THE ROLE OF TURBULENCE IN THE SOLAR WIND, MAGNETOSPHERE, IONOSPHERE DYNAMICS

EDITED BY: Marina Stepanova, Joseph E. Borovsky, Vadim Uritsky, Zoltan Voros, Alessandro Retino and Gaetano Zimbardo

PUBLISHED IN: Frontiers in Astronomy and Space Sciences and Frontiers in Physics

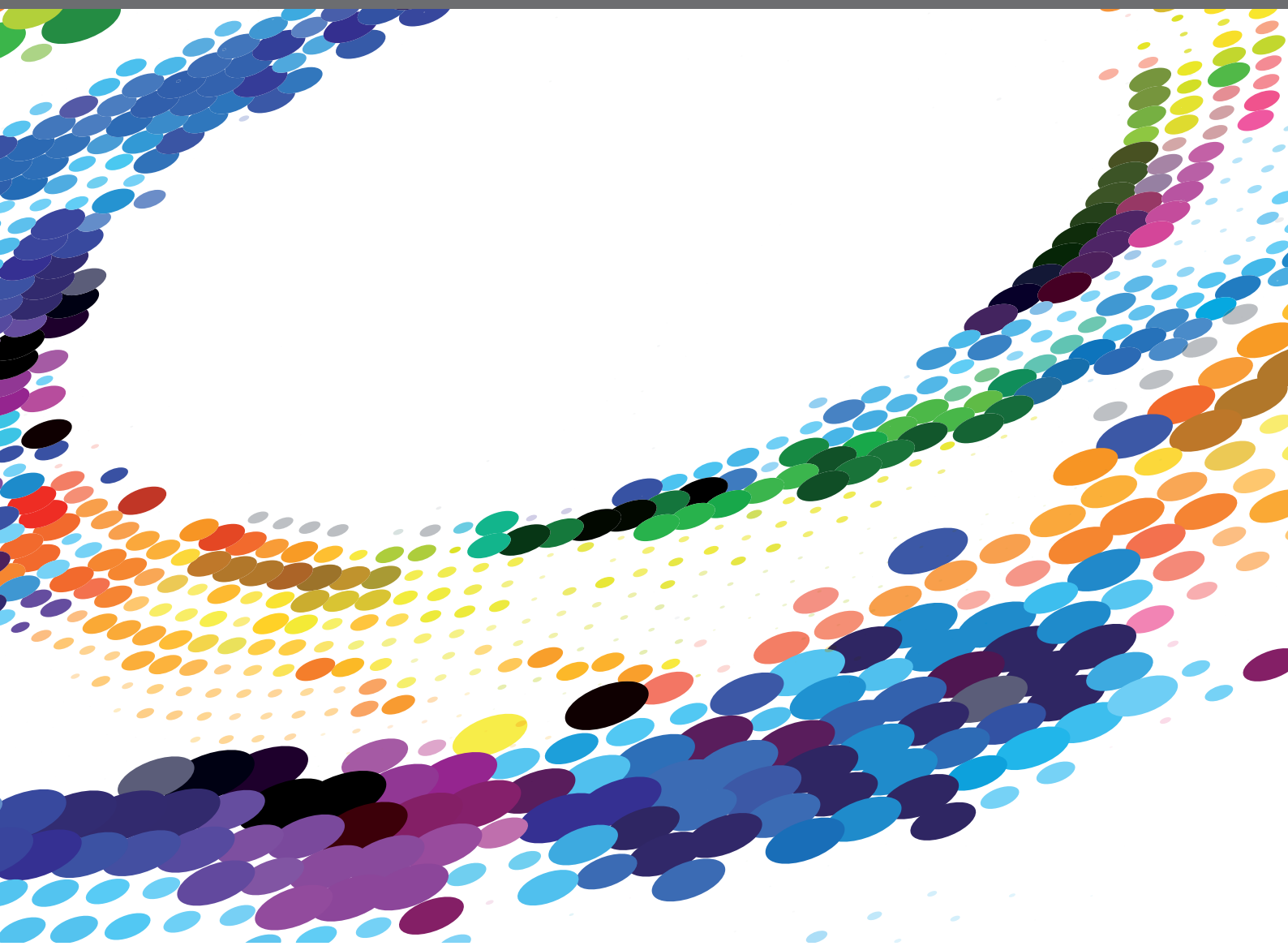

frontiers Research Topics

ISSN 1664-8714
ISBN 978-2-88971-701-9
DOI 10.3389/978-2-88971-701-9

About Frontiers

Frontiers is more than just an open-access publisher of scholarly articles: it is a pioneering approach to the world of academia, radically improving the way scholarly research is managed. The grand vision of Frontiers is a world where all people have an equal opportunity to seek, share and generate knowledge. Frontiers provides immediate and permanent online open access to all its publications, but this alone is not enough to realize our grand goals.

Frontiers Journal Series

The Frontiers Journal Series is a multi-tier and interdisciplinary set of open-access, online journals, promising a paradigm shift from the current review, selection and dissemination processes in academic publishing. All Frontiers journals are driven by researchers for researchers; therefore, they constitute a service to the scholarly community. At the same time, the Frontiers Journal Series operates on a revolutionary invention, the tiered publishing system, initially addressing specific communities of scholars, and gradually climbing up to broader public understanding, thus serving the interests of the lay society, too.

Dedication to Quality

Each Frontiers article is a landmark of the highest quality, thanks to genuinely collaborative interactions between authors and review editors, who include some of the world's best academicians. Research must be certified by peers before entering a stream of knowledge that may eventually reach the public - and shape society; therefore, Frontiers only applies the most rigorous and unbiased reviews.
Frontiers revolutionizes research publishing by freely delivering the most outstanding research, evaluated with no bias from both the academic and social point of view. By applying the most advanced information technologies, Frontiers is catapulting scholarly publishing into a new generation.

What are Frontiers Research Topics?

Frontiers Research Topics are very popular trademarks of the Frontiers Journals Series: they are collections of at least ten articles, all centered on a particular subject. With their unique mix of varied contributions from Original Research to Review Articles, Frontiers Research Topics unify the most influential researchers, the latest key findings and historical advances in a hot research area! Find out more on how to host your own Frontiers Research Topic or contribute to one as an author by contacting the Frontiers Editorial Office: frontiersin.org/about/contact

THE ROLE OF TURBULENCE IN THE SOLAR WIND, MAGNETOSPHERE, IONOSPHERE DYNAMICS

Topic Editors:
Marina Stepanova, University of Santiago, Chile
Joseph E. Borovsky, Space Science Institute, United States
Vadim Uritsky, The Catholic University of America, United States
Zoltan Voros, Space Research Institute, Austrian Academy of Sciences, Austria
Alessandro Retino, UMR7648 Laboratoire de physique des plasmas (LPP), France
Gaetano Zimbardo, University of Calabria, Italy

Citation: Stepanova, M., Borovsky, J. E., Uritsky, V., Voros, Z., Retino, A., Zimbardo, G., eds. (2022). The Role of Turbulence in the Solar Wind, Magnetosphere, Ionosphere Dynamics. Lausanne: Frontiers Media SA. doi: 10.3389/978-2-88971-701-9

Table of Contents

05 ***Editorial: The Role of Turbulence in the Solar Wind, Magnetosphere, Ionosphere Dynamics***
Marina Stepanova, Joseph E. Borovsky, Alessandro Retino, Vadim Uritsky, Zoltán Vörös and Gaetano Zimbardo

08 ***Plasma and Magnetic-Field Structure of the Solar Wind at Inertial-Range Scale Sizes Discerned From Statistical Examinations of the Time-Series Measurements***
Joseph E. Borovsky

21 ***Transport Ratios of the Kinetic Alfvén Mode in Space Plasmas***
Yasuhito Narita, Owen Wyn Roberts, Zoltán Vörös and Masahiro Hoshino

35 ***Some Similarities and Differences Between the Observed Alfvénic Fluctuations in the Fast Solar Wind and Navier–Stokes Turbulence***
Joseph E. Borovsky and Tiziano Mina

55 ***Higher-Order Statistics in Compressive Solar Wind Plasma Turbulence: High-Resolution Density Observations From the Magnetospheric MultiScale Mission***
Owen Wyn Roberts, Jessica Thwaites, Luca Sorriso-Valvo, Rumi Nakamura and Zoltán Vörös

69 ***The Effect of Solar-Wind Turbulence on Magnetospheric Activity***
R. D'Amicis, D. Telloni and R. Bruno

78 ***On the Variation of Intermittency of Fast and Slow Solar Wind With Radial Distance, Heliospheric Latitude, and Solar Cycle***
Anna Wawrzaszek and Marius Echim

87 ***Driving and Dissipation of Solar-Wind Turbulence: What is the Evidence?***
Charles W. Smith and Bernard J. Vasquez

97 ***The Impact of Turbulence on the Ionosphere and Magnetosphere***
Patrick Guio and Hans L. Pécseli

107 ***Plasma and Magnetic Field Turbulence in the Earth's Magnetosheath at Ion Scales***
Liudmila Rakhmanova, Maria Riazantseva and Georgy Zastenker

129 ***Magnetohydrodynamic Turbulence in the Earth's Magnetotail From Observations and Global MHD Simulations***
Mostafa El-Alaoui, Raymond J. Walker, James M. Weygand, Giovanni Lapenta and Melvyn L. Goldstein

145 ***Influence of MHD Turbulence on Ion Kappa Distributions in the Earth's Plasma Sheet as a Function of Plasma*** β ***Parameter***
A. V. Eyelade, C. M. Espinoza, M. Stepanova, E. E. Antonova, I. L. Ovchinnikov and I. P. Kirpichev

159 ***The Impact of Turbulence on Physics of the Geomagnetic Tail***
Elizaveta E. Antonova and Marina V. Stepanova

173 ***An Auroral Alfvén Wave Cascade***
C. C. Chaston

179 ***Langmuir Turbulence in the Auroral Ionosphere: Origins and Effects***
Hassanali Akbari, James W. LaBelle and David L. Newman

201 ***Effects of the Background Turbulence on the Relaxation of Ion Temperature Anisotropy in Space Plasmas***
Pablo S. Moya and Roberto E. Navarro

213 ***Shock Propagation and Associated Particle Acceleration in the Presence of Ambient Solar-Wind Turbulence***
Fan Guo, Joe Giacalone and Lulu Zhao

228 ***Turbulence Upstream and Downstream of Interplanetary Shocks***
A. Pitňa, J. Šafránková, Z. Němeček, T. Ďurovcová and A. Kis

247 ***Plasma Dynamics in Low-Electron-Beta Environments***
Stanislav Boldyrev, Nuno F. Loureiro and Vadim Roytershteyn

253 ***How Turbulent is the Magnetically Closed Corona?***
James A. Klimchuk and Spiro K. Antiochos

258 ***Turbulence in the Magnetospheres of the Outer Planets***
Joachim Saur

265 ***Mesoscale Structure in the Solar Wind***
N. M. Viall, C. E. DeForest and L. Kepko

frontiers in Astronomy and Space Sciences

EDITORIAL
published: 17 February 2022
doi: 10.3389/fspas.2021.763190

Editorial: The Role of Turbulence in the Solar Wind, Magnetosphere, Ionosphere Dynamics

Marina Stepanova[1,2]*, *Joseph E. Borovsky*[3], *Alessandro Retino*[4], *Vadim Uritsky*[5,6], *Zoltán Vörös*[7] and *Gaetano Zimbardo*[8,9]

[1]Physics Department, University of Santiago of Chile (USACH), Santiago, Chile, [2]Center for Interdisciplinary Research in Astrophysics and Space Sciences, University of Santiago of Chile (USACH), Santiago, Chile, [3]Space Science Institute, Boulder, CO, United States, [4]Laboratoire de Physique des Plasmas, CNRS, Observatoire de Paris, Sorbonne Université, Université Paris-Saclay, École Polytechnique, Institut Polytechnique de Paris, Palaiseau, France, [5]Department of Physics, The Catholic University of America, Washington, DC, United States, [6]NASA Goddard Space Flight Center, Greenbelt, MD, United States, [7]Space Research Institute, Austrian Academy of Sciences Graz, Graz, Austria, [8]Dipartimento di Fisica, Universitá della Calabria, Rende, Italy, [9]Istituto Nazionale di Astrofisica, Sezione INAF Presso l'Universitá della Calabria, Rende, Italy

Keywords: turbulence, space plasmas, heliosphere, solar wind, magnetosphere

Editorial on the Research Topic

The Role of Turbulence in the Solar Wind, Magnetosphere, Ionosphere Dynamics

This Research Topic is dedicated to one of the most intriguing and least understood phenomena of space plasma physics: nearly collisionless turbulence. Even at the beginning of space exploration, there was evidence that space plasmas might be turbulent. For example, Ness et al. (1964) analyzed the magnetic field measurements made by the IMP 1 satellite and reported the existence of the region of turbulence between the magnetopause and the bow shock now known as the magnetosheath. Later on, Fairfield and Ness (1970) calculated the power-law spectra of magnetic fluctuations in the magnetosheath using IMP 4 measurements. A highly fluctuating magnetic field in the geomagnetic tail was observed by the IMP 1 Hruška and Hrušková (1969) and IMP 3 Hruška and Hrušková (1970) satellites. Coleman (1968) analyzed the magnetic fluctuations in the solar wind using the data from the Mariner 2 spacecraft. The obtained power spectral density of these fluctuations closely resembled a typical turbulent spectrum. More sophisticated space missions were launched during the following decades, giving more insight about the main characteristics of space plasmas, including fluctuations of all plasma macro-parameters and fields. Nonetheless, turbulence is only one possible interpretation of these fluctuations, and the discussion about what we observe continues. This Research Topic contains different, sometimes even contradictory, points of view on the nature of turbulence and observed phenomena. It covers eight reviews and three mini-reviews, providing the reader with a view of the current state of this field. It also includes original research and prospective papers.

Four papers in this Research Topic are focused on determining what is turbulence and what is mistaken for turbulence. In a perspective article, Klimchuk and Antiochos argue that in the closed corona of the Sun the ubiquitous current sheets arise from the quasi-static twisting of flux tubes rather than from the action of dynamic turbulence. These currents sheets, being the sites of reconnection (nanoflares), could play a key role in the heating of the corona. Similarly, the review article by Borovsky argues that much of the structures (including current sheets) in the solar wind are also not turbulence: his review examines the properties of the structure of the solar wind and the arguments for certain structure types having their origin in the corona. Viall et al. extensively review solar observations, solar-wind measurements, and computer

OPEN ACCESS

Edited and reviewed by:
Rudolf von Steiger,
University of Bern, Switzerland

***Correspondence:**
Marina Stepanova
marina.stepanova@usach.cl

Specialty section:
This article was submitted to Space Physics, a section of the journal Frontiers in Astronomy and Space Sciences

Received: *23 August 2021*
Accepted: *30 August 2021*
Published: *17 February 2022*

Citation:
Stepanova M, Borovsky JE, Retino A, Uritsky V, Vörös Z and Zimbardo G (2022) Editorial: The Role of Turbulence in the Solar Wind, Magnetosphere, Ionosphere Dynamics. Front. Astron. Space Sci. 8:763190. doi: 10.3389/fspas.2021.763190

simulations to explore the issue of what structures in the solar wind are created at the Sun and what structures are created in the wind away from the Sun. Viall et al. assess the current knowledge and outline future steps for progress. Borovsky and Mina perform side-by-side analyses of the measurements of fluctuations in (1) the Navier-Stokes turbulence of a wind tunnel and (2) the Alfvénic solar wind, focusing on the similarities and differences in the statistical and the physical properties of the fluctuations. The question raised is: Why do the Alfvénic fluctuations statistically look like turbulence?

Our Research Topic also includes a set of works dedicated to the study of different types of turbulence in the heliosphere. In particular, Wawrzaszek and Echim concentrate on the study of turbulence intermittency, an important diagnostics of turbulent energy cascade, throughout the heliosphere. Various indicators of intermittency are reviewed, and it is found that intermittency increases with radial distance in Alfvénic solar wind, that the intermittency of fast solar wind at solar minimum decreases with latitude, while at solar maximum the intermittency values are more scattered. Boldyrev et al. review several fluid models for fluctuations in low-to-moderate beta plasmas, which are representative of space plasma environments such as the Earth's magnetosphere and magnetosheath as well as the solar corona. The general physical derivation of the model equations is presented and three special cases are treated in detail, including the derivation of the dispersion relations for linear modes as well as the conserved quantities. Assumptions and limits of applicability of each model are discussed. Guo et al. address the fact that the presence of solar-wind turbulence leads to the rippling of interplanetary-shock surfaces. The role of preexisting upstream turbulence and shock surface rippling in enhancing the acceleration of particles is emphasized, and it is proposed that this may help to solve the injection problem of shock acceleration, in particular at quasi-perpendicular shocks. Pitna et al. point out that while particle acceleration at shocks in the presence of turbulence has been long considered, only recently has the evolution of turbulence itself from upstream to downstream received enough attention. They show that, compared to upstream, the downstream turbulent power in magnetic field, velocity, and density is enhanced by about one order of magnitude, and that downstream turbulence is always more compressive. Both the papers of Guo et al. and Pitna et al. point out that *in-situ* observations of interplanetary shocks provide an invaluable opportunity to understand how shocks interact with large-scale turbulence and accelerate energetic particles.

Smith and Vasquez review the evidence for multi-scale turbulent *in-situ* dynamics that results in the heating of the solar wind. The generation, transport and dissipation of fluctuation energy are critically examined offering a wide discussion of the often controversial scenarios for energy transfer across scales. Perhaps some fundamental questions remain unanswered because of the lack of multi-point measurements and realistic simulations. Roberts et al. investigated intermittency of turbulent electron density fluctuations in the solar wind at sub-ion scales using calibrated spacecraft potential from the Magnetospheric MultiScale mission. The scale-dependent kurtosis is found to increase towards ion scales. Then it plateaus through the sub-ion range. However, discrepancies between statistics of temporal and spatial fluctuation exist, for which several alternative explanations are offered. Based on the linear Vlasov theory, Narita et al. examined the plasma dielectric tensor deriving analytic expressions for transport ratios and scaling laws for the electric and magnetic fields. Fluid-scale properties of the kinetic Alfvén mode are derived from the kinetic treatment of the dielectric tensor. The developed methods are useful for the wave mode identification in spacecraft observations. D'Amicis et al. review recent developments on the complexity of solar wind magnetosphere interactions with the emphasis on solar wind turbulence driven geomagnetic response. The role played by Alfvenic turbulence in the solar wind-magnetosphere coupling is accentuated. It is also emphasized that the geomagnetic response is affected by internal magnetospheric conditions and by the total energy of solar wind fluctuations. Moya and Navarro used quasi-linear kinetic theory to investigate the effects of a turbulence background spectrum on the relaxation of the ion-cyclotron temperature anisotropy instability in the solar wind. Different initial levels of turbulence amplitude and spectral shapes are considered. It is shown that all spectrum shapes can heat protons preferentially in the direction perpendicular to the ambient magnetic field, even if the plasma is initially stable. Possible implications for recent Parker Solar Probe data are discussed.

Turbulence in the magnetosheath is reviewed by Rakhmanova et al. In particular, they discuss the applicability of the Taylor hypothesis, the main features of the spectra of plasma, magnetic fluctuations fitted by power laws for various MHD and kinetic regimes, as well as the intermittent character of turbulence. Of special interest is the study of the plasma fluctuations measured with sufficient time resolution to explore plasma turbulence at kinetic scales, along with the influence of the solar wind turbulence and geometry of the bow shock to the development of the magnetosheath turbulence.

Antonova and Stepanova review the paradigm of the geomagnetic tail as a turbulent wake behind an obstacle and its application to the magnetospheric dynamics. In particular, they examine the role of turbulence on the MHD scales in the plasma transport and mixing, and the stability of the turbulent plasma sheet. Based on their findings, the large-scale two-vortex magnetospheric convection generated by the magnetospheric plasma pressure gradients is proposed as a source of energy for turbulence development and possibly the driving or integral vortex of such turbulence. The turbulent flows in the magnetotail appear during the 3D MHD simulations of the global magnetosphere. Meanwhile, a review by El-Alaoui et al. describes a method to couple the large-scale drivers of MHD turbulence to the local kinetic scales. The obtained power spectral density of magnetic fluctuations is consistent with observations of turbulence in the magnetotail. The authors highlight the role of resistivity as a source of dissipation that contributes to plasma sheet turbulence in two ways. First, on a large scale, it causes reconnection, which drives the turbulent flows, and secondly, it dissipates the energy on smaller scales. They also consider the influence of the Kelvin-Helmholtz instability along the flank boundaries. According to El-Alaoui et al.

turbulent acceleration might lead to the appearance of non-thermal tails in plasma distributions (a kappa distribution). Eyelade et al. established a relation between the turbulent eddy diffusion and kappa indexes for different values of plasma β parameter in the Earth's plasma sheet. They found that several processes related to MHD turbulence lead to either an increase or decrease of the κ index of kappa distribution functions, depending on the value of β and the direction of the turbulent transport with respect to the plasma sheet.

Studies of turbulent processes in the ionosphere are presented in a number of works. The mini-review by Akbari et al. focuses on Langmuir waves and turbulence in the auroral ionosphere caused by magnetospheric electron beams. The review provides a concise but rigorous theoretical description of the Langmuir wave mechanism, and a summary of many years of observations of this phenomenon using spaceborne and ground-based instruments. The importance of conjugate multi-instrument campaigns involving *in situ* wave and particle measurements and incoherent scatter radar data is emphasized. Turbulence in collisionless space plasmas is known to be a major cause of the anomalous transport and resistivity. The paper by Guio and Pecseli addresses these important phenomena, paying particular attention to cross-scale wave mechanisms that contribute to the anomalous resistivity and diffusion. Intermittent kinetic structures able to limit the free flow of charged plasma particles (such as electron and ion phase space vortices) are also discussed. The perspective article by Chaston is dedicated to transient multiscale structures in the auroral acceleration region playing a major part in shaping auroral displays. The author emphasizes the importance of coordinated *in-situ* and ground based observations allowing one to relate the nonlinear forcing of the plasma above auroral arcs with visible auroral forms. The examples presented in the paper provide evidence for a turbulent cascade inside the auroral acceleration region, likely supported by large-amplitude inertial Alfvén waves.

There are a few works dedicated to the turbulence in the magnetospheres of the outer planets and some fundamental aspects of space plasmas. In particular, Saur discusses plasma turbulence at outer planets where conditions are different from those in the solar wind, e.g., existence of a strong planetary magnetic field, stronger plasma inhomogeneities and larger abundance of heavy ions. Spacecraft observations at Jupiter and Saturn are reviewed, namely, in the magnetosphere, magnetosheath and at moons, and implications for plasma heating and particle acceleration are discussed. The need for new measurements from future missions, in particular at Uranus and Neptune, is discussed.

As shown in this editorial, past and present satellite missions have provided us with an unprecedented opportunity to study the turbulence in space plasmas *in situ*. As a result, the heliosphere became the world's largest laboratory for studying various types of plasma turbulence. The majority of turbulent properties obtained are universal and relevant not only for space physics systems but also for other astrophysical objects with similar turbulent processes. We believe that this Research Topic will enable space scientists and astrophysicists, particularly those in their early careers, to understand a variety of aspects of a wide range of sometimes controversial topics and arrive at their own conclusions.

AUTHOR CONTRIBUTIONS

All authors listed have made a substantial, direct and intellectual contribution to the work, and approved it for publication.

FUNDING

MS was supported by the FONDECYT 1211144 and AFOSR N°FA9550-19-1-0384 research grants, JB was supported by the NSF SHINE program, ZV was supported by the Austrian FWF projects P28764-N27.

ACKNOWLEDGMENTS

MS thanks Elizaveta Antonova for helpful conversations.

REFERENCES

Coleman, P. J. J., Jr (1968). Turbulence, Viscosity, and Dissipation in the Solar-Wind Plasma. *Astrophysical J.* 153, 371. doi:10.1086/149674

Fairfield, D. H., and Ness, N. F. (1970). Magnetic Field Fluctuations in the Earth's Magnetosheath. *J. Geophys. Res.* 75 (31), 6050–6060. doi:10.1029/ja075i031p06050

Hruška, A., and Hrušková, J. (1969). Long Time-Scale Magnetodynamic Noise in the Geomagnetic Tail. *Planet. Space Sci.* 17 (8), 1497–1504.

Hruška, A., and Hrušková, J. (1970). Transverse Structure of the Earth's Magnetotail and Fluctuations of the Tail Magnetic Field. *J. Geophys. Res.* 75 (13), 2449–2457.

Ness, N. F., Scearce, C. S., and Seek, J. B. (1964). Initial Results of the Imp 1 Magnetic Field experiment. *J. Geophys. Res.* 69 (17), 3531–3569. doi:10.1029/jz069i017p03531

Conflict of Interest: The authors declare that the research was conducted in the absence of any commercial or financial relationships that could be construed as a potential conflict of interest.

Publisher's Note: All claims expressed in this article are solely those of the authors and do not necessarily represent those of their affiliated organizations, or those of the publisher, the editors, and the reviewers. Any product that may be evaluated in this article, or claim that may be made by its manufacturer, is not guaranteed or endorsed by the publisher.

frontiers in Astronomy and Space Sciences

REVIEW
published: 20 May 2020
doi: 10.3389/fspas.2020.00020

Plasma and Magnetic-Field Structure of the Solar Wind at Inertial-Range Scale Sizes Discerned From Statistical Examinations of the Time-Series Measurements

*Joseph E. Borovsky**

Center for Space Plasma Physics, Space Science Institute, Boulder, CO, United States

OPEN ACCESS

Edited by:
Luca Sorriso-Valvo,
National Research Council, Italy

Reviewed by:
Bernard Vasquez,
University of New Hampshire, United States
Yasuhito Narita,
Austrian Academy of Sciences (OAW), Austria
Julia E. Stawarz,
Imperial College London, United Kingdom

***Correspondence:**
Joseph E. Borovsky
jborovsky@spacescience.org

Specialty section:
This article was submitted to Space Physics, a section of the journal Frontiers in Astronomy and Space Sciences

Received: *03 March 2020*
Accepted: *21 April 2020*
Published: *20 May 2020*

Citation:
Borovsky JE (2020) Plasma and Magnetic-Field Structure of the Solar Wind at Inertial-Range Scale Sizes Discerned From Statistical Examinations of the Time-Series Measurements. Front. Astron. Space Sci. 7:20. doi: 10.3389/fspas.2020.00020

This paper reviews the properties of the magnetic and plasma structure of the solar wind in the inertial range of spatial scales (500–5 $\times$ 10^6 km), corresponding to spacecraft timescales from 1 s to a few hr. Spacecraft data sets at 1 AU have been statistically analyzed to determine the structure properties. The magnetic structure of the solar wind often has a flux-tube texture, with the magnetic flux tube walls being strong current sheets and the field orientation varying strongly from tube to tube. The magnetic tubes also exhibit distinct plasma properties (e.g., number density, specific entropy), with variations in those properties from tube to tube. The ion composition also varies from tube to tube, as does the value of the electron heat flux. When the solar wind is Alfvénic, the magnetic structure of the solar wind moves outward from the Sun faster than the proton plasma does. In the reference frame moving outward with the structure, there are distinct field-aligned plasma flows within each flux tube. In the frame moving with the magnetic structure the velocity component perpendicular to the field is approximately zero; this indicates that there is little or no evolution of the magnetic structure as it moves outward from the Sun. Large sudden velocity shears are seen across the boundaries between the magnetic flux tubes as the magnetic field rotates and the field-aligned flow rotates. The effect of the solar-wind current sheets on the magnetic power spectral density of the solar wind is examined: the current sheets are found to dominate the spectral properties of the solar wind.

Keywords: solar wind, heliospheric structure, turbulence, Alfvén waves, current sheets

INTRODUCTION

This review examines the plasma and magnetic-field structure of the inner heliosphere in the "inertial range" of scale sizes, corresponding to timescales in the solar wind data from about 1 s to about 3 h, equivalent to advected spatial scales of about 500 km to 5 $\times$ 10^6 km. These are MHD scales sizes, larger than ion gyroradii r_{gi} $\sim$ 20–100 km and larger than ion-inertial lengths c/ω_{pi} $\sim$ 50–150 km in the solar-wind plasma at 1 AU.

In this range of timescales, the magnetic-field time series is dominated by strong current sheets (directional discontinuities) and calmer regions between the current sheets. The plasma time series is dominated by sudden jumps in the plasma parameters (e.g., number density, specific entropy, proton temperature, plasma beta, magnetic-field strength, etc.) at the locations of strong current sheets. The proton flow time series is dominated by sudden jumps of the flow vector (abrupt flow shears) at the location of the current sheets, especially for the more-Alfvénic types of solar-wind plasma.

This review explores the properties of the structure of the solar wind in the inner heliosphere as gleaned from spacecraft time-series measurements. This paper is organized as follows. In Section The Flux-Tube Texture of the Heliospheric Magnetic Field the magnetic flux-tube texture of the solar wind is discussed. Section The Motion of the Magnetic Structure through the Solar-Wind Plasma examines the outward motion of the magnetic structure through the solar-wind proton plasma. Section The Alpha-to-Proton Ionic Composition and Magnetic Flux Tubes discusses how the alpha-to-proton ionic composition varies from tube to tube and Section The Electron Heat Flux (Strahl) and Magnetic Flux Tubes discusses how the electron strahl (heat flux) changes from tube to tube. Section Squashing and Stretching of Magnetic Flux Tubes describes the squashing and stretching of magnetic flux tubes in compression and rarefaction regions. Section Mixing discusses the lack of evidence of mixing in the solar wind as it moves outward through the inner heliosphere. Section Current Sheets and the Fourier Power Spectrum explains the impact of solar-wind current sheets on the magnetic power spectrum of the solar wind. Section Current Sheet Thicknesses discusses the thicknesses of the current sheets in the magnetic structure. Abrupt velocity shears in the solar wind are discussed in Section Intense Velocity Shears. Section Alfvénic Domains in Coronal-Hole-Origin Plasma discusses spatial domains of Alfvénicity that are found in the solar wind from coronal holes. Magnetic switchbacks in the solar wind are discussed in Section Magnetic Switchbacks. Section Types of Solar-Wind Plasma and the Inertial-Range Structure reviews the systematic differences in the inertial-range structure of the solar wind in four different types of solar-wind plasma originating from four different types of regions on the Sun. The review is summarized in Section Summary and Discussion, which also contains some suggestions about changes in nomenclature.

THE FLUX-TUBE TEXTURE OF THE HELIOSPHERIC MAGNETIC FIELD

Figure 1 contains a binning of the temporal angular change in the direction of the solar-wind magnetic field in 64-s time-resolution time-series measurements at 1 AU during the years 1998–2008. Two distinct populations can be seen in the occurrence distribution, both fit by exponential functions: a population of large angular changes and a population of smaller angular changes. The large-angular change population is consistent with the spacecraft crossing strong current sheets in the solar-wind plasma, and the small-angular-change population is consistent with magnetic field directional wiggles in the spatial regions between the current sheets. The two distributions are consistent with a picture of magnetic-flux tubes separated by current sheets, with the direction of the magnetic field changing from tube to tube. For a plot similar to **Figure 1** closer to the Sun see the 1-s curve in Figue 3 of Chhiber et al. (2020) and for a plot further from the Sun see Figure 6 of Miao et al. (2011), indicative of a flux-tube texture throughout the inner heliosphere.

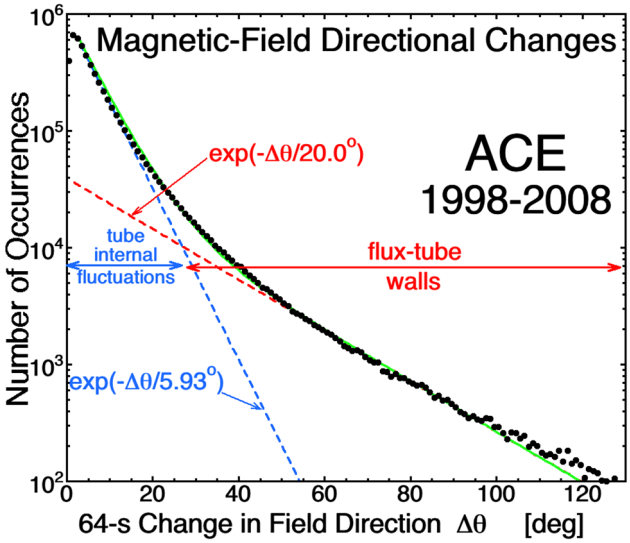

FIGURE 1 | The 64-s change in the solar-wind magnetic-field direction is binned for 11 years of measurements at 1 AU by the ACE Magnetic Fields Experiment (Smith et al., 1998). The sum of the two exponential fit functions appears in green.

A flux-tube texture of the solar wind has been realized since early *in situ* measurements of the solar wind were available (Bartley et al., 1966; McCracken and Ness, 1966; Ness et al., 1966; Michel, 1967). The flux tubes were evident from the sudden changes in the anisotropy directions of energetic particles (Bartley et al., 1966; McCracken and Ness, 1966), from the sudden changes of direction of the magnetic field (Ness et al., 1966; Michel, 1967; Siscoe et al., 1968), and from sudden changes in the plasma flow vector (Thieme et al., 1989).

Depictions of this spaghetti of magnetic flux tubes can be found throughout the literature [cf. Figure 3 of McCracken and Ness (1966); Figure 6 or Bartley et al. (1966); Figures 1, Figure 5, 9 of Michel (1967); Figure 30H of Schatten (1971); Figure 5 of (Bruno et al., 2001); Figure 1A of Borovsky (2008); Figure 22 of Borovsky (2010a); Figures 7, 8 of Bruno and Carbone (2016); Figure 7 of Bruno (2019)]. In the flux-tube structure the walls of the flux tubes are current sheets wherein the magnetic-field direction changes suddenly. At 1 AU the current sheet thicknesses are on the order of 10^3 km (Siscoe et al., 1968; Vasquez et al., 2007) and the flux-tube diameters are on the order of 5×10^5 km (Borovsky, 2008; Zheng et al., 2017). In streamer-belt-origin plasma and coronal-hole-origin plasma the flux tubes meander along the Parker-spiral direction, with a

spread in flux-tube orientations of about 40° about the Parker-spiral direction (Borovsky, 2010a). At 1 AU Tong et al. (2016) statistically measured the characteristic spatial scale $L_{||}$ of flux-tube meandering to be $L_{||} \sim 2 \times 10^6$ km = 370 R_E = 0.016 AU along the Parker-spiral direction.

The origin of the flux-tube magnetic structure of the inner heliosphere is not known (Neugebauer and Giacalone, 2010, 2015; Li and Qin, 2011; Owens et al., 2011; Telloni et al., 2016; Tu et al., 2016; Viall and Borovsky, 2020). Among the possibilities are (a) active MHD turbulence (Dmitruk et al., 2004; Greco et al., 2009), (b) turbulence that has exhausted its energy and left behind a structured magnetic field (Dobrowolny et al., 1980; Telloni et al., 2016), (c) fossil magnetic structure from the corona (Huang et al., 2014; Burkholder et al., 2019; Eselevich, 2019), and (d) steepened Alfvén waves (Malara et al., 1996; Vasquez and Hollweg, 1999).

The flux-tube texture of the heliospheric magnetic field impacts energetic-particle transport in the heliosphere and the physics of particle scattering (Michel, 1967; Qin and Li, 2008), with ducting and weak scattering in the interiors of flux tubes where there are low levels of magnetic fluctuations (Trenchi et al., 2013a,b) and with energetic particles with non-zero gyroradii passing close to the flux-tube walls suffering large-angle scattering. Energetic particles with gyroradii comparable to or larger than flux-tube diameters [cf. Table 4 of Viall and Borovsky (2020)] will suffer scattering associated with the distribution of flux-tube orientations. The $L_{||} \sim 0.16$ AU wiggle of the flux-tube orientations about the Parker spiral will also produce a scattering of energetic particles [e.g., (Webb et al., 2006)].

The driving of the Earth's magnetosphere by the solar wind is very sensitive to the direction of the solar-wind magnetic field (Sonnerup, 1974; Komar et al., 2015). From one flux tube to the neighboring flux tube the magnetic-field direction of the solar wind changes (Bruno et al., 2001; Borovsky, 2008; Bruno and Carbone, 2016), with sudden strong jumps in the magnetic-field direction as a flux-tube wall is crossed. The advection of the flux-tube structure past the Earth produces a magnetic direction that is quasi-steady for 15 min or so, followed by a strong change in the field direction. Depending chiefly on the orientation of each flux tube, some flux tubes are geoeffective and some are not, with the flux-tube structure of the solar wind resulting in an intermittent driving of convection and geomagnetic activity in the Earth's magnetosphere (Borovsky, 2020a).

Statistical analysis of the orientations of the flux tubes at 1 AU finds two populations [cf. Figure 18 of Borovsky (2010a)]: a population that is on average aligned in the Parker-spiral direction with a spread of flux-tube orientations of about 40° about the Parker-spiral direction and a second, smaller, population of flux tubes that are quasi-isotropically oriented (cf. Section Types of Solar-Wind Plasma and the Inertial-Range Structure).

The magnetic-flux-tube structure of the solar wind also corresponds with a plasma-tube structure of the solar wind. When the occurrence distributions of changes of plasma properties are examined [e.g., Figure 3 of Borovsky (2008)], a dual population is seen: a population of large changes and a population of small changes, as in **Figure 1**. This holds for changes in the plasma number density, changes in the specific entropy, changes in the magnetic-field strength, changes in the plasma-β, etc. The locations of the large changes correspond to the locations of current sheets [(Borovsky, 2008; Owens et al., 2011)], i.e., the plasma properties change from flux tube to flux tube. In the slower types of solar wind these plasma changes across the magnetic-tube walls are robust; in the faster coronal-hole-origin wind the plasma changes are more subtle [(Borovsky, 2016)]. As will be discussed in later sections, the magnetic-flux-tube structure also corresponds to a structure in the ion composition of the solar-wind plasma and to a structure in the electron heat flux (strahl intensity) of the solar wind.

Plasma boundaries and magnetic-flux-tube boundaries are, in the MHD nomenclature, discussed as "tangential discontinuities." In Section The Motion of the Magnetic Structure through the Solar-Wind Plasma it will be pointed out that the magnetic structure of the solar wind moves en mass away from the Sun faster than the proton plasma moves outward. It is often stated to be the case that tangential discontinuities do not propagate relative to the plasma [e.g., (Burlaga and Ness, 1969; Tsurutani and Ho, 1999)], but in the case of flux tubes a perturbation transverse to the axis of the tube will propagate axially along the tube relative to the plasma in the tube at a speed related to the Alfvén speed (Edwin and Roberts, 1983; Ruderman and Roberts, 2006; Goossens et al., 2009). Perturbations of interest for the solar wind are the shuffling of flux tubes (= plasma tubes) at the Sun, with this shuffling pattern propagating outward faster than the plasma outflow.

THE MOTION OF THE MAGNETIC STRUCTURE THROUGH THE SOLAR-WIND PLASMA

In Alfvénic solar wind [i.e., in coronal-hole-origin plasma and in streamer-belt-origin plasma (Xu and Borovsky, 2015; D'Amicis et al., 2019)] the flux-tube structure of the magnetic field moves outward from the Sun at a higher speed than the proton plasma does (Borovsky, 2020b; Nemecek et al., 2020). For an interval of solar-wind data, a single reference frame can be found wherein $\mathbf{v} \times \mathbf{B} \approx 0$ where $\mathbf{v}(t)$ is the measured solar-wind proton flow vector and $\mathbf{B}(t)$ is the measured magnetic-field vector. That single reference frame moves with the magnetic structure and it is found to move typically at about $0.7v_A$ in the Parker-spiral direction relative to the proton flow vector of the solar wind, where $v_A = B/(4\pi n_p m_p)^{1/2}$ is the proton Alfvén speed of the solar-wind plasma with number density n_p (Borovsky, 2020b). Nemecek et al. (2020) refer to this frame as the DeHoffman-Teller frame of the solar wind and they find that the alpha-particle beam of the solar wind is at rest in this magnetic-structure reference frame.

In this reference frame of the magnetic structure, there is a Sunward flow of proton plasma within the flux tubes that is everywhere parallel to the local magnetic field, with the flow vector changing across the walls of the flux tubes as the orientation of one flux tube changes relative to its neighboring flux tube. In Alfvénic intervals of solar wind, the perpendicular-to-**B** plasma velocity $v_\perp$ within the structure is found to be in the

noise of the measurements. The fact that $v_\perp \approx 0$ in the reference frame of the magnetic structure indicates that there is little or no evolution of the magnetic structure as it moves outward from the Sun through the inner heliosphere.

The heliospheric magnetic structure with its spaghetti of flux tubes moves en mass through the plasma in the Parker-spiral direction. This outward-moving magnetic structure could be the outward propagation of flux-tube dynamics happening in the corona: the shuffling of flux tubes as they become rearranged by reconnection in the dynamic corona.

When the solar wind at 1 AU is not Alfvénic, a reference frame where $\mathbf{v} \times \mathbf{B} \approx 0$ cannot be found. When the solar wind is not Alfvénic, the solar-wind plasma is found to be inhomogeneous (lumpy) with variations in the proton number density $n_p(t)$. In this inhomogeneous plasma there are strong variations in the local Alfvén speed from flux tube to flux tube. It could be the case that owing to spatial variations in the Alfvén speed the spaghetti of magnetic flux tubes cannot coherently propagate relative to the proton plasma in the Parker-spiral direction; Alfvénic fluctuations from the Sun are not expected to survive into the inner heliosphere when the flux tubes have substantially different internal Alfvén speeds [cf. (Heyvaerts and Priest, 1983; Magyar et al., 2017)]. In these non-Alfvénic-wind cases, the pattern of shuffling of flux tubes at the Sun appears to be advected out into the heliosphere at the solar wind (proton) speed.

THE ALPHA-TO-PROTON IONIC COMPOSITION AND MAGNETIC FLUX TUBES

The alpha-to-proton number-density ratio α/p varies with time in the solar wind, characterized by sudden jumps in the ratio [e.g., (Safrankova et al., 2013; Zastenker et al., 2014)]. [See also Figure 3 of Borovsky (2008)] The jumps in the α/p ratio at 1 AU are statistically co-located with the magnetic walls of flux tubes (Borovsky, 2020c). This is demonstrated in **Figure 2**. Here strong jumps in the alpha-to-proton number-density ratio α/p are collected with the ACE spacecraft and with the WIND spacecraft, these jumps representing boundaries of the ion composition of the solar-wind plasma. For each spacecraft the angular change Δθ of the magnetic-field vector (every 64-s on ACE and every 97-s on WIND) is measured and the superposed-epoch average of Δθ is plotted (in green for ACE and in red for WIND), with the zero epoch being the crossing of each α/p boundary. **Figure 2** shows that the magnetic field tends to undergo a strong change in direction at the α/p boundaries, with a storng change in direction being indicative of the crossing of a strong current sheet (a magnetic-flux-tube wall). Jumps in α/p represent ion-composition boundaries in the solar-wind plasma and ion-composition boundaries can only be created at the Sun; they can be stretched and folded in the solar wind, but they cannot be formed in the solar wind. Hence, the α/p boundaries are fossils from the Sun. This implies that the magnetic boundaries at 1 AU that are co-located with the α/p boundaries (the flux-tube walls) are also fossils from the Sun not created in the solar wind.

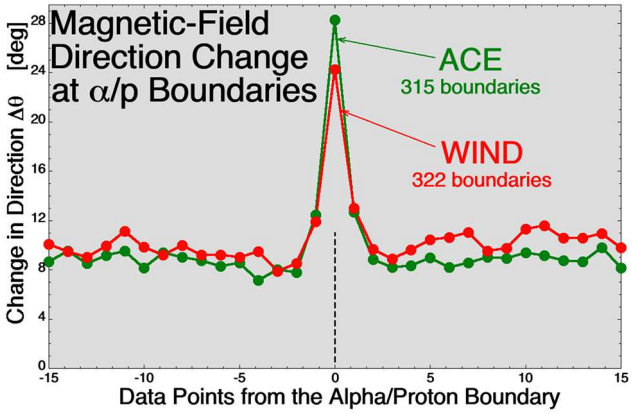

FIGURE 2 | For 315 α/p boundaries located with the ACE spacecraft (green) and for 322 α/p boundaries located with the WIND spacecraft, the superposed-epoch average of the magnetic-field vector direction change (over 64-s for ACE and over 97-s for WIND) is plotted with the zero epoch being the α/p boundary crossing time.

Note that Owens et al. (2011) analyzed fractional changes in the alpha-to-proton number-density ratio α/p in the 64-s ACE data set in comparison with angular changes in the magnetic-field direction and found that about 25% of strong current sheets were associated with strong changes in α/p. Two comments are relevant to this finding. First, there are solar-wind types that exhibit strong plasma inhomogeneity (i.e., sector-reversal-region plasma and streamer-belt-origin plasma) and solar wind that exhibits weak inhomogeneity (coronal-hole-origin plasma), with all exhibiting strong current sheets; the more-homogeneous types of plasma will only rarely show strong fractional jumps in the plasma properties such at α/p. Secondly, the measurements of α/p at 1 AU are notoriously noisy and the measurements from different instruments do not agree [cf. Figure 7E of Borovsky (2016) and discussion therein]; this means that the jumps in the measured values of α/p at current sheets are not that different from the jumps in the measured values of α/p away from the current sheets. The study of Borovsky (2020c) only focused on distinct α/p changes that were above the noise level; those α/p changes are overwhelmingly occurring at strong current sheets.

THE ELECTRON HEAT FLUX (STRAHL) AND MAGNETIC FLUX TUBES

The electron strahl is a magnetic-field-aligned distribution of energetic electrons moving outward from the Sun (Feldman et al., 1976), representing the electron heat flux from the Sun. At 1 AU the measured intensity of the energetic-electron strahl of the solar wind is not steady, rather it undergoes sudden temporal jumps in intensity. Those sudden intensity changes are statistically co-located with the walls of the magnetic flux tubes (Borovsky, 2020c): a superposed-epoch average of the magnetic-field direction change associated with events where the strahl-intensity jump (strahl-intensity boundaries) looks very much

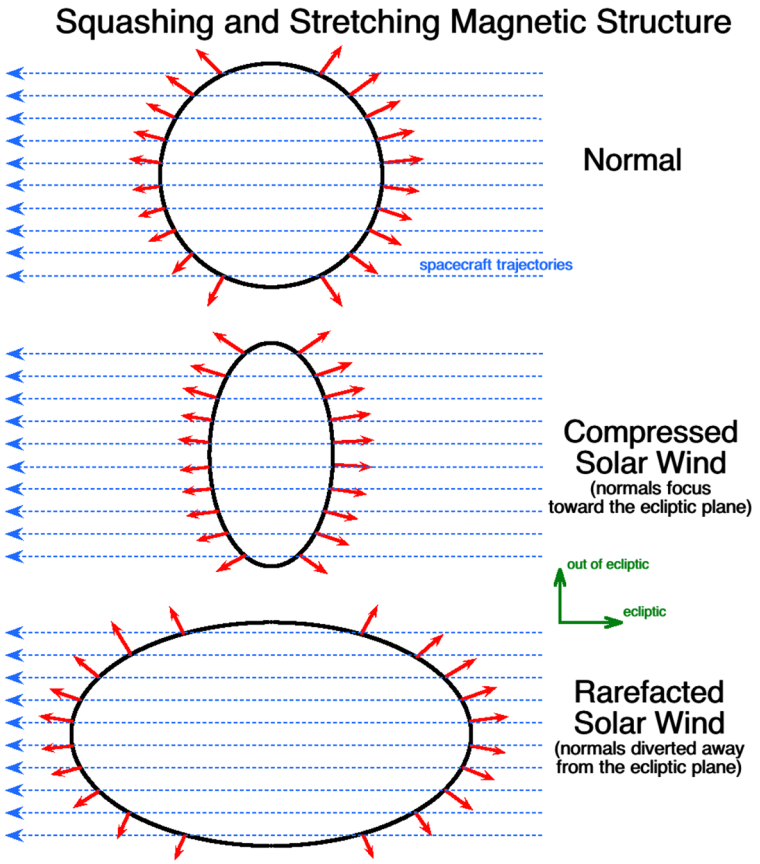

FIGURE 3 | The cross sections of three flux tubes are sketched: a round flux tube **(Top)**, a round flux tube that was compressed **(Middle)**, and a round flux tube that was rafefacted **(Bottom)**. The blue dashed curves are sample spacecraft trajectories through the flux tubes and the red arrows are normals to the flux-tube walls at the point where the spacecraft crosses the wall. The ecliptic plane and normal to the ecliptic plane are noted in green.

like **Figure 2** for α/p boundaries does. I.e., different magnetic flux tubes have different strahl intensities (different values of the heat flux).

The co-location of strahl-intensity boundaries and flux-tube walls implies that there is a long-distance coherence of the flux tubes seen at 1 AU going back toward the Sun. The confinement of solar energetic particles by flux tubes (Trenchi et al., 2013a,b) also implies a long-distance coherence of the magnetic tubes.

The electron strahl is associated with an electron-mobility-driven (electron-pressure-gradient driven) ambipolar interplanetary electric field $E_{||}$ that points outward from the Sun to retard electrons (Lin, 1998; Pierrard et al., 2001; Maksimovic et al., 2005). This $E_{||}$ acts to accelerate solar-wind ions outward to increase the solar wind speed in the inner heliosphere (Jockers, 1972; Lemaire and Pierrard, 2001; Pierrard and Peters, 2014). Between 0.3 AU and 1 AU this interplanetary electric field produces an observed statistical increase in the speed of the slow solar wind (Schwenn et al., 1981; Arya and Freeman, 1991; Lemaire, 2010). The fact that the strahl intensity varies from flux tube to flux tube implies that the interplanetary electric field may act independently in each tube. The acceleration of the solar wind in the heliosphere might vary from tube to tube.

SQUASHING AND STRETCHING OF MAGNETIC FLUX TUBES

When a spacecraft crosses the wall between two flux tubes in the solar wind, the orientation of the current sheet separating the two flux tubes can be obtained using the cross-product method (Burlaga and Ness, 1969; Knetter et al., 2004), taking the normal to the current sheet being in the $B_1 \times B_2$ direction where B_1 and B_2 are the magnetic-field vectors on either side of the current sheet. At 1 AU, the statistical orientations of the current sheets indicate that the magnetic flux tubes are on average round (cylindrical) (Borovsky, 2008). However, in compression and rarefaction regions of the solar wind at 1 AU the magnetic-flux tubes are no longer statistically round, rather they are squashed and stretched into flattened shapes (Borovsky and Denton, 2016). This effect is outlined in **Figure 3**. The top panel depicts the cross section of a round flux tube with red arrows showing a sampling of the orientations of the normals to the current-sheet walls. In the middle and bottom panels a round flux tube that was compressed (middle) and rarefacted (bottom) are depicted along with a sampling of the orientations of the normals. Comparing in **Figure 3** these orientations to the orientations

for the round flux tube, the normals of the compressed tube are more-concentrated toward the equatorial plane and the normals of the rarefacted tube are more-concentrated normal to the ecliptic plane. In corotating interaction regions (CIRs) of the solar wind the compression factor of the solar-wind plasma can be measured by the increase in the magnetic-field strength and in the trailing edges of high-speed streams the rarefaction factor of the solar-wind plasma can be measured by the decrease of the magnetic-field strength. The squashing factor for an initially round flux tube in a compression region and the stretching factor for an initially round flux tube in a rarefaction region can both be predicted knowing the compression or rarefaction factor. Hence, the shape changes of the flux tubes can be predicted, and the systematic variation in the statistical orientations of the current sheets can be predicted. For CIRs and for trailing edges, those flux-tube shape predictions agree with the measured statistics of the current-sheet orientations [cf. Figures 3, 14, and A1 of Borovsky and Denton (2016)]. In compression regions the normals of the walls of the flux tubes tend to be concentrated toward the ecliptic plane and in rarefaction regions the normals of the walls of the flux tubes tend to be concentrated perpendicular to the ecliptic plane. In reality, because the flux tubes are pressed against each other an unperturbed flux tube will not be round, rather it will have a cross section more like the shape of a cell in a Voronoi pattern [cf. Figure 8 of Borovsky (2018a)]. Nevertheless, the statistics of the current-sheet orientations will follow the statistics for round flux tubes and compressed or rarefactive round flux tubes.

If current sheets were being newly created in the solar wind (e.g., by an active MHD turbulence), then the current sheets would be created isotropically giving the statistical impression of round-shaped flux tubes. At 1 AU, CIR compressions and trailing-edge rarefactions have been ongoing for about 100 h. In that 100 h the current sheets were not newly created; rather their orientations reflect the ∼100-h evolution of the compression or rarefaction.

MIXING

A universal process occurring in active turbulence is mixing (Liepmann, 1979; Ottino, 1990; Dimotakis, 2005), involving (1) the stretching and folding of structure and (2) the eventual homogenization of the medium. These two stages of mixing are denoted as mesomixing and micromixing (Paul et al., 2003). In the inhomogeneous slow solar wind, Borovsky (2012a) attempted to quantify these two processes using solar-wind plasma measurements from 0.3 to 1 AU.

The stretching and folding processes produce a temporal evolution of the distribution of structure sizes, with structure sizes decreasing as time increases (cf. Figure 7 of Corrsin (1959)]. Between 0.3 and 1 AU Borovsky (2012a) found no evolution of the distribution of plasma "chunk" sizes, i.e., no evidence for ongoing stretching and folding in the solar-wind plasma.

The homogenization process produces a temporal evolution in the distribution of passive-scalar values in the medium, with the occurrence distribution narrowing with time toward a single value. Between 0.3 and 1 AU Borovsky (2012a) found no evolution in either the occurrence distribution of solar-wind proton number density or the occurrence distribution of solar-wind proton specific entropy, i.e., no evidence for ongoing homogenization of the solar-wind plasma. (A passive scalar is a scalar quantity that is convected by the fluid without perturbing the fluid behavior; density, strictly speaking is not a passive scalar but is still expected to homogenize under the action of stretching and folding followed by diffusion).

The absence of measured mixing seen in the statistics of plasma structure sizes agrees with the observation of the survival of periodic density structures in the solar wind from the corona to the Earth (Kepko and Viall, 2019). Periodic density structures emitted by the corona are imaged by white-light cameras (Viall and Vourlidas, 2015) and seen advecting into the inner heliosphere. Upstream solar-wind monitors at L1 pick up these periodic density structures at Earth, where they excite periodic ULF disturbances in the Earth's magnetosphere (Kepko et al., 2002; Kepko and Spence, 2003). The frequencies of these periodic solar-wind structures are typically 1×10^{-3}-5×10^{-3} Hz (4–17 min periods), in the inertial range of the solar wind. In the inertial range of an MHD turbulence one expects modes to be destroyed and the energy of the modes to be cascaded to higher frequencies (higher wavenumbers), but the action of MHD turbulence in the solar wind does not destroy these periodic perturbations in the ∼100-h travel time from the Sun to the Earth.

CURRENT SHEETS AND THE FOURIER POWER SPECTRUM

The solar wind's magnetic power spectral density in the inertial range of frequencies comes dominantly from the strong current sheets (directional discontinuities) in the solar wind's magnetic structure (Siscoe et al., 1968; Sari and Ness, 1969; Borovsky, 2010b); since the solar wind's magnetic correlation function is the Fourier transform of the magnetic power spectral density, magnetic correlation functions of the solar wind are also dominated by the current sheets. By creating an artificial time series that only contained the occurrence statistics (waiting times) and the amplitudes of the current sheets seen in solar-wind measurements, Borovsky (2010b) was able to reproduce the amplitude and spectral slope of the inertial range of frequencies of the solar wind's trace-B power spectral density with the artificial time series. An implication of this finding is that understanding the origin of the strong current sheets in the solar wind is key to understanding the inertial range of the solar-wind magnetic-field spectra.

At the high-frequency end of the inertial range (at about 1 Hz), the magnetic power spectral density of the solar wind exhibits a breakpoint to a steeper magnetic spectrum above the breakpoint. Using artificial time series wherein the current-sheet thicknesses of the solar wind were stretched in time, Borovsky and Podesta (2015) demonstrated that the frequency at which the magnetic spectral breakpoint occurs is governed by the thicknesses of the strong current sheets in the solar

wind. When the strong current sheets in the solar-wind magnetic time series are thickened by a multiplicative factor X, the magnetic power spectral breakpoint terminating the inertial-range spectrum shifts to lower frequencies by a factor of 1/X (Borovsky and Podesta, 2015; Podesta and Borovsky, 2016). An implication of this finding is that the physics of what governs the breakpoint frequency of the solar-wind spectrum is the physics of what governs current-sheet thicknesses in the solar wind.

With the strong current sheets of the solar wind dominating the Fourier power, and with the thicknesses of the current sheets determining the breakpoint frequency, it follows that the temporal shapes (profiles) of the current sheets should determine the Fourier spectrum at frequencies above the breakpoint. By statistically examining the Fourier transforms of Gaussian-windowed current sheets in the solar-wind magnetic-field measurements, Borovsky and Burkholder (2020) demonstrated the consistency (amplitude and shape) of the high-frequency spectrum of the solar wind with the Fourier spectrum of solar-wind current sheets. An implication of this demonstration is that physical mechanisms acting within solar-wind current sheets should be investigated to understand the high-frequency spectra of the solar wind.

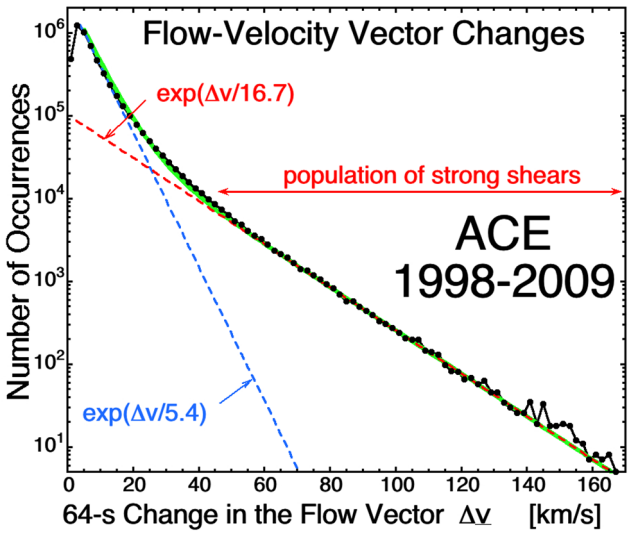

FIGURE 4 | The 64-s change in the solar-wind velocity vector is binned for 11 years of measurements at 1 AU by the ACE SWEPAM instrument (McComas et al., 1998). The sum of the two exponential fit functions appears in green.

CURRENT SHEET THICKNESSES

At 1 AU the current-sheet (directional-discontinuity) thicknesses are on the order of 10^3 km (Siscoe et al., 1968; Vasquez et al., 2007), about 1–3 s in the time series. [The solar-wind current sheets appear to be thicker further from the Sun [cf. Figure 7 of Miao et al. (2011)], and since the high-frequency magnetic Fourier breakpoint appears at higher frequencies closer to the Sun (Bruno and Trenchi, 2014; Duan et al., 2020), the current sheets are probably thinner closer to the Sun]. At 1 AU the current sheets are many times thicker than typical proton gyroradii r_{gp} and typical ion-inertial lengths c/ω_{pi} [cf. Figures 3A,B of Borovsky et al. (2019)]. The thicknesses of solar-wind current sheets may be more consistent with Bohm diffusion $D_B = ck_BT_p/16eB$ (Borovsky, 2006) or gyro-Bohm diffusion $D_{gB} = (ck_BT_p/16eB)(r_{gp}/L)$ acting over the age of the solar-wind plasma. When the scalesizes of gradients in a plasma are much larger than ion gyroradii, it has been argued that Bohm diffusion transitions over to gyro-Bohm diffusion (Perkins et al., 1993; Hannum et al., 2001), which is weakened by a term proportional to the ratio of the gyroradius to the gradient scalelength: r_{gp}/L.

It is well-known that the solar-wind plasma contains weak double layers (time domain structures) [e.g., (Mangeney et al., 1999; Lacombe et al., 2002; Salem et al., 2003a,b; Mozer et al., 2020a)]. Malaspina et al. (2013) point out that the solar-wind time domain structures are localized in the strong current sheets of the solar wind.

INTENSE VELOCITY SHEARS

Figure 4 plots the occurrence distribution (black points) of the 64-s change in the solar-wind flow vector for 11 years of measurements by the ACE spacecraft at 1 AU. As was the case for the magnetic-field direction change distribution in **Figure 1**, the velocity-change distribution shows two distinct populations, both fit by exponential functions: a population of large velocity changes and a population of smaller velocity changes. The population of large velocity changes are abrupt wind shears in the solar-wind plasma that are co-located with the strong current sheets that form the walls of the flux-tube structure [cf. top panels of Figure 3 of Owens et al. (2011)]. As was pointed out in Section The Motion of the Magnetic Structure through the Solar-Wind Plasma, the abrupt wind shears are field-aligned flows in the flux tubes that spatially change direction at the boundaries between flux tubes owing to the change in the magnetic-field direction. The vorticity $\boldsymbol{\omega} = \nabla \times \mathbf{v}$ of these velocity shears is perpendicular to the local magnetic field direction.

The thicknesses of the velocity shear layers in the solar wind are the same as the thicknesses of the current sheets, about 10^3 km (Borovsky and Steinberg, 2014). Note the intense velocity shear in Figure 3A of Borovsky (2020b) at time 9.8 UT where the flow vector of the solar wind is observed to change by 98 km/s in 3 s.

Very strong wind shears, which occur on average about once per day at Earth, can lead to comet-like disconnections of the Earth's magnetotail (Borovsky, 2012b, 2018b).

ALFVÉNIC DOMAINS IN CORONAL-HOLE-ORIGIN PLASMA

In the Alfvénic solar wind from coronal holes, there are patches of solar wind that are highly Alfvénic separated by abrupt non-Alfvénic transitions. Within each patch, the Alfvénicity is very high as measured by a high correlation between the vector $\mathbf{v}$ and the vector $\mathbf{v}_A = \mathbf{B}/(4\pi n_p m_p)^{1/2}$. A set of these Alfvénic domains in coronal-hole-origin plasma appears in Figure 14 of Borovsky

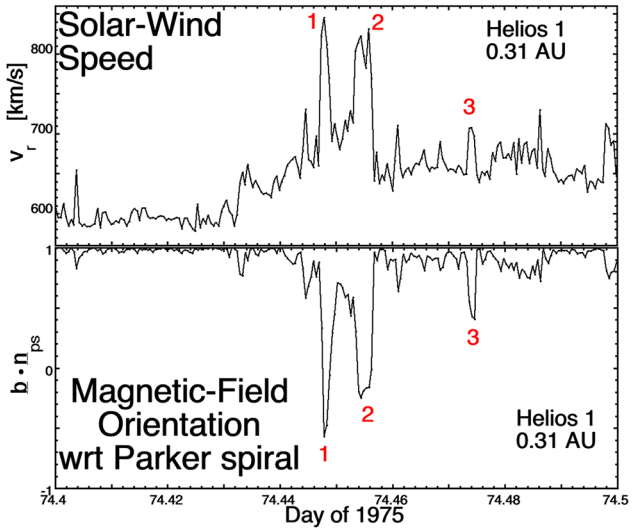

FIGURE 5 | Magnetic switchbacks (labeled 1, 2, and 3) and the associated solar-wind-velocity pulses at 0.31 AU. The curves are 40-s resolution measurements by Helios 1 [cf. Fig. 11 of Borovsky (2016)].

(2016) with the Alfvénic correlation in each domain shown in Figure 14A. Each domain lasts a few hours (corresponding to the lower-frequency end of the inertial range). The Alfvénic domains may represent some larger-than-flux-tube structure of the solar wind at the low-frequency (large-spatial-scale) edge of the inertial range: the Alfvénic-domain spatial scales magnetically map to the expected sizes of supergranules in the coronal-hole photosphere.

MAGNETIC SWITCHBACKS

Localized magnetic-field foldings (magnetic switchbacks, field reversals) are well-known in the coronal-hole plasma at 1 AU [e.g., (Kahler et al., 1996)], further out in the polar coronal-hole plasma of the Ulysses data set [e.g., (Balogh et al., 1999; Yamauchi et al., 2004; Neugebauer and Goldstein, 2013)], at 0.3 AU in the Helios data set (Borovsky, 2016; Horbury et al., 2018), and at 0.17 AU in the Parker Solar Probe data set (Bale et al., 2019). These magnetic-field deviations from the Parker spiral are associated with localized increases in the solar-wind radial velocity: a "velocity excess" [cf. Figure 5 of Michel (1967)], "one-sided Alfvénic fluctuations" (Gosling et al., 2009), or "pulsed Alfvénic fluctuations" (Gosling et al., 2011). An example with three switchbacks appears in **Figure 5**, where 0.1 day = 2.4 h of measurements from the Helios 1 spacecraft at 0.31 AU are plotted. The switchbacks are labeled in red. **Figure 5** (bottom panel) plots the direction of the magnetic field with respect to the local Parker-spiral direction: the switchbacks are noted by the reversal of the field from the Parker-spiral direction. **Figure 5** (bottom panel) plots the radial proton flow velocity, which is locally increased within each switchback. A sketch of a magnetic switchback appears in **Figure 6**, where the flow within a folded flux tube is examined. With the magnetic structure of the solar wind moving en mass outward from the Sun faster than the average proton plasma flow (cf Section The Motion of the Magnetic Structure through the Solar-Wind Plasma), in the reference frame of the magnetic structure there is a Sunward flow of plasma within the magnetic structure that is locally field aligned (red arrows in **Figure 6**). Where there is a fold in the magnetic structure, the flow within the structure is locally anti-Sunward. A spacecraft sees this flow within the field folding as a local increase in the solar-wind speed. These magnetic and velocity structures can often be quite small (10's of R_E), since the switchback structure seen by the WIND and ACE spacecraft, both upstream of the Earth near L1, can be very different [cf. Figure 10 of Borovsky (2016)]. Magnetic switchbacks close to the Sun are presently of great interest for Parker Solar Probe observations [e.g., (Bale et al., 2019; Kasper et al., 2019; de Wit et al., 2020; Horbury et al., 2020; Mozer et al., 2020b; Rouillard et al., 2020; Tenerani et al., 2020)].

Near the Sun (0.3 AU) the magnetic field in coronal-hole-origin plasma tends to be aligned with the Parker spiral direction, but with increasing distance from 0.3 to 2.3 AU the coronal-hole-origin solar-wind magnetic field evolves into a less-aligned state [cf. Figure 13D of Borovsky (2016)].

TYPES OF SOLAR-WIND PLASMA AND THE INERTIAL-RANGE STRUCTURE

Based on unambiguous collections of solar wind from different origins on the Sun, Xu and Borovsky (2015) developed a solar-wind categorization scheme applicable to solar-wind data at 1 AU [see also (Camporeale et al., 2017)]. The scheme categorizes solar wind into four types: (1) coronal-hole-origin plasma, (2) streamer-belt-origin plasma, (3) sector-reversal-region plasma, and (4) ejecta.

In **Table 1** some of the statistical properties of the four types of plasma at 1 AU are collected. The first 3 rows are the wind speed, the number density, and the Alfvén speed, with mean values ± standard deviations as taken from the OMNI2 data set (King and Papitashvili, 2005) from the years 1995–2018. Note the low average Alfvén speed in sector-reversal-region plasma and the high average Alfvén speed in ejecta. For the inertial range of timescales the homogeneity (lumpiness) of the plasma, the magnetic-field orientation, and the Alfvénicity are noted in rows 4–6 of **Table 1**. Coronal-hole-origin plasma and streamer-belt-origin plasma are quasi-homogeneous, they have magnetic fields that tend to be Parker-spiral oriented (plus variations about the Parker-spiral direction), and they tend to be Alfvénic. [Streamer-belt-origin plasma is the "Alfvénic slow wind" (D'Amicis and Bruno, 2015; Bale et al., 2019; D'Amicis et al., 2019; Perrone et al., 2020)]. On the contrary, sector-reversal-region plasma and ejecta tend to be inhomogeneous, with non-Parker-spiral-oriented magnetic fields, and tend to be non-Alfvénic. A Parker-spiral magnetic-field orientation is consistent with a plasma that is continuously emitted from a spot on the Sun; non-Parker-spiral fields are characteristic of impulsive emission of plasma from the Sun. Consistent with this is the strahl (row 7 of **Table 1**): coronal-hole-origin plasma and streamer-belt-origin

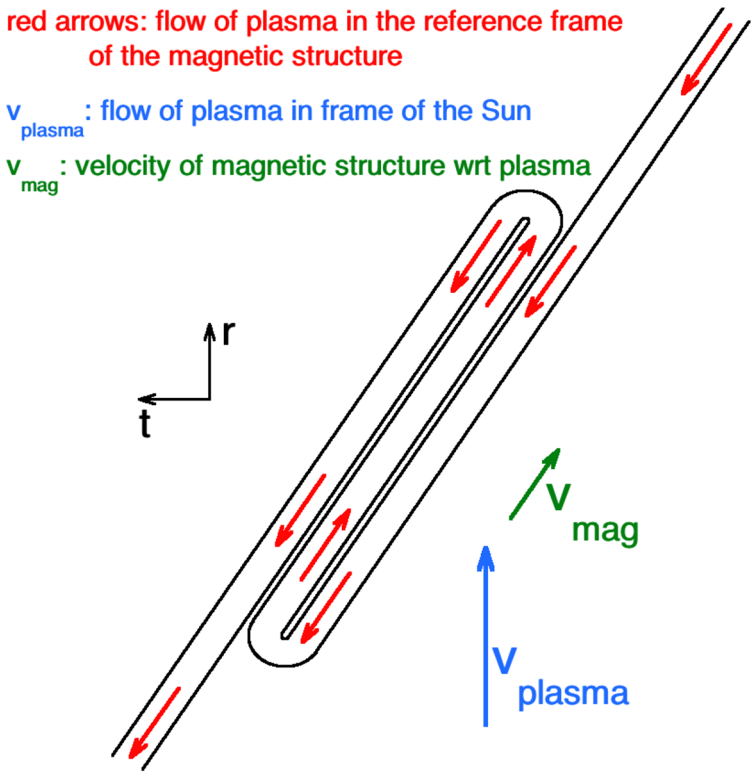

FIGURE 6 | A sketch in the ecliptic plane of a magnetic switchback (folded flux tube) and the associated velocity perturations. The Sun is at the bottom of the sketch. The sketched structure is approximately Parker-spiral aligned (see r-t coordinates in black). The red arrows are the flow of plasma in the reference frame of the magnetic structure, with the structure moving at a velocity v_{mag} (green arrow) with respect to the average plasma flow $v_{plama} = v_{sw}$ (blue arrow). A spacecraft crossing the folded flux tube sees a localized increase in the radial flow velocity where the magnetic field is reversed from the Parker spiral.

TABLE 1 | Some systematic differences in the properties of the four types of solar-wind plasma; the values are from the OMNI2 1-AU data set in the years 1995–2018.

	Coronal-hole -origin plasma	Streamer-belt -origin plasma	Sector-reversal -region plasma	Ejecta plasma
Wind speed v_{sw}	562 ± 80 km/s	410 ± 50 km/s	339 ± 39 km/s	429 ± 98 km/s
Number density n_{sw}	3.2 ± 1.7 cm^{-3}	5.6 ± 3.2 cm^{-3}	10.7 ± 6.5 cm^{-3}	6.4 ± 5.7 cm^{-3}
Alfvén speed v_A	73 ±19 km/s	51 ±13 km/s	30 ± 11 km/s	111 ± 60 km/s
Homogeneity	Quasi-homogeneous	Quasi-homogeneous	Inhomogeneous	Inhomogeneous
Field orientation	Parker-spiral aligned	Parker-spiral aligned	Non-parker-spiral	Non-parker-spiral
Alfvénicity	High	High	None	Weak
Strahl	Unidirectional	Unidirectional	Absent	Bi-Directional
Plasma age at earth τ_{age}	76 ± 11 h	103 ± 12 h	124 ± 14 h	101 ± 19 h
Occurrence rate at earth	23.9%	41.6%	23.9%	11.5%

plasma have unidirectional strahls indicative of one magnetic footpoint on the Sun, sector-reversal-region plasma tends to have no strahl indicative of no magnetic connection to the Sun, and ejecta often has a bidirectional strahl indicative of both magnetic footpoints on the Sun. Row 8 of **Table 1** indicates the age of the plasma at 1 AU (approximated using the velocity of the plasma at 1 AU). Row 9 is the fraction of time each type of plasma was seen at Earth in the years 1995–2018. These fractions vary strongly through the 11-year solar cycle (Xu and Borovsky, 2015).

SUMMARY AND DISCUSSION

A coherent picture of the structure of the magnetic field and plasma of the solar wind in the inner heliosphere is being uncovered. Many of the properties of that structure are as yet underappreciated. The multiple properties of the structure that were discussed in this review are summarized in the final paragraph of Section Introduction.

Examination specifically of the solar-wind spatial structure leads to a description that differs from the description of physics common in the solar wind in the literature, that common description dominated by a Fourier analysis in frequency or a structure-function analysis of time differences (Viall and Borovsky, 2020). Some common terminology in the literature may be biased and not as accurate as another terminology. Five terminology examples are commented upon.

(1) The term "pressure balanced structure" [e.g., (Riazantseva et al., 2005)] might be more-accurately replaced by "plasma boundary"; the term plasma boundary better reflects the inhomogeneity of the solar wind and the fact that the ion composition, the specific entropy, the strahl, etc. can change across the boundary between two flux tubes, whereas a pressure balanced structure could be created by a localized heating of the plasma accompanied by expansion. There will, of course, be pressure balance across a plasma boundary.
(2) The interpretation of plasma number density variations or magnetic-field-strength variations as a signature of "compressibility" [e.g., (D'Amicis and Bruno, 2015)] might be better described as "inhomogeneity" of the solar-wind plasma, or lumpiness of the plasma.
(3) The high-frequency spectral breakpoint of the solar-wind representing an "onset of dissipation" in an eddy-cascade picture of the Fourier fluctuations [e.g., (Gary, 1999)] might be better described as the "physics of current-sheet thicknesses" in collisionless plasmas.
(4) Some of the concern with wave-vector anisotropy in the solar wind [e.g., (Oughton et al., 2015)] might be refocused on the question of current-sheet orientations.
(5) The focus on high-frequency plasma-wave dispersion relations to explain the shape of the high-frequency magnetic spectrum of the solar wind [e.g., (Podesta et al., 2010)] might be refocused on the shapes (profiles) of current sheets in the solar wind.

AUTHOR CONTRIBUTIONS

The author planned, outlined, researched, and wrote the manuscript.

FUNDING

Work at the Space Science Institute was supported by the NSF SHINE program via award AGS-1723416, by the NASA Heliophysics Guest Investigator Program via Grant No. NNX17AB71G, and by NASA Heliophysics LWS TRT program via Grant No. NNX14AN90G.

ACKNOWLEDGMENTS

The author thanks Brandon Burkholder, Mick Denton, Zdenek Nemecek, John Podesta, Chuck Smith, and Nicki Viall for helpful conversations.

REFERENCES

Arya, S., and Freeman, J. W. (1991). Estimates of solar wind velocity gradients between 0.3 and 1 AU based on velocity probability distributions from Helios 1 at perihelion and aphelion. *J. Geophys. Res.* 96, 14183–14187. doi: 10.1029/91JA01135

Bale, S. D., Badman, S. T., Bonnell, J. W., Bowen, T. A., Burgess, D., Case, A. W., et al. (2019). Highly structured slow solar wind emerging from an equatorial coronal hole. *Nature* 576, 237–242. doi: 10.1038/s41586-019-1818-7

Balogh, A., Forsyth, R. J., Lucek, A., Horbury, T. S., and Smith, E. J. (1999). Heliophysics magnetic field polarity inversions at high heliographic latitudes. *Geophys. Res. Lett.* 26, 631–634. doi: 10.1029/1999GL900061

Bartley, W. C., Bakata, R. P., McCracken, K. G., and Rao, U. R. (1966). Anisotropic cosmic radiation fluxes of solar origin. *J. Geophys. Res.* 71, 3297–3304. doi: 10.1029/JZ071i013p03297

Borovsky, J. E. (2006). The eddy viscosity and flow properties of the solar wind: CIRs, CME sheaths, and solar-wind/magnetosphere coupling. *Phys. Plasmas* 13, 056505–056526. doi: 10.1063/1.2200308

Borovsky, J. E. (2008). The flux-tube texture of the solar wind: strands of the magnetic carpet at 1 AU? *J. Geophys. Res.* 113:A08110. doi: 10.1029/2007JA012684

Borovsky, J. E. (2010a). On the variations of the solar-wind magnetic field about the Parker-spiral direction. *J. Geophys. Res.* 115:A09101. doi: 10.1029/2009JA015040

Borovsky, J. E. (2010b). On the contribution of strong discontinuities to the power spectrum of the solar wind. *Phys. Rev. Lett.* 105:111102. doi: 10.1103/PhysRevLett.105.111102

Borovsky, J. E. (2012a). Looking for evidence of mixing in the solar wind from 0.31 to 0.98 AU. *J. Geophys. Res.* 117:A06107. doi: 10.1029/2012JA017525

Borovsky, J. E. (2012b). The effect of sudden wind shear on the Earth's magnetosphere: statistics of wind-shear events and CCMC simulations of magnetotail disconnections. *J. Geophys. Res.* 117:6224. doi: 10.1029/2012JA017623

Borovsky, J. E. (2016). Plasma structure of the coronal-hole solar wind: origins and evolution. *J. Geophys. Res.* 121, 5055–5087. doi: 10.1002/2016JA022686

Borovsky, J. E. (2018a). The spatial structure of the oncoming solar wind at Earth and the shortcomings of a solar-wind monitor at L1. *J. Atmos. Solar-Terr. Phys.* 177, 2–11. doi: 10.1016/j.jastp.2017.03.014

Borovsky, J. E. (2018b). Looking for evidence of wind-shear disconnections of the Earth's magnetotail: GEOTAIL measurements and LFM MHD simulations, *J. Geophys. Res.* 123, 5538–5560. doi: 10.1029/2018JA025456

Borovsky, J. E. (2020a). What magnetospheric and ionospheric researchers should know about the solar wind. *J. Atmos. Solar-Terr. Phys.* 204:105271. doi: 10.1016/j.jastp.2020.105271

Borovsky, J. E. (2020b). On the motion of the heliospheric magnetic structure through the solar wind plasma. *J. Geophys. Res.* 125:e2019JA027377. doi: 10.1029/2019JA027377

Borovsky, J. E. (2020c) The magnetic structure of the solar wind: Ionic composition and the electron strahl. *Geophys. Res. Lett.* 47:e2019GL084586. doi: 10.1029/2019GL084586

Borovsky, J. E., Burkholder, B. L. (2020). On the fourier contribution of strong current sheets to the high-frequency magnetic power spectral density of the solar wind. *J. Geophys. Res.* 125:e2019JA027307. doi: 10.1029/2019JA027307

Borovsky, J. E., and Denton, M. H. (2016). The trailing edges of high-speed streams at 1 AU. *J. Geophys. Res.* 121, 6107–6140. doi: 10.1002/2016JA022863

Borovsky, J. E., Denton, M. H., and Smith, C. W. (2019). Some properties of the solar-wind turbulence at 1 AU statistically examined in the different types of solar-wind plasma. *J. Geophys. Res.* 124, 2406–2424. doi: 10.1029/2019JA026580

Borovsky, J. E., and Podesta, J. J. (2015). Exploring the effect of current-sheet thickness on the high-frequency fourier spectrum of the solar wind, *J. Geophys. Res.* 120, 9256–9268. doi: 10.1002/2015JA021622

Borovsky, J. E., and Steinberg, J. T. (2014). No evidence for the localized heating of solar-wind protons at intense velocity shear zones. *J. Geophys. Res.* 119, 1455–1462. doi: 10.1002/2013JA019746

Bruno, R. (2019). Intermittency in solar wind turbulence from fluid to kinetic scales. *Earth Space Sci.* 6, 656–672. doi: 10.1029/2018EA000535

Bruno, R., and Carbone, V. (2016). Turbulence in the solar wind. *Lecture. Notes Phys.* 928:1. doi: 10.1007/978-3-319-43440-7

Bruno, R., Carbone, V., Veltri, P., Pietropaolo, E., and Bavassano, B. (2001). Identifying intermittency events in the solar wind. *Planet. Space Sci.* 49, 1201–1210. doi: 10.1016/S0032-0633(01)00061-7

Bruno, R., and Trenchi, L. (2014). Radial dependence of the frequency break between fluid and kinetic scales in the solar wind fluctuations. *Astrophys. J. Lett.* 787:L24. doi: 10.1088/2041-8205/787/2/L24

Burkholder, B. L., Otto, A., Delamere, P. A., and Borovsky, J. E. (2019). Magnetic connectivity in the corona as a source of structure in the solar wind. *J. Geophys. Res.* 124, 32–49. doi: 10.1029/2018JA026132

Burlaga, L. F., and Ness, N. F. (1969). Tangential discontinuities in the solar wind. *Solar Phys.* 9, 467–477. doi: 10.1007/BF02391672

Camporeale, E., Care, A., and Borovsky, J. E. (2017). Classification of solar wind with machine learning. *J. Geophys. Res.* 122, 10,910–10,920. doi: 10.1002/2017JA024383

Chhiber, R., Goldstein, M. L., Maruca, B. A., Chasapis, A., Matthaeus, W. H., et al. (2020). Clustering of intermittent magnetic and flow structures near parker solar probe's first perihelion – a partial-variance-of-increments analysis. *Astrophys. J. Suppl. Ser.* 246:31. doi: 10.3847/1538-4365/ab53d2

Corrsin, S. (1959). Outline of some topics in homogeneous turbulent flow. *J. Geophys. Res.* 64:2134. doi: 10.1029/JZ064i012p02134

D'Amicis, R., and Bruno, R. (2015). On the origin of highly alfvénic slow solar wind. *Astrophys. J.* 805:84. doi: 10.1088/0004-637X/805/1/84

D'Amicis, R., Matteini, L., and Bruno, R. (2019). On the slow solar wind with high alfvénicity: from composition and microphysics to spectral properties. *Mon. Not. Roy. Astron. Soc.* 483, 4665–4677. doi: 10.1093/mnras/sty3329

de Wit, T. D., Krasnoselskikh, V., Bale, S. D., Bonnell, J. W., Bowen, T. A., et al. (2020). Switchbacks in the near-sun magnetic field: long memory and impact on the turbulent cascade. *Astrophys. J. Suppl. Ser.* 246:39. doi: 10.3847/1538-4365/ab5853

Dimotakis, P. E. (2005). Turbulent mixing. *Ann. Rev. Fluid. Mech.* 37, 329–56. doi: 10.1146/annurev.fluid.36.050802.122015

Dmitruk, P., Matthaeus, W. H., and Seenu, N. (2004). Test particle energization by current sheets and nonuniform fields in magnetohydrodynamic turbulence. *Astrophys. J.* 617:667. doi: 10.1086/425301

Dobrowolny, M., Mangeney, A., and Veltri, P. (1980). Fully developed anisotropic turbulence in interplanetary space. *Phys. Rev. Lett.* 45:144. doi: 10.1103/PhysRevLett.45.144

Duan, D., Bowen, T. A., Chen, C. H. K., Mallet, A., He, J., et al. (2020). The radial dependence of proton-scale magnetic spectral break in slow solar wind during PSP encounter 2. *Astrophys. J. Suppl. Ser.* 246:55. doi: 10.3847/1538-4365/ab672d

Edwin, P. M., and Roberts, B. (1983). Wave propagation in a magnetic cylinder. *Solar Phys.* 88, 179. doi: 10.1007/BF00196186

Eselevich, V. G. (2019). Diamagnetic structures as a basis of quasi-stationary slow solar wind. *Solar Terr. Phys.* 5, 29–41. doi: 10.12737/stp-53201904

Feldman, W. C., Asbridge, J. R., Bame, S. J., Gary, S. P., Montgomery, M. D., and Zink, S. M. (1976). Evidence for the regulation of solar wind heat flux at 1 AU. *J. Geophys. Res.* 81:5207. doi: 10.1029/JA081i028p05207

Gary, S. P. (1999). Collisionless dissipation wavenumber: linear theory. *J. Geophys. Res.* 104, 6759–6762. doi: 10.1029/1998JA900161

Goossens, M., Trradas, J., Andries, J., Arregui, I., and Ballester, J. L. (2009). On the nature of kink MHD waves in magnetic flux tubes. *Astron. Astrophys.* 503, 213–223. doi: 10.1051/0004-6361/200912399

Gosling, J. T., McComas, D. J., Roberts, D. A., and Skoug, R. M. (2009). A one-sided aspect of alfvénic fluctuations in the solar wind. *Astrophys. J.* 695:L213. doi: 10.1088/0004-637X/695/2/L213

Gosling, J. T., Tian, H., and Phan, T. D. (2011). Pulsed Alfvén waves in the solar wind. *Astrophys. J.* 737:L35. doi: 10.1088/2041-8205/737/2/L35

Greco, A., Matthaeus, W. H., Servidio, S., Chuychai, P., and Dmitruk, P. (2009). Statistical analysis of discontinuities in solar wind ACE data and comparison with intermittent MHD turbulence. *Astrophys. J.* 691:L111. doi: 10.1088/0004-637X/691/2/L111

Hannum, D., Bateman, G., Kinsey, J., Kritz, A. H., Onjun, T., and Pankin, A. (2001). Comparison of high-mode predictive simulations using mixed Bohm/gyro-bohm and multi-mode (MMM95) transport models. *Phys. Plasmas* 8, 964–974. doi: 10.1063/1.1338534

Heyvaerts, J., and Priest, E. R. (1983). Coronal heating by phase-mixed shear alfvén waves. *Astron. Astrophys.* 117, 220–234.

Horbury, T. S., Woolley, T., Laker, R., Matteini, L., Eastwood, J., et al. (2020). Sharp Alfvénic impulses in the near-Sun solar wind. *Astrophys. J. Suppl. Ser.* 246:45. doi: 10.3847/1538-4365/ab5b15

Horbury, T. S., Woolley, T., and Stansby, D. (2018). Short, large-amplitude speed enhancemnts in the near-sun fast solar wind. *Mon. Not. R. Astron. Soc.* 478, 1980–1986. doi: 10.1093/mnras/sty953

Huang, C., Yan, Y., Li, G., Deng, Y., and Tan, B. (2014). Tracking back the solar wind to its photospheric footpoints from wind observations – a statistical study. *Solar Phys.* 289, 3109–3119. doi: 10.1007/s11207-014-0508-8

Jockers, K. (1972). Solar wind models based on exospheric theory. *Astron. Astrophys.* 6:219.

Kahler, S. W., Crooker, N. U., and Gosling, J. T. (1996). The topology of intrasector reversals of the interplanetary magnetic field. *J. Geophys. Res.* 101, 24,373–24,382. doi: 10.1029/96JA02232

Kasper, J. C., Bale, S. D., Belcher, J. W., Berthomier, M., Case, A. W., et al. (2019). Alfvénic velocity spikes and rotational flows in the near-Sun solar wind. *Nature* 576, 228–231. doi: 10.1038/s41586-019-1813-z

Kepko, L., and Spence, H. E. (2003). Observations of discrete, global magnetospheric oscillations directly driven by solar wind density variations. *J. Geophys. Res.* 108:1257. doi: 10.1029/2002JA009676

Kepko, L., Spence, H. E., and Singer, H. J. (2002). ULF waves in the solar wind as direct drivers of magnetospheric pulsations. *Geophys. Res. Lett. (2002)* 29:39-1–39-4. doi: 10.1029/2001GL014405

Kepko, L., and Viall, N. M. (2019). The source, significance, and magnetospheric impact of periodic density structures within stream interaction regions. *J. Geophys. Res.* (2019) 124, 1–22. doi: 10.1029/2019JA026962

King, J. H., and Papitashvili, N. E. (2005). Solar wind spatial scales in and comparisons of hourly Wind and ACE plasma and magnetic field data. *J. Geophys. Res.* 110:2104. doi: 10.1029/2004JA010649

Knetter, T., Neubauer, F. M., Horbury, T., and Balogh, A. (2004). Four-point discontinuity observations using cluster magnetic field data: a statistical survey. *J. Geophys. Res.* 109:A06102. doi: 10.1029/2003JA010099

Komar, C. M., Fermo, R. L., and Cassak, P. A. (2015). Comparative analysis of dayside magnetic reconnection models in global magnetosphere simulations. *J. Geophys. Res.* 120, 276–294. doi: 10.1002/2014JA020587

Lacombe, C., Salem, C., Mangeney, A., Hubert, D., Perche, C., Bougeret, J. L., et al. (2002). Evidence for the interplanetary electric potential? WIND observations of electrostatic fluctuations. *Ann. Geophys.* 20, 609–618. doi: 10.5194/angeo-20-609-2002

Lemaire, J. (2010). Half a century of kinetic solar wind models. *AIP Conf. Proc.* 1216:8. doi: 10.1063/1.3395971

Lemaire, J., and Pierrard, V. (2001). Kinetic models of solar and polar winds. *Astrophys. Space Sci.* 277, 169–180. doi: 10.1007/978-94-010-0904-1_22

Li, G., and Qin, G. (2011). "A solar wind model with current sheets," in *Proceedings of a 5th International Conference Held at San Diego, California, USA 13-18 June 2010*. ed. N.V. Pogorelov (San Francisco: Astronomical Society of the Pacific), 117.

Liepmann, H. W. (1979). The rise and fall of ideas in turbulence. *Amer. Sci.* 67, 221–228.

Lin, R. P. (1998). WIND observations of suprathermal electrons in the interplanetary medium. *Space Sci. Rev.* 86, 61–78. doi: 10.1007/978-94-011-4762-0_4

Magyar, N., Van Doorsselaere, T., and Goosens, M. (2017). Generalized phase mixing: turbulence-like behaviour from unidirectional propagating MHD waves. *Sci. Rep.* 7:14820. doi: 10.1038/s41598-017-13660-1

Maksimovic, M., Zouganelis, I., Chaufray, J. Y., Issautier, K., Scime, E. E., Littleton, J. E., et al. (2005). Radial evolution of the electron distribution functions in the fast solar wind between 0.3 and 1.5 AU. *J. Geophys. Res.* 110:A09104. doi: 10.1029/2005JA011119

Malara, F., Primavera, L., and Veltri, P. (1996). Compressive fluctuations generated by time evolution of Alfvénic perturbations in the solar wind current sheet. *J. Geophys. Res.* 101:21597–21617. doi: 10.1029/96JA01637

Malaspina, D. M., Newman, D. L., Wilson, L. B., Goetz, K., Kellogg, P. J., and Kerstin, K. (2013). Electrostatic solitary waves in the solar wind: evidence for instability at solar wind current sheets. *J. Geophys. Res.* 118, 591–599. doi: 10.1002/jgra.50102

Mangeney, A., Salem, C., Lacombe, C., Bougeret, J. L., Perche, C., Manning, R., et al. (1999). WIND observations of coherent electrostatic waves in the solar wind. *Ann. Geophys.* 17, 307–320. doi: 10.1007/s00585-999-0307-y

McComas, D. J., Blame, S. J., Barker, P., Feldman, W. C., Phillips, J. L., Riley, P., et al. (1998). Solar wind electron proton alpha monitor (SWEPAM) for the advanced composition explorer. *Space Sci. Rev.* 86, 563–612. doi: 10.1007/978-94-011-4762-0_20

McCracken, K. G., and Ness, N. F. (1966). The collimation of cosmic rays by the interplanetary magnetic field. *J. Geophys. Res.* 71, 3315–3318. doi: 10.1029/JZ071i013p03315

Miao, B., Peng, B., and Li, G. (2011). Current sheets from Ulysses observation. *Ann. Geophys.* 29, 237–249. doi: 10.5194/angeo-29-237-2011

Michel, F. C. (1967). Model of solar wind structure. *J. Geophys. Res.* 72:1917. doi: 10.1029/JZ072i007p01917

Mozer, F. S., Agapiov, O. V., Bale, S. D., Bonnell, J. W., Case, T., et al. (2020b) Switchbacks in the solar magnetic field: their evolution, their content, and their effects on the plasma. *Astrophys. J. Suppl. Ser.* 246:68. doi: 10.3847/1538-4365/ab7196

Mozer, F. S., Agapitov, O. V., Bale, S. D., Bonnell, J. W., Goetz, K., Goodrich, R., et al. (2020a) Time domain structures and dust in the solar vicinity: parker solar probe observations. *Astrophys. J. Suppl. Ser.* 246:50. doi: 10.3847/1538-4365/ab5e4b

Nemecek, Z., Durovcova, T., Safrankova, J., Nemec, F., Matteini, L., Stansvy, D., et al. (2020). What is the solar wind frame of reference? *Astrophys. J.* 889:163. doi: 10.3847/1538-4357/ab65f7

Ness, N. F., Scearce, C. S., and Cantarano, S. (1966). Preliminary results fro the pioneer 6 magnetic field experiment. *J. Geophys. Res.* 71:3305. doi: 10.1029/JZ071i013p03305

Neugebauer, M., and Giacalone, J. (2010). Progress in the study of interplanetary discontinuities. *AIP Conf. Proc.* 1216:194. doi: 10.1063/1.3395834

Neugebauer, M., and Giacalone, J. (2015). Energetic particles, tangential discontinuities, and solar flux tubes. *J. Geophys. Res.* 120, 8281–8287. doi: 10.1002/2015JA021632

Neugebauer, M., and Goldstein, B. (2013). E. Double-proton beams and magnetic switchbacks in the solar wind. *AIP Conf. Proc.* 1539:46. doi: 10.1063/1.4810986

Ottino, J. (1990). M. Mixing, chaotic advection, and turbulence. *Ann. Rev. Fluid Mech.* 22, 207–254. doi: 10.1146/annurev.fl.22.010190.001231

Oughton, S., Matthaeus, W. H., Wan, M., and Osman, K. T. (2015). Anisotropy in solar wind plasma turbulence. *Phil. Trans. Roy. Soc. A* 373, 1–23. doi: 10.1098/rsta.2014.0152

Owens, M. J., Wicks, R. T., and Horbury, T. S. (2011). Magnetic discontinuities in the near-Earth solar wind: evidence of in-transit turbulence or remnants of coronal structure? *Solar Phys.* 269, 411–420. doi: 10.1007/s11207-010-9695-0

Paul, E. L., Atiemo-Obeng, V. A., and Kresta, S. M. (2003). *Handbook of Industrial Mixing Wiley-Interscience*. (Hoboken, NJ: Wiley-Interscience; John Wiley & Sons). doi: 10.1002/0471451452

Perkins, F. W., Barnes, C. W., Hohnson, D. W., Scott, S. D., et al. (1993). Nondimensional transport scaling in the tokamak fusion test reactor: is tokamak transport bohm or gyro-bohm? *Phys. Fluids B* 5, 477–498. doi: 10.1063/1.860534

Perrone, D., D'Amicis, R., De Marco, R., Matteini, L., Stansby, D., Bruno, R., Horbury, T. S. (2020). Highly alfvénic slow solar wind at 0.3 AU during a solar minimum: helios insights for parker solar probe and solar orbiter. *Astron. Astrophys.* 633:A166. doi: 10.1051/0004-6361/201937064

Pierrard V, Issautier K, Meyer-Vernet N, Lemaire J. Collisionless model of the solar wind in a spiral magnetic field. *Geophys. Res. Lett.* (2001) 28:223.

Pierrard, V., and Peters, M. (2014). Coronal heating and solar wind acceleration for electrons, protons, and minor ions obtained from kinetic models based on kappa distributions. *J. Geophys. Res.* 119, 9441–9455. doi: 10.1002/2014JA020678

Podesta, J. J., and Borovsky, J. E. (2016). Relationship between the durations of jumps in solar wind time series and the frequency of the spectral break. *J. Geophys. Res.* 121, 1817–1838. doi: 10.1002/2015JA021987

Podesta, J. J., Borovsky, J. E., and Gary, S. P. (2010). A kinetic Alfvén wave cascade subject to collisionless damping cannot reach electron scales in the solar wind at 1 AU. *Astrophys. J.* 712:685. doi: 10.1088/0004-637X/712/1/685

Qin, G., and Li, G. (2008). Effect of flux tubes in the solar wind on the diffusion of energetic particles. *Astrophys. J.* 682:L129 doi: 10.1063/1.2982464

Riazantseva, M. O., Khabarova, O. V., Zastenker, G. N., and Richardson, J. D. (2005). Sharp boundaries of solar wind plasma structures and an analysis of their pressure balance. *Cosmic. Res.* 43, 157–164. doi: 10.1007/s10604-005-0030-8

Rouillard, A. P., Kouloumvakos, A., Vourlidas, A., Kasper, J., Bale, S., et al. (2020). Related streamer flows to density and magnetic structures at the parker solar probe. *Astrophys. J. Suppl. Ser.* 246:37. doi: 10.3847/1538-4365/ab579a

Ruderman, M. S., Roberts, B. Leaky and non-leaky kink oscillations of magnetic flux tubes. *J. Plasma Phys.* (2006) 72, 285–308. doi: 10.1017/S0022377805004101

Safrankova, J., Memecek, Z., Cagas, P., Pavlu, J., Zastenker, G. N., Riazantseva, M. O., et al. (2013). Short-scale variations of the solar wind helium abundance. *Astrophys. J.* 778:25. doi: 10.1088/0004-637X/778/1/25

Salem, C., Hubert, D., Lacombe, C., Bale, S. D., Mangeney, A., Larson, D. E., et al. (2003a). Electron properties and Coulomb collisions in the solar wind at 1 AU: WIND observations. *Astrophys. J.* 585:1147. doi: 10.1086/346185

Salem, C., Lacombe, C., Mangeney, A., Kellogg, P. J., and Bougeret, J. L. (2003b). Weak double layers in the solar wind and their relation to the interplanetary electric field. *AIP Conf. Proc.* 679:513. doi: 10.1063/1.1618647

Sari, J. W., and Ness, N. F. (1969). Power spectra of the interplanetary magnetic field. *Solar Phys.* 8, 155–165. doi: 10.1007/BF00150667

Schatten, K. H. (1971). Large-scale properties of the interplanetary magnetic field. *Rev. Geophys. Space Phys.* 9:773. doi: 10.1029/RG009i003p00773

Schwenn, R., Muhlhauser, K. H., Marsch, E., and Rosenbauer, H. (1981). "Two states of the solar wind at the time of solar activity minimum II. Radial gradients of plasma parameters in fast and slow streams," in *Solar Wind Four* MPAE-W-100-81-31, (Lindau: Max Planck Institut fur eronomie), 126.

Siscoe, G. L., Davis, L., Coleman, P. J., Smith, E. J., and Jones, D. E. (1968). Power spectra and discontinuities of the interplanetary magnetic field: mariner 4. *J. Geophys. Res.* 73:61. doi: 10.1029/JA073i001p00061

Smith, C. W., Acuna, M. H., Burlaga, L. F., L'Heureux, J., Ness, N. F., and Scheifele, J. (1998). The ACE magnetic fields experiment. *Space Sci. Rev.* 86, 611–632. doi: 10.1023/A:1005092216668

Sonnerup, B. U. O. (1974). Magnetopause reconnection rate. *J. Geophys. Res.* 79:1546. doi: 10.1029/JA079i010p01546

Telloni, D., Perri, S., Carbone, V., and Bruno, R. (2016). Selective decay and dynamic alignment in the MHD turbulence: the role of the rugged invariants. *AIP Conf. Proc.* 1720:040015. doi: 10.1063/1.4943826

Tenerani, A., Velli, M., Matteini, L., Reville, V., Shi, C., et al. (2020). Magnetic field kinks and folds in the solar wind. *Astrophys. J. Suppl. Ser.* 246:32. doi: 10.3847/1538-4365/ab53e1

Thieme, K. M., Schwenn, R., and Marsch, E. (1989). Are structures in high-speed streams signatures of coronal fine structures? *Adv. Space Res.* 9, 127–130. doi: 10.1016/0273-1177(89)90105-1

Tong, Y., Borovsky, J. E., Steinberg, J. T. (2016). "Using ACE-Earth magnetic connection events to measure wandering length scale of interplanetary magnetic field in the solar wind," in *2016 Los Alamos Space Weather Summer School Research Reports*, Report LA-UR-16-29471, (Los Alamos: NM: Los Alamos National Laboratory), 55.

Trenchi, L., Bruno, R., D'Amicis, R., Marcucci, M. F., and Telloni, E. (2013b). Observation of IMF coherent structures and their relationship to SEP dropout events. *Ann. Geophys.* 31, 1333–1341. doi: 10.5194/angeo-31-1333-2013

Trenchi, L., Bruno, R., Telloni, D., D'Amicis, R., Marcucci, M. F., Zurbuchen, T. H., et al. (2013a). Solar energetic particle modulation associated with coherent magnetic structures. *Astrophys. J.* 770:11. doi: 10.1088/0004-637X/770/1/11

Tsurutani, B. T., and Ho, C. M. (1999). A review of discontinuities and Alfvén waves in interplanetary space: ulysses results. *Rev. Geophys.* 37, 517–541. doi: 10.1029/1999RG900010

Tu, C. Y., Wang, X., He, J., Marsch, E., and Wang, L. (2016). Two cases of convecting structure in the slow solar wind turbulence. *AIP Conf. Proc.* 1720:040017 doi: 10.1063/1.4943828

Vasquez, B. J., Abramenko, V. I., Haggerty, D. K., and Smith, C. W. (2007). Numerous small magnetic field discontinuities of Bartels rotation 2286 and the potential role of Alfvénic turbulence. *J. Geophys. Res.* 112:A11102. doi: 10.1029/2007JA012504

Vasquez, B. J., and Hollweg, J. V. (1999). Formation of pressure-balanced structures and fast waves from nonlinear Alfvén waves. *J. Geophys. Res.* 104, 4681–4696. doi: 10.1029/1998JA900090

Viall, N. M., Borovsky, J. E. (2020). Nine outstanding questions of solar wind physics. *J. Geophys. Res*. 125. doi: 10.1002/essoar.10502606.1

Viall, N. M., and Vourlidas, A. (2015). Periodic density structures and the origin of the slow solar wind. *Astrophys. J.* 807:176. doi: 10.1088/0004-637X/807/2/176

Webb, G. M., Zank, G. P., Kaghashvili, E. K., and le Roux, J. A. (2006). Compound and perpendicular diffusion of cosmic rays and random walk of the field lines. I. Parallel particle transport models. *Astrophys. J.* 651:211. doi: 10.1086/507415

Xu, F., and Borovsky, J. E. (2015). A new 4-plasma categorization scheme for the solar wind. *J. Geophys. Res.* 120, 70–100. doi: 10.1002/2014JA020412

Yamauchi, Y., Suess, S. T., Steinberg, J. T., and Sakurai, T. (2004). Differential velocity between solar wind protons and alpha particles in pressure balanced structures. *J. Geophys. Res.* 109:A03104. doi: 10.1029/2003JA 010274

Zastenker, G. N., Koloskova, I. V., Riazantseva, M. O., Yurasov, A. S., Safrankova, J., Nemecek, Z., et al. (2014). Observation of fast variations of the helium-ion abundance in the solar wind. *Cosmic. Res.* 52, 25–36. doi: 10.1134/S0010952514010109

Zheng, J., Hu, Q., Chen, Y., and le Roux, J. (2017). Automated detection of small-scale magnetic flux ropes and their association with shocks. *J. Phys. Conf. Ser.* 900:012024. doi: 10.1088/1742-6596/900/1/ 012024

Conflict of Interest: The author declares that the research was conducted in the absence of any commercial or financial relationships that could be construed as a potential conflict of interest.

frontiers in Physics

PERSPECTIVE
published: 29 May 2020
doi: 10.3389/fphy.2020.00166

Transport Ratios of the Kinetic Alfvén Mode in Space Plasmas

Yasuhito Narita[1]*, *Owen Wyn Roberts*[1], *Zoltán Vörös*[1,2] and *Masahiro Hoshino*[3]

[1] Space Research Institute, Austrian Academy of Sciences, Graz, Austria, [2] Research Centre for Astronomy and Earth Sciences, Geodetic and Geophysical Institute, Sopron, Hungary, [3] Graduate School of Science, The University of Tokyo, Tokyo, Japan

Fluctuation properties of the kinetic Alfvén mode, such as polarization of the wave electric and magnetic field around the mean magnetic field, parallel fluctuation to the mean field, ratios of the electric to magnetic field, and density fluctuations are analytically estimated by constructing the dielectric tensor of plasma based on the linear Vlasov theory. The dielectric tensor contains various fluid-picture processes in the lowest order, including polarization drift, Hall current, and diamagnetic current. Major discoveries from the dielectric tensor method in the kinetic Alfvén mode study are (1) identification of the mechanism of the field rotation sense reversal as a result of competition between the Hall and diamagnetic currents, (2) behavior of the parallel magnetic field fluctuation (in the compressive sense). The analytic expression of transport ratios serves as a diagnostic tool to study and identify the kinetic Alfvén mode in space plasma observations in the inner heliospheric domain.

Keywords: kinetic Alfvén mode, dielectric tensor, fluctuation properties, energy spectra, plasma turbulence

OPEN ACCESS

Edited by:
Luca Sorriso-Valvo,
Institute for Science and Technology of Plasmas (NCR), Italy

Reviewed by:
Christian L. Vásconez,
National Polytechnic School, Ecuador
Francesco Malara,
University of Calabria, Italy
Silvio Sergio Cerri,
Princeton University, United States

***Correspondence:**
Yasuhito Narita
yasuhito.narita@oeaw.ac.at

Specialty section:
This article was submitted to Space Physics, a section of the journal Frontiers in Physics

Received: *07 February 2020*
Accepted: *21 April 2020*
Published: *29 May 2020*

Citation:
Narita Y, Roberts OW, Vörös Z and Hoshino M (2020) Transport Ratios of the Kinetic Alfvén Mode in Space Plasmas. Front. Phys. 8:166. doi: 10.3389/fphy.2020.00166

1. INTRODUCTION

Kinetic Alfvén mode is one of the small-scale variants of the shear Alfvén mode in which the electric field parallel to the mean magnetic field direction (excited nearly in the electromagnetic fashion) is balanced against the electron-scale Debye screening when the wavevector becomes nearly perpendicular to the mean field [1]. The kinetic Alfvén mode is considered to play an important role in various space plasma environments and is one of the likely fluctuation constituents in solar wind turbulence. Indeed, various *in situ* observations of the solar wind plasma and magnetic field are favorably interpreted as a realization of the kinetic Alfvén mode from 0.1 to 100 Hz in the spacecraft frame (e.g., [2–8]).

The properties of the kinetic Alfvén mode and its possible realization in solar wind turbulence has also been investigated in numerical experiments [9–21]. In particular, explicit use of spectral ratios in order to characterize kinetic-scale fluctuations has been extensively used in recent kinetic simulations [22–28]. Discussion in Grošelj et al. [28] on the wave-like or coherent-structure nature of the sub-ion-scale fluctuations is of great interest in understanding the solar wind microphysics.

Here we revisit the kinetic Alfvén mode and analytically derive the transport ratios and scaling laws for the electric and magnetic fields in the spirit of developing useful tools for the wave mode identification in the spacecraft observations, particularly in view of the inner heliospheric observations, such as Parker Solar Probe, Solar Orbiter, and BepiColombo's cruise to Mercury. Our derivation is based on the dielectric tensor in the kinetic picture, and treat the dielectric tensor analytically in the leading orders so that the fluid picture properties of kinetic Alfvén mode are derived from the kinetic treatment. We fill the gap between the kinetic derivation and the fluid

picture of kinetic Alfvén waves presented in Hollweg [29] by identifying various terms in the dielectric tensor that are physically relevant to the fluid picture, such as the polarization drift, Hall effect, and diamagnetic current.

2. DIELECTRIC RESPONSE FRAMEWORK

2.1. Dielectric Tensor

Our starting point is the dielectric tensor $\boldsymbol{\epsilon}$ in the linear Vlasov theory, which gives the dispersion relation through the determinant-zero equation for the wave electric field, $\mathbf{D}(\vec{k},\omega)\cdot\vec{E}=0$, or explicitly (cf. Equation 73, Chapter 10 in Stix [30]),

$$\begin{bmatrix} \epsilon_{xx}-N_\parallel^2 & \epsilon_{xy} & \epsilon_{xz}+N_\parallel N_\perp \\ -\epsilon_{xy} & \epsilon_{yy}-N^2 & \epsilon_{yz} \\ \epsilon_{xz}+N_\parallel N_\perp & -\epsilon_{yz} & \epsilon_{zz}-N_\perp^2 \end{bmatrix} \begin{bmatrix} E_x \\ E_y \\ E_z \end{bmatrix} = 0. \quad (1)$$

Here the dispersion matrix $\mathbf{D}$ depends on the refraction indices $N_\parallel = k_\parallel c/\omega$, $N_\perp = k_\perp c/\omega$, and $N = kc/\omega$, and most importantly, the dielectric tensor $\boldsymbol{\epsilon}$. A total refraction index, $N^2 = N_\perp^2 + N_\parallel^2$, appears in the diagonal elements in Equation (1). We use the coordinate system spanning the mean magnetic field in the z-direction and the wavevector in the x-z-plane (denoted by $\vec{k} = (k_x, 0, k_z) = k_\perp, 0, k_\parallel)$). Frequencies are assumed to be sufficiently smaller than the ion cyclotron frequency, $\omega \ll \Omega_i$, where $\Omega_i = eB_0/m_i$. Wavevectors are highly oblique to the mean magnetic field such that $k_\parallel \ll k_\perp$ holds.

Essential information on the wave properties is included in the dielectric tensor, e.g., dispersion relation, fluctuation sense of the wave electric and magnetic field. The elements of dielectric tensor for the kinetic Alfvén mode are evaluated in the paper by Lysak and Lotko [31], which can be simplified in the following way in the spirit of deriving the fluid-picture property of the wave

$$\epsilon_{xx} = 1 + \frac{c^2}{V_A^2}\left(1 - \frac{3}{4}\mu_i\right) \quad (2)$$

$$\epsilon_{yy} = 1 + \frac{c^2}{V_A^2} - \frac{\beta}{2}\frac{k_\perp^2 c^2}{\omega^2} \quad (3)$$

$$\epsilon_{zz} = 1 + \frac{1}{k_\parallel^2 \lambda_{De}^2} \quad (4)$$

$$\epsilon_{xy} = \mathrm{i}\frac{c^2}{V_A^2}\frac{\Omega_i}{\omega}\left(-1 + \frac{3}{2}\mu_i\right) \quad (5)$$

$$\epsilon_{yz} = -\frac{\mathrm{i}}{2}\frac{k_\perp}{k_\parallel}\frac{c^2}{V_A^2}\frac{\Omega_i}{\omega}\left(-1 + \frac{3}{2}\mu_i\right) = -\frac{1}{2}\frac{k_\perp}{k_\parallel}\epsilon_{xy} \quad (6)$$

$$\epsilon_{xz} = -\frac{1}{2}\frac{c^2}{V_A^2}\frac{k_\parallel}{k_\perp}\mu_i. \quad (7)$$

Here, ϵ_{xx} represents an extended form of the current for the polarization drift c^2/V_A^2 by correcting for the thermal motion in the perpendicular direction. The argument μ_i is defined as $\mu_i = k_\perp^2 r_{gi}^2$, which is the square of the perpendicular wavenumbers normalized to the gyroradius of the thermal ions $r_{gi} = v_{th,i}/\Omega_i$ (here $v_{th,i} = (k_B T_i/m_i)^{1/2}$ is the ion thermal speed and Ω_i the ion gyro-frequency). The plasma beta β is defined for both ions and electrons in an additive way, $\beta = 2\mu_0 n k_B (T_i + T_e)/B_0^2$. Quasi-neutrality is assumed, too.

The dielectric tensor method has been used in order to derive the properties of kinetic Alfvén mode fluctuations [32–36]. For example, Boldyrev et al. [34] presents the dielectric tensor method for both the kinetic Alfvén and the whistler modes. Passot and Sulem [36] discuss limits and full expressions for certain fluctuations. Our approach puts an emphasis on retaining the thermal correction (finite Larmor radius) to the polarization current in ϵ_{xx} (Equation 2) and extending the kinetic Alfvén mode to higher frequencies at about the ion cyclotron frequency in ϵ_{yy}, ϵ_{xy}, and ϵ_{yz} (Equations 3–6). We also use the notation with the Alfvén speed in the dielectric tensor using the relation $c^2/V_A^2 = \omega_{pi}^2/\Omega_i^2$, where ω_{pi} and Ω_i denote the ion plasma frequency and ion cyclotron frequency, respectively.

We treat a low-beta plasma case in deriving the properties of kinetic Alfvén mode. The diagonal elements of the dielectric tensor represent the plasma response for three different modes in the low-frequency domain: ϵ_{xx} represents the shear Alfvén mode (through the polarization drift), ϵ_{yy} the fast magnetosonic mode, and ϵ_{zz} the ion acoustic mode, respectively. The off-diagonal elements represent couplings among these modes. In particular, the first term in ϵ_{xy} represents a coupling of the Alfvén mode (incompressible mode) with the fast mode (compressible mode) through the Hall current and the second term a coupling through the diamagnetic current (see Appendix A for the comparison with the fluid picture). The off-diagonal elements relative to the diagonal elements become increasingly more important at shorter wavelengths. For example, the ratio of the xy to xx elements increases quadratically as a function of the perpendicular wavenumber in the dispersive range (retaining the diamagnetic current and simplifying the dispersion relation into $\omega^2 = k_\parallel^2 V_A^2 k_\perp^2 r_{gi}^2 \left(\frac{3}{4} + \frac{T_e}{T_i}\right)$) as

$$\left|\frac{\epsilon_{xy}^{(dm)}}{\epsilon_{xx}}\right| \simeq \frac{3}{2}\tan\theta\frac{v_{th,i}}{V_A}\left(\frac{3}{4} + \frac{T_e}{T_i}\right)^{-1/2}\left(1 + \frac{3}{4}k_\perp^2 r_{gi}^2\right), \quad (8)$$

while the ratio in the MHD range (retaining the Hall term and simplifying the dispersion relation into $\omega^2 = k_\parallel^2 V_A$) is estimated as

$$\left|\frac{\epsilon_{xy}^{(h)}}{\epsilon_{xx}}\right| \simeq \frac{\Omega_i}{\omega} \simeq \frac{\Omega_i}{k_\parallel V_A}. \quad (9)$$

The dispersion relation is obtained by decoupling of the fast mode from the Alfvén mode and solving the determinant-zero equation for the xx, xz, zx, and zz elements [31].

The dispersion relation of kinetic Alfvén mode is obtained by decoupling from the fast mode (represented by the yy element) and solving the reduced equation containing the Alfvén mode fluctuation or polarization drift (represented by the xx element) and the parallel electron motion (represented by the zz element):

$$\begin{bmatrix} \epsilon_{xx}-N_\parallel^2 & \epsilon_{xz}+N_\parallel N_\perp \\ \epsilon_{xz}+N_\parallel N_\perp & \epsilon_{zz}-N_\perp^2 \end{bmatrix} \begin{bmatrix} E_x \\ E_z \end{bmatrix}. \quad (10)$$

Furthermore, if the coupling term ϵ_{xz} is neglected since the wavevector is nearly perpendicular to the mean magnetic field, the determinant-zero condition is obtained as

$$\epsilon_{xx}\epsilon_{zz} - N_\parallel^2\epsilon_{zz} - N_\perp^2\epsilon_{xx} = 0, \tag{11}$$

from which the dispersion relation reads (Equation 2.44 in Hasegawa and Uberoi [1]):

$$\omega^2 = k_\parallel^2 V_A^2\left[1 + k_\perp^2 r_{gi}^2\left(\frac{3}{4} + \frac{T_e}{T_i}\right)\right]. \tag{12}$$

The electron temperature is higher than the proton temperature in the low-speed solar wind (up to a ratio of 4) and lower in the high-speed solar wind (down to about 0.7) [37], with a mean value of $T_e/T_i = 1.64$ and a median of $T_e/T_i = 1.27$ [38].

If the thermal correction is neglected in the polarization current (i.e., in low-beta plasmas), the dispersion relation is simplified into the following form (Equation E18 in Schekochihin et al. [32]; see also Bian et al. [33], or Passot and Sulem [36]):

$$\omega^2 = k_\parallel^2 V_A^2\left(1 + k_\perp^2\rho_s^2\right), \tag{13}$$

where ρ_s is ion-sound gyro-radius or sonic Larmor radius defined as

$$\rho_s^2 = \frac{T_e}{T_i}r_{gi}^2. \tag{14}$$

The concept of ion-sound radius was introduced in the studies of magnetic reconnection during the late 1960's to early 1970's.

At higher values of beta, thermal correction is needed by keeping the coupling ϵ_{xz}, and in that case, the dispersion relation is extended to the following form

$$\omega^2 = k_\parallel^2 V_A^2\left[1 + k_\perp^2 r_{gi}^2\left[\frac{3}{4} + \frac{T_e}{T_i} - k_\parallel^2 r_{gi}^2\frac{T_e}{T_i}\left(1 + \frac{3}{4}k_\perp^2 r_{gi}^2\right)\right]\right]. \tag{15}$$

The dispersion relation of kinetic Alfvén mode (Equation 15) is graphically presented in **Figure 1** for different values of ion beta and propagation angles to the mean magnetic field. The conventional expression (Equation 12) is valid up to wavenumbers of $k_\perp r_{gi} \sim 3$.

Condition of a constant propagation angle (which is observationally supported by multi-spacecraft wave analyses of solar wind fluctuations, such as Perschke et al. [39] and Roberts et al. [40]) is applied in **Figure 1**. The parallel and perpendicular components of the wavevector are related to the wavevector magnitude by $k_\parallel = k\cos\theta$ and $k_\perp = k\sin\theta$, respectively. Different options are possible to plot the dispersion relations. For example, the frequency can be divided by the product of parallel wavenumber and Alfvén speed as $\omega/(k_\parallel V_A)$ [32]; the dispersion relation may be simplified into $\omega \propto k_\parallel k_\perp$ irrespective of wavevector anisotropy [41]; application of critical balance [42]; and intermittency correction [20].

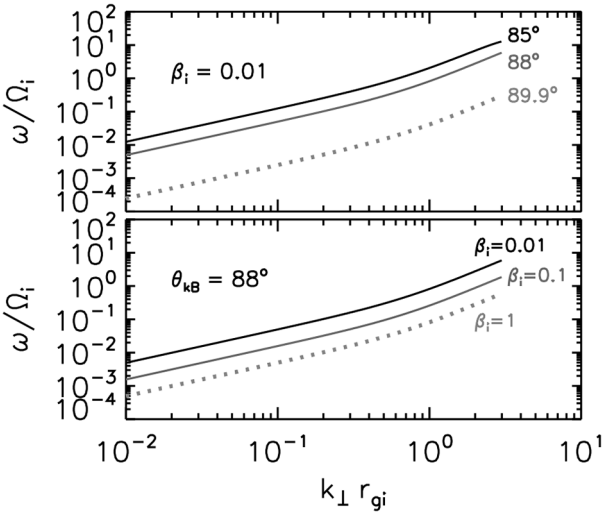

FIGURE 1 | Dispersion relation of kinetic Alfvén mode for different values of ion beta (top) and propagation angles to the mean magnetic field (bottom). Electron-to-ion temperature ratio is set to unity.

2.2. Transport Ratios

2.2.1. Electric Field Polarization

Electric field polarization (field rotation sense around the mean magnetic field) is evaluated by the ratio of the two perpendicular field components, and can directly be obtained from the dispersion tensor as follows:

$$\frac{E_y}{E_x} = \frac{D_{xz}D_{yx} - D_{xx}D_{yz}}{D_{xy}D_{yz} - D_{xz}D_{yy}} \tag{16}$$

$$= \frac{-(\epsilon_{xz} + N_\parallel N_\perp)\epsilon_{xy} - (\epsilon_{xx} - N_\parallel^2)\epsilon_{yz}}{\epsilon_{xy}\epsilon_{yz} - (\epsilon_{xz} + N_\parallel N_\perp)(\epsilon_{yy} - N^2)}, \tag{17}$$

where the dielectric tensor in Equations (2)–(7) is used in deriving Equation (17). Since the yz element of dielectric tensor is proportional to the xy element (Equation 6), the polarization E_y/E_x is proportional to the xy element, $E_y/E_x \propto \epsilon_{xy}$. Change in sense of field rotation is hence associated with the competition between the Hall current and the diamagnetic current.

A more complete expression of the electric field polarization is shown in Appendix B. Approximation at lower wavenumbers $k_\perp r_{gi} < 1$ yet $kd_i > 1$, where $d_i = V_A/\Omega_i$ is the ion inertial length) yields a left-hand polarization (though polarization is highly elliptic)

$$\frac{E_y}{E_x} \simeq i\frac{k_\parallel d_i}{k^2 d_i^2} \tag{18}$$

$$\simeq i\frac{\cos\theta}{kd_i}. \tag{19}$$

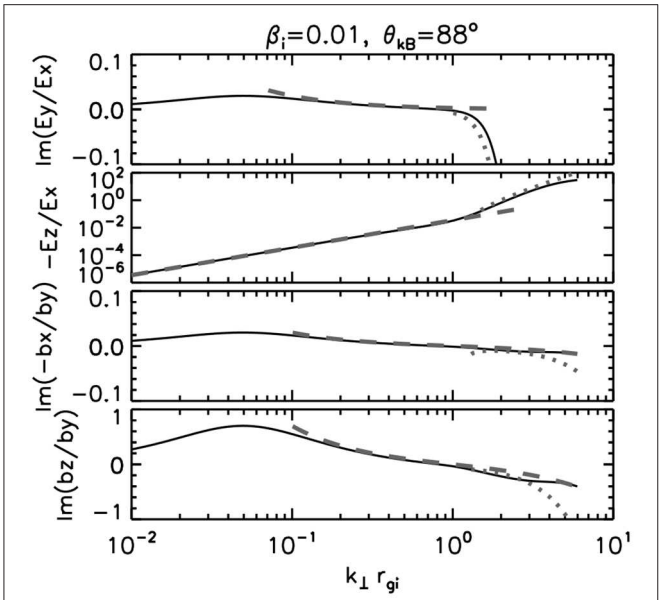

FIGURE 2 | Electric field polarization, parallel electric field, magnetic field polarization, and parallel magnetic field as a function of the perpendicular component of wavevector normalized to the thermal ion gyro-radius. Ion beta 0.01. Propagation angle 88° to the mean magnetic field. Dashed and dotted curves are the low-wavenumber and high-wavenumber approximations, respectively. Electron-to-ion temperature ratio is set to unity. Equations (18), (30), (36), (45) are used for the low-wavenumber approximation (dashed lines). Equations (21), (31), (39), (46) are used for the high-wavenumber approximation (dotted lines).

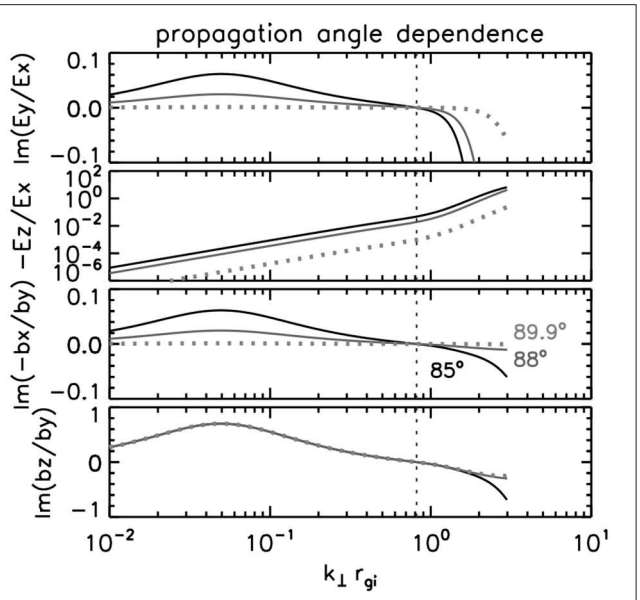

FIGURE 3 | Transport ratios for different values of propagation angle to the mean magnetic field. The parameter set is taken from **Figure 2**.

and approximation at higher wavenumbers ($k_\perp r_{\rm gi} > 1$) yields a right-hand sense of polarization:

$$\frac{E_{\rm y}}{E_{\rm x}} \simeq {\rm i}\frac{3}{4}\frac{v_{\rm th,i}^2}{V_{\rm A}^2}\frac{\omega^3}{\Omega_{\rm i}^3}\left(1-\frac{3}{4}k_\perp^2 r_{\rm gi}^2\right) \tag{20}$$

$$\sim -{\rm i}\frac{9}{16}\frac{v_{\rm th,i}^4}{V_{\rm A}^4}\frac{\omega^3}{\Omega_{\rm i}^3}\tan^2\theta. \tag{21}$$

Electric field polarization is plotted in the top panel of **Figure 2** for the full expression (Equation 17) and the two approximations (Equations 17 and 21).

Dependence on the propagation angle $\theta_{\rm kB} = \tan^{-1}(k_\perp/k_\parallel)$ and the plasma beta (for ions) is displayed in the top panels of **Figures 3**, **4**, respectively. Electric field has a left-hand rotation sense around the mean magnetic field at lower wavenumbers and changes into right-hand rotation sense at $k_\perp r_{\rm gi} = \sqrt{2/3} \simeq 0.816$ and above (marked by vertical dotted lines in **Figures 3**, **4**).

The fluid-picture of field polarization is associated with a simplified version of Equation (17):

$$\frac{E_{\rm y}}{E_{\rm x}} = -\frac{\epsilon_{\rm xy}}{N^2} \tag{22}$$

$$\sim -{\rm i}\frac{\omega}{\Omega_{\rm i}}\frac{\Omega_{\rm i}^2}{k^2 V_{\rm A}^2}\left(-1+\frac{3}{2}k_\perp^2 r_{\rm gi}^2\right) \tag{23}$$

Again, Equation (22) shows that the rotation sense of the wave electric field depends on the sign of the dielectric response $\epsilon_{\rm xy}$, which is a combination of the Hall current with the diamagnetic current.

If the diamagnetic current dominates the dielectric response (or equivalently, when the perpendicular wavenumber is sufficiently large and the electron temperature is lower than that of ions the electric field polarization reduces to that in the fluid picture,

$$\frac{E_{\rm y}}{E_{\rm x}} = -\frac{\epsilon_{\rm xy}^{\rm (dm)}}{N^2} \tag{24}$$

$$= -{\rm i}\frac{3}{2}\frac{\omega}{\Omega_{\rm i}}\frac{\Omega_{\rm i}^2}{k^2 V_{\rm A}^2}k_\perp^2 r_{\rm gi}^2 \tag{25}$$

$$= -{\rm i}\frac{3}{2}\frac{\omega}{\Omega_{\rm i}}\frac{v_{\rm th,i}^2}{V_{\rm A}^2} \tag{26}$$

Equation (23) can be compared with that obtained from the fluid-theoretical approach Equation (46) in Hollweg [29]. Note that Equation (23) is a measure of the out-of-plane component of electric field (to the plane spanning the mean magnetic field and the wavevector) relative to the in-plane component. The inversion of $E_{\rm y}/E_{\rm x}$ from Hollweg's result reflects different choices of the coordinate system Hollweg's paper takes the perpendicular component of wavevector as the y direction, while our paper takes that component as the x direction. The factor 3/2 in Equation 23) originates in the different use of temperature. Hollweg's paper uses the temperature through the sound speed $c_{\rm s}$ by including both the ion and the electrons thermal motions with the respective polytropic index γ, while our paper uses the temperature through the ion thermal speed. Our paper does

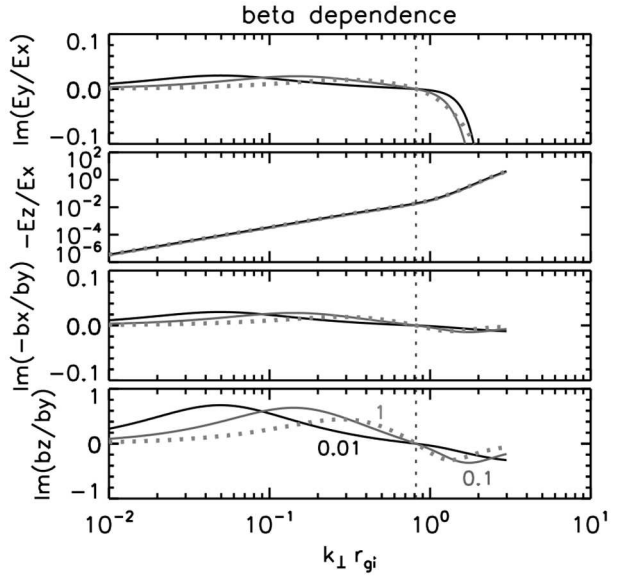

FIGURE 4 | Transport ratios for different values of ion beta. The parameter set is taken from **Figure 2**.

not include the electron thermal effect (such as diamagnetic drift) in the perpendicular direction. Hollweg's result is obtained by replacing $3/2v_{\mathrm{th,i}}^2$ by c_s^2. The factor 3/2 them arises when considering the longitudinal ion motion in the ion sound speed (which makes a factor of $\gamma = 3$) and the two perpendicular components (x and y components) in the ion gyro-motion in the definition of ion thermal speed (which makes a factor of 1/2). Field (temporal) rotation is right-hand, which has the same sense as electron gyro-motion as presented by Gary [43] and Hollweg [29]. If the Hall current dominates, however, the field rotation flips to the left-hand polarized sense.

2.2.2. Parallel Electric Field

The parallel component of electric field is obtained in the same fashion as the polarization in the xy plane. The relation to the dielectric (or dispersion) tensor is

$$\frac{E_z}{E_x} = \frac{D_{xy}D_{zx} - D_{xx}D_{zy}}{D_{xz}D_{zy} - D_{xy}D_{zz}}. \tag{27}$$

Again, the full expression of the ratio E_z/E_x is shown in Appendix B. If the value of beta is sufficiently low, the parallel ratio E_z/E_x is expressed as:

$$\frac{E_z}{E_x} = -\frac{k_\parallel}{k_\perp}\left[\frac{3}{2} - \frac{1}{2}\frac{\omega^2}{k_\parallel^2 V_A^2}\left(1 - \frac{3}{4}k_\perp^2 r_{gi}^2\right)\right] \times \left[-\frac{3}{2} + \frac{\omega^2}{k_\parallel^2 V_A^2}\frac{1}{k_\perp^2 r_{gi}^2 T_e/T_i}\right]^{-1}. \tag{28}$$

Approximation at lower wavenumbers ($k_\perp r_{gi} < 1$) is

$$\frac{E_z}{E_x} \simeq -\frac{T_e}{T_i}k_\parallel k_\perp r_{gi}^2 \tag{29}$$

$$\simeq -\tan\theta\frac{T_e}{T_i}k_\perp^2 r_{gi}^2 \tag{30}$$

and that at higher wavenumbers ($k_\perp r_{gi} > 1$) is

$$\frac{E_z}{E_x} \simeq \frac{1}{2\tan\theta}\left(\frac{3}{4} + \frac{T_e}{T_i}\right)\left[-\frac{3}{2} + \left(\frac{3}{4} + \frac{T_e}{T_i}\right)\left(\frac{T_e}{T_i}\right)^{-1}\right]^{-1} \times k_\perp^2 r_{gi}^2\left(1 - \frac{3}{4}k_\perp^2 r_{gi}^2\right). \tag{31}$$

Equations (28), (30), and (31) are displayed in the second panel of **Figure 2**. The parallel electric field becomes more significant at larger wavenumbers, and exceeds the perpendicular electric field when $k_\perp r_{gi} > 2$, particularly when the wavevector has a moderate deviation from the perpendicular direction (e.g., 85 and 88° in **Figure 3** irrespective of the values of beta (**Figure 4**).

The fluid-approach derivation by Hollweg [29] is obtained as follows:

$$\frac{E_z}{E_x} = -\frac{N_\parallel N_\perp - N_\parallel^2\left(\frac{\omega^2}{k_\parallel V_A^2} - 1\right)\frac{1}{2}\frac{k_\perp}{k_\parallel}}{\left(\frac{1}{k_\parallel^2\lambda_{De}^2} - N_\perp^2 - N_\parallel N_\perp\frac{1}{2}\frac{k_\perp}{k_\parallel}\right)} \tag{32}$$

$$= \frac{\left(\frac{m_e}{m_i}\frac{\omega^2}{k_\parallel^2}\frac{v_{th,e}^2}{V_A^2} - \frac{k_B T_e}{m_i}\right)k_\parallel k_\perp}{\Omega_i^2\left(1 + k_\perp^2\rho_L^2\right)} \tag{33}$$

The low-wavenumber approximation can be derived in a more simplified way:

$$\frac{E_z}{E_x} \simeq -\frac{D_{zx}}{D_{zz}} = -\frac{T_e}{T_i}k_\parallel k_\perp r_{gi}^2. \tag{34}$$

Equation (34) reproduces the second term (leading term) in Equation (16) in Hollweg [29]. The parallel electric field expression E_z/E_x enters directly the dispersion relation, and is essentially proportional to $k_\parallel k_\perp$ normalized to the (fictitious) ion gyroradius using the electron temperature.

2.2.3. Magnetic Field Polarization

Magnetic field polarization is related to the parallel electric field E_z/E_x and the electric field polarization E_y/E_x through the induction equation, $\delta\vec{B} = \omega^{-1}\vec{k}\times\vec{E}$. By noting that the wavevector is in the x–z plane, $\vec{k} = (k_\perp, 0, k_\parallel)$, we define the magnetic field polarization as the imaginary part of $-\delta B_x/\delta B_y$ because δB_y is the most significant component in the fluctuating magnetic field. In the definition above, the positive value of imaginary part of $-\delta B_x/\delta B_y$ corresponds to the left-hand (temporal) rotation sense around the mean magnetic field in an agreement with the construction of the electric field polarization. We obtain the magnetic field polarization as follows.

$$-\frac{\delta B_x}{\delta B_y} = \frac{E_y}{E_x}\left(1 - \frac{k_\perp}{k_\parallel}\frac{E_z}{E_x}\right)^{-1}. \tag{35}$$

At lower wavenumbers ($k_\perp r_{\rm gi} < 1$), the polarization is obtained using Equations (18) and (29) as:

$$-\frac{\delta B_{\rm x}}{\delta B_{\rm y}} \simeq {\rm i}\frac{1}{\tan\theta}\frac{1}{kd_{\rm i}}\left(1-\frac{T_{\rm e}}{T_{\rm i}}k_\perp^2 r_{\rm gi}^2\right). \tag{36}$$

In fact, Equation (36) turns out to be a valid expression even at higher wavenumbers ($k_\perp r_{\rm gi} > 1$) (dashed line in the third panel of **Figure 2**). In the fluid picture, when the diamagnetic current dominates at higher wavenumbers, the magnetic field polarization is obtained in a simpler way from Equations (26) and (34):

$$-\frac{\delta B_{\rm x}}{\delta B_{\rm y}} = -{\rm i}\frac{3}{2}\frac{v_{\rm th,i}^2}{V_{\rm A}^2}\frac{\omega}{\Omega_{\rm i}}\left(1+\frac{T_{\rm e}}{T_{\rm i}}k_\perp^2 r_{\rm gi}^2\right)^{-1} \tag{37}$$

$$\simeq -{\rm i}\frac{3}{2}\frac{k_\parallel^2 v_{\rm th,i}^2}{\omega\Omega_{\rm i}}, \tag{38}$$

where the frequency is approximated to $\omega \sim k_\parallel V_{\rm A}(1 + k_\perp r_{\rm gi}(T_{\rm e}/T_{\rm i})^{1/2})$ in Equation (38). The polarization at higher wavenumbers ($k_\perp r_{\rm gi} > 1$) is obtained using Equations (21) and (31) as:

$$-\frac{\delta B_{\rm x}}{\delta B_{\rm y}} \simeq {\rm i}\frac{9}{16}\frac{v_{\rm th,i}^4}{V_{\rm A}^4}\frac{\omega^3}{\Omega_{\rm i}^3}\frac{\tan^2\theta}{Ck_\perp^2 r_{\rm gi}^2\left(1-\frac{3}{4}k_\perp^2 r_{\rm gi}^2\right)}, \tag{39}$$

where the coefficient C is a numerical factor defined as

$$C = \frac{1}{2}\left(\frac{3}{4}+\frac{T_{\rm e}}{T_{\rm i}}\right)\left[-\frac{3}{2}+\left(\frac{3}{4}+\frac{T_{\rm e}}{T_{\rm i}}\right)\left(\frac{T_{\rm e}}{T_{\rm i}}\right)^{-1}\right]^{-1}. \tag{40}$$

Equation (39), however, turns out to be valid only in a narrow range of wavenumbers (dotted line for $2 < k_\perp r_{\rm gi} < 3$ in the third panel of **Figure 2**). The low-wavenumber approximation (Equation 36) gives a more practical expression of magnetic field polarization.

Magnetic field polarization is plotted in the third panel of **Figure 2**. The field rotation sense of the fluctuating magnetic field inherits the polarization of the electric field, that is left-hand polarized around the mean magnetic field at lower wavenumbers and right-hand polarized at higher wavenumbers. Turnover of the rotation sense occurs at $k_\perp r_{\rm gi} = \sqrt{2/3} \simeq 0.816$. The polarization profile is persistent over different propagation angles (**Figure 3**) and different values of beta (**Figure 4**). Another change in the field rotation sense is associated with the value of beta and the ratio of electron to ion temperature. See the full expression of the magnetic field polarization is presented in Appendix B. A more complete and convenient expression of the polarization exhibiting the secondary change in the field rotation sense is

$$-\frac{\delta B_{\rm x}}{\delta B_{\rm y}} = -{\rm i}\frac{\omega\Omega_{\rm i}}{k^2 V_{\rm A}^2}\left(1-\frac{1}{2}\frac{T_{\rm e}}{T_{\rm i}}k_\perp^2 r_{\rm gi}^2\right)\left(-1+\frac{3}{2}k_\perp^2 r_{\rm gi}^2\right)$$
$$\left(1+\frac{T_{\rm e}}{T_{\rm i}}k_\perp^2 r_{\rm gi}^2\right)\times\left[k_\perp^2 r_{\rm gi}^2\left(\frac{\omega^2}{k_\parallel^2 V_{\rm A}^2}-2\frac{T_{\rm e}}{T_{\rm i}}\right)-1\right]^{-1}. \tag{41}$$

2.2.4. Parallel Magnetic Field

The parallel component of fluctuating magnetic field $\delta B_{\rm z}$ in relation to the in-plane perpendicular component $\delta B_{\rm x}$ is obtained from the induction equation,

$$\frac{\delta B_{\rm z}}{\delta B_{\rm x}} = -\frac{k_\perp}{k_\parallel}. \tag{42}$$

Equation (42) can also be derived from the divergence-free equation for the fluctuating magnetic field, $\vec{k}\cdot\delta\vec{B} = 0$. The x component, $\delta B_{\rm x}$, has the smallest amplitude among the three components of fluctuating magnetic field since the wavevector is nearly in the x direction.

The ratio of $\delta B_{\rm z}$ to $\delta B_{\rm y}$ is obtained from the induction equation as

$$\frac{\delta B_{\rm z}}{\delta B_{\rm y}} = \frac{k_\perp}{k_\parallel}\frac{E_{\rm y}}{E_{\rm x}}\left(1-\frac{k_\perp}{k_\parallel}\frac{E_{\rm z}}{E_{\rm x}}\right)^{-1}. \tag{43}$$

Alternatively, it is more useful to estimate the ratio $\delta B_{\rm z}/\delta B_{\rm y}$ over the in-plane component $\delta B_{\rm x}$:

$$\frac{\delta B_{\rm z}}{\delta B_{\rm y}} = \frac{\delta B_{\rm z}}{\delta B_{\rm x}}\frac{\delta B_{\rm x}}{\delta B_{\rm y}}. \tag{44}$$

The ratio $\delta B_{\rm z}/\delta B_{\rm y}$ at lower wavenumbers is then obtained using Equations (42) and (36)

$$\frac{\delta B_{\rm z}}{\delta B_{\rm y}} \simeq {\rm i}\frac{1}{kd_{\rm i}}\left(1-\frac{T_{\rm e}}{T_{\rm i}}k_\perp^2 r_{\rm gi}^2\right). \tag{45}$$

And the ratio at higher wavenumbers is obtained using Equations (42) and (39)

$$\frac{\delta B_{\rm z}}{\delta B_{\rm y}} \simeq {\rm i}\frac{9}{16}\frac{v_{\rm th,i}^4}{V_{\rm A}^4}\frac{\omega^3}{\Omega_{\rm i}^3}\frac{\tan^3\theta}{Ck_\perp^2 r_{\rm gi}^2\left(1-\frac{3}{4}k_\perp^2 r_{\rm gi}^2\right)}. \tag{46}$$

The bottom panel in **Figure 2** displays the magnetic field polarization as a function of the perpendicular wavenumber (normalized to the thermal ion gyroradius) for the exact expression (Equation 43) and the two approximations (Equations 45 and 46). The parallel (or compressive) component of fluctuating magnetic field is not small but competes against the out-of-plane (incompressible) component, $\delta B_{\rm y}$ both at lower and higher wavenumbers. When the Hall current dominates at lower wavenumbers, the fluctuation sense of parallel magnetic field is left-hand polarized around the x direction or virtually around the wavevector). When the diamagnetic current dominates at higher wavenumbers, the fluctuation sense is right-hand polarized around the x direction. The change in the polarization sense is the same as that of $E_{\rm y}/E_{\rm x}$ and $-B_{\rm x}/E_{\rm y}$. and the turnover of fluctuation sense occurs at $k_\perp r_{\rm gi} = \sqrt{2/3}$ irrespective of propagation angles (**Figure 3**). Like the magnetic field polarization study above, the fitting quality of low-wavenumber approximation (Equation 45, dashed line) turns out to be valid even at higher wavenumbers while that of high-wavenumber approximation (Equation 46, dotted line) degrades at $k_\perp r_{\rm gi} > 3$.

The ratio $\delta B_z/\delta B_y$ can reach a value of about 0.7 at lower wavenumbers ($k_\perp r_{gi} < 1$). The reason for this is that the electric field polarization E_y/E_x becomes amplified by a factor of $\tan\theta$. The peak wavenumber shifts with the increasing value of beta (**Figure 4**), indicating that the compressibility peak at lower wavenumbers is associated with the Hall current around the ion inertial length. Note that the ratio of ion inertial length d_i to the thermal ion gyro-radius is $d_i/r_{gi} = \sqrt{\beta_i/2}$ in our definition of thermal velocity $v_{th,i}^2 = k_B T_i/m_i$.

In the fluid picture, when the diamagnetic current dominates at higher wavenumbers, the parallel component of fluctuating magnetic field is estimated using Equations (37), (42), and (44):

$$\frac{\delta B_z}{\delta B_y} = -i\frac{3}{2}\frac{k_\perp}{k_\parallel}\frac{v_{th,i}^2}{V_A^2}\frac{\omega}{\Omega_i}\left(1+\frac{T_e}{T_i}k_\perp^2 r_{gi}^2\right)^{-1}. \quad (47)$$

The reversal of fluctuation sense from the low-wavenumber domain (Equation 45) is clear in Equation (47).

A useful quantity in the observational studies is the squared ratio of parallel fluctuation to the total fluctuation, which is approximated to $|\delta B_z|^2/|\delta B_y|^2$ at wavelengths around the ion gyro-radius. The y component is dominant among the three components of fluctuating magnetic field. The magnetic field compression is estimated using Equation (47) as:

$$\frac{|\delta B_z|^2}{|\delta B_{total}|^2} \sim \frac{|\delta B_z|^2}{|\delta B_y|^2} \sim \frac{9}{4}\frac{v_{th,i}^2}{V_A^2}k_\perp^2 r_{gi}^2\left(1+\frac{T_e}{T_i}k_\perp^2 r_{gi}^2\right)^{-1}. \quad (48)$$

Equations (38), (42), and (48) are in a good agreement with the numerical results, such as hodograms in Pucci et al. [44] and Vásconez et al. [12].

2.2.5. E–B Ratios

The ratio of electric to magnetic field fluctuations (hereafter, the E-B ratio) also serves as a useful quantity to diagnose the wave property. The E-B ratios can be expressed by a combination of the frequencies, wavenumbers, and ratios of electric field components. For example, the ratio of E_y to δB_x and that to δB_z are obtained directly from the induction equation:

$$\frac{E_y}{\delta B_x} = -\frac{\omega}{k_\parallel} \quad (49)$$

$$\frac{E_y}{\delta B_z} = -\frac{\omega}{k_\perp}. \quad (50)$$

The ratio $E_x/\delta B_y$ is obtained as

$$\frac{E_x}{\delta B_y} = \frac{E_x}{E_y}\frac{E_y}{\delta B_x}\frac{\delta B_x}{\delta B_y} \quad (51)$$

$$= \frac{\omega}{k_\parallel}\left(1-\frac{k_\perp}{k_\parallel}\frac{E_z}{E_x}\right)^{-1}, \quad (52)$$

where Equations (35) and (49) are used in deriving Equation (52). The ratio $E_x/\delta B_z$ is obtained, by using Equations (49) and (42), as

$$\frac{E_x}{\delta B_z} = \frac{E_x}{E_y}\frac{E_y}{\delta B_x}\frac{\delta B_x}{\delta B_z} \quad (53)$$

$$= \frac{\omega}{k_\perp}\frac{E_x}{E_y}. \quad (54)$$

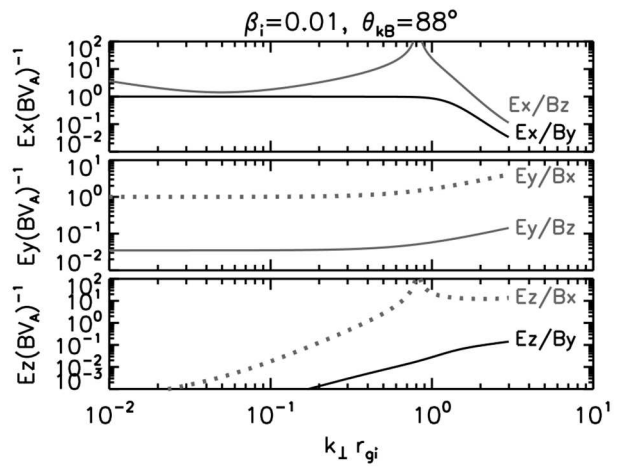

FIGURE 5 | Ratios of the electric field to the fluctuating magnetic field for various combinations.

The ratios $E_z/\delta B_x$ and $E_z/\delta B_y$ are, respectively,

$$\frac{E_z}{\delta B_x} = \frac{E_z}{E_x}\frac{E_x}{E_y}\frac{E_y}{\delta B_x} \quad (55)$$

$$= -\frac{\omega}{k_\parallel}\frac{E_z}{E_x}\frac{E_x}{E_y} \quad (56)$$

and

$$\frac{E_z}{\delta B_y} = \frac{E_z}{E_x}\frac{E_x}{\delta B_y} \quad (57)$$

$$= \frac{\omega}{k_\parallel}\frac{E_z}{E_x}\left(1-\frac{k_\perp}{k_\parallel}\frac{E_z}{E_x}\right)^{-1}. \quad (58)$$

Absolute values of the E-B ratios are normalized to the Alfvén speed V_A and plotted as a function of perpendicular wavenumber $k_\perp r_{gi}$ in **Figure 5**. $E_x/\delta B_z$ and $E_z/\delta B_x$ exhibit a singularity at $k_\perp r_{gi} = \sqrt{2/3}$. $E_x/\delta B_y$ is the dominant component and has a significant contribution when the electric field energy is divided by the total magnetic field fluctuation energy, $|E_x|^2/(|\delta B_x|^2 + |\delta B_y|^2 + |\delta B_z|^2)$ (**Figure 6** top panel). $E_y/\delta B_x$ and $E_y/\delta B_x$ essentially represent the phase speed in the parallel and perpendicular directions to the mean magnetic field, respectively. $E_z/\delta B_y$ is a measure of parallel electric field, and dominates eventually the electric field at higher wavenumbers when plotting $|E_z|^2/(|\delta B_x|^2 + |\delta B_y|^2 + |\delta B_z|^2)$ (**Figure 6** top panel).

The ratio of E_y to δB_y is also of great interest because the both field components are the leading ones in the kinetic domain. Using the induction equation (Equation 49) and the diamagnetic current type magnetic field polarization (Equation 37), the ratio $E_y/\delta B_y$ (with normalization to the Alfvén speed) is

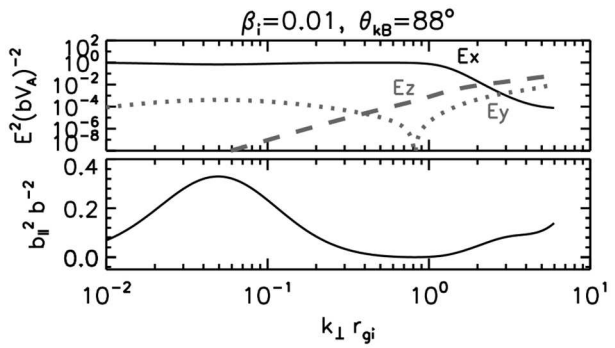

FIGURE 6 | Ratios of the electric field energy to the total magnetic field fluctuation energy (top) and parallel magnetic field energy relative to the total magnetic field fluctuation energy (bottom).

obtained as

$$\frac{1}{V_\mathrm{A}}\frac{E_\mathrm{y}}{\delta B_\mathrm{y}} = \frac{E_\mathrm{y}}{\delta B_\mathrm{x}}\frac{\delta B_\mathrm{x}}{\delta B_\mathrm{y}} \tag{59}$$

$$\simeq -\mathrm{i}\frac{3}{2}\frac{v_{\mathrm{th,i}}^2}{V_\mathrm{A}^2}\frac{k_\parallel V_\mathrm{A}}{\Omega_\mathrm{i}}\left(\frac{3}{4}+\frac{T_\mathrm{e}}{T_\mathrm{i}}\right)\left(\frac{T_\mathrm{e}}{T_\mathrm{i}}\right)^{-1}. \tag{60}$$

By introducing $\tan\theta = k_\perp/k_\parallel$, the squared ratio of Equation (60) is obtained as

$$\frac{1}{V_\mathrm{A}^2}\left|\frac{E_\mathrm{y}}{\delta B_\mathrm{y}}\right|^2 = \frac{9}{4}\frac{v_{\mathrm{th,i}}^2}{V_\mathrm{A}^2}\frac{1}{\tan^2\theta}k_\perp^2 r_\mathrm{gi}^2\left(\frac{3}{4}+\frac{T_\mathrm{e}}{T_\mathrm{i}}\right)^2\left(\frac{T_\mathrm{e}}{T_\mathrm{i}}\right)^{-2}. \tag{61}$$

Equation (61) indicates that the E_y energy spectrum is flatter than the δB_y spectrum by $k_\parallel^2 = k_\perp^2/\tan^2\theta$ (see section 2.3).

2.2.6. Density Fluctuation

The species-wise density fluctuation can be computed through the continuity equation, $\omega\delta n_\mathrm{s} + n_{0,\mathrm{s}}\vec{k}\cdot\vec{u}_\mathrm{s} = 0$, where the flow velocity $\vec{u}_\mathrm{s}$ is associated with the wave electric field through the current density, $\vec{j}_\mathrm{s} = q_\mathrm{s}n_\mathrm{s}\vec{u}_\mathrm{s}$, and Ohm's law, $\vec{j}_\mathrm{s} = \boldsymbol{\sigma}_\mathrm{s}\vec{E}$ as follows (cf., Gary [43]),

$$\vec{u}_\mathrm{s} = -\mathrm{i}\omega\epsilon_0\frac{1}{q_\mathrm{s}n_\mathrm{s}}\left(\boldsymbol{\epsilon}_\mathrm{s}-\boldsymbol{I}\right)\vec{E}. \tag{62}$$

Note that the conductivity is related to the dielectric tensor through $\boldsymbol{\sigma}_\mathrm{s} = -\mathrm{i}\omega\epsilon_0\left(\boldsymbol{\epsilon}_\mathrm{s}-\boldsymbol{I}\right)$. The density fluctuation is linearly proportional to the electric field (through the tensor operation). To obtain the squared density fluctuation in an independent way from the electric field, one may normalize the density fluctuation to the parallel magnetic field fluctuation,

$$\frac{\langle\delta n_\mathrm{s}^2\rangle}{n_{0,\mathrm{s}}^2}\frac{B_0^2}{\langle\delta B_\parallel^2\rangle} = \frac{\Omega_\mathrm{s}^2}{\omega_\mathrm{ps}^4}\frac{1}{\langle\delta B_\parallel^2\rangle}|\vec{k}\cdot\left(\boldsymbol{\epsilon}_\mathrm{s}-\boldsymbol{I}\right)\vec{E}|^2 \tag{63}$$

$$= \frac{\Omega_\mathrm{s}^2}{\omega_\mathrm{ps}^4}\frac{\omega^2}{k_\mathrm{x}^2}\frac{|\vec{k}\cdot\left(\boldsymbol{\epsilon}_\mathrm{s}-\boldsymbol{I}\right)\vec{E}|^2}{E_\mathrm{y}^2}. \tag{64}$$

The ion compressibility is contributed largely by E_x since the parallel electric field is smaller than the perpendicular one, $E_\mathrm{z} \ll E_\mathrm{x}$, and the ion compressibility is approximated to

$$\frac{\langle\delta n_\mathrm{i}^2\rangle}{n_{0,\mathrm{i}}^2}\frac{B_0^2}{\langle\delta B_\parallel^2\rangle} = \frac{4}{9}\frac{V_\mathrm{A}^4}{v_{\mathrm{th,i}}^4}, \tag{65}$$

which essentially agrees with the fluid-derivation except for a factor of $\frac{4}{9}$. This factor is obtained by expressing the temperature not with the thermal velocity but with the sound speed by replacing $3v_{\mathrm{th,i}}/2$ by c_s in Equation (14) in Hollweg [29]. One may extend the expression in Equation 65 by correcting for the ion thermal motion and multiplying a factor of $\left(1-\frac{3}{4}\mu_\mathrm{i}\right)^2$ on the right hand side of Equation (65), which reproduces Equation (22) in Hollweg [29]. The electron compressibility is related to the parallel electric field. The leading term is $k_\mathrm{z}(\epsilon_{zz}-1)E_\mathrm{z}$, yielding the electron compressibility in the same form as Equation (65).

The relation of density fluctuation to the E_x component is

$$\frac{\delta n_\mathrm{i}}{n_{0,\mathrm{i}}} = -\mathrm{i}\frac{k_\perp V_\mathrm{A}}{\Omega_\mathrm{i}}\frac{E_\mathrm{x}}{V_\mathrm{A}B_0} = \mathrm{i}\frac{V_\mathrm{A}^2}{c^2}\frac{d_\mathrm{i}}{\lambda_\mathrm{De}}\frac{1}{k_\parallel\lambda_\mathrm{De}}\frac{E_\mathrm{z}}{V_\mathrm{A}B_0}, \tag{66}$$

where we introduced the ion inertial length $d_\mathrm{i} = V_\mathrm{A}/\Omega_\mathrm{i}$ and used Equation (34). Equation (66) holds for the electrons, too.

2.3. Spectral Signature

The analytic expressions for the kinetic Alfvén mode properties are useful in interpreting results from observations and numerical simulations for kinetic Alfvén turbulence by, e.g., Howes et al. [9], Passot et al. [10]), Franci et al. [13], Told et al. [15], Valentini et al. [19]. Cerri et al. [23], Grošelj et al. [26]). Perrone et al. [21], and Cerri et al. [27]. In some limited cases, the analytic expressions are also useful to estimate the energy spectra for the kinetic Alfvén mode, assuming the turbulent field is primarily composed of linear-mode waves. The ratio of fluctuation energies of the electric field ($|E_\mathrm{x}|^2$, $|E_\mathrm{y}|^2$, $|E_\mathrm{z}|^2$) to that of the total magnetic field fluctuation ($|\delta B_\mathrm{total}|^2 = |\delta B_\mathrm{x}|^2 + |\delta B_\mathrm{y}|^2 + \delta B_\mathrm{z}|^2$) (**Figure 6**) indicate that the x and z components of electric field can be expressed by a scaling law. The x component of electric field to the magnetic field fluctuation is, with the help of Equation (29), written as:

$$\frac{|E_\mathrm{x}|^2}{|\delta B_\mathrm{total}|^2} \simeq \frac{|E_\mathrm{x}|^2}{|\delta B_\mathrm{y}|^2} \tag{67}$$

$$\propto \begin{cases} V_\mathrm{A}^2 & (k_\perp r_\mathrm{gi} < 1) \\ \left(\frac{3}{4}+\frac{T_\mathrm{e}}{T_\mathrm{i}}\right)V_\mathrm{A}^2 k_\perp^{-2} r_\mathrm{gi}^{-2} & (k_\perp r_\mathrm{gi} \sim 1) \end{cases} \tag{68}$$

The y component of electric field becomes larger than x at even higher wavenumbers, and the energy ratio to the magnetic field is (using Equation 61)

$$\frac{|E_\mathrm{y}|^2}{|\delta B_\mathrm{total}|^2} \simeq \frac{|E_\mathrm{y}|^2}{|\delta B_\mathrm{y}|^2} \tag{69}$$

$$\propto \frac{v_{\mathrm{th,i}}^2 k_\perp^2 r_\mathrm{gi}^2}{\tan^2\theta} \quad (k_\perp r_\mathrm{gi} > 1). \tag{70}$$

The z component using Equations (29) and (31) as:

$$\frac{|E_z|^2}{|\delta B_{\rm total}|^2} \simeq \frac{|E_z|^2}{|\delta B_y|^2} \tag{71}$$

$$\propto \begin{cases} (\frac{T_e}{T_i})^2 V_A^2 k_\parallel^2 k_\perp^2 r_{gi}^4 & (k_\perp r_{gi} < 1) \\ \left(\frac{3}{4} + \frac{T_e}{T_i}\right) V_A^2 k_\parallel^2 r_{gi}^2 & (k_\perp r_{gi} > 1) \end{cases} \tag{72}$$

Different scenarios are possible to assess $k_\parallel$ in the scaling law:

1. Filamentation. A parallel-propagating Alfvén wave interacts with a density perturbation in the perpendicular plane to the mean magnetic field and the wave-wave interaction generates daughter waves which propagate in highly oblique directions to the mean field. If the density perturbation has a vanishing parallel wavenumber, the daughter waves retain the parallel wavenumber of the pump Alfvén wave (e.g., [45]). In the filamentation scenario, the parallel wavenumber is a constant,

$$k_\parallel = \text{const.} \tag{73}$$

2. Constant propagation angle. Multi-spacecraft observations indicate that the treatment of constant propagation angle over a wider range of wavenumbers is a valid assumption for dominant wave components in the solar wind [39, 40].

$$k_\parallel = \frac{k_\perp}{\tan\theta}. \tag{74}$$

3. Critical balance. The energy transfer time is modeled as scale-wise balanced between the eddy turnover time in the perpendicular plane to the mean magnetic field $\tau_{ed} = (k_\perp u_\perp)^{-1}$ (which originates in the fluid non-linearity) and the Alfvén time scattering time $\tau_A = (k_\parallel V_A)^{-1}$ along the mean magnetic field (which originates in the hydromagnetic non-linearity):

$$k_\perp u_\perp \sim k_\parallel V_A. \tag{75}$$

The flow velocity in the perpendicular plane is assumed to follow the Richardson-Kolmogorov scaling:

$$u_\perp \sim k_\perp^{-1/3} \epsilon_{\rm turb}^{1/3}, \tag{76}$$

where $\epsilon_{\rm turb}$ denotes the energy transfer rate in the inertial range of fluid turbulence, and is modeled as the flow kinetic energy (proportional to the square of flow velocity, $u_\perp^2$) divided by eddy turnover time $(k_\perp u_\perp)^{-1}$. Combination of Equation (75) with Equation (76) yields a relation between the parallel and perpendicular components of wavevector:

$$k_\parallel \sim k_\perp^{2/3} L^{1/3}, \tag{77}$$

where $L = V_A^3/\epsilon$ is a integration-scale length of the system [42].

Figure 7 displays sketches of the energy spectra deduced from our dielectric tensor method, in particular, using the fluctuation energy ratios shown in **Figure 6**. We assume a Kolmogorov-type spectral slope $-5/3$ at lower wavenumbers (MHD inertial range) and an electron-MHD-type spectral slope $-7/3$ at higher wavenumbers (dispersive range) as presented in the theoretical studies [34, 36] as well as in the hybrid Vlasov-Maxwell numerical study [16]. The small-scale spectrum may be even steeper than $-7/3$. For example, a hybrid simulation study by Franci et al. [13] presents a steepening of the spectral curve from $-5/3$ in the MHD domain to -3 in the kinetic domain while a flattening of the electric field spectrum to a slope of $-2/3$ or -1 and a steepening of magnetic field spectrum (steeper than $-7/3$) are found in the kinetic range by hybrid simulations by Servidio et al. [14], Cerri and Califano [46], Cerri et al. [20], and Arzamasskiey et al. [47]. The observational values of the short-wavelength slope are, e.g., -2.1 [2], -2.5 [48], and -2.6 [49].

The perpendicular electric field spectrum falls with the same slope as the magnetic field energy at lower wavenumbers, and falls more steeply than the magnetic field spectrum by a slope difference -2. Yet, at sufficiently high wavenumbers (higher than the wavenumber for the ion gyro-radius), the perpendicular electric field spectrum exhibits a flattening because the out-of-plane component (E_y component) becomes more significant than the in-plane component (E_x component). The perpendicular electric field spectrum has a slope of $-1/3$ for the constant propagation angle and -1 for the critical balance (assuming that the magnetic field spectrum has a slope of $-7/3$). The parallel electric field spectrum exhibits a different sense of the slope because the parallel electric field spectrum increases rapidly toward higher wavenumbers. Three different scenarios above indicate that the slope difference of the parallel electric field spectrum to the magnetic field spectrum is 2 (filamentation), 4 (constant propagation angle), and 10/3 (critical balance) at lower wavenumbers, and 0 (filamentation), 2 (constant propagation angle), and 4/3 (critical balance). Yet, it should be noted that the Landau damping parallel to the mean magnetic field is not included in our discussion. The dominance of parallel electric field energy depends on several details of the system under consideration, e.g., injection amplitude and separation of scales. The parallel magnetic field does not exhibit a simple scaling to the perpendicular magnetic field. The parallel field becomes enhanced at wavelengths around the ion inertial length and the ion gyro-radius.

From polarization (or transport ratio) point-of-view, the steepening of perpendicular electric field spectrum occurs because E_x fluctuation energy (in-plane component in a nearly electrostatic sense) becomes smaller than the total magnetic field fluctuation energy at shorter wavelengths around the ion gyro-radius. Then E_y (out-of-plane component in a nearly electromagnetic sense) becomes increasingly larger at even shorter wavelengths and the E_y leads to a flattening of perpendicular electric field spectrum. **Figure 5** shows the competition between E_x and E_y components in terms of fluctuation amplitudes, and **Figure 6** the competition in terms of the fluctuation energies. A drop of perpendicular electric field spectral curve at wavelengths close to ion

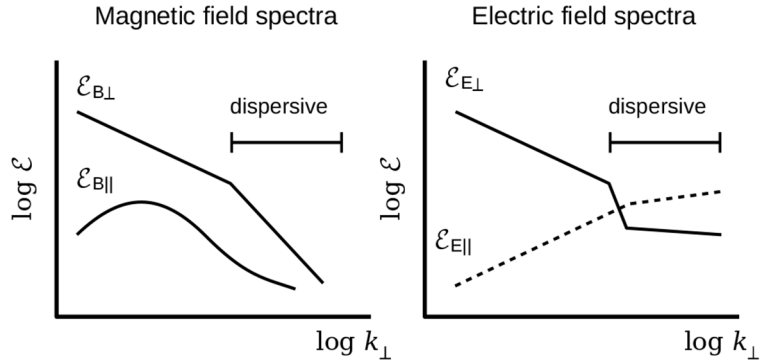

FIGURE 7 | Schematic energy spectra for the magnetic field (left) and electric field (right) of the kinetic Alfvén mode in the perpendicular wavenumber domain.

gyro-radius has, so far, not been clearly identified in the numerical simulation studies or observations. Possible explanations include effects of higher-order correction of the wave properties (through dielectric response) to thermal and kinetic effects and excitation of other fluctuation modes (e.g., linear-mode waves, forced waves by wave-wave interactions, non-linear mode) that mediate energy cascade of kinetic Alfvén turbulence. Component-wise transport ratio studies will help to diagnose the realization of kinetic Alfvén mode in turbulent kinetic plasmas in the observational and simulation studies.

Our naive estimate of spectral signature for kinetic Alfvén turbulence predicts a local minimum of parallel magnetic field spectrum at wavelengths close to the thermal ion gyroradius. This is because the electric field changes the rotation sense of wave field. Hybrid and particle-in-cell simulations [27] show an evidence for a local minimum of the spectral slope in the energy spectrum of parallel magnetic field in the perpendicular wavenumber domain (but not changing the sign of spectral slope). Note that **Figure 7** merely reflects the fluctuation sense studies presented in **Figure 6** on the assumption of two distinct power-law spectral domains for the perpendicular magnetic field fluctuations. Yet, increasing sense of the parallel magnetic field fluctuation and flattening of the perpendicular electric field spectrum (relative to the perpendicular fluctuation) are presented in numerical studies by Told et al. [15]. The parallel electric field spectrum often exhibits a decaying sense of spectral curve toward higher wavenumbers (e.g., [21]). Growing sense of the spectrum (with a positive value of spectral index) is confirmed at lower wavenumbers in the Eulerian hybrid Vlasov-Maxwell simulations but not in the hybrid particle-in-cell simulations [22]. The parallel magnetic field spectrum has the nearly same spectral curve to the perpendicular magnetic field spectrum, and has a smaller energy density than the perpendicular magnetic field spectrum (e.g., [21]). The perpendicular electric field spectrum has a larger energy density than the parallel electric field spectrum, and the spectral curve is flatter than the parallel spectrum in the kinetic domain (e.g., [21]). Flattening of the perpendicular electric field spectrum agrees with the hybrid simulation [13, 14, 20, 46, 47], gyro-kinetic simulation [9], fluid-model simulation [10], and particle-in-cell simulation [26].

3. LESSONS AND OUTLOOK

Analytic derivation of the kinetic Alfvén mode properties is presented in the lowest order picture (which reproduces the transport ratios of the wave in the fluid picture) by assessing the dielectric response in various directions, such as the polarization drift, Debye screening, and Hall and diamagnetic currents and evaluating the transport ratios directly by evaluating the dielectric tensor. The presented method has a wide range of applications in the sense that the dielectric tensor method offers an algorithm to perform higher-order thermal corrections due to the finite Larmor radius and Alfvén wave couplings with the fast and ion-acoustic mode (e.g., treating ϵ_{xz} as a non-zero quantity).

The dielectric tensor method shows that the Hall and diamagnetic currents contribute to the wave properties through the off-diagonal dielectric response. The off-diagonal dielectric response determines the polarization property of the kinetic Alfvén mode without altering the dispersion relation significantly.

The (temporal) rotation of electric field is in the electron gyration sense, right-hand polarized when viewing into the mean magnetic field direction at a fixed point in space. The field rotation sense originates in the diamagnetic current in the wave. Field rotation sense may be reversed when the Hall current dominates in the (off-diagonal) dielectric response, particularly when the perpendicular wavenumber is not sufficiently large.

The obtained analytic expressions are simplified by using approximations, and then are tested against the transport ratios obtained numerically from the dielectric tensor in Equations (2)–(7). From a practical point of view, Equations (18), (21), (30), (31), (36), (45) provide useful tools of fluctuation sense studies, which can easily be implemented for various data analyses and applications to further studies.

The analytic expression of the transport ratios will serve as a useful tool in the spacecraft observations of wave phenomena, e.g., electric and magnetic field fluctuations in the inner

heliospheric region by Parker Solar Probe, Solar Orbiter, and BepiColombo. Even though the measurements are limited to the magnetic field fluctuations only (e.g., the BepiColombo MPO spacecraft measures the interplanetary magnetic field during its 7-years cruise to Mercury) the dielectric tensor method offers a reference model of transport ratios for the kinetic Alfvén mode.

Of course, there could be other modes (both linear and non-linear modes) contributing to the sub-ion-scale fluctuations in solar wind turbulence, which may then show different behavior of the spectral ratios (e.g., [16, 24, 34]) and cause deviations from the expected kinetic Alfvén mode ratios (e.g., [27]). Numerical simulations would play an important role to identify the linear and non-linear modes when the kinetic Alfvén mode evolves into turbulence and to properly associate the transport ratios with various wave modes.

Our study is based on the linear-mode wave properties, in which fluctuation amplitudes are assumed to be sufficiently lower than the mean magnetic field and the waves do not interact with one another (otherwise wave-wave interactions can in general produce forced or pumped waves that differ from the linear mode of the system. Under what condition the mean magnetic field may be treated as a homogeneous and time-stationary field will be an important question when working on the spacecraft data In the case of strong turbulence, fluid non-linearities (eddies and coherent structures) play a more important role.

AUTHOR CONTRIBUTIONS

YN worked on the calculations and manuscript writing. OR, ZV, and MH worked on the discussion of the wave properties and finalization of the manuscript.

FUNDING

The work by YN was financially supported by the Austrian Space Applications Programme (ASAP) at the Austrian Research Promotion Agency under contract 853994 and 865967. YN also acknowledges financial support by the Japan Society for the Promotion of Science, Invitational Fellowship for Research in Japan (Long-term) under grant FY2019 L19527. The work by ZV was supported by the Austrian Science Fund (FWF) project P28764-N27.

ACKNOWLEDGMENTS

YN thanks the research and administration staff members of the Hoshino laboratory group at the University of Tokyo for discussions, supports, and organizations during the fellowship program and the University of Tokyo Mejirodai International Village for the arrangement and hospitality during the pleasant and productive stay in Tokyo.

REFERENCES

1. Hasegawa A, Uberoi C. The Alfvén Wave. Oak Ridge, TN: Tech. Inf. Center, US Dept. of Energy (1982).
2. Bale SD, Kellogg PJ, Mozer FS, Horbury TS, Rème H. Measurement of the electric fluctuation spectrum of magnetohydrodynamic turbulence. *Phys Rev Lett*. (2005) **94**:215002. doi: 10.1103/PhysRevLett.94.215002
3. Sahraoui F, Goldstein ML, Belmont G, Canu P, Rezeau, L. Three dimensional anisotropic k spectra of turbulence at subproton scales in the solar wind. *Phys Rev Lett*. (2010) **105**:131101. doi: 10.1103/PhysRevLett.105.131101
4. Salem CS, Howes GG, Sundkvist D, Bale SD, Chaston CC, Chen CHK, et al. Identification of kinetic Alfvén wave turbulence in the solar wind. *Astrophys J Lett*. (2012) **745**:L9. doi: 10.1088/2041-8205/745/1/L9
5. TenBarge JM, Podesta JJ, Klein KG, Howes GG. Interpreting magnetic variance anisotropy measurements in the solar wind. *Astrophys J*. (2012) **753**:107. doi: 10.1088/0004-637X/753/2/107
6. Chen CHK, Boldyrev S, Xia Q, Perez JC. Nature of subproton scale turbulence in the solar wind. *Phys Rev Lett*. (2013) **110**:225002. doi: 10.1103/PhysRevLett.110.225002
7. Kiyani KH, Chapman SC, Sahraoui F, Hnat B, Fauvarque O, Khotyaintsev YV. Enhanced magnetic compressibility and isotropic scale invariance at sub-ion Larmor scales in solar wind turbulence. *Astrophys J*. (2013) **763**:10. doi: 10.1088/0004-637X/763/1/10
8. Roberts OW, Li X, Li B. Kinetic plasma turbulence in the fast solar wind measured by cluster. *Astrophys J*. (2013) **769**:58. doi: 10.1088/0004-637X/769/1/58
9. Howes GG, TenBarge JM, Dorland W, Quataert E, Schekochihin AA, Numata R, et al. Gyrokinetic simulations of solar wind turbulence from ion to electron scales. *Phys Rev Lett*. (2011) **107**:035004. doi: 10.1103/PhysRevLett.107.035004
10. Passot T, Henri P, Laveder D, Sulum PL. Fluid simulations of ion scale plasmas with weakly distorted magnetic fields. *Eur Phys J D*. (2014) **68**:207. doi: 10.1140/epjd/e2014-50160-1
11. Vásconez CL, Valentini F, Camporeale E, Veltri P. Vlasov simulations of kinetic Alfvén waves at proton kinetic scales. *Phys Plasmas*. (2014) **21**:112107. doi: 10.1063/1.4901583
12. Vásconez C, Pucci F, Valentini F, Servidio S, Matthaeus WH, Malara, F. Kinetic Alfvén wave generation by large-scale phase mixing. *Astrophys J*. (2015) **815**:7. doi: 10.1088/0004-637X/815/1/7
13. Franci L, Landi S, Matteini L, Verdini A, Hellinger P. High-resolution hybrid simulations of kinetic plasma turbulence at proton scales. *Astrophys J*. (2015) **812**:21. doi: 10.1088/0004-637X/812/1/21
14. Servidio S, Valentini F, Perrone D, Greco A, Califano F, Matthaeus WH, et al. A kinetic model of plasma turbulence. *J Plasma Phys*. (2015) **81**:325810107. doi: 10.1017/S0022377814000841
15. Told D, Jenko F, TenBarge JM, Howes GG, Hammett GW. Multiscale nature of the dissipation range in gyrokinetic simulations of Alfvénic turbulence. *Phys Rev Lett*. (2015) **115**:025003. doi: 10.1103/PhysRevLett.115.025003
16. Cerri SS, Califano F, Jenko F, Told D, Rincon F. Subproton-scale cascades in solar wind turbulence: driven hybrid-kinetic simulations. *Astrophys J Lett*. (2016) **822**:L12. doi: 10.3847/2041-8205/822/1/L12
17. Kobayashi S, Sahraoui F, Passot T, Laveder D, Sulem PL, Huang SY, et al. Three-dimensional simulations and spacecraft observations of sub-ion scale turbulence in the solar wind: influence of Landau damping. *Astrophys J*. (2017) **839**:122. doi: 10.3847/1538-4357/aa67f2
18. Hughes RS, Gary SP, Wang J, Parashar TN. Kinetic Alfvén turbulence: electron and ion heating by particle-in-cell simulations. *Astrophys J Lett*. (2017) **847**:L14. doi: 10.3847/2041-8213/aa8b13
19. Valentini F, Vásconez CL, Pezzi O, Servidio S, Malara F, Pucci F. Transition to kinetic turbulence at proton scales driven by large-amplitude kinetic Alfvén fluctuations. *Astron Astrophys*. (2017) **599**:A8. doi: 10.1051/0004-6361/201629240
20. Cerri SS, Kunz MW, Califano F. Dual phase-space cascades in 3D hybrid-Vlasov-Maxwell turbulence. *Astrophys J Lett*. (2018) **856**:L13. doi: 10.3847/2041-8213/aab557
21. Perrone, D, Passot T, Laveder D, Valentini F, Sulem PL, Zouganelis I, et al. Fluid simulations of plasma turbulence at ion scales: comparison with Vlasov-Maxwell simulations. *Phys Plasmas*. (2018) **25**:052302. doi: 10.1063/1.5026656

22. Cerri SS, Franci L, Califano F, Landi S. Plasma turbulence at ion scales: a comparison between particle in cell and Eulerian hybrid-kinetic approaches. *J Plasma Phys*. (2017) **83**:705830202. doi: 10.1017/S0022377817000265
23. Cerri SS, Servidio S, Califano F. Kinetic cascade in solar-wind turbulence: 3D3V hybrid-kinetic simulations with electron inertia. *Astrophys J Lett*. (2017) **846**:L18. doi: 10.3847/2041-8213/aa87b0
24. Grošelj D, Cerri SS, Navarro AB, Willmott C, Told D, Loureiro NF, et al. Fully kinetic versus reduced-kinetic modeling of collisionless plasma turbulence. *Astrophys J*. (2017) **847**:28. doi: 10.3847/1538-4357/aa894d
25. Franci L, Landi S, Verdini A, Matteini L, Hellinger P. Solar wind turbulent cascade from MHD to sub-ion scales: large-size 3D hybrid particle-in-cell simulations. *Astrophys J*. (2018) **853**:26. doi: 10.3847/1538-4357/aaa3e8
26. Grošelj D, Mallet A, Loureiro NF, Jenko F. Fully kinetic simulation of 3D kinetic Alfvén turbulence. *Phys Rev Lett*. (2018) **120**:105101. doi: 10.1103/PhysRevLett.120.105101
27. Cerri SS, Grošelj D, Franci L. Kinetic plasma turbulence: recent insights and open questions from 3D3V simulations. *Front Astron Space Sci*. (2019) **6**:64. doi: 10.3389/fspas.2019.00064
28. Grošelj D, Chen CHK, Mallet A, Samtaney R, Schneider K, Jenko F. Kinetic turbulence in astrophysical plasmas: waves and/or structures? *Phys Rev X*. (2019) **9**:031037. doi: 10.1103/PhysRevX.9.031037
29. Hollweg JV. Kinetic Alfvén wave revisited. *J Geophys Res*. (1999) **104**:14811–9. doi: 10.1029/1998JA900132
30. Stix TH. Waves in Plasmas. New York, NY: AIP-Press (1992).
31. Lysak RL, Lotko W. On the kinetic dispersion relation for shear Alfvén waves. *J Geophys Res*. (1996) **101**:5085–94. doi: 10.1029/95JA03712
32. Schekochihin AA, Cowley SC, Dorland W, Hammett GW, Howes GG, Quataert E, et al. Astrophysical gyrokinetics: kinetic fluid turbulent cascades in magnetized weakly collisional plasmas. *Astrophys J Suppl*. (2009) **182**:310–77. doi: 10.1088/0067-0049/182/1/310
33. Bian NH, Kontar EP, Brown JC. Parallel electric field generation by Alfvén wave turbulence. *Astron Astrophys*. (2010) **519**:A113. doi: 10.1051/0004-6361/201014048
34. Boldyrev S, Horaites K, Xia Q, Perez JC. Toward a theory of astrophysical plasma turbulence at subproton scales. *Astrophys J*. (2013) **777**:41. doi: 10.1088/0004-637X/777/1/41
35. Hunana P, Zank GP. Inhomogeneous nearly incompressible description of magnetohydrodynamic turbulence. *Astrophys J*. (2010) **718**:148–67. doi: 10.1088/0004-637X/718/1/148
36. Passot T, Sulem PL. Imbalanced kinetic Alfvén wave turbulence: from weak turbulence theory to nonlinear diffusion models for the strong regime. *J Plasma Phys*. (2019) **85**:905850301. doi: 10.1017/S0022377819000187
37. Montgomery MD. Average thermal characteristics of solar wind electrons. In: Sonett CP, Coleman PJ, Wilcox JM, editors. Solar Wind. Washington, DC: Scientific and Technical Information Office, National Aeronautics and Space Administration (1972). p. 208.
38. Wilson LB III, Stevens ML, Kasper JC, Klein KG, Maruca BA, Bale SD, et al. The statistical properties of solar wind temperature parameters near 1 au. *Astrophys J Suppl*. (2018) **236**:41. doi: 10.3847/1538-4365/aab71c
39. Perschke C, Narita Y, Motschmann U, Glassmeier KH. Multi-spacecraft observations of linear modes sideband waves in ion-scale solar wind turbulence. *Astrophys J Lett*. (2014) **793**:L25. doi: 10.1088/2041-8205/793/2/L25
40. Roberts OW, Li X, Jeska L. A statistical study of the solar wind turbulence at ion kinetic scales using the k-filtering and cluster data. *Astrophys J*. (2015) **802**:2. doi: 10.1088/0004-637X/802/1/2
41. Boldyrev S, Perez JC. Spectrum of kinetic-Alfvén turbulence. *Astrophys J Lett*. (2012) **758**:L44. doi: 10.1088/2041-8205/758/2/L44
42. Goldreich P, Sridhar S. Toward a theory of interstellar turbulence. II. Strong Alfvénic turbulence. *Astrophys J*. (1995) **438**:763–75. doi: 10.1086/175121
43. Gary SP. Low-frequency waves in a high-beta collisionless plasma: polarization, compressibility, and helicity. *J Plasma Phys*. (1986) **35**:431–47. doi: 10.1017/S0022377800011442
44. Pucci F, Vásconez CL, Pezzi O, Servidio S, Valentini F, Matthaeus WH, et al. From Alfvén waves to kinetic Alfvén waves in an inhomogeneous equilibrium structure. *J Geophys Res Space Phys*. (2016) **121**:1024–45. doi: 10.1002/2015JA022216
45. Comişel H, Narita Y, Motschmann U. Alfvén wave evolution into magnetic filaments in 3-D space plasma. Earth Planet Space. (2020) **72**:32. doi: 10.1186/s40623-020-01156-8
46. Cerri SS, Califano F. Reconnection and small-scale fields in 2D-3V hybrid-kinetic driven turbulence simulations. *New J Phys*. (2017) **19**:025007. doi: 10.1088/1367-2630/aa5c4a
47. Arzamasskiy L, Kunz MW, Chandran BDG, Quataert E. Hybrid-kinetic simulations of ion heatingin Alfvénic turbulence. *Astrophys J*. (2019) **879**:53. doi: 10.3847/1538-4357/ab20cc
48. Sahraoui F, Goldstein ML, Robert P, Khotyaintsev YV. Evidence of a cascade and dissipation of solar-wind turbulence at the electron gyroscale. *Phys Res Lett*. (2009) **102**:231102. doi: 10.1103/PhyRevLett.102.231102
49. Alexandrova O, Carbone V, Veltri P, Sorriso-Valvo L. Small-scale energy cascade of the solar wind turbulence. *Astrophys J*. (2008) **674**:1153–7. doi: 10.1086/524056

Conflict of Interest: The authors declare that the research was conducted in the absence of any commercial or financial relationships that could be construed as a potential conflict of interest.

APPENDIX A: POLARIZATION, HALL, AND DIAMAGNETIC CURRENTS

Polarization current is expressed by the dielectric response as $\epsilon_\mathrm{p} = c^2/V_\mathrm{A}^2$. The polarization current originates in the ion polarization drift velocity, for example in the x direction, as

$$u_\mathrm{x} = -\mathrm{i}\frac{m_\mathrm{i}\omega}{qB^2}E_\mathrm{x}, \tag{78}$$

where m_i is the ion mass, q the electric charge of ions. The polarization current is thus expressed as

$$\begin{aligned} j_\mathrm{x} &= qn_\mathrm{i}u_\mathrm{x} && (79)\\ &= -\mathrm{i}\frac{m_\mathrm{i}n_\mathrm{i}\omega}{B_0^2}E_\mathrm{x} && (80)\\ &= -\mathrm{i}\epsilon_0\omega\frac{c^2}{V_\mathrm{A}^2}E_\mathrm{x}. && (81)\end{aligned}$$

The corresponding conductivity is σ_p

$$\sigma_\mathrm{p} = -\mathrm{i}\epsilon_0\omega\frac{c^2}{V_\mathrm{A}^2}, \tag{82}$$

and the dielectric response ϵ_p is obtained from the conductivity as

$$\begin{aligned} \epsilon_\mathrm{p} &= \frac{\mathrm{i}}{\epsilon_0\omega}\sigma_\mathrm{p} && (83)\\ &= \frac{c^2}{V_\mathrm{A}^2}. && (84)\end{aligned}$$

Hall current (for example in the y direction) is associated with the electric field (in the x direction) through:

$$E_\mathrm{y} = -\frac{1}{n_\mathrm{e}e}j_\mathrm{x}B_0, \tag{85}$$

where n_e is the electron number density and e the electron charge. Using the quasi-neutrality, one may interpret the electron density nearly as ion density, $n_\mathrm{e} \simeq n_\mathrm{i}$. Equation (85) then yields the conductivity in the following form

$$\sigma_\mathrm{h} = -\frac{en_\mathrm{i}}{B_0} \tag{86}$$

and the dielectric response as

$$\begin{aligned} \epsilon_\mathrm{h} &= -\frac{\mathrm{i}}{\epsilon_0\omega}\sigma_\mathrm{h} && (87)\\ &= -\mathrm{i}\frac{en_\mathrm{i}}{\epsilon_0\omega B_0} && (88)\\ &= -\mathrm{i}\frac{c^2}{V_\mathrm{A}^2}\frac{\Omega_\mathrm{i}}{\omega}. && (89)\end{aligned}$$

Diamagnetic current is associated with the pressure gradient as

$$\vec{j} = \frac{\vec{B}\times\nabla p}{B^2}. \tag{90}$$

Using the expression of pressure (for ions) $p_\mathrm{i} = \gamma_\mathrm{i}n_\mathrm{i}k_\mathrm{B}T_\mathrm{i}$ and estimating the density fluctuation through the continuity equation with polarization drift and frozen-in magnetic field ([29])

$$\frac{\delta n_\mathrm{i}}{n_\mathrm{i,0}} = -\mathrm{i}\frac{k_\mathrm{x}}{\Omega_\mathrm{i}}\frac{E_\mathrm{x}}{B_0}, \tag{91}$$

the diamagnetic current in the y direction can be associated with E_x as

$$j_\mathrm{y} = -\frac{\gamma_\mathrm{i}k_\mathrm{B}n_\mathrm{i,0}T_\mathrm{i}}{\Omega_\mathrm{i}B_0^2}k_\mathrm{x}^2E_\mathrm{x}. \tag{92}$$

The conductivity and dielectric response are, respectively,

$$\begin{aligned} \sigma_\mathrm{d} &= \frac{\gamma_\mathrm{i}k_\mathrm{B}n_\mathrm{i,0}T_\mathrm{i}}{\Omega_\mathrm{i}B_0^2}k_\mathrm{x}^2 && (93)\\ \epsilon_\mathrm{d} &= \frac{\mathrm{i}}{\epsilon_0\omega}\sigma_\mathrm{d} && (94)\\ &= \frac{\mathrm{i}\gamma_\mathrm{i}}{2}\frac{c^2}{V_\mathrm{A}^2}\frac{\Omega_\mathrm{i}}{\omega}k_\mathrm{x}^2r_\mathrm{gi}^2. && (95)\end{aligned}$$

APPENDIX B: DIELECTRIC TENSOR CALCULATIONS

The dispersion tensor elements are as follows.

$$\begin{aligned} D_\mathrm{xx} &= \epsilon_\mathrm{xx} - N_\parallel^2 && (96)\\ &= \frac{c^2}{V_\mathrm{A}^2}\left(1-\frac{3}{4}k_\perp^2r_\mathrm{gi}^2\right) - N_\parallel^2 && (97)\\ &= N_\parallel^2\left[\frac{\omega^2}{k_\parallel^2V_\mathrm{A}^2}\left(1-\frac{3}{4}k_\perp^2r_\mathrm{gi}^2\right)-1\right] && (98)\\ D_\mathrm{xy} &= \epsilon_\mathrm{xy} && (99)\\ &= \mathrm{i}\frac{c^2}{V_\mathrm{A}^2}\frac{\Omega_\mathrm{i}}{\omega}\left(-1+\frac{3}{2}k_\perp^2r_\mathrm{gi}^2\right) && (100)\\ D_\mathrm{xz} &= \epsilon_\mathrm{xz} + N_\parallel N_\perp && (101)\\ &= -\frac{1}{2}\frac{c^2}{V_\mathrm{A}^2}\frac{k_\parallel}{k_\perp}k_\perp^2r_\mathrm{gi}^2 + N_\parallel N_\perp && (102)\\ &= N_\parallel N_\perp\left(-\frac{1}{2}\frac{\omega^2}{\Omega_\mathrm{i}^2}\frac{v_\mathrm{th,i}^2}{V_\mathrm{A}^2}+1\right) && (103)\end{aligned}$$

$$D_{yx} = -\epsilon_{xy} \tag{104}$$
$$= -\mathrm{i}\frac{c^2}{V_A^2}\frac{\Omega_i}{\omega}\left(-1+\frac{3}{2}k_\perp^2 r_{gi}^2\right) \tag{105}$$
$$D_{yy} = \epsilon_{yy} - N^2 \tag{106}$$
$$D_{yz} = \epsilon_{yz} \tag{107}$$
$$= -\frac{1}{2}\frac{k_\perp}{k_\parallel}\epsilon_{xy} \tag{108}$$
$$= -\mathrm{i}\frac{1}{2}\frac{k_\perp}{k_\parallel}\frac{c^2}{V_A^2}\frac{\Omega_i}{\omega}\left(-1+\frac{3}{2}k_\perp^2 r_{gi}^2\right) \tag{109}$$
$$D_{zx} = D_{xz} \tag{110}$$
$$D_{zy} = -D_{yz} \tag{111}$$
$$D_{zz} = \epsilon_{zz} - N_\perp^2 \tag{112}$$
$$= \frac{1}{k_\parallel^2\lambda_{De}^2} - N_\perp^2 \tag{113}$$

The electric field polarization is evaluated as:

$$\frac{E_y}{E_x} = \frac{D_{xx}D_{yz} - D_{xz}D_{yx}}{D_{xz}D_{yy} - D_{xy}D_{yz}} \tag{114}$$
$$= -\frac{D_{yx} - D_{xx}D_{yz}/D_{xz}}{D_{yy} - D_{xy}D_{yz}/D_{xz}} \tag{115}$$
$$= -\frac{\epsilon_{xy}}{N^2}\left[\frac{3}{2} - \frac{1}{2}\frac{\omega^2}{k_\parallel^2 V_A^2}\left(1-\frac{3}{4}k_\perp^2 r_{gi}^2\right)\right] \left(1-\frac{1}{2}\epsilon_{xy}^2 N^{-2}N_\parallel^{-2}\right)^{-1} \tag{116}$$
$$= -\mathrm{i}\frac{\Omega_i^2}{k^2 V_A^2}\frac{\omega}{\Omega_i}\left(-1+\frac{3}{2}k_\perp^2 r_{gi}^2\right) \times \left[\frac{3}{2} - \frac{1}{2}\frac{\omega^2}{k_\parallel^2 V_A^2}\left(1-\frac{3}{4}k_\perp^2 r_{gi}^2\right)\right] \times \left[1+\frac{1}{2}\frac{\Omega_i^2}{k^2 V_A^2}\frac{\omega^2}{k_\parallel^2 V_A^2}\left(-1+\frac{3}{2}k_\perp^2 r_{gi}^2\right)^2\right]^{-1} \tag{117}$$

The parallel electric field in ratio to the in-plane perpendicular electric field is evaluated as:

$$\frac{E_z}{E_x} = \frac{D_{xy}D_{zx} - D_{xx}D_{zy}}{D_{xz}D_{zy} - D_{xy}D_{zz}} \tag{118}$$
$$= -\frac{D_{zx} - D_{xx}D_{zy}/D_{xy}}{D_{zz} - D_{xz}D_{zy}/D_{xy}} \tag{119}$$
$$= -\frac{(\epsilon_{xy} + N_\parallel N_\perp) - \frac{1}{2}\frac{k_\perp}{k_\parallel}(\epsilon_{xx} - N_\parallel^2)}{(\epsilon_{zz} - N_\perp^2) - \frac{1}{2}\frac{k_\perp}{k_\parallel}(\epsilon_{xz} + N_\parallel N_\perp)} \tag{120}$$
$$= -\frac{k_\parallel}{k_\perp}\left[\frac{3}{2} - \frac{1}{2}\frac{v_{th,i}^2}{V_A^2}\frac{\omega^2}{\Omega_i^2} - \frac{1}{2}\frac{\omega^2}{k_\parallel^2 V_A^2}\left(1-\frac{3}{4}k_\perp^2 r_{gi}^2\right)\right] \times \left[-\frac{3}{2} - \frac{1}{4}\frac{v_{th,i}^2}{V_A^2}\frac{\omega^2}{\Omega_i^2} + \frac{\omega^2}{k_\parallel^2 V_A^2}\frac{1}{k_\perp^2 r_{gi}^2 T_e/T_i}\right]^{-1} \tag{121}$$

The magnetic field polarization is evaluated using Equations (117) and (121) as:

$$-\frac{\delta B_x}{\delta B_y} = \frac{E_y}{E_x}\left(1-\frac{k_\perp}{k_\parallel}\frac{E_z}{E_x}\right)^{-1} \tag{122}$$
$$= -\mathrm{i}\frac{\Omega_i^2}{k^2 V_A^2}\frac{\omega}{\Omega_i}\left(-1+\frac{3}{2}k_\perp^2 r_{gi}^2\right) \times \left[\frac{3}{2} - \frac{1}{2}\frac{\omega^2}{k_\parallel^2 V_A^2}\left(1-\frac{3}{4}k_\perp^2 r_{gi}^2\right)\right] \times \left[1+\frac{1}{2}\frac{\Omega_i^2}{k^2 V_A^2}\frac{\omega^2}{k_\parallel^2 V_A^2}\left(-1+\frac{3}{2}k_\perp^2 r_{gi}^2\right)^2\right]^{-1} \times \left[1+\left[\frac{3}{2} - \frac{1}{2}\frac{v_{th,i}^2}{V_A^2}\frac{\omega^2}{\Omega_i^2} - \frac{1}{2}\frac{\omega^2}{k_\parallel^2 V_A^2}\left(1-\frac{3}{4}k_\perp^2 r_{gi}^2\right)\right] \times \left[-\frac{3}{2} - \frac{1}{4}\frac{v_{th,i}^2}{V_A^2}\frac{\omega^2}{\Omega_i^2} + \frac{\omega^2}{k_\parallel^2 V_A^2}\frac{1}{k_\perp^2 r_{gi}^2 T_e/T_i}\right]^{-1}\right]^{-1} \tag{123}$$

The parallel magnetic field relative to the out-of-plane component is obtained from Equations(42) to (123) as:

$$\frac{\delta B_z}{\delta B_y} = \frac{\delta B_z}{\delta B_x}\frac{\delta B_x}{\delta B_y} \tag{124}$$
$$= \mathrm{i}\frac{k_\perp}{k_\parallel}\frac{\Omega_i^2}{k^2 V_A^2}\frac{\omega}{\Omega_i}\left(-1+\frac{3}{2}k_\perp^2 r_{gi}^2\right) \times \left[\frac{3}{2} - \frac{1}{2}\frac{\omega^2}{k_\parallel^2 V_A^2}\left(1-\frac{3}{4}k_\perp^2 r_{gi}^2\right)\right] \times \left[1+\frac{1}{2}\frac{\Omega_i^2}{k^2 V_A^2}\frac{\omega^2}{k_\parallel^2 V_A^2}\left(-1+\frac{3}{2}k_\perp^2 r_{gi}^2\right)^2\right]^{-1} \times \left[1+\left[\frac{3}{2} - \frac{1}{2}\frac{v_{th,i}^2}{V_A^2}\frac{\omega^2}{\Omega_i^2} - \frac{1}{2}\frac{\omega^2}{k_\parallel^2 V_A^2}\left(1-\frac{3}{4}k_\perp^2 r_{gi}^2\right)\right] \times \left[-\frac{3}{2} - \frac{1}{4}\frac{v_{th,i}^2}{V_A^2}\frac{\omega^2}{\Omega_i^2} + \frac{\omega^2}{k_\parallel^2 V_A^2}\frac{1}{k_\perp^2 r_{gi}^2 T_e/T_i}\right]^{-1}\right]^{-1} \tag{125}$$

frontiers in Astronomy and Space Sciences

ORIGINAL RESEARCH
published: 31 August 2020
doi: 10.3389/fspas.2020.00053

Some Similarities and Differences Between the Observed Alfvénic Fluctuations in the Fast Solar Wind and Navier–Stokes Turbulence

Joseph E. Borovsky[1]* *and Tiziano Mina*[2,3]

[1] Center for Space Plasma Physics, Space Science Institute, Boulder, CO, United States, [2] Facoltà di Matematica, Università Degli Studi di Torino, Turin, Italy, [3] Los Alamos National Laboratory, Theoretical Division, Los Alamos, NM, United States

Using two long data sets analyzed on equal footing, the properties of Alfvénic fluctuations in the fast (coronal-hole-origin) solar wind and Navier–Stokes turbulence are compared. A 26.4-s-long interval of hot-wire measurements in the ONERA wind tunnel is used, and a 71-h-long interval of unperturbed coronal-hole plasma measured by the WIND spacecraft at 1 AU is used. Similarities and differences between a Navier–Stokes fluid and the collisionless magnetized solar-wind plasma are discussed, as are differences between the physical natures of the advecting evolving turbulent fluctuations and the propagating non-evolving Alfvénic fluctuations. The details of the power spectral densities of the turbulence and the Alfvénic fluctuations are compared. Statistics of first and second time derivatives are examined for the wind-tunnel and solar-wind time series, and the statistics are compared with the statistics of time derivatives of phase-randomized time series. Using running medians, the statistics of flat spots in the time series of Alfvénic fluctuations is examined, which is evidence of a cellular structure to the magnetic field and velocity field. A call for a campaign of expanded coordinated future work is made.

Keywords: solar wind, turbulence, Alfvén waves, heliosphere, coherent structure

OPEN ACCESS

Edited by:
Luca Sorriso-Valvo, Institute for Science and Technology of Plasmas (CNR), Italy

Reviewed by:
Lorenzo Matteini, UMR8109 Laboratoire d'Études Spatiales et d'Instrumentation en Astrophysique (LESIA), France
Federico Fraternale, University of Alabama in Huntsville, United States

***Correspondence:**
Joseph E. Borovsky
jborovsky@spacescience.org

Specialty section:
This article was submitted to Space Physics, a section of the journal Frontiers in Astronomy and Space Sciences

Received: *29 May 2020*
Accepted: *15 July 2020*
Published: *31 August 2020*

Citation:
Borovsky JE and Mina T (2020) Some Similarities and Differences Between the Observed Alfvénic Fluctuations in the Fast Solar Wind and Navier–Stokes Turbulence. Front. Astron. Space Sci. 7:53. doi: 10.3389/fspas.2020.00053

INTRODUCTION

A side-by-side comparison is made between Navier–Stokes turbulence measured in a wind tunnel and Alfvénic fluctuations measured in the fast solar wind. Measurements of the Alfvénic fluctuations in the fast solar wind are often considered to be measurements of magnetohydrodynamics (MHD) turbulence (Tu et al., 1989; Marsch and Tu, 1990a; Bavassano and Bruno, 1992; Wicks et al., 2013; Telloni et al., 2019), although the Alfvénic fluctuations have some properties different from a turbulence. Navier–Stokes fluid turbulence comprised rapidly evolving advecting structures (eddies) that strongly interact with each other, whereas the Alfvénic fluctuations in the solar wind propagate *en masse* through the plasma away from the Sun and are largely non-evolving.

In the theory of MHD turbulence, Alfvénic fluctuations can only be involved in turbulence if there are counterpropagating fluctuations in order to enable non-linear interactions (Kraichnan, 1965; Dobrowolny et al., 1980). If there is turbulence acting in the fast solar wind, it is related to the inward (toward the Sun) propagating Alfvénic fluctuations, which, if they exist, are in the noise of the measurements (Wang et al., 2018). Relatedly, in the reference frame that moves outward away from the Sun at the velocity of the Alfvénic fluctuations, the plasma flow velocity component locally perpendicular to B is in the noise of the measurement, indicating little or no evolution of the magnetic structure as it propagates outward (Borovsky J. E., 2020a).

TABLE 1 | Some properties of the wind-tunnel and Alfvénic solar-wind time series analyzed in this study.

Property	Wind tunnel	Alfvénic solar wind
Mean flow velocity	20.5 m/s	681 km/s
Length of time series	24.6 s (505 m)	71 h (1.74×10^8 km)
Data time resolution	4×10^{-5} s (0.82 mm)	3 s for $\underline{\mathbf{v}}$ (2, 040 km) 0.09375 s for $\underline{\mathbf{B}}$ (64 km)
Low-frequency breakpoint	1 s (20 m)	10^4 s (7×10^6 km)
High-frequency breakpoint	1,250 Hz (1.64 cm)	0.3 s (200 km)

This study will make a systematic comparison of the properties of Alfvénic solar wind fluctuations with true Navier–Stokes Kolmogorov active turbulence, asking what is similar, what is different, and for the properties that are similar asking why they are similar. As will be pointed out, the Navier–Stokes Kolmogorov turbulence measurements in the wind tunnel and the MHD Alfvénic structure propagation measurements in the fast solar wind are observations of two completely different processes. Similarities might point to some universal properties.

For a sample of Navier–Stokes turbulence, hot-wire 4×10^{-5}-s resolution measurements of the streamwise velocity v from the return-flow channel of the ONERA S1 wind tunnel at Modane are used (cf. Kahalerras et al., 1998; Malecot et al., 2000; Gagne et al., 2004; Podesta et al., 2009). The measurements are taken at the axis of the 24-m-diameter return channel. No grid is used in the return channel to generate turbulence; rather, as is the case for pipe flow (cf. Schlichting, 1979), the turbulence is driven by a velocity shear across a boundary layer between the wind flow and the wall (Kim et al., 1971). Some of the properties of this Navier–Stokes–turbulence time series are collected into **Table 1**. Applying the Reynolds-number scaling $R \sim (L_{\rm eddy}/L_{\rm Kolmog})^{4/3}$ (e.g., Equation 7.18 of Frisch, 1995), where $L_{\rm eddy}$ is the large eddy size (taken to be the low-frequency breakpoint of the power spectral density), and $L_{\rm Kolmog}$ is the Kolmogorov scale (taken to be the high-frequency breakpoint of the power spectral density), with the values $L_{\rm eddy} = 20$ m and $L_{\rm Kolmog} = 1.6$ cm in **Table 1**, the large-eddy Reynolds number R for the wind-tunnel turbulence is estimated as $R \sim 1.3 \times 10^4$. Gagne et al. (2004) estimate the Taylor microscale to be $\lambda \approx 2.8$ cm and the Taylor-scale Reynolds number to be $R_\lambda \approx 2{,}260$.

For a sample of Alfvénic fluctuations in the fast solar wind, a 71-h interval of unperturbed coronal-hole-origin plasmas measured by the WIND spacecraft at 1 AU is used. The long sample (13:00 UT on November 4, 2005, to 12:00 UT on November 7, 2005) of data analyzed is from "Flattop 15" in Table 1 of Borovsky (2016). In **Figure 1**, the radial (from the Sun) flow velocity $-v_x$ of the solar wind is plotted as a function of time for the solar-wind high-speed stream that contains Flattop 15. The flat top of the $-v_x$ plot indicates an interval of unperturbed fast wind, unperturbed in the sense that it has not been compressed or rarefacted by interaction with slower-wind streams. The WIND spacecraft measured the plasma flow vector $\underline{\mathbf{v}}$ with 3-s time resolution using the 3DP (three-dimensional plasma) instrument (Lin et al., 1995) and measured the magnetic-field vector $\underline{\mathbf{B}}$ with 0.09375-s time resolution using the MFI (magnetic field instrument) (Lepping et al., 1995). Note that the 3DP velocity measurements are noisier than the MFI magnetic-field measurements, and so some of the analyses will focus on $\underline{\mathbf{B}}$ instead of $\underline{\mathbf{v}}$. WIND spacecraft data are supplied in the GSE (geocentric solar ecliptic) XYZ right-hand coordinate system, where the direction X points from the Earth to the Sun, Y points from the Earth duskward in the ecliptic plane, and Z is normal to the ecliptic plane. During the 71-h interval denoted as Flattop 15 in **Figure 1**, the mean values ± standard deviations for some solar-wind parameters are radial flow speed $-v_x = 681 \pm 32$ km/s, plasma number density $n = 1.47 \pm 0.26$ cm^{-3}, magnetic-field strength $B_{\rm mag} = 4.47 \pm 0.60$ nT, Alfvén speed $v_{\rm A} = 81.1 \pm 10.5$ km/s, Alfvén Mach number $M_{\rm A} = -v_x/v_{\rm A} = 8.6 \pm 2.1$, ion-inertial length $c/\omega_{\rm pi} = 190 \pm 18$ km, and thermal proton gyroradius $r_{\rm gi} = 107 \pm 27$ km. To estimate an effective large-eddy Reynolds number, the Reynolds-number scaling $R_{\rm eff} \sim (L_{\rm eddy}/L_{\rm Kolmog})^{4/3}$ is applied, where the scale size associated with the high-frequency breakpoint is used for $L_{\rm Kolmog}$, even though it is not a Kolmogorov scale where viscosity balances the cascade rate; with the values $L_{\rm eddy} = 7 \times 10^6$ km and $L_{\rm Kolmog} = 200$ km in **Table 1**, the effective Reynolds number R for the Alfvénic fluctuations is estimated as $R_{\rm eff} \sim 1.1 \times 10^6$. At 681 km/s, the transit time of the solar wind (= age of the solar-wind plasma) from the Sun to 1 AU is ∼61 h, which is less than the 71-h duration of the interval; hence (like a wind tunnel), the beginning of the Flattop-15 plasma interval was being measured at 1 AU before the final part of the interval was created at the Sun. This 61-h transit time is also approximately the age of the plasma $\tau_{\rm age}$ when it is measured at 1 AU. A large spatial scale for this interval of coronal-hole-origin solar wind is defined by causality and the age of the plasma: the spatial scale $L_{\rm caus} = v_{\rm A}\tau_{\rm age}$, which is the distance an Alfvénic signal can propagate along the mean field and so represents the "domains of communication" scale size in the plasma. This value is $L = v_{\rm A}\tau_{\rm age} = M_{\rm A}^{-1}\, d$, where $d = 1$ AU $= 1.5 \times 10^8$ km is the distance from the Sun to the WIND spacecraft. It would be associated with a spacecraft timescale $t_{\rm caus} = M_{\rm A}^{-1}\tau_{\rm age} = 7.1$ h. Another large spatial scale in this plasma is the ∼5-h domains of Alfvénicity shown in Figure 14 of Borovsky (2016); it has been suggested that these domains could be associated with the large-scale open-flux-funnel structure of coronal holes. Some properties of this Alfvénic-fluctuation time series are collected into **Table 1**.

In making the comparison between the Navier–Stokes wind-tunnel measurements and the solar-wind fluctuation measurements, it would be useful to normalize the two data sets to each other, perhaps by scaling the amplitudes and the times. Owing to uncertainties, such a normalization is not made for the present study. One-time scaling could be based on the correlation time of each time series; however, the correlation time is ambiguous, and depends on the length of the time series used for its calculation. A less-ambiguous time normalization could be based on the timescale of the high-frequency Fourier breakpoint of the power spectral density of each time series. The analysis of the two time series in *Similarities and Differences in the Statistics of Derivatives* will be based on the timescale difference from the high-frequency breakpoint of the two series.

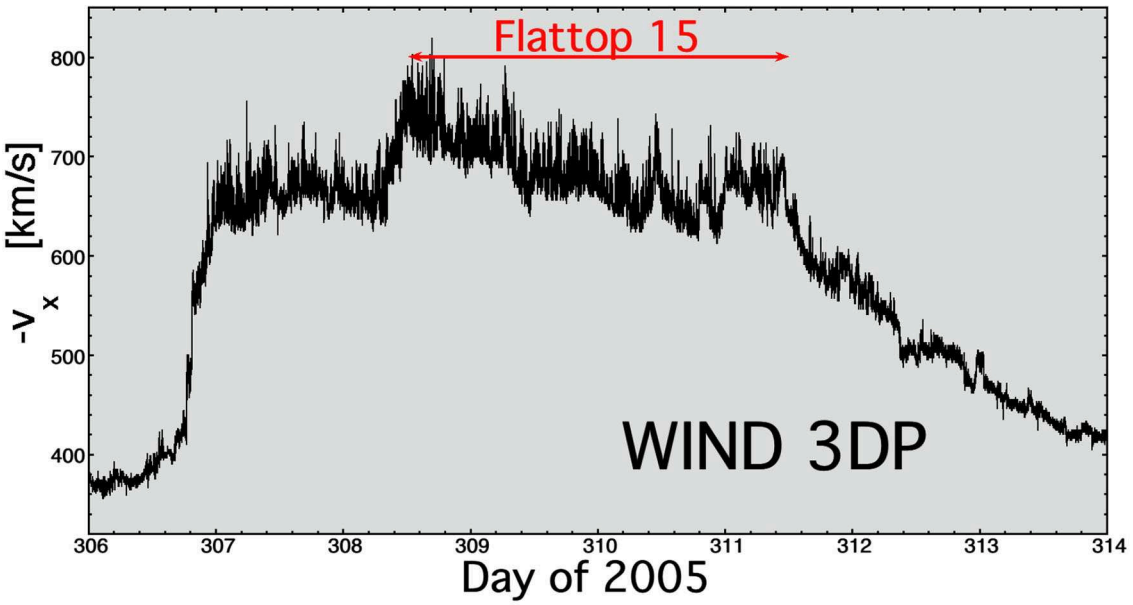

FIGURE 1 | The high-speed stream in November 2005 that contains Flattop 15. The radial-velocity measurements were taken by the WIND spacecraft at 1 AU.

This article is organized as follows. In *Similarities and Differences in the Medium*, similarities and differences between a Navier–Stokes fluid and the magnetized collisionless solar-wind plasma are discussed. In *Similarities and Differences in the Fluctuations*, similarities and differences in the physical nature of the fluctuations in Navier–Stokes turbulence vs. the Alfvénic solar wind are discussed. *Similarities and Differences in the Fourier Spectra* examines the similarities and differences in the power spectral densities of the wind-tunnel Navier–Stokes turbulence vs. the Alfvénic fluctuations in the fast solar wind. *Similarities and Differences in the Statistics of Derivatives* examines the statistics of time derivatives in the wind-tunnel Navier–Stokes turbulence measurements vs. the measurements of the Alfvénic fluctuations of the solar wind. *Level Shifts and Calm Regions* examines flat spots in the measurement time series of the wind tunnel vs. the Alfvénic solar wind. *Summary and Discussion* contains a summary of findings and a discussion about the possible origin of the properties of the Alfvénic fluctuations. *Similarities and Differences in the Medium* also contains a summary. A call for coordinated future work is also made in *Summary and Discussion*.

SIMILARITIES AND DIFFERENCES IN THE MEDIUM

A Navier–Stokes fluid (such as air) is an isotropic medium that obeys the Navier–Stokes equation for momentum transport

$$\rho(\partial \underline{\mathbf{v}}/\partial t + \underline{\mathbf{v}} \bullet \nabla \underline{\mathbf{v}}) = -\nabla P + \rho\nu\nabla^2 \underline{\mathbf{v}}, \qquad (1)$$

where ρ is the mass density of the fluid, P is an isotropic pressure, and ν is the kinematic viscosity. In this medium, momentum is transferred locally from one element of fluid to the adjacent elements via the stress tensor and via ∇P. In transporting momentum long distances, one element transfers its momentum to a neighbor, which in turn transports its momentum to its neighbor, and so forth. In the Navier–Stokes equation, momentum transport occurs at a sound speed $\sim P/\rho$.

A collisionless magnetized plasma (such as the solar wind) is anisotropic on global and local scales. It is anisotropic globally in that the magnetic structure of the plasma can propagate without evolution in the direction of the global mean magnetic-field vector (cf. Figure 7.1 of Parker, 1979; Borovsky J. E., 2020a; Nemecek et al., 2020), and it is anisotropic locally in that the nature of the forces perpendicular and parallel to the local magnetic-field vector $\underline{\mathbf{B}}$ differs. In the MHD description of plasmas, the momentum transport is given by

$$\rho(\partial \underline{\mathbf{v}}/\partial t + \underline{\mathbf{v}} \bullet \nabla \underline{\mathbf{v}}) = -\nabla P + (1/c)\underline{\mathbf{j}} \times \underline{\mathbf{B}} + \rho\nu\nabla^2 \underline{\mathbf{v}}, \qquad (2)$$

where $\underline{\mathbf{j}}$ is the electrical current density in the plasma. In the direction parallel to $\underline{\mathbf{B}}$, the $\underline{\mathbf{j}} \times \underline{\mathbf{B}}$ term of expression (2) vanishes, and the MHD description reduces to the Navier–Stokes equation (expression 1). A collisionless plasma has fluid-like properties in the directions perpendicular to $\underline{\mathbf{B}}$ where the magnetic field constrains the charged particles of the plasma to orbit the magnetic-field lines together (e.g., Chew et al., 1956; Parker, 1957), but in the direction along $\underline{\mathbf{B}}$, the particles of the plasma travel ballistically. In a collisionless plasma parallel to $\underline{\mathbf{B}}$, momentum is transported at the speed of the individual particles (e.g., ions), and momentum is not shared with neighboring parcels of plasma. Occasional warnings have appeared about the use of MHD to describe the collisionless solar wind (e.g., Lemaire and Scherer, 1973; Montgomery, 1992). As pointed out

by Borovsky and Gary (2009), the solar-wind plasma fails fluid-behavior tests in the parallel-to-$\underline{\mathbf{B}}$ direction. Three examples are the following. (1) The ballistic-ion behavior along $\underline{\mathbf{B}}$ observed when the solar-wind plasma and the magnetospheric plasma are magnetically joined by field-line reconnection (Paschmann, 1984; Thomsen et al., 1987); fluid behavior would produce a local sharing of momentum and a separation of the two reconnected plasmas, rather than the long-distance interpenetration of the ion populations that is seen. (2) The inability of the solar-wind plasma to form a stationary bow shock when the shock-normal angle is parallel to the solar-wind magnetic field (Thomsen et al., 1990; Mann et al., 1994; Wilkinson, 2003; Lucek et al., 2004). (3) The strictly particle-kinetic dynamics along $\underline{\mathbf{B}}$ of the solar-wind as it fills in the wake created by flow past the moon (Ogilvie et al., 1996; Farrell et al., 2002).

This difference is noted as item 1 in **Table 2**.

TABLE 2 | A summary of differences between the Navier–Stokes turbulence in the wind tunnel and the Alfvénic fluctuations of the fast solar wind.

#	Navier–Stokes fluid turbulence	Alfvénic fluctuations in coronal-hole-origin plasma
1	Medium is an isotropic fluid	Medium is an anisotropic collisionless plasma
2	Medium is homogeneous	Medium contains magnetic holes and Alfvénicity domains
3	The fluctuations are advecting interacting structures	The fluctuations are propagating, largely non-interacting structures
4	Structure temporally evolving	Interlocking network of non-evolving structure
5	Interaction timescale $\tau_{eddy} \sim L_{fluctuation}/\delta v$	Interaction timescale $>> L_{fluctuation}/\delta v$
6	Fluctuations are locally (near the measurement probe) generated	Fluctuations are generated nearer to the Sun than the measuring spacecraft
7	Energy source is large-scale shear	Energy source is argued to be lower-frequency Alfvénic fluctuations from the Sun
8	Fluctuation structure is not cellular	Fluctuation structure is cellular and tube-like
9	High-frequency breakpoint location is governed by viscous dissipation balancing the energy cascade	High-frequency breakpoint is governed by thicknesses of strong current sheets
10	High-frequency breakpoint location is mvable	High-frequency breakpoint location is fixed by the plasma properties
11	High-frequency spectrum is exponential	High-frequency spectrum is a power law
12	The power spectrum below the low-frequency breakpoint decreases with decreasing frequency	The power spectrum below the low-frequency breakpoint increases with decreasing frequency
13	Coherent structure is restricted to the high-frequency end of the inertial subrange	Coherent structure occurs throughout the inertial subrange

SIMILARITIES AND DIFFERENCES IN THE FLUCTUATIONS

In the Navier–Stokes wind tunnel, the fluctuations $\delta\underline{\mathbf{v}}$ are interacting, "advecting" perturbations with a spatial pattern that evolves with time. Historically, the fluctuations have been described as eddies with a range of spatial scales (Tennekes and Lumley, 1972 sect. 8.2; Frisch, 1995 sect. 7.3); however, there are also coherent structures in the turbulence such as vortex filaments (e.g., Belin et al., 1996; Jimenez and Wray, 1998; Biferale et al., 2010). The eddies are thought to strongly interact with each other, particularly eddies of similar spatial scales, producing eddies of smaller spatial scale during the interaction; those eddy–eddy interactions (along with intermittent-structure interactions) create a cascade of flow kinetic energy from large scales to smaller scales (e.g., Argoul et al., 1989; Ch. 6 of Pope, 2000). Stretching of vorticity structures, important for both Navier–Stokes and MHD (e.g., Figure 8.4 of Tennekes and Lumley, 1972 or Moffatt, 2014), is dominant in the eddy–eddy interactions. Because of the cascade of energy, driving must be present for the Navier–Stokes turbulent fluctuations to persist.

In the Alfvénic solar wind, the fluctuations $\delta\underline{\mathbf{v}}$ and $\delta\underline{\mathbf{B}}$ are non-interacting, "propagating" perturbations with a spatial pattern that does not evolve. Figure 7.1 of Parker (1979) sketches a volume of tangled magnetic field embedded in a uniform field of strength B_o. If the plasma is incompressible, Parker points out that if there are field-aligned flows everywhere within the magnetic structure, then the volume of tangled magnetic field will propagate at the mean-field Alfvén speed $B_o/(4\pi\rho)^{1/2}$ without distortion. Inside the volume, the total field is $(B_o^2 + B_1^2)^{1/2}$, which is greater in strength than B_o, and so the Alfvén speed measured inside the volume $B/(4\pi\rho)^{1/2}$ is greater than the mean-field Alfvén speed $B_o/(4\pi\rho)^{1/2}$, and so the magnetic structure moves at a speed lower than the Alfvén speed measured inside the structure. Borovsky J. E. (2020a) and Nemecek et al. (2020) have developed methodologies to find the moving reference frame of the solar-wind magnetic structure relative to the solar-wind plasma; at 1 AU, they find that the magnetic structure propagates at about 0.7 v_A along the Parker-spiral direction relative to the proton plasma of the solar wind, where v_A is the local Alfvén speed within the magnetic structure. In Figure 2 of Borovsky J. E. (2020a), the velocity of the magnetic structure is plotted as a function of time for Flattop 15. In 1-min resolution measurements of magnetic fluctuations at 1 AU, the angular spread of magnetic-field directions about the Parker-spiral direction is about 40° (cf. row 1 of Table 1 in Borovsky, 2010a). Hence, $B_1 = B_o \tan(40^\circ) = 0.84\, B_o$. Thus, $B = (B_o^2 + B_1^2)^{1/2} = 1.3\, B_o$, and so the structure moving at the Alfvén speed of B_o moves at about $1/1.3 = 0.77$ times the measured Alfvén speed of B. In the reference frame of the magnetic structure, the proton flow vector $\underline{\mathbf{v}}$ is everywhere parallel to the local magnetic field $\underline{\mathbf{B}}$, and the flow components in the structure change as the field direction spatially varies in the magnetic structure. Note, however, that the α-particle "beam" of the solar wind is approximately at rest in the reference frame of the magnetic structure (Nemecek et al., 2020). In the reference frame of the magnetic structure, the magnitude of the perpendicular component of the plasma flow vector is consistent with measurement error: the magnitude of

the measured values of $\underline{\mathbf{v}}_\perp$ is consistent with a purely parallel-to-$\underline{\mathbf{B}}$ velocity $v_{||}$ and the uncertainty in the parallel-to-$\underline{\mathbf{B}}$ vs. perpendicular-to-$\underline{\mathbf{B}}$ directions owing to the angular variation of the direction of $\underline{\mathbf{B}}$ during the time required to obtain a vector $\underline{\mathbf{v}}$ measurement. Such perpendicular-to-$\underline{\mathbf{B}}$ flows would signify an evolution of the propagating magnetic structure, but the measurements do not support the observation of evolution. Note that measurements of the third-order Elsasser moments show evidence of an evolution of the Alfvénic fluctuations of the fast solar wind indicated by a non-zero energy-cascade rate in the fluctuations (e.g., Sorriso-Valvo et al., 2007; MacBride et al., 2008; Stawarz et al., 2010; Podesta, 2011).

There are two other aspects of the solar-wind Alfvénic fluctuations that differ from the Navier–Stokes fluctuations. The parallel-to-$\underline{\mathbf{B}}$ flow of plasma in the reference frame of the magnetic structure gives rise to (1) flow jets at magnetic switchbacks, which produce (2) a solar-wind speed that has a skewed distribution. In the reference frame of the magnetic structure, the proton flow is toward the Sun: at locations where there are localized magnetic-field foldings (denoted as switchbacks or field reversals), the flow is anti-Sunward in the reference frame of the magnetic structure. Going to the reference frame of a spacecraft, which sees the magnetic structure moving outward along the Parker-spiral direction, the spacecraft will see a faster proton flow velocity in the magnetic-field switchback than in the surrounding regions: this localized fast flow gives the impression of a flow jet (Kahler et al., 1996; Balogh et al., 1999; Neugebauer and Goldstein, 2013; Borovsky, 2016; Borovsky J. E., 2020d). As seen by a spacecraft, the solar-wind bulk flow velocity depends on the direction of the magnetic field. This gives rise to the phenomena of one-sided variations of the solar-wind speed (Gosling et al., 2009; Matteini et al., 2014).

These differences are noted in **Table 2** as items 3 and 4.

In the wind tunnel data, the pattern of evolving fluctuations is advected past the probe at a large velocity $v_o \sim 12\delta v$. In the WIND spacecraft measurements of Flattop 15, the pattern of Alfvénic fluctuations is advected past the probe at a large velocity $v_o \sim 21\delta v$.

The Navier–Stokes wind-tunnel turbulence fluctuations are characterized by a velocity perturbation $\delta\underline{\mathbf{v}}$ on a mean flow $\underline{\mathbf{v}}_o$, whereas the Alfvénic solar-wind fluctuations are characterized by a velocity perturbation $\delta\underline{\mathbf{v}}$ and magnetic-field perturbation $\delta\underline{\mathbf{B}}$ on a mean flow $\underline{\mathbf{v}}_o$ and mean magnetic-field vector $\underline{\mathbf{B}}_o$. In the Alfvénic fluctuations, $\delta\underline{\mathbf{B}}(t)$ and $\delta\underline{\mathbf{v}}(t)$ are highly correlated (for a toward-the-Sun mean magnetic field direction) or highly anticorrelated (for an away-from-the-Sun mean magnetic field-direction). In the full Flattop-15 data set, the 3-s data correlation coefficients are $R_{corr} = 0.847$ for $v_x \leftrightarrow B_x$, 0.880 for $v_y \leftrightarrow B_y$, and 0.888 for $v_z \leftrightarrow B_z$, using 15-s changes in the vectors. For Alfvénic fluctuations, it is convenient to describe $\underline{\mathbf{v}}$ and $\underline{\mathbf{B}}$ in terms of the outward-propagating and inward-propagating Elsasser variables $\underline{\mathbf{Z}}_{out} = +\,s\underline{\mathbf{b}}$ and $\underline{\mathbf{Z}}_{in} = \underline{\mathbf{v}} - s\underline{\mathbf{b}}$, where $\underline{\mathbf{b}} = \underline{\mathbf{B}}/(4\pi\rho)^{1/2}$ is the magnetic-field vector normalized to the Alfvén speed and the sign $s = -1$ for toward magnetic sectors and $s = +1$ for away magnetic sectors. The Alfvénic fluctuations of the fast solar wind are described by $\underline{\mathbf{Z}}_{out}$, with the values of $\underline{\mathbf{Z}}_{in}$ in the noise of the $\underline{\mathbf{v}}$ and $\underline{\mathbf{B}}$ measurements (Wang et al., 2018).

An important difference between the turbulent fluctuations in the wind tunnel and the Alfvénic fluctuations propagating outward in the fast solar wind at 1 AU is that the wind-tunnel fluctuations are locally generated near the measurement location, whereas the Alfvénic fluctuations have been generated closer to the Sun and propagated to the measuring spacecraft at 1 AU. It is argued that the source of channel-flow fluid turbulence is large-scale shear in the flow (cf. Ch. 7 of Pope, 2000); in the solar wind, it has been argued that the energy source of the inertial-range turbulent fluctuations is lower-frequency outward-propagating Alfvénic fluctuations that originate at the Sun (Horbury et al., 1996; Zank et al., 1996; Smith et al., 2001; Vasquez et al., 2007; Bruno et al., 2019). These differences are noted in **Table 2** as items 6 and 7.

Four other differences between the solar-wind Alfvénic fluctuations and the Navier–Stokes turbulent fluctuations are described in the following four paragraphs.

(1) The pattern of fluctuations in the solar wind represents a cellular spatial structure wherein the magnetic field undergoes a strong directional change across a "directional discontinuity" (strong current sheet) and then the magnetic-field directional variations are relatively small for an interval of time until another directional discontinuity is crossed. This pattern represents a magnetic cellular structure or flux-tube structure of the plasma wherein the directional discontinuities (current sheets) are the cell walls, and the intervals of small directional changes are the interiors of the cells (cf. Bruno et al., 2001; Borovsky, 2008). The fact that the flux-tube walls of the solar wind also coincide with intensity changes of the intensity of the solar-wind electron heat flux (electron Strahl) (Borovsky J. E., 2020b) implies that the flux-tube structure has a long-distance coherence going from 1 AU back toward the Sun. In the Alfvénic solar wind, the velocity fluctuations also have this cellular spatial structure because, in the reference frame of the magnetic structure, all flow velocities are parallel to $\underline{\mathbf{B}}$ (Borovsky J. E., 2020a). This is noted in **Table 2** as item 8.

(2) The solar-wind Alfvénic fluctuations exhibit matching pairs of current sheets wherein the field and flow vectors $\underline{\mathbf{B}}(t)$ and $\underline{\mathbf{v}}(t)$ are quasi-steady with a particular orientation, then $\underline{\mathbf{B}}$ and $\underline{\mathbf{v}}$ both undergo a sudden change in orientation across a first current sheet, and then after an interval of time, $\underline{\mathbf{B}}$ and $\underline{\mathbf{v}}$ suddenly return to their original orientations across a second current sheet. Two examples of this appear in **Figure 2** [and other examples can be found in the literature (e.g., Gosling et al., 2011; Arnold et al., 2013)]. The event in the left-hand panel has a total duration of 16 s (from the first current sheet to the matching current sheet), with 144 s of data plotted. The event in the right-hand panel has a total duration of 5.5 min with 12 min of data plotted. The velocity components measured by the WIND spacecraft are plotted in red, and the magnetic-field components $\underline{\mathbf{b}}$ (normalized to the Alfvén speed $\underline{\mathbf{b}} = \underline{\mathbf{B}}/(4\pi\rho)^{1/2}$) are plotted in blue. In all panels, the locations of the two current sheets are marked with green arrows. Note the strong correlations in the temporal behaviors of $\underline{\mathbf{v}}$ and $\underline{\mathbf{B}}$ (that is what is meant by

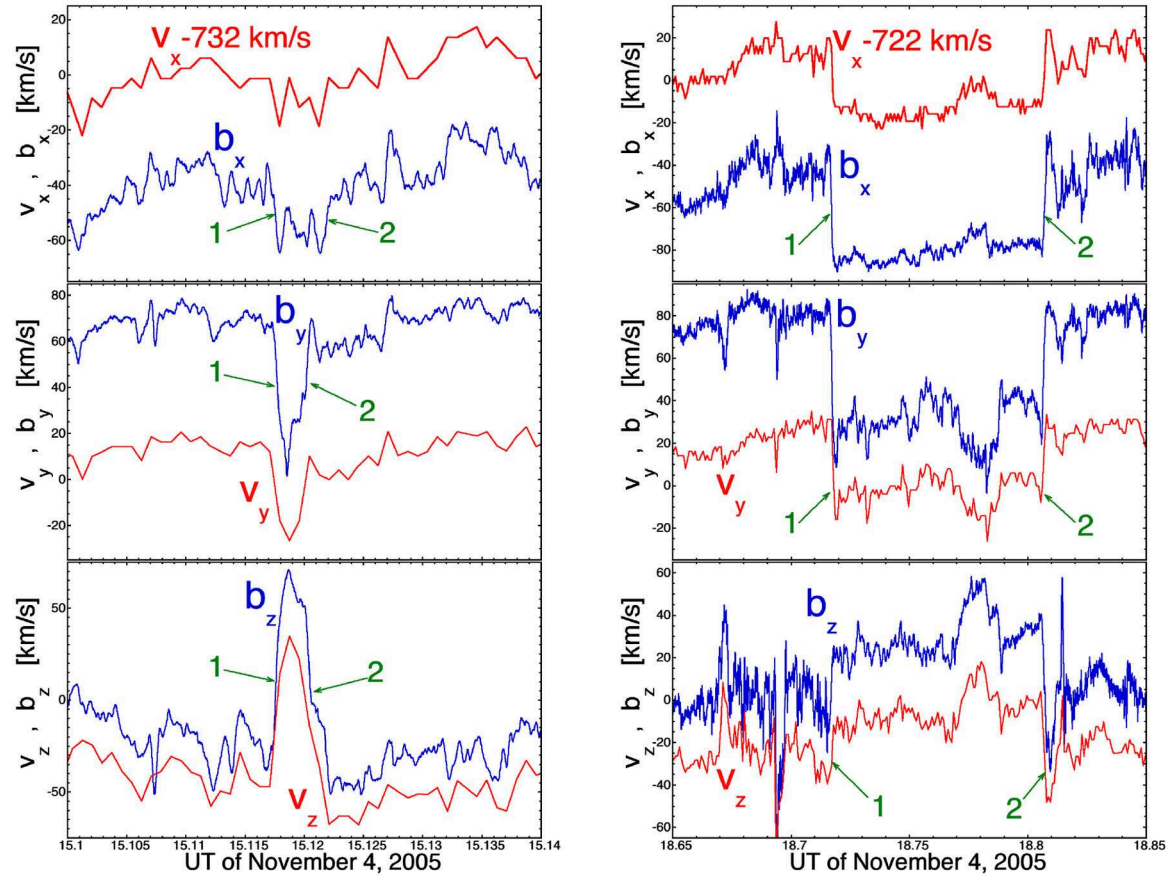

FIGURE 2 | Two examples of paired current sheets, one with an event duration of 16 s (left panel) and one with a duration of 5.5 min (right panel). The velocity (red curves) is measured with 3-s time resolution and the magnetic field (blue curves) is measured with 0.09375-s time resolution. The two current sheets marking the beginning and end of the event are indicated in each panel with green arrows.

the fluctuations being "Alfvénic"). In both panels, the $\underline{\mathbf{v}}$ and $\underline{\mathbf{B}}$ vectors have the same orientations before current sheet "1" and after current sheet "2," but different orientations between the current sheets. Such matching pairs of current sheets are common in the Alfvénic fluctuations of the fast solar wind and lead to a statistically non-randomness of the temporal changes of the magnetic-field direction at 1 AU (cf. Figure 10 of Borovsky J. E., 2020c).

(3) The fast Alfvénic plasma of coronal-hole origin exhibits "domains of Alfvénicity" wherein the $\underline{\mathbf{v}}(t) \leftrightarrow \underline{\mathbf{B}}(t)$ correlation coefficient is very high for a temporal interval, then a non-Alfvénic (poorly correlated) transition of $\underline{\mathbf{v}}$ and $\underline{\mathbf{B}}$ occurs, and then another subsequent highly correlated $\underline{\mathbf{v}}(t) \leftrightarrow \underline{\mathbf{B}}(t)$ temporal interval commences. For Flattop 15, the domains of Alfvénicity are plotted in Figure 14 of Borovsky (2016). At 1 AU, typical durations of a single domain are a few hours. These domains of Alfvénicity seen in coronal-hole-origin solar wind may be associated with open flux funnels in the downflow lanes at the edges of supergranules on the Sun (Dowdy et al., 1987; Tu et al., 2005; Peter, 2007; Kayshap et al., 2015), or they might be associated with magnetic separatrices in the corona (Burkholder et al., 2019). This is noted in **Table 2** as item 2.

(4) The fast solar wind also exhibits magnetic holes (Turner et al., 1977; Winterhalter et al., 2000; Neugebauer et al., 2001; Amariutei et al., 2011), which are spatial regions of various sizes wherein the magnetic-field strength is locally much reduced from the average value. In most of the Alfvénic fluctuations of the solar wind, the direction of the magnetic-field vector $\underline{\mathbf{B}}$ can vary by up to 180°, whereas the strength of the magnetic field B_{mag} essentially does not vary. **Figure 3** shows an example of a magnetic hole in Flattop 15. **Figure 3A** plots the magnetic-field strength (blue), the Alfvén speed (green), and the proton-beta $\beta_p = 8\pi n k_B T_p/B^2$ (red) as functions of time for 9 min of observations. **Figure 3B** plots the magnetic pressure $B^2/8\pi$, the proton pressure nk_BT_p, and the electron pressure nk_BT_e, with the electron properties measured by the SWE (Solar Wind Experiment) instruments (Ogilvie et al., 1995) onboard the WIND spacecraft. Note in **Figure 3B** the hint of pressure balance at the magnetic hole where the magnetic pressure is decreased within the magnetic hole and the particle pressures

are increased. In Fourier analysis of the $B_{\rm mag}(t)$ time series and of the number density n(t) time series, magnetic holes contribute Fourier power to the spectral density where the interpretation of the Fourier power is the degree of compressibility of the solar-wind fluctuations (e.g., Marsch and Tu, 1990b; Goldstein and Roberts, 1999), but the true origin of the power is not in compressions or rarefactions. Note that a magnetic hole with a timescale τ contributes Fourier power at all frequencies. Likewise, magnetic holes make contributions to other $B_{\rm mag}$ and n statistics where they can be interpreted as compressions (Hnat et al., 2005; Matteini et al., 2018). The origins of magnetic holes are not known, and it is a matter of choice to consider them to be a property of the fluctuations (this section) or a property of the medium (*Similarities and Differences in the Medium*). This difference is noted in **Table 2** as item 2. As pointed out in Borovsky J. E. (2020d), the descriptor "compressible" might be more accurately replaced by "inhomogeneous".

SIMILARITIES AND DIFFERENCES IN THE FOURIER SPECTRA

In **Figure 4**, the power spectral densities for the streamwise velocity in the ONERA wind tunnel (**Figure 4A**), the radial proton-plasma velocity component of the solar wind in Flattop 15 (**Figure 4B**), and the radial component of the solar-wind magnetic field (**Figure 4C**) are plotted. The power spectral densities are calculated from the time series of measurements using the periodogram method (Cooley et al., 1970; Otnes and Enochson, 1972), with the power spectral density being the square of the Fourier transform. Data that are not a factor of 4 below the Nyquist frequency are not plotted. Data gaps in the time series are linearly interpolated.

The Inertial Subrange

In **Figure 4A**, the inertial subrange of the Navier–Stokes turbulence spans the frequency range from about 1 to 1,250 Hz, and in **Figures 4B,C**, the inertial subrange of the Alfvénic solar-wind fluctuations spans the frequency range from about 10^{-4} Hz (or lower) to 0.3 Hz.

Both the Navier–Stoke turbulence and the Alfvénic solar wind have power spectral densities that are power laws in the inertial subranges. In **Table 3**, the power-law spectral slopes for the spectra plotted in **Figure 4** are collected, with information about the frequency range used for the power-law fits.

The power-law spectral index of Navier–Stokes turbulence is well-known to be associated with a cascade of fluctuation energy from larger-scale size fluctuations to smaller-scale size fluctuations (cf. section 8.3 of Tennekes and Lumley, 1972; section 5.1 of Frisch, 1995). A power-law spectrum is interpreted as scale invariance or scale similarity (e.g., section 7.3 of Frisch, 1995).

In the Alfvénic solar wind, the inertial-range spectral index of the magnetic power spectral density and the inertial-range spectral index of the velocity power spectral index differ, with the velocity spectra being systematically shallower than the magnetic

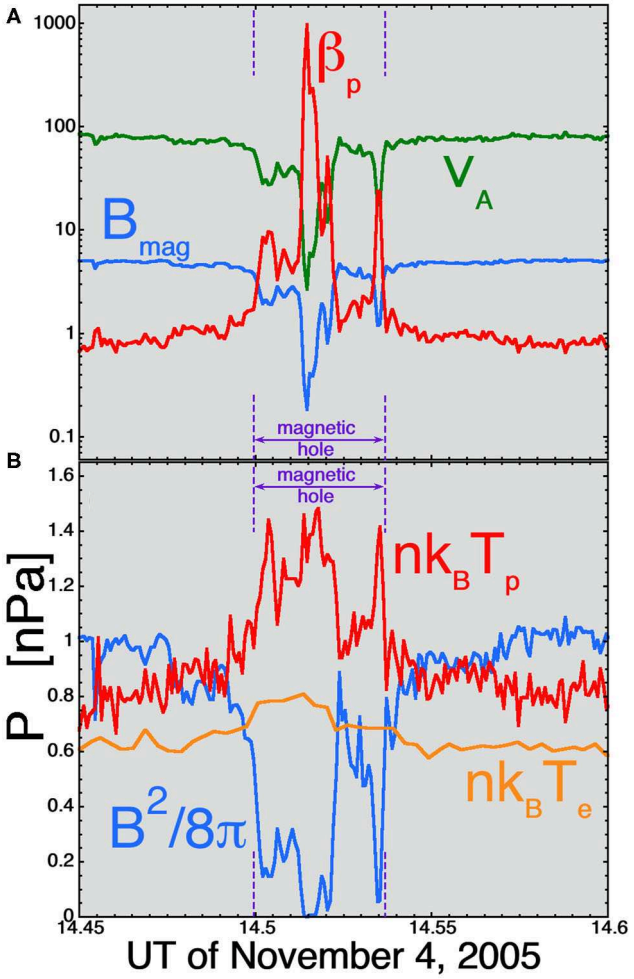

FIGURE 3 | An example of a magnetic hole (denoted in purple) during Flattop 15. Nine minutes of WIND spacecraft data [plasma properties in panel **(A)** and pressures in panel **(B)**] are plotted, and the duration of the magnetic hole as seen by WIND was 130 s.

spectra (Podesta et al., 2007; Tessein et al., 2009; Borovsky, 2012). The amplitude and the spectral slope of the solar-wind magnetic power spectral density in the inertial range is determined by the amplitudes and occurrence distribution of strong current sheets (directional discontinuities) in the solar-wind plasma (Siscoe et al., 1968; Sari and Ness, 1969; Borovsky, 2010b), which are coherent structures. Because $\delta\underline{\mathbf{v}}$ and $\delta\underline{\mathbf{B}}$ are strongly correlated in the Alfvénic solar wind and because strong velocity shears occur at the sites of strong current sheets, it is almost certainly the case that the amplitude and the spectral index of the velocity power spectral density of the Alfvénic solar wind will be determined by the amplitudes and occurrence distribution of intense velocity shears in the solar-wind plasma. The strength of the contribution of coherent structures in the Navier–Stokes turbulence to the Navier–Stokes inertial-range power spectral density is not known.

The energy-transfer timescale in Navier-Stokes turbulence goes as the eddy turnover time $\tau_{\rm eddy} = L_{\rm eddy}/\delta v$, where $L_{\rm eddy}$ is

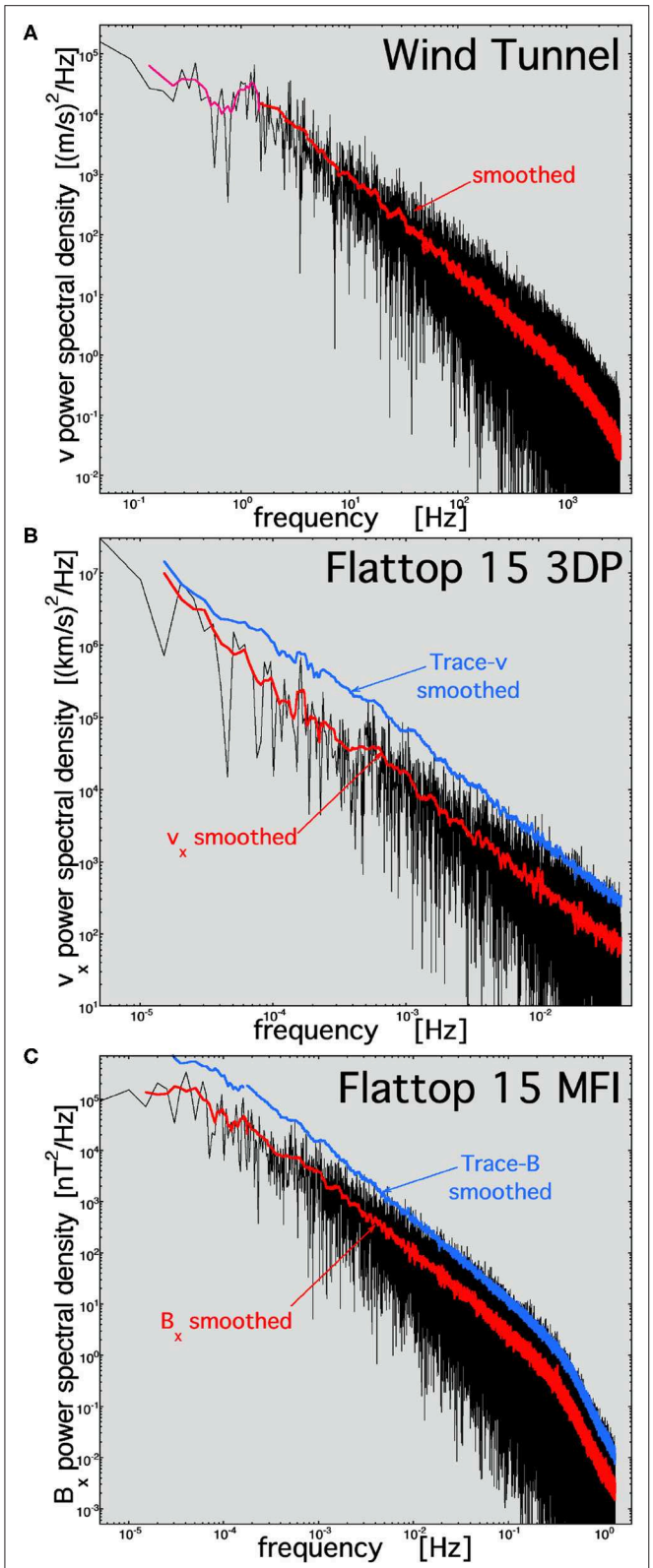

FIGURE 4 | Periodogram power spectral densities for **(A)** the streamwise velocity v in the wind tunnel Navier–Stokes turbulence, **(B)** the radial (from the Sun) velocity v_x for the Alfvénic solar wind fluctuations of Flattop 15, and **(C)** the radial component of the magnetic field B_x for the Alfvénic solar wind fluctuations of Flattop 15.

TABLE 3 | Spectral fits in the inertial subrange.

	Index	Fit range	Data resolution used
v	−1.625	5 to 500 Hz	4×10^{-5} s
B_x	−1.561	10^{-3} to 10^{-1} Hz	0.09375 s
B_y	−1.607	10^{-3} to 10^{-1} Hz	0.09375 s
B_z	−1.548	10^{-3} to 10^{-1} Hz	0.09375 s
Trace B	−1.570	10^{-3} to 10^{-1} Hz	0.09375 s
v_x	−1.404	10^{-3} to 4.16×10^{-2} Hz	3.0 s
v_y	−1.511	10^{-3} to 4.16×10^{-2} Hz	3.0 s
v_z	−1.462	10^{-3} to 4.16×10^{-2} Hz	3.0 s
Trace v	−1.458	10^{-3} to 4.16×10^{-2} Hz	3.0 s

a large-eddy scale size at the low-frequency end of the inertial subrange, and δv is the rms level of velocity fluctuations (cf. Section 7.1 of Frisch, 1995). τ_{eddy} is the evolution timescale (lifetime) of a large eddy. The evolution timescale for the Alfvénic solar-wind fluctuations can be gauged as $\tau_{evol} \sim L_\perp/\delta v_\perp$ where $L_\perp$ is the perpendicular-to-B fluctuation scale size, and $\delta v_\perp$ is the perpendicular-to-B fluctuation velocity. In the reference frame moving with the collective magnetic-field structure, $v_\perp$ is quite small, in the noise of the velocity measurements (Borovsky J. E., 2020a. Hence, the evolutionary timescale τ_{evol} of the Alfvénic fluctuations is long, much longer than an "eddy turnover time." This is akin to the Elsasser-mode evolution timescale for the evolution of outward Elsasser fluctuations ${\tau^{\circ}}^{\text{out}}{}_L \sim L/\delta {Z^{\text{in}}}_L$ (Bruno and Carbone, 2016) where the amplitude $\delta {Z^{\text{in}}}_L$ of the inward Elsasser fluctuations is in the noise of the measurements. This difference is noted in **Table 2** as item 5.

The High-Frequency Breakpoint

Both Navier–Stokes turbulence and the Alfvénic solar wind have breakpoints in their power spectral densities defining the high-frequency end of the inertial subrange, with the power spectra steepening above the breakpoint.

For Navier–Stokes turbulence, the breakpoint is known to be associated with the cascade of energy to smaller spatial scales encountering stronger viscous dissipation of fluctuations at smaller spatial scales. This balance at the breakpoint is at the Kolmogorov dissipation scale. In Navier–Stokes turbulence, the breakpoint frequency (or wavenumber) is movable: if the turbulence is driven harder, the breakpoint moves to higher frequencies.

For solar-wind power spectra, the location of the high-frequency breakpoint is fixed by characteristic scale sizes in the solar-wind plasma: the ion gyroradius and the ion-inertial length (Leamon et al., 1998; Gary, 1999; Gary and Borovsky, 2004, 2008; Bruno and Trenchi, 2014). If the turbulence is driven harder, the frequency (wavenumber) of the breakpoint does not move. These characteristic plasma scale sizes represent a transition from fluid-like behavior at large scales to particle-kinetic behavior at small scales. It is known that the frequency of the high-frequency breakpoint in the magnetic power spectra of the Alfvénic fast solar wind is governed by the thicknesses of strong current sheets in the solar-wind plasma (Borovsky and Podesta, 2015), another strong

effect of coherent structure on the power spectral density of the solar wind.

This difference is noted in **Table 2** as items 9 and 10.

The frequency spectrum above the high-frequency break tends to be exponential-like for Navier–Stokes turbulence (e.g., section 8.4 of Tennekes and Lumley, 1972; Sirovich et al., 1994). For the Alfvénic fluctuations of the solar wind, the frequency spectrum above the high-frequency breakpoint tends to be a power law (cf. **Figure 4B**; Leamon et al., 1998; Alexandrova et al., 2009; Podesta, 2010; Sahraoui et al., 2010; Chen et al., 2014; Bruno et al., 2017). For Flattop 15, the fitted magnetic spectral indices in the 0.5- to 1.333-Hz frequency range above the breakpoint are −3.39 for B_x, −3.62 for B_y, −3.78 for B_z, and −3.66 for trace B. The shape and amplitude of the magnetic power spectral density above the high-frequency breakpoint are consistent with the Fourier spectra of individual solar-wind current sheets (Borovsky and Burkholder, 2020), suggesting that the high-frequency spectra may be governed by the spatial profiles of the solar-wind current sheets or by physical processes ongoing within the current sheets. The origin of the solar-wind high-frequency spectrum is an ongoing research issue, with dissipation, mode conversion, and current-sheet physics being considered (e.g., Podesta et al., 2010; Gary et al., 2012; Podesta and Borovsky, 2016; Mallet et al., 2017). This difference is noted in **Table 2** as item 11.

The Low-Frequency Energy Subrange

At low frequencies, the power law of the inertial subrange ends.

In Navier–Stokes turbulence, the power spectrum rolls over and decreases in amplitude as $f \rightarrow 0$ (e.g., Figure 5.7 of Frisch, 1995; Figure 6.20 of Pope, 2000). The end of the inertial range at low frequency is associated with a large-eddy scale size, usually a fraction of the width of the flow channel. The rolling over of the spectrum indicates an absence of energy in large-spatial-scale (low-frequency) fluctuations.

For fluctuations in the Alfvénic solar wind, the power spectrum at the low-frequency end of the inertial subrange bends to a shallower spectrum that is often characterized by a power-law index. The Alfvénic solar wind power spectrum increases in amplitude as $f \rightarrow 0$. In long streams of coronal-hole-origin plasma, it is observed that the magnitude of the magnetic-field strength B_{mag} stays approximately constant (with the exception of magnetic holes). For the observed Alfvénic fluctuations, $\delta\underline{\mathbf{v}}$ is correlated with $\delta\underline{\mathbf{B}}$ such that $\delta\underline{\mathbf{v}} \approx \pm\, v_A \delta\underline{\mathbf{B}}/B_{\mathrm{mag}}$ (with the + sign for toward magnetic sectors and the – sign for away magnetic sectors). In the magnetic power spectral density, the amplitude δB is larger at lower frequencies. Eventually, going toward lower frequencies a point in the power spectra is reached where $\delta B \approx B_{\mathrm{mag}}$. The amplitudes δB of fluctuations at frequencies lower than this point saturate at $\delta B \approx B_{\mathrm{mag}}$ (Villante, 1980; Matteini et al., 2018; Bruno et al., 2019), and this part of the power spectrum can have a spectral index near f^{-1}, which is fluctuations with the same amplitude but with longer scale sizes (longer periods). The velocity fluctuations also saturate at $\delta v \approx v_A$ because they are tied to the magnetic-field fluctuations. Such a low-frequency saturation does not occur in Navier–Stokes turbulence. Certainly, at periods longer than about 1 day, the solar-wind power spectrum is dominated by surface features on the rotating Sun, with the differing surface features producing plasma with differing properties and differing magnetic structure (e.g., Matthaeus et al., 2007; Borovsky, 2018). It is often argued that the low-frequency energy-subrange outward propagating Alfvénic fluctuations are the energy source for the inertial-range Alfvénic fluctuations (Horbury et al., 1996; Zank et al., 1996; Smith et al., 2001; Vasquez et al., 2007; Bruno et al., 2019; but see Tu and Marsch, 1995 for a contrary argument).

This difference is noted in **Table 2** as item 12.

SIMILARITIES AND DIFFERENCES IN THE STATISTICS OF DERIVATIVES

First and second time derivatives of the wind-tunnel and Flattop-15 time series are calculated over timescales Δt. The first derivative of a function $f(t)$ is calculated as $df/dt = [f(t + 0.5\Delta t) - f(t - 0.5\Delta t)]/\Delta t$, and the second derivative of $f(t)$ is calculated as $d^2f/dt^2 = [-(1/3)f(t - \Delta t) + (16/3)f(t - 0.5\Delta t) - 10f(t) + (16/3)f(t + 0.5\Delta t) - (1/3)f(t - \Delta t)]/\Delta t^2$. The occurrence distributions of the first and second time derivatives of each time series will be compared with the occurrence distributions of the first and second time derivatives of a corresponding phase-randomized time series. The phase-randomized time series are created by (1) Fourier transforming the original time series, (2) randomizing the phase of each Fourier sine-cosine pair while preserving the amplitude, and (3) inverse Fourier transforming the randomized-phase Fourier transform. This process preserves the power spectral density of the time series (as approximated by the periodogram) and approximately preserves the autocorrelation function, which is the Fourier transform of the power spectral density. Examples of the original time series (blue curves) and a corresponding phase-randomized time series are plotted in the three panels of **Figure 5**. Note that a phase-randomized time series differs according to the random numbers chosen. **Figure 5A** plots 0.5 s of wind-tunnel velocity measurements, and **Figures 5B,C** plot 2 h of solar-wind measurements: these durations are a few correlation times. In **Figures 5B,C** note the strong correlation between the blue v_x and B_x curves (similar jumps, maxima, and minima) of the original time series.

Figure 6 bins time derivatives over a timescale Δt that corresponds to a frequency just below the high-frequency breakpoint of the Fourier power spectral density: $\Delta t = 3.2 \times 10^{-3}$ s for the wind tunnel and $\Delta t = 6$ s for the solar wind. These derivatives will correspond to the high-frequency end of the inertial range. In each panel of **Figure 6**, the black curve is the occurrence distribution of the absolute values of the derivatives measured in the wind-tunnel v, Flattop-15 v_x, and Flattop-15 B_x time series. The red curve in each panel of **Figure 6** is the occurrence distribution of the absolute values of derivatives measured in the same time series after the Fourier phases of the time series have been randomized. Note in **Figure 6** that the standard deviations of the distributions of first and second derivatives are the same for the phase-randomized time series as they are for the original time series. The distributions are plotted

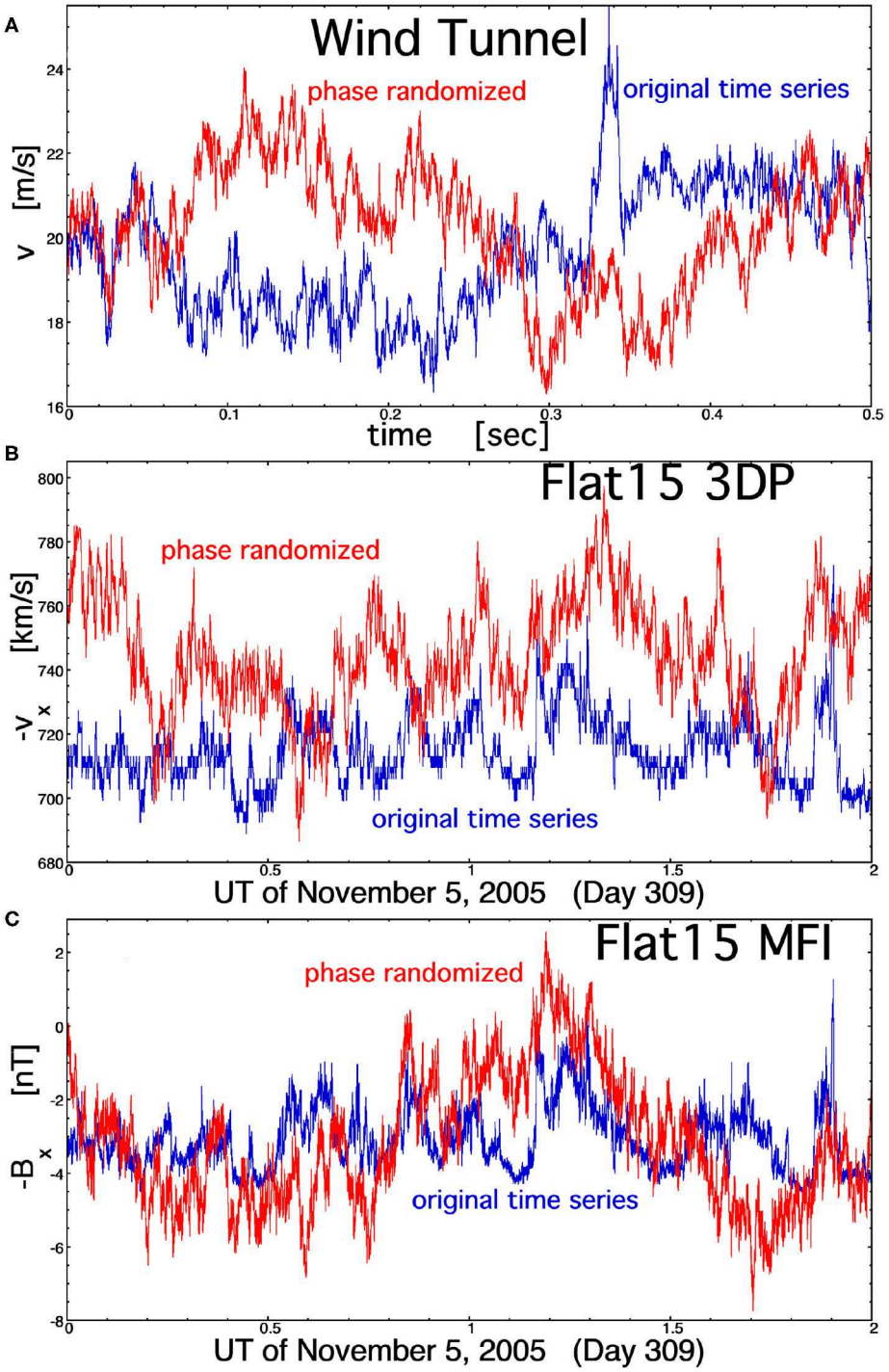

FIGURE 5 | Comparisons of the measurement time series (blue curves) with randomized-phase versions of the time series for **(A)** the streamwise velocity v in the wind tunnel Navier–Stokes turbulence, **(B)** the radial (from the Sun) velocity v_x for the Alfvénic solar wind fluctuations of Flattop 15, and **(C)** the radial component of the magnetic field B_x for the Alfvénic solar wind fluctuations of Flattop 15. The time duration plotted in each panel is a few correlation times.

in a manner such that the width of the randomized distribution is about the same fraction of the horizontal axis in each panel. For the original time series, the kurtosis K of the distribution of signed derivatives (not the absolute values, which are plotted) is noted in each panel of **Figure 6.** Here, the kurtosis K of N-values of x is defined as $K = [N^{-1}\,\Sigma\,(x_i - <x>)^4]/[N^{-2}\,\Sigma\,(x_i - <x>)^2]$

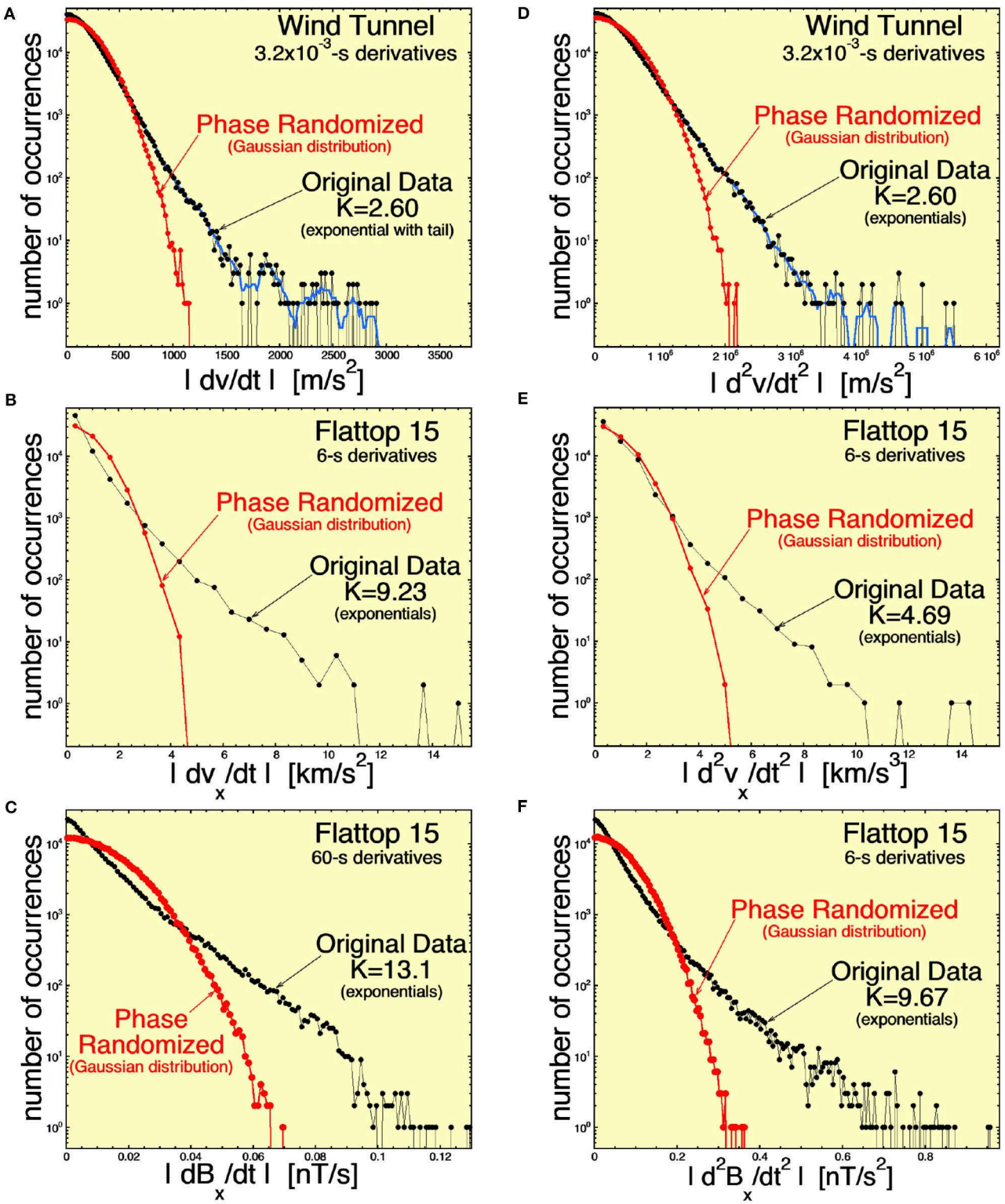

FIGURE 6 | Distributions of the measured first time derivatives **(A–C)** and second time derivatives **(D–F)** for **(A,D)** the streamwise velocity v in the wind tunnel Navier–Stokes turbulence, **(B,E)** the radial (from the Sun) velocity v_x for the Alfvénic solar wind fluctuations of Flattop 15, and **(C,F)** the radial component of the magnetic field B_x for the Alfvénic solar wind fluctuations of Flattop 15. The black curves are time derivatives in the measured time series, and the red curves are time derivatives in phase-normalized versions of the measured time series. The time derivatives are over a timescale pertaining to the higher-frequency portion of the inertial subrange. For the original-data distributions, the kurtosis K of the signed values is noted.

– 3, where Σ is the sum of i from 1 to N. The red distributions of derivatives (corresponding to the phase-randomized data) are all approximately Gaussian. The Gaussian distributions have $K \approx 0$. The distributions of $|dv/dt|$ and $|d^2v/dt^2|$ for the Navier–Stokes turbulence of the wind tunnel (black curves in **Figures 6A,B**) are exponentials, with a weak tail at the end of the exponential. This non-Gaussianity is an indication of coherent structure in the time series of the wind-tunnel turbulence (with coherence being destroyed by phase randomization). The distributions of $|dv_x/dt|$, $|dB_x/dt|$, $|d^2v_x/dt^2|$, and $|d^2B_x/dt^2|$ of the Alfvénic fluctuations in the fast solar wind (black curves in **Figures 6B,C,E,F** are all double exponentials). The second exponentials associated with the larger values can be interpreted as derivatives measured at the locations of strong current sheets and velocity shears in the solar wind, and the first exponentials corresponding to smaller values can be associated with measures of derivatives away from the current sheets and velocity shears. Note in **Figures 6B,C,E,F** that the weaker derivatives away from the current sheets and velocity shears are not Gaussian, indicating coherent structures in addition to the coherent structures of the strong current sheets and velocity shears. In the panels of **Figure 6**, the kurtosis values of the Alfvénic fluctuations of the solar wind are significantly larger than the kurtosis values of the Navier–Stokes–turbulence fluctuations.

In **Figure 7**, the $\Delta t = 6$-s first and second time derivatives are examined for the vector components of $\underline{\mathbf{v}}$ and $\underline{\mathbf{B}}$ in the Alfvénic solar wind of Flattop 15. The derivatives for each randomized-phase time series (all Gaussian distributions) are also plotted. Each component of $\underline{\mathbf{v}}$ and of $\underline{\mathbf{B}}$ exhibits double exponential distributions of the first and second derivatives.

In **Figure 8**, time derivatives are calculated over a timescale Δt that is 10 times longer than those in **Figure 6** ($\Delta t = 3.2 \times 10^{-2}$ s for the wind tunnel and $\Delta t = 60$ s for the solar wind), corresponding to a frequency that is 10 times lower, and in **Figure 9**, derivatives are calculated over a timescale that is 100 times longer ($\Delta t = 0.32$ s for the wind tunnel and $\Delta t = 600$ s $= 10$ min for the solar wind). The distributions of **Figure 6** correspond to the high-frequency end of the inertial subrange, **Figure 8** corresponds to a factor of 10 lower frequency than the high-frequency end, and **Figure 9** corresponds to a factor of 100 lower frequency than the high-frequency end of the inertial subrange. In each panel of **Figures 6**, **8**, **9**, the black curve is the occurrence distribution of time derivatives in the original time series, and the red curve is the occurrence distribution of time derivatives in the corresponding phase-randomized time series. The red phase-randomized distributions are all Gaussian. Note also that the rms values of the black and red occurrence distribution in each panel are equal.

Figure 6A finds that the $|dv/\mathrm{dt}|$ distribution for Navier–Stokes turbulence near the high-frequency end of the inertial subrange is exponential-like (with kurtosis of the signed values $K = 2.60$), indicating the presence of coherent structures. However, **Figure 8A** finds that the distribution of $|dv/dt|$ a factor of 10 lower in frequency is approximately Gaussian (with $K = 0.56$ for the signed values of dv/dt), showing an absence of coherent structure with scale sizes a factor of 10 below the high-frequency end of the inertial subrange. Consistent with this, **Figure 9A** shows an absence of coherent structure in the $|dv/dt|$distribution at a frequency 100 times lower than the high-frequency end of the inertial subrange, with $K = -0.11$ for the signed values.

This lack of lower-frequency coherent structure is not the case for the first time derivatives of v_x and B_x in the Alfvénic fluctuations of the solar wind. **Figures 8B,C**, **9B,C**, show persistent exponential distributions of $|dv_x/dt|$ and $|dB_x/dt|$ at 10 times and 100 times lower frequencies than the high-frequency end of the inertial subrange, with kurtosis values for the signed first derivatives that are strongly non-zero.

Similar cases are found examining the occurrence distributions of the second time derivatives in the right-hand columns of **Figures 6**, **8**, **9**. (1) There is an absence of coherent structure in the wind-tunnel Navier–Stokes turbulence at frequencies lower than the high-frequency end of the inertial subrange (although the disappearance of coherence is not as rapid going down in frequency as was the case for $|dv/dt|$); (2) the coherent structure as indicated by the $|d^2v_x/dt^2|$ and $|d^2B_x/dt^2|$ occurrence distributions persists to at least a factor of 100 below the high-frequency end of the inertial subrange (cf. **Figures 9E,F**).

These differences are noted in **Table 2** as item 13.

LEVEL SHIFTS AND CALM REGIONS

As discussed in *Similarities and Differences in the Fluctuations*, the solar-wind plasma is characterized by a cellular spatial structure wherein the magnetic field undergoes a strong directional change across a "directional discontinuity" (strong current sheet), and then the magnetic-field directional variations are relatively small for an interval of time. In the Alfvénic solar wind, the velocity v, which is everywhere parallel to $\underline{\mathbf{B}}$ in the reference frame of the magnetic structure, also has this cellular spatial structure (Borovsky J. E., 2020a). In the time series of the individual components of $\underline{\mathbf{v}}$ or of $\underline{\mathbf{B}}$, the cell interiors appear as flat spots (with noise).

In **Figure 10**, running medians of the wind-tunnel v(t) time series and of the Flattop-15 $B_x(t)$ time series are plotted. The running median of v(t) is over 4×10^{-3}-s time intervals, and the running median of $B_x(t)$ is over 16-s time intervals: each of these interval lengths corresponds to a frequency that is about a factor of 5 below the high-frequency breakpoints in their respective power spectral densities. The original time series is plotted in red, and the running medians are plotted in blue. The 2 s of wind-tunnel data plotted in **Figure 10A** is ∼500 running-median interval lengths, and the 2 h of Alfvénic solar wind data plotted in **Figure 10B** is about 450 running-median interval lengths. The shifts in levels, resulting in "flat spots," can be seen in the blue B_x running-median curve in **Figure 10B**.

To gauge this effect in the Alfvénic solar-wind fluctuations relative to the Navier–Stokes turbulence, running medians of the time series are calculated, and then time differences in the running-median time series are statistically analyzed looking for an excess of small differences representing flat regions in the time series. The occurrence distributions of the time differences are plotted in **Figure 11**. The red curve is the occurrence distribution

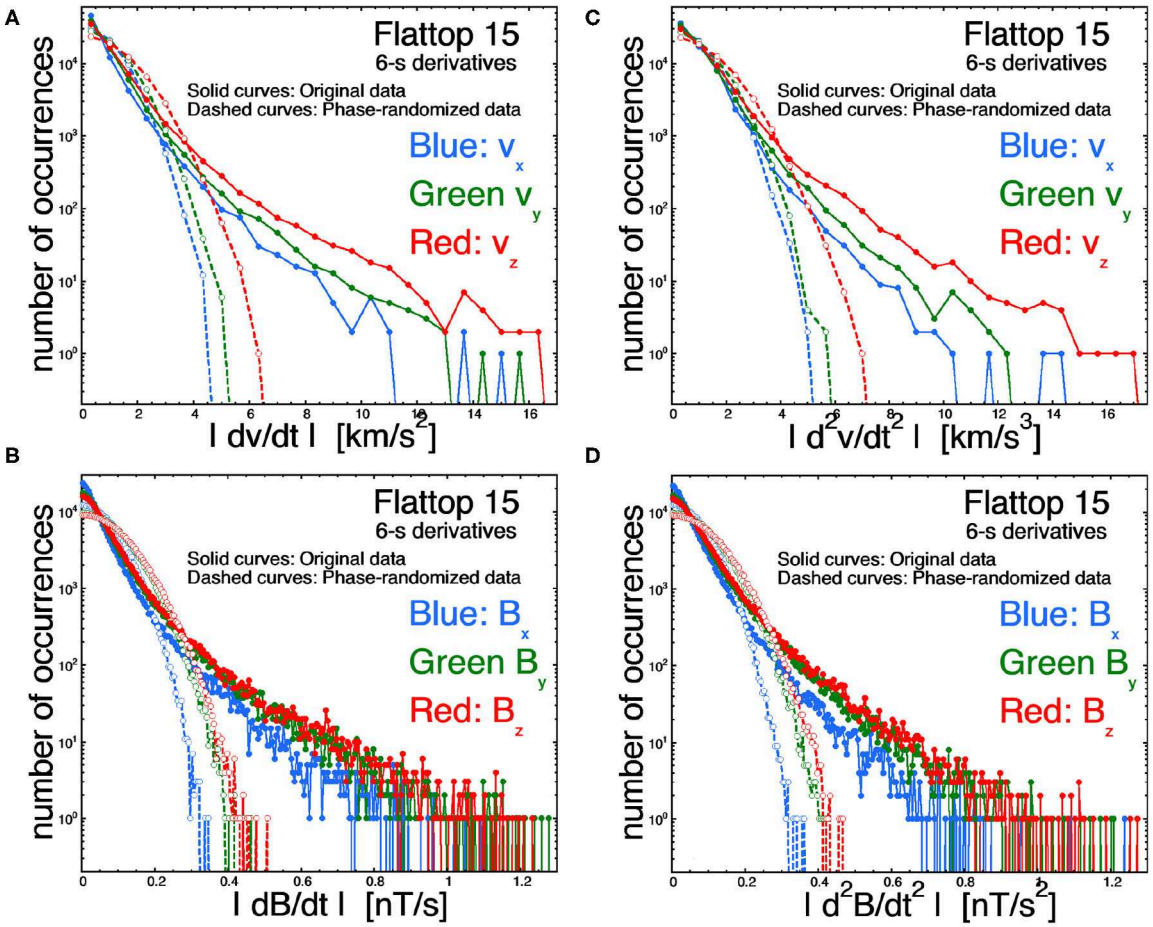

FIGURE 7 | Distributions of the measured first time derivatives **(A,B)** and second time derivatives **(C,D)** for **(A,C)** the radial (from the Sun) velocity v_x for the Alfvénic solar wind fluctuations of Flattop 15, and **(B,D)** the radial component of the magnetic field B_x for the Alfvénic solar wind fluctuations of Flattop 15. As labeled in each panel, three solid curves are for the three components of the measured time series, and three dashed curves are for the phase-normalized versions of the measured time series.

of 8-s changes in $B_x(t)$ after the Flattop-15 $B_x(t)$ time series is subjected to 16-s running medians. The running median of 16 s is approximately five times the period associated with the 0.3-Hz high-frequency breakpoint of the B_x power spectral density (cf. **Figure 4C**). The plotted occurrence distribution is normalized (horizontal axis) so that the root mean square of the distribution of differences is unity. For comparison, the blue curve in **Figure 11** is the occurrence distribution of 2×10^{-3}-s changes in v(t) after the wind-tunnel v(t) time series was subjected to a 4×10^{-3}-s running median. The running median of 4×10^{-3} s is approximately five times the period associated with the 1,250-Hz high-frequency breakpoint of the wind-tunnel v power spectral density (cf. **Figure 4A**). Again, the blue plotted occurrence distribution is normalized so that the root mean square of the distribution of differences is unity. **Figure 11** shows an excess of small differences in the distribution of $B_x(t)$ changes in the Alfvénic fluctuations of the solar wind that are not seen in the v(t) changes of the Navier–Stokes turbulence. This excess indicates a prevalence of flat regions of the Alfvénic-fluctuation time series relative to the Navier–Stokes-turbulence time series. The excess of small differences in $B_x(t)$ changes (cf. **Figure 11**) can also be seen if running averages are taken instead of running medians.

This difference is noted in **Table 2** as item 8.

SUMMARY AND DISCUSSION

As analyzed in the present study, similarities between the Alfvénic fluctuations of the fast (coronal-hole-origin) solar wind and Navier–Stokes turbulence are restricted to the well-known fact that both exhibit an inertial subrange with (1) a power-law functional form with similar spectral indices, (2) a high-frequency breakpoint, and (3) a low-frequency breakpoint. The differences discussed and found are summarized in **Table 2**; the differences cataloged in **Table 2** pertain to the medium (1 and 2), to the physical nature of the fluctuations (3–8), and to the properties of the power spectral densities and statistics of the fluctuations (9–13). The extensive cataloging in **Table 2** of differences between Navier–Stokes turbulence and the Alfvénic

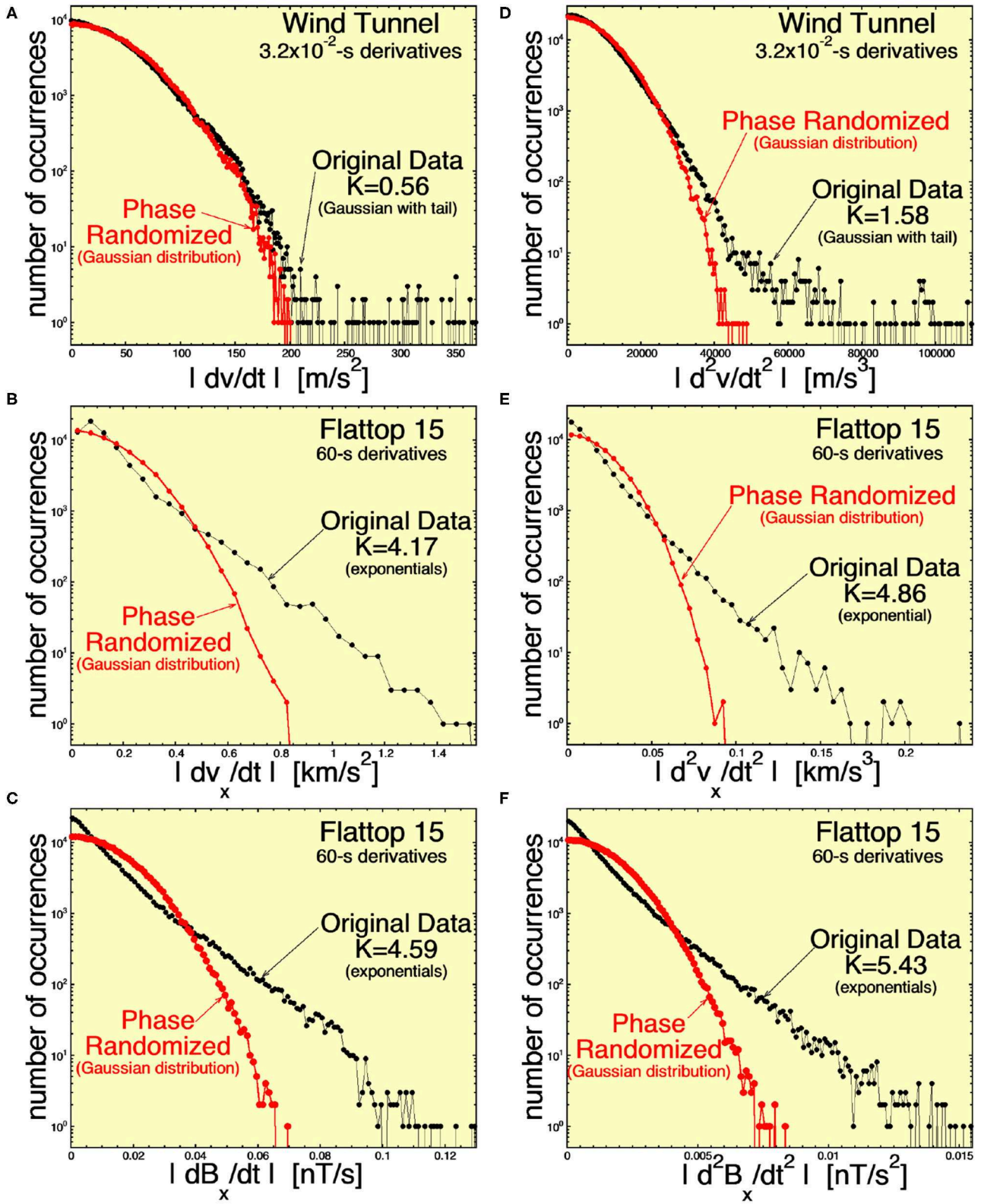

FIGURE 8 | Similar to **Figure 6**, distributions of the measured first time derivatives **(A–C)** and second time derivatives **(D–F)** for **(A,D)** the streamwise velocity v in the wind tunnel Navier–Stokes turbulence **(B,E)** the radial (from the Sun) velocity v_x for the Alfvénic solar wind fluctuations of Flattop 15, and **(C,F)** the radial component of the magnetic field B_x for the Alfvénic solar wind fluctuations of Flattop 15. The black curves are time derivatives in the measured time series, and the red curves are time derivatives in phase-normalized versions of the measured time series. Here, time derivatives are over a timescale a factor of 10 longer than in **Figure 6**. For the original-data distributions, the kurtosis K of the signed values is noted.

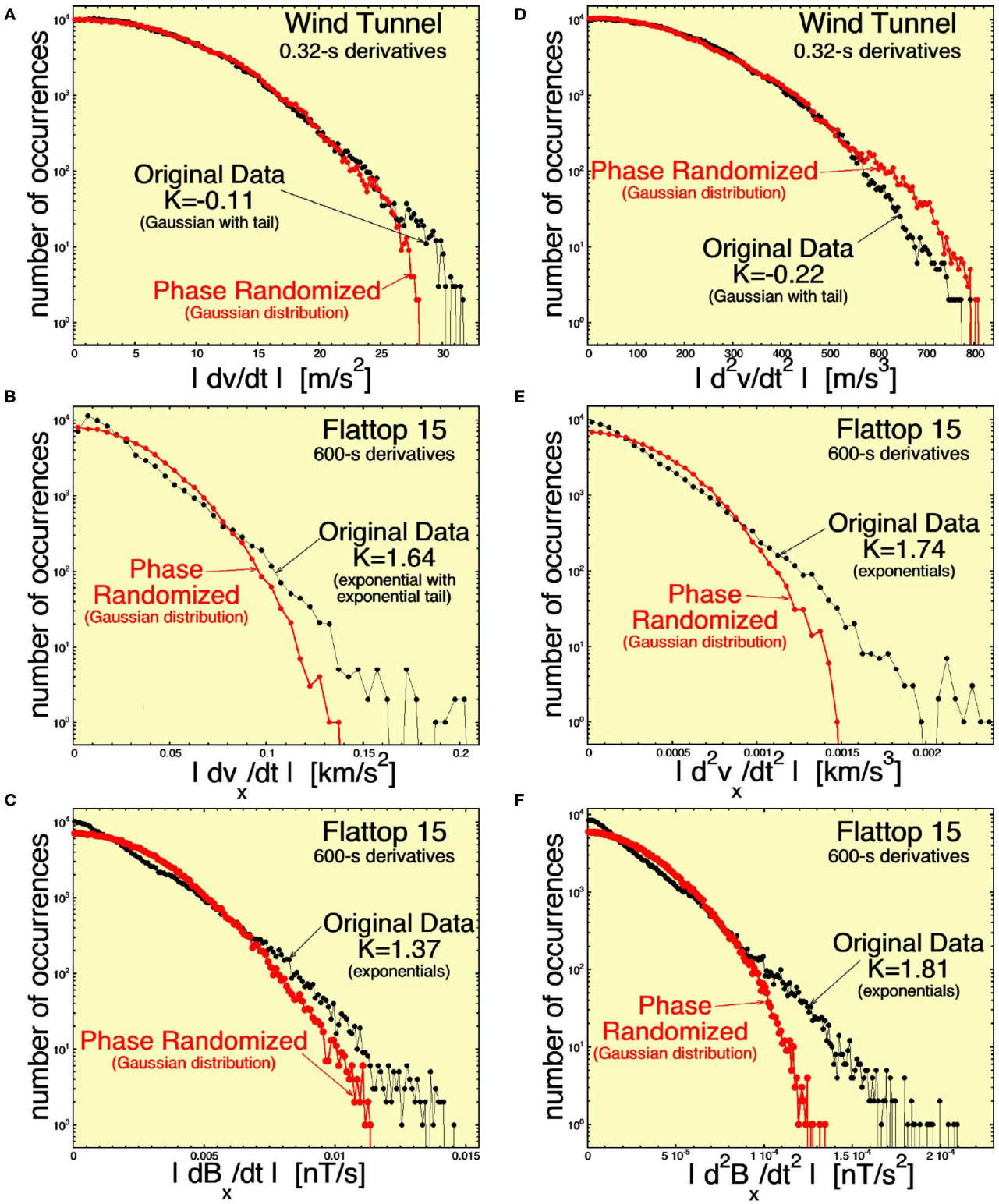

FIGURE 9 | Similar to **Figures 6**, **8**, distributions of the measured first time derivatives **(A–C)** and second time derivatives **(D–F)** for **(A,D)** the streamwise velocity v in the wind tunnel Navier–Stokes turbulence **(B,E)** the radial (from the Sun) velocity v_x for the Alfvénic solar wind fluctuations of Flattop 15, and **(C,D)** the radial component of the magnetic field B_x for the Alfvénic solar wind fluctuations of Flattop 15. The black curves are time derivatives in the measured time series, and the red curves are time derivatives in phase-normalized versions of the measured time series. Here time derivatives are over a timescale a factor of 100 longer than in **Figure 6**. For the original-data distributions, the kurtosis K of the signed values is noted.

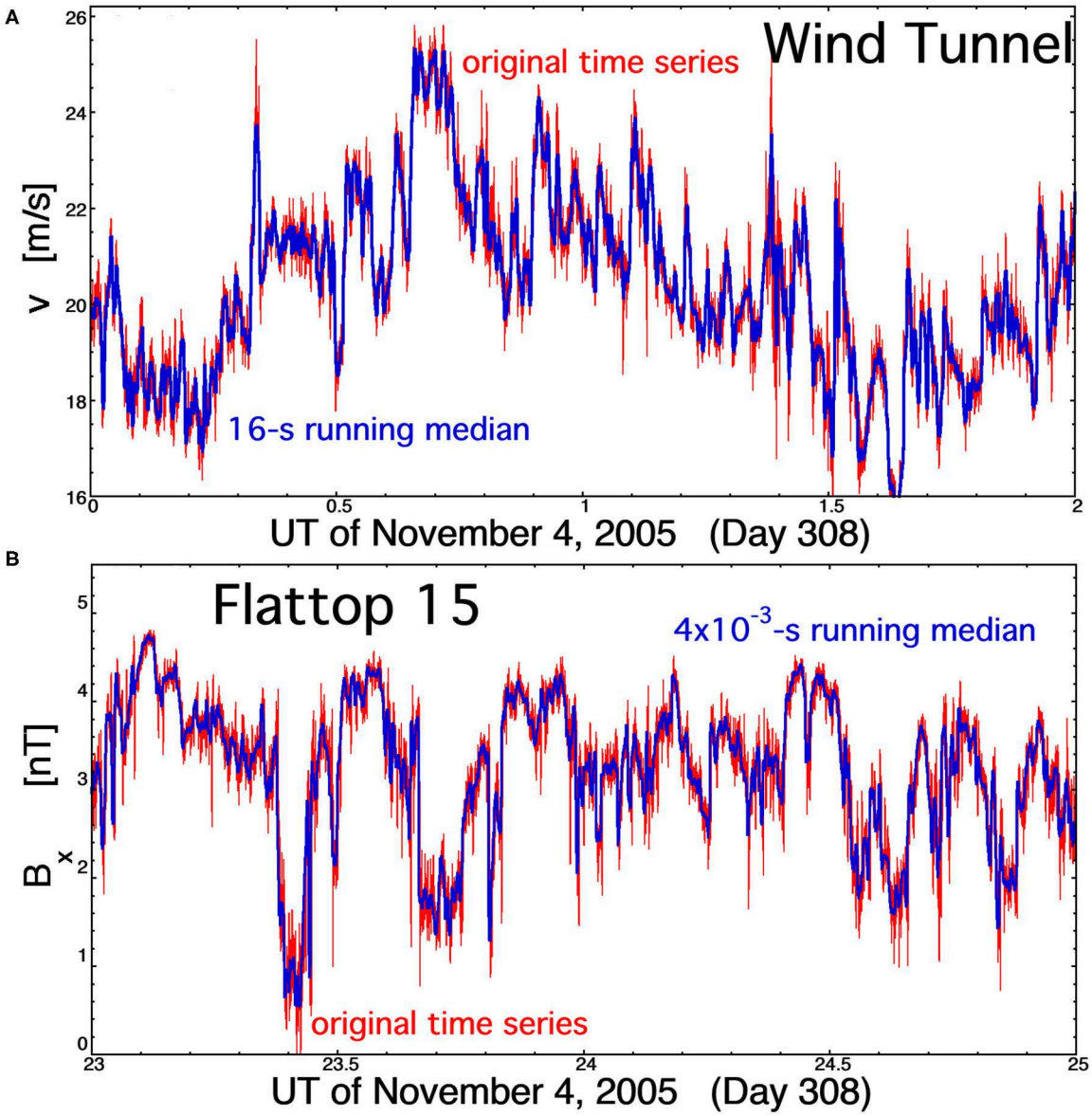

FIGURE 10 | Running medians (blue curves) are compared with the measurement time series (red curves) for **(A)** the streamwise velocity v in the wind tunnel Navier–Stokes turbulence and **(B)** the radial component of the magnetic field B_x for the Alfvénic solar wind fluctuations of Flattop 15. The running medians are over timescales that are about five times longer than the period corresponding to the high-frequency breakpoints of the power spectral densities.

fluctuations of the coronal-hole-origin solar wind is unique to the present study. Difference 13 in **Table 2** is a new finding.

An outstanding question is why would the inertial-range spectral properties of the outward-propagating Alfvénic fluctuations in the solar wind be similar to the properties of Navier–Stokes turbulence? A related question is how the outward-propagating structures obtained their properties? Three possibilities are suggested here. (1) Maybe the outward-propagating fluctuations are fossils of turbulence at the Sun in the sense that the structure seen in the inner heliosphere is the relaxation of an MHD turbulence near the Sun to an Alfvénic state (e.g., Dobrowolny et al., 1980; Matthaeus et al., 2008; Telloni et al., 2016). (2) Maybe the outward propagating fluctuations carry the signal of turbulent footpoint and/or reconnection motions in the corona. (3) Maybe the outward-propagating fluctuations carry the signatures of non-linear interactions that occurred when non-Alfvénic perturbations near the Sun propagate apart into non-evolving Alfvénic perturbations (cf. Section 7.1 of Parker, 1979). Note that Smith et al. (2009) and Stawarz et al. (2010) have suggested that an inverse cascade is ongoing to enforce the dominance of outward propagation in the fast solar wind.

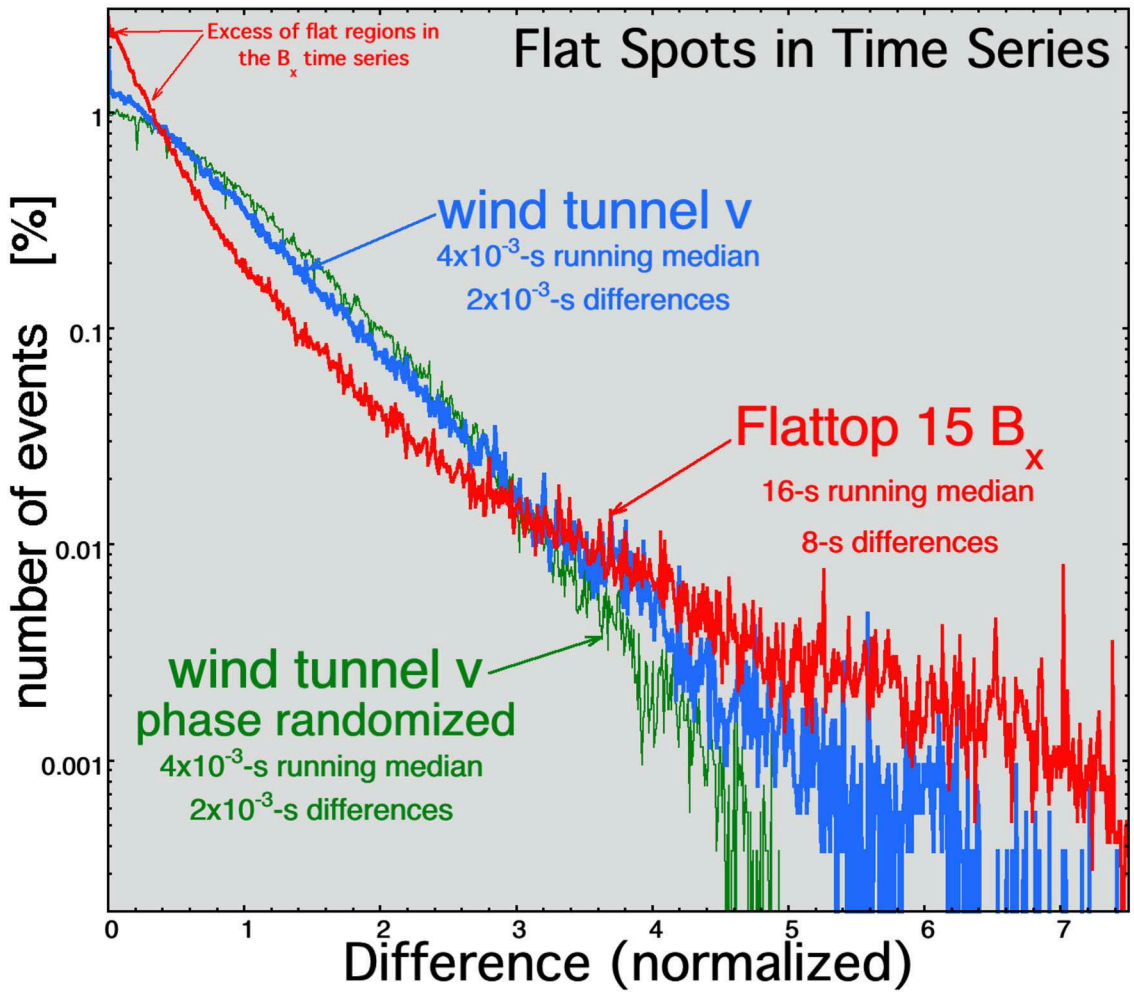

FIGURE 11 | The normalized distribution of 2×10^{-3}-s differences of the streamwise velocity v in the wind tunnel Navier–Stokes turbulence (blue curve) and the normalized distribution of the 8-s differences of the radial component of the magnetic field B_x for the Alfvénic solar wind fluctuations of Flattop 15 (red curve) calculated after 4×10^{-3}-s and 16-s running medians were applied to the time series. The green curve is the normalized distribution of differences of the streamwise wind-tunnel velocity v after the wind-tunnel time series was (1) phase randomized and then (2) processed with a 4×10^{-3}-s running median.

In the present study, two distinct types of fluctuations were analyzed on equal footing with a few different analysis techniques. The differences in the fluctuation properties from the Navier–Stokes fluctuations cited in the present study are specific to the highly Alfvénic fluctuations in coronal-hole-origin plasma: for other types of solar-wind fluctuations in other types of solar-wind plasma, these specific properties and differences (e.g., **Table 2**) do not hold. For the future, there are more types of classical solar-wind data sets and more analysis techniques that can be applied. A future challenge would be to bring together experts in different analysis techniques to simultaneously analyze the various data sets that are characteristic of the different types of solar wind and the different types of solar-wind fluctuations. The two data sets used here are (1) Navier–Stokes turbulence in a wind tunnel and (2) Alfvénic fluctuations in the fast (coronal-hole-origin) solar wind. A third data set would be (3) Alfvénic fluctuations in the slow (streamer-belt-origin) solar wind (e.g., D'Amicis and Bruno, 2015; D'Amicis et al., 2016, 2019; Borovsky et al., 2019), and a fourth data set would be (4) non-Alfvénic slow wind. Candidate long-duration data sets are available in the collection of long pseudostreamer intervals of streamer-belt-origin solar wind that were collected to develop the Xu and Borovsky (2015) solar-wind plasma categorization scheme. A fifth data set would be (5) non-Alfvénic non-Parker-spiral sector-reversal-region plasma. There are long intervals of this plasma that have been collected for use in developing the Xu and Borovsky (2015) solar-wind categorization scheme. Among the analysis techniques that could be applied to each data set are (a) Fourier power-spectral analysis, (b) autocorrelation-function analysis, (c) third-order moments, (d) fractal and multifractal analysis, (e) compressibility analysis, (f) intermittency studies (wavelet, partial variance

of increments), (g) running-median analysis, (h) dimensional analysis, (i) Taylor scale analysis, (j) fractional-derivative analysis, (k) zero-crossing analysis, (l) peak-valley counting statistics, (m) current-sheet orientation statistics, (n) event statistics, and (o) time-series clustering.

DATA AVAILABILITY STATEMENT

Publicly available datasets were analyzed in this study. This data can be found here: https://cdaweb.gsfc.nasa.gov/index.html/.

AUTHOR CONTRIBUTIONS

JB planned, outlined, researched, and drafted the manuscript. TM provided data analysis and mathematical expertise. All authors contributed to the article and approved the submitted version.

FUNDING

This work at the Space Science Institute was supported by the NSF SHINE program via award AGS-1723416, by the NASA Heliophysics Guest Investigator Program via grant NNX17AB71G, and by NASA Heliophysics LWS TRT program via grant NNX14AN90G.

ACKNOWLEDGMENTS

The authors thank Gian Luca Delzanno and Zdenek Nemecek for helpful conversations. Text files of the 4×10^{-5}-s wind-tunnel measurements, the 3-s solar-wind velocity measurements, and the 0.09375-s solar-wind magnetic-field measurements used in this investigation are available at: Borovsky J. (2020, https://zenodo.org/record/3928592#.Xv4MPi2ZP2I).

REFERENCES

Alexandrova, O., Saur, J., Lacombe, C., Mangeney, A., Mitchell, J., Schwartz, S. J., et al. (2009). Universality of solar-wind turbulent spectrum from MHD to electron scales. *Phys. Rev. Lett.* 103:165003. doi: 10.1103/PhysRevLett.103.165003

Amariutei, O. A., Walker, S. N., and Zhang, T. L. (2011). Occurrence rate of magnetic holes between 0.72 and 1 AU: comparative study of cluster and VEX data. *Ann. Geophys.* 29, 717–722. doi: 10.5194/angeo-29-717-2011

Argoul, F., Arneodo, A., Grasseau, G., Gagne, Y., Hopfinger, E. F., and Frisch, U. (1989). Wavelet analysis of turbulence reveals the multiscale nature of the Richardson cascade. *Nature* 338, 51–53. doi: 10.1038/338051a0

Arnold, L., Li, G., Li, X., and Yan, Y. (2013). Observation of flux-tube crossings in the solar wind. *Astrophys. J.* 766, 2 1–6. doi: 10.1088/0004-637X/766/1/2

Balogh, A., Forsyth, R. J., Lucek, E. A., Horbury, T. S., and Smith, E. J. (1999). Heliopsheric magnetic field inversions at high heliographic latitudes. *Geophys. Res. Lett.* 26, 631–634. doi: 10.1029/1999GL900061

Bavassano, B., and Bruno, R. (1992). On the role of interplanetary sources in the evolution of low-frequency Alfvénic turbulence in the solar wind. *J. Geophys. Res.* 97, 19129–19137. doi: 10.1029/92JA01510

Belin, F., Maurer, J., Tabeling, P., and Willaime, H. (1996). Observation of intense filaments in fully developed turbulence. *J. Phys. II France* 6, 573–583. doi: 10.1051/jp2:1996198

Biferale, L., Scagliarini, A., and Toschi, F. (2010). On the measurement of vortex filament lifetimes statistics in turbulence. *Phys. Fluids* 22:065101. doi: 10.1063/1.3431660

Borovsky, J. (2020). Some similarities and differences between the observed Alfvénic fluctuations in the fast solar wind and Navier-Stokes turbulence [data set]. *Zenodo*. doi: 10.5281/zenodo.3928592

Borovsky, J. E. (2008). The flux-tube texture of the solar wind: strands of the magnetic carpet at 1 AU? *J. Geophys. Res.* 113:A08110. doi: 10.1029/2007JA012684

Borovsky, J. E. (2010a). On the variations of the solar-wind magnetic field about the Parker-spiral direction. *J. Geophys. Res.* 115:A09101. doi: 10.1029/2009JA015040

Borovsky, J. E. (2010b). On the contribution of strong discontinuities to the power spectrum of the solar wind. *Phys. Rev. Lett.* 105:111102. doi: 10.1103/PhysRevLett.105.111102

Borovsky, J. E. (2012). The velocity and magnetic-field fluctuations of the solar wind at 1 AU: statistical analysis of Fourier spectra and correlations with plasma properties. *J. Geophys. Res.* 117:A05104. doi: 10.1029/2011JA017499

Borovsky, J. E. (2016). Plasma structure of the coronal-hole solar wind: origins and evolution. *J. Geophys. Res.* 121, 5055–5087. doi: 10.1002/2016JA022686

Borovsky, J. E. (2018). On the origin of the intercorrelations between solar-wind variables. *J. Geophys. Res.* 123, 20–29. doi: 10.1002/2017JA024650

Borovsky, J. E. (2020a). On the motion of the heliospheric magnetic structure through the solar wind plasma. *J. Geophys. Res.* 125:e2019JA027377. doi: 10.1029/2019JA027377

Borovsky, J. E. (2020b). The magnetic structure of the solar wind: ionic composition and the electron strahl. *Geophys. Res. Lett.* 47:e2019GL084586. doi: 10.1029/2019GL084586

Borovsky, J. E. (2020c). What magnetospheric and ionospheric researchers should know about the solar wind. *J. Atmos. Solar Terr. Phys.* 204:105271. doi: 10.1016/j.jastp.2020.105271

Borovsky, J. E. (2020d). The plasma and magnetic-field structure of the solar wind at inertial-range scale sizes discerned from statistical examinations of the time-series measurements. *Front. Astron. Space Sci.* 7:20. doi: 10.3389/fspas.2020.00020

Borovsky, J. E., and Burkholder, B. L. (2020). On the Fourier contribution of strong current sheets to the high-frequency magnetic power spectral density of the solar wind. *J. Geophys. Res.* 125:e2019JA027307. doi: 10.1029/2019JA027307

Borovsky, J. E., Denton, M. H., and Smith, C. W. (2019). Some properties of the solar-wind turbulence at 1 AU statistically examined in the different types of solar-wind plasma. *J. Geophys. Res.* 124, 2406–2424. doi: 10.1029/2019JA026580

Borovsky, J. E., and Gary, S. P. (2009). On viscosity and the Reynolds number of MHD turbulence in collisionless plasmas: Coulomb collisions, Landau damping, and Bohm diffusion. *Phys. Plasmas* 16:082307. doi: 10.1063/1.3155134

Borovsky, J. E., and Podesta, J. J. (2015). Exploring the effect of current-sheet thickness on the high-frequency Fourier spectrum of the solar wind. *J. Geophys. Res.* 120, 9256–9268. doi: 10.1002/2015JA021622

Bruno, R., and Carbone, E. V. (2016). Turbulence in the solar wind. *Lecture Notes Phys.* 928, 1–267. doi: 10.1007/978-3-319-43440-7_1

Bruno, R., Carbone, V., Veltri, P., Pietropaolo, E., and Bavassano, B. (2001). Identifying intermittency events in the solar wind. *Planet. Space Sci.* 49, 1201–1210. doi: 10.1016/S0032-0633(01)00061-7

Bruno, R., Telloni, D., DeIure, D., and Pietropaolo, E. (2017). Solar wind magnetic field background spectrum from fluid to kinetic scales. *Mon. Not. Roy. Astron. Soc.* 472, 1052–1059. doi: 10.1093/mnras/stx2008

Bruno, R., Telloni, D., Sorriso-Valvo, L., Marino, R., De Marco, R., and D'Amicis, R. (2019). The low-frequency break observed in the slow solar wind magnetic spectra. *Astron. Astrophys.* 627:A96. doi: 10.1051/0004-6361/201935841

Bruno, R., and Trenchi, L. (2014). Radial dependence of the frequency break between fluid and kinetic scales in the solar wind fluctuations. *Astrophys. J. Lett.* 787:L24. doi: 10.1088/2041-8205/787/2/L24

Burkholder, B. L., Otto, A., Delamere, P. A., and Borovsky, J. E. (2019). Magnetic connectivity in the corona as a source of structure in the solar wind. *J. Geophys. Res.* 124, 32–49. doi: 10.1029/2018JA026132

Chen, C. H. K., Leung, L., Boldyrev, S., Maruca, B. A., and Bale, S. D. (2014). Ion-scale spectral break of solar wind turbulence at high and low beta. *Geophys. Res. Lett.* 41, 8081–8088. doi: 10.1002/2014GL062009

Chew, G. G., Goldberger, M. L., and Low, F. E. (1956). The Boltzmann equation and the one-fluid equations in the absence of particle collisions. *Proc. Roy. Soc. Lond. A*236, 112–118. doi: 10.1098/rspa.1956.0116

Cooley, J. W., Lewis, P. A. W., and Welch, P. D. (1970). The application of the fast Fourier transform algorithm to the estimation of spectra and cross-spectra. *J. Sound Vibrat.* 12, 339–352. doi: 10.1016/0022-460X(70)90076-3

D'Amicis, R., and Bruno, R. (2015). On the origin of highly Alfvénic slow solar wind. *Astrophys. J.* 805:84. doi: 10.1088/0004-637X/805/1/84

D'Amicis, R., Bruno, R., and Matteini, L. (2016). Characterizing the Alfvénic slow wind: a case study. *AIP Conf. Proc.* 1720:040002. doi: 10.1063/1.4943813

D'Amicis, R., Matteini, L., and Bruno, R. (2019). On the slow solar wind with high Alfvénicity: from composition and microphysics to spectral properties. *Mon. Not. Roy. Astron. Soc.* 483, 4665–4677. doi: 10.1093/mnras/sty3329

Dobrowolny, M., Mangeney, A., and Veltri, P. (1980). Fully developed anisotropic turbulence in interplanetary space. *Phys. Rev. Lett.* 45, 144–147. doi: 10.1103/PhysRevLett.45.144

Dowdy, J. F., Emslie, A. G., and Moore, R. L. (1987). On the inability of magnetically constricted transition regions to account for the 10^5 to 10^5 K plasma in the quiet solar atmosphere. *Solar Phys.* 112, 255–279. doi: 10.1007/BF00148781

Farrell, W. M., Tribble, A. C., and Steinberg, J. T. (2002). Similarities in the plasma wake of the Moon and space shuttle. *J. Spacecr. Rockets* 39, 749–754. doi: 10.2514/2.3874

Frisch, U. (1995). *Turbulence.* Cambridge: Cambridge University Press. doi: 10.1017/CBO9781139170666

Gagne, Y., Castaing, B., Baudet, C., and Malecot, Y. (2004). Reynolds dependence of third-order velocity structure functions. *Phys. Fluids* 16, 482–485. doi: 10.1063/1.1639013

Gary, S. P. (1999). Collisionless dissipation wavenumber: linear theory. *J. Geophys. Res.* 104, 6759–6762. doi: 10.1029/1998JA900161

Gary, S. P., and Borovsky, J. E. (2004). Alfvén-cyclotron fluctuations: linear Vlasov theory. *J. Geophys. Res.* 109:A06105. doi: 10.1029/2004JA010399

Gary, S. P., and Borovsky, J. E. (2008). Damping of long-wavelength kinetic Alfvén fluctuations: linear theory. *J. Geophys. Res.* 113:A12104. doi: 10.1029/2008JA013565

Gary, S. P., Chang, O., and Wang, J. (2012). Forward cascade of whistler turbulence: three-dimensional particle-in-cell simulations. *Astrophys. J.* 755:142. doi: 10.1088/0004-637X/755/2/142

Goldstein, M. L., and Roberts, D. A. (1999). Magnetohydrodynamic turbulence in the solar wind. *Phys. Plasmas* 6, 4154–4160. doi: 10.1063/1.873680

Gosling, J. T., McComas, D. J., Roberts, D. A., and Skoug, R. M. (2009). A one-sided aspect of Alfvénic fluctuations in the solar wind. *Astrophys. J.* 695:L213–L216. doi: 10.1088/0004-637X/695/2/L213

Gosling, J. T., Tian, H., and Phan, T. D. (2011). Pulsed Alfvén waves in the solar wind. *Astrophys. J.* 737:L35. doi: 10.1088/2041-8205/737/2/L35

Hnat, B., Chapman, S. C., and Rowlands, G. (2005). Compressibility in solar wind plasma turbulence. *Phys. Rev. Lett.* 94:204502. doi: 10.1103/PhysRevLett.94.204502

Horbury, T. S., Balogh, A., Forsyth, R. J., and Smith, E. J. (1996). The rate of turbulent evolution over the Sun's poles. *Astron. Astrophys.* 316, 333–341.

Jimenez, J., and Wray, A. A. (1998). On the characteristics of vortex filaments in isotropic turbulence. *J. Fluid Mech.* 373, 255–285. doi: 10.1017/S0022112098002341

Kahalerras, H., Malecot, Y., Gagne, Y., and Casting, B. (1998). Intermittency and Reynolds number. *Phys. Fluids* 10, 910–921. doi: 10.1063/1.869613

Kahler, S. W., Crooker, N. U., and Gosling, J. T. (1996). The topology of intrasector reversals of the interplanetary magnetic field. *J. Geophys. Res.* 101, 24373–24382. doi: 10.1029/96JA02232

Kayshap, P., Banerjee, D., and Srivastava, A. K. (2015). Diagnostics of a coronal hole and the adjacent quiet Sun by the Hinode/EUV Imaging Spectrometer (EIS). *Solar Phys.* 290, 2889–2908. doi: 10.1007/s11207-015-0763-3

Kim, H. T., Kline, S. J., and Reynolds, W. C. (1971). The production of turbulence near a smooth wall in a turbulent boundary layer. *J. Fluid Mech.* 50, 133–160. doi: 10.1017/S0022112071002490

Kraichnan, R. H. (1965). Inertial-range spectrum of hydromagnetic turbulence. *Phys. Fluids* 8, 1385–1387. doi: 10.1063/1.1761412

Leamon, R. J., Smith, C. W., Ness, N. F., Matthaeus, W. H., and Wong, H. K. (1998). Observational constraints on the dynamics of the interplanetary magnetic field dissipation range. *J. Geophys. Res.* 103, 4775–4787. doi: 10.1029/97JA03394

Lemaire, J., and Scherer, M. (1973). Kinetic models of the solar and polar winds. *Rev. Geophys. Space Phys.* 11, 427–468. doi: 10.1029/RG011i002p00427

Lepping, R. P., Acuna, M. H., Burlaga, L. F., Farrell, W. M., Slavin, J. A., Schatten, K. H., et al. (1995). The WIND magnetic field investigation. *Space Sci. Rev.* 71, 207–229. doi: 10.1007/BF00751330

Lin, R. P., Anderson, K. A., Ashford, S., Carlson, C., Curtis, D., Ergun, R., et al. (1995). A three-dimensional plasma and energetic particle investigation for the WIND spacecraft. *Space Sci. Rev.* 71, 125–153. doi: 10.1007/BF00751328

Lucek, E. A., Horbury, T. S., Balogh, A., Dandouras, I., and Reme, H. (2004). Cluster observations of structures at quasi-parallel bow shocks. *Ann. Geophys.* 22, 2309–2313. doi: 10.5194/angeo-22-2309-2004

MacBride, B. T., Smith, C. W., and Forman, M. A. (2008). The turbulent cascade at 1 AU: energy transfer and the third-order scaling for MHD. *Astrophys. J.* 679, 1644–1660. doi: 10.1086/529575

Malecot, Y., Auriault, C., Kahalerras, H., Gagne, Y., Channal, O., Chabaud, B., et al. (2000). A statistical examiner of turbulence intermittency in physical and numerical experiments. *Eur. Phys. J. B* 16, 549–591. doi: 10.1007/s100510070216

Mallet, A., Schekochihin, A. A., and Chandran, B. D. G. (2017). Disruption of Alfvénic turbulence by magnetic reconnection in a collisionless plasma. *J. Plasma Phys.* 83:905830609. doi: 10.1017/S0022377817000812

Mann, G., Luhr, H., and Baumjohann, W. (1994). Statistical analysis of short large-amplitude magnetic field structures in the vicinity of the quasi-parallel bow shock. *J. Geophys. Res.* 99, 13315–13323. doi: 10.1029/94JA00440

Marsch, E., and Tu, C-Y. (1990a). On the radial evolution of MHD turbulence in the inner heliosphere. *J. Geophys. Res.* 95, 8211–8229. doi: 10.1029/JA095iA06p08211

Marsch, E., and Tu, C. Y. (1990b). Spectral and spatial evolution of compressible turbulence in the inner solar wind. *J. Geophys. Res.* 95, 11945–11956. doi: 10.1029/JA095iA08p11945

Matteini, L., Horbury, T. S., Neugebauer, M., and Goldstein, B. E. (2014). Dependence of solar wind speed on the local magnetic field orientation: role of Alfvénic fluctuations. *Geophys. Res. Lett.* 41, 259–265. doi: 10.1002/2013GL058482

Matteini, L., Stansby, D., Horbury, T. S., and Chen, C. H. K. (2018). On the 1/f spectrum in the solar wind and its connection with magnetic compressibility. *Astrophys. J. Lett.* 869:L32. doi: 10.3847/2041-8213/aaf573

Matthaeus, W. H., Breech, B., Dmitruk, P., Bemporad, A., Poletto, G., Velli, M., et al. (2007). Density and magnetic field signatures of interplanetary 1/f noise. *Astrophys. J.* 657, L121–L124. doi: 10.1086/513075

Matthaeus, W. H., Pouquet, A., Mininni, P. D., Dmitruk, P., and Breech, B. (2008). Rapid alignment of velocity and magnetic field in magnetohydrodynamic turvulence. *Phys. Rev. Lett.* 100:085003. doi: 10.1103/PhysRevLett.100.085003

Moffatt, H. K. (2014). Helicity and singular structures in fluid dynamics. *Proc. Nation. Acad. Sci. U.S.A.* 111, 3663–3670. doi: 10.1073/pnas.1400277111

Montgomery, D. (1992). Modifications of magnetohydrodyanics as applied to the solar wind. *J. Geophys. Res.* 97, 4309–4310. doi: 10.1029/92JA00144

Nemecek, Z., Durovcova, T., Safrankova, J., Nemec, F., Matteini, L., Stansvy, D., et al. (2020). What is the solar wind frame of reference? *Astrophys.l J.* 889:163. doi: 10.3847/1538-4357/ab65f7

Neugebauer, M., and Goldstein, B. E. (2013). Double-proton beams and magnetic switchbacks in the solar wind. *AIP Conf. Proc.* 1539, 46–49. doi: 10.1063/1.4810986

Neugebauer, M., Goldstein, B. E., Winterhalter, D., Smith, E. J., MacDowall, R. J., and Gary, S. P. (2001). Ion distributions in large magnetic holes in the fast wind. *J. Geophys. Res.* 106, 5635–5648. doi: 10.1029/2000JA000331

Ogilvie, K. W., Chorney, D. J., Fritzenreiter, R. J., Hunsaker, F., Keller, J., Lobell, J., et al. (1995). SWE, a comprehensive plasma instrument for the WIND spacecraft. *Space Sci. Rev.* 71, 55–77. doi: 10.1007/BF00751326

Ogilvie, K. W., Steinberg, J. T., Fitzenreiter, R. J., Owen, C. J., Lazarus, A. J., Farrell, W. M., et al. (1996). Observations of the lunar plasma wake from the WIND spacecraft on December 27, 1994. *Geophys. Res. Lett.* 23, 1255–1258. doi: 10.1029/96GL01069

Otnes, R. K., and Enochson, L. (1972). *Digital Time Series Analysis*. New York, NY: Wiley.

Parker, E. N. (1957). Newtonian development of the dynamical properties of ionized gases of low density. *Phys. Rev.* 107, 924–933. doi: 10.1103/PhysRev.107.924

Parker, E. N. (1979). *Cosmical Magnetic Fields*. Oxford: Clarendon Press.

Paschmann, G. (1984). "Plasma and particle observations at the magnetopause: implications for reconnection," in *Magnetic Reconnection in Space and Laboratory,* ed E. W. Hones (Washington: American Geophysical Union), 114–123. doi: 10.1029/GM030p0114

Peter, H. (2007). Modeling the (upper) solar atmosphere including the magnetic field. *Adv. Space Res.* 39, 1814–1825. doi: 10.1016/j.asr.2007.03.064

Podesta, J. J. (2010). Solar wind turbulence: advances in observation and theory. *Adv. Plasma Astrophys. Proc. IAU Symp.* 274, 295–301. doi: 10.1017/S1743921311007162

Podesta, J. J. (2011). On the energy cascade rate of solar wind turbulence in high cross helicity flows. *J. Geophys. Res.* 116:A05101. doi: 10.1029/2010JA016306

Podesta, J. J., and Borovsky, J. E. (2016). Relationship between the durations of jumps in solar wind time series and the frequency of the spectral break. *J. Geophys. Res.* 121, 1817–1838. doi: 10.1002/2015JA021987

Podesta, J. J., Borovsky, J. E., and Gary, S. P. (2010). A kinetic Alfvén wave cascade subject to collisionless damping cannot reach electron scales in the solar wind at 1 AU. *Astrophys. J.* 712, 685–691. doi: 10.1088/0004-637X/712/1/685

Podesta, J. J., Forman, M. A., Smith, C. W., Elton, D. C., Malecot, Y., and Gagne, Y. (2009). Accurate estimation of third-order moments from turbulence measurements. *Nonlin. Proc. Geophys.* 16, 99–110. doi: 10.5194/npg-16-99-2009

Podesta, J. J., Roberts, D. A., and Goldstein, M. L. (2007). Spectral exponents of kinetic and magnetic energy spectra in solar wind turbulence. *Astrophys. J.* 664, 543–548. doi: 10.1086/519211

Pope, S. B. (2000). *Turbulent Flows*. Cambridge: Cambridge University Press. doi: 10.1017/CBO9780511840531

Sahraoui, F., Goldstein, M. L., Belmont, G., Canu, P., and Rezeau, L. (2010). Three dimensional anisotropic k spectra of turbulence at subproton scales in the solar wind. *Phys. Rev. Lett.* 105:131101. doi: 10.1103/PhysRevLett.105.131101

Sari, J. W., and Ness, N. F. (1969). Power spectra of the interplanetary magnetic field. *Solar Phys.* 8, 155–165. doi: 10.1007/BF00150667

Schlichting, H. (1979). *Boundary Layer Theory*, 7th Edn. New York, NY: McGraw-Hill.

Sirovich, L., Smith, L., and Yakhot, V. (1994). Energy spectrum of homogeneous and isotropic turbulence in far dissipation range. *Phys. Rev. Lett.* 72, 344–347. doi: 10.1103/PhysRevLett.72.344

Siscoe, G. L., Davis, L., Coleman, P. J., Smith, E. J., and Jones, D. E. (1968). Power spectra and discontinuities of the interplanetary magnetic field: mariner 4. *J. Geophys. Res.* 73, 61–82. doi: 10.1029/JA073i001p00061

Smith, C. W., Matthaeus, W. H., Zank, G. P., Ness, N. F., Oughton, S., and Richardson, J. D. (2001). Heating of the low-latitude solar wind by dissipation of turbulent magnetic fluctuations. *J. Geophys. Res.* 106, 8253–8272. doi: 10.1029/2000JA000366

Smith, C. W., Stawarz, J. E., Vasquez, B. J., and Forman, M. (2009). Turbulent cascade at 1 AU in high cross-helicity flows. *Phys. Rev. Lett.* 103:201101. doi: 10.1103/PhysRevLett.103.201101

Sorriso-Valvo, L., Marino, R., Carbone, V., Noullez, A., Lepreti, F., Veltri, P., et al. (2007). Observation of inertial energy cascade in interplanetary space. *Phys. Rev. Lett.* 99:115001. doi: 10.1103/PhysRevLett.99.115001

Stawarz, J. E., Smith, C. W., Vasaquez, B. J., Forman, M. A., and MacBride, B. T. (2010). The turbulent cascade for high cross-helicity states at 1 AU. *Astrophys. J.* 713, 920–934. doi: 10.1088/0004-637X/713/2/920

Telloni, D., Carbone, V., Bruno, R., Sorriso-Valvo, L., Zank, G. P., Adhikari, L., et al. (2019). No evidence for critical balance in field-aligned Alfvénic solar wind turbulence. *Astrophys. J.* 887:160. doi: 10.3847/1538-4357/ab517b

Telloni, D., Perri, S., Carbone, V., and Bruno, R. (2016). Selective decay and dynamic alignment in the MHD turbulence: the role of the rugged invariants. *AIP Conf. Proc.* 1720:040015. doi: 10.1063/1.4943826

Tennekes, H., and Lumley, J. L. (1972). *A First Course in Turbulence*. Cambridge MA: MIT Press. doi: 10.7551/mitpress/3014.001.0001

Tessein, J. A., Smith, C. W., MacBride, B. T., Matthaeus, W. H., Forman, M. A., and Borovsky, J. E. (2009). Spectral indices for multi-dimensional interplanetary turbulence at 1 AU. *Astrophys. J.* 692, 684–693. doi: 10.1088/0004-637X/692/1/684

Thomsen, M. F., Gosling, J. T., Bame, S. J., and Onsager, T. G. (1990). Two-state ion heating at quasi-parallel shocks. *J. Geophys. Res.* 95, 6363–6374. doi: 10.1029/JA095iA05p06363

Thomsen, M. F., Stansberry, J. A., Bame, S. J., Fuselier, S. A., and Gosling, J. T. (1987). Ion and electron velocity distributions within flux transfer events. *J. Geophys. Res.* 92, 12127–12136. doi: 10.1029/JA092iA11p12127

Tu, C.-Y., and Marsch, E. (1995). Comment on "Evolution of energy containing turbulent eddies in the solar wind" by W. H. Matthaeus, S. Oughton, D. H. Pontius Jr., and Y. Zhou. *J. Geophys. Res.* 100, 12323–12328. doi: 10.1029/95JA01103

Tu, C.-Y., Roberts, D. A., and Goldstein, M. L. (1989). Spectral evolution and cascade constant of solar wind Alfvénic turbulence. *J. Geophys. Res.* 94, 13575–13578. doi: 10.1029/JA094iA10p13575

Tu, C.-Y., Zhou, C., Marsch, E., Xia, L.-D., Zhao, L., Wang, J.-X., et al. (2005). Solar wind origin in coronal funnels. *Science* 308, 519–523. doi: 10.1126/science.1109447

Turner, J. M., Burlaga, L. F., Ness, N. F., and Lemaire, J. F. (1977). Magnetic holes in the solar wind. *J. Geophys. Res.* 82, 1921–1924. doi: 10.1029/JA082i013p01921

Vasquez, B. J., Smith, C. W., Hamilton, K., MacBride, B. T., and Leamon, R. J. (2007). Evaluation of the turbulent energy cascade rates from the upper inertial range in the solar wind at 1 AU. *J. Geophys. Res.* 112:A07101. doi: 10.1029/2007JA012305

Villante, U. (1980). On the role of Alfvénic fluctuations in the inner solar system. *J. Geophys. Res.* 85, 6869–6873. doi: 10.1029/JA085iA12p06869

Wang, X., Tu, C.-Y., He, J.-S., Wang, L.-H., Yao, S., and Zhang, L. (2018). Possible noise nature of Elsässer variable z- in highly Alfvénic solar wind fluctuations. *J. Geophys. Res.* 123, 57–67. doi: 10.1002/2017JA024743

Wicks, R. T., Roberts, D. A., Mallet, A., Sckekochihin, A. A., Horbury, T. S., and Chen, C. H. K. (2013). Correlations at large scales and the onset of turbulence in the fast solar wind. *Astrophys. J.* 778:177. doi: 10.1088/0004-637X/778/2/177

Wilkinson, W. P. (2003). The Earth's quasi-parallel bow shock: review of observations and perspectives for cluster. *Planet. Space Sci.* 51, 629–647. doi: 10.1016/S0032-0633(03)00099-0

Winterhalter, D., Smith, E. J., Neugebauer, M., Goldstein, B. E., and Tsurutani, B. T. (2000). The latitudinal distribution of solar wind magnetic holes. *Geophys. Res. Lett.* 27, 1615–1618. doi: 10.1029/1999GL003717

Xu, F., and Borovsky, J. E. (2015). A new 4-plasma categorization scheme for the solar wind, *J. Geophys. Res.* 120, 70–100. doi: 10.1002/2014JA020412

Zank, G. P., Matthaeus, W. H., and Smith, C. W. (1996). Evolution of turbulent magnetic fluctuation power with heliocentric distance. *J. Geophys. Res.* 101, 17093–17107. doi: 10.1029/96JA01275

Conflict of Interest: The authors declare that the research was conducted in the absence of any commercial or financial relationships that could be construed as a potential conflict of interest.

frontiers in Physics

ORIGINAL RESEARCH
published: 30 October 2020
doi: 10.3389/fphy.2020.584063

Higher-Order Statistics in Compressive Solar Wind Plasma Turbulence: High-Resolution Density Observations From the Magnetospheric MultiScale Mission

Owen Wyn Roberts[1]*, *Jessica Thwaites*[1,2], *Luca Sorriso-Valvo*[3], *Rumi Nakamura*[1] and *Zoltán Vörös*[1,4]

[1]Space Research Institute, Austrian Academy of Sciences, Graz, Austria, [2]University of Wisconsin-Madison, Madison, WI, United States, [3]Istituto per la Scienza e Tecnologia Dei Plasmi (ISTP), Consiglio Nazionale DelleRicerche, Bari, Italy, [4]Geodetic and Geophysical Institute, Research Centre for Astronomy and Earth Sciences (RCAES), Sopron, Hungary

Turbulent density fluctuations are investigated in the solar wind at sub-ion scales using calibrated spacecraft potential. The measurement technique using the spacecraft potential allows for a much higher time resolution and sensitivity when compared to direct measurements using plasma instruments. Using this novel method, density fluctuations can be measured with unprecedentedly high time resolutions for *in situ* measurements of solar wind plasma at 1 a.u. By investigating 1 h of high-time resolution data, the scale dependant kurtosis is calculated by varying the time lag τ to calculate increments between observations. The scale-dependent kurtosis is found to increase towards ion scales but then plateaus and remains fairly constant through the sub-ion range in a similar fashion to magnetic field measurements. The sub-ion range is also found to exhibit self-similar monofractal behavior contrasting sharply with the multi-fractal behavior at large scales. The scale-dependent kurtosis is also calculated using increments between two different spacecraft. When the time lags are converted using the ion bulk velocity to a comparable spatial lag, a discrepancy is observed between the two measurement techniques. Several different possibilities are discussed including a breakdown of Taylor's hypothesis, high-frequency plasma waves, or intrinsic differences between sampling directions.

Keywords: plasma turbulence, intermittancy, solar wind, coherent structure, plasma

OPEN ACCESS

Edited by:
Marian Lazar,
Ruhr-Universität Bochum, Germany

Reviewed by:
Vincenzo Carbone,
Università della Calabria, Italy
David Malaspina,
University of Colorado Boulder, United States

***Correspondence:**
Owen Wyn Roberts
owen.roberts@oeaw.ac.at

Specialty section:
This article was submitted to Space Physics, a section of the journal Frontiers in Physics

Received: *16 July 2020*
Accepted: *17 September 2020*
Published: *30 October 2020*

Citation:
Roberts OW, Thwaites J, Sorriso-Valvo L, Nakamura R and Vörös Z (2020) Higher-Order Statistics in Compressive Solar Wind Plasma Turbulence: High-Resolution Density Observations From the Magnetospheric MultiScale Mission. Front. Phys. 8:584063. doi: 10.3389/fphy.2020.584063

1. INTRODUCTION

The solar wind is an excellent example of turbulent plasma where disordered fluctuations are observed in velocity, temperature, and density as well as in electromagnetic fields [1–5]. At large scales, a fluid description of the plasma is valid and fluctuations transverse to the mean magnetic field direction dominate. This region is often termed the inertial range, where magnetic fields and density are often observed with a power spectral density that has a −5/3 spectral index [6–8]. However, the presence of several different species (protons, electrons, and heavy ions), each with their characteristic scales, causes several different distinct ranges to be present in the plasma [9–11]. When fluctuations approach

proton scales, kinetic effects become important, the magnetic spectra steepen [7], and fluctuations become more compressive [12]. In this range, usually called sub-ion range, the Kolmogorov-like phenomenology can be adapted using Hall-MHD and kinetic models. These predict different spectral scaling exponents, typically near the observed values $\sim -8/3$ (see e.g., Ref. [13]). There are also observations and numerical simulations that suggest the third order law based on Hall MHD is valid, supporting the hypothesis that there is another fluid like cascade in this region [14, 15]. However, the additional presence of kinetic effects, such as Landau damping [16] suggest that another fluid like cascade is not completely sufficient to describe the phenomenology. At smaller scales electron kinetic effects become important and the morphology of the magnetic spectrum is unclear [17–20]. At the sub-ion scales, density measurements are challenging due to the need for high time resolution. Investigating density fluctuations can be especially taxing due to the lower (compared to instruments that measure fields) sampling rates. One novel way to measure the electron density at the same time resolution as electric field measurements is to calibrate the spacecraft potential [3, 21–29]. In the solar wind typically the two dominant currents to and from the spacecraft are the photoelectron current I_{ph} and the electron thermal current I_e. If all other current sources are small it can be assumed that both of these currents are equal and have opposite signs. This is typically the case in the solar wind at 1 a.u. Using lower time resolution electron density and temperature data from plasma instruments, the electron thermal current can be calculated as a function of the spacecraft potential. The variation of the current with the potential can be modelled by a superposition of exponential functions. By using the obtained model and the direct measurement of electron temperature the electron density can be derived from the spacecraft potential.

Turbulent flows tend to develop vortices or eddies, which are intermittently distributed in the flow [30, 31] and are often termed coherent structures. Due to the presence of a strong ambient magnetic field in a plasma, coherent structures become elongated along the magnetic field direction [20, 32, 33]. Furthermore, the plasma allows other types of structures to form such as current sheets, flux ropes, or magnetic vortices [34–38]. These structures are associated with large gradients[1] in the measured variables (such as electron density), which are often investigated by calculating differences of time-lagged or spatially lagged variables and evaluating their scale-dependent statistics. A time-lagged increment is defined as:

$$\delta n_e(t,\tau) = n_e(t+\tau) - n_e(t), \tag{1}$$

where n_e is the plasma electron density, t is the sample time and τ a time scale where $\tau \geq \delta t$ where δt is the time resolution.

Similarly, a spatial lag between two measurement points at position vectors $\overrightarrow{\lambda_1}$ and $\overrightarrow{\lambda_2}$ are defined as

$$\delta n_e\left(\overrightarrow{\lambda_{1,2,t}}\right) = n_e\left(\overrightarrow{\lambda_{1,t}}\right) - n_e\left(\overrightarrow{\lambda_{2,t}}\right). \tag{2}$$

To quantify how intermittent a given time interval is, higher-order statistics of increments such as the kurtosis are calculated. Kurtosis is defined as;

$$\kappa = \frac{\langle \delta n_e^4 \rangle}{\langle \delta n_e^2 \rangle^2}, \tag{3}$$

and measures the deviation of a probability distribution function from being Gaussian, specifically how heavy the tails of the distribution are. For a Gaussian process, the kurtosis is equal to three. An intermittent signal would be expected to have a scale dependence in the kurtosis [e.g., 39–42] and a departure from self-similar or monofractal scaling[2,] [43–46].

Previous studies in the solar wind have shown that the kurtosis of magnetic and velocity fluctuations do exhibit a scale dependence in the inertial range [47, 48], suggesting that the inertial range is strongly intermittent. Furthermore, magnetic field measurements also indicate that this range is characterized by multifractal behavior, a standard framework to model intermittency [12, 44]. Different components of the magnetic field have also been shown to have different intermittency properties. The component of the magnetic field along the mean-field direction (also termed the compressive component) has also been shown to be more intermittent at large scales [49] when compared to the transverse components. This was interpreted as a combination of the transverse fluctuations phases being randomized by large scale Alfvénic fluctuations, in effect reducing the kurtosis[3]. Meanwhile, in the large scale compressive component, Alfvénic fluctuations have very little effect as they are incompressible. Additionally, compressible coherent structures are more prevalent causing the kurtosis to be larger. At smaller scales below proton characteristic scales, there are conflicting observations. In the study of Alexandrova et al. [13] the kurtosis was found to increase rapidly in the sub-ion range. This is similar to the result of Chhiber et al. [42] in the magnetosheath i.e., a rapid increase in the kurtosis of the fluctuations in the sub-ion range. Meanwhile, observations of Kiyani et al. [44] show that the sub-ion range in the solar wind is monofractal, juxtaposing strongly with the multifractal inertial range. Other studies in the solar wind have observed the fluctuations in density Chen et al. [45] and magnetic field Chhiber et al. [42] which do not have a strong increase of the scale-dependent kurtosis in the sub-ion range. A recent analysis based on empirical mode decomposition concluded that the sub-ion scale turbulence of density fluctuations is not intermittent [50]. However, in the study of Sorriso-Valvo et al. [46] different methods applied to density measurements of the same intervals yielded different results. The various different results point to the fact that higher order statistics obtained in plasma turbulence are not universal, but may depend on the specific interval.

[1]A large gradient may be defined from the statistical properties of the fluctuations in a time series, i.e., larger than one standard deviation.

[2]Throughout this paper, the word intermittency refers to intermittency in fully developed turbulence, unless otherwise specified.

[3]It is important to note that coherent structures have constant phase in scale, while waves have constant phase in time. However waves at different scales will have different phases and can shuffle the phases at each scale effectively reducing the cross scale coupling of phase.

The majority of the studies mentioned have used single spacecraft measurements and have used a time lag (**Eq. 1**) to obtain the fluctuation. This is limited to investigating a single direction (i.e., along the bulk velocity vector), and also requires an assumption that the plasma does not evolve over the timescale it requires to be measured, so that the spacecraft see a one-dimensional spatial cut through the plasma. This assumption is termed Taylor's frozen in flow hypothesis [51]. To avoid assuming this, multi-point missions such as Cluster and the Magnetospheric MultiScale mission were developed which allow increments to be calculated using two different spacecraft, overcoming the inherent Spatio-temporal ambiguity associated with single spacecraft observations.

Calculating spatially separated increments defined in **Eq. 2** has the advantage that multiple directions can be sampled, but are limited to a single scale for a tetrahedral constellation of four points i.e., six baselines in different direction of size of order $\left|\overrightarrow{\lambda_{1,2}}\right|$. At the distance of the order of tens of kilometers, magnetic field increments calculated from two points can vary wildly from being close to Gaussian [42], to being strongly leptokurtic [41]. However, due to magnetic field instrument's sensitivity in the sub-ion range, a comparison between time-lagged and spatially lagged measurements is difficult.

The goal of this paper is to use density fluctuations in the solar wind estimated from the spacecraft potential on the Magnetospheric MultiScale mission to obtain an extremely high time resolution measurement of the electron density [52]. Although there are limitations to this technique, it also has several advantages, most notably the higher time resolution, fewer data gaps, and the absence of large errors due to low particle counts. Using this novel method, density fluctuations can be measured with unprecedented time resolutions. Such time resolutions are not possible using plasma measurements, and exceed what has been done in the current literature with spacecraft potential. This method applied to the MMS spacecraft allows density fluctuations to be measured deep into the sub ion range up to 40 Hz. This range of scales has only previously been accessible to magnetic field measurements in the solar wind [e.g., 12]. Previous studies of density with spacecraft potential [e.g., 53, 54] have been limited to ~ 7.5 Hz due to sensitivity or a Nyquist frequency of 16 Hz using a direct measurement [e.g., 40, 46, 55]. The novel spacecraft potential measurement will be compared to the direct measurement from the plasma instrument and to the magnetic field data which are both available but similar to the previous studies [41, 42] are limited to a smaller range of time scales due to the limited sensitivity in the magnetic field measurement in the sub-ion scales. In the following section, we will present the data. This will be followed by the results of the kurtosis of the density fluctuations, a discussion and a conclusion.

2. DATA/METHODOLOGY

Data is used from the Magnetospheric MultiScale mission [56] (MMS) when an hour-long interval of burst mode data in the slow solar wind was available. The MMS mission consists of four identical spacecraft in a tetrahedral configuration optimized for studying magnetic reconnection in the Earth's Magnetosphere. However, there are also intervals of solar wind plasma which have been sampled by MMS. The close spacings of MMS of the order of a few km to tens of km make it an excellent mission to study sub-ion scale turbulence. A 1-h long burst mode interval is analyzed here which was previously studied in [42, 57]. The spacecraft are located at $[x_{GSE}, y_{GSE}, z_{GSE}] = [16.5, 17.5, 6.3]R_E$ and were not magnetically connected to the foreshock. The subscript GSE denotes the Geocentric Solar Ecliptic coordinate system, where the x component points from Earth towards the Sun, z points to the North solar ecliptic. This is very far from the nominal bow shock nose which is approximately at $x_{GSE} = 10R_E$ [58]. Furthermore there are no signatures of backstreaming ions or electric field fluctuations in this interval [52] and the magnetic field is predominantly in y_{GSE} direction meaning that there is no connection with the foreshock. The magnetic field is measured by the fluxgate magnetometers [59] which have a sampling rate of 128 Hz in burst mode and sensitivity which allows the study of the magnetic fluctuations at inertial (fluid scales) and ion kinetic scales before noise becomes significant near 5 Hz for this interval. We do not use the Search coil magnetometer as it is already at the noise level. The plasma measurements are provided by the Fast Plasma Investigation's (FPI) Dual Ion Spectrometers and Dual Electron Spectrometers and have sampling rates of 6.6 and 33 Hz respectively [60].

The Spacecraft potential can be used to estimate the electron density (see e.g., [3, 21–29, 52]). A detailed description of the calibration process and of the spin removal is presented in [52]. It is important to note that the spacecraft have a characteristic charging timescale, and respond to the ambient electron density after that timescale. Assuming constant photoelectron emission this time scale is very large of the order of kiloHertz [32]. This is far outside of our range of interest. Even if we relax the assumption that the photoelectron emission is constant such as when large amplitude electric fields are present the charging timescale is still much larger than the largest scale we survey [61]. Therefore in the solar wind we do not expect any finite charging effects in the solar wind at these scales. The spin is removed by constructing an empirical model of the spacecraft charging by binning the potential based on the spacecraft phase angle. A model is fitted to the median in each bin and then subtracted. For this interval, spin effects were present also in the FPI electron data. These have been removed using the same approach. The spacecraft potential is calculated from measurements performed with the Spin Plane Double Probe instruments [62] and has a sampling rate of 8.192 kHz. The spacecraft potential is measured from the four spin plane probes. The four measured probe to spacecraft potentials are averaged to give the spacecraft potential. If one probe is unavailable i.e. for MMS4 due to one probe becoming unbiased due to a dust strike then the average of two opposing probes is used rather than all four probes [61, 63, 64]. This results in a difference in the quality of the measurement when comparing spacecraft 1 through 3 with 4. The electron density data from FPI the has an upper limit of 3 Hz for electrons due to Poission noise from finite counting statistics. For the spacecraft potential we used the upper limit of 40 Hz to avoid noise from the preamplifier. The limit of 40 Hz was chosen so that

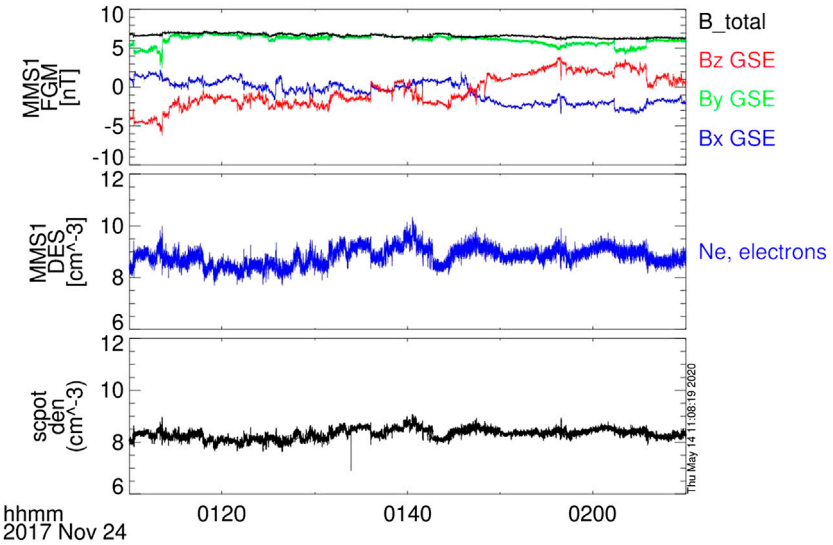

FIGURE 1 | Measured data from MMS1 during the interval studied. Top panel shows the three magnetic field components and the magnitude. Middle panel shows the electron density measured from the FPI-DES instrument. Bottom panel shows the electron density measured from the spacecraft potential calibration method.

the signal from the spacecraft potential is three times larger than a quiet interval when the spacecraft potential is regulated by the Active Spacecraft POtential Control (ASPOC) instrument [65] is operating [52].

An overview of the event is given in **Figure 1**. Both measurement techniques show good agreement for the electron density. An important caveat of the spacecraft potential is that it can be severely affected by dust strikes or similar inverted signatures discussed by [e.g., 66–68]. These events are characterized by an abrupt jump or drop in the density estimation which can affect the calculation of higher-order statistics [69, 70]. In our sample, there is a sharp decrease in the potential at one point which is likely due to a dust strike, or an inverted signature as discussed by [67]. Such strikes, present in the spacecraft potential data set, are removed here by linear interpolation as they are not density perturbations intrinsic to the solar wind. Rather the perturbation in density is the result of the dust vaporizing on contact with the spacecraft and cause a density perturbation due to the dust/spacecraft interaction. This can be seen in the bottom panel of **Figure 1**. The interval has a low ion bulk speed of 377 km s^{-1}, a mean electron density from FPI of 8.8 cm^{-3} and ion and electron plasma beta (dimensionless ratio of plasma pressure to magnetic pressure) of $\beta_i = 0.4$ and $\beta_e = 0.7$. There are no signatures of large scale events such as Interplanetary coronal mass ejections in the day before or the day after the event from OMNI. This means that the interval is characteristic of typical slow solar wind. It is important to note that the measurement of the ion temperature is unreliable from MMS [e.g., 57, 71] and here we use OMNI data [72] for the calculation of the ion plasma beta.

This interval is a typical example of the slow solar wind. The spacecraft separations are in the range $r \in [15, 20]$km. Based on Taylor's frozen in flow hypothesis [51] this corresponds to a timescale of $\tau_{sc} \in [0.04, 0.06]$ s. When considering inter-spacecraft fluctuations, the time resolution needs to be sufficient to distinguish the changes, otherwise some fluctuation may be advected over the spacecraft before it has been sampled [e.g., 57]. Out of the three measurements which we use in this study (magnetic field, electron density from FPI, and electron density from the spacecraft potential), the lowest time resolution is the FPI electrons at 0.03 s. This is sufficiently small so that no blurring of the information occurs when calculating increments between two spacecraft which are radially aligned (i.e., along the solar wind bulk flow direction). That is to say advection time of a fluctuation in the radial direction of 15 km/377 km/s = 0.04 s which is larger than the time resolution of the FPI electrons.

3. RESULTS

The power spectral densities of the spacecraft potential-derived electron density, the trace magnetic field and the magnetic field magnitude are shown in **Figure 2**. The frequencies corresponding to the different spatial scales the ion and electron inertial lengths (d_i, d_e) the ion and electron gyroradii (ρ_i, ρ_e), as well as the combined scales [73], are indicated. A typical inertial range scaling is observed at low frequencies for both the electron density and the magnetic fluctuations, with a power-law scaling exponent close to −5/3. Spectral breaks are found by fitting a power law from either side of the break and is indicated by the vertical dashed black lines. There is a flattening in the magnetic field spectra near 5 Hz which is due to instrumental noise. The decrease at higher frequencies ($f > 10$Hz) is due to an anti-aliasing filter and is not of physical origin. The electron density from the spacecraft potential shows a power law until 100 Hz where the spectrum flattens. In the region above 100 Hz the spectrum is flat indicating white noise, the kurtosis is 3 (see

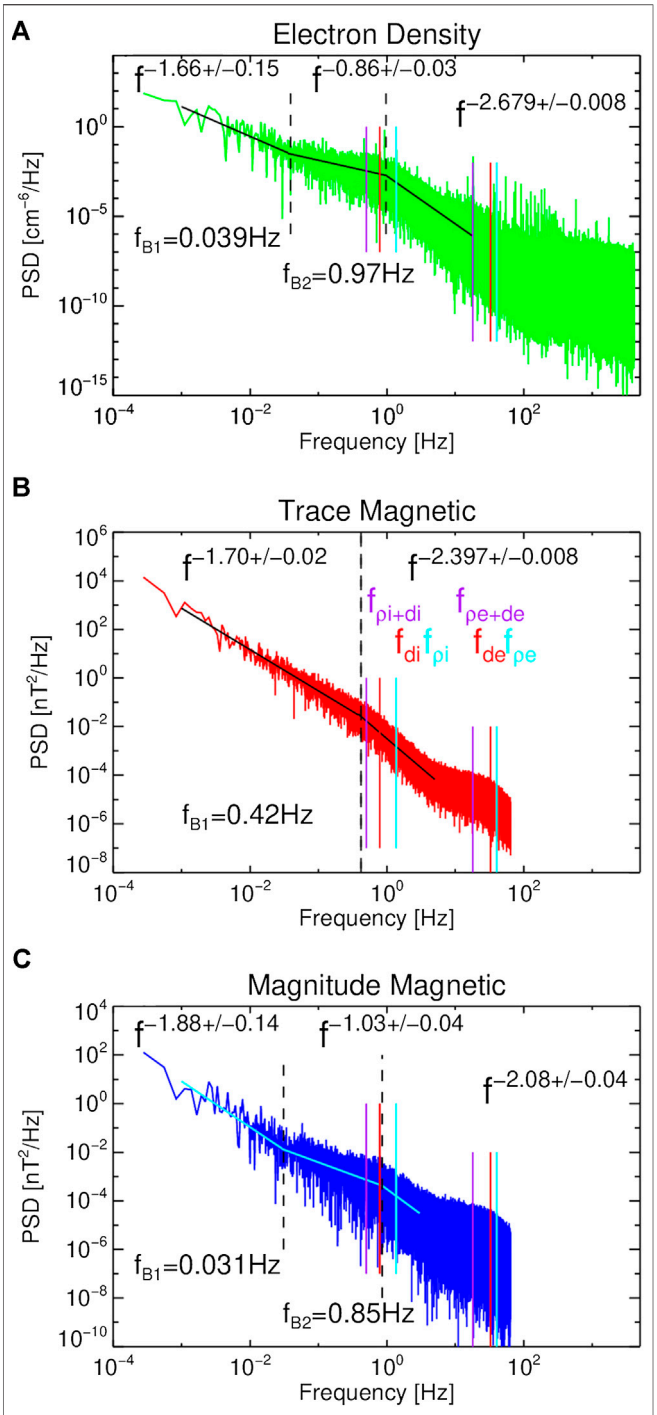

FIGURE 2 | Power spectral densities from MMS1. **(A)** shows the electron density from the spacecraft potential, **(B)** shows the trace magnetic field from the fluxgate magnetometer **(C)** shows the magnetic field magnitude from FGM. The colored lines denote several of the characteristic scales, while the black dashed lines denote the spectral breaks. The power-law fits and the break frequencies are indicated on the plots.

Figure 3) at a value of three and the structure functions are also flat regardless of the order (see **Figure 6**). This is likely due to noise and is consistent with the Poisson noise in the electronics [62]. Although, pre-amplifier noise may be significant at smaller frequencies and has a non-zero spectral index. In order to avoid noise effects, here we limit our analysis to the range up to 40 Hz. At ion scales there is a flattening in the central region of the electron density spectra [45, 74] which we term a transition region.

Figure 3 shows the scale-dependent kurtosis of the density fluctuations calculated from both the direct measurement from FPI and from the spacecraft potential. Both time lags (lines) and spatial lags (points) are used for this calculation. An unfortunate

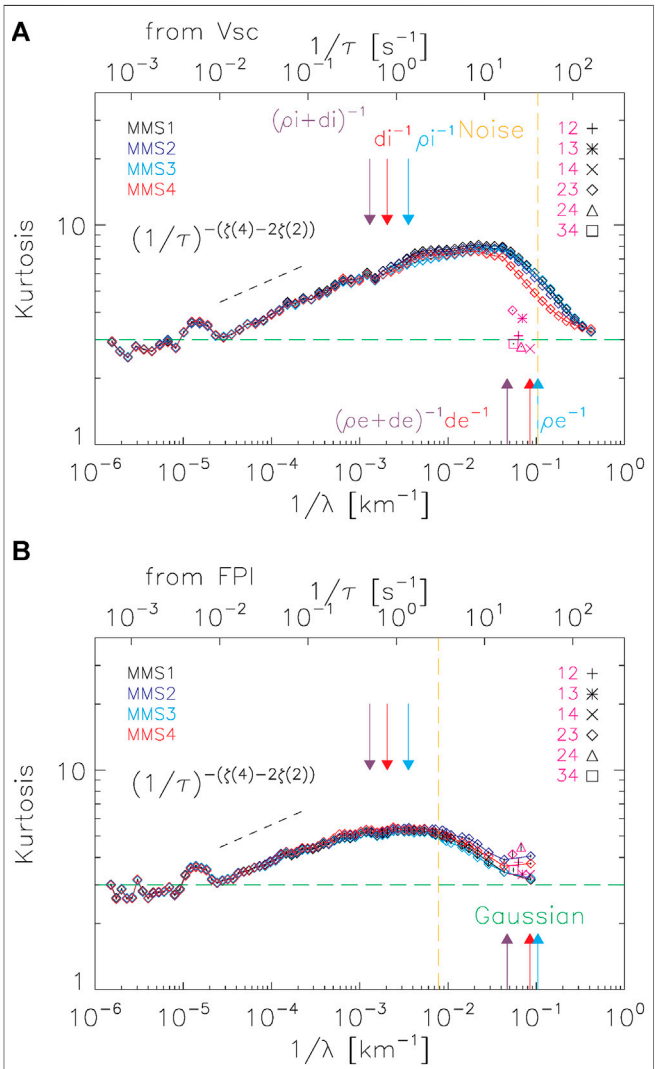

FIGURE 3 | Scale-dependent kurtosis for electron density fluctuations obtained from the spacecraft potential **(A)** and FPI **(B)**. The orange vertical line denotes the region where instrumental noise becomes significant for the two different measurements. The green horizontal line denotes a kurtosis of 3, characteristic of a Gaussian process. The arrows denote the same characteristic scales as previously in **Figure 2**. The lines denote the time-lagged values from different spacecraft, and the pink data points denote the kurtosis calculated from two spacecraft measurements. Black-dashed lines indicate power-laws expected from the scaling of the structure functions, and are displayed for reference. Error bars are indicated based on 100 bootstrap resamplings but they are smaller than the plotting symbols.

consequence of sampling heavily tailed distributions such as turbulent fluctuations is that some large fluctuations might significantly alter higher-order statistics. To ensure better statistical consistency we follow the scheme presented in Kiyani et al. [70]. This involves removing the largest fluctuation in the probability distribution function, recalculating the kurtosis, and repeating until the kurtosis converges. This has the advantage that outliers from either side of the heavy tails will be removed, and do not need any a priori information e.g., the standard deviation [75, 76]. Practically, this does not remove many data points. In our scheme of convergence we set a maximum limit of at most 0.1% removed data points. The error bars, prevalently smaller than the symbols, denote the estimated error from one hundred bootstrap resamplings of the fluctuations.

At the largest scales, the kurtosis $\kappa \simeq 3$ indicates approximately Gaussian distributions. There is a bump in the kurtosis at a scale of $\lambda^{-1} \sim 10^{-5}$ km^{-1} which is likely related to the finite signal length. In the inertial range, the kurtosis increases roughly as a power law, as expected from the scaling properties of turbulence. The expected scaling laws are indicated for reference, the exponents $\simeq 0.1$ being estimated using the structure functions scaling exponents (see below) and **Eq. 4**. As the time lags become smaller near ion scales there is a plateau and then the value of the kurtosis starts to decrease near the combined electron scale before the noise floor. The noise floor is indicated by the orange dashed line at 3 Hz for the FPI data and 40 Hz for the potential data. Both density measurements show similar scale-dependent kurtoses at large scales. However, due to FPI data reaching the noise floor sooner, at a higher frequency they begin to disagree. The time-lagged measurements from the four spacecraft agree well with one another. The data points from MMS4 differ slightly in the spacecraft potential possibly due to the probe failure mentioned previously. This may be a result of two probes being used from MMS4 rather than four probes on the other spacecraft. The PDFs show some skewness. At small scales, this is necessary in order to have non-vanishing odd-order moments. At large scales, we still observe skewed PDFs, which are probably a finite sample effect, for example due to the presence of statistically underrepresented large-scale structures which may affect the statistics. We do not discuss those scales in this paper. The pink data points show the kurtoses calculated from the spatial lags. The values of the kurtosis from the spatial lags are small, close to being Gaussian for both measurements. A salient feature here is that for the FPI data the time and spatial lags agree, however, the time lag is unreliable due to noise. This is a similar result to the magnetic field in [42]. However, the spacecraft potential is less affected by noise and there is a disagreement between the time and spatial lags.

Figure 4 shows the scale-dependent kurtosis for the magnetic field measurements $\mathbf{B}(t)$. To put the fluctuations in a physically relevant co-ordinate system, we convert the fluctuations from the Geocentric Solar Ecliptic system to a mean-field scale-dependent coordinate system [32]. This is defined for each pair of measurements that make an increment as $\mathbf{B}_{loc}(t,\tau) = [\mathbf{B}(t) + \mathbf{B}(t+\tau)]/2$ for a time lag, or $\mathbf{B}_{loc,1,2}(t) = [\mathbf{B}_1(t) + \mathbf{B}_2(t)]/2$ for spatially lagged measurements. The perpendicular components

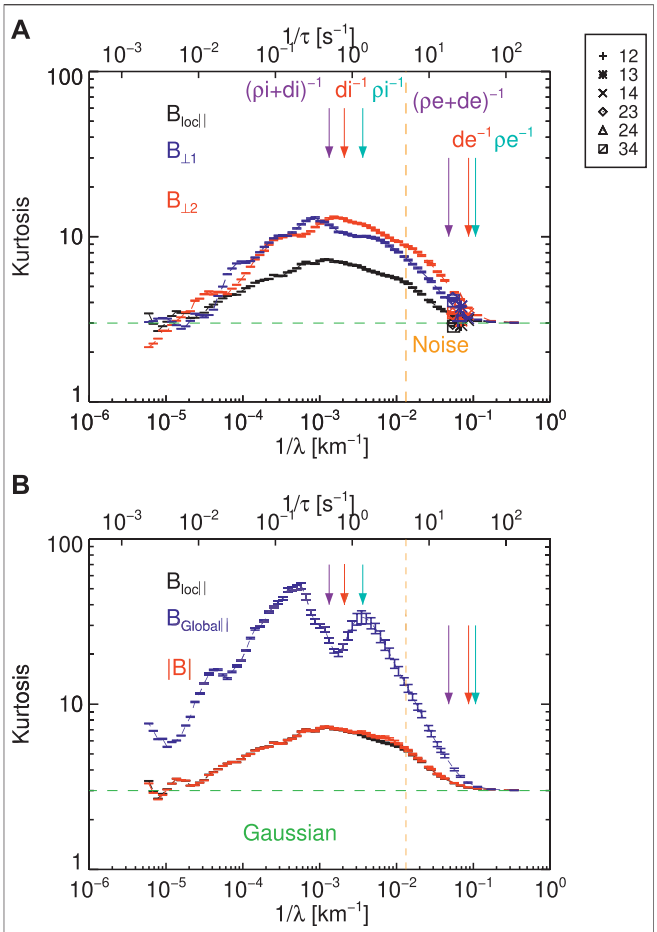

FIGURE 4 | (A) The scale-dependent kurtosis for the magnetic field components in a local mean-field co-ordinate system. The connected lines denote the time-lagged increments and the points denote the spatially lagged values. **(B)** Three different measures of the compressible magnetic field component. Blue denotes the global mean field over the entire interval, red denotes the magnitude of the magnetic field and black denotes the same local mean-field as in **(A)**. The green horizontal line denotes a kurtosis of 3 which corresponds to a Gaussian distribution. The orange vertical line denotes 5 Hz where instrumental noise becomes significant in the fluxgate magnetometer data. The colored arrows denote the characteristic ion scales the cyclotron scale, the inertial length and the Larmor radius.

are defined as the cross product of the local magnetic field and the radial direction from the Sun, and the cross product of the local magnetic field with the first perpendicular direction. The three components of the magnetic field are displayed in **Figure 4** with the lines denoting the time-lagged quantities and the points denoting spatially lagged quantities. We recover the same result as [42], i.e., there is an approximately power-law increase in the inertial range towards ion scales, and then a reduction before the signals become noise dominated. However, as we use a different coordinate system we also have information about the compressive and the transverse components. At these scales, the transverse components seem to dominate the kurtosis.

We also compare our results to other measures of the compressive magnetic field in **Figure 4B**. Here the kurtosis of

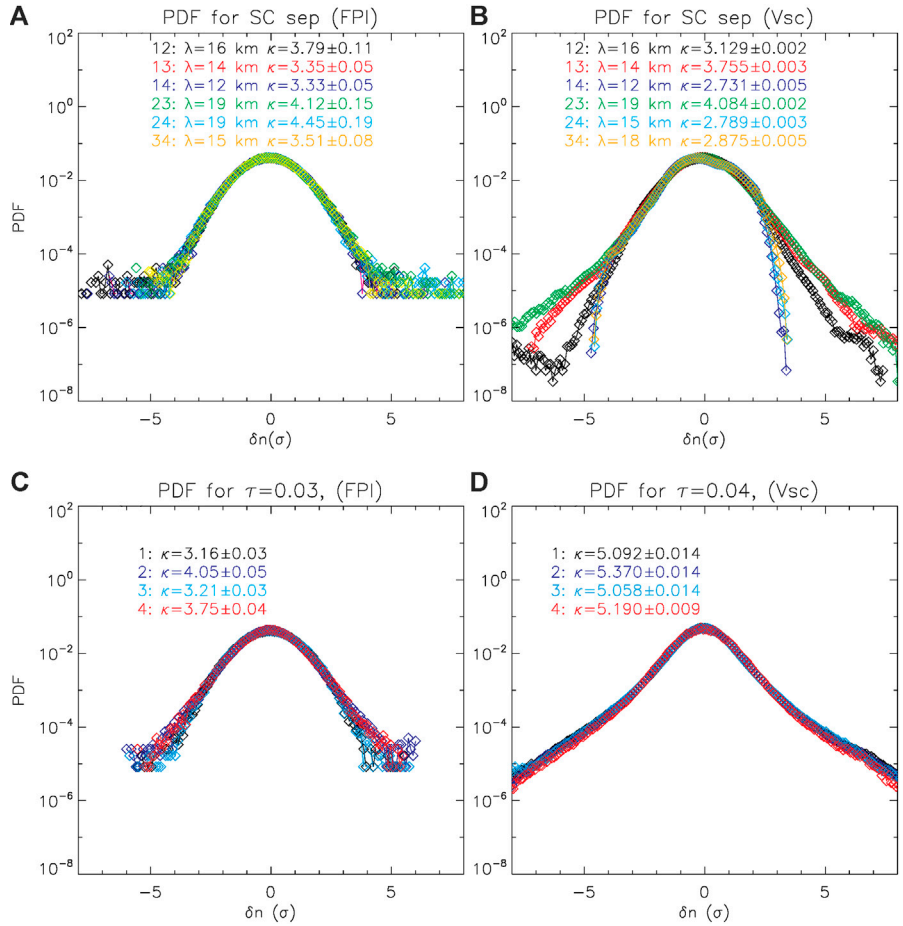

FIGURE 5 | Probability distribution functions for standardized density fluctuations based on spatially lagged measurements from FPI-DES **(A)** from spacecraft potential **(B)** and for time lags at a comparable scale to the spatial lags for FPI **(C)** and for the spacecraft potential **(D)**.

the global magnetic field (which is defined as the mean direction of the field over the entire interval) and of the magnitude of the magnetic field are plotted along with that of the local magnetic field. The local magnetic field and the magnitude agree very well with one another, which is expected for the solar wind as the fluctuations in the magnitude are small $\delta B/B_0 \ll 1$. However, the global magnetic field is much more intermittent. This suggests that when using a global magnetic field some of the intermittent transverse fluctuations might be contributing to the compressible part if there is an abrupt change in the magnetic field direction away from the global mean field direction. On the other hand, the local magnetic field may follow the fluctuations too closely and therefore gradients may not be fully captured, which would result in a lower kurtosis for the local magnetic field definition. This is essentially because the direction of a local magnetic field is not a fixed direction but is also varies in time (or space), reducing the strength of the gradients. For a more detailed discussion on the use of local vs. global mean magnetic field, the reader is directed to the discussion of [77]. Here, we remark that both local and global magnetic fields have limitations, where a local definition may underestimate the intermittency while a global magnetic field may overestimate it.

Figure 5 shows the probability distribution functions (PDF) for the electron density fluctuations from FPI and the spacecraft potential. These PDFs show the spatial lags (b, d) and the time lags (a, c) where τ corresponds to the spatial lag sizes assuming Taylot's hypothesis. The fluctuations here have been normalized to the standard deviation for each scale. Both spatial lags show approximately Gaussian distributions with low kurtosis values. The pairs which include MMS4 for the spacecraft potential are noticeably different which is again likely to the probe failure on MMS4. The time lags based on the FPI data also show a similar distribution. However, the time lags from the spacecraft potential are leptokurtic and show prominent heavy tails.

Figure 6 shows the m-th order structure functions from m = 1 to m = 6. These are defined as:

$$S_m(\tau) = \langle |\delta n_e(t,\tau)|^m \rangle_t \tag{4}$$

For an intermittent signal at higher orders of m ($m > 3$), S_m becomes more difficult to estimate due to the assumptions of ergodicity in the statistical approach and the reality of the finite length of time series [e.g., 69, 70, 78]. Higher orders accentuate the effects of the largest fluctuations and outliers in the data, which can cause the estimation of S_m to degrade if the largest

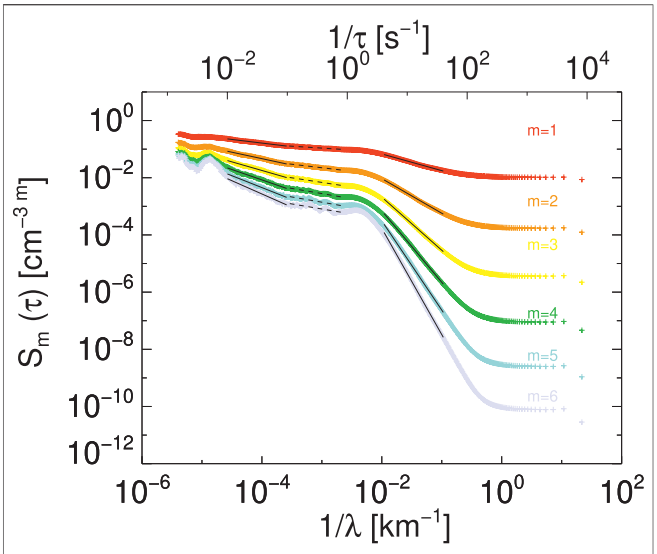

FIGURE 6 | The m-th order structure functions for m = 1 to m = 6. The straight lines denote fits over three different time lag ranges the inertial scales $\frac{1}{\tau} = [0.01, 0.1]s^{-1}$ the transition scales $\frac{1}{\tau} = [0.1, 0.8]s^{-1}$ and the sub-ion range $\frac{1}{\tau} = [4, 40]s^{-1}$.

amplitude fluctuations are not sufficiently sampled in the signal. Therefore the quality of the structure-function obtained is dependent on the statistics of the extreme fluctuations in the signal. In particular, the estimation is difficult when using time lags when the increments at a given time lag have large amplitudes and the time-lagged series is strongly intermittent, which is usually the case in turbulent flows. This can somewhat be mitigated by having a longer time interval so that rare events are sufficiently sampled. However, our data lengths in MMS and Cluster are typically very short [e.g., 41, 79] because of orbital constraints. For MMS at best there are some intervals with a few hours of continuous burst mode in the solar wind.

The maximum order that can be estimated accurately is dependent on the intermittency in the signal, and the length of the time interval used. A rough estimate for the largest order that can be estimated is $\log(N) - 1$ where N is the number of data points. For the number of data points, here $N \simeq 20 \times 10^6$ this corresponds to the largest possible order of 6 [40]. However using the approach of [69], and analyzing a timescale of 0.5s where the scale-dependent kurtosis is near its peak a maximum order of 4 is obtained. Structure functions from orders 1 through 6 are shown in **Figure 6** although orders larger than 4 should be interpreted with caution as discussed.

The structure functions show two distinct ranges with power-law behaviour $S_m(\tau) \propto \tau^{\zeta(m)}$. A possible suggestion of a power-law behaviour is also present in the transition range, at intermediate scales. However, it is difficult to resolve the inertial range and the transition range as they don't cover a very large range of scales.

The variation with the order m of the scaling exponents ζ_m obtained by fitting the structure functions to the inertial range and the sub-ion range is investigated.

For a monofractal scale-invariant process the scaling index expected to vary linearly as $\zeta(m) \propto m$, while for a multifractal process the scaling exponent will have a nonlinear relationship to the order. Physically this means that more than one moment of order m is needed to fully capture the details of the PDF, and the signal is more intermittent. The relationship between the scaling exponent and the order (with step $\delta m = 0.1$) is shown in **Figure 7** for two of the ranges which correspond to the fits shown in black in **Figure 6**. As the transition range is shorter than a decade in scale and the scaling exponents are strongly concave we are not able to fit a p-model to them and we do not display them. The scaling relations of the inertial are concave, while the sub-ion range shows a linear relation. A linear fitting is performed for orders below $m = 3$ which is shown in black and the order four is marked by the orange line. This is one order below the maximum physical m estimated from the technique of [69]. Before m = 4 is reached, the inertial departs from the linear scaling. This suggests that there is multifractality in the inertial range. This is in stark contrast to the sub-ion range which exhibits linear scaling even at orders $m > 4$. Similar relations between the scaling exponent and the order are obtained for the magnetic field in **Figure 8**. However, as there is a smaller range available due to the noise floor occurring at a lower frequency than the electron density meaning that the sub-ion range is fitted over a smaller range of scales and is not as reliable as the electron density. For the two transverse components, there are only two ranges fitted, the ion inertial and the sub-ion range as there is no apparent transition range in the trace spectra in Figure **2A**. Some studies have observed transitions in the trace magnetic spectra between the ion inertial and ion gyroradius scales, which may be related to ion damping, the interplay of Hall and convective terms or plasma instabilities [e.g., see 11, 80 and references therein]. However the spectral signature of this region is different to the flattening observed in the density spectra. Typically the transition observed in the magnetic spectra is very steep ~ -3.4 although the same process may affect the density and magnetic spectra differently. However in this interval we have no evidence of a transition in the trace spectra for this interval. For the compressive component, there are three ranges. However, similarly to the density spectra the transition range is too short to be fitted satisfactorily. The inertial ranges show weak concave relations while the sub-ion range shows mono-fractal behavior. This behavior has been observed in magnetic field observations of [12, 44], and in ion density fluctuations [45].

In order to obtain a more quantitative estimate of the level of intermittency, each scaling exponent curve can be fitted to a standard p-model of intermittent turbulence [81]. In such phenomenological framework, intermittency is modeled as the result of a multifractal multiplicative cascade for the fraction of volume in which the energy is transferred across scales. It predicts a simple relation for the scaling exponents: $\zeta_m = 1 - \log_2[p_{model}^{mH} + (1 - p_{model})^{mH}]$, where H is the Hurst exponent, related to the spectral index through $\alpha = 2H + 1$ or to the structure function scaling exponents through $\zeta_m = mH$, and indicating the roughness of the signal. In the present work, H has been left as a free fitting parameter of the model. The second fitting parameter $p_{model} \in [0.5, 1]$, related to the fraction of volume where the energy transfer is concentrated during the

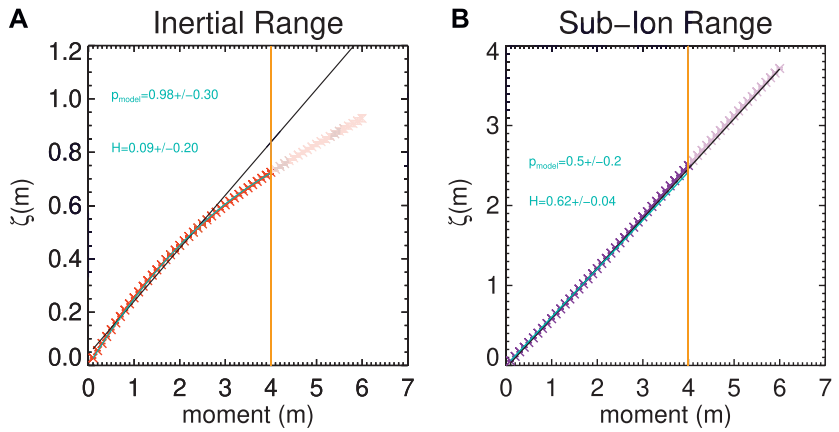

FIGURE 7 | Scaling exponents ζ as a function of the moment *m* for the inertial **(A)** transition **(B)** and sub-ion ranges. The exponents here correspond to the black lines in **Figure 6**. The cyan lines denote p-model fits, and the black line denotes a linear fit to orders below 3.

intermittent cascade, so that larger p_{model} corresponds to larger intermittency.

The scaling exponents presented in the various panels of **Figures 7, 8** have been fitted to a p-model, and the quality of the fit is excellent in all cases. Note that the p-model fit was performed only using exponents up to the fourth order, to ensure statistical convergence. However, we point out that the fitting parameters remain basically unchanged when all six orders are included. We therefore include the higher orders (with lighter colour plotting symbols) in the figures, with the caveat that they might be poorly statistically described. The solid cyan lines in the **Figures 7, 8** represent those fits, and the resulting intermittency

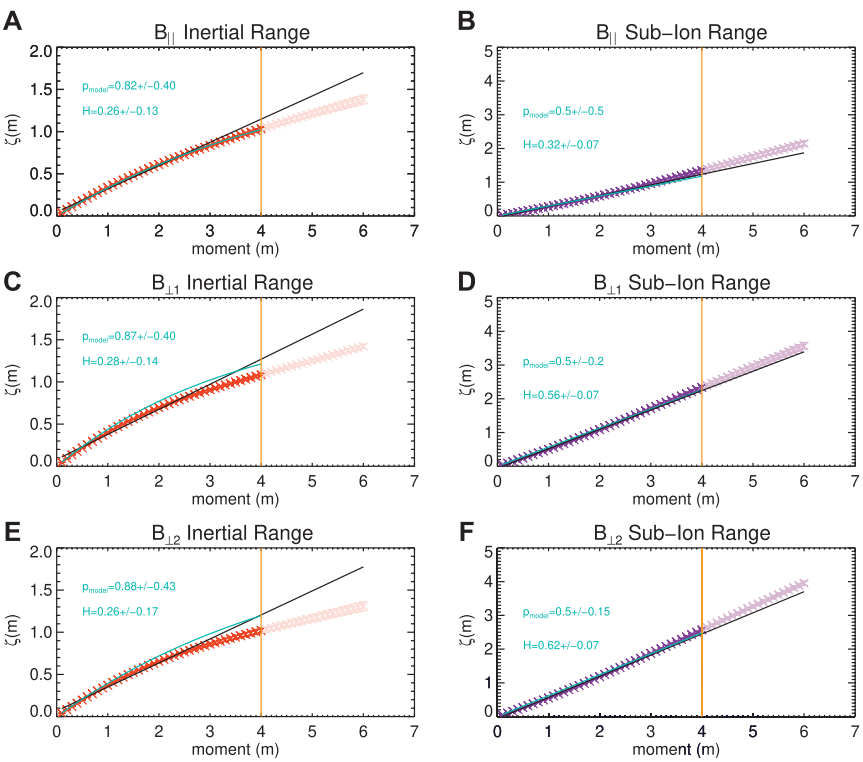

FIGURE 8 | Scaling exponents ζ as a function of the moment *m* for the magnetic field. **(A**, **B)** denote the compressive component for the two ranges mentioned previously. **(C**, **E)** denote the scaling index for the inertial range for the two transverse components **(D**, **F)** denote the scaling exponent for the sub-ion range transverse components.

parameters p_{model} are given in each panel. The fitted values of H are always compatible with the scaling exponents of the second order structure functions, within error bars. This confirms the possibility to describe the turbulence using the P-model, and corroborates the meaningfulness of the intermittency parameter p_{model} For the electron density, a strong intermittency value $p_{model} = 0.98 \pm 0.30$ was found in the inertial range, in agreement with the large scaling exponent of the kurtosis. We do not show the scaling exponents or fit a p-model for the transition range, the bad quality of the fit did not allow modeling the data with the p-model. This is consistent with the extreme curvature of the scaling exponent (not shown), which for large orders m becomes a decreasing function of the order. This feature is typically forbidden for an "ideal" turbulent field, which requires monotonic increase of ζ_m (constant exponents are expected in the presence of topological discontinuities, for example in the absence of dissipation as described by the Burgers equation for neutral flows) [31]. The indication of this observation is that the stochastic fluctuations of the transition region are not simply the result of a turbulent cascade, but other physical processes must occur in generating the exceptionally strong gradients in that range of scale. This is not surprising, since in this range kinetic effects start to be relevant in the dynamics, so that wave-particle interactions may play an additional role in generating density fluctuations. Specifically this may be consistent with damping of compressive slow mode waves which are cascaded as a passive scalar, and are heavily damped as they reach the ion scales, in addition to an active cascade of kinetic Alfvén waves [e.g 74, 82].

In the sub-ion range, the p-model fitting parameter $p_{model} = 0.5 \pm 0.2$ indicates clearly the absence of intermittency, again in agreement with visual description of the PDFs and of the kurtosis, and with recent results on density intermittency [50]. Finally, the magnetic field components present high level of intermittency in the inertial range ($p_{model} \simeq 0.8$), and strictly mono-fractal scaling in the sub-ion range ($p_{model} \simeq 0.5$).

4. DISCUSSION

The evolution of the scale-dependent kurtosis is shown to increase throughout the inertial range until it reaches the proton characteristic scales whereafter it decreases in the magnetic field or plateaus as in the density. This behavior is different from that in the magnetosheath, where the scale-dependent kurtosis continues to increase down to the smallest scales [42]. This may be due to the magnetosheath turbulence being strongly driven by the shock while the solar wind turbulence is decaying and the kurtosis decreases with radial distance [e.g., 83, 84]. This is to say that turbulence in the solar wind at large heliocentric distances is far from the drivers, e.g., velocity shears between streams, shocks, etc. Another possibility is that high-frequency wave activity in the solar wind may act in the sub-ion range to reduce the kurtosis [48]. These waves would need to have the property of having strong wavevector anisotropy $k_\perp \gg k_\parallel$, and approximate equal power in the compressive and stransverse components. In this region of large $k_\perp$these waves could be either Ion Bernstein [e.g., 85] or Kinetic Alfvén waves [e.g., 54]. The damping rates of such waves are highly sensitive to the propagation direction and the plasma beta. In the magnetosheath, due to processing at the shock the ion temperature (and consequently the ion beta) are much higher [e.g., 86]. At higher plasma β, linear plasma waves are typically more heavily damped [87]. This suggests that such waves could exist in the solar wind and act to reduce the kurtosis while in the magnetosheath they cannot exist leading to the magnetosheath being more similar to a neutral fluid.

One of the more puzzling results here is that there is a difference between the time and the spatial lags of the electron density from spacecraft potential. For the magnetic field data and the density from FPI, there is an agreement between the time and the spatial lags. However, this is somewhat misleading as the time lags are heavily affected by instrumental noise. As instrumental noise is uncorrelated between spacecraft the spatial lags are more robust to the effects of noise. In the spacecraft potential data, the time lag corresponding to the spatial separation occurs before instrumental noise becomes significant and show a leptokurtic distribution. The spatial lags show approximately Gaussian distributions. This could be due to several reasons. Firstly, there may be a physical difference between the different directions i.e., that there are more structures in the direction of the bulk flow (time lags) as opposed to other directions (spatial lags). This may be a naturally occurring difference or there could be a sampling effect related to the bulk flow direction [88]. Another possibility is that Taylor's hypothesis breaks down in this region. In the numerical study of [89] they concluded that the Taylor's hypothesis is likely to be violated at small scales for intervals where the Alfvén speed is comparable to the bulk speed [e.g., in the magnetosheath 90]. The geometry of the magnetic field with respect to the bulk velocity direction also plays a role with more radial configurations of the magnetic field being more likely to violate the hypothesis. In this interval $V_{sw}/V_A = 7.6$, the magnetic field makes a large angle ($86 \pm 11^\circ$) with the bulk velocity and the hypothesis should be well satisfied for large scales. However, at small scales such as we study here, the hypothesis may still break down despite the interval having a large bulk speed and a favorable magnetic field configuration. A breakdown in Taylor's hypothesis could be due to wave activity or that structures evolve at faster timescales at these scales. The waves that can exist in the sub-ion range such as kinetic Alfvén waves [91], or fast mode branch waves such as Ion Bernstein waves, or parallel whistler waves [92, 93] are very dispersive. Furthermore wave activity could act to reduce the kurtosis here similarly to how MHD-scale Alfvén waves act at larger scales [49]. Another possibility is that electron scale coherent structures evolve very quickly. For example, vortices could merge such as is discussed in neutral fluid turbulence in a process called vortex collapse [e.g., 94] or could develop or be destroyed on time scales faster than the advection time. This hypothesis could be tested directly with several spacecraft that are aligned with the bulk flow direction at a range of distnaces. Other possibilities are that the timing accuracy is not sufficient to compare inter-spacecraft increments, although this seems unlikely. Another issue could be that the resampling required to put the time series from

different spacecraft on the same timeline causes some issues at the edges of the time series [42]. To ensure that outliers due to this effect are not present data points at the edges (the first and last 4 s) of the resampled time series are removed at each edge. Finally, we remark that coherent structures are characterized by phase coherence across many scales, therefore when looking at time lags larger scale coherent structures may affect the smaller scales, whereas using spatial lags the larger scale fluctuations could be more effectively filtered. It is however important to note that the structure of coherent structures may be complex with larger coherent structures, possibly having smaller "daughter" structures associated with them [95].

The scale-dependent kurtosis of the magnetic field gives complementary information to the density. In **Figure 4** we see that the compressive component is smaller than the transverse components. This is different from observations of larger scales where the opposite is true [49], this may reflect a difference in the nature of coherent structures. At large scales coherent structures are likely strongly compressive, magnetic holes or boundaries between streams, while in the ion ranges the structures may be predominantly incompressible or very weakly compressible such as Alfvénic vortices and current sheets [34, 37]. There is a large difference between the scale-dependent kurtosis using a global mean as opposed to a local mean or the magnitude of the magnetic field. Using a global field may result in a larger kurtosis as it is potentially polluted by some of the transverse coherent structures. However, when using a local field gradients may not be able to be identified. In this case the local magnetic field agrees well with the values of the kurtosis of magnetic field magnitude and the density. The good agreement between the local magnetic field and the magnitude is likley because the fluctuations are small. However as the fluctuations are larger in the magnetosheath the magnitude may not be reliable, and one should use a local definition. However, it should be stressed that both approaches to calculating a local field have advantages and limitations, and the choice has implications for the interpretation of the results as shown here.

When comparing the spatial lags of the magnetic field and the density we see agreement between all of the different methods, that they all have small kurtoses. This complements previous measurements of the power of compressive and transverse fluctuations i.e. that they have similar powers in the sub-ion range [12, 20]. One potential explanation for this is that the fluctuations are kinetic Alfvén wave-like. As the KAW develops a larger wavenumber in the perpendicular direction it becomes strongly compressive. In the sub-ion range, this could account for equal power in the compressive and two transverse components [e.g., 12, 96].

Structure-function anaysis presented in **Figures 7,8** also suggests that the sub-ion range for magnetic and density fluctuations are monofractal. For the density measurements, the scaling exponents are somewhat smaller than what is expected based on the Fourier spectrum in **Figure 2**. This may be due to the flattening in the spectrum at ion scales, meaning that there is a shorter range of scales available for fitting compared to the magnetic field data. The flattening of the spectra at ion scales could be due to the competition of large scale slow waves and small scale kinetic Alfvén waves, Hall effects, or an increase in the compressible coherent structures at this range. In this range, the scaling indices are anomalous[4] suggesting a larger degree of multifractality in the density fluctuations. However, the scale-dependent kurtosis reaches a plateau and is not very different in **Figure 3** when the scales close to the transition range are compared to the sub-ion range. Here we reach a similar conclusion to [46], that different measures of intermittency capture different properties of intermittency. The scaling indices in the sub-ion range of magnetic and density fluctuations suggest monofractal scaling, in agreement with the spatially lagged kurtoses which show predominantly Gaussian statistics. However, the time-lagged measurements show leptokurtic distributions.

5. CONCLUSION

To summarize; we have investigated compressive and incompressive intermittency in the solar wind. Using the exceptionally high resolution data provided from MMS allows a view deep into the sub-ion scale with unprecedented time resolution for an *in situ* measurement of electron density fluctuations. Further more the multiple measurement points allow an investigation of different directions in the plasma. Previous studies of the electron density have been limited to single point measurements and are only able to sample along the bulk flow direction. The results are found to be similar to those found with the magnetic field in [12, 44] and in ion density fluctuations at larger scales than are studied here [45]. In these studies, the scale-dependent kurtosis was not found to evolve significantly and the evolution of scaling index with the order suggested monofractal scaling or only very weak multifractality when juxtaposed with the inertial and transition ranges.

A discrepancy was observed between temporal and spatial lags and we have put forward several possible explanations for this. This could be due to a breakdown in Taylor's hypothesis. This could be investigated using two spacecraft data where the baseline is aligned with the bulk flow. This would give a direct measurement of whether Taylor's hypothesis is valid. However, for this interval none of the spacecraft pairs are aligned closely enough to the bulk velocity direction to make such a comparison. Other possibilities include directional differences. To investigate this possibility detailed comparisons with numerical simulations may be needed, and more sampling points than the four points that MMS or Cluster offer. One strong possibility is high-frequency waves which may affect these scales of randomizing the phases of the signal, reducing the kurtosis. Waves such as those described tend to have strong wavevector anisotropies ($k_\perp \gg k_\parallel$) [e.g., 97, 98] and could cause different kurtoses in different directions. Furthermore, such waves would also be strongly dispersive and could also lead to a violation of Taylor's hypothesis. Alternatively it may be coherent structures in this interval are all much larger than the spacecraft baseline sizes. In this case there would not be much difference between the different spacecraft, whereas the gradients in the time lags would be larger. One final possibility is that there could be a sampling effect inherent

[4]Anomalous refers here to a deviation from self-similar, linear order dependence of the structure functions scaling exponent, typical of intermittency.

with the bulk velocity direction [e.g., 88]. This could cause a bias in the bulk flow direction so that more structures are seen in this direction than compared to others.

The differences in the different measurement techniques support the statement in [46] that to investigate intermittency a variety of different techniques should be employed. We also remark that four-point measurements have revolutionized *in situ* plasma turbulence study. However, four points are inherently limited to providing either homogeneous coverage of the plasma at a single scale or multi-scale coverage at the cost of losing directional information. The natural next step in investigating space plasma turbulence is to go beyond four points to obtain multi-direction multi-scale measurements [99–101].

DATA AVAILABILITY STATEMENT

The Magnetospheric MultiScale mission data are available from https://lasp.colorado.edu/mms/sdc/public/. The processed spacecraft potential can be accessed at https://www.iwf.oeaw.ac.at/en/research/researchnbspgroups/space-plasma-physics/sc-plasma-interaction/mmsaspoc-data-analysis/.

AUTHOR CONTRIBUTIONS

OR, JT and LS, performed the analysis of the data. The initial manuscript was drafted by OR. OR and RN developed of the density dataset. JT, LS, ZV, and RN contributed to the interpretation of the data and several improvements in the manuscript.

FUNDING

The calibration of the spacecraft potential data at IWF is supported by Austrian FFG projects ASAP15/873685. JT was funded by a Fulbright Austria-Marshall Plan grant. RN was supported by Austrian FWF projects I2016-N20. ZV was supported by the Austrian FWF projects P28764-N27.

ACKNOWLEDGMENTS

The authors acknowledge the MMS instrument teams for FPI, FGM, and SDP for providing excellent data which made this study possible.

REFERENCES

1. Bale SD, Kellogg PJ, Mozer FS, Horbury TS, Reme H. Measurement of the electric fluctuation spectrum of magnetohydrodynamic turbulence. *Phys Rev Lett* (2005) 94:215002. doi:10.1103/PhysRevLett.94.215002
2. Podesta JJ, Roberts DA, Goldstein ML. Power spectrum of small-scale turbulent velocity fluctuations in the solar wind. *J Geophys Res* (2006) 111:A10109. doi:10.1029/2006JA011834
3. Roberts OW, Narita Y, Li X, Escoubet CP, Laakso H. Multipoint analysis of compressive fluctuations in the fast and slow solar wind. *J Geophys Res Space Phys* (2017) 122:6940–63. doi:10.1002/2016JA023552
4. Šafránková J, Nemecek Z, Nemec F, Prech L, Chen CHK, Zastenker GN. Power spectral density of fluctuations of bulk and thermal speeds in the solar wind. *Astrophys J* (2016) 825:121. doi:10.3847/0004-637X/825/2/121
5. Roberts OW, Narita Y, Nakamura R, Vörös Z, Gershman D. Anisotropy of the spectral index in ion scale compressible turbulence: MMS observations in the magnetosheath. *Front Phys* (2019) 7: 1–16. doi:10.3389/fphy.2019.00184
6. Tu CY, Marsch E. MHD structures, waves and turbulence in the solar wind: observations and theories. *Space Sci Rev* (1995) 73:1–210. doi:10.1007/BF00748891
7. Smith CW, Vasquez BJ, Hamilton K. Interplanetary magnetic fluctuation anisotropy in the inertial range. *J Geophys Res* (2006) 111:A09111. doi:10.1029/2006JA011651
8. Bruno R, Carbone V. The solar wind as a turbulence laboratory. *Living Rev Sol Phys* (2013) 10, 2. http://www.livingreviews.org/lrsp-2013-2. doi:10.12942/lrsp-2013-2
9. Kiyani KH, Osman KT, Chapman SC. Dissipation and heating in solar wind turbulence: from the macro to the micro and back again. *Phil Trans Math Phys Eng Sci* (2015) 373:20140155. doi:10.1098/rsta.2014.0155
10. Verscharen D, Klein KG, Maruca BA. The multi-scale nature of the solar wind. *Living Rev Sol Phys* (2019) 16:5. doi:10.1007/s41116-019-0021-0
11. Sahraoui F, Hadid L, Huang S. Magnetohydrodynamic and kinetic scale turbulence in the near-Earth space plasmas: a (short) biased review. *Rev Mod Plasma Phys* (2020) 4:4. doi:10.1007/s41614-020-0040-2
12. Kiyani K, Chapman S, Sahraoui F, Hnat B, Fauvarque O, Khotyaintsev YV. Enhanced magnetic compressibility and isotropic scale invariance at sub-ion larmor scales in solar wind turbulence. *Astrophys J* (2013) 763:10. doi:10.1088/0004-637X/763/1/10
13. Alexandrova O, Lacombe C, Mangeney A. Spectra and anisotropy of magnetic fluctuations in the Earth's magnetosheath: cluster observations. *Ann Geophys* (2008) 26:3585–96. doi:10.5194/angeo-26-3585-2008
14. Ferrand R, Galtier S, Sahraoui F, Meyrand R, Andrés N, Banerjee S. On exact laws in incompressible hall magnetohydrodynamic turbulence. *Astrophys J* (2019) 881:50. doi:10.3847/1538-4357/ab2be9
15. Bandyopadhyay R, Sorriso-Valvo L, Chasapis A, Hellinger P, Matthaeus WH, Verdini A, et al. *In situ* observation of hall magnetohydrodynamic cascade in space plasma. *Phys Rev Lett* (2020) 124:225101. doi:10.1103/PhysRevLett.124.225101
16. Chen CH, Klein KG, Howes GG. Evidence for electron Landau damping in space plasma turbulence. *Nat Commun* (2019) 10:740. doi:10.1038/s41467-019-08435-3
17. Alexandrova O, Saur J, Lacombe C, Mangeney A, Mitchell J, Schwartz S, et al. Universality of solar-wind turbulent spectrum from MHD to electron scales. *Phys Rev Lett* (2009) 103:165003. doi:10.1103/PhysRevLett.103.165003
18. Alexandrova O, Lacombe C, Mangeney A, Grappin R, Maksimovic M. Solar wind turbulent spectrum at plasma kinetic scales. *Astrophys J* (2012) 760:121. doi:10.1088/0004-637X/760/2/121
19. Sahraoui F, Huang SY, Belmont G, Goldstein ML, Rétino A, Robert P, et al. Scaling OF the electron dissipation range OF solar wind turbulence. *Astrophys J* (2013) 777:15. doi:10.1088/0004-637X/777/1/15
20. Roberts OW, Narita Y, Escoubet CP. Direct measurement of anisotropic and asymmetric wave vector spectrum in ion-scale solar wind turbulence. *Astrophys J* (2017) 851:L11. doi:10.3847/2041-8213/aa9bf3
21. Pedersen A. Solar wind and magnetosphere plasma diagnostics by spacecraft electrostatic potential measurements. *Ann Geophys* (1995) 13:118–29. doi:10.1007/s00585-995-0118-8
22. Escoubet CP, Pedersen A, Schmidt R, Lindqvist PA. Density in the magnetosphere inferred from ISEE 1 spacecraft potential. *J Geophys Res Space Phys* (1997) 102:17595–609. doi:10.1029/97JA00290
23. Pedersen A, Décréau P, Escoubet CP, Gustafsson G, Laakso H, Lindqvist PA, et al. Four-point high time resolution information on electron densities by the electric field experiments (EFW) on cluster. *Ann Geophys* (2001) 19:1483–9. doi:10.5194/angeo-19-1483-2001
24. Pedersen A, Lybekk B, André M, Eriksson A, Masson A, Mozer FS, et al. Electron density estimations derived from spacecraft potential measurements on cluster in tenuous plasma regions. *J Geophys Res Space Phys* (2008) 113:A07S33. doi:10.1029/2007JA012636
25. Lybekk B, Pedersen A, Haaland S, Svenes K, Fazakerley AN, Masson A, et al. Solar cycle variations of the cluster spacecraft potential and its use for electron density estimations. *J Geophys Res Space Phys* (2012) 117:A01217. doi:10.1029/2011JA016969

26. Yao S, He JS, Marsch E, Tu CY, Pedersen A, Rème H, et al. Multi-scale anti-correlation between electron density and magnetic field strength in the solar wind. *Astrophys J* (2011) 728:146. doi:10.1088/0004-637X/728/2/146.
27. Andriopoulou M, Nakamura R, Torkar K, Baumjohann W, Hoelzl B. Deriving plasma densities in tenuous plasma regions, with the spacecraft potential under active control. *J Geophys Res Space Phys* (2015) 120:9594–616. doi:10.1002/2015JA021472
28. Andriopoulou M, Nakamura R, Wellenzohn S, Torkar K, Baumjohann W, Torbert RB, et al. Plasma density estimates from spacecraft potential using MMS observations in the dayside magnetosphere. *J Geophys Res Space Phys* (2018) 123:2620–9. doi:10.1002/2017JA025086
29. Torkar K, Nakamura R, Wellenzohn S, Jeszenszky H, Torbert RB, Lindqvist PA, et al. Improved determination of plasma density based on spacecraft potential of the magnetospheric multiscale mission under active potential control. *IEEE Trans Plasma Sci* (2019) 47:3636–47. doi:10.1109/TPS.2019.2911425
30. Kolmogorov AN. A refinement of previous hypotheses concerning the local structure of turbulence. *J Fluid Mech* (1962) 13:83–5. doi:10.1017/s0022112062000518
31. Frisch U. *Turbulence: The Legacy of A. N. Kolmogorov*. Cambridge, England: Cambridge University Press (1995)
32. Chen C, Mallet A, Schekochihin A, Horbury T, Wicks RT, Bale S. Three-dimensional structure of solar wind turbulence. *Astrophys J* (2012) 758:2. doi:10.1088/0004-637X/758/2/120
33. Roberts OW, Toledo-Redondo S, Perrone D, Zhao J, Narita Y, Gershman D, et al. Ion-scale kinetic Alfvén turbulence: MMS measurements of the Alfvén ratio in the magnetosheath. *Geophys Res Lett* (2018) 45:7974–84. doi:10.1029/2018GL078498
34. Perrone D, Alexandrova O, Mangeney A, Maksimovic M, Lacombe C, Rakoto V, et al. Compressive coherent structures at ION scales IN the slow solar wind. *Astrophys J* (2016) 826:196. doi:10.3847/0004-637X/826/2/196
35. Roberts OW, Li X, Alexandrova O, Li B. Observation of an MHD Alfvén vortex in the slow solar wind. *J Geophys Res Space Phys* (2016) 121:3870–81. doi:10.1002/2015JA022248
36. Vörös Z, Yordanova E, Echim MM, Consolini G, Narita Y. Turbulence-generated proton-scale structures in the terrestrial magnetosheath. *Astrophys J Lett* (2016) 819:L15 1–6. doi:10.3847/2041-8205/819/1/L15
37. Perrone D, Alexandrova O, Roberts OW, Lion S, Lacombe C, Walsh A, et al. Coherent structures at ion scales in fast solar wind: cluster observations. *Astrophys J* (2017) 849:49. doi:10.3847/1538-4357/aa9022.
38. Wang X, Tu CY, He JS, Wang LH. Ion-scale spectral break in the normal plasma beta range in the solar wind turbulence. *J Geophys Res Space Phys* (2018) 123:68–75. doi:10.1002/2017JA024813.
39. Wu P, Perri S, Osman K, Wan M, Matthaeus W, Shay M, et al. Intermittent heating IN solar wind and kinetic simulations. *Astrophys J Lett* (2013) 763:L30. doi:10.1088/2041-8205/763/2/L30.
40. Chen CHK, Leung L, Boldyrev S, Maruca BA, Bale S. Ion-scale spectral break of solar wind turbulence at high and low beta. *Geophys Res Lett* (2014) 41:8081–88. doi:10.1002/2014GL062009.
41. Chasapis A, Matthaeus WH, Parashar TN, Fuselier SA, Maruca BA, Phan TD, et al. High-resolution statistics of solar wind turbulence at kinetic scales using the magnetospheric multiscale mission. *Astrophys J* (2017) 844:L9. doi:10.3847/2041-8213/aa7ddd.
42. Chhiber R, Chasapis A, Bandyopadhyay R, Parashar TN, Matthaeus WH, Maruca BA, et al. Higher-order turbulence statistics in the Earth's magnetosheath and the solar wind using magnetospheric multiscale observations. *J Geophys Res Space Phys* (2018) 123:9941–54. doi:10.1029/2018JA025768.
43. Macek WM. Multifractality and intermittency in the solar wind. *Nonlinear Process Geophys* (2007) 14:695–700. doi:10.5194/npg-14-695-2007
44. Kiyani KH, Chapman SC, Khotyaintsev YV, Dunlop MW, Sahraoui F. Global scale-invariant dissipation in collisionless plasma turbulence. *Phys Rev Lett* (2009) 103:075006. doi:10.1103/PhysRevLett.103.075006
45. Chen CHK, Sorriso-Valvo L, Šafránková J, Němeček Z. Intermittency OF solar wind density fluctuations from ION to electron scales. *Astrophys J* (2014) 789:L8. doi:10.1088/2041-8205/789/1/L8
46. Sorriso-Valvo L, Carbone F, Leonardis E, Chen CH, Šafránková J, Němeček Z. Multifractal analysis of high resolution solar wind proton density measurements. *Adv Space Res* (2017) 59:1642–51. doi:10.1016/j.asr.2016.12.024
47. Sorriso-Valvo L, Carbone V, Veltri P, Consolini G, Bruno R. Intermittency in the solar wind turbulence through probability distribution functions of fluctuations. *Geophys Res Lett* (1999) 26:1801–4. doi:10.1029/1999GL900270
48. Wan M, Osman KT, Matthaeus WH, Oughton S. Investigation of intermittency in magnetohydrodynamics and solar wind turbulence: scale-dependent kurtosis. *Astrophys J* (2012) 744:171. doi:10.1088/0004-637X/744/2/171
49. Bruno R, Carbone V, Sorriso-Valvo L, Bavassano B. Radial evolution of solar wind intermittency in the inner heliosphere. *J Geophys Res Space Phys* (2003) 108:1130. doi:10.1029/2002JA009615
50. Carbone F, Sorriso-Valvo L, Alberti T, Lepreti F, Chen CHK, Němeček Z, et al. Arbitrary-order hilbert spectral analysis and intermittency in solar wind density fluctuations. *Astrophys J* (2018) 859:27. doi:10.3847/1538-4357/aabcc2
51. Taylor GI. The spectrum of turbulence. *Proc Math Phys Eng Sci* (1938) 164:476–90. doi:10.1098/rspa.1938.0032
52. Roberts OW, Nakamura R, Torkar K, Narita Y, Holmes JC, Voros Z, et al. Sub-ion scale Compressive turbulence in the solar wind: MMS spacecraft potential observations. The Astrophys J Suppl S (2020) 250:35. doi:10.3847/1538-4365/abb45d
53. Chen C, Howes GG, Bonnell JW, Mozer FS, Klein KG, Bale S. Kinetic scale density fluctuations in the solar wind. In: Solar wind 13: proceeding of the thirteenth international solar wind conference solar wind, 1539; Pasadena, CA; (2013) p. 143–6. doi:10.1063/1.4811008
54. Chen C, Boldyrev S, Xia Q, Perez JC. Nature of subproton scale turbulence in the solar wind. *Phys Rev Lett* (2013) 110:225002. doi:10.1103/PhysRevLett.110.225002
55. Safrankova J, Nemecek Z, Prech L, Zastenker G. Ion kinetic scale in the solar wind observed. *Phys Rev Lett* (2013) 110:025004. doi:10.1103/PhysRevLett.110.025004
56. Burch JL, Moore TE, Torbert RB, Giles BL. Magnetospheric multiscale overview and science objectives. *Space Sci Rev* (2016) 199:5–21. doi:10.1007/s11214-015-0164-9
57. Bandyopadhyay R, Chasapis A, Chhiber R, Parashar TN, Maruca BA, Matthaeus WH, et al. Solar wind turbulence studies using MMS fast plasma investigation data. *Astrophys J* (2018) 866:81. doi:10.3847/1538-4357/aade93
58. Jeřáb M, Něměek Z, Šafránková J, Jelínek K, Měrka J. Improved bow shock model with dependence on the IMF strength. *Planet Space Sci* (2005) 53:85–93. doi:10.1016/j.pss.2004.09.032
59. Russell CT, Anderson BJ, Baumjohann W, Bromund KR, Dearborn D, Fischer D, et al. The magnetospheric multiscale magnetometers. *Space Sci Rev* (2016) 199:189–256. doi:10.1007/s11214-014-0057-3
60. Pollock C, Moore T, Jacques A, Burch J, Gliese U, Saito Y, et al. Fast plasma investigation for magnetospheric multiscale. *Space Sci Rev* (2016) 199:331–406. doi:10.1007/s11214-016-0245-4
61. Roberts OW, Nakamura R, Torkar K, Graham DB, Gershman DJ, Holmes J, et al. Estimation of the electron density from spacecraft potential during high frequency electric field fluctuations. *J Geophys Res Space Phys* (2020) 125:e2020JA027854. doi:10.1029/2020JA027854
62. Lindqvist PA, Olsson G, Torbert RB, King B, Granoff M, Rau D, et al. The spin-plane Double probe electric field instrument for MMS. *Space Sci Rev* (2016) 199:137–65. doi:10.1007/s11214-014-0116-9
63. Khotyaintsev YV, Lindqvist PA, Nilsson T. Spin-plane Double Probe instrument/ Axial Double Probe instrument (SDP/ADP) data products guide (2017) Technical Report.
64. Graham DB, Vaivads A, Khotyaintsev YV, Eriksson AI, André M, Malaspina DM, et al. Enhanced escape of spacecraft photoelectrons caused by Langmuir and upper hybrid waves. *J Geophys Res Space Phys* (2018) 123:7534–53. doi:10.1029/2018JA025874
65. Torkar K, Nakamura R, Tajmar M, Scharlemann C, Jeszenszky H, Laky G, et al. Active spacecraft potential control investigation. *Space Sci Rev* (2016) 199:515–44. doi:10.1007/s11214-014-0049-3
66. Ye S, Vaverka J, Nouzak L, Sternovsky Z, Zaslavsky A, Pavlu J, et al. Understanding cassini RPWS antenna signals triggered by dust impacts. *Geophys Res Lett* (2019) 46:10941–50. doi:10.1029/2019GL084150
67. Vaverka J, Pavlů J, Nouzák L, Šafránková J, Němeček Z, Mann I, et al. One-year analysis of dust impact-like events onto the MMS spacecraft. *J Geophys Res Space Phy* 124 (2019) 8179–90. doi:10.1029/2019JA027035

68. Escoubet CP, Hwang KJ, Toledo-Redondo S, Turc L, Haaland SE, Aunai N, et al. Cluster and MMS simultaneous observations of magnetosheath high speed jets and their impact on the magnetopause. *Front Astron Space Sci* (2020) 6:78. doi:10.3389/fspas.2019.00078
69. Dudok de Wit T. Can high-order moments be meaningfully estimated from experimental turbulence measurements? *Phys Rev* (2004) 70:055302. doi:10.1103/PhysRevE.70.055302
70. Kiyani K, Chapman SC, Hnat B. Extracting the scaling exponents of a self-affine, non-Gaussian process from a finite-length time series. *Phys Rev* (2006) 74:051122. doi:10.1103/PhysRevE.74.051122
71. Bandyopadhyay R, Matthaeus WH, Chasapis A, Russell CT, Strangeway RJ, Torbert RB, et al. Direct measurement of the solar-wind taylor microscale using MMS turbulence campaign data. APJ (2020) 899:63. doi:10.3847/1538-4357/ab9ebe
72. King JH, Papitashvili N. Solar wind spatial scales in and comparisons of hourly Wind and ACE plasma and magnetic field data. *J Geophys Res* (2005) 110: A02104. doi:10.1029/2004JA010649
73. Bruno R, Trenchi L. Radial dependence OF the frequency break between fluid and kinetic scales IN the solar wind fluctuations. *Astrophys J Lett* (2014) 787 24. doi:10.1088/2041-8205/787/2/L24
74. Chandran BDG, Quataert E, Howes GG, Xia Q, Pongkitiwanichakul P. Constraining low-frequency alfvenic turbulence in the solar wind using density-fluctuation measurements. *Astrophys J* (2009) 707:1668–75. doi:10.1088/0004-637X/707/2/1668
75. Veltri P. MHD turbulence in the solar wind: self-similarity, intermittency and coherent structures. *Plasma Phys Control Fusion* (1999) 41:A787–95. doi:10.1088/0741-3335/41/3A/071
76. Chapman SC, Hnat B, Rowlands G, Watkins NW. Scalling collapse and structure functions: identifying self-affinity in finite length time series. *Nonlinear Process Geophys* (2005) 12:767–74. doi:10.5194/npg-12-767-2005
77. Oughton S, Matthaeus WH. Critical balance and the physics of magnetohydrodynamic turbulence. *Astrophys J* (2020) 897:37. doi:10.3847/1538-4357/ab8f2a
78. Tennekes H, Wyngaard JC. The intermittent small-scale structure of turbulence: data-processing hazards. *J Fluid Mech* (1972) 55:93–103. doi:10.1017/S0022112072001661
79. Roberts OW, Li X, Jeska L. A statistical study OF the solar wind turbulence at ION kinetic scales using the K -filtering technique and cluster data. *Astrophys J* (2015) 802:1–13. doi:10.1088/0004-637X/802/1/2
80. Alexandrova O, Chen CHK, Sorriso-Valvo L, Horbury TS, Bale SD. Solar wind turbulence and the role of ion instabilities. *Space Sci Rev* (2013) 178:101–39. doi:10.1007/s11214-013-0004-8
81. Meneveau C, Sreenivasan KR. Simple multifractal cascade model for fully developed turbulence. *Phys Rev Lett* (1987) 59:1424–1427. doi:10.1103/PhysRevLett.59.1424
82. Schekochihin AA, Cowley SC, Dorland W, Hammett GW, Howes GG, Quataert E, et al. Astrophysical gyrokinetics: kinetic and fluid turbulent cascades in magnetized weakly collisional plasmas. *Astrophys J Suppl* (2009) 182:310–77. doi:10.1088/0067-0049/182/1/310
83. Wawrzaszek A, Echim M, Macek WM, Bruno R. Evolution of intermittency in the slow and fast solar wind beyond the ecliptic plane. *Astrophys J Lett* (2015) 814: L19. doi:10.1088/2041-8205/814/2/L19
84. Parashar TN, Cuesta M, Matthaeus WH. Reynolds number and intermittency in the expanding solar wind: predictions based on voyager observations. *Astrophys J* 884 (2019) L57. doi:10.3847/2041-8213/ab4a82
85. Narita Y, Plaschke F, Nakamura R, Baumjohann W, Magnes W, Fischer D, et al. Wave telescope technique for MMS magnetometer. *Geophys Res Lett* (2016) 43:4774–80. doi:10.1002/2016GL069035.Received
86. Krasnoselskikh V, Balikhin M, Walker SN, Schwartz S, Sundkvist D, Lobzin V, et al. The dynamic quasiperpendicular shock: Cluster discoveries. *Space Science Reviews* (2013) 178:535–598. doi:10.1007/s11214-013-9972-y
87. Gary S. *Theory of space plasma microinstabilities*. Cambridge, England: Cambridge University Press (1993)
88. Turner AJ, Gogoberidze G, Chapman S, Hnat B, Müller WC. Nonaxisymmetric anisotropy of solar wind turbulence. *Phys Rev Lett* (2011) 107:095002. doi:10.1103/PhysRevLett.107.095002
89. Perri S, Valentini F, Sorriso-Valvo L, Reda A, Malara F. On the estimation of the current density in space plasmas: multi- versus single-point techniques. *Planet Space Sci* (2017) 140:6–10. doi:10.1016/j.pss.2017.03.008
90. Stawarz JE, Eriksson S, Wilder FD, Ergun RE, Schwartz SJ, Pouquet A, et al. Observations of turbulence in a kelvin-helmholtz event on 8 september 2015 by the magnetospheric multiscale mission. *J Geophys Res Space Phy* (2016) 121: 11021–11034. doi:10.1002/2016JA023458
91. Chen C, Bale S, Salem C, Maruca B. Residual energy spectrum of solar wind turbulence. *Astrophys J* (2013) 770:125. doi:10.1088/0004-637X/770/2/125
92. Lacombe C, Alexandrova O, Matteini L, Santolík O, Cornilleau-Wehrlin N, Mangeney A, et al. Whistler mode waves and the electron heat flux in the solar wind: cluster observations. *Astrophys J* (2014) 796:5. doi:10.1088/0004-637X/796/1/5
93. Roberts OW, Alexandrova O, Kajdič P, Turc L, Perrone D, Escoubet CP, et al. Variability of the magnetic field power spectrum in the solar wind at electron scales. *Astrophys J* (2017) 850:120. doi:10.3847/1538-4357/aa93e5
94. Novikov EA, Sedov YB. Vortex collapse. *Sov Phys JETP* (1979) 50:297–301
95. Greco A, Perri S, Servidio S, Yordanova E, Veltri P. The complex structure of magnetic field discontinuities in the turbulent solar wind. *Astrophys J* (2016) 823:L39. doi:10.3847/2041-8205/823/2/L39
96. Narita Y. Non-elliptic wavevector anisotropy for magnetohydrodynamic turbulence. *Ann Geophys* (2015) 33:1413–9. doi:10.5194/angeo-33-1413-2015
97. Roberts OW, Li X, Li B. Kinetic plasma turbulence in the fast solar wind measured by cluster. *Astrophys J* (2013) 769:58. doi:10.1088/0004-637X/769/1/58
98. Roberts OW, Li X. Evidence of the ion cyclotron resonance at proton kinetic scales in the solar wind. *Astrophys J* (2015) 802:1–11. doi:10.1088/0004-637X/802/1/1
99. Klein KG, Alexandrova O, Bookbinder J, Caprioli D, Case AW, Chandran BDG, et al. [Plasma 2020 decadal] Multipoint measurements of the solar wind: a proposed advance for studying magnetized turbulence. Arxiv [Preprint]. 1903.05740. (2019)
100. TenBarge JM, Alexandrova O, Boldyrev S, Califano F, Cerri SS, Chen CHK, et al. [Plasma 2020 decadal] Disentangling the spatiotemporal structure of turbulence using multi-spacecraft data. Arxiv [Preprint]. 1903.05710. (2019)
101. Matthaeus WH, Bandyopadhyay R, Brown MR, Borovsky J, Carbone V, Caprioli D, et al. [Plasma 2020 decadal] The essential role of multi-point measurements in turbulence investigations: the solar wind beyond single scale and beyond the Taylor Hypothesis. Arxiv [Preprint]. 1903.06890 (2019)

Conflict of Interest: The authors declare that the research was conducted in the absence of any commercial or financial relationships that could be construed as a potential conflict of interest.

frontiers in Physics

MINI REVIEW
published: 25 November 2020
doi: 10.3389/fphy.2020.604857

The Effect of Solar-Wind Turbulence on Magnetospheric Activity

R. D'Amicis[1]*, *D. Telloni*[2] *and R. Bruno*[1]

[1]*Institute for National Astrophysics, Institute for Space Astrophysics and Planetology, Rome, Italy,* [2]*Institute for National Astrophysics, Astrophysical Observatory of Turin, Turin, Italy*

The solar wind is a highly turbulent medium exhibiting scalings of the fluctuations ranging over several decades of scales from the correlation length down to proton and electron gyroradii, thus suggesting a self-similar nature for these fluctuations. During its journey, the solar wind encounters the region of space surrounding Earth dominated by the geomagnetic field which is called magnetosphere. The latter is exposed to the continuous buffeting of the solar wind which determines its characteristic comet-like shape. The solar wind and the magnetosphere interact continously, thus constituting a coupled system, since perturbations in the interplanetary medium cause geomagnetic disturbances. However, strong variations in the geomagnetic field occur even in absence of large solar perturbations. In this case, a major role is attributed to solar wind turbulence as a driver of geomagnetic activity especially at high latitudes. In this review, we report about the state-of-art related to this topic. Since the solar wind and the magnetosphere are both high Reynolds number plasmas, both follow a scale-invariant dynamics and are in a state far from equilibrium. Moreover, the geomagnetic response, although closely related to the changes of the interplanetary magnetic field condition, is also strongly affected by the intrinsic dynamics of the magnetosphere generated by geomagnetic field variations caused by the internal conditions.

Keywords: solar wind, interplanetary magnetic field, turbulence, geomagnetic response, geomagnetic activity indices, magnetic storm and substorm

OPEN ACCESS

Edited by:
Joseph Eric Borovsky, Space Science Institute, United States

Reviewed by:
Zoltan Voros, Austrian Academy of Sciences, Austria
Adnane Osmane, University of Helsinki, Finland

***Correspondence:**
R. D'Amicis
raffaella.damicis@inaf.it

Specialty section:
This article was submitted to Space Physics, a section of the journal Frontiers in Physics

Received: *10 September 2020*
Accepted: *27 October 2020*
Published: *25 November 2020*

Citation:
D'Amicis R, Telloni D and Bruno R (2020) The Effect of Solar-Wind Turbulence on Magnetospheric Activity. Front. Phys. 8:604857. doi: 10.3389/fphy.2020.604857

1. INTRODUCTION

Ref. [1] discovered an important connection between the solar wind and the magnetosphere: the level of magnetospheric storminess depends strongly on the direction of the z component of the interplanetary magnetic field (IMF) given in geocentric solar magnetospheric (GSM) coordinates. In particular, the geomagnetic activity is driven mainly by interplanetary structures with intense, long-duration and southward turning of magnetic fields (B_s), reconnecting with the Earth's magnetic field, following the scenario proposed by Ref. [2]. This process initiates the substorm sequence, with a net transfer of solar wind energy to Earth [3–6]. Overall, the magnetospheric activity results into several phenomena including geomagnetic substorms and storms, turbulence, ionospheric currents and auroras, and magnetic reconnection [7], thus determining a system far from equilibrium [8]. The response of the magnetosphere to the forcing exerted by the solar wind is not simply proportional to the input. When a critical threshold is reached, the magnetospheric system tends to reconfigure through a sequence of energy-loading and stress-developing processes [9, 10], determining episodic and abrupt, rather than slow and gradual, changes in the magnetosphere. This behavior motivates the description of the

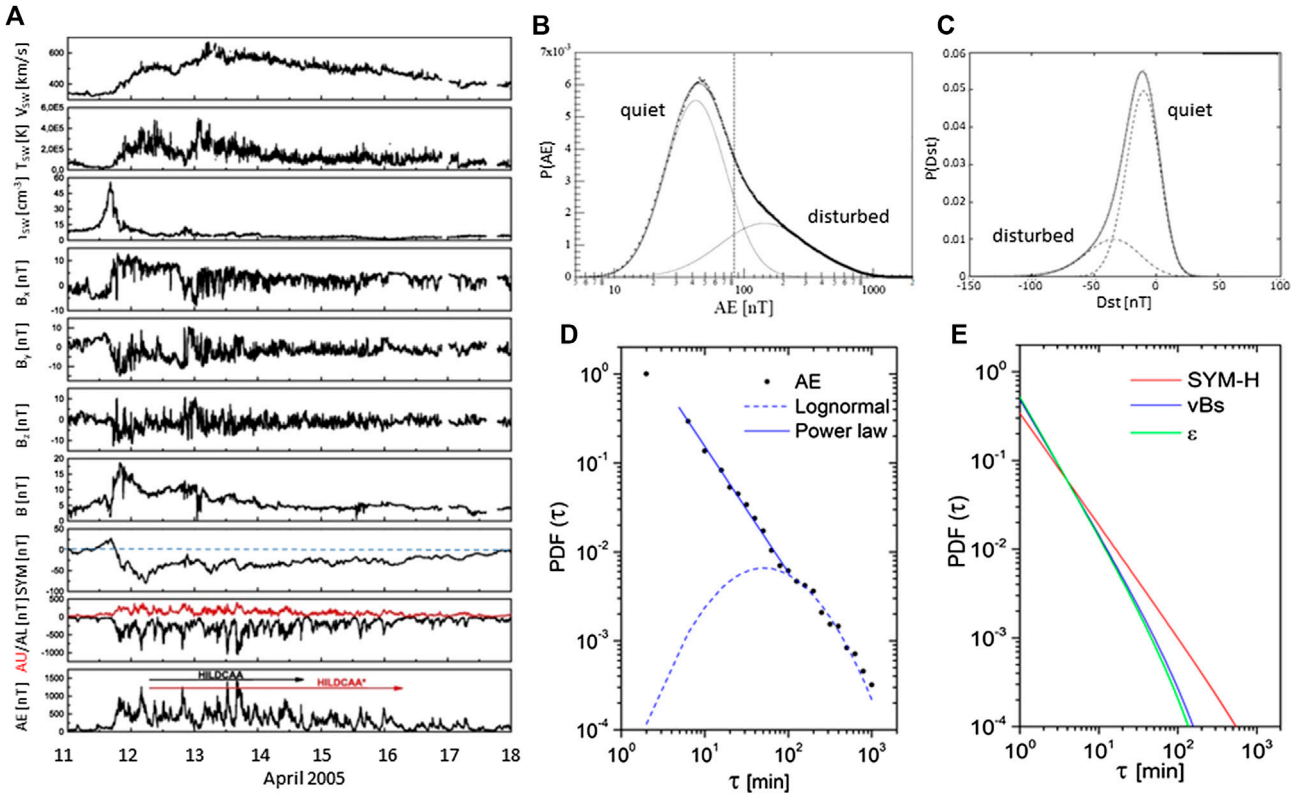

FIGURE 1 | (A) From top to bottom: time series of solar wind bulk speed (V_{SW}), temperature (T_{SW}), number density (n_{SW}); magnetic field components (B_x, B_y, B_z) and magnitude **(B)**; geomagnetic indices: SYM-H, AU/AL and AE. Adapted from Figure 1 of Ref. 31. **(B)** Probability distribution function of AE index, P (AE), (black dots). The solid line refers to a nonlinear best fit obtained as the superposition of two Log-normal distribution functions. The two dotted lines show the two components relative to quiet and active periods, respectively. The vertical dashed line is the threshold discriminating active and quiet periods, evaluated from the data. Adapted from Figure 1 of Ref. 74. **(C)** Probability distribution function of Dst index, P (Dst) (black dots). The solid line refers to a nonlinear best fit obtained as the superposition of two Log-normal distribution functions. The individual lognormal distributions are shown as the dashed and dashed-dot lines. Adapted from Figure 2 of Ref. 115. **(D)** Probability distribution function of AE burst lifetime (black dots) fitted by a power law (solid line) for small timescale and by a lognormal distribution (dashed line) for larger timescales. Adapted from Figure 7 of Ref. 70. **(E)** Comparison of the best fit functions of the burst lifetime distribution functions for SYM-H (red), ϵ (green), and VB_s (blue). Adapted from Figure 2 of Ref. 80.

Earth's magnetosphere as a complex system in which several nonlinearly sub-systems co-exist and are multiply interconnected on a wide range of spatial and temporal scales [11–15]; (and references therein).

Although there is a remarkable literature focusing on the geoeffectiveness of large interplanetary perturbations as Interplanetary counterpart of Coronal Mass Ejections (ICMEs), predominant during maximum of the solar cycle, and Corotating Intercation Regions (CIRs), more frequent during minimum e.g., [16–21], a significant geomagnetic activity is sometimes present even in the absence of such large perturbations. Within this framework and to understand the perspective of this review, a distinguishing feature of the solar wind system driver, namely turbulence, cannot be ignored. In fact, early solar wind observations by Mariner 2 in 1962 provided the first power spectral density (PSD) of magnetic field fluctuations that closely resembled a typical turbulent spectrum [22], interpreted as the proof that non-linear interactions among turbulent eddies were actively transferring energy from large to small scales. References [23, 24] highlighted that the energy cascade process is caused by the non-linear interaction of Alfvén waves. [25, 26], indeed, identified for the first time a strong correlation between velocity and magnetic field fluctuations that correspond to large amplitude Alfvén waves always propagating away from the Sun [27]. On the other hand, observations by Ref. [25] resulted to be critical for the paradigm adopted by Ref. [22] to explain the presence of a turbulence spectrum. As a matter of fact, if all the Alfvén waves were propagating outward, and there were no inward modes to interact with and produce a turbulent cascade, where did the turbulent spectrum observed by Coleman come from? This debate led Ref. [28] to the formulation of a new model in which both inward and outward Alfvén modes, present in the solar wind in different amounts, interact nonlinearly, producing a turbulent energy cascade. In fast solar wind streams mainly, fluctuations show a high Alfvénic character and are non-compressive, or in other words, the fluctuations in the proton density and in the magnitude of the magnetic field are remarkably depleted, being thus purely directional fluctuations, as expected for Alfvén waves. Solar wind turbulence is invoked to explain

different processes occurring not only in the heliosphere (e.g., solar wind heating and acceleration, energetic particle acceleration, and cosmic-ray propagation) but also in the solar wind-magnetosphere coupling with particular reference to the auroral activity caused by reconnection between the southward components of the Alfvénic fluctuations magnetic fields and magnetospheric fields. Without establishing a connection between solar wind turbulence and geomagnetic response, these geomagnetic disturbances have earlier been called high-intensity (AE peak values exceeding 1,000 nT and never droping below 200 nT) long-duration (greater than 2 days) continuous AE-activity or HILDCAA [29] which are separated from magnetic storm main phases. Moreover, the auroral intensifications during HILDCAAs are not substorm expansion events, nor convection bay events [30]. **Figure 1**, panel A), shows an example of solar wind parameters, interplanetary magnetic field and geomagnetic indices of a typical HILDCAA event triggered by Alfvénic fluctuations, following a geomagnetic storm. This figure has been adapted from and has been described in details in Ref. [31].

Within this framework, this review focuses on the effects of solar wind turbulence on the geomagnetic response, providing a brief overview of the state-of-art with particular reference to the scale-invariant dynamics of the solar wind and the magnetosphere (**section 2**) and proposed connection between solar wind turbulence and geomagnetic response (**section 3**). **Section 4** sums up the results and contains a brief discussion.

2. SCALE-INVARIANT DYNAMICS OF THE SOLAR WIND AND THE MAGNETOSPHERE

The solar wind dynamics is associated with many characteristic spatial and temporal scales, thus retaining a multi-scale nature [32]. The PSD of magnetic-field fluctuations cover an extended scale range, from several days to the proton and electron gyroperiods and can generally be characterized by four distinguishable dynamical ranges of scales, usually represented in the frequency domain (e.g., [33–37]; and references therein): i) a scaling of $\sim f^{-1}$ in the energy-containing range [38–41]; ii) a scaling of $f^{-5/3}$ [42] or $f^{-3/2}$ [23, 24] in the inertial range or at magnetohydrodynamics (MHD) scales; iii) a scaling of $\sim f^{-\alpha}$ at sub-ion scales with a broader range of slopes, with α approximately $\in$ [−4, −2] strongly related to the power of the fluctuations in the inertial range [43, 44]; iv) even steeper scaling at electron scales [33–35]. The reader is redirected to other seminal papers and reviews (e.g., [32, 36]; and references therein) for a thorough description of solar wind turbulence, being outside the scope of the present review to go into further detail.

It must be noted, however, that beside the strong connection existing between the solar wind and the magnetosphere via reconnection processes, the solar wind and the magnetosphere are both high Reynolds number plasmas [45]. As a result, we would expect that not only the solar wind but also the magnetosphere shows a scale-invariant dynamics and power-law PSD (e.g., [46–51]). On the other hand, geomagnetic indices are widely used to study the magnetospheric output and are indicative of the most important magnetospheric current systems. Although, historically, the first geomagnetic indices were related to a global description of the geomagnetic activity (Kp index introduced by Ref. [52]; and derived indices), more specific indices are now used. They take into account the separate contribution of the auroral activity, dominated by the auroral electroject dynamics (the auroral electrojet indices, AE, AU, AL, AO defined and developed by Ref. [53], and the low-latitude activity, dominated by the ring current dynamics. The latter includes the disturbance storm, Dst, index derived by Refs. [54, 55] and the a longitudinally asymmetric (ASY) and a symmetric (SYM) disturbance index introduced and derived for both the horizontal (dipole pole) direction H (SYM-H, ASY-H) and the orthogonal (East-West) direction D (SYM-D, ASY-D). In particular, the SYM-H index, derived by Ref. [56] is essentially the same as Sugiura's hourly Dst index, although 1 min values are derived from different sets of stations and a slightly different coordinate system. Both AE and Dst (and SYM-H) show a bimodal behavior being characterized by two components relative to quiet and disturbed periods as shown in **Figure 1** panel B) and C).

Observational evidence of the non-linear behavior of the magnetosphere in terms of the geomagnetic indices was given by Ref. [57] and later by, e.g., [58] who showed that the AE and Dst PSD, respectively, are characterized by a power law. In addition, the AE index has a multifractal (intermittent) structure both in quiet and disturbed periods and its fluctuations are not distributed according to a Gaussian distribution rather by a leptokurtic distribution [59–63], with AE more intermittent at maximum of solar activity than at solar minimum [64, 65].

Reference [66] found that AE burst lifetime (defined as the duration for which the measurement exceeds a given threshold value, see also Ref. [67]) probability distribution functions (PDFs) are characterized by power laws (see also Ref. [68, 69], as shown in **Figure 1**, panel d), adapted from Ref. [70]. References [71, 72] interpreted these results suggesting that the magnetosphere can be described in terms of a stochastic non-linear system that evolves toward metastable configurations identifying a state of self-organized criticality (SOC) [73] independent from initial conditions. The traditional SOC systems are characterized by energy dissipation in the form of avalanches. According to the theory, the events generated in this way are not correlated and would follow a Poissonian distribution. However, observations show waiting time distributions of the geomagnetic indices following power laws as for correlated events (e.g., [70, 74]), thus suggesting to attribute to an external forcing, the solar wind, the long time correlation found in the geomagnetic response, supporting the idea of forced and/or self-organized criticality (FSOC) systems [72, 75]. Evidence suggesting a significant SOC component in the dynamics of substorms in the magnetosphere was presented by Ref. [76] showing observations of bursty bulk flows, fast flows, localized dipolarization plasma turbulence, and multiple localized reconnection sites that would provide the basic avalanche phenomenon in the establishment of SOC in the plasma sheet.

According to Ref. [77]; the magnetosphere can be assimilated to a metastable system, consisting of a collection of temporarily stable states. Some of them are related to the others by relatively quick transition processes, which can be identified as the loading-unloading component during substorms. For a comprehensive review on SOC, the interested reader is redirected to the papers by Refs. [78, 79].

SOC models are invoked also to explain power laws lifetime distributions of the SYM-H index [80] as shown in **Figure 1E**), adapted from Ref. [80]. In particular, the scaling properties of SYM-H for both quiet and active periods are described by power law scaling behaviors, each with a single nonlinear scaling exponent, characteristic of fractional Brownian motion (fBm) [81, 82]. However, the significant differences between quiet and active intervals suggests, according to their interpretation, that the basic dynamics of SYM-H could be captured by a modification to fBm [83], indicating that the SYM-H time series, rather than being monofractal, is probably weakly multifractal.

3. CONNECTING SOLAR WIND TURBULENCE AND GEOMAGNETIC RESPONSE

Significant effort has been made in establishing the relationship between fluctuations in the energy delivered by the solar wind to the magnetosphere and variations in the magnetospheric response. Common quantities, referred as coupling parameters, used to study the coupling between the solar wind and the magnetosphere are vB_s [84] measuring the interplanetary magnetic field advected in the magnetosphere by the reconnection process and the ϵ parameter [85] which estimates the fraction of the solar-wind Poynting flux through the dayside magnetosphere.

Several studies have been performed to compare the behavior of the coupling parameters and the interplanetary magnetic field with the geomagnetic indices. Reference [86] showed that the burst lifetime PDFs of the coupling parameters are finite-range power laws with an exponential cut-off. Although the burst lifetime PDFs of AU, AL and AE have the same power law component, a second component can be recognized in the auroral indices distributions and are highlighted in **Figure 1**, panel B) and d), showing AE PDFs and AE burst lifetime PDFs, respectively, adapted from Refs. [70, 74]; respectively. The power law component is directly linked to the solar wind input at short (about 20 min) lag [87] and it is commonly referred as "directly driven component", in which energy is directly dissipated in the auroral ionosphere and ring current with a delay of about 20 min being due to the inductance of the magnetosphere-ionosphere system. This component is associated with the DP2 current systems consisting of the eastward electrojet centered in the evening sector and the westward electrojet centered in the late morning sector [88–90]. The second component is related to the global magnetospheric output that is an intrinsic property of the magnetosphere. This is linked to the DP1 current system dominated by the westward electrojet in the midnight sector and it is referred as "loading unloading component", indicating that the energy from the solar wind is first stored in the magnetotail and then is suddenly released to be deposited in the auroral ionosphere and ring current as a consequence of external changes in the interplanetary medium or internal triggering processes [87, 91–93] such as, e.g., magnetic reconnection in the tail [94].

Reference [70] confirmed previous results and showed in addition that while the power law associated to the directly driven component depends on the phase of the solar cycle, the second component related to the loading-unloading mechanisms does not change accordingly, supporting the idea that it is related to the intrinsic response of the magnetosphere. Studying the statistical properties of fluctuations in AU, AL and AE indices and in the ϵ parameter, Ref. [95] found that the fluctuations are self-similar up to 4 h for AU and AL and up to 2 h for AE. Fluctuations on shorter time scales are found to have similar long-tailed (leptokurtic) PDFs, consistent with an underlying nonlinear process. [96]; using the Local Intermittency Measure (LIM) technique to extract the intermittent component of the AE index, found that this corresponds to the impulsive unloading process. Further investigations by Ref. [97] focused on the scaling properties of the solar wind driver and geomagnetic indices during solar minimum and maximum. They found that fluctuations in the AL index exhibit scaling properties insensitive to the phase of the solar cycle while the scaling exponent of AU changes with the solar cycle and the trend follows that of the ϵ parameter. This is consistent with the AU index more closely monitoring activity on the dayside and AL reflecting activity in the magnetotail [97].

Similar to Ref [80], ref [86] performed a comparative studies between the behavior of the input parameters and the geomagnetic response at low latitudes by means of the SYM-H index and found power law distributions for all parameters. Although during solar minimum the scaling exponents obtained for SYM-H, vB_s and ϵ were essentially the same, this was not the case for solar maximum. The authors interpreted the similar values between coupling parameters and SYM-H during solar minimum as merely fortuitous and that the scaling properties of the low-latitude magnetosphere are not purely a direct response to the scale-free properties of the solar wind but are due to inherent properties of the magnetosphere. The same authors questioned the role of the solar wind as a direct driver for the SYM-H (or Dst) scaling in agreement with Ref. [98]. This results agrees with SYM-H being the product of a SOC system [99] and would be consistent with the observation that the ring current is frequently the product of multiple spatial and temporal fine structures (e.g., [100]). In this case, Dst (and SYM-H) is produced by superposition of multiple processes, rather than by a single monolithic ring current, which operate in a SOC state. The effect of interplanetary magnetic field fluctuations on the geomagnetic response at low latitudes, using the SYM-H index, was studied using higher order statistical moments [101]. While the asymmetry of the probability density functions (described in terms of the skewness) does not seem to be important as a geoeffective parameter, there is a relationship between the kurtosis of the two parameters, thus appearing to be a representative geoeffective parameter, which can influence the

reconnection process at the Earth's magnetopause and the efficiency of the solar wind–magnetosphere coupling.

Correlations between the basic characteristics of turbulence in the upstream solar wind and various geomagnetic indices have also shown that geomagnetic activity increases with an increase in the amplitude of the turbulence in the solar wind. Reference [45] highlighted that the amplitude of the turbulence in the solar wind upstream of the Earth is strongly correlated with the geomagnetic activity during both northward and southward IMF. During southward B_z, when magnetic reconnection operates at the magnetopause, the antiparallel orientations of interplanetary and magnetospheric magnetic fields are essential. On the contrary, during northward B_z a viscous coupling of the solar wind flow to the magnetosphere is enhanced and therefore the level of turbulence in the solar wind is the key parameter. In this case, an increased upstream turbulence leads to a larger eddy viscosity (which reflects in a larger Reynolds stress), determining more momentum transport from the solar wind flow into the magnetosphere. This causes a greater convection in the magnetosphere, which drives stronger current systems between the magnetosphere and the ionosphere, and which leads to raised geomagnetic indices. This is in agreement with a later study by Ref. [102] on the role of the solar wind fluctuations in geomagnetic activity during southward and northward IMF. They demonstrated that, in both cases, high power fluctuations in B_z systematically result in a greater level of geomagnetic activity on timescales consistent with viscous processes. Within the same framework, Ref. [103] showed that the substorm activity is associated not only to flux loading rather also to high solar wind velocity, causing viscous terms to have an important role in substorm loading or onsets than previously supposed. On the other hand, the triggering of geomagnetic activity can be caused by the passage of a velocity-shear layer determining sudden changes in the cross-polar-cap potential and ionospheric Joule dissipation are seen as the shear layers pass and eventually generating ULF oscillations responsible for the energization of the outer electron radiation belt [104]. It must be noted that a southward direction of the IMF as the primary driver of the geomagnetic activity is not the only crucial parameter. Indeed, an important role is played also by the energy carried by solar wind fluctuations. Reference [105] studied the correlation between the solar wind total (kinetic + magnetic) energy and the Dst index and found that high-energy solar wind plasma can severely perturb the near-Earth space environment even without reconnecting with the geomagnetic field at the dayside magnetopause.

The first statistical evidence of the role played by Alfvénic turbulence in the solar wind-magnetosphere coupling was shown by Ref. [106] who performed a comparitive study over different phases of the solar cycle. In particular, these authors identified the turbulent Alfvénic content of the solar wind fluctuations using the normalized cross-helicity, σ_C, indicating the predominance of an Alfvénic mode (either inward or outward) with respect to the other, and the normalized residual energy, σ_R, indicating a predominance of magnetic energy on kinetic energy or viceversa. For Alfvénic fluctuations, $\sigma_C = \pm 1$ and $\sigma_R = 0$. For further details refer to Ref. [106]. It was found that the level of AE depends not only on the presence of Alfvénic fluctuations but also on the amplitude of such fluctuations as shown in **Figure 2**, panel A) and B), adapted from Ref. [106]. These results were further supported by another study by the same authors [107] who presented the first statistical evidence of the presence of a slow Alfvénic solar wind during maximum of solar activity and found to be very similar to the fast wind on many respects and not only for the Alfvénic content of the fluctuations [44, 108–112]. [107] demonstrated that the nature of these kind of fluctuations plays a major role in the geomagnetic activity rather than the type of wind selected on the basis of the flow speed. On the other hand, the same statistical relationship was not established between solar wind turbulence and low-latitude geomagnetic response (see **Figure 2** panel C), adapted from Ref. [98]. In addition, Ref. [65] performed a statistical study on the intermittency of B_s and AE. They focused on their respective extreme (say intermittent) events and studied the distribution of the elapsed time, or waiting time, between consecutive events, finding distributions characterized by well-defined power laws which would suggest the existence of long term correlations typical of turbulent processes. These events were found to be weakly dependent on the phase of the solar cycle. However, these results have been overall questioned by observations of the turbulent fluctuations downstream of the Earth's bow shock that show that the shock destroys the information from the solar wind. If this is the case, the turbulent spectrum that eventually forms far from the shock is due to the local property of the magnetosheath (e.g., [47]) and therefore, according to this study, the property of power laws in the interplanetary magnetic field does not map into the property of power laws in the inner magnetosphere.

4. DISCUSSION

The solar wind and the magnetosphere are high Reynolds number plasma environments [45], both showing scale-invariant dynamics and power-law PSDs. Several studies have been carried out to investigate the turbulent nature of the solar wind (e.g., [32, 36]; and references therein) and the magnetosphere (e.g., [46–51]) separately, invoking turbulence and a SOC approach to describe the dynamics of the two plasma environments, respectively. At this stage, an obvious question arises: whether SOC is different from turbulence. Since they basically exhibit several similarities (e.g., power-law functions in the power spectrum, scale-free size distributions, and many degrees of freedom), the answer to this question is rather difficult. We refer the reader to Ref. [79] that have been exhaustively discussed this topic, invoking a SOC-turbulence duality as a generic feature of astrophysical plasmas, although the explicit complementarity between the two has not been demonstrated. According to the same authors, SOC can be identified as a state of near-critical turbulence, which is in the transition between the laminar state and the fully developed turbulence state. On the other hand, several models have been used within the SOC approach to reproduce the observed fluctuation spectra in terms of

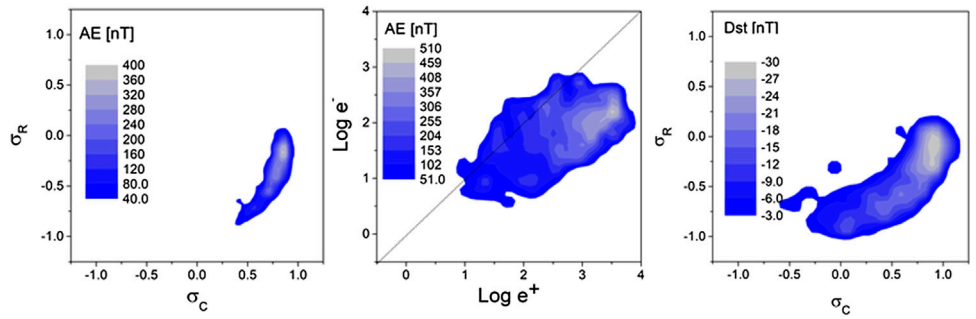

FIGURE 2 | (A) Average AE values (indicated by the color scale) computed over square bins of $\sigma_C - \sigma_R$; **(B)** Average AE values (indicated by the color scale) computed over square bins of $e^+ - e^-$. The solid black line indicates the locus of all points which meets the condition: $e^+ = e^-$. Both adapted from Ref. 106. **(C)** Average Dst values computed for every square bin $\sigma_C - \sigma_R$, adapted from Ref. 98.

sandpile cellular automata models. These models are clearly useful to improve forecasting (or, at least, nowcasting) within the framework of Space Weather studies. Although they are overall capable of reproducing the observations, they also show some limitations in explaining for example the turbulent behavior of the Earth's plasma sheet [13].

On the other hand, since the solar wind and the magnetosphere constitute a coupled system, at a later stage, a scientific effort has been carried out to establish a link between solar wind turbulence and geomagnetic response (e.g., [45, 65, 70, 80, 86, 97, 98, 101, 106, 107]). The previous papers have identified a direct link between the so-called "directly driven component", characteristic of the magnetosphere dynamics at auroral latitudes, and solar wind turbulence. This link is eventually established via reconnection processes between the southward components of the Alfvénic fluctuations magnetic fields and magnetospheric fields. On the other hand, the connection between the turbulent solar wind and the geomagnetic response at low latitudes has been questioned [80, 98], although the magnetic storms recovery phase has been found to be related to large-amplitude Alfvén waves [113, 114]. Conversely, the previous results have been distrusted by observations performed across the Earth's bow shock that would destroy the information from the solar wind. Therefore, according to this study, the property of power laws in the interplanetary magnetic field cannot be directly related to the property of power laws in the inner magnetosphere [47]. This conjecture would allow other interpretations aiming at identifying the trigger of the geomagnetic activity as, for instance, i) the role played by viscous coupling especially during northward IMF [45, 102, 103]; ii) the presence of velocity-shear layers that eventually lead to the generation of ULF oscillations responsible for the energization of the outer electron radiation belt [104], iii) the role of the energy associated to solar wind fluctuations in determining Dst perturbations even without reconnecting with the geomagnetic field at the dayside magnetopause [105].

To summarize, the solar wind and the magnetosphere are nonlinear environments, forming a coupled system, mainly via reconnection processes. The magnetosphere reacts nonlinearly to the system's driver. Being a metastable system characterized by quick transition processes, it loads the energy accumulated in an impulsive way when a critical threshold is reached to reconfigure toward an equilibrium configuration. Given the complexity of the system, the authors are in favor of using a statistical approach rather than a one-to-one study. In this case, there is some evidence of the statistical relationship between solar wind turbulence and the geomagnetic response, although this is cannot be considered, for sure, the only physical mechanism involved in the magnetosphere's dynamics.

AUTHOR CONTRIBUTIONS

All authors listed have made a substantial, direct and intellectual contribution to the work and approved it for publication. In particular, the paper was conceived and written by RD with the support and critical feedback of DT and RB.

FUNDING

DT was partially supported by the Italian Space Agency (ASI) under contract I/013/12/0.

REFERENCES

1. Fairfield DH, Cahill LJ, Jr. Transition region magnetic field and polar magnetic disturbances. *J Geophys Res* (1966) 71:155–69. doi:10.1029/JZ071i001p00155.
2. Dungey JW. Interplanetary magnetic field and the auroral zones. *Phys Rev Lett* (1961) 6:47–8. doi:10.1103/PhysRevLett.6.47.
3. Russell CT, McPherron RL. Semiannual variation of geomagnetic activity. *J Geophys Res* (1973) 78:82–108. doi:10.1029/JA078i001p00092.
4. Baker DN, Akasofu S-I, Baumjohann W, Bieber J, Fairfield JW, Hones EW, Jr., et al. Substorms in the magnetosphere. NASA Publication (1984) NASA RP-1120.

5. Baker DN, Pulkkinen TI, Angelopoulos V, Baumjohann W, McPherron RL. The neutral line model of substorms: past results and present view. *J Geophys Res* (1966) 101:12975–3010. doi:10.1029/95JA03753.
6. Gonzalez WD, Joselyn JA, Kamide Y, Kroehl HW, Rostoker G, Tsurutani BT, et al. What is a geomagnetic storm?. *J Geophys Res* (1994) 99:5771–92. doi:10.1029/93JA02867.
7. Tsurutani BT, Hajra R, Echer E, Gjerloev JW. Extremely intense (SML = -2500 nt) substorms: isolated events that are externally triggered? *Ann Geophys* (2015) 33:519–24. doi:10.5194/angeo-33-519-2015.
8. Consolini G, Michelis PD, Tozzi R. On the Earth's magnetospheric dynamics: nonequilibrium evolution and the fluctuation theorem. *J Geophys Res* (2008) 113:A08222. doi:10.1029/2008JA013074.
9. Klimas J, Uritsky VM, Vassiliadis D, Baker DN. A mechanism for the loading-unloading substorm cycle missing in MHD global magnetospheric simulation models. *Geophys Res Lett* (2005) 32:L14108. doi:10.1029/2005GL022916.
10. Baker DN, Klimas J, Vassiliadis D. Nonlinear dynamics in the Earth's magnetosphere. In: AA Tsonis JB Elsner, editors. *Nonlinear dynamics in geosciences*. Berlin, Germany: Springer (2007) p. 53–67.
11. Chang T. Low-dimensional behavior and symmetry-breaking of stochastic systems near criticality can these effects be observed in space and in the laboratory?. *IEEE Trans Plasma Sci* (1992) 20:691–4. doi:10.1109/27.199515.
12. Klimas AJ, Vassiliadis D, Baker DN, Roberts DA. The organized nonlinear dynamics of the magnetosphere. *J Geophys Res* (1996) 101:13089–114. doi:10.1029/96JA00563.
13. Watkins NW, Freeman MP, Chapman SC, Dendy RO. Testing the soc hypothesis for the magnetosphere. *J Atmos Sol Terr Phys* (2001) 63:1435–45. doi:10.1016/S1364-6826(00)00245-5.
14. Consolini G. Self-organized criticality: a new paradigm for the magnetotail dynamics. *Fractals* (2002) 10:275–83. doi:10.1142/S0218348X02001397.
15. Valdivia J, Rogan J, Munoz V, Gomberoff L, Klimas A, Vassiliadis D, et al. The magnetosphere as a complex system. *Adv Space Res* (2005) 35:961–71. doi:10.1016/j.asr.2005.03.144.
16. Gosling JT, Bame SJ, McComas DJ. Coronal mass ejections and large geomagnetic storms. *Geophys Res Lett* (1990) 17:901–4. doi:10.1029/GL017i007p00901.
17. Tsurutani BT, Gonzalez WD, Gonzalez ALC, Tang F, Arballo JK, Okada M. Interplanetary origin of geomagnetic activity in the declining phase of solar cycle. *J Geophys Res* (1995) 100:21717–33. doi:10.1029/95JA01476.
18. Gonzalez WD, Tsurutani BT, Clua de Gonzalez AL. Interplanetary origin of geomagnetic storms. *Space Sci Rev* (1999) 88:529–62. doi:10.1023/A:1005160129098.
19. Yermolaev YI, Yermolaev MY, Zastenker GN, Zelenyi LM, Petrukovich AA, Sauvaud J-A. Statistical studies of geomagnetic storm dependencies on solar and interplanetary events: a review. *Planet Space Sci* (2005) 53:189–96. doi:10.1016/j.pss.2004.09.044.
20. Laughlin LK, Turner NE. Geoeffectiveness of CIR and CME events: factors contributing to their differences. *J Southeastern Assoc Res Astron* (2008) 2:19–22.
21. Yermolaev YI, Nikolaeva NS, Lodkina IG, Yermolaev MY. Geoeffectiveness and efficiency of CIR, sheath, and ICME in generation of magnetic storms. *J Geophys Res* (2012) 117:A00L07. doi:10.1029/2011JA017139.
22. Coleman PJJ. Turbulence, viscosity and dissipation in the solar wind plasma. *Astrophys J* (1968) 153:371–88. doi:10.1086/149674.
23. Iroshnikov PS. Turbulence of a conducting fluid in a strong magnetic field. *Sov Astron* (1964) 40:742.
24. Kraichnan RH. Inertial-range spectrum of hydromagnetic turbulence. *Phys Fluid* (1965) 8:1385. doi:10.1063/1.1761412.
25. Belcher JW, Davis L. Large-amplitude Alfvén waves in the interplanetary medium, 2. *J Geophys Res* (1971) 76:3534–63. doi:10.1029/JA076i016p03534.
26. Belcher JW, Solodyna CV. Alfvén waves and directional discontinuities in the interplanetary medium. *J Geophys Res* (1975) 80:181–6. doi:10.1029/JA080i001p00181.
27. Belcher JW, Davis LJ, Smith EJ. Large-amplitude Alfvén waves in the interplanetary medium: Mariner 5. *J Geophys Res* (1969) 74:2302–8. doi:10.1029/JA074i009p02302.
28. Tu C-Y, Pu Z-Y, Wei F-S. The power spectrum of interplanetary Alfvénic fluctuations: derivation of governing equation and its solution. *J Geophys Res* (1984) 89:9695–702. doi:10.1029/JA089iA11p09695.
29. Tsurutani BT, Gonzalez WD. The cause of high-intensity long-duration continuous AE activity (HILDCAAs): interplanetary Alfvén wave trains. *Planet Space Sci* (1987) 35:405–12. doi:10.1016/0032-0633(87)90097-3.
30. Tsurutani BT, Gonzalez WD, Guarnieri FL, Kamide Y, Zhou X, Arballo JK. Are high-intensity long-duration continuous AE activity (HILDCAA) events substorm expansion events? *J Atmos Sol Terr Phys* (2004) 66:167–76. doi:10.1016/j.jastp.2003.08.015.
31. Prestes A, Klausner V, González AO, Serra SL. Statistical analysis of solar wind parameters and geomagnetic indices during HILDCAA/HILDCAA* occurrences between 1998 and 2007. *Phys Rev Lett* (2017) 60:1850–65. doi:10.1016/j.asr.2017.06.023.
32. Verscharen D, Klein KG, Maruca BA. The multi-scale nature of the solar wind. *Living Rev Sol Phys* (2019) 16:5. doi:10.1007/s41116-019-0021-0.
33. Alexandrova O, Saur J, Lacombe C, Mangeney A, Mitchell J, Schwartz SJ, et al. Universality of solar-wind turbulent spectrum from MHD to electron scales. *Phys Rev Lett* (2009) 103:165003. doi:10.1103/PhysRevLett.103.165003.
34. Sahraoui F, Goldstein ML, Robert P, Khotyaintsev YV. Evidence of a cascade and dissipation of solar-wind turbulence at the electron gyroscale. *Phys Rev Lett* (2009) 102:231102. doi:10.1103/PhysRevLett.102.231102.
35. Alexandrova O, Chen CHK, Sorriso-Valvo L, Horbury TS, Bale SD. Solar wind turbulence and the role of ion instabilities. *Space Sci Rev* (2013) 178:101–39. doi:10.1007/s11214-013-0004-8.
36. Bruno R, Carbone V. The solar wind as a turbulence laboratory. *Living Rev Sol Phys* (2013) 10:208. doi:10.12942/lrsp-2013-2.
37. Goldstein ML, Wicks RT, Perri S, Sahraoui F. Kinetic scale turbulence and dissipation in the solar wind: key observational results and future outlook. *Philos Trans Roy Soc* (2015) A373:20140147. doi:10.1098/rsta.2014.0147.
38. Matthaeus WH, Goldstein ML. Low-frequency 1/f noise in the interplanetary magnetic field. *Phys Rev Lett* (1986) 57:495–8. doi:10.1103/PhysRevLett.57.495.
39. Dmitruk P, Matthaeus HW. Low-frequency 1/f fluctuations in hydrodynamic and magnetohydrodynamic turbulence. *Phys Rev E* (2007) 76:036305. doi:10.1103/PhysRevE.76.036305.
40. Matteini L, Stansby D, Horbury TS, Chen CHK. On the 1/f spectrum in the solar wind and its connection with magnetic compressibility. *Astrophys J Lett* (2018) 869:L32. doi:10.3847/2041-8213/aaf573.
41. Bruno R, Telloni D, Sorriso-Valvo L, Marino R, Marco RD, D'Amicis R. On the low-frequency break observed in the slow solar wind magnetic spectra. *Astron Astrophys* (2019) 627:A96. doi:10.1051/0004-6361/201935841.
42. Kolmogorov AN. The local structure turbulence in incompressible viscous fluids for very large Reynolds numbers. *Dokl Akad Nauk SSSR* (1941) 30:301–5.
43. Bruno R, Trenchi L, Telloni D. Spectral slope variation at proton scales from fast to slow solar wind. *Astrophys J Lett* (2014) 793:L15. doi:10.1088/2041-8205/793/1/L15.
44. D'Amicis R, Matteini L, Bruno R. On the slow solar wind with high Alfvénicity: from composition and microphysics to spectral properties. *Mon Not Roy Astron Soc* (2019) 483:4665–77. doi:10.1093/mnras/sty3329.
45. Borovsky JE, Funsten HO. Role of solar wind turbulence in the coupling of the solar wind to the Earth's magnetosphere. *J Geophys Res* (2003) 108:1246. doi:10.1029/2002JA009601.
46. Alexandrova O, Lacombe C, Mangeney A. Spectra and anisotropy of magnetic fluctuations in the Earth's magnetosheath: cluster observations. *Ann Geophys* (2008) 26:3585–96. doi:10.5194/angeo-26-3585-2008.
47. Huang SY, Hadid LZ, Sahraoui F, Yuan ZG, Deng XH. On the existence of the Kolmogorov inertial range in the terrestrial magnetosheath turbulence. *Astrophys J Lett* (2017) 836:L10. doi:10.3847/2041-8213/836/1/L10
48. Chhiber R, Chasapis A, Bandyopadhyay R, Parashar TN, Matthaeus WH, Maruca BA, et al. Higher-order turbulence statistics in the Earth's magnetosheath and the solar wind using Magnetospheric multiscale observations. *J Geophys Res* (2018) 123:9941–54. doi:10.1029/2018JA025768
49. Li H, Jiang W, Wang C, Verscharen D, Zeng C, Russell CT, et al. Evolution of the Earth's magnetosheath turbulence: a statistical study based on mms observations. *Astrophys J Lett* (2020) 898:L43. doi:10.3847/2041-8213/aba531
50. Kozak LV, Petrenko BA, Lui ATY, Kronberg EA, Grigorenko EE, Prokhorenkov AS. Turbulent processes in the Earth's magnetotail: spectral and statistical research. *Ann Geophys* (2018) 36:1303–18. doi:10.5194/angeo-36-1303-2018

51. Di Mare F, Sorriso-Valvo L, Retino A, Malara F, Hasegawa H. Evolution of turbulence in the Kelvin-Helmholtz instability in the terrestrial magnetopause. *Atmosphere* (2019) 10:561. doi:10.3390/atmos10090561
52. Bartels J. Potsdamer erdmagnetische. *Ztschrift Geophys* (1938) 14:68–78.
53. Davis TN, Sugiura M. Auroral electrojet activity index AE and its universal time variations. *J Geophys Res* (1966) 71:785–801. doi:10.1029/JZ07i003p00785
54. Sugiura M. Hourly values of equatorial Dst for the IGY. *Ann IGY* (1964) 35:9.
55. Sugiura M, Kamei T. Equatorial Dst index 1957-1986. In: A Berthelier M Menvielle, editors. *IAGA bulletin 40*. Saint Maur, France: Int. Serv. of Geomagn. Indices Publ. Off. (1991) p. 246.
56. Iyemori T. Storm-time magnetospheric currents inferred from mid-latitude geomagnetic field variations. *J Geomagn Geoelectr* (1990) 42:1249–65. doi:10.5636/jgg.42.1249
57. Tsurutani BT, Sugiura M, Iyemori T, Goldstein BE, Gonzalez WD, Akasofu S-I, et al. The nonlinear response of AE to the IMF Bs driver - a spectral break at 5 hours. *Geophys Res Lett* (1990) 17:269–82. doi:10.1029/GL017i003p00279
58. Wei HL, Billings SA, Balikhin M. Analysis of the geomagnetic activity of the Dst index and self-affine fractals using wavelet transforms. *Nonlinear Process Geophys* (2004) 11:303–12. doi:10.5194/npg-11-303-2004
59. Consolini G, Marcucci MF, Candidi M. Multifractal structure of auroral electrojet index data. *Phys Rev Lett* (1996) 76:4082–5. doi:10.1103/PhysRevLett.76.4082
60. Consolini G, Michelis PD. Non-Gaussian distribution function of AE index fluctuations: evidence of time intermittency. *Geophys Res Lett* (1998) 9:419–23. doi:10.1029/1998GL900073
61. Voros Z. On multifractality of high-latitude geomagnetic fluctuations. *Ann Geophys* (2000) 18:1273–82. doi:10.1007/s00585-000-1273-6
62. Dorotovic I, Voros K. On the Earth's plasma sheet response to the magnetic turbulence in the solar wind. In: ADGD Danesy, S Poedts, J Andries, editors.Proceedings of the 11th European solar physics meeting the dynamic Sun: challenges for theory and observations; 2005 Sep 11–16; Leuven, Belgium. Noordwijk, Netherlands: . ESA Publications (2005) p. 13.
63. Rypdal M, Rypdal K. Stochastic modeling of the AE index and its relation to fluctuations in B_z of the IMF on time scales shorter than substorm duration. *J Geophys Res* (2010) 115:A11216. doi:10.1029/2010JA015463
65. Voros Z, Jankovicova D, Kovacs P. Scaling and singularity characteristics of solar wind and magnetospheric fluctuations. *Nonlinear Process Geophys* (2002) 9:149–62. doi:10.5194/npg-9-149-2002
65. D'Amicis R, Bruno R, Bavassano B. Alfvénic turbulence in high speed solar wind streams as a driver for auroral activity. *J Atmos Sol Terr Phys* (2009) 71:1014–22. doi:10.1016/j.jastp.2008.05.002
66. Consolini G. Sandpile cellular automata and magnetospheric dynamics. In: S Aiello, N Iucci, G Sironi, A Traves, U Villante, editors. *Proceedings of the 8th GIFCO conference: cosmic physics in the year 2000*. Bologna, Italy: SIF (1997) p. 123–6.
67. Takalo J. *Correlation dimension of AE data*. [PhD thesis]. Jyväskylä, Finland: University of Jyviskylii (1993)
68. Lui ATY, Chapman SC, Liou K, Newell PT, Mengnad CI, Brittnacher M, et al. Is the dynamic magnetosphere an avalanching system?. *Geophys Res Lett* (2000) 27:911–4. doi:10.1029/1999GL010752
69. Uritsky VM, Klimas AJ, Vassiliadis D, Chua D, Parks G. Scale-free statistics of spatiotemporal auroral emissions as depicted by POLAR UVI images: dynamic magnetosphere is an avalanching system. *J Geophys Res* (2002) 107:1426. doi:10.1029/2001JA000281
70. D'Amicis R, Bruno R, Villante U. A comparative study of probability distribution functions and burst lifetime distributions of B_s and AE at solar maximum and minimum. In: ATY Lui, Y Kamide, G Consolini, editors. *Multiscale coupling of Sun-Earth processes*. Burlington, MA: Elsevier (2005) p. 399–409.
71. Chang TS. Self-organized criticality, multi-fractal spectra, sporadic localized reconnections and intermittent turbulence in the magnetotail. *Phys Plasmas* (1999) 6:4137–45. doi:10.1063/1.873678
72. Consolini G, Chang TS. Magnetic field topology and criticality in geotail dynamics: relevance to substorm phenomena. *Space Sci Rev* (2001) 95:309–21. doi:10.1023/A:1005252807049
73. Bak P, Tang C, Wiesenfeld K. Self-organized criticality: an explanation of the 1/f noise. *Phys Rev Lett* (1987) 59:381. doi:10.1103/PhysRevLett.59.381.
74. Consolini G, Michelis PD. Fractal time statistics of AE-index burst waiting times: evidence of metastability. *Nonlinear Process Geophys* (2002) 9:419–23. doi:10.5194/npg-9-419-2002
75. Sánchez R, Newman DE, Carreras BA. Waiting-time statistics of self-organized-criticality systems. *Phys Rev Lett* (2002) 88:068302. doi:10.1103/PhysRevLett.88.068302
76. Klimas AJ, Valdivia JA, Vassiliadis D, Baker DN, Hesse M, Takalo J. Self-organized criticality in the substorm phenomenon and its relation to localized reconnection in the magnetospheric plasma sheet. *J Geophys Res* (2000) 105:18765–80. doi:10.1029/1999JA000319
77. Sitnov MI, Sharma AS, Papadopoulos K, Vassiliadis D, Valdivia JA, Klimas AJ, et al. Phase transition-like behavior of the magnetosphere during substorms. *J Geophys Res* (2000) 105:12955–74. doi:10.1029/1999JA000279
78. Sharma AS, Aschwanden MJ, Crosby NB, Klimas AJ, Milovanov AV, Morales L, et al. 25 Years of self-organized criticality: space and laboratory plasmas. *Space Sci Rev* (2016) 198:167–216. doi:10.1007/s11214-015-0225-0
79. Aschwanden MJ, Crosby NB, Dimitropoulou M, Georgoulis MK, Hergarten S, McAteer J, et al. 25 Years of self-organized criticality: solar and astrophysics. *Space Sci Rev* (2016) 198:47–166. doi:10.1007/s11214-014-0054-6
80. Wanliss J, Weygand JM. Power law burst lifetime distribution of the SYM-H index. *Geophys Res Lett* (2007) 34:L04107. doi:10.1029/2006GL028235
81. Wanliss J. Nonlinear variability of SYM-H over two solar cycles. *Earth Planets Space* (2004) 56:e13–6. doi:10.1186/BF03352507
82. Wanliss J. Fractal properties of SYM-H during quiet and active times. *J Geophys Res* (2005) 110:A03202. doi:10.1029/2004JA010544
83. Peltier R-F, Lévy-Véhel J. Multifractional brownian motion : definition and preliminary results (1995) INRIA. RR-2645.
84. Burton RK, McPherron RL, Russell CT. An empirical relationship between interplanetary conditions and Dst. *J Geophys Res* (1975) 80:4204. doi:10.1029/JA080i031p04204
85. Perreault P, Akasofu SI. A study of geomagnetic storms. *Geophys J* (1978) 54:547–73. doi:10.1111/j.1365-246X.1978.tb05494.x
86. Freeman M, Watkins NW, Riley DJ. Evidence for a solar wind origin of the power law burst lifetime distribution of the AE indices. *Geophys Res Lett* (2000) 27:1087–90. doi:10.1029/1999GL010742
87. Bargatze LF, Baker DN, McPherron RL, Hones EW. Magnetospheric impulse response for many levels of magnetospheric activity. *J Geophys Res* (1985) 90:6387–94. doi:10.1029/JA090iA07p06387
88. Obayashi T, Nishida A. Large-scale electric field in the magnetosphere. *Space Sci Rev* (1968) 8:3–31. doi:10.1007/BF00362569
89. Nishida A. DP 2 and polar substorm. *Space Sci Rev* (1971) 19:205–21. doi:10.1016/0032-0633(71)90200-5
90. Kamide Y, Baumjohann W. *Magnetosphere-ionosphere coupling*. New York: Springer-Verlag (1993)
91. Tsurutani BT, Slavin JA, Kamide Y, Zwickl RD, King JH, Russell CT. Coupling between the solar wind and the magnetosphere: CDAW 6. *J Geophys Res* (1985) 90:1191–9. doi:10.1029/JA090iA02p01191
92. Rostoker G, Akasofu S-I, Baumjohann W, Kamide Y, McPherron RL. The roles of direct input of energy from the solar wind and unloading of stored magnetotail energy in driving magnetospheric substorms. *Space Sci Rev* (1987) 46:93–111. doi:10.1007/BF00173876
93. Liou K, Newell PT, Meng C-I, Brittnacher M, Parks G. Characteristics of the solar wind controlled auroral emissions. *J Geophys Res* (1998) 103:17543–57. doi:10.1029/98JA01388
94. Angelopoulos V, McFadden JP, Larson D, Carlson CW, Mende SB, Frey H, et al. Tail reconnection triggering substorm onset. *Science* (2008) 321:931–5. doi:10.1126/science.1160495
95. Hnat B, Chapman SC, Rowlands G, Watkins NW, Freeman MP. Scaling of solar wind ϵ and the AU, AL and AE indices as seen by WIND. *Geophys Res Lett* (2002) 29:2078. doi:10.1029/2002GL016054.
96. Consolini G, Michelis PD. Local intermittency measure analysis of AE index: the directly driven and unloading component. *Geophys Res Lett* (2005) 32:L05101. doi:10.1029/2004GL022063
97. Hnat B, Chapman SC, Rowlands G. Scaling and a Fokker-Planck model for fluctuations in geomagnetic indices and comparison with solar wind as seen by Wind and ACE. *J Geophys Res* (2005) 110:A08206. doi:10.1029/2004JA010824
98. D'Amicis R, Bruno R, Bavassano B. Geomagnetic activity driven by solar wind turbulence. *Adv Space Res* (2010) 46:514–20. doi:10.1016/j.asr.2009.08.031

99. Paczuski MS, Boettcher S, Baiesi M. Interoccurrence times in the Bak-Tang-Wiesenfeld sandpile model: a comparison with the observed statistics of solar flares. *Phys Rev Lett* (2005) 95:181102. doi:10.1103/PhysRevLett.95.181102
100. Lui ATY, McEntire RW, Krimigis SM. Evolution of the ring current during two geomagnetic storms. *J Geophys Res* (1987) 92:7459–70. doi:10.1029/JA092iA07p07459
101. Jankovicova D, Voros Z, Simkanin J. The influence of solar wind turbulence on geomagnetic activity. *Nonlinear Process Geophys* (2008) 15:53–9. doi:10.5194/npg-15-53-2008
102. Osmane A, Dimmock AP, Naderpour R, Pulkkinen TI, Nykyri K. The impact of solar wind ulf bz fluctuations on geomagnetic activity for viscous timescales during strongly northward and southward imf. *J Geophys Res* (2015) 120:9307–22. doi:10.1002/2015JA021505
103. Newell PT, Gjerloev JW, Mitchell EJ. Space climate implications from substorm frequency. *J Geophys Res* (2013) 118:6254–65. doi:10.1002/jgra.50597
104. Borovsky JE. The effect of sudden wind shear on the Earth's magnetosphere: statistics of wind shear events and CCMC simulations of magnetotail disconnections. *J Geophys Res* (2012) 117:A06224. doi:10.1029/2012JA017623
105. Telloni D, Carbone F, Antonucci E, Bruno R, Grimani C, Villante U, et al. Study of the influence of the solar wind energy on the geomagnetic activity for Space Weather science. *Astrophys J* (2020) 896:149. doi:10.3847/1538-4357/ab91b9
106. D'Amicis R, Bruno R, Bavassano B. Is geomagnetic activity driven by solar wind turbulence? *Geophys Res Lett* (2007) 34:L05108. doi:10.1029/2006GL028896
107. D'Amicis R, Bruno R, Bavassano B. Response of the geomagnetic activity to solar wind turbulence during solar cycle 23. *J Atmos Sol Terr Phys* (2011) 73:653. doi:10.1016/j.jastp.2011.01.012
108. D'Amicis R, Bruno R. On the origin of highly Alfvénic slow solar wind. *Astrophys J* (2015) 805:84. doi:10.1088/0004-637X/805/1/84
109. Stansby D, Matteini L, Horbury TS, Perrone D, D'Amicis R, Bercic L. The origin of slow Alfvénic solar wind at solar minimum. *Mon Not Roy Astron Soc* (2020) 492:39–44. doi:10.1093/mnras/stz3422
110. Perrone D, D'Amicis R, Marco RD, Matteini L, Stansby D, Bruno R, et al. Highly Alfvénic slow solar wind at 0.3 au during a solar minimum: helios insights for Parker Solar Probe and Solar Orbiter. *Astron Astrophys* (2020) 633:A166. doi:10.1051/0004-6361/201937064
111. D'Amicis R, Matteini L, Bruno R, Velli M. Large amplitude fluctuations in the Alfvénic solar wind. *Sol Phys* (2020) 295:46. doi:10.1007/s11207-020-01606-2
112. Telloni D, Bruno R, D'Amicis R, Carbone F, Marco RD, Perrone D. Wave-polarization analysis of the Alfvénic slow solar wind at kinetic scales. *Astrophys J* (2020) 897:167. doi:10.3847/1538-4357/ab980a
113. Guarnieri FL, Tsurutani BT, Gonzalez WD, Echer E, Gonzalez ALC, Grande M, et al. ICME and CIR storms with particular emphasis on HILDCAA events. In: N Gopalswamy A Bhattacharyya, editors. Solar influence on the heliosphere and Earth's environment: recent progress and prospects; 2006 Feb 19–20; Goa, India. Mumbai, India: Indian Institute of Geomagnetism (2006) p. 266. |
114. Tsurutani BT, Gonzalez WD, Gonzalez ALC, Guarnieri FL, Gopalswamy N, Grande M, et al. Corotating solar wind streams and recurrent geomagnetic activity: a review. *J Geophys Res* (2006) 111:A07S01. doi:10.1029/2005JA011273
115. Wanliss JA, Anh VV, Yu Z-G, Watson S. Multifractal modeling of magnetic storms via symbolic dynamics analysis. *J Geophys Res* (2005) 110:A08214. doi:10.1029/2004JA010996

Conflict of Interest: The authors declare that the research was conducted in the absence of any commercial or financial relationships that could be construed as a potential conflict of interest.

frontiers in Astronomy and Space Sciences

MINI REVIEW
published: 13 January 2021
doi: 10.3389/fspas.2020.617113

On the Variation of Intermittency of Fast and Slow Solar Wind With Radial Distance, Heliospheric Latitude, and Solar Cycle

Anna Wawrzaszek[1]* *and Marius Echim*[2,3]

[1]Centrum Badań Kosmicznych, Polska Akademia Nauk, Warsaw, Poland, [2]The Royal Belgian Institute for Space Aeronomy, Brussels, Belgium, [3]Institute of Space Science, Măgurele, Romania

Intermittency, an important property of astrophysical plasma turbulence, is studied extensively during last decades from *in-situ* measurements of the solar wind plasma and magnetic field in the ecliptic plane and at higher latitudes, and heliocentric distances between 0.3 and 5 Astronomical Units. In this paper, we review the main findings on intermittency derived from investigation of solar wind turbulence for the inertial range of scales. It turns out that our current knowledge on the evolution of intermittency in the heliosphere is based on two missions, Helios two and Ulysses. We discuss the importance of data selection methodologies and applications for heliospheric spacecraft, the different data analysis techniques (the anomalous scaling of the structure function, the non-Gaussianity of the probability distribution functions, the local intermittency measure estimated from a wavelet representation and the multifractal spectrum). Studies show that Alvénic solar wind is less intermittent but reveals increase with the radial distance. Moreover, intermittency is stronger for the magnetic than for velocity fluctuations and is considered to be responsible for the increase with the radial distance of the anisotropy of magnetic fluctuations. The intermittency of fast solar wind at solar minimum decreases with latitude. Finally, the level of intermittency in the solar wind depends on solar cycle phase, reflecting the changes of the state of solar wind and suggesting that the deeper study of origin of fast and slow wind can further improve our understanding of the intermittency.

Keywords: solar wind, turbulence, intermittency, plasma, Interplanetary medium, solar cycle

OPEN ACCESS

Edited by:
Joseph Eric Borovsky, Space Science Institute, United States

Reviewed by:
Luca Sorriso-Valvo, Institute for Space Physics (Uppsala), Sweden
Antonella Greco Università della Calabria, Italy

***Correspondence:**
Anna Wawrzaszek
anna.wawrzaszek@cbk.waw.pl

Specialty section:
This article was submitted to Space Physics, a section of the journal Frontiers in Astronomy and Space Sciences

Received: *14 October 2020*
Accepted: *10 November 2020*
Published: *13 January 2021*

Citation:
Wawrzaszek A and Echim M (2021) On the Variation of Intermittency of Fast and Slow Solar Wind With Radial Distance, Heliospheric Latitude, and Solar Cycle. Front. Astron. Space Sci. 7:617113. doi: 10.3389/fspas.2020.617113

1. INTRODUCTION

The solar wind is considered as natural laboratory to study turbulence of astrophysical plasmas (Bruno and Carbone, 2013, and references therein). Indeed, solar wind Reynolds number is quite large and the spectral properties of magnetic field and plasma velocity fluctuations show power law behavior (Coleman and Paul, 1968; Goldstein et al., 1995; Tu and Marsch, 1995; Biskamp, 2003; Bruno and Carbone, 2013), similar to neutral fluids turbulence. The solar wind power spectral density reveals the existence of an inertial range of scales, where the energy is transferred nonlinearly from larger to smaller scales. The power law exponent, $f^{-\alpha}$, is often found in good agreement with theoretical values derived from dimensional analysis, $\alpha = 5/3$ (Kolmogorov, 1941). It is also found that the high frequency limit of the inertial range extends toward larger values with increasing distance from the Sun (e.g., Horbury et al., 1996; Bruno and Trenchi, 2014). The properties of solar

wind turbulence depend on effects like the radial expansion of the solar wind (Goldstein et al., 1995; Gazis, 1996), the interactions between fast and slow plasma streams and/or dynamic processes related to various types of non-linear structures forming in solar wind plasma. Anisotropy is an ubiquitous feature of the solar wind turbulence (Belcher and Davis, 1971; Bruno et al., 1999; Horbury et al., 2008; Wicks et al., 2010), noticeable in effects related to compressibility (Alexandrova et al., 2008) and affecting the structure of fluctuations at meso (inertial range) (Horbury et al., 2008; Wicks et al., 2010) and kinetic scales (Lacombe et al., 2017), which increases the complexity of the entire phenomenon.

One of the open-question is related to the structure of solar wind turbulence, more specifically, on how irregular is the transfer of energy between scales. The irregularity of the energy transfer rate (see, e.g., Marsch et al., 1996; Horbury et al., 1997) leads to the phenomenon of intermittency (from Latin *intermitere*, to interrupt). This type of irregularity represents a violation of the fundamental hypothesis adopted to derive the classical model of Kolmogorov turbulence and is generally described as a deviation from the perfect self-similarity (Frisch, 1995, ch. 8). Indeed, while in the classical model of turbulence the energy is transferred by nonlinear structures (e.g. vortices) that fully occupy the space at all scales and which are characterized by a constant, scale-independent energy transfer rate, in intermittent turbulence the energy is transferred non-uniformly, by processes whose transfer rate is scale and spatially dependent. The phenomenon of intermittency can be defined as the property of the plasma structures carying the turbulent fluctuations (e.g., eddies, Alfvén vortices) to break down heterogeneously at smaller and smaller scales, i.e. they become scattered in time and/or space (Biskamp, 2003, ch. 7). In solar wind turbulence, intermittency can be detected at scales pertaining to the inertial range, orders of magnitude away from dissipative scales, which is a significant difference between hydrodynamic and MHD turbulence (Frisch, 1995; Biskamp, 2003; Bruno, 2019). Intermittency in solar wind turbulence was first identified by Burlaga, 1991. Since then, it has been widely studied and documented using data from many missions: Voyager (Burlaga, 1991; Burlaga, 1995; Burlaga et al., 1993), Helios (e.g., Marsch and Liu, 1993; Marsch and Tu, 1994; Marsch et al., 1996; Sorriso-Valvo et al., 1999; Veltri and Mangeney, 1999; Sorriso-Valvo et al., 2001; Bruno et al., 2003), Ulysses (e.g., Horbury et al., 1996; Tu et al., 1996; Horbury et al., 1997; Pagel and Balogh, 2001; Pagel and Balogh, 2003; Yordanova et al., 2009; Wawrzaszek et al., 2015, Wawrzaszek et al., 2019), Advanced Composition Explorer and WIND (Hnat et al., 2003; Vörös et al., 2006; Szczepaniak and Macek, 2008; Greco et al., 2009; Salem et al., 2009; Wan et al., 2011), and recently also from Parker Solar Probe (e.g., Alberti et al., 2020; Chhiber et al., 2020; Perrone et al., 2020).

Intermittency can be revealed by several complementary data analysis methodologies. Most of the analysis methods focus on higher-order moments of fluctuations probabilities in order to reveal their scale dependence and a departure from self-similarity expected for intermittent fluctuations (e.g., Frisch, 1995).

(1) A first class of methods estimate intermittency from the anomalous scaling of the Structure Functions (SF) and its deviation from self-similarity quantified by fitting different intermittency models (e.g., Meneveau and Sreenivasan, 1987; Burlaga, 1991; Carbone, 1993; Marsch and Liu, 1993; She and Leveque, 1994; Burlaga, 1995; Horbury et al., 1997).
(2) Another approach evaluates intermittency from the non-Gaussian features of Probability Distribution Functions (PDF) of the solar wind fluctuation (Marsch and Tu, 1994), e.g. by comparison/fitting with Castaing distributions (Castaing et al., 1990; Sorriso-Valvo et al., 1999; Sorriso-Valvo et al., 2001; Pagel and Balogh, 2003; Yang and Tam, 2010) or from the evaluation of the fourth order moment (kurtosis, Flatness Factor) (e.g., Bruno et al., 2003; Yordanova et al., 2009).
(3) A third methodology adopted to evaluate intermittency is based on the so-called Local Intermittency Measure (LIM) computed from the normalized squared module of wavelet coefficients calculated for an incremental measure of the signal, similar to the one used to estimate the PDFs (Farge, 1992; Veltri and Mangeney, 1999; Bruno et al., 2001).
(4) Finally, a fourth approach is based on calculation of the multifractal spectrum of an incremental measure (e.g., Marsch et al., 1996; Burlaga and Ness, 2010; Wawrzaszek and Macek, 2010; Macek et al., 2014; Wawrzaszek et al., 2015).

More details and exhaustive description of each method applied for intermittency can be found in recent reviews like, e.g., Salem et al. (2009), Bruno and Carbone (2013), Matthaeus et al. (2015), Bruno (2019).

Due to the relatively reduced time resolution of most of solar wind data, the methods mentioned above were applied to study intermittency of the inertial range turbulence (e.g., Burlaga, 1991; Marsch and Liu, 1993; Tu et al., 1996; Sorriso-Valvo et al., 1999; Bruno et al., 2003; Wawrzaszek et al., 2015; Wawrzaszek et al., 2019). In this review, we summarize the observations of MHD intermittency in the solar wind, and discuss how intermittency changes with the type of solar wind (fast vs. slow), the radial distance, the heliolatitude, and solar cycle. We also emphasize the importance of using robust data selection algorithms, the impact of various reference systems and how the interpretation of results depends on the characteristics of the different data analysis methods. The study of intermittency in the MHD range of scales is crucial and complementary to investigation of kinetic scales reported recently by (e.g., Perri et al., 2012; Wan et al., 2012; Sorriso-Valvo et al., 2017).

2. SOLAR WIND INTERMITTENCY VERSUS RADIAL DISTANCE AND HELIOLATITUDE

2.1. Radial Evolution of Intermittency in the Ecliptic

The first study of intermittency for different solar wind conditions and for a range of heliocentric distances in the ecliptic plane is due to Marsch and Liu (1993), who

investigated Helios two observations of fast and slow streams (bulk velocity and Alfvén velocity) at two heliocentric distances (0.3 and 1 AU), for scales between 40.5 s and 24 h. Their analysis was based on the structure function approach and found that intermittency is stronger for the small scales, while the fast solar wind reveals generally less intermittent nature than slow wind. It was also shown that the intermittency level in the ecliptic increases with the increasing heliocentric distance for fast wind streams and was suggested that solar wind turbulence results from a mixture of waves, advected sheets and eddies.

Tu et al. (1996) considered 5 cases of Helios two data and detected magnetic intermittency in the range of scales between 81 and 2,500 s. From estimation of the anomalous scaling of structure function they showed that the intermittency in the fast solar wind is relatively stable, but it varies significantly in the slow wind. However, a clear radial evolution trend was not found.

Sorriso-Valvo et al. (1999) analyzed fluctuations of the solar wind at time scales from 81 s to 1 day from four months of Helios two data recorded in 1976 when the heliocentric distance varied from 1 AU to 0.29 AU. They studied intermittency with the Castaing distribution approach and found that the magnetic field intensity presents higher level of intermittency than the bulk speed for fast and slow wind. No significant differences were found between slow and fast wind. Sorriso-Valvo et al. (1999) considered compressive phenomena to be at the origin of the slow solar wind intermittency.

Bruno et al. (1999) investigated the effects of intermittency on anisotropy (defined as the ratio between the total power perpendicular to the minimum variance direction and the power along this direction) for three heliospheric distances, 0.3, 0.7, and 0.9 AU, from magnetic and velocity data provided by Helios 2. It is shown that there is a link between the radial evolution of intermittency and anisotropy. Indeed, it is demonstrated, aided by the computation of the Local Intermittency Measure (LIM), that the increase of magnetic anisotropy with radial distance is mainly due to radial evolution of magnetic intermittency. However, the intermittency of the velocity field does not alter significantly the radial trend of velocity anisotropy.

Bruno et al. (2003) focused on the radial behavior of intermittency in the ecliptic determined from the fourth-order moment (or flatness) of PDFs computed for the compressive and vector fluctuations of the magnetic field and plasma velocity, measured by Helios two at 0.3, 0.7 and 0.9 AU. While previous analyses were based on data representation in the Solar Ecliptic (SE) reference systems (Marsch and Liu, 1993; Tu et al., 1996; Sorriso-Valvo et al., 1999), Bruno et al. (2003) used a Mean Field (MF) reference system (see Appendix D.2 of Bruno and Carbone, 2013). In MF reference frame one component, $B_{\parallel}$, is outwardly oriented and parallel to the mean field $\mathbf{B}_0$, whose value depends on scale, as suggested by Gerick et al. (2017), Macek et al. (2017), see also a discussion by Podesta. (2017). The analysis of Bruno et al. (2003) confirmed previous results and showed that intermittency is stronger for magnetic field fluctuations than for velocity and increases with the distance from the Sun in the fast solar wind. Results showed also that components transverse to the local magnetic field direction, are less intermittent than the parallel one. The intermittency of the parallel component increases much faster with the radial distance than the intermittency of the transversal ones. Bruno et al. (2003) interpreted this trend considering the solar wind turbulence is driven by coherent advected structures and propagating stochastic Alfvénic fluctuations. They concluded that the coherent nature of the advected structures could explain the intermittency increase. On the other hand, intermittency would decrease due to the stochastic nature of Alfvénic fluctuations. However, at larger radial distances the coherent nature of advected structures prevails, thus intermittency increases. The relationship between solar wind Alfvénicity and intermittency was also studied by D'Amicis et al. (2012), who reached similar conclusions.

Yang and Tam (2010) analyzed 39 time intervals of fast solar wind data provided by Helios 1 and 2 at radial distances between 0.3 and 1 AU. From a conditioned flatness analysis and the fitting of Castaing distribution, these authors confirmed that fast solar wind magnetic intermittency increases with larger distance from the Sun. The increase of intermittency with distance in the ecliptic plane was confirmed for two parameters of the fast solar wind (velocity and magnetic field).

Bruno et al. (2014a) considered also the radial evolution of intermittency of density fluctuations in fast solar wind as observed by Helios 2 between 0.3 and 0.9 AU. It is shown that, in contrast to observations for velocity and magnetic field, the density fluctuations show a stronger intermittent character at short heliocentric distances and the level of density intermittency decreases with the distance from the Sun.

Recent analysis of Parker Solar Probe (PSP) data measured during the first two orbits, when slow solar wind dominated, provide insight on intermittency at rather close distances from the Sun. Some studies focused on data measured at 0.17 AU and on the identification coherent structures (Bandyopadhyay et al., 2020; Chhiber et al., 2020), various types of intermittent events like current sheets, vortex-like structures or wave packets (Perrone et al., 2020). Alberti et al. (2020) analyzed magnetic field components measured by PSP at different locations (between 0.17 and 0.7 AU). Authors reveled statistical global self-similar scaling at radial distances below 0.4 AU and scaling properties typical for intermittent turbulence above 0.4 AU. They suggested that around 0.4 AU there is a transition region in which intermittency appears and the scaling in the inertial range changes (Chen et al., 2020).

2.2. Radial Dependence of Intermittency Outside the Ecliptic

In the ecliptic plane, the solar wind turbulence is driven by velocity shears, parametric decay, and the interaction between Alfvénic modes with convected structures (Bruno and Carbone, 2013). Thanks to Ulysses measurements, the radial dependence of the intermittent turbulence can be investigated outside the ecliptic plane. It is found that at higher latitudes solar wind turbulence shows different properties compared to the equatorial regions (Ruzmaikin et al., 1995; Bavassano et al., 2000, Bavassano et al., 2001). The radial evolution of turbulence in the polar wind

is less rapid (e.g., Horbury et al., 1996; Bruno and Trenchi, 2014), what seems to have also influence on the level of magnetic intermittency (e.g., Ruzmaikin et al., 1995; Horbury and Balogh, 2001; Pagel and Balogh, 2002, Pagel and Balogh, 2003; Yordanova et al., 2009).

An analysis of structure function scaling (Pagel and Balogh, 2001) at solar minimum (1994–1995), radial distances between 1.3 and 2.4 AU and heliolatitudes between −80° to +80°, revealed the evolution of intermittency outside the ecliptic. A high level of intermittency was found for a range of scales between 10 and 300 s in the fast solar wind; however, the data in the slow wind were much more variable and difficult to interpret. Nevertheless, it was shown that the transverse magnetic components have a comparable level of intermittency, while the radial component is slightly less intermittent.

Pagel and Balogh (2002) confirmed the radial trends at solar minimum (1994–1995) and maximum (2000–2001) and also found, contrary to previous studies, that the slow solar wind presents a level of intermittency comparable to the fast wind. It is worth to add that authors used wind speed as the criterion to discriminate between two states of solar wind. Bruno and Carbone (2013) suggested that this discrepancy results mainly from the representation of data in the RTN reference system instead of the Mean Field frame.

Pagel and Balogh (2003) analyzed 28 cases of polar coronal fast wind measured during solar minimum (1994–1996) and fitted the PDFs of magnetic field fluctuations with the Castaing distribution, for time scales between 40 and 200 s. Their results showed that intermittency, or non-Gaussianity, of the magnetic field fluctuations increases with the radial distance in the range 1.4–4.1 AU and is stronger for transverse than for radial component. It is suggested that the increase of intermittency with the radial distance is the effect of the increase of the scale range of the inertial range sustained by the radial expansion of the solar wind.

Yordanova et al. (2009) analyzed 21 time intervals without CMEs and, based on kinetic parameters and ions (oxygen) charge states, considered four states of the solar wind, 1) pure fast, 2) fast streams, 3) pure slow, 4) slow streams, from Ulysses data recorded between 1992 and 1997. The results indicated that only pure fast wind (4 cases) show clear trends for radial evolution of the intermittency with the heliocentric distance, between 1.5 AU and 3.0 AU and at heliolatitudes between 50° and 80°. Yordanova et al. (2009) concluded also that pure slow wind measured at 5.1–5.4 AU and at latitudes narrowed to <20° presents the most intermittent state.

Wawrzaszek et al. (2015) studied the radial dependence of magnetic field intermittency as observed by Ulysses during two solar minima (1997–1998, 2007–2008) and one maximum (1999–2001), between 1.4 and 5.4 AU and a heliolatitudes ranging between −80° and +70°. To avoid the problem of mixing of different states of the solar wind, these authors applied a multi-parametric procedure based on several solar wind variables to select data and discriminate between slow and fast wind. Additionally, interplanetary transients like shocks and CMEs have been excluded from the analysis. Thus, they found 98 time intervals of slow (43 time intervals) and fast solar wind (55 time intervals). Wawrzaszek et al. (2015) applied the multifractal formalism to investigate intermittency and limited their analyses to the compressional component. More precisely, they determined multifractal spectra and Δ, the degree of multifractality, as a quantative descriptor of the intermittency level. This study suggests that the level of intermittency decreases with distance in contrast to the previous analyses based on statistical description (Pagel and Balogh, 2003; Yordanova et al., 2009). However, during the identification of the multifractal scaling, authors included also scales less than 16 s, what could have an impact on the results. Nevertheless, the collection of data used by Wawrzaszek et al. (2015) is the largest in terms of number of time intervals and total data (more than 17,000 h), among all studies devoted to intermittency based on Ulysses data.

Wawrzaszek et al. (2019) extended their study by using a larger number of time intervals (126) at solar minima (1997–1998, 2007–2008) and solar maximum (1999–2001). The multifractal analysis were applied for the all magnetic field components in the MHD range of scales (larger than 16 s). Additionally, the authors investigated intermittency of the parallel and perpendicular component in the Mean Field reference system, used previously by Bruno et al. (2003) for Helios two data. Wawrzaszek et al. (2019) confirmed the decrease of intermittency with the radial distance, for all components of the magnetic field, regardless the reference system, RTN or Mean Field. However, the rate of decrease of the intermittency with the distance from the Sun, was influenced by the range of the analyzed scales; smaller scales less than 16 s caused a slowdown of this decrease, interpreted as the influence of compressibility processes that strengthen the phenomenon of intermittency (Alexandrova et al., 2008). In general, Wawrzaszek et al. (2019) reminded the idea that the intermittency in MHD range have solar origin (Pagel and Balogh, 2002; Wawrzaszek et al., 2015) and suggested that the strength of various solar wind drivers like fast and slow streams, shocks interaction, pressure balanced, incompressible current sheets and interplanetary shocks (Veltri and Mangeney, 1999) diminishes with the distance from the Sun leading to a decrease of intermittency. On the other hand, Greco et al. (2012) performing numerical simulation and data analysis from the ecliptic suggested that intermittency is formed in the solar wind through active *in-situ* dynamics. In the light of this suggestion solar wind beyond ecliptic seems to be insufficiently active turbulent medium, the coherent character of advected structures can be somehow reduced with the increase of radial distance.

2.3. Latitudinal Dependence and Solar Cycle Effect

Another possible source for the differences observed between radial variation trends provided by different methodologies can be the mixing of different heliolatitudes in the same dataset. The solar cycle phase can also play a role. In **Table 1** we provide a summary of datasets analyzed in the papers discussed above.

Pagel and Balogh (2002) compared two Ulysses fast-latitude scans at solar minimum and maximum, and did not reveal any

TABLE 1 | Selected papers devoted to the analysis of intermittency in the solar wind beyond the ecliptic plane by using Ulysses measurements.

Paper	Data				Method
	Year	Distance	Latitude	Par(Ref. Sys)	
Pagel and Balogh (2001)	1994–1995	1.3–2.4 AU	−80°–+80°	*B* (RTN)	SF analysis
Pagel and Balogh (2002)	1994–1995 2000–2001	1.3–2.4 AU	−80°–+80°	*B* (RTN)	FF analysis
Pagel and Balogh (2003)	1994–1996	1.4–3.8 AU	−80°–+80°	*B* (RTN)	Castaing dist
Yordanova et al. (2009)	1992–1997	1.4–5.4 AU	−80°–+80°	*B* (RTN)	FF analysis
Wawrzaszek et al. (2015)	1997–1998 1999–2001 2007–2008	1.4–5.4 AU	−80°–+70°	|*B*| (RTN)	Multifractal Spectrum
Wawrzaszek et al. (2019)	1997–1998 1999–2001 2007–2008	1.4–5.4 AU	−80°–+70°	*B* (RTN) *B* (MF)	Multifractal Spectrum

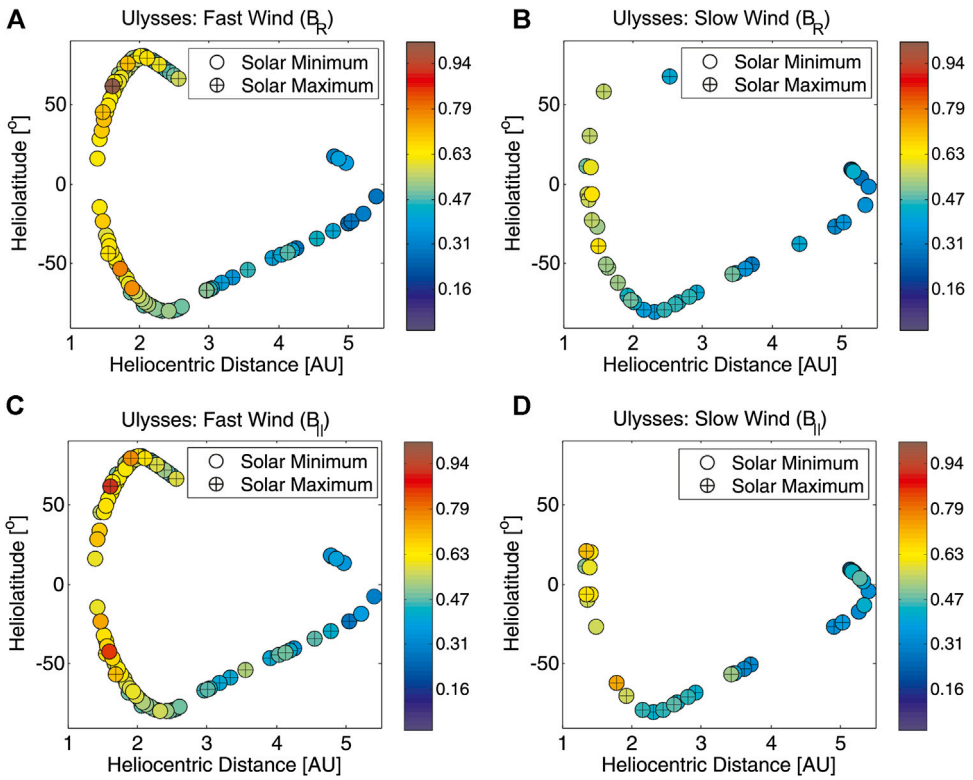

FIGURE 1 | Map of the degree of multifractality as a level of intermittency determined for fast (left panel) and slow (right panel) solar wind during solar minima (1997–1998, 2007–2008) and solar maximum (1999–2001), correspondingly. Color denotes the level of multifractality (intermittency) calculated for the radial components B_R (in RTN reference system, **(A,B)**) and component $B_\parallel$ (parallel to the mean field vector $\mathbf{B}_0$, **(C,D)**), as observed by Ulysses at various heliocentric distances (between 0.3 and 5 AU) and heliographic latitudes (between −80° and +70°). From Wawrzaszek et al. (2019).

latitudinal dependence of intermittency (Wawrzaszek et al., 2015; Wawrzaszek et al., 2019). showed that the fast solar wind at solar minimum exhibit a decrease of intermittency as the latitude increases; the smallest values of intermittency were found near solar poles. An example form Wawrzaszek et al. (2019) is shown in the composite **Figure 1**, where left/right panels refer to the fast/slow solar wind. Color in **Figure 1** denotes the values Δ, the degree of multifractality as an intermittency measure. **Figure 1** presents results for the radial component B_R (in RTN reference system, panels **A** and **B**) and component $B_\parallel$ (parallel to the mean field vector $\mathbf{B}_0$, panels **C** and **D**), respectively. The decrease of intermittency as the latitude increases is observed both in RTN and MF reference systems and confirms the previous conclusions that turbulence at Ulysses is mainly driven by Alfvénic fluctuations (e.g., D'Amicis et al., 2012). Moreover, data reveal the existence of a symmetry with respect to the

ecliptic plane for solar minima (1997–1998, 2007–2008) in coherence with previous observations (Bavassano et al., 2000; Wawrzaszek and Macek, 2010). On the other hand, during the solar maximum (1999–2001) the slow and fast solar wind does not show a latitudinal dependence and symmetry.

The solar cycle trends need more discussion. Indeed, on the one hand trends in the radial dependence of intermittency in the ecliptic were derived from Helios 1 and 2 data recorded during solar cycle 21, between 1974 and 1981. On the other hand, the first, second and third orbit of Ulysses data captured the solar wind properties during cycles 22 and 23, revealing also differences in the state of the solar wind (McComas et al., 2008).

The analysis of solar wind data from each solar cycle confirmed the presence of intermittency, virtually at all radial distances and both at solar minimum and solar maximum (Pagel and Balogh, 2001; Pagel and Balogh, 2002; Pagel and Balogh, 2003; Wawrzaszek et al., 2015, Wawrzaszek et al., 2019). Pagel and Balogh (2002) suggested intermittency varies less with the solar cycle phase than with the type of wind. Analysis of Ulysses data for the years 1992–1997 (Yordanova et al., 2009) and results obtained for the solar minimum (1997–1998) (Wawrzaszek et al., 2015; Wawrzaszek et al., 2019) showed that intermittency is stronger for slow solar wind than for the fast wind. This is in agreement with research performed in the ecliptic (Marsch and Liu, 1993; Bruno et al., 2003). However, the study by (Wawrzaszek et al., 2015; Wawrzaszek et al., 2019) based on data recorded at solar maximum (1999–2001) and minimum (2007–2008) reveals cases when the slow solar wind shows a lower level of intermittency than the fast solar wind. Similar conclusions were given by Pagel and Balogh, (2002), who analyzed data from the same solar maximum and found a high level of intermittency in the fast coronal hole solar wind and a varying and lower level in the slow wind. However, one should note that most of the slow solar wind cases considered in (Pagel and Balogh, 2002; Wawrzaszek et al., 2015, 2019) pertained to solar cycle 23 characterized by specific properties (e.g., McComas et al., 2008; D'Amicis et al., 2011). In particular, the slow wind observed at maximum of solar cycle 23 (the year 2001) showed a degree of Alfvénicity comparable or even higher than for the fast wind observed at the minimum of the same cycle (2007) as discussed by D'Amicis et al. (2011). Moreover, a new type of Alfvénic slow wind is believed to show having some characteristics common to the fast wind (D'Amicis and Bruno, 2015; D'Amicis et al., 2018). Very interesting are recent observations of PSP performed during minimum of solar cycle no. 24, which confirmed the existence of the slow solar wind with high Alfvénicity and its intermittent character (Bandyopadhyay et al., 2020; Chhiber et al., 2020; Perrone et al., 2020).

Finally it is worth to stress that at solar maximum the statistics of slow wind intervals is rather poor (compare cases in **Figure 1B**, **D** marked by circles with a cross for maximum and empty circles for minimum). At solar maximum intermittency spans a larger domain of values, as a confirmation of the complex nature of the solar wind during strong activity of the Sun.

3. SUMMARY AND PERSPECTIVE

In this review we discuss recent findings on solar wind inertial range intermittency observed over a large range of heliocentric distances and latitudes, for different levels of solar activity.

Intermittency is a real and omnipresent characteristic of solar wind turbulence, detected for fluctuations of solar wind magnetic field and plasma parameters (velocity, density), for fast and slow types of wind. The main source of intermittency are magnetic non-Alfvénic coherent structures involved in the radial evolution of solar wind turbulence, different than filaments or vortices observed in neutral fluid turbulence (Bruno and Carbone, 2013; Bruno, 2019). The most intermittent events identified in the inertial range of scales are parallel shocks, slow mode shocks, or tangential discontinuities/current sheets (Veltri and Mangeney, 1999; Bruno et al., 2001; Borovsky, 2008) or planar sheets in MHD flows (Bruno, 2019). Data from Helios and Ulysses show different trends for the radial evolution of intermittency in fast and slow winds. While in the inner heliosphere, in the equatorial plane and at radial distances less than 1 AU intermittency tends to increase with distance, this tendency is reversed outside the ecliptic and for larger radial distances. It is argued that decreasing of intermittency with large radial distances is the result of the interplay between coherent, intermittent structures convected by the wind and propagating Alfvén fluctuations, which tend to reduce intermittency. Examples of solar wind data for which Alfvénic fluctuations are less dominant, are generally more intermittent but do not show a clear radial evolution. Nevertheless, intermittency in the Alfvénic solar wind increases with heliocentric distance. Moreover, data indicate intermittent properties of fast polar wind show a symmetry in the two hemispheres. The fast solar wind at solar minimum exhibits a decrease of intermittency as the latitude increases. However, this trend is less clear at solar maximum, when intermittency values are more scattered. The level of intermittency in the solar wind is solar cycle-dependent, reflecting the changes of the state of solar wind and suggesting that the origin of fast and slow wind is important for the subsequent structure of turbulent transfer of energy within the heliosphere.

Although the studies discussed above provide evidence on the existence of a radial evolution of intermittency beyond the ecliptic plane, it is difficult to define a universal trend and to indicate how intermittency changes with the radial distance for all types of wind, and all phases of the solar cycle. On the one hand, different methodologies capture different aspects of intermittency (Sorriso-Valvo et al., 2017). The multifractal analysis emphasizes the role of the higher-order moments, and collect the measure of intermittency from an estimation of large (positive moments) and small (negative moments) concentrations of measure. The structure function and the flatness approaches are based on positive moments only. On the other hand, the mathematical formalism of the multifractal scalings does not lend itself to a interpretation in terms of coherent structures (Wan et al., 2011). It is certain that the multifractal approach and the analysis based on the structure function, PDFs and their moments capture complementary characteristics of the same phenomenon,

the irregular structure of the energy transfer in astrophysical plasma turbulence. Further studies are expected to illuminate more the intricate relationship between the insight provided by these higher order analyses and the impact on understanding solar wind and astrophysical intermittency.

Nevertheless, some additional analyses should still be performed to better understand solar wind turbulence and intermittent dynamics at MHD scales. As we tried to underline in this short review, a large part of the studies devoted to intermittency are based on a relatively small number of samples selected by different methods, making it difficult to interpret and compare results. Moreover, most often only a subset of plasma or magnetic field measurements were analyzed, and due to the limitations of *in-situ* interplanetary data, similar scaling ranges are seldom considered by different approaches. Therefore, a complementary analysis of intermittency with various descriptors estimated for the same large datasets is still needed. One of the simplest ways to achieve such a goal seems to be using analysis tools designed to perform automatic analysis of large collections of space measurements, *in-situ* or simulations (e.g., Teodorescu and Echim, 2020). Moreover, significant advances in data selection procedures allow to identify more than the two basic states of the solar wind, fast and slow, as discussed by (Landi et al., 2012; Xu and Borovsky, 2015; Camporeale et al., 2017). Such categorization procedures will likely provide further refinement of data analysis and allow for a deeper analysis of solar wind intermittency and its relationship with the various states of solar wind. A continuation of detailed studies of the relationship between solar wind anisotropy and intermittency and of the dependence on the solar wind conditions is also needed. It would allow for new comparisons between turbulence properties revealed by *in-situ* data analysis and the results of numerical simulations and improve our understanding of physical processes like dynamic alignment, critical balance and intermittency. Additionally, a better understanding of the formation, stability and dynamics of solar wind discontinuities can help understanding the origin of intermittency (Borovsky, 2008; Greco et al., 2008; Greco et al., 2009).

Finally, there is a need to advance the understanding of the couplings between the inertial range structure of turbulence and intermittency and the phenomena taking place at smaller, kinetic scales (e.g., Bruno et al., 2014b), for example their influence on field-particle interaction (e.g., Chen et al., 2019; Sorriso-Valvo et al., 2019). As Bruno (2019) reviewed recently, most studies focus now on the analysis of intermittent events at small, kinetic scales as the key to understanding the dissipation mechanisms in the collisionless solar wind plasma. This topic, due to the lack of adequate plasma observations was mainly explored by using plasma numerical simulations. Recently, thanks to new missions like Magnetospheric Multiscale Mission, Parker Solar Probe or Solar Orbiter, new opportunities are opened for the scientific community to analyze the intermittent nature of solar wind turbulence at much smaller scales and in new regions of the heliosphere (at closer distances from the Sun and during new solar cycles). This opens up new research options and makes upcoming years very exciting for the heliospheric community.

AUTHOR CONTRIBUTIONS

AW and ME planned, outlined, researched, and wrote the manuscript.

ACKNOWLEDGMENTS

ME acknowledge support from the Belgian Solar Terrestrial Center of Excellence (STCE) and the Romanian Government UEFISCDI PCCDI Project VESS and Program Nucleu LAPLAS.

REFERENCES

Alberti, T., Laurenza, M., Consolini, G., Milillo, A., Marcucci, M. F., Carbone, V., et al. (2020). On the scaling properties of magnetic-field fluctuations through the inner heliosphere. *Astrophys. J.* 902, 84. doi:10.3847/1538-4357/abb3d2

Alexandrova, O., Carbone, V., Veltri, P., and Sorriso-Valvo, L. (2008). Small-scale energy cascade of the solar wind turbulence. *Astrophys. J.* 674, 1153–1157. doi:10.1086/524056

Bandyopadhyay, R., Matthaeus, W. H., Parashar, T. N., Chhiber, R., Ruffolo, D., Goldstein, M. L., et al. (2020). Observations of energetic-particle population enhancements along intermittent structures near the sun from the parker solar probe. *Astrophys. J. Suppl.* 246, 61. doi:10.3847/1538-4365/ab6220

Bavassano, B., Pietropaolo, E., and Bruno, R. (2000). On the evolution of outward and inward Alfvénic fluctuations in the polar wind. *J. Geophys. Res.* 105, 15959–15964. doi:10.1029/1999JA000276

Bavassano, B., Pietropaolo, E., and Bruno, R. (2001). Radial evolution of outward and inward alfvénic fluctuations in the solar wind: a comparison between equatorial and polar observations by ulysses. *J. Geophys. Res.* 106, 10659–10668. doi:10.1029/2000JA000453

Belcher, J. W., and Davis, L., Jr (1971). Large-amplitude alfven waves in the interplanetary medium, 2. *J. Geophys. Res.* 76, 3534–3563. doi:10.1029/JA076i016p03534

Biskamp, D. (2003). Magnetohydrodynamic turbulence. *Plasma Phys. Contr. Fusion* 45, 1827. doi:10.1088/0741-3335/45/9/701

Borovsky, J. E. (2008). Flux tube texture of the solar wind: strands of the magnetic carpet at 1 au? *J. Geophys. Res.* 113, A08110. doi:10.1029/2007JA012684

Bruno, R., Bavassano, B., Pietropaolo, E., Carbone, V., and Veltri, P. (1999). Effects of intermittency on interplanetary velocity and magnetic field fluctuations anisotropy. *Geophys. Res. Lett.* 26, 3185–3188. doi:10.1029/1999GL010668

Bruno, R., Carbone, V., Sorriso-Valvo, L., and Bavassano, B. (2003). Radial evolution of solar wind intermittency in the inner heliosphere. *J. Geophys. Res.* 108, 1130. doi:10.1029/2002JA009615

Bruno, R., and Carbone, V. (2013). The solar wind as a turbulence laboratory. *Living Rev. Sol. Phys.* 10, 2. doi:10.12942/lrsp-2013-2

Bruno, R., Carbone, V., Veltri, P., Pietropaolo, E., and Bavassano, B. (2001). Identifying intermittency events in the solar wind. *Planet. Space Sci.* 49, 1201–1210. doi:10.1016/S0032-0633(01)00061-7

Bruno, R. (2019). Intermittency in solar wind turbulence from fluid to kinetic scales. *Earth Space Sci.* 6, 656–672. doi:10.1029/2018EA000535

Bruno, R., Telloni, D., Primavera, L., Pietropaolo, E., D'Amicis, R., Sorriso-Valvo, L., et al. (2014a). Radial evolution of the intermittency of density fluctuations in the fast solar wind. *Astrophys. J.* 786, 53. doi:10.1088/0004-637x/786/1/53

Bruno, R., and Trenchi, L. (2014). Radial dependence of the frequency break between fluid and kinetic scales in the solar wind fluctuations. *Astrophys. J.* 787, L24. doi:10.1088/2041-8205/787/2/l24

Bruno, R., Trenchi, L., and Telloni, D. (2014b). Spectral slope variation at proton scales from fast to slow solar wind. *Astrophys. J.* 793, L15. doi:10.1088/2041-8205/793/1/l15

Burlaga, L. F. (1991). Intermittent turbulence in the solar wind. *J. Geophys. Res.* 96, 5847–5851. doi:10.1029/91JA00087

Burlaga, L. F., and Ness, N. F. (2010). Sectors and large-scale magnetic field strength fluctuations in the heliosheath near 110 au: voyager 1, 2009. *Astrophys. J.* 725, 1306. doi:10.1088/0004-637X/725/1/1306

Burlaga, L. F., Perko, J., and Pirraglia, J. (1993). Cosmic-ray modulation, merged interaction regions, and multifractals. *Astrophys. J.* 407, 347–358. doi:10.1086/172517

Burlaga, L. (1995). *Interplanetary mganetohydrodynamics*. 1st Edn. New York, NY: Oxford University Press, 272.

Camporeale, E., Carè, A., and Borovsky, J. E. (2017). Classification of solar wind with machine learning. *J. Geophys. Res.* 122 (10), 910–920. doi:10.1002/2017JA024383

Carbone, V. (1993). Cascade model for intermittency in fully developed magnetohydrodynamic turbulence. *Phys. Rev. Lett.* 71, 1546–1548. doi:10.1103/PhysRevLett.71.1546

Castaing, B., Gagne, Y., and Hopfinger, E. (1990). Velocity probability density functions of high Reynolds number turbulence. *Phys. Nonlinear Phenom.* 46, 177–200. doi:10.1016/0167-2789(90)90035-N

Chen, C. H. K., Bale, S. D., Bonnell, J. W., Borovikov, D., Bowen, T. A., Burgess, D., et al. (2020). The evolution and role of solar wind turbulence in the inner heliosphere. *Astrophys. J. Suppl.* 246, 53. doi:10.3847/1538-4365/ab60a3

Chen, C., Klein, K., and Howes, G. (2019). Evidence for electron Landau damping in space plasma turbulence. *Nat. Commun.* 10, 740. doi:10.1038/s41467-019-08435-3

Chhiber, R., Goldstein, M. L., Maruca, B. A., Chasapis, A., Matthaeus, W. H., Ruffolo, D., et al. (2020). Clustering of intermittent magnetic and flow structures near parker solar probe's first perihelion—a partial-variance-of-increments analysis. *Astrophys. J. Suppl.* 246, 31. doi:10.3847/1538-4365/ab53d2

Coleman, J., and Paul, J. (1968). Turbulence, viscosity, and dissipation in the solar-wind plasma. *Astrophys. J.* 153, 371. doi:10.1086/149674

D'Amicis, R., Bruno, R., and Bavassano, B. (2011). Response of the geomagnetic activity to solar wind turbulence during solar cycle 23. *J. Atmos. Sol. Terr. Phys.* 73, 653–657. doi:10.1016/j.jastp.2011.01.012

D'Amicis, R., and Bruno, R. (2015). On the origin of highly Alfvénic slow solar wind. *Astrophys. J.* 805, 84. doi:10.1088/0004-637x/805/1/84

D'Amicis, R., Consolini, G., Bavassano, B., and Bruno, R. (2012). Conditioned analysis of high-latitude solar wind intermittency. *Astrophys. J.* 755, 63. doi:10.1088/0004-637x/755/1/63

D'Amicis, R., Matteini, L., and Bruno, R. (2018). On the slow solar wind with high Alfvénicity: from composition and microphysics to spectral properties. *Mon. Not. Roy. Astron. Soc.* 483, 4665–4677. doi:10.1093/mnras/sty3329

Farge, M. (1992). Wavelet transforms and their applications to turbulence. *Annu. Rev. Fluid Mech.* 24, 395–458. doi:10.1146/annurev.fl.24.010192.002143

Frisch, U. (1995). *Turbulence. The legacy of A. N. Kolmogorov*. Cambridge, United Kingdom: Cambridge University Press, 296.

Gazis, P. R. (1996). Solar cycle variation in the heliosphere. *Rev. Geophys.* 34, 379–402. doi:10.1029/96RG00892

Gerick, F., Saur, J., and von Papen, M. (2017). The uncertainty of local background magnetic field orientation in anisotropic plasma turbulence. *Astrophys. J.* 843, 5. doi:10.3847/1538-4357/aa767c

Goldstein, M. L., Roberts, D. A., and Matthaeus, W. H. (1995). Magnetohydrodynamic turbulence in the solar wind. *Annu. Rev. Astron. Astrophys.* 33, 283–326. doi:10.1146/annurev.aa.33.090195.001435

Greco, A., Chuychai, P., Matthaeus, W. H., Servidio, S., and Dmitruk, P. (2008). Intermittent mhd structures and classical discontinuities. *Geophys. Res. Lett.* 35, L19111. doi:10.1029/2008GL035454

Greco, A., Matthaeus, W. H., D'Amicis, R., Servidio, S., and Dmitruk, P. (2012). Evidence for nonlinear development of magnetohydrodynamic scale intermittency in the inner heliosphere. *Astrophys. J.* 749, 105. doi:10.1088/0004-637x/749/2/105

Greco, A., Matthaeus, W. H., Servidio, S., Chuychai, P., and Dmitruk, P. (2009). Statistical analysis of discontinuities in solar wind ACE data and comparison with intermittent MHD turbulence. *Astrophys. J.* 691, L111–L114. doi:10.1088/0004-637x/691/2/l111

Hnat, B., Chapman, S. C., and Rowlands, G. (2003). Intermittency, scaling, and the fokker-planck approach to fluctuations of the solar wind bulk plasma parameters as seen by the wind spacecraft. *Phys. Rev. E–Stat. Nonlinear Soft Matter Phys.* 67, 056404. doi:10.1103/PhysRevE.67.056404

Horbury, T., Balogh, A., Forsyth, R., and Smith, E. (1997). Ulysses observations of intermittent heliospheric turbulence. *Adv. Space Res.* 19, 847–850. doi:10.1016/S0273-1177(97)00290-1

Horbury, T. S., Forman, M., and Oughton, S. (2008). Anisotropic scaling of magnetohydrodynamic turbulence. *Phys. Rev. Lett.* 101, 175005. doi:10.1103/PhysRevLett.101.175005

Horbury, T. S., and Balogh, A. (2001). Evolution of magnetic field fluctuations in high-speed solar wind streams: ulysses and helios observations. *J. Geophys. Res.* 106, 15929–15940. doi:10.1029/2000JA000108

Horbury, T. S., Balogh, A., Forsyth, R. J., and Smith, E. J. (1996). The rate of turbulent evolution over the Sun's poles. *Astron. Astrophys.* 316, 333–341.

Khotyaintsev, A., and Macek, W. M. (2008). Asymmetric multifractal model for solar wind intermittent turbulence. *Nonlinear Process Geophys.* 15, 615–620. doi:10.5194/npg-15-615-2008

Kolmogorov, A. (1941). The local structure of turbulence in incompressible viscous fluid for very large Reynolds' numbers. *Akademiia Nauk SSSR Doklady* 30, 301–305.

Lacombe, C., Alexandrova, O., and Matteini, L. (2017). Anisotropies of the magnetic field fluctuations at kinetic scales in the solar wind: cluster observations. *Astrophys. J.* 848, 13. doi:1538-4357/aa8c06

Landi, E., Alexander, R. L., Gruesbeck, J. R., Gilbert, J. A., Lepri, S. T., Manchester, W. B., et al. (2012). Carbon ionization stages as a diagnostic of the solar wind. *Astrophys. J.* 744, 100, doi:10.1088/0004-637X/744/2/100

Macek, W. M., Wawrzaszek, A., and Burlaga, L. F. (2014). Multifractal structures detected by voyager 1 at the heliospheric boundaries. *Astrophys. J. Lett.* 793, L30, doi:10.1088/2041-8205/793/2/L30

Macek, W. M., Wawrzaszek, A., Kucharuk, B., and Sibeck, D. G. (2017). Intermittent anisotropic turbulence detected by THEMIS in the magnetosheath. *Astrophys. J.* 851, L42. doi:10.3847/2041-8213/aa9ed4

Marsch, E., and Liu, S. (1993). Structure functions and intermittency of velocity fluctuations in the inner solar wind. *Ann. Geophys.* 11, 227–238.

Marsch, E., Tu, C.-Y., and Rosenbauer, H. (1996). Multifractal scaling of the kinetic energy flux in solar wind turbulence. *Ann. Geophys.* 14, 259–269. doi:10.1007/s00585-996-0259-4

Marsch, E., and Tu, C. Y. (1994). Non-Gaussian probability distributions of solar wind fluctuations. *Ann. Geophys.* 12, 1127–1138. doi:10.1007/s00585-994-1127-8

Matthaeus, W. H., Wan, M., Servidio, S., Greco, A., Osman, K. T., Oughton, S., et al. (2015). Intermittency, nonlinear dynamics and dissipation in the solar wind and astrophysical plasmas. *Philos Trans A Math Phys Eng Sci* 373, 20140154. doi:10.1098/rsta.2014.0154

McComas, D. J., Ebert, R. W., Elliott, H. A., Goldstein, B. E., Gosling, J. T., Schwadron, N. A., et al. (2008). Weaker solar wind from the polar coronal holes and the whole sun. *Geophys. Res. Lett.* 35, L18103. doi:10.1029/2008GL034896

Meneveau, C., and Sreenivasan, K. R. (1987). Simple multifractal cascade model for fully developed turbulence. *Phys. Rev. Lett.* 59, 1424–1427. doi:10.1103/PhysRevLett.59.1424

Pagel, C., and Balogh, A. (2001). A study of magnetic fluctuations and their anomalous scaling in the solar wind: the Ulysses fast-latitude scan. *Nonlinear Process Geophys.* 8, 313–330. doi:10.5194/npg-8-313-2001

Pagel, C., and Balogh, A. (2002). Intermittency in the solar wind: a comparison between solar minimum and maximum using ulysses data. *J. Geophys. Res.: Space Physics* 107, SSH 6. doi:10.1029/2002JA009331

Pagel, C., and Balogh, A. (2003). Radial dependence of intermittency in the fast polar solar wind magnetic field using ulysses. *J. Geophys. Res.* 108, SSH 2. doi:10.1029/2002JA009498

Perri, S., Goldstein, M. L., Dorelli, J. C., and Sahraoui, F. (2012). Detection of small-scale structures in the dissipation regime of solar-wind turbulence. *Phys. Rev. Lett.* 109, 191101. doi:10.1103/PhysRevLett.109.191101

Perrone, D., Bruno, R., D'Amicis, R., Telloni, D., De Marco, R., Stangalini, M., et al. (2020). Coherent events at ion scales in the inner Heliosphere: arker Solar Probe

observations during the first Encounter. Preprint repository name [Preprint]. Available at: arXiv:2010.02578 (Accessed October 06, 2020).

Podesta, J. J. (2017). How to define the mean square amplitude of solar wind fluctuations with respect to the local mean magnetic field. *J. Geophys. Res.: Space Physics* 122 (11), 835–844. doi:10.1002/2017JA023864

Ruzmaikin, A. A., Feynman, J., Goldstein, B. E., Smith, E. J., and Balogh, A. (1995). Intermittent turbulence in solar wind from the south polar hole. *J. Geophys. Res.* 100, 3395–3403. doi:10.1029/94JA02808

Salem, C., Mangeney, A., Bale, S. D., and Veltri, P. (2009). Solar wind Magnetohydrodynamics turbulence: anomalous scaling and role of intermittency. *Astrophys. J.* 702, 537–553. doi:10.1088/0004-637x/702/1/537

She, Z. S., and Leveque, E. (1994). Universal scaling laws in fully developed turbulence. *Phys. Rev. Lett.* 72, 336–339. doi:10.1103/PhysRevLett.72.336

Sorriso-Valvo, L., Catapano, F., Retinò, A., Le Contel, O., Perrone, D., Roberts, O. W., et al. (2019). Turbulence-driven ion beams in the magnetospheric kelvin-helmholtz instability. *Phys. Rev. Lett.* 122, 035102. doi:10.1103/PhysRevLett.122.035102

Sorriso-Valvo, L., Carbone, F., Leonardis, E., Chen, C. H., Safrankova, J., and Nemecek, Z. (2017). Multifractal analysis of high resolution solar wind proton density measurements. *Adv. Space Res.* 59, 1642–1651. doi:10.1016/j.asr.2016.12.024

Sorriso-Valvo, L., Carbone, V., Giuliani, P., Veltri, P., Bruno, R., Antoni, V., et al. (2001). Intermittency in plasma turbulence. *Planet. Space Sci.* 49, 1193–1200. doi:10.1016/S0032-0633(01)00060-5

Sorriso-Valvo, L., Carbone, V., Veltri, P., Consolini, G., and Bruno, R. (1999). Intermittency in the solar wind turbulence through probability distribution functions of fluctuations. *Geophys. Res. Lett.* 26, 1801–1804. doi:10.1029/1999GL900270

Teodorescu, E., and Echim, M. (2020). Open-source software analysis tool to investigate space plasma turbulence and nonlinear dynamics (odyn). *Earth Space Sci.* 7, e2019EA001004. doi:10.1029/2019EA001004

Tu, C.-Y., Marsch, E., and Rosenbauer, H. (1996). An extended structure-function model and its application to the analysis of solar wind intermittency properties. *Ann. Geophys.* 14, 270–285. doi:10.1007/s00585-996-0270-9

Tu, C. Y., and Marsch, E. (1995). Magnetohydrodynamic structures waves and turbulence in the solar wind - observations and theories. *Space Sci. Rev.* 73, 1–210. doi:10.1007/BF00748891

Vörös, Z., Leubner, M. P., and Baumjohann, W. (2006). Cross-scale coupling-induced intermittency near interplanetary shocks. *J. Geophys. Res.* 111, A02102. doi:10.1029/2005JA011479

Veltri, P., and Mangeney, A. (1999). "Scaling laws and intermittent structures in solar wind MHD turbulence," in *American institute of physics conference series*, Editors. S. R. Habbal, R. Esser, J. V. Hollweg, and P. A. Isenberg (New York : American Institute of Physics Conference Series), Vol. 471, 543–546.

Wan, M., Osman, K. T., Matthaeus, W. H., and Oughton, S. (2011). Investigation of intermittency in magnetohydrodynamics and solar wind turbulence: scale-dependent kurtosis. *Astrophys. J.* 744, 171. doi:10.1088/0004-637x/744/2/171

Wan, M., Matthaeus, W. H., Karimabadi, H., Roytershteyn, V., Shay, M., Wu, P., et al. (2012). Intermittent dissipation at kinetic scales in collisionless plasma turbulence. *Phys. Rev. Lett.* 109, 195001. doi:10.1103/PhysRevLett.109.195001

Wawrzaszek, A., Echim, M., and Bruno, R. (2019). Multifractal analysis of heliospheric magnetic field fluctuations observed by ulysses. *Astrophys. J.* 876, 153. doi:10.3847/1538-4357/ab1750

Wawrzaszek, A., Echim, M., Macek, W. M., and Bruno, R. (2015). Evolution of intermittency in the slow and fast solar wind beyond the ecliptic plane. *Astrophys. J. Lett.* 814, L19. doi:10.1088/2041-8205/814/2/L19

Wawrzaszek, A., and Macek, W. M. (2010). Observation of the multifractal spectrum in solar wind turbulence by ulysses at high latitudes. *J. Geophys. Res.* 115, A07104. doi:10.1029/2009JA015176

Wicks, R. T., Horbury, T. S., Chen, C. H. K., and Schekochihin, A. A. (2010). Power and spectral index anisotropy of the entire inertial range of turbulence in the fast solar wind. *Mon. Not. Roy. Astron. Soc. Lett.* 407, L31–L35. doi:10.1111/j.1745-3933.2010.00898.x

Xu, F., and Borovsky, J. E. (2015). A new four-plasma categorization scheme for the solar wind. *J. Geophys. Res.* 120, 70–100. doi:10.1002/2014JA020412

Yang, Y.-H., and Tam, S. W. (2010). Intermittency analysis and spatial dependence of magnetic field disturbances in the fast solar wind. *J. Atmos. Sol. Terr. Phys.* 72, 97–108. doi:10.1016/j.jastp.2009.10.013

Yordanova, E., Balogh, A., Noullez, A., and von Steiger, R. (2009). Turbulence and intermittency in the heliospheric magnetic field in fast and slow solar wind. *J. Geophys. Res.* 114, A08101. doi:10.1029/2009JA014067

Conflict of Interest: The authors declare that the research was conducted in the absence of any commercial or financial relationships that could be construed as a potential conflict of interest.

frontiers in Astronomy and Space Sciences

REVIEW
published: 25 January 2021
doi: 10.3389/fspas.2020.611909

Driving and Dissipation of Solar-Wind Turbulence: What is the Evidence?

Charles W. Smith and Bernard J. Vasquez*

Physics Department and Space Science Center, Morse Hall, University of New Hampshire, Durham, NH, United States

Fifty years of solar wind observations have provided extensive data that drives an evolving view of the fundamental nature and dynamics of the magnetic, velocity, and density fluctuations that are ubiquitous throughout the heliosphere. Despite the ongoing examination of ever improving data, fundamental questions remain unanswered because there are very few multi-point measurements from a sufficient number of spacecraft in close proximity to fully resolve the three-dimensional dynamics that are at the heart of the problem. Simulations provide new insights and new questions, but most simulations sacrifice one aspect of plasma physics in order to address another. Computers and computational methods remain insufficient to simulate fully compressive, fully nonlinear, collisionless plasma dynamics with sufficient spatial range and dimension to be considered a complete description of solar wind turbulence. For these reasons, there remain multiple divergent opinions as to the underlying dynamics of solar wind turbulence, dissipation, and the observed heating of the thermal plasma. We review observations of solar wind turbulence in so far as they contribute to an understanding of solar wind heating through the existence of energy reservoirs, the dynamics that move energy from the reservoirs to the dissipation scales, and the conversion into heat of energy associated with coherent fluctuations.

Keywords: instabilities, magnetic fields, solar wind, sun: heliosphere, turbulence, waves

OPEN ACCESS

Edited by:
Joseph Eric Borovsky,
Space Science Institute, United States

Reviewed by:
Chuanyi Tu,
Peking University, China
Francesco Malara,
University of Calabria, Italy

****Correspondence:***
Charles W. Smith
Charles.Smith@unh.edu

Specialty section:
This article was submitted to Space Physics, a section of the journal Frontiers in Astronomy and Space Sciences

Received: *29 September 2020*
Accepted: *11 December 2020*
Published: *25 January 2021*

Citation:
Smith CW and Vasquez BJ (2021) Driving and Dissipation of Solar-Wind Turbulence: What is the Evidence?. Front. Astron. Space Sci. 7:611909. doi: 10.3389/fspas.2020.611909

1 INTRODUCTION

For decades the fundamental nature of fluctuations in the solar wind has been the object of debate. Two schools of thought have structured that debate. In the first, fluctuations are described as waves, most often solutions to the linearized dynamical equation, and the leading wave form has been Alfvén waves (Coleman, 1966; Völk and Alpers, 1973; Denskat and Burlaga, 1977; Heinemann and Olbert, 1980). In the second, fluctuations are described as being the result of diverse nonlinear dynamics that are the magnetized plasma equivalent of traditional hydrodynamic turbulence (Coleman, 1968; Bavassano et al., 1982; Matthaeus and Goldstein, 1982; Goldstein et al., 1995).

Early formulations of these ideas were based primarily on the observed power spectrum, fluctuation anisotropy, and cross-field correlation (Belcher and Davis, 1971). The view evolved and became dominant that the fluctuations originated with noncompressive waves in the sub-Alfvénic region of the solar atmosphere. These waves then propagate outward and across the point where the flow becomes super-Alfvénic. This transition acts as a filter for waves propagating at the Alfvén speed resulting solar wind oscillations that are dominated by outward-propagating Alfvén waves. This explains the fact that fluctuations (both magnetic and kinetic) tend to be noncompressive and transverse to the local mean magnetic field with a reproducible power spectrum that reflects the turbulence in the collision-dominated corona.

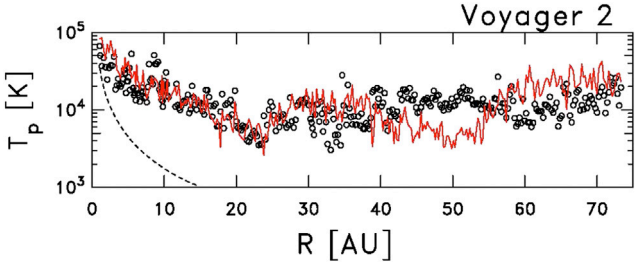

FIGURE 1 | Average solar wind proton temperature as seen by Voyager 2 (circles) and prediction of transport theory (red curve). Dashed line represents predicted proton temperature derived assuming adiabatic expansion from 1 AU (Taken from Smith et al. (2006c).

Attempts to build on this idea led to difficulties where predictions disagreed with observations. Notably, WKB theory that was used to predict the evolution of nonevolving waves with heliocentric distance was unable to account for the apparent ability of the magnetic fluctuations to remain transverse to the local mean magnetic field that rotates according to the Parker spiral (Hollweg, 1990). The local destruction and reformation of the waves would permit the newly formed waves to reorient if the dynamics were anisotropic with regard to the mean magnetic field and simulations indicate that they are (Shebalin et al., 1983; Matthaeus et al., 1990; Matthaeus et al., 1996a, Matthaeus et al., 1998; Ghosh and Goldstein, 1997; Ghosh et al., 1998a; Ghosh et al., 1998b; Cho and Vishniac, 2000; Vasquez et al., 2014). However, that means that processes normally associated with turbulence would be active and wave propagation alone could not explain the observations. At this same time, there was a growing recognition that thermal ions in the solar wind were experiencing *in situ* heating and the source was not recognized. It is a basic attribute of hydrodynamics (HD) that the turbulent fluctuation energy is moved to fluctuations at smaller scales where dissipation results in heating.

In this paper we review the evidence for turbulent *in situ* dynamics that results in the heating of the solar wind. We examine studies of solar wind fluctuations at all scales in an effort to better understand the generation, transport, and dissipation of fluctuation energy that results in the heating of the solar wind.

2 SOLAR WIND HEATING

It has become entirely evident that some *in situ* process heats the ambient thermal proton population of the solar wind. **Figure 1** shows the temperature of solar wind thermal ions as measured by the Voyager 2 spacecraft (Smith et al., 2006c). The departure from adiabatic expansion from 1 AU onward clearly shows the need for some form of heating in the solar wind (Gazis et al., 1994; Richardson et al., 1995). The radial variation of the solar wind proton temperature inside 1 AU as seen by the Helios spacecraft likewise shows the need for a heating source (Marsch et al., 1983; Schwenn, 1983; Lopez and Freeman, 1986; Arya and Freeman, 1991; Freeman et al., 1992; Totten et al., 1995; Verma et al., 1995; Vasquez et al., 2007; Hellinger et al., 2013; Lamarche et al., 2014).

Early attempts to explain the apparent heating often resembled the theories of heating that result in the acceleration of the wind from the solar corona. One notable theory, known as the cyclotron sweep mechanism, asked if it were possible to dissipate a static spectrum of magnetic fluctuations such that as the plasma moved away from the Sun and the spatial scale associated with various dissipation processes increased? Could dissipation of the observed spectrum in this manner provide the necessary energy to account for solar wind heating (Hollweg and Turner, 1978; Tu and Marsch, 1997)? It cannot (Schwartz et al., 1981). It is necessary to replace the energy that is consumed by dissipation processes or some other heating mechanism and associated source must be found to account for the observed energy budget.

Without attempting to identify the source, Vasquez et al. (2007) examined published results of the thermal proton temperature as a function of wind speed and heliocentric distance to obtain the rate of proton heating at 1 AU. They get the following expression:

$$\epsilon_{V\,asquez} = 3.6 \times 10^{-5} T_P V_{SW} \tag{1}$$

where $\epsilon_{Vasquez}$ is given in J/(kg s), T_P is given in Kelvin, and V_{SW} is given in km s^{-1}. For typical solar wind conditions, $\epsilon_{Vasquez}$ varies from 10^2 to 10^4 J/(kg s).

3 THE TURBULENT SPECTRUM

The overriding limitation of turbulence studies in space is that there is rarely more than one spacecraft in a region of interest. It is not possible to directly measure the nonlinear dynamics, or even the multi-dimensional spectrum, of fluctuations with a single spacecraft. There are techniques that attempt to overcome this limitation with interesting results, but in the end what is needed to make real progress in understanding any turbulent system is the ability to make measurements separated at multiple points in close proximity where the spacing of the measurements reflects the scale being studied. HelioSwarm is a proposed NASA MIDEX mission currently in a Phase-A study that will perform the multipoint measurement required to understand solar wind turbulence (Spence, 2019; Hautaluoma and Fox, 2020).

The cadence of magnetic measurements in the solar wind is generally more rapid than it is for thermal ion measurements. Therefore, there are more studies of solar wind turbulence using magnetic field measurements. The magnetic spectrum is generally divided into three ranges. There is the energy-containing range that is seen at 1 AU at spacecraft-frame frequencies $f_{sc} < 10^{-4}$ Hz. These are spatial scales greater than the nominal correlation scale for the fluctuations where dynamics that are thought to originate at the Sun and persisted to the point of observation. In other words, they are direct measure of solar dynamics. The power spectrum of the energy-containing range is typically $P \sim f_{sc}^{-1}$. At lower frequencies the measured spectrum includes signals from large-scale transient solar activity, solar

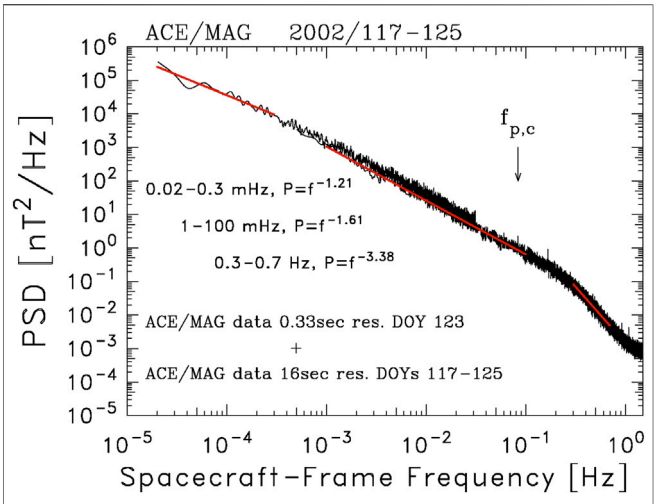

FIGURE 2 | Composite spectrum using a nine-day interval of low-resolution magnetic field data from the ACE spacecraft and a single day of high-resolution data. Frequencies >1 Hz show aliasing from unresolved higher frequencies. The analysis is described in the text.

rotation, and the solar cycle. Between the correlation scale (30 min–1 h at 1 AU) and the dissipation scale (typically ~2–5 s at 1 AU) is the inertial range. This is thought to represent the nondissipative nonlinear dynamics that transport energy through the spatial scales in a conservative manner. The power spectrum of the inertial range is often characterized at $f_{sc}^{-5/3}$, but finite intervals of data can display a wide range of spectral indices and different theories for the dominant nonlinear dynamics predict varying spectral indices (Iroshnikov, 1964; Kraichnan, 1965; Matthaeus and Zhou, 1989; Goldreich and Sridhar, 1995; Goldreich and Sridhar, 1997; Leamon et al., 1999; Oughton and Matthaeus, 2020). At still smaller scales, the spectrum steepens and often demonstrates polarization signatures in association with the onset of dissipation.

Figure 2 shows a typical spectrum of the interplanetary magnetic field to illustrate the above description. It is a composite of two analyses using the Blackman–Tukey spectral technique (Blackman and Tukey, 1958). In the first analysis, nine days of data from days 117 through 125 of 2002 from the Advanced Composition Explorer (ACE) spacecraft with 16 s resolution is used to produce a measured spectrum from 2×10^{-5} to 3×10^{-2} Hz. This is a series of short-lived compression and rarefaction flows, each spanning ~1 day. The frequency range from 2×10^{-5} to 3×10^{-4} Hz is fit with a power law to obtain $f_{sc}^{-1.21 \pm 0.02}$. This is an example of the energy-containing range. In this spectrum, there is a subtle break in the spectral index to a steeper form that occurs at $f_{sc} \sim 5 \times 10^{-4}$ Hz. In the second analysis, overlayed on the same figure, 24 h of high resolution data from day 123 of the same mission is used to produce a measured spectrum from 5×10^{-4} to 1.5 Hz. This is a rarefaction interval of expanding solar wind flow. Two frequency ranges are fit to this spectrum. The first extends from 5×10^{-4} to 0.1 Hz and is fit to a power law $\sim f_{sc}^{-1.61 \pm 0.01}$. This represents the inertial range. The last frequency range extends from 0.3 to 0.7 Hz and is fit to $f_{sc}^{-3.38 \pm 0.01}$. This represents the dissipation range. The spectral break at ~0.2 Hz marks the onset of dissipation.

3.1 The Inertial Range

The inertial range is the most studied portion of the spectrum and the original source of the debate between waves or turbulence? Fluctuations are largely transverse to the local mean magnetic field, which suggests they are noncompressive (Belcher and Davis, 1971). This fluctuation anisotropy has now been shown to be equally correlated to two plasma parameters: the thermal proton $\beta_p = 8\pi N_P k_B T_P B_0^{-2}$ where N_P is the proton number density, k_B is Boltzman's constant, and T_P is the proton temperature and the ratio of the magnetic fluctuation amplitude to the mean field strength $\delta B/B_0$ (Smith et al., 2006b; Pine et al., 2020b). This implies that the relative strength of the compressive fluctuations depends on one of these two parameters.

Belcher and Davis (1971) demonstrated not only the above fluctuation anisotropy, but also that the two components perpendicular to the mean field had slightly different power levels at 5:4. While this fact was widely ignored and thought to be insignificant, Bieber et al. (1996) demonstrated that the ratio of the two perpendicular components is an indication of the anisotropy of the underlying wave vectors. Using their formalism, it is easy to show that the ratio 5:4 with a nominal mean field winding angle of 45° is indicative of a dominant 2D component meaning that the wave vectors as well as the fluctuations are largely confined to the plane perpendicular to the mean magnetic field. Subsequent analyses of many data intervals have supported the assertion that the 2D component is dominant in most solar wind samples (Matthaeus et al., 1990; Leamon et al., 1998a; Dasso et al., 2005; Hamilton et al., 2008; MacBride et al., 2010).

Observations combined with numerous simulations (Matthaeus et al., 1998; Cho and Vishniac, 2000; Müller and Grappin, 2005; Boldyrev et al., 2009; Beresnyak, 2011) have led to the view that the inertial range is composed largely of 2D turbulence with an undetermined underlying dynamic. Wave theories have resurfaced to assert that both the inertial and dissipation range is primarily composed of interacting kinetic Alfvén waves that form a turbulent plasma system (Leamon et al., 1999; Bale et al., 2005; Howes et al., 2008; Howes and Quataert, 2010; Sahraoui et al., 2010; TenBarge et al., 2013; Narita et al., 2020), and while there are problems with this interpretation (Smith et al., 2012; Roberts and Li, 2015; Vasquez et al., 2018a) it remains a popular view.

In HD, Kolmogorov (1941a) argued that the spectral transport of energy through the fluctuation spectrum was isotropic, energy-conserving, and based on dynamics that are local within the spectrum. Using a structure function formalism, this lead to the famous prediction for the omnidirectional inertial-range spectrum

$$P_k = C_K \epsilon^{2/3} k^{-5/3} \tag{2}$$

where $C_K = 1.6$ (Batchelor, 1953), ϵ is the rate of energy transport through the inertial-range spectrum, and k is the wavenumber.

These ideas can be extended to magnetohydrodynamics (MHD) by employing the total energy (magnetic plus kinetic)

and adopting a new coefficient which has been shown to apply to average solar wind conditions at 1 AU (Matthaeus and Zhou, 1989; Vasquez et al., 2007). Integrating the omnidirectional spectrum and allowing for a ratio of magnetic to kinetic energy , the extension of **Eq. (2)** that describes the average rate of energy transport through the spectrum at 1 AU under changing solar wind conditions is

$$\epsilon_{MHD} = f_{sc}^{5/2} P_B^{3/2} 21.8^3 V_{SW}^{-1} N_P^{-3/2} \tag{3}$$

where P_B is the trace of the magnetic power spectral matrix in units of $\mathrm{nT}^2\ \mathrm{Hz}^{-1}$, V_{SW} is the solar wind speed in units of km s^{-1}, N_P is the thermal proton density in units of cm^{-3}, and 21.8 is a conversion factor. The factor V_{SW}^{-1} converts spacecraft-frame frequency to wave number and $N_P^{-3/2}$ converts the magnetic field to units of velocity. This yields ϵ_{MHD} in units of $\mathrm{km}^2\ \mathrm{s}^{-3}$. If we apply **Eq. (3)** to **Figure 2** at $f_{sc} = 10^{-2}$ Hz, using average plasma parameters $V_{\mathrm{SW}} = 400$ km s^{-1} and $N_p = 5\ \mathrm{cm}^{-3}$, we obtain $\epsilon_{MHD} = 7.3 \times 10^{-4}\ \mathrm{km}^2\ \mathrm{s}^{-3}$ cws If we apply **Eq. (1)** to the same data where the average thermal proton temperature is 9.3×10^4 K, we get an estimate for the average heating rate for a sample of this kind to be $\epsilon_{Vasquez} = 1.3 \times 10^{-3}\ \mathrm{km}^2\ \mathrm{s}^{-3}$ which is twice the value obtained from the power spectrum and **Eq. (3)**.

3.2 The Dissipation Range

In traditional HD, dissipation occurs at the smallest scales within the spectrum that are still described by fluid theory. The scale marking the spectral break and the onset of dissipation and the steepening of the spectrum depends on the rate of energy transfer through the inertial range (Smith et al., 2006a). When dissipation becomes competitive with the energy-conserving spectral transport of the inertial range, the spectrum steepens as energy is converted from fluid processes to heat.

In space, this is not the case (Leamon et al., 1999; Smith et al., 2001b; Smith et al., 2006a; Woodham et al., 2018; Pine et al., 2020a). There, the scale where dissipation sets in is determined by the ambient plasma parameters and the spectral slope associated with dissipation changes according to the rate of energy transport through the inertial range (Smith et al., 2006a; Pine et al., 2020a). Dissipation is marked by the breakdown of the fluid approximation and the necessary recovery of kinetic plasma theory. There are varying viewpoints of what dynamical processes are responsible for dissipation including cyclotron damping, Landau and transit time damping, and magnetic reconnection and those processes depend to a large degree on what form the inertial-range fluctuations take as they deliver energy to the dissipation scales (Isenberg, 1984; Isenberg, 1990; Goldstein et al., 1994; Hollweg and Isenberg, 2002; Gary et al., 2005; Isenberg and Vasquez, 2009; Parashar et al., 2009; Svidzinski et al., 2009; Markovskii et al., 2010a; Markovskii and Vasquez, 2010b; Chandran et al., 2010; Chang et al., 2011; Markovskii and Vasquez, 2011; Servidio et al., 2012; Vasquez and Markovskii, 2012; Markovskii and Vasquez, 2013a; Markovskii and Vasquez, 2013b; Bourouaine and Chandran, 2013; Chandran et al., 2013; Karimabadi et al., 2013; Kasper et al., 2013; Wu et al., 2013; Xia et al., 2013; Dalena et al., 2014; Hughes et al., 2014; Saito and Nariyuki, 2014; Servidio et al., 2014; Goldstein et al., 2015; Isenberg and Vasquez, 2015; Servidio et al., 2015; Vásconez et al., 2015; Vasquez, 2015; Wan et al., 2015; Franci et al., 2016; Gary, Hughes and Wang, 2016; Matthaeus et al., 2016; Parashar and Matthaeus, 2016; Pucci et al., 2016; Hughes et al., 2017a; Hughes et al., 2017b; Valentini et al., 2017; Yang et al., 2017; Woodham et al., 2018). Whatever the process, dissipation in space plasmas appears to become important at scales associated with the proton inertial scale or proton cyclotron scale which are strongly correlated in the solar wind at or beyond 1 AU (Pine et al., 2020a).

At the same frequency where the spectrum steepens due to dissipation (or does not if dissipation is weak), the spectrum often becomes polarized. The polarization of the dissipation range is consistent with the removal of outward propagating Alfvén waves via cyclotron damping, but analysis shows that this is only one of several active processes (Leamon et al., 1998b; Hamilton et al., 2008). Alternatively, the polarization sense could be due to the compressive nature of 2D turbulent fluctuations (Markovskii and Vasquez, 2016).

4 TRANSPORT THEORY

There are three basic questions to the turbulent heating the solar wind: (1) what is the energy reservoir, (2) how does the energy get to the dissipation scales, and (3) what is the heating dynamic? Current theory holds that there are two energy reservoirs. The first is the remnant solar wind fluctuations of the energy-containing range. This includes the large-scale flow gradients of the solar wind and it is primarily responsible for the heating of the solar wind inside 10 AU. The second is the various populations of interstellar neutral atoms, primarily hydrogen, that transit the heliosphere. When ionized, they form a pickup population of suprathermal ions that excite magnetic waves at inertial-range scales close to the dissipation range. This is the dominant energy source beyond 10 AU (Zank et al., 1996; Smith et al., 2006c; Pine et al., 2020c).

It is possible to derive a transport theory describing solar wind heating without knowing the actual dissipation processes in a manner analogous to the Taylor-von Kármán approach (Taylor, 1935; von Kármán and Howarth, 1938). Under the assumption that the energy-containing range can be described to predict a rate of energy delivery to inertial-range scales, and with a description of the rate at which interstellar pickup ions excite wave energy, and assuming that all energy that is injected into the inertial range will be transported to the spectrum dissipation scales, it is possible to write equations describing the rate of solar wind heating

$$\frac{\mathrm{d}Z^2}{\mathrm{d}r} = -\frac{A'}{r}Z^2 - \frac{\alpha}{U}\frac{Z^3}{\lambda} + \frac{\dot{E}_{PI}}{U}, \tag{4}$$

$$\frac{\mathrm{d}\lambda}{\mathrm{d}r} = -\frac{C'}{r}\lambda + \frac{\beta}{U}Z - \frac{\beta}{U}\frac{\lambda}{Z^2}\dot{E}_{PI}, \tag{5}$$

$$\frac{\mathrm{d}T}{\mathrm{d}r} = -\frac{4}{3}\frac{T}{r} + \frac{2}{3}\frac{m_p}{k_B}\frac{\alpha}{U}\frac{Z^3}{\lambda}. \tag{6}$$

Application of these equations has focused on the energy-containing scales where Z^2 is the total fluctuation energy

(magnetic plus kinetic) that is typically computed using hourly averages of the measured variables, λ is the similarity scale that is typically taken to be the correlation length, and T is the average temperature of the thermal protons. A', C', α and β, are heavily constrained by rotational symmetry, Taylor–Kármán local phenomenology, and solar wind conditions (Matthaeus et al., 1996b; Matthaeus et al., 1999). **Figure 1** uses $A' = -1.1$, $C' = 1.8$, $\alpha = 1$, and $\beta = 1$. The remaining parameters are the rate of energy injection into the turbulent spectrum by newborn interstellar PUIs E_{PI} which is obtained from other theories, the proton mass m_p, and Boltzmann's constant k_B.

The solution of these equations using parameters from 1 AU are represented by the red curve in **Figure 1**. Other, sometimes more involved, versions of transport theory that follow the same general approach exist that predict a greater range of measurements and a few attempt to build specific dissipation processes into the theory (Zhou and Matthaeus, 1990a, b; Matthaeus et al., 1994; Matthaeus et al., 1996b; Matthaeus et al., 1999; Williams and Zank, 1994; Williams et al., 1995; Richardson et al., 1995; Richardson et al., 1996; Zank et al., 1996; Zank et al., 2012; Zank et al., 2017; Smith et al., 2001a; Smith et al., 2006c; Richardson and Smith, 2003; Isenberg et al., 2003; Isenberg et al., 2010; Isenberg, 2005; Breech et al., 2005; Breech et al., 2008; Breech et al., 2009; Breech et al., 2010; Oughton et al., 2006; Oughton et al., 2011; Ng et al., 2010; Usmanov et al., 2012; Usmanov et al., 2014; Usmanov et al., 2016; Usmanov et al., 2018; Adhikari et al., 2015a; Adhikari et al., b, Adhikari et al., 2017).

The intent of transport theory is that by using reasonable parameterization of the spectrum that is tightly constrained by observation, it is possible to account for the decay of the turbulent spectrum, the evolution of the break between the energy-containing and inertial range, the rate of heating, and the observed plasma temperature. While this alone may not prove that solar wind turbulence is an active heliospheric process that is responsible for the heating, it does set the bar for other theories to match.

5 THIRD-MOMENT THEORY

Where Kolmogorov (1941a) argued a rate of energy transport through the HD inertial range based on local dynamics and dimensional analysis, it is possible to compute a rigorous expression for the rate of energy transport in the HD inertial-range spectrum (Kolmogorov, 1941b). By assuming isotropy, homogeneity, and stationarity, the rate of energy transport through the inertial range is given by

$$-(4/5)\epsilon^{HD}|\mathbf{L}| = \langle [V_L(\mathbf{x}+\mathbf{L}) - V_L(\mathbf{x})]^3 \rangle \tag{7}$$

where V_L is the component of the velocity fluctuation along the separation vector $\mathbf{L}$, $V_L \equiv \mathbf{V}\cdot\mathbf{L}/L$ where $L = |\mathbf{L}|$, ϵ^{HD} is the rate of energy cascade, and $\langle \ldots \rangle$ denote ensemble average. In single-spacecraft studies using the Taylor frozen-in-flx assumtion, V_L is the radial component of the flow.

Politano and Pouquet (1998a, b) extend the Kolmogorov (1941b) analysis to include incompressible MHD turbulence using the Elsässer variables (Elsässer, 1950)

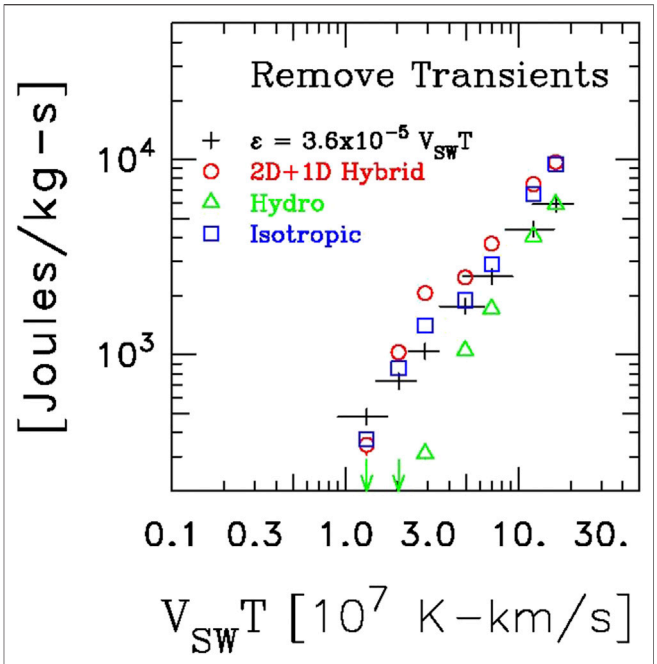

FIGURE 3 | Application of **Eqs (9)** and **(10)** years of data from the Advanced Composition Explorer (ACE) spacecraft [Reproduced from Stawarz et al. (2009)].

$$\mathbf{Z}^{\pm} \equiv \mathbf{V} \pm \mathbf{B}/\sqrt{4\pi\rho} \tag{8}$$

where ρ is the mass density. Their expression for the spectral transport of energy in an isotropic MHD system is

$$(4/3)\epsilon^{\pm}_{ISO} V\tau = \langle \Delta Z^{\mp}_R(\tau) \sum_i [\Delta Z^{\pm}_i(\tau)]^2 \rangle \tag{9}$$

where τ is the positive time lag and $\sum_i$ is the sum over all three vector components. The subscript "R" denotes the Radial component directed from the Sun's center to the point of measurement. The total spectral transport of energy is given by

$$\epsilon^T = (\epsilon^+ + \epsilon^-)/2. \tag{10}$$

It is straightforward to extend this analysis to include other geometries including 2D. When we apply this formalism to the data represented in **Figure 2**, we get an average $\epsilon_T = 3 \times 10^{-4}\,\mathrm{km^2\,s^{-3}}$. This is half the value we obtained from **Eq. (3)** and a fourth the value we obtained from **Eq. (1)**, but Stawarz et al. (2009) and Coburn et al. (2012) found better agreement between the third-moment expression and $\epsilon_{vasquez}$ when averaging a larger sample of observations.

Figure 3 compares the spectral transport of energy as computed using **Eq. (9)** for several different assumptions of geometry along with the scaling shown to be accurate by Vasquez et al. (2007) and the comparison is favorable. Since the results of (Vasquez et al., 2007) were obtained by examining Helios results, it represents a ground truth for the local heating rate at 1 AU. This comparison offers strong evidence that the solar wind fluctuation spectrum is not a static collection of non-

interacting fluctuations and can be described by extensions of the HD concepts to embrace the added dynamics of MHD.

Third-moment analyses have been developed and applied to varying solar wind conditions using single- and multi-spacecraft techniques and with efforts to extend the analysis to compressive fluctuations (MacBride et al., 2005, 2008; Sorriso-Valvo et al., 2007; Marino et al., 2008; Carbone et al., 2009; Smith et al., 2009; Stawarz et al., 2009, 2010, 2011; Wan et al., 2009; Forman et al., 2010; Osman et al., 2011; Coburn et al., 2012, 2014, 2015; Banerjee et al., 2016; Hadid et al., 2017; Vasquez et al., 2018b; Smith et al., 2018; Sorriso-Valvo et al., 2018). The compressive formalisms show agreement with the incompressible formalism under most applications as would be expected since density fluctuations in the solar wind are small.

6 INTERMITTENT HEATING

Intermittency is generally described as the result of nonlocal dynamics contributing to the spectral transport of energy (Kolmogorov, 1962). The leading diagnostic is obtained by comparing the relative value of high-order structure functions. However, if we generalize the concept of intermittency to represent the non-steady transfer of energy, we can make a direct measure of this using the third-moment techniques described above.

Third moments computed at lags corresponding to inertial-range scales are expected to be a linear function of lag with the slope proportional to the rate of energy transport through the spectrum. Using data samples comparable in duration to the measured correlation length of the magnetic fluctuations, it is possible to show that estimates of the third-moment expressions describing spectral transfer vary significantly (Coburn et al., 2014; Coburn et al., 2015). The mean of the distribution of ϵ values agrees well with the average local heating rate of the solar wind under diverse conditions as described above, but the standard deviation is $\sim 10\times$ the mean. Despite this variation, estimates are generally linear functions as expected and yield seemingly convergent functions. However, the correlation length for primitive variables (magnetic field, velocity, density) may not correspond to the correlation length for the third-order functions and it is this length that must be used when combining statistically independent estimates of the spectral transport rate.

Smith et al. (2018) measured the correlation length for third-moment expressions using the same data that produced **Figure 2** and found that the correlation length was 20% of the lag value. This means that the third moment expressions decorrelate in a fraction of the scale of interest, indicating that the nonlinear dynamics of the inertial range changes significantly over any scale of interest. For instance, fluctuations seen at 0.01 Hz in the spacecraft frame have a spatial scale $L = 400/0.01 = 4 \times 10^4$ km assuming a wind speed of 400 km s^{-1}. The nonlinear dynamics associated with this scale can be expected to change significantly over $\sim L/5 = 8 \times 10^3$ km. This is significantly less than the 30 min to 1 h scale over which the primitive variables decorrelate.

The conclusion from this is that the spectral transfer rate is highly variable in both time and scale with energy being transfered to both smaller and larger scales at a mean-square rate that is 10× what is needed to account for the average heating rate. This ongoing redistribution of energy maintains the spectral form despite the fact that newborn interstellar pickup ions (PUIs) are responsible for driving the spectrum beyond 10 AU by depositing energy at scales close to the dissipation scale (Smith et al., 2001a; Smith et al., 2006c; Pine et al., 2020c). Therefore, the nonlinear dynamics that support solar wind turbulence are much stronger than is normally inferred from the average heating rate needed to account for the observed heating.

7 SUMMARY

We began by discussing the multiple views that attempt to describe solar wind turbulence. To date, there is no definitive resolution to that controversy. The general morphology that describes the various ranges of the turbulent spectrum, dividing it into energy-containing, inertial, and dissipation range spans the various views, but those views offer different interpretations of the underlying dynamics. Those various dynamics each lead to predictions for the inertial-range power spectrum analogous to **Eq. (2)**. Different forms of the transport equations, as represented here by **Eqs (4)–(6)**, can be derived based on those same assumptions of the underlying dynamics. However, **Eq. (9)** embraces all underlying dynamics subject to an assumption of the underlying geometry of the wave vectors. In this way, it does provide one example of rigorous universality against which various theories of solar wind turbulence can be tested.

AUTHOR CONTRIBUTIONS

CS lead the effort in this review. BV provided material on solar wind heating and energy cascade rate estimation especially at 1 AU. Both authors contributed to the overall presentation of the review and revised the manuscript before submission.

FUNDING

CS is supported by NASA Grant NNX17AB86G and by the Advanced Composition Explorer mission. BV is supported by NASA Grant 80NSSC19K0832. CS and BV are partially supported by NASA Grant 80NSSC17K0009 and NSF SHINE AGS1622413.

ACKNOWLEDGMENTS

The data used in this analysis are available from the National Space Science Data Center and ACE Science Center.

REFERENCES

Adhikari, L., Zank, G. P., Bruno, R., Telloni, D., Hunana, P., Dosch, A., et al. (2015b). The transport of low-frequency turbulence in the super-Alfvénic solar wind. *J. Phys. Conf. Series* 642, 012001. doi:10.1088/1742-6596/642/1/012001

Adhikari, L., Zank, G. P., Bruno, R., Telloni, D., Hunana, P., Dosch, A., et al. (2015a). The transport of low-frequency turbulence in astrophysical flows. Ii. Solutions for the super-alfvénic solar wind. *APJ (Acta Pathol. Jpn.)* 805, 63. doi:10.1088/0004-637x/805/1/63

Adhikari, L., Zank, G. P., Hunana, P., Shiota, D., Bruno, R., Hu, Q., et al. (2017). II. Transport of nearly incompressible magnetohydrodynamic turbulence from 1 to 75 au. *APJ (Acta Pathol. Jpn.)* 841, 85. doi:10.3847/1538-4357/aa6f5d

Arya, S., and Freeman, J. W. (1991). Estimates of solar wind velocity gradients between 0.3 and 1 AU based on velocity probability distributions from Helios 1 at perihelion and aphelion. *J. Geophys. Res*. 96 (14), 183. doi:10.1029/91ja01135

Bale, S. D., Kellogg, P. J., Mozer, F. S., Horbury, T. S., and Reme, H. (2005). Measurement of the electric fluctuation spectrum of magnetohydrodynamic turbulence. *Phys. Rev. Lett* 94, 215002. doi:10.1103/PhysRevLett.94.215002

Banerjee, S., Hadid, L. Z., Sahraoui, F., and Galtier, S. (2016). Scaling of compressible magnetohydrodynamic turbulence in the fast solar wind. *APJ (Acta Pathol. Jpn.)* 829, L27. doi:10.3847/2041-8205/829/2/l27

Batchelor, G. K. (1953). *The theory of homogeneous turbulence*. New York: Cambridge University Press.

Bavassano, B., Dobrowolny, M., Mariani, F., and Ness, N. F. (1982). Radial evolution of power spectra of interplanetary Alfvénic turbulence. *J. Geophys. Res.* 87, 3617. doi:10.1029/ja087ia05p03617

Belcher, J. W., and Davis, L., Jr. (1971). Large-amplitude Alfvén waves in the interplanetary medium, 2. *J. Geophys. Res.* 76, 3534–3563. doi:10.1029/ja076i016p03534

Beresnyak, A. (2011). Spectral slope and Kolmogorov constant of MHD turbulence. *Phys. Rev. Lett.* 106, 075001. doi:10.1103/PhysRevLett.106.075001

Bieber, J. W., Wanner, W., and Matthaeus, W. H. (1996). Dominant two-dimensional solar wind turbulence with implications for cosmic ray transport. *J. Geophys. Res.* 101, 2511–2522. doi:10.1029/95ja02588

Blackman, R. B., and Tukey, J. W. (1958). *The measurement of power spectra*. Mineola, NY: Dover.

Boldyrev, S., Mason, J., and Cattaneo, F. (2009). Dynamic alignment and exact scaling laws in magnetohydrodynamic turbulence. *APJ (Acta Pathol. Jpn.)* 699, L39. doi:10.1088/0004-637x/699/1/l39

Bourouaine, S., and Chandran, B. D. G. (2013). Observational test OF stochastic heating IN LOW-β fast-solar-wind streams. *APJ (Acta Pathol. Jpn.)* 774, 96. doi:10.1088/0004-637x/774/2/96

Breech, B., Cranmer, S. R., Matthaeus, W. H., Kasper, J. C., and Oughton, S. (2010). "Heating of the solar wind with electron and proton effects," in Twelfth international solar wind conference, 214–217.

Breech, B., Matthaeus, W. H., Minnie, J., Oughton, S., Parhi, S., Bieber, J. W., et al. (2005). Radial evolution of cross helicity in high-latitude solar wind. *Geophys. Res. Lett.* 32, L06103. doi:10.1029/2004gl022321

Breech, B., Matthaeus, W. H., Cranmer, S. R., Kasper, J. C., and Oughton, S. (2009). Electron and proton heating by solar wind turbulence. *J. Geophys. Res.* 114, 287. doi:10.1029/2009ja014354

Breech, B., Matthaeus, W. H., Minnie, J., Bieber, J. W., Oughton, S., Smith, C. W., et al. (2008). Turbulence transport throughout the heliosphere. *J. Geophys. Res.* 113, 333. doi:10.1029/2007ja012711

Carbone, V., Marino, R., Sorriso-Valvo, L., Noullez, A., and Bruno, R. (2009). Scaling laws of turbulence and heating of fast solar wind: the role of density fluctuations. *Phys. Rev. Lett.* 103, 061102. doi:10.1103/PhysRevLett.103.061102

Chandran, B. D. G., Li, B., Rogers, B. N., Quataert, E., and Germaschewski, K. (2010). Perpendicular ion heating by low-frequency alfvén-wave turbulence in the solar wind. *APJ (Acta Pathol. Jpn.)* 720, 503. doi:10.1088/0004-637x/720/1/503

Chandran, B. D. G., Verscharen, D., Quataert, E., Kasper, J. C., Isenberg, P. A., and Bourouaine, S. (2013). Stochastic heating, differential flow, and the alpha-to-proton temperature ratio in the solar wind. *APJ (Acta Pathol. Jpn.)* 776, 45. doi:10.1088/0004-637x/776/1/45

Chang, O., Peter Gary, S., and Wang, J. (2011). Whistler turbulence forward cascade: three-dimensional particle-in-cell simulations. *Geophys. Res. Lett.* 38, 123. doi:10.1029/2011gl049827

Cho, J., and Vishniac, E. T. (2000). The anisotropy of magnetohydrodynamic alfvenic turbulence. *APJ (Acta Pathol. Jpn.)* 539, 273. doi:10.1086/309213

Coburn, J. T., Forman, M. A., Smith, C. W., Vasquez, B. J., and Stawarz, J. E. (2015). Third-moment descriptions of the interplanetary turbulent cascade, intermittency and back transfer. *Phil. Trans. Royal Soc. A*. 373, 20140150. doi:10.1098/rsta.2014.0150

Coburn, J. T., Smith, C. W., Vasquez, B. J., Forman, M. A., and Stawarz, J. E. (2014). Variable cascade dynamics and intermittency in the solar wind at 1 AU. *APJ (Acta Pathol. Jpn.)* 786, 52. doi:10.1088/0004-637x/786/1/52

Coburn, J. T., Smith, C. W., Vasquez, B. J., Stawarz, J. E., and Forman, M. A. (2012). The turbulent cascade and proton heating in the solar wind during solar minimum. *APJ (Acta Pathol. Jpn.)* 754, 93. doi:10.1088/0004-637x/754/2/93

Coleman, P. J. J., Jr. (1968). Turbulence, viscosity, and dissipation in the solar-wind plasma. *APJ (Acta Pathol. Jpn.)* 153, 371–388. doi:10.1086/149674

Coleman, P. J., Jr. (1966). Hydromagnetic waves in the interplanetary plasma. *Phys. Rev. Lett.* 17, 207–211. doi:10.1103/physrevlett.17.207

Dalena, S., Rappazzo, A. F., Dmitruk, P., Greco, A., and Matthaeus, W. H. (2014). Test-particle acceleration in a hierarchical three-dimensional turbulence model. *APJ (Acta Pathol. Jpn.)* 783, 143. doi:10.1088/0004-637x/783/2/143

Dasso, S., Milano, L. J., Matthaeus, W. H., and Smith, C. W. (2005). Anisotropy in fast and slow solar wind fluctuations. *APJ (Acta Pathol. Jpn.)* 635, L181–L184. doi:10.1086/499559

Denskat, K. U., and Burlaga, L. F. (1977). Multispacecraft observations of microscale fluctuations in the solar wind. *J. Geophys. Res.* 82, 2693. doi:10.1029/ja082i019p02693

Elsässer, W. M. (1950). The hydromagnetic equations. *Phys. Rev*. 79, 183. doi:10.1103/physrev.79.183

Forman, M. A., Smith, C. W., and Vasquez, B. J. (2010). Comment on "Scaling laws of turbulence and heating of fast solar wind: the role of density fluctuations". *Phys. Rev. Lett*. 104, 189001. doi:10.1103/PhysRevLett.104.189001

Franci, L., Landi, S., Matteini, L., Verdini, A., and Hellinger, P. (2016). Plasma beta dependence of the ion-scale spectral break of solar wind turbulence: high-resolution 2D hybrid simulations. *APJ (Acta Pathol. Jpn.)* 833, 91. doi:10.3847/1538-4357/833/1/91

Freeman, J. W., Totten, T., and Arya, S. (1992). A determination of the polytropic index of the free streaming solar wind using improved temperature and density radial power-law indices. *EOS. Trans. AGU* 73, 238.

Gary, S. P., Hughes, R. S., and Wang, J. (2016). Whistler turbulence heating of electrons and ions: three-dimensional particle-in-cell simulations. *APJ (Acta Pathol. Jpn.)* 816, 102. doi:10.3847/0004-637x/816/2/102

Gary, S. P., Smith, C. W., and Skoug, R. M. (2005). Signatures of Alfvén-cyclotron wave-ion scattering: Advanced Composition Explorer (ACE) solar wind observations. *J. Geophys. Res* 110, A07108. doi:10.1029/2004ja010569

Gazis, P. R., Barnes, A., Mihalov, J. D., and Lazarus, A. J. (1994). Solar wind velocity and temperature in the outer heliosphere. *J. Geophys. Res*. 99, 6561–6573. doi:10.1029/93ja03144

Ghosh, S., Matthaeus, W. H., Roberts, D. A., and Goldstein, M. L. (1998a). The evolution of slab fluctuations in the presence of pressure-balanced magnetic structures and velocity shears. *J. Geophys. Res* 103 (23), 691–723.704doi:10.1029/98ja02195

Ghosh, S., Matthaeus, W. H., Roberts, D. A., and Goldstein, M. L. (1998b). Waves, structures, and the appearance of two-component turbulence in the solar wind. *J. Geophys. Res.* 103 (23), 705–723. doi:10.1029/98ja02194

Ghosh, S., and Goldstein, M. L. (1997). Anisotropy in Hall MHD turbulence due to a mean magnetic field. *J. Plasma Phys* 57, 129–154. doi:10.1017/s0022377896005260

Goldreich, P., and Sridhar, S. (1997). Magnetohydrodynamic turbulence revisited. *APJ (Acta Pathol. Jpn.)* 485, 680–688. doi:10.1086/304442

Goldreich, P., and Sridhar, S. (1995). Toward a theory of interstellar turbulence. 2: strong alfvenic turbulence. *APJ (Acta Pathol. Jpn.)* 438, 763–775. doi:10.1086/175121

Goldstein, M. L., Roberts, D. A., and Fitch, C. A. (1994). Properties of the fluctuating magnetic helicity in the inertial and dissipation ranges of solar wind turbulence. *J. Geophys. Res.* 99 (11), 519–611. doi:10.1029/94ja00789

Goldstein, M. L., Wicks, R. T., Perri, S., and Sahraoui, F. (2015). Kinetic scale turbulence and dissipation in the solar wind: key observational results and future outlook. *Philos Trans A Math Phys Eng Sci*. 373, 20140147. doi:10.1098/rsta.2014.0147

Goldstein, M. L., Roberts, D. A., and Matthaeus, W. H. (1995). Magnetohydrodynamic turbulence in the solar wind. *Annu. Rev. Astron. Astrophys* 33, 283–325. doi:10.1146/annurev.aa.33.090195.001435

Hadid, L. Z., Sahraoui, F., and Galtier, S. (2017). Energy cascade rate in compressible fast and slow solar wind turbulence. *APJ (Acta Pathol. Jpn.)* 838, 9. doi:10.3847/1538-4357/aa603f

Hamilton, K., Smith, C. W., Vasquez, B. J., and Leamon, R. J. (2008). Anisotropies and helicities in the solar wind inertial and dissipation ranges at 1 AU. *J. Geophys. Res*. 113, a. doi:10.1029/2007ja012559

Hautaluoma, G., and Fox, K. (2020). NASA space weather release, 20-083. Available from: https://www.nasa.gov/press-release/nasa-selects-proposals-for-new-space-environment-missions.

Heinemann, M., and Olbert, S. (1980). Non-WKB Alfvén waves in the solar wind. *J. Geophys. Res.* 85, 1311. doi:10.1029/ja085ia03p01311

Hellinger, P., Trávníček, P. M., Štverák, Š., Matteini, L., and Velli, M. (2013). Proton thermal energetics in the solar wind: Helios reloaded. *J. Geophys. Res. Space Physics* 118, 1351. doi:10.1002/jgra.50107

Hollweg, J. V. (1990). On WKB expansions for Alfvén waves in the solar wind. *J. Geophys. Res.* 95 (14), 873–814. doi:10.1029/ja095ia09p14873

Hollweg, J. V., and Isenberg, P. A. (2002). Generation of the fast solar wind: a review with emphasis on the resonant cyclotron interaction. *J. Geophys. Res.* 107, A071147. doi:10.1029/2001ja000270

Hollweg, J. V., and Turner, J. M. (1978). Acceleration of solar wind He++3. Effects of resonant and nonresonant interactions with transverse waves. *J. Geophys. Res.* 83, 97. doi:10.1029/ja083ia01p00097

Howes, G. G., Dorland, W., Cowley, S. C., Hammett, G. W., Quataert, E., Schekochihin, A. A., et al. (2008). Kinetic simulations of magnetized turbulence in astrophysical plasmas. *Phys. Rev. Lett.* 100, 065004. doi:10.1103/PhysRevLett.100.065004

Howes, G. G., and Quataert, E. (2010). On the interpretation of magnetic helicity signatures in the dissipation range of solar wind turbulence. *APJ (Acta Pathol. Jpn.)* 709, L49. doi:10.1088/2041-8205/709/1/l49

Hughes, R. S., Gary, S. P., and Wang, J. (2014). Electron and ion heating by whistler turbulence: three-dimensional particle-in-cell simulations. *Geophys. Res. Lett.* 41, 8681. doi:10.1002/2014gl062070

Hughes, R. S., Gary, S. P., Wang, J., and Parashar, T. N. (2017a). Kinetic Alfvén turbulence: electron and ion heating by particle-in-cell simulations. *APJ (Acta Pathol. Jpn.)* 847, L14. doi:10.3847/2041-8213/aa8b13

Hughes, R. S., Gary, S. P., and Wang, J. (2017b). Particle-in-cell simulations of electron and ion dissipation by whistler turbulence: variations with electron β. *APJ (Acta Pathol. Jpn.)* 835, L15. doi:10.3847/2041-8213/835/1/l15

Iroshnikov, P. S. (1964). Turbulence of a conducting fluid in a strong magnetic field. *Sov. Astron* 7, 566.

Isenberg, P. A. (1990). Investigations of a turbulence-driven solar wind model. *J. Geophys. Res.* 95, 6437. doi:10.1029/ja095ia05p06437

Isenberg, P. A. (1984). Resonant acceleration and heating of solar wind ions: anisotropy and dispersion. *J. Geophys. Res.* 89, 6613. doi:10.1029/ja089ia08p06613

Isenberg, P. A., Smith, C. W., Matthaeus, W. H., and Richardson, J. D. (2010). Turbulent heating of the distant solar wind by interstellar pickup protons in a decelerating flow. *APJ (Acta Pathol. Jpn.)* 719, 716–721. doi:10.1088/0004-637x/719/1/716

Isenberg, P. A., Smith, C. W., and Matthaeus, W. H. (2003). Turbulent heating of the distant solar wind by interstellar pickup protons. *APJ (Acta Pathol. Jpn.)* 592, 564–573. doi:10.1086/375584

Isenberg, P. A. (2005). Turbulence-driven solar wind heating and energization of pickup protons in the outer heliosphere. *APJ (Acta Pathol. Jpn.)* 623, 502–510. doi:10.1086/428609

Isenberg, P. A., and Vasquez, B. J. (2015). Kinetic evolution of coronal hole protons by imbalanced ion-cyclotron waves: implications for measurements by Solar Probe Plus. *APJ (Acta Pathol. Jpn.)* 808, 119. doi:10.1088/0004-637x/808/2/119

Isenberg, P. A., and Vasquez, B. J. (2009). Preferential acceleration and perpendicular heating of minor ions in a collisionless coronal hole. *APJ (Acta Pathol. Jpn.)* 696, 591. doi:10.1088/0004-637x/696/1/591

Karimabadi, H., Roytershteyn, V., and Wan, M. (2013). Coherent structures, intermittent turbulence, and dissipation in high-temperature plasmas. *Phys. Plasmas.* 20, 012303. doi:10.1063/1.4773205

Kasper, J. C., Maruca, B. A., Stevens, M. L., and Zaslavsky, A. (2013). Sensitive test for ion-cyclotron resonant heating in the solar wind. *Phys. Rev. Lett*. 110, 09110. doi:10.1103/PhysRevLett.110.091102

Kolmogorov, A. N. (1941b). Dissipation of energy in locally isotropic turbulence. *R. Soc. Lond. A* 32, 16–18.

Kolmogorov, A. N. (1941a). The local structure of turbulence in incompressible viscous fluid for very large Reynolds numbers. *R. Soc. Lond. A* 30, 301–305.

Kolmogorov, A. N. (1962). A refinement of previous hypotheses concerning the local structure of turbulence in a viscous incompressible fluid at high Reynolds number. *J. Fluid Mech* 13, 82–85. doi:10.1017/s0022112062000518

Kraichnan, R. H. (1965). Inertial-range spectrum of hydromagnetic turbulence. *Phys. Fluids* 8, 1385–1387. doi:10.1063/1.1761412

Lamarche, L. J., Vasquez, B. J., and Smith, C. W. (2014). Proton temperature change with heliocentric distance from 0.3 to 1 AU according to relative temperatures. *J. Geophys. Res. Space Phys* 119, 3267. doi:10.1002/2013ja019529

Leamon, R. J., Smith, C. W., Ness, N. F., and Wong, H. K. (1999). Dissipation range dynamics: kinetic Alfvén waves and the importance of. *J. Geophys. Res* 104 (22), 331–322. doi:10.1029/1999ja900158

Leamon, R. J., Matthaeus, W. H., Smith, C. W., and Wong, H. K. (1998b). Contribution of cyclotron-resonant damping to kinetic dissipation of interplanetary turbulence. *Astrophys. J. Lett.* 507, L181–L184. doi:10.1086/311698

Leamon, R. J., Smith, C. W., Ness, N. F., Matthaeus, W. H., and Wong, H. K. (1998a). Observational constraints on the dynamics of the interplanetary magnetic field dissipation range. *J. Geophys. Res*. 103, 4775–4787. doi:10.1029/97ja03394

Lopez, R. E., and Freeman, J. W. (1986). Solar wind proton temperature velocity relationship. *J. Geophys. Res.J. Geophys. Res.* 92, 91.

MacBride, B. T., Forman, M. A., Smith, C. W., and ESA, S. P. (2005). "Turbulence and the third moment of fluctuations: Kolmogorov's 4/5 law and its MHD analogues in the solar wind," in *Proceedings of solar wind 11: connecting Sun and heliosphere*. Editors B. Fleck and T. H. Zurbuchen (The Netherlands: European Space Agency), 613–616.

MacBride, B. T., Smith, C. W., and Forman, M. A. (2008). The turbulent cascade at 1 AU: energy transfer and the third-order scaling for MHD. *APJ (Acta Pathol. Jpn.)* 679, 1644–1660. doi:10.1086/529575

MacBride, B. T., Smith, C. W., and Vasquez, B. J. (2010). Inertial-range anisotropies in the solar wind from 0.3 to 1 AU: Helios 1 observations. *J. Geophys. Res.* 115, A07105. doi:10.1029/2009ja014939

Marino, R., Sorriso-Valvo, L., Carbone, V., Noullez, A., Bruno, R., and Bavassano, B. (2008). Heating the solar wind by a magnetohydrodynamic turbulent energy cascade. *APJ (Acta Pathol. Jpn.)* 677, L71–L74. doi:10.1086/587957

Markovskii, S. A., and Vasquez, B. J. (2013a). "Magnetic helicity of strong 2D turbulence in the dissipation range," in Thirteenth international solar wind conference, 239.

Markovskii, S. A., and Vasquez, B. J. (2011). A short-timescale channel of dissipation of the strong solar wind turbulence. *APJ (Acta Pathol. Jpn.)* 739, 22. doi:10.1088/0004-637x/739/1/22

Markovskii, S. A., Vasquez, B. J., and Chandran, B. D. G. (2010a). Perpendicular proton heating due to energy cascade of fast magnetosonic waves in the solar corona. *APJ (Acta Pathol. Jpn.)* 709, 1003. doi:10.1088/0004-637x/709/2/1003

Markovskii, S. A., and Vasquez, B. J. (2013b). Magnetic helicity in the dissipation range of strong imbalanced turbulence. *APJ (Acta Pathol. Jpn.)* 768, 62. doi:10.1088/0004-637x/768/1/62

Markovskii, S. A., and Vasquez, B. J. (2016). Magnetic helicity of ion kinetic turbulence with a nonzero electron temperature. *APJ (Acta Pathol. Jpn.)* 820, 15. doi:10.3847/0004-637x/820/1/15

Markovskii, S. A., and Vasquez, B. J. (2010b). The effect of spectral anisotropy of fast magnetosonic turbulence on the plasma heating at the proton kinetic scales. *Phys. Plasmas* 17, 112902. doi:10.1063/1.3509158

Marsch, E., Mühlhäuser, K. H., Rosenbauer, H., and Schwenn, R. (1983). On the equation of state of solar wind ions derived from Helios measurements. *J. Geophys. Res*. 88, 2982. doi:10.1029/ja088ia04p02982

Matthaeus, W. H., Goldstein, M. L., and Roberts, D. A. (1990). Evidence for the presence of quasi-two-dimensional nearly incompressible fluctuations in the solar wind. *J. Geophys. Res*. 95 (20), 673–720. doi:10.1029/ja095ia12p20673

Matthaeus, W. H., Oughton, S., Pontius, D. H., Jr., and Zhou, Y. (1994). Evolution of energy containing turbulent eddies in the solar wind. *J. Geophys. Res.* 99 (19), 267–319. doi:10.1029/94ja01233

Matthaeus, W. H., Parashar, T. N., Wan, M., and Wu, P. (2016). Turbulence and proton–electron heating in kinetic plasma. *Astrophys. J* 7, 827. doi:10.3847/2041-8205/827/1/l7

Matthaeus, W. H., Ghosh, S., Oughton, S., and Roberts, D. A. (1996a). Anisotropic three-dimensional MHD turbulence. *J. Geophys. Res.* 101, 7619. doi:10.1029/95ja03830

Matthaeus, W. H., and Goldstein, M. L. (1982). Measurement of the rugged invariants of magnetohydrodynamic turbulence in the solar wind. *J. Geophys. Res.* 87, 6011–6028. doi:10.1029/ja087ia08p06011

Matthaeus, W. H., Zank, G. P., and Oughton, S. (1996b). Phenomenology of hydromagnetic turbulence in a uniformly expanding medium. *J. Plasma Phys* 56, 659. doi:10.1017/s0022377800019516

Matthaeus, W. H., Zank, G. P., Smith, C. W., and Oughton, S. (1999). Turbulence, spatial transport, and heating of the solar wind. *Phys. Rev. Lett.* 82, 3444–3447. doi:10.1103/physrevlett.82.3444

Matthaeus, W. H., and Zhou, Y. (1989). Extended inertial range phenomenology of magnetohydrodynamic turbulence. *Phys. Fluid. Plasma Phys* 1, 1929–1931. doi:10.1063/1.859110

Matthaeus, W., Oughton, S., Ghosh, S., and Hossain, M. (1998). Scaling of anisotropy in hydromagnetic turbulence. *Phys. Rev. Lett.* 81, 2056. doi:10.1103/physrevlett.81.2056

Müller, W-C., and Grappin, R. (2005). Spectral energy dynamics in magnetohydrodynamic turbulence. *Phys. Rev. Lett.* 95, 114502. doi:10.1103/physrevlett.95.114502

Narita, Y., Roberts, O. W., Vörös, Z., and Hoshino, M. (2020). Transport ratios of the kinetic Alfven mode in space plasmas. *Front. Phys* 8, 166. doi:10.3389/fphy.2020.00166

Ng, C. S., Bhattacharjee, A., Munsi, D., Isenberg, P. A., and Smith, C. W. (2010). Kolmogorov versus Iroshnikov–Kraichnan spectra: consequences for ion heating in the solar wind. *J. Geophys. Res*. 115, 124. doi:10.1029/2009ja014377

Osman, K. T., Wan, M., Matthaeus, W. H., Weygand, J. M., and Dasso, S. (2011). Anisotropic third-moment estimates of the energy cascade in solar wind turbulence using multispacecraft data. *Phys. Rev. Lett.* 107, 165001. doi:10.1103/PhysRevLett.107.165001

Oughton, S., Dmitruk, P., and Matthaeus, W. H. (2006). A two-component phenomenology for homogeneous magnetohydrodynamic turbulence. *Phys. Plasmas* 13, 042306. doi:10.1063/1.2188088

Oughton, S., and Matthaeus, W. H. (2020). Critical balance and the physics of magnetohydrodynamic turbulence. *APJ (Acta Pathol. Jpn.)* 897, 37. doi:10.3847/1538-4357/ab8f2a

Oughton, S., Matthaeus, W. H., Smith, C. W., Breech, B., and Isenberg, P. A. (2011). Transport of solar wind fluctuations: a two-component model. *J. Geophys. Res.* 116, 277. doi:10.1029/2010ja016365

Parashar, T. N., Shay, M. A., Cassak, P. A., and Matthaeus, W. H. (2009). Kinetic dissipation and anisotropic heating in a turbulent collisionless plasma. *Phys. Plasmas* 16, 032310. doi:10.1063/1.3094062

Parashar, T. N., and Matthaeus, W. H. (2016). Propinquity of current and vortex structures: effects on collisionless plasma heating. *APJ (Acta Pathol. Jpn.)* 832, 57. doi:10.3847/0004-637x/832/1/57

Pine, Z. B., Smith, C. W., Hollick, S. J., Argall, M. R., Vasquez, B. J., Isenberg, P. A., et al. (2020a). Solar wind turbulence from 1 to 45 AU. I. Evidence for dissipation of magnetic fluctuations using Voyager and ACE observations. *APJ (Acta Pathol. Jpn.)* 900, 91. doi:10.3847/1538-4357/abab10

Pine, Z. B., Smith, C. W., Hollick, S. J., Argall, M. R., Vasquez, B. J., Isenberg, P. A., et al. (2020b). Solar wind turbulence from 1 to 45 AU. III. Anisotropy of magnetic fluctuations in the inertial range using Voyager and ACE observations. *APJ (Acta Pathol. Jpn.)* 900, 93. doi:10.3847/1538-4357/abab11

Pine, Z. B., Smith, C. W., Hollick, S. J., Argall, M. R., Vasquez, B. J., Isenberg, P. A., et al. (2020c). Solar wind turbulence from 1 to 45 AU. IV. Turbulent transport and heating of the solar wind using Voyager observations. *APJ (Acta Pathol. Jpn.)* 900, 94. doi:10.3847/1538-4357/abab12

Politano, H., and Pouquet, A. (1998b). Dynamical length scales for turbulent magnetized flows. *Geophys. Res. Lett.* 25, 273. doi:10.1029/97gl03642

Politano, H., and Pouquet, A. (1998a). von Kármán-Howarth equation for magnetohydrodynamics and its consequences on third-order longitudinal structure and correlation functions. *Phys. Rev. E* 57, R21. doi:10.1103/physreve.57.r21

Pucci, F., Vásconez, C. L., Pezzi, O., Servidio, S., Valentini, F., Matthaeus, W. H., et al. (2016). From Alfvén waves to kinetic Alfvén waves in an inhomogeneous equilibrium structure. *J. Geophys. Res. Space Physics* 121, 1024–1045. doi:10.1002/2015ja022216

Richardson, J. D., and Smith, C. W. (2003). The radial temperature profile of the solar wind. *Geophys. Res. Lett* 30, 1206. doi:10.1029/2002gl016551

Richardson, J. D., Paularena, K. I., Lazarus, A. J., and Belcher, J. W. (1995). Evidence for a solar wind slowdown in the outer heliosphere? *Geophys. Res. Lett.* 22, 1469–1472. doi:10.1029/95gl01421

Richardson, J. D., Phillips, J. L., Smith, C. W., and Gray, P. C. (1996). Thermal anisotropies in the solar wind: evidence of heating by interstellar pickup ions?. *Geophys. Res. Lett.* 23, 3259–3262. doi:10.1029/96gl02909

Roberts, O. W., and Li, X. (2015). Evidence of the ion cyclotron resonance at proton kinetic scales in the solar wind. *Astrophys. J* 14, 802. doi:10.1088/0004-637x/802/1/1

Sahraoui, F., Goldstein, M. L., Belmont, G., Canu, P., and Rezeau, L. (2010). Three dimensional anisotropickspectra of turbulence at subproton scales in the solar wind. *Phys. Rev. Lett.* 105, 13. doi:10.1103/physrevlett.105.131101

Saito, S., and Nariyuki, Y. (2014). Perpendicular ion acceleration in whistler turbulence. *Phys. Plasmas* 21, 042303. doi:10.1063/1.4870757

Schwartz, S. J., Feldman, W. C., and Gary, S. P. (1981). The source of proton anisotropy in the high-speed solar wind. *J. Geophys. Res*. 86, 541. doi:10.1029/ja086ia02p00541

Schwenn, R. (1983). The average solar wind in the inner heliosphere: structures and slow variations Cp-2280. *Solar Wind Five* 154, 489.

Servidio, S., Valentini, F., Califano, F., and Veltri, P. (2012). Local kinetic effects in two-dimensional plasma turbulence. *Phys. Rev. Lett*. 108, 045001. doi:10.1103/PhysRevLett.108.045001

Servidio, S., Valentini, F., Perrone, D., Greco, A., Califano, F., Matthaeus, W. H., et al. (2015). A kinetic model of plasma turbulence. *J. Plasma Phys* 81, 325810107. doi:10.1017/s0022377814000841

Servidio, S., Osman, K. T., Valentini, F., Perrone, D., Califano, F., Chapman, S., et al. (2014). Proton kinetic effects in Vlasov and solar wind turbulence. *APJ (Acta Pathol. Jpn.)* 781, L27. doi:10.1088/2041-8205/781/2/l27

Shebalin, J. V., Matthaeus, W. H., and Montgomery, D. (1983). Anisotropy in MHD turbulence due to a mean magnetic field. *J. Plasma Phys* 29, 525. doi:10.1017/s0022377800000933

Smith, C. W., Mullan, D. J., Ness, N. F., Skoug, R. M., and Steinberg, J. (2001b). Day the solar wind almost disappeared: magnetic field fluctuations, wave refraction and dissipation. *J. Geophys. Res* 106 (18), 625–718. doi:10.1029/2001ja000022

Smith, C. W., Stawarz, J. E., Vasquez, B. J., Forman, M. A., and MacBride, B. T. (2009). Turbulent cascade at 1 AU in high cross-helicity flows. *Phys. Rev. Lett.* 103, 201101. doi:10.1103/PhysRevLett.103.201101

Smith, C. W., Hamilton, K., Vasquez, B. J., and Leamon, R. J. (2006a). Dependence of the dissipation range spectrum of interplanetary magnetic fluctuationson the rate of energy cascade. *APJ (Acta Pathol. Jpn.)* 645, L85–L88. doi:10.1086/506151

Smith, C. W., Isenberg, P. A., Matthaeus, W. H., and Richardson, J. D. (2006c). Turbulent heating of the solar wind by newborn interstellar pickup protons. *APJ (Acta Pathol. Jpn.)* 638, 508–517. doi:10.1086/498671

Smith, C. W., Matthaeus, W. H., Zank, G. P., Ness, N. F., Oughton, S., and Richardson, J. D. (2001a). Heating of the low-latitude solar wind by dissipation of turbulent magnetic fluctuations. *J. Geophys. Res*. 106, 8253–8272. doi:10.1029/2000ja000366

Smith, C. W., Vasquez, B. J., Coburn, J. T., Forman, M. A., and Stawarz, J. E. (2018). Correlation scales of the turbulent cascade at 1 AU. *APJ (Acta Pathol. Jpn.)* 858, 21. doi:10.3847/1538-4357/aabb00

Smith, C. W., Vasquez, B. J., and Hamilton, K. (2006b). Interplanetary magnetic fluctuation anisotropy in the inertial range. *J. Geophys. Res*. 111, A09111. doi:10.1029/2006ja011651

Smith, C. W., Vasquez, B. J., and Hollweg, J. V. (2012). Observational constraints on the role of cyclotron damping and kinetic Alfvén waves in the solar wind. *APJ (Acta Pathol. Jpn.)* 745, 8. doi:10.1088/0004-637x/745/1/8

Sorriso-Valvo, L., Carbone, F., Perri, S., Greco, A., Marino, R., and Bruno, R. (2018). On the statistical properties of turbulent energy transfer rate in the inner heliosphere. *Sol. Phys* 293, 10. doi:10.1007/s11207-017-1229-6

Sorriso-Valvo, L., Marino, R., Carbone, V., Noullez, A., Lepreti, F., Veltri, P., et al. (2007). Observation of inertial energy cascade in interplanetary space plasma. *Phys. Rev. Lett* 99, 115001. doi:10.1103/PhysRevLett.99.115001

Spence, H. E. (2019). "HelioSwarm: unlocking the multiscale mysteries of weakly-collisional magnetized plasma turbulence and ion heating," in Fall meeting of the American Geophysical Union. 2019Abstract SH11B-04.

Stawarz, J. E., Smith, C. W., Vasquez, B. J., Forman, M. A., and MacBride, B. T. (2009). The turbulent cascade and proton heating in the solar wind at 1 AU. *APJ (Acta Pathol. Jpn.)* 697, 1119–1127. doi:10.1088/0004-637x/697/2/1119

Stawarz, J. E., Smith, C. W., Vasquez, B. J., Forman, M. A., and MacBride, B. T. (2010). The turbulent cascade for high cross-helicity States at 1 Au. *APJ (Acta Pathol. Jpn.)* 713, 920–934. doi:10.1088/0004-637x/713/2/920

Stawarz, J. E., Vasquez, B. J., Smith, C. W., Forman, M. A., and Klewicki, J. (2011). Third moments and the role of anisotropy from velocity shear in the solar wind. *APJ (Acta Pathol. Jpn.)* 736, 44. doi:10.1088/0004-637x/736/1/44

Svidzinski, V. A., Li, H., Rose, H. A., Albright, B. J., and Bowers, K. J. (2009). Particle in cell simulations of fast magnetosonic wave turbulence in the ion cyclotron frequency range. *Phys. Plasmas* 16, 122310. doi:10.1063/1.3274559

Taylor, G. I. (1935). Statistical theory of turbulenc. *Proc. R. Soc. A* 151, 421–444. doi:10.1098/rspa.1935.0158

TenBarge, J. M., Howes, G. G., and Dorland, W. (2013). Collisionless damping at electron scales in solar wind turbulence. *APJ (Acta Pathol. Jpn.)* 774, 139. doi:10.1088/0004-637x/774/2/139

Totten, T. L., Freeman, J. W., and Arya, S. (1995). An empirical determination of the polytropic index for the free-streaming solar wind using Helios 1 data. *J. Geophys. Res* 100, 13. doi:10.1029/94ja02420

Tu, C.-Y., and Marsch, E. (1997). *Sol. Phys* 171, 363. doi:10.1023/a:1004968327196

Usmanov, A. V., Goldstein, M. L., and Matthaeus, W. H. (2016). A four-fluid MHD model of the solar wind/interstellar medium interaction with turbulence transport and pickup protons as separate fluid. *APJ (Acta Pathol. Jpn.)* 820, 17. doi:10.3847/0004-637x/820/1/17

Usmanov, A. V., Goldstein, M. L., and Matthaeus, W. H. (2012). Three-dimensional magnetohydrodynamic modeling of the solar wind including pickup protons and turbulence transport. *APJ (Acta Pathol. Jpn.)* 754, 40. doi:10.1088/0004-637x/754/1/40

Usmanov, A. V., Goldstein, M. L., and Matthaeus, W. H. (2014). Three-fluid, three-dimensional magnetohydrodynamic solar wind model with eddy viscosity and turbulent resistivity. *APJ (Acta Pathol. Jpn.)* 788, 43. doi:10.1088/0004-637x/788/1/43

Usmanov, A. V., Matthaeus, W. H., Goldstein, M. L., and Chhiber, R. (2018). The steady global corona and solar wind: a three-dimensional MHD simulation with turbulence transport and heating. *APJ (Acta Pathol. Jpn.)* 865, 25. doi:10.3847/1538-4357/aad687

Valentini, F., Vásconez, C. L., Pezzi, O., Servidio, S., Malara, F., and Pucci, F. (2017). Transition to kinetic turbulence at proton scales driven by large-amplitude kinetic Alfvén fluctuations. *A&A* 599, A8. doi:10.1051/0004-6361/201629240

Vásconez, C. L., Pucci, F., Valentini, F., Servidio, S., Matthaeus, W. H., and Malara, F. (2015). Kinetic Alfvén wave generation by large-scale Phase mixing. *APJ (Acta Pathol. Jpn.)* 815, 7. doi:10.1088/0004-637x/815/1/7

Vasquez, B. J., Forman, M. A., Coburn, J. T., Smith, C. W., and Stawarz, J. E. (2018b). The turbulent cascade for high cross-helicity states at 1 au. II. minor energy. *APJ (Acta Pathol. Jpn.)* 867, 156. doi:10.3847/1538-4357/aae6c6

Vasquez, B. J. (2015). Heating rate scaling of turbulence in the proton kinetic regime. *APJ (Acta Pathol. Jpn.)* 806, 33. doi:10.1088/0004-637x/806/1/33

Vasquez, B. J., Markovskii, S. A., and Chandran, B. D. G. (2014). Three-dimensional hybrid simulation study of anisotropic turbulence in the proton kinetic regime. *APJ (Acta Pathol. Jpn.)* 788, 178. doi:10.1088/0004-637x/788/2/178

Vasquez, B. J., Markovskii, S. A., and Smith, C. W. (2018a). The turbulence magnetic helicity signature in the interplanetary medium: a Blackman-Tukey and Morlet wavelet analysis. *APJ (Acta Pathol. Jpn.)* 855, 121. doi:10.3847/1538-4357/aaad0d

Vasquez, B. J., and Markovskii, S. A. (2012). Velocity power spectra from cross-field turbulence in the proton kinetic regime. *APJ (Acta Pathol. Jpn.)* 747, 19. doi:10.1088/0004-637x/747/1/19

Vasquez, B. J., Smith, C. W., Hamilton, K., MacBride, B. T., and Leamon, R. J. (2007). Evaluation of the turbulent energy cascade rates from the upper inertial range in the solar wind at 1 AU. *J. Geophys. Res.* 112, a. doi:10.1029/2007ja012305

Verma, M. K., Roberts, D. A., and Goldstein, M. L. (1995). Turbulent heating and temperature evolution in the solar wind. *J. Geophys. Res.* 100, 839. doi:10.1029/95ja01216

Völk, H. J., and Alpers, W. (1973). The propagation of Alfvén waves and their directional anisotropy in the solar wind. *Astrophys. Space Sci.* 20, 267.

von Kármán, T., and Howarth, L. (1938). On the statistical theory of isotropic turbulence. *Proc. R. Soc. Lond. Ser. A* 164, 192–215.

Wan, M., Matthaeus, W. H., Roytershteyn, V., Karimabadi, H., Parashar, T., Wu, P., et al. (2015). Intermittent dissipation and heating in 3D kinetic plasma turbulence. *Phys. Rev. Lett* 114, 175002. doi:10.1103/PhysRevLett.114.175002

Wan, M., Sevidio, S., Oughton, S., and Matthaeus, W. H. (2009). The third-order law for increments in magnetohydrodynamic turbulence with constant shear. *Phys. Plasmas* 16, 090703. doi:10.1063/1.3240333

Williams, L. L., and Zank, G. P. (1994). Effect of magnetic field geometry on the wave signature of the pickup of interstellar neutrals. *J. Geophys. Res*. 99 (19), 229–319. doi:10.1029/94ja01657

Williams, L. L., Zank, G. P., and Matthaeus, W. H. (1995). Dissipation of pickup-induced waves: a solar wind temperature increase in the outer heliosphere? *J. Geophys. Res.* 100 (17), 059–117. doi:10.1029/95ja01261

Woodham, L. D., Wicks, R. T., Verscharen, D., and Owen, C. J. (2018). The role of proton cyclotron resonance as a dissipation mechanism in solar wind turbulence: a statistical study at ion-kinetic scales. *APJ (Acta Pathol. Jpn.)* 856, 49. doi:10.3847/1538-4357/aab03d

Wu, P., Perri, S., Osman, K., Wan, M., Matthaeus, W. H., Shay, M. A., et al. (2013). Intermittent heating in solar wind and kinetic simulations. *APJ (Acta Pathol. Jpn.)* 763, L30. doi:10.1088/2041-8205/763/2/l30

Xia, Q., Perez, J. C., Chandran, B. D. G., and Quataert, E. (2013). Perpendicular ion heating by reduced magnetohydrodynamic turbulence. *APJ (Acta Pathol. Jpn.)* 776, 90. doi:10.1088/0004-637x/776/2/90

Yang, Y., et al. (2017). Energy transfer, pressure tensor, and heating of kinetic plasma. *Phys. Plasmas* 24, 072306. doi:10.1063/1.4990421

Zank, G. P., Matthaeus, W. H., and Smith, C. W. (1996). Evolution of turbulent magnetic fluctuation power with heliospheric distance. *J. Geophys. Res.* 101 (17), 093–117. doi:10.1029/96ja01275

Zank, G. P., Adhikari, L., Hunana, P., Shiota, D., Bruno, R., and Telloni, D. (2017). Theory and transport of nearly incompressible magnetohydrodynamic turbulence. *APJ (Acta Pathol. Jpn.)* 835, 147. doi:10.3847/1538-4357/835/2/147

Zank, G. P., Dosch, A., Hunana, P., Florinski, V., Matthaeus, W. H., and Webb, G. M. (2012). The transport of low-frequency turbulence in astrophysical flows. I. Governing equations. *APJ (Acta Pathol. Jpn.)* 745, 35. doi:10.1088/0004-637x/745/1/35

Zhou, Y., and Matthaeus, W. H. (1990b). Models of inertial range spectra of interplanetary magnetohydrodynamic turbulence. *J. Geophys. Res.* 95 (14), 881–814. doi:10.1029/ja095ia09p14881

Zhou, Y., and Matthaeus, W. H. (1990a). Transport and turbulence modeling of solar wind fluctuations. *J. Geophys. Res.* 95, 10291–10311. doi:10.1029/ja095ia07p10291

Conflict of Interest: The authors declare that the research was conducted in the absence of any commercial or financial relationships that could be construed as a potential conflict of interest.

frontiers in Astronomy and Space Sciences

MINI REVIEW
published: 25 January 2021
doi: 10.3389/fspas.2020.573746

The Impact of Turbulence on the Ionosphere and Magnetosphere

Patrick Guio[1,2] *and Hans L. Pécseli*[1,3]*

[1]Department of Physics and Technology, University of Tromsø, Oslo, Norway, [2]Department of Physics and Astronomy, University College London, London, United Kingdom, [3]Department of Physics, University of Oslo, Oslo, Norway

An important property associated with turbulence in plasmas and fluids is anomalous transport. Plasma, being a good conductor, can in addition be affected by turbulence causing an anomalous resistivity that can significantly exceed its classical counterpart. While turbulent transport may be adequately described in configuration space, some aspects of the anomalous resistivity are best accounted for in phase space. Kinetic phenomena like electron and ion phase space vortices can thus act as obstacles for the free flow of slow charged particles. Plasma instabilities and large amplitude plasma waves are candidates for contributions to the anomalous resistivity by generating such structures. Langmuir waves can be relevant, but also others, such as upper- as well as lower-hybrid waves in magnetized plasmas. Often these anomalous resistivity effects can be small, but due to the large spatial and temporal scales involved in space plasmas, planetary ionosphere and magnetosphere in particular, even such moderate effects can be important. This mini-review is discussing elements of the description of plasma turbulence with particular attention to wave phenomena that contribute to anomalous resistivity and diffusion. Turbulence effects can have relevance for space weather phenomena as well, where ground based and airborne activities relying on for instance Global Positioning and Global Navigation Satellite Systems are influenced by plasma conditions in geospace.

Keywords: plasma, turbulence, ionosphere, anomalous resistivity, nonlinear waves, diffusion

OPEN ACCESS

Edited by:
Vadim Uritsky,
The Catholic University of America, United States

Reviewed by:
Giuseppe Consolini,
Institute for Space Astrophysics and Planetology (INAF), Italy
Nickolay Ivchenko,
Royal Institute of Technology, Sweden
Arnaud Masson,
European Space Astronomy Centre (ESAC), Spain

***Correspondence:**
Hans L. Pécseli
hans.pecseli@fys.uio.no

Specialty section:
This article was submitted to Space Physics, a section of the journal Frontiers in Astronomy and Space Sciences

Received: *17 June 2020*
Accepted: *30 November 2020*
Published: *25 January 2021*

Citation:
Guio P and Pécseli HL (2021) The Impact of Turbulence on the Ionosphere and Magnetosphere. Front. Astron. Space Sci. 7:573746. doi: 10.3389/fspas.2020.573746

1 INTRODUCTION

Plasmas, magnetized plasmas in particular, can support a variety of wave phenomena, electromagnetic as well as electrostatic. These waves can be excited in laboratory experiments, and are frequently found to be generated by some instability mechanisms in naturally occurring plasmas, in the Earth's ionosphere and magnetosphere in particular, as described by, e.g., Shawhan (1979), Shawhan (1985). Informative summary figures can be found in these works. Controlled laboratory plasma studies often assume conditions where harmonic wave phenomena are excited, but these are rarely met in natural environments where turbulent states are more likely to develop. For some conditions further developed in this review, such turbulent stages can have similarities to classical hydrodynamic turbulence.

In neutral fluids and gases, 'strongly' turbulent states often develop, while in plasmas, turbulence is often observed to be 'weak'. For discussing this distinction, we consider a nonlinear model wave equation (Dupree, 1969; Similon and Sudan, 1990; Galtier, 2009) in the form

$$\frac{\partial Q_\ell(\boldsymbol{k},t)}{\partial t}+i\omega(\boldsymbol{k})Q_\ell(\boldsymbol{k},t)=\sum_{m,n}\sum_{\boldsymbol{k}'}M_{\ell,m,n}(\boldsymbol{k},\boldsymbol{k}')\,Q_m(\boldsymbol{k}',t)Q_n(\boldsymbol{k}-\boldsymbol{k}',t). \quad (1)$$

The indices $\{\ell,m,n\}\in\{x,y,z\}$ label components of the complex vector $\boldsymbol{Q}(\boldsymbol{k},t)$. The nonlinear term in the right hand side contains the coupling coefficients $M_{\ell,m,n}$ between components for wavenumbers $\boldsymbol{k}$ and $\boldsymbol{k}'$. Any quadratically nonlinear partial differential equation with a first order time derivative can be brought in the form of **Eq. 1** by a Fourier series representation of the variables in configuration space. One such example is the Navier-Stokes equation (Kollmann, 2019) where Q_ℓ represents the incompressible fluid velocity component u_ℓ, and $i\omega(\boldsymbol{k})\to k^2\nu$, where ν is the fluid kinematic viscosity. For plasma waves, on the other hand, Q_ℓ can represent the electric field component E_ℓ, while $\omega(\boldsymbol{k})$ is a linear dispersion relation, which may be complex for some wave vector ranges for linearly unstable systems. We let $\mathcal{M}$ be a 'representative' value of $M_{\ell,m,n}$, for the Navier-Stokes equation we have, $\mathcal{M}_{\rm NS}\sim k$. An effective Reynolds number $\mathcal{R}$ can be constructed as $\mathcal{R}=\mathcal{M}Q/\omega(k)$ i.e., the ratio of two time-scales, one originating from the nonlinear part in the right hand side and the other representing the linear part in the left hand side. When **Eq. 1** represents the Navier-Stokes equation, we find $\mathcal{R}_{\rm NS}\approx U/(K\nu)$ where U is a 'representative' velocity and K a 'representative' wavenumber. For a pipe flow, U would be the injected flow velocity and $K\sim 1/D$ the inverse diameter of the pipe. When $U\gg\nu/D$, we expect nonlinearity to dominate and strong turbulence to develop. For fluids and gases, where ν is generally small, this condition is easily fulfilled and we can anticipate that strongly turbulent states can be obtained. In the limit where $\omega(k)$ is negligible, the dynamics of fluids or gases is solely due to nonlinear effects. For the Navier-Stokes equation, this is the case for the limit where $k^2\nu$ is negligible. For a plasma, the situation is frequently the opposite (Dupree, 1969), the linear part $\omega(k)$ is often large. For Langmuir waves $\omega(k)\approx\omega_{pe}$, the electron plasma frequency. The corresponding plasma Reynolds number is $\mathcal{R}_{\rm P}\approx\mathcal{E}\mathcal{M}_P/\omega(K)$, with $\mathcal{E}$ being a representative electrostatic electric field value, and K a representative wavenumber to be determined by some externally imposed parameters, e.g., the geometry. $\mathcal{R}_{\rm P}$ is often a small number, resulting in a weakly turbulent state (Dupree, 1969; Pécseli, 2016). Models for weak turbulence have been developed for plasma sciences (Kadomtsev, 1965; Nicholson, 1983; Horton, 1985; Kono and Škorić, 2010). Depending on the plasma conditions, the magnetization for instance, both strongly and weakly turbulent conditions can be found.

Diagnostic tools involving two-point measurements that can distinguish strong and weak turbulence have been developed (Iwama et al., 1979; Beall et al., 1982; Pécseli, 2015). In some cases, the linear dispersion relation can be identified in the $(\omega,\boldsymbol{k})$-space, thus demonstrating the importance of the $\omega(\boldsymbol{k})$ term in **Eq. 1**, while for strongly turbulent conditions a similar analysis shows enhanced amplitudes for a wide range of wave vectors with no discernible frequency-wavenumber relation.

Classical physics, and thus also plasma physics, used to rest on a two-fold basis: theory and observations, the latter including results from controlled laboratory experiments. With the development of efficient high-speed computing, it has become possible to make numerical simulations on a level competing with laboratory results. Modern physics, also plasma physics, now rests on a basis of three pillars, theory, experiment and numerical simulations (Post and Votta, 2005; Hut, 2006). Use of advanced high performance computing techniques allow massively parallel computations involving tens of thousands of cores. Modern numerical simulations can in many cases serve as a substitute for experiments. Fine details in the variations of the magnetospheric plasma can now be resolved in numerical simulations (von Alfthan et al., 2014). Predictions of such details can be important for instance for space weather phenomena (Morley, 2020) that can have effects being important for activities on ground. Scintillations in the plasma index of refraction affecting Global Positioning Systems (GPS) and Global Navigation Satellite Systems (GNSS) offer examples (Jin et al., 2020). The energy source for intense space weather phenomena is often found in solar outbursts that give rise to fluctuations in the Earth's plasma environment (Sato et al., 2019). Numerical simulations can also give support when interpreting observations made by instrumented spacecraft. If the simulations reproduce the observed data, it can be assumed that the numerical results can be trusted also for information not directly accessible for confirmation by measurements.

2 TURBULENT SPECTRA

2.1 Strong Turbulence in Neutral Fluids

Fully developed strong turbulence in incompressible neutral flows develops a universal continuous power spectrum $F(k)$ for the velocity fluctuations. Ignoring intermittency effects, a spectrum characterizing an inertial subrange for homogeneous and isotropic conditions is found to follow a power law $\sim C_K\epsilon^{2/3}k^{-5/3}$, the Kolmogorov-Obukhov spectrum, where ϵ is the energy dissipation rate per unit fluid mass, and C_K the Kolmogorov constant (Sreenivasan, 1995) which has to be determined experimentally. For shorter wavelengths, Heisenberg (1948) predicted the existence of a viscous spectral subrange following a $\sim k^{-7}$ power law (Heisenberg and Taylor, 1948; Beran, 1968). Although some numerical and experimental studies seem to offer support for this result, it is unlikely to be correct (Landahl and Mollo-Christensen, 1992) since it predicts that, for instance, the integral for spatial derivative spectrum (Bendat, 1958) of mth order, $\int_0^\infty k^{2m}F(k)\,\mathrm{d}k$, diverges for $m\geq 3$. This would imply that the flow develops singular third and higher order spatial derivatives. There are no indications that the Navier-Stokes equation has this property for three-dimensional turbulence with 'smooth' initial conditions (Sulem et al., 1983; Constantin, 1991), and there is no natural wavenumber associated with the Navier-Stokes equation to give an upper limit for a viscous subrange. For turbulence confined to two-spatial dimensions, the situation might be different. The classical Kolmogorov-Obukhov result implicitly assumes the energy dissipation ϵ to be a deterministic quantity. In reality, it is randomly fluctuating so that the dissipation can take place in 'hot spots' i.e., within intermittent spatial regions and time periods (Novikov, 1990; Davidson, 2004; Kollmann, 2019).

When additional energy is injected into a three-dimensional turbulent field, classical turbulence models predicts the energy to cascade toward smaller scales by a 'vortex-stretching' mechanism (Tennekes and Lumley, 1972). One feature of two-dimensional turbulence is that energy can cascade toward *larger* scales. Convincing observations of this process seems to be missing in space plasmas, but it has been amply demonstrated by numerical simulations. Turbulence models in two spatial dimensions (Hasegawa and Mima, 1978; Kraichnan and Montgomery, 1980; Gruzinov and Pogutse, 1986) are relevant for low frequency phenomena confined to a plane $\perp \boldsymbol{B}$ in magnetized plasmas.

2.2 Strong Turbulence in Plasmas

One important parameter classifying plasma conditions is β, the ratio of plasma to magnetic pressure. Note that $\beta \approx (C_s/\mathrm{V_A})^2$, the square ratio of the ion acoustic sound speed to the Alfvén velocity. In the near Earth environment we usually have $\beta \ll 1$. For larger β-values, as in the Solar wind, a coupling between transverse electromagnetic perturbations and compressional modes can be expected in magnetized plasmas.

There are no obvious reasons for turbulent spectra to follow a power law, but it has been found to be the case sometimes also for fully developed strong plasma turbulence. There are thus solid evidences that fully developed strong resistive electrostatic drift-wave turbulence in plasmas confined by strong magnetic fields develops a $\sim k^{-5}$ power-law spectral subrange for fluctuations in the electrostatic potential (Tchen et al., 1980; Pécseli, 2015; Pécseli, 2016). The continuation of this drift-wave spectrum to wavelengths shorter than the ion Larmor radius remains poorly understood.

The conditions in the Earth's ionospheric *E*- and *F*-regions are special due to the importance of collisions between charged and neutral particles. It has been speculated that also some low-frequency ionospheric waves in these regions can develop strong turbulence with universal power law spectra (Ott and Farley, 1974; Sudan and Keskinen, 1977; Sudan, 1983; Hassam et al., 1986), but the conjecture has not been studied systematically in any detail (Pécseli, 2016), although some observations and numerical simulations seem to be consistent with the hypothesis (Kelley, 1989). Studies of rocket data, in particular, have shown power law spectra for both fluctuating plasma density and electrostatic potential (Basu et al., 1988; Krane et al., 2000; Dyrud et al., 2006) in reasonable agreement also with laboratory results (Mikkelsen and Pécseli, 1980). Intermittency is also found to be an issue for plasma turbulence (Dyrud et al., 2008). Parts of it has to do with coherent interactions of large amplitude waves in a background of a low level of turbulence (Vladimirov and Stenflo, 1997).

Fully developed strong plasma turbulence with a large β-value is mostly found in the solar wind as summarized by e.g., Bruno and Carbone (2005), where conditions are well described by magnetohydrodynamics (MHD). Turbulent plasma energy spectra (i.e., the sum of kinetic and magnetic energy), in the form $\sim (\epsilon V_A)^{1/2} k^{-3/2}$, have been predicted by Iroshnikov (1964) and Kraichnan (1965). It has been found that large scale cavities can form in the Earth's magnetosphere (Fritz et al., 2003) where the magnetic field strength is small, thus creating large regions with relatively large β-value where the Iroshnikov-Kraichnan results are also relevant. A worthwhile investigation would be to analyze the energy spectra for these conditions.

2.2.1 Plasma Turbulence as a 'Soliton Gas'

Turbulence is associated with many degrees of freedom being excited. An intermediate scenario has been suggested, where a nonlinear evolution of waves saturate in an ensemble of solitons (Kingsep et al., 1973; Dysthe et al., 1986). Once excited, these solitons will collide but recover their original form after collisions (Drazin and Johnson, 1989). Each of these nonlinear structures are described by a wide band of phase coherent Fourier components, so that each soliton can be described by a reduced number of parameters, such as amplitude, width, position and velocity, where some of these parameters can be interrelated as for instance for Korteweg-de Vries solitons (Drazin and Johnson, 1989). This turbulence model can seem unrealistic since most soliton studies refer to spatially one dimensional problems. Several observations can, however, be discussed in terms of this framework. In these cases the wave field can be accounted for by a random distribution of slowly evolving semi-coherent structures, possibly in a background of random noise. A simple spectral analysis does not account for coherent phase relations and the diagnostic methods have to be supplemented by, for instance, triple correlations or bispectral methods (Kim and Powers, 1978). Large coherent structures are best identified by conditional sampling of the data (Johnsen et al., 1987), possibly supplemented by filtering methods, matched filters for instance (Teliban et al., 2007; Fredriksen et al., 2008).

2.3 Taylor's Hypothesis

Measurements of wavenumber power spectra require a minimum of 'two-point' measurements with movable probes. Often, this is not possible, and only time series obtained at one probe position are available. An almost universally used approximation, the Taylor's hypothesis or frozen turbulence approximation, is relates measured frequencies to wavenumbers (Taylor, 1938; Shkarofsky, 1969; Wyngaard and Clifford, 1977). Here it is implicitly argued that the wave field is swept rapidly past the observation point (onboard e.g., an instrumented rocket or a spacecraft), so that the time variation observed is actually due to a moving spatial variation i.e., $\omega \approx \boldsymbol{k} \cdot \boldsymbol{U} \equiv k_\parallel U$, where ω is the detected frequency, and $\boldsymbol{U}$ the relative velocity between the turbulent medium and the observer. Since the frequency ω is only related to the wave vector component $k_\parallel$ along $\boldsymbol{U}$, application of Taylor's hypothesis may need to be combined with assumptions of homogeneity and isotropy in two or three dimensional space. Both scalar and vector spectra can be defined so that the total power is e.g., $\langle \phi^2 \rangle = \int_0^\infty F(k)\,\mathrm{d}k$, or alternatively $\langle \phi^2 \rangle = \iiint G(\boldsymbol{k})\,\mathrm{d}^3\boldsymbol{k}$. The physical dimension of the spectra *F* and *G* are different, and care should be taken not to confuse them, in particular when comparing theoretical and experimental results (Mikkelsen and Pécseli, 1980). The

distinction of spectral definition is relevant also for power spectra in two spatial dimensions, e.g., in a plane $\perp \boldsymbol{B}$.

3 TURBULENT TRANSPORT

One of the most important properties associated with turbulence is anomalous transport. This is particularly true for confinement of fusion plasmas physic and in many industrial applications. In space, the anomalous transport of plasma across magnetic field lines is important for the spatial distribution of plasma (Horton, 1990). To illustrate this problem, we take a low-β plasma confined by a homogeneous magnetic field $\boldsymbol{B}$. The transport is often due to electrostatic fields, $\boldsymbol{E} = -\nabla\phi$, with frequencies well below the ion cyclotron frequency Ω_{ci}. The ion fluid velocity $\boldsymbol{E}\times\boldsymbol{B}/B^2 + \Omega_{ci}^{-1}\,(B^2\partial\boldsymbol{E}/\partial t + (\boldsymbol{E}\times\boldsymbol{B})\cdot\nabla_\perp\boldsymbol{E})/B^3$ is taken to be perpendicular to the magnetic field. Nonlinearities enter through the ion polarization drifts, being the second bracketed term in the ion flow velocity. Finite ion Larmor radius effects (Knorr et al., 1988; Hansen et al., 1989; Chen, 2016) are usually not accounted for. Allowing for a slight deviation from strictly $\boldsymbol{B}$-normal wave propagation, the electrons can flow along the magnetic field lines to obtain an isothermal Boltzmann equilibrium, $n_e = n_0(\boldsymbol{r}_\perp)\exp(e\phi/T_e)$ where T_e is the electron temperature and $n_0(\boldsymbol{r}_\perp)$ is a reference density allowed to vary across magnetic flux tubes (Chen, 2016) i.e., $\boldsymbol{r}_\perp \perp \boldsymbol{B}$. In the quasi-neutral limit, $n_e \approx n_i \equiv n$, keeping only the terms up to second order, the Hasegawa-Mima (HM) equation (Hasegawa and Mima, 1978; Gruzinov and Pogutse, 1986; Albert et al., 1990) is readily derived. It has been widely applied to study weakly nonlinear electrostatic drift waves in low-β plasmas. Also this equation can be expressed (Albert et al., 1990) in the form of **Eq. 1**. The HM-equation has linearly stable solutions, but it accounts for the interaction of many modes excited by a source. Linearly unstable resistive electrostatic drift waves are described by the Hasegawa-Wakatani (HW) set of equations (Hasegawa and Wakatani, 1983), which extend the HM-equation. Numerical solutions of the HW-equation have been found to evolve into a strongly turbulent state with a continuous power spectrum as summarized elsewhere (Pécseli, 2015). When the magnetic field is weaker, $\beta \sim m_e/m_i$, the electron motion can couple to Alfvén waves and the equations have to be modified, but the possibility for a strongly turbulent state remains.

The space-time variations of low frequency, large spatial scale electromagnetic fluctuations in high-β plasmas is well described by the MHD equations, and strongly turbulent states can develop (Goedbloed and Poedts, 2004; Bruno and Carbone, 2005; Galtier, 2009). Relevant space observations relates, for instance, to clouds in the interstellar medium composed of ionized hydrogen atoms (H II regions), regions with neutral atomic hydrogen (H I) and to diffuse nebula or emission nebula (Cox, 2005). On astronomical scales, we find H I and H II regions to be clearly separated. This can be seen as a paradox since on such large scales relevant for interstellar media we could expect correspondingly large Reynolds numbers. Such a turbulent state should result in a strong mixing smearing out boundaries between the H I and H II regions in contradiction with observations. A possible explanation for the lack of turbulent mixing could be that there is not sufficient free energy available to drive a substantial high-β MHD-turbulence on those scales.

Anomalous transport can be particularly important for the plasma at the boundaries between the solar wind and the magnetosphere i.e., the polar cusps and the magnetopause. The cusps offer a particularly easy access between the two regions (D'Angelo, 1977; Fritz et al., 2000). Solar wind plasma particles can thus get direct access to the Earth's ionosphere through the northern and southern cusp points. The shear flow at the interface between open and closed magnetic field lines can give fluid-like Kelvin-Helmholtz (KH) instabilities that can mediate anomalous transport between the two regions. The nonlinear saturated stage of the KH instability plays a critical role for the solar wind interaction with the Earth's magnetosphere (Johnson et al., 2014; Ma et al., 2017).

The solar wind, supersonic and superalfvenic at 1 AU, is an important source of free energy driving turbulence on large spatial scales in the Earth's magnetosphere. The coupling between the solar wind and the plasma of the Earth magnetosphere can involve magnetic field reconnection, and the efficiency of these processes depends critically on the polarity of the interplanetary magnetic field (IMF) with respect to the Earth's magnetic field. The process will depend on the solar activity as evidenced by its correlation with the distribution and intensity of ionospheric plasma irregularities (Jin et al., 2020). The coupling process itself can be accounted by resistive MHD, but resistivity due to classical collisions is found to be insufficient for the relevant plasma parameters. Anomalous resistivity has been suggested as a remedy for explaining enhanced reconnection rates. Lower hybrid wave turbulence can be one source of such anomalous resistivity (Huba et al., 1977), and this wavetype is indeed observed near the Earth's magnetopause (Graham et al., 2017). There is, however, seemingly no consensus on the detailed nature of the relevant anomalous resistivity, nor agreement concerning the origin of the free energy driving the necessary plasma instabilities (Biskamp, 1997).

The discussion of turbulent transport, so far, dealt with 'absolute turbulent diffusion', a phenomenon that is adequately accounted by considering a single representative particle moving with respect to its origin of release. Alternatively a problem of 'relative diffusion' can be formulated, which can be described by the relative motion of two particles (Misguich et al., 1987). The two problems are substantially different: the first case refers to motion in a fixed frame, the later to the center of mass frame moving randomly itself. Relative motion is important for discussing the expansion of a cloud of contaminants instantly released. This could be a barium cloud released in a controlled experiment described by e.g., Haerendel (2019), or micro meteorites evaporating in the ionosphere. In a magnetized plasma the problems of anomalous transport are strongly anisotropic regarding the directions along and across magnetic field lines.

4 ANOMALOUS RESISTIVITY

Since plasma in space is a highly conductive medium, its dynamics is particularly sensitive to changes in current distributions, and the electric and magnetic fields being induced. In a magnetized plasma under normal conditions, the ions dominate the ***B***-transverse current, while the electrons usually carry the current along the magnetic field lines. Obstacles to the free electron flow can be caused by fluid or by kinetic effects (Dupree, 1970; Papadopoulos, 1977; Büchner and Elkina, 2006). These obstacles can be generated by nonlinear wave phenomena (Davidson and Gladd, 1975; Guio and Forme, 2006). While classical resistivity is caused by particle collisions with known collision frequency, we can find an equivalent nonlinear source induced by kinetic wave-particle interactions giving rise to an anomalous collision frequency affecting the electron as well as the ion dynamics.

Together with other sources, the interaction between the solar wind flow and the Earth's magnetosphere can impose large scale steady state electric fields perpendicular to the magnetic field (Kelley, 1989). This electric field drives the equatorial and the auroral electrojets, predominantly in the ionospheric E-region. The classical resistivity is too small to give any significant energy deposition by this electric field. Low frequency plasma sound waves can, however, be excited in the collisional ionospheric *E*-region due to a modified two-stream instability, the Farley-Buneman (FB) instability found by Farley (1963) and Buneman (1963) independently. It can also develop into a turbulent spectrum (Mikkelsen and Pécseli, 1980; Krane et al., 2000; Pécseli, 2015; Young et al., 2020). An enhanced anomalous collision frequency induced by these fluctuations can give rise to a bulk heating of the plasma while saturating the instability (Schlegel and St.-Maurice, 1981; Primdahl, 1986; Oppenheim et al., 1996). It was anticipated (Pécseli, 2015) that the turbulence generated by the FB instability have similarities with the current driven ion sound instability (Kadomtsev, 1965; Machalek and Nielsen, 1973; Horton, 1985). The stability conditions in the ionospheric *E*- and *F*-regions are complicated by the possibility for two instabilities being present at the same time (Sudan, 1983), a gradient instability and the two-stream FB-instability mentioned before.

The nature of the obstacles inhibiting the free electron flow can be kinetic, while others can adequately be described by a simpler fluid model. Their excitation requires free energy and they can form as a result of a plasma instability, such as current driven instabilities (Büchner and Elkina, 2006), where the nonlinear saturated stage is often found to form phase space vortices, an ubiquitous nonlinear kinetic plasma phenomenon (Bernstein et al., 1957; Morse and Nielson, 1969; Lynov et al., 1979; Saeki et al., 1979; Pécseli et al., 1984; Schamel, 1986; Drake et al., 2003). These vortices are found also as three dimensional forms in magnetized plasmas (Børve et al., 2001; Daldorff et al., 2001), while they appear to be unstable for unmagnetized conditions in two or three spatial dimensions as observed in numerical simulations by Morse and Nielson (1969). Phase space structures are observed in space plasmas (Ergun et al., 1998; Tong et al., 2018; Wang et al., 2020), albeit often with relatively small spatial scales. Laboratory experiments and particle simulations (Morse and Nielson, 1969; Saeki et al., 1979; Pécseli et al., 1984; Guio et al., 2003) demonstrate the existence of structures also at large spatial scales in units of the Debye length. Current driven instabilities can indirectly cause localized potential variations by, in a first step, exciting plasma waves, Langmuir waves for instance. By their nonlinear evolution these structures form localized coherent electrostatic structures. Vortices in ion as well as electron phase space can also be formed by particle beams, or particle bursts (Morse and Nielson, 1969; Sakanaka, 1972; Børve et al., 2001; Guio et al., 2003; Wang et al., 2020). Such beams can have their origin in electrostatic double layers (Sato et al., 1981; Jovanović et al., 1982; Schamel, 1986) separating high and low potential regions connected by magnetic field lines. Such regions are observed as 'inverted V-events' by instrumented space craft (Partamies et al., 2008). Significant plasma wave amplitudes can also be excited during ionospheric heating experiments (Hanssen et al., 1992; Dubois et al., 1993). Here we give a brief discussion of some wave types that can play a role in the nonlinear plasma dynamics.

4.1 Electron Plasma Waves

For unmagnetized plasmas the only high frequency electrostatic waves are the Langmuir waves. In magnetized plasmas, the wave dispersion relation includes upper-hybrid waves propagating at large angles to the magnetic field. The nonlinear features of these electron waves have been studied intensively (Thornhill and ter Haar, 1978; Briand, 2015) with particular attention to the wave-collapse phenomenon, where an initial spatial wave distribution collapses to a singularity in a finite time (Zakharov, 1972; Rasmussen and Rypdal, 1986; Robinson, 1997; Kono and Škorić, 2010). It has been amply demonstrated that Langmuir waves collapse as a physical phenomenon is realizable, but so far there seems to be no evidence that it plays any significant role in nature. In its classical form, the collapse phenomenon refers to an initial value problem where a localized large amplitude wave-field is excited. One element in the phenomenon, cavitation of Langmuir waves, is believed to be important under 'driven' conditions where a continuous external energy source is present. This can be in the form of naturally occurring particle beams (Forme, 1999; Guio and Forme, 2006; Isham et al., 2012; Akbari et al., 2016) or perturbations induced from the ground through ionospheric heating experiments (Hanssen et al., 1992; Dubois et al., 1993). Wave cavities can be described by a random distribution of slowly evolving and weakly interacting structures resembling wave-filled plasma density depletions.

4.2 Lower-Hybrid Waves

In magnetized plasmas, the lower-hybrid waves play a particular role by having an approximately equal distribution of the wave energy between the electron and the ion components. The nonlinear space-time evolution has been studied analytically (Musher and Sturman, 1975; Sotnikov et al., 1978; Shapiro et al., 1993) for these wave types. Such waves have indeed been observed in nature with solid indications of a nonlinear evolution (Kjus et al., 1998; Høymork et al., 2000; Schuck et al., 2003; Schuck et al., 2004), but it remains questionable whether

this evolution can be attributed to wave-collapse phenomena (Pécseli et al., 1996; Pécseli and Trulsen, 2006). The scales of the local wave packets in the $\boldsymbol{B}$-transverse direction are well known from satellite observations, but the magnetic field aligned length scales have not been studied in space. All we know is that these scale lengths are very large, probably limited by collisional mean free paths (Pécseli et al., 1996), and this makes also numerical simulations challenging. Lower-hybrid drift waves excited at steep plasma density gradients can also contribute to anomalous transport and plasma heating as suggested by Davidson and Gladd (1975). Lower-hybrid drift waves have been observed in space (Huba et al., 1978; Bale et al., 2002; Walker et al., 2008; Graham et al., 2017) but the associated transport properties have not been fully documented.

The soliton turbulence model described in **Section 2.1** can seem unrealistic, but observations (Pécseli et al., 1997) of an ensemble of saturated lower-hybrid wave structures show examples that can be interpreted by such a model. The properties of such individual structures have been studied as well, with results summarized by Schuck et al. (2003).

4.3 Whistlers

Electromagnetic waves, whistlers, with frequencies below the electron cyclotron resonance frequency can propagate in magnetized plasmas (Stenzel, 2016). In a limited frequency range, $\Omega_{ci} \ll \omega \ll \omega_{ce}$, whistler waves can be seen as electron equivalents to MHD waves (Kingsep et al., 1990; Biskamp et al., 1999; Stenzel, 1999; Galtier, 2009; Lyutikov, 2013). Such waves are frequently observed in the ionosphere (Yeh and Liu, 1972). Often whistlers appear in form of wide band electromagnetic modes, Chorus (Shawhan, 1985; Li et al., 2019; Aryan et al., 2020), or as Hiss in plasmaspheric plumes (Zhang et al., 2019). Seemingly, whistlers are often observed at modest amplitudes, but evidence for weakly nonlinear effects in form of self-ducting (Karpman et al., 1974, 1990) have been reported by Bell (1985). The basic features of whistlers are well explained by fluid models (Yeh and Liu, 1972) but details in the wave energy distributions need kinetic models to account for nonlinear wave-particle couplings (Dysthe, 1971; Nakamura et al., 2018). The evolution of wide band whistler wave spectra have been studied by fluid models (Biskamp et al., 1999; Cho and Lazarian, 2009) indicating that universal energy power spectral subranges with a $\sim k^{-7/3}$ wavenumber scaling can develop.

5 DISCUSSION

Weakly nonlinear wave phenomena include parametric decay and modulational instabilities, usually described in terms of three and four wave phenomena. Most studies refer to the stability of processes involving modulated plane waves. In nature this condition is unlikely to be found, broad band wave *spectra* are much more often observed. Simple physical arguments (Alber, 1978; Pécseli, 2014) give that a wave-decay or a modulational instability involving wavelengths longer than the correlation length (i.e., the inverse wavenumber spectral width) associated with the spectrum are stable (Alber, 1978; Pécseli, 2014), although details will differ for decay and modulational instabilities. For ocean waves this argument seems to hold promise (Alber, 1978; Dysthe et al., 2003). Heuristic arguments then implie that, due to nonlinear effects, the wavenumber spectra should broaden until some quasi stationary conditions are established. Analytical studies of electron plasma waves in magnetized as well as unmagnetized plasmas (Bhakta and Majumder, 1983; Pécseli, 2014; Kono and Pécseli, 2016; Kono and Pécseli, 2017a; Kono and Pécseli, 2017b) demonstrated that with the given assumptions a wide band spectrum was indeed less unstable than a narrow band. The results did not, however, predict complete modulation- or parametric decay-stabilizations for wide band wavenumber spectra: this could be due to a simplifying quasi-normal (sometimes termed quasi-Gaussian) assumption (Leslie, 1973; Alber, 1978) made in the analysis. The scenario outlined here has not been systematically analyzed experimentally nor numerically for plasma media. For numerical tests it is possible that one dimensional simulations can suffice. The low frequency decay products of modulational as well as oscillating two-stream instabilities do not obey any dispersion relation (Thornhill and ter Haar, 1978; Kono and Škorić, 2010; Pécseli, 2014). This feature is common to BGK-type phase space structures (Bernstein et al., 1957), such as phase space vortices, making it difficult to distinguish the phenomena by remote sensing, e.g., radio wave scattering (Vierinen et al., 2017).

6 CONCLUSION

Turbulence in fluids and plasmas have been studied for over a century but is still considered to represent one of the major unresolved problems in nonlinear physics. Elements in the theory of classical fluid turbulence, intermittency in particular, are not fully understood, but the available understanding suffices to allow adequate predictions for central problems such as turbulent transport also under inhomogeneous conditions. The understanding of plasma turbulence, for magnetized plasmas in particular, has not reached the same level, although convincing agreement between analytical results and observations have been achieved for a number of specific questions. Theories for weak turbulence in plasmas are well established and tested, in particular for the special case of 'quasi linear theory' (Kadomtsev, 1965) which accounts for the spreading in velocity space of an electron beam exciting electron plasma waves (Kontar, 2001; Ratcliffe et al., 2014). Generalizations and extensions of the analysis have been suggested (Orszag and Kraichnan, 1967; Horton, 1985; Similon and Sudan, 1990), but it is not known how well these models perform in comparison with observations, or realistic numerical simulation results of plasma turbulence.

AUTHOR CONTRIBUTIONS

Both authors have made a substantial, and direct, contribution to the work and approved it for publication.

ACKNOWLEDGMENTS

The authors thank Professor Lennart Stenflo and Professor Jan Trulsen for valuable discussions.

REFERENCES

Akbari, H., Guio, P., Hirsch, M. A., and Semeter, J. L. (2016). Zakharov simulations of beam-induced turbulence in the auroral ionosphere. *J. Geophys. Res. Space Phys.* 121, 4811–4825. doi:10.1002/2016JA022605

Alber, I. E. (1978). Effects of randomness on stability of two-dimensional surface wavetrains. *Proc. Roy. Soc. Lond.* 363, 525–546. doi:10.1098/rspa.1978.0181

Albert, J. M., Similon, P. L., and Sudan, R. N. (1990). Almost two–dimensional treatment of drift wave turbulence. *Phys. Fluid. Plasma Phys.* 2, 3032–3039. doi:10.1063/1.859370

Aryan, H., Agapitov, O. V., Artemyev, A., Mourenas, D., Balikhin, M. A., Boynton, R., et al. (2020). Outer radiation belt electron lifetime model based on combined van Allen probes and Cluster VLF measurements. *J. Geophys. Res. Space Physics.* 125, e2020JA028018. doi:10.1029/2020JA028018

Bale, S. D., Mozer, F. S., and Phan, T. (2002). Observation of lower hybrid drift instability in the diffusion region at a reconnecting magnetopause. *Geophys. Res. Lett.* 29, 33–1–33–4. doi:10.1029/2002GL016113

Basu, S., Basu, S., MacKenzie, E., Fougere, P. F., Coley, W. R., Maynard, N. C., et al. (1988). Simultaneous density and electric field fluctuation spectra associated with velocity shears in the auroral oval. *J. Geophys. Res.* 93, 115–136. doi:10.1029/JA093iA01p00115

Beall, J. M., Kim, Y. C., and Powers, E. J. (1982). Estimation of wavenumber and frequency spectra using fixed probe pairs. *J. Appl. Phys.* 53, 3933–3940. doi:10.1063/1.331279

Bell, T. F. (1985). High-amplitude VLF transmitter signals and associated sidebands observed near the magnetic equatorial plane on the ISEE 1 satellite. *J. Geophys. Res.* 90, 2792–2806. doi:10.1029/JA090iA03p02792

Bendat, J. S. (1958). *Principles and applications of random noise theory*. New York: John Wiley & Sons. doi:10.1002/qj.49708536318

Beran, M. J. (1968). *Statistical continuum theories, vol. 9 of monographs in statistical physics and thermodynamics*. New York: Interscience.

Bernstein, I. B., Greene, J. M., and Kruskal, M. D. (1957). Exact nonlinear plasma oscillations. *Phys. Rev.* 108, 546–550. doi:10.1103/PhysRev.108.546

Bhakta, J. C., and Majumder, D. (1983). Effect of finite spectral width on the modulational instability of Langmuir waves. *J. Plasma Phys.* 30, 203–209. doi:10.1017/S0022377800001124

Biskamp, D. (1997). Magnetic reconnection in plasmas. *Astrophys. Space Sci.* 242, 165207. doi:10.1007/BF00645113

Biskamp, D., Schwarz, E., Zeiler, A., Celani, A., and Drake, J. F. (1999). Electron magnetohydrodynamic turbulence. *Phys. Plasmas.* 6, 751–758. doi:10.1063/1.873312

Børve, S., Pécseli, H. L., and Trulsen, J. (2001). Ion phase-space vortices in 2.5-dimensional simulations. *J. Plasma Phys.* 65, 107–129. doi:10.1017/s0022377801008947

Briand, C. (2015). Langmuir waves across the heliosphere. *J. Plasma Phys.* 81, 325810204. doi:10.1017/S0022377815000112

Bruno, R., and Carbone, V. (2005). The solar wind as a turbulence laboratory. *Living Rev. Sol. Phys.* 10, 1–162. doi:10.12942/lrsp-2013-2

Büchner, J., and Elkina, N. (2006). Anomalous resistivity of current-driven isothermal plasmas due to phase space structuring. *Phys. Plasmas.* 13, 082304. doi:10.1063/1.2209611

Buneman, O. (1963). Excitation of field aligned sound waves by electron streams. *Phys. Rev. Lett.* 10, 285–287. doi:10.1103/PhysRevLett.10.285

Chen, F. F. (2016). *Introduction to plasma physics and controlled fusion*. 3rd Edn. Heidelberg: Springer.

Cho, J., and Lazarian, A. (2009). Simulations of electron magnetohydrodynamic turbulence. *Astrophys. J.* 701, 236–252. doi:10.1088/0004-637x/701/1/236

Constantin, P. (1991). "New perspectives in turbulence," in *Remarks on the Navier-Stokes equations*. (Berlin: Springer-Verlag), Chap. 8, 229–261.

Cox, D. P. (2005). The three-phase interstellar medium revisited. *Annu. Rev. Astron. Astrophys.* 43, 337–385. doi:10.1146/annurev.astro.43.072103.150615

Daldorff, L. K. S., Guio, P., Børve, S., Pécseli, H. L., and Trulsen, J. (2001). Ion phase space vortices in 3 spatial dimensions. *Europhys. Lett.* 54, 161–167. doi:10.1209/epl/i2001-00290-6

Davidson, P. A. (2004). *Turbulence. An introduction for scientists and engineers*. United Kingdom: Oxford University Press.

Davidson, R. C., and Gladd, N. T. (1975). Anomalous transport properties associated with the lower-hybrid-drift instability. *Phys. Fluids.* 18, 1327–1335. doi:10.1063/1.861021

Drake, J. F., Swisdak, M., Cattell, C., Shay, M. A., Rogers, B. N., and Zeiler, A. (2003). Formation of electron holes and particle energization during magnetic reconnection. *Science.* 299, 873–877. doi:10.1126/science.1080333

Drazin, P. G., and Johnson, R. S. (1989). *Solitons: an introduction*. Cambridge, UK: Cambridge University Press.

Dubois, D. F., Hanssen, A., Rose, H. A., and Russell, D. (1993). Space and time distribution of HF excited Langmuir turbulence in the ionosphere: comparison of theory and experiment. *J. Geophys. Res.* 98, 17543–17567. doi:10.1029/93JA01469

Dupree, T. H. (1969). "Turbulence in fluids and plasmas," in *Microwave research institute symposia series. Introduction to basic phenomena of turbulence in plasmas*. (Brooklyn, N.Y., Polytechnic Press), Chap. 2, Vol. XVIII, 3–12.

Dupree, T. H. (1970). Theory of resistivity in collisionless plasma. *Phys. Rev. Lett.* 25, 789–792. doi:10.1103/PhysRevLett.25.789

Dyrud, L., Krane, B., Oppenheim, M., Pécseli, H. L., Schlegel, K., Trulsen, J., et al. (2006). Low-frequency electrostatic waves in the ionospheric E-region: a comparison of rocket observations and numerical simulations. *Ann. Geophys.* 24, 2959–2979. doi:10.5194/angeo-24-2959-2006

Dyrud, L., Krane, B., Oppenheim, M., Pécseli, H. L., Trulsen, J., and Wernik, A. W. (2008). Structure functions and intermittency in ionospheric plasma turbulence. *Nonlinear Process Geophys.* 15, 847–862. doi:10.5194/npg-15-847-2008

Dysthe, K. B. (1971). Some studies of triggered whistler emissions. *J. Geophys. Res.* 76, 6915–6931. doi:10.1029/JA076i028p06915

Dysthe, K. B., Pécseli, H. L., and Trulsen, J. (1986). A statistical model for soliton particle interaction in plasmas. *Phys. Scr.* 33, 523. doi:10.1088/0031-8949/33/6/007

Dysthe, K. B., Trulsen, K., Krogstad, H. E., and Socquet-Juglard, H. (2003). Evolution of a narrow-band spectrum of random surface gravity waves. *J. Fluid Mech.* 478, 110. doi:10.1017/S0022112002002616

D'Angelo, N. (1977). Plasma waves and instabilities in the polar cusp: a review. *Rev. Geophys.* 15, 299–307. doi:10.1029/RG015i003p00299

Ergun, R. E., Carlson, C. W., McFadden, J. P., Mozer, F. S., Muschietti, L., Roth, I., et al. (1998). Debye-scale plasma structures associated with magnetic-field-aligned electric fields. *Phys. Rev. Lett.* 81, 826–829. doi:10.1103/PhysRevLett.81.826

Farley, D. T. (1963). Two-stream plasma instability as a source of irregularities in the ionosphere. *Phys. Rev. Lett.* 10, 279–282. doi:10.1103/PhysRevLett.10.279

Forme, F. R. E. (1999). Parametric decay of beam-driven Langmuir wave and enhanced ion-acoustic fluctuations in the ionosphere: a weak turbulence approach. *Ann. Geophys.* 17, 1172–1181. doi:10.1007/s00585005084210.1007/s00585-999-1172-4

Fredriksen, Å., Pécseli, H. L., and Trulsen, J. (2008). Crash and recovery of the potential in a toroidal plasma column, as observed by generalized conditional sampling. *New J. Phys.* 10, 033030. doi:10.1088/1367-2630/10/3/033030

Fritz, T. A., Chen, J., and Sheldon, R. B. (2000). The role of the cusp as a source for magnetospheric particles: a new paradigm?. *Adv. Space Res.* 25, 1445–1457. doi:10.1016/S0273-1177(99)00656-0

Fritz, T. A., Chen, J., and Siscoe, G. L. (2003). Energetic ions, large diamagnetic cavities, and Chapman-Ferraro cusp. *J. Geophys. Res. Space Phys.* 108, 1028. doi:10.1029/2002JA009476

Galtier, S. (2009). Wave turbulence in magnetized plasmas. *Nonlinear Process Geophys.* 16, 83–98. doi:10.5194/npg-16-83-2009

Goedbloed, H., and Poedts, S. (2004). *Principles of magnetohydrodynamics with applications to laboratory and astrophysical plasmas*. Cambridge, UK: Cambridge.

Graham, D. B., Khotyaintsev, Y. V., Norgren, C., Vaivads, A., André, M., Toledo-Redondo, S., et al. (2017). Lower hybrid waves in the ion diffusion and magnetospheric inflow regions. *J. Geophys. Res. Space Phys.* 122, 517–533. doi:10.1002/2016JA023572

Gruzinov, A., and Pogutse, O. (1986). Description of plasma turbulence in a strong magnetic field. *Proc. USSR Acad. Sci.* 290, 322–325.

Guio, P., and Forme, F. (2006). Zakharov simulations of Langmuir turbulence: effects on the ion-acoustic waves in incoherent scattering. *Phys. Plasmas.* 13, 122902. doi:10.1063/1.2402145

Guio, P., Børve, S., Daldorff, L. K. S., Lynov, J. P., Michelsen, P., Pécseli, H. L., et al. (2003). Phase space vortices in collisionless plasmas. *Nonlinear Process Geophys.* 10, 75–86. doi:10.5194/npg-10-75-2003

Haerendel, G. (2019). Experiments with plasmas artificially injected into near-earth space. *Front. Astron. Space Sci.* 6, 29. doi:10.3389/fspas.2019.00029

Hansen, F. R., Knorr, G., Lynov, J. P., Pécseli, H. L., and Rasmussen, J. J. (1989). A numerical plasma simulation including finite Larmor radius effects to arbitrary order. *Plasma Phys. Contr. Fusion*. 31, 173–183. doi:10.1088/0741-3335/31/2/003

Hanssen, A., Mjølhus, E., DuBois, D. F., and Rose, H. A. (1992). Numerical test of the weak turbulence approximation to ionospheric Langmuir turbulence. *J. Geophys. Res.* 97, 12073–12091. doi:10.1029/92JA00874

Hasegawa, A., and Mima, K. (1978). Pseudo-three-dimensional turbulence in magnetized nonuniform plasma. *Phys. Fluids*. 21, 87–92. doi:10.1063/1.862083

Hasegawa, A., and Wakatani, M. (1983). Plasma edge turbulence. *Phys. Rev. Lett.* 50, 682–686. doi:10.1103/PhysRevLett.50.682

Hassam, A. B., Hall, W., Huba, J. D., and Keskinen, M. J. (1986). Spectral characteristics of interchange turbulence. *J. Geophys. Res.* 91, 13513–13522. doi:10.1029/JA091iA12p13513

Heisenberg, W. (1948). Zur statistischen Theorie der Turbulenz. *Z. Phys.* 124, 628–657. doi:10.1007/BF01668899

Heisenberg, W., and Taylor, G. I. (1948). On the theory of statistical and isotropic turbulence. *Proc. Math. Phys. Eng. Sci.* 195, 402–406. doi:10.1098/rspa.1948.0127

Horton, W. (1985). Ion acoustic turbulence and anomalous transport. *J. Stat. Phys.* 39, 739–754. doi:10.1007/BF01008363

Horton, W. (1990). Nonlinear drift waves and transport in magnetized plasma. *Phys. Rep*. 192, 1–177. doi:10.1016/0370-1573(90)90148-U

Høymork, S. H., Pécseli, H. L., Lybekk, B., Trulsen, J., and Eriksson, A. (2000). Cavitation of lower hybrid waves in the Earth's ionosphere: a model analysis. *J. Geophys. Res.* 105, 18519–18536. doi:10.1029/2000JA900017

Huba, J. D., Gladd, N. T., and Papadopoulos, K. (1978). Lower-hybrid-drift wave turbulence in the distant magnetotail. *J. Geophys. Res.* 83, 5217–5226. doi:10.1029/JA083iA11p05217

Huba, J. D., Gladd, N. T., and Papadopoulos, K. (1977). The lower-hybrid-drift instability as a source of anomalous resistivity for magnetic field line reconnection. *Geophys. Res. Lett.* 4, 125–128. doi:10.1029/GL004i003p00125

Hut, P. (2006). Virtual laboratories. *Prog. Theor. Phys. Suppl.* 164, 38–53. doi:10.1143/PTPS.164.38

Iroshnikov, P. S. (1964). Turbulence of a conducting fluid in a strong magnetic field. *Sov. Astron. Lett.* 7, 566–571.

Isham, B., Rietveld, M. T., Guio, P., Forme, F. R. E., Grydeland, T., and Mjølhus, E. (2012). Cavitating Langmuir turbulence in the terrestrial aurora. *Phys. Rev. Lett.* 108, 105003. doi:10.1103/PhysRevLett.108.105003

Iwama, N., Ohba, Y., and Tsukishima, T. (1979). Estimation of wave-number spectrum parameters from fixed probe-pair data. *J. Appl. Phys*. 50, 3197–3206. doi:10.1063/1.326356

Jin, Y., Xiong, C., Clausen, L., Spicher, A., Kotova, D., Brask, S., et al. (2020). Ionospheric plasma irregularities based on *in situ* measurements from the Swarm satellites. *J. Geophys. Res. Space Physics*. 125, e2020JA028103. doi:10.1029/2020JA028103

Johnsen, H., Pécseli, H. L., and Trulsen, J. (1987). Conditional eddies in plasma turbulence. *Phys. Fluids*. 30, 2239–2254. doi:10.1063/1.866158

Johnson, J. R., Wing, S., and Delamere, P. A. (2014). Kelvin Helmholtz instability in planetary magnetospheres. *Space Sci. Rev.* 184, 1–31. doi:10.1007/s11214-014-0085-z

Jovanović, D., Lynov, J. P., Michelsen, P., Pécseli, H. L., Rasmussen, J. J., and Thomsen, K. (1982). Three dimensional double layers in magnetized plasmas. *Geophys. Res. Lett*. 9, 1049–1052. doi:10.1029/GL009i009p01049

Kadomtsev, B. B. (1965). *Plasma turbulence*. New York: Academic Press.

Karpman, V., Hansen, F., Huld, T., Lynov, J., Pécseli, H., and Rasmussen, J. (1990). Nonlinear evolution of the modulational instability of whistler waves. *Phys. Rev. Lett*. 64, 890–893. doi:10.1103/PhysRevLett.64.890

Karpman, V. I., Istomin, J. N., and Shklyar, D. R. (1974). Nonlinear frequency shift and self-modulation of the quasi- monochromatic whistlers in the inhomogeneous plasma (magnetosphere). *Planet. Space Sci.* 22, 859–871. doi:10.1016/0032-0633(74)90155-X

Kelley, M. C. (1989). *The Earth's ionosphere, plasma physics and electrodynamics. International geophysics series*. San Diego, California: Academic Press, Vol. 43.

Kim, Y. C., and Powers, E. J. (1978). Digital bispectral analysis of self-excited fluctuation spectra. *Phys. Fluids*. 21, 1452–1453. doi:10.1063/1.862365

Kingsep, A. S., Chukbar, K. V., and Yan'kov, V. V. (1990). *Electron magnetohydrodynamics. Review plasma physics*. New York: Consultant Bureau, Chap. 3, Vol. 16, 243–291.

Kingsep, A. S., Rudakov, L. I., and Sudan, R. N. (1973). Spectra of strong Langmuir turbulence. *Phys. Rev. Lett*. 31, 1482–1484. doi:10.1103/PhysRevLett.31.1482

Kjus, S. H., Pécseli, H. L., Lybekk, B., Holtet, J., Trulsen, J., Lühr, H., et al. (1998). Statistics of the lower hybrid wave cavities detected by the FREJA satellite. *J. Geophys. Res.* 103, 26633–26647. doi:10.1029/98JA02245

Knorr, G., Hansen, F. R., Lynov, J. P., Pécseli, H. L., and Rasmussen, J. J. (1988). Finite Larmor radius effects to arbitrary order. *Phys. Scripta*. 38, 829–834. doi:10.1088/0031-8949/38/6/014

Kollmann, W. (2019). *Navier-Stokes turbulence: theory and analysis*. Switzerland: Springer.

Kono, M., and Pécseli, H. L. (2016). Parametric decay of wide band Langmuir wave-spectra. *J. Plasma Phys*. 82, 905820606. doi:10.1017/S0022377816001070

Kono, M., and Pécseli, H. L. (2017a). Stability of electron wave spectra in weakly magnetized plasmas. *J. Plasma Phys*. 83, 905830610. doi:10.1017/S0022377817000873

Kono, M., and Pécseli, H. L. (2017b). Stability of electron wave spectra in weakly magnetized plasmas: local spectra and correlations. 1–12. doi:10.5281/zenodo.1035851

Kono, M., and Škorić, M. M. (2010). "Nonlinear physics of plasmas. No. 62," in *Springer series on atomic, optical, and plasma physics*. Heidelberg, Germany: Springer.

Kontar, E. P. (2001). Dynamics of electron beams in the inhomogeneous solar corona plasma. *Sol. Phys*. 202, 131–149. doi:10.1023/A:1011894830942

Kraichnan, R. H. (1965). Inertial-range spectrum of hydromagnetic turbulence. *Phys. Fluids*. 8, 1385–1387. doi:10.1063/1.1761412

Kraichnan, R. H., and Montgomery, D. (1980). Two-dimensional turbulence. *Rep. Prog. Phys*. 43, 547–619. doi:10.1088/0034-4885/43/5/001

Krane, B., Pécseli, H. L., Trulsen, J., and Primdahl, F. (2000). Spectral properties of low-frequency electrostatic waves in the ionospheric E region. *J. Geophys. Res.* 105, 10585–10601. doi:10.1029/1999JA900503

Landahl, M. T., and Mollo-Christensen, E. (1992). *Turbulence and random processes in fluid mechanics*. 2nd Edn. Cambridge, UK: Cambridge University Press.

Leslie, D. C. (1973). *Developments in the theory of turbulence*. Oxford: Oxford University Press.

Li, J., Bortnik, J., An, X., Li, W., Angelopoulos, V., Thorne, R. M., et al. (2019). Origin of two-band chorus in the radiation belt of Earth. *Nat. Commun*. 10, 4672. doi:10.1038/s41467-019-12561-3

Lynov, J. P., Michelsen, P., Pécseli, H. L., Rasmussen, J. J., Saéki, K., and Turikov, V. A. (1979). Observations of solitary structures in a magnetized, plasma loaded waveguide. *Phys. Scr*. 20, 328–335. doi:10.1088/0031-8949/20/3-4/005

Lyutikov, M. (2013). Electron magnetohydrodynamics: dynamics and turbulence. *Phys. Rev. E*. 88, 053103. doi:10.1103/PhysRevE.88.053103

Ma, X., Delamere, P., Otto, A., and Burkholder, B. (2017). Plasma transport driven by the three-dimensional Kelvin-Helmholtz instability. *J. Geophys. Res. Space Phys.* 122 (10), 10382–10395. doi:10.1002/2017JA024394

Machalek, M. D., and Nielsen, P. (1973). Light-scattering measurements of turbulence in a normal shock. *Phys. Rev. Lett*. 31, 439–442. doi:10.1103/PhysRevLett.31.439

Mikkelsen, T., and Pécseli, H. L. (1980). Strong turbulence in partially ionized plasmas. *Phys. Lett*. 77, 159–162. doi:10.1016/0375-9601(80)90179-6

Misguich, J. H., Balescu, R., Pécseli, H. L., Mikkelsen, T., Larsen, S. E., and Xiaoming, Q. (1987). Diffusion of charged particles in turbulent magnetoplasmas. *Plasma Phys. Contr. Fusion*. 29, 825–856. doi:10.1088/0741-3335/29/7/004

Morley, S. K. (2020). Challenges and opportunities in magnetospheric space weather prediction. *Space Weather*. 18, e2018SW002108. doi:10.1029/2018SW002108

Morse, R. L., and Nielson, C. W. (1969). One-, two-, and three-dimensional numerical simulation of two-beam plasmas. *Phys. Rev. Lett*. 23, 1087–1090. doi:10.1103/PhysRevLett.23.1087

Musher, S. L., and Sturman, B. I. (1975). Collapse of plasma waves near the lower hybrid resonance. *JETP Lett*. 22, 265–267.

Nakamura, S., Omura, Y., and Summers, D. (2018). Fine structure of whistler mode hiss in plasmaspheric plumes observed by the van Allen probes. *J. Geophys. Res. Space Physics*. 123, 9055–9064. doi:10.1029/2018JA025803

Nicholson, D. R. (1983). *Introduction to plasma theory*. New York: John Wiley & Sons.

Novikov, E. A. (1990). The effects of intermittency on statistical characteristics of turbulence and scale similarity of breakdown coefficients. *Phys. Fluid. Fluid Dynam*. 2, 814–820. doi:10.1063/1.857629

Oppenheim, M., Otani, N., and Ronchi, C. (1996). Saturation of the Farley-Buneman instability via nonlinear electron E×B drifts. *J. Geophys. Res*. 101, 17273–17286. doi:10.1029/96JA01403

Orszag, S. A., and Kraichnan, R. H. (1967). Model equations for strong turbulence in a Vlasov plasma. *Phys. Fluids*. 10, 1720–1736. doi:10.1063/1.1762351

Ott, E., and Farley, D. T. (1974). The spectrum of ionospheric irregularities. *J. Geophys. Res*. 79, 2469–2472. doi:10.1029/JA079i016p02469

Papadopoulos, K. (1977). A review of anomalous resistivity for the ionosphere. *Rev. Geophys*. 15, 113–127. doi:10.1029/RG015i001p00113

Partamies, N., Donovan, E., and Knudsen, D. (2008). Statistical study of inverted-V structures in FAST data. *Ann. Geophys*. 26, 1439–1449. doi:10.5194/angeo-26-1439-2008

Pécseli, H. L. (2016). *Low frequency waves and turbulence in magnetized laboratory plasmas and in the ionosphere*. United Kingdom: IOP Publishing.

Pécseli, H. L. (2014). Modulational stability of electron plasma wave spectra. *J. Plasma Phys*. 80, 745–769. doi:10.1017/S002237781400035X

Pécseli, H. L. (2015). Spectral properties of electrostatic drift wave turbulence in the laboratory and the ionosphere. *Ann. Geophys*. 33, 875–900. doi:10.5194/angeo-33-875-2015

Pécseli, H. L., and Trulsen, J. (2006). "Tests of time evolutions in deterministic models by random sampling of space plasma phenomena," in *Geospace electromagnetic waves and radiation. Lecture notes in physics*. Berlin: Springer, Chap. 11, Vol. 687, 273–296.

Pécseli, H. L., Iranpour, K., Holter, Ø., Lybekk, B., Holtet, J., Trulsen, J., et al. (1996). Lower hybrid wave cavities detected by the FREJA satellite. *J. Geophys. Res*. 101, 5299–5316. doi:10.1029/95JA03127

Pécseli, H. L., Lybekk, B., Trulsen, J., and Eriksson, A. (1997). Lower-hybrid wave cavities detected by instrumented spacecrafts. *Plasma Phys. Contr. Fusion*. 39, A227. doi:10.1088/0741-3335/39/5A/021

Pécseli, H. L., Trulsen, J., and Armstrong, R. J. (1984). Formation of ion phase-space vortexes. *Phys. Scr*. 29, 241–253. doi:10.1088/0031-8949/29/3/010

Post, D. E., and Votta, L. G. (2005). Computational science demands a new paradigm. *Phys. Today*. 58, 35–41. doi:10.1063/1.1881898

Primdahl, F. (1986). Polar ionospheric E-region plasma wave stabilization and electron heating by wave-induced enhancement of the electron collision frequency. *Phys. Scripta*. 33, 187–191. doi:10.1088/0031-8949/33/2/017

Rasmussen, J. J., and Rypdal, K. (1986). Blow-up in nonlinear Schroedinger equations-I A general review. *Phys. Scr*. 33, 481–497. doi:10.1088/0031-8949/33/6/001

Ratcliffe, H., Brady, C. S., Che Rozenan, M. B., and Nakariakov, V. M. (2014). A comparison of weak-turbulence and particle-in-cell simulations of weak electron-beam plasma interaction. *Phys. Plasmas*. 21, 122104. doi:10.1063/1.4904065

Robinson, P. A. (1997). Nonlinear wave collapse and strong turbulence. *Rev. Mod. Phys*. 69, 507–574. doi:10.1103/RevModPhys.69.507

Saeki, K., Michelsen, P., Pécseli, H. L., and Rasmussen, J. J. (1979). Formation and coalescence of electron solitary holes. *Phys. Rev. Lett*. 42, 501–504. doi:10.1103/PhysRevLett.42.501

Sakanaka, P. H. (1972). Beam-generated collisionless ion-acoustic shocks. *Phys. Fluids*. 15, 1323–1327. doi:10.1063/1.1694084

Sato, H., Jakowski, N., Berdermann, J., Jiricka, K., Heßelbarth, A., Banyś, D., et al. (2019). Solar radio burst events on 6 September 2017 and its impact on GNSS signal frequencies. *Space Weather*. 17, 816–826. doi:10.1029/2019SW002198

Sato, N., Hatakeyama, R., Iizuka, S., Mieno, T., Saeki, K., Rasmussen, J. J., et al. (1981). Ultrastrong stationary double layers in a nondischarge magnetoplasma. *Phys. Rev. Lett*. 46, 1330–1333. doi:10.1103/PhysRevLett.46.1330

Schamel, H. (1986). Electron holes, ion holes and double layers. *Phys. Rep*. 140, 161–191. doi:10.1016/0370-1573(86)90043-8

Schlegel, K., and St.-Maurice, J. P. (1981). Anomalous heating of the polar E region by unstable plasma waves 1. Observations. *J. Geophys. Res*. 86, 1447–1452. doi:10.1029/JA086iA03p01447

Schuck, P. W., Bonnell, J. W., and Kintner, P. M. (2003). A review of lower hybrid solitary structures. *IEEE Trans. Plasma Sci*. 31, 1125–1177. doi:10.1109/TPS.2003.822043

Schuck, P. W., Bonnell, J. W., and Pinçon, J.-L. (2004). Properties of lower hybrid solitary structures: a comparison between space observations, a laboratory experiment, and the cold homogeneous plasma dispersion relation. *J. Geophys. Res. Space Phys*. 109, A01310. doi:10.1029/2002JA009673

Shapiro, V. D., Shevchenko, V. I., Solov'ev, G. I., Kalinin, V. P., Bingham, R., Sagdeev, R. Z., et al. (1993). Wave collapse at the lower-hybrid resonance. *Phys. Fluids, Plasma Phys*. 5, 3148–3162. doi:10.1063/1.860652

Shawhan, S. D. (1979). "Magnetospheric plasma waves," in *Solar system plasma physics*. Amsterdam: North-Holland Publishing Company, Chap. III.1.6, Vol. 54, 213–270.

Shawhan, S. D. (1985). The menagerie of geospace plasma waves. *Space Sci. Rev*. 42, 257–274. doi:10.1007/BF00218235

Shkarofsky, I. P. (1969). "Analytic forms for decaying turbulence functions," in *Turbulence in fluids and plasmas. Microwave research institute symposia series*. Brooklyn, N. Y., USA: Polytechnic Press, Chap. 21, Vol. XVIII, 289–301.

Similon, P. L., and Sudan, R. N. (1990). Plasma turbulence. *Annu. Rev. Fluid Mech*. 22, 317–347. doi:10.1146/annurev.fl.22.010190.001533

Sotnikov, V. I., Shapiro, V. D., and Shevchenko, V. I. (1978). Macroscopic consequences of collapse at the lower hybrid resonance. *Sov. J. Plasma Phys*. 4, 252–257.

Sreenivasan, K. R. (1995). On the universality of the Kolmogorov constant. *Phys. Fluids*. 7, 2778–2784. doi:10.1063/1.868656

Stenzel, R. L. (1999). Whistler waves in space and laboratory plasmas. *J. Geophys. Res*. 104, 14379–14395. doi:10.1029/1998JA900120

Stenzel, R. L. (2016). Whistler waves with angular momentum in space and laboratory plasmas and their counterparts in free space. *Adv. Phys. X*. 1, 687–710. doi:10.1080/23746149.2016.1240017

Sudan, R. N. (1983). Unified theory of Type I and Type II irregularities in the equatorial electrojet. *J. Geophys. Res*. 88, 4853–4860. doi:10.1029/JA088iA06p04853

Sudan, R. N., and Keskinen, M. (1977). Theory of strongly turbulent two-dimensional convection of low-pressure plasma. *Phys. Rev. Lett*. 38, 966–970. doi:10.1103/PhysRevLett.38.966

Sulem, C., Sulem, P.-L., and Frisch, H. (1983). Tracing complex singularities with spectral methods. *J. Comput. Phys*. 50, 138–161. doi:10.1016/0021-9991(83)90045-1

Taylor, G. I. (1938). The spectrum of turbulence. *Proc. R. Soc. A*. 164, 476–490. doi:10.1098/rspa.1938.0032

Tchen, C. M., Pécseli, H. L., and Larsen, S. E. (1980). Strong turbulence in low-β plasmas. *Plasma Phys*. 22, 817–829. doi:10.1088/0032-1028/22/8/005

Teliban, I., Block, D., Piel, A., and Greiner, F. (2007). Improved conditional averaging technique for plasma fluctuation diagnostics. *Plasma Phys. Contr. Fusion*. 49, 485–497. doi:10.1088/0741-3335/49/4/011

Tennekes, H., and Lumley, J. L. (1972). *A first course in turbulence*. Cambridge, Massachusetts: MIT Press.

Thornhill, S. G., and ter Haar, D. (1978). Langmuir turbulence and modulational instability. *Phys. Rep*. 43, 43–99. doi:10.1016/0370-1573(78)90142-4

Tong, Y., Vasko, I., Mozer, F. S., Bale, S. D., Roth, I., Artemyev, A., et al. (2018). Simultaneous multispacecraft probing of electron phase space holes. *Geophys. Res. Lett*. 45, 11513–11519. doi:10.1029/2018GL079044

Vierinen, J., Gustavsson, B., Hysell, D. L., Sulzer, M. P., Perillat, P., and Kudeki, E. (2017). Radar observations of thermal plasma oscillations in the ionosphere. *Geophys. Res. Lett*. 44, 5301–5307. doi:10.1002/2017GL073141

Vladimirov, S. V., and Stenflo, L. (1997). Three-wave processes in a turbulent nonstationary plasma. *Phys. Plasmas*. 4, 1249–1256. doi:10.1063/1.872297

von Alfthan, S., Pokhotelov, D., Kempf, Y., Hoilijoki, S., Honkonen, I., Sandroos, A., et al. (2014). Vlasiator: first global hybrid-Vlasov simulations of Earth's

foreshock and magnetosheath. *J. Atmos. Sol. Terr. Phys.* 120, 24–35. doi:10.1016/j.jastp.2014.08.012

Walker, S. N., Balikhin, M. A., Alleyne, H. S. C. K., Hobara, Y., André, M., and Dunlop, M. W. (2008). Lower hybrid waves at the shock front: a reassessment. *Ann. Geophys.* 26, 699–707. doi:10.5194/angeo-26-699-2008

Wang, R., Vasko, I. Y., Mozer, F. S., Bale, S. D., Artemyev, A. V., Bonnell, J. W., et al. (2020). Electrostatic turbulence and Debye-scale structures in collisionless shocks. *Acta Pathol. Jpn.* 889, L9. doi:10.3847/2041-8213/ab6582

Wyngaard, J. C., and Clifford, S. F. (1977). Taylor's hypothesis and high-frequency turbulence spectra. *J. Atmos. Sci.* 34, 922–929. doi:10.1175/1520-0469(1977)034<0922:THAHTS>2.0.CO;2

Yeh, K. C., and Liu, C. H. (1972). *Theory of ionospheric waves. International geophysics series*. New York, London: Academic Press, Vol. 17.

Young, M. A., Oppenheim, M. M., and Dimant, Y. S. (2020). The Farley-Buneman spectrum in 2-D and 3-D particle-in-cell simulations. *J. Geophys. Res. Space Phys.* 125, e2019JA027326. doi:10.1029/2019JA027326

Zakharov, V. E. (1972). Collapse of Langmuir waves. *Sov. Phys.-JETP.*, 35, 908–914.

Zhang, W., Ni, B., Huang, H., Summers, D., Fu, S., Xiang, Z., et al. (2019). Statistical properties of hiss in plasmaspheric plumes and associated scattering losses of radiation belt electrons. *Geophys. Res. Lett.* 46, 5670–5680. doi:10.1029/2018GL081863

Conflict of Interest: The authors declare that the research was conducted in the absence of any commercial or financial relationships that could be construed as a potential conflict of interest.

frontiers in Astronomy and Space Sciences

REVIEW
published: 28 January 2021
doi: 10.3389/fspas.2020.616635

Plasma and Magnetic Field Turbulence in the Earth's Magnetosheath at Ion Scales

Liudmila Rakhmanova, Maria Riazantseva and Georgy Zastenker*

Space Research Institute, Russian Academy of Sciences, Moscow, Russia

Crossing the Earth's bow shock is known to crucially affect solar wind plasma including changes in turbulent cascade. The present review summarizes results of more than 15 years of experimental exploration into magnetosheath turbulence. Great contributions to understanding turbulence development inside the magnetosheath was made by means of recent multi-spacecraft missions. We introduce the main results provided by them together with first observations of the turbulent cascade based on direct plasma measurements by the Spektr-R spacecraft in the magnetosheath. Recent results on solar wind effects on turbulence in the magnetosheath are also discussed.

OPEN ACCESS

Edited by:
Alessandro Retino, UMR7648 Laboratoire de physique des plasmas (LPP), France

Reviewed by:
Silvia Perri, University of Calabria, Italy
Julia E. Stawarz, Imperial College London, United Kingdom

***Correspondence:**
Liudmila Rakhmanova
rakhlud@gmail.com

Specialty section:
This article was submitted to Space Physics, a section of the journal Frontiers in Astronomy and Space Sciences

Received: *12 October 2020*
Accepted: *18 December 2020*
Published: *28 January 2021*

Citation:
Rakhmanova L, Riazantseva M and Zastenker G (2021) Plasma and Magnetic Field Turbulence in the Earth's Magnetosheath at Ion Scales. Front. Astron. Space Sci. 7:616635. doi: 10.3389/fspas.2020.616635

Keywords: plasma turbulence, solar wind, bow shock, magnetosheath, Sun-Earth's coupling

INTRODUCTION

Coupling between solar wind (SW) and the Earth's magnetosphere is one of the challenging problems of modern geophysics. The presence of a transition layer in front of the magnetopause has been known since the launching of the first spacecraft to the near-Earth space (e.g., Ness et al., 1964; Spreiter et al., 1966). Its presence results from an interaction between the supersonic and superalfvenic SW and the magnetosphere which leads to the formation of the outstanding bow shock (BS) wave.

The role of the magnetosheath (MSH) in Sun-Earth coupling has been focused on for several decades. At the BS plasma decelerates and diverts, it becomes denser and hotter. In general, the MSH plasma flow behind the BS can be described satisfactorily by magnetohydrodynamic (MHD) models (e.g., Spreiter and Stahara, 1980; Kartalev et al., 1996; Tóth et al., 2005; Samsonov et al., 2007; Samsonov et al., 2012). An MHD approach helps to obtain mean values of plasma and magnetic field parameters inside the MSH at large enough scales. However, small-scale variations of the parameters cannot be obtained by these models (e.g., Zastenker et al., 2002; Hayosh et al., 2006). Large amount of small-scale fluctuations, arising inside the MSH do not obey the MHD description of the plasma and may lead to discrepancies between the parameters predicted by the MHD models and the parameters, measured locally during short time intervals. In particular, the magnetic and electric field as well as density profiles which directly affect the magnetopause, were shown to be different from those measured in the SW (e.g., Šafránková et al., 2009; Pulinets et al., 2014; Pulkkinen et al., 2016). These differences are not usually taken into account by models of solar wind-magnetosphere coupling, which may be the reason for their inaccuracies.

Similar to the regions downstream of interplanetary shocks, behind the BS the fluctuations of the plasma and magnetic field parameters have higher amplitude, i.e., higher power spectral density (PSD), than those in the upstream undisturbed SW and fill a wide range of frequencies (or scales). The power of the fluctuations is strongly controlled by the geometry of the BS in the point where plasma enters the MSH (Greenstadt, 1972; Shevyrev et al., 2003; Shevyrev and Zastenker, 2005). This

geometry is usually characterized by the θ_{BN} angle between the local BS normal and interplanetary magnetic field (IMF) vector. Behind the quasi-parallel BS ($\theta_{BN} < 45^{\circ}$), fluctuations are as much as 2–3 times more powerful than behind the quasi-perpendicular BS ($\theta_{BN} > 45^{\circ}$). In some cases, the fluctuations penetrate to the MSH from the SW, but in most of the cases the BS itself and processes inside the MSH are the sources of variations (Zastenker et al., 2002). Fluctuations inside the MSH have various sources. At the bow shock, temperature anisotropy increases resulting in a relaxation of energy via waves and instabilities (Anderson et al., 1994; Lacombe and Belmont, 1995; Schwartz et al., 1996). Upstream foreshock processes contribute to the fluctuations behind the quasi-parallel bow shock (Shevyrev and Zastenker, 2005; Shevyrev et al., 2006; Kozak et al., 2011; Gutynska et al., 2012). Moreover, behind the BS, the fluctuations are superimposed by the MSH dynamics in response to the changes in the upstream SW parameters (e.g., Sibeck and Gosling, 1996). The multifactor dynamics of the MSH fluctuations lead to difficulties in its analysis.

MSH fluctuations have been analyzed via experimental data for a long time in different ways: in statistical descriptions (Němeček et al., 2000; Němeček et al., 2001; Němeček et al., 2002; Shevyrev and Zastenker, 2005; Gutynska et al., 2008; Gutynska et al., 2009; Gutynska et al., 2012; Dimmock et al., 2014), in sets of case studies (Zastenker et al., 2002; Shevyrev et al., 2003; Kozak et al., 2011; Kozak et al., 2012), or as a set of wave modes (Song et al., 1992a; Song et al., 1992b; Hubert, 1994; Lacombe and Belmont, 1995; Lucek et al., 2001; Sahraoui et al., 2003; Alexandrova, 2004; Sahraoui et al., 2004). Recent achievements in hybrid simulations (Blanco-Cano et al., 2006a; Blanco-Cano et al., 2006b; Omidi et al., 2010; Ofman and Gedalin, 2013; Karimabadi et al., 2014; Omidi et al., 2014) also made a great contribution to the understanding of the dynamics of MSH variations and waves. However, MSH fluctuations usually present a set of mixed components such as different wave modes, coherent structures, and external fluctuations of the SW origin, which also present highly complex mixed structures as well (see e.g., Roberts et al., 2013; Perschke et al., 2014; Perrone et al., 2020). One of the ways to deal with the whole ensemble of fluctuations is to consider it in a framework of turbulent cascade.

Turbulence in plasma is usually regarded as the cascade of energy through scales via non-linear interacting eddies (Frisch, 1995). Moreover, in plasmas, a variety of wave modes can exist and the non-linear interaction of these waves also contributes to the formation of the turbulent cascade (e.g., Goldreich and Sridhar, 1995). Turbulence can be found in many of astrophysical and space plasmas like stellar winds, accretion discs, galaxy clusters [see review by Schekochihin et al., (2009)], planetary magnetosheaths, and in laboratory plasma as well (Budaev et al., 2015). Near-Earth space is usually referred to as a natural laboratory to study turbulence in collisionless plasma, as a large set of spacecraft data help to analyze it for different backgrounds and in a wide range of scales–from electron gyroradii up to the scales of large space phenomena (e.g., coronal mass ejections, planetary magnetospheres, etc.).

The largest eddies which form the turbulent cascade determines the scales at which energy is supposed to be injected into the system. At small scales where kinetic processes make a significant contribution to the cascade, the energy is supposed to be partially transferred to the particles (i.e., dissipated) which leads to plasma heating. A feature of systems characterized by very high Reynolds numbers is that the scales at which energy is injected and dissipated differ by many orders of scales. This difference leads to the existence of several ranges of scales in the turbulent cascade. In the energy containing scales (more than $\sim 10^6$ km for the SW plasma), spectra usually follows the $\sim k^{-1}$ power law. Then the spectrum steepens and follows the $k^{-5/3}$ power law, predicted for the velocity fields by Kolmogorov (1941) and described more commonly for plasma flow by Frisch (1995). In the scales of dissipation, the Kolmogorov phenomenology ceases to operate and the turbulent cascade breaks and steepens. This range has been shown to start close to the scales of proton inertial length, or proton gyroradius. Since the beginning of the spacecraft era, a large dataset of *in situ* measurements in the SW has provided a great opportunity to study turbulence in collisionless plasma. Detailed phenomenology of turbulent cascade formation in SW plasma can be found in reviews by Tu and Marsch (1995); Alexandrova et al. (2013); Bruno and Carbone (2013); Chen (2016).

MSH turbulence is studied much less compared to those in the SW, though it has been actively explored during the last few decades. The present review focuses on the experimental study of MSH turbulence around ion scales. It does not claim to present a full unbiased review of turbulence in the MSH, but aims to give an overview of the kinds of experimental studies on turbulence spectra which have been performed during last two decades with the help of different spacecraft and different kinds of measurements. Some of them have already been reviewed by Zimbardo et al. (2010), who provided a comparison between turbulence features in different regions of the near-Earth space. Also, some of the results were included in a recent review by Sahraoui et al. (2020), which summarized several years of the authors' explorations of turbulence in space plasma. A substantial part of the present review is devoted to the exploration of MSH turbulence with the help of high-resolution plasma measurements available on board the Spektr-R spacecraft, which have not been presented in other reviews. The main purpose of the paper is to provide a comparison between statistical studies of turbulence spectra and to point out the importance of plasma fluctuations.

TURBULENT FEATURES OF THE MAGNETOSHEATH FLUCTUATIONS

Spectral Indices and Shapes: Some Features and Case Studies

In the theoretical frameworks, turbulent cascade is usually described in wave vector k space, where the energy spectrum follows the $\sim k^{\alpha}$ law, with α varying for different range of scales. Transition from experimentally obtained frequency spectra to

those in wave vector space is one of the difficulties in comparison between a theory and an experiment. Usually, a Taylor hypothesis is applied for such a comparison (Taylor, 1938). This method assumes that waves, which form the cascade, are much slower than the plasma flow, or in other terms, that the waves have low frequency in a plasma rest frame. Klein et al. (2014) and Howes et al. (2014) checked the validity of the Taylor hypothesis for linear kinetic wave modes in SW plasma. The authors showed that the hypothesis could only be significantly violated in cases of low bulk speed of plasma $V \sim V_A$ [with $V_A = B/(4\pi\rho_m)^{-1/2}$ being the Alfven speed, B being the magnetic field magnitude, and ρ_m being the plasma mass density] and in case of fast or whistler turbulence. The applicability of the Taylor hypothesis was studied via compressive Hall-MHD numerical simulations by Perri et al. (2017). The authors suggested that deviations of real spectra from those measured by a single spacecraft to be significant for the flow speed close to V_A and at sub ion scales in the case of a k-vector parallel to the mean magnetic field. Recently, the validity of the Taylor hypothesis at sub-ion scales was checked via direct comparison between the single-spacecraft time measurements converted to the spatial ones with the help of the hypothesis and the direct spatial measurements between pairs of the MMS spacecraft. The reported results showed that the Taylor hypothesis works well in most of the cases (e.g., Chasapis et al., 2017; Chen and Boldyrev, 2017; Chhiber et al., 2018; Stawarz et al., 2019). However, some of the cases showed a clear violation of the hypothesis (Stawarz et al., 2019). Typically, in the SW the hypothesis is satisfied as well as in the flank MSH as bulk velocity is significantly higher than the Alfven or magnetosonic speeds and whistlers are rarely observed (Rodriguez, 1985). However, a probable mismatch of spatial and temporal variation spectra should be kept in mind when considering subsolar MSH. Huang and Sahraoui (2019) presented a simple check of the validity of the Taylor hypothesis using the ratio between frequencies of ion and electron spectral breaks.

Processing *in situ* measurements is commonly prepared in frequency space. Usually, with the help of Fourier or wavelet analysis, one can distinguish the frequency range of at least 1 decade of scales at which spectra can be approximated with $\sim f^{\alpha}$ with a constant value of α. Another method to obtain features of the turbulent fluctuations is analysis of the probability distribution function (PDF) or analysis of structure functions which represent high order moments of the field and its scaling (Frisch 1995; Bruno and Carbone 2013). Though this method provides a deeper view on the parameters of plasma turbulence, it is rather sensitive to data quality and is difficult to apply for statistical studies. Fourier and wavelet analyses are more commonly used for turbulence exploration (Dudok de Wit et al., 2013).

In theoretical frameworks, different predictions of spectral indices are usually given depending on the processes responsible for turbulence development and dissipation (e.g., Leamon et al., 1998; Smith et al., 2006; Schekochihin et al., 2009; Boldyrev and Perez, 2012). Thus, a comparison of the value of the spectral exponent, obtained by means of experimental data, with theoretical predictions was supposed to give the information of processes governing the space plasma turbulence and was a goal of a number of studies.

Since the first experimental studies of the MSH turbulence, a variety of spectral indices values have been reported. Below a set of distinct results are listed and the causes of differences are discussed in the next sections. In an early review of the magnetic field fluctuations inside the MSH, Fairfield (1976) presented a composed spectrum, obtained by the onboard measurements of different spacecraft—OGO−1,−3,−5, Mariner 4, Explorer 12—in the range of frequencies 10^{-2}–10^{2} Hz. This spectrum followed a two-power-law structure with a break at ∼0.2 Hz. The power exponents were close to −1 and −3 at frequencies lower and higher than the ion spectral break, respectively. Rezeau et al. (1986) analyzed 14 spectra at frequencies 0.5–11 Hz, i.e., above proton gyrofrequency, obtained by the GOES-2 spacecraft in the MSH. The spectral exponent was estimated to be close to the −3 value with the 0.3 standard deviation of the distribution of the exponent's value. Later, a somewhat steeper spectrum was presented for the wider range of scales—0.1–100 Hz (Rezeau et al., 1999). The two-power-law spectrum of magnetic field fluctuation was observed by Dudok de Wit and Krasnosel'Skikh (1996) with the help of AMPTE-UKS measurements downstream from the subsolar quasi-parallel BS. Statistical exploration of the features of magnetic field fluctuations behind the bow shock was provided by Czaykowska et al. (2001). The authors analyzed 132 cases of bow shock crossings by the AMPTE/IRM spacecraft and presented a typical view of the magnetic field fluctuation spectrum behind the bow shock. The spectra exhibited a clear break at ion scales and followed the $\sim f^{-1}$ power law at frequencies below the break while the power exponent ranged from −3 to −2 at sub-ion scales.

Note that in the case of analyzing the fluctuation spectra at scales of transition from MHD to kinetic scales, the uncertainties of the MHD-part slope calculation is higher than those of the kinetic-scale slope. Usually for measurements with high enough time resolution the slope at the kinetic scales can be calculated quite precisely. The scatter of the kinetic-scale slope values reported in various experimental studies is likely to arise from wide statistical distribution rather than errors of estimation.

One of the important factors influencing turbulence development in plasma is intermittency indicated by deviation of the PDF of fluctuations from Gaussian becoming more pronounced toward smaller scales (Tu and Marsch, 1995; Sorriso-Valvo et al., 1999; Macek, 2007; Riazantseva et al., 2015). This was usually interpreted as the concentration of turbulent energy in structures at sub-ion scales, with geometry of the structures affecting the turbulent cascade. In experimental studies, the intermittency can be easily detected by means of the flatness (or kurtosis) value which is the fourth moment of the PDF. An increase of flatness to values above three (analytically determined value for Gaussian PDF) with decreasing scales indicates the presence of intermittency. Note that commonly used theories of turbulence do not involve the intermittent nature of plasma that in some cases may result in discrepancies in the modeled predictions and observations (see reviews by Bruno and Carbone 2013; Budaev et al., 2011). In the MSH, intermittency

has been rarely addressed. Dudok de Wit and Krasnosel'Skikh (1996) used high-order statistics and presented the non-Gaussian distribution of magnetic field fluctuations both upstream and downstream of the BS. Kozak et al. (2012) provided a comparison between the intermittent features of the magnetic field in the SW, MSH, and foreshock and presented an absence of intermittency in the MSH. A recent case study by Chhiber et al. (2018) demonstrated the intermittent nature of turbulence both at the electron and ion scales in front of the magnetopause. Moreover, the authors compared features of PDF in the SW and in the MSH based on two cases of MMS measurements and suggested a more intermittent character of MSH turbulence. The flatness/kurtosis value was shown to constantly increase toward the electron scales in the MSH while in the SW, the kurtosis stopped increasing around the ion scales and then decreased up to three at the electron scales. However, the authors noted that intermittency features can change significantly and rapidly in such a dynamically bounded region as the MSH. Statistical comparison between the intermittency in the SW and in the flank MSH (Riazantseva et al., 2016) showed dependencies of kurtosis on the considered scale for a variety of analyzed cases which included the kurtosis value close to three at all scales, i.e., the absence of intermittency. Thus, the character of intermittency in the MSH and its difference from the intermittency of SW turbulence is still a challenging question.

Active exploration of turbulence in the near-Earth space started in 2001 with the launch of the Cluster satellites (Escoubet et al., 1997). The Cluster measurements were prepared by four spacecraft grouped in a tetrahedron with the sides of the order of ion gyroradius. This advantage in the mission allowed for dividing temporal fluctuations from the spatial and for direct exploration of the turbulence anisotropy at the ion scales. Combined with high-quality magnetic field measurements of high cadence, Cluster data have provided a powerful instrument for the exploration of turbulence at the ion and sub-ion scales. One of the first observations of the magnetic field fluctuation spectrum in the MSH (Rezeau et al., 2001) revealed $\sim f^{-2.31}$ spectrum at frequencies 1–10 Hz when the spacecraft were in the vicinity of the magnetopause at the MSH flank.

The technique of decomposition of fluctuations into frequency and wave vector domains was applied to the Cluster data by Sahraoui et al. (2003). The authors analyzed a period of magnetosheath observation close to the magnetopause. The suggested method called the k-filtering technique helped the authors to determine that the turbulent cascade was dominated by mirror mode fluctuations. Further, the authors performed a comprehensive analysis of Cluster measurements when the spacecraft were separated by ~100 km and presented evidence of anisotropy of the cascade formation in the MSH (Sahraoui et al., 2006). The magnetopause normal was shown to serve as a constraint for the development of the turbulent cascade along with the mean magnetic field vector. Moreover, the authors presented a view of the turbulent cascade in the wave vector space along the flow direction. The spectrum exhibited a clear power law of $\sim k^{-8/3}$ within the range $k\rho = (0.3\ 5)$, where ρ was the proton gyroradius. Note, that the power exponent was shown to differ from $\sim f^{-7/3}$, measured in the frequency space, pointing out the significance of the Doppler shift effect.

Based on Cluster high resolution measurements of the magnetic and electric fields, Alexandrova et al. (2006) managed to detect an Alfven vortex-localized coherent structure in the MSH. Observations were performed in the vicinity of the quasi-perpendicular BS. The authors performed a spectrum of magnetic field fluctuations characterized by a clear bump (or spectral knee) at the scales of transition from MHD to kinetic regimes. At frequencies above the bump, the spectrum followed the $f^{-0.5}$ power law, at smaller scales, the spectrum steepened and followed the $\sim f^{-3}$ power law. Further, the authors presented a similar case with the spectrum following the f^{-4} power law at the kinetic scales and significantly decreased level of compressibility at the scales of the bump (Alexandrova, 2008). The authors concluded that the presence of incompressible Alfven vortices in compressive MSH turbulence is one of the differences between the SW and the MSH.

Based on Cluster data, Sundkvist et al. (2007) explored thin current sheets, identified as ion reconnection regions (Retinò et al., 2007), which were typically found behind the quasi-parallel BS. The magnetic field fluctuations associated with the current sheets were shown to follow two typical power law structures with a break at the range of transition from MHD to kinetic regimes. Kolmogorov scaling was identified at the frequencies below the break while at higher frequencies, the spectrum was characterized with a −3.1 power exponent. The intermittent nature of the fluctuations was also pointed out, which became significant at scales of ~10 ρ.

Breuillard et al. (2016) performed a case study on the turbulence spectrum in the MSH for intervals associated with different instabilities: Alfven ion cyclotron (AIC) and/or mirror instability and their absence. The absence of instabilities as well as presence of both kinds of them was characterized by a nearly isotropic spectra of magnetic field fluctuations. Spectra of fluctuations of every magnetic field component as well as their sum were shown to be close to the $f^{-2.8}$ power law. In the case of dominating mirror instability, the parallel component was more powerful than two perpendicular ones, with the spectrum having a slope of -2.00 ± 0.07 at the sub-ion scales; the perpendicular components had similar a spectra with a -2.65 ± 0.06 slope, and the total magnetic field spectrum followed the $f^{-2.30\pm0.05}$ power law, that was flatter than typically observed inside the MSH. On the opposite side, in the case of AIC wave domination, the perpendicular components were more powerful than the parallel one, with the former having slopes of -2.4 ± 0.06 and -2.38 ± 0.05 while the latter had a slope of -2.65 ± 0.07. The total spectrum of the magnetic field fluctuations in that case were characterized by the power exponent of -2.45 ± 0.05, which is somewhat flatter than typically observed. Thus, spectral slopes were shown to be affected by the presence of instabilities, assuming differences in dissipation processes.

Early performed observations and case studies of the turbulence spectra showed that MSH plasma could also be used to figure out the properties of ion scale processes in plasma. Though generally similar, distinct results provided

somewhat different features of turbulence from case to case. Thus, statistical studies covering various background conditions were required to obtain the typical parameters of the turbulence behind the BS.

Spectral Indices: Statistical Studies of Magnetic Field Fluctuations

Based on Cluster measurements, Mangeney et al. (2006), and Lacombe et al. (2006) performed the first comprehensive statistical analysis of the turbulent fluctuations inside the MSH at sub-ion and up to electron scales. The authors addressed magnetic and electric field fluctuations in frequency ranges of (8, 4000) Hz. Although this range of scales is out of the scope of the current review, these studies and the considered data intervals of the Cluster measurements have inspired a number of works focused on ion-scale turbulence. Moreover, these studies demonstrated the importance of Doppler-shift in the measurements' interpretation.

For the same dataset, Alexandrova et al. (2008) presented the first results on the shape and features of magnetic field fluctuation spectra in the MSH around ion scales for various background conditions. Their study was based on more than 20 h of Cluster measurements in the MSH, mostly behind the quasi-perpendicular BS (one of the cases referred to oblique BS, with $\theta_{BN} = 50^{\circ}$). The advantage of the study was the consideration of fluctuation spectra both below and above the ion spectral break. The authors showed the differences of spectra of compressive fluctuations (namely, fluctuations of the component, which is parallel to the mean magnetic field, $B_{||}$) and those of in-compressive Alfvenic fluctuations (of the component, which is normal to the mean magnetic field, $B_{\perp}$). The compressive fluctuations were shown to be less powerful at the whole range of frequencies–from 10^{-3}–10 Hz. Also, the spectra obtained for different directions had different features. The transverse Alfvenic fluctuations were shown to follow Kolmogorov scaling with $\sim f^{-5/3}$ at the frequencies below ion break and the power-law scaling with the slope ranged from −3 to −2.3 at the frequencies above the break, with no clear dependence of the spectral slope on the background conditions. The compressive component was shown to follow the Alfvenic one at sub-ion scales. Both components were shown to have wave vectors $k_{\perp} >> k_{||}$. The authors showed the evidence of 2-D turbulence domination at sub-ion scales for both components of the fluctuations. This dominance of 2-D turbulence was shown to exist for various values of plasma parameter $\beta = p_T/P_B$, where P_T was plasma thermal pressure and P_B referred to magnetic pressure.

Analyzing the same set of intervals, Matteini et al. (2017) compared the spectra of magnetic and electric field fluctuations in a wide range of scales, covering MHD, ion, and electron scales. The authors showed that for various values of plasma parameter β mutual scaling of electric and magnetic field fluctuations stayed the same: $\delta E/\delta B \sim 1$ at MHD scales and $\delta E/\delta B \sim f$ at sub-ion scales up to electron scales. Similar results were obtained based on MMS data (Stawarz et al., 2016; Breuillard et al., 2018). Matteini et al. (2017) concluded that mutual scaling of electric and magnetic field fluctuations implied a domination of fluctuations with $k_{\perp} >> k_{||}$ at sub-ion scales, consistent with theoretical predictions. The same study presented the ion velocity spectrum at MHD scales following $\sim f^{-3/2}$ scaling while the magnetic field fluctuations followed a spectrum with a −5/3 power exponent. This result was consistent with the findings made for the SW turbulence spectra (Podesta et al., 2006; Borovsky, 2012; Šafránková et al., 2016).

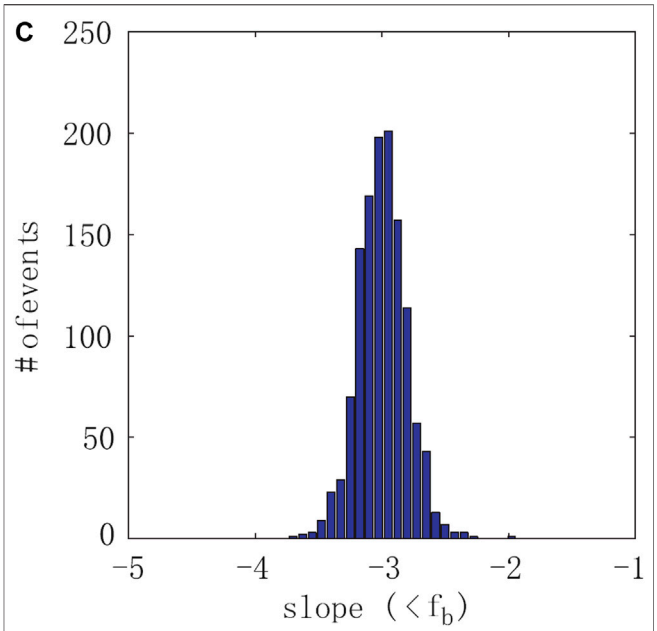

FIGURE 1 | Distribution of the power exponent of magnetic field fluctuations inside the MSH at sub-ion scales [adapted from (Huang et al., 2014), **Figure 5**].

Using the advantages of the multi-spacecraft Cluster mission, He et al. (2011) analyzed the spatial correlation function of the density and both transverse and parallel magnetic field fluctuations for the wide range of angles between the velocity and magnetic field vectors. Although 2-D correlation functions could not be simply recalculated to the 2-D PSDs of the fluctuations, the method was shown to be useful in analyzing anisotropy of both magnetic field and plasma fluctuations. The authors showed the existence of two dominant populations of fluctuations, with the majority of them being extended parallel to the mean magnetic field. The authors suggested this to be a signature of the same two-population view of the PSDs, with the major fluctuations having wave vectors normal to the mean magnetic field and the minor population having a wave vector along the mean field, e.g., $k_{\perp} >> k_{||}$. A surprising similarity was pointed out between the correlation functions for density and transverse magnetic field component. Unlike previous results of a 1-D study by Alexandrova et al. (2008), this study was performed in 2-D space, and the obtained results were consistent. Also, this work presented the flattening of density PSDs at MHD scales with the increasing angle between velocity and magnetic field vectors. The spectral slope changed from −1.6 to −1.2 on average while the angle increased from 20 to 90°. Standard deviations of the slope's

values were ~0.25, so the presented result was statistically reliable. At the same time, for the kinetic scales, the slope changed from −2.8 to −2.3, with standard deviations of ~0.2. For the spectra of transverse magnetic field fluctuations at the kinetic scales, a similar trend was observed (the errors represent standard deviations): at the MHD scales, the slope increased from −3.5 ± 0.4 to −2.90 ± 0.15. For MHD scales, the slope changed from −1.5 ± 0.3 to −1.3 ± 0.2, thus the dependency was insignificant due to large standard deviations.

Huang et al. (2014) presented statistical analysis of the scaling of magnetic field fluctuation spectra at sub-ion scales basing on Cluster measurements. The authors used two-power-law approximation of the spectra with a break around electron scales. The considered dataset included a wide range of background conditions. This paper showed for the first time the wide distribution of power exponents at sub-ion scales (shown in **Figure 1**) which lay between −3.5 and −2.4 with a peak at −2.9. The results were shown to be similar to those in the undisturbed SW.

In situ data of the Cluster and Themis spacecraft in the MSH allowed Hadid et al. (2018) to perform the first quantitative estimate of the energy cascade rate for compressible MHD turbulence behind the BS. The authors examined two sets of the most common types of events – Alfvenic-like and magnetosonic-like which were attributed to the developed turbulence, e.g., with Kolmogorov scaling at MHD scales. The compressible cascade rate was shown to be increased for compressible magnetosonic-like events. Interestingly, density fluctuations, which were known to be powerful inside the MSH were shown to enhance the anisotropy of the cascade rate, suggesting the dominant contribution of slow (or mirror) mode to the cascade formation. Further, Andrés et al. (2019) succeeded in obtaining quantitative estimations of the cascade rate for sub-ion scales as well, based on MMS data and analytical relations (Andrés and Sahraoui, 2017; Andrés et al., 2018; Sahraoui et al., 2020).

Fluctuations of Plasma Parameters Inside the Magnetosheath at Ion and Sub-Ion Scales: Advantages of Spektr-R Measurements

Direct spacecraft measurements revealed the importance of the compressible component in the formation of turbulent cascade in the MSH. Typically the turbulent fluctuations are considered as a mixture of linear MHD wave modes (or their kinetic counterparts) superimposed by pressure balanced structures (Tu and Marsch 1995; Howes et al., 2012; Bruno and Carbone 2013), coherent structures, or waves (e.g., Lion et al., 2016). While the incompressible Alfvenic mode is characterized by zero variations of density and parallel components of the magnetic field, for the compressible magnetosonic and mirror modes these parameters fluctuate. Thus, variations of parallel components of the magnetic field and/or density fluctuations are usually referred to as a representation of compressive fluctuations. Note that recently Borovsky (2020) suggested considering density fluctuations as a signature of plasma inhomogeneity rather than compressibility. As this review aims to summarize the results of experimental studies rather than give their theoretical interpretation, below we refer to the density fluctuations as the compressive component of the cascade consistent with most commonly used terminology. At the scales around the ion spectral break, the compressive component was only usually represented by the parallel component or magnitude of magnetic field fluctuations as measurements of plasma parameters were rare in the MSH at a high enough cadence to observe the spectral break and range of scales around it (e.g., propagation experiment on board ISEE-1 and -2 (Lacombe et al., 1995). In 2011, the Spektr-R spacecraft was launched with a BMSW instrument (Zastenker et al., 2013; Šafránková et al., 2013) on board. The spacecraft was in operation until 2019 and for the first time provided continuous measurements of ion flux value and direction with 0.031 s time resolution. Also, proton density, bulk and thermal velocity measurements with similar time resolution were available, but inside the MSH measurements of this kind were rare, though were often performed in the SW (Šafránková et al., 2015; Šafránková et al., 2016). The BMSW instrument observed both SW and MSH plasmas and for the first time allowed researchers to obtain statistically turbulent properties of directly measured plasma fluctuations at scales around the ion spectral break. As it was shown by Neugebauer et al. (1978), fluctuations of ion flux value mostly represent the fluctuations of proton density. Later, a direct comparison of density and ion flux value fluctuation spectra measured by the BMSW (Pitňa et al., 2016) confirmed their similarity. These arguments allowed for the usage of an ion flux fluctuation spectrum as a proxy of density spectrum. Also, the BMSW instrument provided measurements of the ion flux direction which were more affected by the velocity fluctuations.

The first statistical results of the BMSW measurements in the MSH were presented in Rakhmanova et al. (2016) and Riazantseva et al. (2016). Rakhmanova et al. (2016) dealt with more than 100 h of ion flux value and direction measurements. Most of the cases referred to the MSH flanks. The shape of the spectra, typical for the interplanetary magnetic field fluctuations with two power laws divided by the break only occurred for nearly half of the statistics. The authors obtained distributions of the slopes S_1 and S_2 which characterized the power laws at MHD and kinetic scales, respectively for 290 spectra. **Figure 2** presents the obtained distributions for ion flux value (black columns) and polar angle (gray columns). The polar angle characterized the deviation of the ion flux vector from the Sun-Earth line and its fluctuations were used to analyze differences in density and velocity fluctuation spectra. This study showed that at the MHD scales, the spectra of both ion flux and polar angle fluctuation exhibited, on average, Kolmogorov-like scaling with an $\sim f^{-5/3}$ power law (see **Figure 2A**). On the ion kinetic scales, the mean slope of the ion flux value fluctuations was −2.9 with a standard deviation of 0.3 (see **Figure 2B**), consistent with the statistical results of Huang et al. (2014) for the magnetic field (see **Figure 1**). Thus, ion flux and magnetic field fluctuation spectra were shown statistically to have similar slopes. In the MSH, this consistency was shown for the first time for kinetic scales. The

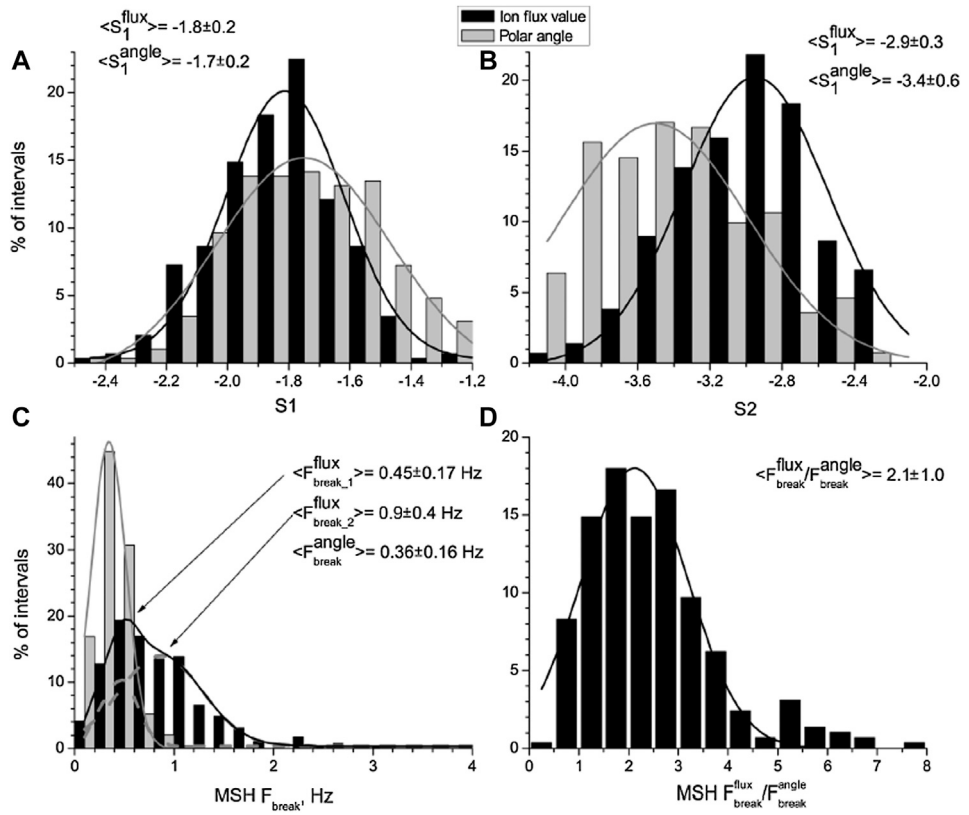

FIGURE 2 | Distribution of spectral slope at MHD **(A)** and kinetic **(B)** scales and the break frequency **(C)** for ion flux value (black) and polar angle (gray) fluctuation spectra in the MSH; distribution of ratio between the break frequencies for the two parameters **(D)** [Adapted from (Rakhmanova et al., 2016)].

spectra of polar angle fluctuations were shown to be steeper at these scales, with a mean value of the slope at −3.4 with a standard deviation of 0.6. This difference was suggested to be a signature of differences in the shapes of density and bulk velocity fluctuations at sub-ion scales in the MSH. Later, a similar result was obtained separately for density and ion velocity fluctuations in Chen and Boldyrev (2017). Also, a general similarity was pointed out between the scaling of ion flux spectra in the MSH and in the upstream SW (Riazantseva et al., 2016).

A significant difference was found between the break frequencies of ion flux value and polar angle fluctuation spectra. The distribution of the break frequency for ion flux value exhibited two maxima (see **Figure 2C**). Note that the two-peak distribution of the break frequency for ion flux fluctuations was also shown by the authors for large statistics in the SW (not shown here). The presence of two peaks may be a signature of two distinct dissipation mechanisms both in SW and MSH plasma. However, the nature of this difference is still not clear. Also, on average, spectra of the ion flux value had a break at scales two times as large as those of the polar angle (see **Figure 2D**). This result also uncovered differences in the spectra of density and velocity fluctuations.

As the measurements of the magnetic field were unavailable at Spektr-R, ion characteristic scales could not be determined directly except for proton inertial length. The results of Rakhmanova et al. (2016) suggested that there was no direct correspondence between the spectral break of ion flux fluctuations and proton inertial length. Also, for a single case study where magnetic field measurements were traced from the Themis-B spacecraft in the MSH, the authors demonstrated the absence of the direct correspondence between the break frequency and the Doppler-shifted proton gyroradius. Chen et al. (2014) and Šafránková et al., (2016) suggested that ion break takes place at different ion scales depending on plasma beta for the SW plasma, i.e., different leading processes are responsible for the dissipation of various background conditions.

As mentioned above, the typical two-power-law spectra were observed only in half of the cases in the MSH. For the other cases, the transition between the MHD and kinetic scales was modified in different ways. Rakhmanova et al. (2018a) demonstrated that the spectra of ion flux fluctuations inside the MSH formed three major groups of spectral shapes, presented in **Figure 3**: with two power laws divided by the break (52% of cases, panel a), with a bump around the break (19% of cases, panel b) and with a plateau around the break (21% of cases, panel c). A similar difference in spectral shape was also demonstrated for the SW though the proportion between the groups of cases was different (Riazantseva et al., 2017). Also, there was a small portion of events (~8%) with non-linear steepening of the spectra at the

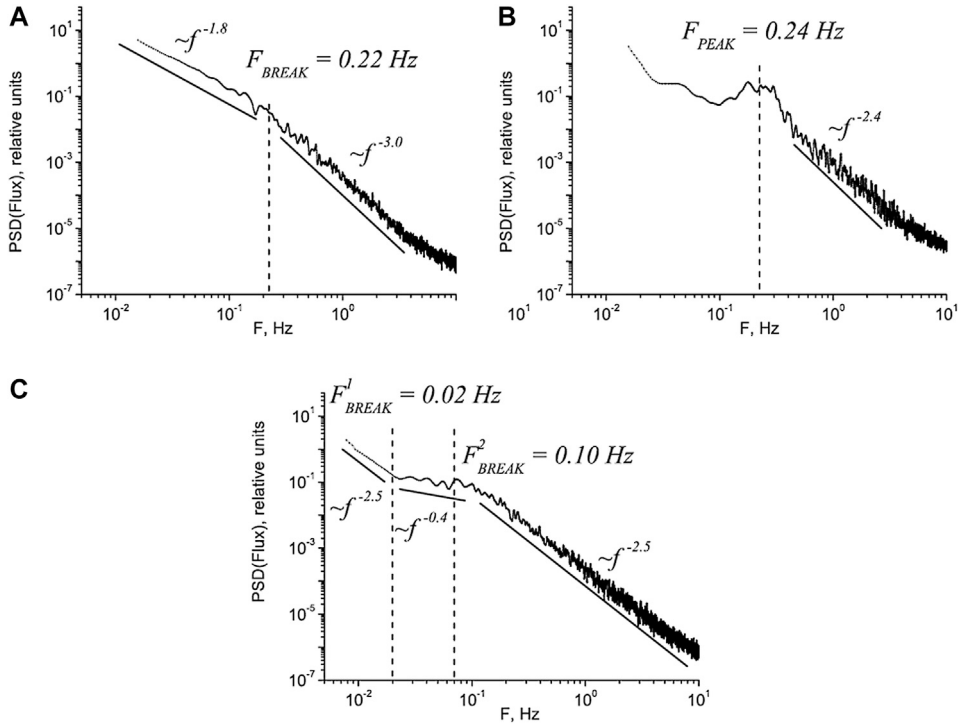

FIGURE 3 | Different shapes of ion flux fluctuations observed inside the magnetosheath: **(A)** with two power laws and break, **(B)** with bump around the spectral break, and **(C)** with plateau around the spectral break [Adapted from (Rakhmanova et al., 2018a), **Figure 3**].

kinetic scales, not shown here (in the SW this type is observed more frequently).

Note that a plateau in spectra of density (or ion flux) fluctuations was observed more often in the SW (Šafránková et al., 2015; Šafránková et al., 2016; Riazantseva et al., 2017) compared to the MSH. According to theoretical suggestions (Chandran et al., 2009), spectra with a plateau can be formed as the superposition of the typical two-power-law spectrum, including density fluctuations passively convected by Alfvenic turbulence, and kinetic Alfven wave fluctuations, which arise at ion scales and are compressive in nature. The occurrence of the plateau was suggested to be influenced by the power of the cascade at large scales and by plasma parameter β. **Figure 4** shows the distribution of PSD value, measured for a frequency range of 0.018–0.022 Hz for the mentioned three groups of spectra in the MSH. Here the statistics of Rakhmanova et al. (2018a) were used which included ~1,100 spectra of ion flux fluctuations. The frequency band was chosen to consider MHD scales according to statistical results (Rakhmanova et al., 2016). The panels in **Figure 4** correspond to spectral shapes, presented in **Figure 3**. The results correspond well to the predictions of Chandran et al. (2009): spectra with plateau are usually less powerful at large scales (here, at the MHD scales) than those with two power laws. However, spectra with a bump are characterized by even smaller power at MHD scales. This may be due to the dominance of instabilities during quiet background conditions. The reasons for this difference are worth analyzing in the future.

Recent Results on Turbulence Exploration by MMS

All the studies mentioned above pointed out the necessity of simultaneous measurements of both plasma and magnetic field parameters to clearly understand the nature of turbulence. In 2015, the MMS mission (Burch et al., 2016) was launched. The mission consisted of four identical satellites, each including a similar set of instruments. Merged data from the magnetometers FGM (Russell et al., 2016) and SCM (Le Contel et al., 2014) allow for the consideration of magnetic field fluctuations at frequencies up to 1 kHz (Fischer et al., 2016). A fast plasma instrument (FPI, Pollock et al., 2016) provides moments of ion distribution function, e.g., density, velocity, and temperature, with a 0.15 s time resolution in the burst mode while the same parameters for electrons are measured with a 0.031 s time resolution. Thus, simultaneous direct measurements of plasma and magnetic field parameters became available for the first time at boundary layers of the near-Earth's space as well as in the SW, with time resolution being sufficient for exploring plasma turbulence at kinetic scales. In this section some of the recent results of turbulence exploration in the MSH by MMS are discussed, while a number of them are described in subsequent sections, where more specific points are focused on.

Chen and Boldyrev (2017) performed a comprehensive case study into MMS data during the 70s in the vicinity of the dusk-side magnetopause. The authors demonstrated both electron density and magnetic field fluctuation spectra to follow the

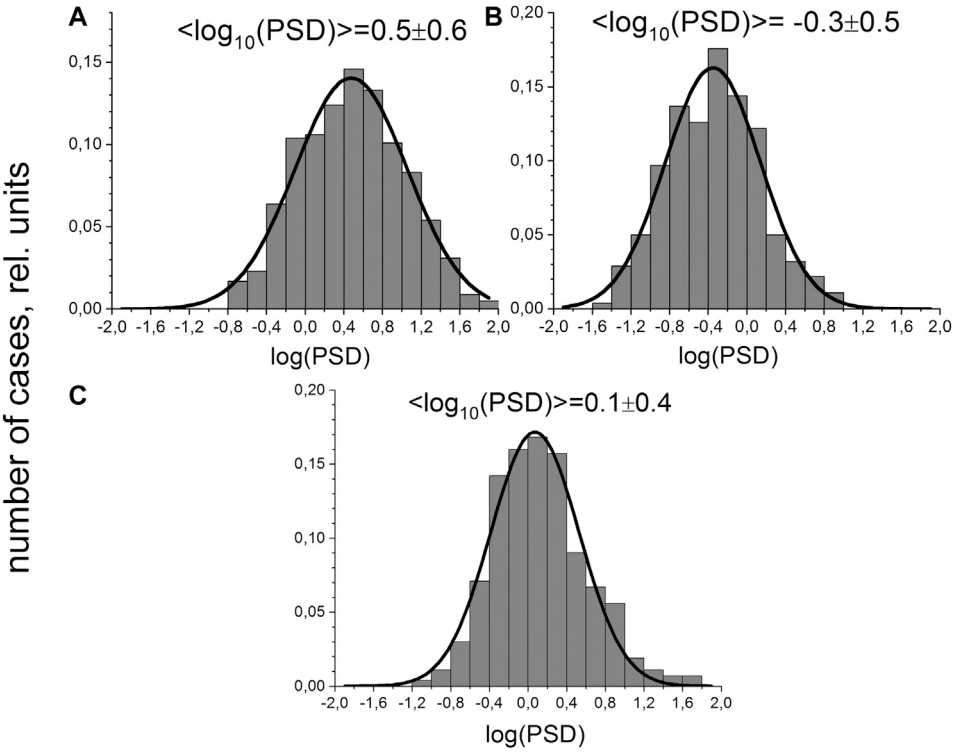

FIGURE 4 | Distribution of MHD-scale PSDs for spectra of ion flux fluctuations, characterized by different shapes: **(A)** two power laws with break, **(B)** with bump, **(C)** with plateau; the corresponding types of spectra are presented in **Figure 3**. (Adapted from PHD work by L. Rakhmanova, 2019).

$f^{-2.8}$ power law between ion and electron scales which was close to the previous observations for the magnetic field by Cluster (Huang et al., 2014) and for ion flux by Spektr-R (Rakhmanova et al., 2016). The ion velocity fluctuations formed a spectrum with a −3.5 power exponent which confirmed the conjectures of Rakhmanova et al. (2016) concerning differences in density and velocity spectra at sub-ion scales. Based on normalized electron density spectra and the coherence analysis, Chen and Boldyrev (2017) suggested the low frequency KAW nature of turbulence. The authors also suggested an inertial kinetic Alfven wave mode to form a turbulent cascade at electron scales.

The nature of turbulent fluctuations was also addressed by Roberts et al. (2018). Based on MMS measurements in the inner MSH, the authors managed to calculate the Alfven ratio and suggested that for the single considered interval the ratio corresponded to KAW turbulence rather than to kinetic slow waves. Kolmogorov scaling was shown to exist at frequencies below the ion spectral break for both the magnetic field and density fluctuations.

Stawarz et al. (2016) performed turbulence exploration in regions, usually dominated by Kelvin-Helmholtz instability, i.e., in the vicinity of the equatorial flanks of the magnetopause. A magnetic field magnitude spectrum was shown to follow Kolmogorov scaling at frequencies below ion break, while above the break, the spectrum followed the $f^{-3.2}$ power law. At the MHD scales, the normal components of ion as well as electron velocity fluctuations followed fluctuations of the normal component of the magnetic field. On the opposite side, at sub-ion scales, the velocity spectra diverged: the normal component of the electron velocity fluctuations flattened and followed the electric field fluctuation spectrum, while the normal component of the ion velocity fluctuations became steeper than for normal magnetic field fluctuations. The authors suggested that this was due to the decoupling of ions at sub-ion scales, while the electron remained frozen in the magnetic field.

MMS measurements allowed for careful studies of turbulence anisotropy inside the MSH. Roberts et al. (2019) presented a case study of anisotropy of turbulent fluctuations both for fields and scalars, i.e., magnetic field, density, velocity, and thermal speed. Consistent with the results of Roberts et al. (2018) and Stawarz et al. (2016), the ion velocity fluctuations were shown to form steeper spectra at ion kinetic scales compared to the spectra of magnetic field fluctuations. Also, the strong anisotropy of spectral indices was pointed out: the spectra of all the considered parameters were steeper in the direction parallel to the magnetic field. The authors suggested that the compressive component of the fluctuations inside the MSH was different from those of the SW and was likely to be formed by compressive coherent structures.

MMS data helped to reveal the importance of the compressive fluctuations in the MSH and their differences from those in the SW. Breuillard et al. (2018) showed highly compressive fluctuations inside the MSH, with the compressibility level

higher behind the quasi-parallel BS vs. quasi-perpendicular. The authors concluded that the MSH turbulence was formed by coherent structures superimposed on the Alfvenic fluctuations.

The MMS data allowed for comprehensive studies of reconnection processes, both at ion and electron scales, and their effects on turbulence and dissipation. Previously *in situ* evidence of the reconnection have been rare (e.g., Retinò et al., 2007). Vörös et al. (2017) managed to test a reconnection event downstream of the quasi-parallel BS, when the MMS spacecraft crossed both ion and electron diffusion regions. Vörös et al. (2019) managed to compare different measures of energy exchange or dissipation based on direct measurements by MMS in the reconnecting current sheets behind the quasi-parallel BS. The authors showed the presence of net irreversible work done in the current sheets by the electric field. Also, for the analyzed case, the dissipation occurred preferentially in a direction parallel to the magnetic field. Stawarz et al. (2019) presented an analysis of two intervals in the MSH close to the BS, probed by MMS. The intervals had a different number of reconnecting current sheets with electron-scale size. The magnetic field fluctuation spectra for the two considered cases exhibited similar features at frequencies up to 10 Hz, i.e., as small as electron scales. The spectra followed the $f^{-1.4}$ power law at MHD scales and the $f^{-2.7}$ and $f^{-2.8}$ power law at sub-ion scales. The differences occurred at electron scales and were attributed to the affection of the electron-scale reconnection on the electrons' dissipation. These results were consistent with the earlier findings of Phan et al. (2018) revealing the reconnection events at electron scales which did not generate ion jets.

Multi-spacecraft MMS data allowed for direct calculations of the energy cascade rate in the MSH. As mentioned above, Andrés et al. (2019) performed quantitative estimations of the energy cascade rate at sub-ion scales. Bandyopadhyay et al. (2018) succeeded to compare energy cascade rates at an energy containing scale, at the inertial range, and at the dissipation range. The authors focused on the interval containing nearly incompressive fluctuations and suggested a higher energy cascade rate in the MSH turbulence than in the SW turbulence. Thus, the authors pointed out significant differences between turbulence upstream and downstream of the BS. Further, the MMS advantages were employed to explore the energy conversion at kinetic scales. Bandyopadhyay et al. (2020) considered the statistical distribution of pressure-strain interactions and compared it to the results of the kinetic simulations. The authors suggested that analyzing the statistics of such interactions gave direct information on internal energy production without employing any conjectures of mechanisms. The conversion of energy was shown to occur near intense current sheets rather than within them.

All the studies based on MMS measurements, available to date, show the great potential of these data in the analysis of MSH turbulence below ion scales. Considering simultaneous measurements of the MMS and Cluster and probable Themis and Spektr-R spacecraft could give a substantial contribution to our understanding of the compressible turbulence in the MSH. Presented case studies as well as statistics provide a basic view of the features of turbulence inside the MSH and its similarity and differences from the turbulence in the undisturbed SW. However, MSH plasma always evolves in the confined space. Also, fluctuations of plasma and magnetic field parameters in the MSH not only include the fluctuations borne at the BS, but also those originating from the upstream SW. Further sections focus on the contribution of these two factors to the development of the MSH turbulence.

MAGNETOSHEATH TURBULENCE INFLUENCED BY THE BOUNDARIES

Turbulence Development Between the Bow Shock and Magnetopause

The above-mentioned case studies showed similarities in spectral shapes for magnetic field and density fluctuations inside the MSH. However, different indices of the fluctuation spectra were demonstrated when considering magnetosheath plasma at regions adjacent to the bow shock and farther from it (Alexandrova et al., 2008; Czaykowska et al., 2001 etc.). Thus, one can suspect that the distance to the BS can contribute to the formation of the cascade.

BS contribution to MSH turbulence recently became a topic of interest. Yordanova et al. (2008) presented a case study of the evolution of structure functions of magnetic field fluctuations with distance from the BS with the help of Cluster data. The study was performed behind the quasi-parallel BS where variations of the field components were of the order of the mean field, i.e., the prevalent direction of the field could not influence the anisotropy of the turbulence. The intermittency level was shown to increase with the distance from the BS together with the anisotropy of magnetic field fluctuations. Also, the authors presented slightly steeper spectra of the magnetic field fluctuations at the kinetic scales at the spacecraft which was located closer to the BS then others (with distance of about 1 R_E). In a study by Gutynska et al. (2009), the slope of the magnetic field magnitude fluctuation spectrum obtained by Cluster at MHD scales was shown to increase gradually from −1.6 to −1 with the distance from the magnetopause.

Rakhmanova et al. (2017) presented a case study of the evolution of turbulence features across the MSH behind the quasi-perpendicular BS. The study considered a single crossing of the MSH by the Spektr-R spacecraft and examined spectra of ion flux fluctuations at ion and sub ion scales. Fourier spectra of ion flux fluctuations were calculated over 8 min intervals shifted in time by 1 min for the whole crossing of the MSH. Though magnetic field measurements were not available at Spektr-R, the MHD modeled predictions were adapted to obtain parameters of the magnetic field for given dynamics of upstream SW parameters. Note that in that case the model did not include ion-scale fluctuations, though it fits for the determination of mean parameters through the analyzed intervals. Results of this study are illustrated in **Figure 5**, adapted from the mentioned paper. The figure presents the evolution of the following parameters during the crossing: **(A)** the ion flux value, **(C)** the mean PSD obtained for each spectrum at frequency band

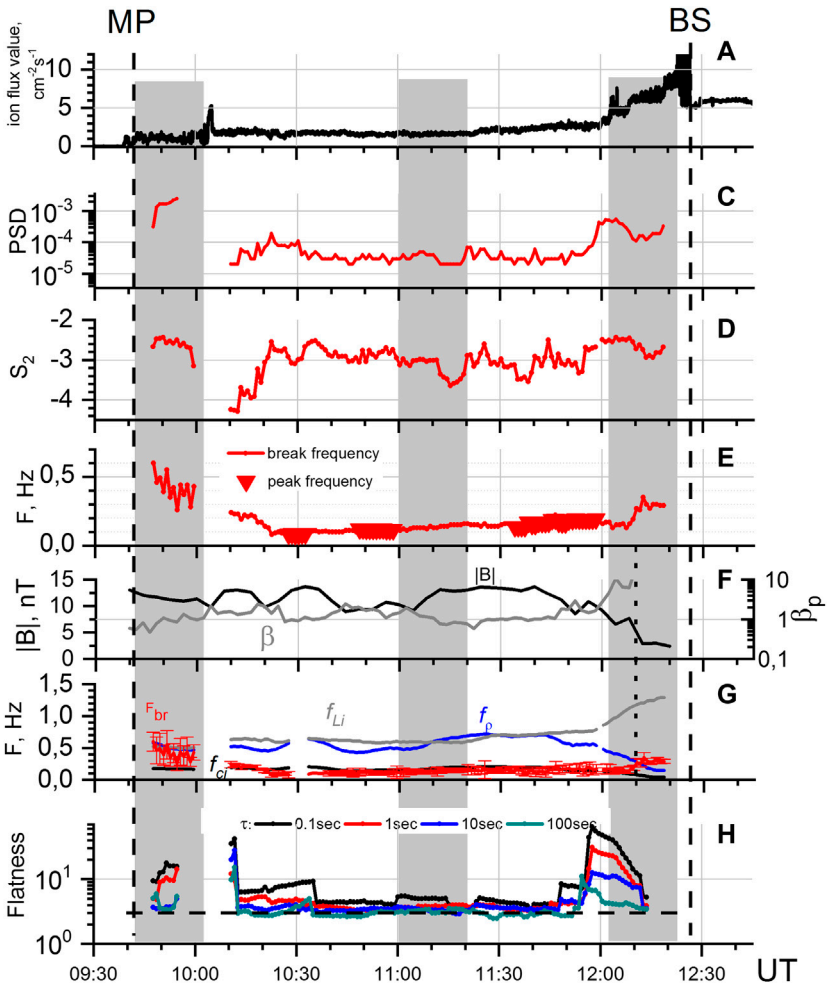

FIGURE 5 | Evolution of the MSH turbulence at ion scales according to Spektr-R observations during single MSH crossing on February 9, 2012: **(A)** ion flux value, **(C)** PSD of ion flux fluctuation spectrum, **(D)** spectral slope at the kinetic scales, **(E)** frequency of spectra break (line) or peak (triangles), **(F)** modeled magnetic field (black) and plasma parameter β (gray), **(G)** plasma characteristic frequencies and the break frequency (red), **(H)** flatness (kurtosis) of ion flux fluctuations, calculated at different scales. (Adapted from Rakhmanova et al., 2017), panel **(B)** and polar angle data were eliminated.

2 ± 0.1 Hz, i.e., at the kinetic scales, **(D)** the spectral slope S_2 at the kinetic scales, **(E)** break frequency of the spectra (in the case of a bump in the spectrum instead of the break, the triangles denote the bump frequency), **(F)** the modeled values of the magnetic field magnitude and proton parameter β, **(G)** plasma characteristic frequencies: ion cyclotron frequency (black line), gyrostructure frequency (blue line), and inertial length frequency (gray line) together with the break frequency (red line), and **(H)** kurtosis/flatness value calculated at the set of time scales: 0.1, 1, 10, and 100 s (shown in different colors). Kurtosis values were calculated over intervals of 15 min duration (~3×10^4 data points) to enable the reliable determination of the parameter. For the parameters calculated over the interval, each point refers to the center of the interval. The figure shows that the break frequency of the ion flux fluctuation spectra followed different characteristic scales across the MSH (see panel g) for steady upstream SW conditions. This change in the break frequency was suggested to be due to differences in dominating processes which governed the dissipation of energy at ion scales at different distances from the BS and magnetopause. Also, signatures of highly intermittent plasma were performed in the regions close to the boundaries, while in the middle MSH, far from the BS and the magnetopause, plasma did not exhibit intermittent features. This can be seen in **Figure 5H** by the increasing of the flatness value with the decreasing scales (or time increments) in regions close to the boundaries. Note that this result was obtained behind the quasi-perpendicular BS, while Yordanova et al. (2008) and Kozak et al. (2012) presented a low intermittency level behind the quasi-parallel BS. On the other hand, an increased level of intermittency was shown in laboratory plasma in the vicinity of edges (Budaev et al., 2011), that show a similarity of the processes developing in turbulence close to the boundaries.

Challenging results in boundaries' influence on MSH turbulence were obtained with statistical studies. Huang et al. (2017) analyzed the modification of spectra throughout the MSH with the help of large statistics of the Cluster magnetic field data.

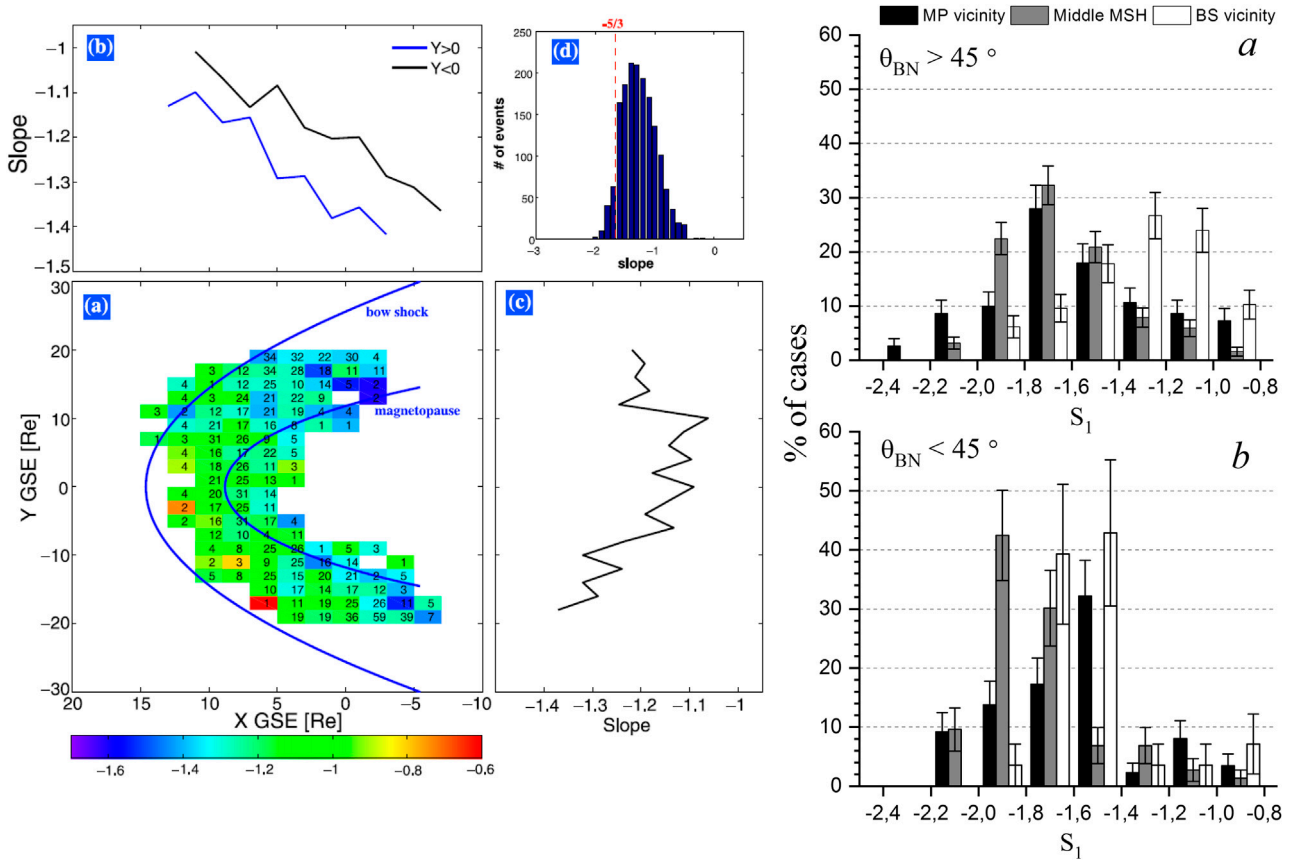

FIGURE 6 | Left columns–mean values of the spectral slope of magnetic field fluctuations at MHD scales at various locations inside the MSH [adapted from (Huang et al., 2017)]; right column–distribution of values of spectral slope of ion flux fluctuations at MHD scales at different distances from the MSH [adapted from (Rakhmanova et al., 2018b)].

The authors considered whole dayside MSH during three years of Cluster operation. In the region close to the subsolar BS, the magnetic field spectra usually follows f^{-1} scaling at the scales above the ion break while farther from the BS and toward the flanks spectra became more like the Kolmogorov spectrum with $f^{-5/3}$ scaling. The authors suggested that crossing the BS resulted in the redistribution of energy in the cascade and the disappearance of the Kolmogorov inertial range, i.e., the energy, injected into the system was dissipated immediately.

Rakhmanova et al. (2018b) also analyzed the dependence of the spectral slopes of ion flux fluctuations at the scales above the break on the distance to the BS and the magnetopause based on statistics of Spektr-R measurements in the MSH. The analysis revealed a wide distribution of spectral slopes peaking at −1.2 in the regions adjacent to the BS. Thus, spectra were significantly flatter than predicted by the theories of developed turbulence and observed in the undisturbed SW. However, spectra with f^{-1} scaling were not always observed in the vicinity of the BS like those shown by Huang et al. (2017). Note that the results of Huang et al. (2017) were obtained in the dayside MSH while the results of Rakhmanova et al. (2018a) mostly referred to the nightside flank MSH. This is the most probable reason for the more pronounced results of Huang et al. (2017). Farther from the BS, the distribution of the spectral slopes had a peak at −5/3, so typically the spectra followed Kolmogorov scaling. Note, that though the values of the slope were scattered, the distributions exhibited a clear difference in the vicinity of the BS and in other parts of the MSH. **Figure 6** demonstrates the comparison between the results of Huang et al. (2017) for magnetic fields fluctuations and Rakhmanova et al. (2018b) for ion flux fluctuations obtained at the MHD scales.

The influence of the BS on the spectra of magnetic field fluctuations at the kinetic scale was suggested to be insignificant (Huang et al., 2017). Rakhmanova et al. (2018a) suggested that there was a slight steepening of the ion flux fluctuation spectra closer to the BS. A comparison between the two studies is presented in **Figure 7** (in the same format as **Figure 6**). Just behind the quasi-perpendicular BS, the spectra had a slope of −3.2 on average while farther from it, the slope was usually closer to −2.8. The standard deviations for the distributions were ~0.4. The evolution of the slope was shown to be even more pronounced behind the quasi-parallel BS (the errors represent standard deviations): spectra of the ion flux fluctuations followed the $f^{-3.4\pm0.3}$ power law in this region while in the middle MSH and close to the magnetopause the slopes were −2.7 ± 0.4 and −3.0 ± 0.5, respectively. Thus,

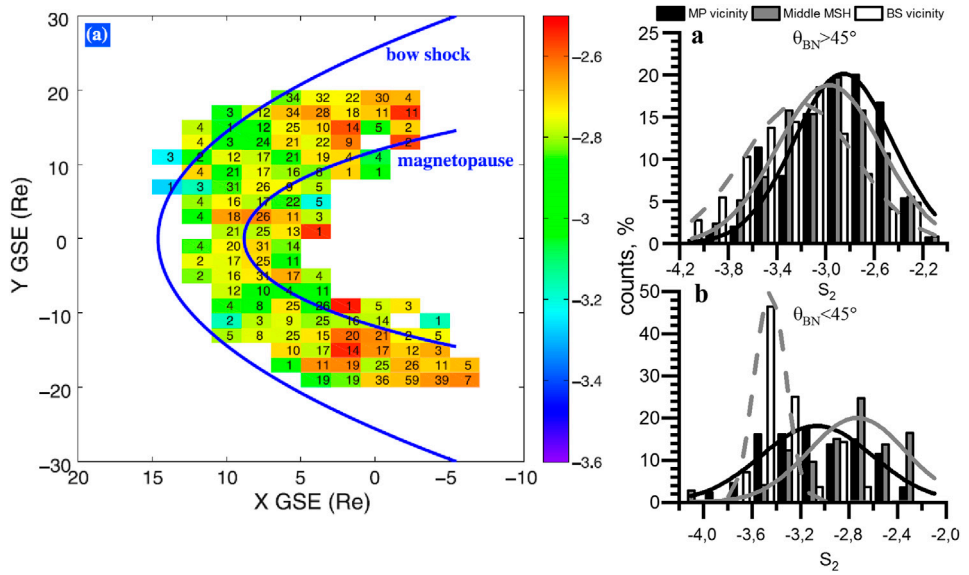

FIGURE 7 | left columns–mean value of the spectral slope of magnetic field fluctuations at kinetic scales at various locations inside the MSH (adapted from Huang et al., 2017); right column–distribution of values of spectral slope of ion flux fluctuations at kinetic scales at different distances from the MSH boundaries [adapted from (Rakhmanova et al., 2018a)].

significant dumping of the compressive fluctuations occurred behind the quasi-parallel bow shock.

Rakhmanova et al. (2018a) also considered differences in the shapes of ion flux fluctuation spectra at various regions of the MSH. The classification of spectral shapes was used which was performed in the Section *Fluctuations of Plasma Parameters Inside the Magnetosheath at Ion and Sub-Ion Scales: Advantages of Spektr-R Measurements*, and the statistics showed that 1) spectra with two power laws were dominant at all distances from the BS, 2) spectra with a bump were most likely to occur in the vicinity of the BS, while 3) spectra with a plateau were usually found in the regions adjacent to the magnetopause. The authors suggested a different scenario of turbulence development in the vicinity of the bow shock and the magnetopause. Spectra were similar to the analytical predictions of Chandran et al. (2009) in the region close to the magnetopause, like it was shown in Section *Fluctuations of Plasma Parameters Inside the Magnetosheath at Ion and Sub-Ion Scales: Advantages of Spektr-R Measurements*. On the other hand, turbulence was strongly dominated by instabilities (most probably, mirror instability) closer to BS which led to the formation of the bump and the damping of compressive fluctuations in the turbulent cascade.

Macek et al. (2018) presented three cases of MMS measurements of magnetic field magnitude and ion velocity value at different distances from the MSH. The cases were observed behind quasi-parallel or oblique BS in nearly subsolar MSH. For the regions close to the boundaries, the authors showed a −2.60 ± 0.06 and −2.68 ± 0.05 power exponent at kinetic scales for fluctuations of magnetic field and velocity, respectively, in accordance with some of the theoretical −8/3 scaling (e.g., Boldyrev and Perez, 2012), which accounted for the geometry of structures. In the middle MSH, spectra of magnetic field fluctuations demonstrated a −2.24 ± 0.09 power exponent at the kinetic scales, which is somewhat flatter than the typical value observed in the statistical studies mentioned above, however, close to −7/3 which was predicted in the framework of KAW turbulence without considering the geometry of structures (e.g., Schekochihin et al., 2009). For this case, no high-resolution plasma measurements were available. However, at MHD scales, the velocity spectrum demonstrated clear Kolmogorov-like scaling with the slope close to −5/3 at frequencies below the break while the spectrum of magnetic field fluctuations was strongly different from the theoretical predictions of the developed turbulence and exhibited $f^{-0.77\pm0.06}$ power law.

Recently, Li et al. (2020) performed large statistics of burst-mode MMS data which covered both flank and subsolar MSH regions at different distances from the boundaries. Magnetic field, density, and velocity fluctuations were analyzed. The authors demonstrated the steepening of the MHD part of magnetic field fluctuation spectra across the MSH, with slopes of on average −1.46 near the BS and −1.91 near the magnetopause. The standard deviations for the reported distributions were ~0.25, thus the observed dependence was statistically significant. For the kinetic scales, only slight flattening of the spectra were presented, with slopes changing from −2.9 to −2.7 from the BS toward the magnetopause. However, the values of the slopes were highly scattered for the region in the vicinity of the BS, so the standard deviation was of about 0.6, making the change of the slope across the MSH negligible. The evolution of magnetic field spectra was shown to be similar behind the quasi-parallel and quasi-perpendicular BS. In the case of density, spectra had a −1.87 slope at MHD scales in the vicinity of the BS of both types. Behind

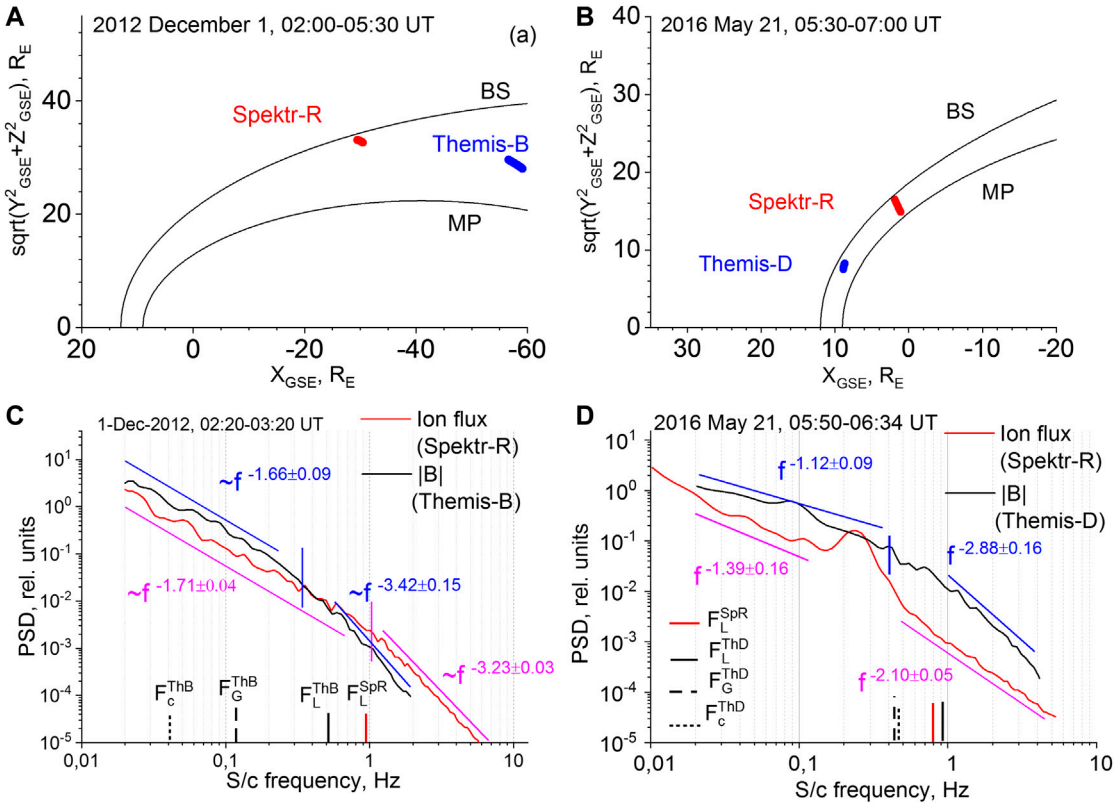

FIGURE 8 | Comparison of the compressive fluctuation spectra **(A,C)** close to the BS (red line) and in the middle MSH (blue line) and **(B,D)** in the vicinity of the BS close to the BS nose (blue line) and at the flank (red line). [Adapted from **Figures 1A**, **3**, **4**, **6** of (Rakhmanova et al., 2020b)].

the quasi-parallel BS, the slope decreased up to −2.44 close to the magnetopause while for the quasi-perpendicular BS, it decreased up to −2.17. However, standard deviations of ~0.6 were performed for the observed averages, which implied no significant dependencies in that case. No differences of velocity fluctuations spectra at MHD scales were shown across the MSH. No dependence was found for kinetic-scale plasma fluctuations on the distance from the BS. Also, the authors demonstrated that at MHD scales, the magnetic field fluctuation spectra were flatter at the flank compared to the subsolar region, which was consistent with Huang et al. (2017), while features of density spectra showed no changes. The presented spectral slopes at the MHD scales were somewhat different to those obtained previously by Huang et al. (2017); Rakhmanova et al. (2018a); Rakhmanova et al. (2018b). Most probably, this difference was due to considering quite short data intervals (~several minutes), which could result in errors in slope determination at MHD scales. However, the obtained dependencies on the position inside the MSH qualitatively corresponded to the previous studies.

Examining the dynamics of the turbulence inside the MSH has several difficult points. First, the turbulent cascade is strongly affected by the set of waves and instabilities arising at the bow shock and in the vicinity of the magnetopause (mirror instabilities, Kelvin-Helmholtz instabilities, etc.) and the presence of local structures like Alfven vortices (Alexandrova et al., 2006). Second, dynamics due to the movement between the boundaries is superimposed by the dynamics of the MSH itself as a response to the changes of the upstream SW conditions. Difficulties of the experimental analysis also come from the limited number of measurements, provided simultaneously from different points inside the MSH at various distances. Recent missions (Cluster, MMS) were focused on sub-ion plasma physics and could consider the evolution of turbulence at distances of the spacecraft separations, i.e., 10–1,000 km. To analyze the evolution of the fluctuation spectra while plasma moves through the MSH, a larger separation (of the order of the MSH thickness and larger) between the spacecraft is required. Such analysis can be prepared with the help of simultaneous data from different spacecraft missions like Themis, Cluster, Spektr-R, and MMS. However, combining data from different sets of instruments is quite difficult due to differences in the organization of spacecraft orbits and the absence of intercalibration for the instruments.

Recently, Rakhmanova et al. (2020b) performed a case study of evolution of compressive turbulence inside the MSH with the help of Spektr-R plasma and Themis magnetic field measurements. For quiet background conditions, the spectra of compressive fluctuations were compared 1) at two points, placed at closely located streamlines at the flank MSH at distances ~30 R_E, and also 2) at two points in the vicinity of the BS, but

at different distances from the BS nose. The sketch of the spacecraft positions and comparison of spectra of ion flux fluctuations from the Spektr-R and magnetic field magnitude fluctuations from the Themis-B/-D are presented in **Figure 8** for the two considered cases. The results demonstrated that 1) at the MHD scales, the spectra of compressive fluctuations could have Kolmogorov scaling in the vicinity of the flank BS and stay unchanged at distances up to 30 R_E; and 2) when plasma crossed the dayside BS, the modification of the spectrum strongly depended on the distance to the BS nose. Note that in that study the cases referred to different types of the BS, which also might contribute to the differences in the results. However, these results first provided direct confirmation of the suggestions which came from statistical studies of Huang et al. (2017); Rakhmanova et al. (2018a); Rakhmanova et al. (2018b) on the evolution of turbulent features across the MSH and differences in BS influence on the downstream turbulence at the dayside and flank MSH.

Differences of turbulent features behind the quasi-parallel and quasi-perpendicular Bow Shock

As mentioned in the introduction, the dynamics of fluctuations inside the MSH strongly depends on the mutual direction of the IMF and the local BS normal. A comparison of different case studies also implies the dependence of turbulence features on an θ_{BN} angle. The current section summarizes the results of the direct comparison of turbulence affected by the BS of different geometry.

Macek et al. (2015) used Themis data to compare the behavior of the Elsässer variables behind the BS with different geometry. The authors showed signatures of the most populated portion of anti-sunward propagating waves compared to those propagating toward the Sun behind the quasi-perpendicular BS. On the opposite side, the populations of waves of different directions are equal behind the quasi-parallel BS. Turbulence behind the quasi-perpendicular BS was shown to be more intermittent compared to the one behind the quasi-parallel BS.

Based on the whole set of MMS data, Breuillard et al. (2018) presented a comparison of spectral indices, anisotropy, and compressibility level behind quasi-parallel and quasi-perpendicular BS. At the MHD scales, density and magnetic field fluctuations (both parallel and transverse component) exhibited similar scaling. Interestingly, behind the quasi-perpendicular BS the spectra were characterized by a −1 power exponent while behind the quasi-parallel bow shock, typical Kolmogorov-like scaling was observed. This difference was similar to the results of the statistical and case studies (Rakhmanova et al., 2018b; Rakhmanova et al., 2020b). Note that results of Breuillard et al. (2018) were obtained in the dayside MSH. At the kinetic scales, four considered spectra showed the same $f^{-2.8}$ power laws both for magnetic field and density fluctuations. Thus, upstream BS geometry does not affect kinetic-scale fluctuations in the MSH.

Yordanova et al. (2020) examined MMS data behind quasi-parallel and quasi-perpendicular BS based on single intervals. The authors analyzed properties of thin current sheets and showed their preferential population behind the quasi-parallel BS and a small amount behind the quasi-perpendicular BS. The study considered turbulent spectra associated with thin current sheets downstream of the quasi-parallel BS and without signatures of current sheets downstream of the quasi-perpendicular BS. The authors presented similar $\sim f^{-2.8}$ scaling of the magnetic field magnitude fluctuation spectra at the kinetic scales behind the BS of both kinds. However, the spectrum behind the quasi-perpendicular BS was dominated by a large bump at the scales of transition from MHD to kinetic scales, and the spectrum was significantly flatter than the Kolmogorov-like spectrum at the MHD scales. On the opposite side, behind the quasi-parallel BS, the spectrum of the magnetic field magnitude fluctuations exhibited clear Kolmogorov scaling and two power laws. The results of the study are presented in **Figure 9**. The results are consistent with the results obtained with the help of Cluster data (Sundkvist et al., 2007) and also with the statistical results by Rakhmanova et al. (2018b) obtained by plasma measurements on board Spektr-R.

Rakhmanova et al. (2020b) statistically analyzed the influence of θ_{BN} angle on the power exponents of ion flux fluctuation spectra at MHD and kinetic scales. Crossing of the quasi-perpendicular BS was shown to result in flattening of the spectra at MHD scales and their deviation from the Kolmogorov scaling (**Figure 10**, top). On the contrary, spectra with a −5/3 power exponent can more often be found behind the quasi-parallel BS. Upstream foreshock processes and an altogether higher level of fluctuations were suggested to result in the formation of the turbulent cascade upstream of the shock, which led to insignificance of the BS effect during the crossing. On the other hand, steady conditions upstream of the quasi-perpendicular BS result in a greater impact on the cascade and disbalance of the energy in it, leading to a deviation of the spectral shape from those predicted by the developed turbulence theories. At the kinetic scales (**Figure 10**, bottom), steeper spectra were usually observed behind the quasi-parallel bow shock which is consistent with Li et al. (2020), and imply damping of plasma fluctuations in this region. On the other hand, the results of Li et al. (2020) demonstrated no differences in magnetic field spectra behind the quasi-parallel and quasi-perpendicular BS.

Rakhmanova et al. (2020a) presented three examples of spectra of ion flux fluctuations just behind the quasi-perpendicular BS ($\theta_{BN} > 70^\circ$) and all three of them were characterized by different spectral slopes at MHD scales - from −5/3 to −1 (see detailed description of the work in the next section). Interestingly, all the analyzed cases occurred in the flank MSH, so the difference in slope was unlikely to be due to distance from the BS nose. Moreover, statistical studies of Huang et al. (2017); Rakhmanova et al. (2018a); Rakhmanova et al. (2018b) did not reveal significant differences of the turbulence features at different MSH flanks. The difference in slopes may be due to a set of factors, which are hard to distinguish, and mainly, differences in the modification of spectra at the BS for various upstream conditions like SW parameters. The next section is dedicated to our first results in analyzing those factors.

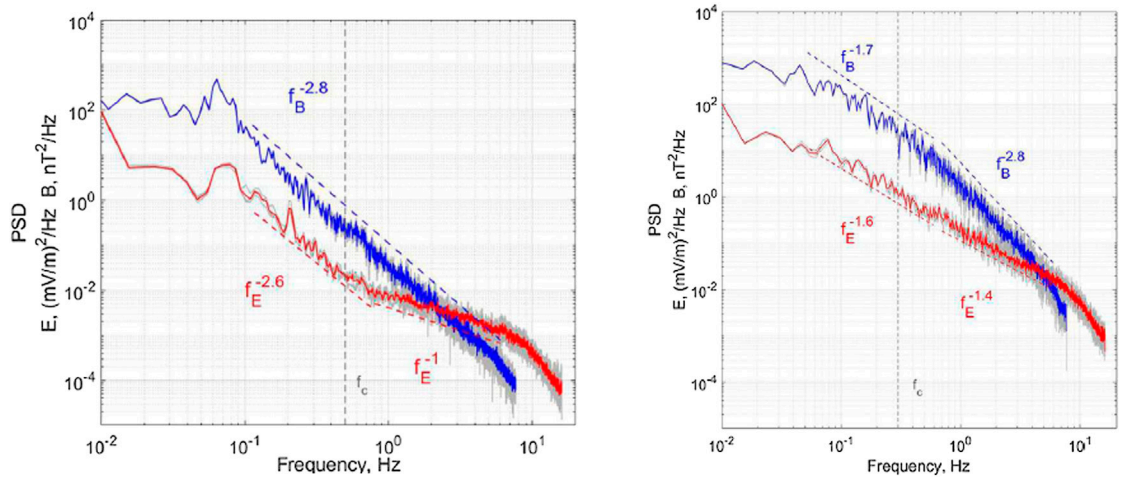

FIGURE 9 | Spectra of magnetic (blue line) and electric (red line) field magnitude fluctuations behind the quasi-perpendicular (left panel) and quasi-parallel (right panel) BS [Adapted from (Yordanova et al., 2020)].

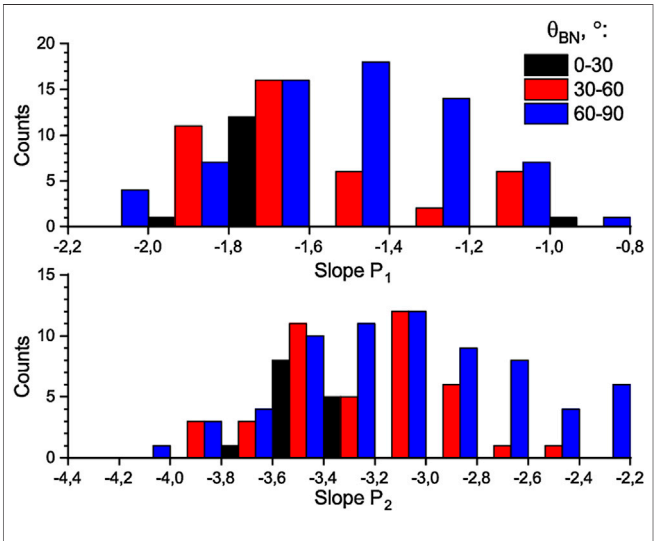

FIGURE 10 | Distribution of the slopes S_1 (top panel) and S_2 (bottom panel) for ion flux fluctuation spectra measured behind the quasi-perpendicular (blue), oblique (red), and quasi-parallel (black) BS [adapted from (Rakhmanova et al., 2020a)].

UPSTREAM PARAMETERS INFLUENCING THE MODIFICATION OF TURBULENT CASCADE AT THE BOW SHOCK

In the SW, the variability of spectral properties has been known for a long time to be controlled by background conditions in plasma, like the angle between the velocity and magnetic field vectors or plasma parameter β (e.g., Chen et al., 2014). For the MSH plasma, distance to the boundaries (BS and magnetopause) was shown to contribute significantly to turbulence development. However, statistical studies (e.g., Rakhmanova et al., 2018a; Rakhmanova et al., 2018b; Li et al., 2020) as well as a large set of case studies revealed wide distributions of spectral indices in the regions close to the BS, including the conservation of Kolmogorov scaling across the BS for some cases as well as its absence for others. Therefore the challenging question is which factors could control the modification of turbulent cascade at the BS.

Rakhmanova et al. (2020a) considered the influence of the characteristics of fluctuation spectrum in the upstream SW on the properties of downstream turbulence. The authors considered three cases of the quasi-perpendicular BS crossing at the flank MSH by the Spektr-R spacecraft and analyzed ion flux fluctuation spectra upstream and downstream from the BS for stable background conditions. Comparisons of the upstream and downstream spectra, adapted from the paper, are presented in **Figure 11**. All three cases referred to typical spectral shapes in the upstream SW: nearly Kolmogorov scaling at frequencies below the break and with the plateau existed at the scales of transitions from MHD to kinetic regimes. However, the spectra were characterized by quite different power law exponents at the kinetic scales, which was attributed to different local background conditions. Direct comparison of the spectra obtained at both sides from the BS demonstrated that at the MHD scales, crossing of the BS could result either in significant flattening of the spectrum with the power exponent ~ −1 (panel a), or in moderate flattening of the spectrum to the power exponent of −1.3 (panel b), or in no changes in the power exponent at all (panel c). At the kinetic scales, on the contrary, crossing of the BS seemed to result only in a slight steepening of the spectrum. Interestingly, slopes of the spectra at kinetic scales seemed to be dependent on the same slope of the upstream spectra. All three analyzed cases referred to similar BS geometry, however, they were observed during periods corresponding to different large-scale SW flows according to the classification by Yermolaev et al. (2009); Yermolaev et al. (2015). The case with the most crucial changes in the MHD part of the spectrum was observed during SW of type "Sheath," e.g., the compressed region in front of the interplanetary

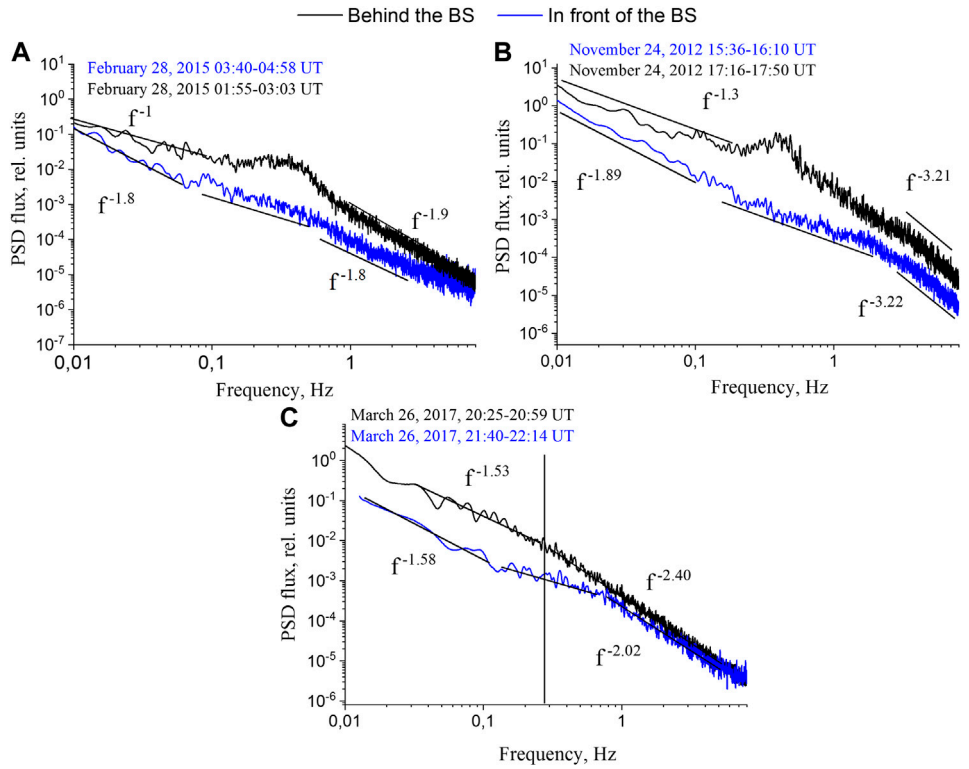

FIGURE 11 | Three case studies of influence of the upstream SW turbulence on the characteristics of turbulence spectrum of compressive fluctuations downstream of the BS. (Adapted from **Figures 1E**, **2** of (Rakhmanova et al., 2020a), colored).

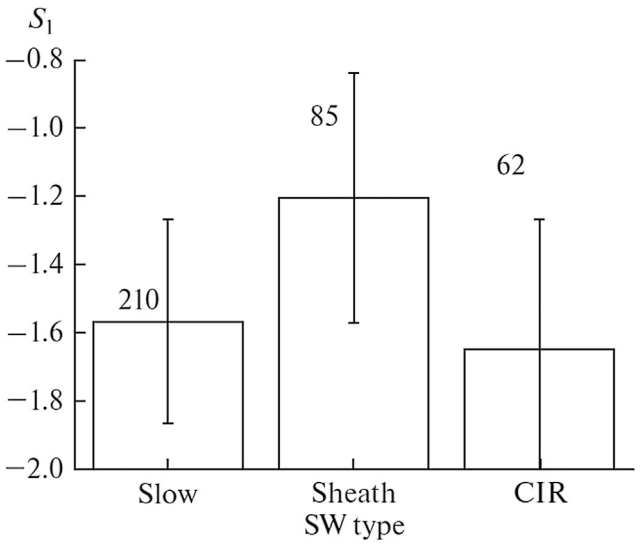

FIGURE 12 | Mean values of the MHD-scale spectral slope S_1 for the ion flux fluctuations in the vicinity of the BS for different upstream large-scale SW types, numbers refer to the number of analyzed data intervals, vertical lines denote standard deviations of the values (Adapted from (Rakhmanova et al., 2020b)).

manifestation of the coronal mass ejection (CME) or in front of the magnetic cloud (MC). The case which was characterized by no changes in the MHD part of spectrum was observed during periods of steady slow SW flow. Another case corresponding to the turbulent cascade developing in the MC was characterized by moderate changes in spectrum during the crossing. A recent study (Rakhmanova et al., 2020a) also demonstrated the Kolmogorov scaling of the MHD part of ion flux fluctuation spectrum in the vicinity of the BS (see **Figure 8**, on the left). The considered spectrum was observed behind the quasi-parallel BS during upstream slow steady SW.

Statistical data by Spektr-R measurements in the MSH adjacent to the BS (Rakhmanova et al., 2020b) demonstrated the influence of the large-scale SW type on the modification of the turbulent cascade at MHD scales at the BS. Significant changes at the BS were shown to be most probable during compressed SW flow of type "Sheath," while steady SW flow was typically accompanied by the nearly Kolmogorov scaling of ion flux fluctuation spectra downstream of the BS similar to the results shown in the previous section. **Figure 12** presents the mean values of spectral slope at the MHD scales behind the BS for different upstream SW types. The interaction of the SW flow of different types with the BS was shown to be accompanied by an occurrence of different spectral shapes of ion flux fluctuations in the MSH. While typically (Rakhmanova et al., 2018a) in the MSH adjacent to the BS, the spectra exhibited two power laws with a break or broad peak instead of the break (see **Figure 3A,B** of the current paper, adapted from (Rakhmanova et al., 2018a)). During the periods of SW of type "Sheath" behind the BS, the spectra were usually characterized by the plateau (see **Figure 3C**).

Differences in the effect of the various SW types on the MSH turbulence may result from differences in turbulence properties in the SW. Riazantseva et al. (2020) demonstrated alterations in sub-ion properties of turbulent spectra when considering SW flow of compressed and non-compressed types. Recent results by Borovsky et al. (2019), Borovsky (2020) also demonstrated distinct properties of MHD-scale fluctuations in large-scale flows of various types and different levels of Alfvenicity. The presented results therefore suggest a strong relationship between upstream SW processes and downstream MSH turbulence.

Note that according to Yermolaev et al. (2009); Yermolaev et al. (2012); Yermolaev et al. (2015), the large-scale SW flows of various types affect the magnetosphere in a different way, with compressed regions like "Sheath" being highly geoeffective. That is, the obtained results may be interesting in the scopes of space weather.

DISCUSSION

The present paper summarizes the experimental achievements in the exploration of highly turbulent plasma in front of the magnetosphere. To date, a number of distinct case studies have been reported together with a few statistical explorations of turbulence features at different parts of the MSH for various background and upstream conditions.

The whole set of studies demonstrates changes in dynamics of the turbulent cascade behind the BS. Unlike the SW, inside the MSH:

- Turbulence is usually characterized by a high level of compressive fluctuations.
- Turbulent cascade is usually modified behind the BS: at the MHD scales spectra are usually shallower than the predicted Kolmogorov spectra for developed turbulence and observed in the SW; at the kinetic scales spectra of compressive fluctuations tend to be steeper than typically observed in the SW and MSH.
- Turbulence at MHD scales develops in a different way for different BS geometry: behind the quasi-perpendicular BS, spectra often exhibit non-Kolmogorov scaling and bump around ion scales, while behind the quasi-parallel BS spectra tend to be more like those observed in the SW, with typical two-power-law shape and Kolmogorov scaling; BS geometry does not affect the kinetic-scale turbulence.
- Dynamics of turbulent cascade seem to be different for various large-scale SW flow types: for slow steady SW, no significant changes in spectra may happen while during compressed SW flow the spectra are usually highly modified at the BS.

Though generally the picture of turbulence development in the MSH can be seen qualitatively from the presented works, there are still a lot of questions worth answering. How does turbulence develop in the confined space? Which conditions in the upstream SW are favorable for the most crucial changes in the turbulent cascade at the BS? What path is required for plasma to recover "developed" turbulent cascade behind the BS? Answering these questions would provide essential knowledge for laboratory plasma as well as for space weather forecasts.

Today, a large set of high quality *in situ* measurements of magnetic and electric fields as well as plasma parameters are available. However, basically the presented data and studies are still scattered. We would like to emphasize the importance of using the whole database of spacecraft measurements in different regions of the MSH that can lead to better understanding of turbulence dynamics in front of the magnetopause. We also hope that this review will be helpful for those who aim to present a reliable theoretical description of turbulence and its evolution inside the MSH and to those who develop models of solar wind-magnetosphere coupling, which include kinetic-scale processes and turbulence.

AUTHOR CONTRIBUTIONS

All authors have made a substantial, direct, and intellectual contribution to the work and approved it for publication.

REFERENCES

Alexandrova, O. (2004). Cluster observations of finite amplitude Alfvén waves and small-scale magnetic filaments downstream of a quasi-perpendicular shock. *J. Geophys. Res.* 109, A05207. doi:10.1029/2003JA010056

Alexandrova, O. (2008). Solar wind vs. magnetosheath turbulence and Alfvén vortices. *Nonlinear Process Geophys.* 15, 95–108. doi:10.5194/npg-15-95-2008

Alexandrova, O., Chen, C. H. K., Sorriso-Valvo, L., Horbury, T. S., and Bale, S. D. (2013). Solar wind turbulence and the role of ion instabilities. *Space Sci. Rev.* 178, 101–139. doi:10.1007/s11214-013-0004-8

Alexandrova, O., Lacombe, C., and Mangeney, A. (2008). Spectra and anisotropy of magnetic fluctuations in the Earth's magnetosheath: cluster observations. *Ann. Geophys.* 26, 3585–3596. doi:10.5194/angeo-26-3585-2008

Alexandrova, O., Mangeney, A., Maksimovic, M., Cornilleau-Wehrlin, N., Bosqued, J.-M., and André, M. (2006). Alfvén vortex filaments observed in magnetosheath downstream of a quasi-perpendicular bow shock. *J. Geophys. Res.* 111, A12208. doi:10.1029/2006JA011934

Anderson, B. J., Fuselier, S. A., Gary, S. P., and Denton, R. E. (1994). Magnetic spectral signatures in the Earth's magnetosheath and plasma depletion layer. *J. Geophys. Res.* 99, 5877. doi:10.1029/93JA02827

Andrés, N., and Sahraoui, F. (2017). Alternative derivation of exact law for compressible and isothermal magnetohydrodynamics turbulence. *Phys. Rev. E.* 96, 053205. doi:10.1103/PhysRevE.96.053205

Andrés, N., Sahraoui, F., Galtier, S., Hadid, L. Z., Ferrand, R., and Huang, S. Y. (2019). Energy cascade rate measured in a collisionless space plasma with MMS data and compressible hall magnetohydrodynamic turbulence theory. *Phys. Rev. Lett.* 123, 245101. doi:10.1103/PhysRevLett.123.245101

Andrés, N., Sahraoui, F., Galtier, S., Hadid, L. Z., Dmitruk, P., and Mininni, P. D. (2018). Energy cascade rate in isothermal compressible magnetohydrodynamic turbulence. *J. Plasma Phys.* 84, 21. doi:10.1017/S0022377818000788

Bandyopadhyay, R., Chasapis, A., Chhiber, V., Parashar, T. N., Matthaeus, W. H., Shay, M. A., et al. (2018). Incompressive energy transfer in the Earth's magnetosheath: magnetospheric multiscale observations. *Astrophys. J.* 866, 106. doi:10.3847/1538-4357/aade04

Bandyopadhyay, R., Matthaeus, W. H., Parashar, T. N., Yang, Y., Chasapis, A., Giles, B. L., et al. (2020). Statistics of kinetic dissipation in the Earth's magnetosheath: MMS observations. *Phys. Rev. Lett.* 124, 255101. doi:10.1103/PhysRevLett.124.255101

Blanco-Cano, X., Omidi, N., and Russell, C. T. (2006a). Macrostructure of collisionless bow shocks: 2. ULF waves in the foreshock and magnetosheath. *J. Geophys. Res.* 111, A10205. doi:10.1029/2005JA011421

Blanco-Cano, X., Omidi, N., and Russell, C. T. (2006b). ULF waves and their influence on bow shock and magnetosheath structures. *Adv. Space Res.* 37, 1522–1531. doi:10.1016/j.asr.2005.10.043

Boldyrev, S., and Perez, J. C. (2012). Spectrum of kinetic alfven turbulence. *Astrophys. J. Lett.* 758 (2), 5. doi:10.1088/2041-8205/758/2/L44

Borovsky, J. E. (2012). The velocity and magnetic field fluctuations of the solar wind at 1 AU: statistical analysis of Fourier spectra and correlations with plasma properties. *J. Geophys. Res. Sp. Phys.* 117, 5104. doi:10.1029/2011JA017499

Borovsky, J. E. (2020). Plasma and magnetic-field structure of the solar wind at inertial-range scale sizes discerned from statistical examinations of the time-series measurements. *Front. Astron. Sp. Sci.* 7, 20. doi:10.3389/fspas.2020.00020

Borovsky, J. E., Denton, M. H., and Smith, C. W. (2019). Some properties of the solar wind turbulence at 1 AU statistically examined in the different types of solar wind plasma. *J. Geophys. Res. Space Phys.* 124, 2406–2424. doi:10.1029/2019JA026580

Breuillard, H., Matteini, L., Argall, M. R., Sahraoui, F., Andriopoulou, M., ContelLe, O., et al. (2018). New insights into the nature of turbulence in the Earth's magnetosheath using magnetospheric multiscale mission data. *Astrophys. J.* 859, 127. doi:10.3847/1538-4357/aabae8

Breuillard, H., Yordanova, E., Vaivads, A., and Alexandrova, O. (2016). The effects of kinetic instabilities on small-scale turbulence in Earth's magnetosheath. *Astrophys. J.* 829, 54. doi:10.3847/0004-637X/829/1/54

Bruno, R., and Carbone, V. (2013). The solar wind as a turbulence laboratory. *Living rev. Sol. Phys.* 10, 7. doi:10.12942/lrsp-2013-2

Budaev, V. P., Savin, S. P., and Zelenyi, L. M. (2011). Investigation of intermittency and generalized self-similarity of turbulent boundary layers in laboratory and magnetospheric plasmas: towards a quantitative definition of plasma transport features. *Phys. Usp.* 54, 875–918. doi:10.3367/ufne.0181.201109a.0905

Budaev, V. P., Zelenyi, L. M., and Savin, S. P. (2015). Generalized self-similarity of intermittent plasma turbulence in space and laboratory plasmas. *J. Plasma Phys.* 81, 395810602. doi:10.1017/S0022377815001099

Burch, J. L., Moore, T. E., Torbert, R. B., and Giles, B. L. (2016). Magnetospheric multiscale overview and science objectives. *Space Sci. Rev.* 199, 5–21. doi:10.1007/s11214-015-0164-9

Chandran, B. D. G., Quataert, E., Howes, G. G., Xia, Q., and Pongkitiwanichakul, P. (2009). Constraining low-frequency alfvénic turbulence in the solar wind using density-fluctuation measurements. *Astrophys. J.* 707, 1668–1675. doi:10.1088/0004-637X/707/2/1668

Chasapis, A., Matthaeus, W. H., Parashar, T. N., Fuselier, S. A., Maruca, B. A., Phan, T. D., et al. (2017). High-resolution statistics of solar wind turbulence at kinetic scales using the magnetospheric multiscale mission. *Astrophys. J. Lett.* 844, L9. doi:10.3847/2041-8213/aa7ddd

Chen, C. H., Leung, L., Boldyrev, S., Maruca, B. A., and Bale, S. D. (2014). Ion-scale spectral break of solar wind turbulence at high and low beta. *Geophys. Res. Lett.* 41, 8081–8088. doi:10.1002/2014GL062009

Chen, C. H. K. (2016). Recent progress in astrophysical plasma turbulence from solar wind observations. *J. Plasma Phys.* 82, 535820602. doi:10.1017/S0022377816001124

Chen, C. H. K., and Boldyrev, S. (2017). Nature of kinetic scale turbulence in the Earth's magnetosheath. *Astrophys. J.* 842, 122. doi:10.3847/1538-4357/aa74e0

Chhiber, R., Chasapis, A., Bandyopadhyay, R., Parashar, T. N., Matthaeus, W. H., Maruca, B. A., et al. (2018). Higher-order turbulence statistics in the Earth's magnetosheath and the solar wind using magnetospheric multiscale observations. *J. Geophys. Res. Space Phys.* 123, 9941–9954. doi:10.1029/2018JA025768

Czaykowska, A., Bauer, T. M., Treumann, R. A., and Baumjohann, W. (2001). Magnetic field fluctuations across the Earth's bow shock. *Ann. Geophys.* 19, 275–287. doi:10.5194/angeo-19-275-2001

Dimmock, A. P., Nykyri, K., and Pulkkinen, T. I. (2014). A statistical study of magnetic field fluctuations in the dayside magnetosheath and their dependence on upstream solar wind conditions. *J. Geophys. Res. Space Phys.* 119, 6231–6248. doi:10.1002/2014JA020009

Dudok de Wit, T., Alexandrova, O., Furno, I., Sorriso-Valvo, L., and Zimbardo, G. (2013). Methods for characterising microphysical processes in plasmas. *Space Sci. Rev.* 178, 665–693. doi:10.1007/s11214-013-9974-9

Dudok de Wit, T., and Krasnosel'Skikh, V. V. (1996). Non-Gaussian statistics in space plasma turbulence: fractal properties and pitfalls. *Nonlinear Process Geophys.* 3, 262–273. doi:10.5194/npg-3-262-1996

Escoubet, C. P., Schmidt, R., and Goldstein, M. L. (1997). Cluster—science and mission overview. *Space Sci. Rev.* 79, 11–32. doi:10.1023/A:1004923124586

Fairfield, D. H. (1976). Magnetic fields of the magnetosheath. *Rev. Geophys.* 14, 117. doi:10.1029/RG014i001p00117

Frisch, U. (1995). *Turbulence : the legacy of A.N. Kolmogorov*. Cambridge, United Kingdom: Cambridge University Press, doi:10.1017/S0022112096210791

Fischer, D., Magnes, W., Hagen, C., Dors, I., Chutter, M. W., Needell, J., et al. (2016). Optimized merging of search coil and fluxgate data for MMS. *Geosci. Instrum. Method. Data Syst.* 5, 521. doi:10.5194/gi-5-521-2016

Fujimoto, A., Šafránková, J., Němeček, Z., Goncharov, O., Němec, F., Přech, L., et al. (2016). Density fluctuations upstream and downstream of interplanetary shocks. *Astrophys. J.* 819, 41. doi:10.3847/0004-637X/819/1/41

Goldreich, P., and Sridhar, S. (1995). Toward a theory of interstellar turbulence. II. Strong alfvenic turbulence. *Astrophys. J.* 438, 763. doi:10.1086/175121

Greenstadt, E. W. (1972). Binary index for assessing local bow shock obliquity. *J. Geophys. Res.* 77, 5467–5479. doi:10.1029/JA077i028p05467

Gutynska, O., Šafránková, J., and Němeček, Z. (2008). Correlation length of magnetosheath fluctuations: cluster statistics. *Ann. Geophys.* 26, 2503–2513. doi:10.5194/angeo-26-2503-2008

Gutynska, O., Šafránková, J., and Němeček, Z. (2009). Correlation properties of magnetosheath magnetic field fluctuations. *J. Geophys. Res. Sp. Phys.* 114, A8. doi:10.1029/2009JA014173

Gutynska, O., Šimůnek, J., Šafránková, J., Němeček, Z., and Přech, L. (2012). Multipoint study of magnetosheath magnetic field fluctuations and their relation to the foreshock. *J. Geophys. Res. Space Phys.* 117, A04214. doi:10.1029/2011JA017240

Hadid, L. Z., Sahraoui, F., Galtier, S., and Huang, S. Y. (2018). Compressible magnetohydrodynamic turbulence in the Earth's magnetosheath: estimation of the energy cascade rate using *in situ* spacecraft data. *Phys. Rev. Lett.* 120, 055102. doi:10.1103/PhysRevLett.120.055102

Hayosh, M., Šafránková, J., and Němeček, Z. (2006). MHD-modelling of the magnetosheath ion plasma flow and magnetic field and their comparison with experiments. *Adv. Space Res.* 37, 507–514. doi:10.1016/j.asr.2005.07.059

He, J.-S., Marsch, E., Tu, C.-Y., Zong, Q.-G., Yao, S., and Tian, H. (2011). Two-dimensional correlation functions for density and magnetic field fluctuations in magnetosheath turbulence measured by the cluster spacecraft. *J. Geophys. Res. Space Phys.* 116, A6. doi:10.1029/2010JA015974

Howes, G. G., Bale, S. D., Klein, K. G., Chen, C. H. K., Salem, C. S., and Tenbarge, J. M. (2012). The slow-mode nature of compressible wave power in solar wind turbulence. *Astrophys. J. Lett.* 753, 19. doi:10.1088/2041-8205/753/1/L19

Howes, G. G., Klein, K. G., and TenBarge, J. M. (2014). Validity of the taylor hypothesis for linear kinetic waves in the weakly collisional solar wind. *Astrophys. J.* 789, 106. doi:10.1088/0004-637X/789/2/106

Huang, S. Y., Hadid, L. Z., Sahraoui, F., Yuan, Z. G., and Deng, X. H. (2017). On the existence of the Kolmogorov inertial range in the terrestrial magnetosheath turbulence. *Astrophys. J. Lett.* 836, L10. doi:10.3847/2041-8213/836/1/L10

Huang, S. Y., and Sahraoui, F. (2019). Testing of the taylor frozen-in-flow hypothesis at electron scales in the solar wind turbulence. *Astrophys. J.* 876, 138. doi:10.3847/1538-4357/ab17d3

Huang, S. Y., Sahraoui, F., Deng, X. H., He, J. S., Yuan, Z. G., Zhou, M., et al. (2014). Kinetic turbulence in the terrestrial magnetosheath: cluster observations. *Astrophys. J.* 789, L28. doi:10.1088/2041-8205/789/2/L28

Hubert, D. (1994). Nature and origin of wave modes in the dayside earth magnetosheath. *Adv. Space Res.* 14, 55–64. doi:10.1016/0273-1177(94)90048-5

Karimabadi, H., Roytershteyn, V., Vu, H. X., Omelchenko, Y. A., Scudder, J., Daughton, W., et al. (2014). The link between shocks, turbulence, and magnetic reconnection in collisionless plasmas. *Phys. Plasmas*. 21, 062308. doi:10.1063/1.4882875

Kartalev, M. D., Nikolova, V. I., Kamenetsky, V. F., and Mastikov, I. P. (1996). On the self-consistent determination of dayside magnetopause shape and position. *Planet. Space Sci.* 44, 1195–1208. doi:10.1016/S0032-0633(96)00040-2

Klein, K. G., Howes, G. G., and Tenbarge, J. M. (2014). The violation of the taylor hypothesis in measurements of solar wind turbulence. *Astrophys. J. Lett.* 790, 20. doi:10.1088/2041-8205/790/2/L20

Kolmogorov, A. N. (1941). The local structure of turbulence in incompressible viscous fluid for very large Reynolds numbers. *Proc.R.Soc. A.* 434, 9. doi:10.1098/rspa.1991.0075

Kozak, L. V., Pilipenko, V. A., Chugunova, O. M., and Kozak, P. N. (2011). Statistical analysis of turbulence in the foreshock region and in the Earth's magnetosheath. *Cosmic Res.* 49, 194–204. doi:10.1134/S0010952511030063

Kozak, L. V., Savin, S. P., Budaev, V. P., Pilipenko, V. A., and Lezhen, L. A. (2012). Character of turbulence in the boundary regions of the Earth's magnetosphere. *Geomagn. Aeron.* 52, 445–455. doi:10.1134/S0016793212040093

Lacombe, C., and Belmont, G. (1995). Waves in the Earth's magnetosheath: observations and interpretations. *Adv. Space Res.* 15, 329–340. doi:10.1016/0273-1177(94)00113-F

Lacombe, C., Belmont, G., Hubert, D., Harvey, C. C., Mangeney, A., Russell, C. T., et al. (1995). Density and magnetic field fluctuations observed by ISEE 1-2 in the quiet magnetosheath. *Ann. Geophys.* 13, 343–357. doi:10.1007/s00585-995-0343-1

Lacombe, C., Samsonov, A. A., Mangeney, A., Maksimovic, M., Cornilleau-Wehrlin, N., Harvey, C. C., et al. (2006). Cluster observations in the magnetosheath. Part 2: intensity of the turbulence at electron scales. *Ann. Geophys.* 24, 3523–3531. doi:10.5194/angeo-24-3523-2006

Le Contel, O., Leroy, P., Roux, A., Coillot, C., Alison, D., Bouabdellah, A., et al. (2014). The search coil magnetometer for MMS. *Space Sci. Rev.* 199, 257–282. doi:10.1007/s11214-014-0096-9

Leamon, R. J., Smith, C. W., and Ness, N. F. (1998). Characteristics of magnetic fluctuations within coronal mass ejections: the January 1997 event. *Geophys. Res. Lett.* 25, 2505–2508. doi:10.1029/98GL00305

Li, H., Jiang, W., Wang, C., Verscharen, D., Zeng, C., Russell, C. T., et al. (2020). Evolution of the Earth's magnetosheath turbulence: a statistical study based on MMS observations. *Astrophys. J.* 898, L43. doi:10.3847/2041-8213/aba531

Lion, S., Alexandrova, O., and Zaslavsky, A. (2016). Coherent events and spectral shape at ion kinetic scales in the fast solar wind turbulence. *Astrophys. J.* 824, 47. doi:10.3847/0004-637X/824/1/47

Lucek, E. A., Dunlop, M. W., Horbury, T. S., Balogh, A., Brown, P., Cargill, P., et al. (2001). Cluster magnetic field observations in the magnetosheath: four-point measurements of mirror structures. *Ann. Geophys.* 19, 1421–1428. doi:10.5194/angeo-19-1421-2001

Macek, W. M. (2007). Multifractality and intermittency in the solar wind. *Nonlinear Process Geophys.* 14, 695–700. doi:10.5194/npg-14-695-2007

Macek, W. M., Krasińska, A., Silveira, M. V. D., Sibeck, D. G., Wawrzaszek, A., Burch, J. L., et al. (2018). Magnetospheric multiscale observations of turbulence in the magnetosheath on kinetic scales. *Astrophys. J.* 864, L29. doi:10.3847/2041-8213/aad9a8

Macek, W. M., Wawrzaszek, A., and Sibeck, D. G. (2015). THEMIS observation of intermittent turbulence behind the quasi-parallel and quasi-perpendicular shocks. *J. Geophys. Res. Space Phys.* 120, 7466–7476. doi:10.1002/2015JA021656

Mangeney, A., Lacombe, C., Maksimovic, M., Samsonov, A. A., Cornilleau-Wehrlin, N., Harvey, C. C., et al. (2006). Cluster observations in the magnetosheath. Part 1: anisotropies of the wave vector distribution of the turbulence at electron scales. *Ann. Geophys.* 24, 3507–3521. doi:10.5194/angeo-24-3507-2006

Matteini, L., Alexandrova, O., Chen, C. H. K., and Lacombe, C. (2017). Electric and magnetic spectra from MHD to electron scales in the magnetosheath. *Mon. Not. R. Astron. Soc.* 466, 945–951. doi:10.1093/mnras/stw3163

Ness, N. F., Scearce, C. S., and Seek, J. B. (1964). Initial results of the imp 1 magnetic field experiment. *J. Geophys. Res.* 69, 3531–3569. doi:10.1029/JZ069i017p03531

Neugebauer, M., Wu, C. S., and Huba, J. D. (1978). Plasma fluctuations in the solar wind. *J. Geophys. Res.* 83, 1027. doi:10.1029/JA083iA03p01027

Němeček, Z., Šafránková, J., Pišoft, P., and Zastenker, G. N. (2001). Statistical study of ion flux fluctuations in the magnetosheath. *Czech. J. Phys.* 51, 853–862. doi:10.1023/A:1011630618180

Němeček, Z., Šafránková, J., Zastenker, G. N., Pišoft, P., and Jelínek, K. (2002). Low-frequency variations of the ion flux in the magnetosheath. *Planet. Space Sci.* 50, 567–575. doi:10.1016/S0032-0633(02)00036-3

Němeček, Z., Šafránková, J., Zastenker, G. N., Pišoft, P., Paularena, K. I., and Richardson, J. D. (2000). Observations of the radial magnetosheath profile and a comparison with gasdynamic model predictions. *Geophys. Res. Lett.* 27, 2801–2804. doi:10.1029/2000GL000063

Ofman, L., and Gedalin, M. (2013). Two-dimensional hybrid simulations of quasi-perpendicular collisionless shock dynamics: gyrating downstream ion distributions. *J. Geophys. Res. Space Phys.* 118, 1828–1836. doi:10.1029/2012JA018188

Omidi, N., Eastwood, J. P., and Sibeck, D. G. (2010). Foreshock bubbles and their global magnetospheric impacts. *J. Geophys. Res. Sp. Phys.* 115, A06204. doi:10.1029/2009JA014828

Omidi, N., Sibeck, D., Gutynska, O., and Trattner, K. J. (2014). Magnetosheath filamentary structures formed by ion acceleration at the quasi-parallel bow shock. *J. Geophys. Res. Space Phys.* 119, 2593–2604. doi:10.1002/2013JA019587

Perri, S., Servidio, S., Vaivads, A., and Valentini, F. (2017). Numerical study on the validity of the Taylor hypothesis in space plasmas. *Astrophys. J. Suppl.* 231, 4. doi:10.3847/1538-4365/aa755a

Perrone, D., Bruno, R., D'Amicis, R., Telloni, D., De Marco, R., Stangalini, M., et al. (2020). Coherent events at ion scales in the inner heliosphere: parker solar probe observations during the first encounter. *Astrophys. J.* 905 (2), 12. doi:10.3847/1538-4357/abc480

Perschke, C., Narita, Y., Motschmann, U., and Glassmeier, K.-H. (2014). Multi-spacecraft observations of linear modes and sideband waves in ion-scale solar wind turbulence. *Astrophys. J. Lett.* 793, L25. doi:10.1088/2041-8205/793/2/L25

Phan, T. D., Eastwood, J. P., Shay, M. A., Drake, J. F., Sonnerup, B. U. Ö., Fujimoto, M., et al. (2018). Electron magnetic reconnection without ion coupling in Earth's turbulent magnetosheath. *Nature.* 557, 202. doi:10.1038/s41586-018-0091-5

Podesta, J. J., Roberts, D. A., and Goldstein, M. L. (2006). Power spectrum of small-scale turbulent velocity fluctuations in the solar wind. *J. Geophys. Res.* 111, A10109. doi:10.1029/2006JA011834

Pollock, C., Moore, T., Jacques, A., Burch, J., Gliese, U., Saito, Y., et al. (2016). Fast plasma investigation for magnetospheric multiscale. *Space Sci. Rev.* 199, 331–406. doi:10.1007/s11214-016-0245-4

Pulinets, M. S., Antonova, E. E., Riazantseva, M. O., Znatkova, S. S., and Kirpichev, I. P. (2014). Comparison of the magnetic field before the subsolar magnetopause with the magnetic field in the solar wind before the bow shock. *Adv. Space Res.* 54, 604–616. doi:10.1016/j.asr.2014.04.023

Pulkkinen, T. I., Dimmock, A. P., Lakka, A., Osmane, A., Kilpua, E., Myllys, M., et al. (2016). Magnetosheath control of solar wind-magnetosphere coupling efficiency. *J. Geophys. Res. Space Phys.* 121, 8728–8739. doi:10.1002/2016JA023011

Rakhmanova, L., Riazantseva, M., and Zastenker, G. (2016). Plasma fluctuations at the flanks of the Earth's magnetosheath at ion kinetic scales. *Ann. Geophys.* 34, 1011–1018. doi:10.5194/angeo-34-1011-2016

Rakhmanova, L. S., Riazantseva, M. O., Zastenker, G. N., and Yermolaev, Y. I. (2017). High-frequency plasma fluctuations in the middle magnetosheath and near its boundaries: Spektr-R observations. *J. Plasma Phys.* 83, 705830204. doi:10.1017/S002237781700023X

Rakhmanova, L., Riazantseva, M., Zastenker, G., and Verigin, M. (2018a). Kinetic-scale ion flux fluctuations behind the quasi-parallel and quasi-perpendicular bow shock. *J. Geophys. Res. Space Phys.* 123, 5300–5314. doi:10.1029/2018JA025179

Rakhmanova, L. S., Riazantseva, M. O., Zastenker, G. N., and Verigin, M. I. (2018b). Effect of the magnetopause and bow shock on characteristics of plasma turbulence in the Earth's magnetosheath. *Geomagn. Aeron.* 58, 718–727. doi:10.1134/S0016793218060129

Rakhmanova, L. S. (2019). Dynamisc of fast plasma variations in the magnetosheath. PhD work. Moscow, Russia: Russian Academy of Sciences.

Rakhmanova, L. S., Riazantseva, M. O., Zastenker, G. N., Yermolaev, Y. I., Lodkina, I. G., and Chesalin, L. S. (2020a). Turbulent cascade in the magnetosheath affected by the solar wind's plasma turbulence. *Cosmic Res.* 57, 443–450. doi:10.1134/S0010952519060066

Rakhmanova, L., Riazantseva, M., Zastenker, G., Yermolaev, Y., and Lodkina, I. (2020b). Dynamics of plasma turbulence at Earth's bow shock and through the magnetosheath. *Astrophys. J.* 901, 30. doi:10.3847/1538-4357/abae00

Retinò, A., Sundkvist, D., Vaivads, A., Mozer, F., André, M., and Owen, C. J. (2007). *In situ* evidence of magnetic reconnection in turbulent plasma. *Nat. Phys.* 3, 235–238. doi:10.1038/nphys574

Rezeau, L., Belmont, G., Cornilleau-Wehrlin, N., Reberac, F., and Briand, C. (1999). Spectral law and polarization properties of the low-frequency waves at the magnetopause. *Geophys. Res. Lett.* 26, 651–654. doi:10.1029/1999GL900060

Rezeau, L., Perraut, S., and Roux, A. (1986). Electromagnetic fluctuations in the vicinity of the magnetopause. *Geophys. Res. Lett.* 13, 1093–1096. doi:10.1029/GL013i011p01093

Rezeau, L., Sahraoui, F., d'Humières, E., Belmont, G., Chust, T., Cornilleau-Wehrlin, N., et al. (2001). A case study of low-frequency waves at the magnetopause. *Ann. Geophys.* 19, 1463–1470. doi:10.5194/angeo-19-1463-2001

Riazantseva, M., Budaev, V., Rakhmanova, L., Zastenker, G., Yermolaev, Y., Lodkina, I., et al. (2017). Variety of shapes of solar wind ion flux spectra: Spektr-R measurements. *J. Plasma Phys.* 83, 705830401. doi:10.1017/S0022377817000502

Riazantseva, M. O., Budaev, V. P., Zelenyi, L. M., Zastenker, G. N., Pavlos, G. P., Safrankova, J., et al. (2015). Dynamic properties of small-scale solar wind plasma fluctuations. *Philos. Trans. R. Soc. A.* 373, 20140146. doi:10.1098/rsta.2014.0146

Riazantseva, M. O., Budaev, V. P., Rakhmanova, L. S., Zastenker, G. N., Šafránková, J., Němeček, Z., et al. (2016). Comparison of properties of small-scale ion flux fluctuations in the flank magnetosheath and in the solar wind. *Adv. Space Res.* 58, 166–174. doi:10.1016/J.ASR.2015.12.022

Riazantseva, M. O., Rakhmanova, L. S., Yermolaev, Yu. I, Lodkina, I. G., Zastenker, G. N., and Chesalin, L. S. (2019). Characteristics of turbulent solar wind flow in plasma compression regions. *Cosmic Res.* 58 (6), 468–477. doi:10.1134/S001095252006009X

Roberts, O. W., Li, X., and Li, B. (2013). Kinetic plasma turbulence in the fast solar wind measured by cluster. *Astrophys. J.* 769, 58. doi:10.1088/0004-637X/769/1/58

Roberts, O. W., Narita, Y., Nakamura, R., Vörös, Z., and Gershman, D. (2019). Anisotropy of the spectral index in ion scale compressible turbulence: MMS observations in the magnetosheath. *Front. Physiol.* 7, 184. doi:10.3389/fphy.2019.00184

Roberts, O. W., Toledo-Redondo, S., Perrone, D., Zhao, J., Narita, Y., Gershman, D., et al. (2018). Ion-scale kinetic Alfvén turbulence: Mms measurements of the Alfvén ratio in the magnetosheath. *Geophys. Res. Lett.* 45, 7974–7984. doi:10.1029/2018GL078498

Rodriguez, P. (1985). Magnetosheath whistler turbulence. *J. Geophys. Res.* 90, 6337. doi:10.1029/JA090iA07p06337

Russell, C. T., Anderson, B. J., Baumjohann, W., Bromund, K. R., Dearborn, D., Fischer, D., et al. (2016). The magnetospheric multiscale magnetometers. *Space Sci. Rev.* 199, 189–256. doi:10.1007/s11214-014-0057-3

Šafránková, J., Hayosh, M., Gutynska, O., Němeček, Z., and Přech, L. (2009). Reliability of prediction of the magnetosheath BZ component from interplanetary magnetic field observations. *J. Geophys. Res. Space Phys.* 114. doi:10.1029/2009JA014552

Šafránková, J., Němeček, Z., Němec, F., Přech, L., Chen, C. H. K., and Zastenker, G. N. (2016). Power spectral density of fluctuations of bulk and thermal speeds in the solar wind. *Astrophys. J.* 825, 121. doi:10.3847/0004-637X/825/2/121

Šafránková, J., Němeček, Z., Němec, F., Přech, L., Pitňa, A., Chen, C. H. K., et al. (2015). Solar wind density spectra around the ion spectral break. *Astrophys. J.* 803, 107. doi:10.1088/0004-637X/803/2/107

Šafránková, J., Němeček, Z., Přech, L., Zastenker, G., Čermák, I., Chesalin, L., et al. (2013). Fast solar wind monitor (BMSW): description and first results. *Space Sci. Rev.* 175, 165–182. doi:10.1007/s11214-013-9979-4

Sahraoui, F., Belmont, G., Rezeau, L., Cornilleau-Wehrlin, N., Pinçon, J. L., and Balogh, A. (2006). Anisotropic turbulent spectra in the terrestrial magnetosheath as seen by the cluster spacecraft. *Phys. Rev. Lett.* 96, 075002. doi:10.1103/PhysRevLett.96.075002

Sahraoui, F., Belmont, G., Pinçon, J. L., Rezeau, L., Balogh, A., Robert, P., et al. (2004). Magnetic turbulent spectra in the magnetosheath: new insights. *Ann. Geophys.* 22 (6), 2283–2288. doi:10.5194/angeo-22-2283-2004

Sahraoui, F., Hadid, L., and Huang, S. (2020). Magnetohydrodynamic and kinetic scale turbulence in the near-Earth space plasmas: a (short) biased review. *Rev. Mod. Phys.* 4, 4. doi:10.1007/s41614-020-0040-2

Sahraoui, F., PinçOn, J. L., Belmont, G., Rezeau, L., Cornilleau-Wehrlin, N., Robert, P., et al. (2003). ULF wave identification in the magnetosheath: the k-filtering technique applied to Cluster II data. *J. Geophys. Res.* 108, 1335. doi:10.1029/2002JA009587

Samsonov, A. A., Alexandrova, O., Lacombe, C., Maksimovic, M., and Gary, S. P. (2007). Proton temperature anisotropy in the magnetosheath: comparison of 3-D MHD modelling with cluster data. *Ann. Geophys.* 25, 1157–1173. doi:10.5194/angeo-25-1157-2007

Samsonov, A. A., Němeček, Z., Šafránková, J., and Jelínek, K. (2012). Why does the subsolar magnetopause move sunward for radial interplanetary magnetic field? *J. Geophys. Res. Space Phys.* 117, A05221. doi:10.1029/2011JA017429

Schekochihin, A. A., Cowley, S. C., Dorland, W., Hammett, G. W., Howes, G. G., Quataert, E., et al. (2009). Astrophysical gyrokinetics: kinetic and fluid turbulent cascades in magnetized weakly collisional plasmas. *Astrophys. J. Suppl.* 182, 310–377. doi:10.1088/0067-0049/182/1/310

Schwartz, S. J., Burgess, D., and Moses, J. J. (1996). Low-frequency waves in the Earth's magnetosheath: present status. *Ann. Geophys.* 14, 1134–1150. doi:10.1007/s00585-996-1134-z

Shevyrev, N. N., and Zastenker, G. N. (2005). Some features of the plasma flow in the magnetosheath behind quasi-parallel and quasi-perpendicular bow shocks. *Planet. Space Sci.* 53, 95–102. doi:10.1016/j.pss.2004.09.033

Shevyrev, N. N., Zastenker, G. N., Eiges, P. E., and Richardson, J. D. (2006). Low frequency waves observed by Interball-1 in foreshock and magnetosheath. *Adv. Space Res.* 37, 1516–1521. doi:10.1016/j.asr.2005.07.072

Shevyrev, N. N., Zastenker, G. N., Nozdrachev, M. N., Němeček, Z., Šafránková, J., and Richardson, J. D. (2003). High and low frequency large amplitude variations of plasma and magnetic field in the magnetosheath: radial profile and some features. *Adv. Space Res.* 31, 1389–1394. doi:10.1016/S0273-1177(03)00008-5

Sibeck, D. G., and Gosling, J. T. (1996). Magnetosheath density fluctuations and magnetopause motion. *J. Geophys. Res. Space Phys.* 101, 31–40. doi:10.1029/95JA03141

Smith, C. W., Hamilton, K., Vasquez, B. J., and Leamon, R. J. (2006). Dependence of the dissipation range spectrum of interplanetary magnetic fluctuations on the rate of energy cascade. *Astrophys. J.* 645, L85–L88. doi:10.1086/506151

Song, P., Russell, C. T., and Thomsen, M. F. (1992a). Slow mode transition in the frontside magnetosheath. *J. Geophys. Res.* 97, 8295. doi:10.1029/92JA00381

Song, P., Russell, C. T., and Thomsen, M. F. (1992b). Waves in the inner magnetosheath: a case study. *Geophys. Res. Lett.* 19, 2191–2194. doi:10.1029/92GL02499

Sorriso-Valvo, L., Carbone, V., Veltri, P., Consolini, G., and Bruno, R. (1999). Intermittency in the solar wind turbulence through probability distribution functions of fluctuations. *Geophys. Res. Lett.* 26, 1801–1804. doi:10.1029/1999GL900270

Spreiter, J. R., and Stahara, S. S. (1980). A new predictive model for determining solar wind-terrestrial planet interactions. *J. Geophys. Res.* 85, 6769–6777. doi:10.1029/JA085iA12p06769

Spreiter, J. R., Summers, A. L., and Alksne, A. Y. (1966). Hydromagnetic flow around the magnetosphere. *Planet. Space Sci.* 14, 223–253. doi:10.1016/0032-0633(66)90124-3

Stawarz, J. E., Eastwood, J. P., Phan, T. D., Gingell, I. L., Shay, M. A., Burch, J. L., et al. (2019). Properties of the turbulence associated with electron-only magnetic reconnection in Earth's magnetosheath. *Astrophys. J.* 877, L37. doi:10.3847/2041-8213/ab21c8

Stawarz, J. E., Eriksson, S., Wilder, F. D., Ergun, R. E., Schwartz, S. J., Pouquet, A., et al. (2016). Observations of turbulence in a kelvin-helmholtz event on 8 september 2015 by the magnetospheric multiscale mission. *J. Geophys. Res. Space Phys.* 121, 11021–11034. doi:10.1002/2016JA023458

Sundkvist, D., Retinò, A., Vaivads, A., and Bale, S. D. (2007). Dissipation in turbulent plasma due to reconnection in thin current sheets. *Phys. Rev. Lett.* 99, 025004. doi:10.1103/PhysRevLett.99.025004

Taylor, G. I. (1938). The spectrum of turbulence. *Proc. R. Soc. A Math. Phys. Eng. Sci.* 164, 476–490. doi:10.1098/rspa.1938.0032

Tóth, G., Sokolov, I. V., Gombosi, T. I., Chesney, D. R., Clauer, C. R., De Zeeuw, D. L., et al. (2005). Space Weather Modeling Framework: a new tool for the space science community. *J. Geophys. Res. Space Phys.* 110. doi:10.1029/2005JA011126

Tu, C.-Y., and Marsch, E. (1995). MHD structures, waves and turbulence in the solar wind. Available at: https://ui.adsabs.harvard.edu/abs/1995mswt.book.T/abstract (Accessesd September 11, 2020)

Vörös, Z., Yordanova, E., Khotyaintsev, Y. V., Varsani, A., and Narita, Y. (2019). Energy conversion at kinetic scales in the turbulent magnetosheath. *Front. Astron. Sp. Sci.* 6, 60. doi:10.3389/fspas.2019.00060

Vörös, Z., Yordanova, E., Varsani, A., Genestreti, K. J., Khotyaintsev, Y. V., Li, W., et al. (2017). MMS observation of magnetic reconnection in the turbulent magnetosheath. *J. Geophys. Res. Space Phys.* 122, 11442–11467. doi:10.1002/2017JA024535

Yermolaev, Y. I., Nikolaeva, N. S., Lodkina, I. G., and Yermolaev, M. Y. (2009). Catalog of large-scale solar wind phenomena during 1976–2000. *Cosmic Res.* 47, 81–94. doi:10.1134/S0010952509020014

Yermolaev, Y. I., Nikolaeva, N. S., Lodkina, I. G., and Yermolaev, M. Y. (2012). Geoeffectiveness and efficiency of CIR, Sheath and ICME in generation of magnetic storms. *J. Geophys. Res.* 117. doi:10.1029/2011JA017139

Yermolaev, Y. I., Lodkina, I. G., Nikolaeva, N. S., and Yermolaev, M. Y. (2015). Dynamics of large-scale solar-wind streams obtained by the double superposed epoch analysis. *J. Geophys. Res. Space Phys.* 120, 7094–7106. doi:10.1002/2015JA021274

Yordanova, E., Vaivads, A., André, M., Buchert, S. C., and Vörös, Z. (2008). Magnetosheath plasma turbulence and its spatiotemporal evolution as observed by the cluster spacecraft. *Phys. Rev. Lett.* 100, 205003. doi:10.1103/PhysRevLett.100.205003

Yordanova, E., Vörös, Z., Raptis, S., and Karlsson, T. (2020). Current sheet statistics in the magnetosheath. *Front. Astron. Sp. Sci.* 7, 2. doi:10.3389/fspas.2020.00002

Zastenker, G. N., Nozdrachev, M. N., Němeček, Z., Šafránková, J., Paularena, K. I., Richardson, J. D., et al. (2002). Multispacecraft measurements of plasma and magnetic field variations in the magnetosheath: comparison with Spreiter models and motion of the structures. *Planet. Space Sci.* 50, 601–612. doi:10.1016/S0032-0633(02)00039-9

Zastenker, G. N., Safrankova, J., Nemecek, Z., Prech, L., Cermak, I., Vaverka, I., et al. (2013). Fast measurements of parameters of the Solar Wind using the BMSW instrument. *Cosmic Res.* 51, 78–89. doi:10.1134/S0010952513020081

Zimbardo, G., Greco, A., Sorriso-Valvo, L., Perri, S., Vörös, Z., Aburjania, G., et al. (2010). Magnetic turbulence in the geospace environment. *Space Sci. Rev.* 156, 89–134. doi:10.1007/s11214-010-9692-5

Conflict of Interest: The authors declare that the research was conducted in the absence of any commercial or financial relationships that could be construed as a potential conflict of interest.

frontiers in Astronomy and Space Sciences

REVIEW
published: 22 March 2021
doi: 10.3389/fspas.2021.620519

Magnetohydrodynamic Turbulence in the Earth's Magnetotail From Observations and Global MHD Simulations

Mostafa El-Alaoui[1,2,3]*, *Raymond J. Walker*[4], *James M. Weygand*[4], *Giovanni Lapenta*[5,6] *and Melvyn L. Goldstein*[6,7]

[1]Department of Physics and Astronomy, UCLA, Los Angeles, CA, United States, [2]Community Coordinated Modeling Center, NASA GSFC, Greenbelt, MD, United States, [3]Department of Physics, CUA, Washington, DC, United States, [4]Department of Earth, Planetary, and Space Sciences, University of California, Los Angeles, CA, United States, [5]Department of Mathematics, KU Leuven, Leuven, Belgium, [6]Space Science Institute, Boulder, CO, United States, [7]University of Maryland Baltimore County, Baltimore, MD, United States

Magnetohydrodynamic (MHD) turbulent flows are found in the solar wind, the magnetosheath and the magnetotail plasma sheet. In this paper, we review both observational and theoretical evidence for turbulent flow in the magnetotail. MHD simulations of the global magnetosphere for southward interplanetary magnetic field (IMF) exhibit nested vortices in the earthward outflow from magnetic reconnection that are consistent with turbulence. Similar simulations for northward IMF also exhibit enhanced vorticity consistent with turbulence. These result from Kelvin-Helmholtz (KH) instabilities. However, the turbulent flows association with reconnection fill much of the magnetotail while the turbulent flows associated with the KH instability are limited to a smaller region near the magnetopause. Analyzing turbulent flows in the magnetotail is difficult because of the limited extent of the tail and because the flows there are usually sub-magnetosonic. Observational analysis of turbulent flows in the magnetotail usually assume that the Taylor frozen-in-flow hypothesis is valid and compare power spectral density vs. frequency with spectral indices derived for fluid turbulence by Kolmogorov in 1941. Global simulations carried out for actual magnetospheric substorms in the tail enable the results of the simulations to be compared directly with observed power spectra. The agreement between the two techniques provides confidence that the plasma sheet plasma is actually turbulent. The MHD results also allow us to calculate the power vs. wave number; results that also support the idea that the tail is turbulent.

Keywords: turbulence, Magnetohydrodynamic, magnetotail, plasma sheet, reconnection

OPEN ACCESS

Edited by:
Gaetano Zimbardo,
University of Calabria, Italy

Reviewed by:
Antonella Greco,
Università della Calabria, Italy
Hui Li,
National Space Science Center (CAS), China

***Correspondence:**
Mostafa El-Alaoui
mostafa@physics.ucla.edu

Specialty section:
This article was submitted to Space Physics, a section of the journal Frontiers in Astronomy and Space Sciences

Received: *23 October 2020*
Accepted: *04 February 2021*
Published: *22 March 2021*

Citation:
El-Alaoui M, Walker RJ, Weygand JM, Lapenta G and Goldstein ML (2021) Magnetohydrodynamic Turbulence in the Earth's Magnetotail From Observations and Global MHD Simulations. Front. Astron. Space Sci. 8:620519. doi: 10.3389/fspas.2021.620519

INTRODUCTION

One of the primary goals of current investigations in space physics is to understand how electromagnetic energy stored in the magnetotail is transferred to plasma energy. Turbulence is a multi-scale phenomenon that mediates the transport of energy, mass, and momentum. Unsteady, but nonrandom fluctuations in the magnetic and electric fields and flows characterize turbulence (e.g., Karimabadi et al., 2013). Turbulent spectra have been observed in many space plasmas. For example, turbulent fluctuation spectra have been found in the solar wind (Coleman, 1968; Matthaeus and Goldstein 1982; Roberts et al., 1987a; Roberts et al., 1987b; Tu et al., 1989; Marsch and Tu, 1990;

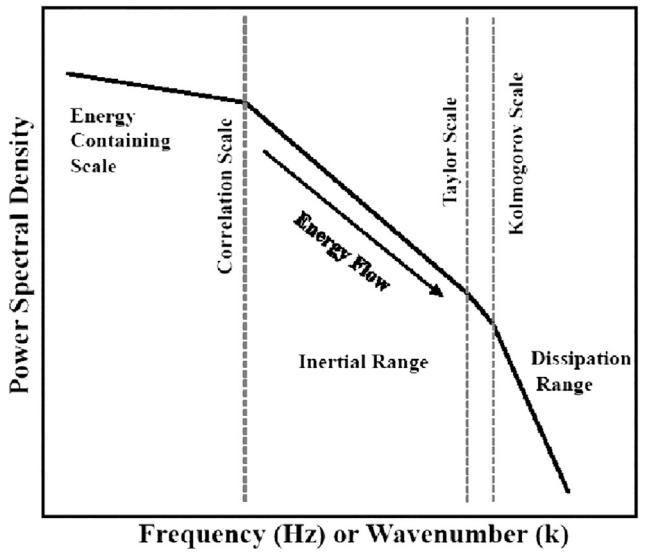

FIGURE 1 | Schematic of a typical power spectral density plot for turbulent solar wind. The lowest frequencies are at the energy containing scales and the dissipation range is at the highest frequencies. The correlation scale (left most dashed gray line) separates energy containing scales and the inertial range while the Kolmogorov scale (right most dashed gray line) is between the inertial range and the dissipation range. The third scale on the schematic is the Taylor scale (middle dashed gray line), the scale at which eddies start to damp out, (Adapted from Goldstein et al. (1995)).

Sahraoui et al., 2010), in the magnetosheath (Zimbardo et al., 2010; Li et al., 2020) and in the magnetosphere (Borovsky et al., 1997; Lui 2001; Weygand 2005; Weygand et al., 2006; Weygandf et al., 2007). In the magnetosphere, turbulence exists over a wide range of scales from large scale magnetohydrodynamic (MHD) flows to kinetic dissipation scales (see Zimbardo et al., (2010) for a review of turbulence studies in the geospace environment including both the magnetosheath and the magnetosphere). Emphasis in this paper is on our understanding of the MHD turbulence, its consequences for transport and dynamics, and, specifically, its relationship to magnetic reconnection, with a focus on the magnetotail. In particular, several studies have presented evidence that turbulence in the plasma sheet is an important mechanism for energizing plasma in the magnetotail (Borovsky et al., 1997; Angelopoulos et al., 1999; Chang, 1999; Klimas, 2000; Borovsky and Funsten 2003; Weygand et al., 2007).

In general, turbulence in plasmas can be thought of as resulting from oscillations in velocity or magnetic field driven by nonlinear processes at large scales (Kadomtsev, 1965) and as vorticity in fluid motion where the inertial forces in the vortices are larger than the forces that are damping the eddies (Leung and Gibson, 2004). The turbulence in any medium transfers energy from the largest scales to small dissipation scales, but, in some circumstances, can involve an inverse transfer from small scales to large scales (Frisch and Kolmogorov, 2001). Observations of turbulent fluctuations in the solar wind have been discussed for decades. For example, one of the primary goals of the Parker Solar Probe mission (Nature 2019) is to find the source of the Alfvénic turbulence in the solar corona. Compared to the solar wind, there are relatively few observational studies of turbulence in the magnetosphere. Such studies as there are include observations of the fluctuations in the magnetic field, plasma, and electric field measurements associated with power in both the inertial range and the dissipation range. A schematic of this process is shown in **Figure 1**. The large scales, or energy containing scales, will drive turbulence to an inertial range that, in fluid turbulence, was shown by Kolmogorov (1941) to have a power spectral index as a function of wave number that is −5/3. In this range of scales, turbulent eddies will break-down until dissipation causes the spectrum to steepen as viscosity damps the eddies. The beginning of the dissipative range is the Taylor scale (Kolmogorov 1941) scale and it is at this (kinetic scale) that heating occurs as the fluctuations are damped. In space, one generally measures time series, so that the power spectra are usually shown as a function of frequency but the validity of such a representation depends on the nature of the background flow and the properties of the fluctuations and often is determined by the validity of the Taylor frozen-in-flow hypothesis (Taylor, 1938), which is discussed in more detail below.

In this review, we first consider in *Observations of Turbulence in the Magnetotail* the observational evidence that turbulence exists in the tail. The approach used for studies of solar wind turbulence is not directly applicable to the magnetotail because contrary to the case in the solar wind, boundary effects are often important and the fluctuations may not satisfy conditions required of a random stationary process (Matthaeus and Goldstein, 1982; Perri and Balogh, 2010) which justifies construction of power spectra. In the super-Alfvénic solar wind flow, one can usually assume the validity of the Taylor frozen-in-flow hypothesis (Taylor, 1938) which justifies the transformation from frequency spectra to wave number. The Taylor hypothesis states that frequency ω relates linearly to the wave vector k (i.e., $\omega = k\,v$, where v is the plasma velocity) when the magnetic field evolves on a timescale longer than the time it takes it to flow past the spacecraft. In the magnetotail, the flow rarely exceeds the Alfvén speed and thus time and spatial scales are difficult to separate and determining the power spectrum of fluctuations as a function of wavenumber is challenging. Therefore, it is difficult to determine unambiguously the spectra of observed fluctuations. The flow speeds in the magnetosheath are usually higher and use of the Taylor hypothesis is frequently valid.

Consequently, we include a discussion of a variety of analysis methods in our discussion of fluctuations in the tail. In addition, analysis techniques used for studies of magnetic reconnection in the magnetotail can be applied to analyze the nature of the observed flows.

A number of generation mechanisms including flow shear instabilities such as the Kelvin-Helmholtz instability and flows from reconnection have been proposed (Matthaeus et al., 1984; Montgomery 1987; Angelopoulos et al., 1993; Borovsky et al., 1997; Lui 2001; Antonova and Ovchinnikov, 2002; Vörös et al., 2003). In *Magnetohydrodynamic Simulations of Turbulence in the Magnetotail*, we review work on evaluating the mechanisms by using MHD simulations. Finally, in *Some Unsolved Questions About Turbulence That can be Addressed Using Modeling*, we

consider several unsolved problems associated with turbulence in the tail and discuss future simulations to address them.

OBSERVATIONS OF TURBULENCE IN THE MAGNETOTAIL

A simplistic method suggesting the presence of turbulent fluctuations in a time series is to examine the spectral index in the inertial range of the power spectra. Kolmogorov (1941) used dimensional analysis to argue that the spectral index for fully developed fluid turbulence should be -5/3 for spectra of power vs. wavenumber. Perhaps surprisingly, this value is frequently observed in the fluctuating magnetic fields of the solar wind and magnetosheath (also see, Podesta et al. (2007)). On the other hand, Kraichnan (1965) found a value of -3/2 for ideal isotropic incompressible MHD turbulence. The difference between the neutral fluid values and magnetized fluid value comes from the number of degrees of freedom in the fluid. In both derivations, the rate of energy transfer from the driving scale of the spectra to the dissipation range of the spectrum was held constant. Whether or not the energy transfer rate is constant is important for differentiating Kraichnan and Kolmogorov type turbulence from intermittent turbulence. In intermittent turbulence, the energy transfer rate may not be constant and the turbulence may not yet be fully developed.

Within the plasma sheet, Borovsky et al. (1997) used ISEE-2 data and found for the plasma flow velocities that the slope of the power spectral density vs. frequency was -0.8 to -2.0 while that for the magnetic fieldit was between −1.6 and −3.0. Borovsky et al. (1997) used a "random sweeping model to approximate the conversion from wavenumber to frequency. (Even though these values include the theoretical value they do not confirm the presence of turbulent flows in the plasma sheet). Several different phenomena can explain these values including waves and/or driving phenomena, or it could be that the time series is neither stationary nor fully developed. Borovsky and Funsten (2003) suggested that this range of spectral indices could result from boundary effects or a combination of driving mechanisms each with different spectral indices. Weygand et al. (2005) found spectral indices in Cluster plasma sheet magnetic field data that were closer to −2 for the inertial range but did not take into account the speed of the flows. Vörös et al. (2004), also using Cluster magnetic field data, obtained a value of −2.6, but it is not clear if this value applies to the inertial range, dissipation range, or somewhere in between. Ergun et al. (2014) used MMS data and found a clear spectral index of −5/3 within the magnetic field inertial range, but a spectral index closer −3/2 in the electric field inertial range data. Chaston et al. (2012) found a similar value within the inertial range for electric field power spectra using THEMIS plasma sheet electric field data. Overall, the studies show that for slow speed flow the Taylor hypothesis is not valid but may be valid for high speed flows like those associated with magnetic reconnection. More work on this is needed.

Kozak et al. (2018) used the magnetic field measurements from four spacecraft of the Cluster mission for the analysis of turbulent processes in Earth's magnetotail. They obtained power-law scaling of the generalized diffusion coefficient indicating the presence of super-diffusion processes. Prior to the dipolarization, the spectral index was in the range between −1.68 and −2.08 while in the dipolarization on larger time scales the index was between −2.2 and −1.53. However, when they examined the data in the dipolarization on smaller time scales they found that the range was −2.89 to −2.35. They also report that the break in the spectra occurs at approximately the average proton gyrofrequency.

The wide range of spectral indices from the magnetic field and electric field data suggests the presence of intermittent turbulence within the plasma sheet. One method of determining the presence of intermittent turbulence is to look for non-self-similar scaling of the fluctuation probability distribution function. A number of studies have demonstrated that non-self-similar scaling of probability distribution functions exists within the plasma sheet (Weygand et al., 2005; Weygand et al., 2006; Stawarz et al., 2015]. To determine if there is non-self-similar scaling, one constructs probability distribution functions of the fluctuations across a range of times and calculates the kurtosis (i.e., fourth moment) for each distribution. If the kurtosis systematically decreases with increasingly temporal separation in the time series, then most likely the turbulence is intermittent (Weygand et al., 2006). All three of these studies found that magnetic field fluctuations observed with Cluster and THEMIS exhibited non-self-similar scaling of probability distributions during geomagnetic active periods within the plasma sheet. Both Stawarz et al. (2015) and Weygand et al. (2005) used single spacecraft observations to show non-self-similar scaling, which requires that the Taylor hypothesis applies, and suggests that the fluctuations are evolving slowly with respect to the time required for the plasma to flow past the spacecraft and are consequently frozen in the flow. Weygand et al. (2006) took this method one step further and avoided assuming the Taylor hypothesis by using pairs of Cluster spacecraft separated in space to show that non-self-similar scaling is present within the plasma sheet magnetic field. This non-self-similar scaling demonstrated the presence of intermittent turbulence in the plasma sheet. Thus much of the prior work suggests that turbulence is present in the plasma sheet, but that it may not be fully developed or may be intermittent.

Assuming that turbulence is present in the plasma sheet, we can determine the three fundamental associated scale lengths, *viz.,* the correlation scale, the Taylor scale, and the Kolmogorov scale (Goldstein et al., 1995; Weygand et al., 2007). The correlation scale is the energy-containing scale and the scale at which the inertial range turbulent cascade begins to exhibit a power spectrum. The Taylor scale is the scale at which the turbulent eddies begin to damp out, and the Kolmogorov scale is the point at which dissipation begins (**Figure 1**). A series of studies by Weygand et al., 2007; Weygand et al., 2009; Weygand et al., 2010) used Cluster spacecraft pairs over many years combining many different intervals to produce two-dimensional cross correlation maps of the magnetic field fluctuations within the plasma sheet. An example of such a map is shown in **Figure 2**. From these maps, we can determine correlation scales and Taylor scales. The correlation scale is the 1/e folding distance on the correlation vs. spacecraft

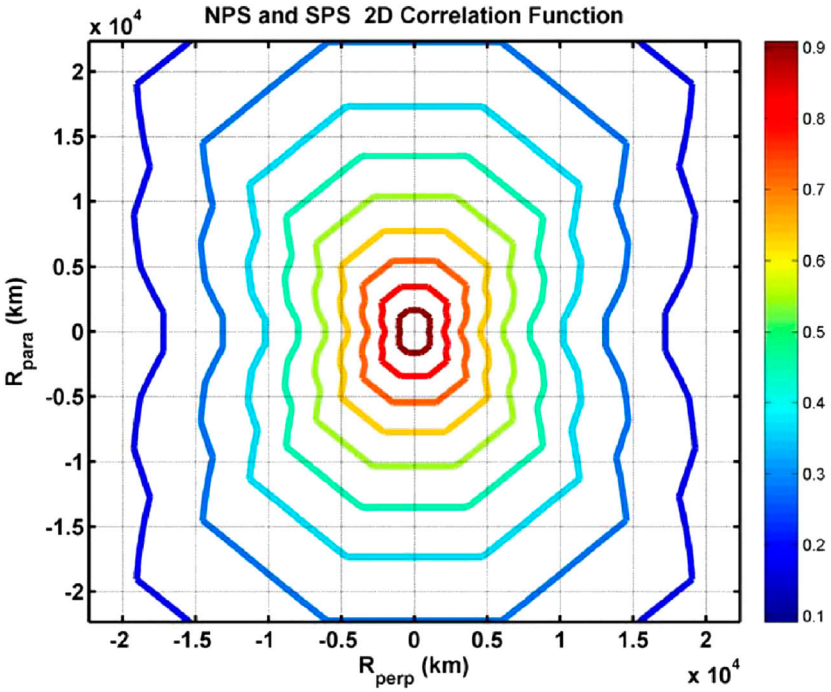

FIGURE 2 | Correlation contour plot for the plasma sheet. Correlations calculated for one quadrant were mirrored into the other quadrants. Rperp is the separation perpendicular to the mean magnetic field direction and Rpara is the separation parallel to the magnetic field direction. The color bar gives the value of the cross correlation coefficient (Weygand et al., 2009).

separation curve and the Taylor scale is the radius of curvature of the two point cross correlation function of the magnetic field fluctuations at the origin (Matthaeus et al., 2005; Weygand et al., 2007). Weygand et al., 2007; Weygand et al., 2009; Weygand et al., 2010) found that the correlation scale and Taylor scale varied with their angle with respect to the mean magnetic field direction for geomagnetically quiet and moderate conditions. The correlation scale and Taylor scale were longest along the mean magnetic field (about 16,400 km and 2900 km, respectively) and shortest perpendicular to the field (9200 km and 1100 km, respectively). In the plasma sheet, the resulting two-dimensional correlation maps were similar to the two-dimensional correlation maps of quasi two-dimensional turbulence observed in the slow solar wind (Dasso et al., 2005; Weygand et al., 2011), suggesting the presence of quasi two-dimensional turbulence within the plasma sheet. Physically, the correlation scale is associated with the approximate thickness of the plasma sheet and/or driving scales and the Taylor scale is expected to be about the same size or larger than an ion gyroradius in the plasma sheet (~700 km). Weygand et al. (2009) suggested that the difference in the Taylor scale size with magnetic field direction (**Figure 2**) might be related to dispersive and dissipative effects. Similar differences were noted in the solar wind in the same paper.

The correlation scale (λ_{CS}) and the Taylor scale (λ_{TS}) derived from the two-dimensional correlation maps can be employed to determine an effective magnetic Reynolds number ($R_{eff} = (\lambda_{CS}/\lambda_{TS})^2$) for the plasma sheet. The effective magnetic Reynolds number (i.e., Lundqvist number) is an important parameter to help validate numerical MHD models and it suggests where dissipation scale or, for Hall effects, dispersion become important. Weygand et al. (2009), Weygand et al., (2010) obtained effective magnetic Reynolds numbers between 10 and 110 for the plasma sheet. These values are similar to Lundqvist numbers for magnetospheric MHD models, but atre significantly smaller than 1600 reported in Vörös et al. (2006). El-Alaoui et al., (2010) estimated the magnetic Reynolds number from an MHD simulation to be between 100 and 1000 except near sites of reconnection where the Reynolds number is less than 10.

The statistical studies used to investigate observations of turbulence can also be applied to simulations, which enables us to compare more directly observations that indicate turbulence with the simulations. The focus of this review is on global MHD calculations of turbulence in the magnetotail but we should mention additional modeling studies using other techniques. Several calculations have modeled particle motion in turbulent fields (e.g. Taktakishvili et al. (2001), Greco et al., (2002), Zimbardo et al. (2003) We discuss the MHD simulation results in more detail in *Magnetohydrodynamic Simulations of Turbulence in the Magnetotail.*

MAGNETOHYDRODYNAMIC SIMULATIONS OF TURBULENCE IN THE MAGNETOTAIL

The MHD equations written in primitive form illustrate the nonlinear terms responsible for MHD turbulence.

$$\frac{\partial \rho}{\partial t} = -\nabla \cdot (\rho \mathbf{v}),$$
$$\rho \frac{\partial \mathbf{v}}{\partial t} = \rho (\mathbf{v} \cdot \nabla)\mathbf{v} + \frac{1}{\mu_o}(\mathbf{B} \cdot \nabla)\mathbf{B} - \nabla\left(P + \frac{B^2}{2\mu_o}\right),$$
$$\frac{\partial p}{\partial t} = (\mathbf{v} \cdot \nabla)p - \gamma p \nabla \cdot \mathbf{v},$$
$$\frac{\partial \mathbf{B}}{\partial t} = \nabla \times (\mathbf{v} \times \mathbf{B}) + \frac{\eta}{\mu_o}\nabla^2 \mathbf{B},$$
$$\nabla \cdot \mathbf{B} = 0,$$

where ρ is the mass density, $\mathbf{v}$ is the plasma flow velocity, $\mathbf{B}$ is the magnetic field vector, P is the thermal pressure, μ_o is the permeability of free space, and $\overline{\eta}$ is the resistivity.

In the magnetotail at the largest scales, well described by MHD, flows driven on the scale of the entire system, break up into structures that cascade to smaller scales in an (energy cascade) (El-Alaoui et al., 2010). Borovsky and Funsten (2003) argue that plasma sheet turbulence is due to vortices, or eddies as shown in two dimensions in Matthaeus and Montgomery (1980). In the plasma sheet, turbulence produces intense mixing (Antonova and Ovchinnikov, 1999; Antonova and Ovchinnikov, 2002). A number of local (e.g. Nykyri and Otto, 2001; Nykyri et al., 2006b) and global MHD simulation studies have shown vortices forming at the magnetopause (e.g., Hwang et al., 2011; El-Alaoui et al., 2012; Hwang et al., 2012; Sorathia et al., 2019) and in the tail (e.g., Ashour-Abdalla et al., 1999; Fairfield et al., 2000; White et al., 2001; Ashour-Abdalla et al., 2002; Slinker et al., 2003; Hasegawa et al., 2004; Walker et al., 2006; Collado-Vega et al., 2007; Claudepierre et al., 2008; Hwang et al., 2011; Sorathia et al., 2019). However, the expected behavior in three dimensions has yet to be studied in any depth. Vortices observed at the magnetopause occur for both northward and southward interplanetary magnetic field (IMF) and have been interpreted as nonlinear Kelvin-Helmholtz waves (e.g. Hwang et al., 2011; El-Alaoui et al., 2012; Hwang et al., 2012; Sorathia et al., 2019). The vortices reported in the tail were, in general, not associated with boundary oscillations. For example, Ashour-Abdalla et al. (2002), Walker et al. (2006) found large-scale vortices in the central plasma sheet during simulations of prolonged intervals with southward IMF.

The results from idealized global MHD simulations of the solar wind-magnetosphere ionosphere system driven by simplified solar wind and IMF conditions (constant solar wind with either southward or northward IMF), exhibit field fluctuations with spectral properties similar to the observations (El-Alaoui et al., 2012). An interesting feature revealed by these simulations is that the fluctuation energy is transported to small regions of high dissipation as described by, for example Wan et al., (2012). However, MHD cannot reveal the processes causing the dissipation. The statistical properties of the observed fluctuations indicate that localized regions of high-dissipation are formed (see, for example, a study carried out in the solar wind by Greco et al., (2009)). The simulations show that these fluctuations are associated with reconnection (El-Alaoui et al., 2009; El-Alaoui et al., 2010). However, it is unknown whether large-scale turbulence enhances, diminishes, breaks up, or otherwise affects the micro-processes involved in magnetic reconnection. Investigating this theoretically requires particle-in-cell (PIC) simulations. However, local PIC simulations of the reconnection region do not include the substantial energy input from large-scale turbulence. It is thus important to include the large scale driving as well as the microscopic dissipation in the same calculation as was done, for example, in Wu et al., (2013).

We have recently introduced a method to couple the large scale drivers to the local kinetic scales. In this approach (Walker et al., 2019), the MHD results provide the initial state and the driving boundary conditions for a particle-in-cell simulation of a substantial portion of the magnetosphere. The use of the implicit moment method as implemented in the iPic3D code (Markidis et al., 2010) allows one to consider larger domain sizes within the kinetic approach. The approach has been shown to introduce correctly the physics of reconnection at electron scales, replicating the presence of electron crescent-shaped distributions (Lapenta et al., 2017) and of unsteady reconnection processes feeding further into the turbulence cascade (Ashour-Abdalla et al., 2016) and resulting in electron (Ashour-Abdalla et al., 2015) and ion (Lapenta et al., 2016) energization. The kinetic level of description also reveals instabilities both near the reconnection site (Lapenta, 2008; Walker et al., 2018) and in the outflow (Divin et al., 2015; Lapenta et al., 2015) that further drive (Pucci et al.,2017; Lapenta et al., 2018) and impact energy exchanges (Lapenta et al., 2016; Lapenta et al., 2020a). For instance, Lapenta et al. (2020b) argue that turbulent acceleration is responsible for the formation of power law tails in the distribution functions of energetic electrons.

Turbulence for idealized conditions

El-Alaoui et al., (2010) examined results from a 3D MHD simulation of the magnetosphere with nominal solar wind parameters and a southward IMF. They demonstrated that flows in the plasma sheet were consistent with turbulence. This global MHD simulation required very small grid spacing (<0.13 R_E) to resolve flow vortices and turbulence in the plasma sheet. The simulation was run with southward IMF (5 nT) for 240 min followed by a northward IMF of the same magnitude. They found that fluctuations and eddies occurred under these steady driving conditions. In the tail, the regions of high grid resolution were large, including the near earth and mid-magnetotail regions. Snapshots taken during the southward IMF interval are in **Figure 3**. Three variables are superimposed in areas on the equatorial plane. The color contours display the B_Z component of the magnetic field, the black arrows show flows in the plane and the white isocontours give the locations of the last closed field lines. Localized reconnection can be identified by flow reversals, from earthward to tailward, associated with reversals in the B_Z component of the magnetic field. The B_Z component was complex during this interval with filament like structure where it was large and positive at several locations. A spacecraft encountering this would see dipolarization front like signatures in the magnetic field. Vortices are apparent earthward of the

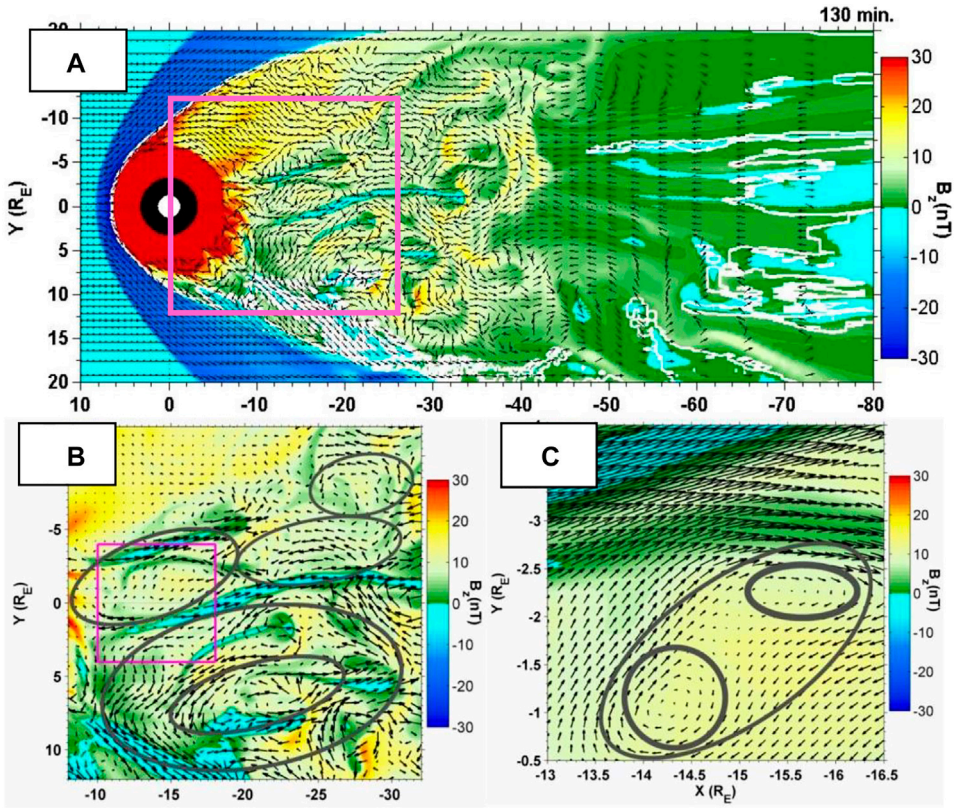

FIGURE 3 | B_Z color contours and flow vectors (arrows) at time 130 min in the equatorial plane. Panel **(A)** shows the global scale configuration; panel **(B)** shows the meso-scale vortices expanded; and panel **(C)** shows further expansion of a selected region. Note that B_z changes sign tailward of about 50 R_E and is very patchy at this time. (After El-Alaoui et al. (2010)).

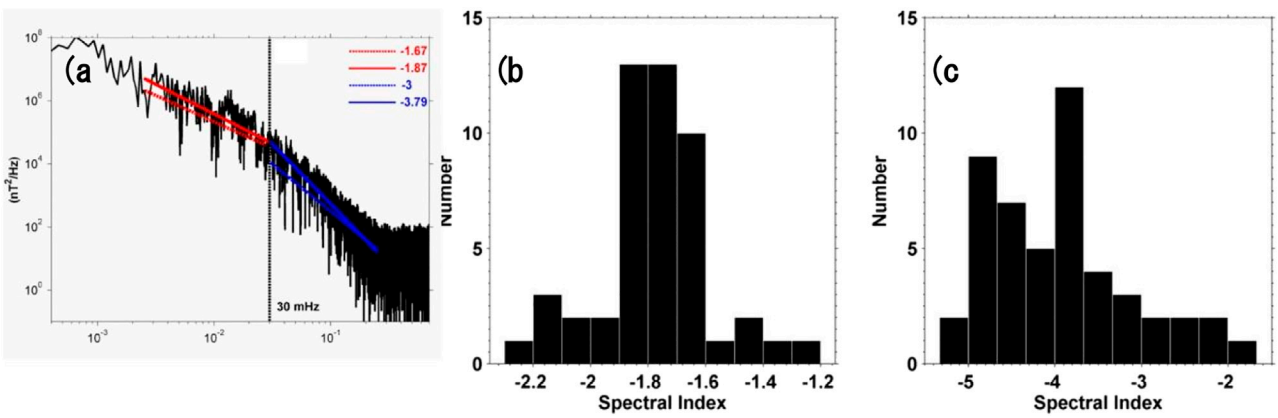

FIGURE 4 | (A) Power spectra for B_Z at $x = -15\ R_E$, $y = -5\ R_E$ and z = 0 for southward IMF. Histograms of **(B)** inertial range PSD slopes **(C)** Dissipative range PSD slopes for southward IMF. (After El-Alaoui et al., 2010).

reconnection (panel a). Nested within the larger vortices are smaller vortices (panel b) and within the smaller vortices we find even small vortices (panel c). This pattern of nested vortices exists throughout the magnetotail earthward of the reconnection sites throughout the simulation.

Figure 4 shows the power spectral density (PSD) in the tail (**Figure 4A**) with the *Kolmogorov* [1941] spectrum superimposed. The slope changes to −3 at ~30 mHz, which we interpret as the dissipation regime. A qualitatively similar change in slope is also observed in the solar wind (e.g., Alexandrova,

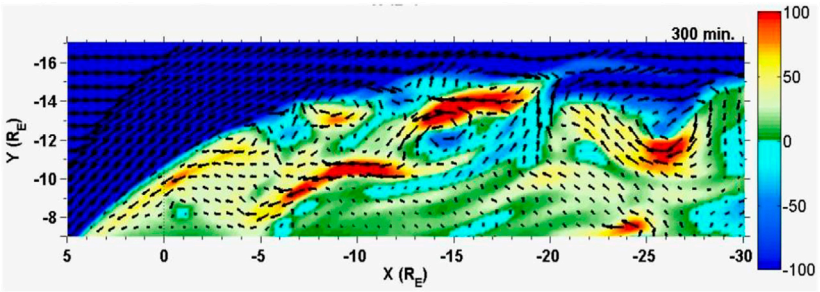

FIGURE 5 | Northward IMF results at 300 min. Shown are color contours of V_x and flow vectors at the dawn flank to show the existence of waves consistent with the Kelvin-Helmholtz instability. (Adapted from El-Alaoui et al. (2010)).

2008; Chen et al., 2010; Sahraoui et al., 2010) and in the magnetosphere (e.g., Vörös et al., 2005; Nykyri et al., 2006a; Matthaeus et al., 2008).

We computed inertial and dissipative range PSD slopes at forty-nine locations in the equatorial magnetotail. All of the PSDs at these locations exhibited the three frequency ranges defined above: the driving (energy containing) range, the inertial range, and the dissipative range. We constructed histograms of the spectral slopes for the inertial ranges (**Figure 4B**) and for dissipative ranges (**Figure 4C**) for southward IMF. We found that the PSDs have a median value of −1.77 while in the dissipative range the median value is −3.9 although the distribution is broad. In a statistical distribution of observed spectra Weygand et al. (2005) found a peak in the distribution of slopes at a spectral index of −2.0 and a weak secondary peak at a slope of −1.6. There is a trend toward more negative slopes for more tailward locations.

MHD simulations require a source of dissipation for reconnection to occur. One way to provide dissipation is to add an extra term of the form ηJ where η is a resistivity and J is the current density in Ohm's law (El-Alaoui, 2001; El-Alaoui et al., 2009). Dissipation in the simulation contributes to plasma sheet turbulence in two ways. On a large scale, it leads to reconnection that drives the turbulent flows and on small scales it dissipates the energy. It is important to have this term in the MHD code. For instance, without this term reconnection does not occur in the tail (Raeder et al., 2001).

While the turbulent flows in these calculations are related to reconnection, turbulent flows in the magnetotail associated with the Kelvin-Helmholtz (KH) instability also have been reported. Observations of changes in the magnetopause position consistent with KH have been discussed by numerous authors (e.g., Sckopke et al., 1981; Song et al., 1988; Chen et al., 1993; Fairfield et al., 2000). Intervals with northward IMF provide an opportunity to investigate boundary oscillations in the absence of strong flows from plasma sheet reconnection. For instance, several studies have reported vortices forming along the flank boundaries from MHD simulations (Li et al., 2009; El-Alaoui et al., 2010; Sorathia et al., 2019). They indicated that the KH instability was likely the source but noted that reconnection also was occurring at high latitudes in the polar cusp region (Hwang et al., 2012). Li et al. (2009) argued that the combined processes form a cold dense boundary layer. All of the papers indicated that the process was turbulent. A typical example of the resulting flows based on the El-Alaoui et al. (2010) simulation is shown in **Figure 5**. Power spectral densities at different locations for the northward IMF interval are shown in **Figure 6**. The PSD power law indices in the inertial range had more variation than in the southward case but were still consistent with turbulence. The PSD power law indices in the dissipative range also varied widely but were generally more negative than in the inertial range.

The pattern of vorticity in the tail was much more extensive for the southward IMF. This suggests that reconnection driven flows are more important than the KH instability for driving the tail into a turbulent state. However, more work needs to be done to quantify the relative contributions of reconnection and KH.

Our ability to correctly resolve the turbulent cascade resulted in large part from recent improvements in the resolution of MHD simulations [e.g., Guild et al., 2008; El-Alaoui et al., 2009). The success in simulating the overall form of turbulent spectrum (**Figure 4**,**6**) gives us confidence That the details of dissipation may not significantly affect that overall turbulent spectrum.

MHD turbulence in simulated substorms

El-Alaoui et al., (2013) investigated the properties of fluctuations during a February 7, 2009 substorm in which the WIND spacecraft provided solar wind data. The simulation of this substorm suggests that the configuration of the tail and its evolution is very complex. The simulation results and THEMIS observations in the magnetotail were remarkably similar to dipolarizations and strong flows (see **Figures 3**,**4** of El-Alaoui et al., (2013) for a detailed comparison between the observed magnetic field and flows and the simulation). As has been reported in previous substorm simulation studies (e.g. Ashour-Abdalla et al., (2015)) a large dipolarization grows by accreting smaller earthward-moving dipolarization fronts (DFs). In this case the dipolarizations were associated with a strong channel of earthward flow that formed a large vortex near earth. **Figure 7** shows two snapshots of the flows, *Bz* and the thermal pressure in the plasma sheet (maximum pressure surface) at two times. The plots on the left are from 0359UT and those on the right are from 0405UT. Dipolarizations from reconnection at about X = −15RE have moved into the inner tail. The flows in these channels, combined with lower velocity return flows, form several large vortices in the plasma sheet.

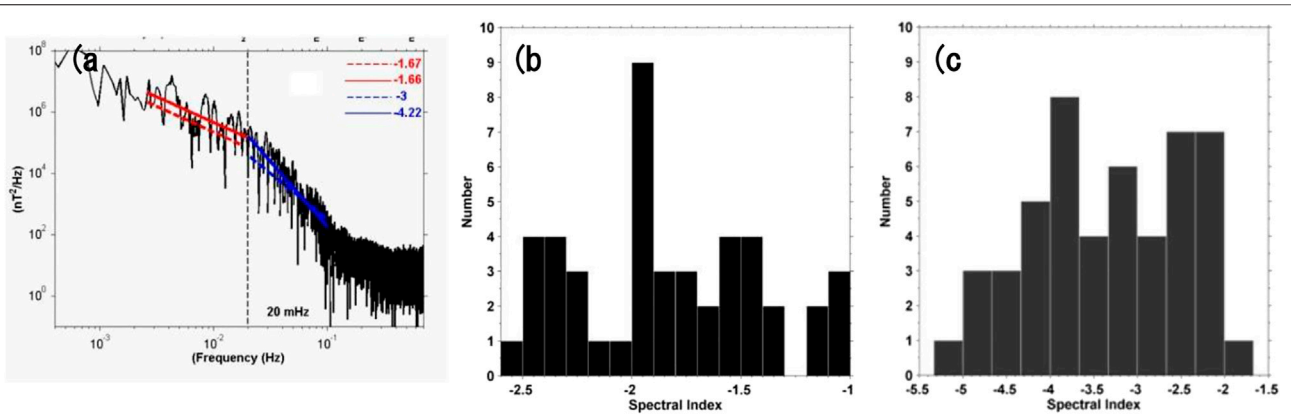

FIGURE 6 | (A) Power spectra for B_Z at $x = -20\ R_E$, $y = -5\ R_E$ and $z = 0$ for northward IMF. Panel **(B)** contains a histogram of **(B)** inertial range PSD slopes and panel **(C)** has dissipative range PSD slopes for northward IMF (After El-Alaoui et al. (2010)).

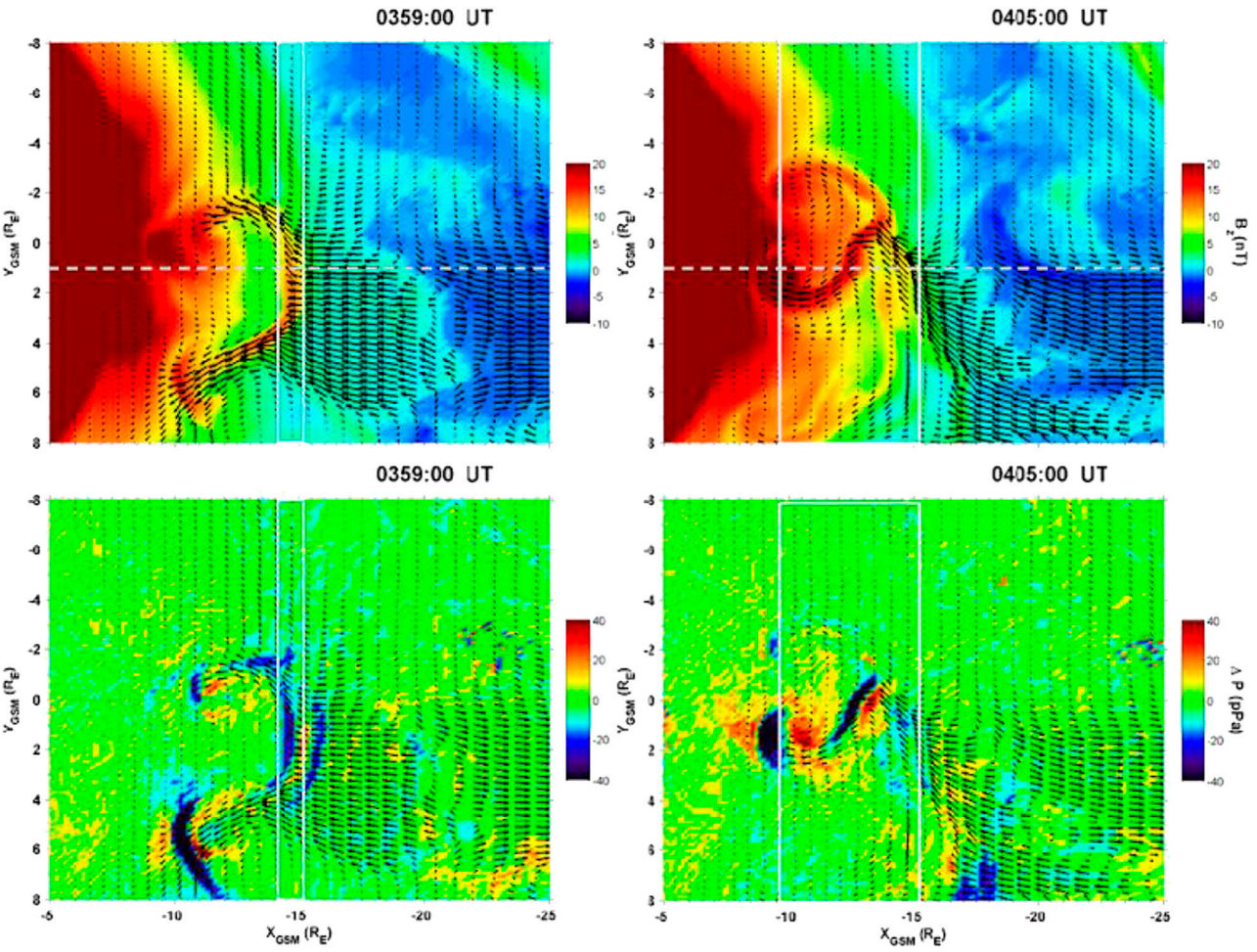

FIGURE 7 | MHD results on the maximum pressure surface at two times (GSM coordinates). In the top panel, color contours show *Bz* and the black arrows give the flow velocity. Dipolarization fronts are located between the vertical white lines. Dipolarization fronts are clearly visible as areas of high magnetic fields which are moving earthward. The bottom panels show the change in thermal pressure from a baseline 10 s before. (After El-Alaoui et al., (2013)).

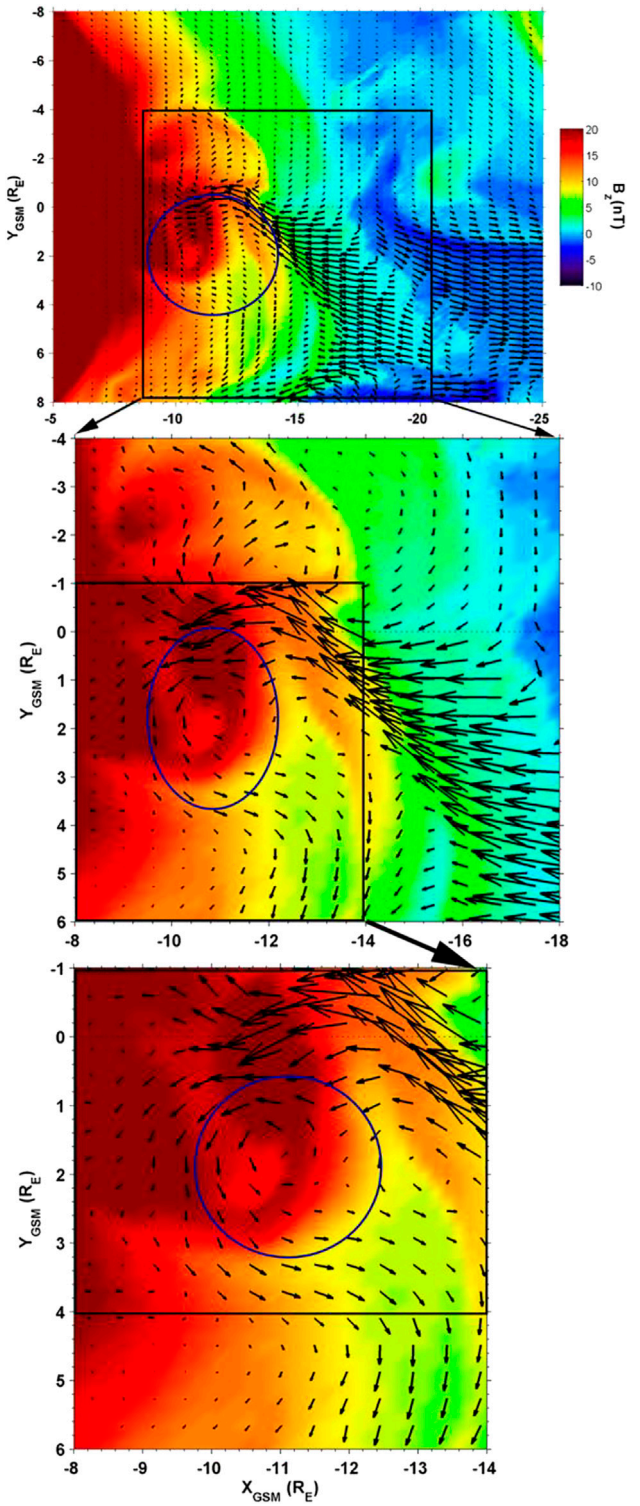

FIGURE 8 | Details on the maximum pressure surface of Bz and the flow showing vortices at 0407 UT. Vortices occur on multiple time and spatial scales. (After El-Alaoui et al., 2013).

The panels in **Figure 8** show successive blowups of *Bz* and the flows at 407UT. Within the larger vortices, we find smaller nested vortices like those found in the generic simulation described above, although the vortex structure is more complex in the event driven case (compare **Figure 3** with **Figures 7**,**8**). These vortices form the low frequency end of the turbulent cascade.

The MHD simulation and the observations show that the magnetotail mesoscale structures (e.g., dipolarizations, flow channels, localized reconnection sites, and flow vortices) during a substorms are in a state of rapid change. In **Figure 9**, we have compared the spectra of Bz from times between 0200 UT and 0500 UT, at $z = -3\ R_E$ and $y = -2\ R_E$ for three x values ($-10\ R_E$, $-12\ R_E$, and $-14\ R_E$) with observations at THEMIS P5. The driving, inertial and dissipative scales appear in both the observations and the simulation. The slope of the spectrum in the MHD results at high frequencies becomes nearly flat as the MHD time-step size (typically between 0.01 and 0.1 s) is approached. The slopes in the upper right corner of the figure come from least squares fits to the results. The simulation (black) power levels in the driving and inertial ranges frequently overlap those observed (red). The spectral indices in the inertial ranges are similar, with an observed index at P5 of −1.74 and values from −1.85 to −1.80 from the simulation. The frequency between the inertial range and the dissipative range appears to be about 30 mHz. This feature is similar to that found in the generic cases. The numerical experiments with generic simulations have shown that the overall level of dissipation in the simulation controls the location of this breakpoint (El-Alaoui et al., 2013) but does not affect the driving and inertial ranges. Although the resistivity in the MHD model gives the observed frequency where the slope changes, it does not tell us which physical mechanisms dissipate energy at the high-frequencies.

Probability distribution functions (PDFs) enable us to characterize the turbulent flows. In particular, the fourth moment of the PDF (the kurtosis) provides a measure of non-Gaussian nature of the wings of the PDF. If the kurtosis of the PDF decreases with increasing lag (τ) the turbulence is said to be intermittent. In plasma flows, intermittent turbulence occurs if dissipation is localized to specific regions of space. **Figure 10** shows the PDFs from this simulation as black curves and PDFs constructed from THEMES P5 observations in red using three lags (10, 200 and 900s). The black dotted line gives values from a Gaussian. The numbers at the top of the panels give the kurtosis. A Gaussian distribution has a kurtosis of three while the larger values reflect energy in the wings of the distributions. The kurtosis tends to decrease for increasing lags consistent with the expectations of intermittency. Similar results in the solar wind were found in Wu et al. (2013).

The vorticity in both the generic case (**Figure 3**) and the event simulation (**Figure 7**) suggest a strong interaction between the reconnection generated flows and the tail

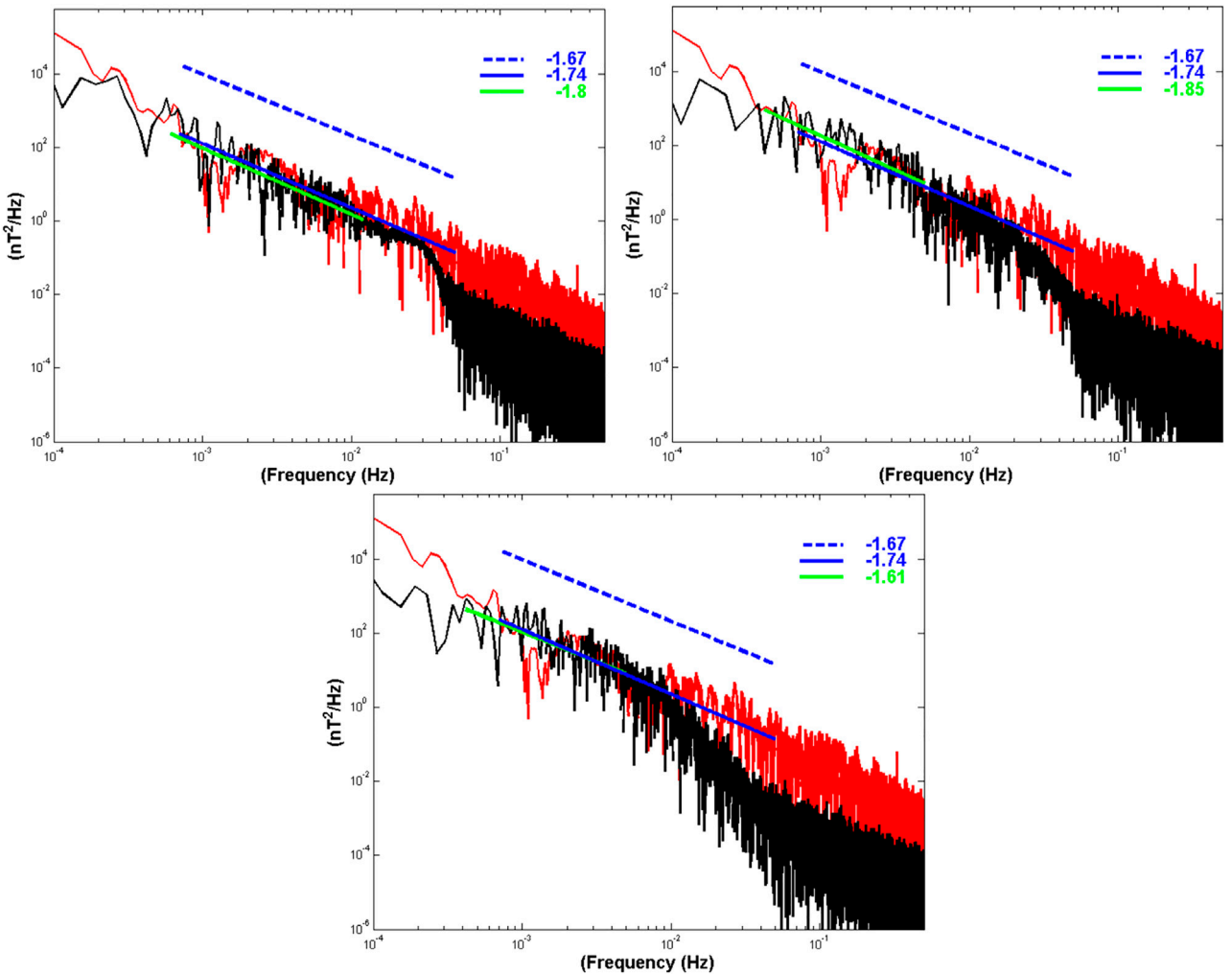

FIGURE 9 | The panels show PSDs for B_Z at the three locations in the MHD simulation. Values from the simulation are black and at THEMIS P5 observations are red. The solid blue (green) lines are least squares fits in the inertial range for the data (MHD results). The dashed blue lines have the slopes of -5//3.

becoming turbulent. As discussed in *Observations of Turbulence in the Magnetotail*, the Taylor hypothesis may not be applicable to the tail under all flow conditions. One advantage of simulations is that we can calculate the power in k space. We computed spatial power spectra in the region between −10 and $-22R_E$ in x and −4 to $8R_E$ in y at the maximum pressure surface (El-Alaoui et al., 2016). The fluctuations in this box were transformed to k space by using a Fourier transform. This yields the power at the allowed wavenumbers in the square domain. These are given by $k_x = 2\pi n/L$ and $k_y = 2\pi m/L$ where L is the length of the box on a side and n and m are integers 0, 1, 2, 3, . . .). Most of the power is at low wavenumbers as expected (**Figure 11**, bottom), since the lowest wavenumbers are dominated by large scale features of the magnetotail including the dipole field and the effects of the box's edges. To display the variations in turbulent power as a function of time, we summed over n and m, excluding the lowest wavenumbers (0, 1, and 2). The mesoscale features with sizes less than or equal to 3 R_E are included, however. We then computed the sum of the power in the remaining modes between 0340 and 0412 UT. Because dipolarizations are characterized by B_z increases and the flow is primarily earthward (V_x), these two parameters are used in the analysis. The plot on bottom left of the figure is a time before a dipolarization front forms while that on the right is after formation. The total power is much higher at the second time (0353 UT). These spectra show that the additional power extends across the k-spectrum, showing that the turbulent power quickly cascades across the wavenumber range.

The top panels of **Figure 11** give the summed power vs. time. The maxima in the Bz and Vx power correspond with the evolution of the mesoscale structures in the magnetotail. The largest feature is a major increase in Vx power starting at 0349 UT and peaking at 0353 UT. An increase in B_z power starts at about the same time and peaks a few minutes later. The start of this increase corresponds to the formation of a narrow, intense flow

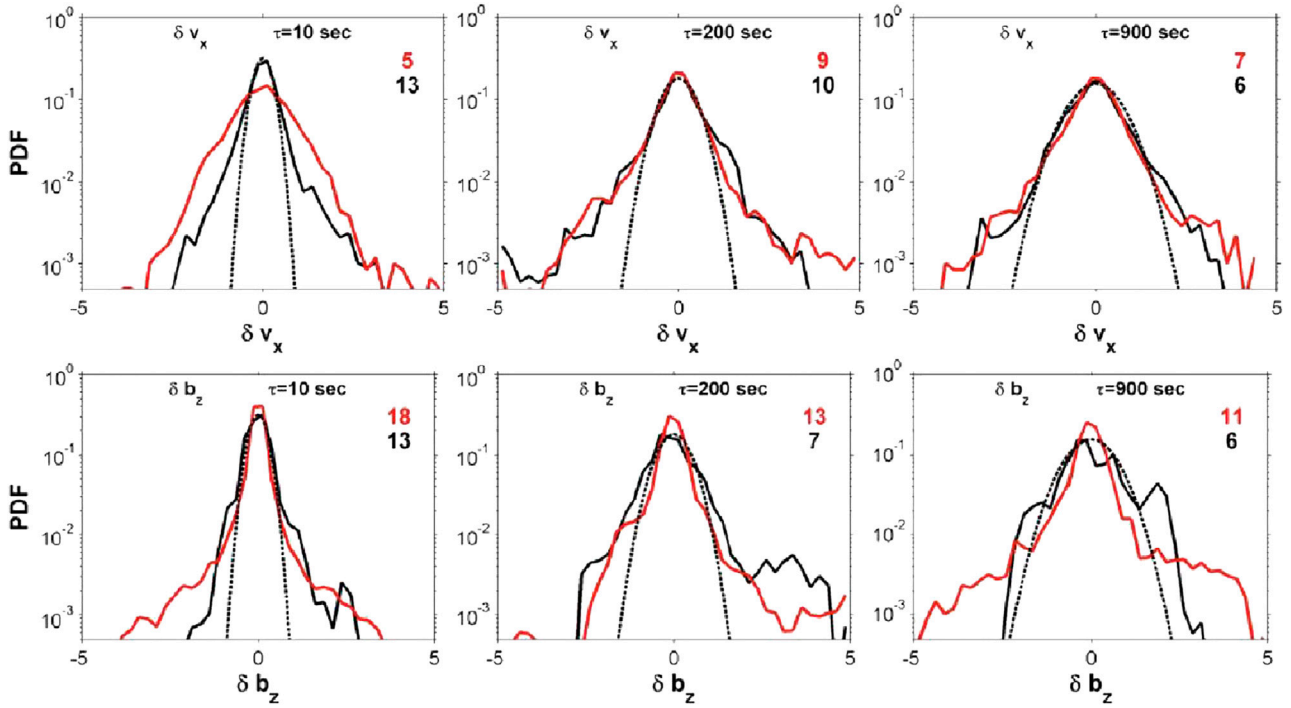

FIGURE 10 | Probability Distribution Functions calculated from the simulation (black) and from THEMIS P5 observations (red). The top panels are based on the Vx component of velocity and bottom panels are based on Bz. The dashed line is a Gaussian fit. The numbers at the top give the kurtosis. (From El-Alaoui et al., 2013).

channel and a large dipolarization noted above. At 0353, this large dipolarization has reached about x = −10.5 R_E.

The February 7, 2009 substorm provides a rare example in the literature of a case where both observations and a simulations have been compared directly. There is considerable work from both the data analysis and the simulations that support the conclusion that localized reconnection-driven earthward flows can generate turbulent fluctuations in the tail. Observations of localized reconnection regions with strong high-speed outflow support the idea that reconnection is an important process driving turbulence in the plasma sheet (Vörös et al., 2006; Angelopoulos et al., 1999). Huang et al., (2012) and Osman et al., (2015) have analyzed the magnetic field fluctuations observed by Cluster during a period of strong earthward plasma sheet flow (~1200 km/s). The magnetic field fluctuations are consistent with turbulence. Localized dissipation may drive these fast flows by enabling localized reconnection. The resulting outflow jets can initiate a turbulent cascade. For example, when a high-speed flow such as a bursty bulk flow (BBF) reaches the near-Earth region, that flow is diverted leading to large vortices that are several R_E across [e.g., Vörös et al., 2006]. The February 7, 2009 MHD simulation of the magnetosphere shows this explicitly. In the MHD results strong narrow flow channels form (Wiltberger et al., 2000; Ashour-Abdalla et al., 2002; Walker et al., 2006; Ge et al., 2011; Birn and Hesse, 2013) at the driving scales for turbulent vortices (e.g., El-Alaoui et al., 2013). In turn, the turbulent eddies can feedback on the reconnection process as well, leading to a very complex interplay between turbulence and dissipation (Matthaeus and Lamkin, 1986; El-Alaoui et al., 2012; Donato et al., 2013). The existence of turbulent eddies may contribute to the patchiness of the reconnection occurring in MHD simulations (El-Alaoui et al., 2010). Borovsky and Funsten (2003) investigated dissipation of the turbulence and argued for small-scale eddy dissipation where the vortices dissipate energy due to reconnection. Overall the results from all of these studies strongly support the idea that fast earthward flows drive large scale vortices that initiate turbulence.

SOME UNSOLVED QUESTIONS ABOUT TURBULENCE THAT CAN BE ADDRESSED USING MODELING

The simulation and data studies discussed make a strong case that flows associated with reconnection are turbulent. However, the dissipation in the MHD models used in this review depends on an additional term in Ohm's law. The extra term has free parameters so the fluid models provide little information about the physics of the dissipation region. One challenge in modeling turbulent flows in the tail is to include the physics of dissipation on a global scale. We need a model that can extend our basic understanding of kinetic turbulence and the transition between fluid and kinetic effects. Such a model would be a combined simulation that would resolve macroscopic motions and at the same time resolve ion and electron scales. It would cover the MHD turbulent cascade at

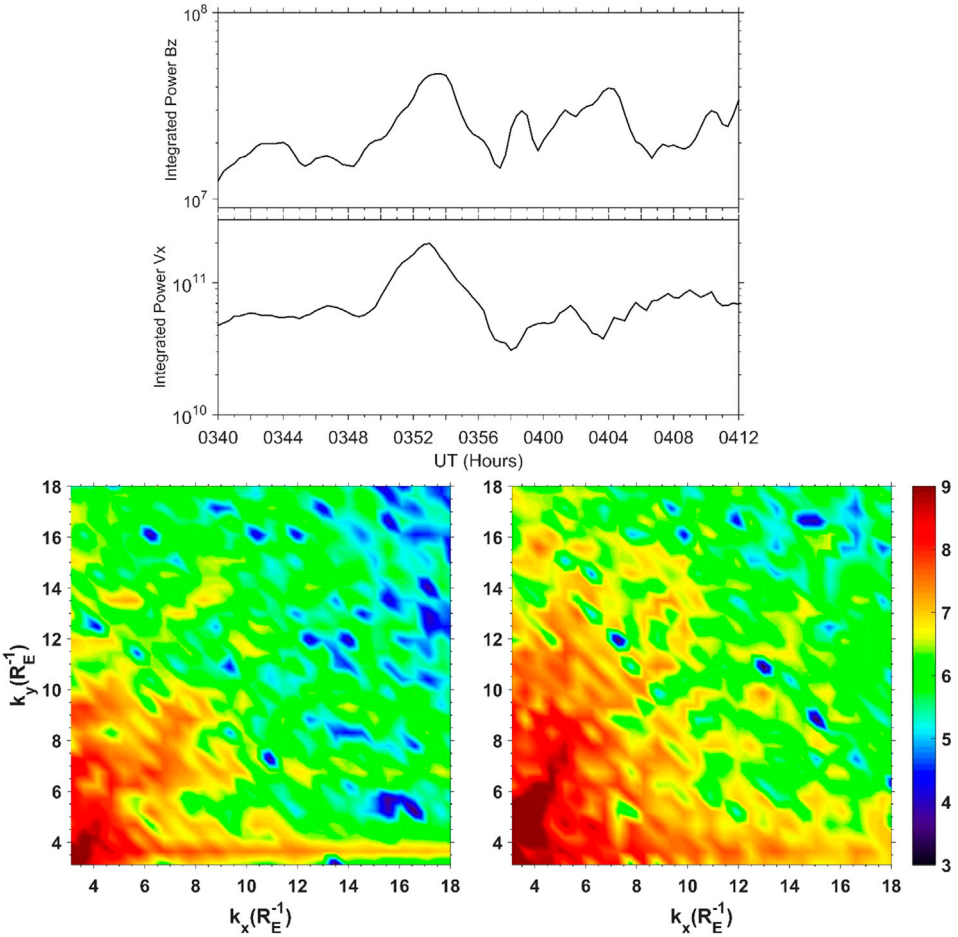

FIGURE 11 | Time history of total small and mesoscale spectral power in the vicinity of flow channels and dipolarizations. For the region between −10 and $-22R_E$ in *x* and −4 to $8R_E$ in y, the sum of the power in all *x* and *y* for mode numbers greater than two was computed (top two panels). The top panel shows the result for B_z, in units of nT^2, and the panel below it shows the result for V_x, in units of $(km/s)^2$. The lower two panels show the power, in units of $(R_E \cdot km/s)^2$, vs. wavenumber at two times, 0344 UT on the left and 0353 UT on the right. (After El-Alaoui et al. (2016)).

large scales (inertial range) as well as Hall (dispersive) and kinetic (dissipation) ranges. Such simulations need to capture energetic exchanges at all scales. Fluid turbulence transfers the energy of large-scale flows to small-scale fluctuations and heat. As turbulence develops, the large-scale flow breaks up into vortices that cascade down to smaller and smaller scales where energy dissipates as heat. This represents a cascade of energy from the large energy-containing scales, through intermediate scales to small scales where heating occurs. In the magnetotail, the energy at the largest scales comes from the interaction between the magnetosphere and the solar wind, while at the smallest scales the dissipation is due to wave particle interactions and reconnection occurring on length scales of the ion Larmor radius or smaller. In the magnetotail, turbulence is complicated by the coupling between velocity and magnetic field fluctuations. Furthermore, turbulence in the kinetic regime involves specific normal modes of the plasma with spatial scales associated with specific waves, e.g., lower hybrid, or ion cyclotron waves.

We have recently developed (Walker et al., 2019) a model that combines simulations that resolve the macroscopic evolution and simulations that resolve ion and electron scales. The new method covers the MHD turbulent cascade at large scales (inertial range) as well as Hall (dispersive) and kinetic (dissipation) ranges. In the application to the study of turbulence, these simulations capture energetic exchanges at all scales. Fluid turbulence transfers the energy of large-scale flows to small-scale fluctuations and heat. As turbulence develops, the large-scale flow breaks up into vortices that cascade down to smaller and smaller scales where energy dissipates as heat. This represents a cascade of energy from the large energy-containing scales, through intermediate scales to small scales where heating occurs. At the magnetopause, the energy at the largest scales comes from the interaction between the magnetosphere and the solar wind, while at the smallest scales the dissipation is due to wave particle interactions and reconnection occurring on length scales of the ion Larmor radius or smaller. In the magnetotail, turbulence is complicated by the coupling between velocity and magnetic field fluctuations. Furthermore, turbulence in the kinetic regime

involves specific normal modes of the plasma with spatial scales associated with specific waves, e.g., lower hybrid, or ion cyclotron waves. It has long been recognized that the plasma distributions in the tail have non-thermal tails (a κ distribution). Recently, Lapenta et al. (2020b) have used this approach to model the acceleration of tail plasma to form this high-energy tail distribution. They argue that the main acceleration mechanism is turbulent acceleration. A similar conclusion was reached by Ergun et al. (2020) based on observations from the Magnetospheric Multi-Scale (MMS) mission.

The MMS observations come from four closely spaced satellites that provide the opportunity to investigate the turbulence in wave number space without the necessity of invoking the Taylor hypothesis. Combined with the latest kinetic simulation, these data (e.g., Ergun et al., 2018; Li et al., 2020; Ergun et al., 2020) offer great potential for understanding the importance of turbulence for acceleration in the tail and provide the community with a way to better understand the mechanisms of dissipation.

Specific issues that need to be examined include the scale of the dissipation region and its distribution in space. Fluid turbulence can develop into a state with dissipation localized in small regions of sharp gradients. How does this dissipation work in the plasma sheet when kinetic physics is included? How does dissipation occur in different regions? Is dissipation found near structures like thin current sheets (as in Wu et al., 2013), dipolarization fronts and the separatrices the result of distinct or the same processes? How do the flows become turbulent (e.g. velocity shears as in Ruffolo et al. (2020))? How important are turbulent flows for plasma heating by energy transfer from magnetic energy to particle and wave energy?

The magnetotail provides a unique laboratory for studying turbulence and reconnection. In the solar wind, turbulence has been investigated in depth for a long time (e.g. Coleman, 1968; Roberts et al., 1987a; Roberts et al., 1987b) but it is driven from the Sun over very large distances and long times but there is also evidence of reconnection driven turbulence in the solar wind (Gosling et al., 2010). In contrast in the magnetotail plasma sheet, the driving forces are well confined and comparatively short-term, developing in a few minutes over just tens of thousands of km.

AUTHOR CONTRIBUTIONS

All authors listed have made a substantial, direct, and intellectual contribution to the work and approved it for publication.

FUNDING

This work was supported by NASA NNX17AB83G and NSF-2040319. We also acknowledge NASA THEMIS contract NAS5-02099 and NASA HPDE contract 80GSFC17C0018 at UCL. The MHD computations were performed by using the Comet supercomputer at San Diego, part of the Extreme Science and Engineering Discovery Environment (XSEDE). This program is supported by grant number ACI-1548562 from the National Science Foundation. The data produced by the simulations are stored on local machines and are available upon request to the lead author.

REFERENCES

Alexandrova, O. (2008). Solar wind vs magnetosheath turbulence and Alfvén vortices. *Nonlin. Process. Geophys.* 15, 95–108. doi:10.5194/npg-15-95-2008

Angelopoulos, V., Kennel, C. F., Coroniti, F. V., Pellat, R., Spence, H. E., Kivelson, M. G., et al. (1993). Characteristics of ion flow in the quiet state of the inner plasma sheet. *Geophys. Res. Lett.* 20 (16), 1711–1714. doi:10.1029/93GL00847

Angelopoulos, V., Mukai, T., and Kokubun, S. (1999). Evidence for intermittency in Earth's plasma sheet and implications for self-organized criticality. *Phys. Plasmas* 6 (11), 4161. doi:10.1063/1.873681

Antonova, E. E., and Ovchinnikov, I. L. (1999). Magnetostatically equilibrated plasma sheet with developed medium-scale turbulence: structure and implications for substorm dynamics. *J. Geophys. Res.* 104 (A8), 17289. doi:10.1029/1999JA900141

Antonova, E. E., and Ovchinnikov, I. L. (2002). Reconnection in the conditions of developed turbulence. *Adv. Space Res.* 29 (7), 1063–1068. doi:10.1016/S0273-1177(02)00022-4

Ashour-Abdalla, M., El-Alaoui, M., Coroniti, F. V., Walker, R. J., and Peroomian, V. (2002). A new convection state at substorm onset: results from an MHD study. *Geophys. Res. Lett.* 29 (20), 26. doi:10.1029/2002GL015787

Ashour-Abdalla, M., El-Alaoui, M., Peroomian, V., Walker, R. J., Zelenyi, L. M., Frank, L. A., et al. (1999). Localized reconnection and substorm onset on Dec. 22, 1996. *Geophys. Res. Lett.* 26, 3545. doi:10.1029/1999gl003630

Ashour-Abdalla, M., Lapenta, G., Walker, R., El-Alaoui, M., Liang, H., Zhou, M., and Goldstein, M. L. (2016). Identifying the electron diffusion region in a realistic simulation of Earth's magnetotail. *Geophys. Res. Lett.* 43 (12), 6005–6011.

Ashour-Abdalla, M., Lapenta, G., Walker, R. J., El-Alaoui, M., and Liang, H. (2015). Multiscale study of electron energization during unsteady reconnection events. *J. Geophys. Res. Space Phys.* 120 (6), 4784–4799.

Birn, J., and Hesse, M. (2013). The substorm current wedge in MHD simulations. *J. Geophys. Res. Space Phys.* 118 (6), 3364–3376. doi:10.1002/jgra.50187

Borovsky, J. E., Elphic, R. C., Funsten, H. O., and Thomsen, M. F. (1997). The Earth's plasma sheet as a laboratory for flow turbulence in high-β MHD. *J. Plasma Phys.* 57 (1), 1–34. doi:10.1017/S0022377896005259

Borovsky, J. E., and Funsten, H. O. (2003). MHD turbulence in the Earth's plasma sheet: dynamics, dissipation, and driving. *J. Geophys. Res.* 108 (A7). doi:10.1029/2002JA009625

Chang, T. (1999). Self-organized criticality, multi-fractal spectra, sporadic localized reconnections and intermittent turbulence in the magnetotail. *Phys. Plasmas* 6 (1), 4137–4145. doi:10.1063/1.873678

Chaston, C. C., Bonnell, J. W., Clausen, L., and Angelopoulos, V. (2012). Energy transport by kinetic-scale electromagnetic waves in fast plasma sheet flows. *J. Geophys. Res.* 117, A09202. doi:10.1029/2012JA017863

Chen, C. H., Horbury, T. S., Schekochihin, A. A., Wicks, R. T., Alexandrova, O., and Mitchell, J. (2010). Anisotropy of solar wind turbulence between ion and electron scales. *Phys. Rev. Lett.* 104 (2), 255002. doi:10.1103/PhysRevLett.104.255002

Chen, S., Doolen, G., Herring, J., Kraichnan, R., Orszag, S., and She, Z. (1993). Far-dissipation range of turbulence. *Phys. Rev. Lett.* 70 (20), 3051–3054. doi:10.1103/PhysRevLett.70.3051

Claudepierre, S. G., Elkington, S. R., and Wiltberger, M. (2008). Solar wind driving of magnetospheric ULF waves: pulsations driven by velocity shear at the magnetopause. *J. Geophys. Res.* 113, A05218. doi:10.1029/2007JA012890

Coleman, P. J. J., Jr. (1968). Turbulence, viscosity, and dissipation in the solar-wind plasma. *ApJ* 153, 371. doi:10.1086/149674

Collado-Vega, Y. M., Kessel, R. L., Shao, X., and Boller, R. A. (2007). MHD flow visualization of magnetopause boundary region vortices observed during high-speed streams. *J. Geophys. Res.* 112, A06213. doi:10.1029/2006JA012104

Dasso, S., Milano, L. J., Matthaeus, W. H., and Smith, C. W. (2005). Anisotropy in fast and slow solar wind fluctuations. *ApJ* 635, L181–L184. doi:10.1086/499559

Divin, A., Khotyaintsev, Y. V., Vaivads, A., André, M., Markidis, S., and Lapenta, G. (2015). Evolution of the lower hybrid drift instability at reconnection jet front. *J. Geophys. Res. Space Phys.* 120 (4), 2675–2690. doi:10.1002/2014ja020503

Donato, S., Greco, A., Matthaeus, W. H., Servidio, S., and Dmitruk, P. (2013). How to identify reconnecting current sheets in incompressible Hall MHD turbulence. *J. Geophys. Res. Space Phys.* 118 (7), 4033–4038. doi:10.1002/jgra.50442

El-Alaoui, M. (2001). Current disruption during November 24, 1996, substorm. *J. Geophys. Res.* 106 (A4), 6229–6245.

El-Alaoui, M., Ashour-Abdalla, M., Richard, R. L., Goldstein, M. L., Weygand, J. M., and Walker, R. J. (2010). Global magnetohydrodynamic simulation of reconnection and turbulence in the plasma sheet. *J. Geophys. Res.* 115, A12236. doi:10.1029/2010JA015653

El-Alaoui, M., Ashour-Abdalla, M., Walker, R. J., Peroomian, V., Richard, R. L., Angelopoulos, V., et al. (2009). Substorm evolution as revealed by THEMIS satellites and a global MHD simulation. *J. Geophys. Res.* 114, A08221. doi:10.1029/2009JA014133

El-Alaoui, M., Richard, R. L., Ashour-Abdalla, M., Goldstein, M. L., and Walker, R. J. (2013). Dipolarization and turbulence in the plasma sheet during a substorm: THEMIS observations and global MHD simulations. *J. Geophys. Res. Space Phys.* 118 (12), 7752–7761. doi:10.1002/2013JA019322

El-Alaoui, M., Richard, R. L., Ashour-Abdalla, M., Walker, R. J., and Goldstein, M. L. (2012). Turbulence in a global magnetohydrodynamic simulation of the Earth's magnetosphere during northward and southward interplanetary magnetic field. *Nonlin. Process. Geophys.* 19 (2), 165–175. doi:10.5194/npg-19-165-2012

El-Alaoui, M., Richard, R. L., Nishimura, Y., and Walker, R. J. (2016). Forces driving fast flow channels, dipolarizations, and turbulence in the magnetotail. *J. Geophys. Res. Space Phys.* 121 (11), 63–111. doi:10.1002/2016JA023139

Ergun, R. E., Ahmadi, N., Kromyda, L., Schwartz, S. J., Chasapis, A., Hoilijoki, S., et al. (2020). Observations of particle acceleration in magnetic reconnection-driven turbulence. *ApJ* 898, 154. doi:10.3847/1538-4357/ab9ab6

Ergun, R. E., Goodrich, K. A., Stawarz, J. E., Andersson, L., and Angelopoulos, V. (2015). Large-amplitude electric fields associated with bursty bulk flow braking in the Earth's plasma sheet. *J. Geophys. Res. Space Phys.* 120, 1832–1844. doi:10.1002/2014JA020165

Ergun, R. E., Goodrich, K. A., Wilder, F. D., Ahmadi, N., Holmes, J. C., Eriksson, S., et al. (2018). Magnetic reconnection, turbulence, and particle acceleration: observations in the earth's magnetotail. *Geophys. Res. Lett.* 45, 3338–3347. doi:10.1002/2018gl076993

Fairfield, D. H., Otto, A., Mukai, T., Kokubun, S., Lepping, R. P., Steinberg, J. T., et al. (2000). Geotail observations of the Kelvin-Helmholtz instability at the equatorial magnetotail boundary for parallel northward fields. *J. Geophys. Res.* 105 (A9), 21159–21173. doi:10.1029/1999ja000316

Frisch, U., and Kolmogorov, A. N. (2001). *Turbulence: the legacy of A.N. Kolmogorov*. Cambridge, United Kingdom: Cambridge University Press

Ge, Y. S., Raeder, J., Angelopoulos, V., Gilson, M. L., and Runov, A. (2011). Interaction of dipolarization fronts within multiple bursty bulk flows in global MHD simulations of a substorm on 27 February 2009. *J. Geophys. Res.* 116 (A5), 57. doi:10.1029/2010JA015758

Goldstein, M. L., Roberts, D. A., and Matthaeus, W. H. (1995). Magnetohydrodynamic turbulence in the solar wind. *Annu. Rev. Astron. Astrophys.* 33, 283–325. doi:10.1146/annurev.aa.33.090195.001435

Gosling, J. T., Teh, W.-L., and Eriksson, S. (2010). A torsional Alfvén wave embedded within a small magnetic flux rope in the solar wind. *ApJ* 719, L36. doi:10.1088/2041-8205/719/1/L36

Greco, A., Matthaeus, W. H., Servidio, S., Chuychai, P., and Dmitruk, P. (2009). Statistical analysis of discontinuities in solar wind ACE data and comparison with intermittent MHD turbulence. *ApJ* 691 (2), L111–L114. doi:10.1088/0004-637X/691/2/L111

Greco, A., Taktakishvili, A. L., Zimbardo, G., Veltri, P., and Zelenyi, L. M. (2002). Ion dynamics in the near-Earth magnetotail: magnetic turbulence versus normal component of the average magnetic field. *J. Geophys. Res.* 107 (A10), 1267. doi:10.1029/2002JA009270

Guild, T. B., Spence, H. E., Kepko, E. L., Merkin, V., Lyon, J. G., Wiltberger, M., et al. (2008). Geotail and LFM comparisons of plasma sheet climatology: 2. Flow variability. *J. Geophys. Res. Atmos.* 113 (A4). doi:10.1029/2007JA012613

Hasegawa, H., Fujimoto, M., Phan, T. D., Rème, H., Balogh, A., Dunlop, M. W., et al. (2004). Transport of solar wind into Earth's magnetosphere through rolled-up Kelvin-Helmholtz vortices. *Nature* 430 (7001), 755–758. doi:10.1038/nature02799

Huang, S. Y., Zhou, M., Sahraoui, F., Vaivads, A., Deng, X. H., André, M., et al. (2012). Observations of turbulence within reconnection jet in the presence of guide field. *Geophys. Res. Lett.* 39 (11), L11104. doi:10.1029/2012GL052210

Hwang, K.-J., Goldstein, M. L., Kuznetsova, M. M., Wang, Y., Viñas, A. F., and Sibeck, D. G. (2012). The first *in situ* observation of Kelvin-Helmholtz waves at high-latitude magnetopause during strongly dawnward interplanetary magnetic field conditions. *J. Geophys. Res.* 117 (A8), a. doi:10.1029/2011JA017256

Hwang, K.-J., Kuznetsova, M. M., Sahraoui, F., Goldstein, M. L., Lee, E., and Parks, G. K. (2011). Kelvin-Helmholtz waves under southward interplanetary magnetic field. *J. Geophys. Res.* 116, A08210. doi:10.1029/2011JA016596

Kadomtsev, B. B. (1965). *Plasma turbulence*. New York, NY: Academic Press.

Karimabadi, H., Roytershteyn, V., Wan, M., Matthaeus, W. H., Daughton, W., Wu, P., et al. (2013). Coherent structures, intermittent turbulence, and dissipation in high-temperature plasmas. *Phys. Plasmas* 20 (1), 012303. doi:10.1063/1.4773205

Klimas, A. J., Valdivia, J. A., Vassiliadis, D., Baker, D. N., Hesse, M., and Takalo, J. (2000). Self-organized criticality in the storm phenomenon and its relation to localized reconnection in the magnetospheric plasma sheet. *J. Geophys. Res.* 105 (A8), 18765–18780. doi:10.1029/1999ja000319

Kolmogorov, A. N. (1941). The local structure of turbulence in incompressible viscous fluid for very large Reynolds' numbers. *Dokl. Akad. Nauk SSSR* 30, 301–305.

Kozak, L. V., Petrenko, B. A., Lui, A. T. Y., Kronberg, E. A., Grigorenko, E. E., and Prokhorenkov, A. S. (2018). Turbulent processes in the Earth's magnetotail: spectral and statistical research. *Ann. Geophys.* 36, 1303–1318. doi:10.5194/angeo-36-1303-2018

Kraichnan, R. H. (1965). Inertial-range spectrum of hydromagnetic turbulence. *Phys. Fluids* 8, 1385. doi:10.1063/1.1761412

Lapenta, G., Ashour-Abdalla, M., Walker, R. J., and El Alaoui, M. (2016). A multiscale study of ion heating in Earth's magnetotail. *Geophys. Res. Lett.* 43 (2), 515–524. doi:10.1002/2015gl066689

Lapenta, G., Berchem, J., El Alaoui, M., and Walker, R. (2020b). Turbulent energization of electron power law tails during magnetic reconnection. *Phys. Rev. Lett. Appear.* 125 (22), 225101. doi:10.1103/PhysRevLett.125.225101

Lapenta, G., Berchem, J., Zhou, M., Walker, R. J., El-Alaoui, M., Goldstein, M. L., et al. (2017). On the origin of the crescent-shaped distributions observed by MMS at the magnetopause. *J. Geophys. Res. Space Phys.* 122, 2024–2039. doi:10.1002/2016JA023290

Lapenta, G., El Alaoui, M., Berchem, J., and Walker, R. (2020a). Multiscale MHD-kinetic PIC study of energy fluxes caused by reconnection. *J. Geophys. Res. Space Phys.* 125, e2019JA027276. doi:10.1029/2019ja027276

Lapenta, G., Goldman, M. V., Newman, D. L., and Markidis, S. (2016). Energy exchanges in reconnection outflows. *Plasma Phys. Controlled Fusion* 59 (1), 014019. doi:10.1088/0741-3335/59/1/014019

Lapenta, G., Markidis, S., Goldman, M. V., and Newman, D. L. (2015). Secondary reconnection sites in reconnection-generated flux ropes and reconnection fronts. *Nat. Phys* 11 (8), 690–695. doi:10.1038/nphys3406

Lapenta, G., Pucci, F., Olshevsky, V., Servidio, S., Sorriso-Valvo, L., Newman, D. L., et al. (2018). Nonlinear waves and instabilities leading to secondary reconnection in reconnection outflows. *J. Plasma Phys.* 84 (1). doi:10.1017/s002237781800003x

Lapenta, G. (2008). Self-feeding turbulent magnetic reconnection on macroscopic scales. *Phys. Rev. Lett.* 100 (23), 235001. doi:10.1103/PhysRevLett.100.235001

Leung, P.-T., and Gibson, C. H. (2004). Turbulence and fossil turbulence in oceans and lakes. *Chin. J. Ocean. Limnol.* 22, 1–23. doi:10.1007/bf02842796

Li, W., Raeder, J., Øieroset, M., and Phan, T. D. (2009). Cold dense magnetopause boundary layer under northward IMF: results from THEMIS and MHD simulations. *J. Geophys. Res.* 114, A00C15. doi:10.1029/2008JA013497

Lui, A. T. Y. (2001). Multifractal and intermittent nature of substorm-associated magnetic turbulence in the magnetotail. *J. Atmos. Solar-Terrestrial Phys.* 63 (13), 1379–1385. doi:10.1016/S1364-6826(00)00239-X

Markidis, S., Lapenta, G., and Rizwan-Uddin, G. (2010). Multi-scale simulations of plasma with iPIC3D. *Mathematics Comput. Simulation* 80, 1509–1519. doi:10.1016/j.matcom.2009.08.038

Marsch, E., and Tu, C.-Y. (1990). On the radial evolution of MHD turbulence in the inner heliosphere. *J. Geophys. Res.* 95 (A6), 8211. doi:10.1029/JA095iA06p08211

Matthaeus, W. H., Dasso, S., Weygand, J. M., Milano, L. J., Smith, C. W., and Kivelson, M. G. (2005). Spatial correlation of solar-wind turbulence from two-point measurements. *Phys. Rev. Lett.* 95 (2), 231101. doi:10.1103/PhysRevLett.95.231101

Matthaeus, W. H., Pouquet, A., Mininni, P. D., Dmitruk, P., and Breech, B. (2008). Rapid alignment of velocity and magnetic field in magnetohydrodynamic turbulence. *Phys. Rev. Lett.* 100 (8), 085003. doi:10.1103/PhysRevLett.100.085003

Matthaeus, W. H., Ambrosiano, J. J., and Goldstein, M. L. (1984). Particle acceleration by turbulent magnetohydrodynamic reconnection. *Phys. Rev. Lett.* 53 (15), 1449–1452. doi:10.1103/PhysRevLett.53.1449

Matthaeus, W. H., and Lamkin, S. L. (1986). Turbulent magnetic reconnection. *Phys. Fluids* 29 (8), 2513. doi:10.1063/1.866004

Matthaeus, W. H., and Goldstein, M. L. (1982). Stationarity of magnetohydrodynamic fluctuations. *J. Geophys. Res. Atmos.* 87 (A12), 10347–10354. doi:10.1029/JA087iA12p10347

Matthaeus, W. H., and Montgomery, D. C. (1980). "Selective decay hypothesis at high mechanical and magnetic Reynolds numbers," in *Nonlinear dynamics*. Editors H. H. G. Hellman (New York, NY: New York Academy of Sciences), 203.

Montgomery, D. (1987). "Remarks on the MHD problem of generic magnetospheres and magnetotails," in *Magnetotail physics*. Editor A. T. Y. Lui (Baltimore, MD: Johns Hopkins University Press), 203–204.

Nykyri, K., Grison, B., Cargill, P. J., Lavraud, B., Lucek, E., Dandouras, I., et al. (2006a). Origin of the turbulent spectra in the high-altitude cusp: Cluster spacecraft observations. *Ann. Geophys.* 24, 1057–1075. doi:10.5194/angeo-24-1057-2006

Nykyri, K., Otto, A., Lavraud, B., Mouikis, C., Kistler, L. M., Balogh, A., et al. (2006b). Cluster observations of reconnection due to the Kelvin-Helmholtz instability at the dawnside magnetospheric flank. *Ann. Geophys.* 24, 2619. doi:10.5194/angeo-24-2619-2006

Nykyri, K., and Otto, A. (2001). Plasma transport at the magnetospheric boundary due to reconnection in Kelvin-Helmholtz vortices. *Geophys. Res. Lett.* 28, 3565. doi:10.1029/2001gl013239

Osman, K. T., Kiyani, K. H., Matthaeus, W. H., Hnat, B., Chapman, S. C., and Khotyaintsev, Yu. V. (2015). Multi-spacecraft measurement of turbulence within a magnetic reconnection jet. Available at: http://arxiv.org/abs/1508.04179.

Perri, S., and Balogh, A. (2010). Stationarity in solar wind flows, *ApJ*, 714, 937. doi:10.1088/0004-637X/714/1/937

Podesta, J. J., Roberts, D. A., and Goldstein, M. L. (2007). Spectral exponents of kinetic and magnetic energy spectra in solar wind turbulence. *ApJ* 664, 543. doi:10.1086/519211

Pucci, F., Servidio, S., Sorriso-Valvo, L., Olshevsky, V., Matthaeus, W. H., Malara, F., et al. (2017). Properties of turbulence in the reconnection exhaust: numerical simulations compared with observations. *ApJ* 841 (1), 60. doi:10.3847/1538-4357/aa704f

Raeder, J., McPherron, R. L., Frank, L. A., Kokubun, S., Lu, G., Mukai, T., et al. (2001). Global simulation of the Geospace Environment Modeling substorm challenge event. *J. Geophys. Res.* 106 (A1), 323–337. doi:10.1029/2000JA000605

Roberts, D. A., Goldstein, M. L., Klein, L. W., and Matthaeus, W. H. (1987b). Origin and evolution of fluctuations in the solar wind: helios observations and Helios-Voyager comparisons. *J. Geophys. Res.* 92 (A11), 12023. doi:10.1029/JA092iA11p12023

Roberts, D. A., Klein, L. W., Goldstein, M. L., and Matthaeus, W. H. (1987a). The nature and evolution of magnetohydrodynamic fluctuations in the solar wind: Voyager observations. *J. Geophys. Res.* 92 (A10), 11021. doi:10.1029/JA092iA10p11021

Ruffolo, D., Matthaeus, W. H., Chhiber, R., Usmanov, A. V., Yang, Y. R., and Bandyopadhyay, R. (2020). Shear-driven transition to Isotropically turbulent solar wind outside the Alfvén critical zone. *ApJ* 902, 94. doi:10.3847/1538-4357/abb594

Sahraoui, F., Goldstein, M. L., Belmont, G., Canu, P., and Rezeau, L. (2010). Three dimensional anisotropic k spectra of turbulence at subproton scales in the solar wind. *Phys. Rev. Lett.* 105 (13), 13–24. doi:10.1103/PhysRevLett.105.131101

Sckopke, N., Paschmann, G., Haerendel, G., Sonnerup, B. U. Ö., Bame, S. J., Forbes, T. G., et al. (1981). Structure of the low-latitude boundary layer, *J. Geophys. Res.*, 86, 2099.

Slinker, S. P., Fedder, J. A., Sibeck, D. G., Lyon, J. G., Frank, L. A., and Mukai, T. (2003). Simulation of magnetopause oscillations observed January 9, 1996. *Geophys. Res. Lett.* 30 (11), 1569. doi:10.1029/2003GL017063

Song, Y., and Lysak, R. L. (1988). Turbulent generation of auroral currents and fields-A spectral simulation of two-dimensional MHD turbulence. *Geophys. Monogr. Ser.* 44, 197–203. doi:10.1029/GM044p0197

Sorathia, K., Merkin, V. G., Ukhorskiy, A. Y., Allen, R. C., Nykyri, K., and Wing, S. (2019). Solar wind ion entry into the magnetosphere during northward IMF. *J. Geophys. Res. Space Phys.* 124, 5461–(5481.)

Stawarz, J. E., Ergun, R. E., and Goodrich, K. A. (2015). Generation of high-frequency electric field activity by turbulence in the Earth's magnetotail. *J. Geophys. Res. Space Phys.* 120, 1845–1866. doi:10.1002/2014JA020166

Taktakishvilli, A. L., Greco, A., Veltri, P., Zimbardo, G., Zelenyi, L. M., and Milovanov, A. V. (2001). Magnetic turbulence and ion dynamics in the magnetotail. *Astrophysics Space Sci.* 277, 71–79.

Taylor, G. I. (1938). The spectrum of turbulence. *Proc. R. Soc. London, Ser. A.* 164, 476–490. doi:10.1098/rspa.1938.0032

Tu, C.-Y., Marsch, E., and Thieme, K. M. (1989). Basic properties of solar wind MHD turbulence near 0.3 AU analyzed by means of Elsässer variables. *J. Geophys. Res.* 94 (A9), 11739. doi:10.1029/JA094iA09p11739

Vörös, Z., Baumjohann, W., Nakamura, R., Volverk, M., Schwarzl, H., Balogh, A., et al. (2005). Dissipation scale in the Earth's plasma sheet estimated from Cluster measurements, *Nonlin. Processes Geophys.* 12, 725–732. doi:10.5194/npg-12-725-2005

Vörös, Z., Baumjohann, W., Nakamura, R., Runov, A., Zhang, T. L., Volwerk, M., et al. (2003). Multi-scale magnetic field intermittence in the plasma sheet. *Ann. Geophys.* 21 (9), 1955–1964. doi:10.5194/angeo-21-1955-2003

Vörös, Z., Baumjohann, W., Nakamura, R., Volwerk, M., and Zhang, T. L. (2004). Wavelet analysis of magnetic turbulence in the Earth's plasma sheet, Phys. Plasmas, 11. *J. Geophys. Res. Space Phys.* 109, 1333.

Vörös, Z., Leubner, M. P., and . Baumjohann, W. (2006). Cross-scale coupling-induced intermittency near interplanetary shocks. *J. Geophys. Res.* 111 (A2). doi:10.1029/2005JA011479

Walker, R. J. M., Ashour-Abdalla, M., El Alaoui, M., and Coroniti, F. V. (2006). Magnetospheric convection during prolonged intervals with southward interplanetary magnetic field. *J. Geophys. Res.* 111, A10219. doi:10.1029/2005JA011541

Walker, R. J., Lapenta, G., Berchem, J., El-Alaoui, M., and Schriver, D. (2019). Embedding particle-in-cell simulations in global magnetohydrodynamic simulations of the magnetosphere. *J. Plasma Phys.* 85 (1), 905850109. doi:10.1017/S0022377819000072

Walker, R. J., Lapenta, G., Liang, H., Berchem, J., El-Alaoui, M., and Goldstein, M. L. (2018). Structure and dynamics of three-dimensional magnetotail reconnection. *J. Geophys. Res. Space Phys.* 123 (10), 8241–8260. doi:10.1029/2018JA025509

Wan, M., Matthaeus, W. H., Karimabadi, H., Roytershteyn, V., Shay, M., Wu, P., et al. (2012). Intermittent dissipation at kinetic scales in collisionless plasma turbulence. *Phys. Rev. Lett.* 109 (19). doi:10.1103/PhysRevLett.109.195001

Weygand, J. M., Kivelson, M. G., Khurana, K. K., Schwarzl, H. K., Thompson, S. M., McPherron, R. L., et al. (2005). Plasma sheet turbulence observed by cluster II. *J. Geophys. Res.* 110, A01205. doi:10.1029/2004JA010581

Weygand, J. M., Kivelson, M. G., Khurana, K. K., Schwarzl, H. K., Walker, R. J., Balogh, A., et al. (2006). Non-self-similar scaling of plasma sheet and solar wind probability distribution functions of magnetic field fluctuations. *J. Geophys. Res.* 111 (A11), A08102. doi:10.1029/2006JA011820

Weygand, J. M., Matthaeus, W. H., Dasso, S., and Kivelson, M. G. (2011). Correlation and Taylor scale variability in the interplanetary magnetic field fluctuations as a function of solar wind speed. *J. Geophys. Res.* 116 (A8), A08102. doi:10.1029/2011JA016621

Weygand, J. M., Matthaeus, W. H., Dasso, S., Kivelson, M. G., Kistler, L. M., and Mouikis, C. (2009). Anisotropy of the Taylor scale and the correlation scale in plasma sheet and solar wind magnetic field fluctuations. *J. Geophys. Res.* 114 (A), 07213. doi:10.1029/2008JA013766

Weygand, J. M., Matthaeus, W. H., Dasso, S., Kivelson, M. G., and Walker, R. J. (2007). Taylor scale and effective magnetic Reynolds number determination from plasma sheet and solar wind magnetic field fluctuations. *J. Geophys. Res.* 112 (A10), A10201. doi:10.1029/2007JA012486

Weygand, J. M., Matthaeus, W. H., El-Alaoui, M., Dasso, S., and Kivelson, M. G. (2010). Anisotropy of the Taylor scale and the correlation scale in plasma sheet magnetic field fluctuations as a function of auroral electrojet activity. *J. Geophys. Res. Space Phys.* 115 (A), A12250. doi:10.1029/2010JA01599

White, W. W., Shoendorf, J. A., Siebert, K. D., Maynard, N. C., Weimer, D. R., Wilson, G. L., et al. (2001). MHD simulation of magnetospheric transport at the mesoscale. in *Space weather*. Editors P. Song, H. Singer, and G. Siscoe (Washington, DC: AGU).

Wiltberger, M., Pulkkinen, T. I., Lyon, J. G., and Goodrich, C. C. (2000). MHD simulation of the magnetotail during the December 10, 1996, substorm. *J. Geophys. Res.* 105 (A12), 27649. doi:10.1029/1999JA000251

Wu, P., Perri, S., Osman, K., Wan, M., Matthaeus, W. H., Shay, M. A., et al. (2013). Intermittent heating in solar wind and kinetic simulations. *Astrophys. J. Lett.* 763 (2), L30. doi:10.1088/2041-8205/763/2/L30

Zimbardo, G., Greco, A., Sorriso-Valvo, L., Perri, S., Vörös, Z., Aburjania, G., et al. (2010). Magnetic turbulence in the geospace environment. *Space Sci. Rev.* 156 (1–4), 89–134. doi:10.1007/s11214-010-9692-5

Zimbardo, G., Greco, A., Taktakishvili, A. L., Veltri, P., and Zelenyi, L. M. (2003). Magnetic turbulence and particle dynamics in the Earth's magnetotail, *Ann. Geophysicae, Eur. Geosciences Union* 21, 1947–1953.

Conflict of Interest: The authors declare that the research was conducted in the absence of any commercial or financial relationships that could be construed as a potential conflict of interest.

frontiers in Astronomy and Space Sciences

ORIGINAL RESEARCH
published: 23 March 2021
doi: 10.3389/fspas.2021.647121

Influence of MHD Turbulence on Ion Kappa Distributions in the Earth's Plasma Sheet as a Function of Plasma β Parameter

A. V. Eyelade[1,2]*, *C. M. Espinoza*[1,2], *M. Stepanova*[1,2]*, *E. E. Antonova*[3,4], *I. L. Ovchinnikov*[3] *and I. P. Kirpichev*[4]

[1] Physics Department, University of Santiago of Chile, Santiago, Chile, [2] Center for Interdisciplinary Research in Astrophysics and Space Sciences, University of Santiago of Chile, Santiago, Chile, [3] Skobeltsyn Institute of Nuclear Physics, Moscow State University, Moscow, Russia, [4] Space Research Institute, Russian Academy of Science, Moscow, Russia

The possible influence of MHD turbulence on the energy distributions of ions in the Earth's plasma sheet was studied using data taken by the THEMIS satellites. Turbulence levels were traced using eddy diffusion coefficients (D), of which we measured one for each Geocentric Solar Magnetospheric (GSM) coordinates every 12 min. Ion fluxes between 1.75 and 210.5 keV during the same time windows that correspond to mainly suprathermal populations were fitted to Kappa distribution functions, which approximate a Maxwellian distribution when the κ-index (κ) is large. We found that the distribution of the eddy diffusion coefficients is bimodal, independently of both the eddy diffusion component and the plasma beta (β) parameter, which is defined as the ratio between plasma and magnetic pressures. The main peak corresponds to turbulent plasma flows with $D > 10^3$ km^2 s^{-1}. In such cases, the impact of turbulence on the κ index depends on the value of β and also on the direction of the turbulent transport. For eddy diffusion perpendicular to the neutral sheet, the values of κ decrease as D_{ZZ} increases for $\beta < 2$; while for higher values of β, κ increases with D_{ZZ}. For the other two directions, the values of κ decrease as D increases. This last tendency is stronger for $\beta \sim 1$ but almost null for $\beta \sim 10$. The secondary peak in the distribution of D values might represent quasi-laminar flows forming part of very large vortices, correct detection and description of which is beyond the scope of this study.

Keywords: turbulence, Kappa distributions, plasma sheet, magnetotail, substorms

OPEN ACCESS

Edited by:
Luca Sorriso-Valvo, Institute for Space Physics (Uppsala), Sweden

Reviewed by:
Ivan Vasko, University of California, Berkeley, United States
Marian Lazar, Ruhr-Universität Bochum, Germany

***Correspondence:**
A. V. Eyelade
adetayo.eyelade@usach.cl
M. Stepanova
marina.stepanova@usach.cl

Specialty section:
This article was submitted to Space Physics, a section of the journal Frontiers in Astronomy and Space Sciences

Received: *29 December 2020*
Accepted: *25 February 2021*
Published: *23 March 2021*

Citation:
Eyelade AV, Espinoza CM, Stepanova M, Antonova EE, Ovchinnikov IL and Kirpichev IP (2021) Influence of MHD Turbulence on Ion Kappa Distributions in the Earth's Plasma Sheet as a Function of Plasma β Parameter. Front. Astron. Space Sci. 8:647121. doi: 10.3389/fspas.2021.647121

1. INTRODUCTION

Since the beginnings of the Space Age, it is known that various regions of the Earth's magnetosphere are filled with turbulent plasmas (see, for example, Sonett, 1960; Ness et al., 1961). Such dynamics are somewhat expected if the Earth's magnetic field is considered as an obstacle in the path of the incoming turbulent, supersonic, and superalfvenic solar wind, which leads to turbulent wake formation. Nonetheless, the magnetotail presents a more complex structure than an ordinary wake, as the plasma density and beta (β) parameter in the plasma sheet are much higher than in the tail lobes, and the plasma sheet is much more turbulent (e.g. Antonova, 1985; Montgomery, 1987; Angelopoulos et al., 1993; Borovsky et al., 1997). This behavior constitutes one of the many unsolved problems in magnetospheric physics (Borovsky et al., 2020).

Detailed studies of the properties of plasma sheet turbulent flows in the magnetotail started at the end of the 90's. For instance, Borovsky et al. (1997, 1998) showed that unpredictable random fluctuations of flow velocity are observed in the plasma sheet and that their amplitudes are much larger than the mean flow velocities. They also obtained the probability distributions and autocorrelation times of flow velocity and concluded that the observed properties correspond to magnetohydrodynamic (MHD) turbulence. The flow velocities were normally shown to be sub-Alfvenic, which is especially important for frozen-in condition applicability and the observed properties of turbulent fluctuations. Borovsky and Funsten (2003) later confirmed that the observed turbulence is essentially formed by eddies (eddy turbulence) and determined that the typical scale of such eddies is 4,000–10,000 km, or even greater, with a mean value of about 1.6 Earth Radii (R_E). Later, though Weygand et al. (2005) obtained somewhat smaller estimates of 6,000 km for the eddy sizes. Successful direct observations of eddy vortices in the plasma sheet are only possible if measurements are carried out fairly simultaneously by two or more satellites separated by long distances, such as THEMIS satellite mission (Time History of Events and Macroscale Interactions during Substorms; Angelopoulos, 2008). Plasma vortices of such scales were observed by Keika et al. (2009), Keiling et al. (2009), Panov et al. (2010) using THEMIS data. The eddy diffusion coefficients are a useful way to quantify MHD turbulence. Borovsky et al. (1998) proposed a method for calculating this coefficient using data from a single satellite as a function of the root mean square velocity and autocorrelation time.

Many authors have carried out measurements of eddy diffusion coefficients in the plasma sheet using data from different satellites. In general, most results point to $D_{\alpha\alpha} \sim 10^5$ km^2/s (e.g. Ovchinnikov et al., 2000; Troshichev et al., 2002). Subsequent studies of turbulent eddy diffusion in the plasma sheet have shown that eddy-diffusion coefficients increase with Earth distance toward the tail (Stepanova et al., 2009, 2011; Pinto et al., 2011), but are nearly constant at mid distances and slightly decrease in the distant tail (Troshichev et al., 2002). The eddy diffusion was also found to be sensitive to the geomagnetic activity, increasing during geomagnetic substorms, especially during the expansion phase process (Stepanova et al., 2009, 2011).

Studies of the stability of the plasma sheet commonly consider laminar flows only (see Petrukovich et al., 2015; Sitnov et al., 2019). Nonetheless, the presence of turbulence requires to modify this approach. In this case, the stability of a turbulent plasma sheet can be reached due to a balance between regular and turbulent transports: Large-scale dawn-dusk electric field allows plasma advects toward the tail center; meanwhile, turbulent transport could compensate for this advection, thereby forming a stable plasma sheet (Antonova and Ovchinnikov, 1996, 1997, 1999, 2001; Antonova, 2002; Stepanova and Antonova, 2011). The same approach can be applied to explain the dawn-dusk asymmetry in the thickness of the turbulent low latitude boundary layer: a balance between the regular transport and transport due to turbulent eddy diffusion is assumed in combination with a dependence of this thickness on the orientation of the interplanetary magnetic field (IMF) (Antonova, 2005).

However, strictly speaking, the MHD approach for describing magnetospheric plasmas is valid only when the particle distribution functions are Maxwellian. Meanwhile, this may not be the case, as the energy distributions of particles in the magnetosphere, especially in the plasma sheet, are generally not Maxwellian. In fact, enhanced high energy tails are often observed in the energy distributions (e.g. Christon et al., 1989; Espinoza et al., 2018).

Kappa distribution functions (Livadiotis, 2017) have proven to be useful representations of the differential particle fluxes in the magnetosphere (e.g. Olbert, 1968; Christon et al., 1989; Haaland et al., 2010; Navarro et al., 2015; Runov et al., 2015; Viñas et al., 2015; Yoon and Livadiotis, 2017; Kirpichev and Antonova, 2020). In general, these functions will recover more information than a Maxwellian function, albeit the addition of one more parameter: the kappa index (κ). While high kappa values imply a higher slope of the distribution at the highest energies (hence a more Maxwellian behavior); low kappa values indicate the presence of a substantial population of energetic particles. Their presence can partially be understood by the fact that particle collisions are rare in these plasmas, and there seems not to be an efficient mechanism to thermalize them (evolve the distribution toward a Maxwellian function) over timescales shorter than the main dynamical scales that govern the systems. In this regard, although the derivation of the Kappa distribution from first principles is under strong debate, the Kappa function might be understood as a generalized case of the Maxwellian distribution (Olbert, 1968; Vasyliunas, 1968; Tsallis, 1988, 2004, 2009; Collier, 1993, 1999; Nauenberg, 2003, 2004; Livadiotis and McComas, 2013; Livadiotis, 2015; Treumann and Baumjohann, 2020).

The general form of the Kappa distribution is denoted by f:

$$f(E; n, \kappa, E_c) = n \left(\frac{m}{2\pi E_c}\right)^{\frac{3}{2}} \frac{\Gamma(\kappa)}{\Gamma(\kappa - \frac{1}{2})\sqrt{\kappa}} \times \left[1 + \frac{E}{\kappa E_c}\right]^{-(\kappa+1)} , \quad (1)$$

where f is the phase space density, E is the kinetic energy, n is the particle density, m is the particle mass, Γ is the Euler gamma function, and κ and E_c are the κ-parameter and characteristic or core energy, respectively. The κ index is a measure of the energy spectrum slope of the suprathermal particles forming the tail of the velocity distribution function. Indeed, for $\kappa \to \infty$, Equation (1) becomes identical to the Maxwellian distribution. The Kappa distributions given by Equation (1) exhibit a thermal core with characteristic energy E_c and suprathermal tails, such that the total characteristic particle kinetic energy E_{total} is given by

$$E_{\text{total}} = E_c \frac{\kappa}{\kappa - 3/2} , \quad (2)$$

which enables a straightforward comparison between Kappa and Maxwellian distributions, and to outline the effects of suprathermals as shown by Lazar et al. (2015, 2016).

Over the last decades, it has become clear that Kappa Distributions can successfully describe ion distribution functions

in the plasma sheet. For instance, Christon et al. (1989, 1991) used the particle instruments onboard the International Sun-Earth Explorer 1 (ISEE 1) and found that kappa-index ranges between 4 and 8 for both ions and electrons, with a most probable value between 5 and 6. Later, Haaland et al. (2010) found that the κ-index ranges between 3 and 6, using data from the Cluster satellites.

Espinoza et al. (2018) also used the Kappa approximation to model ions and electrons flux spectra along the plasma sheet. Their statistical results reveal that the electrons have smaller kappa κ_e than ion kappa κ_i, which suggests electrons non-thermal properties are stronger than ions. Besides, their results in the relative numbers of energetic ions show a significant dawn-dusk asymmetry, being lower in the dusk-side, which increases during substorms. This is consistent with the previous study of Wing et al. (2005).

Stepanova and Antonova (2015) utilized Kappa distributions to fit ion and electron flux spectra for five events in which the THEMIS satellites were oriented in the plasma sheet. They obtained snapshots of kappa index properties that show a tendency for the electron κ-index to be high toward tailward direction; while the situation with the ion κ-index is less clear. In two of the five events analyzed, the kappa-index decreased toward the tail. To explain this, it was proposed that the stochastic acceleration responsible for the diffusion in energy space could lead to hardening of particle spectra (low kappa values) near the Earth region. Simultaneously, the diffusion in velocity space could lead to softening of particle spectra (Collier, 1999). Considering that for some events, the relaxation took place further away from the Earth, it was proposed that plasma transport from the Earth to the tail takes enough time for the relaxation of spectra (*aging*).

Nonetheless, it is well-known that the dawn-dusk electric field drives a regular transport toward the Earth. On the other hand, the bursty bulk flows mainly produce much of the particle transport earthward, which is faster than regular convection. The dipolarization fronts also produce plasma transport in the earthward direction (Runov et al., 2012). At the same time, the form of ion spectra fitted by Kappa distribution is conserved during the dipolarization, and on average, no non-adiabatic acceleration of ions in dipolarization flux bundles were present (Runov et al., 2015). Consequently, none of these sources of plasma transport could explain the gradual increase of kappa toward the tail due to tailward plasma transport accompanied by the "aging" of the distribution function.

Stepanova and Antonova (2015) proposed that particle transport from the inner magnetosphere toward the tail could be attributed to turbulent eddy diffusion. In this case, the time available for Kappa distribution function relaxation to Maxwellian will depend on balance between the processes leading to both transport directions. The characteristic time of turbulent transport between 3 and 12 h were estimated. At the same time, they calculated the average bulk velocity and found that most velocities were directed toward the Earth. However, there are points at which the bulk velocity was directed tailward, thus reducing the time available for relaxation. Whereas, the low kappa values were found precisely for these events, suggesting that Kappa distribution evolution is mainly due to relaxation in the velocity space. It could be that MHD turbulence is what modifies the particle distribution functions. To date, there are no specific studies about a possible relation between the kappa index and MHD turbulence—considering turbulent transport, local turbulent acceleration, or conversely turbulent mixing; that might lead to the Maxwellization of the distribution functions. In this study, we explore the relation between the ion kappa index and the eddy diffusion coefficients. This result contributes to a better understanding of the possible influence that MHD turbulence may have on the departure of the ion distribution functions from Maxwellian.

The organization of this paper is as follows: In section 2, we describe the instruments and methodology used to obtain the ion Kappa distribution parameters; In section 3, we present the results of the analyses and explore the relationship between kappa and three components of the eddy diffusion tensor. In section 4, we discuss the results; and in section 5, we summarize and conclude our findings.

2. INSTRUMENTATION, DATA SELECTION, AND ANALYSIS

We utilized data taken by the THEMIS mission (Time History of Events and Macroscale Interactions during Substorms; Angelopoulos, 2008) during the years 2008–2009, downloaded via the THEMIS ftp website.[1] Quasi-static magnetic field measurements were taken using the Flux Gate Magnetometer (FGM; Auster et al., 2008). Ion spectra were obtained by combining the measurements of the Electrostatic Analyzers (ESA; McFadden et al., 2008), which operates at lower energies, from a few eV to 25 keV, and the Solid State Telescopes (SST; Angelopoulos, 2008), which is sensitive to energies above 30 keV. We used level 2 full particle energy flux spectrogram. The angular distributions are not considered in the measured data since the pitch angle dependency has been averaged. Taking into consideration that ions in the plasma sheet are typically isotropic, the loss of anisotropy information is not critical. Moreover, due to the average process the number of counts in each energy channel increases, which is beneficial for the study of energy distributions. A mass-spectrometer was not included in the THEMIS instruments and it is impossible to differentiate ions of different species; therefore, we refer to them as just ions.

We restricted our analyses to ions energy range of 1.75–210.5 keV, to ensure that the actual fits of the tail and core parts of ion distribution function are obtained following the method used by Espinoza et al. (2018). We discarded lower energies due to contamination from the photoelectrons and spacecraft potential. Similarly, we discarded higher energies due to contamination by solar cosmic rays, energetic electrons, and a low number of counts. This energy range does not contain relativistic ions, hence we use the ordinary $\kappa-$distribution function, without the relativistic corrections suggested by Scherer et al. (2018, 2019), Lazar et al. (2020).

Example of ion energy flux spectra measured by combining both particle instruments (ESA and SST) onboard THEMIS

[1] http://themis.ssl.berkeley.edu/index.shtml

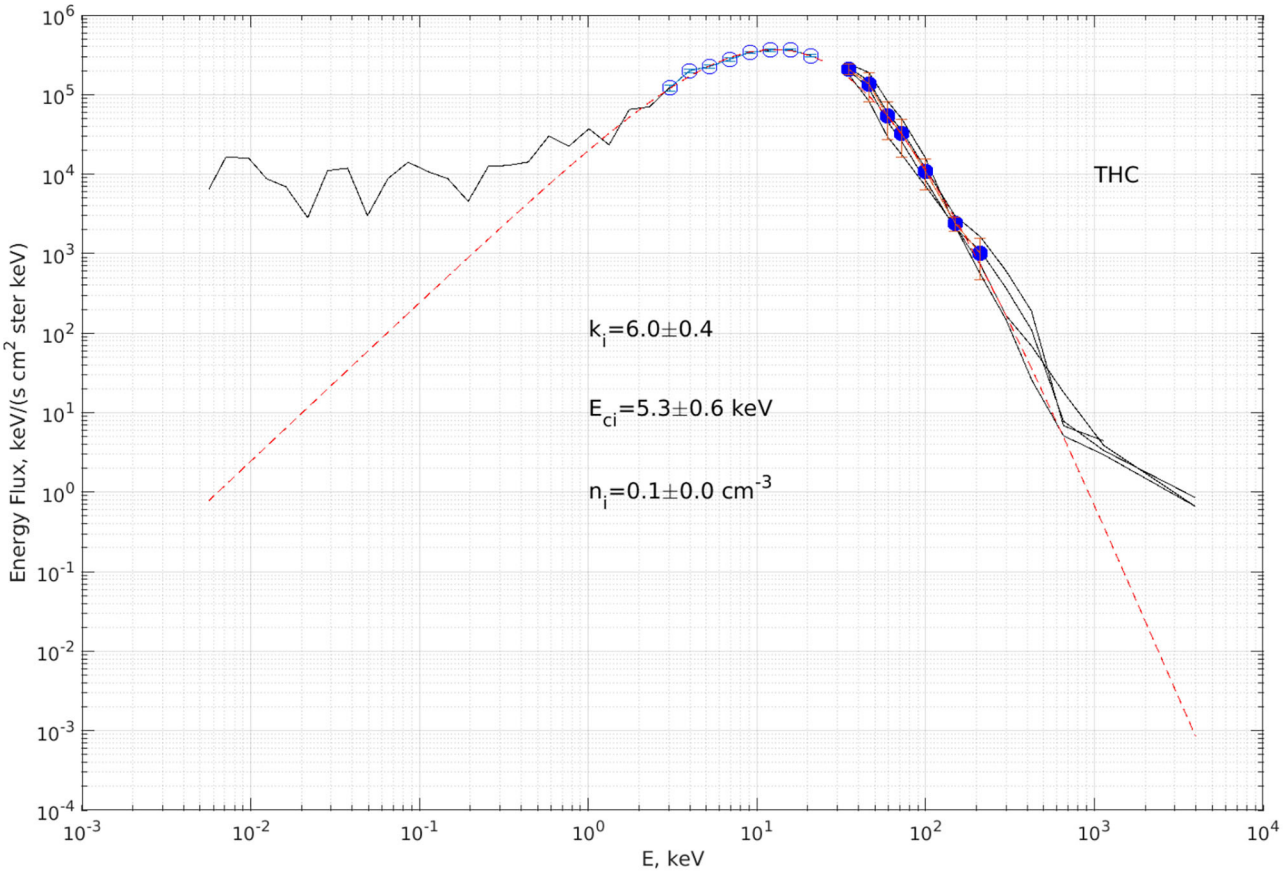

FIGURE 1 | Example of the fit of κ−distribution to the flux spectra of ions measured by THEMIS-C (THC), on 14th February 2008, at 12.8 UT, GSM coordinate $(X, Y, Z) = (-15.8, -0.82, -4.10)$ R_E. The solid black lines are sub-datasets taken over a total of 12 min. Open circles represent averages of the subsets measurements of low energy particles (ESA), and filled circles represent averages of the subsets of measurements of high energy particles (SST). The red dash-line is the Kappa function curve fitted to the open and filled circles.

satellites (solid lines) is illustrated in **Figure 1**. The circles on the plots are the average of the spectra obtained for the 12 min time windows. The open circles represent measurements from the ESA, while the filled circles represent the SST. For the average flux data, the error bars represent the spread between the maximum and minimum values observed. The error bars were found to vary significantly between the ESA and SST data, so they were normalized in the same way as Espinoza et al. (2018). The inverse squared of the error bars is used to define weights for the fits, which were performed over the averaged data using a non-linear least-squares method combined with the Levenberg-Mardquart algorithm. We inspected hundreds of spectra visually and decided to work only with the fits that give a reduced chi-squared $\chi^2 < 100$.

The observed differential energy spectra of ions were fitted to the model obtained by transforming the Kappa distribution from Equation (1) to differential energy fluxes:

$$F(E) = \frac{1}{\pi} \frac{n}{\sqrt{2\pi m}} \frac{E^2}{E_c^{3/2}} \frac{\Gamma(\kappa)}{\Gamma(\kappa - \frac{1}{2})\sqrt{\kappa}} \left[1 + \frac{E}{\kappa E_c}\right]^{-(\kappa+1)} . \quad (3)$$

This expression agrees with the expression of the differential particle flux ($I(E)$) used, for example, by Vasyliunas (1968), Christon et al. (1989), Olsson and Janhunen (1998). As in Stepanova and Antonova (2015), Espinoza et al. (2018), here we use the differential energy flux, that is $F(E) = E \cdot I(E)$ (Lyons et al., 1985; Baumjohann and Treumann, 1997). The differential energy flux was used since this is how the information related to particle distribution functions is given by the THEMIS team.

Following Borovsky et al. (1998, see their appendix), to estimate the eddy-diffusion coefficient D_{zz}, the eddy transport is assumed to be a Markov process (i.e., each plasma displacement Δ_z is independent of previous displacements). This is valid when displacements are separated in time by the autocorrelation time τ_{auto} of the flow velocity. In the Markovian picture, the diffusion coefficient is given as;

$$D_{zz} = \frac{\langle (\Delta_z)^2 \rangle}{2\,\tau_{auto}} \quad (4)$$

A typical Δ_z displacement which has a z-component of fluid velocity is $\Delta_z = V_z \tau_{auto}$. With this, the turbulent transport is

evaluated by determining the eddy diffusion coefficient tensor denoted as $D_{\alpha\alpha}$:

$$D_{\alpha\alpha} = \frac{V^2_{\mathrm{rms},\alpha\alpha}\tau_{\alpha\alpha}}{2} \quad , \tag{5}$$

where $\tau_{\alpha\alpha}$ is the decay time of the autocorrelation function of the ion bulk velocity component V_α; which acts as a measure of the persistence of a fluctuating bulk velocity, and V_{rms} is the root mean square (rms) of the α component of the velocity fluctuations around a mean value, which can be determined from

$$V_{\mathrm{rms},\alpha\alpha} = \sqrt{\frac{\sum \left(V_\alpha(i) - \langle V_\alpha \rangle\right)^2}{N}} \quad . \tag{6}$$

Both the diffusion coefficients and the parameters of the kappa fits were obtained from 12-min intervals shifted every 6 min. This allowed us to use about 240 bulk velocity measurements in each interval to calculate V_{rms} and $\tau_{\alpha\alpha}$, as described in Stepanova et al. (2011). All measurements were constrained to the following Geocentric Solar Magnetospheric (GSM) coordinate system: $X \leq -10$ R_E, $-30 \leq Y \leq 30$ R_E, $-5 \leq Z \leq 5$ R_E. To ensure that the measurements are performed in plasma sheet-like plasmas, the time intervals were selected based on the following criteria: ion number density (n_i), ion temperature (T_i), x components of the magnetic field (B_x), bulk velocity (V_x) were restricted to $n_i \geq 0.1$ cm^{-3}, $T_i \geq 1$ keV, $|B_x| < 20$ nT, and $|V_x| < 300$ km/s.

As well, we considered only cases in which $\beta > 0.1$; where β is the ion plasma parameter defined as the ratio of the ion plasma pressure to magnetic pressure: $\beta = (\frac{P_i}{B^2/2\,\mu_0})$, where B is the total magnetic field strength and μ_0 is the magnetic permeability, and P_i is the plasma pressure. The values of P_i and ion bulk velocity were taken directly from the level 2 data products containing the ESA macro-parameters (see the SPEDAS THEMIS documentation[2]). The contribution of ions with energies above 25 keV (detected by the SST, Angelopoulos, 2008) to the bulk velocity has been evaluated and found to be negligible (Lee and Angelopoulos, 2014), hence the influence of SST on macro parameters, such as P_i, is not strong. Thus, we utilized only the ESA measurements to calculate beta parameter and rms velocities.

Figure 2 illustrates the data analysis described above, using data obtained from THEMIS C satellite on February 26, 2008, between 05 to 08 UT during quiet geomagnetic conditions. In this case, the satellite was inside the plasma sheet until ∼7:45 UT. Both the eddy diffusion coefficients and the κ index were obtained while $|B_x| < -20$ nT. As mentioned at the beginning of this section, we used 12-min time intervals to calculate the eddy diffusion and kappa parameters. Nonetheless, we acknowledge that this choice for the duration of the interval might interfere with the calculation of the eddy diffusion coefficients. To estimate this effect we present two hodograms in **Figure 3**, which show the evolution of particles velocities in the (V_x,V_y) and (V_x, V_z) planes. We calculated both the average and the root mean square velocities (V_{rms}) for a 3-h long interval, as well as for selected 12 min intervals. As it can be seen, the average velocities calculated over 12-min intervals are of the same order as the average value over 3-h. This suggests that the 12-min intervals are enough to recover eddy diffusion coefficients.

Figure 4 illustrates the spatial coverage of the selected intervals projected in the X-Ygsm and X-Zgsm planes in the geocentric solar magnetospheric system. Each interval is represented by a dot, which is color-coded with the measured plasma β parameter. Furthermore, the intervals selected correspond to the quiet time geomagnetic conditions, which were identified using the criteria applied by Stepanova et al. (2011). They are based on the variation of the high resolution (1-min) auroral electrojet lower index (AL) obtained from the OMNI database. This was achieved by subjecting the 1-min resolution of the AL index to AL ≥ -100 nT and the slope absolute value $|s|$ to $\leq 1/2$ nT/min, which indicate how fast the AL-index changed during a minute (more details about this analysis are given in Stepanova et al., 2011).

3. RESULTS

As seen in **Figure 2**, for relatively low β the values of κ in some intervals anti-correlate with the eddy diffusion coefficients. However, whether this behavior persists for all orbits and for all values of β is unclear. Thus we made an extensive statistical study of a set of hundreds of thousands quiet time 12-min-long intervals, for which we have calculated D, κ, and β. Considering that both D and β cover a few orders of magnitude, we define a grid in the logarithmic (β, D) space using a cell size of $\Delta \log_{10} \beta = 0.2$, and $\Delta \log_{10} D = 0.5$ within the range $-1 < \log_{10} \beta < 2$ and $0 < \log_{10} D < 7$. This was used to create the color-coded plots shown in **Figure 5**.

Figure 5 shows the number of measurements (N) and the average values of κ_i, in each bin. The empty bins contain less than ten measurements. As it can be seen in the left column [panels (A), (C), and (E)], for all eddy diffusion coefficients components, and for all values of β, the distributions of eddy diffusion coefficients have two maxima. The main peak corresponds to turbulent plasma, with D between 10^4 and 10^6 km^2/s. These high values are the main contribution to the values of the eddy diffusion coefficients averaged within each β bin, which are shown with a white solid line in the figure. The secondary maximum might correspond to nearly laminar flows ($D \sim 10^2$ km^2/s), which could be part of vortices larger than the maximum vortex size that we are able to detect (determined by the 12-min intervals chosen for this study). In such case, the rms velocity would be low, and the autocorrelation time would exceed 12 min, hence could not be measured correctly. In other words, this method may be insensitive to very large vortices, especially considering that the satellite velocity is often of the same order of magnitude as the plasma velocity averaged over turbulent eddies. Therefore, we restrict the following analysis of a possible relation between κ and $D_{\alpha\alpha}$ to turbulent flows only.

In order to understand whether there is a relation between κ and $D_{\alpha\alpha}$ for a fixed value of β (as suggested by the right panels of **Figure 5**), we use the linear function $\kappa = A \log_{10} D + B$ to fit κ

[2]http://themis.igpp.ucla.edu/software_docs.shtml

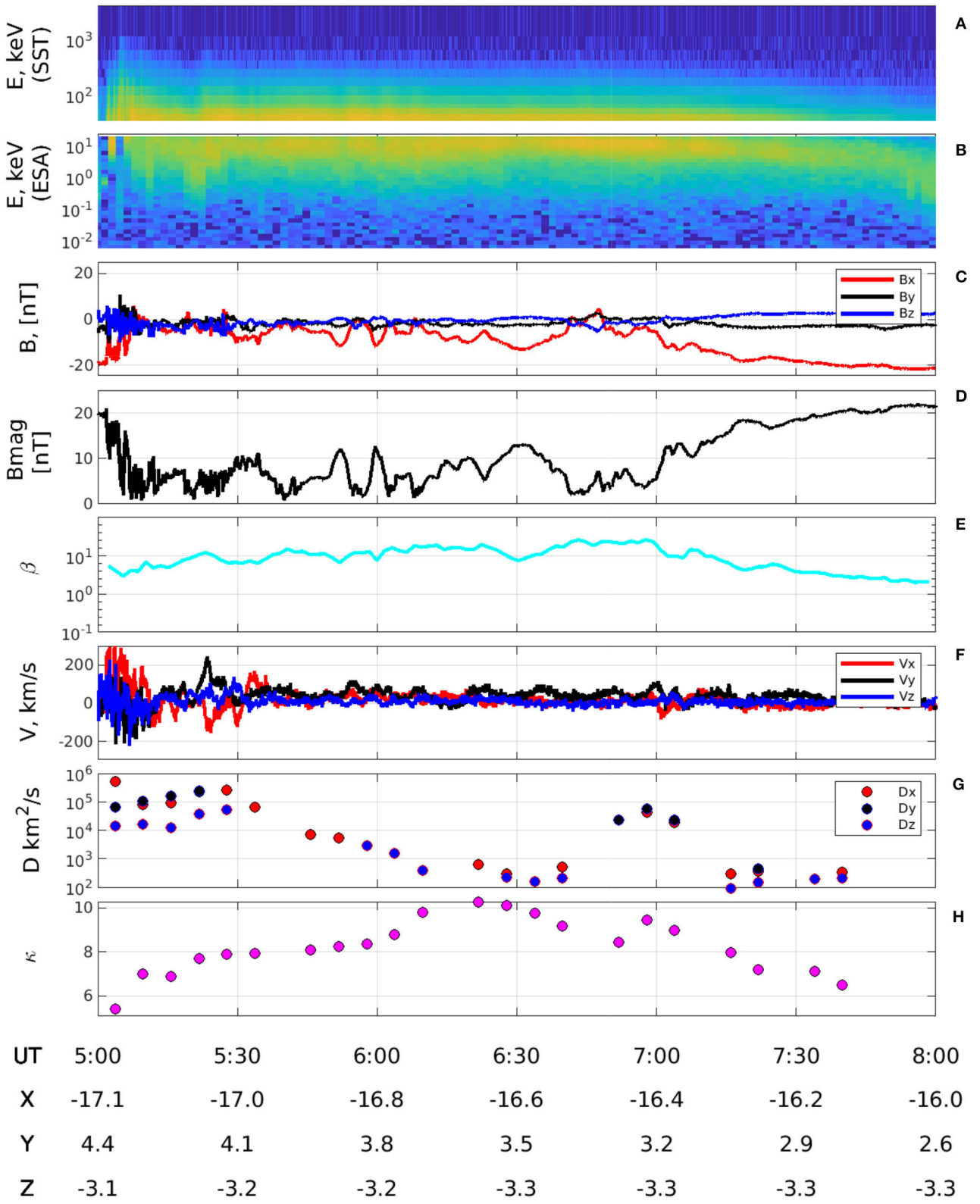

FIGURE 2 | Panels from top to bottom are the: **(A)** Ion spectrogram (SST), **(B)** Ion spectrogram (ESA), **(C)** Magnetic field components, **(D)** Magnetic field magnitude, **(E)** plasma β parameter, **(F)** Bulk velocity components, **(G)** Eddy diffusion coefficient, and **(H)** ion kappa-index obtained from the on-board moments of ion distribution function measured between 5 and 8 UT by THEMIS-C (THC) on 26 February 2008.

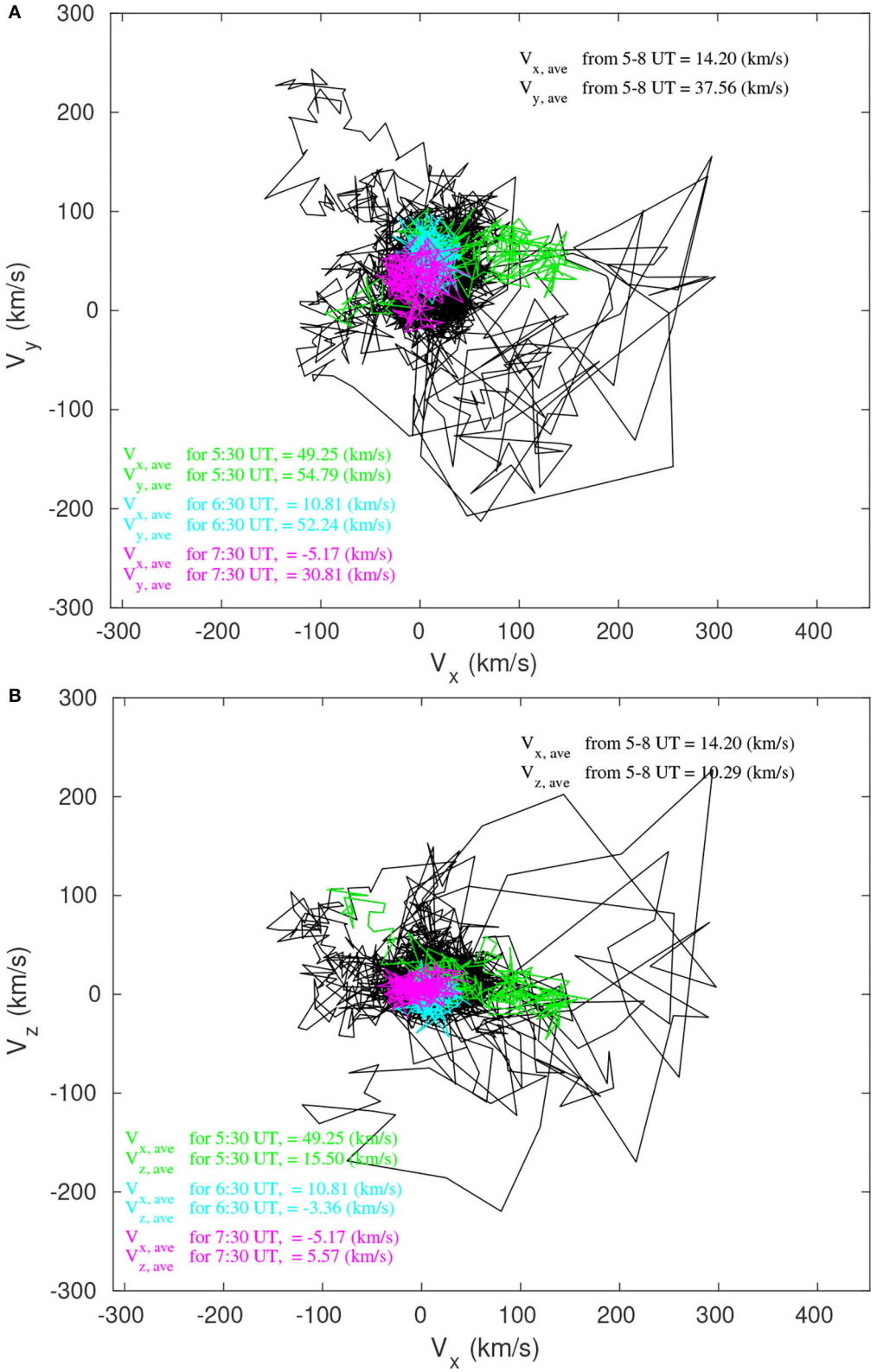

FIGURE 3 | Hodograms of flow measured between 5 and 8 UT by THEMIS-C (THC) on 26 February 2008 and during three 12 min intervals. Panels from top to bottom are: **(A)** V_x and V_y, **(B)** V_x and V_z bulk velocity components. The colors represent 12 min intervals centered at the time indicated in the lower left corner by the same color together with the average bulk velocity calculated for each interval.

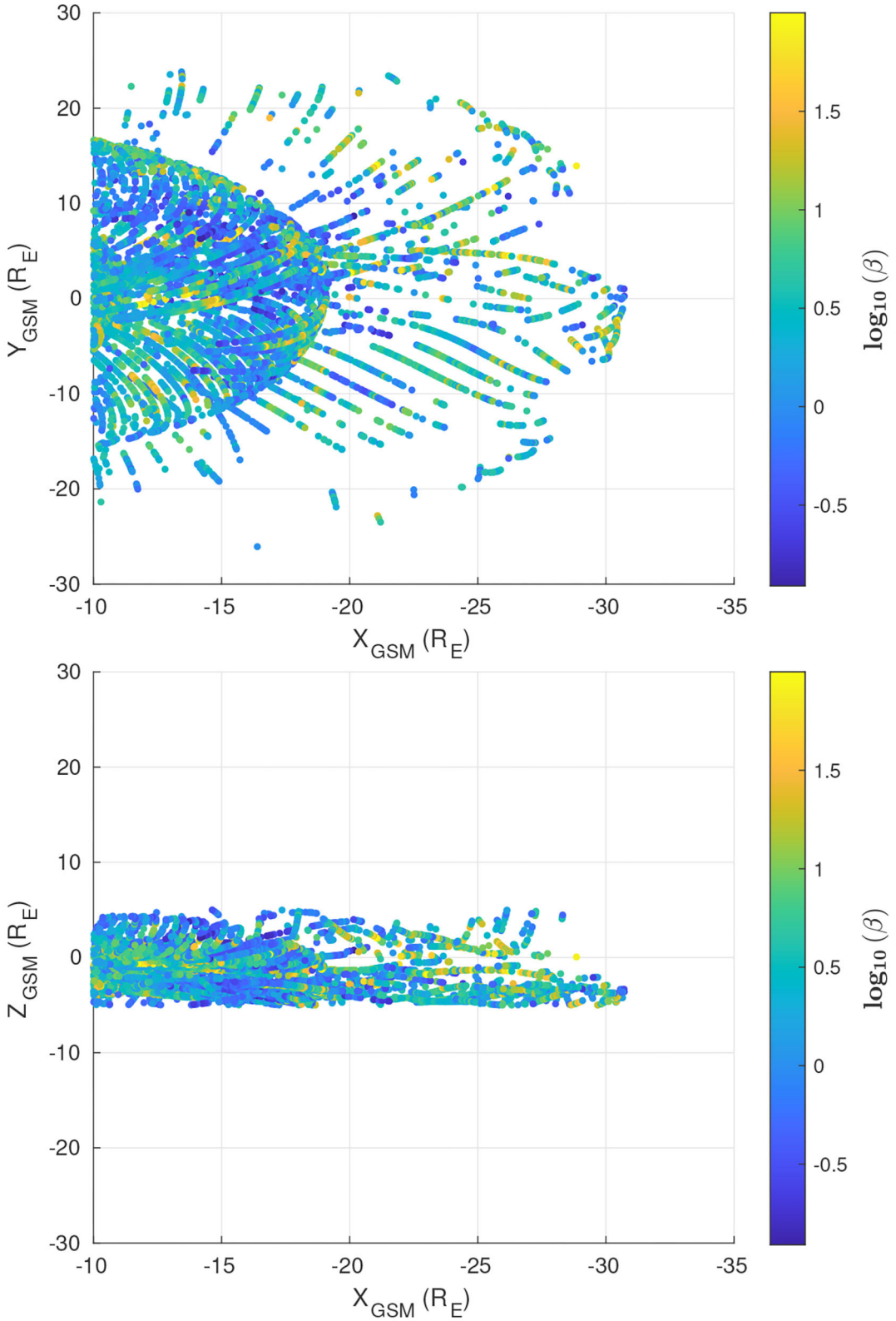

FIGURE 4 | Spatial coverage of the time intervals used in the study. (Top) The *X*-*Y*gsm plane. (Bottom) The *X*-*Z*gsm plane. The 12-min averaged plasma β at each location is represented with the color scale.

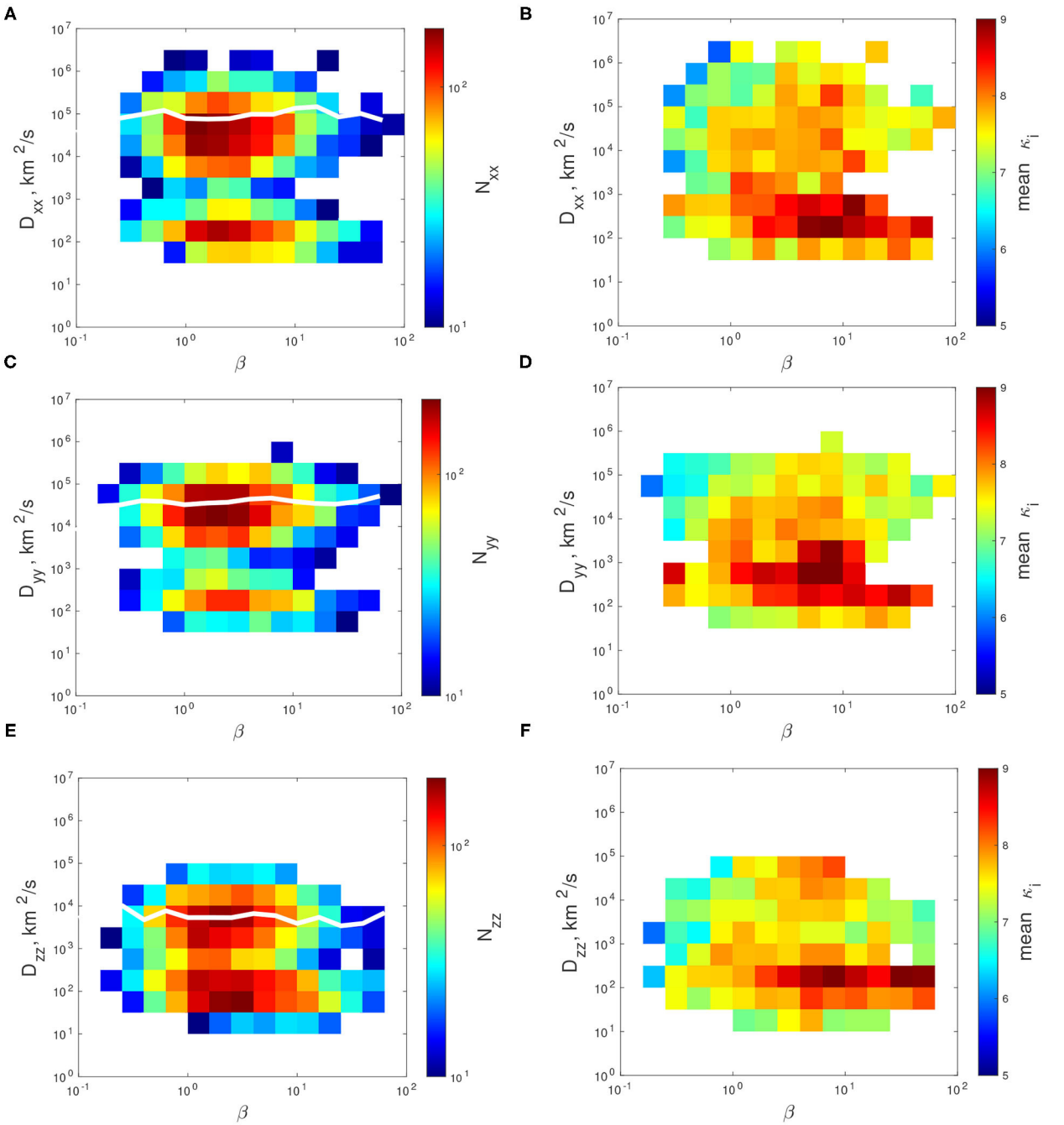

FIGURE 5 | Eddy diffusion coefficients and κ indices as a function of β. Left column **(A,C,E)**: the number of measurements in each cell. Right column **(B,D,F)**: average values of the κ index. Only bins with 10 or more measurements are colored.

and $\log_{10} D$. **Figure 6** shows these dependencies for some selected values of β. The fitted data, corresponding to turbulent flows, are plotted with filled circles ($D > 10^3$ km^2/s). The vertical error bars represent the standard deviation of the κ values within each bin; meanwhile, the horizontal error bars reflect the D bin's width.

Despite the strong dispersion of the κ values in each bin, there are systematic trends in the behavior of the measured slopes (A) and intercept (B), as β increases (**Figure 7**). These trends are different for each $D_{\alpha\alpha}$ component. For the x-component the κ indices almost do not depend on D: $A_{xx} \sim 0$ except for $\beta \sim 1$, for which A_{xx} is minimum and negative; thereby implying that the κ-index decreases with D_{xx}. The trend for Y is similar to the one observed for X but clearer. The behavior of A_{zz} is different: it monotonically increases with β and changes its sign, implying

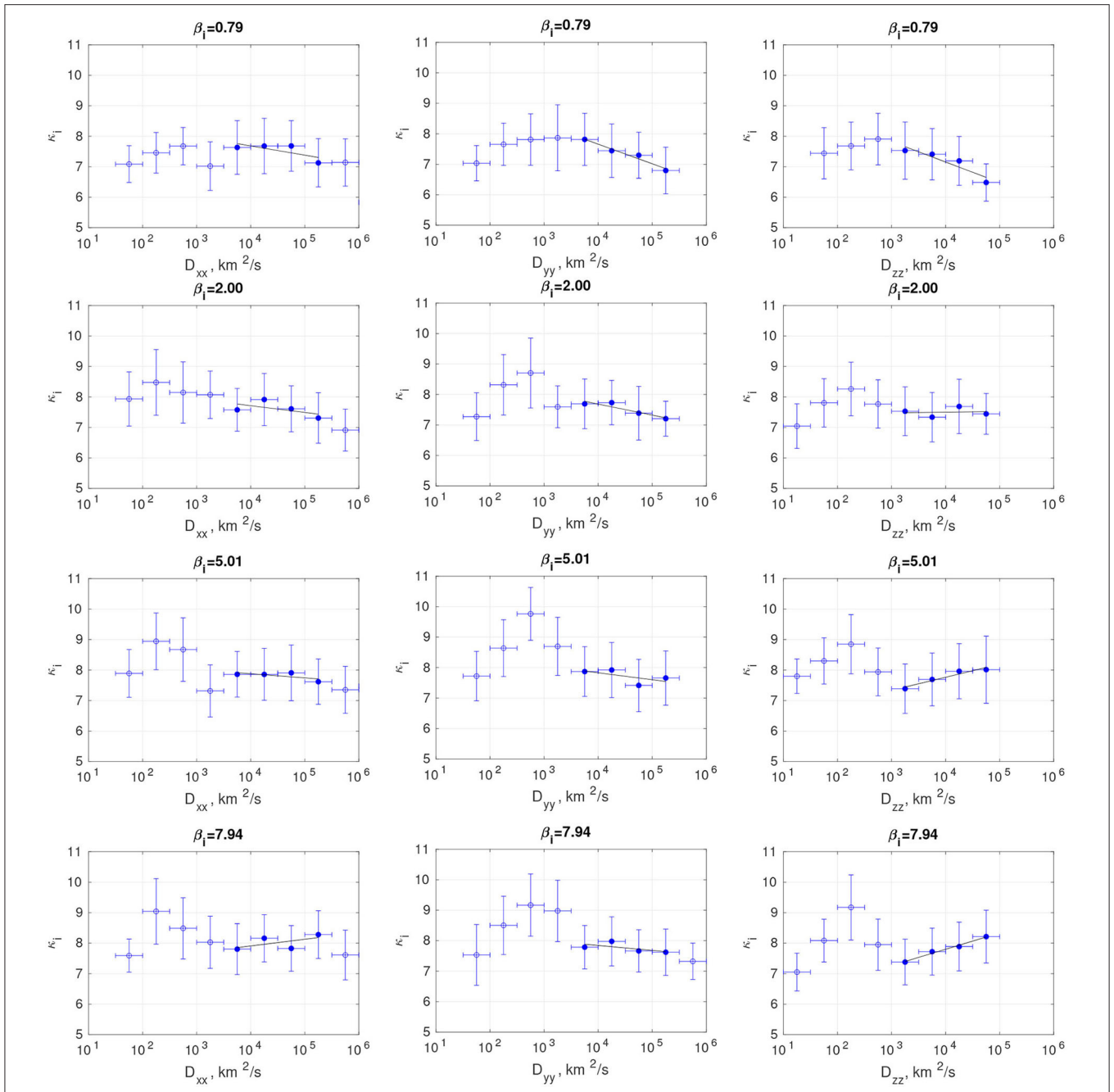

FIGURE 6 | Dependence of ion κ indices on mean $\log_{10} D$ for different plasma β. The first column is for D_{xx}, while second and third columns are for D_{yy} and D_{zz}, respectively. The function $\kappa = A \log_{10} D + B$ was fitted to the points plotted with filled circles, and the results are plotted with a solid line.

that while κ decreases with D for low β, κ increases with D for $\beta \geq 2$. The latter suggests that eddy diffusion in plasmas with high β might make the distribution functions more Maxwellian.

4. DISCUSSION

Our study shows that MHD turbulence in the plasma sheet might have an intermittent character. As seen in **Figure 5**, for most β values the eddy diffusion coefficients vary over a wide range (10^1–$10^6\,\mathrm{km}^2/\mathrm{s}$) and present two peaks. The majority of the coefficients concentrate around 10^4–10^5 km^2/s, which correspond to medium scale vortices with scales of $\sim$ 10,000 km that contribute to turbulent transport.

The eddy diffusion coefficients lower than $10^3\,\mathrm{km}^2/\mathrm{s}$ may correspond to very large vortices for which the coefficients are underestimated due to the 6-min limit in the determination of the autocorrelation time (half of the 12-min-long windows used

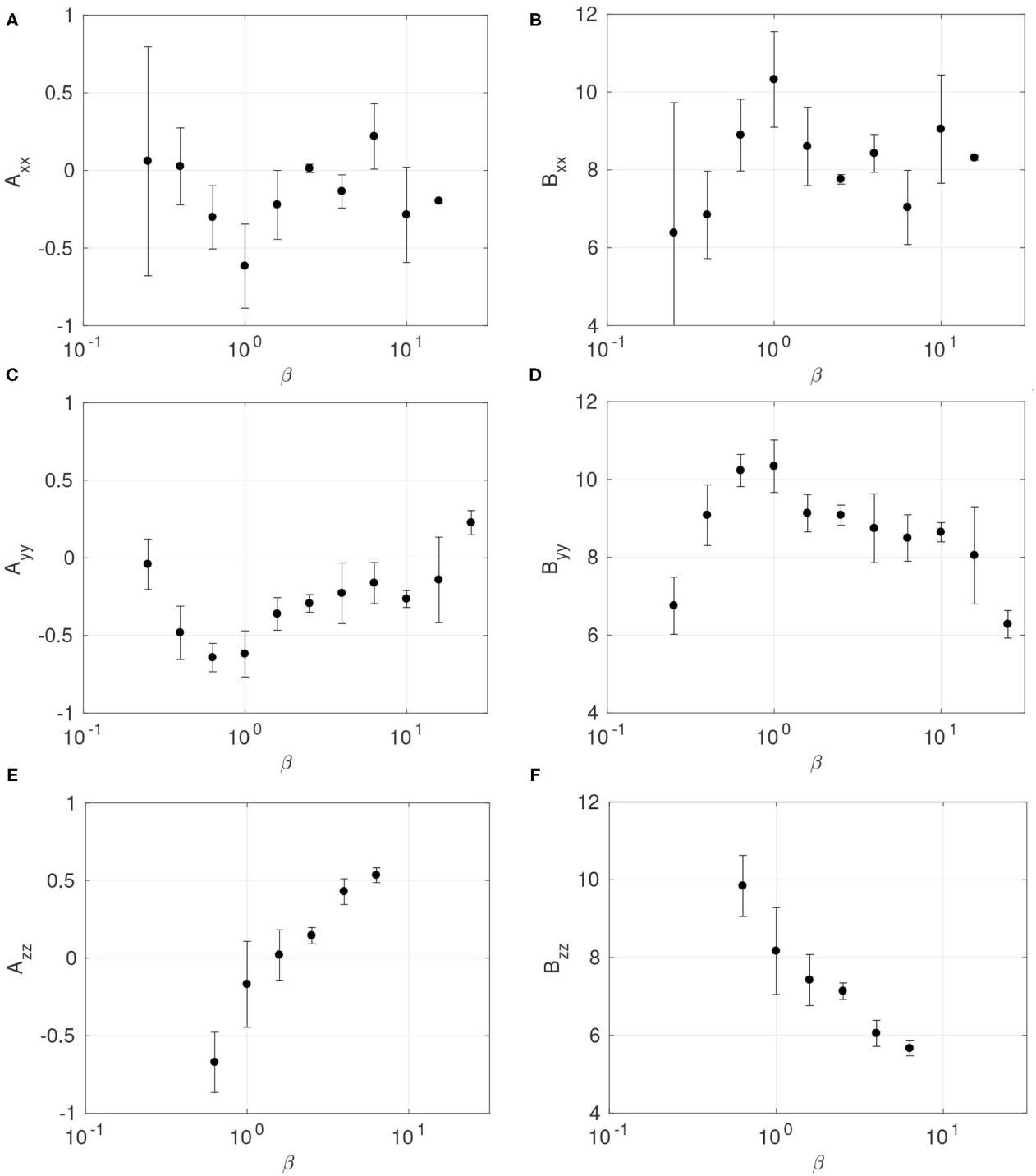

FIGURE 7 | Slopes **(A)** and intercepts **(B)** obtained from fits of κ vs. $\log_{10} D$ data for different β values. The first row **(A,B)** is for D_{xx}, while the second **(C,D)** and third rows **(E,F)** are for D_{xx} and D_{xx}, respectively.

for the analyses). The duration of the time interval used can also affect the values of the average V_{rms} over the interval. Borovsky et al. (1997) used a 2-h interval and obtained average bulk velocity values of the order of 10 km/s. In our study, these averages range between a few km/s to a few hundreds km/s, while the typical values are a few tens km/s. Inside big vortices the average V_{rms} will be low, because within the vortex the velocity of the vortex is subtracted and only small fluctuations remain.

On the other hand, the presence of stable quasi-laminar flows would agree with the results of Angelopoulos et al. (1999), who analyzed the properties of velocity fluctuations and concluded that the geomagnetic tail is a system that has properties of intermittent turbulence and exhibits sporadic variability. This fact is also reflected in multi-scale features of magnetic fluctuations in the near-Earth magnetosphere (Lui, 2001; Consolini et al., 2005). The intermittent behavior can be observed over all the plasma sheet for example see **Figure 2**, also (Stepanova and Antonova, 2011; Stepanova et al., 2011). However, the average values of the eddy diffusion coefficients are 10^4-10^5 km^2/s (solid white lines in **Figure 5**), indicating a strong presence of turbulence, and suggesting that turbulent transport may play an important role in magnetospheric dynamics.

The evolution observed of κ toward the geomagnetic tail has been associated with the transport of particles induced by turbulent eddy diffusion. For slow plasma transport from the Earth to the tail, there is enough time for the Kappa distribution to relax toward Maxwellian distribution due to diffusion in the velocity space (*aging*). This mechanism of relaxation (proposed by Collier, 1999) explains also the increase of the κ-index with the E_c that has been observed (Kirpichev and Antonova, 2020; Eyelade et al., 2021).

Our results show that low values of κ are observed for the highest eddy diffusion coefficients D_{xx} and D_{yy}. In this case, turbulent transport in the X and Y directions is faster, and the available time for Kappa distribution functions to relax to a Maxwellian is shorter. Thus the Kappa distributions cannot thermalize, which is reflected in the low κ indices.

However, some energetic tails might also be the consequence of reconnection outflows, as observed in many experiments and also modeled by El-Alaoui et al. (2010, 2012). These outflows appear as part of turbulent cascades during MHD simulations, when the computer codes combine both low resistivity and small grid spacing, thereby obtaining comparatively large values of the magnetic Reynolds number. El-Alaoui et al. (2010, 2012), argued that the formation of localized reconnection regions is the main process driving turbulence in the plasma sheet. These processes would also lead to a decrease in κ-index.

On the other hand, for the Z direction the eddy diffusion seems to increase with the κ-index, for high values of β. This could be related to turbulent mixing, which is commonly observed in the plasma sheet. The mixing length of the average plasma sheet is ∼10,000 km (Borovsky et al., 1998), leading to equalization of temperature across the plasma sheet, which is commonly observed (Huang and Frank, 1994). The plasma sheet extends to thousands of Earth's radii toward the tail in the X direction, while in the Y direction to tens of radii and just about ten Earth's radii in the direction perpendicular to the neutral sheet Z. This might explain why our results show that turbulent plasma mixing might prevail in the Z direction; meanwhile the fast turbulent transport and local reconnection is relevant in the X and Y directions. The efficiency of all the aforementioned processes could depend on the plasma β parameter, as reflected in our study. Nonetheless, more exhaustive statistical studies are necessary to untangle these effects.

5. CONCLUSIONS

Observations of ion Kappa distribution made by the multi-satellite THEMIS mission in the magnetotail plasma sheet were statistically explored in conjunction with eddy diffusion coefficients D and the plasma β parameter. Our study reveals the presence of turbulent flows ($D \sim 10^4 - 10^6$ km^2/s) alternated with quasi-laminar flows ($D \sim 10^2$ km^2/s), which might belong to large vortexes that are beyond the detection limits of our method. For turbulent plasmas, several processes related to MHD turbulence lead to either an increase or decrease of the κ index, depending on the value of β and the direction of the turbulent transport with respect to the plasma sheet.

DATA AVAILABILITY STATEMENT

The raw data supporting the conclusions of this article will be made available by the authors, without undue reservation.

AUTHOR CONTRIBUTIONS

All the research analysis in this study was carried out by AE, CE, and MS, while IK assisted in analyzing Kappa distribution functions. IO was engaged in the analysis of eddy diffusion transport, while EA was involved in the theoretical interpretation of the results. All authors contributed to the manuscript revisions and approved the final version of the manuscript.

FUNDING

This work was supported by Agencia Nacional de Investigación y Desarrollo de Chile (ANID) grants 21181777 and 1191351. MS acknowledges support from University of Santiago Chile through DICYT grant number 042031S. CE and MS acknowledge support from AFOSR (FA9550-19-1-0384).

ACKNOWLEDGMENTS

We acknowledge NASA contract NAS5-02099 and V. Angelopoulos for the use of THEMIS mission data, specifically C. W. Carlson and J. P. McFadden for ESA data, D. Larson for SST data, and K. H. Glassmeier, U. Auster, and W. Baumjohann for FGM data. THEMIS satellite mission data used in this paper are available on the THEMIS mission website: http://themis.ssl.berkeley.edu/index.shtml.

REFERENCES

Angelopoulos, V. (2008). The themis mission. *Space Sci. Rev.* 141, 5–34. doi: 10.1007/s11214-008-9336-1

Angelopoulos, V., Kennel, C. F., Coroniti, F. V., Pellat, R., Spence, H. E., Kivelson, M. G., et al. (1993). Characteristics of ion flow in the quiet state of the inner plasma sheet. *Geophys. Res. Lett.* 20, 1711–1714. doi: 10.1029/93GL00847

Angelopoulos, V., Mukai, T., and Kokubun, S. (1999). Evidence for intermittency in earth's plasma sheet and implications for self-organized criticality. *Phys. Plasmas* 6, 4161–4168. doi: 10.1063/1.873681

Antonova, E. (2002). Magnetostatic equilibrium and turbulent transport in earth's magnetosphere: a review of experimental observation data and theoretical approach. *Geomagn. Aeron.* 3, 117–130. Available online at: http://ijga.agu.org/v03/gai00358/gai00358.htm

Antonova, E. E. (1985). The nonadiabatic character of diffusion and the equalization of concentration and temperature in the plasma sheet of the earth magnetosphere. *Geomagn. Aeron.* 25, 623–627.

Antonova, E. E. (2005). The structure of the magnetospheric boundary layers and the magnetospheric turbulence. *Planet. Space Sci.* 53, 161–168. doi: 10.1016/j.pss.2004.09.041

Antonova, E. E., and Ovchinnikov, I. L. (1996). The equilibrium of turbulent current sheet and the current sheet of the earth's magnetotail. *Geomagn. Aeron.* 36, 7–14.

Antonova, E. E., and Ovchinnikov, I. L. (1997). Current sheet with medium scale developed turbulence and the formation of the plasma sheet of earth's magnetosphere and solar prominences. *Adv. Space Res.* 19, 1919–1922. doi: 10.1016/S0273-1177(97)00101-4

Antonova, E. E., and Ovchinnikov, I. L. (1999). Magnetostatically equilibrated plasma sheet with developed medium-scale turbulence: structure and implications for substorm dynamics. *J. Geophys. Res.* 104, 17289–17298. doi: 10.1029/1999JA900141

Antonova, E. E., and Ovchinnikov, I. L. (2001). The model of turbulent plasma sheet during IMF $B_z > 0$. *Adv. Space Res.* 28, 1747–1752. doi: 10.1016/S0273-1177(01)00541-5

Auster, H., Glassmeier, K., Magnes, W., Aydogar, O., Baumjohann, W., Constantinescu, D., et al. (2008). The themis fluxgate magnetometer. *Space Sci. Rev.* 141, 235–264. doi: 10.1007/s11214-008-9365-9

Baumjohann, W., and Treumann, R. (1997). *Basic Space Plasma Physics*. London: Imperial College Press.

Borovsky, J. E., Delzanno, G. L., Valdivia, J. A., Moya, P. S., Stepanova, M., Birn, J., et al. (2020). Outstanding questions in magnetospheric plasma physics: the Pollenzo view. *J. Atmos. Sol. Terres. Phys.* 208:105377. doi: 10.1016/j.jastp.2020.105377

Borovsky, J. E., Elphic, R. C., Funsten, H. O., and Thomsen, M. F. (1997). The Earth's plasma sheet as a laboratory for flow turbulence in high-[beta] MHD. *J. Plasma Phys.* 57, 1–34. doi: 10.1017/S0022377896005259

Borovsky, J. E., and Funsten, H. O. (2003). MHD turbulence in the Earth's plasma sheet: dynamics, dissipation, and driving. *J. Geophys. Res.* 108:1284. doi: 10.1029/2002JA009625

Borovsky, J. E., Thomsen, M. F., and Elphic, R. C. (1998). The driving of the plasma sheet by the solar wind. *J. Geophys. Res.* 103, 17617–17640. doi: 10.1029/97JA02986

Christon, S. P., Williams, D. J., Mitchell, D. G., Frank, L. A., and Huang, C. Y. (1989). Spectral characteristics of plasma sheet ion and electron populations during undisturbed geomagnetic conditions. *J. Geophys. Res.* 94, 13409–13424. doi: 10.1029/JA094iA10p13409

Christon, S. P., Williams, D. J., Mitchell, D. G., Huang, C. Y., and Frank, L. A. (1991). Spectral characteristics of plasma sheet ion and electron populations during disturbed geomagnetic conditions. *J. Geophys. Res.* 96, 1–22. doi: 10.1029/90JA01633

Collier, M. R. (1993). On generating kappa-like distribution functions using velocity space Levy flights. *Geophys. Res. Lett.* 20, 1531–1534. doi: 10.1029/93GL01702

Collier, M. R. (1999). Evolution of kappa distributions under velocity space diffusion: a model for the observed relationship between their spectral parameters. *J. Geophys. Res.* 104, 28559–28564. doi: 10.1029/1999JA900355

Consolini, G., Kretzschmar, M., Lui, A. T., Zimbardo, G., and Macek, W. M. (2005). On the magnetic field fluctuations during magnetospheric tail current disruption: a statistical approach. *J. Geophys. Res.* 110:10–11. doi: 10.1029/2004JA010947

El-Alaoui, M., Ashour-Abdalla, M., Richard, R. L., Goldstein, M. L., Weygand, J. M., and Walker, R. J. (2010). Global magnetohydrodynamic simulation of reconnection and turbulence in the plasma sheet. *J. Geophys. Res.* 115:2–5. doi: 10.1029/2010JA015653

El-Alaoui, M., Richard, R., Ashour-Abdalla, M., Walker, R., and Goldstein, M. (2012). Turbulence in a global magnetohydrodynamic simulation of the earth's magnetosphere during northward and southward interplanetary magnetic field. *Nonlin. Process. Geophys.* 19, 165–175. doi: 10.5194/npg-19-165-2012

Espinoza, C. M., Stepanova, M., Moya, P. S., Antonova, E. E., and Valdivia, J. A. (2018). Ion and electron kappa distribution functions along the plasma sheet. *Geophys. Res. Lett.* 45:6362. doi: 10.1029/2018GL078631

Eyelade, A. V., Stepanova, M., Espinoza, C. M., and Moya, P. S. (2021). On the relation between kappa distribution functions and the plasma beta parameter in the earth magnetosphere: THEMIS observations. *arXiv* 2101.07305.

Haaland, S., Kronberg, E. A., Daly, P. W., Fränz, M., Degener, L., Georgescu, E., et al. (2010). Spectral characteristics of protons in the Earth's plasmasheet: statistical results from cluster CIS and RAPID. *Ann. Geophys.* 28, 1483–1498. doi: 10.5194/angeo-28-1483-2010

Huang, C., and Frank, L. (1994). A statistical survey of the central plasma sheet. *J. Geophys. Res.* 99, 83–95. doi: 10.1029/93JA01894

Keika, K., Nakamura, R., Volwerk, M., Angelopoulos, V., Baumjohann, W., Retinò, A., et al. (2009). Observations of plasma vortices in the vicinity of flow-braking: a case study. *Ann. Geophys.* 27, 3009–3017. doi: 10.5194/angeo-27-3009-2009

Keiling, A., Angelopoulos, V., Weygand, J. M., Amm, O., Spanswick, E., Donovan, E., et al. (2009). THEMIS ground-space observations during the development of auroral spirals. *Ann. Geophys.* 27, 4317–4332. doi: 10.5194/angeo-27-4317-2009

Kirpichev, I., and Antonova, E. (2020). Dependencies of kappa parameter on the core energy of kappa distributions and plasma parameter in the case of the magnetosphere of the earth. *Astrophys. J.* 891:35. doi: 10.3847/1538-4357/ab700f

Lazar, M., Fichtner, H., and Yoon, P. (2016). On the interpretation and applicability of κ-distributions. *Astron. Astrophys.* 589:A39. doi: 10.1051/0004-6361/201527593

Lazar, M., Poedts, S., and Fichtner, H. (2015). Destabilizing effects of the suprathermal populations in the solar wind. *Astron. Astrophys.* 582:A124. doi: 10.1051/0004-6361/201526509

Lazar, M., Scherer, K., Fichtner, H., and Pierrard, V. (2020). Toward a realistic macroscopic parametrization of space plasmas with regularized κ-distributions. *Astron. Astrophys.* 634:A20. doi: 10.1051/0004-6361/201936861

Lee, J. H., and Angelopoulos, V. (2014). On the presence and properties of cold ions near earth's equatorial magnetosphere. *J. Geophys. Res.* 119, 1749–1770. doi: 10.1002/2013JA019305

Livadiotis, G. (2015). Introduction to special section on origins and properties of kappa distributions: statistical background and properties of kappa distributions in space plasmas. *J. Geophys. Res.* 120, 1607–1619. doi: 10.1002/2014JA020825

Livadiotis, G. (2017). *Kappa Distributions: Theory and Applications in Plasmas*. Elsevier.

Livadiotis, G., and McComas, D. (2013). Understanding kappa distributions: a toolbox for space science and astrophysics. *Space Sci. Rev.* 175, 183–214. doi: 10.1007/s11214-013-9982-9

Lui, A. (2001). Multifractal and intermittent nature of substorm-associated magnetic turbulence in the magnetotail. *J. Atmos. Sol. Terres. Phys.* 63, 1379–1385. doi: 10.1016/S1364-6826(00)00239-X

Lyons, L., Williams, D., and Prigancova, A. (1985). Book-review-quantitative aspects of magnetospheric physics-geophysics and astrophysics monographs. *Astrophys. Space Sci.* 113:423. doi: 10.1007/BF00650979

McFadden, J., Carlson, C., Larson, D., Ludlam, M., Abiad, R., Elliott, B., et al. (2008). The themis esa plasma instrument and in-flight calibration. *Space Sci. Rev.* 141, 277–302. doi: 10.1007/s11214-008-9440-2

Montgomery, D. (1987). "Remarks on the MHD problem of generic magnetospheres and magnetotails," in *Magnetotail Physics,* ed A. T. Y. Liu (Baltimore, MD: Johns Hopkins University Press), 203.

Nauenberg, M. (2003). Critique of q-entropy for thermal statistics. *Phys. Rev. E* 67:036114. doi: 10.1103/PhysRevE.67.036114

Nauenberg, M. (2004). Reply to "comment on 'critique of q-entropy for thermal statistics'". *Phys. Rev. E* 69:038102. doi: 10.1103/PhysRevE.69.038102

Navarro, R. E., Moya, P. S., Muñoz, V., Araneda, J. A., Viñas, A. F., and Valdivia, J. A. (2015). Magnetic alfven-cyclotron fluctuations of anisotropic non-thermal plasmas. *J. Geophys. Res.* 120, 2382–2396. doi: 10.1002/2014JA020550

Ness, N. F., Harrison, J. C., and Slichter, L. B. (1961). Observations of the free oscillations of the earth. *J. Geophys. Res.* 66, 621–629. doi: 10.1029/JZ066i002p00621

Olbert, S. (1968). "Summary of experimental results from MIT detector on IMP-1," in *Physics of the Magnetosphere*, eds R. L. Carovillano, J. F. McClay, and H. R. Radoski (Dordrecht: Springer), 641–659. doi: 10.1007/978-94-010-3467-8_23

Olsson, A., and Janhunen, P. (1998). Field-aligned conductance values estimated from Maxwellian and kappa distributions in quiet and disturbed events using freja electron data. *Ann. Geophys.* 16, 298–302. doi: 10.1007/s00585-998-0298-0

Ovchinnikov, I. L., Antonova, E. E., and Yermolaev, Y. I. (2000). Determination of the turbulent diffusion coefficient in the plasma sheet using the project interball data. *Cosmic Res.* 38, 557–561. doi: 10.1023/A:1026686600686

Panov, E. V., Nakamura, R., Baumjohann, W., Sergeev, V. A., Petrukovich, A. A., Angelopoulos, V., et al. (2010). Plasma sheet thickness during a bursty bulk flow reversal. *J. Geophys. Res.* 115:A05213. doi: 10.1029/2009JA014743

Petrukovich, A., Artemyev, A., Vasko, I., Nakamura, R., and Zelenyi, L. (2015). Current sheets in the earth magnetotail: plasma and magnetic field structure with cluster project observations. *Space Sci. Rev.* 188, 311–337. doi: 10.1007/s11214-014-0126-7

Pinto, V., Stepanova, M., Antonova, E. E., and Valdivia, J. A. (2011). Estimation of the eddy-diffusion coefficients in the plasma sheet using THEMIS satellite data. *J. Atmos. Sol. Terres. Phys.* 73, 1472–1477. doi: 10.1016/j.jastp.2011.05.007

Runov, A., Angelopoulos, V., Gabrielse, C., Liu, J., Turner, D. L., and Zhou, X. Z. (2015). Average thermodynamic and spectral properties of plasma in and around dipolarizing flux bundles. *J. Geophys. Res.* 120, 4369–4383. doi: 10.1002/2015JA021166

Runov, A., Angelopoulos, V., and Zhou, X. Z. (2012). Multipoint observations of dipolarization front formation by magnetotail reconnection. *J. Geophys. Res.* 117:14. doi: 10.1029/2011JA017361

Scherer, K., Fichtner, H., Fahr, H. J., and Lazar, M. (2019). On the applicability of κ-distributions. *Astrophys. J.* 881:93. doi: 10.3847/1538-4357/ab2df9

Scherer, K., Fichtner, H., and Lazar, M. (2018). Regularized κ-distributions with non-diverging moments. *Europhys. Lett.* 120:50002. doi: 10.1209/0295-5075/120/50002

Sitnov, M., Birn, J., Ferdousi, B., Gordeev, E., Khotyaintsev, Y., Merkin, V., et al. (2019). Explosive magnetotail activity. *Space Sci. Rev.* 215:31. doi: 10.1007/s11214-019-0599-5

Sonett, C. P. (1960). "Space research, proceedings of the first international space science symposium," *Nice*, ed H. K. Bijl (New York, NY: North-Holland Publishing Amsterdam), 921.

Stepanova, M., and Antonova, E. E. (2011). Modeling of the turbulent plasma sheet during quiet geomagnetic conditions. *J. Atmos. Sol. Terres. Phys.* 73, 1636–1642. doi: 10.1016/j.jastp.2011.02.009

Stepanova, M., and Antonova, E. E. (2015). Role of turbulent transport in the evolution of the κ distribution functions in the plasma sheet. *J. Geophys. Res.* 120:2014JA020684. doi: 10.1002/2014JA020684

Stepanova, M., Antonova, E. E., Paredes-Davis, D., Ovchinnikov, I. L., and Yermolaev, Y. I. (2009). Spatial variation of Eddy-diffusion coefficients in the turbulent plasma sheet during substorms. *Ann. Geophys.* 27, 1407–1411. doi: 10.5194/angeo-27-1407-2009

Stepanova, M., Pinto, V., Valdivia, J. A., and Antonova, E. E. (2011). Spatial distribution of the Eddy diffusion coefficients in the plasma sheet during quiet time and substorms from THEMIS satellite data. *J. Geophys. Res.* 116:1637. doi: 10.1029/2010JA015887

Treumann, R., and Baumjohann, W. (2020). Olbertian partition function in scalar field theory. *arXiv* 2011.03445. doi: 10.3389/fphy.2020.610625

Troshichev, O. A., Antonova, E. E., and Kamide, Y. (2002). Inconsistency of magnetic field and plasma velocity variations in the distant plasma sheet: violation of the "frozen-in" criterion? *Adv. Space Res.* 30, 2683–2687. doi: 10.1016/S0273-1177(02)80382-9

Tsallis, C. (1988). Possible generalization of boltzmann-gibbs statistics. *J. Stat. Phys.* 52:479. doi: 10.1007/BF01016429

Tsallis, C. (2004). Comment on "critique of q-entropy for thermal statistics". *Phys. Rev. E* 69:038101. doi: 10.1103/PhysRevE.69.038101

Tsallis, C. (2009). *Introduction to Nonextensive Statistical Mechanics*. New York, NY: Springer.

Vasyliunas, V. M. (1968). A survey of low-energy electrons in the evening sector of the magnetosphere with OGO1 and OGO3. *J. Geophys. Res.* 73, 2839–2884. doi: 10.1029/JA073i009p02839

Viñas, A. F., Moya, P. S., Navarro, R. E., Valdivia, J. A., Araneda, J. A., and Muñoz, V. (2015). Electromagnetic fluctuations of the whistler cyclotron and firehose instabilities in a maxwellian and tsallis-kappa-like plasma. *J. Geophys. Res.* 120, 3307–3317. doi: 10.1002/2014JA020554

Weygand, J. M., Kivelson, M. G., Khur ana, K. K., Schwarzl, H. K., Thompson, S. M., McPherron, R. L., et al. (2005). Plasma sheet turbulence observed by cluster II. *J. Geophys. Res.* 110:A01205. doi: 10.1029/2004JA010581

Wing, S., Johnson, J., Newell, P., and Meng, C. I. (2005). Dawn-dusk asymmetries, ion spectra, and sources in the northward interplanetary magnetic field plasma sheet. *J. Geophys. Res.* 110:7–8. doi: 10.1029/2005JA011086

Yoon, P. H., and Livadiotis, G. (2017). "Chapter 8–nonlinear wave-particle interaction and electron kappa distribution," in *Kappa Distributions,* ed G. Livadiotis (Amsterdam: Elsevier), 363–398. doi: 10.1016/B978-0-12-804638-8.00008-5

Conflict of Interest: The authors declare that the research was conducted in the absence of any commercial or financial relationships that could be construed as a potential conflict of interest.

frontiers in Astronomy and Space Sciences

REVIEW
published: 23 March 2021
doi: 10.3389/fspas.2021.622570

The Impact of Turbulence on Physics of the Geomagnetic Tail

Elizaveta E. Antonova[1,2]* *and Marina V. Stepanova*[3]*

[1]Skobeltsyn Institute of Nuclear Physics, Lomonosov Moscow State University, Moscow, Russia, [2]Space Research Institute RAS, Moscow, Russia, [3]Physics Department, University of Santiago, Santiago, Chile

There is a vast amount of evidence that suggests that the geomagnetic tail is like a turbulent wake behind an obstacle. Large-scale vortices in the wake are able to generate turbulent transport that takes place both along the plasma sheet, in the *X* and *Y* directions, and across the plasma sheet, in the *Z* direction. Thus, turbulent fluctuations in all directions should be taken into consideration when analyzing plasma transport in the plasma sheet, and stability of the plasma sheet configurations. In this review, we summarize and discuss the main results of large and middle scale magnetospheric turbulence yielded by data analysis and modeling. We also identify changes in the description of the magnetospheric dynamics connected with the existence of turbulent fluctuations in the tail.

Keywords: magnetosphere, plasma sheet, medium and large-scale turbulence, pressure balance, substorm

OPEN ACCESS

Edited by:
Luca Sorriso-Valvo, Institute for Space Physics (Uppsala), Sweden

Reviewed by:
Gaetano Zimbardo, University of Calabria, Italy
Takuma Nakamura, Austrian Academy of Sciences (OeAW), Vienna, VIE, Austria
Christian L. Vásconez, Department of Physics, National Polytechnic School, Ecuador

***Correspondence:**
Elizaveta E. Antonova
elizaveta.antonova@gmail.com
Marina V. Stepanova
marina.stepanova@usach.cl

Specialty section:
This article was submitted to Space Physics, a section of the journal Frontiers in Astronomy and Space Sciences

Received: *28 October 2020*
Accepted: *10 February 2021*
Published: *23 March 2021*

Citation:
Antonova EE and Stepanova MV (2021) The Impact of Turbulence on Physics of the Geomagnetic Tail. Front. Astron. Space Sci. 8:622570. doi: 10.3389/fspas.2021.622570

INTRODUCTION

Formation of turbulent wake behind an obstacle is a well-known phenomenon observed in the gas and fluid flows with a high Reynolds number. An example of such a wake behind a flying bullet can be seen in **Figure 1** adapted from (http://waterocket.explorer.free.fr/aerodynamics.htm). As it is well known, the sound and Alfvénic Reynolds numbers in the magnetosphere of the Earth are larger than $\sim 10^{11}$ (Borovsky and Funsten, 2003a). The magnetic field of the Earth represents an obstacle for the solar wind flow. That is why the formation of a turbulent wake behind such obstacle is very natural even in the case of a laminar flow in front of it. In fact, the solar wind flow is not laminar, and there are many works describing its turbulent properties. On the other hand, the existence of well-defined structures and the lack of evidence of mixing in the solar wind as it moves outward through the inner heliosphere is now intensively discussed (Borovsky, 2008; Borovsky, 2020a; Borovsky, 2020b). Regardless, the main solar wind macro parameters are highly fluctuating, and the properties of the turbulent flow behind the Earth's magnetic dipole should depend on those random fluctuations. The effect of the solar wind turbulence on the magnetospheric activity was discussed by D'Amicis et al. (2020). They show "the major role of the solar wind turbulence as a driver of geomagnetic activity especially at high latitudes" and at the same time "the geomagnetic response strongly affected by the intrinsic dynamics of the magnetosphere". They also stressed, that "strong variations in the geomagnetic field occur even in absence of large solar wind perturbations."

The change of the solar wind flow at the bow shock leads to the formation of a turbulent magnetosheath behind it. The level of fluctuations in the magnetosheath is an order of magnitude larger than in the solar wind. Although the term "turbulent magnetosheath" does exist since the first space measurements (Antonova et al., 2012), the attention to the importance of the study of this phenomenon was captured mainly during the last years. Detailed reviews of such studies can be found in the current Topic Issue. The existence of turbulent magnetosheath should be taken into account during the analysis of the properties of magnetospheric turbulence and the magnetospheric dynamics.

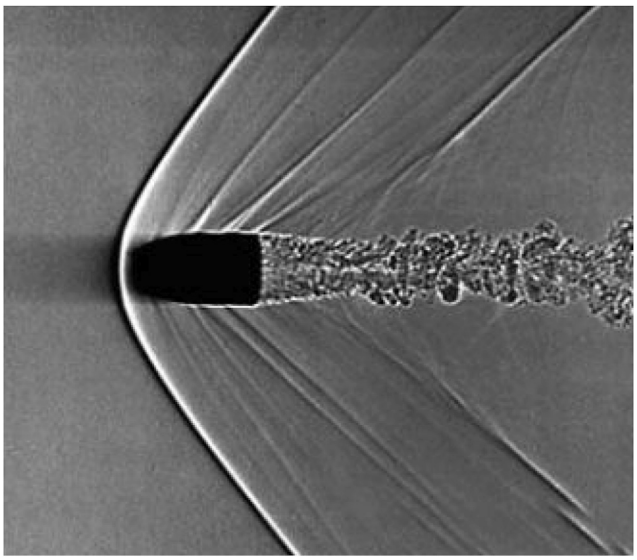

FIGURE 1 | Turbulent flow behind a flying bullet (the shadowgraph).

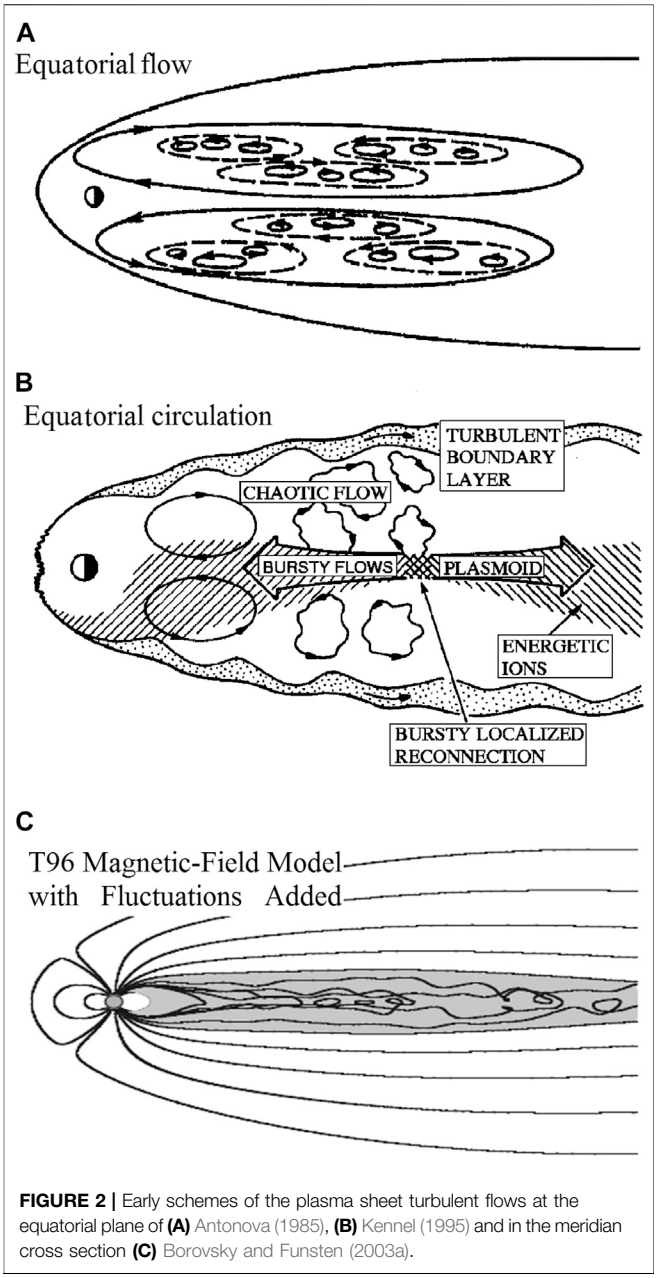

FIGURE 2 | Early schemes of the plasma sheet turbulent flows at the equatorial plane of **(A)** Antonova (1985), **(B)** Kennel (1995) and in the meridian cross section **(C)** Borovsky and Funsten (2003a).

Currently there are a lot of studies of turbulence in the Earth's magnetosphere at the MHD scale [see, for example, references in (Borovsky et al., 2020)]. Despite this, until now the most popular analytical and computer models that describe the magnetospheric dynamics consider only the laminar flows in the geomagnetic tail. In this paper, we summarize the main results of the study of magnetospheric turbulence and try to understand the reasons of why the laminar flow models are so widely used. We also try to analyze the results of the models, which consider the turbulent transport as one of the main factors that determines the magnetospheric dynamics. A complete review of all results obtained is beyond the scope of this paper. We only try to identify the key unsolved topics in the study of the magnetospheric turbulence and to show why such studies are very important for the solution of a number of the key magnetospheric problems. Our current work is mainly concentrated on the analysis of the inertial or driving scales of tail turbulence, leaving the dissipative scale beyond the scope of this review.

The paper is organized as follows: The second section contains the historical review of the main stages of the study of the magnetospheric turbulence as well as the analysis of the properties of the turbulent transport in the geomagnetic tail. The third section contains the analysis of the main reasons, which make the studies of magnetospheric turbulent wake difficult. The fourth section is dedicated to the discussion of the results of the turbulent plasma sheet modeling. In this section, we also analyze the advantages of studies of the magnetostatic equilibrium that take into account the turbulence for the description of several magnetospheric processes. The fifth section contains the discussion of the connection between the plasma sheet turbulence and the large-scale magnetospheric convection. The six section contains the analyzes the role of the eddy diffusion in solving problems caused by the use of models based on laminar flow. The last section is dedicated to discussions and conclusions.

STUDY OF MAGNETOSPHERIC TURBULENCE AND ITS MAIN CHARACTERISTICS

A clear manifestation of the existence of low frequency magnetospheric turbulence was obtained through spectral analysis of geomagnetic indexes [see (Consolini et al., 1996; Uritsky and Pudovkin, 1998; Stepanova et al., 2003; etc.)]. Consolini et al. (1996) examined the structure of fluctuations in the auroral electrojet index and found them to be multifractal.

The noncoincidence of forms of Fourier-spectra of the solar wind parameters and the AE-fluctuation spectra shown by Uritsky and Pudovkin (1998) evidenced the existence of the inner magnetospheric sources of turbulent fluctuations of the auroral electrojets. Such finding was in close agreement with the numerous low altitude auroral observations of fluctuating electric fields, amplitudes of which are much larger than the large-scale dawn-dusk electric field. Numerous results of auroral plasma measurements also clearly demonstrated the existence of nonequipotential magnetic field lines. Turbulent fluctuations of the electric field in the plasma sheet were observed by Maynard et al. (1982), Petersen et al. (1984), Hoshino et al. (1994), etc. These fluctuations have mainly electrostatic nature.

Even the first observations in the geomagnetic tail (Sonett et al., 1960) showed the presence of strong fluctuations of the main magnetospheric parameters. It is necessary to mention that James Dungey, the author of the first theory, explaining the dependence of magnetospheric dynamics on the direction and value of the interplanetary magnetic field (IMF), considered the observed fluctuations as the main difficulty for the validity of his approach (Dungey, 1961; Dungey, 1962). He stressed the importance to study "the effect of turbulence." However, at the beginning of the space age, the possibilities to analyze turbulent flows were limited and the systematic study of the characteristics of turbulent plasma flows have started only during the last decades.

Antonova (1985) summarized the results of magnetospheric observations leading to the suggestion about the dominant role of turbulence in the dynamics of the magnetospheric plasma sheet. It was suggested that the observed turbulence is mainly connected to the excitation of drift instabilities due to the nonhomogeneous distribution of magnetospheric plasma. It was also suggested that the magnetospheric turbulence includes embedded vortices connected to the large scale two vortex magnetospheric convection. **Figure 2A** shows a system of such vortices. Simultaneously Montgomery (1987) pointed out that the plasmas of the Earth's magnetotail should not behave in a laminar-flow fashion, owing to the high fluid and magnetic Reynolds numbers of the plasma sheet. He stressed that laminar-flow models of the magnetosphere and magnetotail "seem unlikely." Unfortunately, despite of these works, most researches were convinced that it would be possible to describe the main processes in the magnetosphere in the frame of the laminar models of plasma flow.

The study of plasma sheet turbulence was driven by the discovery of the bursty-bulk-flow (BBF) events by Baumjohann et al. (1989), Baumjohann et al. (1990a) and the analysis of plasma sheet bulk velocity and magnetic field fluctuations (Angelopoulos et al., 1992; Angelopoulos et al., 1996; Angelopoulos et al., 1999; Borovsky et al., 1997; Borovsky et al., 1998). It was clearly shown, that the observed picture of plasma flow at the equatorial plane strongly differs from the large scale magnetospheric convection. **Figure 2B** shows the adapted from Kennel (1995) and discussed by Angelopoulos et al. (1999) scheme of localized bursty-flows that drive the vortical turbulent flows. It was suggested that the BBF appears as a result of reconnection processes. Not only the bulk velocity, but also the magnetic field in the plasma sheet is highly fluctuating and can result in a snarling of the magnetic field lines. **Figure 2C** adapted from (Borovsky and Funsten, 2003a) shows a sketch of the turbulent magnetic field of the plasma sheet constructed by adding noise to the Tsyganenko-96 magnetic field model.

The quantitative study of the hydrodynamic properties of plasma sheet turbulence started with the papers of (Borovsky et al., 1997; Borovsky et al., 1998; Borovsky and Funsten, 2003a). It was shown using the ISEE-2 plasma and magnetic field measurements that the amplitudes of the bulk velocity fluctuations are much larger than the average velocities: $\delta Vx/Vx>>1$, $\delta Vy/Vy>>1$ and amplitudes of the magnetic field fluctuations are comparable with its mean value $\delta B/B \sim 0.5$. Later, Yermolaev et al. (1995) obtained the same picture in the Z and Y directions using data of the Interball/Tail probe. According to Borovsky et al. (1997), Borovsky et al. (1998), the correlation time for velocity fluctuations at geocentric distance ~20 R_E is ~2 min, and for the magnetic field is ~8 min. The mixing length of the average plasma sheet is ~10,000 km (Borovsky et al., 1998). It was shown that the distributions of the occurrence of the plasma-sheet bulk flows $P(v_x)$ and $P(v_y)$ has two components: i) an isotropic distribution of flows at low flow velocities and ii) an anisotropic distribution of fast flows. Such asymmetry appears due to the presence of BBF in the X and Y components of the inner plasma sheet flows. The distribution of slower flows was fitted by Borovsky et al. (1997) by the exponential functions: $P(V_x) = 0.32\exp(-|V_{x-8}|/41)$, $P(V_y) = 0.31\exp(-|V_{y-5}|/54)$, where Vx and Vy are the velocities in X and Y directions, and the velocities have units of km·s^{-1}, reaching a very high correlation with the correlation coefficients equal to 0.98. The distribution of fast BBF flows was fitted by $P(V_x) = 0.300\exp(-|V_X|/149)$ for $V_x > 0$ and $P(V_x) = 0.011\exp(-|V_x|/159)$ for $V_x < 0$. The analysis of the properties of velocity fluctuations made it possible to conclude [see (Angelopoulos et al., 1999)] that the geomagnetic tail is a system that exhibits sporadic variability and has properties of intermittent turbulence. This conclusion was supported by the subsequent studies showing that magnetic fluctuations in the near-Earth magnetosphere exhibit multiscale features (Lui, 2001; Consolini et al., 2005).

Borovsky et al. (1997) and Borovsky and Funsten (2003a) showed that the plasma-sheet material appears to be well mixed in density and temperature. They stressed that the persistent (many-minute) laminar flow is not observed and the turbulence may be strongly driven rather than well developed. It is interesting to mention that the values of plasma flow are significantly larger during the intervals of steady magnetospheric convection than they are during active times. Neagu et al. (2002), Neagu et al. (2005) found no significant dependence of the amplitude of the ion velocity and magnetic field fluctuations on the distance from the Earth toward the geomagnetic tail, the dawn-tail distance and on the distance from the neutral sheet.

Subsequent results obtained by Antonova (2000), Ovchinnikov et al. (2000), Schödel et al. (2001), Ovchinnikov

et al. (2002), Troshichev et al. (2002), Uritsky et al. (2002), Neagu et al. (2002), Uritsky et al. (2003), Neagu et al. (2005), Stepanova et al. (2005), Stepanova et al. (2006), Antonova (2008), Uritsky et al. (2008), Stepanova et al. (2009), Uritsky et al. (2009), Stepanova et al. (2011), etc. supported the validity of early findings and permitted to obtain a number of statistical dependencies. Ovchinnikov et al. (2002), Stepanova et al. (2005), Stepanova et al. (2009), Stepanova et al. (2011) showed that the level of velocity fluctuations strongly depends on the phase of magnetospheric substorm. It increases after a substorm onset and then slowly decreases during 1–2 h.

The BBFs are frequently considered as the main source of the observed plasma sheet fluctuations. They are composed by flow bursts lasting ~1 min and are commonly observed at substorm growth, expansion and recovery phases. Nonetheless, many BBF occur without classical substorm signatures during pseudo-breakups and auroral brightening. The BBF occurrence rate peaks close to midnight, and the variance of the remnant flow during high AE is stronger at midnight than at nearby sectors. This result supports the conclusion of Kennel (1995) that the geomagnetic tail is in a state of bimodal convection, whereby the potential flow is stagnant unless it is driven by localized flow bursts. Nagai et al. (1998) showed using the Geotail observations that the fast flows tend to be observed around the near-Earth pre-midnight sector. Petrukovich et al. (2001) calculated the angles between the vectors of fast earthward plasma flow and the local magnetic field. In the low-β (where β is the plasma parameter) parts of the geomagnetic tail, the fast flows were found to be nearly field-aligned. In the high-β plasma sheet the average angle was larger than 45°. The width of the flow channel, which represents the typical large-scale characteristic scale of the flow used to calculate the Reynolds number, has been estimated from the statistical analysis of Cluster spacecraft multi-point measurements by Sergeev et al. (2000), Nakamura et al. (2004). It was shown that the full width of the flow channel is 2–3 R_E in the "dawn-dusk" direction and 1.5–2 R_E in the "north-south" direction. Recently Sitnov et al. (2019) summarized the main results of the BBF study.

Borovsky et al. (1997) found that within the plasma sheet the slope of the power spectral density vs. frequency for plasma flow velocity and magnetic field varied from −0.8 to −2.0 and from −1.6 to −3.0, respectively. Different types of Reynolds numbers can be derived for the flows in the plasma sheet reflecting different aspects of turbulent flows (Borovsky and Funsten 2003a; Weygand et al., 2005). In particular, Weygand et al., (2005) showed that the level of intermittency in the central plasma sheet differs from that observed for the outer plasma sheet. They examined the magnetic field spectral indices in the field-aligned coordinate system and found that their range was quite broad (average of −2.0 ± 0.4). The transverse magnetic field component inside the central plasma sheet in the *Y* direction had a spectra index of −1.56 ± 0.04, and the mean eddy scale size found in this study was 6,000 km.

The study of plasma velocity fluctuations has been limited by a low time resolution of particle spectra measurements in comparison to the magnetic measurements, and by contamination caused by many sources. That is why the main progress in the study of plasma sheet turbulence was done due to the analysis of spectra of magnetic fluctuations using Cluster magnetometer observations (Vörös et al., 2003; Vörös et al., 2004; Vörös et al., 2006; Vörös et al., 2019; Volwerk et al., 2004; Weygand et al., 2005). It was shown, that the turbulence in the plasma sheet is a mixture of Alfvénic wavy turbulence and of eddy 2-D turbulence. A strong correlation between the maximum perpendicular flow velocity and the turbulence power for maximum velocities $150 \leq v_{\perp max} \leq 400$ km/s was found. It was also shown that the presence of BBFs significantly changes the spectral index or scaling index. Hoshino et al. (1994) showed that fluctuations of the magnetic field observed in the distant plasma sheet are characterized by a "kink" Fourier power law spectrum that can be approximated by two power law functions with two different spectral indices (Zelenyi et al., 2015).

The behavior of magnetospheric turbulence is hard to comprehend because it is almost impossible to discriminate between spatial and temporal variations even using data from multipoint satellite missions as THEMIS, CLUSTER and MMS. That is why the determination of properties of magnetospheric turbulence in most cases is still limited to the method proposed by Borovsky et al. (1997), Borovsky et al. (1998) for calculations of fluctuations of hydrodynamic velocities and their autocorrelation times [see also (Ovchinnikov et al. (2000), Antonova (2000), Ovchinnikov et al. (2002), Antonova (2008); Troshichev et al. (2002)] for the implementation of this method). It allows us to determine the turbulent flow velocities v_{rms} and their components and the autocorrelation time τ_{auto} when the mean flow velocity is small compared with the turbulent flow velocities. Borovsky et al. (1997) considered the autocorrelation time as a measure of the persistence of a fluctuating velocity and calculated it by analyzing the autocorrelation function:

$$A(\tau) = \frac{\Sigma\,(V_{rms}(t) - V_{rms}(t))\,(V_{rms}(t+\tau) - V_{rms}(t+\tau))}{(V_{rms}(t) - V_{rms}(t))^2} \quad (1)$$

Four methods were proposed for the determination of τ_{auto} (Borovsky et al., 1997), the most popular of which is based on the determination of the time interval during which the curve $A(\tau)$ has fallen to the value $A(\tau) = 1/e$. Finally, the method proposed by Borovsky et al. (1998) permits to estimate the coefficient of eddy diffusion as:

$$D = (V_{rms})^2 \tau_{auto}/2 \quad (2)$$

and analyze the transport of the plasma sheet material.

The first evaluation of the coefficient of eddy diffusion made by Borovsky et al. (1998) gave a very high value of $D = 2.6{\cdot}10^5$ km^2 s^{-1}. Nearly the same eddy diffusion coefficients were reported by (Ovchinnikov et al., 2000; Stepanova et al., 2005; 2009; Stepanova et al., 2011; Pinto et al., 2011). In particular, Stepanova et al. (2009), Stepanova et al. (2011) obtained the statistical distribution of the coefficients of eddy diffusion for quiet time and different phases of magnetospheric substorm. The use of the Interball/Tail probe satellite data allowed Stepanova et al. (2009) to determine D_{zz} and D_{yy} components of the eddy diffusion tensor, meanwhile the use of the THEMIS satellites permitted to obtain all three diagonal components of this tensor D_{zz}, D_{yy} and D_{xx} (Stepanova et al., 2011). However, it is necessary to mention that the presence of

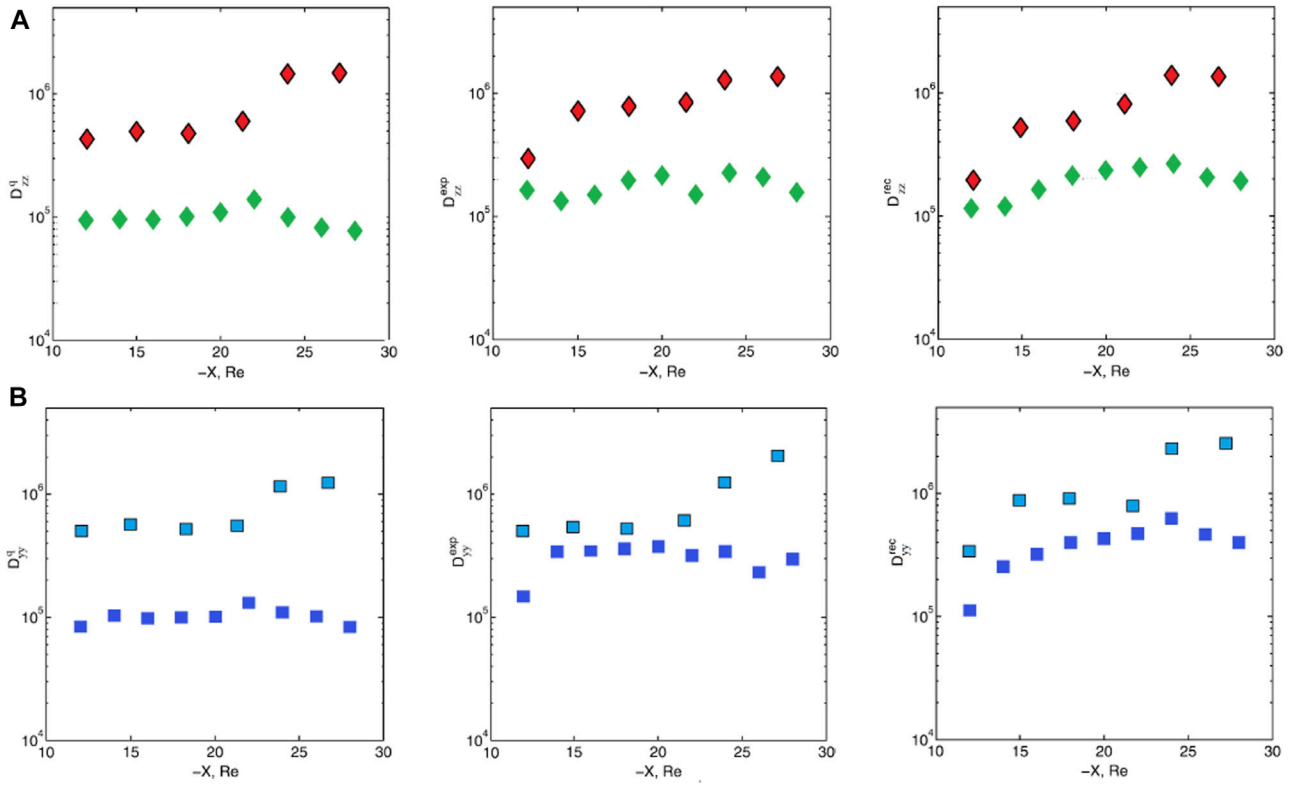

FIGURE 3 | Comparison of the dependencies of D_{zz} **(A)** and D_{yy} **(B)** on the radial distance and on the phase of magnetospheric substorm (q, quiet; exp, expansion; rec, recovery) from (Stepanova et al., 2009) (red diamonds and blue squares) and (Stepanova et al., 2011) (green diamonds and dark blue squares).

BBF might strongly affect the results of D_{xx} calculations and this value should be used with caution. **Figure 3A** shows the comparison of the dependence of D_{zz} on the radial distance for different phases of the magnetospheric substorm from (Stepanova et al., 2009) (red diamonds) and (Stepanova et al., 2011) (green diamonds). **Figure 3B** shows the same results for D_{yy} from (Stepanova et al., 2009) (blue squares) and (Stepanova et al., 2011) (dark blue squares). It is possible to note that the eddy diffusion coefficients obtained using the data from the THEMIS mission are smaller than the coefficients obtained from the Interball/Tail probe observations. It can be explained considering that during the first years of the THEMIS mission the geomagnetic activity was very low, and the eddy diffusion is expected to be lower for the time interval used for that studies (2008–2010). Pinto et al. (2011) obtained the instantaneous radial distribution of eddy diffusion coefficients using the data of the THEMIS satellites located along the midnight meridian. It was shown that the level of turbulence is greatly decreased at geocentric distances smaller than ~10 R_E. Slightly lower values of eddy diffusion coefficients were obtained in the distant tail by Troshichev et al. (2002). The same eddy diffusion coefficient values ~10^5 km^2/s were obtained by Nagata et al. (2008) for northward IMF orientation. Wang et al. (2010) analyzed plasma sheet transport and estimated the diffusion coefficients D_{yy} and D_{xx} associated with fluctuating drift to be ~10^5–10^6 km^2/s.

As it will be shown in the next sections, the introduction of eddy diffusion transport makes it possible to overcome the limitations of the ordinary MHD approach for the description of large-scale magnetospheric processes. To date, the necessary formalism has been developed only for gases in the absence of a magnetic field (Klimontovich, 1990; Klimontovich, 1999). Nonetheless, even a simplified analysis could be very useful.

REASONS FOR THE POPULARITY OF LAMINAR FLOW MODELS

Our analysis of characteristics of turbulent plasma flows leads to a natural question: Why do the most popular models describe the magnetospheric plasma flows in a laminar fashion? They have been developed in parallel with the models of the radiation belts formation, where the radial diffusion is recognized as the most important mechanism. The simplest answer is because of the real simplicity of such models and the possibility in a number of cases to obtain more or less reasonable results. Nonetheless, the explanation of this popularity is not so simple and can be related to three main reasons.

The first reason is a comparatively small number of works dedicated to the magnetospheric turbulence in comparison with the solar wind turbulence. It is related to the viability of use of the Taylor's hypothesis for the solar wind, which allows us to

transform the length scale l into the time scale t via a simple relation: $l = t \times V_{SW}$, where V_{SW} is the solar wind velocity. This relation permits in case of the solar wind to obtain spectra of turbulent fluctuations in a wide range of scales, meanwhile it is very difficult or even impossible to separate spatial and temporal variations inside the magnetosphere, especially for large vortices, even using multisatellite observation.

The second reason is that the plasma sheet configuration differs from the turbulent wake in hydrodynamic fluid. The scale of plasma sheet in Z direction is much smaller than the scale in Y direction. The formation of the plasma sheet is possible to model using global MHD codes and assuming the preexistence of particle sources in the magnetosphere [see (Watanabe and Sato, 1990) and results of later MHD simulations]. As a result of this modeling, the plasma sheet region extends widely in the equatorial plane and is considerably compressed perpendicular to it. However, taking into account the high values of the coefficient of eddy diffusion D_{zz} it is difficult to understand why such configuration could exist for a comparatively long time. In the next section we shall show that the observed structure of the quasistable magnetospheric turbulent wake as a sheet-like structure can be clearly explained taking into account the compression of this wake by the dawn-dusk electric field.

The third, and from our point of view the most important reason is related to the problem of the auroral oval mapping. Even the first results of auroral observations (Chamberlain, 1961) showed that the quiet time auroral arcs could exist for many hours, which is difficult to imagine if the roots of such arcs are embedded into the turbulent medium. For a long time, it has been widely assumed that the auroral oval maps to the plasma sheet. This assumption was based on the use of the magnetic field models with predefined configuration of current systems (Antonova et al., 2018). Nonetheless, the results of the topological mapping, based on the use of the plasma pressure as a "tracer" along a magnetic field line, indicated (Antonova et al., 2014; Antonova et al., 2015), that most of auroral oval is mapped to the surrounding the Earth plasma ring at geocentric distances from ~7 to ~10 R_E (Kirpichev et al., 2016). As the level of velocity and magnetic field fluctuations decreases at the distances <10 R_E (Stepanova et al., 2009; Stepanova et al., 2011; Pinto et al., 2011), the roots of quiet auroral arcs can be formed in a comparatively stable region. Therefore, the third obstacle to model the magnetosphere as a turbulent wake is caused by an erroneous auroral oval mapping.

TURBULENT PLASMA SHEET MODELING

The experimental evidences of high levels of fluctuations having a turbulent character encourage the development of models that would take into account both the turbulent transport and the modification of particle distribution functions due to interaction with turbulent electric and magnetic fields. It is an endeavor that could be reached in the future. For now, we can only present a few results, which can be useful for the future studies.

MHD Models and Plasma Sheet Turbulence

The most popular models of the large scale magnetospheric dynamics, known as the ideal MHD models, are developed using the MHD finite difference codes. That is why the results of such modeling should be used with caution taking into account the effect of numerical resistivity. Frequently such numerical codes break the frozen-in condition and are not able to produce high magnetic Reynolds numbers. These models reproduce the magnetic field line reconnection in the geomagnetic tail at different distances depending on the grid spacing scale. Nonetheless, even this kind of models reproduce the formation of medium scale vortexes in the plasma sheet after reconnection (Birn et al., 1999; Birn et al., 2011). It is necessary to mention also that MHD models describe the formation of vortices that appeared due to development of Kelvin-Helmholtz instability at the magnetospheric flanks stating from (Miura, 1984). Latest results employed the fully kinetic model were obtained by (Nakamura et al., 2020).

When the computer codes combine both the low resistivity and small grid spacing, it is possible to obtain comparatively large values of the magnetic Reynolds number and to model the formation of the turbulent plasma sheet under idealized southward (El-Alaoui et al., 2010) and northward (El-Alaoui et al., 2012) IMF. These models were able to reproduce some features of the plasma sheet turbulence, including the nested vortices at multiple scales. The largest scales were associated with the reconnection outflows and the diversion of high-speed flows. El-Alaoui et al. (2010), El-Alaoui et al. (2012) also found that the power spectral densities (PSDs) had the characteristics of a turbulent flow and showed the three scale ranges expected from theory: the energy-containing range, the inertial range, and the dissipative range. They selected the formation of localized reconnection regions as the main process driving turbulence in the plasma sheet.

However, the appearance of numerical resistivity is not the unique and even not the main problem of the ideal MHD models. It is necessary to take into account that the contribution of the pressure gradients in the generalized Ohm's law can be significant. In collisionless plasma, this law has the form:

$$\mathbf{E} + [\mathbf{V} \times \mathbf{B}] = \frac{[\mathbf{j} \times \mathbf{B}]}{ne} - \frac{\nabla p_e}{ne} + \left[\frac{\partial \mathbf{j}}{\partial t} + \nabla \cdot (\mathbf{jV} + \mathbf{Vj})\right] \frac{m_e}{ne^2} \quad (3)$$

where m_e and n_e are the mass and density of electrons, m_i and n_i are the mass and density of ions, $m = m_i + m_e$, $n = (m_i n_i + m_e n_e)/m$ is the density, $V = (m_i n_i v_i) + (m_e n_e v_e)/_{mn}$ is the plasma velocity, $\mathbf{j} = en\,(\mathbf{v\_v_e})$ is the current density, $\mathbf{E}$ is the electric field. The frozen-in approximation can be used only in the regions where the right-hand side of the generalized Ohm's law is much smaller than its left-hand side (Baumjohan and Treuman, 1996; Priest and Forbes, 2000; Paschmann et al., 2002; etc.). It is necessary to mention that the ideal MHD do not consider the electrostatic field and the induction equation can be written as (Priest and Forbes, 2000):

$$\frac{\partial \mathbf{B}}{\partial t} = \nabla \times \left([\mathbf{V} \times \mathbf{B}] - \frac{1}{ne}[\mathbf{j} \times \mathbf{B}] - \frac{\nabla p_e}{ne} - \frac{m_e}{ne^2}\frac{\partial \mathbf{j}}{\partial t} \right) \quad (4)$$

The first term in the right-hand side of **Eq. 3** is named the Hall term. Priest and Forbes (2000) stressed that only in case of strong collisional plasma in weak magnetic field this term can be neglected. The scale of the Hall term if $V \neq V_A$ is equal (Priest and Forbes, 2000):

$$L_{Hall} = \lambda_i \frac{V_A}{V} \quad (5)$$

where $\lambda_i = c/\omega_{pi}$ is the ion inertial length, $\omega_{pi} = [(e^2 ne)/(\varepsilon_0 m_i)]^{1/2}$ is the ion plasma frequency, c is the velocity of light, ε_0 is the vacuum dielectric constant. Therefore, in the regions of slow flow velocity where $V_A >> V$, the ideal MHD becomes inapplicable and the Hall MHD must be used. The ideal MHD models are used in thermonuclear researches for the description of the aperiodic instabilities and the study of quick processes. The slow plasma processes can be described using the Hall MHD, which requires large computer capacities. However, it is clear that inside regions of turbulent flow in the plasma sheet only regions with near to Alfvénic plasma flow can be analyzed properly using the ideal MHD approach. **Eqs. 3**, **4** contain also the term, which depends on the electron pressure gradient. This leads to the validity of the frozen in conditions for the electron motion by neglecting the electron inertia term (Baumjohan and Treuman, 1996):

$$\frac{\partial \mathbf{B}}{\partial \mathbf{t}} = \nabla \times [\mathbf{v_e} \times \mathbf{B}] \quad (6)$$

This means that in collisionless MHD with Hall currents, the electrons are the unique plasma component, which is frozen to the magnetic field. The plasma flow in such a case deviates from the motion of the magnetic field lines. Hall currents are observed in the magnetotail [see Nagai et al. (2003) and later observations]. The validation of the frozen in condition for electrons and electron reconnection was one of the main goals of the MMS mission (Burch et al., 2016a). The electron reconnection was used to explain the observations of the super-Alfvénic electron jets, not accompanied by the ion outflows (Burch et al., 2016b; Phan et al., 2018). Although the MMS observations captivated the attention to the study and modeling of the turbulent processes at small and medium scales [see (Stawarz et al., 2015; Ergun et al., 2018; Califano et al., 2020) and references therein], it is not clear how these studies could help to clarify the main properties of the large-scale magnetospheric dynamics.

Therefore, in spite of significant advantages of different MHD models in the analysis of magnetospheric turbulence and dynamics, there are some important problems which solution requires a different approach. This includes the magnetospheric configurations with slow in comparison with the Alfvén velocity plasma motions like the central plasma sheet where the averaged flow velocities are ~30 km/s (Angelopoulos et al., 1993), and hence $V << V_A$. At the same time, for this and similar regions it is necessary to take into account the presence of the turbulent eddy diffusion and the role of the turbulent transport due to the large values of obtained eddy diffusion coefficients.

It is well known that when the flow velocity is much smaller than the Alfvén and sound velocities, the analyzed plasma configuration is in magnetostatic equilibrium $[\mathbf{j} \times \mathbf{B}] = \nabla p$. Here we discuss the simplest case of the isotropic plasma pressure. Plasma velocity across the plasma sheet is fast only in case of the tail flapping; meanwhile plasma velocity along the sheet is comparable with the Alfvén velocity only inside the BBF. Therefore, it is possible to analyze the properties of the plasma sheet using the condition of magnetostatic equilibrium as it was done in many papers. It is necessary to note that the existence of stress balance $p + (B^2/2\mu_0) \approx$const across the plasma sheet and the plasma pressure isotropy were experimentally verified by Baumjohann et al. (1990b), Kistler et al. (1993), Petrukovich et al. (1999), Wang et al. (2013), etc. The plasma sheet is a well-defined structure that exists in spite of the presence of turbulent fluctuations. Therefore, it is necessary to understand why such structure is formed and how it is supported in the collisionless plasma with turbulent fluctuations. It is necessary to mention that the existence of high level of turbulent fluctuations can lead to the appearance of eddy viscosity (Borovsky and Funsten, 2003b). Nonetheless, the eddy diffusion transport is more relevant for the Earth's plasma sheet where plasma pressure is nearly isotropic.

Model of the Turbulent Plasma Sheet Including Eddy Diffusion and Pressure Balance Across the Plasma Sheet

In order to include the turbulent transport to the description of the large-scale processes in the geomagnetic tail it is necessary to use a special system of hydrodynamic transport equations. To our knowledge, such system of equations has not been developed for collisionless plasma yet. However, the turbulent diffusion was included to the system of hydrodynamic equations by Klimontovich (1990), starting from the equation of mass conservation, which can be written as:

$$\frac{\partial \rho}{\partial t} + \frac{\partial}{\partial \mathbf{r}}\left(\rho \mathbf{V} - D\frac{\partial \rho}{\partial \mathbf{r}} \right) = 0 \quad (7)$$

where ρ is the mass density, $\mathbf{V}$ is the bulk velocity (averaged on turbulent fluctuations) and D is the space diffusion coefficient. In a presence of the magnetic field, the coefficients of space diffusion can have different values along and perpendicular to the magnetic field and are determined by the properties of the turbulence. Taking into account such feature, **Eq. 7** can be used in the first approximation for the description of plasma transport. It shows that the distribution of plasma density does not change if the expression in round brackets is equal to zero, leading to the appearance of quasistatic distributions.

Observed conservation of pressure balance across the plasma sheet permits to use the condition of magnetostatic equilibrium as an empirical relation thereby connecting the magnetic field and the plasma pressure. A more careful analysis will require the inclusion of magnetic field fluctuations. However, at first approximation it is possible to suggest that they are not so large in comparison with the regular field [~0.5 in accordance with (Borovsky et al., 1997)]. In this case, it is possible to solve the

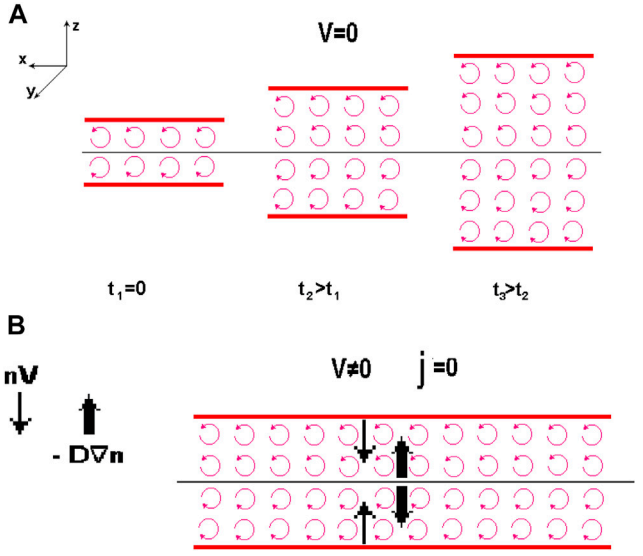

FIGURE 4 | Scheme illustrating the formation of the turbulent plasma sheet. Case **(A)** corresponds to the expansion of the sheet due to eddy diffusion when the regular flow velocity $V = 0$, case **(B)** corresponds to the quasistable configuration, when the regular velocity to the tail center compensates the eddy diffusion.

Grad-Shafranov equation and to determine the magnetic field distribution across the plasma sheet in the tail approximation of Birn and Schindler (1983).

Such approach was used in the Antonova and Ovchinnikov (1996a; Antonova and Ovchinnikov,1996b; Antonova and Ovchinnikov, 1999; Antonova and Ovchinnikov, 2001) model developed to explain the existence of the quasistable plasma sheet in the presence of turbulent transport. As it was mentioned in *Reasons for the Popularity of Laminar Flow Models*, the concept of the plasma sheet as a turbulent wake behind an obstacle has attracted little attention due to an unusual configuration of such turbulent wake, in comparison to the wake commonly observed in ordinary fluids. In the geomagnetic tail, it only takes up part of the volume behind the obstacle and is located between the tail lobes. However, it is well known that such configuration is observed only under southward IMF orientation (IMF Bz < 0). When the IMF turns northward for a comparatively long time, the tail lobes fill with plasma from the plasma sheet (Frank et al., 1986). Such filling leads to the appearance of polar cap arcs and the formation of theta-aurora. One of the main differences between the periods of IMF Bz < 0 and of IMF Bz > 0 is the value of the dawn-dusk electric field, which is much stronger for the southward IMF orientation. The particle drift along the Z axis in the SM coordinate system generates the lobe plasma flow directed from the tail lobes to the center of the plasma sheet, where the plasma density has a maximum. **Eq. 5** shows that the turbulent transport, directed opposite to the plasma pressure gradient, can compensate the regular transport if the averaged bulk velocity $V_z D_{zz} \rho^{-} d\rho/dz$. Due to the intense plasma mixing, the plasma temperature variations across the plasma sheet are much smaller than the variations of the plasma density. Therefore, the plasma density can be obtained from the condition of the pressure balance across the plasma sheet, considering that the temperature is constant. The regular velocity V_z can be evaluated using, for example, the models of the dawn-dusk electric field. By equating regular and turbulent transports, it is possible to obtain the value D_{zz} necessary for the existence of the plasma sheet between the tail lobes, as shown schematically in **Figure 4**.

Figure 5 shows an example of plasma pressure distribution obtained using (Antonova and Ovchinnikov, 1996a; Antonova and Ovchinnikov,1996b; Antonova and Ovchinnikov, 1999) model at geocentric distances $X = -30\ R_E$ when $B_z^{IMF} < -4nT$ (a), and at $B_z^{IMF} > +4nT$ (b). The values of the dawn-dusk electric field were obtained from the Volland-Stern electrostatic field model at ionospheric altitudes, and subsequent mapping to the tail using the Tsyhanenko-87W magnetic field model. The ratio of plasma pressure values between neighboring contours is $e^{1/2}$. This model explains the thinning of the plasma sheet during the substorm growth phase due to the increase of the dawn-dusk electric field. It also explains the plasma sheet thickening after substorm onset due to the increase of the level of turbulence and the eddy diffusion. The filling of the tail lobes during IMF Bz > 0 was explained due to strong reduction of the dawn-dusk electric field under the northward IMF orientation.

The main achievement of the discussed model is the prediction of the value of the eddy diffusion coefficient D_{zz} by Antonova and Ovchinnikov (1996a), Antonova and Ovchinnikov (1996b), before it was obtained experimentally in many works, starting from Borovsky et al. (1998) [see the discussion in (Antonova, 2000; Ovchinnikov et al., 2000; Ovchinnikov and Antonova, 2017)]. Later, Stepanova and Antonova (2011) made a direct verification of the main predictions of the model. Despite its simplicity, the discussed model shows how the existence of turbulent transport could explain the observed formation of quasistable structures, which are compressed by the regular plasma motions, compared with the classical schemes where such compression leads to the appearance of reconnection.

LARGE SCALE MAGNETOSPHERIC VORTICES AND MAGNETOSPHERIC TURBULENCE

To date the mechanisms of the formation of the plasma sheet turbulence are not clear, and continue to be discussed. The formation of the large-scale vortices with scales ~10,000 km is of particular interest, as they make the main contribution to the turbulent transport. The existence of magnetospheric vortices was first demonstrated using data of simultaneous ISSE-1 and ISEE-2 observations by Hones et al. (1979) and analyzed in detail by Birn et al. (1985). Study and modeling of such vortices were later connected to the development of Kelvin-Helmholtz instability at the magnetospheric flanks. Latest analysis of Nakamura et al. (2020) showed how the formation of vortices is related to the level of solar wind fluctuations.

Study of BBF formation leads to the description of vortex formation at the center of the plasma sheet. According to the

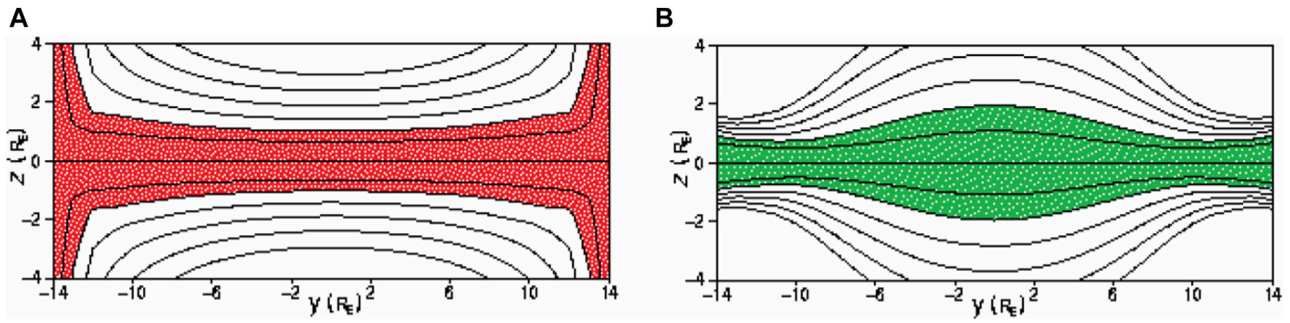

FIGURE 5 | An example of plasma pressure distribution in the plasma sheet at geocentric distance $X = -30\ R_E$, **(A)** when $B_z^{IMF} < -4nT$ and **(B)** at $B_z^{IMF} > +4nT$, in accordance with the model of Antonova and Ovchinnikov (1999).

model of Birn et al. (1999), Birn et al. (2011), the vortices could appear as a result of reconnection. The large-scale vortices of such type were successfully identified in many works using multisatellite observations (Keiling, et al., 2009; Keika et al., 2009; Panov et al., 2010; Tang, 2012; etc.). Unfortunately, these studies were done in (*X*, *Y*) plane only, and the structure of vortices in *Z* direction remains unclear.

El-Alaoui et al. (2010), El-Alaoui et al. (2012) considered the energy-containing scale of magnetospheric turbulence as the largest scale being associated with reconnection outflows and the diversion of high-speed flows. Therefore, the eddy vortices were considered as a driving or integral scale of the tail turbulence. Nonetheless, the appearance of such vortices is a consequence of the large-scale magnetospheric flows. These flows increase when IMF Bz < 0. That shows their deep connection with the large-scale magnetospheric convection. A strong connection between the eddy diffusion and the large-scale magnetospheric convection is also described in the model of the turbulent plasma sheet proposed by Antonova and Ovchinnikov (1996a), bAntonova and Ovchinnikov (1996b), Antonova and Ovchinnikov (1999).

Properties of the large-scale magnetospheric convection have been obtained by many tools and are well known [see (Weimer, 1996)]. The nature of the observed large-scale magnetospheric convection was widely discussed in multiple works since the beginning of Space Age. The viscous interaction and reconnection models were the most popular ones for a long time. However, both mechanisms were not considered a source of large-scale vortices at driving or integral scale of turbulence. Borovsky et al. (2020) stressed that the viscous interaction is neither quantified nor understood. The observed high level of magnetosheath and plasma sheet turbulence is the main obstacle to the applicability of the Dungey (1961) reconnection model.

The discovery of a system of large-scale field-aligned currents by Iijima and Potemra (1976) was crucial for the understanding of the large-scale magnetospheric convection. It became clear that the dawn-dusk electric field in the polar cap and, hence, the large-scale two vortex magnetospheric convection are supported by the Region I field-aligned currents of Iijima and Potemra. The source of the Region 1 currents in the equatorial plane is located inside the plasma sheet and the outer part of the ring current (Antonova et al., 2006; Xing et al., 2009; Antonova et al., 2018). The most probable mechanism of generation of both Region II and Region I currents is related to the existence of the plasma pressure gradients. Strong arguments in favor this mechanism were provided by Troshichev (1982). In particular, Antonova and Ganushkina (1997) showed that the Region I field-aligned currents can be supported by the azimuthal plasma pressure gradients, which appear due to azimuthal asymmetry of the magnetoshere modulated by the IMF. The detailed discussion about the action of this mechanism is beyond the scope of this paper. For the description of turbulent processes in the magnetosphere, it is only important to stress that such mechanism produces the large-scale two vortex convection flows.

The inverted V structures in the auroral oval containing the field-aligned potential drop are a clear result of a medium scale vortex formation in the region of the upward field-aligned current (see **Figure 1** in (Antonova and Ovchinnikov, 1999) which schematically shows the structure of the electrostatic field and its equipotentials typically observed in the inverted-V quiet auroral band). It is necessary to remind that the electric field in the inverted V structure is much larger than the large-scale dawn-dusk electric field, and it increases with the distance from the ionosphere. We assume that the medium-scale vortices such as inverted-V structures should form part of the plasma sheet turbulence. However, their connection with smaller vortices that produce the eddy diffusion in the plasma sheet is not clear yet.

Our analysis shows that mechanisms of generation of the plasma sheet turbulence are deeply connected to the plasma pressure gradients in the magnetosphere, including the driving or integral scale vortices–the two-vortex convection and the eddy vortices, responsible for the eddy diffusion transport.

HOW THE INCORPORATION OF THE EDDY DIFFUSION HELPS TO SOLVE PROBLEMS CAUSED BY THE USE OF MODELS BASED ON LAMINAR FLOW

The convection crisis is one of the main problems of the slow motion of plasma from the tail to the Earth inside the plasma

sheet. Ericson and Wolf (1980), Birn and Schindler (1983) showed that the adiabatic plasma transport in case of the laminar convection should lead to an increase of plasma pressure in the plasma sheet, which was never observed. The adiabatic laminar convection assumes the conservation of particles in a magnetic flux tube and an increase of their temperature in accordance with the adiabatic law, i.e. particle and heat fluxes between the flux tubes are not allowed. Analyzing this problem, Kivelson and Spence (1988) showed that under quiet geomagnetic conditions a quasi-static adiabatic convection is possible in a magnetotail of finite width. However, the problem continued to exist for more disturbed conditions. The existence of turbulent electric field fluctuations and eddy diffusion naturally removes this problem (Antonova, 1985; Antonova and Tverskoy, 1998), as the turbulent fluctuations of the magnetic field do not allow to use such concepts as the magnetic flux tube and the adiabatic transport. It is necessary to note also that particle trajectory in fluctuating magnetic and therefore fluctuating electric field becomes stochastic, when the Larmor radius of a particle is comparable with the field inhomogeneity. In contrast to the commonly used adiabatic model, the behavior of particle pressure in the plasma sheet was determined by Antonova and Ovchinnikov (1996a), Antonova and Ovchinnikov (1996b), Antonova and Ovchinnikov (1999) as the pressure balance in Z direction described by the flaring-tail model of Tverskoy (1968) and Kennel (1995).

Consideration of the high level of plasma sheet fluctuations is also fundamental for the understanding of the nature of magnetospheric substorms. According to (Akasofu, 1964), an isolated substorm onset starts with the brightening of the equatorward auroral arc. Such arc is mapped to the equatorial plane at geocentric distance ~7 R_E [see arguments summarized by Antonova et al. (2018)], i.e., near the inner boundary of the outer part of the ring current. Dispersionless injection boundary is also located at such distances (Lopez et al., 1990; Spanswick et al., 2010). Such features mean the development of an instability able to produce auroral brightening and local particle acceleration. It is difficult to imagine how this instability would develop in the presence of turbulent fluctuations in the plasma sheet, assuming that the auroral oval is mapped to that region, as suggested in many works. On the contrary, the mapping of the auroral oval to the outer part of the ring current does not lead to such consequences, considering that the level of turbulent fluctuations before substorm vanishes in this region, as mentioned in *Study of Magnetospheric Turbulence and Its Main Characteristics*.

It is necessary to mention, that the BBFs are frequently discussed as an onset trigger in the tail. They are observed during the substorm growth, expansion and recovery phases. Nonetheless, many BBFs occur without classical substorm signatures during pseudo-breakups and auroral brightening and produce the auroral streamers. Many substorm onsets are not preceded by the arrival of streamers [see references in (Antonova et al., 2009; Sitnov et al., 2019)]. Therefore, the existence of plasma sheet turbulence including BBFs is a strong argument in favor of the location of the instability responsible for a substorm onset at comparatively small geocentric distances, that agrees with the onset observations.

During a long history of study of substorms different mechanisms of substorm onset were discussed. Most models based on the reconnection in the tail suppose the existence of the laminar plasma flow and the regular character of the magnetic field before the reconnection onset including the models which take into account the Hall term and electron inertia [see, for example (Shay et al., 2003)]. Therefore, variations of plasma sheet velocity and magnetic field constantly observed in the plasma sheet create real difficulties for such models, giving preference for models of substorm onset located at geocentric distances <10 R_E such as the current disruption models (Lui, 2001) and development of upward field-aligned current instability (Antonova, 2002; Stepanova et al., 2002).

One more problem, which naturally appears in connection with the plasma sheet turbulence, is the presence of beams and fast plasma motions, which are attributed to the magnetic reconnection leading to the change of a large-scale magnetic configuration. However, as was mentioned earlier, most of the BBFs do not produce any substantial changes like generation of geomagnetic substorms. To understand such contradiction, it is necessary to remind that the plasma sheet turbulence is a mixture of the Alfvénic wavy turbulence and eddy 2-D turbulence. Therefore, the Alfvénic disturbances constantly exist in the plasma sheet. Relations (3) and (4) show that the ideal MHD in such a case is applicable when the scale of perturbed region is larger than the ion inertial length. This means that the traditional reconnection models can describe the processes inside such regions, which can be only a small part of the entire turbulent region. In such a case, the local reconnection phenomena can be considered as an intrinsic property of the collisionless turbulence and local reconnection phenomena leading to the BBF formation as a part of the tail turbulence development. The reconnection-like phenomena observed inside the turbulent magnetosheath (Yordanova et al., 2016; Vörös et al., 2017) and the plasma sheet (El-Alaoui et al., 2013) are strong evidences in favor of such approach. The magnetostatically quasistable configuration with slow averaged flow velocity can be formed in such a case.

SUMMARY AND CONCLUSION

In this review, we have summarized published results in which the plasma sheet in Earth's magnetosphere has been regarded as a turbulent wake behind an obstacle formed due to high Reynolds number values. Traditional hydrodynamics shows that a turbulent wake should be formed even in the case of a laminar flow before an obstacle. In the magnetosphere, we deal not only with high Reynolds numbers, but also with the interaction between the geomagnetic field and the turbulent solar wind. These solar wind turbulent fluctuations are strongly amplified after crossing the bow shock, forming the plasma flows in the magnetosheath. Here, we have briefly summarized the results of plasma velocity and magnetic field fluctuations in the geomagnetic tail, focusing on the MHD scales, as turbulent motion on such scales makes the main contribution to the plasma transport and mixing. Despite an evident analogy between the turbulent wake behind an obstacle observed in the ordinary flows

and the turbulent geomagnetic tail, this approach for the magnetospheric dynamics is not popular. In the following, we analyzed the potential reasons leading to this situation. We consider that in addition to simplicity of laminar models it is possible to identify three reasons:

- The difficulties in studies of turbulent plasma flows and especially in the detection of large vortices, even using data of multisatellite observations.
- The sheet-like structure of the plasma sheet, which is located between the tail lobes with a very low plasma density, meanwhile the ordinary turbulent wake fills up all region behind an obstacle.
- The erroneous assumption of the mapping of the auroral oval to the plasma sheet, which contradicts the observations of nearly stationary auroral arcs during quiet periods.

In this paper, we have shown that it is possible to overcome all the above mentioned difficulties by considering the latest observational and theoretical works about the morphological mapping of the auroral oval into the equatorial plane. It is important to stress that these works showed that the main part of the auroral oval maps to the outer part of the ring current.

We analyze results of theoretical studies of tail turbulence using the results of the ideal MHD models and the model of the plasma sheet, in which regular flow across the sheet is compensated by eddy diffusion. Here we have pointed out the real advantages of such approach. We have also analyzed the main difficulties of the ideal MHD models, which commonly have not been discussed, connected to the inapplicability of the frozen-in condition. It is well known that in the magnetosphere the averaged plasma velocity is much smaller than the Alfvén velocity. In this case we cannot use the aforementioned approach and the ideal MHD cannot describe plasma systems in magnetostatic equilibrium. Nevertheless, it was possible to obtain the results of near to ideal MHD modeling reproducing the main features of plasma sheet turbulence including comparatively large-scale vortices.

The model of the plasma sheet based on the validity of the plasma and magnetic field pressure balance across the sheet is able to explain the plasma sheet thinning during substorm growth phase due to increase of the dawn-dusk electric field. This model also explains its thickening during expansion phase due to an increase in turbulence and eddy diffusion. It can also help to understand the mechanism of tail lobe filling by the plasma sheet plasma during IMF $B_z > 0$. Development of such mechanism permitted to predict the values of the eddy diffusion coefficients, which were obtained later experimentally, using data of ISEE-2, Interball/Tail Probe, Geotail, CLUSTER and Themis satellites. It takes away the problem of a sheet like turbulent wake behind an obstacle. Nonetheless, this model requires further development and additional verification.

Direct observations of vortices on the scales of ~1–2 R_E showed the reliability to consider the plasma sheet as a turbulent wake behind an obstacle. We discuss a deep connection between the plasma sheet turbulence and the large-scale magnetospheric convection. This relation is analyzed with the aim to identify the vortices corresponding to the driving or integral scale of the tail turbulence. We consider that the large-scale two-vortex magnetospheric convection generated by the magnetospheric plasma pressure gradients is a real source of energy for the turbulence development and may be the driving or integral vortex of such turbulence. However, these suggestions require further investigation.

In this paper we have discussed a number of long standing magnetospheric problems, which are removed due to the existence of the turbulent plasma sheet, including the convection crisis problem. This problem ceases to exist because in case of the turbulent plasma sheet a number of particles in the magnetic flux tube is not conserved, and the approximation of adiabatic compression is not valid for the slow plasma motion. The problem of the location of the substorm expansion phase onset inside the magnetosphere at geocentric distances ~7 R_E also obtains a reasonable explanation as the instability leading to the first auroral arc brightening can be developed only in a region which is comparatively stable before an onset.

We suggest that the long-standing problem of the role of reconnection phenomena on the magnetospheric dynamics obtain new aspect that requires additional discussion. It became clear that the reconnection phenomena are observed inside the turbulent regions and can be considered as a part of the turbulent tail dynamics.

In summary, the plasma sheet turbulence corresponds to an important part of the magnetospheric dynamics and should be studied in detail for the adequate description of the magnetospheric processes.

AUTHOR CONTRIBUTIONS

All authors listed have made a substantial, direct, and intellectual contribution to the work and approved it for publication.

FUNDING

The work of MS was supported by Universidad de Santiago de Chile through the grant: DICYT N° 042031S.

ACKNOWLEDGMENTS

We are grateful for numerous and fruitful discussions on this topic with our colleagues from the Skobeltsyn Institute of Nuclear Physics Moscow State University, the Space Research Institute RAS in Russian Federation, and the Physics Departments at the Universidad de Santiago and Universidad de Chile.

REFERENCES

Akasofu, S.-I. (1964). The development of the auroral substorm. *Planet. Space Sci.* 12, 273–282. doi:10.1016/0032-0633(64)90151-5

Angelopoulos, V., Baumjohann, W., Kennel, C. F., Coroniti, F. V., Kivelson, M. G., Pellat, R., et al. (1992). Bursty bulk flows in the inner central plasma sheet. *J. Geophys. Res.* 97 (A4), 4027–4039. doi:10.1029/91JA02701

Angelopoulos, V., Kennel, C. F., Coroniti, F. V., Pellat, R., Spence, H. E., Kivelson, M. G., et al. (1993). Characteristics of ion flow in the quiet state of the inner plasma sheet. *Geophys. Res. Lett.* 20, 1711–1714. doi:10.1029/93GL00847

Angelopoulos, V., Coroniti, F. V., Kennel, C. F., Kivelson, M. G., Walker, R. J., Russell, C. T., et al. (1996). Multipoint analysis of a bursty bulk flow event on April 11, 1985. *J. Geophys. Res.* 101 (A5), 4967–4989. doi:10.1029/95JA02722

Angelopoulos, V., Mukai, T., and Kokubun, S. (1999). Evidence for intermittency in Earth's plasma sheet and implications for self-organized criticality. *Phys. Plasmas* 6 (11), 4161–4168. doi:10.1063/1.873681

Antonova, E. E. (1985). On nonadiabatic diffusion and adjustment of concentration and temperature in the plasma sheet of the Earth's magnetosphere. *Geomagn. Aeron.* 25, 623–627.

Antonova, E. E. (2000). Large scale magnetospheric turbulence and the topology of magnetospheric currents. *Adv. Space Res.* 25 (7/8), 1567–1570. doi:10.1016/S0273-1177(99)00669-9

Antonova, E. E. (2002). The results of Interball/Tail probe observations the inner magnetosphere substorm onset and particle acceleration. *Adv. Space Res.* 30 (7), 1671–1676. doi:10.1016/S0273-1177(02)00434-9

Antonova, E. E. (2008). Magnetospheric turbulence and properties of magnetospheric dynamics. *Adv. Space Res.* 41, 1677–1681. doi:10.1016/j.asr.2007.05.057

Antonova, E. E., and Ganushkina, N. Y. (1997). Azimuthal hot plasma pressure gradients and dawn-dusk electric field formation. *J. Atmos. Solar-Terrestrial Phys.* 59, 1343–1354. doi:10.1016/S1364-6826(96)00169-1

Antonova, E. E., and Ovchinnikov, I. L. (1996a). Equilibrium of a turbulent current sheet and the current sheet of geomagnetic tail. *Geomagn. Aeron. (Engl. Transl.).* 36, 597–601.

Antonova, E. E., and Ovchinnikov, I. L. (1996b). Current sheet with medium scale developed turbulence and the formation of the plasma sheet of Earth's magnetosphere and solar prominences. *Adv. Space Res.* 19, 1919–1922. doi:10.1016/S0273-1177(97)00101-4

Antonova, E. E., and Ovchinnikov, I. L. (1999). Magnetostatically equilibrated plasma sheet with developed medium-scale turbulence: structure and implications for substorm dynamics. *J. Geophys. Res.* 104, 17289–17297. doi:10.1029/1999JA900141

Antonova, E. E., and Ovchinnikov, I. L. (2001). The model of turbulent plasma sheet during IMF Bz > 0. *Adv. Space Res.* 28 (12), 1747–1752. doi:10.1016/S0273-1177(01)00541-5

Antonova, E. E., and Tverskoy, B. A. (1998). On the nature of electric fields in the Earth's inner magnetosphere (a review). *Int. J. Geomagn. Aeron.* 1 (1), 9–21.

Antonova, E. E., Kirpichev, I. P., and Stepanova, M. V. (2006). Field-aligned current mapping and the problem of the generation of magnetospheric convection. *Adv. Space Res.* 38, 1637–1641. doi:10.1016/j.asr.2005.09.042

Antonova, E. E., Kornilov, I. A., Kornilova, T. A., Kornilova, T. A., Kornilov, O. I., and Stepanova, M. V. (2009). Features of auroral breakup obtained using data of ground-based television observations: case study. *Ann. Geophys.* 27, 1413–1422. doi:10.5194/angeo-27-1413-2009

Antonova, E. E., Pulinets, M. S., Riazantseva, M. O., Znatkova, S. S., Kirpichev, I. P., and Stepanova, M. V. (2012). Turbulence in the magnetosheath and the problem of plasma penetration inside the magnetosphere. *Exploring the solar wind*, ed. M. Lazar (INTECHOPEN.COM). Chapter 18, pp. 417–438.

Antonova, E. E., Vorobjev, V. G., Kirpichev, I. P., and Yagodkina, O. I. (2014). Comparison of the plasma pressure distributions over the equatorial plane and at low altitudes under magnetically quiet conditions. *Geomagn. Aeron.* 54, 278–281. doi:10.1134/S0016793214030025

Antonova, E. E., Vorobjev, V. G., Kirpichev, I. P., Yagodkina, O. I., and Stepanova, M. V. (2015). Problems with mapping the auroral oval and magnetospheric substorms. *Earth Planets Space* 67, 166. doi:10.1186/s40623-015-0336-6

Antonova, E. E., Stepanova, M., Kirpichev, I. P., Ovchinnikov, I. L., Vorobjev, V. G., Yagodkina, O. I., et al. (2018). Structure of magnetospheric current systems and mapping of high latitude magnetospheric regions to the ionosphere. *J. Atmos. Solar-Terrestrial Phys.* 177, 103–114. doi:10.1016/j.jastp.2017.10.013

Baumjohan, W., and Treuman, R. (1996). *Basic space plasma Physics*. London, UK: Imperial College Press, 156–158.

Baumjohann, W., Paschmann, G., and Cattell, C. A. (1989). Average plasma properties in the central plasma sheet. *J. Geophys. Res.* 94, 6597–6606. doi:10.1029/JA094iA06p06597

Baumjohann, W., Paschmann, G., and Lühr, H. (1990a). Characteristics of high-speed ion flows in the plasma sheet. *J. Geophys. Res.* 95, 3801–3809. doi:10.1029/JA095iA04p03801

Baumjohann, W., Paschmann, G., and Lühr, H. (1990b). Pressure balance between lobe and plasma sheet. *Geophys. Res. Lett.* 17 (1), 45–48. doi:10.1029/GL017i001p00045

Birn, J., Hones, E. W., Bame, S. J., and Russell, C. T. (1985). Analysis of 16 plasma vortex events in the geomagnetic tail. *J. Geophys. Res.* 90, 7449–7456. doi:10.1029/JA090iA08p07449

Birn, J., Hesse, M., Haerendel, G., Baumjohann, W., and Shiokawa, K. (1999). Flow braking and the substorm current wedge. *J. Geophys. Res.* 104, 19895–19903. doi:10.1029/1999JA900173

Birn, J., Nakamura, R., Panov, E. V., and Hesse, M. (2011). Bursty bulk flows and dipolarization in MHD simulations of magnetotail reconnection. *J. Geophys. Res.* 116. doi:10.1029/2010JA016083

Birn, J., and Schindler, K. (1983). Self-consistent theory of three-dimensional convection in the geomagnetic tail. *J. Geophys. Res.* 88 (A9), 6969–6980. doi:10.1029/GL007i011p0089710.1029/ja088ia09p06969

Borovsky, J. E., Elphic, R. C., Funsten, H. O., and Thomsen, M. F. (1997). The Earth's plasma sheet as a laboratory for flow turbulence in high-β MHD. *J. Plasma Phys.* 57, 1–34. doi:10.1017/S0022377896005259

Borovsky, J. E., Thomsen, M. F., Elphic, R. C., and Elphic, R. C. (1998). The driving of the plasma sheet by the solar wind. *J. Geophys. Res.* 103 (A8), 17617–17639. doi:10.1029/97JA02986

Borovsky, J. E. (2008). Flux tube texture of the solar wind: strands of the magnetic carpet at 1 AU? *J. Geophys. Res.* 113. doi:10.1029/2007JA012684

Borovsky, J. E., and Funsten, H. O. (2003a). MHD turbulence in the Earth's plasma sheet: dynamics, dissipation, and driving. *J. Geophys. Res.* 108 (A7), 1284. doi:10.1029/2002JA009625

Borovsky, J. E., and Funsten, H. O. (2003b). Role of solar wind turbulence in the coupling of the solar wind to the Earth's magnetosphere. *J. Geophys. Res.* 108 (A6), 1246. doi:10.1029/2002JA009601

Borovsky, J. E. (2020a). Plasma and magnetic-field structure of the solar wind at inertial-range scale sizes discerned from statistical examinations of the time-series measurements. *Front. Astron. Space Sci.* 7, 20. doi:10.3389/fspas.2020.00020

Borovsky, J. E. (2020b). The compression of the heliospheric magnetic structure by interplanetary shocks: is the structure at 1AU a manifestation of solar-wind turbulence or is it fossil structure from the sun? *Front. Astron. Space Sci.* 7, 582564. doi:10.3389/fspas.2020.582564

Borovsky, J. E., Delzanno, G. L., Valdivia, J. A., Moya, P. S., Stepanova, M., Birn, J., et al. (2020). Outstanding questions in magnetospheric plasma physics: the pollenzo view. *J. Atmos. Solar-Terrestrial Phys.* 208, 105377. doi:10.1016/j.jastp.2020.105377

Burch, J. L., Torbert, R. B., Phan, T. D., Chen, L. J., Moore, T. E., Ergun, R. E., et al. (2016b). Electron-scale measurements of magnetic reconnection in space. *Science* 352, aaf2939. doi:10.1126/science.aaf2939

Burch, J. L., Moore, T. E., Torbert, R. B., and Giles, B. L. (2016a). Magnetospheric multiscale overview and science objectives. *Space Sci. Rev.* 199, 5–21. doi:10.1007/s11214-015-0164-9

Califano, F., Cerri, S. S., Faganello, M., Laveder, D., Sisti, M., and Kunz, M. W. (2020). Electron-only reconnection in plasma turbulence. *Front. Phys.* 8, 317. doi:10.3389/fphy.2020.00317

Chamberlain, J. W. (1961). *Physics of the aurora and airglow*. New York and London: Academic Press.

Consolini, G., Marcucci, M. F., and Candidi, M. (1996). Multifractal structure of auroral electrojet index data. *Phys. Rev. Lett.* 76, 4082–4085. doi:10.1103/PhysRevLett.76.4082

Consolini, G., Kretzschmar, M., Lui, A. T. Y., Zimbardo, G., and Macek, W. M. (2005). On the magnetic field fluctuations during magnetospheric tail current

disruption: a statistical approach. *J. Geophys. Res.* 110, A07202. doi:10.1029/2004JA010947

Dungey, J. W. (1961). Interplanetary magnetic field and the auroral zones. *Phys. Rev. Lett.* 6 (1), 47–48. doi:10.1103/PhysRevLett.6.47

Dungey, J. W. (1962). The interplanetary magnetic field and the auroral zones. Tech. Rep. 157. Pennsylvania, USA: The Pennsylvania State University, Scientific Report, University Park.

D'Amicis, R., Telloni, D., and Bruno, R. (2020). The effect of solar-wind turbulence on magnetospheric activity. *Front. Phys.* 8, 604857. doi:10.3389/fphy.2020.604857

El-Alaoui, M., Ashour-Abdalla, M., Richard, R. L., Goldstein, M. L., Weygand, J. M., and Walker, R. J. (2010). Global magnetohydrodynamic simulation of reconnection and turbulence in the plasma sheet. *J. Geophys. Res.* 115. doi:10.1029/2010JA015653

El-Alaoui, M., Richard, R. L., Ashour-Abdalla, M., Walker, R. J., and Goldstein, M. L. (2012). Turbulence in a global magnetohydrodynamic simulation of the Earth's magnetosphere during northward and southward interplanetary magnetic field. *Nonlin. Process. Geophys.* 19, 165–175. doi:10.5194/npg-19-165-2012

El-Alaoui, M., Richard, R. L., Ashour-Abdalla, M., Goldstein, M. L., and Walker, R. J. (2013). Dipolarization and turbulence in the plasma sheet during a substorm: THEMIS observations and global MHD simulations. *J. Geophys. Res. Space Phys.* 118, 7752–7761. doi:10.1002/2013JA019322

Ergun, R. E., Goodrich, K. A., Wilder, F. D., Ahmadi, N., Holmes, J. C., Eriksson, S., et al. (2018). Magnetic reconnection, turbulence, and particle acceleration: observations in the Earth's magnetotail. *Geophys. Res. Lett.* 45, 3338–3347. doi:10.1002/2018GL076993

Ericson, G. M., and Wolf, R. A. (1980). Is the steady convection possible in the Earth's magnetotail. *Geophys. Res. Lett.* 7 (11), 897–900. doi:10.1029/GL007i011p00897

Frank, L. A., Craven, J. D., Gurnett, D. A., Shawhan, S. D., Weimer, D. R., Burch, J. L., et al. (1986). The theta aurora. *J. Geophys. Res.* 91 (A3), 3177–3224. doi:10.1029/JA091iA03p03177

Hones, E. W., Paschmann, G., Bame, S. J., Asbridge, J. R., Sckopke, N., and Schindler, K. (1978). Vortices in magnetospheric plasma flow. *Geophys. Res. Lett.* 5, 1059–1062. doi:10.1029/GL005i012p01059

Hoshino, M., Nishida, A., Yamamoto, T., and Kokubun, S. (1994). Turbulent magnetic field in the distant magnetotail: bottom-up process of plasmoid formation? *Geophys. Res. Lett.* 21, 2935–2938. doi:10.1029/94GL02094

Iijima, T., and Potemra, T. A. (1976). The amplitude distribution of field-aligned currents at northern high latitudes observed by Triad. *J. Geophys. Res.* 81, 2165–2174. doi:10.1029/JA081i013p02165

Keika, K., Nakamura, R., Volwerk, M., Angelopoulos, V., Baumjohann, W., Retinò, A., et al. (2009). Observations of plasma vortices in the vicinity of flow-braking: a case study. *Ann. Geophys.* 27, 3009–3017. doi:10.5194/angeo-27-3009-2009

Keiling, A., Angelopoulos, V., Runov, A., Weygand, J., Apatenkov, S. V., Mende, S., et al. (2009). Substorm current wedge driven by plasma flow vortices: THEMIS observations. *J. Geophys. Res.* 114, a. doi:10.1029/2009JA014114

Kennel, C. F. (1995). *Convection and substorms. Paradigm of magnetospheric phenomenology*. Oxford University Press, 408.

Kirpichev, I. P., Yagodkina, O. I., Vorobjev, V. G., and Antonova, E. E. (2016). Position of projections of the nightside auroral oval equatorward and poleward edges in the magnetosphere equatorial plane. *Geomagn. Aeron.* 56, 407–414. doi:10.1134/S001679321604006X

Kistler, L. M., Baumjohann, W., Nagai, T., and Möbius, E. (1993). Superposed epoch analysis of pressure and magnetic field configuration changes in the plasma sheet. *J. Geophys. Res.* 98 (A6), 9249–9258. doi:10.1029/93JA00630

Kivelson, M. G., and Spence, H. E. (1988). On the possibility of quasi-static convection in the quiet magnetotail. *Geophys. Res. Lett.* 15 (13), 1541–1544. doi:10.1029/GL015i013p01541

Klimontovich, Y. L. (1990). *Turbulent motion and the structure of chaos. The new approach to the statistical theory of open systems*. Dordrecht: Kluwer Academic Publishers, 317.

Klimontovich, Y. L. (1999). *Statistical theory of open systems*. Moscow: Yanus-K, 1.

Lopez, R. E., Sibeck, D. G., McEntire, R. W., and Krimigis, S. M. (1990). The energetic ion substorm injection boundary. *J. Geophys. Res.* 95, 109–117. doi:10.1029/JA095iA01p00109

Lui, A. T. Y. (2001). Multifractal and intermittent nature of substorm-associated magnetic turbulence in the magnetotail. *J. Atmos. Solar-Terrestrial Phys.* 63, 1379–1385. doi:10.1016/S1364-6826(00)00239-X

Maynard, N. C., Heppner, J. P., and Aggson, T. L. (1982). Turbulent electric fields in the nightside magnetosphere. *J. Geophys. Res.* 87 (A3), 1445–1454. doi:10.1029/JA087iA03p01445

Miura, A. (1984). Anomalous transport by magnetohydrodynamic Kelvin-Helmholtz instabilities in the solar wind-magnetosphere interaction. *J. Geophys. Res.* 89, 801–818. doi:10.1029/JA089iA02p00801

Montgomery, D. (1987). "Remarks on the mhd problem of generic magnetospheres and magnetotails," in *Magnetotail Physics*. Editor A. T. Y. Lui (Baltimore: Johns Hopkins University Press), 203.

Nagai, T., Fujimoto, M., Saito, Y., Machida, S., Terasawa, T., Nakamura, R., et al. (1998). Structure and dynamics of magnetic reconnection for substorm onsets with Geotail observations. *J. Geophys. Res.* 103, 4419–4440. doi:10.1029/97JA02190

Nagai, T., Shinohara, I., Fujimoto, M., Machida, S., Nakamura, R., Saito, Y., et al. (2003). Structure of the Hall current system in the vicinity of the magnetic reconnection site. *J. Geophys. Res.* 108 (A10), 1357. doi:10.1029/2003JA009900

Nagata, D., Machida, S., Ohtani, S., Saito, Y., and Saito, T. (2008). Solar wind control of plasma number density in the near-Earth plasma sheet: three-dimensional structure. *Ann. Geophys.* 26, 4031–4049. doi:10.5194/angeo-26-4031-2008

Nakamura, R., Baumjohann, W., Mouikis, C., Kistler, L. M., Runov, A., Volwerk, M., et al. (2004). Spatial scale of high-speed flows in the plasma sheet observed by Cluster. *Geophys. Res. Lett.* 31, a. doi:10.1029/2004GL019558

Nakamura, T. K. M., Stawarz, J. E., Hasegawa, H., Narita, Y., Franci, L., Wilder, F. D., et al. (2020). Effects of fluctuating magnetic field on the growth of the kelvin-helmholtz instability at the Earth's magnetopause. *J. Geophys. Res. Space Phys.* 125, e2019JA027515. doi:10.1029/2019JA027515

Neagu, E., Borovsky, J. E., Gary, S. P., Jorgensen, A. M., Baumjohann, W., and Treumann, R. A. (2005). Statistical survey of magnetic and velocity fluctuations in the near-Earth plasma sheet: international Sun Earth Explorer (ISEE-2) measurements. *J. Geophys. Res.* 110, A05203. doi:10.1029/2004JA010448

Neagu, E., Borovsky, J. E., Thomsen, M. F., Gary, S. P., Baumjohann, W., and Treumann, R. A. (2002). Statistical survey of magnetic field and ion velocity fluctuations in the near-Earth plasma sheet: active Magnetospheric Particle Trace Explorers/Ion Release Module (AMPTE/IRM) measurements. *J. Geophys. Res.* 107, 1098. doi:10.1029/2001JA000318

Ovchinnikov, I. L., and Antonova, E. E. (2017). Turbulent transport of the Earth magnitisphere: review of the results of observations and modeling. *Geomagn. Aeron.* 57 (6), 655–663. doi:10.1134/S0016793217060081

Ovchinnikov, I. L., Antonova, E. E., and Yermolaev, Y. I. (2000). Determination of the turbulent diffusion coefficient in the plasma sheet using the project INTERBALL data. *Cosmic Res.* 38, 557–561. doi:10.1023/a:1026686600686

Ovchinnikov, I. L., Antonova, E. E., and Yermolaev, Y. I. (2002). Plasma sheet heating during substorm and the values of the plasma sheet diffusion coefficient obtained on the base of interball/tail probe observations. *Adv. Space Res.* 30 (7), 1821–1824. doi:10.1016/S0273-1177(02)00456-8

Panov, E. V., Nakamura, R., Baumjohann, W., Angelopoulos, V., Petrukovich, A. A., Retinò, A., et al. (2010). Multiple overshoot and rebound of a bursty bulk flow. *Geophys. Res. Lett.* 37, L08103. doi:10.1029/2009GL041971

Paschmann, G., Haaland, S., and Treumann, R. (2002). Auroral plasma physics. *Space Sci. Rev.* 103 (1-4), 1–485. doi:10.1023/A:1023030716698

Petersen, A., Cattell, C. A., Falthammar, C. G., Formisano, V., Lindqvist, P. A., Mozer, F., et al. (1984). Quasistatic electric field measurements with spherical double probes on the GEOS and ISEE satellites. *Space Sci. Rev.* 37 (3/4), 269–312. doi:10.1007/BF00226365

Petrukovich, A. A., Baumjohann, W., Nakamura, R., Schödel, R., and Mukai, T. (2001). Are earthward bursty bulk flows convective or field-aligned? *J. Geophys. Res.* 106 (A10), 21211–21215. doi:10.1029/2001JA900019

Petrukovich, A. A., Mukai, T., Kokubun, S., Romanov, S. A., Saito, Y., Yamamoto, T., et al. (1999). Substorm-associated pressure variations in the magnetotail plasma sheet and lobe. *J. Geophys. Res.* 104 (A3), 4501–4513. doi:10.1029/98JA02418

Phan, T. D., Eastwood, J. P., Shay, M. A., Drake, J. F., Sonnerup, B. U. Ö., Fujimoto, M., et al. (2018). Electron magnetic reconnection without ion coupling in Earth's turbulent magnetosheath. *Nature* 557, 202–206. doi:10.1038/s41586-018-0091-5

Pinto, V., Stepanova, M., Antonova, E. E., and Valdivia, J. A. (2011). Estimation of the eddy-diffusion coefficients in the plasma sheet using THEMIS satellite data. *J. Atmos. Solar-Terrestrial Phys.* 73, 1472–1477. doi:10.1016/j.jastp.2011.05.007

Priest, E., and Forbes, T. (2000). "Introduction," in *Magnetic reconnection: MHD theory and applications* (Cambridge: Cambridge University Press), 1–47. doi:10.1017/CBO9780511525087.002

Schödel, R., Baumjohann, W., Nakamura, R., Sergeev, V. A., and Mukai, T. (2001). Rapid flux transport in the central plasma sheet. *J. Geophys. Res.* 106 (A1), 301–313. doi:10.1029/2000JA90015910.1029/2000ja900139

Sergeev, V. A., Sauvaud, J.-A., Popescu, D., Kovrazhkin, R. A., Liou, K., Newell, P. T., et al. (2000). Multiple-spacecraft observation of a narrow transient plasma jet in the Earth's plasma sheet. *Geophys. Res. Lett.* 27 (6), 851–854. doi:10.1029/1999GL010729

Shay, M. A., Drake, J. F., Swisdak, M., Dorland, W., and Rogers, B. N. (2003). Inherently three dimensional magnetic reconnection: a mechanism for bursty bulk flows? *Geophys. Res. Lett.* 30, 1345. doi:10.1029/2002GL016267

Sitnov, M., Birn, J., Ferdousi, B., Gordeev, E., Khotyaintsev, Y., Merkin, V., et al. (2019). Explosive magnetotail activity. *Space Sci. Rev.* 215, 31. doi:10.1007/s11214-019-0599-5

Sonett, C. P., Judge, D. L., Sims, A. R., Sims, A. R., and Kelso, J. M. (1960). A radial rocket survey of the distant geomagnetic field. *J. Geophys. Res.* 65, 55–68. doi:10.1029/JZ065i001p000551960

Spanswick, E., Reeves, G. D., Donovan, E., and Friedel, R. H. W. (2010). Injection region propagation outside of geosynchronous orbit. *J. Geophys. Res.* 115. doi:10.1029/2009JA015066

Stawarz, J. E., Ergun, R. E., and Goodrich, K. A. (2015). Generation of high-frequency electric field activity by turbulence in the Earth's magnetotail. *J. Geophys. Res. Space Phys.* 120, 1845–1866. doi:10.1002/2014JA020166

Stepanova, M. V., Antonova, E. E., Bosqued, J. M., Kovrazhkin, R. A., and Aubel, K. R. (2002). Asymmetry of auroral electron precipitations and its relationship to the substorm expansion phase onset. *J. Geophys. Res.* 107 (A7), 1134. doi:10.1029/2001JA003503

Stepanova, M. V., Antonova, E. E., and Troshichev, O. A. (2003). Intermittency of magnetospheric dynamics through non-Gaussian distribution function of PC-index fluctuations. *Geophys. Res. Lett.* 30 (3), 1127. doi:10.1029/2002GL0107010.1029/2002gl016070

Stepanova, M., Vucina-Parga, T., Antonova, E., Ovchinnikov, I., and Yermolaev, Y. (2005). Variation of the plasma turbulence in the central plasma sheet during substorm phases observed by the Interball/tail satellite. *J. Atmos. Solar-Terrestrial Phys.* 67, 1815–1820. doi:10.1016/j.jastp.2005.01.013

Stepanova, M. V., Antonova, E. E., Foppiano, A. J., and Rosenberg, T. J. (2006). Intermittency in the auroral absorption fluctuations as manifestation of magnetospheric turbulence. *Adv. Space Res.* 37 (3), 559–565. doi:10.1016/j.asr.2005.04.112

Stepanova, M., Antonova, E. E., Paredes-Davis, D., Ovchinnikov, I. L., and Yermolaev, Y. I. (2009). Spatial variation of eddy-diffusion coefficients in the turbulent plasma sheet during substorms. *Ann. Geophys.* 27, 1407–1411. doi:10.5194/angeo-27-1407-200910.5194/angeo-27-1407-2009

Stepanova, M., and Antonova, E. E. (2011). Modeling of the turbulent plasma sheet during quiet geomagnetic conditions. *J. Atmos. Solar-Terrestrial Phys.* 73, 1636–1642. doi:10.1016/j.jastp.2011.02.009

Stepanova, M., Pinto, V., Valdivia, J. A., and Antonova, E. E. (2011). Spatial distribution of the eddy diffusion coefficients in the plasma sheet during quiet time and substorms from THEMIS satellite data. *J. Geophys. Res.* 116, A00I24. doi:10.1029/2010JA015887

Tang, C. L. (2012). A plasma flow vortex in the magnetotail and its related ionospheric signatures. *Ann. Geophys.* 30, 537–544. doi:10.5194/angeo-30-537-2012

Troshichev, O. A. (1982). Polar magnetic disturbances and field-aligned currents. *Space Sci. Rev.* 32, 275–360. doi:10.1007/BF00167945

Troshichev, O. A., Antonova, E. E., and Kamide, Y. (2002). Inconsistency of magnetic field and plasma velocity variations in the distant plasma sheet: violation of the "frozen-in" criterion? *Adv. Space Res.* 30 (12), 2683–2687. doi:10.1016/S0273-1177(02)80382-9

Tverskoy, B. A. (1968). *Dynamics of radiation belts of the Earth*. Moscow: Nauka.[in Russian].

Uritsky, V. M., and Pudovkin, M. I. (1998). Low frequency 1/f-like fluctuations of the AE-index as a possible manifestation of self-organized criticality in the magnetosphere. *Ann. Geophys.* 16 (12), 1580–1588. doi:10.1007/s00585-998-1580-x

Uritsky, V. M., Klimas, A. J., Vassiliadis, D., Chua, D., and Parks, G. (2002). Scale-free statistics of spatiotemporal auroral emissions as depicted by POLAR UVI images: dynamic magnetosphere is an avalanching system. *J. Geophys. Res.* 107 (A12), 1426. doi:10.1029/200100028110.1029/2001ja000281

Uritsky, V. M., Klimas, A. J., and Vassiliadis, D. (2003). Evaluation of spreading critical exponents from the spatiotemporal evolution of emission regions in the nighttime aurora. *Geophys. Res. Lett.* 30 (15), 1813. doi:10.1029/2002GL016556

Uritsky, V. M., Donovan, E., Klimas, A. J., and Spanswick, E. (2008). Scale-free and scale-dependent modes of energy release dynamics in the nighttime magnetosphere. *Geophys. Res. Lett.* 35, L21101. doi:10.1029/2008GL035625

Uritsky, V. M., Donovan, E., Klimas, A. J., and Spanswick, E. (2009). Collective dynamics of bursty particle precipitation initiating in the inner and outer plasma sheet. *Ann. Geophys.* 27, 745–753. doi:10.5194/angeo-27-745-2009

Volwerk, M., Vörös, Z., Baumjohann, W., Nakamura, R., Runov, A., Zhang, T. L., et al. (2004). Multi-scale analysis of turbulence in the Earth's current sheet. *Ann. Geophys.* 22, 2525–2533. doi:10.5194/angeo-22-2525-2004

Vörös, Z., Baumjohann, W., Nakamura, R., Runov, A., Zhang, T. L., Volwerk, M., et al. (2003). Multi-scale magnetic field intermittence in the plasma sheet. *Ann. Geophys.* 21, 1955–1964. doi:10.5194/angeo-21-1955-2003

Vörös, Z., Baumjohann, W., Nakamura, R., Volwerk, M., Runov, A., Zhang, T. L., et al. (2004). Magnetic turbulence in the plasma sheet. *J. Geophys. Res.* 109, A11215. doi:10.1029/2004JA010404

Vörös, Z., Baumjohann, W., Nakamura, R., Volwerk, M., and Runov, A. (2006). Bursty bulk flow driven turbulence in the Earth's plasma sheet. *Space Sci. Rev.* 122, 301–311. doi:10.1007/s11214-006-6987-7

Vörös, Z., Yordanova, E., Varsani, A., Genestreti, K. J., Khotyaintsev, Y. V., Li, W., et al. (2017). MMS observation of magnetic reconnection in the turbulent magnetosheath. *J. Geophys. Res. Space Phys.* 122, 11,442–11,467. doi:10.1002/2017JA024535

Vörös, Z., Yordanova, E., Khotyaintsev, Y. V., Varsani, A., and Narita, Y. (2019). Energy conversion at kinetic scales in the turbulent magnetosheath. *Front. Astron. Space Sci.* 6, 60. doi:10.3389/fspas.2019.00060

Wang, C.-P., Lyons, L. R., Nagai, T., Weygand, J. M., and Lui, A. T. Y. (2010). Evolution of plasma sheet particle content under different interplanetary magnetic field conditions. *J. Geophys. Res.* 115. doi:10.1029/2009JA015028

Wang, C.-P., Yue, C., Zaharia, S., Xing, X., Lyons, L., Angelopoulos, V., et al. (2013). Empirical modeling of plasma sheet pressure and three-dimensional force-balanced magnetospheric magnetic field structure: 1. observation. *J. Geophys. Res. Space Phys.* 118, 6154–6165. doi:10.1002/jgra.50585

Watanabe, K., and Sato, T. (1990). Global simulation of the solar wind-magnetosphere interaction: the importance of its numerical validity. *J. Geophys. Res.* 95 (A1), 75–88. doi:10.1029/JA095iA01p00075

Weimer, D. R. (1996). A flexible, IMF dependent model of high-latitude electric potentials having "Space Weather" applications. *Geophys. Res. Lett.* 23 (18), 2549–2552. doi:10.1029/96GL02255

Weygand, J. M., Kivelson, M. G., Khurana, K. K., Schwarzl, H. K., Thompson, S. M., McPherron, R. L., et al. (2005). Plasma sheet turbulence observed by Cluster II. *J. Geophys. Res.* 110, A01205. doi:10.1029/2004JA010581

Xing, X., Lyons, L. R., Angelopoulos, V., Larson, D., McFadden, J., Carlson, C., et al. (2009). Azimuthal plasma pressure gradient in quiet time plasma sheet. *Geophys. Res. Lett.* 36, L14105. doi:10.1029/2009GL038881

Yermolaev, Y. I., Petrukovich, A. A., Zelenyj, L. M., Antonova, E. E., Ovchinnikov, I. L., and Sergeev, V. A. (1995). Investigation of the structure and dynamics of the plasma sheet: the CORALL experiment of the INTERBALL project. *Kosmicheskie Issledovaniia* 38 (1), 16–(22.) [In Russian].

Yordanova, E., Vörös, Z., Varsani, A., Graham, D. B., Norgren, C., Khotyaintsev, Y. V., et al. (2016). Electron scale structures and magnetic reconnection signatures in the turbulent magnetosheath. *Geophys. Res. Lett.* 43, 5969–5978. doi:10.1002/2016GL069191

Zelenyi, L., Artemyev, A., and Petrukovich, A. (2015). Properties of magnetic field fluctuations in the Earth's magnetotail and implications for the general problem of structure formation in hot plasmas. *Space Sci. Rev.* 188, 287–310. doi:10.1007/s11214-014-0037-7

Conflict of Interest: The authors declare that the research was conducted in the absence of any commercial or financial relationships that could be construed as a potential conflict of interest.

frontiers in Astronomy and Space Sciences

PERSPECTIVE
published: 25 March 2021
doi: 10.3389/fspas.2021.618429

An Auroral Alfvén Wave Cascade

C. C. Chaston *

Space Sciences Laboratory, University of California, Berkeley, CA, United States

Folding, kinking, curling and vortical optical forms are distinctive features of most bright auroral displays. These forms are symptomatic of non-linear forcing of the plasma above auroral arcs resulting from the intensification of electrical currents and Alfvén waves along high-latitude geomagnetic field-lines during periods of disturbed space weather. Electrons accelerated to energies sufficient to carry these currents impact the atmosphere and drive visible emission with spatial structure and dynamics that replicate the morphology and time evolution of the plasma region where the acceleration occurs. Movies of active auroral displays, particularly when combined with conjugate *in-situ* fields and plasma measurements, therefore capture the physics of a driven, non-linearly evolving space plasma system. Here a perspective emphasizing the utility of combining *in-situ* measurements through the auroral acceleration region with high time and spatial resolution auroral imaging for the study of space plasma turbulence is presented. It is demonstrated how this special capacity reveals the operation of a cascade of vortical flows and currents through the auroral acceleration region regulated by the physics of Alfvén waves similar to that thought to operate in the Solar wind.

Keywords: Alfvén waves 1, turbulence 2, aurora 3, vorticity 4, cascades 5

OPEN ACCESS

Edited by:
Gaetano Zimbardo,
University of Calabria, Italy

Reviewed by:
Giuseppe Consolini,
Institute for Space Astrophysics and Planetology (INAF), Italy
Robert Lysak,
University of Minnesota Twin Cities, United States
R. P. Sharma,
Indian Institute of Technology Delhi, India

***Correspondence:**
C. C. Chaston
ccc@ssl.berkeley.edu

Specialty section:
This article was submitted to Space Physics, a section of the journal Frontiers in Astronomy and Space Sciences

Received: *16 October 2020*
Accepted: *09 February 2021*
Published: *25 March 2021*

Citation:
Chaston CC (2021) An Auroral Alfvén Wave Cascade. Front. Astron. Space Sci. 8:618429. doi: 10.3389/fspas.2021.618429

INTRODUCTION

Earth's discrete aurora is a consequence of the closure of geomagnetic field-aligned electric currents through the ionosphere and propagating Alfvén waves. The concentration of Earthward field-aligned current from a magnetospheric source due to the convergence of the geomagnetic field requires electron acceleration (Knight, 1973). The region where this acceleration occurs is known as the auroral acceleration region (Paschmann et al., 2003). Qualitatively, this region is bound at low altitudes by the topside ionosphere, below which densities rapidly increase, and at high altitudes by the capacity of hot ambient electrons to carry the current with little or no acceleration. Observations show that the auroral acceleration region extends from >2,000 to ~10,000km in altitude depending on local time, season and solar activity (Karlsson, 2012).

The auroral acceleration region is host to a variety of non-linear processes including the formation of double layers and phase space holes (Ergun et al., 2004) as well as meso-scale plasma instabilities (Selyer and Wu, 2001) that shape the evolving form of auroral displays. These processes decouple magnetospheric convection from the ionosphere through the formation of parallel electric fields. An outer-scale for the operation of these dynamics can be defined by considering the relationship between the cross-field potential in the magnetospheric generator region and that in the ionosphere. Observations above discrete aurora suggest that the field-aligned current ($J_\parallel$) and the potential ϕ along an auroral the field-line can be modeled by the current voltage relation $J_{\parallel I} = K(\phi_M - \phi_I)$ (Lyons, 1981) where the M and I subscripts refer to locations in the magnetosphere and ionosphere respectively. Here, $K = \int \sigma dz$ is the conductance along the geomagnetic field and σ the local conductivity. On the other hand, Ohm's law at the ionosphere provides $J_{\parallel I} = \sum_P \nabla^2_{\perp I} \phi_I$ where Σ_P is the height integrated ionospheric Pedersen conductivity and $\nabla \cdot J = 0$ is used to replace the horizontal

current, $J_{\perp i}$ with $J_{\parallel I}$. Equating $J_{\parallel I}$ from the current voltage relation with that from Ohm's law provides,

$$\phi_M = \left(1 - \lambda_{MI}^2 \lambda \nabla_{\perp I}^2\right)\phi_I \quad (1)$$

after Lysak and Song (1996) where $\lambda_{MI} = (\Sigma_P/\mathrm{K})^{1/2}$ is the magnetosphere-ionosphere coupling scale length. Typically, λ_{MI} = 50–100 km at 100 km altitude. It is apparent from **Eq. 1** that for gradient scale-lengths less than λ_{MI} the majority of the cross-field potential of the generator will not map to the ionosphere but instead will appear along the geomagnetic field above the ionosphere in the form of parallel electric fields. The altitude range over which these parallel fields exist is the auroral acceleration region.

For time varying potential structures or Alfvén waves the same procedure can be performed by replacing the current voltage relation with the cold plasma wave impedance relationship (Stasiewicz et al., 2000),

$$E_\perp = b_\perp V_A \sqrt{1 + k_\perp^2 \lambda_e^2} \quad (2)$$

and using Ampere's law with $E_\perp \approx -\nabla_\perp \phi_\perp$, to provide the result,

$$\phi_M \geq \mu_o \Sigma_P \sqrt{V_{AM} V_{AI}}\left(1 + k_{\perp M}^2 \lambda_{eM}^2\right)\phi_I \quad (3)$$

Here, λ_{eM} and $k_{\perp M}^2$ are the electron inertial length and perpendicular wavenumber in the magnetosphere, and the wave is mapped along the geomagnetic field to the ionosphere using the WKB approximation. Reflection of incoming Alfvén wave Poynting flux from inhomogeneities, particularly at the base of the acceleration region (Chaston, 2006), means that the WKB estimate provides an upper limit for the magnitude of ϕ_I relative to ϕ_M - hence the inequality in **Eq. 3**. Here, it has also been assumed that $n_M/n_I \ll B_{0M}/B_{0I}$ so we can take $k_{\perp I}^2 \lambda_{eI}^2 \to 0$ (n is the plasma density and B_0 is the geomagnetic field strength). For an acceleration region at 1 Earth radius above the surface and densities of the order of 1 and 10^5 cm^{-3} in the acceleration region and ionosphere respectively, one finds $\phi_I/\phi_M < 1$ for a weakly conducting ionosphere (Σ_P = 1 *mho*) but more typically $\phi_I/\phi_M \ll 1$ above auroral arcs where the conductivity is large and the transverse scales are often of the order of acceleration region λ_e (Borovsky, 1993).

For the interpretation of auroral imagery the large size of ϕ_M, relative to ϕ_I, has the significant implication that fast transverse motions in auroral luminosity on scales less than λ_{MI} more likely correspond to structured $E \times B$ flows in the magnetosphere than flows in the ionosphere. These flows advect acceleration structures whose motion is projected onto the ionosphere/upper atmosphere by the precipitating accelerated electrons that such structures drive. The guiding center of these electrons follow ballistic trajectories below the acceleration region subject to the conservation of the first adiabatic invariant along the geomagnetic field before depositing their energy in the upper atmosphere. These trajectories are largely independent of the plasma dynamics operating below the acceleration region and through the topside ionosphere except via coupling/feedback on the acceleration region fields (Lysak, 1990) that drive them Earthward. While the low altitude dynamics may have a turbulent character (Kintner and Seyler,

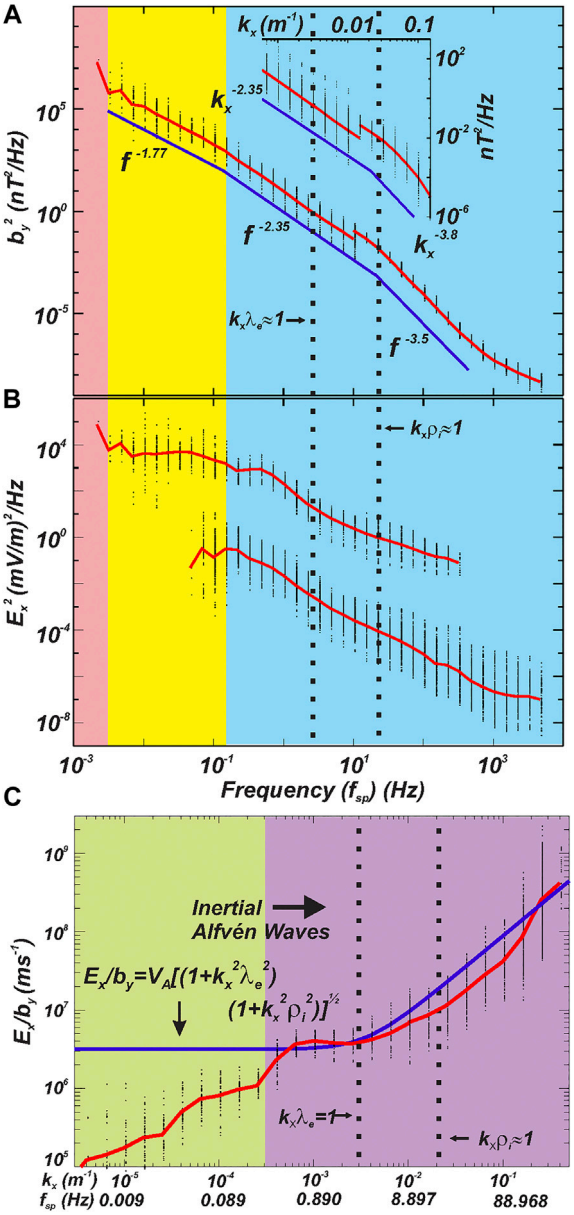

FIGURE 1 | Spectral statistics above "Alfvenic" aurora. **(A)** Average spectral energy density in magnetic field variations (b_Y) perpendicular to the geomagnetic field as a function of frequency (f_{sp}) measured in the spacecraft frame. The inset plot shows the same result but as a function of the wavenumber measured perpendicular to the geomagnetic field (k_x). The offset in these curves at ~10 Hz is due to the transition from fluxgate to search coil magnetometer measurements. The later are recorded only during intervals of enhanced auroral activity where spectral energy densities are larger leading to the offset. **(B)** Average spectral energy density in electric field variations (E_x) perpendicular to both the geomagnetic field and the magnetic field variations shown in part **(A)**. The two curves shown correspond to measurements made in survey and burst instrument modes with the burst mode data downshifted by 4 orders of magnitude for visibility. The black bars are composed of points representing individual measurements in each frequency bin. **(C)** Observed average value (red) of the ratio E_x/b_y as a function of perpendicular wavenumber (k_x) and f_{sp}. The blue line shows the ratio given by the dispersion relation for inertial Alfvén waves based on locally observed parameters [Modified from Chaston et al. (2008)].

1985; Pécseli, 2015) this turbulence is not the topic of this "Perspective" article. This distinction is supported by the fact that observed ionospheric electric fields in and around auroral arcs (e.g., Vondrak, 1981) are insufficient to account for the rapid motions of optical features in the aurora; while in contrast, the electric fields observed *in-situ*, in and around regions of auroral electron acceleration have magnitudes and orientations consistent with these motions (Hallinan, 1981). Consequently, the motion of optical elements within regions of luminosity provide the capacity to image flows and electric fields in the acceleration region (Hallinan, 1981). This capacity is augmented by the fact that auroral luminosity for the most commonly observed lines in bright discrete aurora is proportional to the energy flux of field-aligned precipitating electrons (Rees and Jones, 1973). This relationship has been demonstrated via simulation and observations specifically for Alfven wave accelerated electron distributions (Chaston et al., 2003). The motion and intensity of bright discrete auroral forms can therefore be considered projections of the plasma dynamics and field-line integrated dissipation through the auroral acceleration region.

In the following we draw on previously reported observations to present a perspective on the relationship between the spectral scaling of field structures through the acceleration region and the motions of optical elements within auroral forms. The consistency of the spectral scaling observed *in-situ* with that observed via auroral imaging supports the connection of $E \times B$ drifts through the acceleration region to small-scale auroral motions and provides evidence for the operation of a turbulence-like Alfvén wave cascade above bright dynamic auroral arcs.

THE TURBULENT ALFVÉNIC AURORA

Figure 1 shows spectrograms of the spectral energy density in electric and magnetic fields through the auroral acceleration region as derived from statistics reported from the FAST mission (Chaston et al., 2008). FAST had the unique capacity to measure the electric field at several points in the spacecraft spin plane allowing unambiguous measurement of $k_\perp$ (k_x in **Figure 1**). Under the assumption that at each spacecraft frame frequency this measurement applies to both the magnetic and electric fields, the k-spectra in $b_\perp$ (b_y in **Figure1A**) and $E_\perp$ (E_x in **Figure1B**) were derived. The measurements shown in **Figure 1**, apply specifically to what is termed the "Alfvénic" aurora. The "Alfvénic" aurora is characterized by electric and magnetic field variations that obey the local Alfvénic impedance relation of **Eq. 2**, as shown in **Figure 1C** where the finite gyro-radius term is included. In the example shown here, the Alfvénic nature of the fields extends over the range $10^{-4} \lesssim k_\perp \lesssim 10^{-1}\ \mathrm{m}^{-1}$ or scales from ~60 km, representative of λ_{MI}, down to 10 s of meters, encompassing λ_e and even reaching ion gyro-radii (ρ_i). Significantly, over the range from $10^{-4} \lesssim k_\perp \lesssim 10^{-2}\ \mathrm{m}^{-1}$ there exists a distinct power-law scaling where the energy density of the fluctuation varies as $b_\perp^2/\Delta k_\perp \propto k_\perp^{-7/3}$. These relationships along with an analysis of structure functions motivated Chaston et al. (2008) to suggest the operation of a Kolmogorov-like turbulent cascade above "Alfvenic" aurora much in the manner of critically balanced cascades postulated by Goldreich and Sridhar (1997) and more recently by Howes et al. (2008) in the Solar wind. The operation of such a cascade above dynamic aurora was first proposed by Seyler (1990) based on 3-D fluid-kinetic simulations.

Indeed, the measurements shown in **Figure 1** bear remarkable similarity to those reported in turbulent Alfvénic fields on kinetic scales in the solar wind. In the work of Bale et al., (2005), for example, spectral energy densities with a Kolmogorov $b_\perp^2/\Delta k_\perp \propto k_\perp^{-5/3}$ dependency are observed on scales larger than Alfvén wave dispersive scale lengths, while within the dispersive range (i.e. $k_\perp \rho_i \gtrsim 1$) a scaling close to $b_\perp^2/\Delta k_\perp \propto k_\perp^{-7/3}$ is found. While this is much like that shown in **Figure 1** an important difference, is that above aurorae, $\beta < m_e/m_i$ where β is plasma beta and m_e and m_i are respectively the electron and ion masses. Under these circumstances the largest dispersive scale length for Alfvén waves is λ_e rather than ρ_i. As a consequence, while the turbulent fields on kinetic scales in the solar wind are sometimes described as kinetic Alfvén waves, in the auroral acceleration region a more appropriate description is that of inertial Alfvén waves (Stasiewicz et al., 2000). Here, the reflection of magnetospherically driven Earthward propagating waves off the ionosphere naturally provides the counter-propagation required to facilitate the cross-scale cascade. The study of the operation and consequences of this cascade process above aurorae has the special advantage that its operation is manifest in visible emissions that can be imaged.

IMAGING AN ALFVÉNIC CASCADE

The Reimei spacecraft (Sakanoi et al., 2003) provided conjugate measurements of accelerated electrons and high temporal/spatial resolution imaging of evolving auroral luminosity. Example measurements of a rapidly evolving "Alfvénic" auroral arc are shown in **Figure 2**. This identification is based on the relatively flat electron spectra shown in **Figure 2A** as opposed to the clear mono-energetic peak or inverted-V attributed to "quasi-static" discrete aurora. The snapshots in **Figure 2B-F** show luminosity over a 66 by 66 km field of view (FOV) at 110 km altitude and ~670 nm on a logarithmic scale. Note that this prompt emission is a consequence of energetic electron precipitation (Lanchester et al., 2009; Frey et al., 2010). A bright feature with evolving vortical forms at the upper edge of the region of luminosity can be identified in each snapshot. This feature moves upward through the FOV with the location of the magnetic foot-point of the spacecraft on each image shown by the white box. This allows identification of the electron spectrogram in **Figure 2A** driving the luminosity at that location. Following this bright "arc" is a region of swirling variations in luminosity corresponding to larger vortical features. These snapshots are at a cadence of 0.6 s or every fifth frame retuned by the Reimei camera.

By cross-correlating the consecutive images at full resolution it is possible to measure the velocity field of the features observed in regions of luminosity. At the time of these observations the camera looked along the geomagnetic field nearly normal to the Earth's surface so that the velocities observed are perpendicular to B_0, The cross-correlation is performed using a wavelet approach as described in Chaston et al. (2010). This technique allows the

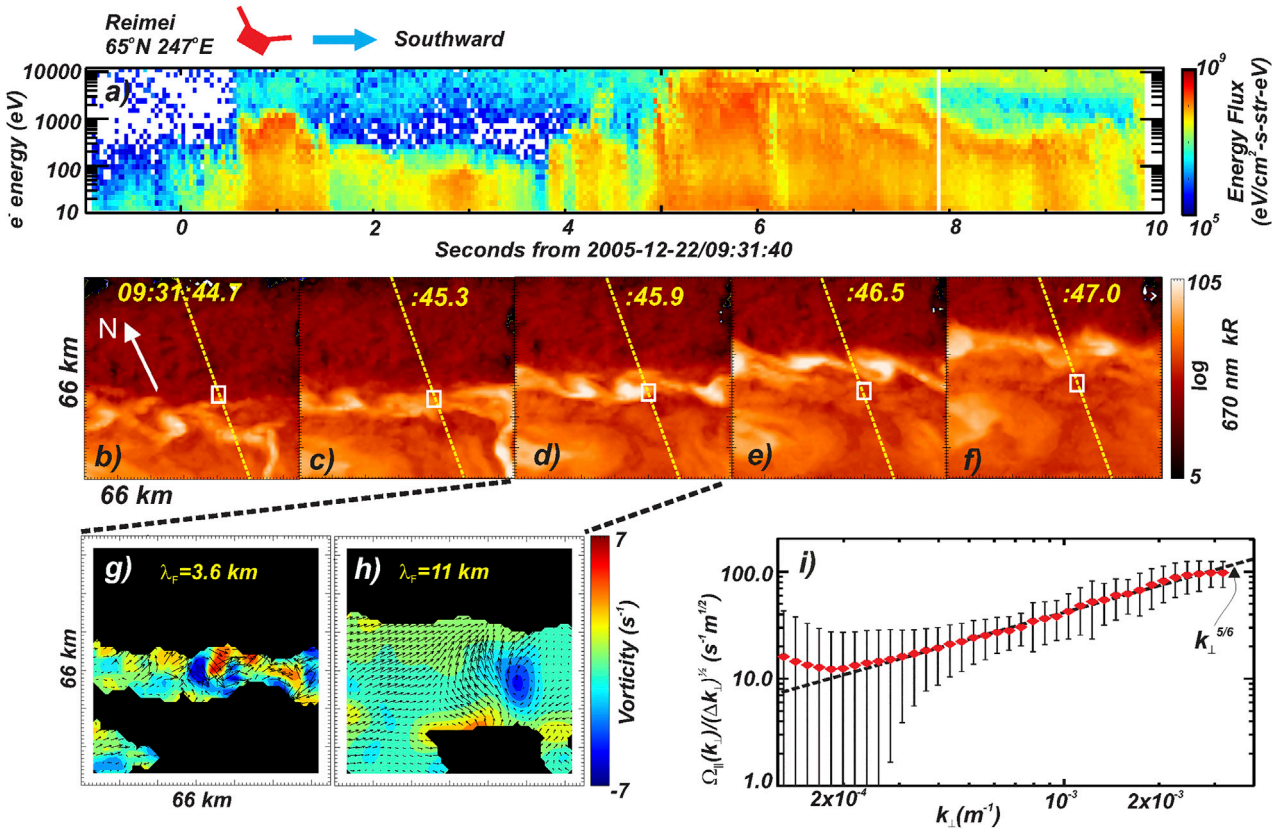

FIGURE 2 | Reimei spacecraft measurements above an "Alfvenic" auroral arc. **(A)** Omni-directional electron energy spectrogram. **(B–F)** Snapshots at ~670 nm of the evolving luminosity. Yellow trace shows the trajectory of the spacecraft mapped onto each image with the white box indicating the spacecraft magnetic foot-point at the snapshot time. **(G–H)** Optical vorticity measurements derived from cross-spectral analysis between snapshot d and the next frame capture (not shown) at the scales indicated. Arrows show optical flow direction and relative speed. **(I)** Vorticity spectrum derived from the full resolution measurements over the time-range comprising the sequence **(B–F)**. Red dots show the log normal average in each $k_\perp$ bin while the error bars show 1 standard deviation.

decomposition of the optical motions as a function of scale subject to a cross-spectral correlation factor that allows the removal of noise. The analysis is performed on the 2-D spatial derivative of the luminosity on scales defined by the wavelet used. Results from this analysis using Paul wavelets (Torrence and Compo, 1998) applied to the central snapshot shown in **Figures 2D**, and the snapshot 0.12 s later (not shown) for scales of 3.6 and 11 km are presented in **Figures 2G,H**. Here the arrows indicate the direction and magnitude of the velocity at half resolution while the color scale shows the vorticity ($\Omega_\parallel = \nabla \times v_\perp$) derived by finite differencing the velocity field measurements. B_0 is into the page with blue showing clockwise rotation about B_0 while red is anticlockwise. If these flows correspond to $E \times B$ drifts, then blue corresponds to converging electric fields, or negative space charge for electrostatic fields. The regions in black in each frame indicate those regions where a reliable determination could not be found.

Figure 2G shows there is considerable structure in the vorticity on small scales distributed over the width of the bright "arc". As indicated by the arrows these features arise from fast motions of the order of 20 km/s composed of both shears and rotational flows. Nested regions of positive and negative vorticity are observed representing structured electric fields on kilometer scales. On larger scales the flow is smoother and a prominent peak in negative vorticity or clockwise rotation can be identified in the center right portion of **Figure 2H**. Performing the same analysis for subsequent image pairs shows rapid temporal variations in the small-scale vorticity with these features advected in the larger scale flow. Compiling statistics over the whole image sequence shown in **Figures 2B–F** provides the spectrum presented in **Figure 2I**. Here, each point represents the average of the distribution in vorticity at each scale normalized by the bandwidth occupied by each spectral bin in k-space. The error bars shown correspond to the standard deviation. The spectrum is well described by a power law varying as $\Omega_\parallel(k_\perp)/\Delta k_\perp^{1/2} \propto k_\perp^{5/6}$ over the range $2 \times 10^{-4} \lesssim k_\perp < 3 \times 10^{-3}$ where $k_\perp = 2\pi/\lambda_F$ and λ_F is the Fourier wavelength of the wavelet (Torrence and Compo, 1998).

DISCUSSION AND CONCLUSION

The *in-situ* measurements and auroral imagery presented above suggest the operation of a turbulent cascade of inertial Alfvén waves

in the auroral acceleration region. Over a range of scales extending from ~60 km down to 10 s of meters perpendicular to B_0 the relationship between the electric and magnetic fields is that expected from a broad k-spectrum of Alfvén waves. This range comprises physical length scales extending from λ_{MI}, down to less than λ_e in the acceleration region. The spectral scaling of the magnetic field over the wavenumber subrange from $10^{-4} \lesssim k_\perp \lesssim 10^{-2}$ m^{-1} is well described by the power law, $b_\perp^2/\Delta k_\perp \propto k_\perp^{-7/3}$ while the imaged optical vorticity, within the same range, scales as $\Omega_\parallel(k_\perp)/\Delta k_\perp^{1/2} \propto k_\perp^{5/6}$. A direct comparison between the *in-situ* fields measurements and imaged vorticity measurements requires conjugate measurements, however these spectral results are statistical in nature and both pertain to "Alfvénic" aurora. This allows a test to determine if the motions observed in the luminosity are statistically consistent with those expected of flows in the measured *in-situ* electromagnetic fields, and moreover, if the spectral trends observed reflect those expected from a turbulent cascade of Alfvén waves.

In inertial Alfvén waves the plasma moves at the $E \times B$ drift speed so that the eddy turnover time is $\tau \sim 1/k_\perp v_\perp = B_0/b_\perp k_\perp V_A \sqrt{1 + k_\perp^2 \lambda_e^2}$ where based on the result shown in **Figure 1C** we use $E_\perp = b_\perp V_A \sqrt{1 + k_\perp^2 \lambda_e^2}$ (**Eq. 2**). On the other hand, the energy transport rate through the cascade is $\varepsilon(k) = H(k)/\tau(k)$, So taking $H = b_\perp^2/2\mu_o$ and substituting for τ provides $\varepsilon(k) = b_\perp^3 k_\perp V_A \sqrt{1 + k_\perp^2 \lambda_e^2}/2\mu_o B_0$. Noting that in classical turbulence, $\varepsilon(k)$ is invariant with scale (Frisch, 1995) one finds after rearranging,

$$b_\perp^2 \Big/ dk_\perp \propto k^{-5/3} \left(1 + k_\perp^2 \lambda_e^2\right)^{-1/3} \tag{4}$$

which for $k_\perp \lambda_e > 1$ provides $b_\perp^2/dk_\perp \propto k^{-7/3}$ as observed. On the other hand, defining the vorticity as $\Omega_\parallel = \nabla \times v_\perp$ and again using $E_\perp = b_\perp V_A \sqrt{1 + k_\perp^2 \lambda_e^2}$ with $b_\perp^2/dk_\perp \propto k^{-7/3}$ provides,

$$\Omega_\parallel(k_\perp) \Big/ dk_\perp^{1/2} \propto k_\perp^{-1/6} \sqrt{1 + k_\perp^2 \lambda_e^2} \tag{5}$$

which in the limit $k_\perp \lambda_e > 1$ returns $\Omega_\parallel(k_\perp)/dk_\perp^{1/2} \propto k_\perp^{5/6}$ as derived from the imagery. **Eq. 4** and **Eq. 5** provide an internally consistent description of the observed spectral scaling in the fields and optical vorticity for $k_\perp \lambda_e > 1$ based on the constancy of energy transport across scales through a cascade of Alfvén waves. The same scalings are returned by 3-D fluid-kinetic simulations of auroral structures (Chaston et al., 2011)

While this model may describe the large wavenumber portion of the spectrum, **Figures 1A** and **2I** respectively show that the $b_\perp^2/dk_\perp \propto k_\perp^{-7/3}$ and $\Omega_\parallel(k_\perp)/dk_\perp^{1/2} \propto k_\perp^{5/6}$ scalings extend to $k_\perp \lambda_e \lesssim 1$. Consequently, there is additional physics operating at large scales or small $k_\perp \lambda_e$. A clue as to the nature of this physics is provided by the fact that the lower limit of the range over which this scaling prevails is qualitatively consistent with the M-I coupling scale length which depends on the effective field-line conductivity. If we define $\sigma = \frac{1}{\mu_o \lambda_e^2 \nu}$, where ν is an anomalous collision frequency, the impedance relationship for the inertial Alfvén wave becomes (Lysak and Carlson, 1981),

$$E_\perp = b_\perp V_A \sqrt{1 + k_\perp^2 \lambda_e^2 (1 + i\nu/\omega)} \tag{6}$$

Where ω is the wave frequency. Re-deriving **Eq. 4** and **Eq. 5** using **Eq. 6** shows that the expression under the radical in both cases is replaced by that in **Eq. 6**. Since $\omega \ll \Omega_i$, ν can be quite small relative to Ω_i while still providing $\left|k_\perp^2 \lambda_e^2 (1 + i\nu/\omega)\right| > 1$ even if $k_\perp \lambda_e \lesssim 1$. Under these circumstances the observed scaling relations, $b_\perp^2/dk_\perp \propto k_\perp^{-7/3}$ and $\Omega_\parallel(k_\perp)/dk_\perp^{1/2} \propto k_\perp^{5/6}$, will be retained in the Alfvén wave model on scales larger than several inertial lengths.

An estimate for the value of ν, independent of that required to account for the observed spectral scaling, is not currently available and the physics it represents goes beyond the scope of this article. It may however, be a consequence of localized irregularities in phase space (Ergun et al., 1998) or non-local kinetic effects (Rankin et al., 1999) intrinsic to current closure in Alfvén waves for finite electron temperatures in the converging geomagnetic field. In either case, the requirement for finite field-line conductance on large scales parameterized here in terms of ν, highlights the importance of electron kinetics in defining the cross-scale cascade observed in "Alfvénic" aurora.

Finally, an analysis similar to that above has been performed to examine the scale dependency of variations in auroral luminosity (Chaston, 2015), albeit within an "inverted-V" or "quasi-static" auroral arc with a different scaling in $b_\perp^2/dk_\perp$. That analysis showed that the integrated dissipation through the acceleration region predicted by the Alfvén wave cascade model reproduces the observed scale dependency of luminosity, and, similar to those results derived above, requires an effective field-line conductivity to reproduce the observed scaling at small $k_\perp \lambda_e$. Given that this dissipation should reduce the spectral index of the energy cascade it is surprising how well the observed k-spectra in $b_\perp^2/dk_\perp$ replicates the predicted spectral-scaling from the Kolmogorov-like treatment developed above. This result suggests that either the energy transport rate across scales is sufficiently rapid that the losses through dissipation are relatively small, or that the dissipation on scales less than λ_{MI} is such that the effect is uniform across the observed range. This a topic requiring further investigation. Nonetheless, the fact that the observed statistics describing the spectral scaling in k-space of the magnetic energy density, vorticity and luminosity can all be derived from the assumption of a constant cross-scale energy transport rate is evidence that a turbulent cascade operates above "Alfvénic" aurora.

DATA AVAILABILITY STATEMENT

Publicly available datasets were analyzed in this study. This data can be found here: the JAXA website https://darts.isas.jaxa.jp/stp/

reimei/ and the FAST data repository at https://cdaweb.gsfc.nasa.gov/index.html.

AUTHOR CONTRIBUTIONS

CC performed the analysis/interpretation in this report and is solely responsible for the results described.

FUNDING

This research was supported by NASA grant NNX17AI55G.

ACKNOWLEDGMENTS

CC thanks the FAST and Reimei teams for the providing the calibrated measurements used in this research.

REFERENCES

Bale, S. D., Kellogg, P. J., Mozer, F. S., Horbury, T. S., and Reme, H. (2005). Measurement of the electric fluctuation spectrum of magnetohydrodynamic turbulence. *Phys. Rev. Lett.* 94, 215002. doi:10.1103/PhysRevLett.94.215002

Borovsky, J. E. (1993). Auroral arc thicknesses as predicted by various theories. *J. Geophys. Res.* 98 (A4), 6101–6138. doi:10.1029/92JA02242

Chaston, C. C., Peticolas, L. M., Bonnell, J. W., Carlson, C. W., Ergun, R. E., and McFadden, J. P. (2003). The width and brightness of auroral arcs driven by inertial Alfvén waves. *J. Geophys. Res.* 108, 1091. doi:10.1029/2001ja007537

Chaston, C. C., Salem, C., Bonnell, J. W., Carlson, C. W., Ergun, R. E., Strangeway, R. J., et al. (2008). The turbulent Alfvénic aurora. *Phys. Rev. Lett.* 100, 175003. doi:10.1103/PhysRevLett.100.175003

Chaston, C. C. (2015). "Inverted-V auroral arcs and Alfvén waves," in *Auroral dynamics and space weather*. Editors Y. Zhang and L. J. Paxton (Hoboken, NJ: John Wiley & Sons). doi:10.1002/9781118978719.ch3

Chaston, C. C., Seki, K., Sakanoi, T., Asamura, K., Hirahara, M., and Carlson, C. W. (2011). Cross-scale coupling in the auroral acceleration region. *Geophys. Res. Lett.* 38, L20101. doi:10.1029/2011GL049185

Chaston, C. C., Seki, K., Sakanoi, T., Asamura, K., and Hirahara, M. (2010). Motion of aurorae. *Geophys. Res. Lett.* 37, L08104. doi:10.1029/2009GL042117

Chaston, C. C. (2006). ULF waves and auroral electrons. *Geophys. Monogr. Ser.*, 169, 239. doi:10.1029/169GM16

Ergun, R. E., Carlson, C. W., McFadden, J. P., Mozer, F. S., Delory, G. T., Peria, W., et al. (1998). FAST satellite observations of large-amplitude solitary structures. *Geophys. Res. Lett.* 25, 2041.

Ergun, R. E., Andersson, L., Main, D., Su, Y.-J., Newman, D. L., Goldman, M. V., et al. (2004). Auroral particle acceleration by strong double layers: the upward current region. *J. Geophys. Res.* 109, A12220. doi:10.1029/2004JA010545

Frey, H. U., Amm, O., Chaston, C. C., Fu, S., Haerendel, G., Juusola, L., et al. (2010). Small and meso-scale properties of a substorm onset auroral arc. *J. Geophys. Res.* 115, A10209. doi:10.1029/2010JA015537

Frisch, U. (1995). *Turbulence: the legacy of A. N. Kolmogorov*. Cambridge, England: Cambridge University Press.

Goldreich, P., and Sridhar, S. (1997). Magnetohydrodynamic turbulence revisited. *Astrophys. J.* 485, 680–688. doi:10.1086/304442

Hallinan, T. J. (1981). "The distribution of vorticity in auroral arcs," in *Physics of auroral arc formation, Geophys. Monogr. Ser.* Editors S.-I. Akasofu and J. R. Kan (Washington, DC: AGU), Vol. 25, 42. doi:10.1029/GM025p0042

Howes, G. G., Cowley, S. C., Dorland, W., Hammett, G. W., Quataert, E., and Schekochihin, A. A. (2008). A model of turbulence in magnetized plasmas: implications for the dissipation range in the solar wind. *J. Geophys. Res.* 113, A05103. doi:10.1029/2007JA012665

Karlsson, T. (2012). "The acceleration region of stable auroral arcs," in *Auroral phenomenology and magnetospheric processes: Earth and other planets, Geophysical Monograph, 197*. Editors A. Keiling, E. Donovan, F. Bagenal, and T. Karlsson (Washington, DC: AGU). doi:10.1029/2011GM001179

Kintner, P. M., and Seyler, C. E. (1985). The status of observations and theory of high latitude ionospheric and magnetospheric plasma turbulence. *Space Sci. Rev.* 41, 91–12. doi:10.1007/bf00241347

Knight, S. (1973). Parallel electric fields. *Planet. Space Sci.* 21, 741–750. doi:10.1016/0032-0633(73)90093-7

Lanchester, B. S., Ashrafi, M., and Ivchenko, N. (2009). Simultaneous imaging of aurora on small scale in OI (777.4 nm) and N21P to estimate energy and flux of precipitation. *Ann. Geophys.* 27, 2881–2891. doi:10.5194/angeo-27-2881-2009

Lyons, L. R. (1981). "The field aligned current versus electric potential relation and auroral electrodynamics," in *Physics of auroral arc formation, Geophys. Monogr. Ser.* Editors S.-I. Akasofu and J. R. Kan (Washington, DC: AGU), Vol. 25, 252.

Lysak, R. L., and Carlson, C. W. (1981). The effect of microscopic turbulence on magnetosphere-ionosphere coupling. *Geophys. Res. Lett.* 8, 269–272. doi:10.1029/gl008i003p00269

Lysak, R. L. (1990). Electrodynamic coupling of the magnetosphere and ionosphere. *Space Sci. Rev.* 52, 33. doi:10.1007/BF00704239

Lysak, R. L., and Song, Y. (1996). Coupling of Kelvin-Helmholtz and current sheet instabilities to the ionosphere: a dynamic theory of auroral spirals. *J. Geophys. Res.* 101, 15411–15422. doi:10.1029/96JA00521

G. Paschmann, S. Haaland, and R. Treumann (Editors) (2003). *Auroral plasma physics*. Dodrecht, Netherlands: Kluwer Academic.

Pécseli, H. L. (2015). Spectral properties of electrostatic drift wave turbulence in the laboratory and the ionosphere. *Ann. Geophys.* 33, 875–900. doi:10.5194/angeo-33-875-2015

Rankin, R., Samson, J. C., and Tikhonchuk, V. T. (1999). Parallel electric fields in dispersive shear Alfvén waves in the dipolar magnetosphere. *Geophys. Res. Lett.* 26, 3601. doi:10.1029/1999gl010715

Rees, M. H., and Jones, R. A. (1973). Time dependent studies of the aurora-II. Spectroscopic morphology. *Planet. Space Sci.* 21, 1213. doi:10.1016/0032-0633(73)90207-9

Sakanoi, T., Okano, S., Obuchi, Y., Kobayashi, T., Ejiri, M., Asamura, K., et al. (2003). Development of the multi-spectral auroral camera onboard the INDEX satellite. *Adv. Space Res.* 32, 379–384. doi:10.1016/s0273-1177(03)90276-6

Seyler, C. E. (1990). A mathematical model of the structure and evolution of small-scale discrete auroral arcs. *J. Geophys. Res.* 95 (A10), 17199–17215. doi:10.1029/JA095iA10p17199

Seyler, C. E., and Wu, K. (2001). Instability at the electron inertial scale. *J. Geophys. Res.* 106, 21623–21644. doi:10.1029/2000JA000410

Stasiewicz, K., Bellan, P., Chaston, C., Kletzing, C., Lysak, R., Maggs, J., et al. (2000). Small scale Alfvénic structure in the aurora. *Space Sci. Rev.* 92, 423–533. doi:10.1023/a:1005207202143

Torrence, C., and Compo, G. P. (1998). A practical guide to wavelet analysis. *Bull. Am. Meteorol. Soc.* 79, 61–78. doi:10.1175/1520-0477(1998)079<0061:apgtwa>2.0.co;2

Vondrak, R. R. (1981). "Chatanika radar measurements of the electrical properties of auroral arcs," in *Physics of auroral arc formation*. Editors S.-I. Akasofu and J. Kan. doi:10.1029/GM025p0185

Conflict of Interest: The author declares that the research was conducted in the absence of any commercial or financial relationships that could be construed as a potential conflict of interest.

frontiers in Astronomy and Space Sciences

REVIEW
published: 30 March 2021
doi: 10.3389/fspas.2020.617792

Langmuir Turbulence in the Auroral Ionosphere: Origins and Effects

Hassanali Akbari[1]*, *James W. LaBelle*[2] *and David L. Newman*[3]

[1]Heliophysics Science Division, NASA Goddard Space Flight Center, Greenbelt, MD, United States, [2]Department of Physics and Astronomy, Dartmouth College, Hanover, NH, United States, [3]Center for Integrated Plasma Studies, University of Colorado Boulder, Boulder, CO, United States

Theory and observations of Langmuir waves and turbulence induced in the auroral ionosphere by electron beams of magnetospheric-origin are reviewed. The theoretical discussions include a brief description of the electrostatic dispersion relation, excitation of Langmuir waves by electron beams, and the stability of beam distributions. The theory of Langmuir turbulence—including the parametric decay instability and wave collapse—is also briefly discussed. The main focus of the review, however, is on the observations of Langmuir waves and turbulence in the ionosphere by *in-situ* and ground-based sensors. A summary of five decades of *in-situ* wave and particle observations is presented and combined with a collection of more recent results from ground-based instruments. The ground-based observations include signatures of Langmuir turbulence in the form of coherent echoes in incoherent scatter radar measurements; signatures of electron beams in the form of auroral morphologies recorded by high-speed, high-resolution optical imagers; and electromagnetic emissions received on the ground at high latitudes. Uniting the various observations obtained by the vastly different sensors is shown to provide further insight into the micro-scale processes that occur in the ionosphere. Also discussed in this review is the potential of the ground-based sensors to provide a broader spatial and temporal context for single-point *in-situ* measurements of such processes.

Keywords: Langmuir turbulence, auroral ionosphere, beam-plasma interactions, plasma waves, radar echoes

OPEN ACCESS

Edited by:
Zoltan Voros,
Space Research Institute, Austrian Academy of Sciences, Austria

Reviewed by:
Peter Haesung Yoon,
University of Maryland, College Park, United States
Huishan Fu,
Beihang University, China
Evgeny V. Mishin,
Air Force Research Laboratory, United States

***Correspondence:**
Hassanali Akbari
hassanali.akbari@nasa.gov

Specialty section:
This article was submitted to Space Physics, a section of the journal Frontiers in Astronomy and Space Sciences

Received: *15 October 2020*
Accepted: *21 December 2020*
Published: *30 March 2021*

Citation:
Akbari H, LaBelle JW and Newman DL (2021) Langmuir Turbulence in the Auroral Ionosphere: Origins and Effects. Front. Astron. Space Sci. 7:617792. doi: 10.3389/fspas.2020.617792

1 INTRODUCTION

The Earth's auroral ionosphere is characterized by the presence of intense particle precipitation from the magnetosphere. The large amount of energy deposited by accelerated electrons and ions in this region induces a range of multi-scale processes that ultimately shape the plasma dynamics at high latitudes. In the same region, collision-less interactions of the streaming electrons with the background plasma leads to the appearance of micro-scale phenomena—which, although they have smaller effects on large-scale plasma dynamics, are extremely rich in physics. Excitation of Langmuir waves by electron beams is an example of such processes.

With typical amplitudes of tens to hundreds of mV/m, Langmuir waves are among the strongest electrostatic waves in the auroral ionosphere (e.g., McFadden et al., 1986; Kintner et al., 1995). The waves are known to be very common and are detected on nearly every auroral zone pass in which precipitating electrons are observed (Kintner et al., 1995). A large body of observational works from satellites such as Freja (Lundin et al., 1994), FAST (Pfaff et al., 2001), as well as sounding rockets have uncovered an extremely wide range of processes associated with the waves. These include nonlinear

wave-wave interactions, linear mode conversions, modifications of electron distributions by the waves, etc. Explaining such observational features has inspired intense research over the past several decades.

While the large body of theoretical, numerical, and experimental works on Langmuir waves in space plasmas have significantly advanced our understanding of these processes on the fundamental level, certain observational features from ground-based sensors at high latitudes have emerged in the past several years that deserve further attention. For example, Langmuir caviton formation and collapse induced by natural electron beams—as one of the most discussed feature of Langmuir turbulence—has been consistently absent in measurements by *in-situ* instruments in the ionosphere. Nevertheless, in the past decade or two, incoherent scatter radars at high latitudes have commonly detected echoes from the auroral ionosphere that include signatures of Langmuir collapse (e.g., Akbari et al., 2012; Isham et al., 2012). Furthermore, despite their large amplitudes and their abundance in the auroral plasma, possible effects of Langmuir waves on the local plasma dynamics have remained largely unaddressed by the *in-situ* observations. This is partly due to sparsity and limitations of single-point measurements by rockets and satellites. Such limitations, however, do not apply to volumetric measurements by stationary ground-based instruments. Under favored situations signatures of Langmuir turbulence could appear and last for several minutes in radar's field-of-view over an extended altitude range, allowing to identify any modification of the ionosphere by the micro-scale processes.

In what follows, we briefly discuss the various regimes of beam-plasma interactions under which Langmuir waves grow. We then provide a brief description of the theory of Langmuir turbulence. This is followed by a review of five decades of *in-situ* observations of Langmuir waves in the ionosphere as well as more recent results from a collection of ground-based incoherent scatter radars, high-resolution auroral imagers, and electromagnetic receivers. The wide range of observations summarized allows us to review the topic of Langmuir waves in the auroral ionosphere and discuss a number of open questions. By uniting the various observations, one goal of this work is to introduce the potential of the ground-based instruments to provide a broader spatial and temporal context for single-point *in-situ* measurements of micro-scale processes.

Although the review is meant to be comprehensive, it only includes the basic concepts. Many details and discussions from the literature are not repeated here—for which, readers are routinely guided to the referenced original papers. Furthermore, this review only includes studies related to Langmuir waves produced naturally by electron beams in space plasmas and does not cover laboratory studies, results observed during injection of artificial electron beams in the ionosphere (a review provided by Mishin (2019)), or Langmuir turbulence induced in ionospheric modification experiments.

2 GENERAL DESCRIPTION OF BEAM-PLASMA INTERACTIONS AND LANGMUIR TURBULENCE

2.1 Beam-Plasma Interactions

2.1.1 Plasma Dispersion Relation

In a plasma consisting of a background population $f_e(v)$ and an electron beam $f_b(v)$, electrostatic plasma oscillations and their growth rates can be obtained by solving the dispersion relation (Clemmow, 2018):

$$\varepsilon = 1 + \sum_s \chi_s(\boldsymbol{k}, \omega) = 0 \tag{1}$$

Here, $\chi_s(\boldsymbol{k}, \omega)$ is the susceptibility for species's'—which includes a core electron population 'e', background ions 'i', and beam electrons 'b'—and is given by:

$$\chi_s(\boldsymbol{k}, \omega) = \frac{\omega_s^2}{k^2} \int \mathrm{d}^3 v \sum_{n=-\infty}^{\infty} J_n^2\left(\frac{k_\perp v_\perp}{\Omega_s}\right) \times \frac{\left[k_\parallel \left(\partial f_s / \partial v_\parallel\right) + \left(n\Omega_s / k_\perp v_\perp\right) k_\perp \left(\partial f_s / \partial v_\perp\right)\right]}{\omega - n\Omega_s - k_\parallel v_\parallel} \tag{2}$$

In this equation, ω is the wave frequency, $\boldsymbol{k}$ is the wave vector, ω_s and Ω_s are the plasma and cyclotron frequencies of species's', J_n is the Bessel function of the first kind of order n, and the subscript $\parallel$ and $\perp$ indicate the directions parallel and perpendicular to the magnetic field B, respectively.

The dispersion relation 1 needs to be solved for a real wave vector $\boldsymbol{k}$, and a complex frequency $\omega = \omega_R + j\gamma$, where γ is the growth/damping rate at $\omega = \omega_R$. In the limit $\omega_R \gg \gamma$, Taylor expansion of $\varepsilon \equiv \varepsilon_R + j\varepsilon_I$ about ω_R leads to the following descriptions for the wave modes and their growth rates, respectively: $\varepsilon_R = 0$ and $\gamma = -\varepsilon_I / (\partial \varepsilon_R / \partial \omega_R)_{\omega_R}$. Focusing on high-frequency waves (and thus ignoring ion dynamics), the dispersion relation $\varepsilon_R = 0$ describes several electrostatic modes—including the upper-hybrid, Langmuir, and the electrostatic whistler—that can be amplified in the presence of an electron beam. A detailed discussion on amplification of the electrostatic modes by auroral electron beams is given by Kaufmann et al. (1978).

In the auroral ionosphere, **Eq. 1** should ideally include an additional term for the secondary or the scattered electrons which dominate the electron distribution function in the suprathermal energy range from a few eV to several keV. As will be discussed later in this review, the suprathermal electrons can introduce additional Landau damping for plasma waves and consequently affect the collisionless interaction of an electron beam with the ionospheric plasma (Lotko and Maggs, 1979; Mishin and Telegin, 1986; Newman et al., 1994c, b). Such effects of the suprathermal electrons, however, are ignored for the moment but will be discussed in **Section 2.2** in the context of beam-generated Langmuir turbulence.

Considering the complexity of the dispersion relation given by **Eq. 1**, the analytical approach to investigate beam-plasma interactions often requires some level of approximation. For wave vector $\boldsymbol{k}$ strictly parallel to B (i.e., $\boldsymbol{k}_\perp = 0$), the arguments

of the Bessel functions J_n in **Eq. 2** vanish and only the $n = 0$ term contributes to the sum over n. In this limit, the unmagnetized susceptibility reduces to

$$\chi_s(k,\omega) = \frac{\omega_s^2}{k^2}\int \mathrm{d}v_\parallel \frac{k_\parallel(\partial F_s/\partial v_\parallel)}{\omega - k_\parallel v_\parallel} \tag{3}$$

where $F_s(v_\parallel)$ is the *reduced* distribution function

$$F_s(v_\parallel) = \int \mathrm{d}^2 v_\perp f_s(\boldsymbol{v}). \tag{4}$$

When there is no ambiguity regarding the use of a 1D model, the notation is often simplified by making the following substitutions: $F_s \to f_s$; $k_\parallel \to k$; and $v_\parallel \to v$. After further limiting consideration to the case of two electron populations (background electrons designated by $s \to e$ and beam electrons designated by $s \to b$), with ions forming an immobile neutralizing background (i.e., $\chi_i = 0$), the dispersion relation reduces to the familiar form (Stix, 1962):

$$1 + \frac{\omega_e^2}{k^2}\int_{-\infty}^{\infty} \mathrm{d}v \frac{k(\partial f_e/\partial v)}{\omega - kv} + \frac{\omega_b^2}{k^2}\int_{-\infty}^{\infty} \mathrm{d}v \frac{k(\partial f_b/\partial v)}{\omega - kv} = 0 \tag{5}$$

Although the $k_\perp \to 0$ limit assumes the presence of a non-zero magnetic field, the 1D susceptibility is valid even in the limit $|\mathbf{B}| \to 0$. In the *unmagnetized* case, the product $k_\parallel(\partial F_s/\partial v_\parallel)$ can be replaced by $\boldsymbol{k}\cdot\nabla_v F_s(\boldsymbol{v})$, where the reduced distribution F_s is now understood as being the integral over velocities perpendicular to $\boldsymbol{k}$ rather than perpendicular to **B** as in the magnetized case. The above substitution, in which $\boldsymbol{k}$ can point in an arbitrary direction, leads directly to the general 2D and 3D dispersion in the unmagnetized limit.

From the linear stability analysis of **Eq. 5** it is found that the details of beam-plasma instability and the characteristics of the growing waves highly depend on the parameters of the beam (i.e., beam number density n_b, beam velocity v_b, and beam velocity spread Δv_b) and the background plasma (O'neil and Malmberg, 1968; Peter Gary, 1985). Specifically, for relatively dense, cold, and fast electron beams such that $P = (n_b/\mathrm{n}_0)^{1/3}(v_b/\Delta v_b) > 6$, the instability is fluid (also called 'reactive') and arises as a growing wave bunches the beam electrons at certain points of its oscillation in space to produce an electric field, which then enhances the modulation of the beam particle (e.g., Cairns, 1989; Cairns and Nishikawa, 1989). The fastest-growing modes, in this case, occur on the 'beam mode' with the dispersion relation $\omega \approx v_b k$. The beam mode is not a normal mode of plasma and appears in a beam-plasma system due to the contribution of χ_b to the real part of the dielectric function ε_R. The term 'reactive' refers to the fact that the interactions are dominated by the real (or reactive) component of ε_R which also contributes to growth rates. The reactive instability is often saturated by trapping of beam electrons in potential wells of the self-generated electrostatic waves or via an increase in the thermal spread of the beam (Cairns and Nishikawa, 1989; Klimas, 1990). The interaction of the electron beam with the background plasma is then passed onto the kinetic domain (Nishikawa and Cairns, 1991; Dum and Nishikawa, 1994). Observational features associated with the instability in space plasmas when $P > 6$ include electrostatic oscillations with frequencies below and above the local plasma frequency in planetary foreshocks (e.g., Etcheto and Faucheux, 1984; Fuselier et al., 1985; Cairns, 1989).

In contrast to the reactive limit, for relatively weak, warm, and slow electron beams such that $P < 1$, the instability is kinetic (Cairns, 1989). In this case, modification of the real part of the dispersion relation 1 by χ_b is small and the solutions of the dispersion relation are close to the normal modes of the plasma. The beam primarily modifies the imaginary (resistive) component of the dielectric function and as such the instability is sometimes referred to as 'resistive'. In this regime, the fastest-growing waves occur on the Langmuir dispersion relation with $\omega \geq \omega_p$ and grow due to inverse Landau damping associated with a positive slope in the one-dimensional (reduced) electron distribution function. The growth rate is given by Shapiro and Shevchenko (1988):

$$\gamma = \frac{\pi\omega_e^2}{2n_0k^2}\omega_L \frac{\partial}{\partial v}(f_e + f_b)_{\omega/k} \tag{6}$$

where n_0 is the background plasma density and ω_L is the wave frequency. It is in this kinetic regime where unstable Langmuir waves grow to high intensities and result in Langmuir turbulence.

Numerical investigation of the dispersion relation for conditions in between the two limits above is discussed in the literature (Cairns, 1989; Dum, 1989). It is shown that by increasing P from below 1 to above 6, a smooth transition occurs in the shape of the dispersion curve, the frequency of the fastest-growing waves, and the kinetic versus reactive nature of the instability. Here, we do not further discuss the reactive regime of the beam-plasma instability since the ionospheric observations that are subject of this review fall well into the kinetic domain.

While the use of **Eq. 5** greatly simplifies the analytical approach, it also eliminates a considerable amount of physics. Specifically, the one-dimensional unmagnetized description ignores the presence of several wave modes—such as the electrostatic whistler, upper-hybrid, and the electron Bernstein modes—which are described by the general electrostatic dispersion relation and are commonly observed in the auroral ionosphere. This reduction is evident in **Eq. 2** where the assumption of $k_\perp = 0$ leads to $J_n\left(\frac{k_\perp v_\perp}{\Omega_s}\right) = 0$ for $n \neq 0$. With respect to the growth rates, the term associated with $n = 0$ becomes equivalent to the growth rate given by **Eq. 6** and is referred to as the 'Landau resonance'. The $n > 0$ terms are referred to as the 'cyclotron resonances'—which are often responsible for amplification of oblique waves with $k_\perp \gg k_\parallel$—whereas, the $n < 0$ terms are sometimes referred to as the 'anomalous Doppler resonances'. For further discussions of the growth of various wave modes and their competition for the free energy provided by auroral electron beams readers are referred to Kaufmann et al. (1978); McFadden et al. (1986); Ergun et al. (1993); Dum and Nishikawa (1994); Muschietti et al. (1997).

2.1.2 Saturation of the Bump-on-Tail Instability

In a uniform plasma, and in the absence of nonlinear wave-wave interactions, saturation of the bum-on-tail instability is due to

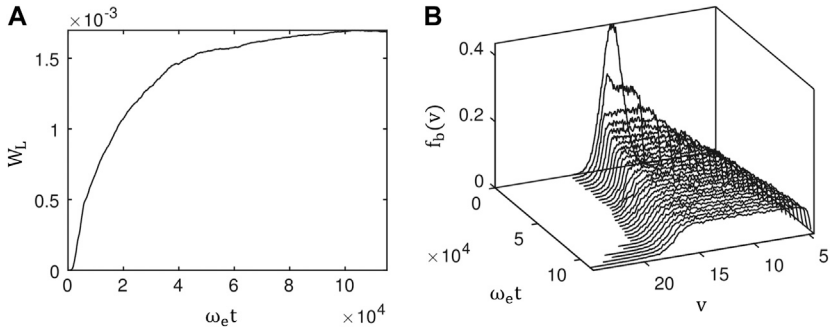

FIGURE 1 | Adapted from Krafft et al. (2015): Results from one-dimensional simulations describing quasi-linear relaxation of an electron beam. **(A)** Time variation of the normalized energy density of beam-generated Langmuir waves (W_L). And, **(B)** evolution of the beam distribution in velocity space (v) as a function of time. Here, v is in the unit of electron thermal velocity defined as $V_{e,th} = \sqrt{k_B T_e/m_e}$. The simulation corresponds to choices of $n_0 = 5 \times 10^6\,\mathrm{m}^{-3}$, $T_e = 20\,\mathrm{eV}$, $n_b/n_0 = 5 \times 10^{-5}$ and $v_b = 2\,\mathrm{keV}$, comparable to observations in the solar wind.

quasi-linear beam flattening. In this process, the waves that are in resonance with the positive slope of the beam grow to large intensities, to the point that they react back on the distribution function, converting the positive slope into a plateau. **Figure 1**, from Krafft et al. (2015), shows an example from a one-dimensional simulation of beam-plasma instability in the solar wind, where quasi-linear relaxation of a 2 keV electron beam is described. Saturation of the bump-on-tail instability by quasi-linear beam flattening occurs on time scales of the order of $\tau_{ql} \sim (n_0/n_b)\omega_e^{-1}$ (Davidson, 1972; Papadopoulos, 1975). The time scale is several milliseconds for the plasma parameters at about 1000 km and in the order of tens of millisecond for the plasma parameters at 300 km. Electron distribution measurements with instruments onboard sounding rockets and satellites have shown that the phase-space distribution of energetic electrons in the keV energy range—i.e., the so-called 'inverted V' electron beams—often consist of a plateau rather than a positive slope at the F region altitudes (e.g., Kaufmann et al., 1978), implying that the electron distributions have already stabilized by quasi-linear diffusion by the time the beams reach to ionospheric altitudes.

Despite the relatively short timescales (equivalently, short distances) on which quasi-linear beam flattening occurs, Langmuir waves have been commonly observed in the solar wind and in the ionosphere far from the generation point of the source electron beams. Several scenarios have been proposed to resolve this contradiction. One scenario involves velocity dispersion, whereby faster beam electrons continuously precede the slower ones, momentarily reproducing a positive slope which is then quickly flattened (e.g., Lin et al., 1981; McFadden et al., 1986). The constant formation and flattening of the positive slope leads to a marginally unstable distribution which can travel to long distances. Another scenario involves nonlinear wave-wave interactions that are not included in the quasi-linear theory. In this scenario, the beam-resonant unstable waves undergo a parametric instability by which their energy quickly transfers to waves that are not in resonance with the beam and, thus, not in direct energy exchange. The beam-resonant waves, therefore, remain at a lower energy level and are less effective in altering the beam distribution (Papadopoulos and Coffey, 1974; Galeev, 1975; Galeev et al., 1977b; Muschietti and Dum, 1991; Goldman et al., 1996). Whether or not the beam flattening is significantly limited by the nonlinear wave-wave interactions depends on the timescales on which the two processes occur. Numerical simulations have demonstrated that for the parameters of the auroral ionosphere, ~1000 km, the parametric decay of Langmuir waves and wave-particle interactions occur on similar timescales and as such both are important in determining the evolution of a beam-plasma system (Sanbonmatsu et al., 1997, 2001).

The presence of spatial and temporal variations in electron beams and background plasma can also significantly affect the growth of electrostatic waves and, consequently, the evolution of a beam distribution. Several examples include 1) propagation of the beam-resonant waves out of the region where the beam exists—for example, oblique propagation of waves outside of an auroral arc (Maggs, 1976, 1978; Maggs and Lotko, 1981); 2) change in the phase velocity of the enhanced waves due to the presence of background density gradient (e.g., Akbari et al., 2013); and 3) temporal variations within the beam and the background plasma that alter the growth rate as a function of time and space. Accounting for the random spatiotemporal variations of the beam and the background plasma has led to the development of the so-called Stochastic Growth Theory (SGT) (Robinson, 1995; Cairns and Robinson, 1997; Cairns et al., 2000; Cairns and Menietti, 2001). At the heart of this theory is a particle distribution that is and remains close to time- and space-averaged marginal stability but includes stochastic fluctuations—due to variations in the beam and background plasma—that cause linear wave growth at random times and locations. This theory provides an intrinsic explanation for certain observational features of Langmuir waves in space plasmas such as the burstiness of the wave fields and their observations far from the source region of the unstable distribution. One prediction of SGT is that the amplitude of the observed waves should follow a log-normal distribution. This prediction has been verified experimentally for several Langmuir wave observations in the solar wind (Cairns et al.,

2000), in planetary foreshocks (Cairns and Robinson, 1997), as well as the Earth's topside ionosphere (Samara et al., 2008).

Other processes that may contribute to the stability of electron beams and their interactions with background plasma involve electron-neutral collisions (e.g., Volokitin and Mishin, 1979). Theoretical calculations show that for electron-neutral collision frequencies, ν_e, greater than a threshold ($\nu_e > \pi\omega_e n_b/n_0$), the increased linear collisional damping can stop the plateau formation and preserve the positive slope. Above a threshold, electron-neutral collisions may also influence the transfer of turbulence energy to dissipative scales by wave collapse (this will be further discussed in the next section), leading to an increased level of wave energy compared to the collisionless case (e.g., Volokitin and Mishin, 1979). Such collisional effects may manifest in the E region of the auroral ionosphere where the exponential increase in the neutral density causes a rapid transition from collisionless to collisional turbulence. It has been proposed that this transition can lead to the appearance of a thin layer in altitude, called the plasma turbulence layer (PTL), in which wave energy is elevated (e.g., Mishin and Telegin, 1989). The dissipation of wave energy in the turbulence layer has been proposed to explain thin layers of enhanced electron temperature and density (e.g, Swider and Narcisi, 1977; Wahlund et al., 1989; Schlesier et al., 1997), as well as auroral luminosity (i.e., the so-called 'Enhanced Aurora') (e.g., Stenbaek-Nielsen and Hallinan, 1979; Dziubenko et al., 1980; Mishin et al., 1981; Hallinan et al., 1985) commonly observed by ground-based incoherent scatter radars and optical instruments at high latitudes.

2.2 Langmuir Turbulence

Langmuir turbulence is a result of nonlinear coupling between Langmuir waves and ion density perturbations. In plasmas, the refractive index is a function of plasma density, with a lower density corresponding to a higher refractive index. An existing density depression, therefore, forms a region of higher refractive index, which tends to concentrate the distribution of wave energy inside. On the other hand, a nonuniform distribution of Langmuir energy acts to push the plasma toward the area of weaker field strength (i.e., outside of the cavity) via the Ponderomotive force $\boldsymbol{F}_P = -\frac{q^2}{4\pi\omega_e^2}\nabla\left|\boldsymbol{E}\right|^2$. As a result of this positive feedback, instabilities emerge that lead to strong responses in electric fields and density perturbations which are referred to as Langmuir turbulence. Langmuir turbulence includes the phenomena of linear parametric instabilities, as well as the completely nonlinear phenomenon of caviton formation and wave collapse. It is known to occur in a variety of space and astrophysical plasmas—including pulsar magnetospheres (Asseo and Porzio, 2006), lower solar corona (Nulsen et al., 2007), the solar wind (e.g., Thejappa et al., 2012a, b; Graham et al., 2012; Graham and Cairns, 2014), planetary foreshocks (e.g., Robinson and Newman, 1991; Thiessen and Kellogg, 1993), and the Earth's ionosphere (e.g., Akbari et al., 2012; Isham et al., 2012)—as well as laboratory laser-plasma (e.g., Kline et al., 2006) and beam-plasma experiments (e.g., Wong and Quon, 1975).

Langmuir turbulence is often modeled by numerical integration of a set of coupled, nonlinear, partial differential equations known as the Zakharov equations (e.g., Newman et al., 1994b; Robinson, 1997; Guio and Forme, 2006). The Zakharov equations for an unmagnetized plasma in multiple dimensions can be expressed as:

$$\nabla\cdot\left(j\frac{\partial}{\partial t}+j\nu_e\times\ +\frac{3}{2}\omega_e\lambda_D^2\nabla^2\right)\boldsymbol{E}=\frac{\omega_e}{2n_0}\nabla\cdot(\delta n\boldsymbol{E}) \tag{7}$$

$$\left(\frac{\partial^2}{\partial t^2}+2\nu_i\times\frac{\partial}{\partial t}-C_s^2\nabla^2\right)\delta n=\frac{1}{16\pi m_i}\nabla^2|\boldsymbol{E}|^2 \tag{8}$$

Here, $\boldsymbol{E}$ is the slowly varying envelope of the high-frequency electrostatic wave field, and δn is the quasineutral plasma density fluctuations. ν_e and ν_i are damping coefficients for Langmuir and ion-acoustic waves. The coefficients are wavenumber-dependent and are implemented by incorporating the convolution product operator ×. Also, λ_D, C_s, and, m_i are the Debye length, ion sound velocity, and ion mass, respectively. In order to account for thermal spontaneous emission of Langmuir and ion-acoustic waves, stochastic complex source terms may also be added to the right-hand side of the two equations (e.g., Guio and Forme, 2006). Electron beams are often accounted for by including their wavenumber-dependent inverse Landau damping in the damping coefficient ν_e. More generally, both the damping and dispersion of Langmuir waves can depend on the direction of **k** due to anisotropy of the plasma. For example, in (Newman et al., 1994b), the Laplacian operator ∇^2 in **Eq. 7** is replaced by a generalized dispersion operator D^2 that includes magnetic corrections to the dispersion relation. The Zakharov equations can be understood in the light of the description provided in the previous paragraph and by noting that 1) the Fourier transform of the expressions in parentheses on the left side of the equations represent the linear dispersion relation of the Langmuir and ion-acoustic waves; 2) the term on the right side of **Eq. 8** represents the Ponderomotive force which couples the ion dynamics to Langmuir field; and 3) that the right side of **Eq. 7** represents the non-uniform plasma density—i.e., the variations of the refractive index.

The standard description of beam-induced Langmuir turbulence in one dimension is as follows (Robinson, 1997): in the kinetic domain of the beam-plasma instability, Langmuir waves with phase velocities in the vicinity of the positive slope of the distribution function (i.e., $k_L \sim \omega_e/v_b$) experience a linear exponential growth according to **Eq. 6**. Provided that $k_L > k^*/2$ and $W < k\lambda_D(m_e/\mathrm{m_i})^{1/2}$ (i.e., region I in Figure 3 of Robinson, 1997)—where, $W = \frac{\varepsilon_0 E_L^2}{4n_0 k_B T_e}$ is the ratio of the Langmuir electric field energy density to the plasma kinetic energy density, $k^* = \frac{2}{3\lambda_D}(\gamma m_e/\mathrm{m_i})^{1/2}$, λ_D is the Debye length and $\gamma = 1 + 3T_i/T_e$—and for sufficiently large wave amplitudes, the nonlinear transfer rate of energy into a daughter mode will exceed its damping rate and the waves become unstable to the parametric decay instability (PDI). Subsequently, the energy quickly transfers from the beam-resonant Langmuir waves to a daughter Langmuir wave with a wavenumber $k_{L'} \approx -k_L + k^*$ and an ion acoustic wave at $k_s \approx 2k_L - k^*$. The change of sign of $k_{L'}$ with respect to k_L for $|k_L| > |k^*|$ indicates that the daughter wave propagates in the

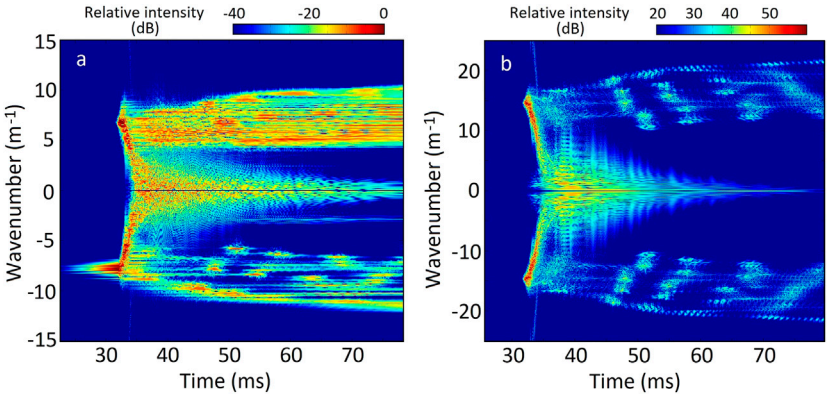

FIGURE 2 | Adapted from Akbari et al. (2016): Results from a one-dimensional simulation of Langmuir turbulence induced in the nightside F region auroral plasma with a 125 eV electron beam. The left and right panels show the evolution of the electric field and ion density perturbations, respectively, as a function of time and wavenumber. A cascade of parametric decay instabilities is seen after t ~32 ms following an exponential amplification of beam-resonant Langmuir waves at $k \sim 8\,\mathrm{m}^{-1}$. Other parameters of the electron beam are $n_b/n_0 = 6 \times 10^{-6}$ and $\Delta v_b/v_b = 0.3$.

direction opposite to that of the original wave. Provided that there is enough input energy to the system, the daughter wave becomes unstable, producing its own set of product waves, transferring energy to yet smaller wavenumbers. A cascade of parametric decay instabilities then could be initiated which ultimately leads to the concentration of energy in the low wavenumber part of the spectrum. Results from a one-dimensional simulation illustrating the energy transfer from an electron beam to beam-resonant Langmuir waves at $k \sim 8\ m^{-1}$ and subsequently to a broad spectrum of waves is shown in **Figure 2**.

In multiple spatial dimensions, the above description of a cascade of parametric decays is slightly altered since the participating waves are now allowed to obtain wave vectors in arbitrary directions—that is, as long as the wave vector matching condition $\boldsymbol{k_L} = \boldsymbol{k_{L'}} + \boldsymbol{k_s}$ is satisfied. In two or three dimensions, therefore, the parametric decay instability may result in product waves that spread over broad arc-like features in k-space while transferring energy to lower wavenumbers. An example of a cascade of PDIs in two spatial dimensions is shown in Figure 5 of Robinson (1997).

In the absence of significant linear damping (collision and Landau damping), dissipation of the concentrated energy at small wavenumbers is achieved by the nonlinear process of caviton formation and collapse. The process is as follows: at $k < k^*/2$, the long-wavelength, relatively uniform Langmuir waves become unstable to the modulational instability by which a wave packet breaks-up into a train of smaller-scale modulations (see Figure 10 of Goldman, 1984). The modulational instability leads to the formation of plasma density cavities of the same scale in which Langmuir waves are trapped. If the intensity of a Langmuir packet is higher than a threshold $(E_c\,(L) \geq \sqrt{\frac{170\, n_0 k_B T_e V_s}{\varepsilon_0 V_{e,th}}}\sqrt{\frac{\lambda_D}{L}}$, where $V_{e,th} = (k_B T_e/\mathrm{m_e})^{1/2}$ and $V_s = (\gamma m_e/\mathrm{m_i})^{1/2} V_{e,th}$ are the electron thermal velocity and the ion sound speed, respectively) (Cairns and Robinson, 1995), collapse initiates—i.e., the Ponderomotive force of the high-frequency field progressively pushes the plasma out of the

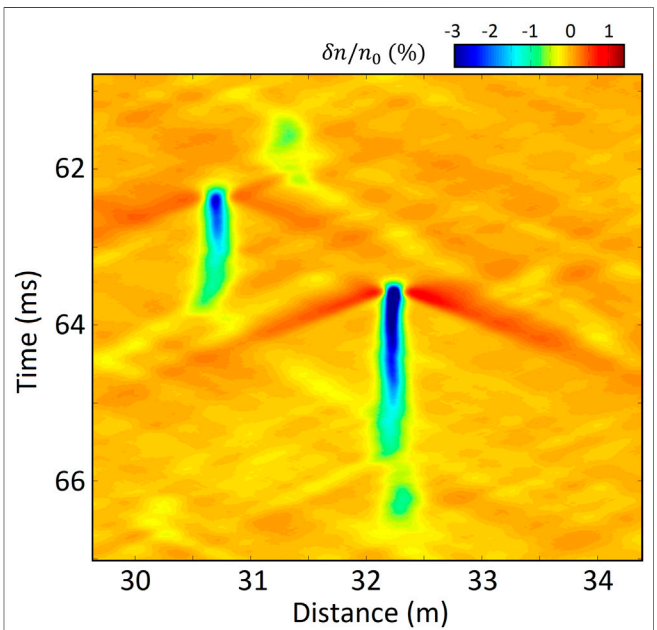

FIGURE 3 | Adapted from Akbari et al. (2016): Results from a one-dimensional simulation of Langmuir turbulence in the nightside F region auroral plasma. Normalized ion density fluctuations are shown in real space as a function of time. The feature located in the center of the plot illustrates a cycle of nucleation–collapse–dissipation.

corresponding density well, further deepening and narrowing the cavity, intensifying the trapped electric field inside. At very small scales (tens of Debye lengths), the collapsing wave packet experiences strong transit-time damping (Robinson, 1997, and references therein), which dissipates the electric field, releasing the energy in the form of accelerated electrons (e.g., Newman et al., 1990; Wang et al., 1996). The density cavity, now unsupported by Ponderomotive force, slowly relaxes in place (in the case of significant ion-acoustic damping) or breaks up

into ion sound pulses that propagate in either direction (in the case of small ion-acoustic damping) (Doolen et al., 1985; Russell et al., 1988).

The relevance of the modulational instability at $k < k^*/2$ in the above description has been discussed by various works (Robinson, 1997, and references therein). Specifically, it has been argued that in a broadband turbulence produced by successive parametric decays, the modulational instability is likely stable (see Sec. III.C of Robinson, 1997). Collapse is instead expected to occur via the alternate 'nucleation' mechanism. This mechanism relies on the fact that, in the presence of density fluctuations, localized Langmuir eigenmodes exist in the form of trapped standing waves in density depressions (e.g., McAdams et al., 2000). The trapped waves may accumulate energy from the background turbulence, for example via three-wave decays, and undergo collapse. An example from a one-dimensional simulation is presented in **Figure 3** where an ion density cavity undergoes nucleation and collapse. Here, collapse is seen at the initial stage of the time development of the feature at x ~32.2 m, during which the cavity steepens and the pushed-aside plasma density propagates to the sides in the form of two ion sound pulses. After the dissipation stage, the density cavity relaxes in place, gradually becoming shallower. This is a consequence of the large ion damping rate chosen in this simulation ($T_e/T_i = 3$) that is suitable for the F region auroral plasma. What remains of the density cavity may later re-nucleate energy, initiating another cycle of nucleation-collapse-dissipation (Doolen et al., 1985; Russell et al., 1988). A fully developed Langmuir turbulence in this picture simultaneously consists of linear Langmuir and ion-acoustic waves along with collapsing cavitons in the turbulence region.

The picture described above is the standard description of Langmuir turbulence that applies to unmagnetized or weakly magnetized plasmas ($\omega_e > \Omega_e$). Several modifications to the description above are discussed in the literature. First, in the presence of a moderate magnetic field ($\Omega_e > \omega_e$)—applicable to environments such as the lower solar corona and the topside F region of the ionosphere—the topological changes to the Langmuir dispersion relation due to the magnetic field suppress self-focusing of wave energy in density cavities. In such environments, therefore, wave collapse is not possible (Newman et al., 1994a). On the other hand, the altered Langmuir dispersion relation allows the three-wave decay to directly transfer energy to larger wavenumbers where dissipation via Landau damping is significant. This is in contrast to the unmagnetized case where the kinematics of the parametric decay only allows energy transfer to lower wavenumbers.

It has been pointed out recently (Layden et al., 2013; Cairns and Layden, 2018) that the modification of the Langmuir dispersion relation to the generalized forms (Willes and Cairns, 2000) of the Langmuir-z mode for weakly magnetized plasmas ($\omega_e > \Omega_e$) and that of the Langmuir-whistler mode for strongly/moderately magnetized plasmas ($\Omega_e > \omega_e$) may also affect the standard description of Langmuir turbulence. Specifically, the deviation of the dispersion relation from that of the electrostatic Langmuir curve at small wavenumbers allows the parametric decay instability to be kinematically viable even for $k < k^*/2$. This is, again, contrary to the unmagnetized case and may potentially affect wave collapse due to the competition between the parametric decay instability and the modulational instability at small wavenumbers.

Another important consideration for Langmuir turbulence in the auroral plasma is the presence of the secondary and the scattered electrons which dominate the electron distribution function in the suprathermal energy range from a few eV to several keV (Mishin and Telegin, 1986). These electrons substantially enhance Landau damping of Langmuir waves at intermediate wavenumbers, causing the cascade of parametric decays to truncate. This, in turn, prevents the accumulation of energy at low wavenumbers, disabling wave collapse even when $\omega_e > \Omega_e$ (Newman et al., 1994c, c). Furthermore, the damping enhances as the angle between $\boldsymbol{k}$ and $\mathbf{B}$ increases. Another effect of the suprathermal electrons is, therefore, to confine the turbulence to within ~10° from the magnetic field direction. This is consistent with various observations by *in-situ* and ground-based sensors.

The above description of Langmuir turbulence, which is mainly developed based on the Zakharov equations, are limited to interactions of Langmuir and ion-acoustic waves and does not include the direct excitation of waves on the lower hybrid/whistler branch by the beam or the parametric decay of Langmuir waves into such wave modes (Stasiewicz et al., 1996; Bonnell et al., 1997; Lizunov et al., 2001; Singh et al., 2001). The electrostatic Zakharov equations also exclude the well-known parametric decay instabilities involving the first and second harmonics of the electromagnetic radiation near the local plasma frequency (e.g., Li et al., 2005a; Li et al., 2005b).

As we wrap up the theoretical discussions, we note that Langmuir turbulence—as would result from nonlinear interactions of warm, tenuous electron beams with background plasma—has also been investigated within the framework of the plasma weak turbulence theory (e.g., Ziebell et al., 2001; Yoon, 2006; Ziebell et al., 2008; Yoon et al., 2012b, and references therein). One advantage of the weak turbulence formalism is that it combines quasi-linear diffusion and wave kinetic equations and, as such, self-consistently describes the evolution of electron beams along with wave-wave interactions and wave-particle scattering effects. The weak turbulence framework has been extensively employed to investigate the generation of Langmuir waves in the solar wind, their conversion to electromagnetic emission near the plasma frequency and its harmonics, as well as their role in the generation of energetic tails in electron distribution functions (e.g., Yoon et al., 2005; Gaelzer et al., 2008; Yoon et al., 2012a; Ziebell et al., 2015; Lee et al., 2019). The weak turbulence theory properly describes three-wave interactions, such as the parametric decay instability, however, does not describe coherent phenomena such as caviton collapse or modulational instabilities. A detailed description of the equations of the weak

turbulence theory is beyond the scope of this work; we instead refer the readers to the references mentioned above.

3 OBSERVATIONS OF LANGMUIR WAVES/ TURBULENCE IN THE IONOSPHERE

3.1 *In-situ* Observations

In-situ observations of particles and fields by instruments onboard satellites and sounding rockets have played a major role in establishing that Langmuir waves are common in the high-latitude plasma environment and identifying their features and consequences. There have been many comparable *in-situ* observations of upper-hybrid waves, including similar physical effects as those reported for Langmuir waves, but this review concentrates on the modes with nearly parallel wave vectors.

Early spacecraft traversing the auroral zone included wave receivers that detected signals around the local plasma frequency (Gregory, 1969, and references therein). Bauer and Stone (1968), for example, combined many of these observations to estimate the electron density profile far into the topside. The Porcupine series of rockets launched in 1977 from Esrange, Sweden, detected Langmuir waves with amplitudes few to tens of mV/m in subsecond bursts both in the natural auroral environment and trapped in an artificial barium cloud (Carlson et al., 1987). Another 1977 rocket launch from Churchill, Manitoba, detected narrow-band signals near 2.3 MHz, tentatively identified as Langmuir waves, with estimated amplitudes 50 mV/m, occurring in bursts of approximately 100 ms duration, and correlated with energetic electrons beams (Kellogg et al., 1978). The bursty nature of auroral Langmuir waves and their correlation with magnetospheric-origin electron beams have been subsequently confirmed by many *in-situ* observations (e.g., Boehm, 1987; Kintner et al., 1995; LaBelle et al., 2010).

McFadden et al. (1986), for example, analyzed data from a 1982 rocket launched to over 600 km from Cape Perry, Canada, observing small amplitude (few mV/m) bursty Langmuir waves associated with ~1.5 keV inverted V electron beams and others associated with broadband lower energy electrons below 375 eV. Through detailed consideration of the stability of measured electron distributions, they concluded that the primary source of energy for the waves was the positive slope in the parallel component of the electron distribution function. They also argued that the small amplitudes of the observed waves required processes to limit wave growth, such as propagation on a density gradient that could result in shifting the waves out of resonance with the beam. Significantly larger amplitude Langmuir wave bursts, up to and exceeding 800 mV/m, were later observed in many experiments (e.g., Boehm, 1987; Ergun et al., 1991a; Kintner et al., 1995; Kletzing et al., 2005; Samara et al., 2008; LaBelle et al., 2010); which also showed that Langmuir waves were more common at altitude above 600 km. In contrast to the small-amplitude waves, the large ~V/m amplitude events require a mechanism to keep Langmuir waves in resonance longer, such as wave reflection or trapping discussed by Boehm (1987), or larger growth rates provided by electron beams.

Repeated *in-situ* observations (e.g., Kletzing et al., 2016) have shown that large-amplitude Langmuir waves in the ionosphere are often observed in conjunction with bursts of broadband (with energies from tens to thousands of eV), field-aligned electrons that are accelerated by the parallel electric field of inertial Alfvén waves (e.g., Kletzing and Hu, 2001). One characteristic of the field-aligned electron bursts is their velocity dispersion, by which the faster, higher energy electrons are observed first, followed by the slower electrons. The free energy for Langmuir waves is attributed to such modulations in the electron flux which lead to the appearance of a transient positive slope in the one-dimensional electron distribution function (McFadden et al., 1986). As was described in **Section 2.1**, the appearance of the transient positive slope, and thus the amplitude of the resulting waves, is determined by the competition between quasi-linear beam flattening, nonlinear parametric instabilities of Langmuir waves, and variations in the electron flux which can occur on similar timescales at ionospheric altitudes. Large-amplitude Langmuir waves in the ionosphere are often not associated with intense, energetic (keV) inverted V electron beams. Such beams, however, could be unstable in oblique directions and give rise to electrostatic whistler and upper-hybrid waves (Maggs, 1976; Kaufmann et al., 1978; Maggs, 1978; Lotko and Maggs, 1981; Maggs and Lotko, 1981; Gough et al., 1990).

3.1.1 Spectral and Temporal Characteristics of Langmuir Waves

A wealth of information on various linear and nonlinear processes involving Langmuir waves and electromagnetic emissions associated with them can be obtained by a careful investigation of their spectral and temporal features. Data from the AUREOL/ARCAD-3 satellite at 400-2000 km, for example, showed evidence of frequency structure associated with auroral Langmuir waves (Beghin et al., 1989). This data set also established the ubiquity of the phenomenon, with occurrence rates up to 80% on the dayside and 60% on the nightside. Wave structures extended above the plasma frequency when $\omega_e > \Omega_e$ and extended below the plasma frequency when $\omega_e < \Omega_e$. McAdams and LaBelle (1999) made continuous measurements of the waveform up to 5 MHz on a sounding rocket PHAZE-2 launched to 945 km into the nightside aurora from Alaska, revealing detailed frequency structure of the Langmuir waves. As found by Beghin et al. (1989), the structure depended on the value of ω_e/Ω_e. For the 'underdense' case ($\omega_e < \Omega_e$), emissions appear in the form of relatively long-lasting monochromatic, banded structures below ω_e, often punctuated by intense waves where the wave frequency matches local plasma frequency (McAdams et al., 1999). These were interpreted as mode conversion of Langmuir wave bursts into whistler waves that propagate long distances particularly as their frequency becomes well below local ω_e away from the source. The banded structure arises because the causative Langmuir waves consist of short-duration bursts. For the 'overdense' case ($\omega_e > \Omega_e$), short-duration frequency-drifting signals called "chirps" were detected just above ω_e in association with electron density irregularities with scales sizes meters to a kilometer. The chirps have bandwidths of 300–600 Hz, amplitudes of

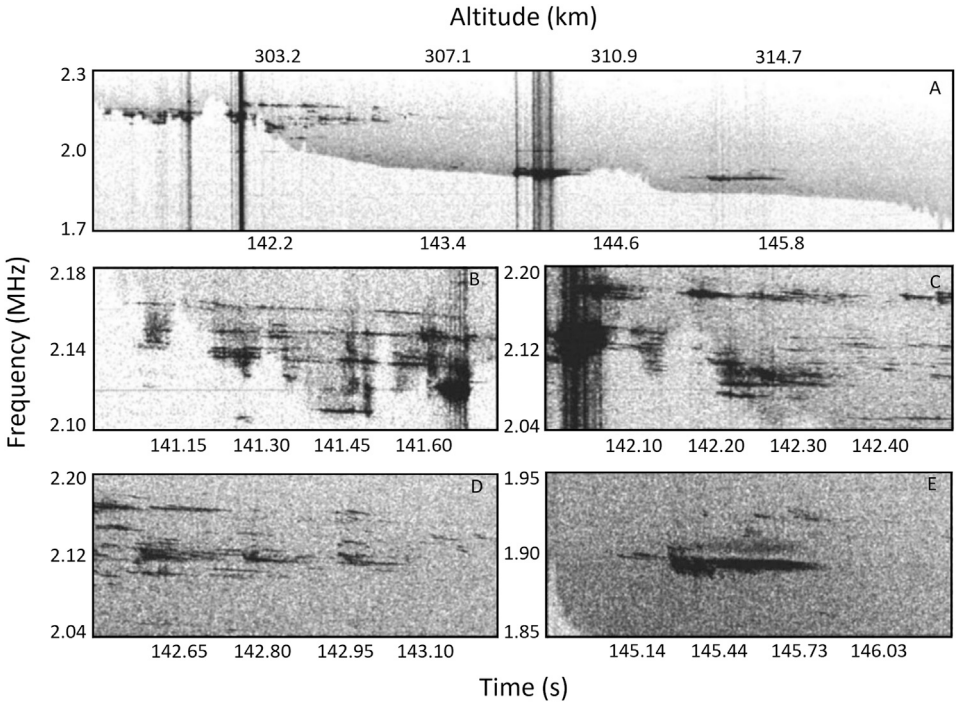

FIGURE 4 | Adapted from McAdams and LaBelle (1999): Spectrograms of electric field measured with a 30-cm double-probe antenna at ~310 km altitude with the PHAZE-2 sounding rocket. Top panel: overview spectrogram showing Langmuir emissions at and just above the plasma frequency, associated with density structures. Bottom panels: zoomed-in spectrograms showing the detailed structure of the Langmuir waves.

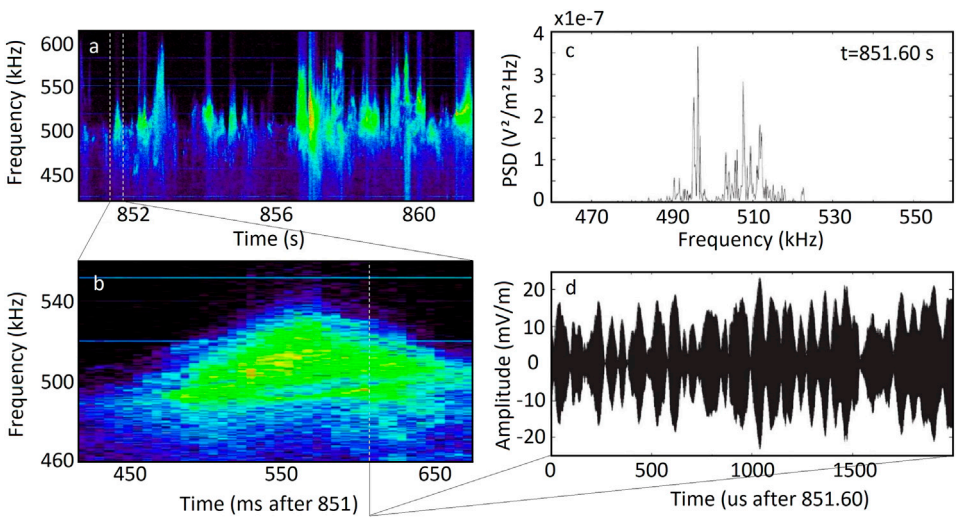

FIGURE 5 | Adapted from LaBelle et al. (2010): Langmuir wave electric fields measured with a 30-cm double-probe antenna at 967–894 km with the TRICE sounding rocket launched from Andoya, Norway on December 10, 2007. Left panels: overview spectrogram showing Langmuir wave bursts **(top)**, and zoomed-in spectrogram showing Langmuir wave structure **(bottom)**. Right panels: selected spectrum showing a forest of peaks at and below f_p **(top)**, and time series waveform showing typical Langmuir wave modulations.

~0.7 mV/m, and last about tens of ms. They often appear in pairs or multiplets.

Figure 4 (from McAdams and LaBelle, 1999) shows spectral data of Langmuir waves measured in the overdense nightside aurora with the PHAZE-2 sounding rocket. The top panel shows Langmuir waves at and above the plasma frequency, that is identified by the lower cutoff descending from 2.2 to 1.7 MHz. The structured Langmuir waves are associated with density

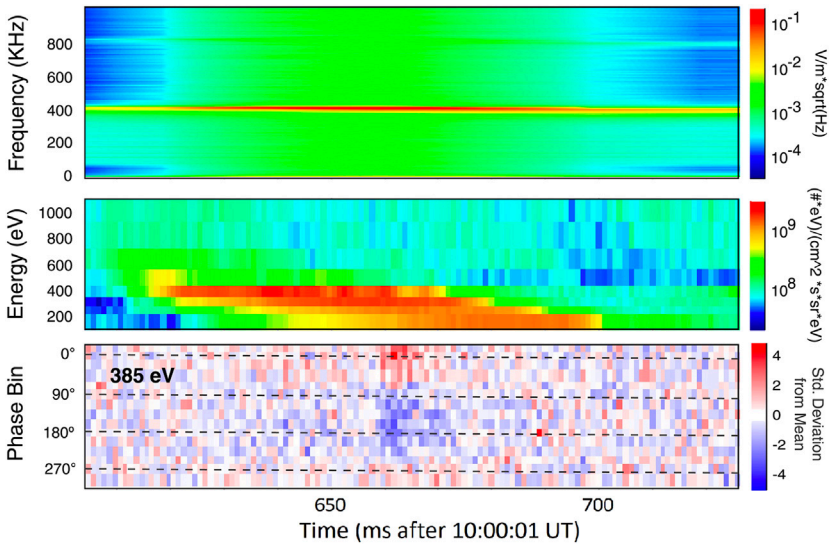

FIGURE 6 | Adapted from Kletzing et al. (2017): Langmuir wave electric field, particle, and wave-particle correlator data measured near 725 km altitude with the CHARM-2 sounding rocket. Top panel: electric field spectrogram showing extremely monochromatic Langmuir waves slightly above 400 kHz. Middle panel: energy flux spectrogram of downgoing electrons showing broadband dispersed feature below 500 eV coincident with the Langmuir waves. Bottom panel: the output of the wave-particle correlator showing significant bunching of 385 eV downgoing electrons in the field of the wave at 10:00:01.66 UT, evidenced by count rates significantly above or below expected values in most of the sixteen phase bins.

enhancements of around 1 km spatial scale believed to be caused by electron impact ionization from the same electron beam which generates the waves. Lower panels B–E show expanded views of the Langmuir wave fine structure, consisting of multiplet structures "chirps".

McAdams et al. (2000) put forth a model of the HF "chirp" emissions as quasi-trapped eigenmodes in a field-aligned density depletion. Observed frequency spacings of the "chirps" (0.1–1.4 kHz) and observed density cavity sizes and depths agreed with predictions of the linear theory of the waves in the depletions using equivalent of WKB approximation. The model also correctly predicts that the modes are evenly spaced, as well as the number of modes predicted for a given density cavity. Yoon and LaBelle (2005) extend the model to a wider class of density irregularities. These observations motivated the analysis discovering analogous eigenmodes of Langmuir waves observed by STEREO spacecraft in the solar wind (Ergun et al., 2008). Samara and LaBelle (2006) review observations of "chirp" features on three different rocket experiments, showing a greater variety of "chirp" frequency variations (upward as well as downward) and a typical 3-km distance scale of decay of amplitudes of escaping chirps as a function of distance from their sources.

Another, clearly noticeable, characteristic of Langmuir waves is their amplitude modulation at very low frequencies (VLF), typically between 1 and 60 kHz. Boehm (1987), for example, reported up to 100% modulations in Langmuir wave amplitudes suggesting nonlinear wave-wave interactions. Such amplitude modulations of Langmuir waves have since been confirmed in many experiments and have resulted in several possible explanations. The proposed mechanisms include beating between Langmuir waves of different frequencies (Newman et al., 1994b; Burinskaya et al., 2003; LaBelle et al., 2010); nonlinear wave-wave interaction involving low-frequency waves such as ion-acoustic, lower hybrid, or ion Bernstein waves (Ergun et al., 1991a; Stasiewicz et al., 1996; Bonnell et al., 1997; Khotyaintsev et al., 2001; Lizunov et al., 2001; Singh et al., 2001), as well as purely kinetic processes where electron motions are affected by the electrostatic potential of the generated waves (Muschietti et al., 1995, 1996; Akimoto et al., 1996; Umeda, 2006).

An example of such modulations is presented in **Figure 5** (adapted from LaBelle et al., 2010) which shows Langmuir waves measured in the dayside aurora with the TRICE sounding rocket. Here, panel a shows a spectrogram from an 11-s interval covering a 200 kHz band centered on the plasma frequency which is near 500 kHz. This panel illustrates the bursty nature of the Langmuir waves. Panel b shows a spectrogram of a relatively long individual burst lasting nearly 200 ms. The upper bound of the waves rises and then falls during the burst, interpreted as evidence of a plasma density enhancement in which the Langmuir waves are trapped. Panel c shows a selected spectrum, at the time of the vertical white dashed line in panel b, showing that the Langmuir waves consist of a forest of spectral peaks spanning about 40 kHz. The coherence and duration of the peaks can be inferred from the spectrogram. Panel d shows waveform data during a 2-ms interval illustrating envelope modulations with amplitudes approaching 100%, typical of auroral Langmuir wave observations.

Bonnell et al. (1997) present a statistical study of several hundred modulated Langmuir wave bursts observed with the Freja satellite at 1400-1700 km and the Scifer sounding rocket launched from Norway to 1450 km in the cusp. They find modulation frequencies from 1 kHz, an instrumental lower limit, to 60 kHz. They demonstrate that parametric decay into oblique Langmuir waves and whistler/lower hybrid waves is kinematically possible and could account for modulation frequencies above 7 kHz. They, furthermore, suggest that below 7 kHz, modulations require involvement of ion sound waves. In none of the preceding studies, however, is the low-frequency daughter wave observed. Stasiewicz et al. (1996), in contrast, shows case studies of Langmuir wave-wave interactions observed with the Freja satellite, in which the low-frequency wave is detected. In some cases, the presence of the low-frequency wave are interpreted as parametric decay of Langmuir waves into lower hybrid waves and in other cases as wave coalescence involving pre-existing lower hybrid waves. Khotyaintsev et al. (2001) and Lizunov et al. (2001) provide support for this mechanism. LaBelle et al. (2010) studies 41 Langmuir bursts out of 1000 estimated to occur during the TRICE rocket experiment launched to 1146 km from Norway into the cusp. They confirm modulation frequencies ranging to above 50 kHz but also find about 10% of events have modulation frequencies below 1 kHz, near the limit of detectability in bursts lasting tens of ms. They suggest interference of independently generated Langmuir wave modes as the source of the modulations. This is based on the statistical distribution of electric fields in the waves, which at the low field end exhibits a power-law spectrum. Li et al. (2010) show that such a distribution is expected for a superposition of random modes. Burinskaya et al. (2003) also suggest wave beating as the source of structure in 1–40 mV/m Langmuir waves detected at 2–3.5 Earth radii at high latitudes by the INTERBALL spacecraft. In contrast, Boehm (1987) originally rejected superposition of independent modes as being too improbable requiring too similar amplitudes to produce nearly 100% modulations.

3.1.2 Polarization

Polarization is another aspect of *in-situ* observations of Langmuir waves. Although, partly because of the large data rates involved, relatively few instruments have measured multiple components of the wave electric fields. McFadden et al. (1986) using measurements of two components of electric field were able to ascertain that the parallel field dominated, possibly by a factor of three or more, in the low amplitude Langmuir waves they measured. The TRICE sounding rocket launched into the cusp from Norway obtained, via small baseline antennas, snapshots of three components of electric field of waveforms at Langmuir wave frequencies. Dombrowski et al. (2012) found that the nature of the observed modulated Langmuir waves, in which the modulation nulls and peaks were not aligned between all three electric field components, could only be explained by mixing of different polarizations of waves, including both linear and elliptically polarized modes. Colpitts and LaBelle (2008) used statistics of the spin dependence of Langmuir wave detection with a single spinning electric field antenna, combined with Monte Carlo simulations, to probe the polarization of observed Langmuir waves.

3.1.3 Wave-Particle Correlators

The relationship of auroral Langmuir waves to the causative electron distribution, subject of linear theory tested by McFadden et al. (1986) and Beghin et al. (1989), has been investigated more deeply using large geometric factor particle instruments and/or wave-particle correlators. Such instruments are designed to sort detected electrons according to the phase of simultaneously measured Langmuir waves, thereby probing the detailed wave-particle interaction. Early versions of this type of experiment detected various levels (5–30%) of modulations of 4–7 keV electrons at megahertz frequencies, in some cases simultaneous with detections of positive slopes in the electron distribution functions (Spiger et al., 1976; Gough and Urban, 1983; Gough et al., 1990).

Ergun et al. (1991b), using a wave-particle correlator that sorted electrons according to the quadrant of the Langmuir wave phase, detected electron bunching at the few percent level in the fields of ~100 mV/m, ~100 ms Langmuir wave bursts, establishing the resonant energy, hence obtaining the parallel wavelength of 15 m. Ergun et al. (1991b) followed up by determining that the electron bunching was in 0 or 180 phase with the electric field, implying wave growth or damping. Simulations suggested that growth/in-phase bunching should be followed by trapping/quadrature bunching, but the latter was not observed, perhaps due to stationarity issues, finite size of the wave packet, or insufficient energy resolution as suggested by Kletzing and Muschietti (2006), who showed that the trapping signature is bimodal in energy and hence requires higher energy resolution to detect. Kletzing et al. (2005, 2016) developed a wave-particle correlator that sorted electrons into sixteen phase bins locked to the Langmuir wave phase. The instruments were flown on two sounding rockets (RACE and Charm-2) launched into the nightside aurora from Alaska and found evidence of electron bunching where the phase relation indicated trapping of electrons in wave fields, in contrast to the result of Ergun et al. (1991b).

Figure 6 adapted from Kletzing et al. (2017) shows an expanded view of 120 ms of data from the CHARM-2 rocket flight. The top panel shows a 0–1 MHz spectrogram where a monochromatic Langmuir wave emission slightly above 400 kHz is observed. The middle panel shows a spectrogram of downgoing electrons where a time-dispersed signature at energies below 500 eV is present. The bottom panel show outputs of the wave-particle correlator for several energies of electrons within the time-dispersed electron flux feature, with Langmuir wave phase bin on the vertical axis and color scale representing standard deviation. The latter is a measure of the degree of electron bunching. Significant correlation is observed in many of the energy channels. The phase bunching is positive near a phase of 180 or 0 degrees relative to the electric potential, indicating reactive phase bunching where electrons are trapped in the wave field.

Dombrowski et al. (2019) analyzed 57 Langmuir wave bursts from the CHARM-2 rocket flight, in which significant correlations were detected between electrons and Langmuir

wave phases. In their observations, signatures of energy exchange slightly dominated over those of particle trapping. Moreover, they observed that at times when the electron beam flux was increasing with time, the phase of the electron bunching indicated energy transfer from the electron beam to the waves, and at times when the beam electron flux was decreasing, the reverse. Test particle simulations showed that short term enhancements in the growth or damping of the Langmuir waves due to time-of-flight effects on the electron distribution could plausibly explain the observations.

3.1.4 Non-thermal Features of the Electron Distribution Function as Signatures of Langmuir Turbulence

Among important signatures of Langmuir turbulence are non-thermal features of the electron distribution function in the form of energetic tails and accelerated suprathermal populations. The non-thermal features are the consequences of nonlinear stabilization of a beam-plasma system and are produced as the parametric instabilities spread the wave energy in k-space from $k_L \sim \omega_e/v_b$ to lower and higher wavenumbers. The common observations of electron velocity distributions with energetic tails at energies above a beam in the solar wind (e.g., Ergun et al., 1998; Fitzenreiter et al., 1998), for example, are reproduced in Langmuir turbulence simulations based on the weak turbulence theory. Here the tail formation is associated with the dissipation of wave energy that is transferred to smaller wavenumbers by the parametric decay and scattering processes (Yoon et al., 2005, 2006; Ryu et al., 2007). This mechanism is shown to be able to produce both symmetric and asymmetric energetic tails (Gaelzer et al., 2008; Yoon et al., 2012a).

Suprathermal electron populations at intermediate energies—between thermal electrons and an energetic beam—with fluxes larger than those predicted from collisional interaction of the beam with the neutral atmosphere, are also commonly observed by *in-situ* instruments in the auroral ionosphere (e.g, Arnoldy and Choy, 1973; Reasoner and Chappell, 1973; Bryant et al., 1978; Fung and Hoffman, 1988; Ogasawara et al., 2017). An explanation based on collisionless beam-plasma interactions has been provided for such observations. In this scenario, modulational instability transfers the energy from beam-resonant waves to higher wavenumbers (i.e., lower phase velocities), making energy exchange possible between the electrostatic waves and the electrons on the tail of the background population (Papadopoulos and Coffey, 1974; Matthews et al., 1976).

Acceleration of electrons to suprathermal energies is also a well-known process associated with the dissipation of collapsing cavitons (e.g., Galeev et al., 1977a; Newman et al., 1990; Wang et al., 1996). In this case, efficient energy exchange could occur as electrons pass through the intense wave packets that are localized in density cavities. Electron acceleration occurs provided that the phase of a Langmuir oscillation during the energy exchange is such that it leads to a net energy gain for the particle. Generation of a suprathermal tail by Langmuir turbulence consisting of collapsing cavitons is an important outcome in the ionospheric modification (heating) experiments. In these experiments, high-power, high-frequency (HF) electromagnetic waves, that is injected into the bottom-side F region, artificially induce Langmuir turbulence, heating the plasma and accelerating electrons (e.g., DuBois et al., 1990, 1993; Isham et al., 1999; Mishin et al., 2004). Collisional interaction of the accelerated electrons with neutral species then produces enhanced ionization and artificial aurora that are detectable with ground-based incoherent scatter radars and optical instruments (e.g., Carlson et al., 1982; Bernhardt et al., 1989; Mishin et al., 2004; Pedersen et al., 2010; Mishin and Pedersen, 2011; Eliasson et al., 2012).

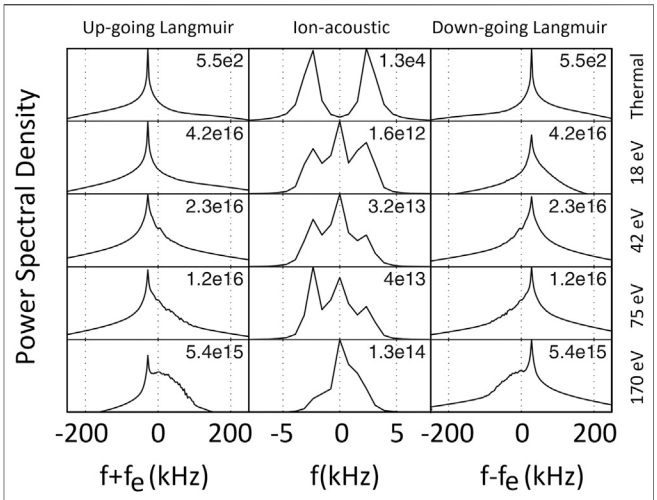

FIGURE 7 | Adapted from Isham et al. (2012): Results from a one-dimensional simulation with plasma parameters of the auroral F region. The spectra of up and down-going Langmuir and ion-acoustic waves are calculated for a wavelength of about 0.67 m ($k \approx 9.4$ m^{-1}), approximately matching the Bragg backscatter condition of the European Incoherent Scatter Scientific Association (EISCAT) 224-MHz radar located near Tromsø, Norway. Modification of the spectra due to Langmuir turbulence produced by downward-going beams of electrons at beam energies of 18, 42, 75, and 170 eV are shown. The appearance of the zero-frequency peak in the ion-acoustic channel and the broadened spectral peaks associated with Langmuir waves are signatures of caviton formation and wave collapse. $\Delta v_b/v_b = 0.3$ and $n_b/n_0 = 2 \times 10^{-5}$ are adopted for the beams. The parameters result in $P \approx 0.09$, corresponding to the kinetic regime of beam-plasma instability. The numbers at the top right section of each panel indicate the peak value of each spectrum.

3.2 Ground-Based Observations

Over the past decade or two, a type of anomalous non-thermal echo from the F region auroral ionosphere has been detected by various incoherent scatter radars (ISRs) (e.g., Strømme et al., 2005; Ekeberg et al., 2010; Akbari et al., 2012; Isham et al., 2012; Schlatter et al., 2014; Akbari et al., 2016). The echoes are often characterized by simultaneous enhancement of spectral peaks in the ISR spectrum that are associated with ion-acoustic and Langmuir waves. They, therefore, indicate the occurrence of naturally produced Langmuir turbulence within the plasma volume illuminated by the radar pulse.

A detailed description of the incoherent scatter radar theory will not be provided here. The following brief description is, however, necessary to provide a proper context for the results presented in this section. For a detailed description of the ISR theory, readers are referred to a review by Akbari et al. (2017)

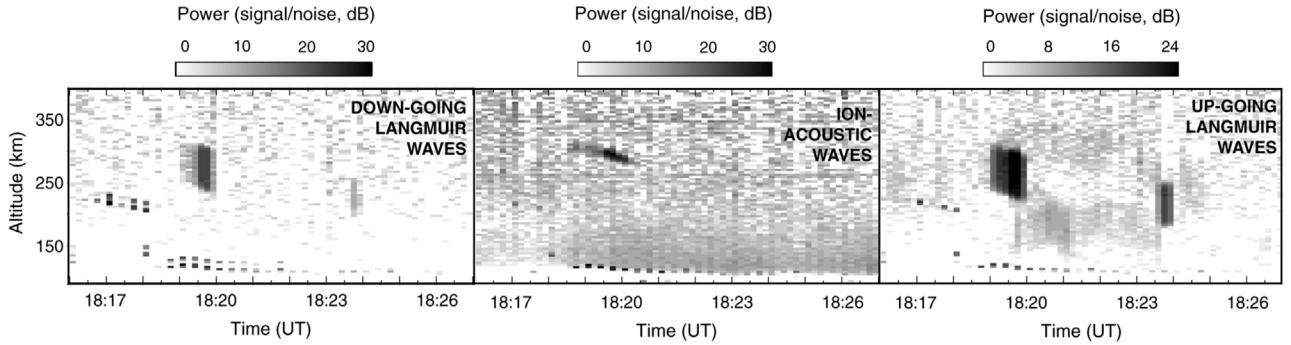

FIGURE 8 | Adapted from Isham et al. (2012): Range-Time-Intensity plot of received power associated with ion-acoustic (middle) and down- and up-going Langmuir waves (left and right, respectively) obtained by the EISCAT 224-MHz radar on November 11, 1999. The simultaneous amplification of ion-acoustic and Langmuir waves is a signature of Langmuir turbulence.

which focuses on Langmuir wave observations by incoherent scatter radars and their numerous applications in ionospheric studies. The fundamental measurement of an incoherent scatter radar is the ISR spectrum. The ISR spectrum is directly related to the frequency spectrum of plasma density fluctuations at a single spatial Fourier component (wavenumber). It is, therefore, related to a cut through the electrostatic dispersion surface along a single wave vector $\boldsymbol{k} = \boldsymbol{k}_{\text{detection}}$, where $\boldsymbol{k}_{\text{detection}}$ is determined by the radar's geometry and operating frequency. The electrostatic solutions of the plasma dispersion relation—such as the ion-acoustic and Langmuir waves—then appear in the ISR spectrum as spectral peaks at frequency offsets that satisfy the relevant dispersion relations for the specific $\boldsymbol{k}$. Example simulated ISR spectra associated with a thermal plasma are shown in the top panels of **Figure 7** (from Isham et al., 2012). The spectra include two resonance lines associated with up- and down-going (more accurately, propagating away and toward the radar) ion-acoustic waves which are closely located in the vicinity of zero Doppler frequency (see top row, middle panel in **Figure 7**) and two resonance lines associated with up- and down-going Langmuir waves with offset Doppler frequencies of about $-f_e$ and $+f_e$, respectively. In the presence of a beam-generated Langmuir turbulence (shown in other panels of **Figure 7**) the resonance lines may be significantly enhanced due to amplification of ion-acoustic and Langmuir waves, and additional features, associated with caviton formation and collapse, may appear in the spectra. The latter signatures may appear in the form of a central peak at zero Doppler and a broadened or additional spectral peaks in the vicinity of $\pm f_e$.

Figure 8, from Isham et al. (2012), shows example ISR data, obtained by the European Incoherent Scatter Scientific Association (EISCAT) 224-MHz radar on November 11, 1999, for a single radar beam in $\mathbf{B} \parallel$ direction. Shown are the total scattered power associated with Langmuir and ion-acoustic waves—i.e., the area under the power spectral density features—as a function of altitude and time. Several distinct sources of scattering can be identified. The dark background in the ion-acoustic channel is backscatter from thermal-level ion-acoustic waves. The repeated 10-s-long enhancements seen in all three channels at about 225 and 125 km before and after 18:18:30, respectively, are experimental features irrelevant to our discussions. The intense features occurring between 18:18:30 and 18:20:30 UT near 300 km and at 18:23:30 UT near 250 km are backscatter signals associated with amplified Langmuir and ion-acoustic waves which indicate the occurrence of parametric decay instability in the local plasma. Echoes similar to those detected by the 224-MHz EISCAT VHF radar, at the detecting wavenumber $|\boldsymbol{k}| \sim 9.4\ \text{m}^{-1}$, have also been commonly observed by other radars, including the 500-MHz EISCAT Svalbard radar at $|\boldsymbol{k}| \sim 21\ \text{m}^{-1}$ (e.g., Strømme et al., 2005; Ekeberg et al., 2010; Schlatter et al., 2014), the 931-MHz EISCAT UHF radar at $|\boldsymbol{k}| \sim 39\ \text{m}^{-1}$ (e.g., Schlatter et al., 2013), and the 450-MHz Poker Flat Incoherent Scatter Radar (PFISR) at $|\boldsymbol{k}| \sim 19\ \text{m}^{-1}$ (e.g., Akbari et al., 2012; Michell et al., 2014). For the rest of this manuscript, such coherent echoes are referred to as 'Langmuir turbulence echoes' or 'LT echoes'. In addition to the simultaneous amplification of ion-acoustic and Langmuir waves, many observations, commonly include important spectral details (not shown here) such as additional peaks in the ISR spectra at zero Doppler frequency and in the vicinity of the local plasma frequency (Akbari et al., 2012; Isham et al., 2012; Schlatter et al., 2013, 2014; Akbari et al., 2016), similar to the simulation results shown in **Figure 7** when electron beams are included. Such spectral features are signatures of Langmuir wave collapse which involve stationary (thus, resulting in a zero Doppler shift) ion density cavities in which Langmuir waves are trapped. These experimental features are considered as the first conclusive evidence of naturally induced Langmuir collapse anywhere in space plasmas.

ISR experimental features very similar to those shown in **Figures 7** and **8** are also commonly obtained in ionospheric modification experiments, where Langmuir turbulence and wave collapse are artificially induced in the ionosphere by the injection of powerful high frequency electromagnetic waves (e.g., DuBois et al., 1990, 1993; Isham et al., 1999). A difference between the results discussed in this review and those from ionospheric heating experiments is the source of the free energy for the turbulence—which for the case of natural turbulence, is thought be the magnetosphere-origin electron beams.

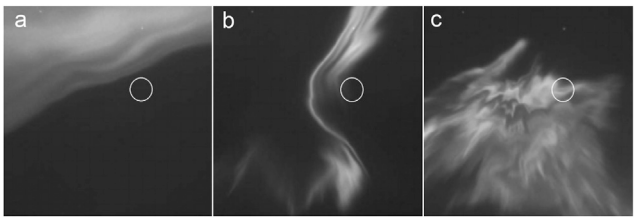

FIGURE 9 | Adapted from Semeter et al. (2008) and Akbari et al. (2012): Auroral morphologies recorded by a high-speed, high-resolution optical imager when coherent echoes appeared in the Poker Flat incoherent scatter radar's field of view (represented by the white circles) on March 23, 2007. The auroral arcs in panels a and b consist of small-scale features, thought to be associated with dispersive-scale Alfvén waves, and are recorded at times when the radar detected LT echoes. The auroral morphology in panel c is different than those in panels **(A)** and **(B)**. At the time of this image, the radar detected a type of coherent echo known as the Naturally Enhanced Ion Acoustic Line.

Correlating LT echoes with optical images of the aurora reveals that natural Langmuir turbulence underlying radar echoes may occur on the edge of auroral arcs and just outside of regions of energetic electron precipitation (Akbari et al., 2013). Two examples are shown in **Figures 9A,B**—here, the optical images are recorded when LT echoes appear in the field of view of the Poker Flat incoherent scatter radar, represented by the white circles. Analysis of high-speed ground-based auroral imagery often indicates the presence of dispersive-scale Alfvén waves at the time of LT echoes, suggesting a relationship between the two. The signatures of dispersive-scale Alfvén waves are seen in **Figures 9A,B** in the form of small-scale structures of the auroral arcs (Semeter and Blixt, 2006; Semeter et al., 2008). Association of LT echoes with auroral forms is further studied by Michell and Samara (2013) and Michell et al. (2014), where correlation with active arcs consisting of small-scale features similar to those shown in **Figures 9A,B** is found. Some radar studies, furthermore, find a correlation between coherent echoes and high-energy flux of precipitating electrons which produce enhanced E region ionization (e.g., Dahlgren et al., 2017). In **Figure 9**, the auroral morphology shown in panel c is different than those in the left two panels. At the time of this image, the radar detected a type of coherent echo known as the Naturally Enhanced Ion Acoustic Line. This will be further discussed in the following. For more discussions on **Figure 9** and the detected radar echoes see the original referenced work.

The radar echoes underlying the natural Langmuir turbulence are primarily observed in radar beam directions parallel to the magnetic field. They are often observed in thin layers (thickness of < 10 km) at or close to the F region peak between 200 and 300 km and are occasionally accompanied by a secondary layer some tens of km below the main layer (e.g. Akbari et al., 2013; Michell et al., 2014; Schlatter et al., 2014). Such localization of the turbulence in multiple thin layers is very intriguing and requires an explanation. The duration of the echoes is typically only a few seconds in radar's field-of-view but events lasting as long as several minutes have been observed. In an apparent contradiction to the explanation of the radar signatures in terms of Langmuir turbulence, often a one-to-one correlation between enhanced echoes associated with amplified Langmuir and ion-acoustic waves is not observed. In **Figure 8**, for example, the enhanced signals associated with Langmuir waves between 18:23:30 and 18:24:00 are not accompanied by an enhancement in the middle panel. A statistical study by Schlatter et al. (2014), using a dataset collected by the 500-MHz European Incoherent Scatter Svalbard Radar, shows that only about 25% of ion-acoustic echoes are accompanied by Langmuir echoes (provided that the frequency of the Langmuir waves fall within the pass-band of the receive channels). The lack of one-to-one correlation between enhanced ion-acoustic and Langmuir waves, however, may arise from the wavenumber matching requirement for detecting wave activities by radars, combined with the fact that ion-acoustic and Langmuir waves involved in a parametric decay instability have different wavenumbers—all of which may not satisfy $k_{\mathrm{wave}} = k_{\mathrm{detection}}$. Schlatter et al. (2014), furthermore, find a maximum occurrence rate of ~0.09% for LT echoes at 21 Magnetic Local Time (MLT). The occurrence rate is shown to increase with geomagnetic activity to ~0.6% for the Kelvin (K) index of 5. This maximum detection rate is small compared to the detection rate of Langmuir waves by *in-situ* instruments and is most likely due to the strict detection criteria of radars.

Based on experimental evidence that Langmuir turbulence echoes appear at altitudes where the vertical background plasma density gradient is minimal—i.e., at the peak of the F region and the valley between the E and F regions—a potential explanation for the localization of the turbulence in thin layers has been described by Akbari et al. (2013). They argue that, while destabilizing features of electron beams may exist on a given field line over an extended altitude range, propagation of waves in a vertical plasma density gradient, which leads to a change in their phase velocity, could drive the waves out of resonance with electron beams, limiting wave growth. Given the group velocity of Langmuir waves and the parameters of the auroral ionosphere, waves could fall out of resonance within tens of milliseconds. This is comparable to the timescales of quasi-linear beam flattening and those of nonlinear wave-wave interactions in the F region. Outside of the turbulence layer, therefore, the amplitude of Langmuir waves likely remains small. When the plasma density gradient is negligible, Langmuir waves may grow to large amplitudes and produce a broadband turbulence that is detectable by incoherent scatter radars. A similar mechanism, based on variations of the background density gradient, has been considered in the auroral E region to explain thin layers of enhanced ionospheric response during electron precipitation events (Voronkov and Mishin, 1993; Mishin and Khazanov, 2006).

Propagation of Langmuir waves in density gradient outside of the turbulence layers can eventually lead to linear mode conversion of the waves into electromagnetic radiation. LaBelle (2011) proposed a scenario where Langmuir waves driven in the topside ionosphere by low-energy electron beams of a few hundred eV, propagate downward to regions of higher plasma density and linearly convert to radiation when they cross the dispersion relation of the LO-mode at small wavenumber. This

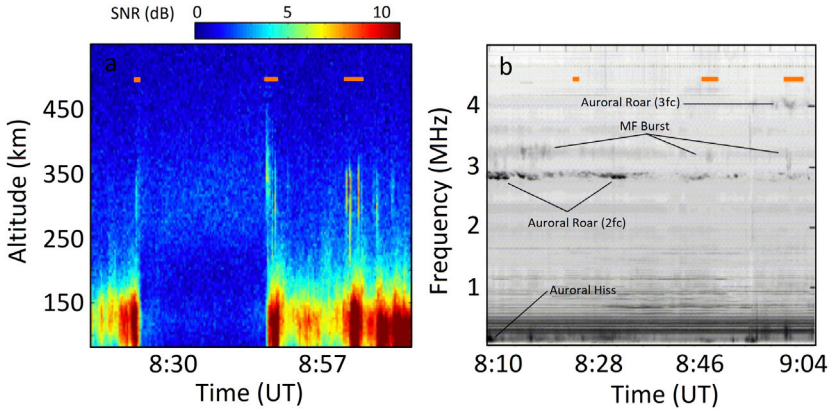

FIGURE 10 | Adapted from Akbari et al. (2013): Correlation of Langmuir turbulence echoes and MF Burst. **(A)** Range–Time–Intensity plot of received power in the ion line channel from the Poker Flat incoherent scatter radar, showing the occurrence of coherent echoes in three intervals on April 5, 2012. **(B)** Spectrogram of natural electromagnetic emissions recorded at Toolik Lake, AK. For aiding the comparison, the locations of the LT echoes are marked on the two panels with orange bars.

scenario is proposed as an underlying generation mechanism for the "medium frequency burst (MF burst)"—an impulsive, broadband emission at 1.3–4.5 MHz often detected via ground-based electromagnetic receivers at the onset of substorms (Weatherwax et al., 1994; LaBelle, 2011; Broughton et al., 2014). Interestingly, LT echoes and medium frequency bursts have simultaneously been detected by the Poker Flat incoherent scatter radar and electromagnetic receivers located in Alaska. An example, obtained on April 5, 2012, is shown in **Figure 10**. **Figure 10A** presents a Range–Time–Intensity plot of the received power in the ion line channel where coherent echoes are observed during three intervals, marked by orange bars, at 250–400 km. Here, the intermittent enhanced power below 200 km is due to increased E region ionization by energetic electron precipitation. **Figure 10B** shows spectrogram of natural electromagnetic emissions recorded at Toolik Lake, AK at the time of the radar data. Four types of EM emissions occur sporadically during the one-hour interval. The emissions include $2f_c$ and $3f_c$ auroral roars, which are narrowband emissions near 2.9 and 4.0 MHz presumed to result from upper-hybrid waves; auroral Hiss at frequencies below 1 MHz; and four occurrences of auroral MF burst, exceeding 2 min duration and spanning approximately 2.9–3.3 MHz. Two of the three radar echoes detected with the PFISR, centered at 8:49 and 9:03 UT, coincide with two of the four MF burst events. However, considering the vastly different conditions under which Langmuir turbulence and MF Burst are detected, the correlation between the two phenomena is difficult to establish. Conversion of Langmuir waves to LO-mode waves through the window for parallel propagation at $f = f_e$ may also explain narrowband signals, perhaps related to MF-burst, observed occasionally at South Pole Station (Broughton et al., 2014). Ground-based studies provide some support for this mechanism (e.g., Broughton et al., 2012; Burnett and LaBelle, 2020), but it has yet to be confirmed with *in-situ* data.

It was discussed in this section that a collection of ground-based observations from incoherent scatter radars, high-speed, high-resolution auroral imagers, and electromagnetic receivers have the potential to uncover a range of complex micro-scale plasma processes that occur in the ionosphere—topics that have historically been investigated via *in-situ* measurements. In the discussion section below, we combine the understandings from the *in-situ* and ground-based observations and discuss several open questions regarding the origin and effects of Langmuir turbulence in the ionosphere.

4 DISCUSSION OF SEVERAL OPEN QUESTIONS

Observations of Langmuir turbulence with *in-situ* instruments and incoherent scatter radars are in many cases complementary. This is due to the widely different natures of the measurement techniques. The most important differences arise from the fact that radars only sense a single spatial Fourier component of the plasma density fluctuations. Wave activities at different scales, regardless of their intensity, remain undetectable to the radar. This is a strong contrast to *in-situ* measurements where attention is often focused on the strongest temporal/spectral components of the measured signal. The inherent sensitivity of radars to wavenumber allows to precisely determine the phase velocity, $v_\phi = \omega/k_{\text{detection}}$, of the detected waves and thus the energy of the Landau resonant electrons $E = \frac{1}{2}m_e v_\phi^2$. Such calculations generally indicate that Langmuir waves underlying LT echoes are in direct energy exchange with low energy electrons in the range ~5–20 eV. Langmuir waves generated by a more energetic electron beam would obtain wavenumbers smaller than $k_{\text{detection}}$—from which the energy is expected to transfer to yet smaller wavenumber via parametric decay, bypassing detection by radars. The detection of turbulence by incoherent scatter radars would then require a mechanism to transfer the energy to larger wavenumbers—perhaps via Langmuir collapse.

The apparent inconsistency between the common detection of signatures of collapse in radar data and the lack of such observations in *in-situ* measurements may have its roots in the altitude of various observations. Radar echoes are consistently observed in the vicinity of the F region peak where the local plasma frequency is often a factor of 2–3 greater than the electron

gyro-frequency of $\Omega_e \approx 1.5$ MHz. At higher altitudes, the domain of many *in-situ* observations, plasma frequency could drop to below the electron gyrofrequency, where collapse is inhibited by the altered topology of the Langmuir dispersion relation. The effect of the enhanced damping introduced by the suprathermal electrons exits at both the altitudes of the radar observations and *in-situ* measurements. The enhanced damping could truncate the cascade of parametric decays, preventing the transfer of energy to $k \approx 0$ where collapse may initiate via the modulational instability. This, however, may be a secondary issue since as was discussed in **Section 2.2**, modulational instability at small wavenumbers is not the only path to collapse. Nucleation in density cavities and direct wave collapse of sufficiently intense Langmuir waves (for which $W > (k\lambda_D)^2$) (Nicholson and Goldman, 1978) can still lead to wave collapse at larger wavenumbers.

Another curious aspect of Langmuir wave observations in the auroral ionosphere is the near-complete absence of harmonic wave detection at multiples of plasma frequency. An exception to this is the study of Boehm (1987) where they detected short (~1 s) intervals of waves near $2f_e$ in the presence of Langmuir waves when $2f_e$ matched the cyclotron frequency. They found the observations to be consistent with second harmonic generation in the upper-hybrid mode just above f_c. Electrostatic or electromagnetic harmonic waves at multiples of f_e are commonly observed during intense Langmuir wave events in type III radio burst source regions as well as in planetary foreshocks (e.g., Kellogg et al., 2010; Malaspina et al., 2010, and references therein). A diverse range of mechanisms has been proposed to explain the harmonic fields. These include electromagnetic emission by coalesce of oppositely-directed Langmuir waves (e.g., Cairns and Melrose, 1985; Cairns, 1987), electrostatic Langmuir wave harmonic generation (e.g., Klimas, 1983; Gaelzer et al., 2003; Umeda et al., 2003; Yoon et al., 2003), electromagnetic emission from collapsing cavitons (Galeev and Krasnoselskikh, 1976; Goldman et al., 1980; Akimoto et al., 1988), antenna radiation (Papadopoulos and Freund, 1978; Malaspina et al., 2013), electron trapping (Kellogg et al., 2010), and wave rectification in spacecraft's plasma sheath (Boehm et al., 1994; Graham et al., 2014).

With respect to the source of free energy for Langmuir turbulence in the ionosphere, *in-situ* measurements have shown that intense Langmuir waves are often associated with dispersive, field-aligned electron bursts that are accelerated by inertial Alfvén waves. On the other hand, conjugate measurements by radars and high-resolution optical imagers have shown that LT echoes are associated with dynamic small-scale auroral structures likely related to dispersive-scale Alfvén waves (see **Figures 9A,B**). Results from one-dimensional Zakharov simulations suggest that the measured ISR spectra are best reproduced numerically when the modeled electron beams extend a positive slope to energies as low as 5 eV, such that ion-acoustic waves are induced by parametric decays at wavenumbers greater than $k_{\text{detection}}$ (Akbari et al., 2015). Such low energy components of an electron beam, however, would likely be significantly modified by collisions at altitudes of some radar observations between 180 and 300 km. This leads to a speculation that perhaps an unstable feature of the electron distribution function which eventually gives rise to LT echoes is produced locally at ionospheric heights in response to electron precipitation (Akbari et al., 2015). Such a speculation, however, is not backed with concrete evidence. The source of the free energy for the turbulence, thus, remains unknown.

As a result of several decades of experimental, theoretical, and numerical investigations, various aspects of Langmuir wave observations in the ionosphere—including their evolution into turbulence and their interactions with the streaming and the background electrons—are now reasonably understood. Less understood, however, are the possible consequences of the micro-scale processes for the ionosphere on a larger scale. Often mentioned in the literature, is the role of Langmuir waves in the energy exchange chain, in which a part of energy carried by energetic electrons become available to the background particles via excitation of Langmuir waves, their decay into other wave modes, and the subsequent damping (e.g., Beghin et al., 1989; Kintner et al., 1995; Stasiewicz et al., 1996; Lizunov et al., 2001; Singh et al., 2001). The applicability of these scenarios to the plasma of the F region ionosphere is open to investigation thanks to the spatiotemporal context that is provided by ground-based instruments.

Examination of several events where enhanced Langmuir and ion-acoustic signatures continuously persist in radar's field of view for several minutes reveals that the bulk of the ionospheric plasma in the vicinity of the turbulence layers, is not significantly affected by the turbulence—that is, no significant change in the background electron temperature, ion temperature, or bulk plasma drift at altitudes above the layers are observed. It is, however, not clear whether the lack of ionospheric response is due to the nature of the instabilities, the energetics of the process, or a limited spatial extent over which they exist. Conjugate auroral imagery at the time of echoes indicates that similar optical morphologies observed on the magnetic field lines probed by the radar often exists over a wider spatial extent in field-perpendicular directions. This, however, does not necessarily imply that the turbulence is active over the same spatial extents. Answering this question would ideally require *in-situ* measurements from within the turbulence layers.

An ionospheric phenomenon that is potentially relevant to the discussions above is the so-called 'Naturally Enhanced Ion Acoustic Lines (NEIALs)'. NEIAL—a well-known terminology in the incoherent scatter radar community—refers to the sudden intensification of the ion-acoustic peaks in the ISR spectrum. At high-latitudes, NEIALs are often detected along the magnetic field lines over an extended altitude range (several hundred km). An example is shown in the left panels of **Figure 11** where received backscatter power in the ion line channel is shown for three radar beam directions within two degrees from ∥ **B**. The streaks with power >10 dB are all NEIALs. Similar to the low-frequency components of the Langmuir turbulence echoes, NEIALs are manifestations of large-amplitude ion-acoustic waves. The two types of echoes, however, are easily distinguished given the different altitudinal and spectral features they pose (see for example Michell et al. (2014).) Several mechanisms have been proposed to explain the occurrence of NEIALs—each of which remains plausible. These include the electron-ion streaming instability (Foster et al., 1988), ion-ion

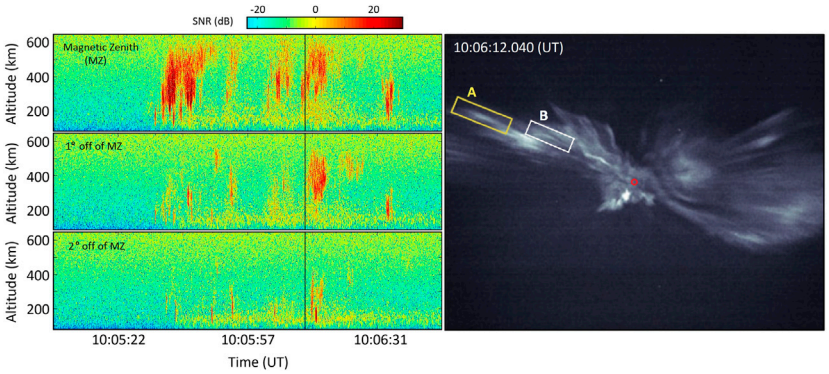

FIGURE 11 | Adapted from Dahlgren et al. (2013) and Akbari and Semeter (2014): Naturally Enhanced Ion Acoustic Lines and conjugate auroral features. The left panels show the Range–Time–Intensity plots of received power in the ion line channel for three radar beams during a period when a substorm expansion crossed through the PFISR beam configuration. Mentioned in parentheses are angles with respect to the magnetic-zenith. The right panel shows an image captured by a high-speed, high-resolution imager at 10:06:12.040 UT, marked by the vertical line in the left panels. Example optical features identified as 'A' and 'B' show flaming motion in the radial direction with respect to the red circle which marks the location of the magnetic zenith over Poker Flat, AK. A video of a sequence of optical images are available from Dahlgren et al. (2013).

streaming instability (Wahlund et al., 1992a), ion cyclotron waves (Bahcivan and Cosgrove, 2008), as well as the parametric decay of beam-generated Langmuir waves (Forme, 1993). The plausibility of a number of these mechanisms is discussed in a review by Sedgemore-Schulthess and Maurice (2001).

Despite the fact that enhanced Langmuir waves are generally not detected in conjunction with NEIALs (potentially, due to the different wavenumbers of Langmuir and ion-acoustic waves involved in a parametric decay), the plausibility of the latter mechanism has been demonstrated by several theoretical and numerical works (Forme, 1999; Kontar and Pécseli, 2005; Guio and Forme, 2006; Sullivan et al., 2008; Pavan et al., 2010; Diaz et al., 2011; Ziebell et al., 2011; Diaz et al., 2012). An evidence suggesting a connection between Langmuir waves and NEIALs comes from conjugate optical and radar observations. Such observations have shown that NEIALs are detected in association with aurora that contains large fluxes of low energy electrons as well as optical features often referred to as the "flaming" aurora (Blixt et al., 2005; Dahlgren et al., 2013; Michell et al., 2014). An example of the latter is shown in the right panel of **Figure 11**. The flaming aurora—the apparent upward motion of localized auroral features along the magnetic field lines—is the optical manifestation of field-aligned dispersive electron bursts where a flux of high energy electrons reach the ionosphere first, depositing energy at lower altitudes, followed by less energetic electrons which increasingly deposit energy at higher altitudes. As discussed in the previous section, field-aligned electron bursts are linked to large-amplitude Langmuir waves and their nonlinear evolution in the auroral ionosphere. In **Figure 11A**, significant variations in the backscatter power are observed from beam to beam. The echoes at higher altitudes (>250 km) in the magnetic zenith beam (top panel) are less pronounced at 1° offset and almost completely disappear at 2° offset. This is consistent with a generation mechanism based on parametric decay of Langmuir waves—which has been shown, theoretical and experimentally, to be confined within small angles from the magnetic field direction.

One significance of NEIALs is their relation with strong modification of the bulk ionospheric plasma. NEIALs are often observed along with significant electron temperature enhancements, up to 8000 K, and upward motion of cold ions with velocities in excess of 0.5 km/s (Wahlund et al., 1992b; Forme et al., 1995; Forme and Fontaine, 1999; Ogawa et al., 2000). It has been suggested that the enhanced electron heating and the ion upflow may be direct consequences of the turbulence (e.g., Wahlund et al., 1993; Forme et al., 1993). NEIALs are, therefore, reminders that the micro-scale processes that are discussed in this review may have larger-scale effects on the bulk ionospheric plasma. Regardless of such effects, however, the extremely rich range of plasma processes that are involved—which are relevant to observations in many space and astrophysical plasmas far from Earth, including planetary foreshocks (e.g., Robinson and Newman, 1991; Thiessen and Kellogg, 1993), the solar wind (e.g., Thejappa et al., 2012a, b; Graham et al., 2012; Graham and Cairns, 2014), the lower solar corona (e.g., Nulsen et al., 2007), and pulsar magnetospheres (e.g., Asseo and Porzio, 2006)—themselves, underline their importance and justify and call for more focused investigations.

AUTHOR CONTRIBUTIONS

All authors listed have made a substantial, direct, and intellectual contribution to the work and approved it for publication.

ACKNOWLEDGMENTS

HA is supported by the NASA Postdoctoral Program (NPP) administrated by USRA. Work at Dartmouth College was supported by NASA Grant NNX17AF92G and sub-award W000726838 to NASA Grant NNX15AL08G.

REFERENCES

Akbari, H., Bhatt, A., La Hoz, C., and Semeter, J. L. (2017). Incoherent scatter plasma lines: observations and applications. *Space Sci. Rev.* 212, 249–294. doi:10.1007/s11214-017-0355-7

Akbari, H., Guio, P., Hirsch, M. A., and Semeter, J. L. (2016). Zakharov simulations of beam-induced turbulence in the auroral ionosphere. *J. Geophys. Res. Space Phys.* 121, 4811–4825. doi:10.1002/2016ja022605

Akbari, H., Semeter, J., Dahlgren, H., Diaz, M., Zettergren, M., Strømme, A., et al. (2012). Anomalous isr echoes preceding auroral breakup: evidence for strong Langmuir turbulence. *Geophys. Res. Lett.* 39. doi:10.1029/2011gl050288

Akbari, H., and Semeter, J. L. (2014). Aspect angle dependence of naturally enhanced ion acoustic lines. *J. Geophys. Res. Space Phys.* 119, 5909–5917. doi:10.1002/2014ja019835

Akbari, H., Semeter, J. L., Hirsch, M. A., Guio, P., and Nicolls, M. J. (2015). Evidence for generation of unstable suprathermal electron population in the auroral f region. *Geophys. Res. Lett.* 42, 185–192. doi:10.1002/2014gl062598

Akbari, H., Semeter, J. L., Nicolls, M. J., Broughton, M., and LaBelle, J. W. (2013). Localization of auroral Langmuir turbulence in thin layers. *J. Geophys. Res. Space Phys.* 118, 3576–3583. doi:10.1002/jgra.50314

Akimoto, K., Omura, Y., and Matsumoto, H. (1996). Rapid generation of Langmuir wave packets during electron beam-plasma instabilities. *Phys. Plasmas* 3, 2559–2563. doi:10.1063/1.871963

Akimoto, K., Rowland, H. L., and Papadopoulos, K. (1988). Electromagnetic radiation from strong Langmuir turbulence. *Phys. Fluids* 31, 2185–2189. doi:10.1063/1.866618

Arnoldy, R. L., and Choy, L. W. (1973). Auroral electrons of energy less than 1 kev observed at rocket altitudes. *J. Geophys. Res.* 78, 2187–2200. doi:10.1029/ja078i013p02187

Asseo, E., and Porzio, A. (2006). Strong Langmuir turbulence in a pulsar emission region: statistical analysis. *Month. Notices R. Astronom. Soc.* 369, 1469–1490. doi:10.1111/j.1365-2966.2006.10386.x

Bahcivan, H., and Cosgrove, R. (2008). Enhanced ion acoustic lines due to strong ion cyclotron wave fields. *Ann. Geophys.* 26, 2081–2095. doi:10.5194/angeo-26-2081-2008

Bauer, S. J., and Stone, R. G. (1968). Satellite observations of radio noise in the magnetosphere. *Nature* 218, 1145. doi:10.1038/2181145a0

Beghin, C., Rauch, J. L., and Bosqued, J. M. (1989). Electrostatic plasma waves and hf auroral hiss generated at low altitude. *J. Geophys. Res.* 94, 1359–1378. doi:10.1029/ja094ia02p01359

Bernhardt, P. A., Tepley, C. A., and Duncan, L. M. (1989). Airglow enhancements associated with plasma cavities formed during ionospheric heating experiments. *J. Geophys. Res.* 94, 9071–9092. doi:10.1029/ja094ia07p09071

Blixt, E., Grydeland, T., Ivchenko, N., Hagfors, T., La Hoz, C., Lanchester, B., et al. (2005). *Dynamic rayed aurora and enhanced ion-acoustic radar echoes*. Berlin: Springer.

Boehm, M. H., Carlson, C. W., McFadden, J. P., Clemmons, J. H., Ergun, R. E., and Mozer, F. S. (1994). Wave rectification in plasma sheaths surrounding electric field antennas. *J. Geophys. Res.* 99, 21361–21374. doi:10.1029/94ja01766

Boehm, M. H. (1987). Waves and static electric fields in the auroral acceleration region. Ph.D. thesis. Berkeley: University of California.

Bonnell, J., Kintner, P., Wahlund, J.-E., and Holtet, J. A. (1997). Modulated Langmuir waves: observations from freja and scifer. *J. Geophys. Res.* 102, 17233–17240. doi:10.1029/97ja01499

Broughton, M. C., LaBelle, J., Roberg-Clark, G. T., McCready, M., and Bunch, N. L. (2012). Experimental tests of a topside generation mechanism for auroral medium frequency radio emissions. *J. Geophys. Res.* 117, 33. doi:10.1029/2012JA018034

Broughton, M. C., LaBelle, J., and Yoon, P. H. (2014). A new natural radio emission observed at South Pole Station. *J. Geophys. Res. Space Phys.* 119, 566. doi:10.1002/2013JA019467

Bryant, D. A., Hall, D. S., and Lepine, D. R. (1978). Electron acceleration in an array of auroral arcs. *Planet. Space Sci.* 26, 81–92. doi:10.1016/0032-0633(78)90039-9

Burinskaya, T. M., Rusanov, A. A., Rauch, J. L., Miles, A., Mogilevsky, M. M., Trotignon, J. G., et al. (2003). Small-scale bursts of Langmuir waves in the polar cap. *Adv. Space Res.* 31, 1247–1252. doi:10.1016/s0273-1177(02)00937-7

Cairns, I. H. (1989). Electrostatic wave generation above and below the plasma frequency by electron beams. *Phys. Fluids B: Plasma Phys.* 1, 204–213. doi:10.1063/1.859088

Cairns, I. H., and Layden, A. (2018). Kinematics of electrostatic 3-wave decay of generalized Langmuir waves in magnetized plasmas. *Phys. Plasmas* 25, 082309. doi:10.1063/1.5037300

Cairns, I. H., and Melrose, D. B. (1985). A theory for the 2fpradiation upstream of the Earth's bow shock. *J. Geophys. Res.* 90, 6637–6640. doi:10.1029/ja090ia07p06637

Cairns, I. H., and Menietti, J. D. (2001). Stochastic growth of waves over Earth's polar cap. *J. Geophys. Res.* 106, 29515–29529. doi:10.1029/2000ja000422

Cairns, I. H., and Nishikawa, K.-I. (1989). Simulations relevant to the beam instability in the foreshock. *J. Geophys. Res.* 94, 79–88. doi:10.1029/ja094ia01p00079

Cairns, I. H., Robinson, P. A., and Anderson, R. R. (2000). Thermal and driven stochastic growth of Langmuir waves in the solar wind and Earth's foreshock. *Geophys. Res. Lett.* 27, 61–64. doi:10.1029/1999gl010717

Cairns, I. H., and Robinson, P. A. (1997). First test of stochastic growth theory for Langmuir waves in Earth's foreshock. *Geophys. Res. Lett.* 24, 369–372. doi:10.1029/97gl00084

Cairns, I. H., and Robinson, P. A. (1995). Inconsistency of ulysses millisecond Langmuir spikes with wave collapse in type iii radio sources. *Geophys. Res. Lett.* 22, 3437–3440. doi:10.1029/95gl03513

Cairns, I. H. (1987). Second harmonic plasma emission involving ion sound waves. *J. Plasma Phys.* 38, 179–198. doi:10.1017/s0022377800012502

Carlson, C., Ergun, R. E., Mallinckrodt, A. J., and Haerendel, G. (1987). *Observations of intense electron bernstein wave emissions in an auroral plasma*. Unpublished manuscript

Carlson, H. C., Wickwar, V. B., and Mantas, G. P. (1982). Observations of fluxes of suprathermal electrons accelerated by hf excited instabilities. *J. Atmos. Terrestrial Phys.* 44, 1089–1100. doi:10.1016/0021-9169(82)90020-4

Clemmow, P. C. (2018). *Electrodynamics of particles and plasmas*. Boca Raton, FL: CRC Press, Taylor and Francis Group.

Colpitts, C. A., and LaBelle, J. (2008). Mode identification of whistler mode, Z-mode, and Langmuir/Upper Hybrid mode waves observed in an auroral sounding rocket experiment. *J. Geophys. Res.* 113, 27. doi:10.1029/2007JA012325

Dahlgren, H., Schlatter, N. M., Ivchenko, N., Roth, L., and Karlsson, A. (2017). Relation of anomalous f region radar echoes in the high-latitude ionosphere to auroral precipitation. *Ann. Geophys.* 35, 475–479. doi:10.5194/angeo-35-475-2017

Dahlgren, H., Semeter, J. L., Marshall, R. A., and Zettergren, M. (2013). The optical manifestation of dispersive field-aligned bursts in auroral breakup arcs. *J. Geophys. Res. Space Phys.* 118, 4572–4582. doi:10.1002/jgra.50415

Davidson, R. C. (1969). *Nonlinear plasma theory*. New York: Academic Press.

Diaz, M., Oppenheim, M., Semeter, J., and Zettergren, M. (2011). Particle-in-cell simulation of incoherent scatter radar spectral distortions related to beam-plasma interactions in the auroral ionosphere. *J. Geophys. Res. Space Phys.* 116, 39–43. doi:10.1029/2010ja016096

Diaz, M., Zettergren, M., Semeter, J., and Oppenheim, M. (2012). Plasma parameter analysis of the Langmuir decay process via particle-in-cell simulations. *Annales Geophysicae* 30, 1169. doi:10.5194/angeo-30-1169-2012

Dombrowski, M., LaBelle, J., Rowland, D., Pfaff, R., and Kletzing, C. (2012). Interpretation of vector electric field measurements of bursty Langmuir waves in the cusp. *J. Geophys. Res. Space Phys.* 117, 1173. doi:10.1029/2012ja017741

Dombrowski, M. P., LaBelle, J., Kletzing, C. A., Bounds, S. R., Cairns, I. H., and Kaeppler, S. R. (2019). Statistical study of electron bunching in auroral Langmuir waves. *J. Geophys. Res. Space Phys.* 124, 5956. doi:10.1029/2018JA026262

Doolen, G. D., DuBois, D. F., and Rose, H. A. (1985). Nucleation of cavitons in strong Langmuir turbulence. *Phys. Rev. Lett.* 54, 804. doi:10.1103/physrevlett.54.804

DuBois, D. F., Hansen, A., Rose, H. A., and Russell, D. (1993). Excitation of strong Langmuir turbulence in the ionosphere: comparison of theory and observations. *Phys. Fluids B: Plasma Phys.* 5, 2616–2622. doi:10.1063/1.860699

DuBois, D. F., Rose, H. A., and Russell, D. (1990). Excitation of strong Langmuir turbulence in plasmas near critical density: application to hf heating of the ionosphere. *J. Geophys. Res.* 95, 21221–21272. doi:10.1029/ja095ia12p21221

Dum, C. T., and Nishikawa, K. I. (1994). Two-dimensional simulation studies of the electron beam-plasma instability. *Phys. Plasmas* 1, 1821–1826. doi:10.1063/1.870636

Dum, C. T. (1989). Transition in the dispersive properties of beam-plasma and two-stream instabilities. *J. Geophys. Res.* 94, 2429–2442. doi:10.1029/ja094ia03p02429

Dziubenko, N., Ivchenko, V., Milinevskii, G., and Mishin, E. (1980). Influence of plasma collective effects on the structure of the aurora borealis streamers. *Soviet J. Exp. Theor. Phys. Lett.* 31, 607–610.

Ekeberg, J., Wannberg, G., Eliasson, L., and Stasiewicz, K. (2010). Ion-acoustic solitary waves and spectrally uniform scattering cross section enhancements. *Annales Geophysicae* 28, 1299–1306. doi:10.5194/angeo-28-1299-2010

Eliasson, B., Shao, X., Milikh, G., Mishin, E. V., and Papadopoulos, K. (2012). Numerical modeling of artificial ionospheric layers driven by high-power hf heating. *J. Geophys. Res. Space Phys.* 117, 67. doi:10.1029/2012ja018105

Ergun, R. E., Carlson, C. W., McFadden, J. P., Clemmons, J. H., and Boehm, M. H. (1991a). Evidence of a transverse Langmuir modulational instability in a space plasma. *Geophys. Res. Lett.* 18, 1177–1180. doi:10.1029/91gl01563

Ergun, R. E., Carlson, C. W., McFadden, J. P., Clemmons, J. H., and Boehm, M. H. (1991b). Langmuir wave growth and electron bunching: results from a wave-particle correlator. *J. Geophys. Res.* 96, 225–238. doi:10.1029/90ja01596

Ergun, R. E., Delory, G. T., Klementis, E., Carlson, C. W., McFadden, J. P., Roth, I., et al. (1993). Vlf wave growth from dispersive bursts of field-aligned electron fluxes. *J. Geophys. Res.* 98, 3777–3787. doi:10.1029/92ja02193

Ergun, R. E., Larson, D., Lin, R. P., McFadden, J. P., Carlson, C. W., Anderson, K. A., et al. (1998). WindSpacecraft observations of solar impulsive electron events associated with solar type III radio bursts. *ApJ* 503, 435. doi:10.1086/305954

Ergun, R., Malaspina, D., Cairns, I. H., Goldman, M., Newman, D., Robinson, P., et al. (2008). Eigenmode structure in solar-wind Langmuir waves. *Phys. Rev. Lett.* 101, 051101. doi:10.1103/physrevlett.101.051101

Etcheto, J., and Faucheux, M. (1984). Detailed study of electron plasma waves upstream of the Earth's bow shock. *J. Geophys. Res.* 89, 6631–6653. doi:10.1029/ja089ia08p06631

Fitzenreiter, R. J., Ogilvie, K. W., Chornay, D. J., and Keller, J. (1998). Observations of electron velocity distribution functions in the solar wind by the wind spacecraft: high angular resolution strahl measurements. *Geophys. Res. Lett.* 25, 249–252. doi:10.1029/97gl03703

Forme, F., and Fontaine, D. (1999). Enhanced ion acoustic fluctuations and ion outflows. *Annales Geophysicae* 17, 182–189. doi:10.1007/s00585-999-0182-6

Forme, F. (1999). Parametric decay of beam-driven Langmuir wave and enhanced ion-acoustic fluctuations in the ionosphere: a weak turbulence approach. *Annales Geophysicae* 17, 1172–1181. doi:10.1007/s00585-999-1172-4

Forme, F. R. E. (1993). A new interpretation on the origin of enhanced ion acoustic fluctuations in the upper ionosphere. *Geophys. Res. Lett.* 20, 2347–2350. doi:10.1029/93gl02490

Forme, F. R. E., Fontaine, D., and Wahlund, J. E. (1995). Two different types of enhanced ion acoustic fluctuations observed in the upper ionosphere. *J. Geophys. Res.* 100, 14625–14636. doi:10.1029/94ja01093

Forme, F. R. E., Wahlund, J.-E., Opgenoorth, H. J., Persson, M. A. L., and Mishin, E. V. (1993). Effects of current driven instabilities on the ion and electron temperatures in the topside ionosphere. *J. Atmos. terrestrial Phys.* 55, 647–666. doi:10.1016/0021-9169(93)90011-m

Foster, J. C., Del Pozo, C., Groves, K., and St. Maurice, J.-P. (1988). Radar observations of the onset of current driven instabilities in the topside ionosphere. *Geophys. Res. Lett.* 15, 160–163. doi:10.1029/gl015i002p00160

Fung, S. F., and Hoffman, R. A. (1988). On the spectrum of the secondary auroral electrons. *J. Geophys. Res.* 93, 2715–2724. doi:10.1029/ja093ia04p02715

Fuselier, S. A., Gurnett, D. A., and Fitzenreiter, R. J. (1985). The downshift of electron plasma oscillations in the electron foreshock region. *J. Geophys. Res.* 90, 3935–3946. doi:10.1029/ja090ia05p03935

Gaelzer, R., Yoon, P. H., Umeda, T., Omura, Y., and Matsumoto, H. (2003). Harmonic Langmuir waves. ii. turbulence spectrum. *Phys. Plasmas* 10, 373–381. doi:10.1063/1.1537239

Gaelzer, R., Ziebell, L. F., Viñas, A. F., Yoon, P. H., and Ryu, C. M. (2008). Asymmetric solar wind electron superthermal distributions. *ApJ* 677, 676. doi:10.1086/527430

Galeev, A., and Krasnoselskikh, V. (1976). Strong Langmuir turbulence in the earth's magnetosphere as a source of kilometer radio emission. *Soviet J. Exp. Theor. Phys. Lett.* 24, 515–517.

Galeev, A. (1975). *Plasma turbulence in the magnetosphere with special regard to plasma heating. Physics of the hot plasma in the magnetosphere*. Berlin: Springer, 251–270.

Galeev, A., Sagdeev, R., Shapiro, V., and Shevchenko, V. (1977a). Langmuir turbulence and dissipation of high frequency energy. *Soviet J. Exp. Theor. Phys.* 73, 1352–1369.

Galeev, A., Sagdeev, R., Shapiro, V., and Shevchenko, V. (1977b). Relaxation of high-current electron beams and the modulational instability. *Soviet J. Exp. Theor. Phys.* 45, 266–271.

Goldman, M. V., Newman, D. L., Wang, J. G., and Muschietti, L. (1996). Langmuir turbulence in space plasmas. *Phys. Scr.*, T63, 28. doi:10.1088/0031-8949/1996/t63/003

Goldman, M. V., Reiter, G. F., and Nicholson, D. R. (1980). Radiation from a strongly turbulent plasma: application to electron beam-excited solar emissions. *Phys. Fluids* 23, 388–401. doi:10.1063/1.862982

Goldman, M. V. (1984). Strong turbulence of plasma waves. *Rev. Mod. Phys.* 56, 709. doi:10.1103/revmodphys.56.709

Gough, M. P., Christiansen, P. J., and Wilhelm, K. (1990). Auroral beam-plasma interactions: particle correlator investigations. *J. Geophys. Res.* 95, 12287–12294. doi:10.1029/ja095ia08p12287

Gough, M. P., and Urban, A. (1983). Auroral beam/plasma interaction observed directly. *Planet. Space Sci.* 31, 875.

Graham, D. B., and Cairns, I. H. (2014). Dynamical evidence for nonlinear Langmuir wave processes in type iii solar radio bursts. *J. Geophys. Res. Space Phys.* 119, 2430–2457. doi:10.1002/2013ja019425

Graham, D. B., Cairns, I. H., Malaspina, D. M., and Ergun, R. E. (2012). Evidence against the oscillating two-stream instability and spatial collapse of Langmuir waves in solar type iii radio bursts. *ApJ* 753, L18. doi:10.1088/2041-8205/753/1/l18

Graham, D. B., Cairns, I. H., and Malaspina, D. M. (2014). Harmonic waves and sheath rectification in type iii solar radio bursts. *J. Geophys. Res. Space Phys.* 119, 723–741. doi:10.1002/2013ja019317

Gregory, P. C. (1969). Radio emission from auroral electrons. *Nature* 221, 350. doi:10.1038/221350a0

Guio, P., and Forme, F. (2006). Zakharov simulations of Langmuir turbulence: effects on the ion-acoustic waves in incoherent scattering. *Phys. Plasmas* 13, 122902. doi:10.1063/1.2402145

Hallinan, T. J., Stenbaek-Nielsen, H. C., and Deehr, C. S. (1985). Enhanced aurora. *J. Geophys. Res.* 90, 8461–8475. doi:10.1029/ja090ia09p08461

Isham, B., La Hoz, C., Rietveld, M. T., Hagfors, T., and Leyser, T. B. (1999). Cavitating Langmuir turbulence observed during high-latitude ionospheric wave interaction experiments. *Phys. Rev. Lett.* 83, 2576. doi:10.1103/physrevlett.83.2576

Isham, B., Rietveld, M., Guio, P., Forme, F., Grydeland, T., and Mjølhus, E. (2012). Cavitating Langmuir turbulence in the terrestrial aurora. *Phys. Rev. Lett.* 108, 105003. doi:10.1103/physrevlett.108.105003

Kaufmann, R. L., Dusenbery, P. B., and Thomas, B. J. (1978). Stability of the auroral plasma: parallel and perpendicular propagation of electrostatic waves. *J. Geophys. Res.* 83, 5663–5669. doi:10.1029/ja083ia12p05663

Kellogg, P. J., Goetz, K., and Monson, S. (2010). Harmonics of Langmuir waves in the earth's foreshock. *J. Geophys. Res. Space Phys.* 115, 63. doi:10.1029/2009ja014635

Kellogg, P. J., Monson, S. J., and Whalen, B. A. (1978). Rocket observation of high frequency waves over a strong aurora. *Geophys. Res. Lett.* 5, 47. doi:10.1029/gl005i001p00047

Khotyaintsev, Y., Lizunov, G., and Stasiewicz, K. (2001). Langmuir wave structures registered by freja: analysis and modeling. *Adv. Space Res.* 28, 1649–1654. doi:10.1016/s0273-1177(01)00485-9

Kintner, P. M., Bonnell, J., Powell, S., Wahlund, J.-E., and Holback, B. (1995). First results from the freja hf snapshot receiver. *Geophys. Res. Lett.* 22, 287–290. doi:10.1029/94gl02549

Kletzing, C. A., and Hu, S. (2001). Alfvén wave generated electron time dispersion. *Geophys. Res. Lett.* 28, 693–696. doi:10.1029/2000gl012179

Kletzing, C. A., LaBelle, J., Bounds, S. R., Dolan, J., Kaeppler, S. R., and Dombrowski, M. (2017). Phase sorting wave-particle correlator. *J. Geophys. Res. Space Phys.* 122, 2069–2078. doi:10.1002/2016ja023334

Kletzing, C. A., LaBelle, J., Bounds, S. R., Dolan, J., Kaeppler, S. R., and Dombrowski, M. (2017). Phase sorting wave-particle correlator. *J. Geophys. Res. Space Phys.* 122, 2069. doi:10.1002/2016JA023334

Kletzing, C., Bounds, S., LaBelle, J., and Samara, M. (2005). Observation of the reactive component of Langmuir wave phase-bunched electrons. *Geophys. Res. Lett.* 32, 112. doi:10.1029/2004gl021175

Kletzing, C., and Muschietti, L. (2006). *Phase correlation of electrons and Langmuir waves. Geospace electromagnetic waves and radiation.* Berlin: Springer, 313–337.

Klimas, A. J. (1983). A mechanism for plasma waves at the harmonics of the plasma frequency in the electron foreshock boundary. *J. Geophys. Res.* 88, 9081–9091. doi:10.1029/ja088ia11p09081

Klimas, A. J. (1990). Trapping saturation of the bump-on-tail instability and electrostatic harmonic excitation in Earth's foreshock. *J. Geophys. Res.* 95, 14905–14924. doi:10.1029/ja095ia09p14905

Kline, J., Montgomery, D., Yin, L., DuBois, D., Albright, B., Bezzerides, B., et al. (2006). Different k λ d regimes for nonlinear effects on Langmuir waves. *Phys. Plasmas* 13, 055906. doi:10.1063/1.2178777

Kontar, E., and Pécseli, H. (2005). Nonlinear wave interactions as a model for naturally enhanced ion acoustic lines in the ionosphere. *Geophys. Res. Lett.* 32. doi:10.1029/2004gl022182

Krafft, C., Volokitin, A. S., and Krasnoselskikh, V. V. (2015). Langmuir wave decay in inhomogeneous solar wind plasmas: simulation results. *ApJ* 809, 176. doi:10.1088/0004-637x/809/2/176

LaBelle, J. (2011). An explanation for the fine structure of mf burst emissions. *Geophys. Res. Lett.* 38, 114. doi:10.1029/2010gl046218

LaBelle, J., Cairns, I. H., and Kletzing, C. (2010). Electric field statistics and modulation characteristics of bursty Langmuir waves observed in the cusp. *J. Geophys. Res. Space Phys.* 115, 139. doi:10.1029/2010ja015277

Layden, A., Cairns, I. H., Li, B., and Robinson, P. (2013). Electrostatic decay in a weakly magnetized plasma. *Phys. Rev. Lett.* 110, 185001. doi:10.1103/physrevlett.110.185001

Lee, S.-Y., Ziebell, L. F., Yoon, P. H., Gaelzer, R., and Lee, E. S. (2019). Particle-in-cell and weak turbulence simulations of plasma emission. *ApJ* 871, 74. doi:10.3847/1538-4357/aaf476

Lefeuvre, A. C., and LaBelle, J. (2020). Estimating polar cap density and medium-frequency burst source heights using 2fce roar radio emissions. *J. Geophys. Res. Space Phys.* 125, e2020JA028166. doi:10.1029/2020ja028166

Li, B., Cairns, I. H., Robinson, P., LaBelle, J., and Kletzing, C. (2010). Waveform and envelope field statistics for waves with stochastically driven amplitudes. *Phys. Plasmas* 17, 032110. doi:10.1063/1.3353092

Li, B., Willes, A. J., Robinson, P. A., and Cairns, I. H. (2005a). Dynamics of fundamental electromagnetic emission via beam-driven Langmuir waves. *Phys. Plasmas* 12, 052324. doi:10.1063/1.1906214

Li, B., Willes, A. J., Robinson, P. A., and Cairns, I. H. (2005b). Second harmonic electromagnetic emission via beam-driven Langmuir waves. *Phys. Plasmas* 12, 012103. doi:10.1063/1.1812274

Lin, R. P., Potter, D. W., Gurnett, D. A., and Scarf, F. L. (1981). Energetic electrons and plasma waves associated with a solar type iii radio burst. *ApJ* 251, 364–373. doi:10.1086/159471

Lizunov, G. V., Khotyaintsev, Y., and Stasiewicz, K. (2001). Parametric decay to lower hybrid waves as a source of modulated Langmuir waves in the topside ionosphere. *J. Geophys. Res.* 106, 24755–24763. doi:10.1029/2001ja900074

Lotko, W., and Maggs, J. E. (1981). Amplification of electrostatic noise in cyclotron resonance with an adiabatic auroral beam. *J. Geophys. Res.* 86, 3449–3458. doi:10.1029/ja086ia05p03449

Lotko, W., and Maggs, J. E. (1979). Damping of electrostatic noise by warm auroral electrons. *Planet. Space Sci.* 27, 1491–1506. doi:10.1016/0032-0633(79)90095-3

Lundin, R., Haerendel, G., and Grahn, S. (1994). The freja project. *Geophys. Res. Lett.* 21, 1823–1826. doi:10.1029/94gl01424

Maggs, J. E. (1976). Coherent generation of vlf hiss. *J. Geophys. Res.* 81, 1707–1724. doi:10.1029/ja081i010p01707

Maggs, J. E. (1978). Electrostatic noise generated by the auroral electron beam. *J. Geophys. Res.* 83, 3173–3188. doi:10.1029/ja083ia07p03173

Maggs, J. E., and Lotko, W. (1981). Altitude dependent model of the auroral beam and beam-generated electrostatic noise. *J. Geophys. Res.* 86, 3439–3447. doi:10.1029/ja086ia05p03439

Malaspina, D. M., Cairns, I. H., and Ergun, R. E. (2010). The 2fp radiation from localized Langmuir waves. *J. Geophys. Res. Space Phys.* 115, 339. doi:10.1029/2009ja014609

Malaspina, D. M., Graham, D. B., Ergun, R. E., and Cairns, I. H. (2013). Langmuir wave harmonics due to driven nonlinear currents. *J. Geophys. Res. Space Phys.* 118, 6880–6888. doi:10.1002/2013ja019309

Matthews, D. L., Pongratz, M., and Papadopoulos, K. (1976). Nonlinear production of suprathermal tails in auroral electrons. *J. Geophys. Res.* 81, 123–129. doi:10.1029/ja081i001p00123

McAdams, K. L., Ergun, R. E., and LaBelle, J. (2000). Hf chirps: eigenmode trapping in density depletions. *Geophys. Res. Lett.* 27, 321–324. doi:10.1029/1999gl003655

McAdams, K. L., and LaBelle, J. (1999). Narrowband structure in hf waves above the electron plasma frequency in the auroral ionosphere. *Geophys. Res. Lett.* 26, 1825–1828. doi:10.1029/1999gl900428

McAdams, K. L., LaBelle, J., Trimpi, M. L., Kintner, P. M., and Arnoldy, R. A. (1999). Rocket observations of banded structure in waves near the Langmuir frequency in the auroral ionosphere. *J. Geophys. Res.* 104, 28109–28122. doi:10.1029/1999ja900379

McFadden, J. P., Carlson, C. W., and Boehm, M. H. (1986). High-frequency waves generated by auroral electrons. *J. Geophys. Res.* 91, 12079–12088. doi:10.1029/ja091ia11p12079

Michell, R. G., Grydeland, T., and Samara, M. (2014). Characteristics of poker flat incoherent scatter radar (pfisr) naturally enhanced ion-acoustic lines (neials) in relation to auroral forms. *Ann. Geophys.* 32, 1333–1347. doi:10.5194/angeo-32-1333-2014

Michell, R. G., and Samara, M. (2013). Observability of neials with the sondrestrom and poker flat incoherent scatter radars. *J. Atmos. Solar-Terrestrial Phys.* 105-106, 299–307. doi:10.1016/j.jastp.2012.12.008

Mishin, E., Burke, W., and Pedersen, T. (2004). On the onset of hf-induced airglow at haarp. *J. Geophys. Res. Space Phys.* 109, 112. doi:10.1029/2003ja010205

Mishin, E., and Khazanov, G. (2006). Tether-induced airglow: collisionless effects. *Geophys. Res. Lett.* 33, 127. doi:10.1029/2006gl026220

Mishin, E., and Pedersen, T. (2011). Ionizing wave via high-power hf acceleration. *Geophys. Res. Lett.* 38, 139. doi:10.1029/2010gl046045

Mishin, E., and Telegin, V. (1989). Effects of plasma turbulence on auroras. *Geomagn. Aeron* 29, 1–13.

Mishin, E., and Telegin, V. (1986). Spectrum of suprathermal electrons in the auroral plasma. *Plasma Phys. Rep.* 12, 509–510.

Mishin, E. V. (2019). Artificial aurora experiments and application to natural aurora. *Front. Astron. Space Sci.* 6, 14. doi:10.3389/fspas.2019.00014

Mishin, E. V., Ivchenko, V. N., and Milinevskii, G. P. (1981). Fine structure of artificial auroral rays. *Adv. Space Res.* 1, 163–165. doi:10.1016/0273-1177(81)90286-6

Muschietti, L., and Dum, C. T. (1991). Nonlinear wave scattering and electron beam relaxation. *Phys. Fluids B: Plasma Phys.* 3, 1968–1982. doi:10.1063/1.859665

Muschietti, L., Roth, I., and Delory, G. (1997). Oblique turbulence driven by field-aligned electron fluxes in the auroral ionosphere. *J. Geophys. Res.* 102, 27217–27226. doi:10.1029/97ja02532

Muschietti, L., Roth, I., and Ergun, R. E. (1995). Kinetic localization of beam-driven Langmuir waves. *J. Geophys. Res.* 100, 17481–17490. doi:10.1029/95ja00595

Muschietti, L., Roth, I., and Ergun, R. E. (1996). On the formation of wave packets in planetary foreshocks. *J. Geophys. Res.* 101, 15605–15613. doi:10.1029/96ja00926

Newman, D. L., Goldman, M. V., Ergun, R. E., and Boehm, M. H. (1994c). Langmuir turbulence in the auroral ionosphere: 1. linear theory. *J. Geophys. Res.* 99, 6367–6376. doi:10.1029/93ja03182

Newman, D. L., Goldman, M. V., and Ergun, R. E. (1994a). Langmuir turbulence in moderately magnetized space plasmas*. *Phys. Plasmas* 1, 1691–1699. doi:10.1063/1.870672

Newman, D. L., Goldman, M. V., and Ergun, R. E. (1994b). Langmuir turbulence in the auroral ionosphere: 2. nonlinear theory and simulations. *J. Geophys. Res.* 99, 6377–6391. doi:10.1029/93ja03183

Newman, D. L., Winglee, R. M., Robinson, P. A., Glanz, J., and Goldman, M. V. (1990). Simulation of the collapse and dissipation of Langmuir wave packets. *Phys. Fluids B: Plasma Phys.* 2, 2600–2622. doi:10.1063/1.859385

Nicholson, D. R., and Goldman, M. V. (1978). Cascade and collapse of Langmuir waves in two dimensions. *Phys. Fluids* 21, 1766–1776. doi:10.1063/1.862093

Nishikawa, K.-I., and Cairns, I. H. (1991). Simulation of the nonlinear evolution of electron plasma waves. *J. Geophys. Res.* 96, 19343–19351. doi:10.1029/91ja01738

Nulsen, A., Cairns, I. H., and Robinson, P. (2007). Field distributions and shapes of Langmuir wave packets observed by ulysses in an interplanetary type iii burst source region. *J. Geophys. Res. Space Phys.* 112. doi:10.1029/2006ja011873

Ogasawara, K., Livadiotis, G., Grubbs, G. A., Jahn, J.-M., Michell, R., Samara, M., et al. (2017). Properties of suprathermal electrons associated with discrete auroral arcs. *Geophys. Res. Lett.* 44, 3475–3484. doi:10.1002/2017gl072715

O'neil, T., and Malmberg, J. (1968). Transition of the dispersion roots from beam-type to landau-type solutions. *Phys. Fluids* 11, 1754–1760.

Papadopoulos, K., and Coffey, T. (1974). Nonthermal features of the auroral plasma due to precipitating electrons. *J. Geophys. Res.* 79, 674–677. doi:10.1029/ja079i004p00674

Papadopoulos, K., and Freund, H. P. (1978). Solitons and second harmonic radiation in type iii bursts. *Geophys. Res. Lett.* 5, 881–884. doi:10.1029/gl005i010p00881

Papadopoulos, K. (1975). Nonlinear stabilization of beam plasma interactions by parametric effects. *Phys. Fluids* 18, 1769–1777. doi:10.1063/1.861096

Park, P. H., Rhee, T., and Ryu, C.-M. (2005). Self-consistent generation of superthermal electrons by beam-plasma interaction. *Phys. Rev. Lett.* 95, 215003. doi:10.1103/physrevlett.95.215003

Pavan, J., Ziebell, L., Yoon, P., and Gaelzer, R. (2010). Ionospheric ion-acoustic enhancements by turbulent counterstreaming electron beam-plasma interaction. *J. Geophys. Res. Space Phys.* 115, 237. doi:10.1029/2009ja014448

Pedersen, T., Gustavsson, B., Mishin, E., Kendall, E., Mills, T., Carlson, H., et al. (2010). Creation of artificial ionospheric layers using high-power hf waves. *Geophys. Res. Lett.* 37, 119. doi:10.1029/2009gl041895

Peter Gary, S. (1985). Electrostatic instabilities in plasmas with two electron components. *J. Geophys. Res.* 90, 8213–8221. doi:10.1029/ja090ia09p08213

Pfaff, R., Carlson, C., Watzin, J., Everett, D., and Gruner, T. (2001). *An overview of the fast auroral snapshot (fast) satellite. The FAST mission*. Berlin: Springer, 1–32.

Reasoner, D. L., and Chappell, C. R. (1973). Twin payload observations of incident and backscattered auroral electrons. *J. Geophys. Res.* 78, 2176–2186. doi:10.1029/ja078i013p02176

Robinson, P. A., and Newman, D. L. (1991). Strong plasma turbulence in the Earth's electron foreshock. *J. Geophys. Res.* 96, 17733–17749. doi:10.1029/91ja01734

Robinson, P. A. (1997). Nonlinear wave collapse and strong turbulence. *Rev. Mod. Phys.* 69, 507. doi:10.1103/revmodphys.69.507

Robinson, P. A. (1995). Stochastic wave growth. *Phys. Plasmas* 2, 1466–1479. doi:10.1063/1.871362

Russell, D., DuBois, D. F., and Rose, H. A. (1988). Nucleation in two-dimensional Langmuir turbulence. *Phys. Rev. Lett.* 60, 581. doi:10.1103/physrevlett.60.581

Ryu, C.-M., Rhee, T., Umeda, T., Yoon, P. H., and Omura, Y. (2007). Turbulent acceleration of superthermal electrons. *Phys. Plasmas* 14, 100701. doi:10.1063/1.2779282

Samara, M., LaBelle, J., and Cairns, I. (2008). Statistics of auroral Langmuir waves. *Annales Geophysicae*. 26, 3885–3895. doi:10.5194/angeo-26-3885-2008

Samara, M., and LaBelle, J. (2006). Structured waves near the plasma frequency observed in three auroral rocket flights. *Ann. Geophys.* 24, 2911. doi:10.5194/angeo-24-2911-2006

Sanbonmatsu, K. Y., Doxas, I., Goldman, M. V., and Newman, D. L. (1997). Non-markovian electron diffusion in the auroral ionosphere at high Langmuir-wave intensities. *Geophys. Res. Lett.* 24, 807–810. doi:10.1029/97gl00669

Sanbonmatsu, K. Y., Newman, D. L., and Goldman, M. V. (2001). Quasi-linear zakharov simulations of Langmuir turbulence at rocket altitudes in the auroral ionosphere. *J. Geophys. Res.* 106, 10519–10535. doi:10.1029/2000ja000270

Schlatter, N. M., Ivchenko, N., and Häggström, I. (2014). On the relation of Langmuir turbulence radar signatures to auroral conditions. *J. Geophys. Res. Space Phys.* 119, 8499–8511. doi:10.1002/2013ja019457

Schlatter, N. M., Ivchenko, N., Sergienko, T., Gustavsson, B. J., and Brändström, B. (2013). Enhanced eiscat uhf backscatter during high-energy auroral electron precipitation. *Copernicus* 31, 1681–1687. doi:10.5194/angeo-31-1681-2013

Schlesier, A., Mishin, E., and Schlegel, K. (1997). "Non-collisional" ionization and temperature layers in the auroral E/F1layer: EISCAT observations. *Geophys. Res. Lett.* 24, 1407–1410. doi:10.1029/97gl01178

Sedgemore-Schulthess, F., and St. Maurice, J.-P. (2001). Naturally enhanced ion-acoustic spectra and their interpretation. *Surv. Geophys.* 22, 55–92. doi:10.1023/a:1010691026863

Semeter, J., and Blixt, E. (2006). Evidence for alfvén wave dispersion identified in high-resolution auroral imagery. *Geophys. Res. Lett.* 33, 121. doi:10.1029/2006gl026274

Semeter, J., Zettergren, M., Diaz, M., and Mende, S. (2008). Wave dispersion and the discrete aurora: new constraints derived from high-speed imagery. *J. Geophys. Res. Space Phys.* 113, 211. doi:10.1029/2008ja013122

Shapiro, V., and Shevchenko, V. (1988). Astrophysical plasma turbulence. i. *Sov. Sci. Rev. Sect. E* 6, 425–546.

Sharber, Y., Fujii, R., Buchert, S. C., Nozawa, S., Watanabe, S., and Van Eyken, A. P. (2000). Simultaneous eiscat svalbard and vhf radar observations of ion upflows at different aspect angles. *Geophys. Res. Lett.* 27, 81–84. doi:10.1029/1999gl010665

Singh, N., Loo, S. M., Wells, B. E., and Lakhina, G. S. (2001). Evolution of electron beam generated waves resulting in transverse ion heating and filamentation of the plasma. *J. Geophys. Res.* 106, 21165–21181. doi:10.1029/2000ja000335

Spiger, R. J., Murphree, J. S., Anderson, H. R., and Loewenstein, R. F. (1976). Modulation of auroral electron fluxes in the frequency range 50 khz to 10 mhz. *J. Geophys. Res.* 81, 1269–1278. doi:10.1029/ja081i007p01269

Stasiewicz, K., Holback, B., Krasnoselskikh, V., Boehm, M., Boström, R., and Kintner, P. M. (1996). Parametric instabilities of Langmuir waves observed by freja. *J. Geophys. Res.* 101, 21515–21525. doi:10.1029/96ja01747

Stenbaek-Nielsen, H. C., and Hallinan, T. J. (1979). Pulsating auroras: evidence for noncollisional thermalization of precipitating electrons. *J. Geophys. Res.* 84, 3257–3271. doi:10.1029/ja084ia07p03257

Stix, T. H. (1962). *The theory of plasma waves*. New York City, NY: McGraw-Hill.

Strømme, A., Belyey, V., Grydeland, T., La Hoz, C., Løvhaug, U., and Isham, B. (2005). Evidence of naturally occurring wave-wave interactions in the polar ionosphere and its relation to naturally enhanced ion acoustic lines. *Geophys. Res. Lett.* 32.

Sullivan, J. M., Lockwood, M., Lanchester, B. S., Kontar, E. P., Ivchenko, N., Dahlgren, H., et al. (2008). An optical study of multiple neial events driven by low energy electron precipitation. *Ann. Geophys.* 26, 2435–2447. doi:10.5194/angeo-26-2435-2008

Swider, W., and Narcisi, R. S. (1977). Auroral e-region: ion composition and nitric oxide. *Planet. Space Sci.* 25, 103–116. doi:10.1016/0032-0633(77)90014-9

Thejappa, G., MacDowall, R., and Bergamo, M. (2012a). *In situ* detection of strong Langmuir turbulence processes in solar type iii radio bursts. *J. Geophys. Res. Space Phys.* 117, 267. doi:10.1029/2012ja017695

Thejappa, G., MacDowall, R. J., Bergamo, M., and Papadopoulos, K. (2012b). Evidence for the oscillating two stream instability and spatial collapse of Langmuir waves in a solar type iii radio burst. *ApJ* 747, L1. doi:10.1088/2041-8205/747/1/l1

Thiessen, J. P., and Kellogg, P. J. (1993). Langmuir wave decay and collapse in the jovian foreshock. *Planet. Space Sci.* 41, 823–832. doi:10.1016/0032-0633(93)90089-k

Umeda, T., Omura, Y., Yoon, P. H., Gaelzer, R., and Matsumoto, H. (2003). Harmonic Langmuir waves. iii. vlasov simulation. *Phys. Plasmas* 10, 382–391. doi:10.1063/1.1537240

Umeda, T. (2006). Vlasov simulation of amplitude-modulated Langmuir waves. *Phys. Plasmas* 13, 092304. doi:10.1063/1.2348088

Volokitin, A., and Mishin, E. (1979). Relaxation of an electron beam in a plasma with infrequent collisions. *Soviet J. Plasma Phys.* 5, 654–656.

Voronkov, I., and Mishin, Y. (1993). Quasilinear regime of Langmuir turbulence in the auroral e region of the ionosphere. *Geomagn. Aeronom. C/C Geomagn. Aeronom.* 33, 350.

Wahlund, J.-E., Forme, F. R. E., Opgenoorth, H. J., Persson, M. A. L., Mishin, E. V., and Volokitin, A. S. (1992a). Scattering of electromagnetic waves from a plasma: enhanced ion acoustic fluctuations due to ion-ion two-stream instabilities. *Geophys. Res. Lett.* 19, 1919–1922. doi:10.1029/92gl02101

Wahlund, J.-E., Opgenoorth, H. J., Forme, F. R. E., Persson, M. A. L., Häggström, I., and Lilensten, J. (1993). Electron energization in the topside auroral ionosphere:

on the importance of ion-acoustic turbulence. *J. Atmos. terrestrial Phys.* 55, 623–645. doi:10.1016/0021-9169(93)90010-v

Wahlund, J.-E., Opgenoorth, H. J., Häggström, I., Winser, K. J., and Jones, G. O. L. (1992b). Eiscat observations of topside ionospheric ion outflows during auroral activity: Revisited. *J. Geophys. Res.* 97, 3019–3037. doi:10.1029/91ja02438

Wahlund, J.-E., Opgenoorth, H. J., and Rothwell, P. (1989). Observations of thin auroral ionization layers by eiscat in connection with pulsating aurora. *J. Geophys. Res.* 94, 17223–17233. doi:10.1029/ja094ia12p17223

Wang, J. G., Payne, G. L., DuBois, D. F., and Rose, H. A. (1996). Comparison of zakharov simulation and open boundary vlasov simulation of strong Langmuir turbulence. *Phys. Plasmas* 3, 111–121. doi:10.1063/1.871837

Weatherwax, A. T., LaBelle, J., and Trimpi, M. L. (1994). A new type of auroral radio emission observed at medium frequencies (~1,350–3,700 kHz) using ground-based receivers. *Geophys. Res. Lett.* 21, 2753–2756. doi:10.1029/94gl02512

Willes, A. J., and Cairns, I. H. (2000). Generalized Langmuir waves in magnetized kinetic plasmas. *Phys. Plasmas* 7, 3167–3180. doi:10.1063/1.874180

Wong, A. Y., and Quon, B. H. (1975). Spatial collapse of beam-driven plasma waves. *Phys. Rev. Lett.* 34, 1499. doi:10.1103/physrevlett.34.1499

Yoon, P. H., Gaelzer, R., Umeda, T., Omura, Y., and Matsumoto, H. (2003). Harmonic Langmuir waves. i. nonlinear dispersion relation. *Phys. Plasmas* 10, 364–372. doi:10.1063/1.1537238

Yoon, P. H., Hong, J., Kim, S., Lee, J., Lee, J., Park, J., et al. (2012a). Asymmetric solar wind electron distributions. *ApJ* 755, 112. doi:10.1088/0004-637x/755/2/112

Yoon, P. H., and LaBelle, J. (2005). Discrete Langmuir waves in density structure. *J. Geophys. Res.* 110, 39–47. doi:10.1029/2005JA011186

Yoon, P. H., Rhee, T., and Ryu, C.-M. (2006). Self-consistent formation of electron κ distribution: 1. theory. *J. Geophys. Res. Space Phys.* 111, 233. doi:10.1029/2006ja011681

Yoon, P. H. (2006). Statistical theory of electromagnetic weak turbulence. *Phys. Plasmas* 13, 022302. doi:10.1063/1.2167587

Yoon, P. H., Ziebell, L. F., Gaelzer, R., and Pavan, J. (2012b). Electromagnetic weak turbulence theory revisited. *Phys. Plasmas* 19, 102303. doi:10.1063/1.4757224

Ziebell, L. F., Gaelzer, R., and Yoon, P. H. (2001). Nonlinear development of weak beam-plasma instability. *Phys. Plasmas* 8, 3982–3995. doi:10.1063/1.1389863

Ziebell, L. F., Yoon, P. H., Petruzzellis, L. T., Gaelzer, R., and Pavan, J. (2015). Plasma emission by nonlinear electromagnetic processes. *ApJ* 806, 237. doi:10.1088/0004-637x/806/2/237

Ziebell, L., Gaelzer, R., Pavan, J., and Yoon, P. (2008). Two-dimensional nonlinear dynamics of beam–plasma instability. *Plasma Phys. Control. Fusion* 50, 085011. doi:10.1088/0741-3335/50/8/085011

Ziebell, L., Yoon, P., Pavan, J., and Gaelzer, R. (2011). Ion-acoustic enhancements generated by beam-plasma instability in an auroral cavity. *J. Geophys. Res. Space Phys.* 116, 111. doi:10.1029/2010ja016147

Conflict of Interest: The authors declare that the research was conducted in the absence of any commercial or financial relationships that could be construed as a potential conflict of interest.

frontiers in Physics

ORIGINAL RESEARCH
published: 14 April 2021
doi: 10.3389/fphy.2021.624748

Effects of the Background Turbulence on the Relaxation of Ion Temperature Anisotropy in Space Plasmas

Pablo S. Moya[1]* *and Roberto E. Navarro*[2]*

[1] Departamento de Física, Facultad de Ciencias, Universidad de Chile, Santiago, Chile, [2] Departamento de Física, Facultad de Ciencias Físicas y Matemáticas, Universidad de Concepción, Concepción, Chile

Turbulence in space plasmas usually exhibits two regimes separated by a spectral break that divides the so called inertial and kinetic ranges. Large scale magnetic fluctuations are dominated by non-linear MHD wave-wave interactions following a −5/3 or −2 slope power-law spectrum. After the break, at scales in which kinetic effects take place, the magnetic spectrum follows a steeper power-law $k^{-\alpha}$ shape given by a spectral index $\alpha > 5/3$. Despite its ubiquitousness, the possible effects of a turbulent background spectrum in the quasilinear relaxation of solar wind temperatures are usually not considered. In this work, a quasilinear kinetic theory is used to study the evolution of the proton temperatures in an initially turbulent collisionless plasma composed by cold electrons and bi-Maxwellian protons, in which electromagnetic waves propagate along a background magnetic field. Four wave spectrum shapes are compared with different levels of wave intensity. We show that a sufficient turbulent magnetic power can drive stable protons to transverse heating, resulting in an increase in the temperature anisotropy and the reduction of the parallel proton beta. Thus, stable proton velocity distribution can evolve in such a way as to develop kinetic instabilities. This may explain why the constituents of the solar wind can be observed far from thermodynamic equilibrium and near the instability thresholds.

Keywords: space plasma physics, turbulence, ion-cyclotron waves, quasilinear theory, temperature anisotropy instability

OPEN ACCESS

Edited by:
Zoltan Voros,
Austrian Academy of Sciences, Austria

Reviewed by:
Luca Franci,
Queen Mary University of London, United Kingdom
Silvio Sergio Cerri,
Princeton University, United States

***Correspondence:**
Pablo S. Moya
pablo.moya@uchile.cl
Roberto E. Navarro
roberto.navarro@udec.cl

Specialty section:
This article was submitted to Space Physics, a section of the journal Frontiers in Physics

Received: *01 November 2020*
Accepted: *18 March 2021*
Published: *14 April 2021*

Citation:
Moya PS and Navarro RE (2021) Effects of the Background Turbulence on the Relaxation of Ion Temperature Anisotropy in Space Plasmas. Front. Phys. 9:624748. doi: 10.3389/fphy.2021.624748

1. INTRODUCTION

In many space environments the media is filled by a weakly collisional plasma. Although Coulomb collisions represent an efficient mechanism for relaxing plasma parcels toward a thermodynamic equilibrium state in which the particle Velocity Distribution Functions (VDFs) achieve a Maxwellian profile [1, 2], when collisions are scarce Coulomb scattering becomes ineffective in establishing equilibrium. Subsequently, kinetic collisionless processes may dominate the dynamics of the system and be responsible for many of the observed macroscopic and microscopic properties of the plasma. Under these conditions the plasma VDF usually develops non-Maxwellian characteristics that can provide the necessary free energy to excite micro-instabilities that subsequently can induce changes on the macroscopic properties of the plasma [3–7]. Among the fundamental problems of plasma physics belongs the understanding of the excitation and relaxation processes of these poorly collisional plasmas and the resultant state of nearly equipartition energy

density between plasma particles and electromagnetic turbulence [8]. In particular, these processes play an important role in space plasma environments, such as the solar wind [9–12] and the Earth's magnetosphere [13–15], specially at kinetic scales [4, 16, 17].

It is well-known that in space plasmas, turbulence usually exhibits two distinct regimes separated by a spectral break dividing the fluctuations power spectrum. In the case of magnetic field fluctuations these two regimes are known as the inertial MHD range (at larger scales) and the kinetic range (at ionic and sub-ionic scales) [12, 18]. Large scale magnetic fluctuations are dominated by MHD non-linear wave-wave interactions following a $-5/3$ or -2 slope power-law spectrum [19]. After the break the spectrum follows a steeper power-law $k^{-\alpha}$ shape given by a spectral index $\alpha > 5/3$, as it has been shown from observations [20], 2.5D simulations [21], and full 3D simulations [22]. The break is related with the scales in which kinetic effects, such as wave-particle interactions [23–25] take place, or ion-scale current sheets are disrupted due to the onset magnetic reconnection [26–30]. Depending on the local plasma conditions the break can coincide with the ion inertial length λ_i, or the ion gyroradius $\rho_i = \sqrt{\beta}\lambda_i$, where β is the plasma beta parameter, as observed in space plasmas [31, 32] and numerical simulations [33]. In particular, for small values of the proton plasma beta, the scale of the break seems to be related to λ_i; while for larger values of beta to ρ_i. Also, different plasma environments can exhibit different spectral indices. For example, considering Van Allen Probes observations, Gamayunov et al. [34] have found $\alpha \sim 2$ in the inner magnetosphere, and Chaston et al. [35] and Moya et al. [16] observed $\alpha \sim 4$ associated with Kinetic Alfvén Waves turbulent spectra measured during geomagnetic storms in the Ring Current region. Similarly, Alexandrova et al. [36] found $\alpha \sim 7/3$ using Cluster data, and Goldstein et al. [37] observed $\alpha \sim 4.2$ considering Wind observations in the case of the solar wind at 1 AU from the Sun. In addition, using data from the recent Parker Solar Probe mission, Franci et al. [38] have found $\alpha \sim 7/2$ during the first perihelion of the spacecraft, at about 36 solar radii from the Sun. Further, all these results are consistent with kinetic scale simulations [22, 38, 39]. Besides the recent progress, how the turbulent energy is dissipated in all these almost collisionless plasma systems is still under debate and corresponds to one of the outstanding open questions in space plasma physics [20, 40].

In a magnetized plasma, such as the solar wind or the Earth's magnetosphere, one of the most typical deviations from the Maxwellian equilibrium is the bi-Maxwellian distribution, i.e., a composed Maxwellian VDF that exhibits different thermal spreads (different temperatures) in the directions along and perpendicular to the background magnetic field. These distributions are susceptible to temperature anisotropy driven micro-instabilities that can effectively reduce the anisotropy and relax the plasma toward more isotropic states. However, in the absence of enough collisions, these instabilities are usually not able to lead the system fully into thermodynamic equilibrium, and the plasma allows a certain level of anisotropy up to the so called kinetic instability thresholds [4, 41]. From the theoretical kinetic plasma physics point of view, on the basis of the linear and quasilinear theory approximations of the dynamics of the plasma, it is possible to predict the thresholds in the temperature anisotropy and plasma beta parameter space that separate the stable and unstable regimes, and how the plasma evolves toward such states. These models are useful to study the generation and first saturation of the electromagnetic energy at the expense of the free energy carried by the plasma. To do so, in general quasilinear calculations consider initial conditions with a small level of magnetic field energy that grows as the temperature anisotropy relaxes. A comprehensive review of linear and quasilinear analysis of these instabilities considering a bi-Maxwellian model can be found in Yoon [42] and references therein.

Since the first studies by Weibel [43] and Sagdeev and Shafranov [44], the research about temperature anisotropy driven modes and the stability of the plasma have been widely studied in the last decades, and represent an important topic for space plasmas physics [45–49]. Predictions based on a bi-Maxwellian description of the plasma are qualitatively in good agreement with observations of solar wind protons (see e.g., Hellinger and Trávníček [6], Bale et al. [11]) and electrons (see e.g., Hellinger et al. [50], Adrian et al. [51]). However, as mentioned, turbulence is ubiquitous in space environments and all these relaxation processes should occur in the presence of a background turbulent magnetic spectrum. To the best of our knowledge, only a few quasilinear studies, such as Moya et al. [49, 52] have considered a background spectrum but nonetheless a study focused on the possible effects of a magnetic field background spectrum is yet to be done. Here we perform such systematic study by computing the quasilinear relaxation of the ion-cyclotron temperature anisotropy instability, considering different choices of the initial level of the magnetic field fluctuations, and the shape of the spectrum. We analyze their effect on the relaxation of the instability and the time evolution of the macroscopic properties of the plasma that are involved.

Several studies of the solar wind electromagnetic turbulence near the spectral break as a function of wave number $|k| = \sqrt{k_\perp^2 + k_\parallel^2}$, where $k_\perp$ and $k_\parallel$ are the wave vector components parallel and perpendicular to the magnetic field, respectively, have shown that the fluctuation spectrum is anisotropic and that the power spectrum sometimes is greater at quasi-perpendicular propagation $k_\perp \gg k_\parallel$ (see e.g., Dasso et al. [53], Horbury et al. [54]) than at quasi-parallel propagation $k_\perp \ll k_\parallel$. However, for small plasma beta ($\beta < 1$) as in this study, the compressibility of the magnetic fluctuations is small in the solar wind at 1 AU (see e.g., Bale et al. [11]), which is consistent with propagation of Alfvén ion-cyclotron waves. Therefore, as a first approximation we consider the fluctuations to be magnetically non-compressive and propagating strictly along the background magnetic field ($k = k_\parallel$), and also have and focused on small β values. In the next section we present the details of our quasilinear model, and then, in sections 3 and 4 we present and discuss all our numerical results. Finally, in the last section we summarize our findings and present the main conclusions of our work.

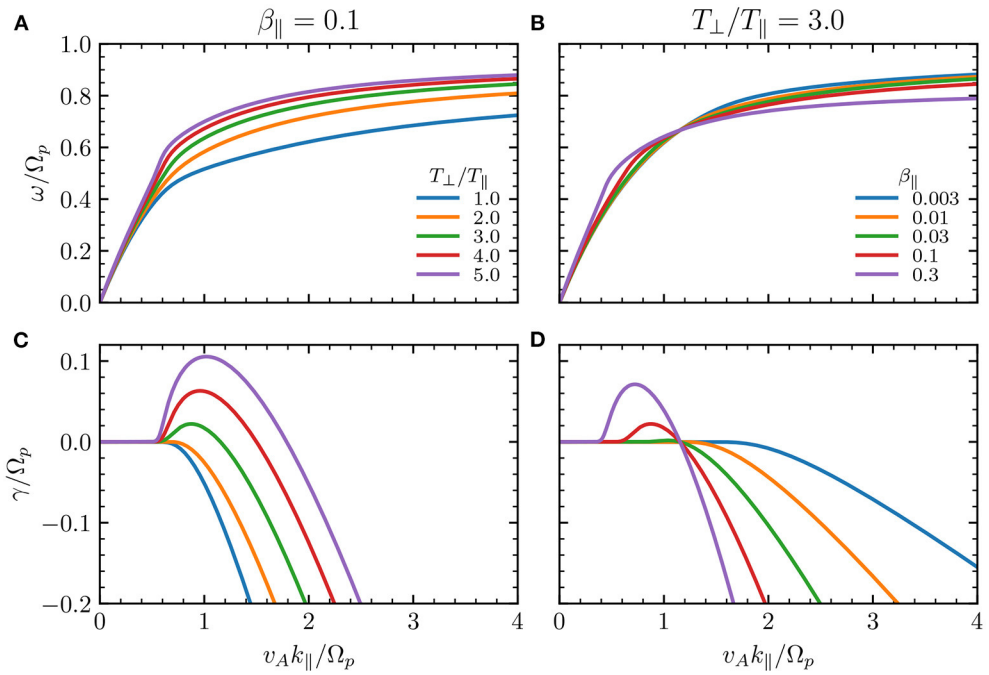

FIGURE 1 | (A,B) Frequency and **(C,D)** growth/damping rate of Alfvén-cyclotron waves as a function of wavenumber, as calculated from the dispersion relation Equation (1). **(A,C)** $\beta_\parallel = 0.1$ and different values of $T_\perp/T_\parallel$. **(B,D)** $T_\perp/T_\parallel = 3$ and different values of $\beta_\parallel$. Plots for $k_\parallel < 0$ can be obtained through the parity condition $\omega_{-k} = -\omega_k^*$.

2. QUASILINEAR TEMPERATURE EVOLUTION

We consider a magnetized plasma composed of bi-Maxwellian protons and cold electrons. The kinetic dispersion relation of left-handed circularly polarized waves, propagating along a background magnetic field $\vec{B}_0$ is given by [52, 55, 56].

$$\frac{v_A^2 k_\parallel^2}{\Omega_p^2} = A + (A\xi^- + \xi)Z(\xi^-) - \frac{\omega_k}{\Omega_p}, \tag{1}$$

where $\omega_k = \omega + i\gamma$ is the complex frequency that depends on the wavenumber $k_\parallel$; $v_A = B_0/\sqrt{4\pi n_p m_p}$ is the Alfvén speed, with n_p and m_p the density and mass of protons, respectively; $\Omega_p = eB_0/m_p c$ is the proton gyrofrequency with c the speed of light; $A = T_\perp/T_\parallel - 1$ where $T_\perp/T_\parallel$ is the temperature anisotropy; $T_\perp$ and $T_\parallel$ are the proton temperatures perpendicular and parallel with respect to $\vec{B}_0$, respectively; $\xi = \omega_k/k_\parallel u_\parallel$ and $\xi^- = (\omega_k - \Omega_p)/k_\parallel u_\parallel$ are resonance factors [57]; $u_\parallel = \sqrt{2k_B T_\parallel/m_p}$ is the parallel proton thermal speed, and k_B the Boltzmann constant. $Z(\xi)$ is the plasma dispersion function [58], which is calculated numerically with the Faddeeva function provided by scipy. We also define the parallel proton $\beta_\parallel = u_\parallel^2/v_A^2$. In Equation (1), we have assumed charge neutrality (i.e., zero net charge such that the electron density is $n_e = n_p$), and $v_A/c \ll 1$. Numerical roots of Equation (1) are calculated through the Muller's method [59] using our own Python code. The dispersion relation Equation (1) supports an infinite number of solutions for ω_k for each value of $k_\parallel$, most of them being sound-like heavily damped modes with frequencies above and below the proton gyrofrequency [5, 60]. Here, we focus on the quasilinear evolution of the plasma due to Alfvén-Cyclotron Wave (ACW) instabilities (for more details about this instability in the context of space plasmas see e.g., Moya et al. [61], Jian et al. [62], Wicks et al. [63], Yoon [42], and references therein).

Figure 1A shows the real part of the ACW complex frequency for $\beta_\parallel = 0.1$ and several values of the temperature anisotropy $T_\perp/T_\parallel$. Similarly, **Figure 1B** shows the effects of $\beta_\parallel$ on the ACW real frequency at a fixed anisotropy $T_\perp/T_\parallel = 3$. In all cases with $\beta_\parallel < 0.1$, the real part of the frequency seems to approach asymptotically to $\omega = \Omega_p$ at large wavenumbers. This description is very similar to the solutions of the dispersion relation Equation (1) in the cold-plasma approximation [64, 65]. However, for $T_\perp/T_\parallel > 1$ (**Figure 1A**) or $\beta_\parallel > 0.01$ (**Figure 1B**), the frequency curve deviates from the cold-plasma approximation for wavelengths around the proton inertial length v_A/Ω_p.

Kinetic effects can damp ACWs of large wavenumbers even at low beta, and large temperature anisotropies can drive part of the wave spectrum unstable. **Figures 1C,D** show the imaginary part of the complex frequency for the same parameters as in **Figures 1A,B**, respectively. The wave is damped if its frequency satisfies $\mathrm{Im}(\omega_k) = \gamma < 0$, or it is unstable if $\gamma > 0$. **Figure 1C** shows that even a small value of $\beta_\parallel = 0.1$ allows the growth of a kinetic instability when $T_\perp/T_\parallel \gtrsim 2$ in a small range of wavenumbers $0.6 \lesssim v_A k_\parallel/\Omega_p \lesssim 2$. The maximum value of γ

increases, and its wavenumber also increases, as the anisotropy rises above $T_\perp/T_\parallel \gtrsim 2$. On the other hand, for $v_A k_\parallel/\Omega_p \gtrsim 2$ and $\beta_\parallel = 0.1$ the ACW is always damped, with damping rate γ decreasing almost linearly with $k_\parallel$. The wave is also marginally stable ($\gamma \approx 0$) for long wavelengths compared with the ion inertial length ($v_A k_\parallel/\Omega_p \lesssim 0.5$).

Notice in **Figure 1D** that the ACW is marginally stable ($\gamma = 0$) at a fixed wavenumber value $v_A k_\parallel/\Omega_p \sim 1.15$ and $T_\perp/T_\parallel = 3$ independently of the value of $\beta_\parallel$. It can be shown from Equation (1) that this happens at $(v_A k_\parallel/\Omega_p)^2 = (R-1)^2/R$ [66]. Thus, for a lower value of the temperature anisotropy the waves are marginally stable at lower wavenumbers, as seen in **Figure 1C**, and the damping becomes stronger as the anisotropy approaches $T_\perp/T_\parallel = 1$. Also, the instability decreases both with lower $\beta_\parallel$ and lower $T_\perp/T_\parallel$. It is important to mention that a semi-cold approximation of the plasma ($\xi^- \gg 1$) fails to describe these properties, making it inappropriate for the quasilinear evolution of the plasma temperature.

The quasilinear moments approximation assumes that the macroscopic parameters of the plasma evolve adiabatically, thus $\omega_k = \omega_k(t)$ solves the dispersion relation Equation (1) instantaneously at all times. The quasilinear evolution of the perpendicular and parallel thermal speeds are given by [52, 61]

$$\frac{\partial u_\perp^2}{\partial t} = -\mathrm{Im}\,\frac{4}{L}\frac{e^2}{m_p^2}\int_{-\infty}^{\infty} dk_\parallel \frac{|B_k|^2}{c^2 k_\parallel^2}\left[(2i\gamma - \Omega_p)\left(\frac{v_A^2 k_\parallel^2}{\Omega_p^2} + \frac{\omega_k}{\Omega_p}\right) + \omega_k\right], \tag{2}$$

$$\frac{\partial u_\parallel^2}{\partial t} = \mathrm{Im}\,\frac{8}{L}\frac{e^2}{m_p^2}\int_{-\infty}^{\infty} dk_\parallel \frac{|B_k|^2}{c^2 k_\parallel^2}\left[(\omega_k - \Omega_p)\left(\frac{v_A^2 k_\parallel^2}{\Omega_p^2} + \frac{\omega_k}{\Omega_p}\right) + \omega_k\right]. \tag{3}$$

where L is the characteristic length of the plasma, and $|B_k|^2$ is the spectral wave energy satisfying

$$\frac{\partial |B_k|^2}{\partial t} = 2\gamma(t)|B_k|^2, \tag{4}$$

such that Equations (1)–(4) form a closed system to address the quasilinear evolution of the ACW instability. The quasilinear approach summarized in Equations (1)–(4) is a widely used theoretical approach to study non-linear effects in the evolution of plasma waves as they interact with the media. Comparisons between quasilinear solutions and hybrid or particle-in-cell simulations [42, 67, 68] have shown that the approach is valid (theoretical and numerical results are in relatively good agreement) when the amplitude of the waves is finite but relatively small, especially for resonant instabilities (such as the ACW instability). Moreover, comparisons have also shown that the agreement between simulations and quasi-linear models is remarkable during the exponential growth of the instability (see e.g., Yoon [42]). Thus, for our calculations we have restricted the initial magnetic energy to $W_B(0) = \int dk_\parallel |B_k(0)|^2/B_0^2 \leq 0.1$ (corresponding to $B_k/B_0 \lesssim 0.1$ for a uniform spectrum), and have followed the quasilinear time evolution up to $\Omega_p t = 150$ ensuring that the plasma reaches a stationary state.

In the next sections we explore the effects of the B_k spectrum on the relaxation of the proton anisotropy.

3. NUMERICAL RESULTS. THE EFFECT OF A BACKGROUND SPECTRUM

In order to solve numerically the system of differential equations given by Equations (1)–(4) we use a fourth order Runge-Kutta method. In this section, for academic purposes, we consider three distinct shapes for the magnetic spectrum $|B_k|^2$ to illustrate the effects that different initial magnetic field background spectra can produce on the quasilinear evolution of the macroscopic parameters of the plasma. The three initial background spectra considered here are a uniform noise $|B_k(0)|^2 = A$, a Gaussian spectrum

$$|B_k(0)|^2 = A\, e^{-(v_A k_\parallel/\Omega_p)^2}, \tag{5}$$

and a Lorentzian spectrum

$$|B_k(0)|^2 = \frac{A}{1 + (v_A k_\parallel/\Omega_p)^\alpha}, \tag{6}$$

where the normalization constant A is adjusted depending on the initial total magnetic energy $W_B(0)$, with the integral calculated in the range $10^{-3} < v_A k_\parallel/\Omega_p < 8$. The large-wavenumber tails $v_A k_\parallel/\Omega_p > 8$ of the spectrum shapes considered here do not contribute to the quasilinear plasma evolution. For these $k_\parallel$ values the waves are heavily damped as **Figure 1** shows for $\beta_\parallel > 0.003$. Thus, if energy is stored at those $k_\parallel$ values, they are quickly transferred to the particles until the wave energy is depleted. For greater values of $k_\parallel$, this process is faster. Therefore, most of the quasilinear evolution at late stages will be carried by energy transfer around $v_A k_\parallel/\Omega_p = 1$ where the wave is marginally stable and an instability is likely to appear.

Figure 2 shows the quasilinear time evolution of the temperature anisotropy, the perpendicular $\beta_\perp$ and parallel $\beta_\parallel$, and the total magnetic energy W_B. The initial conditions are chosen as $T_\perp(0)/T_\parallel(0) = 1$ and $\beta_\parallel = 0.1$, parameters that are close to the most observed values in the solar wind at 1 AU in which quasi-parallel propagation seems to be dominant [11]. For every magnetic shape spectrum, we also compare the effects of different values of the initial level of magnetic fluctuations $W_B(0) = 0.003$ through 0.1. According to linear theory, the plasma is stable for the chosen initial parameters. In fact, for $\beta_\parallel = 0.1$, an isotropic velocity distribution $T_\perp/T_\parallel = 1$ has no free energy to excite an instability (see blue line in **Figure 1C**). Thus, we should expect that the temperatures will remain almost constant in time [60]. However, an striking feature for all the spectrum shapes, is that the anisotropy can grow in time if a sufficient level of magnetic energy is provided.

For an uniform spectrum of total level $W_B(0) = 0.1$ (blue lines in **Figure 2**), the anisotropy can grow up to high values $T_\perp/T_\parallel \simeq 5$ in a small time frame. This results in a sharp increase in the perpendicular beta from $\beta_\perp = 0.1$ to ≈ 0.16,

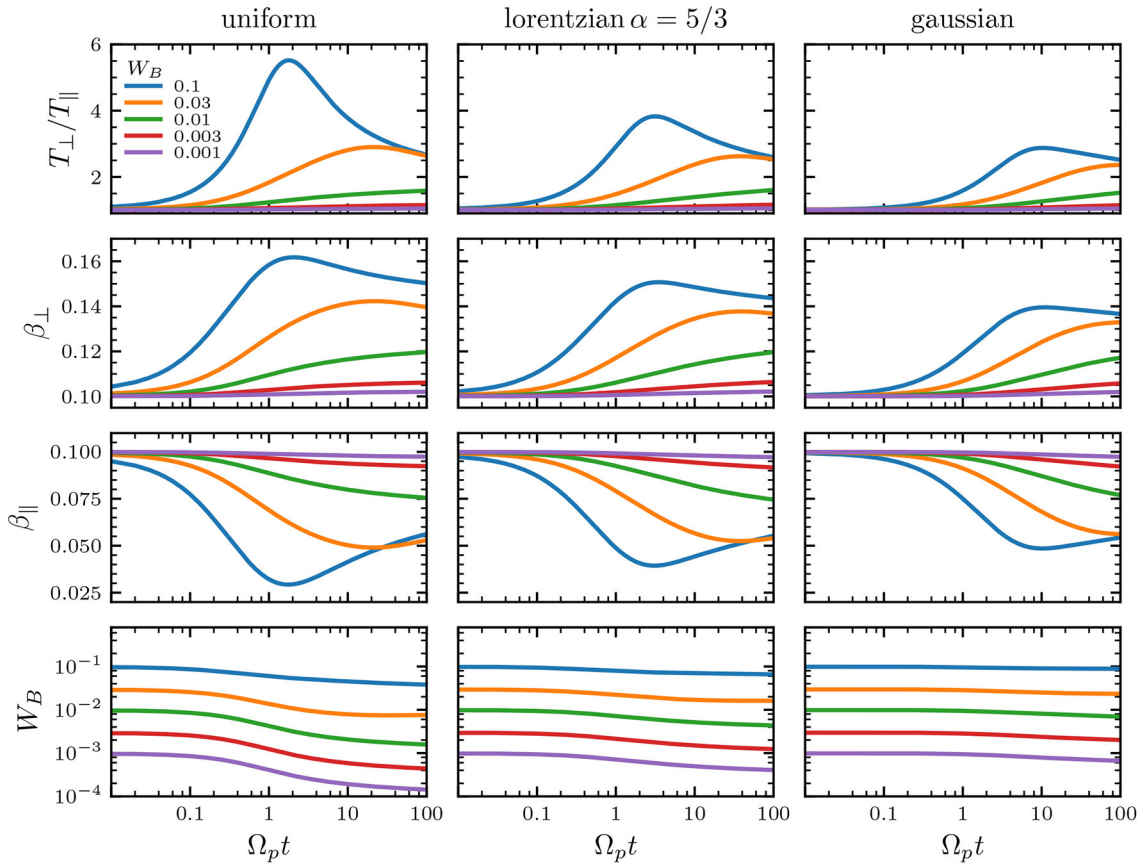

FIGURE 2 | Quasilinear evolution of (upper row) the temperature anisotropy, (second row) perpendicular $\beta_\perp$, (third row) parallel $\beta_\parallel$, and (lower row) total magnetic energy. Initial conditions for all cases were chosen as $\beta_\parallel(0) = 0.1$, $T_\perp(0)/T_\parallel(0) = 1$, and different values of the initial magnetic energy: (blue) $W_B(0) = 0.001$, (orange) $W_B(0) = 0.003$, (green) $W_B(0) = 0.01$, (red) $W_B(0) = 0.03$, and (purple) $W_B(0) = 0.1$. Each column shows (left) a uniform, (middle) $\alpha = 5/3$ Lorentzian, and (right) Gaussian initial background spectrum. Time and W_B axes are in logarithmic scale.

and consistently a rapid fall in the parallel $\beta_\parallel = 0.1$ toward ≈ 0.03. Afterwards, the anisotropy decreases while $\beta_\parallel$ rises, both steadily, toward a quasi-stationary state around $T_\perp/T_\parallel \simeq 3$ and $\beta_\parallel \approx 0.6$. We note that this anisotropy growth is not as explosive for a Lorentzian (with $\alpha = 5/3$, right column in **Figure 2**) and a Gaussian spectrum (middle column) compared to a uniform spectrum, although they all relax to a final state around the same temperature anisotropy. This shows that high levels of a power spectrum may play a role on the regulation of the temperature anisotropies observed in different plasma environments.

For a smaller value of $W_B(0) = 0.03$ (orange lines in **Figure 2**), the anisotropy also grows until it reaches a stationary state around $T_\perp/T_\parallel \simeq 3$. However, this growth is monotonous and does not show a sharp increase nor a saturation in the early stages of the simulation, compared with $W_B(0) = 0.1$. Similarly, $\beta_\parallel$ decreases almost monotonically from 0.1 toward 0.05. For even smaller values of the magnetic field intensity, e.g., $W_B(0) = 0.01$, 0.003, 0.001 (green, red, and purple lines in **Figure 2**), the anisotropy growth is limited and a stationary stage is reached at lower values near $T_\perp/T_\parallel \simeq 1$. As $W_B(0)$ is lowered to noise levels $W_B(0) < 10^{-5}$ (not shown), the anisotropy and other parameters remain almost constant, which is consistent with the fact that the plasma is in an equilibrium state for $\beta_\parallel = 0.1$, $T_\perp/T_\parallel = 1$, and low levels of the magnetic energy. In all cases, we observe that the total magnetic energy decreases monotonously, meaning that the quasilinear approximation is valid through every step of simulation runs.

In the earlier stages of the simulation runs, most of the energy transfer from the waves to the particles occurs at $v_A k_\parallel/\Omega_p \gtrsim 2$ since, according to the linear dispersion relation, the ACWs are heavily damped. This explains why a sufficient level of magnetic energy can heat the particles such that the anisotropy rises. Also, in this wavenumber range an initially uniform wave spectrum stores more energy compared to the Lorentzian one, meaning that the former can transfer more energy to particles compared to the latter in the same time lapse. A similar description holds as the Lorentzian is more energetic than the Gaussian in the $v_A k_\parallel/\Omega_p \gtrsim 2$ range, explaining why the anisotropy can reach higher values for the uniform spectrum compared to the Lorentzian and Gaussian cases. After the field energy is exhausted for long wavenumbers, the anisotropy saturates. If this occurs for anisotropy values in which a kinetic instability is excited, which

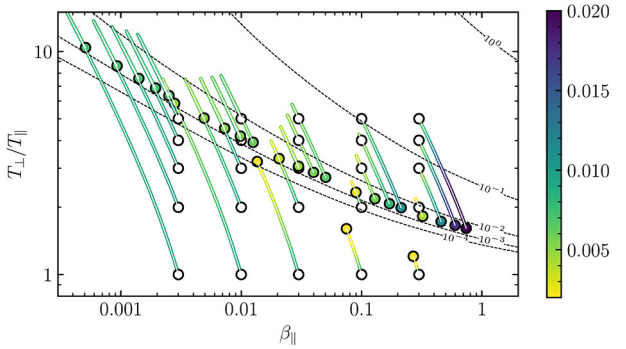

FIGURE 3 | Quasilinear evolution of the proton $\beta_\parallel$ and anisotropy $T_\perp/T_\parallel$. Initial conditions (white circles) were chosen evenly spaced in the range $0.003 \leq \beta_\parallel \leq 0.3$ and $1 \leq T_\perp/T_\parallel \leq 5$, with a uniform magnetic wave spectrum of power $W_B(0) = 0.01$ for all cases. The colorbar represents the instantaneous value of $W_B(t)$. Dashed lines are contours of the proton-cyclotron instability with maximum growth-rates $\gamma/\Omega_p = 10^{-4}$ through 10^0, as calculated from the dispersion relation Equation (1). Colorized circles correspond to the final (stationary) state of the plasma simulations.

should happen around $v_A k_\parallel/\Omega_p = 1$, then the energy transfer is reversed from the particles to the wave so that the anisotropy starts to decrease, and the wave energy around $v_A k_\parallel/\Omega_p = 1$ grows at an instantaneous growth-rate 2γ. However, as **Figure 2** shows, this localized wave energy growth does not translate to total growth in W_B, probably because other parts of the spectrum are still transferring energy to the particles. If the saturated anisotropy is not enough to excite kinetic instabilities, or if the instability is weak, then energy transfer is a slow process and the plasma reaches a quasi-stationary state just after saturation, as shown in all cases with $W_B \leq 0.03$ in **Figure 2**.

Figure 3 shows the time evolution of $\beta_\parallel$, $T_\perp/T_\parallel$, and W_B. A set of numerical simulations with evenly spaced (in log space) initial conditions were chosen in the range $0.003 \leq \beta_\parallel \leq 0.3$ and $1 \leq T_\perp/T_\parallel \leq 5$, marked with white circles, with an initial uniform magnetic wave spectrum of power $W_B(0) = 0.01$ for all cases. The colored lines represent the quasilinear path of the system in the diagram, and their colors represent the instantaneous magnetic energy W_B. The colored circles represent the final state of the system at $\Omega_p t = 150$, long after the system has reached a stationary state, with color matching the instantaneous W_B.

A subset of these initial conditions can excite an instability as shown in **Figures 1C,D**. Thus, in **Figure 3**, contours of the maximum growth-rate $\gamma_{\max}/\Omega_p$ are included as segmented lines. For numerical reasons, we will refer to the contour $\gamma/\Omega_p = 10^{-4}$ as the instability threshold, and points below this line will be considered as stable according to the numerical solutions of the dispersion relation Equation (1). In general, the simulations with initial conditions below the instability threshold evolve so that the wave energy W_B decreases monotonously from $W_B(0) = 0.01$ to values between $0.002 < W_B(t_{\rm sat}) < 0.01$, which is consistent with results from **Figure 2**. On the other hand, for initially unstable conditions, the magnetic energy W_B rises up to values below $0.01 < W_B < 0.02$.

In almost all simulated cases starting below the instability threshold, $\beta_\parallel$ drops rapidly while the temperature anisotropy increases to high values above the stability thresholds. Afterwards, the magnetic wave power is not enough to supply energy to protons, so that $T_\perp/T_\parallel$ slowly relaxes toward values where the maximum growth-rate of the ACW instability is of the order of $\gamma/\Omega_p \simeq 0.001$. Of all the cases, however, there are three exceptions for $T_\perp(0)/T_\parallel(0) = 1$ and $\beta_\parallel(0) = 0.03$, 0.1, and 0.3, whose evolution reaches the final stationary state far below the instability threshold because the initial supplied energy $W_B(0) = 0.1$ is insufficient to push the system to higher anisotropies. This may explain why most of the observed plasma parameters in the solar wind are close to $\beta_\parallel = 1$ and $T_\perp/T_\parallel = 1$, since plasmas in this state are not heavily influenced by the background spectrum.

Notice that for simulations starting far below or far above the instability threshold, e.g., $\beta_\parallel(0) = 0.003$ and $T_\perp/T_\parallel(0) = 1$, or $\beta_\parallel(0) = 0.3$ and $T_\perp/T_\parallel(0) = 5$, the anisotropy can grow up to very high values above the instability thresholds. This effect is damped as the starting anisotropy is near the instability threshold. Thus, the effects of the starting anisotropy, which is a measure of the free energy available to excite an instability, can compete with the effects of the starting magnetic energy to regulate the anisotropy growth. Although not shown here, the quasilinear evolution in the cases of a Gaussian or Lorentzian power spectrum are similar. They all excite some level of proton perpendicular heating in the initial stage of the simulations, and then relax slowly toward a quasi-stationary state near the instability threshold, with properties similar to the ones shown in **Figure 2**.

In summary, we have illustrated how the initial shape magnetic field background spectrum can produce different results on the evolution of macroscopic parameters of the plasma. However, solar wind observations show that the plasma is mostly in a state below the instability thresholds, far from the isotropic state [6, 9], with a non-negligible level of magnetic fluctuations [11, 60], and that the magnetic field has a spectral break around the ion inertial length [31, 32]. The inertial range for transverse fluctuations propagating along the magnetic field $v_A k_\parallel/\Omega_p < 1$ typically shows a power-law spectrum $B_k^2 \propto k_\parallel^{-2}$ [19]. For ion or sub-ions scales (in the kinetic range) the turbulent spectrum steepens to $k_\parallel^{-\alpha}$, with $\alpha \geq 2.0$, arguably due to the characteristics of the dispersion relation of Alfvén or other waves in that range [69–72]. Thus, the results presented here for three arbitrary spectral shapes may not remain the same when a solar wind-like spectrum is considered. This will be the focus of the next section.

4. NUMERICAL RESULTS. THE EFFECT OF A TURBULENT SPECTRUM WITH A SPECTRAL BREAK

Here we compute the quasilinear relaxation considering a quasi-parallel solar wind-like spectrum, including a spectral break at the ion inertial range scale, given by:

$$|B_k(0)|^2 = \begin{cases} Ak_\parallel^{-2} & v_A k_\parallel/\Omega_p < 1\,, \\ Ak_\parallel^{-\alpha} & v_A k_\parallel/\Omega_p > 1\,, \end{cases} \tag{7}$$

where A is chosen depending on the initial total magnetic energy $W_B(0)$, with the integral calculated in the range $10^{-3} < v_A|k_\parallel|/\Omega_p < 8$. Notice that we are restricting to a reduced 1D background spectrum in $k_\parallel$. In this case, a $k_\parallel^{-2}$ reduced spectrum in the MHD range is the result of the integration in $k_\perp$ of a 2D spectrum of quasi-perpendicular fluctuations, whose corresponding reduced $k_\perp$ spectrum exhibit a $-5/3$ power law and a spectral anisotropy of $k_\parallel \sim k_\perp^{2/3}$. In general, the spectral slopes are determined by the conservation of total energy, i.e., that $\int dk_\parallel E(k_\parallel) = \int dk_\perp E(k_\perp)$; and by the assumed spectral anisotropy, e.g., $k_\parallel \sim k_\perp^{d/3}$. So, if the reduced perpendicular 1D spectrum is $k_\perp^{-\mu}$, then the corresponding parallel reduced spectrum scales as $k_\parallel^{-\alpha}$ with $\alpha = [3(\mu-1)+d]/d$. The spectral anisotropy (represented by the parameter d) is still a matter of great debate. Typical values of such anisotropy are $d = 1$ [standard kinetic-Alfvén-wave (KAW) turbulence for which $\mu = 7/3$, giving $\alpha = 5$], $d = 2$ (intermittency corrected KAW turbulence [73], for which $\mu = 8/3$, giving $\alpha = 7/2$), or some reconnection-mediated scenario where $d = 3$ (i.e., $k_\parallel \sim k_\perp$, to which $\alpha = \mu$). Sometimes it has been found $\alpha = \mu = 3$ in simulations [74].

Therefore, following the several observations mentioned here and in the Introduction section, we have considered four values of the spectral index, namely $\alpha = 2$, 7/3, 7/2, and 5. Notice that the case with $\alpha = 2$ corresponds to fluctuations without a break spectrum, which is unrealistic as a break is always observed around the ion characteristic scales and the spectrum is always steeper at smaller scales. Nevertheless we include such case for comparison purposes. Also notice that existing theories of plasma turbulence predict power laws in $k_\parallel$ with e.g., $\alpha = 2$ in the MHD range (see e.g., Howes [75]), in consistency with solar wind observations [19], although this heavily relies on the assumed spectral anisotropy of the turbulent fluctuations, which is still a matter of great debate when it comes to the kinetic range. Moreover, regarding the validity of a purely parallel (instead of quasi-parallel) model, it is important to mention that, as shown by Gaelzer et al. [76] and Kim et al. [77], results considering quasi-parallel propagation may differ only by a multiplicative scaling factor with respect to the purely parallel propagation case considered in this work.

In what follows, the initial anisotropy and total magnetic energy are chosen as $T_\perp(0)/T_\parallel(0) = 1$ and $W_B(0) = 0.1$ for all simulation runs. For an initially low $\beta_\parallel(0) = 0.001$, **Figure 4** (left column) shows that the proton distribution is cooled in the parallel direction with respect to the background magnetic field, as the parallel $\beta_\parallel$ decreases in time. Similarly, protons are heated in the transverse direction for all tested values of α. It is interesting to note that the magnetic energy decreases just 1% from the initial value, but causing a monotonous growth in the temperature anisotropy from $T_\perp/T_\parallel = 1$ to $\simeq 1.4$ for $\alpha = 2$. For larger values of α, this parallel cooling and transverse heating is less efficient. This can be explained as a steepened magnetic field spectrum for $v_A k_\parallel/\Omega_p > 1$ do not contain enough energy to be transferred to the particles compared to the $\alpha = 2$ case.

For $\beta_\parallel(0) = 0.01$ and 0.1, we see in **Figure 4** that the parallel cooling and transverse heating still occurs. It is worth noticing that the magnetic energy actually decreases more, but the parallel cooling and transverse heating is less efficient than in cases with the same value of α and lower $\beta_\parallel(0) = 0.001$. Comparing with **Figure 3**, we see that all three cases $\beta_\parallel = 0.001$, 0.01, and 0.1, with $T_\perp/T_\parallel = 1$, correspond to linearly stable plasmas. However, $\beta_\parallel = 0.1$ is closer to the instability thresholds, meaning that the quasilinear evolution will likely reach a stationary state with lower anisotropies near the stability margins. Also, in the cases we tested for high $\beta_\parallel(0) \geq 0.1$, the temperature evolution seems to be independent of α. Moreover, as an initially anisotropic plasma can drive instabilities depending on the plasma beta, in order to compare with the initially isotropic case (always stable) shown in **Figures 4**, **5** shows results for the same set of parameters as in **Figure 4**, but for an initially anisotropic plasma with $T_\perp/T_\parallel(0) = 3$. The cases with $\beta_\parallel(0) = 0.001$ and 0.01 show similar qualitative characteristics for both **Figures 4**, **5**. However, the case with $\beta_\parallel(0) = 0.1$ is initially unstable (see the green line in **Figure 1C**). This results in the reduction of the anisotropy and the increase in $\beta_\parallel$.

Finally, **Figure 6** shows the spectral wave energy density at several intermediate time steps between $\Omega_p t = 0$ and $\Omega_p t = 140$, considering the initial conditions $W_B(0) = 0.1$, $\alpha = 7/2$, $T_\perp(0)/T_\parallel(0) = 1$ (top), $T_\perp(0)/T_\parallel(0) = 3$ (bottom), and the same three values of $\beta_\parallel(0)$ as in **Figures 4**, **5**. For other values of α the description of these figures are almost identical. As time goes on, the wave spectrum is dampened for high values of $k_\parallel$ in all cases, which is consistent with results of **Figure 1**. For $\beta_\parallel(0) = 0.001$, the spectral break is unmodified at all times of the simulation run, but the spectrum steepens for $v_A k_\parallel/\Omega_p > 2$ for both $T_\perp(0)/T_\parallel(0) = 1$ and 3. For $\beta_\parallel(0) = 0.01$ and $T_\perp(0)/T_\parallel(0) = 1$ and 3, this happens at $v_A k_\parallel/\Omega_p > 1.2$ and the spectral break is still visible. For $\beta_\parallel(0) = 0.1$, the spectral break disappears and the wave spectrum becomes smooth around $v_A k_\parallel/\Omega_p = 1$. In all these cases, transference of energy from the wave to protons results in a monotonous drop in magnetic energy as discussed in **Figures 4**, **5**.

For $\beta_\parallel(0) = 0.1$ and $T_\perp/T_\parallel(0) = 3$, in the first stages of the simulation the electromagnetic wave loses energy at high values of $v_A k_\parallel/\Omega_p > 1$ as in the previous cases. However, since the wave is unstable in this case around $0.6 < v_A k_\parallel/\Omega_p \lesssim 1.2$ (see green line in **Figure 1C**), then the magnetic field amplitude starts to grow for those wavenumbers resulting in a bump in the spectral wave energy just below the spectral break. This results in the decrease of the temperature anisotropy and increment of $\beta_\parallel$, as shown in **Figure 5**, which is also consistent with the discussion of **Figure 3**. Comparing with **Figure 1**, this implies that the range of unstable wavenumbers shifts toward smaller values, which in turns means that the bump in the spectral wave energy also shifts to smaller values of $k_\parallel$. At the same time, previously unstable modes with higher $v_A k_\parallel/\Omega_p > 1$ become damped. Thus, the wave transfers energy to protons for values of $v_A k_\parallel/\Omega_p > 1$, resulting in a steep spectrum near the initial spectral break. At larger times and since the rate at which the wave damps is negligible compared to its growth, this results in a total growth of magnetic energy as shown in the lower right panel of **Figure 5**, which is consistent with the description of **Figure 3** for initially unstable plasma states.

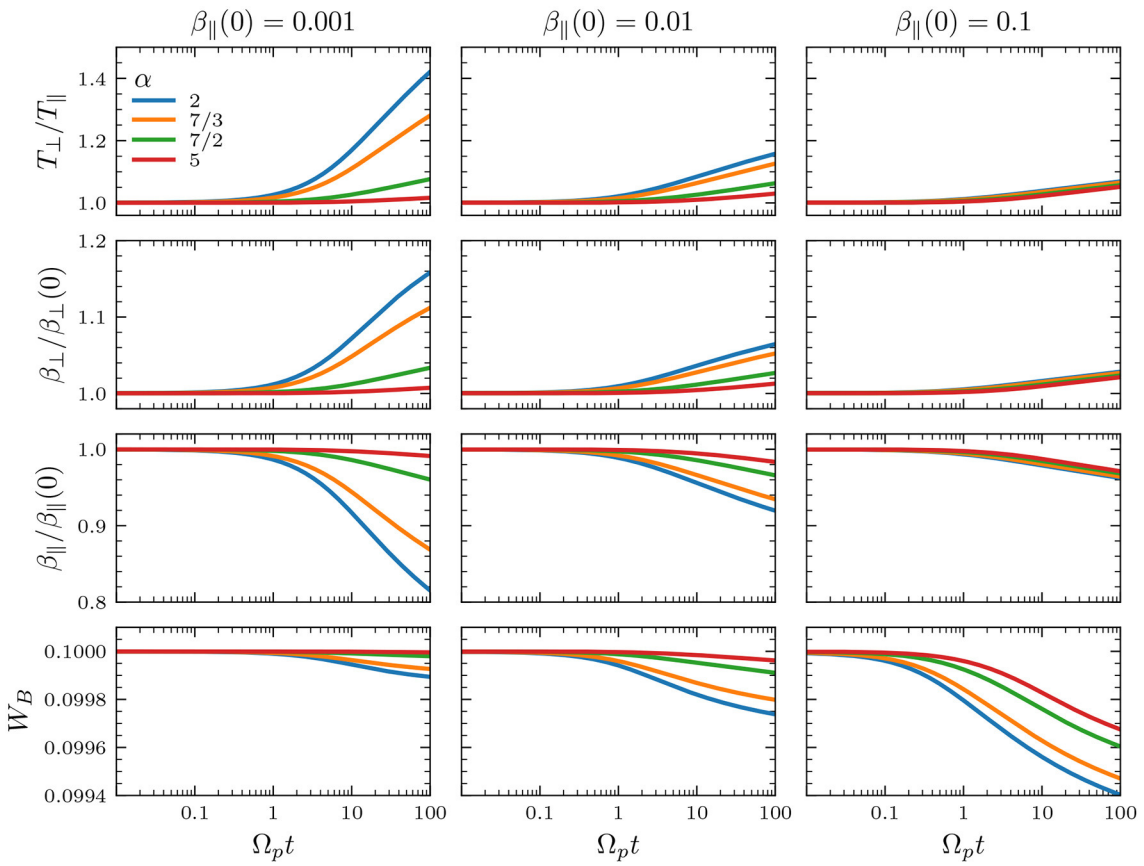

FIGURE 4 | Quasilinear evolution of $T_\perp/T_\parallel$, $\beta_\perp$, $\beta_\parallel$, and total magnetic energy W_B for a solar-wind like spectrum Equation (7) with different values of $2 \leq \alpha \leq 5$. Initially, $T_\perp/T_\parallel(0) = 1$, $W_B(0) = 0.1$, and (left column) $\beta_\parallel(0) = 0.001$, (middle column) $\beta_\parallel(0) = 0.01$, and (right column) $\beta_\parallel(0) = 0.1$.

5. DISCUSSION AND CONCLUSIONS

Turbulence is ubiquitous in space environments and any relaxation process should occur in the presence of a background turbulent magnetic spectrum, e.g., relaxation to quasi-stationary states out of thermodynamic equilibrium, non-Maxwellian characteristics in poorly collisional plasmas, and temperature anisotropy regulation by micro-instabilities or other processes, among others. Here, we have focused on the possible effects of a magnetic field background spectrum on the quasilinear relaxation of the Alfvén ion-cyclotron temperature anisotropy instability. We have compared four different choices of the initial magnetic field spectrum shape $|B_k|^2$: (a) uniform noise, (b) Lorentzian, (c) Gaussian, and (d) the more realistic solar wind-like spectrum with a spectral break at $v_A k_\parallel/\Omega_p = 1$ and the kinetic ion or sub-ion range $v_A k_\parallel/\Omega_p > 1$ with a spectrum $\propto k^{-\alpha}$ with varying $\alpha \geq 2$.

Considering a plasma composed of bi-Maxwellian protons and cold electrons, with electromagnetic fluctuations propagating along a background magnetic field $\vec{B}_0$, it is shown that all the spectrum shapes considered here can heat protons preferentially in the direction perpendicular with respect to $\vec{B}_0$, provided the initial wave has enough energy power to be transferred to protons, even if the plasma is initially stable. Thus, isotropic protons can be heated toward high anisotropies $T_\perp/T_\parallel > 1$. If $T_\perp/T_\parallel$ reaches high enough values, then an Alfvén-cyclotron instability is excited during the quasilinear evolution. Afterwards, the anisotropy production saturates and the plasma relaxes to a quasi-stationary state with a maximum instability growth-rate $\gamma/\Omega_p \approx 10^{-3}$. If the initial wave energy is insufficient then kinetic instabilities are not excited, although transverse heating may still occur.

It is noted that for simulations starting far below the instability threshold (defined here as the contour where $\gamma_{\max}/\Omega_p = 10^{-4}$ in the $\beta_\parallel$ and $T_\perp/T_\parallel$ parameter space), the anisotropy grows, and $\beta_\parallel$ and the wave energy are reduced, such that the final quasi-stationary state lies near the instability thresholds. This means that simulations of stable protons ($T_\perp/T_\parallel = 1$) starting with low $\beta_\parallel < 0.01$ experience stronger perpendicular heating compared to simulations starting with $\beta_\parallel > 0.01$ for the same initial wave energy W_B. For higher values of $\beta_\parallel > 0.1$, a wave energy $W_B < 0.1$ may not be sufficient to be transferred to protons, as it must compete with kinetic effects as measured by the beta parameter, thus the quasi-stationary state is reached for anisotropy values far below the instability thresholds although transverse heating can still be observed. On the other hand, simulations where the

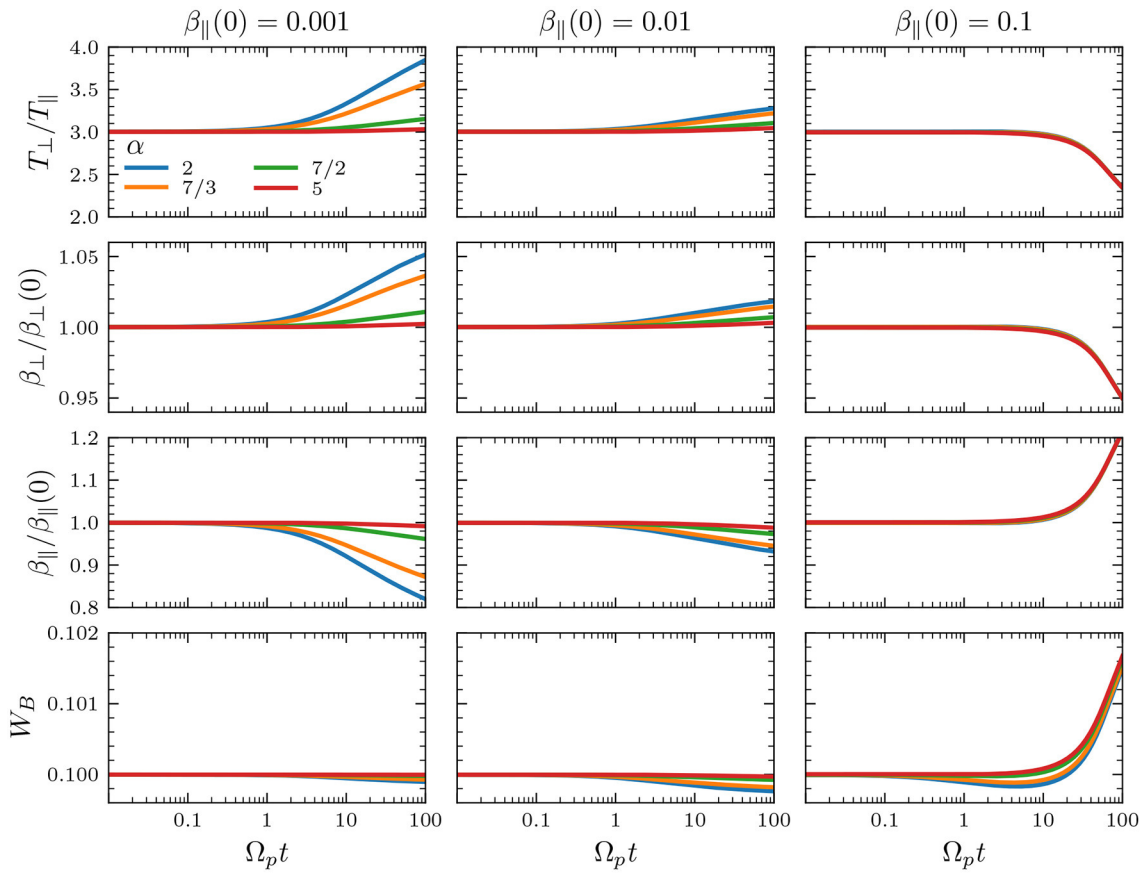

FIGURE 5 | Same as in **Figure 4** but for an initial anisotropy $T_\perp/T_\parallel(0) = 3$.

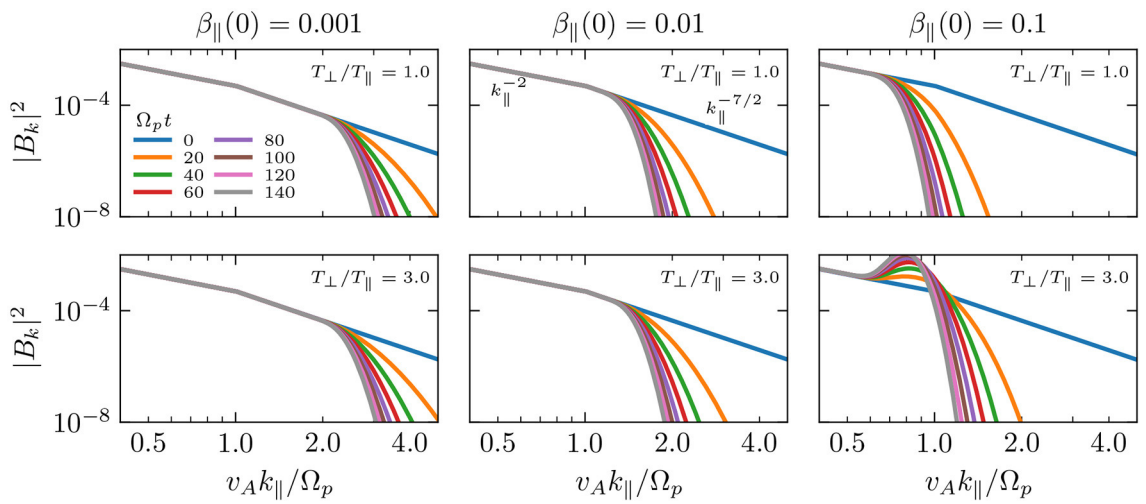

FIGURE 6 | Spectral wave energy $|B_k|^2$ as a function of the normalized wavenumber $v_A k_\parallel/\Omega_p$ for several time steps. Initial conditions are $W_B(0) = 0.1$ for a solar wind-like spectrum with $\alpha = 7/2$. (Top) $T_\perp/T_\parallel(0) = 1$ and (Bottom) $T_\perp/T_\parallel(0) = 3$. (Left) $\beta_\parallel(0) = 0.001$, (Middle) $\beta_\parallel(0) = 0.01$, and (Right) $\beta_\parallel(0) = 0.1$.

plasma is initially unstable (for anisotropies above the instability thresholds), the kinetic instability is dominant over the effects of energy transfer from the turbulent wave to protons. This results in an effective transverse cooling, i.e., reduction of the anisotropy and growth of $\beta_\parallel$. The wave energy also grows due to the presence of the instability. Nevertheless, and similarly

to the previous description, the quasilinear evolution reaches a stationary state around the instability thresholds. Thus, there exists competition between the energy transfer from turbulent waves and the presence of kinetic instabilities, and they are effectively balanced near the instability thresholds.

Our numerical results show that the proton transverse heating by the waves is efficient depending on the energy stored in the tail of the magnetic spectrum ($v_A k_\parallel/\Omega_p > 1$ which lies in the kinetic range). This happens because the waves are heavily damped in the kinetic range according to the linear kinetic dispersion relation, and energy transfer from the waves to protons should occur first for those wavenumbers according to the quasilinear description. As anticipated from the previous results, in the case of a solar wind-like turbulent power-law spectra with a spectral break, the perpendicular heating is more effective for lower values of α as the tails of the spectrum can store more energy to be transferred to the particles. For values of $\beta_\parallel(0) > 0.01$, transverse preferential heating still occurs, however it seems to be independent of α, and it is less efficient than for lower values of $\beta_\parallel(0) < 0.01$. This means that for high values of $\beta_\parallel$, the shape of the wave spectrum is less relevant for perpendicular heating, and other kinetic effects become dominant. Finally, if the plasma is initially unstable, i.e., with large enough temperature anisotropy (e.g., $T_\perp/T_\parallel = 3$ for $\beta_\parallel = 0.1$), then the wave spectrum grows in time because it absorbs energy from the particles in a range of wavenumbers $v_A k_\parallel/\Omega_p < 1$. This produces a bump in the spectral wave energy just below the spectral break, the growth of the total magnetic energy, and the subsequent reduction of the proton temperature anisotropy toward the instability thresholds. It is worth mentioning that a bump has been sometimes observed in the magnetic field spectrum in correspondence of the ion characteristic scales near the Sun [78]. Thus, our results suggest that such characteristic may be related with resonant wave-particle interactions between unstable ion populations and turbulence near the spectral break.

The above being said, it is important to mention that turbulence in the solar wind correspond to an anisotropic cascade following critical balance with $k_\perp \neq 0$. However, as a first approximation here we have considered the fluctuations to follow the parallel propagating ($k_\perp = 0$) Alfvén Ion-Cyclotron mode dispersion relation, since for small values of plasma beta, the compressibility of the fluctuations is small as pointed out by Bale et al. [11], which is consistent with Alfvén Ion-Cyclotron modes. Under this context we have considered that the plasma will only interact with transverse fluctuations with respect to the mean field, and therefore we have neglected the effect of other fluctuations with $k_\perp \neq 0$. We recognize, however, that this may be considered a crude approximation but at the same time we believe that our simplified approach provides valuable insights to the problem of the heating of the solar wind, that is generally observed in an anisotropic state. We expect to expand the scope of our approach and results with a subsequent study considering oblique propagating waves, hopefully corroborating or improving the results of our reduced model.

In summary, our results suggest a possible mechanism to explain why the solar wind plasma can be observed in a stationary state with $T_\perp/T_\parallel > 1$ near the instability thresholds or far from thermodynamic equilibrium, as has been observed in the Earth's magnetosphere or the solar wind. A sufficient level of turbulent magnetic spectrum can drive an initially stable proton plasma toward higher values of the temperature anisotropy, i.e., far from thermodynamic equilibrium and preventing the plasma to remain in an isotropic state. However, measurements of solar wind protons at different space environments show that proton velocity distributions can also exhibit anisotropic states with $T_\perp/T_\parallel < 1$ [11]. There are several possible explanations for this apparent discrepancy, as in this work we have not considered other effects that can effectively reduce the production of anisotropy, or compete with the Alfvén-cyclotron instability and the turbulent energy transfer, but are nonetheless worth of study. For example, radial expansion from the Sun [52, 79, 80], collisional effects [42], the role of compressive fluctuations [81], oblique propagation and the corresponding anisotropic turbulent cascade [19, 54, 75], oblique instabilities, such as the mirror or oblique firehose instabilities [48], other non-Maxwellian distributions, such as kappa distributions, the presence of heavy ions [56], or the kinetic effects of electrons. Also, the amplitude of magnetic fluctuations decays mostly with $\beta_\parallel$ [11, 60], imposing a severe restriction on the wave energy available for anisotropy production in space plasmas. However, steep spectra (larger α values) have been typically observed in association with small values of the plasma beta and large levels of turbulent fluctuations, both recently in near-Sun environment by Parker Solar Probe, and also previously in the near-Earth environment by WIND [82]. Moreover, Parker Solar Probe measurements have also shown an enhanced perpendicular proton heating possibly due to stochastic heating related to the strong turbulent fluctuations particularly in the fast solar wind (see e.g., Martinović et al. [83]) that could compete with all the mentioned mechanisms, including the heating mechanism suggested in this paper.

DATA AVAILABILITY STATEMENT

The original contributions presented in the study are included in the article/supplementary material, further inquiries can be directed to the corresponding author/s.

AUTHOR CONTRIBUTIONS

All authors listed have made a substantial, direct and intellectual contribution to the work, and approved it for publication. All authors contributed equally to this work.

FUNDING

This work was supported by ANID, Chile, through FONDECyT grants No. 11180947 (RN), and No. 1191351 (PM), and CONICyT-PAI grant No. 79170095 (RN).

REFERENCES

1. Spitzer L. *Physics of Fully Ionized Gases*. New York, NY: John Wiley & Sons, Inc. (1962).
2. Marsch E, Goldstein H. The effects of Coulomb collisions on solar wind ion velocity distributions. *J Geophys Res*. (1983) 88:9933–40. doi: 10.1029/JA088iA12p09933
3. Marsch E, Mühlhäuser KH, Rosenbauer H, Schwenn R, Neubauer F. Solar wind helium ions: observations of the Helios solar probes between 0.3 and 1 AU. *J Geophys Res*. (1982) 87:35–51. doi: 10.1029/JA087iA01p00035
4. Gary SP. *Theory of Space Plasma Microinstabilities*. Cambridge: Cambridge University Press (1993).
5. Astudillo HF. High-order modes of left-handed electromagnetic waves in a solar-wind-like plasma. *J Geophys Res*. (1996) 101:24433. doi: 10.1029/96JA01586
6. Hellinger P, Trávníček P. Parallel and oblique proton fire hose instabilities in the presence of alpha/proton drift: hybrid simulations. *J Geophys Res*. (2006) 111:A01107. doi: 10.1029/2005JA011318
7. López RA, Lazar M, Shaaban SM, Poedts S, Moya PS. Alternative high-plasma beta regimes of electron heat-flux instabilities in the solar wind. *Astrophys J Lett*. (2020) 900:L25. doi: 10.3847/2041-8213/abaf56
8. Klimontovich YL. Physics of collisionless plasma. *Physics-Uspekhi*. (1997) 40:21. doi: 10.1070/PU1997v040n01ABEH000200
9. Kasper JC, Lazarus AJ, Gary SP. Wind/SWE observations of firehose constraint on solar wind proton temperature anisotropy. *Geophys Res Lett*. (2002) 29:20-1–20-4. doi: 10.1029/2002GL015128
10. Marsch E. Kinetic physics of the solar corona and solar wind. *Living Rev Solar Phys*. (2006) 3:1. doi: 10.12942/lrsp-2006-1
11. Bale SD, Kasper JC, Howes GG, Quataert E, Salem C, Sundkvist D. Magnetic fluctuation power near proton temperature anisotropy instability thresholds in the solar wind. *Phys Rev Lett*. (2009) 103:211101. doi: 10.1103/PhysRevLett.103.211101
12. Bruno R, Carbone V. The solar wind as a turbulence laboratory. *Living Rev Solar Phys*. (2013) 10:2. doi: 10.12942/lrsp-2013-2
13. Heinemann M. Role of collisionless heat flux in magnetospheric convection. *J Geophys Res Space Phys*. (1999) 104:28397–410. doi: 10.1029/1999JA900401
14. Matsumoto Y, Hoshino M. Turbulent mixing and transport of collisionless plasmas across a stratified velocity shear layer. *J Geophys Res Space Phys*. (2006) 111:A05213. doi: 10.1029/2004JA010988
15. Espinoza CM, Stepanova M, Moya PS, Antonova EE, Valdivia JA. Ion and electron κ distribution functions along the plasma sheet. *Geophys Res Lett*. (2018) 45:6362–70. doi: 10.1029/2018GL078631
16. Moya PS, Pinto VA, Viñas AF, Sibeck DG, Kurth WS, Hospodarsky GB, et al. Weak kinetic Alfvén waves turbulence during the 14 November 2012 geomagnetic storm: Van Allen Probes observations. *J Geophys Res Space Phys*. (2015) 120:5504–23. doi: 10.1002/2014JA020281
17. Narita Y, Roberts OW, Vörös Z, Hoshino M. Transport ratios of the kinetic Alfvén mode in space plasmas. *Front Phys*. (2020) 8:166. doi: 10.3389/fphy.2020.00166
18. Sahraoui F, Goldstein ML, Belmont G, Canu P, Rezeau L. Three dimensional anisotropic k spectra of turbulence at subproton scales in the solar wind. *Phys Rev Lett*. (2010) 105:131101. doi: 10.1103/PhysRevLett.105.131101
19. Horbury TS, Forman M, Oughton S. Anisotropic scaling of magnetohydrodynamic turbulence. *Phys Rev Lett*. (2008) 101:175005. doi: 10.1103/PhysRevLett.101.175005
20. Chen CHK. Recent progress in astrophysical plasma turbulence from solar wind observations. *J Plasma Phys*. (2016) 82:535820602. 535820602. doi: 10.1017/S0022377816001124
21. González CA, Parashar TN, Gomez D, Matthaeus WH, Dmitruk P. Turbulent electromagnetic fields at sub-proton scales: two-fluid and full-kinetic plasma simulations. *Phys Plasmas*. (2019) 26:012306. doi: 10.1063/1.5054110
22. Cerri SS, Grošelj D, Franci L. Kinetic plasma turbulence: recent insights and open questions from 3D3V simulations. *Front Astron Space Sci*. (2019) 6:64. doi: 10.3389/fspas.2019.00064
23. Howes GG, Cowley SC, Dorland W, Hammett GW, Quataert E, Schekochihin AA. A model of turbulence in magnetized plasmas: implications for the dissipation range in the solar wind. *J Geophys Res Space Phys*. (2008) 113:A05103. doi: 10.1029/2007JA012665
24. Maneva Y, Viñas AF, Moya PS, Wicks RT, Poedts S. Dissipation of parallel and oblique Alfvén-cyclotron waves-Implications for heating of alpha particles in the solar wind. *Astrophys J*. (2015) 814:33. doi: 10.1088/0004-637X/814/1/33
25. Sulem PL, Passot T. Landau fluid closures with nonlinear large-scale finite Larmor radius corrections for collisionless plasmas. *J Plasma Phys*. (2015) 81:325810103. doi: 10.1017/S0022377814000671
26. Cerri SS, Califano F. Reconnection and small-scale fields in 2D-3V hybrid-kinetic driven turbulence simulations. *New J Phys*. (2017) 19:025007. doi: 10.1088/1367-2630/aa5c4a
27. Franci L, Cerri SS, Califano F, Landi S, Papini E, Verdini A, et al. Magnetic reconnection as a driver for a sub-ion-scale cascade in plasma turbulence. *Astrophys J*. (2017) 850:L16. doi: 10.3847/2041-8213/aa93fb
28. Loureiro NF, Boldyrev S. Collisionless reconnection in magnetohydrodynamic and kinetic turbulence. *Astrophys J*. (2017) 850:182. doi: 10.3847/1538-4357/aa9754
29. Mallet A, Schekochihin AA, Chandran BDG. Disruption of Alfvénic turbulence by magnetic reconnection in a collisionless plasma. *J Plasma Phys*. (2017) 83:905830609. doi: 10.1017/S0022377817000812
30. Papini E, Franci L, Landi S, Verdini A, Matteini L, Hellinger P. Can hall magnetohydrodynamics explain plasma turbulence at sub-ion scales? *Astrophys J*. (2019) 870:52. doi: 10.3847/1538-4357/aaf003
31. Chen CHK, Leung L, Boldyrev S, Maruca BA, Bale SD. Ion-scale spectral break of solar wind turbulence at high and low beta. *Geophys Res Lett*. (2014) 41:8081–8. doi: 10.1002/2014GL062009
32. Wang X, Tu CY, He JS, Wang LH. Ion-scale spectral break in the normal plasma beta range in the solar wind turbulence. *J Geophys Res Space Phys*. (2018) 123:68–75. doi: 10.1002/2017JA024813
33. Franci L, Landi S, Matteini L, Verdini A, Hellinger P. Plasma beta dependence of the ion-scale spectral break of solar wind turbulence: high-resolution 2D hybrid simulations. *Astrophys J*. (2016) 833:91. doi: 10.3847/1538-4357/833/1/91
34. Gamayunov KV, Engebretson MJ, Zhang M, Rassoul HK. Source of seed fluctuations for electromagnetic ion cyclotron waves in Earth's magnetosphere. *Adv Space Res*. (2015) 55:2573–83. doi: 10.1016/j.asr.2015.02.024
35. Chaston CC, Bonnell JW, Wygant JR, Mozer F, Bale SD, Kersten K, et al. Observations of kinetic scale field line resonances. *Geophys Res Lett*. (2014) 41:209–15. doi: 10.1002/2013GL058507
36. Alexandrova O, Carbone V, Veltri P, Sorriso–Valvo L. Small–scale energy cascade of the solar wind turbulence. *Astrophys J*. (2008) 674:1153–7. doi: 10.1086/524056
37. Goldstein ML, Wicks RT, Perri S, Sahraoui F. Kinetic scale turbulence and dissipation in the solar wind: key observational results and future outlook. *Phil Trans R Soc A*. (2015) 373:20140147. doi: 10.1098/rsta.2014.0147
38. Franci L, Sarto DD, Papini E, Giroul A, Stawarz JE, Burgess D, et al. Evidence of a "current-mediated" turbulent regime in space and astrophysical plasmas. *arXiv*. (2020) 2010.05048. Available online at: https://arxiv.org/abs/2010.05048
39. Franci L, Landi S, Matteini L, Verdini A, Hellinger P. High-resolution hybrid simulations of kinetic plasma turbulence at proton scales. *Astrophys J*. (2015) 812:21. doi: 10.1088/0004-637X/812/1/21
40. Matthaeus WH, Yang Y, Wan M, Parashar TN, Bandyopadhyay R, Chasapis A, et al. Pathways to dissipation in weakly collisional plasmas. *Astrophys J*. (2020) 891:101. doi: 10.3847/1538-4357/ab6d6a
41. Viñas AF, Moya PS, Navarro RE, Valdivia JA, Araneda JA, Muñoz V. Electromagnetic fluctuations of the whistler cyclotron and firehose instabilities in a Maxwellian and Tsallis-kappa-like plasma. *J Geophys Res*. (2015) 120, 3307–17. doi: 10.1002/2014JA020554
42. Yoon PH. Kinetic instabilities in the solar wind driven by temperature anisotropies. *Rev Mod Plasma Phys*. (2017) 1:4. doi: 10.1007/s41614-017-0006-1
43. Weibel ES. Spontaneously growing transverse waves in a plasma due to an anisotropic velocity distribution. *Phys Rev Lett*. (1959) 2:83–4. doi: 10.1103/PhysRevLett.2.83
44. Sagdeev R, Shafranov V. On the instability of a plasma with an anisotropic distribution of velocities in a magnetic field. *J Exptl Theoret Phys (USSR)*. (1960) 29:181.

45. Kennel CF, Petschek HE. Limit on stably trapped particle fluxes. *J Geophys Res*. (1966) 71:1–28. doi: 10.1029/JZ071i001p00001
46. Viñas AF, Goldstein ML, Acuña MH. Spectral analysis of magnetohydrodynamic fluctuations near interplanetary shocks. *J Geophys Res*. (1984) 89:3762–74. doi: 10.1029/JA089iA06p03762
47. Brinca AL, Tsurutani BT. Unusual characteristics of electromagnetic waves exited by cometary newborn ions with large perpendicular energies. *Astron Astrophys*. (1987) 187:311–9. doi: 10.1007/978-3-642-82971-0_57
48. Yoon PH. Quasilinear evolution of Alfvén-ion-cyclotron and mirror instabilities driven by ion temperature anisotropy. *Phys Fluids B*. (1992) 4:3627–37. doi: 10.1063/1.860371
49. Moya PS, Navarro R, Viñas AF, Muñoz V, Valdivia JA. Weak turbulence cascading effects in the acceleration and heating of ions in the solar wind. *Astrophys J*. (2014) 781:76. doi: 10.1088/0004-637X/781/2/76
50. Hellinger P, Trávníček PM, Decyk VK, Schriver D. Oblique electron fire hose instability: particle-in-cell simulations. *J Geophys Res*. (2014) 119:59–68. doi: 10.1002/2013JA019227
51. Adrian ML, Viñas AF, Moya PS, Wendel DE. Solar wind magnetic fluctuations and electron non-thermal temperature anisotropy: survey of wind-SWE-VEIS observations. *Astrophys J*. (2016) 833:49. doi: 10.3847/1538-4357/833/1/49
52. Moya PS, Viñas AF, Muñoz V, Valdivia JA. Computational and theoretical study of the wave-particle interaction of protons and waves. *Ann Geophys*. (2012) 30:1361–9. doi: 10.5194/angeo-30-1361-2012
53. Dasso S, Milano LJ, Matthaeus WH, Smith CW. Anisotropy in fast and slow solar wind fluctuations. *Astrophys J*. (2005) 635:L181–4. doi: 10.1086/499559
54. Horbury TS, Forman MA, Oughton S. Spacecraft observations of solar wind turbulence: an overview. *Plasma Phys Controll Fusion*. (2005) 47:B703–17. doi: 10.1088/0741-3335/47/12B/S52
55. Gomberoff L, Muñoz V, Valdivia JA. Ion cyclotron instability triggered by drifting minor ion species: Cascade effect and exact results. *Planet Space Sci*. (2004) 52:679–84. doi: 10.1016/j.pss.2004.01.004
56. Navarro RE, Muñoz V, Valdivia JA, Moya PS. Feasibility of ion-cyclotron resonant heating in the solar wind. *Astrophys J*. (2020) 898:L9. doi: 10.3847/2041-8213/aba0ae
57. Gary SP, Tokar RL. The second-order theory of electromagnetic hot ion beam instabilities. *J Geophys Res*. (1985) 90:65–72. doi: 10.1029/JA090iA01p00065
58. Fried BD, Conte SD. *The Plasma Dispersion Function*. San Diego, CA: Academic (1961).
59. Muller DE. A method for solving algebraic equations using an automatic computer. *Math Tables Other Aids Comput*. (1956) 10:208–15. doi: 10.2307/2001916
60. Navarro RE, Moya PS, Muñoz V, Araneda JA, Viñas AF, Valdivia JA. Solar wind thermally induced magnetic fluctuations. *Phys Rev Lett*. (2014) 112:1–5. doi: 10.1103/PhysRevLett.112.245001
61. Moya PS, Muñoz V, Rogan J, Valdivia JA. Study of the cascading effect during the acceleration and heating of ions in the solar wind. *J Atmos Solar Terres Phys*. (2011) 73:1390–7. doi: 10.1016/j.jastp.2011.01.009
62. Jian LK, Moya PS, Viñas AF, Stevens M. Electromagnetic cyclotron waves in the solar wind: wind observation and wave dispersion analysis. *AIP Conf Proc* (Weihai). (2016) 1720:040007. doi: 10.1063/1.4943818
63. Wicks RT, Alexander RL, Stevens M, III LBW, Moya PS, Viñas A, et al. A proton-cyclotron wave storm generated by unstable proton distribution functions in the solar wind. *Astrophys J*. (2016) 819:6. doi: 10.3847/0004-637X/819/1/6
64. Krall NA, Trivelpiece AW. *Principle of Plasma Physics*. San Francisco Press Inc. (1986).
65. Stix TH. *Waves in Plasmas*. American Institute of Physics (1992). Available online at: http://books.google.com/books?id=OsOWJ8iHpmMC
66. Yoon PH, Seough JJ, Kim KH, Lee DH. Empirical versus exact numerical quasilinear analysis of electromagnetic instabilities driven by temperature anisotropy. *J Plasma Phys*. (2012) 78:47–54. doi: 10.1017/S0022377811000407
67. Seough J, Yoon PH, Hwang J. Quasilinear theory and particle-in-cell simulation of proton cyclotron instability. *Phys Plasmas*. (2014) 21:062118. doi: 10.1063/1.4885359
68. Seough J, Yoon PH, Hwang J. Simulation and quasilinear theory of proton firehose instability. *Phys Plasmas*. (2015) 22:012303. doi: 10.1063/1.4905230
69. Galtier S, Bhattacharjee A. Anisotropic weak whistler wave turbulence in electron magnetohydrodynamics. *Phys Plasmas*. (2003) 10:3065–76. doi: 10.1063/1.1618648
70. Gary SP, Smith CW. Short-wavelength turbulence in the solar wind: linear theory of whistler and kinetic Alfvén fluctuations. *J Geophys Res Space Phys*. (2009) 114:A12105. doi: 10.1029/2009JA014525
71. Schekochihin AA, Cowley SC, Dorland W, Hammett GW, Howes GG, Quataert E, et al. Astrophysical gyrokinetics: kinetic and fluid turbulent cascades in magnetized weakly collisional plasmas. *Astrophys J Suppl Ser*. (2009) 182:310–77. doi: 10.1088/0067-0049/182/1/310
72. Boldyrev S, Horaites K, Xia Q, Perez JC. Toward a theory of astrophysical plasma turbulence at subproton scales. *Astrophys J*. (2013) 777:41. doi: 10.1088/0004-637X/777/1/41
73. Boldyrev S, Perez JC. Spectrum of kinetic-Alfvén turbulence. *Astrophys J*. (2012) 758:L44. doi: 10.1088/2041-8205/758/2/L44
74. Arzamasskiy L, Kunz MW, Chandran BDG, Quataert E. Hybrid-kinetic simulations of ion heating in Alfvénic turbulence. *Astrophys J*. (2019) 879:53. doi: 10.3847/1538-4357/ab20cc
75. Howes GG. A dynamical model of plasma turbulence in the solar wind. *Phil Trans R Soc A*. (2015) 373:20140145. doi: 10.1098/rsta.2014.0145
76. Gaelzer R, Yoon PH, Kim S, Ziebell LF. On the dimensionally correct kinetic theory of turbulence for parallel propagation. *Phys Plasmas*. (2015) 22:032310. doi: 10.1063/1.4916054
77. Kim S, Yoon PH, Choe GS. Spontaneous emission of electromagnetic and electrostatic fluctuations in magnetized plasmas: quasi-parallel modes. *Phys Plasmas*. (2016) 23:022111. doi: 10.1063/1.4941707
78. Bowen TA, Bale SD, Bonnell JW, Dudok de Wit T, Goetz K, Goodrich K, et al. A merged search-coil and fluxgate magnetometer data product for parker solar probe FIELDS. *J Geophys Res Space Phys*. (2020) 125:e2020JA027813. doi: 10.1029/2020JA027813
79. Hellinger P, Matteini L, Landi S, Verdini A, Franci L, Trávnícek PM. Plasma turbulence and kinetic instabilities at ion scales in the expanding solar wind. *Astrophys J*. (2015) 811:L32. doi: 10.1088/2041-8205/811/2/L32
80. Yoon PH, Sarfraz M. Interplay of electron and proton instabilities in expanding solar wind. *Astrophys J*. (2017) 835:246. doi: 10.3847/1538-4357/835/2/246
81. Yan H, Lazarian A. Cosmic ray transport through gyroresonance instability in compressible turbulence. *Astrophys J*. (2011) 731:35. doi: 10.1088/0004-637X/731/1/35
82. Bruno R, Trenchi L, Telloni D. Spectral slope variation at proton scales from fast to slow solar wind. *Astrophys J*. (2014) 793:L15. doi: 10.1088/2041-8205/793/1/L15
83. Martinović MM, Klein KG, Kasper JC, Case AW, Korreck KE, Larson D, et al. The enhancement of proton stochastic heating in the near-sun solar wind. *Astrophys J Suppl Ser*. (2020) 246:30. doi: 10.3847/1538-4365/ab527f

Conflict of Interest: The authors declare that the research was conducted in the absence of any commercial or financial relationships that could be construed as a potential conflict of interest.

frontiers in Astronomy and Space Sciences

REVIEW
published: 22 April 2021
doi: 10.3389/fspas.2021.644354

Shock Propagation and Associated Particle Acceleration in the Presence of Ambient Solar-Wind Turbulence

Fan Guo[1,2]*, *Joe Giacalone*[3] *and Lulu Zhao*[4]

[1]Los Alamos National Laboratory, Theoretical Division, Los Alamos, NM, United States, [2]New Mexico Consortium, Los Alamos, NM, United States, [3]Lunar and Planetary Laboratory, University of Arizona, Tucson, AZ, United States, [4]Department of Climate and Space Sciences and Engineering, University of Michigan, Ann Arbor, MI, United States

The topic of this review paper is on the influence of solar wind turbulence on shock propagation and its consequence on the acceleration and transport of energetic particles at shocks. As the interplanetary shocks sweep through the turbulent solar wind, the shock surfaces fluctuate and ripple in a range of different scales. We discuss particle acceleration at rippled shocks in the presence of ambient solar-wind turbulence. This strongly affects particle acceleration and transport of energetic particles (both ions and electrons) at shock fronts. In particular, we point out that the effects of upstream turbulence is critical for understanding the variability of energetic particles at shocks. Moreover, the presence of pre-existing upstream turbulence significantly enhances the trapping near the shock of low-energy charged particles, including those near the thermal energy of the incident plasma, even when the shock propagates normal to the average magnetic field. Pre-existing turbulence, always present in space plasmas, provides a means for the efficient acceleration of low-energy particles and overcoming the well known injection problem at shocks.

Keywords: particle acceleration, collisionless shocks, turbulence, energetic particles, solar wind

OPEN ACCESS

Edited by:
Gaetano Zimbardo, University of Calabria, Italy

Reviewed by:
Yasuhito Narita, Austrian Academy of Sciences (OeAW), Austria
Xochitl Blanco-Cano, National Autonomous University of Mexico, Mexico

***Correspondence:**
Fan Guo
guofan.ustc@gmail.com

Specialty section:
This article was submitted to Space Physics, a section of the journal Frontiers in Astronomy and Space Sciences

Received: *21 December 2020*
Accepted: *11 February 2021*
Published: *22 April 2021*

Citation:
Guo F, Giacalone J and Zhao L (2021) Shock Propagation and Associated Particle Acceleration in the Presence of Ambient Solar-Wind Turbulence. Front. Astron. Space Sci. 8:644354. doi: 10.3389/fspas.2021.644354

1 INTRODUCTION

Understanding shocks and its particle acceleration in the solar wind is an important topic in heliophysics, for both the effects of space weather and basic physics of shocks and particle energization. Near the Sun, the shocks emerge in front of the solar drivers and accelerate solar energetic particles (SEPs) (Reames, 1999; Desai and Giacalone, 2016). However, those shocks are farther away from most of the spacecraft, making them difficult to observe directly. At 1 astronomical unit (AU), these shocks are mostly driven by coronal mass ejections, with a smaller population driven by Stream Interaction Regions (SIRs) (Sheeley et al., 1985; Richardson and Cane, 2010; Borovsky, 2020). Strong energetic particles observed in the vicinity of interplanetary shocks are often termed as "Energetic Storm Particles" (ESP) (Bryant et al., 1962; Gosling et al., 1981), to distinguish them from the solar energetic particles (SEPs) accelerated close to the Sun, although the SEPs can be well accelerated by the coronal counterpart of the interplanetary shock driven by the same coronal mass ejection (Kallenrode, 1996; Reames, 1999). Most interplanetary shocks are weak compared to planetary bow shocks. Because of the Parker spiral magnetic field, the interplanetary shocks at 1 AU are mostly quasi-perpendicular, meaning the angle between the un-shocked, upstream magnetic field and the unit normal to the shock θ_{Bn} is usually larger than 45 degree. Decades of spacecraft observations by Helios, IMP, ISEE, ACE, Wind, STEREO and others have accumulated tremendous

amount of shock events (as many as several dozens per year at solar maximum) for study (Neugebauer, 2013; Dresing et al., 2016), including two widely used shock lists collected by ACE[1] and Wind[2]. Newly launched Parker Solar Probe and Solar Orbiter provide shock and energetic particle observations close to the Sun, and will further reveal the physics of interplanetary shocks and their associated energetic particles. The upcoming IMAP mission will provide high resolution measurements of suprathermal ions and provide further observation insight, especially on the variability of energetic particles in the vicinity of the shocks (McComas et al., 2018).

In addition to the mean, Parker spiral magnetic field, the solar wind is well known to be filled with numerous magnetic structures (Borovsky, 2008; Neugebauer and Giacalone, 2010) and turbulence (Tu and Marsch, 1995; Goldstein et al., 1995). In situ measurements of the solar wind have long established the existence of turbulence that has a Kolmogorov-like power spectrum with a correlation scale of about 10^6 km at 1 AU and increases in the outer heliosphere, but could also be contributed by magnetic structures and discontinuities (Borovsky, 2010). Unlike Earth's bow shock that is on a much smaller spatial scale and more suitable for kinetic studies, the interplanetary shocks provide a natural laboratory for physical processes involving high energy charged particles and large scale magnetic field fluctuations. Compared to other shock-turbulence systems like the solar wind termination shock and supernova remnant shocks, interplanetary shocks are frequently observed, with a wealth amount of data accumulated. The propagation and evolution of interplanetary shocks in the solar wind are influenced by fluctuations in magnetic fields, velocity, and density. The turbulent magnetic field can interact with the shock waves, distorting their surfaces, leading to shock ripples (Neugebauer and Giacalone, 2005) and enhance the downstream magnetic fluctuations (Zank et al., 2003; Lu et al., 2009). It is also important for efficient particle acceleration (Giacalone, 2005; Jokipii and Giacalone, 2007; Guo et al., 2010; Guo and Giacalone, 2010; Guo and Giacalone, 2015). These nonplanar ripples at the shock surface, coupled with turbulent upstream magnetic fields, lead to substantial variations of energetic particle flux, which has been pointed out, but never been understood in a systematic way (Giacalone and Neugebauer, 2008; Guo et al., 2010; Kóta, 2010).

The diffusive shock acceleration (DSA) theory describes the basic process of acceleration of particles at the shock front. A review of the mechanism is given by Drury (1983) [see also Desai and Giacalone (2016)], and was independently discovered by Krymskii (1977), Axford et al. (1977), Bell (1978), and Blandford and Ostriker (1978)). For the often considered one-dimensional solution, this gives the classical results:

$$f_s(p) = f_0 p^{-3r/(r-1)} H(p-p_0) \begin{cases} \exp(xU_1/\kappa) & x<0 \\ 1 & x \geq 0 \end{cases} \quad (1)$$

where f_0 is a normalization constant, r is the ratio of the downstream to upstream density, U_1 is the upstream flow speed in the shock frame, and H(p) is the Heaviside step function. This solution is obtained by solving the Parker transport equation (see a discussion in **Section 3**) for a one-dimensional time-steady shock at x = 0.

However, this result has only received limited success when applied to the interplanetary shocks. While there has been claims that an excellent agreement can be made between observations (Kennel et al., 1986) and theory (Lee, 1983) for an interplanetary shock event measured on November 12, 1978, even for that particular event, the observation over a longer time scale shows more complicated variation (Scholer et al., 1983). In fact, most of energetic particle profiles in the vicinity of interplanetary shocks are not consistent with the 1-D solution (Lario et al., 2003). While in some cases particles that interact with interplanetary shocks may have been accelerated in solar events (Li and Zank, 2005), this variation can also be induced by the fact that the 1-D solution fails due to the large-scale magnetic fluctuation, even without previous events (e.g., Neugebauer et al., 2006; Giacalone and Neugebauer, 2008). We will discuss the modification of the shock front due to the solar wind turbulence in **Section 2**. The pre-existing fluctuations are particularly important for the acceleration of particles at quasi-perpendicular shocks. We will discuss the effects of solar wind turbulence on the acceleration of protons and electrons at shocks in **Sections 3** and **4**, respectively.

Understanding shock-turbulence interaction and particle acceleration in the turbulent solar wind also has strong implication to other turbulence system, such as the magnetic field amplification when supernova shocks sweeping through the interstellar medium density and the roles of magnetic field fluctuations on particle acceleration (e.g., Giacalone and Jokipii, 2007; Inoue et al., 2009; Guo et al., 2012; Fraschetti, 2013).

Rest of this paper is organized as follows: We discuss the nonplanar shock effects led by the solar wind turbulence in **Section 2**. A discussion on the acceleration of protons is given in **Section 3**, focusing on the injection problem of protons. We discuss the issue about electron acceleration at interplanetary shock in **Section 4**. We emphasize the variability of energetic particles caused by turbulence in **Section 5**. We leave some final remarks in **Section 6**.

2 NONPLANAR SHOCKS LED BY TURBULENCE

As interplanetary shocks sweep through the turbulent solar wind, their surfaces naturally distort and fluctuate on a variety of scales. This fluctuation in the warped shock surfaces occurs not only in the large scale due to the large-scale turbulent plasma and magnetic fields (Zank et al., 2003; Giacalone, 2005; Li and Zank, 2006; Giacalone and Neugebauer, 2008; Guo and Giacalone, 2010, Guo and Giacalone, 2012b; Trotta et al., 2020), but at small scale as well, due to instabilities caused by ion reflection (Lowe and Burgess, 2003; Burgess, 2006; Yang et al., 2012; Hao et al., 2016; Trotta and Burgess, 2019). Using hybrid

[1]ACE shock list http://www.ssg.sr.unh.edu/mag/ace/ACElists/obs_list.html#shocks

[2]Wind shock list https://www.cfa.harvard.edu/shocks/

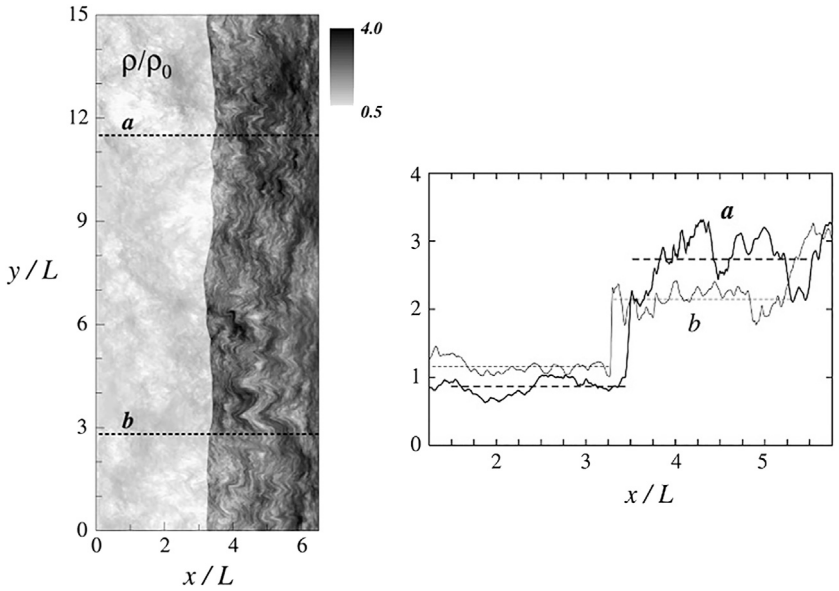

FIGURE 1 | Left panel shows a gray-scale representation of simulated plasma density from a two-dimensional MHD simulation. *L* is the correlation scale of the turbulent fluctuations. The shock is rippled as it swept through the turbulent upstream plasma. Right panel shows two cuts for density profiles at different y positions indicated on the left panel [adapted from Giacalone and Neugebauer, 2008]. Reproduced by permission of the AAS.

kinetic simulations (fluid electrons and kinetic ions) and MHD simulations, Giacalone (2005), Giacalone and Neugebauer (2008), and Guo and Giacalone (2010) have shown that the shock surface is wrapped due to the pre-existing upstream magnetic fluctuations. The angle between the shock normal and the incident magnetic field, θ_{Bn}, vary along the shock surface. **Figure 1** shows plasma density in a 2D MHD simulations where the shock propagates through a fluctuating plasma. It clearly shows that the shock is rippled in various scales from that comparable to the system size down to very small scales. The density profiles can be quite variable as indicated by two cuts across the shock.

The idea that interplanetary shock surface is wrapped in turbulence has been tested in the solar wind by Neugebauer and Giacalone (2005). They analysed 26 well-defined quasi-perpendicular interplanetary shocks that were observed by five spacecraft or more. They used the four spacecraft method to obtain five (five in the six spacecraft event) independent sets of normals and speeds. They also calculated normals and speeds using single-spacecraft methods. Furthermore, they estimated the shock radius of curvature with different methods. Most of the shocks were inconsistent with planar structures, or spherical structures with a radius of 1AU. In other words, the shocks were found to be rippled. They reported that the average local radius of curvature is ~3×10^6 km (~500R_E) which is close to the observed correlation scale of the fluctuating interplanetary magnetic field. Note that the size of the ripples they could observe was limited from below by the spacecraft separations, which were of the order of 10^5 km, corresponding to 10^3 ion inertial lengths for typical solar wind conditions. Thus they were not able to discern any smaller scale (a few times of the ion inertial length) ripples existing at the same time, though such were evident in the 2D hybrid simulations presented in the same article. Later, Koval and Szabo, 2010 confirmed this basic conclusion. The scale of measured shock ripples is similar to the correlation length of the interplanetary turbulence (e.g., Coleman and Paul, 1968; Matthaeus and Goldstein, 1982; Chen et al., 2012). In a recent study, irregular surface of interplanetary shocks at ion scales has been verified by multispacecraft observations of the Cluster mission (Kajdič et al., 2019).

The shock ripples and large-scale magnetic fluctuations have also been invoked to explain the variability of interplanetary type II radio bursts (Bale et al., 1999; Pulupa and Bale, 2008; Knock et al., 2003). Bale et al. (1999) and Pulupa and Bale (2008) observed electron foreshocks and related Langmuir waves upstream of interplanetary shocks. These events appeared to be associated with irregular shock surfaces with spatial scales ~ 10^5 km, in rough consistency with Neugebauer and Giacalone, 2005. They proposed that the complex upstream electron events result from large-scale irregularities in the shock surface.

3 THE PHYSICS ON THE INJECTION PROBLEM AND ITS IMPORTANCE TO UNDERSTANDING THE SOURCE OF SOLAR ENERGETIC PARTICLES

Pre-existing turbulence also has an important effect on low-energy charged particles, including so-called suprathermal particles whose distribution function connects smoothly to the thermal part of the incident plasma distribution. In order to

understand this, it is important to first discuss the physics of particle acceleration more generally. This is directly related to the understanding, and determination of the source of high-energy particles accelerated at shocks. It is also critical to understand the so-called 'injection problem' at shocks.

The mechanism for DSA has been discussed in many dedicated papers mentioned in **Section 1**, and it is generally accepted that this mechanism applies above some 'injection' energy, E_i. In this section we focus on the question of what happens at energies below E_i, and how it relates to the intensity and shape of the spectrum above this energy.

On the one hand, stated simply, the theory of diffusive shock acceleration does not address the injection process; thus, it might be easiest to just assume that there exists a pre-existing population of particles and that these are the particles which are further accelerated by shocks (e.g., Mewaldt et al., 2012). Moreover, the largest energetic particle events associated with coronal mass ejections often come from large active regions on the Sun which commonly also produce a number of smaller CMEs and transient shocks. It is reasonable to expect that these smaller events produce energetic particles that could be accelerated further at the later shock (c.f. Desai and Giacalone, 2016, for a review of observations). It is not clear, however, whether it is the existence of the pre-existing population of energetic particles, or the fact that the later shock moves through a more (magnetically) turbulent medium, which increases the trapping of the particles at the later shock, leading to a higher acceleration rate, which causes the higher fluxes of particles at very high energies.

On the other hand, it is important to examine the physics of particle acceleration at low energies, and to determine the conditions under which DSA theory is applicable. DSA is based on the Parker transport equation, which is given by **Eq. 10**, and was first derived by Parker (1965). This equation assumes the particle's distribution is nearly isotropic.

3.1 The Proper Frame of Reference for the Energy-Change Term in the Parker Transport Equation

We start with an analysis of the term that is responsible for the acceleration, paying particular attention to the proper frame of reference since the pitch-angle distribution of low-energy particles varies considerably between the shock frame and the plasma frame.

We now show that this term follows directly from the basic physics of charged (test) particle motion in electric and magnetic fields. We follow closely the approach of Jokipii (2012), which has rarely been cited in the literature, suggesting that this important derivation has largely been forgotten. We add some more steps to this derivation which did not appear in the original manuscript, for completeness.

The motion of a charged particle, with charge q, in a plasma containing an electric field $\mathbf{E}$ and magnetic field $\mathbf{B}$ is given by:

$$\frac{d\mathbf{p}}{dt} = q\mathbf{E} + \frac{q}{c}\mathbf{w}\times\mathbf{B} \tag{2}$$

where $\mathbf{p}$ is the momentum of the particle, $\mathbf{w}$ is the velocity vector, and c is the speed of light. Gravity and radiation pressure, two forces which are commonly included in macroscopic equations because these forces are negligible in most situations of interest regarding the acceleration of particles.

The rate of change of the kinetic energy K, of a charged particle is obtained by taking the vector dot product of the particle velocity with **Eq. 2**, given by:

$$\frac{dK}{dt} = q\mathbf{w}\cdot\mathbf{E} \tag{3}$$

We consider the case in which the electric field is given by that of ideal magnetohydrodynamics: $\mathbf{E} = -\mathbf{U}\times\mathbf{B}/c$, where $\mathbf{U}$ is the velocity of the bulk plasma which carries with it the magnetic field $\mathbf{B}$. Thus, we have

$$\frac{dK}{dt} = -\frac{q}{c}\mathbf{w}\cdot(\mathbf{U}\times\mathbf{B}) \tag{4}$$

We next consider the kinetic energy in the frame moving with the bulk plasma. Using a prime to denote quantities in the plasma frame of reference, we have

$$K' = K - \mathbf{p}\cdot\mathbf{U} + \frac{1}{2}mU^2 \tag{5}$$

Inserting this into **Eq. 4**, and using **Eq. 2** and a vector identity, after some simple manipulation it follows that:

$$\frac{dK'}{dt} = -(\mathbf{p} - m\mathbf{U})\cdot\frac{d\mathbf{U}}{dt} = -\mathbf{p}'\cdot\frac{d\mathbf{U}}{dt} = -\mathbf{p}'\cdot\left(\frac{\partial\mathbf{U}}{\partial t} + \mathbf{w}'\cdot\nabla\mathbf{U}\right) \tag{6}$$

where the middle term on the right is from the definition of the momentum in the plasma frame, and the last term on the right follows by noting that the total time derivative is that along the particle trajectory in which the plasma velocity can change both temporally and spatially; hence, the use of the advective derivative is appropriate.

We note that the kinetic energy depends on the vector momentum and velocity, and, thus not only the magnitude of these quantities but also their direction: i.e., the particle pitch angle and phase angle. We now consider a distribution of particles and average **Eq. 6** over pitch and phase angle. Denoting this average with the angle-bracket notation, we have

$$\frac{d\langle K'\rangle}{dt} = \left\langle -\mathbf{p}'\cdot\left(\frac{\partial\mathbf{U}}{\partial t} + \mathbf{w}'\cdot\nabla\mathbf{U}\right)\right\rangle \tag{7}$$

It is important to note that the average is taken over the plasma-frame pitch-angle distribution. We assume that the magnetic fluctuations will 'scatter' the particles and alter particles' pitch angles (Jokipii, 1971) with their energy conserved upon each scattering in the plasma frame. If the time between scatterings is shorter than the time variation of the plasma velocity, then the first term inside the parenthesis on the right of **Eq. 7** is small and can be neglected. Switching to index notation for the vectors, we have:

$$\frac{d\langle K'\rangle}{dt} = -\langle p'_i w'_j\rangle\partial_j U_i \tag{8}$$

In deriving this expression, one must also assert that the variation in space of the fluid velocity is on a scale larger than the scattering

mean-free path of the particles, which is simply the magnitude of the particle velocity times the scattering time. Assuming that the distribution is isotropic, the term inside the angle brackets in this equation only gives an answer when i = j and also gives a factor of 1/3 times the magnitude of the momentum and velocity. **Eq. 8** also permits contributions from fluid shear (Parker, 1965; Earl et al., 1988; Li et al., 2018; Du et al., 2018).

Noting also that the kinetic energy can be written in terms of the momentum ($dK'/dt = w'dp'/dt$), **Eq. 8**, in terms of the rate of change of the momentum in the plasma frame for a nearly isotropic distribution, is given by:

$$\frac{d\langle p'\rangle}{dt} = -\frac{1}{3}p'\nabla\cdot\mathbf{U} \tag{9}$$

This represents the rate of change of the magnitude of the momentum, in the *plasma frame* of reference, in a plasma with bulk velocity **U**. We note that energy change only occurs when the plasma has a finite divergence, either rarefactions or compressions of the plasma. In the case of a shock wave, the plasma velocity decreases across the shock, in the shock frame of reference, so that the divergence is negative. Thus, the plasma-frame momentum of the particles increases across the shock, and the energy change occurs directly at the shock. This will be discussed further below.

In the cosmic-ray (or Parker) transport equation first derived by Parker (1965), given by **Eq. 10** below, the term representing the energy change of an isotropic distribution of particles is of the same form as **Eq. 9**. Thus, in the Parker equation, the momentum variable is that measured in the plasma frame of reference. The Parker equation is given by:

$$\frac{\partial f}{\partial t} + \mathbf{U}\cdot\nabla f = \nabla\cdot\left(\kappa\nabla f\right) + \frac{1}{3}\nabla\cdot\mathbf{U}\frac{\partial f}{\partial \ln p} + S - L \tag{10}$$

where the first term on the right represents spatial diffusion, and is discussed further below. The second term on the right is energy change, as discussed above, while the last two terms of the Parker equation represent sources and losses.

The spatial diffusion tensor appearing in the Parker equation depends on the magnetic field, both its turbulent, fluctuating component, as well as its average component. It can be decomposed into components along and across the average magnetic field, and a term which represents drift motions associated with gradient and curvature drifts, according to:

$$\kappa = \kappa_{ij} = \kappa_\perp\delta_{ij} + \left(\kappa_\parallel - \kappa_\perp\right)\frac{B_iB_j}{B^2} + \epsilon_{ijk}\kappa_A\frac{B_k}{B} \tag{11}$$

where the vector B_i represents the average magnetic field. $\kappa_\perp$ and $\kappa_\parallel$ are the diffusion coefficients across and along the magnetic field and these coefficients depend on rigidity of the particles as well as the turbulent component of the magnetic field (Jokipii, 1971; Giacalone and Jokipii, 1999). κ_A represents particle drifts, including those associated with the curvature and gradient of the average magnetic field (Isenberg and Jokipii, 1979).

It is important to note here that the only assumption is that the distribution is isotropic, in the local plasma frame of reference. Above, when we derived the form of the energy-change term, we noted that the momentum was that in the plasma frame. Of course, for very high energy particles, the particle speed is many times greater than the bulk plasma speed, thus, the distinction between the plasma and inertial frames is not much. However, it is important in the context of understanding the acceleration at low energies, and the injection problem, since we are particularly interested in the lowest energy to which the diffusive shock acceleration theory is applicable.

3.2 The Injection Problem: The Perspective from the Diffusive Shock Acceleration Theory

In this review we are particularly interested in the injection problem of energetic particles at shock waves with different shock angles θ_{Bn}. Without loss of generality, we can take the magnetic field to be in the $x - z$ plane, and the unit normal to the shock in the $-x$ direction, which is also common. Thus, the component of the symmetric diffusion tensor normal to the shock, for example, can be written in terms of θ_{Bn} as:

$$\kappa_{xx} = \kappa_\perp\sin^2\theta_{Bn} + \kappa_\parallel\cos^2\theta_{Bn} \tag{12}$$

It is straightforward to solve the Parker equation for a shock-like discontinuity and the solution is given by **Eq. 1**. We note that the momentum, or energy, distribution in the shocked plasma has a power-law dependence on momentum (or energy), with an index that is only a function of the ratio of the upstream to downstream plasma velocity across the shocks. This is also the ratio of the downstream to upstream plasma density, or the shock density jump factor. This result is well known, and the physics is well studied. However, the Parker equation is a purely test-particle treatment and must assume an initial energy of the particles. It does not address where the particles at this initial energy come from, or their intensity and contribution to the overall energetics of the entire plasma. It is therefore instructive to consider the limits of applicability of the Parker equation in order to understand this particular issue better.

The Parker equation is derived by assuming the distribution is nearly isotropic in pitch and phase angle. Thus, it is averaged over these quantities, and neither appear in the equation. Thus, it is implicitly assumed that the distribution is nearly isotropic. Yet, because the equation has a diffusive term, there exists a diffusive anisotropy. In order for this equation to be internally consistent, this diffusive anisotropy must be small. At a shock, the distribution at any given energy, upstream of the shock, decays exponentially from the shock towards the upstream region (see our derivation below). The gradient in the particle intensity, in this case is purely diffusive, and leads to a diffusive streaming flux along the shock-normal direction, S_x, of the form: $S_x = -\kappa_{xx}\nabla f$. The normalized diffusive anisotropy is $\delta = 3S_x/(wf)$, where w is the particle speed. The diffusive length scale associated with the exponential decay of particles away from the shock in the upstream region is κ_{xx}/U_1 (c.f. **Eq. 1**), where U_1 is the upstream plasma velocity, so that by using **Eq. 5** in our expression for S_x,

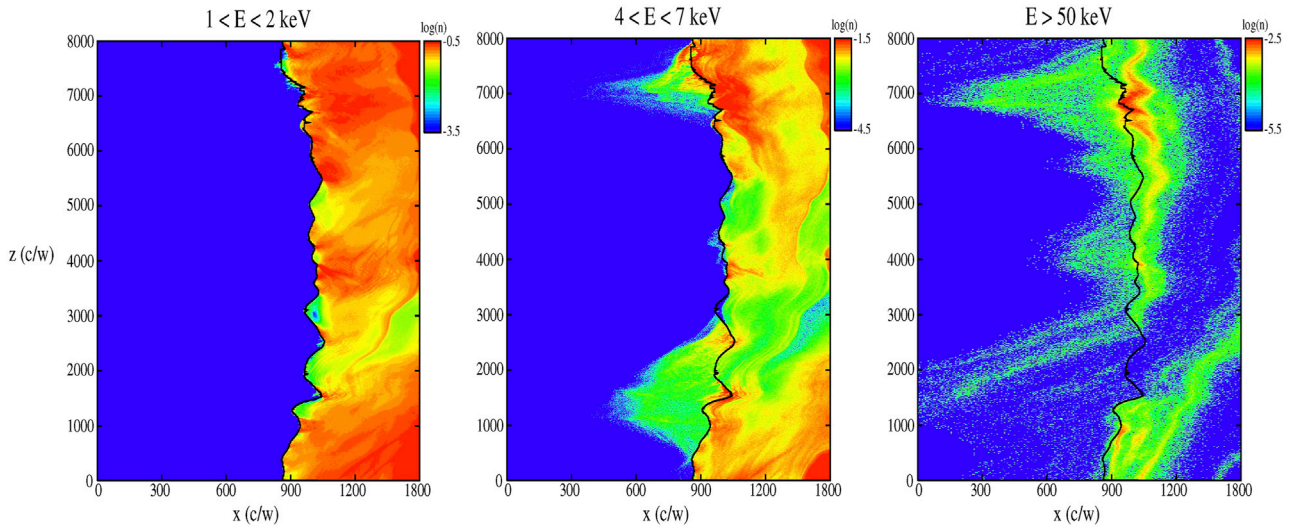

FIGURE 2 | A hybrid simulation of a quasi-perpendicular shock ($< \theta_{Bn} > = 70^\circ$), with parameters consistent with those of the DOY 118, 2001 interplanetary shock measured by ACE. Shown are suprathermal proton densities at $\Omega_{ci}t = 500$ with energies measured in local plasma frame. This result is similar to Giacalone (2005).

requiring $\delta \ll 1$, and after some manipulation, one obtains the following constraint on the applicability of the Parker equation applied to a shock:

$$w \gg 3U_1\left[1 + \frac{\eta^2 \sin^2\theta_{Bn} + (1+\epsilon^2)\sin^2\theta_{Bn}\cos^2\theta_{Bn}}{(\epsilon \sin^2\theta_{Bn} + \cos^2\theta_{Bn})^2}\right]^{1/2} \quad (13)$$

where $\epsilon = \kappa_\perp/\kappa_\parallel$ and $\eta = \kappa_A/\kappa_\parallel$. This expression was first derived by Giacalone and Jokipii (1999) and Zank et al. (2006).

The smallest possible value of the second term inside the brackets (inside the radical) is zero. It cannot be negative. Thus, for any value of θ_{Bn}, the Parker equation is only valid for $w \gg 3U_1$. Defining the sonic Mach number, M, as the ratio of the upstream flow speed to the upstream sound speed, we have: $w \gg 3Mv_{th,1}$. Since the most intense energetic particle events are presumably associated with shocks of fairly high Mach number, this is a particularly stringent requirement. This is true equally for both parallel ($\theta_{Bn} = 0^o$) and perpendicular shocks ($\theta_{Bn} = 90^\circ$).

Under certain conditions, the injection speed given by **Eq. 13** has a very strong dependence on the shock-normal angle. For $\eta \ll 1$ and $\epsilon \ll 1$, this gives $w \approx 3U_1\sec^2\theta_{Bn}$ which is the (3× the) speed of a particle moving with the intersection point of a (perfectly straight) field line and the shock front. This leads to the notion of an injection threshold problem for nearly perpendicular shocks since w is very large as $\theta_{Bn} = 90^\circ$. Some hybrid simulations, which satisfy these conditions, confirm this (Giacalone and Ellison, 2000; Caprioli and Spitkovsky, 2014). These conditions are not realistic for a wide variety of heliospheric and astrophysical shocks, however. The conditions noted above unrealistically neglects particle motion normal to the average magnetic field. In the limit $\theta_{Bn} = 90^\circ$, **Eq. 13** reduces to $w = 3U_1(1+\eta^2/\epsilon^2)^{1/2}$, whereas in the limit $\theta_{Bn} = 0^\circ$, we get $w = 3U_1$. These differ only by the value $(\eta/\epsilon)^2 = (\kappa_A/\kappa_\perp)^2$ which depends on the magnetic field, including its turbulent component and is not necessarily large. Field-line wandering, caused mostly by the largest scales in the fluctuating component of the magnetic field, significantly enhances the motion of particles across the mean magnetic field such that this term can be small. This is why pre-existing

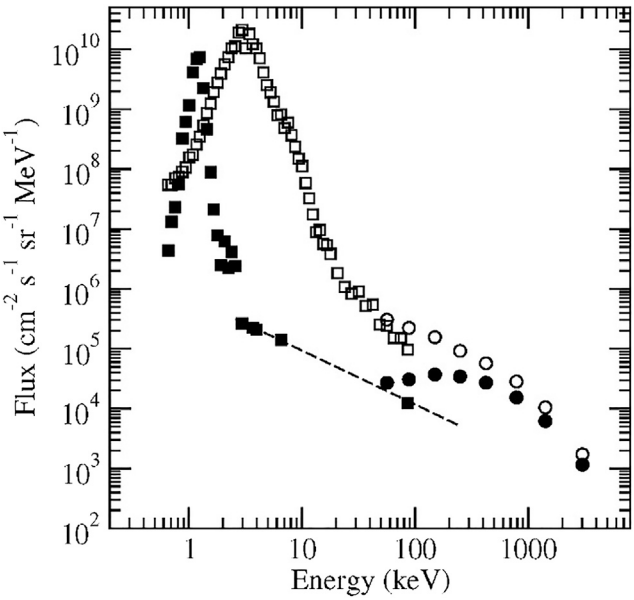

FIGURE 3 | Data from Lario et al. (2019); panels (b) and (f) of their Figure 10. The filled symbols are spectra about 30 min prior to the crossing of a shock. The open symbols are about 12 min after the shock crossing. The circles are ACE/EPAM data, and the squares are ACE/SWICS data.

turbulence is fundamentally important to the injection problem. In this case, the acceleration of low-energy particles at a perpendicular shock can be nearly as efficient as that at a parallel shock.

Hybrid simulations of shocks moving through pre-existing broadband magnetic turbulence have revealed that even thermal plasma is efficiently accelerated at a perpendicular shock (Giacalone, 2005). **Figure 2** shows a new hybrid simulation with parameters similar to those of strong, quasi-perpendicular interplanetary shocks. For this case, the Alfven Mach number is 5.8, the total plasma beta is 0.54, and the angle between average magnetic field and the x direction is 70°. Other parameters are similar to those presented in Giacalone (2005) (see also Giacalone, 2017b). Similarly, in this simulation, the initial magnetic field is a combination of a mean component and a turbulent component. The turbulent component is based on a power spectrum which contains a range of scales from the size of the box down to the ion inertial length. The large scales leads to field-line meandering, which leads to a variation in the angle between the local magnetic field and the unit normal to the shock, whose surface is rippled, as discussed previously. In several places along the shock front, the local shock-normal angle is near perpendicular, as was observed for the interplanetary shock on DOY 118, 2001 by the *Advanced Composition Explorer* (ACE) (Lario et al., 2019), which had similar parameters to those simulated. The model also includes kinetic processes which lead to heating of the particles across the shock and the formation of a suprathermal tail which are ions accelerated directly from the thermal population. The energy spectra of protons from this particular simulation are shown in **Figure 4**.

Observations often show significant enhancements of low-energy ions at quasi-perpendicular IP shocks (e.g., Zank et al., 2006; Giacalone, 2012; Neergaard Parker et al., 2014) suggesting the injection energy does not depend strongly on the shock-normal angle. Low-energy ions were also enhanced by over an order of magnitude at the termination shock (Decker et al., 2005; Decker et al., 2008), which is a good example of a nearly perpendicular shock. The energy of these ions is far less than the theoretical injection threshold (**Eq. 13**) for the nearly perpendicular termination shock, which, is readily shown to be several MeV. Moreover, as we discuss below, there are examples of nearly perpendicular interplanetary shocks which also show a very significant enhancement of very low energy ions (Lario et al., 2019). It is a common misconception that nearly perpendicular shocks are unable to accelerate low-energy ions.

3.3 The Source Population

Neergaard Parker and Zank (2012) derived the solution of diffusive shock acceleration for the case of an arbitrary distribution of pre-existing particles, either from previous events or pre-existing in the solar wind, far upstream of the shock, and also included a separate source at the shock itself (c.f. **Eq. 6** in their paper). Assuming that the pre-existing population is the only source of particles, we can rewrite their solution for the distribution function downstream of the shock, as:

$$f_2(p) = \alpha p^{-\alpha} \int p^{\alpha-1} f_s(p) dp \tag{14}$$

where f is the distribution function and the subscript 2 refers to the post-shock region, and the S subscript refers to the pre-existing population of particles. p is the momentum, and $\alpha = 3U_1/(U_1 - U_2)$, where U_1 and U_2 are the upstream and downstream bulk plasma speeds as measured in the normal incidence frame (shock rest frame).

The pre-existing source distribution is often described in terms of a kappa distribution. As we have discussed previously, the lowest energy for which the Parker equation is valid, is much higher than $\frac{1}{2}mU_1^2$; thus, only the high-energy part of the kappa distribution is important. This is simply a power-law distribution. Thus, it is sufficient to assume a pre-existing source function of the form:

$$f_s(p) = \begin{cases} 0 & p < p_0 \\ f_0 \left(\frac{p}{p_0}\right)^{-\delta} & p \geq p_0 \end{cases} \tag{15}$$

where f_0 is a normalization constant, and p_0 can be regarded as the injection momentum. Later we will fit analytic solutions to observed distributions, and it turns out that p_0 is a free parameter. This is discussed further below.

The complete solution for the downstream distribution is obtained by inserting **Eq. 15** into **Eq. 14**, and is given by.

$$f_2(p) = \frac{\alpha}{\alpha - \delta} f_0 \left[\left(\frac{p}{p_0}\right)^{-\delta} - \left(\frac{p}{p_0}\right)^{-\alpha} \right] \tag{16}$$

It should be noted that at $p = p_0$, the downstream distribution is zero. This is because the source is upstream of the shock, and because of acceleration at the shock, there are no particles with a plasma-frame momentum p_0 downstream of the shock.

In the limit $\delta \to \infty$, the pre-existing source only has a value at p_0 and this expression reduces to $f_2(p) = C(p/p_0)^{-\alpha}$, valid for $p > p_0$, where C is a constant[3]. This is the usual result from diffusive shock acceleration. In particular, the spectral index depends only on the ratio of U_1 to U_2, which is the plasma density jump across the shock.

However, it is interesting to note that this solution implies that if the pre-existing source has a much harder spectrum than that from the acceleration at the shock (i.e., $\delta \ll \alpha$), the resulting distribution downstream of the shock retains the spectral index of the source spectrum, but that the intensity increases across the shock by the factor $\alpha/(\alpha - \delta)$. This might be the case when a very weak shock, with a density jump near unity, encounters a pre-existing population of particles with a rather flat energy spectrum. This suggests that weak shocks do not alter the spectral index of the energetic particle distributions compared to the pre-existing population, but rather, simply boost the intensity. Provided, of course, the pre-existing population has sufficiently hard energy spectrum.

[3]Note that if we take the density of the source population to be n_0, and assume the source distribution is isotropic, then we find $f_0 = n_0(\delta - 3)/(4\pi p_0^3)$, which leads to $C = n_0/(4\pi p_0^3)$.

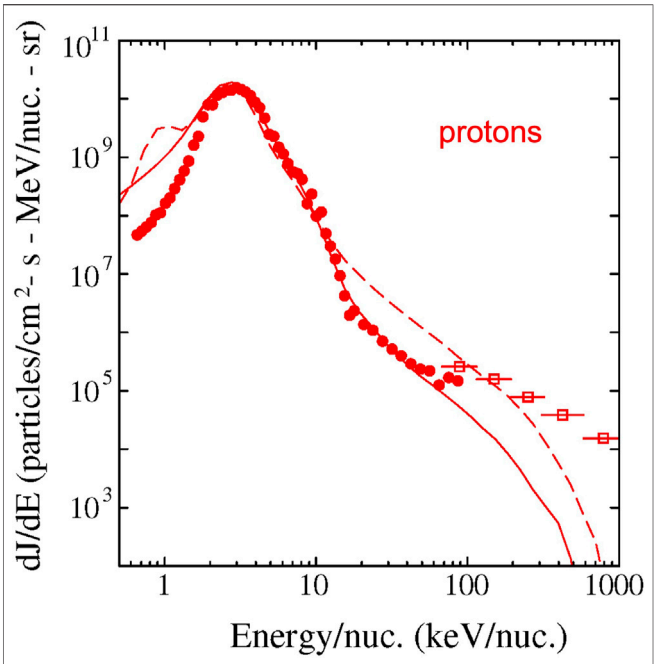

FIGURE 4 | Energy spectra at two regions downstream of the shock in the hybrid simulation shown in **Figure 2** (solid curve $1300 < x\omega_{pi}/c < 1500$ and $6300 < z\omega_{pi}/c < 7400$) and (dashed curve $1100 < x\omega_{pi}/c < 1300$ and $6300 < z\omega_{pi}/c < 7400$). Observed downstream spectrum on DOY 118, 2001 by Lario et al. (2019) is also plotted for comparison.

In contrast, however, if the pre-existing source has a spectrum which is steeper than that from acceleration at the shock, the shock primarily accelerates particles from the lower-energy portion of the pre-existing distribution, and the shock-accelerated spectrum is consistent with that predicted by diffusive shock acceleration theory. We also note from **Eq. 16** that the initial momentum, p_0, is an important parameter in determining the resulting intensity downstream of the shock.

It is instructive to consider the special case in which the pre-existing spectrum has a slope such that $\alpha = \delta$.

$$f_2(p) = \alpha f_0 \left(\frac{p}{p_0}\right)^{-\alpha} \ln\left(\frac{p}{p_0}\right) \tag{17}$$

Thus, the ratio of the shock-accelerated to pre-existing spectrum is $\ln(p/p_0)^{\alpha}$. At a given momentum (higher than p_0), the enhancement factor depends on the injection momentum, p_0. Thus, for this case, in which the pre-existing spectrum has a spectral exponent equal to α (the spectral index from simple DSA theory), the injection momentum plays a critical role in determining by what factor the intensity increases. Moreover, the resulting shock-accelerated spectrum is not even a simple power law. We now consider a specific application of this case.

Figure 3 is adapted from Lario et al. (2019). The data shown in this figure is from panels (b) and (f) of their Figure 10, and was provided to us by the authors. The data shows energy spectra upstream and downstream of an interplanetary shock which crossed the spacecraft ACE on DOY 118, 2001. Data from two instruments, SWICS and EPAM, are shown. The original figure, in Lario et al. (2019), also shows error bars, which are omitted here. The spectra cover a broad range of energy which includes the thermal-peak at low energies, through the suprathermal range, to high energies. Also plotted as a dashed line is the one-count level. as was also done in the original image.

From **Figure 3**, we note that the pre-existing distribution cannot have an intensity larger than the one-count level indicated by the dashed line; thus, at an energy of 250 keV, which is approximately the energy at which the dashed line ends in this figure, the intensity cannot be larger than $5000\,\mathrm{cm^{-2}s^{-1}sr^{-1}MeV^{-1}}$. The shock-accelerated particles, downstream of the shock, at this energy have an intensity of $10^5\,\mathrm{cm^{-2}s^{-1}sr^{-1}MeV^{-1}}$ (open circle at $E = 250$ kev). Thus, the ratio of the shock-accelerated to pre-existing intensity cannot be smaller than 20 ($= 10^5/5000$). Moreover, since the spectral index of the one-count curve in **Figure 3** is approximately the same as that of the shock-accelerated spectrum in the vicinity of 250 keV, **Eq. 17** above can be used to determine the value of the injection energy E_0. Note also that the ratio of the distribution functions upstream and downstream are the same as the ratio of the differential intensity, in this case, because we are taking the ratio at the same energy. Thus, setting $\ln(p/p_0)^{\alpha} = 20$, or, in terms of energy, $\ln(E/E_0)^{\alpha/2} = 20$, we obtain $E_0 = E\exp(-40/\alpha)$. α is the spectral index of the distribution function vs. momentum, which can be readily shown to be $2(\gamma + 1)$, where γ is the spectral exponent of the differential intensity vs. energy, as shown in **Figure 3**. By inspection of **Figure 3**, we find $\gamma \approx 1.1$, and $\alpha = 4.2$, so that $E_0 = (250\,\mathrm{keV})\exp(-40/4.2) \approx 0.02$ keV. This is well below the so-called ram energy of the shock (the kinetic energy of the plasma as it enters the shock), and is near that of the thermal energy of the solar wind.

From the above considerations, we conclude that is not possible to explain the shock-accelerated distribution in this event simply by the 'lifting up' of the pre-existing distribution. The intensity of the shock-accelerated particles indicates that the particles were accelerated from a much-lower energy source; and the most-abundant source is the solar wind. We conclude that for this event, the source of the accelerated particles is the solar wind.

It is also noteworthy that the reported shock parameters for this particular event (Table 1 of Lario et al., 2019) gives a shock-normal angle of $\theta_{Bn} = 88 \pm 2$. This is a very nearly perpendicular shock. Thus, this event shows a clear example of a nearly perpendicular shock which locally accelerates particles from very low energies, forming a high-energy rail. This is consistent with analytic theory and self-consistent plasma simulations which include pre-existing large-scale magnetic fluctuations with parameters consistent with those observed in the solar wind (**Figure 2**; Giacalone, 2003, Giacalone, 2005).

In **Figure 4** we plot the downstream energy spectra from the hybrid simulation mentioned above (c.f. **Figure 2**) at averaged over two different regions downstream of the shock, and compare it with the downstream spectrum seen by ACE. The regions were identified by finding regions for which the local shock normal angle (at the location of the shock for the particular value of z chosen) was very nearly perpendicular, as in the observations. Note that the simulation results, represented as either solid or

dashed curves are both taken downstream of the shock, yet show differences. This means that the spectrum depends on location along the shock in these simulations which suggests this may also be the case in real interplanetary shocks. It is noteworthy that in this simulation, the initial distribution is purely Maxwellian so that the high-energy particles were accelerated (by the shock) from an initially thermal distribution. Moreover, despite the variation along the shock, the intensity of the tail particles is either consistent with, or even larger than the observations, suggesting that the efficiency of accelerating the thermal solar wind in this case is enough to account for the observations.

Consideration of kinetic physics is required to understand the process by which very low-energy ions, including those from the thermal solar wind, are accelerated by a shock. It is well known that supercritical collisionless shocks require a dissipation mechanism other than that afforded by anomalous resistivity (e.g., Kennel et al., 1985). It was established 40 years ago that such shocks extract a small fraction of the thermal population incident upon a shock, creating a population of 'specularly reflected' ions which are reflected in the shock ramp and gyrate in the upstream magnetic field, and are ultimately advected downstream with the plasma flow. This process is well studied at Earth's bow shock (Gosling and Thomsen, 1985). The reflected particles have an energy that is about the plasma ram energy as measured in the plasma frame of reference. This is much larger than the thermal energy, thus, these particles represent a suprathermal population, albeit with the still rather low energy of the plasma ram energy. It is reasonable to expect that a fraction of these particles can undergo a further reflection at the shock, this time gaining even more energy; and some can be reflected more than once, gaining even more energy. Thus, these particles are the likely source of the high-energy tail in supercritical shocks, including those CME-driven interplanetary shocks that produce the largest SEP events observed, such as the one presented above.

4 ELECTRON ACCELERATION AT COLLISIONLESS SHOCKS MOVING THROUGH A TURBULENT MAGNETIC FIELD

Collisionless shocks are efficient accelerators for a variety of energetic charged particles observed in the heliosphere. However, the acceleration of electrons at collisionless shocks is generally considered to be more difficult than that of ions. This is primarily due to the fact that the gyroradii of non-relativistic electrons are much smaller compared with that of protons at the same energy (by a factor of $\sqrt{m_p/m_e} \sim 43$), therefore low-energy electrons cannot resonantly interact with the large-scale magnetic turbulence or ion-scale waves close to the shock front. In fact, statistical results have shown that electrons are less commonly accelerated at interplanetary shocks (Lario et al., 2003).

4.1 Observations of Electron Acceleration in the Vicinity of Interplanetary Shocks

At interplanetary shocks, electrons with energy up to ~ 100 keV have been observed close to quasi-perpendicular shocks with θ_{Bn} is larger than 45° (Dresing et al., 2016; Yang et al., 2018; Yang et al., 2019). Tsurutani and Lin (1985) reported the observations of energetic electrons associated with interplanetary shocks showing "spike-like" flux enhancements for energies >2 keV. The spike events were observed at quasi-perpendicular shocks with $\theta_{Bn} \geq 70°$. Some shock crossings had no enhancements of energetic electrons that were reported to be associated with low shock speeds and/or small θ_{Bn}. Simnett et al., 2005 presented data which show that energetic electrons are accelerated close to shock front. They also showed some accelerated electrons can escape far upstream of quasi-perpendicular interplanetary shocks. As we will show below, this can be explained by simulations that include large scale fluctuations (Guo and Giacalone, 2010). The clear evidence of electron acceleration at interplanetary shocks by DSA is rare, but an example discussed by Shimada et al. (1999) shows evidence of the importance of whistler waves (a high frequency wave that can resonantly interact with low-energy electrons) close to a quasi-perpendicular shock (see also Wilson et al., 2012). This seems to be different from acceleration at Earth's bow shock, where new observations have found whistler waves strongly contribute to the electron acceleration process (Oka et al., 2019; Amano et al., 2020), although more observations with high time cadences will definitely be needed to finally resolve this. The observation by Voyager 1 at the termination shock showed a spike-like enhancement of energetic electrons (Decker et al., 2005). Voyager 2 observed an exponential increase upstream of the termination shock and roughly constant downstream in the heliosheath, similar to what is predicted from DSA (Decker et al., 2008). Both of the Voyager spacecraft have observed that electrons are accelerated to at least MeV range, indicating that the termination shock can efficiently accelerate electrons.

4.2 One-Dimensional Scattering-Free Theory

In order to explain the energization of electrons within the shock layer, Wu (1984) and Leroy and Mangeney (1984) developed analytic models for electron acceleration from thermal energies by adiabatic reflection by a quasi-perpendicular shock (see also Ball and Melrose, 2001). This process is known as fast-Fermi acceleration, where electrons are reflected by the fast-moving shock along the upstream magnetic field in the de Hoffmann-Teller frame. This theory describes a scatter-free electron acceleration process in a planar, time-steady shock. It obtains a qualitative agreement with observations at Earth's bow shock in terms of the loss-cone pitch-angle distribution and energy range of accelerated electrons, but cannot explain observed power-low-like downstream energy distribution (Gosling et al., 1989; Krauss-Varban and Wu, 1989) used the combination of electron test-particle simulation and one-dimensional (1D) hybrid simulation and verified Wu's basic conclusions. The main energy source of

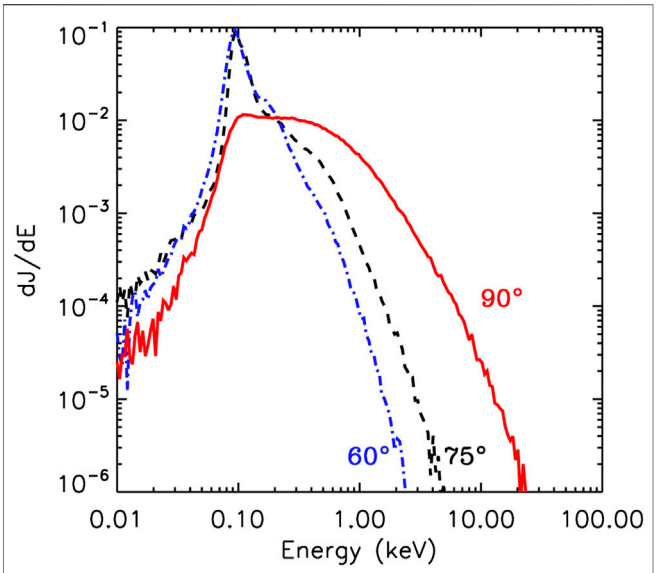

FIGURE 5 | Energy flux spectra of electrons for different averaged shock normal angles. Results of hybrid simulations with test-particle electrons adapted from Guo and Giacalone (2010). Reproduced by permission of the AAS.

fast-Fermi acceleration comes from the $-\mathbf{u} \times \mathbf{B}/c$ electric field which is the same as shock drift acceleration (SDA). It can also be demonstrated that fast-Fermi acceleration and SDA are the same process in two different frames of reference (Krauss-Varban and Wu, 1989). Thus, one would expect electrons to drift in the direction perpendicular to the flow and magnetic field. For a single reflection, the fraction and energies of accelerated particles are limited (Ball and Melrose, 2001). Holman and Pesses (1983) proposed the basic outline for type II solar radio bursts in which energetic electrons are accelerated through SDA. It is expected that multiple reflections are required in order to explain herringbone structures in type II bursts, where the electrons are accelerated to a fraction of the speed of light.

4.3 Effects of Large-Scale Magnetic Fluctuations and Shock Ripples

While the scattering provided by whistler waves (Shimada et al., 1999) is one possibility, Jokipii and Giacalone, 2007 proposed an attractive mechanism for accelerating electrons to high energy that does not require strong pitch-angle scattering, i.e., conserving the first adiabatic invariant. The idea is that the low-rigidity particles, especially electrons, can move rapidly along meandering magnetic field lines and thus travel back and forth between shock fronts. The particles gain energy from the difference between upstream and downstream flow velocities. Guo and Giacalone (2010, 2012a, 2012b) have used hybrid simulations combined with test-particle electrons to simulate effects of large-scale, preexisting magnetic fluctuations on electron acceleration at shocks. They found that efficient electron acceleration can happen after considering large-scale pre-existing upstream magnetic turbulence. The turbulent magnetic field leads to field-line meandering that allows the electrons to get accelerated at a shock front multiple times. The rippled surface of the shock front also contributes to the acceleration by mirroring electrons between the ripples. **Figure 5** shows electron energy spectra at different averaged shock angles suggesting perpendicular shocks can accelerate electrons more efficiently when upstream magnetic fluctuations exist.

Energetic particles are often seen upstream of the interplanetary shocks, known as foreshocks. We note that the spatial distribution of energetic electrons is determined not only by the ripples in the shock front, but also by the global topology of the magnetic field lines. An example is shown in **Figure 6**, which shows the spatial distribution of energetic electrons and profiles of the number of energetic electrons as a function of x, for the case of $(\theta_{Bn}) = 90^\circ$ in Guo and Giacalone (2010). The black solid line is the profile at $z = 200c/\omega_{pi}$, and the red dash line shows the profile at $z = 800c/\omega_{pi}$. The corresponding positions of the shock front at each of these values of z are represented using dot lines. At $z = 200c/\omega_{pi}$, it is observed that the energetic electrons travel far upstream. However, the profile at $z = 800c/\omega_{pi}$ shows no significant upstream energetic electron flux. The upstream energetic electron profiles show irregular features similar to *in situ* observations reported by Tsurutani and Lin (1985) and Simnett et al. (2005). The irregular features are controlled by the global topology of the large-scale turbulent magnetic field lines, along which the accelerated electrons could travel far upstream. Additionally, energetic electron profiles in the x-direction generally show "spike" structures close to the shock front, which is usually observed in interplanetary shocks and Earth's bow shock. Observation by Voyager 1 at the termination shock and in the heliosheath also shows the evidence of electron spike-like enhancements at the shock front (Decker et al., 2005). The upstream spatial distribution of energetic electrons shows irregular features which depend on both the irregularity in the shock surface and the global topology of magnetic field lines. At first the electrons are accelerated and reflected at the shock front, and then they travel upstream along the magnetic field lines. The electrons could be taken far upstream due to field-line meandering. This result can possibly lead to an interpretation to the complex electron foreshock events observed to be associated with interplanetary shocks (Bale et al., 1999; Pulupa and Bale, 2008).

The relation between upstream magnetic field turbulence and energetic electrons at shocks has been further studied by Guo and Giacalone (2015) through numerical integrating test-particle electron trajectories at a shock that propagates through a prespecified, kinematically defined turbulent magnetic field. **Figure 7** shows the efficiency of electron acceleration to above 10 keV (from the initial energy 1 keV). The acceleration is strongest at perpendicular shocks for all wave variance up to $\sigma = <\delta B^2/B_0^2> = 10$, but quasi-parallel shocks can accelerate electrons when upstream fluctuation amplitude is sufficiently large. This trend in general agrees with observations of electron acceleration in the vicinity of interplanetary shocks (Tsurutani and Lin, 1985; Yang et al., 2019). The acceleration at parallel shock when the wave amplitude is strong enough to explain recent observation at Saturn's bow shock (Masters et al., 2013).

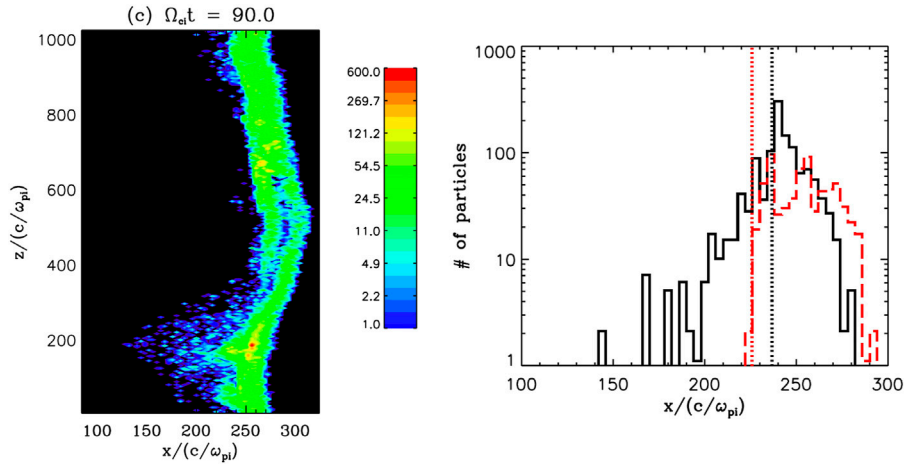

FIGURE 6 | Left: Number of energetic electrons with energies $E > 10E_0$ in the shock region, where the injected electron energy is $E_0 = 100eV$. **Right:** two profiles at $z = 200c/\omega_{pi}$ (black) and at $z = 800c/\omega_{pi}$ (red). Adapted from Guo and Giacalone (2010). Reproduced by permission of the AAS.

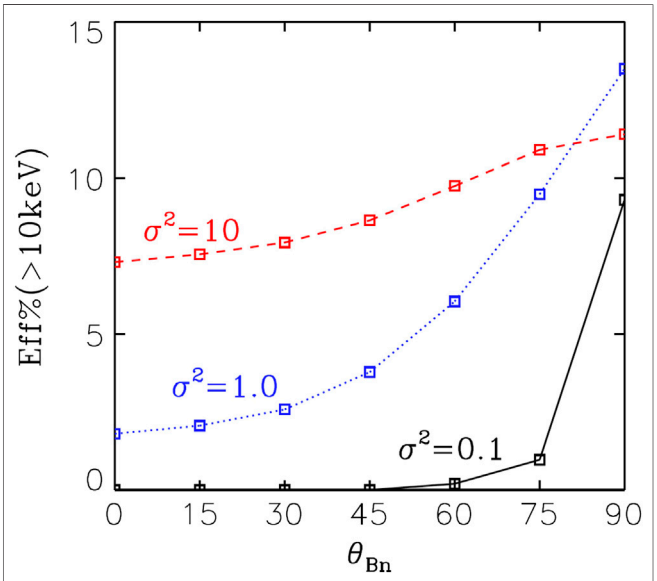

FIGURE 7 | Effiency of electron acceleration for various wave variances as a function of shock angle. The efficiency is defined by the fraction of electrons that is accelerated to more than 10 keV at the end of test-particle simulations (adapted from Guo and Giacalone (2015). Reproduced by permission of the AAS.

5 IMPLICATIONS TO VARIABILITY OF ENERGETIC PARTICLES

Large-scale magnetic field line meandering due to magnetic turbulence is ubiquitous in the heliosphere and other astrophysical environments (Jokipii, 1966; Jokipii and Parker, 1969; Parker, 1979). Including the effects of pre-existing magnetic turbulence is necessary for a complete theory of shock acceleration. Although the 1-D steady state DSA solution gives a very elegant description for the acceleration of charged particles at the shock front, nonplanar shock and fluctuating magnetic field effects could play significant role during the acceleration and transport. These may explain many of the observed varabilities of energetic particles at shocks. Lario et al. (2003) have shown that the energetic particle profiles in the vicinity of interplanetary shocks are often not consistent with the 1-D diffusive shock acceleration and many of the profiles are 'irregular'. A remarkable example is the *in situ* observation at the termination shock and in the heliosheath by Voyager 1 (Stone et al., 2005), which found that the intensity of anomalous cosmic rays (ACRs) was not saturated at the place where Voyager 1 crossed the termination shock and kept increasing after entering the heliosheath (although the low energy intensity does peak at the termination shock (Decker et al., 2005)), which strongly indicates that a simple planar shock model is inadequate to interpret the acceleration of ACRs. Numerical simulations and analytical studies suggest that possible solutions can be made by considering the temporary and/or spatial variation of magnetic field and the shock surface (Florinski and Zank, 2006; McComas and Schwadron, 2006; Guo et al., 2010; Senanayake and Florinski, 2013; Kóta, 2010). Neugebauer et al. (2006) have found that the details of energetic particle fluxes in the vicinity of interplanetary shocks are different between ACE and Wind spacecraft for the same IP shocks. The local shock parameters can significantly change, even change from quasi-parallel to quasi-perpendicular, or vice versa. The spatial scale of persistent energetic particle features is about 3×10^6 km, which is roughly the same as the correlation length of the interplanetary magnetic field (Neugebauer and Giacalone, 2005).

The acceleration of charged-particles in collisionless shocks has been shown to be strongly affected by magnetic-field turbulence at different scales (Giacalone, 2005; Giacalone and Neugebauer, 2008). The large-scale magnetic field variation will have important effects on the shock acceleration since the transport of charged particles is different in the direction parallel and perpendicular to the magnetic field, as shown in

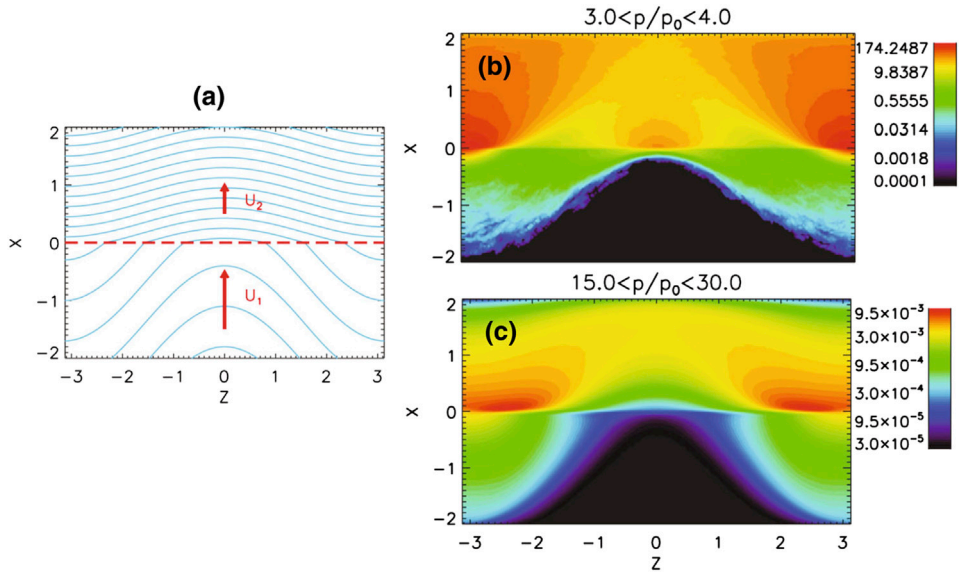

FIGURE 8 | (a) Shock and magnetic field geometry for an upstream average magnetic field perpendicular to the shock normal. The blue lines represent the magnetic field lines and the red dashed line indicates the shock wave. **(b)** Representation of density contour of accelerated particles, for the energy range $3.0 < p/p_0 < 4.0$, where p_0 is the initially injected momentum. **(c)** similar to **(b)** but for $15.0 < p/p_0 < 30.0$ (adapted from Guo et al., 2010). Reproduced by permission of the AAS.

early work (Jokipii, 1982; Jokipii, 1987). Blunt shocks or shocks with fluctuating fronts (Li and Zank, 2006) that have a similar geometry, are also relevant to this problem. Guo et al. (2010) analyzed the effect of the large-scale spatial variation of magnetic field on DSA by considering a simple system that captures the basic physical ideas (**Figure 8**). They solve numerically the Parker transport equation for a shock in the presence of large-scale sinusoidal magnetic-field variations. They demonstrated that the familiar planar-shock results can be significantly altered as a consequence of large-scale, meandering magnetic lines of force. Because the perpendicular diffusion coefficient $\kappa_\perp$ is generally much smaller than the parallel diffusion coefficient $\kappa_\parallel$, energetic charged particles are trapped and preferentially accelerated along the shock front in regions where the connection points of magnetic field lines intersecting the shock surface converge, and thus create "hot spots" of accelerated particles (see also Kong et al., 2017; Kong et al., 2019a). For regions where the connection points are separated from each other, the acceleration to high energies will be suppressed. Furthermore, the particles diffuse away from the "hot spot" regions and modify the spectra of downstream particle distribution. These results are potentially important for particle acceleration at shocks propagating in turbulent magnetized plasmas as well as those that contain large-scale nonplanar structures. For example, in many interplanetary shocks, the peak of the energetic particle intensity is in the downstream rather than at the shock transition (Lario et al., 2003).

6 DISCUSSION AND SUMMARY

In this review, we have discussed the effects of solar wind turbulence on the propagation of shock waves and on particle acceleration and transport in the vicinity of the shocks. The propagation of interplanetary shocks in the turbulent solar wind leads to rippling shock surfaces on various scales. These structures, along with the upstream and downstream magnetic fluctuations likely contribute to the observed energetic particles close to the interplanetary shocks. We emphasized the role of pre-existing upstream turbulence in enhancing the acceleration of low-energy particles at the shock wave, providing a promising means for solving the well known injection problem, especially at quasi-perpendicular shocks. Upstream turbulence is also important to understand the acceleration of electrons and observations at interplanetary shocks. As a remark, solar wind turbulence may be the key for interpreting the variability of energetic particles at interplanetary shocks. This, however, has not been understood in a quantitative way. Observations of interplanetary shocks provide a unique opportunity to systematically understand the system where shocks interact with large-scale turbulence and accelerate energetic particles. Understanding how these processes work is also important to many other space, solar and astrophysical systems (Giacalone, 2017a; Kong et al., 2019b).

AUTHOR CONTRIBUTIONS

All authors listed have made a substantial, direct, and intellectual contribution to the work and approved it for publication.

FUNDING

FG and JG acknowledge the support in part by NASA LWS program grant 80HQTR21T0005. FG is also supported by NSF

grant AST-1735414 and DOE grant DESC0018240. JG is also supported by the IS⊙IS instrument suite on NASA's Parker Solar Probe Mission, contract NNN06AA01C, and by the Interstellar Mapping and Acceleration Probe (IMAP) under NASA contract 80GSFC19C0027. LZ is supported in part by NASA under Grants 80NSSC19K0076, 80NSSC20K1849, and 80NSSC18K0644.

ACKNOWLEDGMENTS

FG thanks Drs. Senbei Du and Xiaocan Li for discussion on the acceleration of particles and Dr. Mitsuo Oka for discussion on the observations of electron acceleration at interplanetary shocks.

REFERENCES

Amano, T., Katou, T., Kitamura, N., Oka, M., Matsumoto, Y., Hoshino, M., et al. (2020). Observational evidence for stochastic shock drift acceleration of electrons at the Earth's bow shock. *Phys. Rev. Lett.* 124, 065101. doi:10.1103/PhysRevLett.124.065101

Axford, W. I., Leer, E., and Skadron, G. (1977). The acceleration of cosmic rays by shock waves. *Internatl. Cosmic Ray Conf.* 11, 132.

Bale, S. D., Reiner, M. J., Bougeret, J. L., Kaiser, M. L., Krucker, S., Larson, D. E., et al. (1999). The source region of an interplanetary type II radio burst. *Geophys. Res. Lett.* 26, 1573–1576. doi:10.1029/1999GL900293

Ball, L., and Melrose, D. B. (2001). Shock drift acceleration of electrons. *Publ.Astron. Soc. Aust.* 18, 361–373. doi:10.1071/AS01047

Bell, A. R. (1978). The acceleration of cosmic rays in shock fronts – I. *Monthly Notices R. Astronom. Soc.* 182, 147–156. doi:10.1093/mnras/182.2.147

Blandford, R. D., and Ostriker, J. P. (1978). Particle acceleration by astrophysical shocks. *Astrophys. J.* 221, L29–L32. doi:10.1086/182658

Borovsky, J. E. (2020). A statistical analysis of the fluctuations in the upstream and downstream plasmas of 109 strong-compression interplanetary shocks at 1 AU. *J. Geophys. Res. Space Phys.* 125, e27518. doi:10.1029/2019JA027518

Borovsky, J. E. (2010). Contribution of strong discontinuities to the power spectrum of the solar wind. *Phys. Rev. Lett.* 105, 111102. doi:10.1103/PhysRevLett.105.111102

Borovsky, J. E. (2008). Flux tube texture of the solar wind: strands of the magnetic carpet at 1 AU? *J. Geophys. Res.* 113, A08110. doi:10.1029/2007JA012684

Bryant, D. A., Cline, T. L., Desai, U. D., and McDonald, F. B. (1962). Explorer 12 observations of solar cosmic rays and energetic storm particles after the solar flare of September 28, 1961. *J. Geophys. Res.* 67, 4983–5000. doi:10.1029/JZ067i013p04983

Burgess, D. (2006). Simulations of electron acceleration at collisionless shocks: the effects of surface fluctuations. *Astrophys. J.* 653, 316–324. doi:10.1086/508805

Caprioli, D., and Spitkovsky, A. (2014). Simulations of ion acceleration at non-relativistic shocks. I. Acceleration efficiency. *Astrophys. J.* 783, 91. doi:10.1088/0004-637X/783/2/91

Chen, C. H. K., Mallet, A., Schekochihin, A. A., Horbury, T. S., Wicks, R. T., and Bale, S. D. (2012). Three-dimensional structure of solar wind turbulence. *Astrophys. J.* 758, 120. doi:10.1088/0004-637X/758/2/120

Coleman, J., and Paul, J. (1968). Turbulence, viscosity, and dissipation in the solar-wind plasma. *Astrophys. J.* 153, 371. doi:10.1086/149674

Decker, R. B., Krimigis, S. M., Roelof, E. C., Hill, M. E., Armstrong, T. P., Gloeckler, G., et al. (2008). Mediation of the solar wind termination shock by non-thermal ions. *Nature* 454, 67–70. doi:10.1038/nature07030

Decker, R. B., Krimigis, S. M., Roelof, E. C., Hill, M. E., Armstrong, T. P., Gloeckler, G., et al. (2005). Voyager 1 in the foreshock, termination shock, and heliosheath. *Science* 309, 2020–2024. doi:10.1126/science.1117569

Desai, M., and Giacalone, J. (2016). Large gradual solar energetic particle events. *Living Rev. Sol. Phys.* 13, 3. doi:10.1007/s41116-016-0002-5

Dresing, N., Theesen, S., Klassen, A., and Heber, B. (2016). Efficiency of particle acceleration at interplanetary shocks: statistical study of STEREO observations. *Astron. Astrophys.* 588, A17. doi:10.1051/0004-6361/201527853

Drury, L. O. C. (1983). Review article: an introduction to the theory of diffusive shock acceleration of energetic particles in tenuous plasmas. *Rep. Prog. Phys.* 46, 973–1027. doi:10.1088/0034-4885/46/8/002

Du, S., Guo, F., Zank, G. P., Li, X., and Stanier, A. (2018). Plasma energization in colliding magnetic flux ropes. *Astrophys. J.* 867, 16. doi:10.3847/1538-4357/aae30e

Earl, J. A., Jokipii, J. R., and Morfill, G. (1988). Cosmic-ray viscosity. *Astrophys. J.* 331, L91. doi:10.1086/185242

Florinski, V., and Zank, G. P. (2006). Particle acceleration at a dynamic termination shock. *Geophys. Res. Lett.* 33, L15110. doi:10.1029/2006GL026371

Fraschetti, F. (2013). Turbulent amplification of a magnetic field driven by the dynamo effect at rippled shocks. *Astrophys. J.* 770, 84. doi:10.1088/0004-637X/770/2/84

Giacalone, J., and Ellison, D. C. (2000). Three-dimensional numerical simulations of particle injection and acceleration at quasi-perpendicular shocks. *J. Geophys. Res.* 105, 12541–12556. doi:10.1029/1999JA000018

Giacalone, J. (2012). Energetic charged particles associated with strong interplanetary shocks. *Astrophys. J.* 761, 28. doi:10.1088/0004-637X/761/1/28

Giacalone, J., and Jokipii, J. R. (2007). Magnetic field amplification by shocks in turbulent fluids. *Astrophys. J.* 663, L41–L44. doi:10.1086/519994

Giacalone, J., and Jokipii, J. R. (1999). The transport of cosmic rays across a turbulent magnetic field. *Astrophys. J.* 520, 204–214. doi:10.1086/307452

Giacalone, J., and Neugebauer, M. (2008). The energy spectrum of energetic particles downstream of turbulent collisionless shocks. *Astrophys. J.* 673, 629–636. doi:10.1086/524008

Giacalone, J. (2005). Particle acceleration at shocks moving through an irregular magnetic field. *Astrophys. J.* 624, 765–772. doi:10.1086/429265

Giacalone, J. (2017a). The acceleration of charged particles at a spherical shock moving through an irregular magnetic field. *Astrophys. J.* 848, 123. doi:10.3847/1538-4357/aa8df1

Giacalone, J. (2017b). The acceleration of thermal ions at a strong, quasi-parallel interplanetary shock: a hybrid simulation. *J. Phys. Conf. Ser.* 900, 012008. doi:10.1088/1742-6596/900/1/012008

Giacalone, J. (2003). The physics of particle acceleration by collisionless shocks. *Planet. Space Sci.* 51, 659–664. doi:10.1016/S0032-0633(03)00101-6

Goldstein, M. L., Roberts, D. A., and Matthaeus, W. H. (1995). Magnetohydrodynamic turbulence in the solar wind. *Annu. Rev. Astron. Astrophys.* 33, 283–325. doi:10.1146/annurev.aa.33.090195.001435

Gosling, J. T., Asbridge, J. R., Bame, S. J., Feldman, W. C., Zwickl, R. D., Paschmann, G., et al. (1981). Interplanetary ions during an energetic storm particle event: the distribution function from solar wind thermal energies to 1.6 MeV. *J. Geophys. Res.* 86, 547–554. doi:10.1029/JA086iA02p00547

Gosling, J. T., Thomsen, M. F., Bame, S. J., and Russell, C. T. (1989). Suprathermal electrons at Earth's bow shock. *J. Geophys. Res.* 94, 10011–10025. doi:10.1029/JA094iA08p10011

Gosling, J. T., and Thomsen, M. F. (1985). Specularly reflected ions, shock foot thicknesses, and shock velocity determination in space. *J. Geophys. Res.* 90, 9893–9896. doi:10.1029/JA090iA10p09893

Guo, F., and Giacalone, J. (2015). The acceleration of electrons at collisionless shocks moving through a turbulent magnetic field. *Astrophys. J.* 802, 97. doi:10.1088/0004-637X/802/2/97

Guo, F., and Giacalone, J. (2012a). Particle acceleration at a flare termination shock: effect of large-scale magnetic turbulence. *Astrophys. J.* 753, 28. doi:10.1088/0004-637X/753/1/28

Guo, F., and Giacalone, J. (2012b). "The acceleration of electrons at perpendicular shocks and its implication for solar energetic particle events," in *American Institute of Physics Conference Series*. Editors Q. Hu, G. Li, G. P. Zank, X. Ao, O. Verkhoglyadova, and J. H. Adams (Palm Springs, CA: American Institute of Physics Conference Series), 1500, 93–99.

Guo, F., and Giacalone, J. (2010). The effect of large-scale magnetic turbulence on the acceleration of electrons by perpendicular collisionless shocks. *Astrophys. J.* 715, 406–411. doi:10.1088/0004-637X/715/1/406

Guo, F., Jokipii, J. R., and Kota, J. (2010). Particle acceleration by collisionless shocks containing large-scale magnetic-field variations. *Astrophys. J.* 725, 128–133. doi:10.1088/0004-637X/725/1/128

Guo, F., Li, S., Li, H., Giacalone, J., Jokipii, J. R., and Li, D. (2012). On the amplification of magnetic field by a supernova blast shock wave in a turbulent medium. *Astrophys. J.* 747, 98. doi:10.1088/0004-637X/747/2/98

Hao, Y., Lembege, B., Lu, Q., and Guo, F. (2016). Formation of downstream high-speed jets by a rippled nonstationary quasi-parallel shock: 2-D hybrid simulations. *J. Geophys. Res. Space Phys.* 121, 2080–2094. doi:10.1002/2015JA021419

Holman, G. D., and Pesses, M. E. (1983). Solar type II radio emission and the shock drift acceleration of electrons. *Astrophys. J.* 267, 837–843. doi:10.1086/160918

Inoue, T., Yamazaki, R., and Inutsuka, S. I. (2009). Turbulence and magnetic field amplification in supernova remnants: interactions between a strong shock wave and multiphase interstellar medium. *Astrophys. J.* 695, 825–833. doi:10.1088/0004-637X/695/2/825

Isenberg, P. A., and Jokipii, J. R. (1979). Gradient and curvature drifts in magnetic fields with arbitrary spatial variation. *Astrophys. J.* 234, 746–752. doi:10.1086/157551

Jokipii, J. R. (2012). "Acceleration of energetic charged particles: shocks, reconnection or turbulence?," in *Physics of the Heliosphere: A 10 Year Retrospective*. Editors J. Heerikhuisen, G. Li, N. Pogorelov, and G. Zank (Maui, HI: American Institute of Physics Conference Series), 144–156.

Jokipii, J. R. (1966). Cosmic-ray propagation. I. Charged particles in a random magnetic field. *Astrophys. J.* 146, 480. doi:10.1086/148912

Jokipii, J. R., and Giacalone, J. (2007). Adiabatic compression acceleration of fast charged particles. *Astrophys. J.* 660, 336–340. doi:10.1086/513064

Jokipii, J. R., and Parker, E. N. (1969). Stochastic aspects of magnetic lines of force with application to cosmic-ray propagation. *Astrophys. J.* 155, 777. doi:10.1086/149909

Jokipii, J. R. (1982). Particle drift, diffusion, and acceleration at shocks. *Astrophys. J.* 255, 716–720. doi:10.1086/159870

Jokipii, J. R. (1971). Propagation of cosmic rays in the solar wind. *Rev. Geophys.* 9, 27–87. doi:10.1029/RG009i001p00027

Jokipii, J. R. (1987). Rate of energy gain and maximum energy in diffusive shock acceleration. *Astrophys. J.* 313, 842. doi:10.1086/165022

Kajdič, P., Preisser, L., Blanco-Cano, X., Burgess, D., and Trotta, D. (2019). First observations of irregular surface of interplanetary shocks at ion scales by cluster. *Astrophys. J. Lett.* 874, L13. doi:10.3847/2041-8213/ab0e84

Kallenrode, M. B. (1996). A statistical survey of 5-MeV proton events at transient interplanetary shocks. *J. Geophys. Res.* 101, 24393–24410. doi:10.1029/96JA01897

Kennel, C. F., Coroniti, F. V., Scarf, F. L., Livesey, W. A., Russell, C. T., Smith, E. J., et al. (1986). A test of Lee's quasi-linear theory of ion acceleration by interplanetary traveling shocks. *J. Geophys. Res.* 91, 11917–11928. doi:10.1029/JA091iA11p11917

Kennel, C. F., Edmiston, J. P., and Hada, T. (1985). A quarter century of collisionless shock research. *Geophys. Mono. Series* 34, 1–36. doi:10.1029/GM034p0001

Knock, S. A., Cairns, I. H., and Robinson, P. A. (2003). Type II radio emission predictions: multiple shock ripples and dynamic spectra. *J. Geophys. Res.* 108, 1361. doi:10.1029/2003JA009960

Kong, X., Guo, F., Chen, Y., and Giacalone, J. (2019a). The acceleration of energetic particles at coronal shocks and emergence of a double power-law feature in particle energy spectra. *Astrophys. J.* 883, 49. doi:10.3847/1538-4357/ab3848

Kong, X., Guo, F., Giacalone, J., Li, H., and Chen, Y. (2017). The acceleration of high-energy protons at coronal shocks: the effect of large-scale streamer-like magnetic field structures. *Astrophys. J.* 851, 38. doi:10.3847/1538-4357/aa97d7

Kong, X., Guo, F., Shen, C., Chen, B., Chen, Y., Musset, S., et al. (2019b). The acceleration and confinement of energetic electrons by a termination shock in a magnetic trap: an explanation for nonthermal loop-top sources during solar flares. *Astrohys. J.* 887, L37. doi:10.3847/2041-8213/ab5f67

Kóta, J. (2010). Particle acceleration at near-perpendicular shocks: the role of field-line topology. *Astrophys. J.* 723, 393–397. doi:10.1088/0004-637X/723/1/393

Koval, A., and Szabo, A. (2010). Multispacecraft observations of interplanetary shock shapes on the scales of the Earth's magnetosphere. *J. Geophys. Res.* 115, A12105. doi:10.1029/2010JA015373

Krauss-Varban, D., and Wu, C. S. (1989). Fast Fermi and gradient drift acceleration of electrons at nearly perpendicular collisionless shocks. *J. Geophys. Res.* 94, 15367–15372. doi:10.1029/JA094iA11p15367

Krymskii, G. F. (1977). A regular mechanism for the acceleration of charged particles on the front of a shock wave. *Akademiia Nauk SSSR Doklady* 234, 1306–1308.

Lario, D., Berger, L., Decker, R. B., Wimmer-Schweingruber, R. F., Wilson, L. B., et al. (2019). Evolution of the suprathermal proton population at interplanetary shocks. *Astrophys. J.* 158, 12. doi:10.3847/1538-3881/ab1e49

Lario, D., Ho, G. C., Decker, R. B., Roelof, E. C., Desai, M. I., and Smith, C. W. (2003). "ACE observations of energetic particles associated with transient interplanetary shocks," in *Solar Wind Ten*, Pisa, Italy. Editors M. Velli, R. Bruno, F. Malara, and B. Bucci (American Institute of Physics Conference Series), 640–643.

Lee, M. A. (1983). Coupled hydromagnetic wave excitation and ion acceleration at interplanetary traveling shocks. *J. Geophys. Res.* 88, 6109–6120. doi:10.1029/JA088iA08p06109

Leroy, M. M., and Mangeney, A. (1984). A theory of energization of solar wind electrons by the Earth's bow shock. *Ann. Geophys.* 2, 449–456.

Li, G., and Zank, G. P. (2005). Mixed particle acceleration at CME-driven shocks and flares. *Geophys. Res. Lett.* 32, L02101. doi:10.1029/2004GL021250

Li, G., and Zank, G. P. (2006). "Particle acceleration at a rippling termination shock," in *Physics of the Inner Heliosheath*. Editors J. Heerikhuisen, V. Florinski, G. P. Zank, and N. V. Pogorelov (Oahu, HI: American Institute of Physics Conference Series), 858, 183–189.

Li, X., Guo, F., Li, H., and Birn, J. (2018). The roles of fluid compression and shear in electron energization during magnetic reconnection. *Astrophys. J.* 855, 80. doi:10.3847/1538-4357/aaacd5

Lowe, R. E., and Burgess, D. (2003). The properties and causes of rippling in quasi-perpendicular collisionless shock fronts. *Ann. Geophys.* 21, 671–679. doi:10.5194/angeo-21-671-2003

Lu, Q., Hu, Q., and Zank, G. P. (2009). The interaction of alfvén waves with perpendicular shocks. *Astrophys. J.* 706, 687–692. doi:10.1088/0004-637X/706/1/687

Masters, A., Stawarz, L., Fujimoto, M., Schwartz, S. J., Sergis, N., Thomsen, M. F., et al. (2013). Electron acceleration to relativistic energies at a strong quasi-parallel shock wave. *Nat. Phys.* 9, 164–167. doi:10.1038/nphys2541

Matthaeus, W. H., and Goldstein, M. L. (1982). Measurement of the rugged invariants of magnetohydrodynamic turbulence in the solar wind. *J. Geophys. Res.* 87, 6011–6028. doi:10.1029/JA087iA08p06011

McComas, D. J., Christian, E. R., Schwadron, N. A., Fox, N., Westlake, J., Allegrini, F., et al. (2018). Interstellar mapping and acceleration Probe (IMAP): a new NASA mission. *Space Sci. Rev.* 214, 116. doi:10.1007/s11214-018-0550-1

McComas, D. J., and Schwadron, N. A. (2006). An explanation of the Voyager paradox: particle acceleration at a blunt termination shock. *Geophys. Res. Lett.* 33, L04102. doi:10.1029/2005GL025437

Mewaldt, R. A., Mason, G. M., and Cohen, C. M. S. (2012). "The dependence of solar energetic particle fluences on suprathermal seed-particle densities," in *Space Weather: the Space Radiation Environment: 11th Annual International AstroPhysics Conference*, Palm Springs, CA. Editors Q. Hu, G. Li, G. P. Zank, X. Ao, O. Verkhoglyadova, and J. H. Adams (American Institute of Physics Conference Series), 128–133.

Neergaard Parker, L., Zank, G. P., and Hu, Q. (2014). Particle acceleration at quasi-perpendicular shock waves: theory and observations at 1 AU. *Astrophys. J.* 782, 52. doi:10.1088/0004-637X/782/1/52

Neergaard Parker, L., and Zank, G. P. (2012). Particle acceleration at quasi-parallel shock waves: theory and observations at 1 AU. *Astrophys. J.* 757, 97. doi:10.1088/0004-637X/757/1/97

Neugebauer, M., Giacalone, J., Chollet, E., and Lario, D. (2006). Variability of low-energy ion flux profiles on interplanetary shock fronts. *J. Geophys. Res.* 111, A12107. doi:10.1029/2006JA011832

Neugebauer, M., and Giacalone, J. (2005). Multispacecraft observations of interplanetary shocks: nonplanarity and energetic particles. *J. Geophys. Res.* 110, A12106. doi:10.1029/2005JA011380

Neugebauer, M., and Giacalone, J. (2010). "Progress in the study of interplanetary discontinuities," in *Twelfth International Solar Wind Conference*, Saint-Malo, France. Editors M. Maksimovic, K. Issautier, N. Meyer-Vernet, M. Moncuquet, and F. Pantellini (American Institute of Physics Conference Series), 194–197.

Neugebauer, M. (2013). Propagating shocks. *Space Sci. Rev.* 176, 125–132. doi:10.1007/s11214-010-9707-2

Oka, M., Otsuka, F., Matsukiyo, S., Wilson, L. B., Argall, M. R., et al. (2019). Electron scattering by low-frequency whistler waves at Earth's bow shock. *Astrophys. J.* 886, 53. doi:10.3847/1538-4357/ab4a81

Parker, E. N. (1979). "Cosmical magnetic fields," in *Their Origin and Their Activity* (Oxford: The International Series of Monographs on Physics, Clarendon Press).

Parker, E. N. (1965). The passage of energetic charged particles through interplanetary space. *Planet. Space Sci.* 13, 9–49. doi:10.1016/0032-0633(65)90131-5

Pulupa, M., and Bale, S. D. (2008). Structure on interplanetary shock fronts: type II radio burst source regions. *Astrophys. J.* 676, 1330–1337. doi:10.1086/526405

Reames, D. V. (1999). Particle acceleration at the Sun and in the heliosphere. *Space Sci. Rev.* 90, 413–491. doi:10.1023/A:1005105831781

Richardson, I. G., and Cane, H. V. (2010). Interplanetary circumstances of quasi-perpendicular interplanetary shocks in 1996–2005. *J. Geophys. Res.* 115, A07103. doi:10.1029/2009JA015039

Scholer, M., Ipavich, F. M., Gloeckler, G., and Hovestadt, D. (1983). Acceleration of low-energy protons and alpha particles at interplanetary shock waves. *J. Geophys. Res.* 88, 1977–1988. doi:10.1029/JA088iA03p01977

Senanayake, U. K., and Florinski, V. (2013). Is the acceleration of anomalous cosmic rays affected by the geometry of the termination shock? *Astrophys. J.* 778, 122. doi:10.1088/0004-637X/778/2/122

Sheeley, J., N. R., Howard, R. A., Michels, D. J., Koomen, M. J., Schwenn, R., Muehlhaeuser, K. H., et al. (1985). Coronal mass ejections and interplanetary shocks. *J. Geophys. Res.* 90, 163–176. doi:10.1029/JA090iA01p00163

Shimada, N., Terasawa, T., Hoshino, M., Naito, T., Matsui, H., Koi, T., et al. (1999). Diffusive shock acceleration of electrons at an interplanetary shock observed on 21 feb 1994. *Astrophys. Space Sci.* 264, 481–488. doi:10.1023/A:1002499513777 10.1007/978-94-011-4203-8_37

Simnett, G. M., Sakai, J. I., and Forsyth, R. J. (2005). Proton and electron acceleration by quasi-perpendicular fast magnetosonic shocks in interplanetary space. *Astrophys. Astron.* 440, 759–766. doi:10.1051/0004-6361:20040229

Stone, E. C., Cummings, A. C., McDonald, F. B., Heikkila, B. C., Lal, N., and Webber, W. R. (2005). Voyager 1 explores the termination shock region and the heliosheath beyond. *Science* 309, 2017–2020. doi:10.1126/science.1117684

Trotta, D., and Burgess, D. (2019). Electron acceleration at quasi-perpendicular shocks in sub- and supercritical regimes: 2D and 3D simulations. *Mon. Notices Royal Astron. Soc.* 482, 1154–1162. doi:10.1093/mnras/sty2756

Trotta, D., Valentini, F., Burgess, D., and Servidio, S. (2020). The interaction between shocks and plasma turbulence: phase space transport. arXiv e-prints arXiv:2011.10417.

Tsurutani, B. T., and Lin, R. P. (1985). Acceleration of >47 keV Ions and >2 keV electrons by interplanetary shocks at 1 AUkeV ions and keV electrons by interplanetary shocks at 1 AU. *J. Geophys. Res.* 90, 1–11. doi:10.1029/JA090iA01p00001

Tu, C. Y., and Marsch, E. (1995). Magnetohydrodynamic structures waves and turbulence in the solar wind – observations and theories. *Space Sci. Rev.* 73, 1–210. doi:10.1007/BF00748891

Wilson, L. B., Koval, A., Szabo, A., Breneman, A., and Cattell, C. A. (2012). Observations of electromagnetic whistler precursors at supercritical interplanetary shocks. *Geophys. Res. Lett.* 39, L08109. doi:10.1029/2012GL051581

Wu, C. S. (1984). A fast Fermi process: energetic electrons accelerated by a nearly perpendicular bow shock. *J. Geophys. Res.* 89, 8857–8862. doi:10.1029/JA089iA10p08857

Yang, L., Wang, L., Li, G., Wimmer-Schweingruber, R. F., He, J., Tu, C., et al. (2019). Electron acceleration by ICME-driven shocks at 1 au. *Astrophys. J.* 875, 104. doi:10.3847/1538-4357/ab1133

Yang, L., Wang, L., Li, G., Wimmer-Schweingruber, R. F., He, J., Tu, C., et al. (2018). The strongest acceleration of > 40 keV electrons by ICME-driven shocks at 1 au. *Astrophys. J.* 853, 89. doi:10.3847/1538-4357/aaa245

Yang, Z. W., Lembège, B., and Lu, Q. M. (2012). Impact of the rippling of a perpendicular shock front on ion dynamics. *J. Geophys. Res.* 117, A07222. doi:10.1029/2011JA017211

Zank, G. P., Li, G., Florinski, V., Hu, Q., Lario, D., and Smith, C. W. (2006). Particle acceleration at perpendicular shock waves: model and observations. *J. Geophys. Res.* 111, A06108. doi:10.1029/2005JA011524

Zank, G. P., Zhou, Y., Matthaeus, W. H., and Rice, W. K. M. (2003). "The interaction of turbulence with shock waves," in *Solar Wind Ten*, Pisa, Italy. Editors M. Velli, R. Bruno, F. Malara, and B. Bucci (American Institute of Physics Conference Series), 417–420.

Conflict of Interest: The authors declare that the research was conducted in the absence of any commercial or financial relationships that could be construed as a potential conflict of interest.

frontiers in Physics

REVIEW
published: 28 April 2021
doi: 10.3389/fphy.2020.626768

Turbulence Upstream and Downstream of Interplanetary Shocks

A. Pitňa[1]*, *J. Šafránková*[1], *Z. Němeček*[1], *T. Ďurovcová*[1] *and A. Kis*[2]

[1]*Department of Surface and Plasma Science, Faculty of Mathematics and Physics, Charles University, Prague, Czechia,* [2]*Institute of Earth Physics and Space Science, Eötvös Loránd Research Network, Sopron, Hungary*

The paper reviews the interaction of collisionless interplanetary (IP) shocks with the turbulent solar wind. The coexistence of shocks and turbulence plays an important role in understanding the acceleration of particles via Fermi acceleration mechanisms, the geoeffectiveness of highly disturbed sheaths following IP shocks and, among others, the nature of the fluctuations themselves. Although our knowledge of physics of upstream and downstream shock regions has been greatly improved in recent years, many aspects of the IP-shock/turbulence interaction are still poorly known, for example, the nature of turbulence, its characteristics on spatial and temporal scales, how it decays, its relation to shock passage and others. We discuss properties of fluctuations ahead (upstream) and behind (downstream) of IP shock fronts with the focus on observations. Some of the key characteristics of the upstream/downstream transition are 1) enhancement of the power in the inertial range fluctuations of the velocity, magnetic field and density is roughly one order of magnitude, 2) downstream fluctuations are always more compressible than the upstream fluctuations, and 3) energy in the inertial range fluctuations is kept constant for a significant time after the passage of the shock. In this paper, we emphasize that–for one point measurements–the downstream region should be viewed as an evolutionary record of the IP shock propagation through the plasma. Simultaneous measurements of the recently launched spacecraft probing inner parts of the Solar System will hopefully shed light on some of these questions.

Keywords: interplanetary shock, turbulence, solar wind, decay, sheath, upstream/downstream

OPEN ACCESS

Edited by:
Joseph Eric Borovsky,
Space Science Institute, United States

Reviewed by:
Gary Zank,
University of Alabama in Huntsville, United States
Ian Richardson,
University of Maryland, College Park, United States

***Correspondence:**
Pitňa A.
alexander.pitna@gmail.com

Specialty section:
This article was submitted to Space Physics, a section of the journal Frontiers in Physics

Received: *06 November 2020*
Accepted: *15 December 2020*
Published: *28 April 2021*

Citation:
Pitňa A, Šafránková J, Němeček Z, Ďurovcová T and Kis A (2021) Turbulence Upstream and Downstream of Interplanetary Shocks. Front. Phys. 8:626768. doi: 10.3389/fphy.2020.626768

1 INTRODUCTION

The physical processes connected with the formation and propagation of MHD shocks, the role of these shocks in acceleration of particles and their coupling to the Earth's magnetosphere has been studied for decades. Although many discoveries were made within these areas, the nature of upstream and downstream fluctuations in the framework of turbulence has been studied less intensively and basic questions have not been fully addressed yet. For example, what regime of turbulence, if any, would describe the observed level of upstream or downstream fluctuations, how intermittent are these fluctuations, etc. Considering that the energy of the downstream fluctuations can reach levels unmatched in a pristine solar wind, with a potential to couple with the Earth's magnetic field, this phenomenon is worthy of further investigations.

Shocks and their drivers have been so far studied in frame of space weather because they are often associated with significant disturbances of the geomagnetic field–geomagnetic storms. Two major types of drivers of geomagnetic storms were identified: 1) interplanetary coronal mass ejections

(ICMEs) that is preceded by a shock and sheaths and 2) corotating interaction regions (CIRs) where a fast stream from a coronal hole overtakes a leading slow stream [16, 17, 34, 111].

ICMEs are the solar wind counterparts of coronal mass ejections (CMEs) observed near the Sun and they play a role in the variation of the strength of the Interplanetary Magnetic Field (IMF) during the solar cycle [99]. They are of interest because, apart of the effects in the geomagnetic field (e.g., [38, 147]), they are responsible for energetic particle events through acceleration by shocks they drive (e.g., [23, 24]).

Magnetic clouds (MCs), a subset of ICMEs, are formed as twisted magnetic flux tubes that carry a large amount of magnetic helicity from the Sun to the interplanetary medium and they transport significant amount of magnetic flux, mass, and energy [22]. MCs are responsible for some major geomagnetic storms [16, 133] because they are often associated with shocks and large southward IMF [69].

The turbulent region bounded by the shock ramp on one side and the front surface of a particular ICME on the other side is called the ICME sheath. Magnetic field fluctuations in the sheaths can be transmitted from the upstream solar wind and/or generated within the sheath, due to physical processes at the shock and due to draping of the magnetic field around the driving ejecta (e.g., [47, 61, 121]). [122] have simulated and compared ICMEs and other heliophysical sheaths and have shown that the sheath of expanding ICMEs (the so-called the expansion sheath that forms around an object that expands but does not propagate relative to the solar wind) differs from the sheath formed by the propagation of steady-state ICMEs (the propagation sheath). Sheaths have been identified also as important drivers of geomagnetic storms (e.g., [38, 64, 128, 139, 147]). Southward excursions of the magnetic field due to fluctuating magnetic fields in the sheath can occasionally generate super-intense storms (e.g., [38, 147]), similarly as can southward fields in the ICME, especially if this is a magnetic cloud with a flux rope structure.

Geomagnetic storms associated with the other type of large-scale solar-wind structures, the quasi-steady CIRs (e.g., [8, 146]) are usually only weak to moderate in strength but they are more frequent than ICMEs, especially during solar minimum [57, 58]. If the relative speed gradients between interacting streams are sufficiently large, fast forward and reverse MHD shocks form and Alfvénic fluctuations in the rarefaction region at the CIR trailing edge may drive prolonged high-latitude activity [63].

In addition, the shock impact angle (i.e., the angle between the shock normal and the Sun–Earth line) affects the geomagnetic response. We note that CIRs are generally associated with larger impact angle, i.e., being more inclined than ICME-driven shocks [59, 67, 95].

The characteristics of fluctuations in the upstream/downstream plasma would be of value to understanding the geoeffectivness of the downstream fluctiations. For example, if one could predict the character of the downstream fluctuations, e.g., the IMF Bz component, from the upstream ones, then we can make a qualitative judgment about the influence of the incoming ICME on the space weather [47].

As discussed above, the connection between upstream and downstream interplanetary (IP) shock fluctuations and space weather effects is a subject of numerous review papers (e.g., [63, 64]). However, the nature of the IP shock induced changes of turbulence has been addressed by a few authors only. For this reason, the present paper concentrates on these fluctuations themselves with a focus on observable characteristics. First, we introduce collisionless shocks and discuss their main drivers within the heliosphere, ICMEs, and CIRs. Next, we focus on the nature of upstream fluctuations of quasi-parallel shocks and downstream fluctuations of both quasi-parallel and quasi-perpendicular shocks, addressing their turbulent nature and their spatial and temporal decay. Finally, we summarize the review and suggest directions for future investigations.

2 COLLISIONLESS SHOCKS

Collisionless shocks arise from the interaction of a large obstacle with a supersonic plasma flow, where "large" refers to a characteristic dimension of the obstacle being larger than characteristic ion kinetic scales and "supersonic" means that characteristic upstream wave speed V_w, is smaller than the relative speed of the obstacle and the flow V_{flow}, i.e., Mach number, $M = V_{flow}/V_w > 1$. The wave speed refers to the group velocity of either the Alfvén, fast or slow magnetosonic wave modes. The flow is deflected around the obstacle and at some distance, a region where the flow is decelerated to the Mach number below unity is termed the shock front. The thickness of the shock front is of the order of characteristic kinetic scales [93], therefore it can be viewed as a discontinuity.

Unlike the hydrodynamic shocks, where we can create, control, and display the formation of a shock in a controlled set-up, the collisionless shocks are difficult to study in laboratory conditions (see references in [6]). The solar wind introduces a unique environment where we can investigate both macrostructure and microstructure of these shocks in details. In last decades, a great progress has been made in the understanding of shock formation, its characteristic scales, dissipation rate, an important role of the reflected paricles and wave-particle interactions and other topics (e.g., [6, 21, 43, 93, 114, 126, 129]).

A standard set of Rankine-Hugoniot (R-H) jump conditions that couple the parameters of upstream and downstream plasma of any MHD discontinuity can be derived from the macroscopic MHD equations (for a full set of the R-H equation see, e.g., [94]. We introduce the two most transparent conditions,

$$\boldsymbol{n} \cdot [N\boldsymbol{V}] = 0 \tag{1}$$

and

$$\boldsymbol{n} \times [\boldsymbol{B}] = 0, \tag{2}$$

where n is the shock normal unit vector, N is the plasma density, $\boldsymbol{V}$ is the plasma speed and $\boldsymbol{B}$ is the magnetic field vector. Square brackets indicate that the quantities are conserved across the discontinuity. We focus on the solutions that exclude contact, tangential and rotational discontinuities, i.e., the solutions with the increase of the entropy, normal speed and plasma density across the boundary.

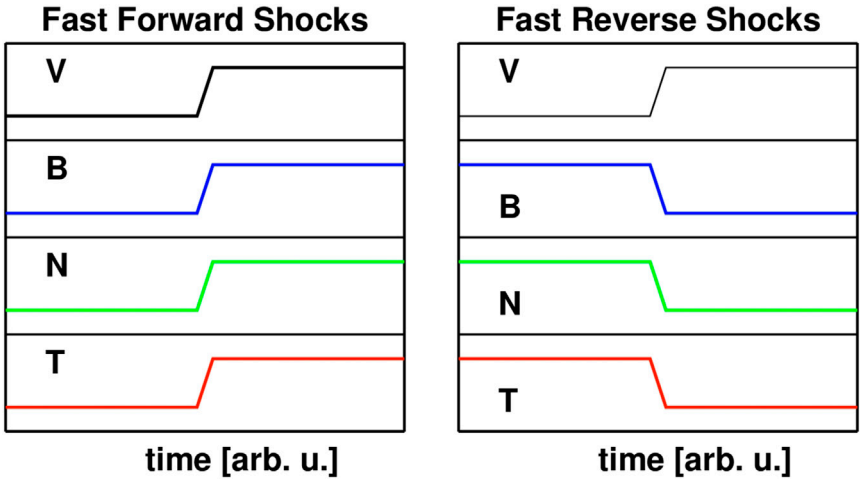

FIGURE 1 | Profiles of the solar wind velocity, *V*, magnetic field magnitude, *B*, density, *N*, and temperature, *T*, across Fast Forward and Fast Reverse shocks.

One of the most important shock characteristics is its criticality [81]. For a shock with Mach number above some critical value, $M > M_c$, the dissipation mechanism that supports the shock front (responsible for entropy production, heating and retardation of the flow) changes [6]. The reflection of some fraction of the incoming particles back upstream now serves as an additional dissipation mechanism.

The angle between the shock normal and upstream magnetic field, θ_{Bn}, plays an important role in the shock dynamics. An angle of $\theta_{Bn} = 45^o$ serves as a boundary between two types of shocks: the quasi-perpendicular, $\theta_{Bn} > 45^o$ and quasi-parallel, $\theta_{Bn} < 45^o$ shocks. For quasi-perpendicular supercritical shocks, the reflected particles cannot escape from the shock front into upstream and they perform one gyration orbit and return back to the shock. A collective effect of the reflected particles creates a so-called foot of the shock ramp (e.g., [71]). For quasi-parallel shocks, particles reflected from the shock escape along magnetic field lines, stream upstream and via multiple ion-beam instabilities they significantly affect the upstream (and thus downstream) plasma, therefore putting R-H relations into question. One point of view is that the whole region affected by the reflected particles is generally the shock transition itself, a highly structured region dominated by wave-particle interactions with continuously reforming shock ramp. On the other hand, there certainly should be a region upstream of the shock ramp that we could call "unaffected", however, defining the boundary between the "unaffected" plasma and the shock transition is difficult. Indeed, observations show that the reflected particles can travel huge distances into upstream [10]. The waves excited by a plethora of wave-particle instabilities [42] would deplete the free energy residing in the non-Maxwellian Velocity Distribution Function (VDF) and interfere with the waves already present in the upstream plasma. The behavior of these new-born waves depends on the parameters of both waves and background plasma. For example, if the wave has a sufficient amplitude, a Parametric Instability Decay (PID) may play a major role in its evolution [25, 125].

In the solar wind, we encounter two types of shocks, fast and slow IP shocks; the former being more frequent than the later. The fast shock forms when the upstream speed of the plasma (relative to an obstacle) exceeds the fast magnetosonic speed within the upstream. On the other hand, the slow shock forms when the upstream speed exceeds the slow magnetosonic speed, while the plasma should not support the growth of fast waves. Thus, formation of a slow shock requires special solar wind conditions [95] and therefore, there are only sparse measurements and reports on them (e.g., [134, 136]) and we will not discuss them.

A shock that propagates away from the Sun is called forward shock while the shock propagating towards the Sun in the plasma frame is called reverse. Thus the jumps of plasma parameters in the spacecraft frame of reference differ for forward/reverse, fast/slow shocks. **Figure 1** shows the qualitative changes of the density, pressure, magnetic field strength, and bulk solar wind speed across the shock in the s/c frame.

These basic characteristics are crucial in understanding upstream (prior to or shock generated) and downstream fluctuations in the framework of turbulence. As an example, one would make a natural conclusion that the upstream medium of supercritical fast forward quasi-perpendicular IP shocks cannot be affected by the reflected particles that are confined to the shock foot. Locally, this should hold true, however, two factors distort this picture: 1) the level of upstream turbulent fluctuations, $\delta B/B_0$ can reach a value of the order of 1 at scales that are relatively small ($l \approx 0.01$ AU) compared to the whole region in which the shock expands into. These fluctuations change a shock geometry and one can find the reflected particles far upstream of shock that was at a given time and location characterized as quasi-perpendicular. These suprathermal particles then can excite waves that become a part of the prior upstream turbulence. The upstream medium can be thus affected by the microphysical processes within the shock ramp and can influence the level of turbulent fluctuations. On the other hand, the downstream medium should be

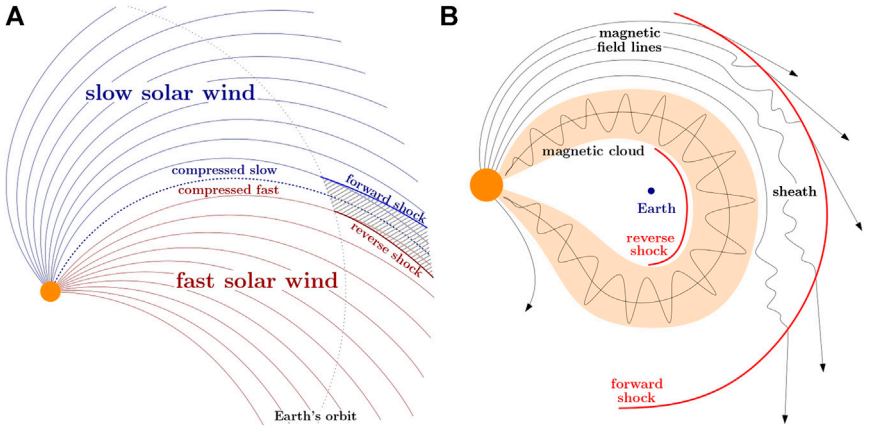

FIGURE 2 | (A) Schematics of the Co-rotating Interaction Region (CIR) which leads to a formation of CIR bounded by forward and reverse shocks; **(B)** A fast forward shock formation in front of an ICME and a possible reverse shock at the trailing edge of the magnetic cloud.

influenced by the shock even more, e.g., the levels of downstream fluctuations can be order of magnitude higher than in upstream [14, 66, 80].

3 ICME VS CIR

Apart from bow shocks arising from the interactions of the solar wind with, the magnetospheres of planets and comets, two sources of collisionless shocks in the heliosphere are ICMEs and CIRs, as noted. **Figure 2A** shows schematically a formation of forward and reverse IP shocks associated with a CIR. The interaction region develops when the solar wind from a coronal hole interacts with preceding slower solar wind. The shocks bounding this region are predominantly formed at distances beyond the Earth's orbit [112], however, already developed CIRs can also be found at 1 AU [36, 67]. Due to the average IMF orientation and the overall CIR topology, both of which follow a Parker spiral [100, 102], shocks that arise from the interaction of slow and fast winds in the region of stream interface are mainly quasi-perpendicular fast shocks.

Figure 2B presents a sketch of ICME with a leading fast forward magnetosonic shock, the sheath region, and the driver—a flux rope. Unlike the CIR shocks, the ICME-driven shock fronts form very close to the Sun and can be readily identified on coronographic images, e.g., of the SOHO mission [35, 96]. Again, taking into account the average direction of the Parker spiral, a parallel shock should be formed close to the Sun (e.g., [45]) and as the shock propagates further into the heliosphere, the normal of the shock front will be gradually more perpendicular to the IMF, thus eventually transforming into a quasi-perpendicular shock. This scenario can be applied for the CME head whereas shocks (if any) at the CME flanks can be quasi-perpendicular even near the Sun. However, a majority of observations come from ~ 1 AU where the angle between the average magnetic field orientation and velocity is approx. 45° that is also the transition from quasi-parallel to quasi perpendicular shock geometry but the IMF fluctuations can change the shock geometry significantly [132]. Moreover, if a pressure inside ICME is larger than that of the surrounding solar wind, the reverse shock can form at the trailing edge of such overexpanding ICME at larger distances from the Sun as Ulysses observations have shown [48].

It should be noted that the processes reported in upstream and downstream of the Earth's bow shock have also been observed at ICMEs and/or CIRs (e.g., presence of ULF waves in the upstream of fast magnetosonic IP shocks [60]). However, the spatial extent of shocks connected with ICMEs and CIRs is orders of magnitude larger than that of the Earth's bow shock, thus, new phenomena can emerge from the interaction of the pristine solar wind with these huge structures, such as accumulation of a plasma in front of a magnetic cloud that drives an ICME shock [63], the formation of Planar Magnetic Structures (PMSs) within ICME sheaths [91, 101] and many others.

One could expect that the changing of θ_{Bn} of ICME shocks as they move away from the Sun will have consequences on the nature of downstream turbulence within the sheath region. At 1 AU, the leading part of the sheath can be characterized as a downstream region of the quasi-perpendicular shock, whereas the sheath region close to the driving CME was affected by shock passage much earlier when the shock was quasi-parallel (see chapter 5). These two regions could exhibit different characteristics because they were shocked at different times and the trailing region had more time for its evolution.

Considering both ICME and CIR related reverse shocks (see **Figure 1**) schematically depicted in **Figures 2A,B**, there are virtually no studies that address the changes of fluctuations from upstream to downstream medium. This is because they are much less frequent and much weaker than the fast shocks at 1 AU. Nonetheless, they may provide a new insight into the evolution of downstream fluctuations (see chapter 5.2) because spacecraft inherently detect first a plasma that was shocked closer to the Sun (thus it had more time for its evolution) and only later a plasma that is being shocked more recently. In the case of a forward shock, the situation is opposite. The difference between two scenarios is most clearly seen in the reference frame of an IP

shock: for a forward shock, a spacecraft moves from upstream to downstream and for a reverse shock, from downstream to upstream. Therefore, a comparison of the evolution of the turbulent fluctuations along two paths through a shocked plasma would be interesting.

Finally, apart from the geoeffectievness of IP shock sheaths, it is of great importance to understand the nature and evolution of sheath fluctuations alone. What energy resides within these fluctuations? What compressibility they exhibit? These and many other questions arise.

We attempt to answer some of these questions in the following sections. The discussion above implies that sheaths of CIR driven shocks are much simple than those in front of CMEs for two reasons. First, CIR driven shocks are quasi-perpendicular on a global scale although we cannot rule out local deviations toward parallel geometry due to variations in the upstream region. Second, the CIR forward shocks propagate always into the slow solar wind whereas both slow and fast winds can be observed upstream the CME driven shocks. In order to cover the whole spectrum of possible scenarios, we discuss mainly CME driven shocks in the manuscript.

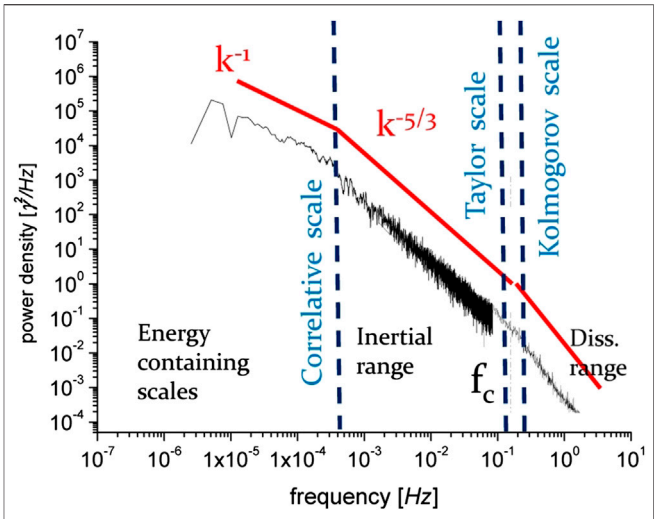

FIGURE 3 | Power spectrum of magnetic field fluctuations at 1 AU. The figure is adapted from [18]; copyright by Springer Nature, licensed under CC BY 4.0.

4 SOLAR WIND TURBULENCE

In this section, we briefly summarize the turbulent nature of the solar wind fluctuations. We note that this topic is still heavily debated and it is not yet fully understood. However, the main properties of the turbulent fluctuations have been established from decades of solar wind observations, i.e., the character of slow and fast solar wind plasma and magnetic field variations and their evolution with the heliocentric distance (e.g., [18]).

According to the present understanding, the solar wind fluctuations can be viewed as a system of nonlinearly interacting Alfvén-like wave packets traveling in opposite directions [56, 70]. The nonlinear interaction between counter streaming Alfvén waves of similar wavelengths is responsible for the generation of Alfvén waves with smaller wavelengths, i.e., the energy within the Alfvénic fluctuations is transferred to smaller scales and the fluctuations become gradually more anisotropic [120]. Furthermore, observations of [9, 39, 85] supported by theoretical works of [143, 144] suggest that solar wind fluctuations are dominated by quasi-2D turbulent fluctuations with a minority "slab" component, meaning that there are two populations of fluctuations, the first have their wave vectors parallel to the background magnetic field, B_0, while the second have the wave vectors perpendicular to B_0. The ratio of energies residing within the quasi-2D and slab fluctuations is roughly 4 : 1 (e.g., [9]. **Figure 3** shows the composite power spectral density of magnetic field fluctuations measured by the Helios 2 and Wind spacecraft [18]. This triple power law is systematically observed in the solar wind and it is frequently interpreted as follows: 1) on large scales, where the power spectrum is a power law with the exponent −1 [19], fluctuations are not yet turbulent and they become part of the turbulent cascade later on, 2) in the inertial range, the energy injected from large scales cascades into smaller scales, exhibiting a power law with the exponent ranging from −1.5 to −2 [28]. Finally, the cascaded energy reaches the characteristic ion scales below which a power spectrum steepens into the power law with even greater variability of the exponent from ≈ −2 to −4 [74, 115]. It is believed that within this so-called kinetic/dissipation range, the cascaded energy is dissipated into random particle motion.

Focusing on the large scale fluctuations in the solar wind, many authors investigated their characteristics to explain their origin. Their findings are consistent with the picture that the fluctuations within the so-called "1/*f*" range are not a simple mixture of non-interacting waves, but more likely these waves may undergo a nonlinear evolution, for example, parametric decay (e.g., [33, 83] and/or nonlinear cascade (e.g., [25, 131]). [84] found that the break between the injection and inertial ranges corresponds to condition $\delta B/B_0 \sim 1$, implying that some process limits the compressibility of the fluctuations at largest scales. Recently, due to Parker Solar Probe (PSP) and Solar orbiter launches, much progress has already been made or is expected. [27] investigated the radial dependence of the power spectra of magnetic fluctuations with the heliocentric distance employing PSP measurements and noted consistency with aforementioned results. Furthermore, the evolution of fluctuations within 1 AU in the framework of Nearly Incompressible (NI) turbulence transport equations [140] was studied by [2]. Using PSP measurements, they estimated the evolution of the kinetic energy, correlation length, density variance and temperature between ∼ 35 R_s and 130 R_s and have found a good correspondence with the NI turbulent transport model that assumed an 80:20 ratio between quasi-2D and slab turbulent populations.

Within the inertial range, which is usually inferred from the estimated power spectrum of the magnetic field fluctuations, the energy flux through the scales $\varepsilon(l)$ is constant, i.e., the free energy that is cascading from the large scales with the rate ε_{inj} is equal to the dissipation rate ε_k. The physical reason for the existence of the inertial range is that the energy supplied at the correlative scale (see

Figure 3) cannot be effectively dissipated. It is transferred into smaller scales, eventually reaching the scales where, in the case of MHD turbulence, dissipative processes act and the cascaded energy is transformed into random particle motion. It follows that the nature of the inertial range cascade should not be sensitive to the dissipative processes, at least in the first approximation. The typical characteristic of the inertial range fluctuations is their anisotropy [52] in a multiple sense: (a) the power within the fluctuations perpendicular to the mean magnetic field is larger than the power within the parallel ones [8], (b) the fluctuations wave vectors are not populated isotropically within the inertial range [85] and (c) power spectrum of fluctuations exhibit different scaling $P(k) \propto k^{-\alpha}$ for different sampling directions [51]. The scaling laws of power spectral densities of the physical fields (N, B, V, T) and the relevant anisotropies inferred from spacecraft observations (e.g., [13, 28, 115, 130]), or state-of-the-art computer simulations (see, [40]; and references therein) serve as key factors in understanding the dynamics of the inertial range. Specifically, they can answer the question which turbulent framework [98, 144, 149] is consistent with observations.

It is believed that the dissipative processes that are responsible for the heating of the solar wind act at the sub-ion range. Therefore, physics of this range has been studied observationally (e.g., [4, 30, 106, 109, 116]), theoretically [11, 53, 119] and by computer simulations [40, 49, 54]. Both observations and simulations show that the transition from inertial to dissipation range corresponds to the spatial scale of the proton thermal gyroradius ρ_{gp} or to the inertial length of the proton ρ_{ip} [31, 41]. The character of the fluctuations at the transition and below these characteristic ion scales is still an unresolved issue. A natural candidate for the plasma mode that the fluctuation may exhibit is the kinetic Alfvén wave (KAW) because it is a continuation of a shear Alfvén wave mode for highly perpendicular wave vectors, $k_\perp \gg k_\parallel$, for which a condition $k_\perp \rho_{gp} \gtrsim 1$ is satisfied. Since the KAW mode is low frequency [11] wave, i.e., $\omega \gg k_\perp v_{th,i}$, $v_{th,i}$ being the ion thermal speed, it exhibits non-negligible density fluctuations around the scale of ρ_{gp}, which are manifested as a plateau around the transition from inertial to dissipation range [26, 30, 115]. Recently, a number of authors [73, 106, 113, 137] shows that the character of fluctuations below the scale of the proton thermal gyroradius, i.e., $k\rho_{gp} \gtrsim 1$, is consistent with KAW-like fluctuations and recently developed KAW turbulent phenomenology [11, 148]. However, the nature of the kinetic range is still heavily debated and alternative/complementary hypotheses are investigated [15].

Due to large spatial dimensions, the spectrum of fluctuations as depicted in **Figure 3** can be significantly affected by the IP shocks. In principle, all three power-law segments can change their slope and amplitude or a power law may not even be formed and the power spectral density profile could be fitted by an exponential function [104].

5 IP SHOCKS AND TURBULENCE

An excellent opportunity to illustrate the complexity of the interaction of turbulence and IP shocks and its dependence on surrounding environment is presented by an example of three consecutive IP shocks observed at 1 AU on June 21 and 22, 2015 [46, 78]. We follow [78] and mark the IP shocks as shown in **Figure 4**: the first shock (S1) was detected at the Wind spacecraft at 16:05 UT on June 21, 2015, the second shock (S2) at 05:02 UT on June 22, 2015 and the third shock (S3) at 18:08 UT on June 22, 2015. Parameters of the shocks are listed in **Table 1**. One of the most important factors that distinguish these three shocks are the upstream conditions. Upstream of S1, the solar wind plasma has extremely high proton beta, $\beta_p \approx 30$ and a very low level of magnetic field fluctuations. Upstream of S2 seems to be the driver of S1, i.e., the magnetic cloud. Finally, upstream of S3 looks like the sheath of S2.

Figure 5 shows the power spectra of upstream and downstream fluctuations of the magnetic field components, the magnetic field strength and the magnetic field strength normalized by the average background magnetic field B_0 for all three shocks at the time scale of 1 h. The intervals used for computations are shown by color bars in the top panel of **Figure 4**. Note that the difference in the fluctuation power between the downstream of S3 (solid blue) and upstream of S1 (dashed red) is roughly four orders of magnitude. Focusing on the changes of levels of fluctuations from upstream to downstream, one can see that S1 and S3 are similar, i.e., the enhancement in δB, $\delta|B|$, and $\delta|B|/B_0$ is roughly the same, while the enhancement of these quantities is much less for S2. Considering an overall level of fluctuations, downstream of S3 is unique because: 1) the IP shock propagates into already disturbed medium of the S2 sheath and 2) the compression ratio of this shock reaches the theoretical limit of 4 for adiabatic index $\gamma = 5/3$ [6].

5.1 Upstream Fluctuations

As it has been pointed out in **Section 2**, the upstream regions of supercritical IP shocks can be substantially disturbed by the microphysical processes that take place at the shock front. These processes influence both upstream and downstream regions. In this section, we discuss upstream fluctuations and how they are coupled with processes such as shock reformation.

Particles reflected from the quasi-parallel shock escape in the upstream region and move away from the shock along the magnetic field lines. These ions interact with the incoming solar wind through a number of wave generation mechanisms and plasma instabilities, which basically develop into an extended foreshock. The complex and highly coupled interaction between waves and particles in the foreshock, where waves are generated by energetic particles and, on the other hand, the energetic particles are scattered by these waves, also defines the energetic coupling between waves and particles. The coupling was described in a self-consistent model by [75, 76, 110]. The main approach of this model is a linear relationship between the energetic particle energy density and the wave energy density. The wave energy density is a partial energy density, calculated in the frequency range that is in resonant condition with the energetic particles. In other words, the energy density of the waves and fluctuations is determined by the energetic and/or accelerated particles. [89] analyzed two upstream ion events and found a good agreement between the measured and predicted

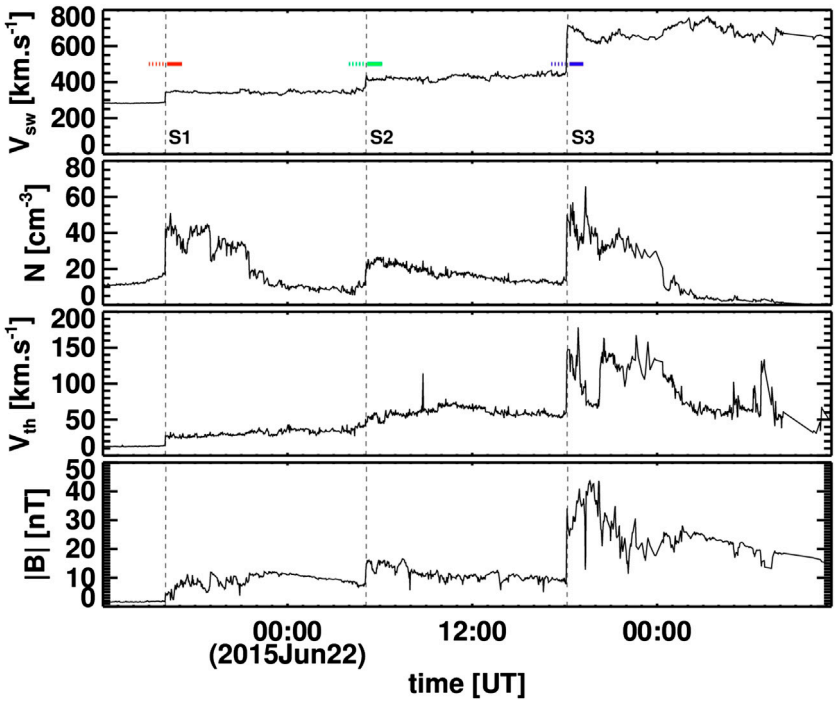

FIGURE 4 | Bulk parameters of the solar wind during 2 days when Wind encountered three quasi-perpendicular fast forward IP shocks. From top to bottom: Profiles of the solar wind velocity, V_{sw}, density, N, thermal speed, V_{th}, and magnetic field magnitude, B. Dashed vertical lines show IP shock fronts. Colored horizontal lines mark the intervals for estimations of the power spectra of magnetic field fluctuations in **Figure 5**. Dashed/solid lines cover 1 h upstream/downstream of each shock (excluding 5 min adjacent to the shock front).

TABLE 1 | Parameters of the shocks S1, S2, and S3 at 1 AU as measured by Wind; parameters are taken from the database of http://ipshocks.fi. B_d/B_u, N_d/N_u, and T_d/T_u are the ratios of downstream/upstream magnetic field magnitude, proton number density, and proton temperature, respectively. V_{sh} is the shock speed in the spacecraft frame of reference, M_{ms} is the fast magnetosonic Mach number and K is the time conversion constant estimated from the shock parameters by **Eq. 4**.

	B_d/B_u	N_d/N_u	T_d/T_u	β_u	θ_{Bn}	V_{sh} [km · s^{-1}]	M_{ms}	K
S1	2.41	2.62	3.82	29.2	84	309	2.3	7.6
S2	1.99	2.2	2.4	1.5	82	424	1.7	6.9
S3	3.34	3.63	6.7	2.2	62	767	4.1	7.9

wave energy density. In a statistical study by [127]; about 300 events were studied and they found a very good correlation value of 0.89 between the observed and predicted wave energy density. This study also demonstrates that the correlation does not depend on the velocity jump across the event. It has been shown by [62] that also in the case of interplanetary shocks, the predicted wave power (spectral) density agrees well with the observed wave intensity values. Lately, [68, 97] demonstrated that in the case when a strong Field Aligned Beam (FAB) is formed at the Earth's bow shock, the waves generated by the beam can influence the wave field in the foreshock region resulting in a significantly higher wave intensity than usual.

In the context of upstream turbulence generated by the suprathermal particles, [7] reported that the upstream magnetic field spectra exhibit a power law scaling of −3/2. They argued that the estimated power spectra show the competition of wave growth [76] and turbulent wave diffusion of the Iroshnikov-Kraichnan weak turbulence theory. Their finding is consistent with the current models of imbalanced turbulence [77, 103, 107] that predict the spectral index of −3/2. In the upstream region, cross helicity σ_c may be significantly increased because the energetic ions amplify the anti-sunward propagating Alfvén waves. Moreover, [27, 28], have shown that the IMF in the solar wind exhibits −3/2 scaling for intervals with high cross helicity.

On the other hand, [92] have shown that in the Earth's foreshock, power spectra in the wave number domain extracted from four-point Cluster measurements exhibit Kolmogorov scaling of −5/3, i.e., $P(k) \propto k^{-5/3}$. They argued that the classical concept of an inertial range can be applicable, i.e., the first waves are excited at low wave numbers, and then they resonantly interact with other waves, creating daughter waves that interact again, etc.

A few studies reported observations of ULF waves (spacecraft frame frequencies 10^{-2}–10^{-1} Hz) upstream both quasi-parallel and quasi-perpendicular IP shocks. [10] reported that unlike the ULF waves in the Earth's foreshock, where these waves can be highly compressive and may steepen into shocklets or Short Large Amplitude Magnetic Structures (SLAMS) (e.g., [135]), ULF waves

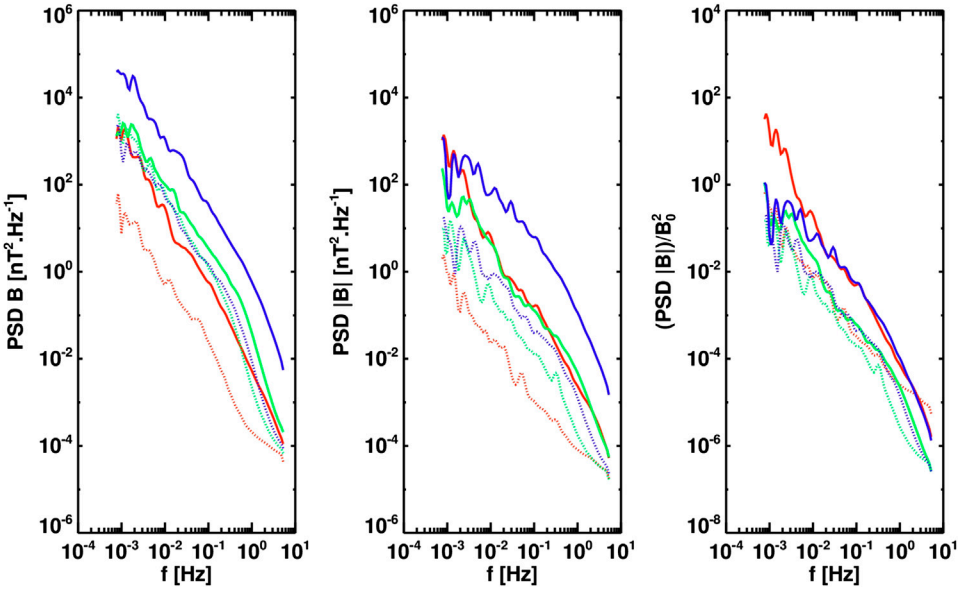

FIGURE 5 | Left: Trace power spectral densities of magnetic field fluctuations for upstream (dashed) and downstream (solid) intervals of S1 (red), S2 (green), and S3 (blue); **middle:** power spectrum of magnetic field magnitude fluctuations, and **right:** the same power spectrum but normalized to the average $|B|$ in the particular interval.

upstream of IP shocks are only weakly compressional. The Alfvénic nature of ULF waves may be explained by a small average Mach number of the shocks they investigated. Since their dataset contained both CIR and ICME shocks, they estimated the extent of the foreshocks for both types. They found that quasi-parallel CIR shocks exhibit foreshocks with a small spatial extent $\Delta r \approx 0.05$ AU, while for ICME shocks $\Delta r \approx 0.1$ AU. They attributed this difference to the shock age; CIR shocks form at larger distances from the Sun (compared to ICME shocks), thus they have less time for acceleration of particles that are the ultimate source of the extended foreshock.

A simulation study of [72] focused on the Mach number dependence of upstream and downstream properties of quasi-parallel shocks. Other simulation studies (e.g., [20]; and references therein), have shown that the reformation of the shock front and its cyclic nature could play a pivotal role in understanding the downstream fluctuations. Due to the shock front reformation that is characteristic of high Mach number shocks, the upstream large amplitude fluctuations are directly convected into the downstream region. In other words, the energy of the reflected and accelerated particles is converted into the downstream wave energy. Even for low Mach number shocks, ULF waves impact the shock front, change the local θ_{Bn} and lead to larger than expected amplification of the wave amplitude.

Focusing on quasi-perpendicular shocks, it is difficult to imagine how multiple crossings of the shock front (essential for particle acceleration) could be achieved because the reflected particles return to the shock in one gyroperiod. However, large amplitude turbulence that the particle would follow may enhance the cross-field diffusion [44]. [142] have shown that power-law spectra of energetic particles upstream of highly quasi-perpendicular IP shocks can be successfully explained in the framework of diffusive shock acceleration.

5.2 Downstream Fluctuations

A key relation that connects the time of observation of the downstream plasma in the spacecraft frame, t_{sp}, with the age of this shocked plasma relative to the shock passage, t_{sh} was derived by [105] and it reads,

$$t_{sh} = t_{sp} K, \tag{3}$$

where K is a time conversion constant that characterizes a particular shock and it is defined as

$$K = \frac{v_{sh}}{v_{sh} - \boldsymbol{v}_d \cdot \boldsymbol{n}}, \tag{4}$$

v_{sh} is the shock speed, v_d is the downstream solar wind speed and n is the shock normal. Calculation of K for S1 yields $K = 7.6$. This value is not universal, it changes with the shock and wind parameters. [105] reported an average value of $K = 6$ for a set of 174 IP shocks, while [14] proposed to use a value of $K = 5.5$. A rough estimation of maximum t_{sh} for $S1$ yields[1] $t_{sh} = 5.5\,\text{h} \cdot 7.6 = 42\,\text{h}$, that is shorter than the propagation time of the ICME from the solar surface up to L1, $t_{prop} \cong 70\,\text{h}$ [46]. Consequently, the downstream region of the IP shock captures the evolution of the shocked plasma from a close proximity of the Sun to L1. It suggests that estimations of the power spectrum of the whole ICME sheath (e.g., S1 sheath in **Figure 4**) is

[1]A rough estimation of the sheath crossing time ($t_{sp} = 5.5$ h) was inferred from the density and magnetic field profiles in **Figure 4**.

problematic due to its inherent "non-stationarity" in the following sense: the leading edge of a sheath is a plasma that has been just shocked, while the trailing edge of the sheath is a plasma that has been shocked closer to the Sun, tens of hours ago. Thus, the determined energy levels of the power spectrum at largest scales seem to lack a proper physical meaning. This leads to the following question: what is the largest scale at which the spectrum can be estimated? Later on, we will introduce a phenomenological argument that addresses this question.

As already mentioned above, two aspects affect the character of sheath fluctuations, 1) the gradual change of the average magnetic field that should roughly follow the Parker spiral and 2) changes of the magnetic field direction due to its inherent fluctuations. The later effect was addressed by [14] who showed that it might enhance the levels of compressibility of downstream fluctuations.

The character of upstream and downstream fluctuations differs for the quasi-parallel and quasi-perpendicular geometry. Ignoring any complicating factors, the simple condition on conservation of the normal component (**Eq. 2**) leads to a conclusion that upstream and downstream magnetic field vectors are the same for $\theta_{Bn} = 0^o$, implying that small deviations in the upstream magnetic field magnitude are not enhanced by the shock, whereas the perpendicular fluctuations can be. On the other hand, for $\theta_{Bn} = 90^o$, a shock can enhance both Alfvén-like (non-compressive) and compressive fluctuations. This leads to a conclusion that the relative change of the compressibility, $(\delta B_\parallel/\delta B_\perp)^2$ is different for these two shock geometries. A more realistic scenario of oblique shocks was treated by [88]. They analytically calculated the transmission coefficients of incident Alfvén wave striking the bow shock on the basis of hydromagnetic shocks. They deduced that an incident Alfvén wave excites two downstream Alfvén waves. This process was consistent with the findings of [79] who used two-dimensional hybrid simulation of the interaction of Alfvén waves with the quasi-perpendicular shock. Both studies report that the fluctuation level of downstream waves is roughly order of magnitude larger than the level of the upstream fluctuations. They found that a shape of the shock front is affected by upstream turbulence, e.g., it exhibits an irregular shape when the upstream is populated by a mix of Alfvén waves. This confirms the finding of [5]; who investigated the interaction of turbulence and IP shock by perturbation analysis of 2D inviscid Burgers' equation. They found that a shape of the quasi-perpendicular shock front is significantly affected by upstream waves which results in complex downstream state and, moreover, they predict the variability of a compression ratio for different regions.

The interaction of turbulence and shocks was investigated both theoretically and observationally by [1, 145]. [1] compared solutions of equations for a turbulent transport with the observations of IP shocks by the Wind spacecraft. They derived four-coupled equations for a perpendicular shock and six-coupled equations for a parallel shock from the turbulent transport equations of [141]. In particular, they have found that the sum of kinetic and magnetic energies within turbulent fluctuations increases across the shock, while the normalized cross-helicity can either increase or decrease. Although the simplified equations are 1D, many important turbulent quantities like total turbulent energy, cross-helicity, residual energy can be reasonably estimated. They have found a good agreement between numerical solutions and observations of both upstream/downstream fluctuations.

However, the uncertainties in estimation of turbulent energies from observations are often huge because each upstream/downstream profile is significantly "noisy" and it may put the analysis of each particular IP shock into question. An approach that solves the problem of under-sampling of turbulent quantities can be based on a large statistical set of IP shocks (e.g., [14]).

[66] studied dynamic pressure and magnetic field fluctuations in the inertial range via a superposed analysis of sheaths driven by ICMEs. The authors estimated the power of the fluctuations in the range of periods 3 – 10 min. They observed a mismatch between the occurrence of the peaks in the ULF power of magnetic field fluctuations and the peaks in dynamic pressure P_{dyn} fluctuations. The ULF power was enhanced at the leading part of the sheath, while the P_{dyn} was enhanced at its trailing part. They attributed this mismatch to the effect of piling of the solar wind in front of ICME and geometric constraints of the magnetic field within the sheath. They also analyzed magnetic field ULF power for each B_x, B_y, and B_z (GSM) component for the estimation of space weather effects. The ULF power for B_z and B_y showed enhancements at the sheath leading part, while the ULF power of the B_x component did not. They focused the analysis mainly on a role of the B_z component and divided 41 sheath regions into various subgroups (fast vs slow ICMEs, central vs intermediate encounters with ICMEs), and reported that the greatest difference of power profiles of ULF B_z fluctuations is between fast and slow ICMEs. While there is a strong increase of the power towards the shock for fast ICMEs, slow ICMEs show a relatively flat profile through the whole sheath.

A different approach in analyzing ICME sheath fluctuations was used by [90]; they focused on carefully constructed averages of magnetic field anisotropy $A = P_\perp/(2P_\parallel)$, compressibility $C = P_\parallel/(P_\parallel + P_\perp)$, where $P_\parallel$ and $P_\perp$ are the fluctuation powers parallel and perpendicular to a local magnetic field, and total fluctuation power P, in the solar wind, sheath and magnetic cloud. They discussed 42 events from the [82] list of well-defined and isolated magnetic cloud driven sheaths. The frequency range for the estimation of relevant quantities was set to $2 \cdot 10^{-3}$–$5 \cdot 10^{-2}$ Hz, i.e., similar as in [66]. The main results of their analysis is that the upstream solar wind and driving magnetic cloud have similar fluctuation powers ($P_{sw} \sim P_{mc} \sim 0.9\,nT^2$), while the fluctuation power within the sheath is roughly order of magnitude larger ($P_{sh} \sim 9\,nT^2$). Moreover, the power anisotropy in the sheaths ($A_{sh} \sim 5$) tends to be much lower than that in the solar wind ($A_{sw} \sim 10$) and in the magnetic cloud ($A_{mc} \sim 36$). The authors found a good correlation ($Cor \sim 0.54$) between the power, P_{sh} and the speed of the magnetic cloud v_{mc}, which can be expected because high-speed MCs drive stronger shocks [65] with a higher compression ratio that leads in average to the enhancement of the fluctuation power. A level of sheath fluctuations, P_{sh} correlates ($Cor \sim 0.42$) with the level of upstream solar wind fluctuations, P_{sw}, consistent with [14] who reported a similar correlation ($Cor \sim 0.48$).

Perhaps the greatest limitation of the [90] study is the use of average values because the level of magnetic field fluctuations generally decreases with the distance from the shock [66, 105]. However, the authors show that significant correlations revealing true physical phenomena can be found even when one omits a time evolution within the sheaths. On the other hand, it would be important to estimate the above mentioned characteristics of fluctuations in different regions of ICME sheaths, and more generally, downstream of any IP shock.

Recently [65] addressed the evolution of magnetic field fluctuations starting from the upstream solar wind and in three separate sheath regions: near the shock, in middle of the sheath and close to the ejecta. Each studied interval have 1 h duration in the spacecraft frame of reference. Their study was based on analysis of three distinctly different IP shocks observed at L1 by the Wind spacecraft. They analyzed magnetic field fluctuation amplitudes, compressibility, spectral properties in inertial and kinetic ranges, and various intermittency measures. Their findings are consistent with the previous studies, e.g., the inertial range spectral indices are mostly steeper in the sheath region compared to the preceding solar wind, but not for the case where the IP shock propagates into a high speed solar wind [14]. However, no ultimate conclusion can be made because the value of the upstream spectral index is likely to be influenced by foreshock-related wave activity. They concluded that the sheath regions exhibit characteristics of turbulence in the slow solar wind (higher compressibility, $\delta|B|/\delta B \lesssim 0.2$) and suggested that sheath turbulence is not fully developed.

A number of studies focus on the nature of compressive fluctuations downstream of IP shocks or/and on the change of the compressibility from upstream to downstream. The basic analysis of three IP shocks in **Section 5** suggests that the compressibility defined as $\delta B^2/B_0^2$ is higher in the downstream. Indeed [14] showed that both $\delta N/N_0$ and $\delta B/B_0$ increase across the shock by a factor of ~ 1.5 and ~ 2, respectively. The author observed the increase for all four distinct types of solar wind plasma [138] the shock propagates through. They explained the increase in inhomogeneity (lumpiness) by invoking the spaghetti-like structure of the solar wind [12]. The main idea is that the change of average magnetic field vector between adjacent flux tubes causes the change of the shock θ_{Bn} which drives the changes of the compression ratio of the shock. The increase of the lumpiness was also reported by [104]; who analyzed the changes of upstream/downstream power spectra of the ion flux (which served as a proxy for density fluctuations).

Important characteristics of turbulence are spectral slopes. Recently [14] comprehensively analyzed upstream/downstream trace-B and V_{sw} spectral indexes in the inertial range. He has shown that there is a little correlation between the corresponding upstream and downstream values ($Cor \lesssim 0.20$) for both B and V_{sw} while there is a small steepening of both spectral indices from upstream to downstream in average (see Figure 12 in [14]). Interestingly, when an IP shock propagates into a coronal-hole-origin plasma, virtually no steepening is observed (based on 15 shocks). Considering the Alfvén ratio r_A (ratio of the kinetic and magnetic energies of the fluctuations), IP shocks propagating through each type of solar wind exhibit a decrease of this ratio, with the greatest reduction occurring for shocks propagating through plasma of coronal hole origin.

Considering the evolution of the upstream and downstream spectral slopes of trace-B and V_{sw} with respect to the distance from the shock front [14] observed flatter spectra (spectral indices ~ -1.5) within 1 h adjacent to the shock front. A similar finding was reported by [55] who analyzed inertial and kinetic range magnetic field fluctuations in different regions of the terrestrial magnetosheath. They showed that closer to the bow shock, the inertial range power spectra of B exhibit '$1/f$' scaling. The flattening reported by both studies is in a qualitative agreement, though the values of indices are substantially different. The difference may be elucidated by examining the spatial/time scales of the fluctuations in these two studies. The significant difference is between the measurements of Cluster [55] and Wind [14]; the Cluster is virtually standing still with respect to the IP shock front, while at Wind, the downstream fluctuations are sweeping past the spacecraft at the speed of the downstream solar wind velocity (with respect to shock front). The corresponding spacecraft time frame for a simulated Wind measurement of the magnetosheath region (e.g., at the nose) can be roughly estimated as $t_{sp}^{W} = L_{magnetosheath}/v_{sw}$. For typical solar wind conditions, t_{sp}^{W} is in the order of minutes. Therefore, the whole magnetosheath region would correspond to just a fraction of the immediate downstream region analyzed by [14] using Wind. Nonetheless, the qualitative similarity of the flattening probably indicates a common physical origin.

Finally, we note that the range of upstream spectral indices is roughly two times wider than the range of the downstream indices (see Figure 12 in [14]). A similar behavior was shown by [104] for the spectral index of the ion flux power spectra in the inertial range (**Figure 6**). We believe that this is not accidental, however, there is no explanation for such observation.

5.2.1 Kinetic Range

The properties of kinetic range fluctuations, for example, which kinetic wave mode they resemble, what power-law scaling they obey, what levels of compressibility they have, etc., are not fully established yet, in particular because obtaining observations of these fluctuations upstream/downstream of IP shocks is challenging.

The number of studies that have analyzed the downstream IP shock kinetic range spectra is very limited but there are plenty of observations of kinetic turbulence in the terrestrial magnetosheath (e.g., [118]; and references therein). However, their relevance to the large scale sheaths of IP shocks is limited due to a small spatial extent of the magnetosheath. Immediately downstream the bow shock, the character of wave/turbulence should not be strongly affected by the presence of the magnetopause. However, deeper in the magnetosheath, magnetospheric processes like reconnection can influence the fluctuations and thus we will focus on the studies that investigated kinetic scale fluctuations closer to the bow shock.

[108] analyzed the 6 years of ion flux measurements of the Spektr-R spacecraft. In the magnetosheath, they found that the ion flux power spectra can be divided into three categories, a)

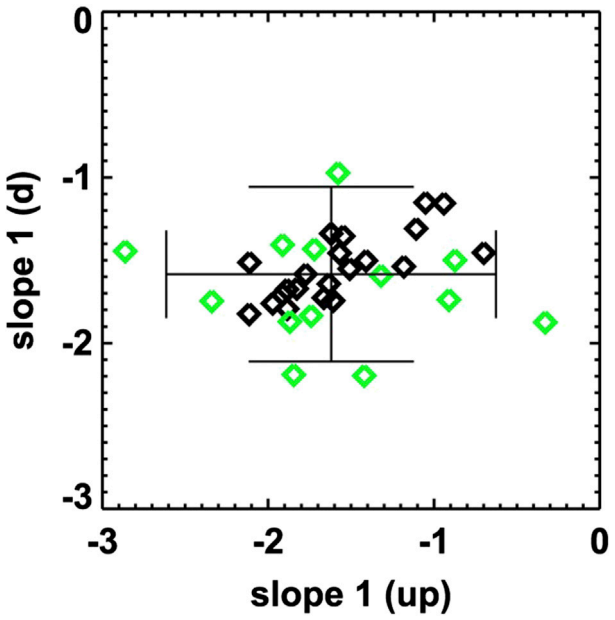

FIGURE 6 | Upstream vs. downstream spectral indices of inertial range fluctuations of the ion flux for a set of 34 IP shocks of [104]. Color symbols show the reliability of estimated slopes (black denotes a more reliable estimation). The horizontal and vertical lines in the middle mark the average spectral index of slope1 in the downstream and upstream regions, respectively. The shorter horizontal and vertical lines denote 2 standard deviations from the averages of the downstream and upstream spectral indices, respectively. The plot shows that for more reliable estimated slopes, the upstream and downstream indices seem to be correlated. On the other hand, the whole set (34 cases) shows that the spread of the indices is roughly two times larger in the upstream than in the downstream region. Image adapted from [104] and reproduced by permission of the AAS.

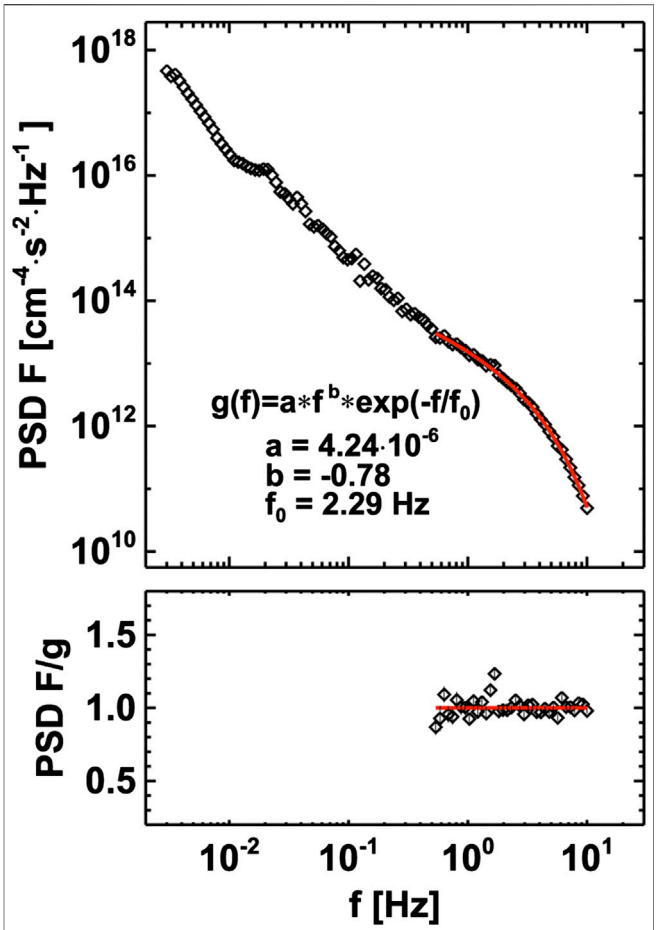

FIGURE 7 | Upper plot: The power spectral density of the ion flux downstream of a particularly strong IP shock detected at Spektr-R on September 12, 2014. The red line shows the fit by an exponentially truncated power-law model function, $g(f)$. Lower plot: The ratio of the measured spectrum, *PSDF*, and the resulted fit, g. Image adapted from [104] and reproduced by permission of the AAS.

two power laws separated by a break, b) two power laws with a bump around the break, and c) two power laws connected by a plateau (power law with spectral index −1). They reported that the bumpy spectra are more likely to occur close to the bow shock and they attributed this bump to kinetic instabilities such as mirror instability but they were not able to give a definitive answer due to the lack of magnetic field measurements. They observed a power law index of −3.2 in the vicinity of the bow shock, which is steeper than values reported in the solar wind [30, 115]. This finding is consistent with [104] who reported that ion flux spectrum is steeper within the downstream region of IP shocks.

[104] have shown that the scaling of fluctuations downstream of IP shocks of the ion flux in the kinetic range can be modeled as an exponentially truncated power law $P(f) \propto a \times f^b \times e^{-f/f_0}$ (**Figure 7**), which has not been reported in previous studies of kinetic-range spectra. A rule-of-thumb for these spectra in the solar wind is that they obey a power law with the scaling index that ranges from ~ -2 to ~ -4 [74, 115, 116]. An exponential power law may imply a fundamentally different physical mechanism that operates at sub-ion scales in the sheaths of IP shocks.

Employing fast MMS measurements [29] combined observations and theory to study plasma turbulence at kinetic scales in the Earth's magnetosheath. They estimated the spectra of the magnetic field, density and electric field, and found that just below characteristic ion scales the spectra follow the predictions for the kinetic Alfvén turbulence. Namely, the dimensionless ratio of normalized density and magnetic field fluctuations $\delta n^2/\delta b^2$ [11, 30, 106] follows the kinetic Alfvén prediction over a wide range of sub-ion frequencies. Similarly [137] concluded that the sub-ion fluctuations are consistent with the two-fluid predictions of KAWs for various dimensionless ratios. [29] proposed a new mode of KAWs–inertial kinetic Alfvén wave–that arises when the plasma exhibits temperature anisotropy $T_i \gg T_e$ while $\beta_i \sim 1$. In this regime, compressibility of fluctuations below the electron inertial length increases from the KAW-predicted value toward inertial KAW-predicted value of ~ 1 at electron gyroradius. This wave mode and its nonlinear dynamics could play an important role in the sheaths of IP shocks since the ions are often hotter than electrons there.

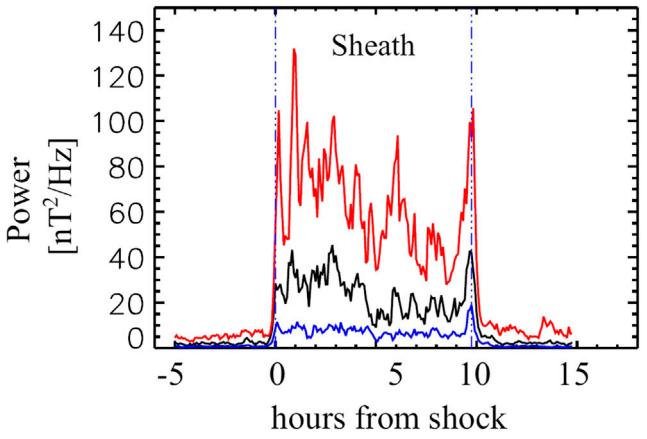

FIGURE 8 | ULF power of B_z component of IMF in sheaths of ICMEs (superposed analysis of sheath profiles that have been re-scaled to 10 h). The black line in the middle shows the median while the red and blue lines denote the upper and lower quartiles, respectively. For details, see [66]. The figure is adapted from [63]; copyright by Springer Nature, licensed under CC BY 4.0.

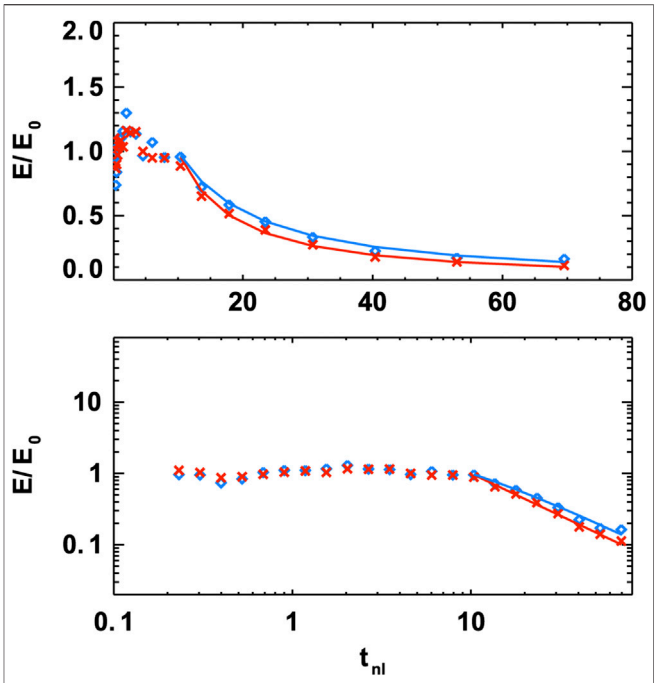

FIGURE 9 | Average downstream evolution of the kinetic (red crosses) and magnetic (blue diamonds) energies for the set of 174 IP shocks analyzed by [105]. Upper/lower panel shows the evolution in a linear scale/log-log scale, respectively. E_0 signifies that the profile of each shock was normalized by its immediate downstream value. Corresponding colored lines show the fit by a phenomenological power law function defined by **Eq. 5**. Image adapted from [105] and reproduced by permission of the AAS.

Although the solar wind is populated predominantly with Alfvénic and slow mode fluctuations [117], the mirror mode (MM) waves are frequently observed in shock sheaths. Due to the quasi-perpendicular shock compression, ions heat preferentially in the perpendicular direction which leads to an increase of temperature anisotropy and the instability threshold ($\beta_\perp/\beta_\parallel - 1 - 1/\beta_\perp = 0$) can be easily reached. Several studies identified peak and dip like large amplitude fluctuations in the Earth magnetosheath (e.g. [123, 124]). [3] investigated MMs in sheaths of 91 ICME driven shocks and among other findings, they reported that 1) the key shock parameter that controls the occurrence of MMs is the Mach number (higher M_A means higher occurrence rate), 2) the amplitudes of MMs were largest near the shock and (3) MMs are predominantly dip like structures and occurred in the mirror stable plasma. They concluded that the source of free energy for MMs is the shock compression and that MMs found deeper in the sheath are remnants of MMs generated closer to the shock front.

Since the average duration of MMs (in the spacecraft frame) in the study of [3] is $\Delta T \sim 12$ s, their large average amplitude is $A \sim 3.5$ nT, a fact that MMs are compressive structures and their occurrence rate is higher for high Mach number IP shocks, these observations may provide a basis for an explanation of the exponential power spectra reported by [104]. However, a definitive answer could only be made by analyzing both the magnetic field vector and number density in IP shock sheaths with sufficient cadence. Then, the nature of fluctuations (KAWs, MMs, Alfvén Ion Cyclotron waves, Whistler mode waves) and their particular contribution to the overall shape of the power spectrum can be estimated.

5.2.2 Decay of Turbulent Fluctuations

[66] have shown that the power within ULF B_z fluctuations decreases with a distance from the shock front. Generally, **Figure 8** (adapted from [63]) shows a relatively flat (although spiky) profile of ULF B_z power in a few hours downstream of the shock front and then decreases roughly from the middle of the sheath. This observation is qualitatively consistent with the findings of [105] who showed that the enhanced power of downstream fluctuations in the inertial range does not decrease immediately after the passage of an IP shock.

[105] analyzed a set of 174 fast forward IP shocks with respect to the evolution of the kinetic and magnetic fluctuations in the downstream region. They estimated the kinetic and magnetic energies, E_k and E_m, in the fluctuations on the time scale of 30 min. A superposed analysis of energy profiles is depicted in **Figure 9**. The profile of each shock was normalized by its immediate downstream value E_0. The main difference between their study and [66] is that the time is transformed into the natural units for turbulent energy decay, i.e., the eddy turnover time, τ_{nl}. The average energy profile for E_k and E_m is very similar and can be fitted by a phenomenological model function

$$E(t_{nl}) = \left(\frac{t_{nl} - t_0}{t_d - t_0}\right)^n \quad (5)$$

where t_0 and n are free parameters of the model, while $t_d = 10$ is a constant determined from the profiles in **Figure 9**. This constant may be interpreted as an average time that turbulence needs to adjust itself after the amplification at the shock. The constant profile up to $t = t_d$ and a Kolmogorov like power-law in the

inertial range suggest that turbulence is in a forced state. This forcing can have two origins (1) the kinetic processes in the shock front provide a free energy that can favor an inverse cascade of the fluctuation energy [105] and (2) the forcing from the large scales is constant. An important caveat for the constant t_d = 10 is that the time scale of 30 min for the estimation of the nonlinear time may not be the proper time scale. One should estimate τ_{nl} on the spatial scale of the injection scale $\tau_{nl}(k_{inj})$ that is usually attributed to the low frequency break in the power spectrum of the magnetic field (see **Figure 3**). Invoking a standard formula for Kolmogorov turbulence, $\tau_{nl} \sim k^{-2/3} \sim f^{-2/3}$ and assuming that the factor of t_d= 10 comes from the underestimation of the true nonlinear time, one can estimate the spacecraft frame frequency corresponding to $\tau_{nl}(f_{inj})$ using the ratio $\tau_{nl}(f_{inj})/\tau_{nl}(f_{30}) = (f_{inj}/f_{30})^{-2/3}$= 10, where f_{30} is simply the spacecraft frame frequency that corresponds to the time scale of 30 min, which yields $f_{inj}/f_{30} \sim 0.03$. This implies that the time scale in the spacecraft frame for the injection scale would correspond to roughly 15 h. That seems to be an overestimation of f_{inj}, at least for the fast solar wind where this time scale is usually lower than 1 h. However, in the slow wind, it may reach such values [19]. In any case, the conclusions of [105] that the power-law decay in time does not start immediately after the IP shock front will not change.

One could expect that the turbulent energy within the enhanced level of fluctuations downstream of the shock eventually cascades to smaller scales and dissipates into heat. Consequently, we should observe an increase of the temperature further in the downstream. The temperature profiles downstream of three shocks (see **Figure 4**) show a gradual rise of the temperature in time for S1 and S2. This rise could be caused by 1) the turbulent heating due to the enhancement of turbulent energy at the shock (left panel in **Figure 5**), 2) it could be just accidental or 3) caused by some another physical mechanism. A superposed analysis of 109 temperature profiles by [14] shows that there is no such an increase even 3 h after the passage of the IP shock (see **Figure 6** in [14]). Our example of three consecutive shocks in **Figure 4** shows that the downstream temperature profiles can be very different and thus the superposed profile can depend on the set of shocks used for analysis. In order, to check downstream temperature independently, **Figure 10** shows the evolution of profiles of the proton temperature T, proton number density N, magnetic field strength B and specific entropy S, 5 h upstream and downstream from the shock passage for 174 IP shocks analyzed by [105]. The profiles are qualitatively similar to those reported by [14]; e.g., a slight increase of the temperature and density towards the shock front in upstream, roughly constant temperature and a slight decrease of the density in downstream. On the basis of the constant downstream temperature profile, [14] suggested that no new active turbulence is generated. However, two observational facts: i) an increased level of turbulent energy and ii) no temperature increase seems to be in contradiction and should be further addressed.

An explanation for this discrepancy may be as it follows. A higher level of fluctuations implies a higher level of the turbulent cascade rate. However, this only means that the energy is dissipated

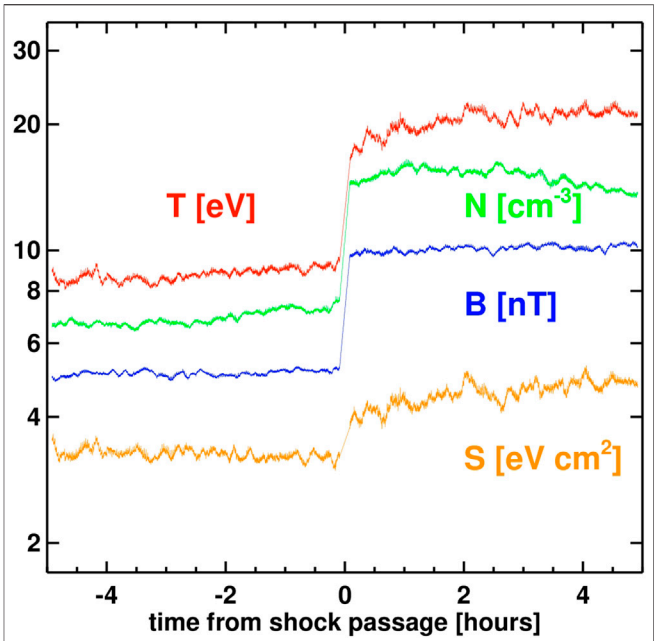

FIGURE 10 | A superposed epoch analysis of 140 fast forward IP shocks analyzed in [105]. The plot shows average profiles of proton temperature (red), proton number density (green), magnetic field magnitude (blue) and specific entropy (orange) for 5 h of upstream/downstream plasma. Note that the statistical set is reduced from the original set of 174 IP shocks due to additional requirements on the temperature measurements.

with the higher rate while the temperature increase is proportional to the energy contained within the largest turbulent eddies. In the solar wind, this scale is of the order of 10^6 km [87], which translates into roughly 1 h of data in the spacecraft frame. If one estimates the power spectrum of fluctuations during the first hour of downstream plasma, it may be unwise to infer the levels of turbulent energy contained within the largest scales from such a spectrum, because the interval is highly non-stationary. Generally, it is a mix that consists of just shocked plasma, on the one side, and the plasma evolved by 5 – 6 h on the other side; it is due to the fact that the time at which the plasma was shocked t_{sh} is usually much longer than the downstream time of a particular plasma parcel observation t_{sp} (see chapter 5). A rule of thumb is, t_{sh}= 5.5 · t_{sp} [14, 105]. One may even ask a question, whether the energy in the injection scale can be estimated. Empirical finding that the temperature is not increasing with the distance from the shock [14] may suggest that there is no new turbulent energy added/enhanced on the largest scale that would eventually heat the plasma.

On the other hand, the constant temperature profile can be consistent with the solar wind turbulent heating. Under assumptions that 1) the heat needed for the non-adiabatic cooling of the solar wind is provided by the turbulent cascade and 2) the cooling rate does not depend on the temperature, the amount of the heat needed for the observed cooling rate $T(r) \propto r^{0.8}$ [37, 50] should increase with a temperature. The temperature increases across the shock by a

factor of 4 (**Figure 10**) and thus the amount of heat that should be provided by the turbulent cascade to keep the same rate of non-adiabatic cooling should increase by a similar factor. It means that the average increase of the fluctuation power and average increase of temperature would be related. This suggestion is in line with observations shown in **Figures 4**, **5**. The thermal velocity V_{th} increases by a factor of 2 across S1 but two orders of magnitude enhancement of PSD B is observed (**Figure 5**, red lines). This large enhancement of the fluctuation level leads to a gradual rise of the downstream temperature. On the other hand, similar enhancement of PSD B across S3 is not sufficient to support much larger rise of V_{th} and rather a decrease of V_{th} is observed through downstream. These speculations need an extended statistical study to be confirmed or rejected. In addition, two aspects that make the analysis even more difficult are: 1) the ratio of downstream/upstream temperatures T_d/T_u can change with the heliocentric distance on the spatial scales of interest and 2) the relative temperature increase with respect to the adiabatic cooling may be too small to discern it in data on small spatial/temporal scales of few hours[2] (e.g., **Figure 10**).

5.3 Comment to the Ratio of Characteristic Time Scales

Further insight into the question of an amplification of turbulence due to shock passage may come from the understanding of how this enhancement develops. Generally, in order to increase the level of turbulent fluctuations, the simplest and straightforward way how to achieve this, is to increase it simultaneously for every wave vector. However, the IP shock is "increasing" the level of fluctuations by an opposite way. At each moment, only local magnetic field increases. Two extreme scenarios are: 1) when the characteristic time of evolution of Alfvénic fluctuations (characteristic eddy nonlinear time, τ_{nl} or characteristic time of decay according to the WKB prediction) is much larger than the time it takes for the shock to travel across this fluctuation, then the enhancement can be viewed as sudden and simultaneous. However, when the opposite is true, i.e., 2) the fluctuations evolve much quicker than the characteristic time of IP shock passage, then the situation becomes more complex.

We can quantify the above considerations by defining a ratio R: the ratio of the characteristic time of a significant change of Alfvénic fluctuations, t_{ch}, and the time for which an IP shock sweeps through fluctuations, t_{sh}:

$$R = \frac{t_{ch}}{t_{sh}} \tag{6}$$

This ratio can be estimated in the upstream and downstream regions separately. We introduce a simple considerations for the both regions, thus illustrating the relevance of R.

In upstream, R^u may be estimated if we identify t_{ch} with the characteristic nonlinear time of turbulent fluctuations, $\tau^u_{nl} = 1/(kZ^u)$ [86], $(Z^u)^2$ is the sum of kinetic and magnetic energies; and we express $t^u_{sh} = 1/(kv^u_A M_A)$, where v^u_A is the upstream Alfvén speed and M_A is the Alfvén Mach number. Thus, $R^u = v^u_A M_A/Z^u$. For a sub-Alfvénic turbulence ($Z \sim \delta v_{sw} < v_A$), $R^u \gtrsim M_A$ should then hold. We see that for large scales, R^u may serve as a proxy for M_A. As anticipated, R^u should be larger than unity even for scales comparable to the coherence length.

In downstream, R^d may be evaluated in a similar manner, $t_{ch} = 1/(kZ^d)$ and $t^d_{sh} = 1/(kv^d_{sh})$, where v^d_{sh} is the downstream plasma speed in the shock frame. Hence, $R^d = v^d_{sh}/Z^d$. We know that $v^d_{sh} < v^d_A$, therefore $R^d \lesssim v^d_A/Z^d$. Note, that $R^d \sim 1$ signifies a change from sub-Alfvénic into super-Alfvénic turbulence [32]. In general, this condition seems hard to be ever satisfied in the solar wind, however, for shocks that propagate into coronal-hole-origin plasma, it may be possible due to the large levels of downstream fluctuations (see Figure 14 of [14]). We hypothesize that for some downstream IP shocks, the regime of super-Alfvénic turbulence may be relevant.

In the previous paragraphs, we derived the expressions for R in a convenient reference frame where the shock is stationary. Focusing on the downstream, we may roughly estimate this ratio from the spacecraft measurements as it follows: expression for t_{ch} is the same as before, $\tau^d_{nl} = 1/(kZ^d)$ while $t^d_{sh} = t_{sp} \cdot K$ (**Eq. 3**), where $t_{sp} = 1/(kv^d_{sp})$, v^d_{sp} being the downstream solar wind speed in the spacecraft frame of reference. Then, $R^d = v^d_{sp}/(Z^d K)$. Note that $R^d = R^d(k)$ since $Z^d = Z^d(k)$. Assuming Kolmogorov scaling in the inertial range, $Z \propto k^{-5/6}$, then $R^d \propto k^{5/6}$ and R^d decreases for larger scales. If we directly evaluate R^d for some average conditions at large scales, e.g., $K = 5.5$, $v^d_{sp} = 400\,\mathrm{km \cdot s^{-1}}$, $(Z^d)^2 = 2000\,\mathrm{km^2 \cdot s^{-2}}$, then $R^d = 1.6$. Whether the value of R^d corresponds to the injection scale or to the break between the inertial and injection ranges depends on specific values of v^d_{sp}, K and Z^d.

Finally, the question whether the constant energy profile up to t_d and the constant temperature profile (**Figure 10**) are causally related, remains open. However, in the view of the new parameter R (**Eq. 6**), this issue should be investigated in the future studies. Analyses of the energy and temperature profiles with respect to the type of a plasma through which an IP shock propagates, as it was suggested by [14] can help in this respect.

6 CONCLUDING REMARKS

The interaction of interplanetary shocks and solar wind turbulence has been investigated for decades focusing mainly on the particle acceleration and geoeffectiveness of IP shocks and their sheaths. The nature of the fluctuations alone were addressed in more detail only recently.

[2]For example, 3 h in the spacecraft frame translates into ~ 17 hours for the age of the shocked plasma (see **Eq. 3**). Assuming the solar wind speed of 500 km·s^{-1}, then the shock encountered the plasma at a distance of ~ 0.8 AU. If the whole temperature increase from 0.8 to 1 AU is due to the turbulent heating, we can estimate the relative temperature increase, $R_t = T(1\,\mathrm{AU})/T_a(1\,\mathrm{AU}) \sim 1.13$, where $T_a(1\,\mathrm{AU})$ is the prediction for the adiabatic temperature decrease.

The key aspects of this interaction have been discussed in this paper. Considering the changes from upstream to downstream of quasi-perpendicular IP shocks: 1) enhancement of the power in the inertial range fluctuations of the velocity, magnetic field and density is roughly one order of magnitude, 2) IP shock reduces the Alfvénicity of fluctuations, 3) the power in the inertial range fluctuations is kept constant for a significant time after the passage of the shock, 4) lumpiness of fluctuations is enhanced due to the changing θ_{Bn} induced by the non-compressive fluctuations, 5) power spectra of inertial range fluctuations resemble those in the solar wind, though they are steeper on average.

A major point of this review is that the downstream region of an IP shock should be viewed as a history of the IP shock propagation through the plasma. This simple perspective then serves as a starting point for the interpretation of the observed phenomena, it constrains the potential questions and most importantly it opens new questions about the nature and evolution of the downstream turbulent fluctuations.

While our knowledge of the processes in upstream and downstream regions of IP shocks has greatly improved in recent years, there are still more questions than answers. Focusing on downstream quasi-perpendicular shocks, the major open problem is what state/regime of turbulence can be ascribed to these fluctuations? On one hand, the inertial range spectra closely resemble those of the turbulent solar wind, while these fluctuations do not evolve (decay) significantly within many hours after the shock passage. Closely connected with this issue is a questionable estimation of the scale of the break between the injection and inertial ranges and the energy that resides within the injection scales. Connected to the issue still is a role of the solar wind expansion: a simple fact that a time for the shock front to propagate through a structure with the spatial extent of correlative/integral scale may be smaller than the characteristic time of evolution of such a structure (WKB/turbulent decay/other). A ratio of these two time scales may prove to be a useful tool in future analysis of upstream/downstream IP shock turbulence.

Finally, understanding the evolution of the IP shock sheath's fluctuations using single point measurements is difficult. Upcoming simultaneous measurements of Parker Solar Probe, Solar Orbiter and the spacecraft located at L1 will hopefully provide a unique opportunity to study the aforementioned evolution of the shock sheaths through the rising phase of the current solar cycle.

DATA AVAILABILITY STATEMENT

All used data are from open-access sources via (http://cdaweb.gsfc.nasa.gov/cdaweb/), the Spektr-R data are available via http://aurora.troja.mff.cuni.cz/spektr-r/project/. Parameters of IP shocks can be accessed at http://ipshocks.fi.

AUTHOR CONTRIBUTIONS

AP drafted the initial manuscript and performed the analysis of the data. JS and ZN significantly improved the manuscript and provided interpretation of the data. TD provided one figure and suggested improvements of the manuscript. AK worked on one section and on the finalization of the manuscript.

FUNDING

The work of the Czech authors was supported partly by the Czech Science Foundation under Contract 19-18993S and by the Grant Agency of the Charles University under the project number 264220.

ACKNOWLEDGMENTS

The authors thank all spacecraft teams for the velocity and magnetic field data.

REFERENCES

1. Adhikari L, Zank GP, Hunana P, and Hu Q. The Interaction of Turbulence with Parallel and Perpendicular Shocks: theory and Observations at 1 au. *Astrophys J* (2016) 833:218. doi:10.3847/1538-4357/833/2/218
2. Adhikari L, Zank GP, Zhao LL, Kasper JC, Korreck KE, Stevens M, et al. Turbulence transport modeling and first orbit parker solar Probe (PSP) observations. *Astrophys J Suppl Ser* (2020) 246:38. doi:10.3847/1538-4365/ab5852
3. Ala-Lahti MM, Kilpua EKJ, Dimmock AP, Osmane A, Pulkkinen T, and Souček J. Statistical analysis of mirror mode waves in sheath regions driven by interplanetary coronal mass ejection. *Ann Geophys* (2018) 36:793–808. doi:10.5194/angeo-36-793-2018
4. Alexandrova O, Lacombe C, Mangeney A, Grappin R, and Maksimovic M. Solar wind turbulent spectrum at plasma kinetic scales. *Astrophys J* (2012) 760:121. doi:10.1088/0004-637X/760/2/121
5. Ao X, Zank GP, Pogorelov NV, and Shaikh D. Interaction of a thin shock with turbulence. I. Effect on shock structure: analytic model. *Phys Fluids* (2008) 20:127102. doi:10.1063/1.3041706
6. Balogh A, and Treumann RA. *Physics of collisionless shocks*. 1st ed. edn. New York: Springer-Verlag (2013).
7. Bamert K, Kallenbach R, le Roux JA, Hilchenbach M, Smith CW, and Wurz P. Evidence for iroshnikov-kraichnan-type turbulence in the solar wind upstream of interplanetary traveling shocks. *Astrophys J Lett* (2008) 675:L45–8. doi:10.1086/529491
8. Belcher JW, and Davis L. Large-amplitude Alfvén waves in the interplanetary medium, 2. *J Geophys Res* (1971) 76:3534–63. doi:10.1029/JA076i016p03534
9. Bieber JW, Wanner W, and Matthaeus WH. Dominant two-dimensional solar wind turbulence with implications for cosmic ray transport. *J Geophys Res* (1996) 101:2511–22. doi:10.1029/95JA02588
10. Blanco-Cano X, Kajdič P, Aguilar-Rodríguez E, Russell CT, Jian LK, and Luhmann JG. Interplanetary shocks and foreshocks observed by STEREO during 2007-2010. *J Geophys Res Space Phys* (2016) 121:992–1008. doi:10.1002/2015JA021645
11. Boldyrev S, Horaites K, Xia Q, and Perez JC. Toward a theory of astrophysical plasma turbulence at subproton scales. *Astrophys J* (2013) 777:41. doi:10.1088/0004-637X/777/1/41

12. Borovsky JE. Flux tube texture of the solar wind: strands of the magnetic carpet at 1 AU? *J Geophys Res Space Phys* (2008) 113:A08110. doi:10.1029/2007JA012684
13. Borovsky JE. The velocity and magnetic field fluctuations of the solar wind at 1 AU: statistical analysis of Fourier spectra and correlations with plasma properties. *J Geophys Res Space Phy* (2012) 117:A05104. doi:10.1029/2011JA017499
14. Borovsky JE. A statistical analysis of the fluctuations in the upstream and downstream plasmas of 109 strong-compression interplanetary shocks at 1 au. *J Geophys Res Space Phys* (2020) 125:e2019JA027518. doi:10.1029/2019JA027518
15. Borovsky JE, and Burkholder BL. On the fourier contribution of strong current sheets to the high-frequency magnetic power SpectralDensity of the solar wind. *J Geophys Res Space Phys* (2020) 125:e27307. doi:10.1029/2019JA027307
16. Borovsky JE, and Denton MH. Differences between CME-driven storms and CIR-driven storms. *J Geophys Res Space Phys* (2006) 111:A07S08. doi:10.1029/2005JA011447
17. Borovsky JE, and Denton MH. The differences between storms driven by helmet streamer CIRs and storms driven by pseudostreamer CIRs. *J Geophys Res Space Phys* (2013) 118:5506–21. doi:10.1002/jgra.50524
18. Bruno R, and Carbone V. The solar wind as a turbulence laboratory. *Living Rev Solar Phys* (2013) 10:2. doi:10.12942/lrsp-2013-2
19. Bruno R, Carbone V, Vörös Z, D'Amicis R, Bavassano B, Cattaneo MB, et al. Coordinated study on solar wind turbulence during the venus-express, ACE and Ulysses alignment of august 2007. *Earth Moon and Planets* (2009) 104:101–4. doi:10.1007/s11038-008-9272-9
20. Burgess D, and Scholer M. Microphysics of quasi-parallel shocks in collisionless plasmas. *Space Sci Rev* (2013) 178:513–33. doi:10.1007/s11214-013-9969-6
21. Burgess D, and Scholer M. *Microphysics of quasi-parallel shocks in collisionless plasmas*. Boston, MA: Springer US (2014). p. 437–57.
22. Burlaga L, Sittler E, Mariani F, and Schwenn R. Magnetic loop behind an interplanetary shock: voyager, Helios, and IMP 8 observations. *J Geophys Res* (1981) 86:6673–84. doi:10.1029/JA086iA08p06673
23. Cane HV, and Lario D. An introduction to CMEs and energetic particles. *Space Sci Rev* (2006) 123:45–56. doi:10.1007/s11214-006-9011-3
24. Cane HV, Reames DV, and von Rosenvinge TT. The role of interplanetary shocks in the longitude distribution of solar energetic particles. *J Geophys Res* (1988) 93:9555–67. doi:10.1029/JA093iA09p09555
25. Chandran BDG. Parametric instability, inverse cascade and the 1/f range of solar-wind turbulence. *J Plasma Phys* (2018) 84:905840106. doi:10.1017/S0022377818000016
26. Chandran BDG, Quataert E, Howes GG, Xia Q, and Pongkitiwanichakul P. Constraining low-frequency alfvénic turbulence in the solar wind using density-fluctuation measurements. *Astrophys J* (2009) 707:1668–75. doi:10.1088/0004-637x/707/2/1668
27. Chen CHK, Bale SD, Bonnell JW, Borovikov D, Bowen TA, Burgess D, et al. The evolution and role of solar wind turbulence in the inner heliosphere. *Astrophys J Suppl Ser* (2020) 246:53. doi:10.3847/1538-4365/ab60a3
28. Chen CHK, Bale SD, Salem CS, and Maruca BA. Residual energy spectrum of solar wind turbulence. *Astrophys J* (2013) 770:125. doi:10.1088/0004-637X/770/2/125
29. Chen CHK, and Boldyrev S. Nature of kinetic scale turbulence in the earth's magnetosheath. *Astrophys J* (2017) 842:122. doi:10.3847/1538-4357/aa74e0
30. Chen CHK, Boldyrev S, Xia Q, and Perez JC. Nature of subproton scale turbulence in the solar wind. *Phys Rev Lett* (2013) 110:225002. doi:10.1103/PhysRevLett.110.225002
31. Chen CHK, Leung L, Boldyrev S, Maruca BA, and Bale SD. Ion-scale spectral break of solar wind turbulence at high and low beta. *Geophys Res Lett* (2014) 41:8081–8. doi:10.1002/2014GL062009
32. Cho J, and Lazarian A. Compressible magnetohydrodynamic turbulence: mode coupling, scaling relations, anisotropy, viscosity-damped regime and astrophysical implications. *Monthly Notices R Astron Soc* (2003) 345:325–39. doi:10.1046/j.1365-8711.2003.06941.x
33. Del Zanna L. Parametric decay of oblique arc-polarized Alfvén waves. *Geophys Res Lett* (2001) 28:2585–8. doi:10.1029/2001GL012911
34. Denton MH, Borovsky JE, Skoug RM, Thomsen MF, Lavraud B, Henderson MG, et al. Geomagnetic storms driven by ICME- and CIR-dominated solar wind. *J Geophys Res Space Phys* (2006) 111:A07S07. doi:10.1029/2005JA011436
35. Domingo V, Fleck B, and Poland AI. The SOHO mission: an overview. *Solar Phys* (1995) 162:1–37. doi:10.1007/BF00733425
36. Ďurovcová T, Němeček Z, and Šafránková J. Evolution of the α-proton differential motion across stream interaction regions. *Astrophys J* (2019a) 873:24. doi:10.3847/1538-4357/ab01c8
37. Ďurovcová T, Šafránková J, and Němeček Z. Evolution of relative drifts in the expanding solar wind: Helios observations. *Solar Phys* (2019b) 294:97. doi:10.1007/s11207-019-1490-y
38. Echer E, Gonzalez WD, and Tsurutani BT. Interplanetary conditions leading to superintense geomagnetic storms (Dst <= -250 nT) during solar cycle 23. *Geophys Res Lett* (2008) 35:L06S03. doi:10.1029/2007GL031755
39. Forman MA, Wicks RT, and Horbury TS. Detailed fit of "critical balance" theory to solar wind turbulence measurements. *Astrophys J* (2011) 733:76. doi:10.1088/0004-637X/733/2/76
40. Franci L, Landi S, Matteini L, Verdini A, and Hellinger P. High-resolution hybrid simulations of kinetic plasma turbulence at proton scales. *Astrophys J* (2015) 812:21. doi:10.1088/0004-637X/812/1/21
41. Franci L, Landi S, Matteini L, Verdini A, and Hellinger P. Plasma beta dependence of the ion-scale spectral break of solar wind turbulence: high-resolution 2D hybrid simulations. *Astrophys J* (2016) 833:91. doi:10.3847/1538-4357/833/1/91
42. Gary SP. *Theory of space plasma microinstabilities*. CambridgeCambridge, UK: Cambridge University Press (1993).
43. Gedalin M. Ion reflection at the shock front revisited. *J Geophys Res* (1996) 101:4871–8. doi:10.1029/95JA03669
44. Giacalone J, and Jokipii JP. Injection and acceleration at non-parallel shocks. In: B Sripathi Acharya, S Gupta, P Jagadeesan, A Jain, S Karthikeyan, S Morris, et al. editors. 29th International Cosmic Ray Conference (ICRC29); 2005 August 3-10; Pune, India. Mumbai: Tata Institute of Fundamental Research (2005). Vol 3:265
45. Good SW, Ala-Lahti M, Palmerio E, Kilpua EKJ, and Osmane A. Radial evolution of magnetic field fluctuations in an interplanetary coronal mass ejection sheath. *Astrophys J* (2020) 893:110. doi:10.3847/1538-4357/ab7fa2
46. Gopalswamy N, Mäkelä P, Akiyama S, Yashiro S, Xie H, and Thakur N. Sun-to-earth propagation of the 2015 June 21 coronal mass ejection revealed by optical, EUV, and radio observations. *J Atmos Solar-Terrestrial Phys* (2018) 179:225–38. doi:10.1016/j.jastp.2018.07.013
47. Gosling JT, and McComas DJ. Field line draping about fast coronal mass ejecta: a source of strong out-of-the-ecliptic interplanetary magnetic fields. *Geophys Res Lett* (1987) 14:355–8. doi:10.1029/GL014i004p00355
48. Gosling JT, Riley P, McComas DJ, and Pizzo VJ. Overexpanding coronal mass ejections at high heliographic latitudes: observations and simulations. *J Geophys Res Space Phys* (1998) 103:1941–54. doi:10.1029/97JA01304
49. Grošelj D, Mallet A, Loureiro NF, and Jenko F. Fully kinetic simulation of 3D kinetic alfvén turbulence. *Phys Rev Lett* (2018) 120:105101. doi:10.1103/PhysRevLett.120.105101
50. Hellinger P, Matteini L, Štverák Š, Trávníček PM, and Marsch E. Heating and cooling of protons in the fast solar wind between 0.3 and 1 AU: Helios revisited. *J Geophys Res Space Phys* (2011) 116:A09105. doi:10.1029/2011JA016674
51. Horbury TS, Forman M, and Oughton S. Anisotropic scaling of magnetohydrodynamic turbulence. *Phys Rev Lett* (2008) 101:175005. doi:10.1103/PhysRevLett.101.175005
52. Horbury TS, Wicks RT, and Chen CHK. Anisotropy in space plasma turbulence: solar wind observations. *Space Sci Rev* (2012) 172:325–42. doi:10.1007/s11214-011-9821-9
53. Howes GG, Cowley SC, Dorland W, Hammett GW, Quataert E, and Schekochihin AA. Astrophysical gyrokinetics: basic equations and linear theory. *Astrophys J* (2006) 651:590–614. doi:10.1086/506172
54. Howes GG, Dorland W, Cowley SC, Hammett GW, Quataert E, Schekochihin AA, et al. Kinetic simulations of magnetized turbulence in astrophysical plasmas. *Phys Rev Lett* (2008) 100:065004. doi:10.1103/PhysRevLett.100.065004

55. Huang SY, Hadid LZ, Sahraoui F, Yuan ZG, and Deng XH. On the existence of the Kolmogorov inertial range in the terrestrial magnetosheath turbulence. *Astrophys J Lett* (2017) 836:L10. doi:10.3847/2041-8213/836/1/L10
56. Iroshnikov PS. Turbulence of a conducting fluid in a strong magnetic field. *Sov Astron* (1963) 40:742.
57. Jian LK, Russell CT, and Luhmann JG. Comparing solar minimum 23/24 with historical solar wind records at 1 AU. *Solar Phys* (2011) 274:321–44. doi:10.1007/s11207-011-9737-2
58. Jian LK, Russell CT, Luhmann JG, Galvin AB, and Simunac KDC. Solar wind observations at STEREO: 2007 - 2011. In: GP Zank, J Borovsky, R Bruno, J Cirtain, S Cranmer, H Elliott, et al. editors. 13th International Solar Wind Conference (Solar Wind); 2012 Jun 17–22; HI. Melville, NY: AIP Publishing LLC. Vol. 1539 (2013). p. 191–4.
59. Jurac S, Kasper JC, Richardson JD, and Lazarus AJ. Geomagnetic disturbances and their relationship to Interplanetary shock parameters. *Geophys Res Lett* (2002) 29:1463. doi:10.1029/2001GL014034
60. Kajdič P, Blanco-Cano X, Aguilar-Rodriguez E, Russell CT, Jian LK, and Luhmann JG. Waves upstream and downstream of interplanetary shocks driven by coronal mass ejections. *J Geophys Res Space Phys* (2012) 117. doi:10.1029/2011JA017381
61. Kataoka R, Watari S, Shimada N, Shimazu H, and Marubashi K. Downstream structures of interplanetary fast shocks associated with coronal mass ejections. *Geophys Res Lett* (2005) 32:L12103. doi:10.1029/2005GL022777
62. Kennel CF, Coroniti FV, Scarf FL, Livesey WA, Russell CT, Smith EJ, et al. A test of Lee's quasi-linear theory of ion acceleration by interplanetary traveling shocks. *J Geophys Res* (1986) 91:11917–28. doi:10.1029/JA091iA11p11917
63. Kilpua E, Koskinen HEJ, and Pulkkinen TI. Coronal mass ejections and their sheath regions in interplanetary space. *Living Rev Solar Phys* (2017a) 14:5. doi:10.1007/s41116-017-0009-6
64. Kilpua EKJ, Balogh A, von Steiger R, and Liu YD. Geoeffective properties of solar transients and stream interaction regions. *Space Sci Rev* (2017b) 212:1271–314. doi:10.1007/s11214-017-0411-3
65. Kilpua EKJ, Fontaine D, Good SW, Ala-Lahti M, Osmane A, Palmerio E, et al. Magnetic field fluctuation properties of coronal mass ejection-driven sheath regions in the near-earth solar wind. *Ann Geophys* (2020) 38:999–1017. doi:10.5194/angeo-38-999-2020
66. Kilpua EKJ, Hietala H, Koskinen HEJ, Fontaine D, and Turc L. Magnetic field and dynamic pressure ulf fluctuations in coronal-mass-ejection-driven sheath regions. *Ann Geophys* (2013) 31:1559–67. doi:10.5194/angeo-31-1559-2013
67. Kilpua EKJ, Lumme E, Andreeova K, Isavnin A, and Koskinen HEJ. Properties and drivers of fast interplanetary shocks near the orbit of the earth (1995–2013). *J Geophys Res Space Phys* (2015) 120:4112–25. doi:10.1002/2015JA021138
68. Kis A, Matsukiyo S, Otsuka F, Hada T, Lemperger I, Dandouras I, et al. Effect of upstream ULF waves on the energetic ion diffusion at the earth's foreshock. II. Observations. *Astrophys J* (2018) 863:136. doi:10.3847/1538-4357/aad08c
69. Klein LW, and Burlaga LF. Interplanetary magnetic clouds at 1 AU. *J Geophys Res* (1982) 87:613–24. doi:10.1029/JA087iA02p00613
70. Kraichnan RH. Inertial range spectrum of hydromagnetic turbulence. *Phys Fluids* (1965) 8:1385–7. doi:10.1063/1.1761412
71. Krasnoselskikh V, Balikhin M, Walker SN, Schwartz S, Sundkvist D, Lobzin V, et al. The dynamic quasiperpendicular shock: cluster discoveries. *Space Sci Rev* (2013) 178:535–98. doi:10.1007/s11214-013-9972-y
72. Krauss-Varban D, and Omidi N. Structure of medium mach number quasi-parallel shocks: upstream and downstream waves. *J Geophys Res* (1991) 96:17715–31. doi:10.1029/91JA01545
73. Lacombe C, Alexandrova O, and Matteini L. Anisotropies of the magnetic field fluctuations at kinetic scales in the solar wind: cluster observations. *Astrophysical J* (2017) 848:45. doi:10.3847/1538-4357/aa8c06
74. Leamon RJ, Smith CW, Ness NF, Matthaeus WH, and Wong HK. Observational constraints on the dynamics of the interplanetary magnetic field dissipation range. *J Geophys Res* (1998) 103:4775. doi:10.1029/97JA03394
75. Lee MA. Coupled hydromagnetic wave excitation and ion acceleration upstream of the earth's bow shock. *J Geophys Res* (1982) 87:5063–80. doi:10.1029/JA087iA07p05063
76. Lee MA. Coupled hydromagnetic wave excitation and ion acceleration at interplanetary traveling shocks. *J Geophys Res* (1983) 88:6109–20. doi:10.1029/JA088iA08p06109
77. Lithwick Y, Goldreich P, and Sridhar S. Imbalanced strong MHD turbulence. *Astrophys J* (2007) 655:269–74. doi:10.1086/509884
78. Liu YD, Hu H, Wang R, Yang Z, Zhu B, Liu YA, et al. Plasma and magnetic field characteristics of solar coronal mass ejections in relation to geomagnetic storm intensity and variability. *Astrophys J Lett* (2015) 809:L34. doi:10.1088/2041-8205/809/2/L34
79. Lu Q, Hu Q, and Zank GP. The interaction of alfvén waves with perpendicular shocks. *Astrophys J* (2009) 706:687–92. doi:10.1088/0004-637X/706/1/687
80. Luttrell AH, and Richter AK. A study of MHD fluctuations upstream and downstream of quasi-parallel interplanetary shocks. *J Geophys Res* (1987) 92:2243–52. doi:10.1029/JA092iA03p02243
81. Marshall W, and Bullard EC. The structure of magneto-hydrodynamic shock waves. *Proc R Soc Lond Ser A. Math Phys Sci* (1955) 233:367–76. doi:10.1098/rspa.1955.0272
82. Masías-Meza JJ, Dasso S, Démoulin P, Rodriguez L, and Janvier M. Superposed epoch study of ICME sub-structures near Earth and their effects on Galactic cosmic rays. *Astron Astrophys* (2016) 592:A118. doi:10.1051/0004-6361/201628571
83. Matteini L, Landi S, Del Zanna L, Velli M, and Hellinger P. Parametric decay of linearly polarized shear Alfvén waves in oblique propagation: one and two-dimensional hybrid simulations. *Geophys Res Lett* (2010) 37:L20101. doi:10.1029/2010GL044806
84. Matteini L, Stansby D, Horbury TS, and Chen CHK. On the 1/f spectrum in the solar wind and its connection with magnetic compressibility. *Astrophys J Lett* (2018) 869:L32. doi:10.3847/2041-8213/aaf573
85. Matthaeus WH, Goldstein ML, and Roberts DA. Evidence for the presence of quasi-two-dimensional nearly incompressible fluctuations in the solar wind. *J Geophys Res* (1990) 95:20673–83. doi:10.1029/JA095iA12p20673
86. Matthaeus WH, Oughton S, Osman KT, Servidio S, Wan M, Gary SP, et al. Nonlinear and linear timescales near kinetic scales in solar wind turbulence. *Astrophys J* (2014) 790:155. doi:10.1088/0004-637X/790/2/155
87. Matthaeus WH, Smith CW, and Oughton S. Dynamical age of solar wind turbulence in the outer heliosphere. *J Geophys Res* (1998) 103:6495–502. doi:10.1029/97JA03729
88. McKenzie JF, and Westphal KO. Transmission of Alfvén waves through the Earth's bow shock. *Planet Space Sci* (1969) 17:1029–37. doi:10.1016/0032-0633(69)90107-X
89. Möbius E, Scholer M, Sckopke N, Lühr H, Paschmann G, and Hovestadt D. The distribution function of diffuse ions and the magnetic field power spectrum upstream of Earth's bow shock. *Geophys Res Lett* (1987) 14:681–4. doi:10.1029/GL014i007p00681
90. Moissard C, Fontaine D, and Savoini P. A study of fluctuations in magnetic cloud-driven sheaths. *J Geophys Res Space Phys* (2019) 124:8208–26. doi:10.1029/2019JA026952
91. Nakagawa T, Nishida A, and Saito T. Planar magnetic structures in the solar wind. *J Geophys Res Space Phys* (1989) 94:11761–75. doi:10.1029/JA094iA09p11761
92. Narita Y, Glassmeier KH, and Treumann RA. Wave-number spectra and intermittency in the terrestrial foreshock region. *Phys Rev Lett* (2006) 97:191101. doi:10.1103/PhysRevLett.97.191101
93. Němeček Z, Š afránková J, Goncharov O, Přech L, and Zastenker GN. Ion scales of quasi-perpendicular low-Mach-number interplanetary shocks. *Geophys Res Lett* (2013) 40:4133–7. doi:10.1002/grl.50814
94. Oliveira D. Magnetohydrodynamic shocks in the interplanetary space: a theoretical review. *Braz J Phys* (2016) 47:81–95. doi:10.1007/s13538-016-0472-x
95. Oliveira D, and Samsonov A. Geoeffectiveness of interplanetary shocks controlled by impact angles: a review. *Adv Space Res* (2018) 61:1–44. doi:10.1016/j.asr.2017.10.006
96. Ontiveros V, and Vourlidas A. Quantitative measurements of coronal mass ejection-driven shocks from LASCO observations. *Astrophys J* (2009) 693:267–75. doi:10.1088/0004-637X/693/1/267
97. Otsuka F, Matsukiyo S, Kis A, Nakanishi K, and Hada T. Effect of upstream ULF waves on the energetic ion diffusion at the earth's foreshock. I. Theory

and simulation. *Astrophysical J* (2018) 853:117. doi:10.3847/1538-4357/aaa23f
98. Oughton S, and Matthaeus WH. Critical balance and the physics of magnetohydrodynamic turbulence. *Astrophys J* (2020) 897:37. doi:10.3847/1538-4357/ab8f2a
99. Owens MJ, and Crooker NU. Coronal mass ejections and magnetic flux buildup in the heliosphere. *J Geophys Res (Space Physics)* (2006) 111:A10104. doi:10.1029/2006JA011641
100. Owens MJ, and Forsyth RJ. The heliospheric magnetic field. *Living Rev Solar Phys* (2013) 10:5. doi:10.12942/lrsp-2013-5
101. Palmerio E, Kilpua EKJ, and Savani NP. Planar magnetic structures in coronal mass ejection-driven sheath regions. *Ann Geophys* (2016) 34:313–22. doi:10.5194/angeo-34-313-2016
102. Parker EN. Dynamics of the interplanetary gas and magnetic fields. *Astrophys J* (1958) 128:664. doi:10.1086/146579
103. Perez JC, and Boldyrev S. Role of cross-helicity in magnetohydrodynamic turbulence. *Phys Rev Lett* (2009) 102:025003. doi:10.1103/PhysRevLett.102.025003
104. Pitňa A, Šafránková J, Němeček Z, Goncharov O, Němec F, Přech L, et al. Density fluctuations upstream and downstream of interplanetary shocks. *Astrophys J* (2016) 819:41. doi:10.3847/0004-637X/819/1/41
105. Pitňa A, Šafránková J, Němeček Z, and Franci L. Decay of solar wind turbulence behind interplanetary shocks. *Astrophys J* (2017) 844:51. doi:10.3847/1538-4357/aa7bef
106. Pitňa A, Šafránková J, Němeček Z, Franci L, Pi G, and Montagud Camps V. Characteristics of solar wind fluctuations at and below ion scales. *Astrophys J* (2019) 879:82. doi:10.3847/1538-4357/ab22b8
107. Podesta JJ, and Borovsky JE. Scale invariance of normalized cross-helicity throughout the inertial range of solar wind turbulence. *Phys Plasmas* (2010) 17:112905. doi:10.1063/1.3505092
108. Rakhmanova LS, Riazantseva MO, Zastenker GN, and Verigin MI. Effect of the magnetopause and bow shock on characteristics of plasma turbulence in the earth's magnetosheath. *Geomagnetism Aeronomy* (2018) 58:718–27. doi:10.1134/S0016793218060129
109. Riazantseva MO, Rakhmanova LS, Zastenker GN, Yermolaev YI, Lodkina IG, and Chesalin LS. Small-scale plasma fluctuations in fast and slow solar wind streams. *Cosmic Res* (2020) 57:434–42. doi:10.1134/S0010952519060078
110. Rice WKM, Zank GP, and Li G. Particle acceleration and coronal mass ejection driven shocks: shocks of arbitrary strength. *J Geophys Res Space Phys* (2003) 108:1369. doi:10.1029/2002JA009756
111. Richardson IG. Identification of interplanetary coronal mass ejections at Ulysses using multiple solar wind signatures. *Solar Phys* (2014) 289:3843–94. doi:10.1007/s11207-014-0540-8
112. Richardson IG. Solar wind stream interaction regions throughout the heliosphere. *Living Rev Solar Phys* (2018) 15:1. doi:10.1007/s41116-017-0011-z
113. Roberts OW, Toledo-Redondo S, Perrone D, Zhao J, Narita Y, Gershman D, et al. Ion-scale kinetic alfvén turbulence: MMS measurements of the alfvén ratio in the magnetosheath. *Geophys Res Lett* (2018) 45:7974–84. doi:10.1029/2018GL078498
114. Russell CT. Physics of collisionless shocks. *Adv Space Res* (1995) 15:403.
115. Safránková J, Němeček Z, Němec F, Přech L, Pitňa A, Chen CHK, et al. Solar wind density spectra around the ion spectral break. *Astrophys J* (2015) 803:107. doi:10.1088/0004-637X/803/2/107
116. Safránková J, Němeček Z, Němec F, Přech L, Chen CHK, and Zastenker GN. Power spectral density of fluctuations of bulk and thermal speeds in the solar wind. *Astrophysical J* (2016) 825:121. doi:10.3847/0004-637X/825/2/121
117. Safránková J, Němeček Z, Němec F, Verscharen D, Chen CHK, Ďurovcová T, et al. Scale-dependent polarization of solar wind velocity fluctuations at the inertial and kinetic scales. *Astrophys J* (2019) 870:40. doi:10.3847/1538-4357/aaf239
118. Sahraoui F, Hadid L, and Huang S. Magnetohydrodynamic and kinetic scale turbulence in the near-Earth space plasmas: a (short) biased review. *Rev Mod Plasma Phys* (2020) 4:4. doi:10.1007/s41614-020-0040-2
119. Schekochihin AA, Cowley SC, Dorland W, Hammett GW, Howes GG, Quataert E, et al. Astrophysical gyrokinetics: kinetic and fluid turbulent cascades in magnetized weakly collisional plasmas. *Astrophys J Suppl* (2009) 182:310–77. doi:10.1088/0067-0049/182/1/310
120. Shebalin JV, Matthaeus WH, and Montgomery D. Anisotropy in MHD turbulence due to a mean magnetic field. *J Plasma Phys* (1983) 29:525–47. doi:10.1017/S0022377800000933
121. Siscoe G, MacNeice PJ, and Odstrcil D. East-west asymmetry in coronal mass ejection geoeffectiveness. *Space Weather* (2007) 5:S04002. doi:10.1029/2006SW000286
122. Siscoe G, and Odstrcil D. Ways in which ICME sheaths differ from magnetosheaths. *J Geophys Res Space Phys* (2008) 113:A00B07. doi:10.1029/2008JA013142
123. Soucek J, Escoubet CP, and Grison B. Magnetosheath plasma stability and ulf wave occurrence as a function of location in the magnetosheath and upstream bow shock parameters. *J Geophys Res Space Phys* (2015) 120:2838–50. doi:10.1002/2015JA021087
124. Soucek J, Lucek E, and Dandouras I. Properties of magnetosheath mirror modes observed by cluster and their response to changes in plasma parameters. *J Geophys Res Space Phys* (2008) 113. doi:10.1029/2007JA012649
125. Spangler SR, Leckband JA, and Cairns IH. Observations of the parametric decay instability of nonlinear magnetohydrodynamic waves. *Phys Plasmas* (1997) 4:846–55. doi:10.1063/1.872183
126. Stone RG, and Tsurutani BT. *Collisionless shocks in the heliosphere. A tutorial review. Geophysical Monograph Series*. Washington DC: American Geophysical Union (1985), 34. doi:10.1029/GM034
127. Trattner KJ, Mobius E, Scholer M, Klecker B, Hilchenbach M, and Luehr H. Statistical analysis of diffuse ion events upstream of the Earth's bow shock. *J Geophys Res* (1994) 99:13389–400. doi:10.1029/94JA00576
128. Tsurutani BT, Gonzalez WD, Tang F, Akasofu SI, and Smith EJ. Origin of interplanetary southward magnetic fields responsible for major magnetic storms near solar maximum (1978-1979). *J Geophys Res* (1988) 93:8519–31. doi:10.1029/JA093iA08p08519
129. Tsurutani BT, and Stone RG. *Collisionless shocks in the heliosphere: reviews of current research. Geophysical Monograph Series*. Washington, DC: American Geophysical Union (1985), 35.
130. Tu C-Y, and Marsch E. MHD structures, waves and turbulence in the solar wind: observations and theories. *Space Sci Rev* (1995) 73:1–210. doi:10.1007/BF00748891
131. Velli M, Grappin R, and Mangeney A. Turbulent cascade of incompressible unidirectional alfvén waves in the interplanetary medium. *Phys Rev Lett* (1989) 63:1807–10. doi:10.1103/PhysRevLett.63.1807
132. Volkmer PM, and Neubauer FM. Statistical properties of fast magnetoacoustic shock waves in the solar wind between 0.3 AU and 1 AU: Helios-1, 2 observations. *Ann Geophys* (1985) 3:1–12.
133. Webb DF, Cliver EW, Crooker NU, Cry OCS, and Thompson BJ. Relationship of halo coronal mass ejections, magnetic clouds, and magnetic storms. *J Geophys Res* (2000) 105:7491–508. doi:10.1029/1999JA000275
134. Whang YC, Zhou J, Lepping RP, and Ogilvie KW. Interplanetary slow shock observed from wind. *Geophys Res Lett* (1996) 23:1239–42. doi:10.1029/96GL01358
135. Wilson LB, Koval A, Sibeck DG, Szabo A, Cattell CA, Kasper JC, et al. Shocklets, SLAMS, and field-aligned ion beams in the terrestrial foreshock. *J Geophys Res Space Phys* (2013) 118:957–66. doi:10.1029/2012JA018186
136. Wu CC, Wu ST, and Dryer M. Generation and evolution of interplanetary slow shocks. *Ann Geophysicae* (1996) 14:375–82. doi:10.1007/s00585-996-0375-1
137. Wu H, Verscharen D, Wicks RT, Chen CHK, He J, and Nicolaou G. The fluid-like and kinetic behavior of kinetic alfvén turbulence in space plasma. *Astrophys J* (2019) 870:106. doi:10.3847/1538-4357/aaef77
138. Xu F, and Borovsky JE. A new four-plasma categorization scheme for the solar wind. *J Geophys Res Space Phys* (2015) 120:70–100. doi:10.1002/2014JA020412
139. Yermolaev YI, Lodkina IG, Nikolaeva NS, and Yermolaev MY. Statistical study of interplanetary condition effect on geomagnetic storms. *Cosmic Res* (2010) 48:485–500. doi:10.1134/S0010952510060018
140. Zank GP, Adhikari L, Hunana P, Shiota D, Bruno R, and Telloni D. Theory and transport of nearly incompressible magnetohydrodynamic turbulence. *Astrophys J* (2017) 835:147. doi:10.3847/1538-4357/835/2/147

141. Zank GP, Dosch A, Hunana P, Florinski V, Matthaeus WH, and Webb GM. The transport of low-frequency turbulence in astrophysical flows. I. Governing equations. *Astrophys J* (2012) 745:35. doi:10.1088/0004-637X/745/1/35
142. Zank GP, Li G, Florinski V, Hu Q, Lario D, and Smith CW. Particle acceleration at perpendicular shock waves: model and observations. *J Geophys Res Space Phys* (2006) 111:A06108. doi:10.1029/2005JA011524
143. Zank GP, and Matthaeus WH. Nearly incompressible fluids. II: magnetohydrodynamics, turbulence, and waves. *Phys Fluids A* (1993) 5: 257–73. doi:10.1063/1.858780
144. Zank GP, Nakanotani M, Zhao LL, Adhikari L, and Telloni D. Spectral anisotropy in 2D plus slab magnetohydrodynamic turbulence in the solar wind and upper corona. *Astrophys J* (2020) 900:115. doi:10.3847/1538-4357/abad30
145. Zank GP, Zhou Y, Matthaeus WH, and Rice WKM. The interaction of turbulence with shock waves: a basic model. *Phys Fluids* (2002) 14:3766–74. doi:10.1063/1.1507772
146. Zhang J, Richardson IG, and Webb DF. Interplanetary origin of multiple-dip geomagnetic storms. *J Geophys Res Space Phys* (2008) 113:A00A12. doi:10.1029/2008JA013228
147. Zhang J, Richardson IG, Webb DF, Gopalswamy N, Huttunen E, Kasper JC, et al. Solar and interplanetary sources of major geomagnetic storms (Dst <= -100 nT) during 1996-2005. *J Geophys Res Space Phys* (2007) 112: A10102. doi:10.1029/2007JA012321
148. Zhao JS, Voitenko Y, Yu MY, Lu JY, and Wu DJ. Properties of short-wavelength oblique alfvén and slow waves. *Astrophys J* (2014) 793:107. doi:10.1088/0004-637X/793/2/107
149. Zhou Y, Matthaeus WH, and Dmitruk P. Colloquium: magnetohydrodynamic turbulence and time scales in astrophysical and space plasmas. *Rev Mod Phys* (2004) 76:1015–35. doi:10.1103/RevModPhys.76.1015

Conflict of Interest: The authors declare that the research was conducted in the absence of any commercial or financial relationships that could be construed as a potential conflict of interest.

frontiers in Astronomy and Space Sciences

MINI REVIEW
published: 05 May 2021
doi: 10.3389/fspas.2021.621040

Plasma Dynamics in Low-Electron-Beta Environments

Stanislav Boldyrev[1,2]*, *Nuno F. Loureiro*[3] *and Vadim Roytershteyn*[2]

[1]Department of Physics, University of Wisconsin-Madison, Madison, WI, United States, [2]Center for Space Plasma Physics, Space Science Institute, Boulder, CO, United States, [3]Plasma Science and Fusion Center, Massachusetts Institute of Technology, Cambridge, MA, United states

Recent *in situ* measurements by the MMS and Parker Solar Probe missions bring interest to small-scale plasma dynamics (waves, turbulence, magnetic reconnection) in regions where the electron thermal energy is smaller than the magnetic one. Examples of such regions are the Earth's magnetosheath and the vicinity of the solar corona, and they are also encountered in other astrophysical systems. In this brief review, we consider simple physical models describing plasma dynamics in such low-electron-beta regimes, discuss their conservation laws and their limits of applicability.

Keywords: collisionless plasma, magnetic fields, heliosphere, solar wind, solar corona, earth magnetosheath, earth magnetosphere, plasma turbulence

OPEN ACCESS

Edited by:
Alessandro Retino, UMR7648 Laboratoire de physique des plasmas (LPP), France

Reviewed by:
Francesco Malara, University of Calabria, Italy
Mikhail V. Medvedev, University of Kansas, United States

***Correspondence:**
Stanislav Boldyrev
boldyrev@wisc.edu

Specialty section:
This article was submitted to Space Physics, a section of the journal Frontiers in Astronomy and Space Sciences

Received: *24 October 2020*
Accepted: *25 January 2021*
Published: *05 May 2021*

Citation:
Boldyrev S, Loureiro NF and Roytershteyn V (2021) Plasma Dynamics in Low-Electron-Beta Environments. Front. Astron. Space Sci. 8:621040. doi: 10.3389/fspas.2021.621040

INTRODUCTION

Astrophysical plasmas (e.g., the Interstellar medium, solar wind, etc) are often in a state of a rough equipartition between the kinetic energies of the particles and the energy of the magnetic fields. However, there are important astrophysical and space environments, such as the Earth's magnetosphere and magnetosheath, and the solar corona and its vicinity, that are characterized by low electron plasma beta, that is, low ratio of electron thermal to magnetic energy, $\beta_e = 8\pi n_e T_e/B^2$ (e.g., Cranmer et al., 2009; Štverák et al., 2015; Bale et al., 2016; Chen et al., 2014), where n_e and T_e are the electron density and temperature, and B is the magnetic field strength. Such plasmas are also nearly collisionless in that the characteristic times of turbulent fluctuations are much shorter than the Coulomb collision times. The interest in plasma dynamics in low-beta regimes is also fueled by recent *in situ* measurements by NASA's MMS and Parker Solar Probe missions, as well as by the measurements expected from the Solar Orbiter spacecraft (e.g., Phan et al., 2018; Chen et al., 2020; Bale et al., 2019; Kasper et al., 2019). In this contribution we briefly review the theoretical frameworks for studying collisionless low-electron-beta plasma dynamics.

In a weakly collisional plasma, the electrons and the ions do not exchange energy efficiently due to the strong difference in their masses. Therefore, it is a common situation that the ion temperature is different from the electron one. In our treatment of the problem we will, therefore, distinguish between the ion and electron betas $\beta_s = 8\pi n_s T_s/B^2$, where $s = \{e, i\}$. While we will concentrate on the case of small electron beta $\beta_e \ll 1$, we will not necessarily assume the same for the ion beta, and will consider the cases of $\beta_i \ll 1$ as well as $\beta_i \sim 1$. For example, the Earth's magnetosphere is characterized by $\beta_i \ll m_e/m_i$, $\beta_e \ll m_e/m_i$, the solar corona and its vicinity correspond to $\beta_e \lesssim 0.01$ and $\beta_i \lesssim 0.1$, the Earth's magnetosheath $\beta_e \sim 0.1$, $\beta_i \lesssim 1$. Other environments with low electron beta include downstream regions of collisionless shocks and magnetospheres of accretion discs (e.g., Quataert, 1998; Vink et al., 2015; Ghavamian et al., 2013).

The most rigorous treatment of a collisionless plasma is provided by the kinetic framework. However, kinetic framework presents considerable challenges for theoretical and especially numerical treatments (but see some examples in e.g. (Schekochihin et al., 2009; Servidio et al.,

2012; Valentini et al., 2017; Grošelj, 2019; Roytershteyn et al., 2019; Franci et al., 2020)). In many important cases, a simplified fluid-like description is possible that is much more physically transparent and allows for efficient numerical studies of plasma waves, turbulence, magnetic reconnection, structure formation, etc. The derivations of such simplified models can be performed using various approaches (reduced two-fluid, gyrofluid, gyrokinetic, kinetic, etc.), and such derivations are scattered in the literature. In this brief review, we discuss several models which we believe are relevant for the above mentioned space physics applications. Our goal is to present a unifying physical derivation of the governing equations, describe the corresponding conservation laws, and discuss the limits of applicability of each of the models. We hope our presentation will be useful for space physicists or astrophysicists who are not necessarily experts in plasma physics.

Model Equations

In this section we present a general derivation of the model equations, and then consider the limits of β_i and β_e mentioned in the introduction. As it is generally the case in magnetized plasma turbulence, we assume the presence of a uniform magnetic field (the guide field), which mimics the magnetic field of external sources (i.e., magnetospheric field) or the magnetic field generated by large-scale turbulent motions. At small scales, the magnetic fluctuations are small, so we separate them from the guide field $\mathbf{B} = B_0\widehat{\boldsymbol{z}} + \delta\mathbf{B}$.[1] We consider the case of small electron beta, so it will be easy to start with the equations describing the electron dynamics where we can neglect the effects related to the electron gyroradius. There are analytical and observational reasons to believe that small-scale fluctuations are oblique in that their wavenumbers along the guide field are much smaller than the wavenumbers in the perpendicular direction, $k_\parallel \ll k_\perp$ (e.g., Shebalin et al., 1983; Chen, 2016). Moreover, in the case of strong developed turbulence, the magnetic fluctuations tend to approach the so-called critical balance state (e.g., Goldreich and Sridhar, 1995; Perez and Boldyrev, 2010), which can be expressed by the following self-consistent ordering of the perturbation parameters,

$$k_\parallel/k_\perp \sim |\delta\mathbf{B}|/B_0 \sim \delta n/n_0 \ll 1. \tag{1}$$

Our general approach in this section is similar to that adopted in (e.g., Chen and Boldyrev, 2017; Milanese et al., 2020), while more refined derivations can be found in (Passot et al., 2017; Passot et al., 2018) where finite Larmor radius corrections are taken into account. In a collisionless plasma, the electron gyro orbits drift in the field-perpendicular direction. The modes we are interested in have frequencies that are much lower than the electron cyclotron frequency Ω_e. To the zeroth and first orders in the small parameter ω/Ω_e, this motion consists of the standard $E\times B$ drift and the polarization drift,

$$\mathbf{v}_\perp = \mathbf{v}_E - \frac{m_e c}{eB^2}\mathbf{B}\times\frac{d_E}{dt}\mathbf{v}_E, \tag{2}$$

where $\mathbf{v}_E = c(\mathbf{E}\times\mathbf{B})/B^2$ is the $E\times B$ drift, the total time derivative is $d_E/dt \equiv \partial/\partial t + \mathbf{v}_E\cdot\nabla$, and e is the modulus of the electron charge. (Obviously, for $\omega \ll \Omega_i$ an equation similar to **Eq. 2** can be written for the ions as well.) In the zeroth-order term (the $\mathbf{v}_E$ velocity) we need to substitute the magnetic field expanded up to the first order, that is, $\mathbf{B} = \mathbf{B}_0 + \delta\mathbf{B}$ and $B^2 \approx B_0^2 + 2B_0\delta B_z$, while in the polarization drift (the second term in **Eq. 2**) we keep only the zeroth-order magnetic field. The magnetic field does not constrain the electron motion in the field-parallel direction, so that the fluctuating parallel electric field will drive the electric current $J_\parallel$. It is easy to see, however, that due to their large masses, the ions will respond to the fluctuating electric field with much smaller velocities, so that the current will be dominated by the electrons, $J_\parallel = -ne v_\parallel$. Since, due to small fluctuations, the magnetic-field lines deviate from the z-direction only slightly, the field-parallel components of the vector fields are very close to their z-components, i.e., $J_\parallel \approx J_z$. This, however, is not true for nearly field-perpendicular wave vectors, so that $k_\parallel \neq k_z$. For this reason, the gradient in the field-parallel direction will be given to the first order in magnetic field fluctuations by

$$\nabla_\parallel = \frac{\mathbf{B}}{B}\cdot\nabla = \partial/\partial z + (\delta\mathbf{B}_\perp/B_0)\cdot\nabla, \tag{3}$$

which is also consistent with the adopted ordering **(1)**. In the same approximation, the field-perpendicular gradients are the same as gradients in the horizontal coordinate plane, $\nabla_\perp = (\partial/\partial x, \partial/\partial y)$.

Finally, we need to relate the parallel electric current to the fluctuating magnetic and electric fields. From the Ampere-Maxwell equation, we have

$$J_z = -\frac{c}{4\pi}\nabla_\perp^2 A_z + \frac{1}{4\pi c}\frac{\partial^2}{\partial t^2}A_z \approx -\frac{c}{4\pi}\nabla_\perp^2 A_z, \tag{4}$$

where $\mathbf{A}$ is the vector potential, $\delta\mathbf{B}_\perp = -\widehat{\mathbf{z}}\times\nabla_\perp A_z$, the Lorentz gauge is assumed for simplicity, and in the last line we neglected the time derivative of the vector potential, since $\omega \sim k_\parallel v_A \ll k_\perp c$. Here v_A is the Alfven speed. The last condition amounts to neglecting the displacement current in the Ampere-Maxwell equation. We can now substitute $\mathrm{v}_\perp$ and $v_\parallel$ expressed through the electric and magnetic potentials, in the electron continuity equation $\partial_t n_e + \nabla_\perp(n_e\mathbf{v}_\perp) + \nabla_\parallel(n_e v_\parallel) = 0$, and get after somewhat lengthy but straightforward algebra (for a more detailed discussion we refer the reader to (Chen and Boldyrev, 2017; Milanese et al., 2020):

$$\frac{\partial}{\partial t}\left(\frac{\delta n_e}{n_0} - \frac{\delta B_z}{B_0} + \frac{m_e c^2}{eB_0^2}\nabla_\perp^2\phi\right) + \frac{c}{B_0}\left(\widehat{z}\times\nabla_\perp\phi\right)\cdot\nabla_\perp\left(\frac{\delta n_e}{n_0} - \frac{\delta B_z}{B_0} + \frac{m_e c^2}{eB_0^2}\nabla_\perp^2\phi\right) = -\frac{c}{4\pi n_0 e}\nabla_\parallel\nabla_\perp^2 A_z, \tag{5}$$

[1]Such a set up is an approximation based on two properties that are believed to be characteristic of strong magnetic turbulence. First is the locality of turbulence, implying that significant nonlinear interaction occurs among fluctuations of comparable scales. Second is the observation that the dynamics at a given small scale are mediated by the presence of a guide magnetic field. However, the strongest magnetic fluctuations are provided by the largest eddies, therefore, such a magnetic field is almost uniform at the small scales of interest.

where ϕ is the electric potential.

In order to proceed further, we need to specify what particular limits we consider. We will do this in the following sections. Here, we simply assume that the electron and ion gyroradii are sufficiently small and we address the scales above the ion and electron gyroradii. We also assume that the frequencies of the fluctuations are much smaller than the cyclotron frequencies of the plasma species. In this case, we can write an equation analogous to **Eq. 5** for the ions (by replacing $m_e \to m_i$, $e \to -e$, and neglecting $v_\parallel$ in the ion equation because of ion inertia), and subtract one equation from the other. As a result, we get

$$\frac{\partial}{\partial t}\left(\rho - \frac{n_0 m_i c^2}{B_0^2}\nabla_\perp^2\phi\right) + \frac{c}{B_0}\left(\hat{z}\times\nabla_\perp\phi\right)\cdot\nabla_\perp\left(\rho - \frac{n_0 m_i c^2}{B_0^2}\nabla_\perp^2\phi\right) = \frac{c}{4\pi}\nabla_\parallel\nabla_\perp^2 A_z, \tag{6}$$

where $\rho = (\delta n_i - \delta n_e)e$ is the density of the electric charge, and we assume singly charged ions. In this equation, we have neglected the electron polarization drift velocity as it is smaller than the ion one by m_e/m_i. By using Gauss's law $\rho = -(1/4\pi)\nabla_\perp^2\phi$, and normalizing the variables as

$$\tilde{\phi} = \phi c/B_0, \quad \tilde{A}_z = A_z\Big/\sqrt{4\pi n_0 m_i}, \tag{7}$$

one rewrites this equation as a charge continuity equation:

$$\frac{\partial}{\partial t}\nabla_\perp^2\phi + \left(\hat{z}\times\nabla_\perp\phi\right)\cdot\nabla_\perp\nabla_\perp^2\phi = -\frac{v_A}{1+v_A^2/c^2}\nabla_\parallel\nabla_\perp^2 A_z, \tag{8}$$

where for simplicity we have omitted the overtilde signs. In this equation, $v_A = B_0/\sqrt{4\pi m_i n_0}$ is the Alfvén velocity and, in the normalized variables (7), the parallel gradient has the form

$$\nabla_\parallel = \partial/\partial z - v_A^{-1}\left(\hat{z}\times\nabla_\perp A_z\right)\cdot\nabla_\perp. \tag{9}$$

The term $v_A^2/c^2 = \Omega_i^2/\omega_{pi}^2$ reflects the deviation from quasineutrality of the plasma. Here, Ω_i is the ion cyclotron frequency and ω_{pi} is the ion plasma frequency. When this term is small, $\Omega_i^2/\omega_{pi}^2 \ll 1$, we have $|\delta n_i - \delta n_e| \ll \delta n$, and the charge density fluctuations can be neglected in the charge continuity equation, $\partial\rho/\partial t \ll \nabla_\perp\cdot\mathbf{J}_\perp$. Interestingly, even a mild breakdown of the analogous quasineutrality condition for the electrons, $\Omega_e^2/\omega_{pe}^2 \ll 1$, leads to a difference between the electron and ion density fluctuations, which may be significant for the plasma dynamics (e.g., Roytershteyn et al., 2019). We will assume in our consideration that the quasineutrality condition holds for both species as it is a common situation in many natural applications (obviously, it always holds better for the heavier particles). We however mention that when this condition is broken for the electrons, that is, $\Omega_e^2/\omega_{pe}^2 \gtrsim 1$ (we will call this case the low plasma density case), our derivation has narrower limits of applicability. Indeed, from **Eq. 4** for the electron parallel current, we can estimate for the electron velocity fluctuations at scale $\lambda \sim 1/k_\perp$, $v_{\parallel,\lambda}^2/c^2 \sim (k_\perp d_e)^2(\delta B_\lambda/B_0)^2(\Omega_e/\omega_{pe})^2$ Here $d_e = c/\omega_{pe}$ is the electron inertial scale. As our case is nonrelativistic, we therefore have to require

$$(k_\perp d_e)^2(\delta B_\lambda/B_0)^2 \ll \omega_{pe}^2\Big/\Omega_e^2, \tag{10}$$

which imposes an additional restriction on the fluctuations amplitudes and scales in the low-density case. When restriction **(10)** is not satisfied, we cannot neglect the relativistic effects and the displacement current, and cannot assume the ordering $k_\parallel \ll k_\perp$.

We need to supplement the charge continuity **Eq. 8** with the equation for the parallel component of the electron velocity field, which reads

$$\frac{\partial \boldsymbol{v}_\parallel}{\partial t} + (\boldsymbol{v}_E\cdot\nabla_\perp)\boldsymbol{v}_\parallel = -\frac{e}{m_e}E_\parallel - \frac{1}{m_e n_0}\nabla_\parallel p_e. \tag{11}$$

Expressing the parallel velocity field through the electric current, and substituting for the electric field $E_\parallel = -\nabla_\parallel\phi - \partial A_z/\partial t$ (where we use the previously discussed approximation $A_\parallel \approx A_z$) we obtain using the same normalization for A_z and ϕ as in **Eq. 7**,

$$\frac{\partial}{\partial t}\left(1-d_e^2\nabla_\perp^2\right)A_z + \left(\hat{z}\times\nabla_\perp\phi\right)\cdot\nabla_\perp\left(1-d_e^2\nabla_\perp^2\right)A_z = -v_A\frac{\partial}{\partial z}\phi + \frac{d_i}{n_0 m_i}\nabla_\parallel p_e. \tag{12}$$

In general, there is no rigorous closure for the pressure term p_e in hydrodynamic-type equations describing a collisionless plasma. One, however, can consider several limiting cases, when approximate expressions may be obtained.

Case of $\beta_e \ll m_e/m_i$ and $\beta_i \ll 1$ (Cold Electrons and Ions)

First is the case of cold electrons, when the typical phase velocity of the fluctuations is larger than the thermal velocity of the electrons, $\omega/k_\parallel \gg v_{Te}$; the equations that we discuss in this section have been considered in (Loureiro and Boldyrev, 2018; Milanese et al., 2020). Assuming that the fluctuations are of the Alfvén type, this condition means that $\beta_e \ll m_e/m_i$. For the ions, it means $\beta_i \ll 1$. In this case, we may neglect the electron pressure in **Eq. 12**. We can therefore use the following system of equations in the case of cold plasma:

$$\frac{\partial}{\partial t}\nabla_\perp^2\phi + \left(\hat{z}\times\nabla_\perp\phi\right)\cdot\nabla_\perp\nabla_\perp^2\phi = -v_A\nabla_\parallel\nabla_\perp^2 A_z, \tag{13}$$

$$\frac{\partial}{\partial t}\left(1-d_e^2\nabla_\perp^2\right)A_z + \left(\hat{z}\times\nabla_\perp\phi\right)\cdot\nabla_\perp\left(1-d_e^2\nabla_\perp^2\right)A_z = -v_A\frac{\partial}{\partial z}\phi. \tag{14}$$

The linear modes supported by this system of equations have the dispersion relation

$$\omega^2 = \frac{k_z^2 v_A^2}{1+k_\perp^2 d_e^2}, \tag{15}$$

and are known as the inertial Alfvén modes. At large scales $k_\perp d_e \ll 1$, they turn into the magnetohydrodynamic shear Alfvén modes as the governing system **(13)**, **(14)** itself turns into the reduced MHD equations (e.g., Kadomtsev and Pogutse, 1974; Strauss, 1976; Biskamp, 2003; Tobias et al., 2013). The term containing the electron inertial scale d_e should be kept if this scale is larger than the ion gyroscale, ρ_i. Since $d_e^2/\rho_i^2 = (m_e/m_i)/\beta_i$, the electron inertial effects are, therefore, relevant when $\beta_i \ll m_e/m_i$. In the opposite limit, the electron inertial terms are negligible and

Eqs. 13, **14** turn into the reduced MHD equations in the whole range of scales $k_\perp^2\rho_i^2 \ll 1$. It is interesting to point out the conservation laws of these equations, the energy and generalized helicity

$$E = \int \left[(\nabla_\perp A_z)^2 + d_e^2 \left(\nabla_\perp^2 A_z\right)^2 + \left(\nabla_\perp \phi\right)^2 \right] d^3 x, \tag{16}$$

$$H = \int \left[\nabla_\perp^2 \phi \left(1 - d_e^2 \nabla_\perp^2\right) A_z \right] d^3 x. \tag{17}$$

The generalized helicity conservation law for this case has been considered in Loureiro and Boldyrev (2018) and Milanese et al. (2020). The latter paper also discusses its nontrivial role in the turbulent energy cascade at kinetic scales $k_\perp d_e > 1$, in particular, in establishing the so-called dynamic phase alignment of magnetic and velocity fluctuations at small scales.

Case of $m_e/m_i \ll \beta_e \ll 1$ and $\beta_i \ll 1$ (Hot Electrons, Cold Ions)

In the considered limit, the systems of equations have been derived in e.g., (Camargo et al., 1996; Terry et al., 2001; Boldyrev et al., 2015). In this case the electrons are hot in that their thermal velocity is much larger than the phase velocity of the waves. The electron could thus be expected to quickly adjust to the electric potential ϕ' built in a plasma, $\delta n_e/n_0 \approx e\phi'/T_e$ with $T_e = const$. However, this is the electric potential existing in a fluid element drifting with the $E \times B$ velocity. Such an electric potential is different from the electric potential ϕ measured in the lab frame, therefore, the above formula is not very helpful. Instead, we express the pressure as $p_e = nT_e$, and use **Eq. 5** for the electron density. We notice that in this equation, the magnetic fluctuations $\delta B_z/B_0$ are smaller than $\delta n/n_0$ in a low beta regime. Indeed, from the plasma momentum equation (the sum of the electron and ion momentum equations), one can derive to the leading order the (total) pressure balance condition $\nabla_\perp p = 0$, which gives $(\delta B_z/B_0) = -(\beta_e/2)(\delta n/n_0)$. We can, therefore, neglect the magnetic fluctuations in **Eq. 5**. We also neglect the electron polarization drift, and obtain

$$\frac{\partial}{\partial t}\left(\frac{\delta n}{n_0}\right) + \left(\hat{z} \times \nabla_\perp \phi\right) \cdot \nabla_\perp \left(\frac{\delta n}{n_0}\right) = -d_i \nabla_\parallel \nabla_\perp^2 A_z, \tag{18}$$

which, together with **Eqs. 12**, **13**, forms a closed system of equations for the considered case.

The dispersion relation for the linear waves in this case is:

$$\omega^2 = \frac{k_z^2 v_A^2 \left(1 + k_\perp^2 \rho_s^2\right)}{\left(1 + k_\perp^2 d_e^2\right)}, \tag{19}$$

where $\rho_s^2 = v_s^2/\Omega_i^2$ is the ion-acoustic radius and $v_s^2 = T_e/m_i$ is the ion acoustic speed. Since $\rho_s^2/d_e^2 = \beta_e/(m_e/m_i)$, this formula shows that depending on the value of the electron beta, either the ion-acoustic scale or the electron inertial scale becomes dominant. The quadratic conservation laws for this case are the energy and generalized enstrophy:

$$E = \int \left[(\nabla_\perp A_z)^2 + d_e^2 \left(\nabla_\perp^2 A_z\right)^2 + \left(\nabla_\perp \phi\right)^2 + \rho_s^2 \left(\frac{\delta n}{n_0}\right)^2 \right] d^3 x, \tag{20}$$

$$\Omega_2 = \int \left(\frac{\delta n}{n_0} - \frac{1}{\Omega_i}\nabla_\perp^2 \phi\right)^2 d^3 x. \tag{21}$$

In fact, there are infinitely many conserved integrals of the form

$$\Omega_n = \int \left(\frac{\delta n}{n_0} - \frac{1}{\Omega_i}\nabla_\perp^2 \phi\right)^n d^3 x, \tag{22}$$

which simply reflects the fact that the two-dimensional $E \times B$ flow is incompressible, and the integrand in Ω_n is passively advected by such a flow.

Case of $m_e/m_i \ll \beta_e \ll 1$ and $\beta_i \lesssim 1$ (Hot Electrons and Ions)

We now consider the case of relatively high temperatures of the electrons and the ions. In this case, the ion gyroscale is not small. At scales close to the ion gyroscale, fluid-like models are generally not accurate, and one has to use full kinetic treatment. However, at larger and smaller scales one can formulate simplified models. Obviously, at hydrodynamic scales $k_\perp^2\rho_i^2 \ll 1$, a good description is provided by the reduced MHD model. Here we will be interested in scales smaller than the ion gyroscale, $k_\perp^2\rho_i^2 \gg 1$. In this limit, the system of equations has been derived in (Chen and Boldyrev, 2017; Passot et al., 2017; Passot et al., 2018). As can be checked later, in this case the ions can be considered hot, $\omega^2 \ll k^2 v_{Ti}^2$, and non magnetized. Therefore, their density, and by quasineutrality the density of the electrons, will adjust to the electric potential existing in a plasma according to the Boltzmann law, $\delta n/n_0 \approx -e\phi/T_i$. Similarly to the previous case, the magnetic intensity fluctuations can be evaluated from the momentum equation, where both the ion and the electron temperatures can be easily taken into account as both species are now hot:

$$(\delta B_z/B_0) = -(\beta_e/2 + \beta_i/2)(\delta n/n_0) \approx -(\beta_i/2)(\delta n/n_0). \tag{23}$$

We can now remove the density and magnetic field fluctuations in the electron **Eqs. 5, 12** in favor of the electric potential, and obtain:

$$\frac{\partial}{\partial t}\left(1 + \frac{2}{\beta_i} - d_e^2 \nabla_\perp^2\right)\phi = v_A d_i^2 \nabla_\parallel \nabla_\perp^2 A_z, \tag{24}$$

$$\frac{\partial}{\partial t}\left(1 - d_e^2 \nabla_\perp^2\right) A_z + \left(\hat{z} \times \nabla_\perp \phi\right) \cdot \nabla_\perp \left(1 - d_e^2 \nabla_\perp^2\right) A_z = -v_A \frac{\partial}{\partial z}\phi. \tag{25}$$

The linear modes described by this system have the dispersion relation:

$$\omega^2 = \frac{k_z^2 v_A^2 k_\perp^2 d_i^2}{\left(1 + k_\perp^2 d_e^2\right)\left(1 + 2/\beta_i + k_\perp^2 d_e^2\right)}; \tag{26}$$

such modes were termed the inertial kinetic-Alfvén modes in Chen and Boldyrev (2017). A particular case of these waves, corresponding to the limit $2/\beta_i \gg 1 + k_\perp^2 d_e^2$, has been previously analyzed in Shukla et al. (2009), Agarwal et al. (2011); such an additional constraint obviously implies a more limited region of applicability of the model, namely, $k_\perp^2 \rho_i^2 \ll m_i/m_e$. The considered system has two quadratic conservation laws, the energy and generalized helicity (Boldyrev and Loureiro, 2020):

$$E = \int \left[\phi\left(1 + \frac{2}{\beta_i} - d_e^2 \nabla_\perp^2\right)\phi - d_i^2 \left(\nabla_\perp^2 A_z\right)\left(1 - d_e^2 \nabla_\perp^2\right) A_z \right] d^3x, \tag{27}$$

$$H = \int \left(1 + \frac{2}{\beta_i} - d_e^2 \nabla_\perp^2\right)\phi \left(1 - d_e^2 \nabla_\perp^2\right) A_z \, d^3x. \tag{28}$$

The derived conservation laws play an important role in turbulent cascades as well as in the formation of current sheets that may become subject to the tearing instability and magnetic reconnection (e.g., Boldyrev and Loureiro, 2019; Vega et al., 2020). Interestingly, this system of equations turns out to be rather universal. It is structurally identical to the system describing the nonlinear whistler modes at sub-ion scales (Chen and Boldyrev, 2017), moreover, at scales $k_\perp^2 d_e^2 \gg 1 + 2/\beta_i$ it is also applicable to a nonrelativistic pair plasma (Loureiro and Boldyrev, 2018) as well as to rapidly rotating non-conducting fluids, see, e.g., (Milanese et al., 2020).

CONCLUSION

We have described several physical models of nonlinear plasma dynamics at low electron beta, which are relevant for space physics applications ranging from the Earth's magnetosphere to the magnetosheath to the solar corona. These models may be helpful for understanding turbulent cascades (that are generally nontrivial in the presence of two conserved quantities (Loureiro and Boldyrev, 2018; Milanese et al., 2020), processes of magnetic reconnection (e.g., Boldyrev and Loureiro, 2019; Loureiro and Boldyrev, 2020), and other linear and nonlinear wave phenomena. Our fluid-like models do not include dissipation effects, like Landau damping, that cannot be rigorously treated in fluid-like models and that require kinetic approach (e.g., Chen et al., 2019; Horvath et al., 2020). The kinetic dissipation effects are especially relevant when the scales of fluctuations approach the gyroscales of plasma species or when the phase velocities of the waves are comparable to the thermal velocities of the particles, see, for instance the kinetic treatment developed for the case $\beta_e \sim m_e/m_i$ in Zocco and Schekochihin (2011). However, it should be noted that the ordering assumed in our models implies that the linear and nonlinear terms are on the same order (the co-called critical balance condition), which means that dissipative kinetic terms may be included as linear terms in our equations (e.g., Li et al., 2016; Passot et al., 2017; Passot et al., 2018), which should not qualitatively alter the nonlinear dynamics captured by the discussed models.

AUTHOR CONTRIBUTIONS

SB, NL, and VR performed the research; SB wrote the paper.

FUNDING

The work of SB was partly supported by the NSF under Grant Nos. NSF PHY-1707272 and NSF PHY-2010098, by the NASA under Grant No. NASA 80NSSC18K0646, and by DOE Grant No. DE-SC0018266. NFL was partially funded by NSF CAREER Award No. 1654168 and by the NSF-DOE Partnership in Basic Plasma Science and Engineering, Award No. PHY-2010136. VR was partially supported by DOE Grant No. DE-SC0019315.

REFERENCES

Agarwal, P., Varma, P., and Tiwari, M. S. (2011). Study of inertial kinetic Alfven waves around cusp region. *Planet. Space Sci.* 59, 306–311. doi:10.1016/j.pss.2010.11.006

Bale, S. D., Goetz, K., Harvey, P. R., Turin, P., Bonnell, J. W., Dudok de Wit, T., et al. (2016). The FIELDS instrument suite for solar Probe plus. Measuring the coronal plasma and magnetic field, plasma waves and turbulence, and radio signatures of solar transients. *Space Sci. Rev.* 204, 49–82. doi:10.1007/s11214-016-0244-5

Biskamp, D. (2003). *Magnetohydrodynamic turbulence*. Cambridge, United Kingdom: Cambridge University Press.

Boldyrev, S., Chen, C. H. K., Xia, Q., and Zhdankin, V. (2015). Spectral breaks of alfvénic turbulence in a collisionless plasma. *Astrophys. J.* 806, 238. doi:10.1088/0004-637X/806/2/238

Boldyrev, S., and Loureiro, N. F. (2019). Role of reconnection in inertial kinetic-AlfvÃ©n turbulence. *Phys. Rev. Res.* 1, 012006. doi:10.1103/PhysRevResearch.1.012006

Boldyrev, S., and Loureiro, N. F. (2020). Tearing instability in AlfvÃ©n and kinetic-AlfvÃ©n turbulence. *J. Geophys. Res. Space Phys.* 125, e2020JA028185. doi:10.1029/2020JA028185

Camargo, S. J., Scott, B. D., and Biskamp, D. (1996). The influence of magnetic fluctuations on collisional drift-wave turbulence. *Phys. Plasmas* 3, 3912–3931. doi:10.1063/1.871580

Chen, C. H. K., Bale, S. D., Bonnell, J. W., Borovikov, D., Bowen, T. A., Burgess, D., et al. (2020). The evolution and role of solar wind turbulence in the inner heliosphere. *Astrophy. J. Suppl.* 246, 53. doi:10.3847/1538-4365/ab60a3

Chen, C. H., and Boldyrev, S. (2017). Nature of kinetic scale turbulence in the earth's magnetosheath. *Astrophy. J.* 842, 122. doi:10.3847/1538-4357/aa74e0

Chen, C. H. K., Klein, K. G., and Howes, G. G. (2019). Evidence for electron landau damping in space plasma turbulence. *Nat. Commun.* 10, 740. doi:10.1038/s41467-019-08435-3

Chen, C. H. K., Leung, L., Boldyrev, S., Maruca, B. A., and Bale, S. D. (2014). Ion-scale spectral break of solar wind turbulence at high and low beta. *Geophys. Res. Lett.* 41, 8081–8088. doi:10.1002/2014GL062009

Chen, C. H. K. (2016). Recent progress in astrophysical plasma turbulence from solar wind observations. *J. Plasma Phys.* 82, 121. doi:10.1017/S0022377816001124

Cranmer, S. R., Matthaeus, W. H., Breech, B. A., and Kasper, J. C. (2009). Empirical constraints on proton and electron heating in the fast solar wind. *Astrophy. J.* 702, 1604–1614. doi:10.1088/0004-637X/702/2/1604

Bale, S. D., Badman, S. T., Bonnell, J. W., Bowen, T. A., Burgess, D., Case, A. W., et al. (2019). Highly structured slow solar wind emerging from an equatorial coronal hole. *Nature* 576, 237–242. doi:10.1038/s41586-019-1818-7

Franci, L., Stawarz, J. E., Papini, E., Hellinger, P., Nakamura, T., Burgess, D., et al. (2020). Modeling MMS observations at the earth's magnetopause with hybrid

simulations of alfvénic turbulence. *Astrophy. J.* 898, 175. doi:10.3847/1538-4357/ab9a47

Ghavamian, P., Schwartz, S. J., Mitchell, J., Masters, A., and Laming, J. M. (2013). Electron-ion temperature equilibration in collisionless shocks: the supernova remnant-solar wind connection. *Space Sci. Rev.* 178, 633–663. doi:10.1007/s11214-013-9999-0

Goldreich, P., and Sridhar, S. (1995). Toward a theory of interstellar turbulence. 2: strong alfvenic turbulence. *Astrophy. J.* 438, 763–775. doi:10.1086/175121

Grošelj, D. (2019). *Thesis: fully kinetic simulations of microscale turbulence is space and astrophysical plasmas*. MS dissertation. Munich: Ludwig-Maximilians-Universität München.

Horvath, S. A., Howes, G. G., and McCubbin, A. J. (2020). *Electron landau damping of kinetic Alfvén waves in simulated magnetosheath turbulence*. arXiv e-printsarXiv:2009.05010.

Kadomtsev, B. B., and Pogutse, O. P. (1974). Nonlinear helical perturbations of a plasma in the tokamak. *Soviet J. Exp. Theor. Phys.* 38, 283–290.

Kasper, J. C., Bale, S. D., Belcher, J. W., Berthomier, M., Case, A. W., Chandran, B. D. G., et al. (2019). Alfvénic velocity spikes and rotational flows in the near-Sun solar wind. *Nature* 576, 1–4. doi:10.1038/s41586-019-1813-z

Li, T. C., Howes, G. G., Klein, K. G., and TenBarge, J. M. (2016). Energy dissipation and Landau damping in two and three-dimensional plasma turbulence. *Astrophy. J. lett.* 832, L24. doi:10.3847/2041-8205/832/2/L24

Loureiro, N. F., and Boldyrev, S. (2020). Nonlinear reconnection in magnetized turbulence. *Astrophy. J.* 890, 55. doi:10.3847/1538-4357/ab6a95

Loureiro, N. F., and Boldyrev, S. (2018). Turbulence in magnetized pair plasmas. *Astrophy. J. lett.* 866, L14. doi:10.3847/2041-8213/aae483

Milanese, L. M., Loureiro, N. F., Daschner, M., and Boldyrev, S. (2020). Dynamic phase alignment in inertial Alfvén turbulence. *Phys. Rev. Lett.* 125, 265101. doi:10.1103/PhysRevLett.125.265101

Passot, T., Sulem, P. L., and Tassi, E. (2017). Electron-scale reduced fluid models with gyroviscous effects. *J. Plasma Phys.* 83, 715830402. doi:10.1017/S0022377817000514

Passot, T., Sulem, P. L., and Tassi, E. (2018). Gyrofluid modeling and phenomenology of low-β_e Alfvén wave turbulence. *Phys. Plasmas* 25, 042107. doi:10.1063/1.5022528

Perez, J. C., and Boldyrev, S. (2010). Numerical simulations of imbalanced strong magnetohydrodynamic turbulence. *Astrophy. J. lett.* 710, L63–L66. doi:10.1088/2041-8205/710/1/L63

Phan, T. D., Eastwood, J. P., Shay, M. A., Drake, J. F., Sonnerup, B. U. Ö., Fujimoto, M., et al. (2018). Electron magnetic reconnection without ion coupling in Earth's turbulent magnetosheath. *Nature* 557, 202–206. doi:10.1038/s41586-018-0091-5

Quataert, E. (1998). Particle heating by Alfvénic turbulence in hot accretion flows. *Astrophy. J.* 500, 978–991. doi:10.1086/305770

Roytershteyn, V., Boldyrev, S., Delzanno, G. L., Chen, C. H. K., Grošelj, D., and Loureiro, N. F. (2019). Numerical study of inertial kinetic-Alfvén turbulence. *Astrophy. J.* 870, 103. doi:10.3847/1538-4357/aaf288

Schekochihin, A. A., Cowley, S. C., Dorland, W., Hammett, G. W., Howes, G. G., Quataert, E., et al. (2009). Astrophysical gyrokinetics: kinetic and fluid turbulent cascades in magnetized weakly collisional plasmas. *Astrophy. J. Supp.* 182, 310–377. doi:10.1088/0067-0049/182/1/310

Servidio, S., Valentini, F., Califano, F., and Veltri, P. (2012). Local kinetic effects in two-dimensional plasma turbulence. *Phys. Rev. Lett.* 108, 045001. doi:10.1103/PhysRevLett.108.045001

Shebalin, J. V., Matthaeus, W. H., and Montgomery, D. (1983). Anisotropy in MHD turbulence due to a mean magnetic field. *J. Plasma Phys.* 29, 525–547. doi:10.1017/S0022377800000933

Shukla, N., Varma, P., and Tiwari, M. S. (2009). Study of kinetic Alfven wave in inertial regime. *Indian J. Pure Appl. Phys.* 47, 350–355.

Strauss, H. R. (1976). Nonlinear, three-dimensional magnetohydrodynamics of noncircular tokamaks. *Phys. Fluids* 19, 134–140. doi:10.1063/1.861310

Štverák, Š., Trávníček, P. M., and Hellinger, P. (2015). Electron energetics in the expanding solar wind via Helios observations. *J. Geophys. Res.* 120, 8177–8193. doi:10.1002/2015JA021368

Terry, P. W., McKay, C., and Fernandez, E. (2001). The role of electron density in magnetic turbulence. *Phys. Plasmas* 8, 2707–2721. doi:10.1063/1.1362531

Tobias, S. M., Cattaneo, F., and Boldyrev, S. (2013). "Ten chapters in turbulence," in *MHD dynamos and turbulence*. Editors P. A. Davidson, Y. Kaneda, and K. R. Sreenivasan (Cambridge: Cambridge University Press), 351–404.

Valentini, F., Vásconez, C. L., Pezzi, O., Servidio, S., Malara, F., and Pucci, F. (2017). Transition to kinetic turbulence at proton scales driven by large-amplitude kinetic Alfvén fluctuations. *Astron. Astrophys.* 599, A8. doi:10.1051/0004-6361/201629240

Vega, C., Roytershteyn, V., Delzanno, G. L., and Boldyrev, S. (2020). Electron-only reconnection in kinetic-alfvén turbulence. *Astrophys. J. Lett.* 893, L10. doi:10.3847/2041-8213/ab7eba

Vink, J., Broersen, S., Bykov, A., and Gabici, S. (2015). On the electron-ion temperature ratio established by collisionless shocks. *Astron. Astrophys.* 579, A13. doi:10.1051/0004-6361/201424612

Zocco, A., and Schekochihin, A. A. (2011). Reduced fluid-kinetic equations for low-frequency dynamics, magnetic reconnection, and electron heating in low-beta plasmas. *Phys. Plasmas* 18, 102309–102324. doi:10.1063/1.3628639

Conflict of Interest: The authors declare that the research was conducted in the absence of any commercial or financial relationships that could be construed as a potential conflict of interest.

frontiers in Astronomy and Space Sciences

PERSPECTIVE
published: 18 May 2021
doi: 10.3389/fspas.2021.662861

How Turbulent is the Magnetically Closed Corona?

James A. Klimchuk and Spiro K. Antiochos*

Heliophysics Science Division, NASA Goddard Space Flight Center, Greenbelt, MD, United States

We argue that the magnetically closed corona evolves primarily quasi-statically, punctuated by many localized bursts of activity associated with magnetic reconnection at a myriad of small current sheets. The sheets form by various processes that do not involve a traditional turbulent cascade whereby energy flows losslessly through a continuum of spatial scales starting from the large scale of the photospheric driving. If such an inertial range is a defining characteristic of turbulence, then the magnetically closed corona is not a turbulent system. It nonetheless has a complex structure that bears no direct relationship to the pattern of driving.

Keywords: turbulence, magnetically closed corona, current sheets, energy power spectrum, inertial range, nanoflares

OPEN ACCESS

Edited by:
Joseph Eric Borovsky,
Space Science Institute, United States

Reviewed by:
Steven Spangler,
The University of Iowa, United States
Sergey Bogachev,
the Russian Academy of Sciences (RAS), Russia

****Correspondence:***
James A. Klimchuk
James.A.Klimchuk@nasa.gov

Specialty section:
This article was submitted to Space Physics, a section of the journal Frontiers in Astronomy and Space Sciences

Received: *01 February 2021*
Accepted: *05 May 2021*
Published: *18 May 2021*

Citation:
Klimchuk JA and Antiochos SK (2021) How Turbulent is the Magnetically Closed Corona?. Front. Astron. Space Sci. 8:662861. doi: 10.3389/fspas.2021.662861

INTRODUCTION

The surface of the Sun—the photosphere—undergoes incessant chaotic motions associated with the convective transport of energy from below. A portion of that energy is transported into the corona by the magnetic field and heats the gas to million-degree temperatures. Some of the surface flows change direction rapidly and launch Alfven waves that subsequently dissipate. Most are much longer-lived, however, and provide heating in a different manner. The details of how this occurs are the subject of this "perspective" article. We deal specifically with the magnetically closed corona, where field lines are rooted to the surface at both ends, allowing magnetic stresses to develop readily. This is the realm of active regions and the quiet Sun. Magnetically open coronal holes and the solar wind cannot support significant stress and are heated primarily by waves (Cranmer et al., 2017). Although still debated, it seems that non-wave heating dominates in the closed corona, especially within active regions; see the recent reviews of observations and models by Van Doorsselaere et al. (2020) and Viall et al. (2021) as well as the recent work by Howson et al. (2020).

There two competing views for how magnetic stresses are built up and released in the corona. In one picture, the evolution is mostly quasi-static but punctuated by many small, localized bursts of activity. The other picture is fully dynamic, with flows having a wide range of spatial scales completely filling the system. This is the turbulence view of the corona. Electric current sheets play an important role in both cases. They are the sites of magnetic reconnection events—often called nanoflares (Parker, 1983)—that are the primary agents of heating. The fundamental difference between the two pictures is how current sheets form. Both possibilities may occur in the actual corona, but our perspective is that one of them dominates.

In driven hydrodynamic systems with small viscosity, nonlinear interactions cause large-scale flows to break up into smaller and smaller eddies. The system organizes such that kinetic energy flows without loss from the largest scales at which it is injected, through a continuum of ever-smaller scales, ultimately reaching a scale where gradients are steep enough that viscous heating is effective. The intermediate range of lossless energy cascade is known as the inertial range and is a fundamental property of turbulence (Kolmogorov, 1941; Biskamp, 1993). In MHD systems, turbulence is more

complicated due to the presence of a magnetic field, but an inertial range is still a defining feature. Magnetic reconnection is an additional energy-dissipation mechanism, obviously not present in hydrodynamics. Reconnection occurs at current-sheet scales larger than the viscous and resistive dissipation scales, but still much smaller than the scale of the driving. Spatially and temporally intermittent behavior is present in hydrodynamic turbulence, but it is much more prominent in MHD turbulence because of reconnection.

Photospheric driving can create current sheets by at least three processes different from a turbulent cascade:

First, even smooth large-scale flows immediately create current sheets at magnetic topological boundaries called separatrix surfaces and quasi-separatrix layers (QSLs) (Priest et al., 2002). These boundaries occur because the field is highly fragmented in the photosphere, with much of the flux concentrated in structures known as kilogauss flux tubes. The tubes expand rapidly with height to become space filling in the low-β corona; thus, they are separated in the photosphere but in contact in the corona. Such contact boundaries are QSLs. Magnetogram observations indicate that a single active region contains roughly 10^5 photospheric concentrations of kiloGauss field, implying a comparable number of current sheets in the corona above (Klimchuk 2015). Partial reconnection of adjacent flux tubes will double the number of topologically distinct structures as described in Klimchuk (2015); therefore, we can expect the actual number of sheets in an active region to far exceed 10^5.

Second, even without the clumping of field described above, a complex evolution for the photospheric flows—including flows that are smooth and large-scale—will cause current structures to form in the corona and thin at an exponential rate (e.g., van Ballegooijen, 1986; Pontin and Hornig, 2020). A stagnation point flow is representative of the basic effect. The footpoints of two nearby field lines may move together for some time, but then diverge as the stagnation point is approached. A quantitative demonstration of this effect can be found in Antiochos and Dahlburg (1997).

Third, current sheets can form highly dynamically from coronal instabilities. The resistive internal kink instability is one example, whereby the distributed volume currents in a twisted flux tube are rapidly converted into multiple thin sheets (Hood et al., 2009). Also, when reconnection is patchy, multiple new current sheets are dynamically created through a process known as reconnection driven current filamentation (Karpen et al., 1996).

We conclude that current sheets and the resulting coronal heating can readily occur without the need of a turbulent cascade; but how can we determine which of these two competing views of the corona is correct: fundamentally turbulent or mostly quasi-static? Important insight may be provided by the spatial energy spectrum, as we now discuss.

ENERGY SPECTRA

Turbulence theory predicts that the lossless energy cascade at intermediate scales—the inertial range—has a distinctive spectrum of the form: $E(k) \propto k^{-a}$, where E is energy and k is wavenumber. The spectral index α has the famous value 5/3 for the kinetic energy in hydrodynamic turbulence (Kolmogorov, 1941). For MHD turbulence in open systems, there is equipartition between magnetic and kinetic energies, and they both have the same spectral index, ranging between 1.5 and two depending on whether the turbulence is weak or strong, isotropic or anisotropic. We must keep in mind that the corona is a closed system and may have different spectral properties from an open system if turbulence exists (Rappazzo et al., 2007; Rappazzo et al., 2008; Rappazzo and Velli 2011).

Many numerical simulations have been performed to study the coronal energy spectrum resulting from slow photospheric driving (Hendrix and Van Hoven, 1996; Dmitruk et al., 2003; Rappazzo et al., 2007; Rappazzo et al., 2008; Rappazzo et al., 2010; Rappazzo et al., 2013; Rappazzo and Velli, 2011). They begin with a uniform magnetic field in a box that spans two opposing boundaries representing positive and negative polarity parts of the photosphere. Essentially, the curved coronal field is straightened out. Flows are imposed at the boundaries that have a random aspect representative of photospheric convection. To avoid the generation of waves, the flows are either steady or their correlation times are long compared to the Alfven travel time.[1]

In all cases, the system responds in a well-behaved manner initially. Magnetic stresses slowly increase as the field becomes twisted and tangled, but the evolution remains everywhere quasi-static even when the stresses become large, thereby demonstrating that nonlinear interactions do not break up smooth flows into smaller and smaller eddies, as occurs with hydrodynamic turbulence. The stiffness of the line-tied, low-β magnetic field lines resists any bending by the plasma. Significant dynamics can result only from imbalances between the two magnetic forces—tension and magnetic pressure gradient—not from fluid effects.

The system becomes dynamic only when a magnetic instability sets in. Kinking and tearing instabilities are the most common. The critical level of twist for kinking depends on the twist profile (Bareford et al., 2010); for example, our simulations require three full turns for instability (Klimchuk et al., 2010).[2] The length-to-diameter aspect ratio in our model is eight, so the field is highly stressed and nonlinear with $B_\phi/B_z \sim 1$.

When the initial instability occurs, it usually produces magnetic complexity and current sheet formation. This leads to reconnection, which produces additional complexity leading to more reconnection and a proliferation of current sheets. Eventually, the system settles into a statistical steady state in which the energy released by the reconnection events balances the

[1]Some studies intentionally launch waves (e.g., van Ballegooijen, et al., 2011; Howson, et al., 2020), but those are not considered here.

[2]We use full MHD and impose a driving pattern in which vorticity is non-constant on streamlines—a condition said to be necessary to activate the nonlinear terms in the equations (Rappazzo et al., 2008). Despite this, no "nonlinear dynamics" occurs until kinking sets in.

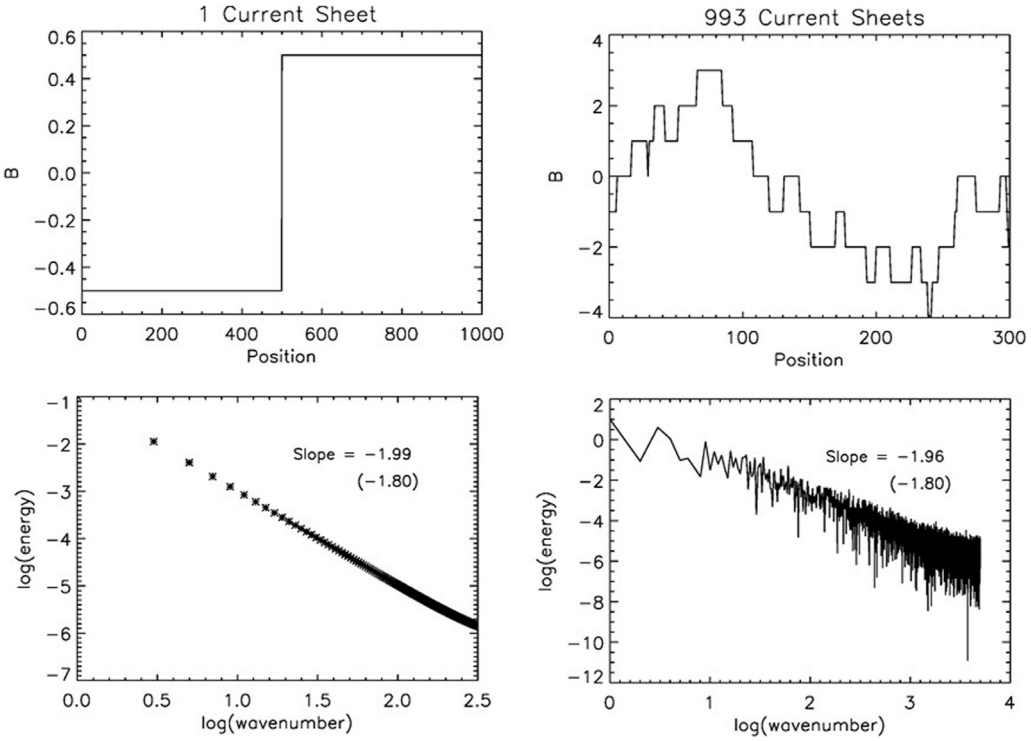

FIGURE 1 | Spatial profile of transverse magnetic field (top) and Fourier power spectrum (bottom) for a single current sheet (left) and 993 currents sheets with random spacing and random sign (right). Only a portion of the profile is shown for the multi-sheet case.

Poynting flux input at the boundaries from the work done on the field by the driving.

Kinetic and magnetic energy spectra for this system are computed from the square of the Fourier transforms of the transverse (i.e., perpendicular to the initial magnetic field direction) components of velocity and magnetic field. They are sometimes called the fluctuating components, though this can be misleading, as we argue below. The spectra from multiple studies are found to obey approximate power laws at intermediate wavenumbers, with the kinetic index being much smaller than the magnetic index: $\alpha_K \approx 0.5$ and $\alpha_M \approx 2$–3. Furthermore, magnetic energy exceeds kinetic energy by roughly two orders of magnitude: $E_M \approx 100\ E_K$ (Hendrix and Van Hoven, 1996; Dmitruk et al., 2003; Rappazzo et al., 2007; Rappazzo et al., 2008; Rappazzo et al., 2010; Rappazzo et al., 2013; Rappazzo and Velli, 2011). These results differ dramatically from the theoretical predictions for an open turbulent system. They are nonetheless cited as evidence for an inertial range, with the discrepancy being attributed to the effects of line-tying. We claim that this interpretation is premature and propose an alternative explanation below.

Note that observationally derived magnetic and kinetic energy spectra do not exist for the magnetically closed corona like they do for the solar wind. Remote sensing measurements of the magnetic and velocity vectors are neither sufficiently accurate nor on sufficiently small scales. Furthermore, the optically thin nature of the corona means there is spatially averaging along the line of sight.

The Fourier power spectrum (square of the transform) is usually interpreted as a measure of the distribution of the different spatial scales that are present in a system. This is not necessarily the case, however. Spatial discontinuities have a power spectrum that is a power law with spectral index 2 (Nahin, 2001). This is demonstrated by the two simple examples of **Figure 1**. On the top left is a step function that might represent the abrupt jump in the transverse component of magnetic field across a current sheet. The corresponding power spectrum is below. The right side shows the magnetic profile and spectrum for 993 sheets with random spacing and random sign (positive or negative jump in the field). Both spectra are nearly straight lines in the log-log plots, but deviate slightly at high wavenumbers, likely due to the discretization in the model. Linear fits have slopes of −1.8 if the full range is included, and very close to −2.0 if high wavenumbers are excluded (above 10^2 on the left and above 10^3 on the right).

The fact that discontinuities have spectral index of two has led some to suggest that the observed power spectra of the solar wind may be an indication of discontinuities (current sheets) rather than a turbulent cascade (Roberts and Goldstein, 1987; Borovsky, 2010). We propose that the MHD simulations representing the magnetically closed corona, discussed above, can be interpreted in the same way. This would explain why the spectral indices for magnetic and kinetic energy differ greatly from each other and from the expected value. It would also explain why the magnetic energy is two orders of magnitude larger than the kinetic energy, rather than equal as expected for turbulence.

The background field in the simulations is initially uniform and potential, but a large transverse component develops as stresses are built up quasi-statically during the pre-dynamics phase. Presumably, some of these stresses remain when the system transitions to a statistical steady state, especially if the driving is steady, as is often the case. If the transverse component of the background field greatly exceeds that of the dynamic fluctuations, the magnetic spectral index will be primarily a measure of the slowly evolving background rather than the fluctuations. If current sheets are prevalent, the index should be near two.

This alone does not argue against turbulence. There could be a hidden turbulent part of the magnetic energy that does not affect the index and that is in equipartition with kinetic energy. The problem is that the kinetic index in the simulations is near 0.5, far smaller than the expected theoretical value of 1.5–2. This would need to be rigorously explained, though see the discussion in Rappazzo and Velli (2011). Another possibility, of course, is that there is no hidden turbulent component in the magnetic spectrum, and the velocity spectrum is due to something entirely different from turbulence.

DISCUSSION

We have described are two competing pictures of the corona in which slow photospheric driving creates a myriad of current sheets that reconnect sporadically to heat the plasma. In the turbulence picture, the corona is a fully dynamic system. Current sheets are produced at the end of a systematic and lossless cascade of energy through a continuum of spatial scales that starts at the large scale of the driving. The competing picture is primarily quasi-static, with current sheets forming by a variety of processes that do not involve an organized system of spatial scales. Many different scales are present, but they are not connected in the manner of an inertial range. In both pictures, the corona has a complex structure that bears no direction relationship to the pattern of driving.

Magnetic and kinetic energy spectra in numerical simulations have been offered as evidence for the turbulence picture. In our opinion, however, the properties of these spectra argue as much against turbulence as for it. Furthermore, the well-behaved nature of the simulations before the first occurrence of a magnetic instability—often far into the nonlinear regime—is difficult to reconcile with traditional turbulence.

Some may argue that the quasi-static picture is just another type of turbulence because of its complex nature. We recommend against this label and suggest that the term be reserved for systems in which a majority the volume is undergoing a lossless energy cascade beginning at the scale of the driving. Magnetic reconnection can be very chaotic depending on the properties of the current sheet (Daughton et al., 2011; Huang and Bhattacharjee, 2016; Leake et al., 2020), and it is possible that the quasi-static picture we advocate includes localized regions where an inertial range is temporarily established. Whether these regions account for a sizable fraction of the coronal volume depends on several factors: the number density of current sheets; the frequency with which they reconnect; the fraction of events that develop an inertial range; and the rate at which the activity decays. Note that the inertial range would begin at the scale of the current sheet, which is far smaller than the scale of the driving, so this would not fit our definition of a turbulent system in any case.

There is much more work to be done before a comprehensive understanding of the corona is achieved. We believe the quasi-static picture serves as a good foundation. The magnetic spectral index found in simulations can likely be explained, at least in part, by the preponderance of current sheets. Why the index is sometimes significantly larger than two is possibly related to the distribution of current sheet spacings, but that has yet to be investigated. The kinetic spectral index of ~0.5 must also be explained. An avalanche-like behavior of reconnection events is one possibility (Knizhnik et al., 2018). We must remember that, because of topological complexities such as separators and QSLs, the velocity pattern in the photosphere—which may be dominated by one scale—is translated into a different velocity pattern in corona, likely involving a range of scales. This will affect the shape of the spectrum. Finally, we note that $\alpha_K < 1$ indicates that small spatial scales contain more energy than large scales, which is fundamentally at odds with turbulence. It would be expected, on the other hand, if the dominant flows are due to reconnection rather than being a direct result of the driving.

DATA AVAILABILITY STATEMENT

The raw data supporting the conclusion of this article will be made available by the authors, without undue reservation.

AUTHOR CONTRIBUTIONS

JK and SA both contributed to the content of the article.

ACKNOWLEDGMENTS

This work was supported by the GSFC Internal Scientist Funding Model (competitive work package program). We thank Marco Velli, Franco Rappazzo, Daniel Gomez, Ben Chandran, Russell Dahlburg, Peter Cargill, Francesco Malara, Andrew Hillier, Aaron Roberts, Giuseppina Nigro, and Vadim Uritsky for a number of helpful discussions in recent years. We also thank the referees for their comments and suggestions.

REFERENCES

Antiochos, S. K., and Dahlburg, R. B. (1997). The Implications of 3D for Solar MHD Modelling. *Solar Phys.* 174, 5–19. doi:10.1023/a:1004905432428

Bareford, M. R., Browning, P. K., and Van der Linden, R. A. M. (2010). A Nanoflare Distribution Generated by Repeated Relaxations Triggered by Kink Instability. *A&A* 521, A70. doi:10.1051/0004-6361/201014067

Biskamp, D. (1993). *Nonlinear Magnetohydrodynamics*. Cambridge: Cambridge Univ. Press. doi:10.1017/cbo9780511599965

Borovsky, J. E. (2010). *PRL* 105, 111102. doi:10.1103/physrevlett.105.111102

Cranmer, S. R., Gibson, S. E., and Riley, P. (2017). Origins of the Ambient Solar Wind: Implications for Space Weather. *Space Sci. Rev.* 212, 1345–1384. doi:10.1007/s11214-017-0416-y

Daughton, W., Roytershteyn, V., Karimabadi, H., Yin, L., Albright, B. J., Bergen, B., et al. (2011). Role of Electron Physics in the Development of Turbulent Magnetic Reconnection in Collisionless Plasmas. *Nat. Phys* 7, 539–542. doi:10.1038/nphys1965

Dmitruk, P., Gómez, D. O., and Matthaeus, W. H. (2003). Energy Spectrum of Turbulent Fluctuations in Boundary Driven Reduced Magnetohydrodynamics. *Phys. Plasmas* 10, 3584–3591. doi:10.1063/1.1602698

Hendrix, D. L., and Van Hoven, G. (1996). Magnetohydrodynamic Turbulence and Implications for Solar Coronal Heating. *ApJ* 467, 887. doi:10.1086/177663

Hood, A. W., Browning, P. K., and Van der Linden, R. A. M. (2009). Coronal Heating by Magnetic Reconnection in Loops with Zero Net Current. *A&A* 506, 913–925. doi:10.1051/0004-6361/200912285

Howson, T. A., De Moortel, I., and Fyfe, L. E. (2020). The Effects of Driving Time Scales on Heating in a Coronal Arcade. *A&A* 643, A85. doi:10.1051/0004-6361/202038869

Huang, Y.-M., and Bhattacharjee, A. (2016). Turbulent Magnetohydrodynamic Reconnection Mediated by the Plasmoid Instability. *ApJ* 818, 20. doi:10.3847/0004-637x/818/1/20

Karpen, J. T., Antiochos, S. K., and DeVore, C. R. (1996). Reconnection-driven Current Filamentation in Solar Arcades. *ApJL* 460, L73. doi:10.1086/309965

Klimchuk, J. A. (2015). Key Aspects of Coronal Heating. *Phil. Trans. R. Soc. A.* 373, 20140256. doi:10.1098/rsta.2014.0256

Klimchuk, J. A., Nigro, G., Dahlburg, R. B., and Antiochos, S. K. (2010). The Existence and Origin of Turbulence in Solar Active Regions. *BAAS* 41, 847.

Knizhnik, K. J., Uritsky, V. M., Klimchuk, J. A., and DeVore, C. R. (2018). Power-law Statistics of Driven Reconnection in the Magnetically Closed Corona. *ApJ* 853, 82. doi:10.3847/1538-4357/aaa0d9

Kolmogorov, A. N. (1941). The Local Structure of Turbulence in Incompressible Viscous Fluid for Very Large Reynolds' Numbers. *Dokl. Akad. Nauk. SSSR* 30, 301.

Leake, J. E., Daldorff, L. K. S., and Klimchuk, J. A. (2020). The Onset of 3D Magnetic Reconnection and Heating in the Solar Corona. *ApJ* 891, 62. doi:10.3847/1538-4357/ab7193

Nahin, P. J. (2001). *The Science of Radio*. New York: Springer-Verlag. doi:10.1007/978-1-4613-0173-8

Parker, E. N. (1983). Magnetic Neutral Sheets in Evolving Fields - Part Two - Formation of the Solar Corona. *ApJ* 264, 642. doi:10.1086/160637

Pontin, D. I., and Hornig, G. (2020). The Parker Problem: Existence of Smooth Force-free Fields and Coronal Heating. *Living Rev. Sol. Phys.* 17, 5. doi:10.1007/s41116-020-00026-5

Priest, E. R., Heyvaerts, J. F., and Title, A. M. (2002). A Flux-Tube Tectonics Model for Solar Coronal Heating Driven by the Magnetic Carpet. *ApJ* 576, 533–551. doi:10.1086/341539

Rappazzo, A. F., Velli, M., Einaudi, G., and Dahlburg, R. B. (2007). Coronal Heating, Weak MHD Turbulence, and Scaling Laws. *ApJ* 657, L47–L51. doi:10.1086/512975

Rappazzo, A. F., Velli, M., Einaudi, G., and Dahlburg, R. B. (2008). Nonlinear Dynamics of the Parker Scenario for Coronal Heating. *ApJ* 677, 1348–1366. doi:10.1086/528786

Rappazzo, A. F., Velli, M., and Einaudi, G. (2013). Field Lines Twisting in a Noisy Corona: Implications for Energy Storage and Release, and Initiation of Solar Eruptions. *ApJ* 771, 76. doi:10.1088/0004-637x/771/2/76

Rappazzo, A. F., Velli, M., and Einaudi, G. (2010). Shear Photospheric Forcing and the Origin of Turbulence in Coronal Loops. *ApJ* 722, 65–78. doi:10.1088/0004-637x/722/1/65

Rappazzo, A. F., and Velli, M. (2011). Magnetohydrodynamic Turbulent Cascade of Coronal Loop Magnetic Fields. *Phys. Rev. E* 83, 065401. doi:10.1103/physreve.83.065401

Roberts, D. A., and Goldstein, M. L. (1987). Spectral Signatures of Jumps and Turbulence in Interplanetary Speed and Magnetic Field Data. *J. Geophys. Res.* 92, 10105. doi:10.1029/ja092ia09p10105

van Ballegooijen, A. A., Asgari-Targhi, M., Cranmer, S. R., and DeLuca, E. E. (2011). Heating of the Solar Chromosphere and Corona by Alfvén Wave Turbulence. *ApJ* 736, 3. doi:10.1088/0004-637x/736/1/3

van Ballegooijen, A. A. (1986). Cascade of Magnetic Energy as a Mechanism of Coronal Heating. *ApJ* 311, 1001. doi:10.1086/164837

Van Doorsselaere, T., Srivastava, A. K., Antolin, P., Magyar, N., Vasheghani Farahani, S., Tian, H., et al. (2020). Coronal Heating by MHD Waves. *SSR* 216, 140. doi:10.1007/s11214-020-00770-y

Viall, N. M., De Moortel, I., Downs, C., Klimchuk, J. A., Parenti, S., and Reale, F. (2021). in *Space Physics and Aeronomy Collection Vol. 1: At the Doorstep of Our Star: Solar Physics and Solar Wind, Geophys. Monograph 258*. Editors N. E. Raoufi and A. Vourlidas (San Francisco: John Wiley & Sons).

Conflict of Interest: The authors declare that the research was conducted in the absence of any commercial or financial relationships that could be construed as a potential conflict of interest.

frontiers in Astronomy and Space Sciences

MINI REVIEW
published: 20 May 2021
doi: 10.3389/fspas.2021.624602

Turbulence in the Magnetospheres of the Outer Planets

*Joachim Saur**

Institute of Geophysics and Meteorology, University of Cologne, Cologne, Germany

The magnetospheres of the outer planets exhibit turbulent phenomena in an environment which is qualitatively different compared to the solar wind or the interstellar medium. The key differences are the finite sizes of the magnetospheres limited by their physical boundaries, the presence of a strong planetary background magnetic field and spatially very inhomogeneous plasma properties within the magnetospheres. Typical turbulent fluctuations possess amplitudes much smaller than the background field and are characterized by Alfvén times, which can be smaller than the non-linear interaction time scales. The magnetospheres of the outer planets are thus interesting laboratories of plasma turbulence. In Jupiter's and Saturn's magnetospheres, turbulence is well-established thanks to the *in-situ* measurements by several spacecraft, in particular the Galileo and Cassini orbiter. In contrast, the fluctuations in Uranus' and Neptune's magnetospheres are poorly understood due to the lack of sufficient data. Turbulence in the outer planets' magnetospheres have important effects on the systems as a whole. The dissipation of the turbulent fluctuations through wave-particle interaction is a significant heat source, which can explain the large magnetospheric plasma temperatures. Similarly, turbulent wave fluctuations strongly contribute to the acceleration of particles responsible for the planet's auroras.

Keywords: turbulence, outer planets, magnetosphere, wave turbulence, wave-particle interaction, aurora

OPEN ACCESS

Edited by:
Joseph Eric Borovsky,
Space Science Institute, United States

Reviewed by:
Fran Bagenal,
University of Colorado Boulder, United States
Mostafa El-Alaoui,
UCLA Department of Physics and Astronomy, United States

***Correspondence:**
Joachim Saur
saur@geo.uni-koeln.de

Specialty section:
This article was submitted to Space Physics, a section of the journal Frontiers in Astronomy and Space Sciences

Received: *31 October 2020*
Accepted: *23 March 2021*
Published: *20 May 2021*

Citation:
Saur J (2021) Turbulence in the Magnetospheres of the Outer Planets. Front. Astron. Space Sci. 8:624602. doi: 10.3389/fspas.2021.624602

1. INTRODUCTION AND ORIGIN OF TURBULENCE

All four outer planets of the solar system, Jupiter, Saturn, Uranus, and Neptune, possess strong internal dynamo magnetic fields with polar field strength of $\sim$ 2,000,000, 40,000, 100,000, and 90,000 nT, respectively (Connerney, 2007; Ness, 2010). They are also fast rotators with periods of 9.9, 10.7, 17.2, and 16.1 h, respectively (Seidelmann et al., 2002). These two effects lead to large and rotationally dominated magnetospheres with average magnetopause standoff distances on the sub-solar side of 65, 20, 20, and 26 planetary radii, respectively (Bagenal, 2009, 2013; Vasyliūnas, 2009).

One of the most important difference between the magnetospheres of the outer planets and the magnetosphere of Earth is the presence of large mass sources well inside the outer planets' magnetospheres and the resultant effects generated by the associated radial mass transport. In case of Jupiter, its inner Galilean moon Io, located deeply within the magnetosphere at 6 R_J, produces about 10^3 kg s^{-1} of SO_2, which eventually gets ionized (Thomas et al., 2004). An additional, but smaller source of mass is its moon Europa with about 50 kg s^{-1} of H_2O (Bagenal and Dols, 2020). In case of Saturn, the mass source is the moon Enceladus, with a time-variable injection rate of 200–1,000 kg s^{-1} of H_2O (Dougherty et al., 2009; Fleshman et al., 2010; Saur et al., 2011; Hedman et al., 2013). In case of Uranus and Neptune, also major moons orbit within their magnetosphere. However, their mass loss rates are not well-constrained. They are considered

smaller compared to those in the magnetospheres of Jupiter and Saturn based on the significantly smaller mass densities in the magnetospheres of Uranus and Neptune (e.g., Bagenal, 2009, 2013).

The centrifugal force in the fast rotating magnetospheres causes the plasma to be concentrated near the equatorial regions (called plasma sheets, see **Figure 1**) and drives transport of plasma radially outward. Due to conservation of angular momentum the outward moving plasma does not to fully corotate with the planet. This generates two types of magnetospheric stresses: Stretched magnetic field lines in the radial direction from the radial transport (see **Figure 1**) and bend backed magnetic field lines in azimuthal direction due to the subcorotating plasma. These magnetic stresses couple to the planets' ionospheres and cause transport of angular momentum between the planets' ionospheres and magnetospheres (Hill, 2001; Goldreich and Farmer, 2007). The stress balance is however not in steady state, but constantly disturbed due to non-continuous radial transport of plasma, which is observed to occur through the interchange of mass loaded magnetic flux tubes with adjacent less loaded flux tubes further out (Kivelson et al., 1997). The imbalance of magnetic stresses cause Alfvén waves to propagate along the magnetic field to achieve stress balance. The Alfvén wave packages are partially reflected at the ionospheres or other boundaries, such as large density gradients of the plasma sheet. The resulting counter-propagating Alfvén wave packages interact non-linearly and thus generate a turbulent cascade (Saur et al., 2002; Saur et al., 2018). On the MHD scales the magnetospheric plasma sheet is thought to be a key region where the cascade is being driven (Saur et al., 2002).

The non-linear interaction of counter-propagating wave packages is the fundamental building block of MHD and plasma turbulence. It is established observationally, theoretically and in numerical modeling (e.g., Goldreich and Sridhar, 1995; Howes and Nielson, 2013). There are several key differences between turbulence in the solar wind (e.g., Bruno and Carbone, 2013) and the turbulence in the magnetospheres of the outer planets. The magnetospheric fluctuations are small amplitude fluctuations $\delta B \ll B_0$ compared to the dominant magnetospheric background field B_0. The magnetospheres are also finite in size. This implies that turbulent scales are bound and a maximum length scale for the inertial range of turbulence exists. It also causes reflection of the wave packages at the ionospheric boundaries. Additionally the magnetospheres are highly inhomogeneous with large densities and small magnetic field strength in the magnetospheric plasma sheets and vice versa at high latitudes (see **Figure 1**). Therefore, the generator region, i.e., where the turbulent cascade is driven, and the dissipation regions of the turbulent fluctuations do not need to be spatially collocated (Saur et al., 2018). Another interesting difference between the solar wind and the magnetospheres of the outer planets is that the composition of ions has a much larger spread in mass. The solar wind is mostly composed of H^+ and He^{++} compared to H^+, O^+, S^+, H_2O^+ ... in Jupiter's or Saturn's magnetospheres. This causes a larger spread of gyro frequencies and inertial length scales and will influence the pathways of turbulent dissipations.

In the reminder of this review we will present observations of turbulent fluctuations in Jupiter's and Saturn's magnetospheres. Additionally, we discuss their impact on overall properties of these magnetospheres such as aurora or temperature structure.

2. MAGNETOSPHERIC TURBULENCE

Turbulence and its implications for the magnetospheres of Jupiter and Saturn have been studied by a number of authors. There are no published studies about turbulence in the magnetospheres of Uranus and Neptune due to a lack of appropriate data.

2.1. Jupiter Magnetosphere

Turbulence in Jupiter's magnetosphere has been investigated on various levels of detail. Before the Galileo epoch, Nishida (1976) considered whistler mode turbulence for pitch angle diffusion of energetic electrons and ions. Barbosa (1981) and Barbosa et al. (1984) investigated ion heating due to high-frequency kilohertz plasma wave turbulence and low frequency Alfvénic turbulence, respectively. Glassmeier (1995) suggests a Kolmogorov-type of turbulence in the very low-frequency, milli-Hertz, range based on Voyager magnetic field measurements.

Magnetic field measurements by the Galileo orbiter led to a dedicated turbulence analysis by Saur et al. (2002). The analysis covered the magnetic field fluctuations in Jupiter's middle magnetosphere (9–24 R_J) within the magnetohydrodynamic (MHD) range between 2.8×10^{-4} and 3.6×10^{-2} Hz, i.e., below the ion cyclotron frequency. Even though the relative velocity between the magnetospheric plasma and the spacecraft is much smaller compared to spacecraft in the solar wind, the Taylor theorem can still be applied (Saur et al., 2013). The properties of the magnetic field fluctuations in Jupiter's middle magnetosphere differ from those in the solar wind. In the Jovian system, the ratio of the magnetic fluctuations δB compared to the background magnetic field B_0 is less than 10^{-1}, while it is of order unity in the solar wind. A weak turbulence cascade is expected in Jupiter's middle magnetosphere based on the ratio $\epsilon = \tau_A/\tau_{nl}$ between the Alfvén time τ_A and the non-linear interaction time τ_{nl}. This ratio ϵ lies in the range of 0.06 to 0.34 and is indicative of weak turbulence (Ng and Bhattacharjee, 1997; Galtier et al., 2000). Magnetic field fluctuations parallel to the background magnetic field exhibit a power law with spectral index of –2 (Saur et al., 2002) also indicative of weak turbulence (Ng and Bhattacharjee, 1997; Galtier et al., 2000). The other components often show deviations from clear power laws possibly due to other perturbations in the Jupiter's highly dynamic magnetosphere or locally non-fully developed turbulent cascades.

Turbulence in Jupiter's magnetosphere has subsequently been analyzed by Tao et al. (2015) who combined low and high-time resolution magnetic field data of the Galileo spacecraft within MHD and kinetic scales, i.e., within 1×10^{-4} Hz to 1 Hz. The resultant magnetic field spectra show spectral breaks well-organized by the ion scales (i.e., ion cyclotron frequency, the Doppler-shifted ion inertial length scales and the ion gyroradius, which assume similar values in Jupiter's middle magnetosphere). For frequencies smaller than those associated with the ion

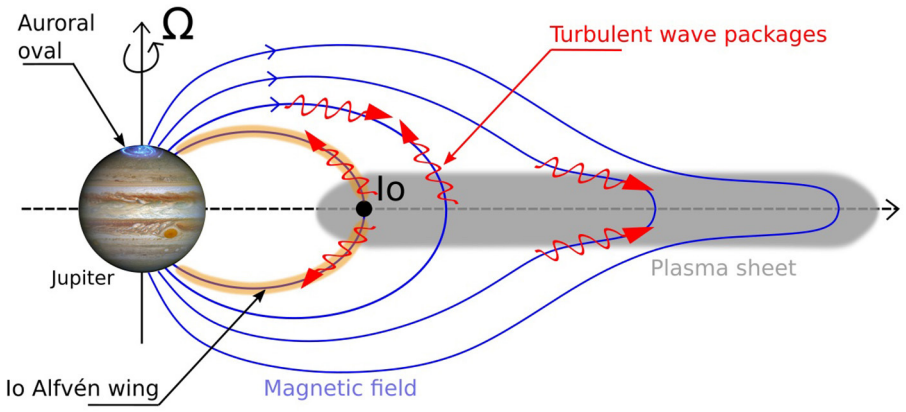

FIGURE 1 | Sketch of turbulent wave packages in Jupiter's magnetosphere. The interaction of counter-propagating Alfvén wave packages generates a turbulent cascade. Waves packages are reflected at the ionosphere of Jupiter or other density gradients in the magnetosphere.

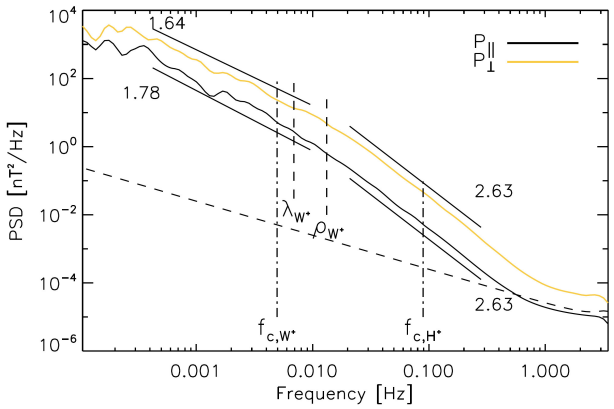

FIGURE 2 | Power spectral density (PSD) of turbulent magnetic field fluctuations in Saturn's magnetosphere (from von Papen et al., 2014). $P_\perp$ and $P_\parallel$ refer to the power spectral densities of fluctuations perpendicular and parallel to the background magnetic field, respectively. λ_{W+} and ρ_{W+} indicate the Doppler shifted ion inertial length scale and gyroradius of water ions, respectively, and $f_{c,W+}$ and $f_{c,H+}$ are the cyclotron frequencies of water ions and protons, respectively.

scales, the spectral indices lie in the range of −0.6 and −1.9 and for higher frequencies within the range of −1.7 and −2.5 (Tao et al., 2015). The authors also show that the turbulence is intermittent, in particular in the equatorial region of Jupiter's magnetospheric plasma.

2.2. Saturn Magnetosphere

Saturn's magnetosphere also hosts small scale turbulent magnetic field fluctuations as demonstrated by von Papen et al. (2014). The average amplitudes of the fluctuations compared to the magnetospheric background field assumes values of $\delta B/B = 0.07$. An exemplary spectrum is shown in **Figure 2**. On MHD scales the spectral slope of the fluctuations perpendicular and parallel to the background magnetic field varies between −0.8 and −1.7. At ion scales, i.e., near the ion inertial length scale or the Doppler-shifted ion gyroradius, a spectral break occurs, with a sub-ion, i.e., high-frequency, slope of −2.3 inside of a radial distances of 9 R_S (see **Figure 2**). Further outside in the magnetosphere the sub-ion spectrum steepens to −2.6. These slopes could be consistent with turbulence of kinetic Alfvén waves. The probability density function of the fluctuations have non-Gaussian tails and a power law increase of the flatness indicates that the turbulence is intermittent (von Papen et al., 2014). The turbulence on the kinetic scales is estimated to be strong in Saturn's magnetosphere with $\epsilon > 1$, i.e., the non-linear time is shorter than the wave propagation time, which could result from Saturn's weaker planetary magnetic field compared to Jupiter's field.

In a follow-up study, von Papen and Saur (2016) investigated the spatial and temporal structure of the magnetospheric turbulence. In local time coordinates, enhanced fluctuations are seen at noon, possibly resulting from flux tube interchanges (e.g., Kivelson et al., 1997), which are considered a prime source of the turbulence. In a frame rotating with Saturn, increased fluctuations are seen at 65° southern and 250° northern magnetic phase. The later correlation is enigmatic and is related to the still unresolved planetary period oscillations of Saturn (Espinosa and Dougherty, 2000; Gurnett et al., 2009; Provan et al., 2009; von Papen and Saur, 2016). The oscillations might result from a coupling between Saturn's atmosphere, ionosphere and magnetosphere. The variability in the turbulence can thus be considered as an effect of the Alfvénic energy fluxes underlying these coupling processes. The spatial variability of the turbulent fluctuations in Saturn's magnetosphere has been subsequently studied by Kaminker et al. (2017). The authors also found enhanced fluctuations between 10 hr and 20 hr local time and the turbulence to be more quiet between 3 hr and 9 hr local time.

2.3. Large Scale Implications of Turbulence

In addition to serving as a laboratory for turbulence studies, the fluctuations in the outer planets' magnetospheres have major implications on overall properties of their planetary systems.

2.3.1. Magnetospheric Heating

The magnetospheres of Jupiter and Saturn possess ion temperatures which strongly increase from the plasma source regions radially outwards by approximately two orders of magnitude to values up to nearly 10^8 K (Bagenal and Delamere, 2011). These observations are considered a long standing puzzle since major energy input rates are required to explain these temperature increases. Otherwise the radial transport of magnetospheric plasma would lead to adiabatic cooling with distance. Dissipation of turbulent magnetic field fluctuations is a very powerful energy source which can explain the temperature increase.

First suggestions of the importance of turbulent heating in Jupiter's magnetosphere in addition to pickup energization and subsequent radial transport date back to Barbosa et al. (1984). Based on the observed spatial distribution of the magnetic field fluctuations and a model for a weak turbulent cascade, Saur (2004) calculated the dissipation rate in Jupiter's middle magnetosphere to a total amount of 5×10^{12} W and demonstrated that this rate and its spatial distribution can explain the observed radial temperature profile (Frank and Paterson, 2002). To a similar conclusion came Ng et al. (2018) who used a radial transport model based on advection and not on flux tube diffusion as in Saur (2004). The turbulent dissipation rates are consistent with the required heating rate independently extracted from Galileo spacecraft observations by Bagenal and Delamere (2011). A possible dissipation mode could be ion cyclotron damping in particular of the heavy sulfur and oxygen ions of Jupiter's magnetosphere (Saur et al., 2018). In Saturn's magnetosphere the dissipation of the magnetic field fluctuations based on a strong turbulence model could provide power on the order of 10^{11} W (von Papen and Saur, 2016; Kaminker et al., 2017; Neupane et al., 2021), which is roughly consistent with the energy needed to heat the magnetosphere to its observed temperatures (Bagenal and Delamere, 2011).

2.3.2. Aurora

Jupiter's main auroral oval lies on magnetic field lines that map to an equatorial distance of about 20–30 R_J (e.g., Clarke et al., 1998, 2002; Hill, 2001) The turbulent power of the magnetic fluctuations in Jupiter's magnetosphere maximizes at the same radial distance (Saur et al., 2003). This distance is also the region where the corotation of Jupiter's magnetosphere breaks down and magnetospheric-ionospheric coupling currents maximize as derived by Hill (1979, 2001) and Cowley and Bunce (2001). The turbulent fluctuations result from the non-steady radial transport and the resultant imbalanced stresses between the magnetosphere and Jupiter's ionosphere. The stress balance is achieved by Alfvén waves propagating between both regions. When the Alfvén waves reach the polar regions of the magnetosphere, the perpendicular length scales of the Alfvén waves grow small due to Jupiter's increasing magnetic field. Just above the ionosphere, the electron inertial length scale assumes its large values of ∼50 km due to the low electron density. When the turbulent cascade reaches this scale, the fluctuations are subject to electron Landau damping resulting in stochastically accelerated electrons (Saur et al., 2018). This process is consistent with the bi-directional and energetically broad band electron distributions recently measured by the Juno spacecraft (e.g., Mauk et al., 2017; Clark et al., 2018). These electrons are one of the key contributors to Jupiter's main auroral oval. Magnetic field fluctuations measured by the Juno spacecraft near the auroral particle acceleration region showed a spectrum with a slope of -2.29 ± 0.09 within 0.5–5×10^{-1} Hz (Gershman et al., 2019). They could be due to kinetic/inertial Alfvén waves, however, the underlying turbulent processes for this spectrum are not fully clear yet as, e.g., the Alfvén velocity is close to the speed of light in this region. The aurora of Saturn is less well-understood, but also within Saturn's magnetosphere bi-directional energetically broad band electron beams have been observed on field lines which are connected to the aurora (Saur et al., 2006; Mitchell et al., 2009) and which appear to be driven by stochastic, turbulent processes (von Papen and Saur, 2016).

2.4. Turbulence in Alfvén wings of the Moons

A new and evolving area of turbulence research in the outer planets' magnetosphere are the Alfvén wings generated by the moons. In **Figure 1**, we exemplarily show Jupiter's moon Io. The moon is an obstacle to the rotating magnetospheric plasma and generates Alfvén waves, which propagate along the rotating background magnetic field toward Jupiter. In the rest frame of each moon two standing waves develop (north and south, respectively). They are referred to as Alfvén wings (Goertz, 1980; Neubauer, 1980, 1998; Saur et al., 2013). The moons can thus be considered as gigantic Alfvén wave antenna. The Alfvén wings are reflected at gradients of the background density and generate filamented structures (Chust et al., 2005; Hess et al., 2011). The magnetic field fluctuations in Io's Alfvén wings at high latitudes have been recently measured by the Juno spacecraft. Their spectrum is consistent with a power law spectral index of -2.35 ± 0.07 within 0.1–800 Hz (Sulaiman et al., 2020). When the filamented waves approach kinetic scales, wave-particle interaction sets in and can energize electrons through electron Landau damping and ions through cyclotron damping (Hess et al., 2010; Saur et al., 2018; Szalay et al., 2018, 2020b). Similar particle acceleration processes have also been observed in the Alfvén wings of Europa (Allegrini et al., 2020) and Ganymede (Szalay et al., 2020a).

2.5. Magnetosheaths' of Jupiter and Saturn

Turbulence in the magnetosheaths of the outer planets has received very little attention to date. Turbulence in the magnetosheaths is distinct from turbulence within the outer planets' magnetospheres. The magnetosheaths are characterized by large amplitude magnetic fluctuations $\delta B/B_0 \sim 1$ (Hadid et al., 2015). The ultimate source of free energy stems from the shocked solar wind plasma with Alfvén Mach numbers as high as ∼100 (Masters et al., 2013), which causes enhanced plasma temperatures and large plasma beta turbulence.

Alexandrova and Saur (2008) analyzed turbulent magnetic field fluctuations in Saturn's magnetosheath obtained the Cassini spacecraft and identified Alfvén vortices similar to those found in Earth's magnetosheath. Alfvén vortices are non-linear magnetic structures associated with sheared velocity perturbations propagating obliquely to the external field. Hadid et al. (2015) also studied Saturn's magnetosheath and calculated power-spectral energy densities of the magnetic field fluctuations with a $\sim f^{-1}$ scaling at MHD scales and an $\sim f^{-2.6}$ scaling at sub-ion scales. The authors also found based on the compressibility of magnetic and density fluctuations that compressible magnetosonic slow modes at MHD scales dominate rather than the Alfvén mode. Magnetic field turbulence in Jupiter's magnetosheath was studied by Bolzan and Echer (2014) based on Ulysses measurements. Bolzan and Echer (2014) considered a similar frequency range as Hadid et al. (2015), but fitted the power spectral density to only one power law instead of two and thus found an average slope of around −2.

3. DISCUSSION: OUTSTANDING ISSUES AND OUTLOOK

For a more comprehensive understanding of turbulence in the outer planets' magnetospheres further measurements and studies are required. The Galileo spacecraft recorded only a small fraction of its mission in a high-frequency modus. The Juno spacecraft is currently exploring the high latitude regions of Jupiter's magnetosphere including the moons' Alfvén wings. With its instrumentation and its polar orbit detailed studies of turbulence and the associated wave-particle processes of turbulent dissipation are on their way.

New missions with appropriate instrumentation to Uranus and Neptune are being discussed (e.g., Arridge et al., 2014), but no mission has been decided upon. The orientations of the planetary magnetic moments at Uranus and Neptune are highly tilted compared to the planets' spin axis. Also the plasma densities and the magnetic field fluctuations in these magnetospheres are much smaller compared to those of Jupiter and Saturn. It will be interesting to see how these properties influences the possible turbulent nature of the field and plasma fluctuations.

Further studies are warranted on where and what types of turbulent cascades are driven in the magnetospheres of the outer planets. For example, are there cascades on kinetic scales outside the plasma sheets? Also a better understanding of the nature of the dissipation mechanisms of the turbulent fluctuations and the resultant ion or electron distribution functions is an important matter. Further observational studies might aim to better resolve the effects of the various dissipation and turbulent break scales expected to occur at the inertial lengths scales and the gyroradii of the electrons and the various ion species, respectively. Because the magnetospheres are highly inhomogeneous, the spatial variability of these parameters and their effects can be more easily studied compared to the solar wind. Suggestions for the roles of Landau and ion cyclotron damping of Alfvénic turbulence in the magnetosphere of Jupiter have been made (e.g., Saur et al., 2018). However, the role of other wave modes or non-resonant wave-particle interaction processes warrant further analysis.

Numerical simulations with hybrid or particle-in-cell models can be a useful tool to better understand the dissipation mechanisms and the associated transport of particles and energy (e.g., Delamere et al., 2021). Future models could focus on more realistic magnetic field geometries with current sheets and inhomogeneous plasma densities along field lines.

Turbulence in the magnetosheaths of the outer planets have not received much attention. Dedicated study might investigate the structure of turbulence downstream of the planets' bow shocks to test the universality of turbulent evolution in Earth's and other planets' magnetosheaths. In the much larger magnetosheath of the outer planets' turbulence might evolve toward a more fully developed turbulent states compared to Earth. While turbulence in the middle magnetospheres of Jupiter and Saturn is unique due to the plasma of the moons and the fast rotating planets, the existence of turbulence in the magnetospheric tails and the magnetosheaths could be universal across all magnetized planets.

Turbulent fluctuations might be used as a diagnostic tool to probe the interior of the icy moons in the outer solar system. Icy moons, such as Europa or Ganymede, possess subsurface water oceans (Kivelson et al., 2000, 2002; Saur et al., 2010, 2015). These saline and thus electrically conductive oceans have been detected through electromagnetic induction caused by time-variable magnetospheric fields. For existing observations only the ∼10 h rotation period of Jupiter could be applied. Turbulent fluctuations provide a broad range of frequencies which can be used in future induction studies to additionally probe the interior of the moons (e.g., with JUICE or Europa Clipper data).

In summary, compared to the solar wind or the interstellar medium, the magnetospheres of the outer planets are complementary laboratories to study plasma turbulence. These magnetospheres are distinct due the planets' large background magnetic fields, the bound and inhomogeneous nature of the turbulent systems, where the location of the turbulent cascade and the turbulent dissipation are not necessarily collocated.

AUTHOR CONTRIBUTIONS

JS selected the material for this review and wrote the manuscript.

FUNDING

This project has received funding from the European Research Council (ERC) under the European Union's Horizon 2020 research and innovation programme (Grant Agreement No. 884711).

ACKNOWLEDGMENTS

JS thanks Sascha Janser for helpful comments on the manuscript and Filip Elekes for the graphics support.

REFERENCES

Alexandrova, O., and Saur, J. (2008). Alfvén vortices in Saturn's magnetosheath: cassini observations. *Geophys. Res. Lett.* 35:L15102. doi: 10.1029/2008GL034411

Allegrini, F., Gladstone, G. R., Hue, V., Clark, G., Szalay, J. R., Kurth, W. S., et al. (2020). First report of electron measurements during a Europa footprint tail crossing by juno. *Geophys. Res. Lett.* 47:e89732. doi: 10.1029/2020GL089732

Arridge, C. S., Achilleos, N., Agarwal, J., Agnor, C. B., Ambrosi, R., André, N., et al. (2014). The science case for an orbital mission to Uranus: exploring the origins and evolution of ice giant planets. *Planet. Space Sci.* 104, 122–140. doi: 10.1016/j.pss.2014.08.009

Bagenal, F. (2009). "Comparative planetary environmnents," in *Heliophysics: Plasma Physics of the Local Cosmos*, eds G. Siscoe and C. J. Schrijver (Cambridge: Cambridge University Press), 360

Bagenal, F. (2013). "Planetary magnetospheres," in *Planets, Stars and Stellar Systems. Volume 3: Solar and Stellar Planetary Systems*, eds T. D. Oswalt, L. M. French, and P. Kalas (Dordrecht: Springer, Media), 251. doi: 10.1007/978-94-007-5606-9_6

Bagenal, F., and Delamere, P. A. (2011). Flow of mass and energy in the magnetospheres of Jupiter and Saturn. *J. Geophys. Res. Space Phys.* 116:A05209. doi: 10.1029/2010JA016294

Bagenal, F., and Dols, V. (2020). The space environment of Io and Europa. *J. Geophys. Res. Space Phys.* 125:e27485. doi: 10.1029/2019JA027485

Barbosa, D. (1981). Dissipation and turbulent heating of plasma in Jupiter's magnetosphere. *Geophys. Res. Lett.* 8, 1111–1114.

Barbosa, D., Eviatar, A., and Siscoe, G. (1984). On the acceleration of energetic ions in Jupiter's magnetosphere. *J. Geophys. Res.* 89, 3789–3800.

Bolzan, M. J. A., and Echer, E. (2014). A multifractal approach applied to the magnetic field turbulence in Jupiter's magnetosheath. *Planet. Space Sci.* 91, 77–82. doi: 10.1016/j.pss.2013.12.004

Bruno, R., and Carbone, V. (2013). The solar wind as a turbulence laboratory. *Liv. Rev. Solar Phys.* 10:2. doi: 10.12942/lrsp-2013-2

Chust, T., Roux, A., Kurth, W. S., Gurnett, D. A., Kivelson, M. G., and Khurana, K. K. (2005). Are Io's Alfvén wings filamented? Galileo observations. *Planet. Space Sci.* 53, 395–412.

Clark, G., Tao, C., Mauk, B. H., Nichols, J., Saur, J., Bunce, E. J., et al. (2018). Precipitating electron energy flux and characteristic energies in jupiter's main auroral region as measured by Juno/JEDI. *J. Geophys. Res. Space Phys.* 123, 7554–7567. doi: 10.1029/2018JA025639

Clarke, J. T., Ajello, J., Ballester, G. E., Jaffel, L. B., Connerney, J. E. P., Gérard, J.-C., et al. (2002). Ultaviolet emissions from the magnetic footprints of Io, Ganymede and Europa on Jupiter. *Nature* 415, 997–1000. doi: 10.1038/415997a

Clarke, J. T., Ballester, G. E., Trauger, J., Ajello, J., Pryor, W., Tobiska, K., et al. (1998). Hubble Space Telescope imaging of Jupiter's UV aurora during the Galileo orbiter mission. *J. Geophys. Res.* 103, 20217–20236.

Connerney, J. E. P. (2007). "Planetary magnetism," in *Planets and Moons, Treatise on Geophysics*, ed G. Schubert (Amsterdam: Elsevier), 281–298.

Cowley, S. W. H., and Bunce, E. J. (2001). Origin of the main auroral oval in Jupiter's coupled magnetosphere-ionosphere system. *Planet. Space Sci.* 49, 1067–1088. doi: 10.1016/S0032-0633(00)00167-7

Delamere, P. A., Ng, C. S., Damiano, P. A., Neupane, B. R., Johnson, J. R., Burkholder, B., et al. (2021). Kelvin-helmholtz related turbulent heating at Saturn's magnetopause boundary. *J. Geophys. Res. Space Phys.* 126:e28479. doi: 10.1029/2020JA028479

Dougherty, M. K., Esposito, L. W., and Krimigis, S. M. (2009). *Saturn From Cassini-Huygens*. Dordrecht: Springer.

Espinosa, S., and Dougherty, M. (2000). Periodic perturbations in saturn's magnetic field. *Geophys. Res. Lett.* 27, 2785–2788. doi: 10.1029/2000GL000048

Fleshman, B. L., Delamere, P. A., and Bagenal, F. (2010). A sensitivity study of the Enceladus torus. *J. Geophys. Res. Planets* 115:E04007. doi: 10.1029/2009JE003372

Frank, L. A., and Paterson, W. R. (2002). Galileo observations of electron beams and thermal ions in Jupiter's magnetosphere and their relationship to the auroras. *J. Geophys. Res.* 107:1478. doi: 10.1029/2001JA009150

Galtier, S., Nazarenko, S. V., Newell, A. C., and Pouquet, A. (2000). A weak turbulence theory for incompressible magnetohydrodynamics. *J. Plasma Phys.* 63, 447–488. doi: 10.1017/S0022377899008284

Gershman, D. J., Connerney, J. E. P., Kotsiaros, S., DiBraccio, G. A., Martos, Y. M., Viñas, A. F., et al. (2019). Alfvénic fluctuations associated with jupiter's auroral emissions. *Geophys. Res. Lett.* 46, 7157–7165. doi: 10.1029/2019GL082951

Glassmeier, K.-H. (1995). Ultralow-frequency pulsations: Earth and Jupiter compared. *Adv. Space Res.* 16, 209–218.

Goertz, C. K. (1980). Io's interaction with the plasma torus. *J. Geophys. Res.* 85, 2949–2956.

Goldreich, P., and Farmer, A. J. (2007). Spontaneous axisymmetry breaking of the external magnetic field at Saturn. *J. Geophys. Res. Space Phys.* 112:A05225. doi: 10.1029/2006JA012163

Goldreich, P., and Sridhar, S. (1995). Toward a theory of interstellar turbulence. II. Strong Alfvénic turbulence. *Astrophys. J.* 438, 763–775.

Gurnett, D. A., Lecacheux, A., Kurth, W. S., Persoon, A. M., Groene, J. B., Lamy, L., et al. (2009). Discovery of a north-south asymmetry in Saturn's radio rotation period. *Geophys. Res. Lett.* 36:L16102. doi: 10.1029/2009GL039621

Hadid, L. Z., Sahraoui, F., Kiyani, K. H., Retinò, A., Modolo, R., Canu, P., et al. (2015). Nature of the MHD and kinetic scale turbulence in the magnetosheath of Saturn: cassini observations. *Astrophys. J. Lett.* 813:L29. doi: 10.1088/2041-8205/813/2/L29

Hedman, M. M., Gosmeyer, C. M., Nicholson, P. D., Sotin, C., Brown, R. H., Clark, R. N., et al. (2013). An observed correlation between plume activity and tidal stresses on Enceladus. *Nature* 500, 182–184. doi: 10.1038/nature12371

Hess, S. L. G., Delamere, P., Dols, V., Bonfond, B., and Swift, D. (2010). Power transmission and particle acceleration along the Io flux tube. *J. Geophys. Res. Space Phys.* 115:A06205. doi: 10.1029/2009JA014928

Hess, S. L. G., Delamere, P. A., Dols, V., and Ray, L. C. (2011). Comparative study of the power transferred from satellite-magnetosphere interactions to auroral emissions. *J. Geophys. Res. Space Phys.* 116:A01202. doi: 10.1029/2010JA015807

Hill, T. W. (1979). Inertial limit on corotation. *J. Geophys. Res.* 84, 6554–6558.

Hill, T. W. (2001). The Jovian auroral oval. *J. Geophys. Res.* 106, 8101–8107. doi: 10.1029/2000JA000302

Howes, G. G., and Nielson, K. D. (2013). Alfvén wave collisions, the fundamental building block of plasma turbulence. I. Asymptotic solution. *Phys. Plasmas* 20:072302. doi: 10.1063/1.4812805

Kaminker, V., Delamere, P. A., Ng, C. S., Dennis, T., Otto, A., and Ma, X. (2017). Local time dependence of turbulent magnetic fields in Saturn's magnetodisc. *J. Geophys. Res. Space Phys.* 122, 3972–3984. doi: 10.1002/2016JA023834

Kivelson, M. G., Khurana, K. K., Russell, C. T., Volwerk, M., Walker, J., and Zimmer, C. (2000). Galileo magnetometer measurements: a stronger case for a subsurface ocean at Europa. *Science* 289, 1340–1343. doi: 10.1126/science.289.5483.1340

Kivelson, M. G., Khurana, K. K., Russell, C. T., and Walker, R. J. (1997). Intermittent short-duration magnetic field anomalies in the Io torus: evidence for plasma interchange? *grl* 24, 2127. doi: 10.1029/97GL02202

Kivelson, M. G., Khurana, K. K., and Volwerk, M. (2002). The permanent and inductive magnetic moments of Ganymede. *Icarus* 157, 507–522. doi: 10.1006/icar.2002.6834

Masters, A., Stawarz, L., Fujimoto, M., Schwartz, S. J., Sergis, N., Thomsen, M. F., et al. (2013). Electron acceleration to relativistic energies at a strong quasi-parallel shock wave. *Nat. Phys.* 9, 164–167. doi: 10.1038/nphys2541

Mauk, B. H., Haggerty, D. K., Paranicas, C., Clark, G., Kollmann, P., Rymer, A. M., et al. (2017). Juno observations of energetic charged particles over Jupiter's polar regions: analysis of monodirectional and bidirectional electron beams. *Geophys. Res. Lett.* 44, 4410–4418. doi: 10.1002/2016GL072286

Mitchell, D. G., Kurth, W. S., Hospodarsky, G. B., Krupp, N., Saur, J., Mauk, B. H., et al. (2009). Ion conics and electron beams associated with auroral processes on Saturn. *J. Geophys. Res. Space Phys.* 114:A02212. doi: 10.1029/2008JA013621

Ness, N. F. (2010). Space exploration of planetary magnetism. *Space Sci. Rev.* 152, 5–22. doi: 10.1007/s11214-009-9567-9

Neubauer, F. M. (1980). Nonlinear standing Alfvén wave current system at Io: theory. *J. Geophys. Res.* 85, 1171–1178.

Neubauer, F. M. (1998). The sub-Alfvénic interaction of the Galilean satellites with the Jovian magnetosphere. *J. Geophys. Res.* 103, 19843–19866.

Neupane, B. R., Delamere, P. A., Ma, X., Ng, C. S., Burkholder, B., and Damiano, P. (2021). On the nature of turbulent heating and radial transport in Saturn's magnetosphere. *J. Geophys. Res. Space Phys.* 126:e27986. doi: 10.1029/2020JA027986

Ng, C. S., and Bhattacharjee, A. (1997). Scaling of anisotropic spectra due to the weak interaction of shear-Alfvén wave packets. *Phys. Plasma* 4, 605–610.

Ng, C. S., Delamere, P. A., Kaminker, V., and Damiano, P. A. (2018). Radial transport and plasma heating in Jupiter's magnetodisc. *J. Geophys. Res. Space Phys.* 123, 6611–6620. doi: 10.1029/2018JA025345

Nishida, A. (1976). Outward diffusion of energetic particles from the Jovian radiation belt. *J. Geophys. Res.* 81, 1771–1773.

Provan, G., Andrews, D. J., Arridge, C. S., Coates, A. J., Cowley, S. W. H., Milan, S. E., et al. (2009). Polarization and phase of planetary-period magnetic field oscillations on high-latitude field lines in Saturn's magnetosphere. *J. Geophys. Res. Space Phys.* 114, A02225. doi: 10.1029/2008JA013782

Saur, J. (2004). Turbulent heating of Jupiter's magnetosphere. *Astrophys. J. Lett.* 602, L137–L140. doi: 10.1086/382588

Saur, J., Duling, S., Roth, L., Jia, X., Strobel, D. F., Feldman, P. S., et al. (2015). The search for a subsurface ocean in Ganymede with Hubble Space Telescope observations of its auroral ovals. *J. Geophys. Res. Space Phys.* 120, 1715–1737. doi: 10.1002/2014JA020778

Saur, J., Feldman, P. D., Roth, L., Nimmo, F., Strobel, D. F., Retherford, K. D., et al. (2011). Hubble space telescope/Advanced camera for surveys observations of Europa's atmospheric ultraviolet emission at Eastern elongation. *Astrophys. J.* 738:153. doi: 10.1088/0004-637X/738/2/153

Saur, J., Grambusch, T., Duling, S., Neubauer, F. M., and Simon, S. (2013). Magnetic energy fluxes in sub-Alfvénic planet star and moon planet interactions. *Astron. Astrophys.* 552:A119. doi: 10.1051/0004-6361/201118179

Saur, J., Janser, S., Schreiner, A., Clark, G., Mauk, B. H., Kollmann, P., et al. (2018). Wave-particle interaction of Alfvén waves in jupiter's magnetosphere: auroral and magnetospheric particle acceleration. *J. Geophys. Res. Space Phys.* 123, 9560–9573. doi: 10.1029/2018JA025948

Saur, J., Mauk, B. H., Mitchell, D. G., Krupp, N., Khurana, K. K., Livi, S., et al. (2006). Anti-planetward auroral electron beams at Saturn. *Nature* 439, 699–702. doi: 10.1038/nature04401

Saur, J., Neubauer, F. M., and Glassmeier, K.-H. (2010). Induced magnetic fields in solar system bodies. *Space Sci. Rev.* 152, 391–421. doi: 10.1007/s11214-009-9581-y

Saur, J., Politano, H., Pouquet, A., and Matthaeus, W. (2002). Evidence for weak MHD turbulence in the middle magnetosphere of Jupiter. *Astron. Astrophys.* 386:699. doi: 10.1051/0004-6361:20020305

Saur, J., Pouquet, A., and Matthaeus, W. (2003). An acceleration mechanism for the generation of the main auroral oval on Jupiter. *Geophys. Res. Lett.* 30:1260. doi: 10.1029/2002GL015761

Seidelmann, P. K., Abalakin, V. K., Bursa, M., Davies, M. E., de Bergh, C., Lieske, J. H., et al. (2002). Report of the IAU/IAG Working Group on Cartographic Coordinates and Rotational Elements of the Planets and Satellites: 2000. *Celest. Mech. Dynam. Astron.* 82, 83–111. doi: 10.1023/A:1013939327465

Sulaiman, A. H., Hospodarsky, G. B., Elliott, S. S., Kurth, W. S., Gurnett, D. A., Imai, M., et al. (2020). Wave-particle interactions associated with io's auroral footprint: evidence of alfven, ion cyclotron, and whistler modes. *Geophys. Res. Lett.* 47:e2020GL088432. doi: 10.1029/2020GL088432

Szalay, J. R., Allegrini, F., Bagenal, F., Bolton, S. J., Bonfond, B., Clark, G., et al. (2020a). Alfvénic acceleration sustains Ganymede's footprint tail aurora. *Geophys. Res. Lett.* 47:e86527. doi: 10.1029/2019GL086527

Szalay, J. R., Bagenal, F., Allegrini, F., Bonfond, B., Clark, G., Connerney, J. E. P., et al. (2020b). Proton acceleration by Io's Alfvénic interaction. *J. Geophys. Res. Space Phys.* 125:e27314. doi: 10.1029/2019JA027314

Szalay, J. R., Bonfond, B., Allegrini, F., Bagenal, F., Bolton, S., Clark, G., et al. (2018). *In situ* observations connected to the Io footprint tail aurora. *J. Geophys. Res. Planets* 123, 3061–3077. doi: 10.1029/2018JE005752

Tao, C., Sahraoui, F., Fontaine, D., Patoul, J., Chust, T., Kasahara, S., et al. (2015). Properties of Jupiter's magnetospheric turbulence observed by the Galileo spacecraft. *J. Geophys. Res. Space Phys.* 120, 2477–2493. doi: 10.1002/2014JA020749

Thomas, N., Bagenal, F., Hill, T. W., and Wilson, J. K. (2004). "The Io neutral clouds and plasma torus," in *Jupiter: The Planet, Satellites and Magnetosphere*, Vol. 1, eds F. Bagenal, T. E. Dowling, and W. B. McKinnon (Cambridge: Cambridge University Press), 561–591.

Vasyliūnas, V. M. (2009). "Fundamentals of planetary magnetospheres," in *Heliophysics: Plasma Physics of the Local Cosmos*, eds G. Siscoe and C. J. Schrijver (Cambridge: Cambridge University Press), 256.

von Papen, M., and Saur, J. (2016). Longitudinal and local time asymmetries of magnetospheric turbulence in Saturn's plasma sheet. *J. Geophys. Res. Space Phys.* 121, 4119–4134. doi: 10.1002/2016JA022427

von Papen, M., Saur, J., and Alexandrova, O. (2014). Turbulent magnetic field fluctuations in Saturn's magnetosphere. *J. Geophys. Res. Space Phys.* 119, 2797–2818. doi: 10.1002/2013JA019542

Conflict of Interest: The author declares that the research was conducted in the absence of any commercial or financial relationships that could be construed as a potential conflict of interest.

frontiers in Astronomy and Space Sciences

REVIEW
published: 25 August 2021
doi: 10.3389/fspas.2021.735034

Mesoscale Structure in the Solar Wind

N. M. Viall[1]*, *C. E. DeForest*[2] *and L. Kepko*[1]

[1]NASA Goddard Space Flight Center, Greenbelt, MD, United States, [2]Department of Space Studies, Southwest Research Institute, Boulder, CO, United States

Structures in the solar wind result from two basic mechanisms: structures injected or imposed directly by the Sun, and structures formed through processing en route as the solar wind advects outward and fills the heliosphere. On the largest scales, solar structures directly impose heliospheric structures, such as coronal holes imposing high speed streams of solar wind. Transient solar processes can inject large-scale structure directly into the heliosphere as well, such as coronal mass ejections. At the smallest, kinetic scales, the solar wind plasma continually evolves, converting energy into heat, and all structure at these scales is formed en route. "Mesoscale" structures, with scales at 1 AU in the approximate spatial range of 5–10,000 Mm and temporal range of 10 s–7 h, lie in the orders of magnitude gap between the two size-scale extremes. Structures of this size regime are created through both mechanisms. Competition between the imposed and injected structures with turbulent and other evolution leads to complex structuring and dynamics. The goal is to understand this interplay and to determine which type of mesoscale structures dominate the solar wind under which conditions. However, the mesoscale regime is also the region of observation space that is grossly under-sampled. The sparse in situ measurements that currently exist are only able to measure individual instances of discrete structures, and are not capable of following their evolution or spatial extent. Remote imaging has captured global and large scale features and their evolution, but does not yet have the sensitivity to measure most mesoscale structures and their evolution. Similarly, simulations cannot model the global system while simultaneously resolving kinetic effects. It is important to understand the source and evolution of solar wind mesoscale structures because they contain information on how the Sun forms the solar wind, and constrains the physics of turbulent processes. Mesoscale structures also comprise the ground state of space weather, continually buffeting planetary magnetospheres. In this paper we describe the current understanding of the formation and evolution mechanisms of mesoscale structures in the solar wind, their characteristics, implications, and future steps for research progress on this topic.

Keywords: sun, heliosphere, solar wind, geospace, space weather, turbulence, solar variability, mesoscales

OPEN ACCESS

Edited by:
Marina Stepanova,
University of Santiago, Chile

Reviewed by:
Roberto Elías Navarro,
University of Concepcion, Chile
Daniel Verscharen,
University College London,
United Kingdom

***Correspondence:**
N. M. Viall
nicholeen.m.viall@nasa.gov

Specialty section:
This article was submitted to Space Physics, a section of the journal Frontiers in Astronomy and Space Sciences

Received: *02 July 2021*
Accepted: *10 August 2021*
Published: *25 August 2021*

Citation:
Viall NM, DeForest CE and Kepko L (2021) Mesoscale Structure in the Solar Wind. Front. Astron. Space Sci. 8:735034. doi: 10.3389/fspas.2021.735034

1 INTRODUCTION

The solar corona is comprised of a hot, ≥1 MK plasma that expands outward into the solar system, carrying magnetic field with it, and reaching flow speeds greater than the Alfvén speed. This flow is the solar wind, and defines the heliosphere. The solar wind is not laminar, but is dynamic and filled with structures on many spatial and temporal scales, from the large down through kinetic dissipation scales. The largest scales are directly imposed onto or injected into the solar wind, and include the

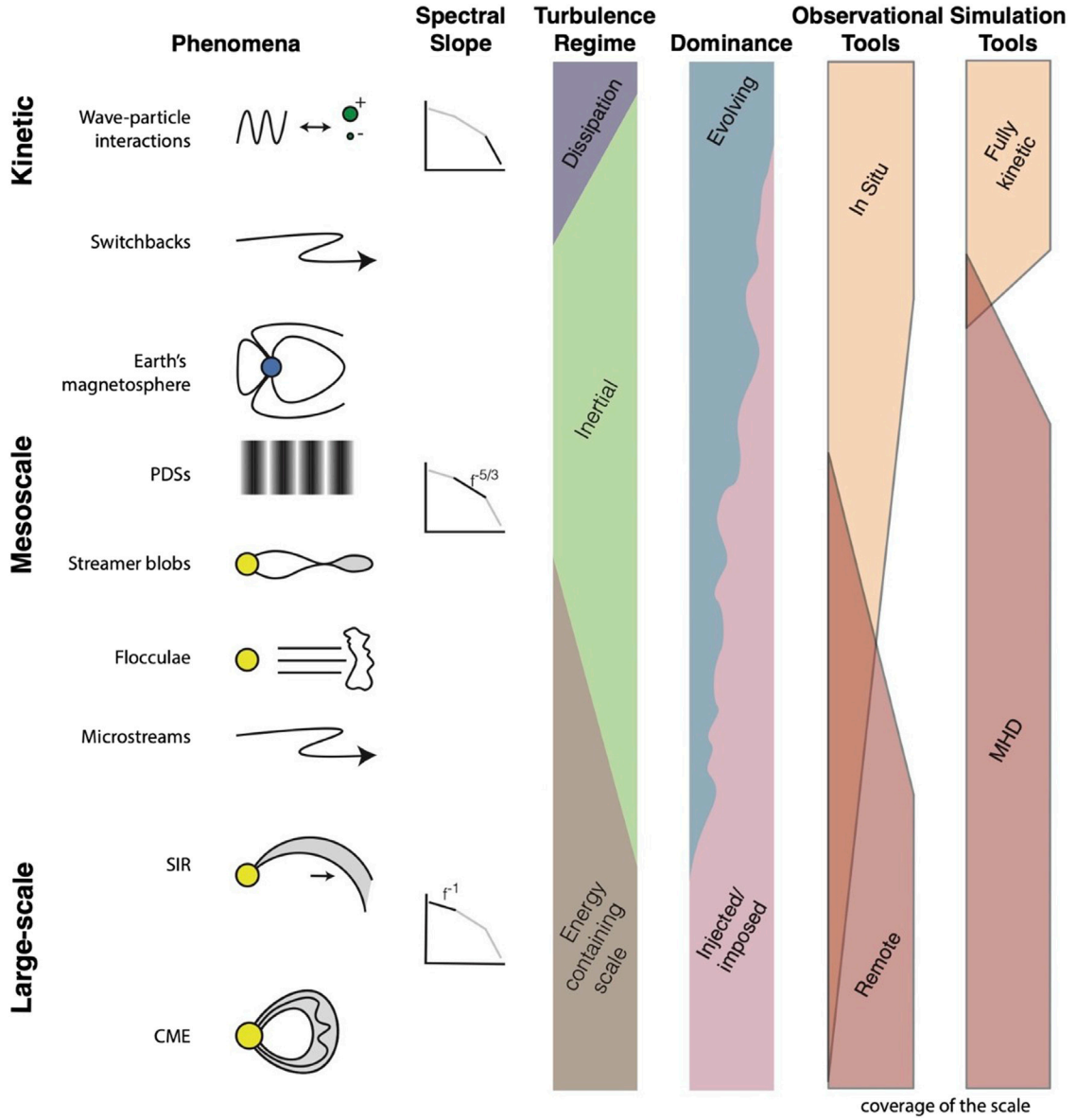

FIGURE 1 | The spatial scales of solar wind phenomena span from the kinetic (<the ion inertial length) to a large fraction of the Heliosphere. The three spatial regimes, kinetic, mesoscale, and large-scale roughly parallel the three turbulence regimes, dissipation, inertial, and energy containing. Structure at the large-scale is clearly injected and imposed by the Sun; structure at the smallest scales has evolved en route. Mesoscale structures are created through evolution and injected/imposed, and which mechanism dominates is ambiguous due to insufficient observations (both *in situ* and remote) and the inability of current numerical simulations to span from kinetic through mesoscales to large-scale.

timescale of solar rotation, the spatial scales associated with the global coronal magnetic field, and phenomena such as coronal mass ejections (CMEs). At the other end of the size spectrum are the smallest scales, those where electron- and ion-scale kinetic physics and dissipation occur, which are all formed through evolution en route. There is a many-orders-of magnitude spread in scale sizes between the large-scale structure and the kinetic dissipation scales of the solar wind (Verscharen et al., 2019). Neither observations nor simulations are currently capable of spanning the mesoscales. We define mesoscales to include this multiple-decade size range that is larger than the dissipation scale and similar plasma scales, and smaller than the largest-scale structures. Unlike the large scale structures, which are always imposed/injected, and the small scale structures, which evolve en route, mesoscale structures can be created through either mechanism. At 1 AU, mesoscales occur between approximately 5–10,000 Mm, or 10 s to 7 h under the assumption that the structures are strictly advecting. For *in situ* measurements, which measure the solar wind at a single point, the spatial scale is related to the measured temporal scale

by $L = V_{sw} * duration$, while in images both spatial and temporal scales can be directly measured.

In **Figure 1** we show a conceptual view of the full range of scales in the solar wind, and highlight representative examples of solar wind phenomena observed at the different scales. The y-axis shows the range of scale sizes from large-scale to kinetic. From left to right, we provide representative cartoon examples of each scale, example spectral slopes of the measured plasma variations, the corresponding turbulence regime, whether the scales' creation is dominated by injected/imposed versus evolution, the ability of current observations to measure them, and the ability of current simulations to model them.

At the smallest scale lies the kinetic scale, where plasma dynamics and structure are dictated by the motion of individual particles. The transition between the kinetic and the mesoscale is generally considered to be related to the ion inertial length, d_i, or the ion gyroradius. At 1 AU, the observed break in the spectra of magnetic field fluctuations from the inertial range to the dissipation scales typically is observed to occur at advected time scales of several seconds (Leamon et al., 1999), or equivalently on spatial scales on the order of hundreds of km through a few Mm via the Taylor hypothesis (that spatial crossing time dominates temporal behavior of the solar wind as measured *in situ*). This scale is close to the proton cyclotron frequency (Verscharen et al., 2019) though multiple mechanisms have been suggested to explain this spectral break (Leamon et al., 1999). Note also that the Taylor hypothesis has limitations in the context of turbulence (Treumann et al., 2019; Bourouaine and Perez, 2020; Perez et al., 2021). At these small scales, all of the structure and dynamics are created as a result of processing and evolution en route to 1 AU. Any injected or imposed structure from the corona begins to evolve on timescales as rapid as the wave-particle interaction time scale (Bruno and Carbone, 2013); structural evolution on small scales has been observed both *in-situ* (Elliott et al., 2016) and (on larger scales) remotely (DeForest et al., 2015).

The largest scale solar wind structures are all imposed/injected from the Sun. For example, the traditional solar wind separation by speed into "fast" and "slow" wind (Neugebauer and Snyder, 1962; Neugebauer and Snyder, 1966; McComas et al., 1998), are empirically associated with and imposed by the large scale solar structures coronal holes and coronal streamers, respectively. Co-rotating interaction regions (CIR) and stream interaction regions (SIR) form due to adjacent faster and slower wind regions in combination with solar rotation, producing compression regions where the fast wind catches up with the slow, and rarefaction regions behind (Gosling and Pizzo, 1999). This is an example of directly imposed structures that have been observed in white light and tracked to 1 AU using combined STEREO SECCHI Heliospheric imager data and L1 *in situ* observations (Rouillard et al., 2009; Rouillard et al., 2010a; Rouillard et al., 2010b), and evidence of them survives out to 10 AU (Richardson, 2018).

The transition from the large scale to the mesoscale range is more ambiguous than the transition from small scale to mesoscales. For the purposes of this paper, we define the mesoscales to be the scales at 1 AU at which structures can be both imposed/injected from the Sun as well as generated en route. The upper end is roughly 10,000 Mm (or 7 h), based on observational and theoretical evidence for mesoscale structures that were created in both ways. These sources of mesoscale structure are not mutually exclusive, as structures from the solar atmosphere will also evolve as they advect. Thus, the complexity in this mesoscale regime is a result of the presence of both imposed/injected and evolved structures, and the interplay between them. Determining the fractional amount of mesoscale structures formed through imposed/injected versus evolved is important for understanding both solar wind formation and turbulent evolution, and the answer is likely dependent on solar wind type and radial distance (evolution time) from the Sun.

Mesoscale solar wind structures are important to study for at least three reasons. First, like the solar wind, the Sun is also dynamic and filled with structures of many scales. Many of the spatial structures are imposed directly onto the heliosphere, and many of the transient dynamics are injected directly into the solar wind as it is formed. Thus, the solar wind and its structures contain imprints of the physical processes that heat the corona and that release and accelerate the solar wind (Viall and Borovsky, 2020). In particular, the traditional bimodal solar wind classification by speed overly simplifies the inherent nature and mesoscale structure of the solar wind. Furthermore, the bimodal classification does not account for solar wind observed to be of other "types" with distinct properties (Roberts et al., 2020a), e.g., slow wind that is highly Alfvénic (Roberts et al., 1987; D'Amicis and Bruno, 2015). Rather than only two types of solar wind, solar wind formation can occur via many different pathways, or combinations of physical mechanisms and source locations (Viall and Borovsky, 2020), each of which injects and imposes different structures with unique properties into the solar wind. Some pathways to solar wind formation result in solar wind plasma with properties and mesoscale structures that cannot be interpreted with the simple bimodal classification.

A key aspect of the new framework that allows for many pathways to solar wind formation is that it considers the time history of the solar plasma as it becomes the solar wind. This oft-ignored time history of solar wind formation imparts unique, observable imprints of the physical regime and processes that dominate each step; mesoscale structures can be one of the results. Observations of collisionality (Kasper et al., 2008; Kasper et al., 2017) and composition (Zurbuchen et al., 2002) are also examples where the solar wind exhibits a continuum of states rather than bimodality, and are examples where the time history of the plasma likely influences the resulting solar wind characteristics. The three steps of solar wind formation time history are source, release, and acceleration. The first step is the source of the plasma–i.e., whether it originates from a coronal hole (CH), which are tenuous and cooler, an active region (AR), which are dense and hot, or from the quiet sun (QS), which are of medium temperatures and densities. Separating the solar wind source into these three types of locations in the corona, which themselves are associated with different solar magnetic field configurations and plasma conditions, is essentially an

empirical proxy for coronal heating (Viall et al., 2021). The second step is the release of plasma–whether the plasma is on open magnetic field lines, with one footpoint rooted in the Sun and the other already open to the heliosphere, or whether the plasma is on closed magnetic field lines, with both magnetic footpoints rooted in the Sun, requiring reconnection for the plasma to be released into solar wind. The third step is plasma acceleration, a process that continues through the high corona. All three steps can occur through a single physical process, such as turbulence; in such cases, the coronal heating mechanism, solar wind release, and solar wind acceleration all result from the same process (Cranmer et al., 2017). However, whenever the second step is reconnection, then steps one and three are necessarily separate processes because they occur in different physical regimes, thus leaving distinct plasma observables and structures in that parcel of solar wind. This time history of solar wind formation provides the seeding for eventual turbulence, and can also lead to the direct creation of mesoscale structures.

The second reason for studying mesoscales is that as the solar wind advects outward, these structures evolve, decay, and generate new mesoscale structures through turbulence, and thus represent a "laboratory" for studying this fundamental process (Bruno and Carbone, 2013).

The third reason for studying mesoscales is that dynamic solar wind and embedded mesoscale structures continually buffet all of the planets in our solar system, and are the medium through which larger structures and energetic particles propagate. Mesoscale structures and dynamics provide a fundamental transfer of energy from the Sun to Geospace, and constitute the ground-state of space weather–the every-day driving of Geospace that happens even during ambient conditions.

In the next three sections we delve into further detail on structures in the solar wind, represented in **Figure 1**, and elaborate on the three above-mentioned reasons that understanding mesoscale structures in the solar wind is critical for advancing our understanding of solar wind formation and evolution. In **Section 2**, we describe evidence of imposed and injected structures that leave imprints of coronal heating, and of the solar wind release and acceleration mechanisms. In **Section 3** we describe evidence of turbulent evolution destroying and creating structures. In **Section 4** we describe how these different types of mesoscale structures drive dynamics in the magnetosphere. Finally, in **Section 5** we discuss the interplay and ambiguity between evolution vs. injection/imposing of these structures, when and under what conditions each mechanism may dominate, and outline potential paths forward for scientific understanding of this complex interconnection.

2 IMPOSED AND INJECTED STRUCTURE IN THE SOLAR WIND

Much of the mesoscale structure and variability in the solar wind, especially observed within 1 AU, is imposed and injected from the Sun. For decades, researchers have speculated that many *in-situ* detected solar wind structures have a solar origin (Crooker et al., 1993; Crooker et al., 1996b), predating observations that were capable of conclusively and routinely differentiating between possible sources. Some fraction of the injected or imposed structures provide the energy for the turbulent cascade, or otherwise evolve as they advect, which we will describe in **Section 3**. In this section we focus on identifiable structures that are unambiguously of solar origin.

There exist two main observational methods for unambiguously identifying structures that were injected/imposed from the Sun. The first and most direct method is through remote imaging. This is typically done in white light, which is sensitive to electron density and location relative to the Thomson Surface (Vourlidas and Howard, 2006; Howard and DeForest, 2012), or extreme ultraviolet (EUV) emission, which is sensitive to electron density squared and is a function of temperature. When remote images exist with sufficient cadence and coverage, structures can be tracked in time from the solar corona as they accelerate outward into the solar wind (Sheeley et al., 1999; Viall et al., 2010; Viall and Vourlidas, 2015-07; DeForest et al., 2016; Alzate and Morgan, 2017; Rouillard et al., 2020; Alzate et al., 2021).

The second method is to use *in situ* observations of ionic and charge state composition. These quantities are frozen into the plasma at heights in the corona at which the collisional ionization and recombination rates are small. Therefore, above these heights these properties do not evolve, thus compositional changes observed *in situ* indicate that the structure was formed in the chromosphere and/or corona. The ionic charge states are generally frozen in by 1.5–3 solar radii, but some elements are not frozen in until as high as four or five solar radii (Landi et al., 2012). The relative abundance of elements with low first ionization potential (FIP) are set lower down in the chromosphere and a relative enhancement of the abundance of low FIP elements is an indicator of plasma release from the closed field corona (Peter, 1998; Laming, 2015). Recent theoretical work argues that the relative abundance of the element sulfur may be a unique indicator of the release of plasma from previously closed-magnetic field lines (Laming et al., 2019). The relative amount of ions as a function of mass can also change in the corona through gravitational effects (Raymond et al., 1997; Weberg et al., 2012-11). This could be the result of closed magnetic field lines with flows that are small enough such that gravitational settling occurs (Feldman et al., 1998). The relative amount of He 2++, or alpha/proton (AHe) ratio is also set in the solar atmosphere, but it is currently unknown which physical mechanism(s) determines the final ratio observed in the solar wind. AHe could be the result of mass dependent processes, particularly when closed field lines open to the solar wind, and lighter protons escape faster than alpha particles (Endeve et al., 2005-05). Currently, observations indicate that AHe is largely the result of FIP fractionation through the chromosphere (Rakowski and Laming, 2012), with an AHe "shutoff" (a rapid depletion in AHe) occurring prior to solar cycle onset that is likely the result of a mechanism near or below the photosphere (Alterman et al., 2021). In summary, the nature of the compositional change are linked to the physical processes involved in creating the solar wind and mesoscale structures that

are injected/imposed from the Sun. Thus, such mesoscale structures contain imprints of the physical mechanisms that heat the solar corona and release and accelerate the solar wind.

Related, although specific entropy (T/n^{γ}) is not a conserved quantity, as it evolves with distance from the Sun, it is anticorrelated with the conserved quantity of charge state and therefore it can also be used as a proxy indicator of imposed or injected structures (Pagel et al., 2004). Likewise, temperature changes, which are not conserved, can be used when observed close to the Sun as a tracer of solar-created structures by the release of hotter plasma from closed-magnetic field lines on the sun through reconnection (Stansby and Horbury, 2018; DiMatteo et al., 2019). For example, in recent work on mesoscale-sized patches of switchbacks using data from Parker Solar Probe, (Woodham et al., 2020) argued that, based on enhanced $T_{\parallel}$ in the patches relative to their surroundings, the patches themselves could be structure injected from reconnection in the solar corona.

In a few isolated cases, which we describe in the examples below, it has been possible to directly link remote observations with *in situ* measurements of injected and imposed mesoscale structures and follow them from their creation at the Sun out into the Heliosphere. However, in most cases it is unknown how far out into the heliosphere the remotely observed structures survive. Likewise, even when compositional changes observed *in situ* indicate a solar creation mechanism, it is usually not known precisely which solar structures created the in situ-determined structures. When mesoscale structures are observed without compositional variations, their source is ambiguous, and could have been due to evolution en route, or imposed/injected structure. Thus, most connections between specific *in situ* phenomena and remote phenomena are qualitative.

The largest structure that the Sun imposes on the Heliosphere is that of its magnetic field, in which the global magnetic polarity inversion line in the corona results in the structure of the Heliospheric Current Sheet (HCS). As the solar cycle progresses, the Sun's magnetic field becomes more complex, and can even form multiple HCSs. The HCS as a structure imposed from the Sun was confirmed through predictions using the magnetic field extrapolated from the photospheric measurements (Hoeksema et al., 1983) as well as with the AHe changes associated with the HCS (Gosling et al., 1981). There is evidence that the Sun also imposes spatial structures on mesoscales that survive at least through the inner heliosphere, and possibly out as far as Ulysses measurements (1–5 AU). The complexity of the photospheric magnetic field produces a web of separatrices, the S-web, (Antiochos et al., 2011; Linker et al., 2011; Titov et al., 2011; Pontin and Wyper, 2015) in the solar corona on mesoscales. Separatrices in the corona are regions where reconnection-released solar wind is most likely to occur. Thus, the imprint of the spatial structure of the S-web is predicted to impose boundaries between reconnection-released wind and open-field wind in the heliosphere on mesoscales (Crooker et al., 2004; Crooker and McPherron, 2012; Aslanyan et al., 2021). Recent simulations of interchange reconnection, which is induced at the lanes between cells of magnetic footpoint driving, predict that remnants of the scale size and pattern of photospheric driving by supergranular flows should be imposed along S-web corridors and into the solar wind (Aslanyan et al., 2021).

Another example of imposed mesoscale structure may be a type of pressure balance structure (PBS) observed by Ulysses, in which the changes in plasma pressure are approximately balanced by the changes in magnetic pressure and have a timescale of less than a day (McComas et al., 1995). There is evidence that polar plumes observed in polar coronal holes may be imposing these heliospheric counterparts as imprints in the polar solar wind (Poletto, 2015). Even in the ecliptic, fast speed streams observed by Helios also showed evidence of PBSs that were correlated with those expected from a superradial expansion of plumes into the heliosphere (Thieme et al., 1989; Thieme et al., 1990). Though PBSs can also be created through mechanisms en route such as slow mode waves (Yao et al., 2013a; Yao et al., 2013b), the high beta portion of the type of PBSs observed by Ulysses were highly correlated with AHe, and therefore likely of solar origin (Reisenfeld et al., 1999). Given the association of the observations with high latitudes during solar minimum (and therefore likely polar coronal holes), and the association with the high beta portion of the structures, (Reisenfeld et al., 1999) suggested that the structures were polar plume extensions. However, the structures' observed frequency did not follow the expected frequency vs. latitude distribution for co-rotating features, and PBS signatures may also be susceptible to instability and mixing (Parhi et al., 1999).

Towards the middle range of the mesoscales, (Borovsky, 2008) studied the scale size of flux tubes observed at 1 AU and found a median scale size of ~440 Mm, and suggested that they were fossilized structures imposed by structures from the Sun. (Borovsky, 2016) examined what they classified as "unperturbed coronal hole plasma" between 0.3 and 2.3 AU and found the plasma to be structured in many of its components, including in AHe and proton specific entropy variations, confirming a solar source to much of the coronal hole wind variability. They argued the radial size scales measured at the spacecraft correspond to longitudinal scales at the Sun as a result of solar rotation. Assuming this geometry, they concluded that the longitudinal scales of the corresponding structures at the Sun would be a significant fraction of a supergranule (which are 30–35 Mm diameter in the photosphere). Thus, they could be due to open magnetic field funnels imposing structure on the solar wind. Examining the boundaries between these mesoscale structures, (Borovsky, 2020b) showed that discontinuous changes in AHe are correlated with discontinuities in the magnetic field direction, i.e., current sheets. They showed that this correlation applies to all types of solar wind, and that the discontinuities are weaker away from the changes in AHe. Lastly, they showed that sharp changes in electron strahl intensity also corresponded to larger discontinuities in the magnetic field direction. Together, these observations support the interpretation that much of the mesoscale structure in the solar wind is likely imposed flux-tube structure from the solar corona.

There are also time-dynamic processes in the solar atmosphere that inject structure into the solar wind and heliosphere. The

largest injected transient structures are CMEs. These are explosive events that can have speeds of up to thousands of km/s. They involve the buildup and release of magnetic energy at a magnetic polarity inversion line. Though large CMEs are generally considered to be created by different phenomena than the ambient solar wind, the same mechanism of magnetic energy build up at a polarity inversion line and subsequent release that creates CMEs is likely also responsible for a spectrum of mesoscale structures in the solar corona from pseudostreamer jets (Kumar et al., 2021) down to small X-ray and EUV jets (Sterling et al., 2015; Wyper et al., 2017). It is predicted that such jets in polar coronal holes could inject mesoscale structures into the solar wind that could be observed in the near-Sun environment with Parker Solar Probe (Roberts et al., 2018). However, based on empirically-determined jet rates and filling factors (Savcheva et al., 2007; Sako et al., 2013), (Roberts et al., 2018) estimated that Parker Solar Probe would only encounter an average coronal hole jet about once in 50–100 days of observations. While it is currently unknown how far out into the heliosphere distinguishable jet signatures survive, it has long been thought that microstreams observed in Ulysses could be remnants of x-ray or EUV jets. Microstreams have velocities ± 35 km/s relative to background, last 6 h or longer, and occur in conjunction with large angle magnetic discontinuities. They have higher kinetic temperatures, proton flux, and a slight enhancement of low FIP elements compared to the average fast solar wind. The compositional changes associated with microstreams indicate a solar origin (Neugebauer et al., 1995; Neugebauer et al., 1997). (Neugebauer, 2012) argued specifically for coronal x-ray jets as the solar source, but polar plumes are also a possibility due to their association with x-ray jets (Neugebauer et al., 1997; Poletto, 2015). Using simulations of jets, (Karpen et al., 2016) demonstrated that the associated Alfvén wave and density and velocity enhancements produced by jets are sustained through the outer corona, and are consistent with *in situ* observations of microstreams. Similarly, (Velli et al., 2011) simulated polar plumes and demonstrated that the observed velocity increase in microstreams could be explained by different heat deposition in plumes. Evidence suggests that plumes are driven by jetting activity at their base (Raouafi et al., 2016), thus for progress it is likely necessary to treat x-ray jets and plumes as different observable manifestations of a common process.

At the large scales, but at slower speeds, are slow helmet streamer blowout CMEs, a subset of which are the so-called "stealth" CMEs, that do not have an obvious signature in the low corona (Howard and Tappin, 2008; Robbrecht et al., 2009). Stealth CMEs originate higher up in the corona, are slow (about 300 km/s) (Ma et al., 2010; Howard and Harrison, 2013), and, though "stealthy," their connection through the global-scale coronal magnetic field to the low corona can be identified through advanced image processing (Alzate and Morgan, 2017). (Lynch et al., 2016) modeled a stealth CME by imposing a large scale global shear meant to represent the effects of differential rotation on the global coronal magnetic field. They showed that the footpoint energization in such driving takes place across the polarity inversion line associated with the HCS and helmet streamers, as opposed to a polarity inversion line in an active region.

As with explosive CMEs, streamer blowout CMEs likely also represent the large end of a continuum of structures created through a common physical mechanism. There is an abundance of mesoscale structures that are also associated with the HCS. (Crooker et al., 1993; Crooker et al., 1996a) identified mesoscale structures within the HCS *in situ* at L1, which they demonstrated could not be due to a wavy HCS traversed by the spacecraft. Instead, they suggested a solar source to the structures because the observed structures were consistent with tangled flux ropes, and flux ropes are generally considered a signature of reconnection. (Suess et al., 2009) expanded on prior *in situ* studies of the AHe depletions occurring at the HCS, and showed that the AHe changes are not centered on the HCS. The offset AHe changes are consistent with solar reconnection-injected structure near the HCS, rather than a static HCS. Thus, the imposed large scale structure of the HCS is also comprised of injected structures at mesoscales; this picture is most recently confirmed by Parker Solar Probe *in situ* observations close to the Sun (Lavraud et al., 2020). Also consistent with this picture, mesoscale plasma blobs are observed in remote white light imaging to be released from the tips of helmet streamers on scales of many hours (Sheeley et al., 1997; Wang et al., 1998; Wang et al., 2000; Harrison et al., 2009; Rouillard et al., 2009; Sheeley and Rouillard, 2010). Their continued acceleration is observed out to 30 solar radii, where they reach typical speeds of around 300 km/s. In some cases, streamer blobs have been tracked from their helmet streamer release out to their observation *in situ* at 1 AU (Rouillard et al., 2010a; Rouillard et al., 2010b), and Parker Solar Probe *in situ* data taken around 30 solar radii (Rouillard et al., 2020). Reconnection at the helmet streamer seems to be fundamental to the release of blobs. Observations in white light of raining inflows (Sheeley et al., 1997; Wang et al., 2000) and the dipolarizations associated with blobs (Sanchez-Diaz et al., 2017), suggests that the reconnection often occurs around four to five solar radii. MHD models (Higginson and Lynch, 2018; Lynch, 2020) and 2D thermal models (Allred and MacNeice, 2015; Endeve et al., 2005-05) also show that helmet streamer tips are dynamic and prone to reconnection. This general picture of streamer reconnection led (Lynch et al., 2016) to argue that stealth CMEs represents the middle of the continuum between fast CMEs and mesoscale helmet streamer blobs, wherein the same universal process of shear across a polarity inversion line leads to reconnection-released plasma into the heliosphere.

On mesoscales of tens of minutes to a couple of hours are puffs and periodic density structures. Some of these have been observed in white light images to originate at the Sun as low as 2.5 solar radii, and can be followed out to about 50 solar radii (Sheeley et al., 1997; Viall et al., 2010; Viall and Vourlidas, 2015-07; DeForest et al., 2016; DeForest et al., 2018). As with helmet streamer blobs, periodic density structures occur preferentially near the HCS (Viall and Vourlidas, 2015-07). They occur at several characteristic scales, including 90 min (Viall and Vourlidas, 2015-07) and shorter (DeForest et al., 2018). In a simulation of reconnection at the helmet streamer, (Réville et al., 2020) demonstrated that periodic density structures at the HCS could be the result of the tearing mode. On the other hand, (Allred and MacNeice, 2015) and (Schlenker

et al., 2021) argued that the periodicity was determined by the interplay between heating and expansion of the last closed field lines, and the retraction of field lines after reconnection. (Pylaev et al., 2017) argued for a third mechanism, wherein a standing shock at the 90 min acoustic cutoff frequency of the corona drives reconnection. Regardless of the precise mechanism, the timescale of the resulting density structures is a constraint on how magnetic reconnection occurs at the helmet streamers. With limitations of current remote white light instruments in terms of sensitivity, and temporal and spatial resolution, periodic density structures are too small and faint to see in more tenuous wind outside of streamers, or beyond about 50 Rsun where the density and associated signal is too weak. However, (DiMatteo et al., 2019) identified several instances of 90 min periodic density structures at the HCS close to the Sun in Helios data. They were associated with temperature changes, and thus determined to be of solar origin. At 1 AU, (Kepko et al., 2016) showed an example of 90 min periodic density structures associated with compositional changes, and (Viall et al., 2009b) showed an example of 30 min periodic density structures associated with AHe changes. Thus, at least some periodic density structures survive through the inner heliosphere. Both (Kepko et al., 2016) and (DiMatteo et al., 2019) showed evidence that at least one of the structures in the periodic density train was a flux rope, and so consistent with reconnection as their formation mechanism.

More generally, mesoscale structures in the heliosphere away from the HCS are expected as a result of interchange reconnection at the boundaries between open and closed fields or S-web arcs (Higginson et al., 2017a; Higginson et al., 2017b). Indeed, (Mason et al., 2019) observed evidence of interchange reconnection at a null-point topology (i.e., a distinct closed magnetic field structure from the helmet streamer) in the corona. With current sensitivity limitations in EUV data, it was not possible to see the solar wind outflows associated with the reconnection. In one event of periodic density structures observed close to the Sun by Helios, the solar coronal source was confirmed via concurrent temperature changes, and the location was determined to be far from the HCS, an important test of the S-web theory of reconnection-released solar wind (DiMatteo et al., 2019). Analyzing 25 years of Wind solar wind density data, (Kepko et al., 2020) identified periodic density structures in all types of solar wind, including fast, ecliptic wind. They occurred at particular timescales, or equivalent radial length scales, that were associated with the solar cycle, and the terminator (McIntosh et al., 2019). Since the 25 years Wind study used all periodic density structures that were identified, without testing for associated compositional changes, it is possible that not all of those were created at the Sun. Even for those that are, further investigation is required to determine if their properties are a function of different types of solar wind sources, e.g. reconnection at the HCS versus other S-web arcs.

3 TURBULENT STRUCTURING IN THE SOLAR WIND

Structuring and/or destruction of mesoscale solar wind structures can also occur through turbulence. As **Figure 1** shows, the scales of observed solar wind mesoscales also correspond to the energy containing and inertial range scales expected from turbulence. Both fluid and MHD turbulence are driven by nonlinearities represented by the underlying equations of motion. These nonlinearities lead to cross-scale cascades of energy first described by Kolmogorov (1941) and Kraichnan (1967) and treated by many authors (Frisch, 1995; Bruno and Carbone, 2013). The turbulent cascade carries energy and structure from the large energy-containing scale through a very broad inertial range of scales (roughly encompassing the mesoscales defined above) that are dominated by the turbulent cascade, to a dissipation scale where the energy becomes a source of heat (Leamon et al., 1998). In the case of the solar wind, the energy containing scales are determined by dynamics and structure of the corona itself (Tu and Marsch, 1995; Chae et al., 1998; Cranmer et al., 1999). A large variety of mechanisms including hydrodynamics, MHD modes, and magnetic reconnection, can give rise to turbulent cascades; once the system develops a cross-scale energy cascade and characteristic spectral power-law signature, it is considered "turbulent" regardless of the specific mechanism. The importance of a cross-scale cascade is that it gives rise to perturbations in all major measurable parameters of the flow, including density, velocity and magnetic fields, and other structural identifiers. The specific relationship between different types of perturbation depends on the mechanism itself.

There are many lines of evidence indicating that the solar wind is processed by turbulence as it moves through the solar system, e.g., see review by (Matthaeus and Velli, 2011). To measure the turbulence properties using *in situ* data requires the inclusion of the Taylor approximation that the dominant source of variability is spatial structures sweeping over the spacecraft. Therefore, time spectra yield equivalent spatial spectra of perturbations in all major wind parameters (Matthaeus and Velli, 2011); the validity of the Taylor approximation is also corroborated by multi-spacecraft measurements of at least some coherence parameters (e.g., Matthaeus et al. (2005)). That corroboration is important, because the Taylor approximation is known to be limited in the context of turbulence (Klein et al., 2014; Bandyopadhyay et al., 2020).

The presence of a turbulent cascade at 1 AU has long been inferred from time spectra of *in situ* measurements (Coleman, 1966; Horbury et al., 2005). Comparisons of the magnetic field spectra measurements show that the break point between the energy containing scales and the inertial range evolves with distance from the Sun. In the fast wind, this break point occurs near 10 mHz at 0.3 AU and steadily evolves to lower frequencies at larger distances of less than 0.1 mHz at 4.8 AU (Bruno et al., 2009; Bruno and Carbone, 2013). Those results also showed that the slow wind is not observed to have a corresponding break between the inertial and energy containing scales, but more recent results with Parker Solar Probe show that the slow wind has a break to energy containing scales, but at a lower frequency than the fast wind (Chen et al., 2021).

The correlation length is often used to define the large end of the inertial range of scale, under the assumption that it represents the largest scale of turbulent eddies. Multi-spacecraft

measurements have yielded 1,000–2000 Mm as the correlation scale at 1 AU (Matthaeus et al., 2005), corresponding to 1–2 h crossing time, although the measurement itself is sensitive to analysis technique (Isaacs et al., 2015) and may be longer. While *in-situ* measurements are limited to statistical analyses of the overall character of the solar wind, imaging measurements afford direct detection of individual features. The coherence length result is corroborated by test particle analysis using features in comet Encke's tail (DeForest et al., 2015), which also identified an eddy size scale of approximately 1,000–2000 Mm (i.e., with roughly 90 min crossing time) at 1AU. However, the comet tail result may be affected by a turbulent "vortex street" from interaction between the solar wind and the comet (Nisticò et al., 2018), and therefore may differ from the turbulent field of the bulk solar wind itself. This uncertainty associated with the characteristic coherence length is reflective of the difficulty of measuring the "native" solar wind flow. While ample spectral signatures indicate the presence of a turbulent cascade, definitively measuring the spectral limits of the cascade - and therefore the dominant processes affecting solar wind variability at different scales - remains an open problem, in part because different solar wind parameters yield different spectral characteristics (Bruno and Carbone, 2013).

In addition to direct spectral measurements and correlation lengths, several other key results demonstrate that the statistical characteristics of the solar wind evolve with propagation, approaching a state consistent with turbulent processing. Tracing of the cross-helicity evolution with distance from the Sun provided one of the first clear lines of evidence that nonlinear dynamical evolution occurs in the solar wind (Roberts et al., 1987). More recently (Telloni et al., 2021) measured a stream of solar wind at 0.1 and 1.0 AU and showed that the magnetic spectral density, flatness, and higher order moment scaling laws were consistent with Alfvénic fluctuations near the Sun evolving into fully developed turbulence. Similarly, (Chen et al., 2020) showed that turbulence evolves between 0.17 and 1 AU: at 0.17 AU the data showed increased energy spectral density, a slope of −3/2, lower magnetic compressibility, and increased relative amount of outward propagating Alfvénic fluctuations compared to inward. Close to the Sun, both the magnetic field and velocity spectra have a slope of −3/2, but only the magnetic spectra is observed to steepen with distance, and the outward dominance of the Alfvénic fluctuations is observed to decrease with distance (Chen et al., 2021; Shi et al., 2021). The evolution of the outward wave dominance as well as the evolution of the spectral break point with distance is supported by MHD simulations of turbulence (Roberts et al., 1991). As physics-based models of turbulence become more complex, they are able to reproduce many of the observed characteristics of the solar wind (Roberts and Ofman, 2019; Adhikari et al., 2021).

The dissipation scale, which defines the small-scale end of the turbulent inertial range of scales, varies with plasma condition and with distance from the Sun; a useful benchmark at 1 AU is 2 s (Leamon et al., 1998), or approximately 600 km. At scales much smaller than this, the spectrum steepens as kinetic phenomena convert the perturbations to fully randomized heat. More recent work has demonstrated that the relationship between temperature and velocity evolves with distance in a way that is consistent with turbulent processing (Elliott et al., 2012; Lionello et al., 2014). Entropy also increases and has less variability with distance, indicating heating and turbulent processing (Roberts et al., 2005). The so-called switchbacks observed by Parker Solar Probe exhibit different break scales between inertial and dissipation scales and increased level of intermittency than the surrounding wind, perhaps contributing to the turbulent heating in the inner heliosphere (Martinović et al., 2021).

Importantly for the purposes of this paper, active turbulence would process any injected or imposed mesoscale structures from the Sun. A general trend of processing and statistical modification is observed to continue to over 30 AU as solar wind features are "worn down" by dynamic interaction with other parcels of wind (Elliott et al., 2016). The solar wind at 0.33 AU was observed with the Helios spacecraft to contain more and sharper spikes in velocity (Horbury et al., 2018) than further away from the Sun, and the trend continues inward to the corona itself in the form of switchbacks observed by Parker Solar Probe (Bale et al., 2019; Kasper et al., 2019). Indeed, the microstreams observed by Ulysses - likely related to the larger of the switchbacks that do survive - are themselves observed to evolve in distance from the Sun (Reisenfeld et al., 1999). This corroborates the picture of a solar wind whose structure evolves from the "young" state with spatial and temporal structure injected by coronal processes, to a more processed state that reflects the observed turbulent spectrum further from the Sun.

There is also evidence that turbulence generates new structures in the solar wind on mesoscales. As one example, there is an active debate as to whether the switchbacks observed by Parker Solar Probe (and described above) are created through turbulence or not, with many arguing that their observed characteristics are consistent with turbulent formation (Squire et al., 2020; Tenerani et al., 2020; Shoda et al., 2021). In another example, work by (DeForest et al., 2016) showed that at least some compact bright features in the images form in the solar wind as it propagates. They identified "flocculae" that are observed to "fade in" to the overall flow between 20 and 80 solar radii from the Sun (see **Figure 1**). Typical flocculae are oblong: about the same size as streamer puffs (~1 solar radius at 30 solar radii altitude) but 3x–10x wider. These have been interpreted as signs of the isotropization of shear-driven turbulence (Chhiber et al., 2019), which may arise locally or be excited as anisotropic magnetically-guided turbulence carried from the outer corona itself (Cranmer, 2012; Cranmer and Woolsey, 2015; Oughton et al., 2015). Similarly, analysis of Helios data showed that the heliospheric current sheet becomes more complex with distance, as indicated by more current-sheet crossings (Roberts et al., 2005). In contrast, a statistical analysis of Helios, IMP8, Wind, ACE and Ulysses data also showed that the occurrence rate of flux ropes in the HCS decreases in frequency and and flux ropes are larger in size with distance from the Sun (Cartwright and Moldwin, 2008; Cartwright and Moldwin, 2010), indicating that they likely merge.

Taken as a whole, these results indicate that solar wind is turbulent. Structure at or below 1,000 Mm observed at 1 AU are well within the turbulent cascade, in a sequence that begins with

both spatial and temporal driving in the corona and processes the imprinted structure through turbulent evolution of shear flows and eddies. Large-scale turbulent eddies appear to form and be isotropized at or shortly above the transition from the low-β corona to moderate-β solar wind, likely about 0.3 AU from the Sun (DeForest et al., 2016), and the cascade appears to fully develop between this distance and 1 AU although the turbulence may remain anisotropic toward the smaller-scale end of the inertial range (Bruno and Carbone, 2013). However, many injected and imposed structures observed on scales of tens of minutes and scales of hundreds to several thousand Mm have been observed to survive to at least 1 AU. We return to the inherent ambiguity of these results and its interpretation in the context of mesoscale structures in **Section 5**.

4 MAGNETOSPHERIC IMPACT OF STRUCTURES

The structured solar wind impacts the magnetosphere in several ways. The solar wind dynamic pressure, $p_{dyn} = n_i m_i v_i^2$, is the primary driver of the magnetopause standoff distance and the size of the magnetosphere. Any mesoscale solar wind structures that are comprised of changes in density and/or velocity will alter the magnetic field magnitude inside the magnetosphere. The interaction between the solar wind dynamic pressure and magnetosphere can be considered quasi-stationary in the response to any solar wind structures that have scales larger than the dayside magnetosphere. As shown in **Figure 1** even the small end of the mesoscales (down to about 100 Mm) in the solar wind are as large as Earth's magnetosphere and, therefore, can drive dynamics in a quasi-stationary way. At ~100 Mm, equivalent to a 4 min duration structure advecting at 400 km/s, the scale size of the structure is approximately similar to the size of the dayside magnetosphere. The temporal scale of the interaction is also near the timescale that information propagates across the magnetosphere, the so-called Alfvénic travel time. Therefore, the quasi-static assumption breaks down for solar wind structures on scales smaller than 100 Mm and/or shorter than 4 min, and propagation effects through the magnetosphere need to be considered. Regardless of the exact timescale of the interaction, solar wind dynamic pressure variability injects compressional energy into the Earth's magnetosphere, where it can affect particle energization, diffusion, and transport.

Large scale solar wind structures, such as CIRs or SIRs that form when a faster wind overtakes a slower wind, are important drivers of magnetospheric activity (Gosling and Pizzo, 1999; Tsurutani et al., 2006; Kilpua et al., 2017). In particular, for Earth's radiation belts it has been recognized for decades that there is a strong correlation between solar wind speed and the flux of relativistic electrons, particularly in the outer zone and for V_{sw} > 500 km/s (Paulikas and Blake, 1979; Miyoshi and Kataoka, 2005; Borovsky and Denton, 2006; Bortnik et al., 2006; Yuan and Zong, 2012). While CMEs are often considered to be large drivers of space weather, SIR-driven geomagnetic storms often exhibit higher fluxes of radiation belt electrons compared to CME-driven storms (Borovsky and Denton, 2006; Kataoka and Miyoshi, 2006; Kilpua et al., 2015; Turner et al., 2019), especially at larger radial distances (>4.5 R_E) and during the declining phase of the solar cycle. The general process of radiation belt enhancements is energization via local chorus waves combined with radial diffusion (see review by Li and Hudson (2019)). While the comparatively long overall SIR scale is important for radiation belt flux enhancements, the mesoscale structures embedded within that large scale structure appear to be an important contributor as well. The compression region between the fast and slow wind is filled with dynamic pressure fluctuations that provide a source of broadband compressional power that drives magnetospheric ultra low frequency (ULF) waves (Kilpua et al., 2013; Kepko and Viall, 2019). ULF waves are known to be an important magnetospheric process that can lead to enhanced radial diffusion, energization, or even loss to atmospheric precipitation. When combined with high solar wind dynamic pressure, this externally driven ULF wave activity can scatter electrons to large radial distances where they can fill a broad region of the radiation belts, or can be lost due to magnetopause shadowing (Turner et al., 2012; Hietala et al., 2014). The entire SIR driving of the magnetosphere can take several days, with the loss of outer zone electrons apparently more dominant during the early part of the SIR, and a net increase in the flux of energetic electrons over the course of the entire SIR event. This highlights the importance of understanding all of the mesoscale aspects of solar wind driving within large scale events.

The subset of mesoscale structure that manifest as periodic density structures are of particular interest for magnetospheric dynamics, because they can drive magnetospheric ULF pulsations at discrete periodicities for extended intervals. There is now a substantial body of research demonstrating magnetospheric pulsations that are directly-driven by solar wind periodic density structures (Kepko et al., 2002; Stephenson and Walker, 2002; Kepko and Spence, 2003; Viall et al., 2009a; Villante et al., 2013; DiMatteo and Villante, 2017). This includes observations of solar wind-driven pulsations in ground magnetometer data (Villante and Tiberi, 2016), high latitude ionospheric radar observations (Fenrich and Waters, 2008), polar UV imaging data (Liou et al., 2008), and even the equatorial ionosphere (Dyrud et al., 2008). MHD simulations have confirmed that cyclic solar wind dynamic pressure structures directly drive magnetospheric oscillations, and locations of field line resonance will even amplify the waves (Claudepierre et al., 2010; Hartinger et al., 2014). The apparent frequencies of periodic density structures in the frame of the magnetosphere is often between 0.5 and 4 mHz (Viall et al., 2009a; Kepko et al., 2020), which is similar to the drift period of radiation belt particles. Kepko and Viall (2019) showed an event where radiation belt particles were precipitating to the atmosphere with a periodicity determined by the solar wind periodic density driver. Recent work utilizing Balloon Array for Radiation-belt Relativistic Electron Losses (BARREL) measurements of particle precipitation suggests an association between solar wind periodic density structures and electromagnetic ion cyclotron (EMIC) wave power enhancements, which scatters energetic electrons into the loss

cone where they are then lost to Earth's atmosphere (Breneman et al., 2020).

An additional mesoscale solar wind structure-magnetosphere interaction that needs to be considered are intervals of large interplanetary magnetic field (IMF) that could lead to enhanced reconnection at the dayside magnetopause. Earth's magnetic field points northward at the magnetopause, and therefore when the IMF has a large southward component (B_{south}), magnetic reconnection is likely to occur. Dayside magnetic reconnection is the primary mechanism by which solar wind energy enters the magnetosphere, and is the ultimate source of much of the dynamics that occur, including geomagnetic storms and substorms. High speed solar wind (>750 km/s) is known to be dominated by large amplitude Alfvén waves (Tsurutani et al., 1994). Within SIRs, these Alfvén waves are compressed and increase in amplitude as the high speed flow impinges upon the slower flow ahead, leading to a pile-up of large amplitude fluctuations in solar wind IMF B_{south}. The combination of high solar wind speed, density, and B_{south} often leads to intense geomagnetic activity. The auroral activity driven by this solar wind interaction has been termed High Intensity Long Duration Continuous AE Activity (HILDCAA) (Tsurutani and Gonzalez, 1987). The relationship between these large amplitude Alfvén waves and the mesocale density structures that are also inherent to SIRs is an area ripe for study.

In some ways, the magnetospheric impact of solar wind structures is independent of whether the solar wind structures are injected/imposed versus formed en route through turbulence. On the other hand, while turbulence and coronal processes can both produce mesoscale structures in the geoeffective size scale range of 100 Mm and greater, coronal processes may produce mesoscale structures with different properties. For example, it seems that unique processes in the corona make them periodic (Kepko et al., 2016; Viall et al., 2009b; Viall and Vourlidas, 2015-07). In another example, (Kepko and Viall, 2019) demonstrated that SIRs compress and amplify existing periodic density structures in the slow wind, thereby increasing their impact on Earth's magnetosphere. This is a clear example of where both the injection mechanisms and evolution impacted Earth's response. In summary, for full predictability of space weather at Earth and the nature of the magnetospheric driving, it is important to understand how much and which types of mesoscale structures are formed through turbulence, or injected/imposed from the solar corona.

5 DISCUSSION

Figure 1 describes the phenomenological structure in the solar wind, from kinetic through mesoscale to large-scale. The turbulence regimes discussed in **Section 3**, and the injected and imposed structures from the Sun discussed in **Section 2**, both produce solar wind structures at mesoscales. There is a clear interplay between imposed and injected structure, the evolution of such structure en route to 1 AU, and turbulence creating new structures, all of which comprise the zoo of mesoscale structures at 1 AU. The goal is to understand this interplay and to determine which type of structures dominate the solar wind under which conditions.

5.1 Differentiating Injected/Imposed vs. Turbulent Structure

There exist many solar wind phenomena on mesoscales for which we cannot determine with certainty whether the associated structures are injected/imposed or are generated en route. As **Figure 1** shows, this is due to lack of both *in situ* and remote observations as well as a lack of applicable models with simultaneous coverage and resolution. Many observations are non-unique to either formation process. When structures are observed *in situ* without compositional changes or a direct link to tracked structures in images, their source is ambiguous, and could have been created via either mechanism (Owens et al., 2011).

Correlation lengths and power law spectra are commonly interpreted in terms of turbulence. However, many physical processes, e.g., any autoregressive process, can result in power law spectra and correlation lengths. Time series of discontinuities can produce a power law with a slope of −5/3 (Borovsky, 2010). There is strong evidence (Borovsky and Burkholder, 2020) that the high frequency end of the magnetic power spectra corresponds to the break point associated with the thickness of the current sheets at strong tangential discontinuities, and the amplitude is associated with the time between current sheets. Likewise, turbulence or other nonlinear processes are likely involved in heating the solar corona (Rappazzo et al., 2008; Cranmer et al., 2017; Klimchuk and Antiochos, 2021). If such mechanisms also affect the creation of the structures in the solar wind, then the spectra and correlation lengths could reflect the remnants of that process, rather than actively evolving turbulence (Viall and Borovsky, 2020). Related, the spectra of velocity, magnetic field, and density each have different spectral slopes, which flatten differently, and different break points (Roberts, 2010; Šafránková et al., 2015). Caution should be taken when inferring the properties of variability in one plasma parameter from the properties of variability in the others. These considerations, together with the evidence of continued wind processing with distance (Elliott et al., 2016), yield an ambiguous picture: there is no clear indicator that either turbulence or solar structuring is the primary driver of solar wind mesoscale structure far from the Sun itself.

There do exist indications that both solar and turbulent processes are important to shaping the solar wind. For example, as described in **Section 2**, there is a population of *in-situ* detected magnetic flux ropes that have been observed simultaneously in white light that are unambiguously formed at the helmet streamer tip through reconnection and advect along the HCS. But the population of all flux ropes in the solar wind, including those at the HCS, could also be due to turbulence (Cartwright and Moldwin, 2008; Cartwright and Moldwin, 2010; Zheng and Hu, 2018; Zhou et al., 2021), and there is evidence that both populations of flux ropes exist in the inner heliosphere (Murphy et al., 2020). Active reconnection is observed to be taking place far out into the solar wind (Gosling and Szabo, 2008), and reconnection across the HCS is very prevalent close to the

Sun (Phan et al., 2021), as well as at the boundaries of switchbacks (Froment et al., 2021). This determination is itself subject to discussion: flux rope identification *in situ* is a difficult problem, and different criteria can result in very different event lists (Feng et al., 2007). Torsional Alfvén waves injected from the Sun, for example, can share properties with flux ropes (Higginson and Lynch, 2018), and flux ropes, plasmoids and magnetic islands can exhibit similar features in the data (Khabarova et al., 2021). Furthermore, turbulent processing is nearly certain to shred and/or merge existing flux tubes or flux ropes in a process analogous to the "magnetochemistry" observed in the photospheric magnetic field (Schrijver et al., 1997), further emphasizing the need for cross-scale measurements to identify those processes.

Switchbacks are another example of mesoscale structures that could be remnants of reconnection at the Sun, or shear flows from structure at the Sun, or turbulence. (Martinović et al., 2021) presented evidence of their formation via turbulence, while (Larosa et al., 2021) argue for the firehose instability to play a role, since only 73% of switchbacks are Alfvénic. (Drake et al., 2021) argue that switchbacks are the result of flux ropes created through interchange reconnection in the corona, and (Tenerani et al., 2020) modeled switchbacks and showed that they persist for up to hundreds of Alfvén crossing times, and thus could be formed in the corona. To date, no single model has been able to explain all the observed features of switchbacks, and the struggle has been to identify unique distinguishing observations that could differentiate the generation mechanisms. It is possible that multiple mechanisms are acting. Whatever their creation, switchbacks are an important mesoscale feature of the solar wind, with many of their signatures persisting further out into the solar wind (where the larger ones were often called microstreams), in observations made by Helios (Horbury et al., 2018), ACE (Gosling et al., 2009) and Ulysses (Neugebauer et al., 1995).

5.2 Injected and Imposed Structures and the Turbulent Cascade

A natural question is how mesoscale structures injected and imposed into the solar wind survive to 1 AU, rather than being wiped out by the turbulent cascade, since they populate the same range of spatial scales. In an analysis of Helios, ACE, Wind and Ulysses observations of AHe and flux tube boundaries, (Borovsky, 2012) showed that there is no evidence of mixing across flux tube boundaries or of stretching and folding of boundaries. As described in **Section 2**, PBSs measured by Ulysses showed a correlation with AHe, suggesting that those PBSs survived through the inner heliosphere (Reisenfeld et al., 1999). This correlation decreased with distance from the Sun, consistent with the eventual evolution and mixing of the polar plume plasma with other plasma (Parhi et al., 1999). This indicates that turbulence is acting, but suggests that 1 AU is still early in the processing of mesoscale structures. The turbulent processing of mesoscale structures may even be a function of latitude, because the effects of solar rotation increases dynamical interactions between streams in the ecliptic. In fact, microstreams and pressure balance structures are easier to detect in Ulysses high-latitude data than ecliptic data (Suess, 2001), and this is thought to be because enhanced dynamic interactions in the ecliptic make it more difficult to detect them.

One possibility is that in the inner heliosphere, some imposed and injected mesoscale structures persist, and turbulence grows within and is bounded by those structures. For example, (Roberts and Goldstein, 1987) showed the magnetic field spectra have a slope of −2 due to sharp jumps in the data, but the spectra follow −5/3 after removal of the jumps. (Borovsky, 2008) argues for fossil, or imposed, flux tubes wherein the turbulence evolves within the flux tubes. Different solar wind streams have different turbulence characteristics (Roberts et al., 2005), and speed is not as important as solar wind source in determining those properties (Shi et al., 2021), indicating that the initial conditions of turbulence on individual flux tubes plays a role. As a final example, if the injected and imposed structures result in large shear flows as implied by the flows measure in (DeForest et al., 2018), turbulence could occur and grow preferentially at such boundaries.

5.3 Importance of Mesoscale Structures as Propagation Medium

CIRs, SIRs and CMEs were mentioned in **Section 1** and shown in **Figure 1** as examples of injected and imposed large-scale structures that persist far into the Heliosphere. Their nature is affected by the solar wind into which they propagate, and there is evidence that these large-scale phenomena may have sub structures that evolve en route. Recent work showed several examples of injected density structures that are compressed and swept up by a higher speed stream behind (Kepko and Viall, 2019). These structures existed in the solar wind, injected at the time of solar wind formation, and were simply swept up with little evolution other than compression. Along these same lines, (Borovsky and Denton, 2010; Borovsky, 2020a) provided evidence that CIRs and interplanetary shocks are not regions of enhanced turbulence. Rather, turbulence measures changed steadily across CIRs, in correlation with source region changes from fast coronal hole wind to slower streamer belt wind. Similarly, the planar magnetic structures upstream of CMEs are thought to be the result of the alignment and compression of preexisting mesoscale structures in the solar wind (Neugebauer et al., 1993) and this resulting structuring is important for geomagnetic impact (Palmerio et al., 2016).

Energetic particle propagation is also highly dependent on the solar wind structure, as the magnetic field can funnel particles, while fluctuations of the magnetic field and density (Reid and Kontar, 2010; Klein and Dalla, 2017) can scatter particles. Many observations of energetic particles have been shown to be consistent with the random walk of field lines from turbulence (Jokipii, 1966; Chhiber et al., 2020). Dropouts in energetic particles and electron strahl also indicate changes in the magnetic topology such as HCS crossings or local kinks in the magnetic field (Crooker et al., 1982; Borovsky, 2008). Strahl intensity and width is correlated with magnetic discontinuities (Borovsky, 2021); more generally, energetic particle changes

during ambient solar wind conditions are correlated with changes in magnetic field and plasma at tangential discontinuities (Neugebauer and Giacalone, 2015; Tessein et al., 2015). (Rosenvinge et al., 2009) showed that STEREO energetic particle data exhibit intensity variations that suggested a linkage to flux tubes with diameters ~ 6,000 Mm, with additional variations suggesting flux tube-funneling on scales down to 500 Mm. On smaller scales are dropouts, where the intensity (particle counts per energy bin) in energetic particles decreased, which was also attributed to trapping along flux tubes (Mazur et al., 2000; Chollet and Giacalone, 2008). The dropouts were attributed to flux tubes on the scales of 10–100 Mm (Giacalone et al., 2000; Chollet and Giacalone, 2011). Interestingly, strahl particles respond to switchback structure observed in Parker Solar Probe, but higher energy particles energies do not, possibly because their larger gyroradius may not be able to respond to steep rotational discontinuities (Bandyopadhyay et al., 2021).

6 Future Progress

As shown in the right part of **Figure 1**, sparse observations have been a limiting factor in understanding the nature and evolution of mesoscale structure in the solar wind. Capturing the imposed and injected structure from the Sun, as well as the subsequent evolution and creation of new structures, requires continuous imaging from the low, through the middle, to the high corona, e.g., from the photosphere through at least five solar radii. This is where the closed magnetic field lines, and non-radial corona transitions to a radial, flow-dominated wind. Higher still, the wind undergoes additional physical transitions up through, for example, near 30 Rsun, where the solar wind exceeds the Alfvén speed and many mesoscale structures are "frozen" into the solar wind flow. The highly structured nature of the solar wind implies that there is not likely a single radius that this transition occurs at, but rather a zone over which the Alfvénic transition occurs (DeForest et al., 2018). This requires observations that are continuously sampled in time and have spatial coverage such that structures in the solar wind can be followed from their source in the solar atmosphere to the solar wind. Simultaneously, the observations must have the spatial and temporal resolution and sensitivity to capture the size scales of interest. Remote observations such as from SDO, STEREO, SOHO, shown in **Figure 1**, currently covers a large fraction of this transition. However, coverage is still not global, as it is limited in latitude, and has gaps in coverage in distance from the Sun. Furthermore, the sensitivity and resolution achieved is just able to sample the largest of the mesoscale range. WISPR has the potential to make measurements at the small mesoscale range, and could help fill this gap. In the future, the Polarimeter to UNify the Corona and Heliosphere (PUNCH) mission will have the combined global spatial coverage with temporal and spatial resolution and sensitivity to address the source of mesoscale structures, their propagation through the inner heliosphere, and interplay between injected and imposed structures with turbulence. The COronal Diagnostic EXperiment (CODEX) mission will measure temperature and velocity simultaneously with density and will be able to image changes in temperature and flow injected and imposed from the Sun. Finally, all images of the solar corona and solar wind have been taken from the ecliptic, limiting the ability to measure the azimuthal extent of structures. The solar polar viewpoint is uniquely able to sample the effects of rotation on the solar wind. Solar Orbiter (Müller et al., 2020) will reach an orbital inclination of approximately 30° during the extended phase of the mission, which will provide azimuthal measurements of mesoscale structures and some constraints on rotational effects. A solar-polar mission that images with a sustained view from above 70° could determine the role of co-rotation with the corona on the creation of mesoscale structures, and the azimuthal structuring and scale sizes of such structures.

At the other end of the spectrum, *in situ* measurements of the small scale kinetics have been well studied with magnetospheric missions like MMS (Burch et al., 2016; Bandyopadhyay et al., 2018; Roberts et al., 2020b; Chasapis et al., 2020) and Cluster (Escoubet et al., 1997; Osman and Horbury, 2006; Sahraoui et al., 2009; Roberts et al., 2013) when they are in the solar wind, and the radial dimension of mesoscale structures are captured well with the 1AU assets Wind, ACE, SOHO, STEREO. With the limited *in situ* sampling currently available, these measurements are sparse, so require long averages to build statistics and a global picture. The connection between the global scales and mesoscales can not be done without constellations of *in situ* measurements. Even with ideal separation of the STEREO spacecraft with each other and L1, connecting mesoscales to global scales, and disentangling time dynamics from spatial structure is not possible (Jian et al., 2009; Simunac et al., 2009) using these data alone.

Current computational ability is also limited. Computations that span the global scales down to kinetic scales of the solar wind are not currently possible. As with observations, it is at the mesoscales that simulations are incapable of placing constraints on theories. The highest resolution MHD models of the heliosphere can only resolve scales of >150 Mm (Merkin et al., 2016; Gombosi et al., 2018), capturing the global-mesoscale transition, but not the full cascade through the mesoscales. On the other hand, it is too computationally expensive to expand kinetic simulations up beyond dissipation scales to capture the mesoscales. Hybrid simulations, even if they resolve the same spatial range as MHD, still need to resolve a finer temporal range (gyromotion) and more degrees of freedom (velocity space), with a resultant sacrifice in the simulation size. As we enter the age of exascale supercomputing (10^{18} computations per second), better resolved hybrid simulations will become possible, including 6-days Vlasov codes, as well as new approaches for mesocale simulations, such as spectral and implicit kinetic solvers, which would enable simulation of the full mesoscale range.

7 CONCLUSION

The solar wind contains structures that are injected and imposed directly by the Sun and structures that are generated and evolve en route due to turbulence. At the

extremes of the spatial scales, it is simple to differentiate these creation mechanisms. Yet there exists a several orders of magnitude gap between these two scales, the mesoscale. In this regime, with a size scale at 1 AU of ~5–10,000 Mm and time scales of 10 s–7 h, both injected/imposed and structures generated en route co-exist, and it is often difficult to disentangle the two. Competition between the imposed and injected structures with turbulent and other evolution leads to complex structuring and dynamics. Injected mesoscales carry imprints of the processes that release solar plasma and heats and accelerates the solar wind, and therefore studying them can provide insight into the generation of the solar wind. The mesoscale regime is also the region of observation space that is grossly under-sampled. Sparse *in situ* measurements are limited to radial profiles of the solar wind as the wind advects past the spacecraft, and remote imaging currently cannot resolve many mesoscales. There is very limited azimuthal coverage, and even less out of the ecliptic coverage. Understanding mesoscale structures is important as they are drivers of Earth's magnetosphere, and important upstream conditions for the structuring of CMEs, CIRs, and the propagation of energetic particles.

AUTHOR CONTRIBUTIONS

NMV led the development of the overall structure of the manuscript and the section on imposed and injected structures. CED took the lead on the turbulence section. LK took the lead on magnetospheric impacts and created the figure. All authors contributed to the discussion.

FUNDING

NMV and LK were supported by the NASA competed Internal Scientist Funding Model (ISFM). CED was supported by NASA's Heliophysics Explorers program (PUNCH mission).

ACKNOWLEDGMENTS

The authors acknowledge Simone Di Matteo, Aaron Roberts, and the ISFM team "Connecting the corona to solar wind structure and magnetospheric impact using modeling and remote and *in situ* observations" for their helpful discussion on this topic.

REFERENCES

Adhikari, L., Zank, G. P., Zhao, L. L., Telloni, D., Horbury, T. S., O'Brien, H., et al. (2021). Evolution of Anisotropic Turbulence in the Fast and Slow Solar Wind: Theory and Solar Orbiter Measurements. *Astron. Astrophysics* [Epub ahead of print]. doi:10.1051/0004-6361/202140672

Allred, J. C., and MacNeice, P. J. (2015). An MHD Code for the Study of Magnetic Structures in the Solar Wind. *Comput. Sci. Discov.* 8, 015002. doi:10.1088/1749-4680/8/1/015002

Alterman, B. L., Kasper, J. C., Leamon, R. J., and McIntosh, S. W. (2021). Solar Wind Helium Abundance Heralds Solar Cycle Onset. *Solar Phys.* 296, 67. doi:10.1007/s11207-021-01801-9

Alzate, N., and Morgan, H. (2017). Identification of Low Coronal Sources of "Stealth" Coronal Mass Ejections Using New Image Processing Techniques. *Astrophysical J.* 840, 103. doi:10.3847/1538-4357/aa6caa

Alzate, N., Morgan, H., Viall, N., and Vourlidas, A. (2021). Connecting the Low to High Corona: A Method to Isolate Transients in STEREO/COR1 Images. *ApJ accepted in press*

Antiochos, S. K., Mikić, Z., Titov, V. S., Lionello, R., and Linker, J. A. (2011). A Model for the Sources of the Slow Solar Wind. *Astrophysical J.* 731, 112. doi:10.1088/0004-637x/731/2/112

Aslanyan, V., Pontin, D. I., Wyper, P. F., Scott, R. B., Antiochos, S. K., and DeVore, C. R. (2021). Effects of Pseudostreamer Boundary Dynamics on Heliospheric Field and Wind. *Astrophysical J.* 909, 10. doi:10.3847/1538-4357/abd6e6

Bale, S. D., Badman, S. T., Bonnell, J. W., Bowen, T. A., Burgess, D., Case, A. W., et al. (2019). Highly Structured Slow Solar Wind Emerging from an Equatorial Coronal Hole. *Nature* 576, 237–242. doi:10.1038/s41586-019-1818-7

Bandyopadhyay, R., Chasapis, A., Chhiber, R., Parashar, T. N., Maruca, B. A., Matthaeus, W. H., et al. (2018). Solar Wind Turbulence Studies Using MMS Fast Plasma Investigation Data. *Astrophysical J.* 866, 81. doi:10.3847/1538-4357/aade93

Bandyopadhyay, R., Matthaeus, W. H., Chasapis, A., Russell, C. T., Strangeway, R. J., Torbert, R. B., et al. (2020). Direct Measurement of the Solar-Wind taylor Microscale Using MMS Turbulence Campaign Data. *Astrophysical J.* 899, 63. doi:10.3847/1538-4357/ab9ebe

Bandyopadhyay, R., Matthaeus, W. H., McComas, D. J., Joyce, C. J., Szalay, J. R., Christian, E. R., et al. (2021). Energetic Particle Behavior in Near-Sun Magnetic Field Switchbacks from PSP. *Astron. Astrophysics* 650, L4. doi:10.1051/0004-6361/202039800

Borovsky, J. E., and Burkholder, B. L. (2020). On the Fourier Contribution of Strong Current Sheets to the High-Frequency Magnetic Power SpectralDensity of the Solar Wind. *J. Geophys. Res. Space Phys.* 125, e2019JA027307. doi:10.1029/2019ja027307

Borovsky, J. E. (2010). Contribution of Strong Discontinuities to the Power Spectrum of the Solar Wind. *Phys. Rev. Lett.* 105, 111102. doi:10.1103/physrevlett.105.111102

Borovsky, J. E., and Denton, M. H. (2006). Differences between CME-Driven Storms and CIR-Driven Storms. *J. Geophys. Res. Space Phys.* 111, A07S08. (c) 2006: American Geophysical Union. doi:10.1029/2005ja011447

Borovsky, J. E., and Denton, M. H. (2010). Solar Wind Turbulence and Shear: A Superposed-Epoch Analysis of Corotating Interaction Regions at 1 AU. *J. Geophys. Res. Space Phys.* 115, n/a. doi:10.1029/2009ja014966

Borovsky, J. E. (2021). Exploring the Properties of the Electron Strahl at 1 AU as an Indicator of the Quality of the Magnetic Connection between the Earth and the Sun. *Front. Astron. Space Sci.* 8, 646443. doi:10.3389/fspas.2021.646443

Borovsky, J. E. (2008). Flux Tube Texture of the Solar Wind: Strands of the Magnetic Carpet at 1 AU?. *J. Geophys. Res. Space Phys.* 113, n/a. doi:10.1029/2007ja012684

Borovsky, J. E. (2012). Looking for Evidence of Mixing in the Solar Wind from 0.31 to 0.98 AU. *J. Geophys. Res. Space Phys.* 117, n/a. doi:10.1029/2012ja017525

Borovsky, J. E. (2020a). The Compression of the Heliospheric Magnetic Structure by Interplanetary Shocks: Is the Structure at 1AU a Manifestation of Solar-Wind Turbulence or Is it Fossil Structure from the Sun?. *Front. Astron. Space Sci.* 7, 582564. doi:10.3389/fspas.2020.582564

Borovsky, J. E. (2020b). The Magnetic Structure of the Solar Wind: Ionic Composition and the Electron Strahl. *Geophys. Res. Lett.* 47, e2019GL084586. doi:10.1029/2019gl084586

Borovsky, J. E. (2016). The Plasma Structure of Coronal Hole Solar Wind: Origins and Evolution. *J. Geophys. Res. Space Phys.* 121, 5055–5087. doi:10.1002/2016ja022686

Bortnik, J., Thorne, R. M., O'Brien, T. P., Green, J. C., Strangeway, R. J., Shprits, Y. Y., et al. (2006). Observation of Two Distinct, Rapid Loss Mechanisms during the 20 November 2003 Radiation belt Dropout Event. *J. Geophys. Res. Space Phys.* 111, A12216. doi:10.1029/2006ja011802

Bourouaine, S., and Perez, J. C. (2020). Interpreting Solar Wind Turbulent Spectra beyond Taylor's Hypothesis. *Astrophysical J.* 893, L32. doi:10.3847/2041-8213/ab7fb1

Breneman, A. W., Halford, A. J., Millan, R. M., Woodger, L. A., Zhang, X., Sandhu, J. K., et al. (2020). Driving of Outer Belt Electron Loss by Solar Wind Dynamic

Pressure Structures: Analysis of Balloon and Satellite Data. *J. Geophys. Res. Space Phys.* 125. doi:10.1029/2020ja028097

Bruno, R., and Carbone, V. (2013). The Solar Wind as a Turbulence Laboratory. *Living Rev. Solar Phys.* 10, 2. doi:10.12942/lrsp-2013-2

Bruno, R., Carbone, V., Vörös, Z., D'Amicis, R., Bavassano, B., Cattaneo, M. B., et al. (2009). Coordinated Study on Solar Wind Turbulence during the Venus-Express, ACE and Ulysses Alignment of August 2007. *Earth, Moon, and Planets* 104, 101–104. doi:10.1007/s11038-008-9272-9

Burch, J. L., Moore, T. E., Torbert, R. B., and Giles, B. L. (2016). Magnetospheric Multiscale Overview and Science Objectives. *Space Sci. Rev.* 199, 5–21. doi:10.1007/s11214-015-0164-9

Cartwright, M. L., and Moldwin, M. B. (2008). Comparison of Small-Scale Flux Rope Magnetic Properties to Large-Scale Magnetic Clouds: Evidence for Reconnection across the HCS?. *J. Geophys. Res. Space Phys.* 113, n/a. doi:10.1029/2008ja013389

Cartwright, M. L., and Moldwin, M. B. (2010). Heliospheric Evolution of Solar Wind Small-Scale Magnetic Flux Ropes. *J. Geophys. Res. Space Phys.* 115, A08102. doi:10.1029/2009JA014271

Chae, J., Schuhle, U., and Lemaire, P. (1998). SUMER Measurements of Nonthermal Motions: Constraints on Coronal Heating Mechanisms. *Astrophysical J.* 505, 957–973. doi:10.1086/306179

Chasapis, A., Matthaeus, W. H., Bandyopadhyay, R., Chhiber, R., Ahmadi, N., Ergun, R. E., et al. (2020). Scaling and Anisotropy of Solar Wind Turbulence at Kinetic Scales during the MMS Turbulence Campaign. *Astrophysical J.* 903, 127. doi:10.3847/1538-4357/abb948

Chen, C. H. K., Bale, S. D., Bonnell, J. W., Borovikov, D., Bowen, T. A., Burgess, D., et al. (2020). The Evolution and Role of Solar Wind Turbulence in the Inner Heliosphere. *Astrophysical J. Suppl. Ser.* 246, 53. doi:10.3847/1538-4365/ab60a3

Chen, C. H. K., Chandran, B. D. G., Woodham, L. D., Jones, S. I., Perez, J. C., Bourouaine, S., et al. (2021). The Near-Sun Streamer belt Solar Wind: Turbulence and Solar Wind Acceleration. *Astron. Astrophysics* 650, L3. doi:10.1051/0004-6361/202039872

Chhiber, R., Goldstein, M. L., Maruca, B. A., Chasapis, A., Matthaeus, W. H., Ruffolo, D., et al. (2020). Clustering of Intermittent Magnetic and Flow Structures Near Parker Solar Probe 's First Perihelion—A Partial-Variance-Of-Increments Analysis. *Astrophysical J. Suppl. Ser.* 246, 31. doi:10.3847/1538-4365/ab53d2

Chhiber, R., Usmanov, A. V., Matthaeus, W. H., and Goldstein, M. L. (2019). Contextual Predictions for the Parker Solar Probe . I. Critical Surfaces and Regions. *Astrophysical J. Suppl. Ser.* 241, 11. doi:10.3847/1538-4365/ab0652

Chollet, E. E., and Giacalone, J. (2011). Evidence of Confinement of Solar-Energetic Particles to Interplanetary Magnetic Field Lines. *Astrophysical J.* 728, 64. doi:10.1088/0004-637x/728/1/64

Chollet, E. E., and Giacalone, J. (2008). Multispacecraft Analysis of Energetic Ion Flux Dropouts. *Astrophysical J.* 688, 1368–1373. doi:10.1086/592378

Claudepierre, J. S. G., Hudson, M. K., Lotko, W., Lyon, J. G., and Denton, R. E. (2010). Solar Wind Driving of Magnetospheric ULF Waves: Field Line Resonances Driven by Dynamic Pressure Fluctuations. *J. Geophys. Res.* 115, A11202. doi:10.1029/2010JA015399

Coleman, P. J. (1966). Variations in the Interplanetary Magnetic Field: Mariner 2: 1. Observed Properties. *J. Geophys. Res.* 71, 5509–5531. doi:10.1029/jz071i023p05509

C. P. Escoubet, C. T. Russell, and R. Schmidt (1997). *Cluster - Science and Mission Overview* (Dordrecht: Springer Netherlands). doi:10.1007/978-94-011-5666-0/_/1

Cranmer, S. R., Field, G. B., and Kohl, J. L. (1999). Spectroscopic Constraints on Models of Ion Cyclotron Resonance Heating in the Polar Solar Corona and High-Speed Solar Wind. *Astrophysical J.* 518, 937–947. doi:10.1086/307330

Cranmer, S. R., Gibson, S. E., and Riley, P. (2017). Origins of the Ambient Solar Wind: Implications for Space Weather. *Space Sci. Rev.* 212, 1345–1384. doi:10.1007/s11214-017-0416-y

Cranmer, S. R. (2012). Self-Consistent Models of the Solar Wind. *Space Sci. Rev.* 172, 145–156. doi:10.1007/s11214-010-9674-7

Cranmer, S. R., and Woolsey, L. N. (2015). Driving Solar Spicules and Jets with Magnetohydrodynamic Turbulence: Testing a Persistent Idea. *Astrophysical J.* 812, 71. doi:10.1088/0004-637x/812/1/71

Crooker, N. U., Burton, M. E., Phillips, J. L., Smith, E. J., and Balogh, A. (1996). Heliospheric Plasma Sheets as Small-Scale Transients. *J. Geophys. Res.* 101, 2467–2474. doi:10.1029/95ja03148

Crooker, N. U., Burton, M. E., Siscoe, G. L., Kahler, S. W., Gosling, J. T., and Smith, E. J. (1996). Solar Wind Streamer belt Structure. *J. Geophys. Res. Space Phys.* 101, 24331–24341. doi:10.1029/96ja02412

Crooker, N. U., Huang, C. L., Lamassa, S. M., Larson, D. E., Kahler, S. W., and Spence, H. E. (2004). Heliospheric Plasma Sheets. *J. Geophys. Res. - Space Phys.* 109, A03107. doi:10.1029/2003ja010170

Crooker, N. U., and McPherron, R. L. (2012). Coincidence of Composition and Speed Boundaries of the Slow Solar Wind. *J. Geophys. Res. Space Phys.* 117, A09104. doi:10.1029/2012ja017837

Crooker, N. U., Siscoe, G. L., Russell, C. T., and Smith, E. J. (1982). Factors Controlling Degree of Correlation between ISEE 1 and ISEE 3 Interplanetary Magnetic Field Measurements. *J. Geophys. Res. Space Phys.* 87, 2224–2230. doi:10.1029/ja087ia04p02224

Crooker, N. U., Siscoe, G. L., Shodhan, S., Webb, D. F., Gosling, J. T., and Smith, E. J. (1993). Multiple Heliospheric Current Sheets and Coronal Streamer belt Dynamics. *J. Geophys. Res. Space Phys.* 98, 9371–9381. doi:10.1029/93ja00636

D'Amicis, R., and Bruno, R. (2015). On the Origin of the Highly Alfvénic Slow Solar Wind. *Astrophysical J.* 805, 84. doi:10.1088/0004-637x/805/1/84

DeForest, C. E., Howard, R. A., Velli, M., Viall, N., and Vourlidas, A. (2018). The Highly Structured Outer Solar Corona. *Astrophysical J.* 862, 18. doi:10.3847/1538-4357/aac8e3

DeForest, C. E., Matthaeus, W. H., Howard, T. A., and Rice, D. R. (2015). Turbulence in the Solar Wind Measured with Comet Tail Test Particles. *Astrophysical J.* 812, 108. doi:10.1088/0004-637x/812/2/108

DeForest, C. E., Matthaeus, W. H., Viall, N. M., and Cranmer, S. R. (2016). Fading Coronal Structure and the Onset of Turbulence in the Young Solar Wind. *Astrophysical J.* 828, 66. doi:10.3847/0004-637x/828/2/66

DiMatteo, S., Viall, N. M., Kepko, L., Wallace, S., Arge, C. N., and MacNeice, P. (2019). Helios Observations of Quasiperiodic Density Structures in the Slow Solar Wind at 0.3, 0.4, and 0.6 AU. *J. Geophys. Res. Space Phys.* 124, 837–860. doi:10.1029/2018ja026182

DiMatteo, S., and Villante, U. (2017). The Identification of Solar Wind Waves at Discrete Frequencies and the Role of the Spectral Analysis Techniques. *J. Geophys. Res. Space Phys.* 122, 4905–4920. doi:10.1002/2017ja023936

Drake, J. F., Agapitov, O., Swisdak, M., Badman, S. T., Bale, S. D., Horbury, T. S., et al. (2021). Switchbacks as Signatures of Magnetic Flux Ropes Generated by Interchange Reconnection in the corona. *Astron. Astrophysics* 650, A2. doi:10.1051/0004-6361/202039432

Dyrud, L. P., Behnke, R., Kepko, E. L., Sulzer, M., and Zafke, S. (2008). Ionospheric ULF Oscillations Driven from above Arecibo. *Geophys. Res. Lett.* 35, L14101. doi:10.1029/2008gl034073

Elliott, H. A., Henney, C. J., McComas, D. J., Smith, C. W., and Vasquez, B. J. (2012). Temporal and Radial Variation of the Solar Wind Temperature-Speed Relationship. *J. Geophys. Res. Space Phys.* 117, n/a. doi:10.1029/2011ja017125

Elliott, H. A., McComas, D. J., and DeForest, C. E. (2016). Long-term Trends in the Solar Wind Proton Measurements. *Astrophysical J.* 832, 66. doi:10.3847/0004-637x/832/1/66

Endeve, E., Lie-Svendsen, O., Hansteen, V. H., and Leer, E. (2005). Release of Helium from Closed-Field Regions of the Sun. *Astrophysical J.* 624, 402–413. doi:10.1086/428938

Feldman, U., Schühle, U., Widing, K. G., and Laming, J. M. (1998). Coronal Composition above the Solar Equator and the North Pole as Determined from Spectra Acquired by the SUMER Instrument on SOHO. *Astrophysical J.* 505, 999–1006. doi:10.1086/306195

Feng, H. Q., Wu, D. J., and Chao, J. K. (2007). Size and Energy Distributions of Interplanetary Magnetic Flux Ropes. *J. Geophys. Res. Space Phys.* 112, n/a. doi:10.1029/2006ja011962

Fenrich, F. R., and Waters, C. L. (2008). Phase Coherence Analysis of a Field Line Resonance and Solar Wind Oscillation. *Geophys. Res. Lett.* 35, 4. (c) 2008: American Geophysical Union. doi:10.1029/2008gl035430

Frisch, U. (1995). *Turbulence. The Legacy of A.N. Kolmogorov*. (UK): Cambridge University Press.

Froment, C., Krasnoselskikh, V., Wit, T. D. d., Agapitov, O., Fargette, N., Lavraud, B., et al. (2021). Direct Evidence for Magnetic Reconnection at the Boundaries

of Magnetic Switchbacks with Parker Solar Probe. *Astron. Astrophysics* 650, A5. doi:10.1051/0004-6361/202039806

Giacalone, J., Jokipii, J. R., and Mazur, J. E. (2000). Small-scale Gradients and Large-Scale Diffusion of Charged Particles in the Heliospheric Magnetic Field. *Astrophysical J.* 532, L75–L78. doi:10.1086/312564

Gombosi, T. I., Holst, B. v. d., Manchester, W. B., and Sokolov, I. V. (2018). Extended MHD Modeling of the Steady Solar corona and the Solar Wind. *Living Rev. Solar Phys.* 15, 4. doi:10.1007/s41116-018-0014-4

Gosling, J., and Pizzo, V. (1999). Formation and Evolution of Corotating Interaction Regions and Their Three Dimensional Structure. *Space Sci. Rev.* 89, 21–52. doi:10.1023/a:1005291711900

Gosling, J. T., Borrini, G., Asbridge, J. R., Bame, S. J., Feldman, W. C., and Hansen, R. T. (1981). Coronal Streamers in the Solar Wind at 1 AU. *J. Geophys. Res. Space Phys.* 86, 5438–5448. doi:10.1029/ja086ia07p05438

Gosling, J. T., McComas, D. J., Roberts, D. A., and Skoug, R. M. (2009). A One-Sided Aspect of Alfvenic Fluctuations in the Solar Wind. *Astrophysical J.* 695, L213–L216. doi:10.1088/0004-637x/695/2/l213

Gosling, J. T., and Szabo, A. (2008). Bifurcated Current Sheets Produced by Magnetic Reconnection in the Solar Wind. *J. Geophys. Res. Space Phys.* 113, 8. doi:10.1029/2008ja013473

Harrison, R. A., Davies, J. A., Rouillard, A. P., Davis, C. J., Eyles, C. J., Bewsher, D., et al. (2009). Two Years of the STEREO Heliospheric Imagers. *Solar Phys.* 256, 219–237. doi:10.1007/s11207-009-9352-7

Hartinger, M. D., Welling, D., Viall, N. M., Moldwin, M. B., and Ridley, A. (2014). The Effect of Magnetopause Motion on Fast Mode Resonance. *J. Geophys. Res. Space Phys.* 119, 8212–8227. doi:10.1002/2014ja020401

Hietala, H., Kilpua, E. K. J., Turner, D. L., and Angelopoulos, V. (2014). Depleting Effects of ICME-Driven Sheath Regions on the Outer Electron Radiation belt. *Geophys. Res. Lett.* 41, 2258–2265. doi:10.1002/2014gl059551

Higginson, A. K., Antiochos, S. K., DeVore, C. R., Wyper, P. F., and Zurbuchen, T. H. (2017). Dynamics of Coronal Hole Boundaries. *Astrophysical J.* 837, 113. doi:10.3847/1538-4357/837/2/113

Higginson, A. K., Antiochos, S. K., DeVore, C. R., Wyper, P. F., and Zurbuchen, T. H. (2017). Formation of Heliospheric Arcs of Slow Solar Wind. *Astrophysical J.* 840, L10. doi:10.3847/2041-8213/aa6d72

Higginson, A. K., and Lynch, B. J. (2018). Structured Slow Solar Wind Variability: Streamer-Blob Flux Ropes and Torsional Alfvén Waves. *Astrophysical J.* 859, 6. doi:10.3847/1538-4357/aabc08

Hoeksema, J. T., Wilcox, J. M., and Scherrer, P. H. (1983). The Structure of the Heliospheric Current Sheet: 1978–1982. *J. Geophys. Res. Space Phys.* 88, 9910–9918. doi:10.1029/ja088ia12p09910

Horbury, T. S., Forman, M. A., and Oughton, S. (2005). Spacecraft Observations of Solar Wind Turbulence: an Overview. *Plasma Phys. Controlled Fusion* 47, B703. doi:10.1088/0741-3335/47/12b/s52

Horbury, T. S., Matteini, L., and Stansby, D. (2018). Short, Large-Amplitude Speed Enhancements in the Near-Sunfast Solar Wind. *Monthly Notices R. Astronomical Soc.* 478, 1980–1986. doi:10.1093/mnras/sty953

Howard, T. A., and DeForest, C. E. (2012). The Thomson Surface. I. Reality and Myth. *Astrophysical J.* 752, 130. doi:10.1088/0004-637x/752/2/130

Howard, T. A., and Harrison, R. A. (2013). Stealth Coronal Mass Ejections: A Perspective. *Solar Phys.* 285, 269–280. doi:10.1007/s11207-012-0217-0

Howard, T. A., and Tappin, S. J. (2008). Three-Dimensional Reconstruction of Two Solar Coronal Mass Ejections Using the STEREO Spacecraft. *Solar Phys.* 252, 373–383. doi:10.1007/s11207-008-9262-0

Isaacs, J. J., Tessein, J. A., and Matthaeus, W. H. (2015). Systematic Averaging Interval Effects on Solar Wind Statistics. *J. Geophys. Res. Space Phys.* 120, 868–879. doi:10.1002/2014ja020661

Jian, L. K., Russell, C. T., Luhmann, J. G., Galvin, A. B., and MacNeice, P. J. (2009). Multi-Spacecraft Observations: Stream Interactions and Associated Structures. *Solar Phys.* 259, 345. doi:10.1007/s11207-009-9445-3

Jokipii, J. R. (1966). Cosmic-Ray Propagation. I. Charged Particles in a Random Magnetic Field. *Astrophysical J.* 146, 480. doi:10.1086/148912

Karpen, J. T., DeVore, C. R., Antiochos, S. K., and Pariat, E. (2016). Reconnection-driven Coronal-Hole Jets with Gravity and Solar Wind. *Astrophysical J.* 834, 62. doi:10.3847/1538-4357/834/1/62

Kasper, J. C., Bale, S. D., Belcher, J. W., Berthomier, M., Case, A. W., Chandran, B. D. G., et al. (2019). Alfvénic Velocity Spikes and Rotational Flows in the Near-Sun Solar Wind. *Nature* 576, 228–231. doi:10.1038/s41586-019-1813-z

Kasper, J. C., Klein, K. G., Weber, T., Maksimovic, M., Zaslavsky, A., Bale, S. D., et al. (2017). A Zone of Preferential Ion Heating Extends Tens of Solar Radii from the Sun. *Astrophysical J.* 849, 126. doi:10.3847/1538-4357/aa84b1

Kasper, J. C., Lazarus, A. J., and Gary, S. P. (2008). Hot Solar-Wind Helium: Direct Evidence for Local Heating by Alfvén-Cyclotron Dissipation. *Phys. Rev. Lett.* 101, 261103. doi:10.1103/physrevlett.101.261103

Kataoka, R., and Miyoshi, Y. (2006). Flux Enhancement of Radiation belt Electrons during Geomagnetic Storms Driven by Coronal Mass Ejections and Corotating Interaction Regions. *Space Weather* 4, n/a. doi:10.1029/2005sw000211

Kepko, L., and Spence, H. E. (2003). Observations of Discrete, Global Magnetospheric Oscillations Directly Driven by Solar Wind Density Variations. *J. Geophys. Res. Space Phys.* 108, 1257. (c) 2003: American Geophysical Union. doi:10.1029/2002ja009676

Kepko, L., Spence, H. E., and Singer, H. J. (2002). ULF Waves in the Solar Wind as Direct Drivers of Magnetospheric Pulsations. *Geophys. Res. Lett.* 29, 39-1–39-4. doi:10.1029/2001gl014405

Kepko, L., Viall, N. M., Antiochos, S. K., Lepri, S. T., Kasper, J. C., and Weberg, M. (2016). Implications of L1 Observations for Slow Solar Wind Formation by Solar Reconnection. *Geophys. Res. Lett.* 43, 4089–4097. doi:10.1002/2016gl068607

Kepko, L., and Viall, N. M. (2019). The Source, Significance, and Magnetospheric Impact of Periodic Density Structures within Stream Interaction Regions. *J. Geophys. Res. Space Phys.* 124, 7722– 7743. doi:10.1029/2019ja026962

Kepko, L., Viall, N. M., and Wolfinger, K. (2020). Inherent Length Scales of Periodic Mesoscale Density Structures in the Solar Wind over Two Solar Cycles. *J. Geophys. Res. Space Phys.* 125, e2020JA028037. doi:10.1029/2020ja028037

Khabarova, O., Malandraki, O., Malova, H., Kislov, R., Greco, A., Bruno, R., et al. (2021). Current Sheets, Plasmoids and Flux Ropes in the Heliosphere. *Space Sci. Rev.* 217, 38. doi:10.1007/s11214-021-00814-x

Kilpua, E. K. J., Balogh, A., Steiger, R. v., and Liu, Y. D. (2017). Geoeffective Properties of Solar Transients and Stream Interaction Regions. *Space Sci. Rev.* 212, 1271–1314. doi:10.1007/s11214-017-0411-3

Kilpua, E. K. J., Hietala, H., Koskinen, H. E. J., Fontaine, D., and Turc, L. (2013). Magnetic Field and Dynamic Pressure ULF Fluctuations in Coronal-Mass-Ejection-Driven Sheath Regions. *Ann. Geophysicae* 31, 1559–1567. doi:10.5194/angeo-31-1559-2013

Kilpua, E. K. J., Hietala, H., Turner, D. L., Koskinen, H. E. J., Pulkkinen, T. I., Rodriguez, J. V., et al. (2015). Unraveling the Drivers of the Storm Time Radiation belt Response. *Geophys. Res. Lett.* 42, 3076–3084. doi:10.1002/2015gl063542

Klein, K.-L., and Dalla, S. (2017). Acceleration and Propagation of Solar Energetic Particles. *Space Sci. Rev.* 212, 1107–1136. doi:10.1007/s11214-017-0382-4

Klein, K. G., Howes, G. G., and TenBarge, J. M. (2014). The Violation of the Taylor Hypothesis in Measurements of Solar Wind Turbulence. *Astrophysical J.* 790, L20. doi:10.1088/2041-8205/790/2/l20

Klimchuk, J. A., and Antiochos, S. K. (2021). How Turbulent Is the Magnetically Closed Corona?. *Front. Astron. Space Sci.* 8, 662861. doi:10.3389/fspas.2021.662861

Kolmogorov, A. (1941). The Local Structure of Turbulence in Incompressible Viscous Fluid for Very Large Reynolds' Numbers. *Akademiia Nauk SSSR Doklady* 30, 301–305.

Kraichnan, R. H. (1967). Inertial Ranges in Two-Dimensional Turbulence. *Phys. Fluids* 10, 1417. doi:10.1063/1.1762301

Kumar, P., Karpen, J. T., Antiochos, S. K., Wyper, P. F., DeVore, C. R., and Lynch, B. J. (2021). From Pseudostreamer Jets to Coronal Mass Ejections: Observations of the Breakout Continuum. *Astrophysical J.* 907, 41. doi:10.3847/1538-4357/abca8b

Laming, J. M. (2015). The FIP and Inverse FIP Effects in Solar and Stellar Coronae. *Living Rev. Solar Phys.* 12, 2. doi:10.1007/lrsp-2015-2

Laming, J. M., Vourlidas, A., Korendyke, C., Chua, D., Cranmer, S. R., Ko, Y.-K., et al. (2019). Element Abundances: A New Diagnostic for the Solar Wind. *Astrophysical J.* 879, 124. doi:10.3847/1538-4357/ab23f1

Landi, E., Gruesbeck, J. R., Lepri, S. T., Zurbuchen, T. H., and Fisk, L. A. (2012). Charge State Evolution in the Solar Wind. II. Plasma Charge State Composition in the Inner corona and Accelerating Fast Solar Wind. *Astrophysical J.* 761, 48. doi:10.1088/0004-637x/761/1/48

Larosa, A., Krasnoselskikh, V., Wit, T. D. d., Agapitov, O., Froment, C., Jagarlamudi, V. K., et al. (2021). Switchbacks: Statistical Properties and

Deviations from Alfvénicity. *Astron. Astrophysics* 650, A3. doi:10.1051/0004-6361/202039442

Lavraud, B., Fargette, N., Réville, V., Szabo, A., Huang, J., Rouillard, A. P., et al. (2020). The Heliospheric Current Sheet and Plasma Sheet during Parker Solar Probe's First Orbit. *Astrophysical J.* 894, L19. doi:10.3847/2041-8213/ab8d2d

Leamon, R. J., Smith, C. W., Ness, N. F., Matthaeus, W. H., and Wong, H. K. (1998). Observational Constraints on the Dynamics of the Interplanetary Magnetic Field Dissipation Range. *J. Geophys. Res. Space Phys.* 103, 4775–4787. doi:10.1029/97ja03394

Leamon, R. J., Smith, C. W., Ness, N. F., and Wong, H. K. (1999). Dissipation Range Dynamics: Kinetic Alfvén Waves and the Importance of β_e. *J. Geophys. Res. Space Phys.* 104, 22331–22344. doi:10.1029/1999ja900158

Li, W., and Hudson, M. (2019). Earth's Van Allen Radiation Belts: From Discovery to the Van Allen Probes Era. *J. Geophys. Res. Space Phys.* 124, 8319–8351. doi:10.1029/2018ja025940

Linker, J. A., Lionello, R., Mikić, Z., Titov, V. S., and Antiochos, S. K. (2011). The Evolution of Open Magnetic Flux Driven by Photospheric Dynamics. *Astrophysical J.* 731, 110. doi:10.1088/0004-637x/731/2/110

Lionello, R., Velli, M., Downs, C., Linker, J. A., and Mikić, Z. (2014). Application of a Solar Wind Model Driven by Turbulence Dissipation to a 2D Magnetic Field Configuration. *Astrophysical J.* 796, 111. doi:10.1088/0004-637x/796/2/111

Liou, K., Takahashi, K., Newell, P. T., and Yumoto, K. (2008). Polar Ultraviolet Imager Observations of Solar Wind-Driven ULF Auroral Pulsations. *Geophys. Res. Lett.* 35, 16101. doi:10.1029/2008gl034953

Lynch, B. J. (2020). A Model for Coronal Inflows and In/Out Pairs. *Astrophysical J.* 905, 139. doi:10.3847/1538-4357/abc5b3

Lynch, B. J., Masson, S., Li, Y., DeVore, C. R., Luhmann, J. G., Antiochos, S. K., et al. (2016). A Model for Stealth Coronal Mass Ejections. *J. Geophys. Res. Space Phys.* 121 (10677–10), 697. doi:10.1002/2016ja023432

Ma, S., Attrill, G. D. R., Golub, L., and Lin, J. (2010). Statistical Study of Coronal Mass Ejections with and without Distinct Low Signatures. *Astrophysical J.* 722, 289–301. doi:10.1088/0004-637x/722/1/289

Martinović, M. M., Klein, K. G., Huang, J., Chandran, B. D. G., Kasper, J. C., Lichko, E., et al. (2021). Multiscale Solar Wind Turbulence Properties inside and Near Switchbacks Measured by the Parker Solar Probe. *Astrophysical J.* 912, 28. doi:10.3847/1538-4357/abebe5

Mason, E. I., Antiochos, S. K., and Viall, N. M. (2019). Observations of Solar Coronal Rain in Null Point Topologies. *Astrophysical J.* 874, L33. doi:10.3847/2041-8213/ab0c5d

Matthaeus, W. H., Dasso, S., Weygand, J. M., Milano, L. J., Smith, C. W., and Kivelson, M. G. (2005). Spatial Correlation of Solar-Wind Turbulence from Two-Point Measurements. *Phys. Rev. Lett.* 95, 231101. doi:10.1103/physrevlett.95.231101

Matthaeus, W. H., and Velli, M. (2011). Who Needs Turbulence?. A Review of Turbulence Effects in the Heliosphere and on the Fundamental Process of Reconnection. *Space Sci. Rev.* 160, 145–168. doi:10.1007/s11214-011-9793-9

Mazur, J. E., Mason, G. M., Dwyer, J. R., Giacalone, J., Jokipii, J. R., and Stone, E. C. (2000). Interplanetary Magnetic Field Line Mixing Deduced from Impulsive Solar Flare Particles. *Astrophysical J.* 532, L79–L82. doi:10.1086/312561

McComas, D. J., Bame, S. J., Barraclough, B. L., Feldman, W. C., Funsten, H. O., Gosling, J. T., et al. (1998). Ulysses' Return to the Slow Solar Wind. *Geophys. Res. Lett.* 25, 1–4. doi:10.1029/97gl03444

McComas, D. J., Barraclough, B. L., Gosling, J. T., Hammond, C. M., Phillips, J. L., Neugebauer, M., et al. (1995). Structures in the Polar Solar Wind: Plasma and Field Observations from Ulysses. *J. Geophys. Res. Space Phys.* 100, 19893–19902. doi:10.1029/95ja01634

McIntosh, S. W., Leamon, R. J., Egeland, R., Dikpati, M., Fan, Y., and Rempel, M. (2019). What the Sudden Death of Solar Cycles Can Tell Us about the Nature of the Solar Interior. *Solar Phys.* 294, 88. doi:10.1007/s11207-019-1474-y

Merkin, V. G., Lyon, J. G., Lario, D., Arge, C. N., and Henney, C. J. (2016). Time-dependent Magnetohydrodynamic Simulations of the Inner Heliosphere. *J. Geophys. Res. Space Phys.* 121, 2866–2890. doi:10.1002/2015ja022200

Miyoshi, Y., and Kataoka, R. (2005). Ring Current Ions and Radiation belt Electrons during Geomagnetic Storms Driven by Coronal Mass Ejections and Corotating Interaction Regions. *Geophys. Res. Lett.* 32,L21105. doi:10.1029/2005gl024590

Müller, D., Cyr, O. C. S., Zouganelis, I., Gilbert, H. R., Marsden, R., Nieves-Chinchilla, T., et al. (2020). The Solar Orbiter mission. *Astron. Astrophysics* 642, A1. doi:10.1051/0004-6361/202038467

Murphy, A. K., Winslow, R. M., Schwadron, N. A., Lugaz, N., Yu, W., Farrugia, C. J., et al. (2020). A Survey of Interplanetary Small Flux Ropes at Mercury. *Astrophysical J.* 894, 120. doi:10.3847/1538-4357/ab8821

Neugebauer, M., Clay, D. R., and Gosling, J. T. (1993). The Origins of Planar Magnetic Structures in the Solar Wind. *J. Geophys. Res. Space Phys.* 98, 9383–9389. doi:10.1029/93ja00216

Neugebauer, M. (2012). Evidence for Polar X-ray Jets as Sources of Microstream Peaks in the Solar Wind. *Astrophysical J.* 750, 50. doi:10.1088/0004-637x/750/1/50

Neugebauer, M., and Giacalone, J. (2015). Energetic Particles, Tangential Discontinuities, and Solar Flux Tubes. *J. Geophys. Res. Space Phys.* 120, 8281–8287. doi:10.1002/2015ja021632

Neugebauer, M., Goldstein, B. E., McComas, D. J., Suess, S. T., and Balogh, A. (1995). Ulysses Observations of Microstreams in the Solar Wind from Coronal Holes. *J. Geophys. Res. Space Phys.* 100, 23389–23395. doi:10.1029/95ja02723

Neugebauer, M., Ruzmaikin, A., and McComas, D. J. (1997). Wavelet Analysis of the Structure of Microstreams in the Polar Solar Wind. *AIP Conf. Proc.* 385, 41–46. doi:10.1063/1.51765

Neugebauer, M., and Snyder, C. W. (1966). Mariner 2 Observations of the Solar Wind: 1. Average Properties. *J. Geophys. Res.* 71, 4469–4484. doi:10.1029/jz071i019p04469

Neugebauer, M., and Snyder, C. W. (1962). Solar Plasma Experiment. *Science* 138, 1095–1097. doi:10.1126/science.138.3545.1095-a

Nisticò, G., Vladimirov, V., Nakariakov, V. M., Battams, K., and Bothmer, V. (2018). Oscillations of Cometary Tails: a Vortex Shedding Phenomenon?. *Astron. Astrophysics* 615, A143. doi:10.1051/0004-6361/201732474

Osman, K. T., and Horbury, T. S. (2006). Multispacecraft Measurement of Anisotropic Correlation Functions in Solar Wind Turbulence. *Astrophysical J.* 654, L103–L106. doi:10.1086/510906

Oughton, S., Matthaeus, W. H., Wan, M., and Osman, K. T. (2015). Anisotropy in Solar Wind Plasma Turbulence. *Philos. Trans. R. Soc. A: Math. Phys. Eng. Sci.* 373, 20140152. doi:10.1098/rsta.2014.0152

Owens, M. J., Wicks, R. T., and Horbury, T. S. (2011). Magnetic Discontinuities in the Near-Earth Solar Wind: Evidence of In-Transit Turbulence or Remnants of Coronal Structure?. *Solar Phys.* 269, 411–420. doi:10.1007/s11207-010-9695-0

Pagel, A. C., Crooker, N. U., Zurbuchen, T. H., and Gosling, J. T. (2004). Correlation of Solar Wind Entropy and Oxygen Ion Charge State Ratio. *J. Geophys. Res. Space Phys.* 109. doi:10.1029/2003ja010010

Palmerio, E., Kilpua, E. K. J., and Savani, N. P. (2016). Planar Magnetic Structures in Coronal Mass Ejection-Driven Sheath Regions. *Ann. Geophysicae* 34, 313–322. doi:10.5194/angeo-34-313-2016

Parhi, S., Suess, S. T., and Sulkanen, M. (1999). Can Kelvin-Helmholtz Instabilities of Jet-like Structures and Plumes Cause Solar Wind Fluctuations at 1 AU?. *J. Geophys. Res. Space Phys.* 104, 14781–14787. doi:10.1029/1999ja900041

Paulikas, G. A., and Blake, J. B. (1979). Effects of the Solar Wind on Magnetospheric Dynamics: Energetic Electrons at the Synchronous Orbit. *Quantitative Model. magnetospheric Process. Geophys. Monogr. Ser.* 21, 180–202. doi:10.1029/gm021p0180

Perez, J. C., Bourouaine, S., Chen, C. H. K., and Raouafi, N. E. (2021). Applicability of Taylor's Hypothesis during Parker Solar Probe Perihelia. *Astron. Astrophysics* 650, A22. doi:10.1051/0004-6361/202039879

Peter, H. (1998). Element Separation in the Chromosphere Ionization-Diffusion Models for the FIP-Effect. *Space Sci. Rev.* 85, 253–260. doi:10.1023/a:1005150500590

Phan, T. D., Lavraud, B., Halekas, J. S., Øieroset, M., Drake, J. F., Eastwood, J. P., et al. (2021). Prevalence of Magnetic Reconnection in the Near-Sun Heliospheric Current Sheet. *Astron. Astrophysics* 650, A13. doi:10.1051/0004-6361/202039863

Poletto, G. (2015). Solar Coronal Plumes. *Living Rev. Solar Phys.* 12, 7. doi:10.1007/lrsp-2015-7

Pontin, D. I., and Wyper, P. F. (2015). The Effect of Reconnection on the Structure of the Sun's Open-Closed Boundary. *Astrophysical J.* 805, 39. doi:10.1088/0004-637x/805/1/39

Pylaev, O. S., Zaqarashvili, T. V., Brazhenko, A. I., Melnik, V. N., Hanslmeier, A., and Panchenko, M. (2017). Oscillation of Solar Radio Emission at Coronal

Acoustic Cut-Off Frequency. *Astron. Astrophysics* 601, A42. doi:10.1051/0004-6361/201629218

Rakowski, C. E., and Laming, J. M. (2012). On the Origin of the Slow Speed Solar Wind: Helium Abundance Variations. *Astrophysical J.* 754, 65. doi:10.1088/0004-637x/754/1/65

Raouafi, N. E., Patsourakos, S., Pariat, E., Young, P. R., Sterling, A. C., Savcheva, A., et al. (2016). Solar Coronal Jets: Observations, Theory, and Modeling. *Space Sci. Rev.* 201, 1–53. doi:10.1007/s11214-016-0260-5

Rappazzo, A. F., Velli, M., Einaudi, G., and Dahlburg, R. B. (2008). Nonlinear Dynamics of the Parker Scenario for Coronal Heating. *Astrophysical J.* 677, 1348–1366. doi:10.1086/528786

Raymond, J. C., Kohl, J. L., Noci, G., Antonucci, E., Tondello, G., Huber, M. C. E., et al. (1997). Composition of Coronal Streamers from the SOHO Ultraviolet Coronagraph Spectrometer. *Solar Phys.* 175, 645–665. doi:10.1023/a:1004948423169

Reid, H. A. S., and Kontar, E. P. (2010). Solar Wind Density Turbulence and Solar Flare Electron Transport from the Sun to the Earth. *Astrophysical J.* 721, 864. doi:10.1088/0004-637x/721/1/864

Reisenfeld, D. B., McComas, D. J., and Steinberg, J. T. (1999). Evidence of a Solar Origin for Pressure Balance Structures in the High-Latitude Solar Wind. *Geophys. Res. Lett.* 26, 1805. doi:10.1029/1999gl900368

Réville, V., Velli, M., Rouillard, A. P., Lavraud, B., Tenerani, A., Shi, C., et al. (2020). Tearing Instability and Periodic Density Perturbations in the Slow Solar Wind. *Astrophysical J.* 895, L20. doi:10.3847/2041-8213/ab911d

Richardson, I. G. (2018). Solar Wind Stream Interaction Regions throughout the Heliosphere. *Living Rev. Solar Phys.* 15, 1. doi:10.1007/s41116-017-0011-z

Robbrecht, E., Berghmans, D., and Linden, R. A. M. V. d. (2009). Automated LASCO CME Catalog for Solar Cycle 23: Are CMEs Scale Invariant?. *Astrophysical J.* 691, 1222–1234. doi:10.1088/0004-637x/691/2/1222

Roberts, D. A. (2010). Demonstrations that the Solar Wind Is Not Accelerated by Waves or Turbulence. *Astrophysical J.* 711, 1044–1050. doi:10.1088/0004-637x/711/2/1044

Roberts, D. A., Ghosh, S., Goldstein, M. L., and Mattheaus, W. H. (1991). Magnetohydrodynamic Simulation of the Radial Evolution and Stream Structure of Solar-Wind Turbulence. *Phys. Rev. Lett.* 67, 3741–3744. doi:10.1103/physrevlett.67.3741

Roberts, D. A., Goldstein, M. L., Klein, L. W., and Matthaeus, W. H. (1987). Origin and Evolution of Fluctuations in the Solar Wind: Helios Observations and Helios-Voyager Comparisons. *J. Geophys. Res. Space Phys.* 92, 12023–12035. doi:10.1029/ja092ia11p12023

Roberts, D. A., and Goldstein, M. L. (1987). Spectral Signatures of Jumps and Turbulence in Interplanetary Speed and Magnetic Field Data. *J. Geophys. Res. Space Phys.* 92, 10105–10110. doi:10.1029/ja092ia09p10105

Roberts, D. A., Karimabadi, H., Sipes, T., Ko, Y.-K., and Lepri, S. (2020). Objectively Determining States of the Solar Wind Using Machine Learning. *Astrophysical J.* 889, 153. doi:10.3847/1538-4357/ab5a7a

Roberts, D. A., Keiter, P. A., and Goldstein, M. L. (2005). Origin and Dynamics of the Heliospheric Streamer belt and Current Sheet. *J. Geophys. Res. Space Phys.* 110,A06102. doi:10.1029/2004ja010541

Roberts, D. A., and Ofman, L. (2019). Hybrid Simulation of Solar-wind-like Turbulence. *Solar Phys.* 294, 153. doi:10.1007/s11207-019-1548-x

Roberts, M. A., Uritsky, V. M., DeVore, C. R., and Karpen, J. T. (2018). Simulated Encounters of the Parker Solar Probe with a Coronal-Hole Jet. *Astrophysical J.* 866, 14. doi:10.3847/1538-4357/aadb41

Roberts, O. W., Li, X., and Li, B. (2013). Kinetic Plasma Turbulence in the Fast Solar Wind Measured by Cluster. *Astrophysical J.* 769, 58. doi:10.1088/0004-637x/769/1/58

Roberts, O. W., Nakamura, R., Torkar, K., Narita, Y., Holmes, J. C., Vörös, Z., et al. (2020). Sub-ion Scale Compressive Turbulence in the Solar Wind: MMS Spacecraft Potential Observations. *Astrophysical J. Suppl. Ser.* 250, 35. doi:10.3847/1538-4365/abb45d

Rosenvinge, T. T. v., Richardson, I. G., Reames, D. V., Cohen, C. M. S., Cummings, A. C., Leske, R. A., et al. (2009). The Solar Energetic Particle Event of 14 December 2006. *Solar Phys.* 256, 443–462. doi:10.1007/s11207-009-9353-6

Rouillard, A. P., Davies, J. A., Lavraud, B., Forsyth, R. J., Savani, N. P., Bewsher, D., et al. (2010). Intermittent Release of Transients in the Slow Solar Wind: 1. Remote Sensing Observations. *J. Geophys. Res. Space Phys.* 115, n/a. doi:10.1029/2009ja014471

Rouillard, A. P., Kouloumvakos, A., Vourlidas, A., Kasper, J., Bale, S., Raouafi, N.-E., et al. (2020). Relating Streamer Flows to Density and Magnetic Structures at the Parker Solar Probe. *Astrophysical J. Suppl. Ser.* 246, 37. doi:10.3847/1538-4365/ab579a

Rouillard, A. P., Lavraud, B., Davies, J. A., Savani, N. P., Burlaga, L. F., Forsyth, R. J., et al. (2010). Intermittent Release of Transients in the Slow Solar Wind: 2. *In Situ* Evidence. *J. Geophys. Res. Space Phys.* 115, n/a. doi:10.1029/2009ja014472

Rouillard, A. P., Savani, N. P., Davies, J. A., Lavraud, B., Forsyth, R. J., Morley, S. K., et al. (2009). A Multispacecraft Analysis of a Small-Scale Transient Entrained by Solar Wind Streams. *Solar Phys.* 256, 307–326. doi:10.1007/s11207-009-9329-6

Šafránková, J., Němeček, Z., Němec, F., Přech, L., Pitňa, A., Chen, C. H. K., et al. (2015). Solar Wind Density Spectra Around the Ion Spectral Break. *Astrophysical J.* 803, 107. doi:10.1088/0004-637x/803/2/107

Sahraoui, F., Goldstein, M. L., Robert, P., and Khotyaintsev, Y. V. (2009). Evidence of a Cascade and Dissipation of Solar-Wind Turbulence at the Electron Gyroscale. *Phys. Rev. Lett.* 102, 231102. doi:10.1103/physrevlett.102.231102

Sako, N., Shimojo, M., Watanabe, T., and Sekii, T. (2013). A Statistical Study of Coronal Active Events in the north Polar Region. *Astrophysical J.* 775, 22. doi:10.1088/0004-637x/775/1/22

Sanchez-Diaz, E., Rouillard, A. P., Davies, J. A., Lavraud, B., Pinto, R. F., and Kilpua, E. (2017). The Temporal and Spatial Scales of Density Structures Released in the Slow Solar Wind during Solar Activity Maximum. *Astrophysical J.* 851, 32. doi:10.3847/1538-4357/aa98e2

Savcheva, A., Cirtain, J., DeLuca, E. E., Lundquist, L. L., Golub, L., Weber, M., et al. (2007). A Study of Polar Jet Parameters Based on Hinode XRT Observations. *Publications Astronomical Soc. Jpn.* 59, S771–S778. doi:10.1093/pasj/59.sp3.s771

Schlenker, M., Antiochos, S., MacNeice, P., and Mason, E. (2021). The Effect of Thermal Non-ewuilibrium on Helmet Streamers. *Astrophysical J.* 916 (2), 115. doi:10.3847/1538-4357/ac069d

Schrijver, C. J., Title, A. M., van Ballegooijen, A. A., Hagenaar, H. J., and Shine, R. A. (1997). Sustaining the Quiet Photospheric Network: The Balance of Flux Emergence, Fragmentation, Merging, and Cancellation. *Astrophysical J.* 487, 424–436. doi:10.1086/304581

Sheeley, N. R., and Rouillard, A. P. (2010). Tracking Streamer Blobs into the Heliosphere. *Astrophysical J.* 715, 300. doi:10.1088/0004-637x/715/1/300

Sheeley, N. R., Walters, J. H., Wang, Y., and Howard, R. A. (1999). Continuous Tracking of Coronal Outflows: Two Kinds of Coronal Mass Ejections. *J. Geophys. Res. Space Phys.* 104, 24739–24767. doi:10.1029/1999ja900308

Sheeley, N. R., Wang, Y.-M., Hawley, S. H., Brueckner, G. E., Dere, K. P., Howard, R. A., et al. (1997). Measurements of Flow Speeds in the corona between 2 and 30 R.. *Astrophysical J.* 484, 472–478. doi:10.1086/304338

Shi, C., Velli, M., Panasenco, O., Tenerani, A., Réville, V., Bale, S. D., et al. (2021). Alfvénic versus Non-alfvénic Turbulence in the Inner Heliosphere as Observed by Parker Solar Probe. *Astron. Astrophysics* 650, A21. doi:10.1051/0004-6361/202039818

Shoda, M., Chandran, B. D. G., and Cranmer, S. R. (2021). Turbulent Generation of Magnetic Switchbacks in the Alfvénic Solar Wind. *Astrophysical J.* 915, 52. doi:10.3847/1538-4357/abfdbc

Simunac, K. D. C., Kistler, L. M., Galvin, A. B., Lee, M. A., Popecki, M. A., Farrugia, C., et al. (2009). *In Situ* Observations of Solar Wind Stream Interface Evolution. *Solar Phys.* 259, 323. doi:10.1007/s11207-009-9393-y

Squire, J., Chandran, B. D. G., and Meyrand, R. (2020). In-situ Switchback Formation in the Expanding Solar Wind. *Astrophysical J.* 891, L2. doi:10.3847/2041-8213/ab74e1

Stansby, D., and Horbury, T. S. (2018). Number Density Structures in the Inner Heliosphere. *Astron. Astrophysics* 613, A62. doi:10.1051/0004-6361/201732567

Stephenson, J. A. E., and Walker, A. D. M. (2002). HF Radar Observations of Pc5 ULF Pulsations Driven by the Solar Wind. *Geophys. Res. Lett.* 29, 8–1–8–4. doi:10.1029/2001gl014291

Sterling, A. C., Moore, R. L., Falconer, D. A., and Adams, M. (2015). Small-scale Filament Eruptions as the Driver of X-ray Jets in Solar Coronal Holes. *Nature* 523, 437–440. doi:10.1038/nature14556

Suess, S. (2001). "Fine Structure in the Corona and Solar Wind at High Heliographic Latitudes at Solar Maximum," in *The 3-D Heliosphere at Solar Maximum, Proceedings of the 34th ESLAB Symposium* (Netherlands: Noordwijk), 55–58. doi:10.1007/978-94-017-3230-7_10

Suess, S. T., Ko, Y., Steiger, R. v., and Moore, R. L. (2009). Quiescent Current Sheets in the Solar Wind and Origins of Slow Wind. *J. Geophys. Res. Space Phys.* 114, n/a. doi:10.1029/2008ja013704

Telloni, D., Sorriso-Valvo, L., Woodham, L. D., Panasenco, O., Velli, M., Carbone, F., et al. (2021). Evolution of Solar Wind Turbulence from 0.1 to 1 au during the First Parker Solar Probe–Solar Orbiter Radial Alignment. *Astrophysical J. Lett.* 912, L21. doi:10.3847/2041-8213/abf7d1

Tenerani, A., Velli, M., Matteini, L., Réville, V., Shi, C., Bale, S. D., et al. (2020). Magnetic Field Kinks and Folds in the Solar Wind. *Astrophysical J. Suppl. Ser.* 246, 32. doi:10.3847/1538-4365/ab53e1

Tessein, J. A., Ruffolo, D., Matthaeus, W. H., Wan, M., Giacalone, J., and Neugebauer, M. (2015). Effect of Coherent Structures on Energetic Particle Intensity in the Solar Wind at 1 AU. *Astrophysical J.* 812, 68. doi:10.1088/0004-637x/812/1/68

Thieme, K., Marsch, E., and Schwenn, R. (1990). Spatial Structures in High-Speed Streams as Signatures of fine Structures in Coronal Holes. *Ann. Geophysicae* 8, 713–723.

Thieme, K., Schwenn, R., and Marsch, E. (1989). Are Structures in High-Speed Streams Signatures of Coronal fine Structures?. *Adv. Space Res.* 9, 127–130. doi:10.1016/0273-1177(89)90105-1

Titov, V. S., Mikić, Z., Linker, J. A., Lionello, R., and Antiochos, S. K. (2011). Magnetic Topology of Coronal Hole Linkages. *Astrophysical J.* 731, 111. doi:10.1088/0004-637x/731/2/111

Treumann, R. A., Baumjohann, W., and Narita, Y. (2019). On the Applicability of Taylor's Hypothesis in Streaming Magnetohydrodynamic Turbulence. *Earth, Planets and Space* 71, 41. doi:10.1186/s40623-019-1021-y

Tsurutani, B. T., Gonzalez, W. D., Gonzalez, A. L. C., Guarnieri, F. L., Gopalswamy, N., Grande, M., et al. (2006). Corotating Solar Wind Streams and Recurrent Geomagnetic Activity: A Review. *J. Geophys. Res. Space Phys.* 111, A07S01. doi:10.1029/2005ja011273

Tsurutani, B. T., and Gonzalez, W. D. (1987). The Cause of High-Intensity Long-Duration Continuous AE Activity (HILDCAAS) - Interplanetary Alfven Wave Trains. *Planet. Space Sci.* 35, 405. doi:10.1016/0032-0633(87)90097-3

Tsurutani, B. T., Ho, C. M., Smith, E. J., Neugebauer, M., Goldstein, B. E., Mok, J. S., et al. (1994). The Relationship between Interplanetary Discontinuities and Alfvén Waves: Ulysses Observations. *Geophys. Res. Lett.* 21, 2267–2270. doi:10.1029/94gl02194

Tu, C. Y., and Marsch, E. (1995). MHD Structures, Waves and Turbulence in the Solar Wind: Observations and Theories. *Space Sci. Rev.* 73, 1–210. doi:10.1007/bf00748891

Turner, D. L., Kilpua, E. K. J., Hietala, H., Claudepierre, S. G., O'Brien, T. P., Fennell, J. F., et al. (2019). The Response of Earth's Electron Radiation Belts to Geomagnetic Storms: Statistics from the Van Allen Probes Era Including Effects from Different Storm Drivers. *J. Geophys. Res. Space Phys.* 124, 1013–1034. doi:10.1029/2018ja026066

Turner, D. L., Shprits, Y., Hartinger, M., and Angelopoulos, V. (2012). Explaining Sudden Losses of Outer Radiation belt Electrons during Geomagnetic Storms. *Nat. Phys.* 8, 208. doi:10.1038/nphys2185

Velli, M., Lionello, R., Linker, J. A., and Mikić, Z. (2011). Coronal Plumes in the Fast Solar Wind. *Astrophysical J.* 736, 32. doi:10.1088/0004-637x/736/1/32

Verscharen, D., Klein, K. G., and Maruca, B. A. (2019). The Multi-Scale Nature of the Solar Wind. *Living Rev. Solar Phys.* 16, 5. doi:10.1007/s41116-019-0021-0

Viall, N. M., and Borovsky, J. E. (2020). Nine Outstanding Questions of Solar Wind Physics. *J. Geophys. Res. Space Phys.* 125, e2018JA026005. doi:10.1029/2018ja026005

Viall, N. M., Kepko, L., and Spence, H. E. (2009). Relative Occurrence Rates and Connection of Discrete Frequency Oscillations in the Solar Wind Density and Dayside Magnetosphere. *J. Geophys. Res. Space Phys.* 114, n/a. (c) 2009: American Geophysical Union. doi:10.1029/2008ja013334

Viall, N., De Moortel, I., Downs, C., Klimchuk, J. A., Parenti, S., and Reale, F. (2021). "The Heating of the Solar Corona," in *Solar Physics and Solar Wind*. Editors N. E. Raouafi, A. Vourlidas, Y. Zhang, and L. J. Paxton, 35–82. doi:10.1002/9781119815600.ch2

Viall, N. M., Spence, H. E., and Kasper, J. (2009). Are Periodic Solar Wind Number Density Structures Formed in the Solar corona?. *Geophys. Res. Lett.* 36, 23102. doi:10.1029/2009gl041191

Viall, N. M., Spence, H. E., Vourlidas, A., and Howard, R. (2010). Examining Periodic Solar-Wind Density Structures Observed in the SECCHI Heliospheric Imagers. *Solar Phys.* 267, 175–202. (c) 2010: Springer Science+Business Media B.V. doi:10.1007/s11207-010-9633-1

Viall, N. M., and Vourlidas, A. (2015). Periodic Density Structures and the Origin of the Slow Solar Wind. *Astrophysical J.* 807, 176. doi:10.1088/0004-637x/807/2/176

Villante, U., Corpo, A. D., and Francia, P. (2013). Geomagnetic and Solar Wind Fluctuations at Discrete Frequencies: A Case Study. *J. Geophys. Res. Space Phys.* 118, 218–231. doi:10.1029/2012ja017971

Villante, U., and Tiberi, P. (2016). Occurrence and Characteristics of Nighttime ULF Waves at Low Latitude: The Results of a Comprehensive Analysis. *J. Geophys. Res. Space Phys.* 121, 4300–4315. doi:10.1002/2015ja022137

Vourlidas, A., and Howard, R. A. (2006). The Proper Treatment of Coronal Mass Ejection Brightness: A New Methodology and Implications for Observations. *Astrophysical J.* 642, 1216–1221. doi:10.1086/501122

Wang, Y.-M., Sheeley, N. R., Socker, D. G., Howard, R. A., and Rich, N. B. (2000). The Dynamical Nature of Coronal Streamers. *J. Geophys. Res. Space Phys.* 105, 25133. doi:10.1029/2000ja000149

Wang, Y. M., Sheeley, N. R., Walters, J. H., Brueckner, G. E., Howard, R. A., Michels, D. J., et al. (1998). Origin of Streamer Material in the Outer Corona. *Astrophysical J.* 498, L165–L168. doi:10.1086/311321

Weberg, M. J., Zurbuchen, T. H., and Lepri, S. T. (2012). ACE/SWICES Observations of Heavy Ion Dropouts within the Solar Wind. *Astrophysical J.* 760, 30. doi:10.1088/0004-637x/760/1/30

Woodham, L. D., Horbury, T. S., Matteini, L., Woolley, T., Laker, R., Bale, S. D., et al. (2020). Enhanced Proton Parallel Temperature inside Patches of Switchbacks in the Inner Heliosphere. *A&A* 650, L1. doi:10.1051/0004-6361/202039415

Wyper, P. F., Antiochos, S. K., and DeVore, C. R. (2017). A Universal Model for Solar Eruptions. *Nature* 544, 452–455. doi:10.1038/nature22050

Yao, S., He, J. S., Tu, C. Y., Wang, L. H., and Marsch, E. (2013). Small-scale Pressure-Balanced Structures Driven by Mirror-Mode Waves in the Solar Wind. *Astrophysical J.* 776, 94. doi:10.1088/0004-637X/776/2/94

Yao, S., He, J. S., Tu, C. Y., Wang, L. H., and Marsch, E. (2013). Small-scale Pressure-Balanced Structures Driven by Oblique Slow Mode Waves Measured in the Solar Wind. *Astrophysical J.* 774, 59. doi:10.1088/0004-637X/774/1/59

Yuan, C. J., and Zong, Q. (2012). Quantitative Aspects of Variations of 1.5–6.0 MeV Electrons in the Outer Radiation belt during Magnetic Storms. *J. Geophys. Res. Space Phys.* 117, n/a. doi:10.1029/2011ja017346

Zheng, J., and Hu, Q. (2018). Observational Evidence for Self-Generation of Small-Scale Magnetic Flux Ropes from Intermittent Solar Wind Turbulence. *Astrophysical J.* 852, L23. doi:10.3847/2041-8213/aaa3d7

Zhou, M., Man, H. Y., Deng, X. H., Pang, Y., Khotyaintsev, Y., Lapenta, G., et al. (2021). Observations of Secondary Magnetic Reconnection in the Turbulent Reconnection Outflow. *Geophys. Res. Lett.* 48, e2020GL091215. doi:10.1029/2020gl091215

Zurbuchen, T. H., Fisk, L. A., Gloeckler, G., and Steiger, R. v. (2002). The Solar Wind Composition throughout the Solar Cycle: A Continuum of Dynamic States. *Geophys. Res. Lett.* 29, 66–1–66–4. doi:10.1029/2001gl013946

Conflict of Interest: The authors declare that the research was conducted in the absence of any commercial or financial relationships that could be construed as a potential conflict of interest.

Advantages of publishing in Frontiers

OPEN ACCESS
Articles are free to read for greatest visibility and readership

FAST PUBLICATION
Around 90 days from submission to decision

HIGH QUALITY PEER-REVIEW
Rigorous, collaborative, and constructive peer-review

TRANSPARENT PEER-REVIEW
Editors and reviewers acknowledged by name on published articles

Frontiers
Avenue du Tribunal-Fédéral 34
1005 Lausanne | Switzerland

Visit us: www.frontiersin.org
Contact us: frontiersin.org/about/contact

REPRODUCIBILITY OF RESEARCH
Support open data and methods to enhance research reproducibility

DIGITAL PUBLISHING
Articles designed for optimal readership across devices

FOLLOW US
@frontiersin

IMPACT METRICS
Advanced article metrics track visibility across digital media

EXTENSIVE PROMOTION
Marketing and promotion of impactful research

LOOP RESEARCH NETWORK
Our network increases your article's readership